

NUMISHEET 2022

Proceedings of the 12th International Conference and Workshop on Numerical Simulation of 3D Sheet Metal Forming Processes

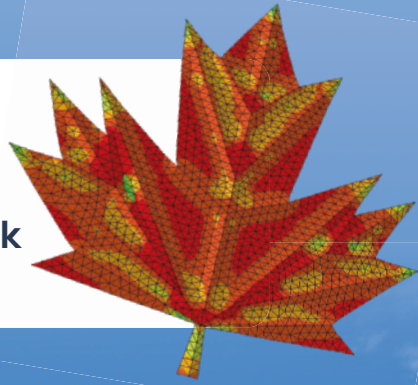
EDITED BY

Kaan Inal

Julie Levesque

Michael Worswick

Cliff Butcher



TMS

 **Springer**

The Minerals, Metals & Materials Series

Kaan Inal · Julie Levesque · Michael Worswick ·
Cliff Butcher
Editors

NUMISHEET 2022

Proceedings of the 12th International
Conference and Workshop on Numerical
Simulation of 3D Sheet Metal Forming
Processes

TMS

 Springer

Editors

Kaan Inal
University of Waterloo
Waterloo, ON, Canada

Julie Levesque
Quebec Metallurgy Center
Montreal, QC, Canada

Michael Worswick
University of Waterloo
Waterloo, ON, Canada

Cliff Butcher
University of Waterloo
Waterloo, ON, Canada

ISSN 2367-1181

ISSN 2367-1696 (electronic)

The Minerals, Metals & Materials Series

ISBN 978-3-031-06211-7

ISBN 978-3-031-06212-4 (eBook)

<https://doi.org/10.1007/978-3-031-06212-4>

© The Minerals, Metals & Materials Society 2022

This work is subject to copyright. All rights are reserved by the Publisher, whether the whole or part of the material is concerned, specifically the rights of translation, reprinting, reuse of illustrations, recitation, broadcasting, reproduction on microfilms or in any other physical way, and transmission or information storage and retrieval, electronic adaptation, computer software, or by similar or dissimilar methodology now known or hereafter developed.

The use of general descriptive names, registered names, trademarks, service marks, etc. in this publication does not imply, even in the absence of a specific statement, that such names are exempt from the relevant protective laws and regulations and therefore free for general use.

The publisher, the authors and the editors are safe to assume that the advice and information in this book are believed to be true and accurate at the date of publication. Neither the publisher nor the authors or the editors give a warranty, expressed or implied, with respect to the material contained herein or for any errors or omissions that may have been made. The publisher remains neutral with regard to jurisdictional claims in published maps and institutional affiliations.

This Springer imprint is published by the registered company Springer Nature Switzerland AG
The registered company address is: Gewerbestrasse 11, 6330 Cham, Switzerland

Contents

Part I Numerical Implementation of Advanced Constitutive Models	
A New Trial Stress for Newton’s Iteration Based on Plastic Strain Rate Potential	3
Seung-Yong Yang and Wei Tong	
Anisotropic Time-Dependent Continuum Damage-Coupled Plasticity Model for Predicting Ductile Fracture of 6xxx Series Aluminum Alloys	15
Mustapha Makki, Georges Ayoub, Andrey Ilinich, and Ghassan Kridli	
Characterization of Impurities in Nanomaterials	25
Kemi Y. Adewale and Mathew O. Aibinu	
Constructing Exact Solutions to Modelling Problems	39
Mathew O. Aibinu, Surendra C. Thakur, and Sibusiso Moyo	
Crystal Plasticity Modelling of Localization in Precipitation Hardened AA6060	49
Y. Larry Li, Christopher P. Kohar, Raja K. Mishra, and Kaan Inal	
Deformation and Fracture in Micro-stamping Process	61
Peng Zhang, Michael P. Pereira, Buddhika Abeyrathna, Bernard F. Rolfe, Daniel E. Wilkosz, Peter Hodgson, and Matthias Weiss	
Die Design for Flashless Forging of a Polymer Insulator Fitting	71
Pedram Khazaie and Sajjad Moein	
DP1180 Material Calibration Between Sheet Metal Simulation and Prototype	81
L. I. U. Rongfeng and L. I. Dayong	
Evolution of the R-value and Its Determination Based on Reverse Fitting for Sheet Metal	91
Jun Zhao, Zhenkai Mu, Qingdang Meng, and Haoran Wang	

Modelling Transient Mechanical Behavior of Aluminum Alloy During Electric-Assisted Forming	105
Jai Tiwari, Hariharan Krishnaswamy, and Murugaiyan Amirthalingam	
Numerical Prediction of Failure in Single Point Incremental Forming Using a New Yield Criterion for Sheet Metal	115
H. Quach, X. Xiao, J. J. Kim, and Y. S. Kim	
Part II Modeling of Sheet Metal Forming: In Memory of Prof. Jean-Claude Gelin	
3D-Swivel-Bending—A Flexible and Scalable Forming Technology	125
Michael Schiller, Peter Frohn-Sörensen, and Bernd Engel	
A Comparative Study of Incremental Sheet Forming Process to Achieve Optimal Accuracy	141
Jaekwang Shin, Dohyun Leem, Newell Moser, Ankush Bansal, Randy Cheng, Kornel Ehmann, Jian Cao, Alan Taub, and Mihaela Banu	
A Virtual Laboratory Based on Full-Field Crystal Plasticity Simulations to Predict the Anisotropic Mechanical Properties of Advanced High Strength Steels	155
Haiming Zhang, Qian Li, Dongkai Xu, and Zhenshan Cui	
Development of a Numerical 3D Model for Analyzing Clinched Joints in Versatile Process Chains	165
C. R. Bielak, M. Böhnke, M. Bobbert, and G. Meschut	
Experimental and Finite Element-Based Analyses of FLCs for AA5052 and AA5083 Alloys	173
Shahin Ahmad, Vilas Tathavadkar, Alankar Alankar, and K. Narasimhan	
Finite Element and Experimental Investigation of Multi-stage Deep Drawing of Stainless Steel 304 Sheets at Elevated Temperature ...	185
Vipin Yadav, Kanhu Nayak, and Prashant Date	
Formability Analysis of Metal–Polymer Sandwich Composites Made of Al and PE Sheets Using Numerical Simulations	197
Tsegaye Bekele, Perumalla Janaki Ramulu, Habtamu Beri, Amrela Siraji, and P. Praveen Kumar Reddy	
Numerical Modeling and Optimization of Fiber Metal Laminates	209
Sheng Sijia and Lang Lihui	
Investigation of the Effect of Blank Holding Force on Earing Defect During Circular Deep Drawing Process Through Finite Element Analysis and Experimentation Using AA6061 and Low-Carbon Steel Sheets	219
Amirela Siraji, Tsegaye Bekele, Perumalla Janaki Ramulu, Habtamu Beri, and P. Venkateswar Reddy	

On the Generalized Plane-Strain Constraints for Orthotropic Plasticity Modeling of Sheet Metals 231
 Jie Sheng, Seung-Yong Yang, and Wei Tong

Springback Investigation of Advanced Path-Dependent Constitutive Models for Sheet Metal Forming 241
 Yanfeng Yang, Hocine Chalal, Cyrille Baudouin, Gabriela Vincze, and Tudor Balan

Stretch-Flanging Behavior of Dual-Phase Steel Using Single-Point Incremental Forming Process 251
 Sandeep Pandre, Ayush Morchhale, Nitin Kotkunde, Kurra Suresh, and Swadesh Kumar Singh

Three-Dimensional Control Point Based Surface Description for Data Reduction, Reverse Engineering and Springback Compensation in Sheet Metal Forming 263
 L. Maier, C. Hartmann, B. Ünver, and W. Volk

Time-Dependent Method for the Inverse Evaluation of Yield Locus Using Nakazima Experiments 275
 K. Barth, B. Berisha, and P. Hora

Part III Mechanics and Materials of Sheet Forming: In Honor of Thomas B. Stoughton

A Novel Testing Methodology for In Situ Microstructural Characterisation During Continuous Strain Path Change 287
 Sisir Dhara, Scott Taylor, Łukasz Figiel, Darren Hughes, Barbara Shollock, and Sumit Hazra

Comparison of Experimental and Finite Element Analysis Results of a Car Body Part with the Optimization of Material Parameters 301
 M. E. Tamer, S. Bortucen, and U. Sahinoglu

Draw Die Development to Maximize Aluminum Formability Potential for Making Styling Featured Outer Panels 309
 Zhi Deng, Anil K. Sachdev, and Raj Dasu

Hydroforming Behaviour of TIG-Welded Tubes of Austenitic Stainless Steel 321
 M. Krishnamraju, Sandeep Sahu, Amarjeet Kumar Singh, and K. Narasimhan

Influence of Kinematic Hardening on Clinch Joining of Dual-Phase Steel HCT590X Sheet Metal 329
 Johannes Friedlein, Julia Mergheim, and Paul Steinmann

Lightweighting Through Stiffening Dart Formation and Its Rigidity Evaluation	345
Dohyun Leem, Lu Huang, Joshua Solomon, Hui-ping Wang, and Jian Cao	
Modeling of the Anisotropic Evolution of Yield Surface Based on Non-associated Flow Rule	355
Namsu Park, Gihyun Bae, Jung Han Song, Jong Sup Lee, Thomas B. Stoughton, and Jeong Whan Yoon	
On Strain Hardening Modeling in Associated and Non-Associated Orthotropic Plasticity	365
Jie Sheng, Mohammed Alharbi, Seung-Yong Yang, and Wei Tong	
Prediction of Ductile Fracture in Bainitic Steel with Dependence on Stress States and Loading Orientation	375
Fuhui Shen, Sebastian Münstermann, and Junhe Lian	
Shape Optimization of a Cruciform-Like Specimen for Combined Tension and Shear Loading	389
Minki Kim, Jinjin Ha, and Yannis P. Korkolis	
Part IV Machine Learning and Big Data	
Data-Based Prediction Model for an Efficient Matching Process in the Body Shop	401
Arndt Birkert, Johannes Weber, Moritz Nowack, Christian Schwarz, Benjamin Hartmann, and Philipp Zimmermann	
Deep Learning-Based Defect Inspection in Sheet Metal Stamping Parts	411
Aru Ranjan Singh, Thomas Bashford-Rogers, Sumit Hazra, and Kurt Debattista	
Part V Multiscale Modeling of Deformation and Fracture Behavior of Metallic Materials	
Analysis of Damage and Fracture Mechanisms in Steel Sheets: Biaxial Experiments and Numerical Simulations	423
Michael Brünig, Moritz Zistl, and Steffen Gerke	
Damage Evolution in DP600 Sheets Using a Combined Finite Element—Cellular Automata Model	433
Iman Sari Sarraf, Daniel E. Green, Yang Song, and Javad Samei	
Deformation and Failure Behavior of Steel Under High Strain Rate and Multiaxial Loading	445
Chongyang Zeng and Xiangfan Fang	

Forming–Structural–Coupled Analysis: The Method to Predict Die Deformation Using Quick Simulations 457
 K. H. Yun, S. H. Jun, M. S. Moon, J. S. Kim, and H. S. Kim

Investigating the Formability and Failure Mechanism of an Advanced High Strength Steel by a Microstructure-Based Hierarchy Modeling Approach 471
 Haiming Zhang, Shuai Luo, Jiaru Liu, and Zhenshan Cui

Investigation on the High Strain Rate Formability of Al-Cu-Mg Alloy by Solid–Liquid Coupling Simulation 483
 Shi-Hong Zhang and Da-Yong Chen

Neutron Diffraction and Crystal Plasticity Analysis on Q&P Steel in Deformation 491
 Hao Yang, Dayong Li, Huamiao Wang, Yinghong Peng, and Peidong Wu

Predicting the Flow and Failure Properties of Dual-Phase Steel Using Phenomenological Models 499
 Arshdeepsingh Sardar, Amin L. Vanjani, A. Bardelcik, and C. H. M. Simha

Part VI Modelling of Thermo-Mechanical Sheet Forming

Development of a Hot Cutting Process for Functional Parts by Stress State-Dependent Damage Modeling 511
 C. Löbbe, J. Martschin, D. Putschkat, H. Sulaiman, A. Jäger, and A. E. Tekkaya

Impact of Thermal Conditions on Predicted Formability of TRIP Steels 523
 Daniel S. Connolly, Christopher P. Kohar, Raja K. Mishra, and Kaan Inal

Local Heat Treatment for Springback Reduction in Deep Drawing of Advanced High-Strength Steel 539
 Josef Domitner, Vladimir Boskovic, Iris Baumgartner, Florian Grünbart, Christof Sommitsch, and Mustafa Kičin

Strain and Stress-Based Forming Limit Diagrams for Inconel 718 Alloy 549
 Gauri Mahalle, Prathamesh Takalkar, Nitin Kotkunde, Amit Kumar Gupta, and Swadesh Kumar Singh

Validation of Comprehensive Material and Friction Models for Simulation of Thermo-Mechanical Forming of High-Strength Aluminium Alloys Using HFQ Technology 557
 Damian Szegda, Mohamed Mohamed, Yogendra Joshi, and Mustapha Ziane

Part VII Modelling of Failure

Development of a Modified Punch Test for Investigating the Failure Behavior in Sheet Metal Materials	575
M. Böhnke, Ch.R. Bielak, M. Bobbert, and G. Meschut	
Effect of Width/Thickness Effect of Sheet Metals on Bendability	585
M. M. Shahzamanian, D. J. Lloyd, and P. D. Wu	
Investigation of a Pre-strain-Specific Edge Crack Sensitivity Factor and Its Implementation in FEM	595
Alexander Kindsmueller, Roman Norz, Niko Manopulo, and Wolfram Volk	
Prediction of Deformation and Failure Anisotropy for Magnesium Sheets Under Mixed-Mode Loading	607
Dirk Steglich and Jacques Besson	
Prediction of Necking Initiation in Case of Abrupt Changes in the Loading Direction	617
R. Norz, N. Manopulo, M. Sigvant, A. R. Chezan, and W. Volk	
Strain Rate-Dependent Hardening Behavior of Weld Metal in Laser Welded Blanks with GEN3 AHSS	627
Minki Kim, Jiahui Gu, and Hyunok Kim	
The Importance of the Choice of the Yield Criterion in Triaxiality Evaluation for Highly Anisotropic Zirlo Sheets	635
Felix Rickhey and Seokmoo Hong	

Part VIII Modelling of Friction

A Numerical Study of Local Elastic Tool Deformation in Sheet Metal Forming Simulation	645
Mats Larsson and Daniel Wiklund	
Analysis and Evaluation of the Clamping Force on the Tool Surface During the Blanking Process	655
Philipp Schumann, Daniel M. Martin, Christian Kubik, Timo Schneider, and Peter Groche	
Evaluating Lubricants for Warm Forming of Aluminum 6xxx Alloys	671
Tom Feister, Laura Zoller, Mehdi Shafiei, Paul Bosler, and Hyunok Kim	
Implementation of Real Contact Areas Into Sheet Metal Forming Simulations Using Digital Spotting Images	679
P. Essig, M. Liewald, C. Bolay, and J. Hol	

Optimization of Slip Conditions in Roll Forming by Numerical Simulation 693
 Marco Becker and Peter Groche

Surface Texture Design for Sheet Metal Forming Applications 703
 Meghshyam Shisode, Ton van den Boogaard, and Javad Hazrati

Part IX Challenges and Opportunities in Forming Aluminum

Effect of Thermal Treatment on Deep Drawability of AA3xxx Alloy 715
 Vivek Srivastava, Sumit Gahlyan, Manali Khandelwal, and Akshay Deshpande

Sensitivity Study of Plastic Anisotropy on Failure Prediction in Hole-Expansion 727
 Jinjin Ha and Yannis P. Korkolis

Dynamic Deformation Behaviour of Al-Li Alloys Under High Strain Rate Deformation 733
 Ali Abd El-Aty, Yong Xu, Shi-Hong Zhang, Ma Yan, Xunzhong Guo, Jie Tao, Yong Hou, and Myoung-Gyu Lee

Research on Electric Current-Assisted Draw Bending of AA7075-T6 Sheet 747
 Hongrui Dong, Xiaoqiang Li, Dongsheng Li, Luyi Dou, Haibo Wang, Yanfeng Yang, and Xuebin Zheng

Part X Other Topics

Numerical Modeling for Progressive Crushing of Composite and Hybrid Metal—Composite Structures 757
 Saarvesh Jayakumar, Lorenz Stolz, Sharath Anand, Amir Hajdarevic, and Xiangfan Fang

A New Sample for Oscillation-Free Force Measurement at High Strain Rates and Its Physical Principles 773
 Xiangfan Fang

A Novel Benchmark Test for Validating the Modelling and Simulation Methodology of Modern Gas-Based Hot Sheet Metal Forming Processes 785
 Naveen Krishna Baru, Tobias Teeuwen, David Bailly, and Gerhard Hirt

Analysis on Deformation Behavior of High-Strength Steel Using the Finite Element Method in Conjunction with Constitutive Model Considering the Elongation at Yield Point 803
 S. C. Yoon, K. J. Kim, G. H. Yim, J. S. Hyun, and Y. D. Chung

Automatic Extraction and Conversion of the Bending Line from Parametric and Discrete Data for the Free-Form Bending Process 813
Lorenzo Scandola, Daniel Maier, Matthias Konrad Werner, Christoph Hartmann, and Wolfram Volk

Characterization of Cohesive Zone Model Properties of Laminated Metal Sheet with a Thin Adhesive Layer 827
Hyeonil Park, Se-Jong Kim, Jinwoo Lee, and Daeyong Kim

Clinching in In Situ CT—A Novel Validation Method for Mechanical Joining Processes 833
Daniel Köhler, Robert Kupfer, Juliane Troschitz, and Maik Gude

Design Guideline of the Bolt Hole Based on the Parametric Formability Analysis 841
Inje Jang, Gihyun Bae, Junghan Song, Namsu Park, Jongsup Lee, Sehwan Jeong, and Heejong Lee

Experimental and Numerical Evaluation of DP600 Fracture Limits 849
Yang Song, Iman Sari Sarraf, and Daniel E. Green

FE Simulations About the Influence of Work Hardening Derived from Embossing Process on Hole-Expansion of Duplex Embossed Sheet 861
You Yu, Wuyang Liu, and Takashi Iizuka

Identification and Validation of Brass Material Parameters Using Single Point Incremental Forming 873
Ehssen Betaieb, Laurent Duchêne, and Anne Marie Habraken

Improvement of the Strength of an Aluminum Liner by Beading Under Consideration of Internal Pressure and Low Temperatures 885
A. Reimer, C. Hartmann, R. Norz, P. Sturm, and W. Volk

Influence of Loading Direction on the Mechanical Parameters of Pre-formed Materials in Tensile Test 899
R. Norz and W. Volk

Microstructure Modelling of the HEC Behaviour of a Novel Vanadium DP980 Cold Rolled Alloy 909
Bruce Williams, Khaled Abu-Samk, Jia Xue, Babak Shalchi Amirkhiz, and Colin Scott

Numerical Description of the Physical Properties of Stretch Web Connectors in Progressive Die Stamping 921
Florian Steinlehner, Annika Weinschenk, Sven Kolb, Stefan Laumann, and Wolfram Volk

Numerically Coupled Tools for Double-Sided Incremental Sheet Forming 937
Vincent Raymond and Jean Savoie

Overcoming Major Obstacles of Springback Compensation by Nonlinear Optimization 949
Luca Hornung, Sebastian Denz, and Vojtech Cvrcek

Sheet Metal Forming Simulation System Strongly Coupled with Die Tool Deformation 963
Masahi Arai and Naoki Ichijo

Author Index 975

Subject Index 979

Part I
Numerical Implementation of Advanced
Constitutive Models

A New Trial Stress for Newton's Iteration Based on Plastic Strain Rate Potential



Seung-Yong Yang and Wei Tong

Abstract It is known that Newton's iteration can be divergent for highly anisotropic yield functions with a large strain increment in finite element analysis of plastic deformation. One of the reasons of the divergence is inaccurate estimation of the initial stress by elastic trial stress. The line search strategy cannot completely remove the problem. A new method to predict the trial stress by plastic strain rate potential was proposed in this work. The new method was applied to Hill's quadratic yield function and Hershey-Hosford yield function. It was shown that the number of iterations can be reduced significantly for plane stress biaxial loading, and computation time can be saved for 3-dimensional finite element simulation.

Keywords Newton iteration · Plasticity potentials · Trial stress

Introduction

Finite element analysis of plastic deformation requires constitutive update of the stress and plastic strain of the material along the loading path, and the new state of the structure will be found by solving a system of equations for the nodal displacements in the main program. The constitutive equations of plastic materials are nonlinear, and a numerical solution of the equations for the stress and plastic strain needs an iterative process in the material routine. Newton's method is widely used for the iterative solution procedure.

If the material exhibits highly anisotropic behavior in the plastic deformation and the load increment is large, Newton's iteration can diverge and more sophisticated methods are necessary to obtain a converged solution. It was reported that Newton's iteration can be divergent for a highly anisotropic yield function or a higher value of

S.-Y. Yang (✉)

Korea University of Technology and Education, Chungnam 31253, Korea
e-mail: ysy@koreatech.ac.kr

W. Tong

Southern Methodist University, Dallas, TX 75275, USA
e-mail: wtong@smu.edu

© The Minerals, Metals & Materials Society 2022

K. Inal et al. (eds.), *NUMISHEET 2022*, The Minerals, Metals & Materials Series,
https://doi.org/10.1007/978-3-031-06212-4_1

the exponent in the Hershey-Hosford yield when a large strain increment is imposed [1]. Line search method was proposed to resolve this issue and enhance the convergence property of the Newton method [1, 2]. In these methods, they assumed an elastic trial stress with vanishing plastic strain increment, and then the line search method was applied to choose an appropriate plastic strain increment to reduce error in the iteration. However, the line search method cannot provide a complete solution to the problem, and the iteration still can be divergent. One of the main reasons for the problem seems that the elastic trial stress is overwhelmingly large when the strain increment is large. Manik [3] proposed a radial return method to improve the convergence of Newton iteration and saved computation time for Hill's quadratic and Yld2004-18p yield functions.

In this paper, a plastic trial stress was proposed to replace the conventional elastic trial stress for the Newton iteration. The new trial stress is based on dual plastic strain rate potential which is a function of plastic strain rate and dual to the yield function. If a plastic strain rate is assumed approximately, then a stress state on the yield surface can be obtain by using the orthogonality condition to the dual plastic strain rate potential and the stress will be closer to the actual stress than the elastic prediction. This yield stress was used as the initial trial stress for the Newton iteration. The effectiveness of the new plastic trial stress in the iterative procedure and finite element analysis was presented in comparison to the conventional elastic trial stress. A review of Newton's method and the proposal of the plastic trial stress will be presented in the framework of the associated flow rule in next sections, and the plastic strain rate potentials for Hill's quadratic yield function and Hershey-Hosford yield function will be described in the following section. The proposed algorithm was implemented in ABAQUS user material subroutine (UMAT) and its numerical superiority will be displayed in comparison for simple biaxial loadings and a general 3-D loading.

Newton's Method and Plastic Trial Stress

Newton Iteration

Stress-based yield potentials are useful in elasto-plastic deformation analyses. Newton's iteration based on the yield function $f(\boldsymbol{\sigma})$ will be described in this section. That is, the yield condition will be applied and the plastic strain increment should satisfy the normality rule to the yield surface. Suppose we are given a stress and equivalent plastic strain at the current time t and a strain increment $\Delta\boldsymbol{\epsilon}$ for the next time $t + \Delta t$. If the corresponding yield function to the elastic trial stress is large enough to satisfy the current yield condition, the material will undergo plastic deformation. Then the new yield condition and the normality rule should be satisfied at the new time $t + \Delta t$, i.e.,

$$r = f(\boldsymbol{\sigma}(t) + \Delta\boldsymbol{\sigma}) - \sigma_f(\bar{\epsilon}^P(t) + \Delta\bar{\epsilon}^P) = 0 \quad (1)$$

$$\mathbf{R} = (\Delta\boldsymbol{\epsilon} - \mathbf{C}^{-1}\Delta\boldsymbol{\sigma}) - \Delta\bar{\epsilon}^P \frac{\partial f}{\partial \boldsymbol{\sigma}}(\boldsymbol{\sigma}(t) + \Delta\boldsymbol{\sigma}) = \mathbf{0} \quad (2)$$

where $\Delta\bar{\epsilon}^P$ is the increment of the equivalent plastic strain during Δt . The small deformation assumption was used, so that the total strain increment is the sum of the elastic and plastic parts in Eq. (2). The flow potential is the same as the yield function in the associated plasticity. The solution of the above two equations are $\Delta\bar{\epsilon}^P$ and $\Delta\boldsymbol{\sigma}$. If a trial value is assumed for $\Delta\bar{\epsilon}^P$ in Eq. (2) and the Taylor expansion is considered, then Eq. (2) will give $\Delta\boldsymbol{\sigma}$. These trial $\Delta\bar{\epsilon}^P$ and $\Delta\boldsymbol{\sigma}$ are substituted in Eq. (1) to check whether the equation is satisfied. If not, some modification on the assumed $\Delta\bar{\epsilon}^P$ is made until the yield condition is satisfied. This procedure can be formulated in the framework of Newton's method to give a systematic modification on the increments of the equivalent plastic strain and stress. That is, the following variations can be derived.

$$\delta\Delta\bar{\epsilon}^P = \frac{r + \mathbf{n} : \mathbf{L}\mathbf{R}}{\mathbf{n} : \mathbf{L}\mathbf{n} + h} \quad (3)$$

$$\delta\Delta\boldsymbol{\sigma} = \mathbf{L}(\mathbf{R} - \delta\Delta\bar{\epsilon}^P\mathbf{n}) \quad (4)$$

where r and \mathbf{R} are the current residuals and \mathbf{n} , \mathbf{L} and h are defined in Eqs. (5)–(7). Modified new increments are to be given by the sum of the old increments and the variations of (3) and (4).

$$\Delta\bar{\epsilon}^P(\text{new}) = \Delta\bar{\epsilon}^P(\text{old}) + \delta\Delta\bar{\epsilon}^P$$

$$\Delta\boldsymbol{\sigma}(\text{new}) = \Delta\boldsymbol{\sigma}(\text{old}) + \delta\Delta\boldsymbol{\sigma}.$$

Newton's iteration will continue until these $\Delta\bar{\epsilon}^P(\text{new})$ and $\Delta\boldsymbol{\sigma}(\text{new})$ satisfy Eqs. (1) and (2) with enough accuracy (that is, the residuals r and \mathbf{R} are small enough). The following variables need to be updated during the iteration.

$$\mathbf{n} = \frac{\partial}{\partial \boldsymbol{\sigma}} f(\boldsymbol{\sigma}(t) + \Delta\boldsymbol{\sigma}) \quad (5)$$

$$h = \frac{\partial}{\partial \Delta\bar{\epsilon}^P} \sigma_f(\bar{\epsilon}^P + \Delta\bar{\epsilon}^P) \quad (6)$$

$$\mathbf{L} = \left(\mathbf{C}^{-1} + \Delta\bar{\epsilon}^P \frac{\partial^2}{\partial \boldsymbol{\sigma}^2} f(\boldsymbol{\sigma}(t) + \Delta\boldsymbol{\sigma}) \right)^{-1} \quad (7)$$

To initiate Newton's iteration described above, $\Delta\bar{\epsilon}^P$ and $\Delta\boldsymbol{\sigma}$ need to be assumed first. The number of iterations will depend on how much accurately the initial guesses were made close to the true solution. This entails the concept of the plastic trial stress described in the next section.

Plastic Trial Stress

In conventional numerical procedure for plasticity, the elastic trial stress is assumed by $\Delta\boldsymbol{\sigma} = \mathbf{C}\Delta\boldsymbol{\epsilon}$ and vanishing plastic strain increment ($\Delta\bar{\boldsymbol{\epsilon}}^p = 0$) is used as the initial value for Newton's iteration. These trial values seem straightforward, but they can be inaccurate if the strain increment is large, and many iterations can be caused or the iteration can be divergent for highly anisotropic materials. To obtain better trial increments, plastic stress which is based on the plastic strain rate potential will be considered as the new trial stress in place of the elastic trial stress.

Yield stress state can be given by the orthogonality condition to the plastic strain rate in the theory of dual plastic potentials [4].

$$\boldsymbol{\sigma}(t + \Delta t) = \nu \frac{\partial}{\partial \Delta\boldsymbol{\epsilon}^p} q(\Delta\boldsymbol{\epsilon}^p) \quad (8)$$

where the parameter ν is equal to the yield strength along the rolling direction, $\nu = \sigma_f(\bar{\boldsymbol{\epsilon}}^p(t) + \Delta\bar{\boldsymbol{\epsilon}}^p)$ in the associated plasticity. There can be many possible options for the plastic strain increment $\Delta\boldsymbol{\epsilon}^p$ and $\Delta\bar{\boldsymbol{\epsilon}}^p$. One simple way is to assume $\Delta\boldsymbol{\epsilon}^p = \Delta\boldsymbol{\epsilon}$ and $\Delta\bar{\boldsymbol{\epsilon}}^p = q(\Delta\boldsymbol{\epsilon}^p)$. These assumptions can define a plastic trial stress by Eq.(8). Another more sophisticated approach is to take only a fraction of the full strain increment for the plastic strain increment in reference to Manik's paper [3]. He proposed a radial projection of the elastically predicted stress $\boldsymbol{\sigma}^{tr}$ on the current yield surface as

$$f((1 - \alpha_y)\boldsymbol{\sigma}^{tr}) = \sigma_f(\bar{\boldsymbol{\epsilon}}^p(t))$$

where $\alpha_y \in [0, 1]$ is the solution of the above equation. Then $(1 - \alpha_y)\boldsymbol{\epsilon}$ will be the corresponding total elastic strain, and the remaining $\alpha_y\boldsymbol{\epsilon}$ will be the plastic strain increment. Hence $\Delta\boldsymbol{\epsilon}^p = \alpha_y\boldsymbol{\epsilon}$ was chosen as the trial plastic strain increment to define the equivalent plastic strain increment and equivalent stress as follows

$$\begin{aligned} \Delta\bar{\boldsymbol{\epsilon}}^p &= q(\alpha_y\boldsymbol{\epsilon}) \\ \bar{\boldsymbol{\sigma}} &= \sigma_f(\bar{\boldsymbol{\epsilon}}^p(t) + \Delta\bar{\boldsymbol{\epsilon}}^p) \end{aligned}$$

These equations will be combined with Eq. (8) to give the plastic trial stress. Then $\Delta\bar{\boldsymbol{\epsilon}}^p$ and $\boldsymbol{\sigma}(t + \Delta t)$ will be used as the initial guess of the plastic strain increment and stress, and Newton's iteration will continue until an accurate enough numerical solution is obtained. The error of the iteration is defined based on the scalar and tensor residuals r and \mathbf{R} as

$$E = \left(\frac{r}{2\mu}\right)^2 + \mathbf{R} : \mathbf{R} \quad (9)$$

where μ is the shear modulus. If the error is small enough during the iteration, for example $E < 10^{-10}$, then the approximate solution was regarded as being close enough to the true solution, and the iteration is terminated.

Yield Functions and Their Plastic Strain Rate Potentials

Hill's Quadratic Yield Function

Hill's quadratic yield function $f(\boldsymbol{\sigma})$ is defined by [5]

$$\begin{aligned} 2f^2(\boldsymbol{\sigma}) &= F(\sigma_{yy} - \sigma_{zz})^2 + G(\sigma_{zz} - \sigma_{xx})^2 + H(\sigma_{xx} - \sigma_{yy})^2 \\ &\quad + 2L\tau_{yz}^2 + 2M\tau_{zx}^2 + 2N\tau_{xy}^2 \\ &= 2A_1(\sigma_{xx} - \sigma_{zz})^2 + 2A_2(\sigma_{xx} - \sigma_{zz})(\sigma_{yy} - \sigma_{zz}) \\ &\quad + 2A_3(\sigma_{yy} - \sigma_{zz})^2 + 2A_4\tau_{xy}^2 + 2A_5\tau_{yz}^2 + 2A_6\tau_{zx}^2 \end{aligned} \quad (10)$$

where the following identities hold.

$$\begin{aligned} 2A_1 &= G + H, \quad 2A_2 = -2H, \quad 2A_3 = F + H, \\ A_4 &= N, \quad A_5 = L, \quad A_6 = M \end{aligned}$$

The dual plastic strain rate function is assumed in the similar form as

$$q^2(\dot{\boldsymbol{\epsilon}}^p) = B_1(\dot{\epsilon}_x^p)^2 + B_2\dot{\epsilon}_x^p\dot{\epsilon}_y^p + B_3(\dot{\epsilon}_y^p)^2 + B_4(\dot{\gamma}_{xy}^p)^2 + B_5(\dot{\gamma}_{yz}^p)^2 + B_6(\dot{\gamma}_{zx}^p)^2 \quad (11)$$

Under these assumptions, relations between the yield function and the dual plastic strain rate potential can be derived analytically. That it, one can use the property that the plastic strain rates should have the same value of the equivalent plastic strain rate, $q(\dot{\boldsymbol{\epsilon}}^p(\boldsymbol{\sigma})) = \dot{\bar{\epsilon}}^p$, whereas the stresses are on a given yield surface. The following relations should hold between A_i and B_i .

$$\begin{aligned} B_1 &= \frac{4A_3}{4A_1A_3 - A_2^2}, \quad B_2 = -\frac{4A_2}{4A_1A_3 - A_2^2} \\ B_3 &= \frac{4A_1}{4A_1A_3 - A_2^2}, \quad B_4 = \frac{1}{A_4}, \quad B_5 = \frac{1}{A_5}, \quad B_6 = \frac{1}{A_6} \end{aligned}$$

Hershey-Hosford Yield Function

Hershey-Hosford yield function is a non-quadratic isotropic yield function. It generalizes von Mises yield function and approaches to Tresca model as the exponent

increases. Hence the flow direction can vary rapidly at the corners of the yield locus for a big exponent a .

$$f^a(\boldsymbol{\sigma}) = \frac{|\sigma_1 - \sigma_2|^a + |\sigma_2 - \sigma_3|^a + |\sigma_3 - \sigma_1|^a}{2} \quad (12)$$

where σ_i are the principal stresses. For the exact dual potential cannot be derived analytically, the following approximate dual plastic strain rate potential was assumed.

$$q^b(\dot{\boldsymbol{\epsilon}}^p) = \frac{|\dot{\epsilon}_1^p|^b + |\dot{\epsilon}_2^p|^b + |\dot{\epsilon}_3^p|^b}{1 + 2^{1-b}} = \frac{|\dot{\epsilon}_1^p|^b + |\dot{\epsilon}_2^p|^b + |\dot{\epsilon}_1^p + \dot{\epsilon}_2^p|^b}{1 + 2^{1-b}} \quad (13)$$

The value of b can be obtained by the least square method to minimize the deviation from a set of discrete plastic strain rates computed from the yield function [6]. For example, one can obtain $b = 1.51523$ for $a = 6$, and $b = 1.34194$ for $a = 8$.

Numerical Results

To test the convergence behavior of Newton's method, Hill's quadratic yield function and Hershey-Hosford yield function were considered. In this section, we will make use of numerical tests similar to Scherzinger's in [1] to show the superiority of the proposed plastic trial stress for the convergence of Newton's iteration.

The material parameters of Hill's quadratic yield function were given as

$$\begin{aligned} A_1 &= 1.0, & A_2 &= -1.0513, & A_3 &= 1.0908, \\ A_4 &= A_5 = A_6 &= 2.9926. \end{aligned}$$

The quadratic yield function in Eq. (10) with these parameters characterizes AA6111-T4 sheet metal [7]. The exponent $a = 8$ was used for the Hershey-Hosford yield function in Eq. (12). The Swift power law was used for the hardening as

$$\sigma_f(\bar{\epsilon}^p) = 462.79 (0.007961 + \bar{\epsilon}^p)^{0.2} \text{ MPa}$$

Young's modulus is 69 GPa and Poisson's ratio is 0.3.

First, the on-axis plane stress biaxial loading condition was considered to find how many iterations are needed to achieve convergence for the elastic trial stress and plastic trial stress, respectively. The stress state and the plastic strain were assumed zero at time $t = 0$, and a large enough strain increment was applied during time step Δt so that the yield condition is satisfied and the plastic deformation occurs. Procedures in reference [8] was used to impose the plane stress condition on the material technically. The applied plane stress condition can be represented as a point on the biaxial stress plane when the shear stress vanishes. 3200 trial cases which are beyond the initial yield locus and less than 40 times the initial yield stress σ_0 along the

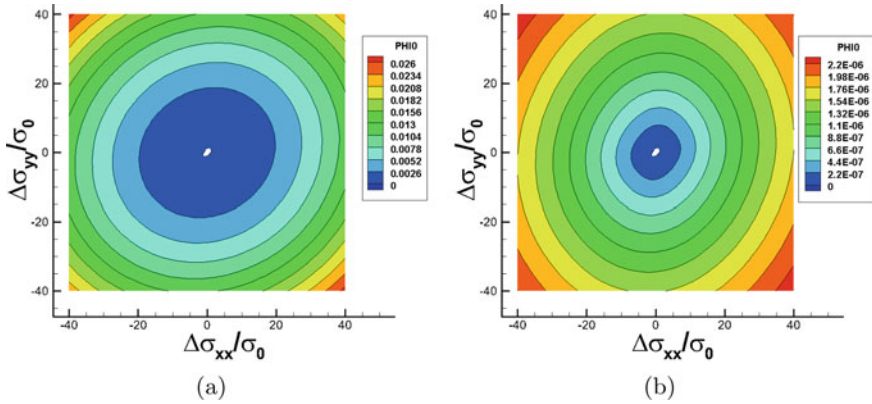


Fig. 1 Error in Eq. (9) by the trial state in the case of **a** elastic trial stress, and **b** plastic trial stress. (Hill's YLD)

rolling direction were examined to test the convergence behavior. The initial residual error in Eq. (9) caused by the trial state before the initiation of the Newton iteration was plotted in Fig. 1a, b for the elastic and plastic trial stresses, respectively, and the number of iterations was plotted for the corresponding trial stresses as shown in Fig. 2. The horizontal axis is the elastic trial stress increment $\Delta\sigma_{xx}$ normalized by the initial yield stress σ_0 , and the vertical axis is $\Delta\sigma_{yy}$ normalized by σ_0 . The normalized elastic stresses were used to represent the strain increments. The initial error is quite large for the elastic trial stress compared to that of the plastic trial stress as shown in Fig. 1. The number of iterations increased as the elastic trial stress is used even though the line search method was used. Meanwhile, the iteration converged in 1 or 2 iterations without the line search strategy, if the plastic trial stress was used as presented in Fig. 2b. Similar behavior was observed for the Hershey-Hosford model as shown in Figs. 3 and 4. If the elastic trial stress was used then the initial error was huge and the iteration diverged for large loading increments as shown in Fig. 4a (if the number of iterations is greater than 20, then the iteration was regarded as being divergent) although the line search method was applied. Newton's iteration with the plastic trial stress converged very quickly as exhibited in Fig. 4b. These results prove the excellent convergence property of the plastic trial stress.

While it has been shown that the plastic trial stress requires much less iterations for the convergence in the on-axis plane stress biaxial loading, it is necessary to examine if the plastic trial stress actually can reduce the computation time in finite element simulation. ABAQUS/Standard FEA analysis was utilized to compare the computation times for a tensile specimen shown in Fig. 5 which was used by Manik [3]. The specimen has notches and some thickness, so that more general stress conditions can be imposed on the material points. Tensile displacement boundary condition was applied at the end of the specimen along the rolling direction. The constitutive equations were implemented in ABAQUS UMAT subroutine. It is known that the time increment should be reduced to achieve a converged solution in FEA, if the mate-

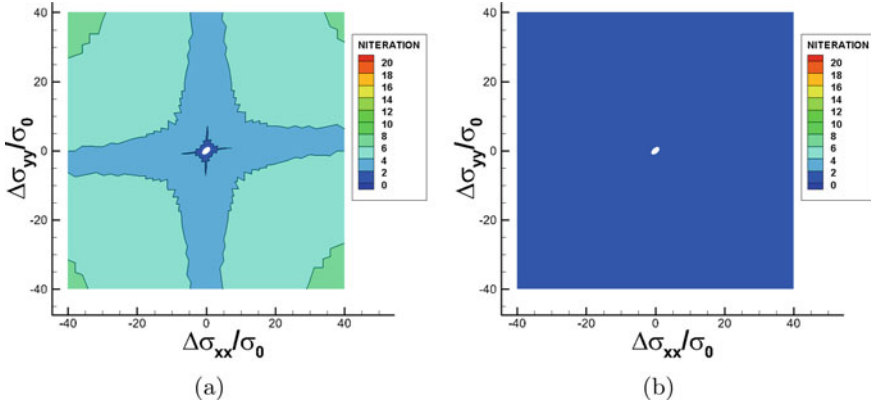


Fig. 2 The number of iterations for the convergence in the case of **a** elastic trial stress, and **b** plastic trial stress. (Hill’s YLD)

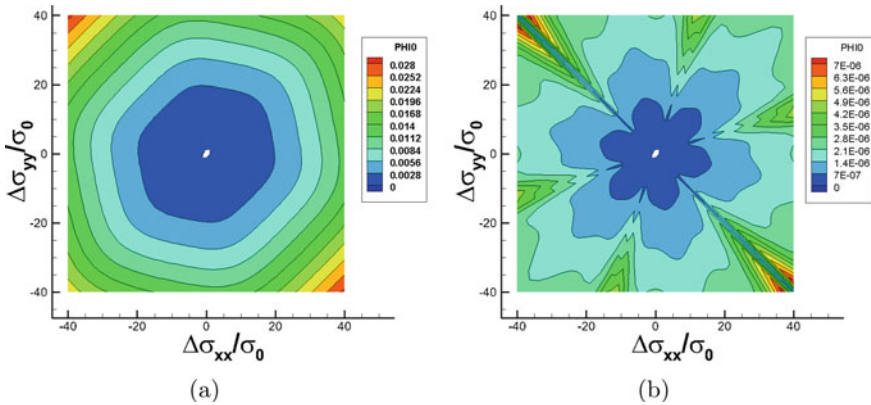


Fig. 3 Error in Eq. (9) by the trial state in the case of **a** elastic trial stress, and **b** plastic trial stress. (Hershey-Hosford YLD with $a = 8$ and $b = 1.34194$)

rial’s behavior deviates significantly from the isotropic von Mises plasticity. There are two-time increment options in ABAQUS/Standard, i.e., fixed and automatic. If the time increment is small enough, then the computations have converged for both elastic trial stress and plastic trial stress and the computation times were almost the same. But the time increment is large, then the time increment was automatically controlled and reduced to obtain a converged solution by the ABAQUS main solver. It was observed that the elastic trial stress required a smaller time step for convergence, and more computation time was spent to complete the job as shown in Table 1 for Hill’s yield function. The total tensile strain was about 0.06 in the gage section of the specimen. The typical strain increment in the gage section was about 0.0001 for the elastic trial stress, which is smaller than 0.00018 for the plastic trial stress. These strain increments turned out to be much smaller than strain increments for conver-

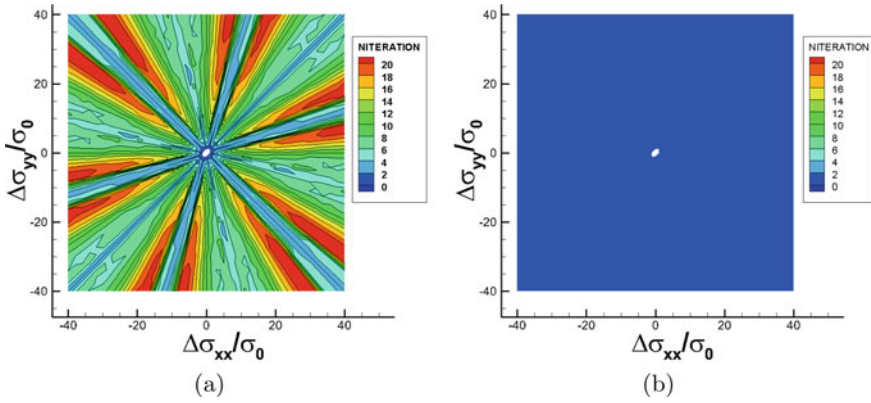


Fig. 4 The number of iterations for the convergence in the case of **a** elastic trial stress, and **b** plastic trial stress. (Hershey-Hosford YLD with $a = 8$ and $b = 1.34194$)

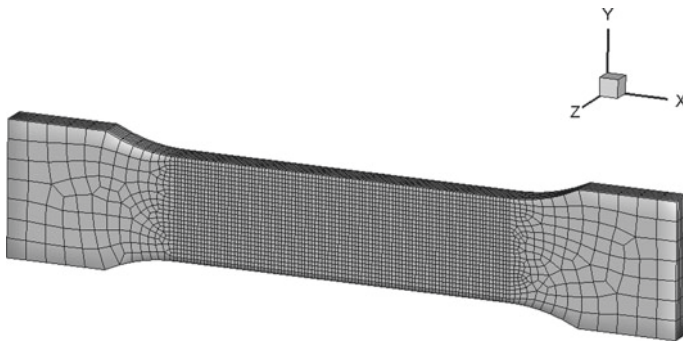


Fig. 5 Tensile specimen [3]

gence in the simple on-axis biaxial loading conditions $\Delta\sigma/\mu$ shown in Figs. 2 and 4. Complicated loading condition in the 3-dimensional specimen seems to restrict the strain increment to the smaller values. ABAQUS intrinsic material library provides Hill's quadratic anisotropic yield function, and the total computation time was more or less similar to the time used in the case of the plastic trial stress, which is significantly less than the time of the elastic trial stress. The line search method was not implemented for the case of the plastic trial stress. If the convergence norm is reduced, then the elastic trial stress and the plastic trial stress required a similar time increment and the total computation times were about the same. ABAQUS does not provide Hershey-Hosford material model, so comparison was made only between the elastic and plastic trial stresses in terms of UMAT as shown in Table 2. The strain increment was about 6×10^{-5} for the elastic trial stress, and the strain increment was 1.4×10^{-4} for the plastic trial stress. Computation time was saved significantly by the usage of the plastic trial stress in Hershey-Hosford model as well.

Table 1 Comparison of computation times of ABAQUS Hill's model and UMATs

Hill	CPU time (s)
ABAQUS Intrinsic material	291.9
Elastic trial stress (UMAT)	652.0
Plastic trial stress (UMAT)	285.0

Table 2 Comparison of computation times of Hershey-Hosford model by UMATs

H-H	CPU time (s)
Elastic trial stress (UMAT)	1508.1
Plastic trial stress (UMAT)	487.8

Discussion and Conclusions

The concept of plastic trial stress was applied to develop an efficient trial stress in Newton's iteration. Hill's quadratic yield and Hershey-Hosford yield were considered for the application and evaluation of the new trial stress. As can be shown by the residual error in biaxial plane stress loading, the plastic trial stress was closer to the true solution than the conventional elastic trial stress, and much less number of iterations was necessary to make convergence in the tests. The plastic trial stress was implemented in ABAQUS/UMAT and 3-dimensional finite element simulation of a tensile test showed that the computation time can be saved by the usage of the plastic trial stress in the material routine without invoking line search strategy.

Only associated flow rule has been assumed and the yield surface was identical to the flow surface in this work. If non-associated flow rule is used, then the flow function will be different to the yield function in general. The concept of the dual plasticity potentials can be applied to non-associated plasticity as well. In that case, the plastic strain rate potential and the flow potential will be in the dual relation as pointed out in [6]. A similar yield potential-based elasto-plastic numerical scheme can be developed in terms of Newton's method, and the concept of the plastic trial stress can be adopted in the non-associated framework. Our future effort will be made on the verification of the numerical efficiency of the plastic trial stress in the non-associated plasticity model.

References

1. Scherzinger WM (2017) A return mapping algorithm for isotropic and anisotropic plasticity models using a line search method. *Comput Methods Appl Math* 317:526–553
2. Perez-Foguet A, Armero F (2002) On the formulation of closest-point projection algorithms in elastoplasticity-part II: globally convergent schemes. *Int J Num Methods Eng* 53:331–374

3. Manik T (2021) A natural vector/matrix notation applied in an efficient and robust return-mapping algorithm for advanced yield functions. *Euro J Mech A Solids* 90. <https://doi.org/10.1016/j.euromechsol.2021.104357>
4. Ziegler H (1983) *An introduction to thermomechanics*. North-Holland Pub. Com.
5. Hill R (1950) *The mathematical theory of plasticity*. Oxford (1950)
6. Yang S, Tong W (2022) Non-quadratic pseudo dual potentials for plastic flow modeling. In: *IDDRG 2022 conference*. Lorient, France
7. Yang S, Sheng J, Alharbi M, Tong W (2021) On edge crack initiation of an aluminum sheet metal. In: *The 13th international conference on the technology of plasticity*
8. de Souza Neto EA, Peric D, Owen DRJ (2008) *Computational methods for plasticity, theory and applications*. Wiley, New York

Anisotropic Time-Dependent Continuum Damage-Coupled Plasticity Model for Predicting Ductile Fracture of 6xxx Series Aluminum Alloys



Mustapha Makki, Georges Ayoub, Andrey Ilinich, and Ghassan Kridli

Abstract An accurate prediction of the fracture strain under different stress states is essential for designing metal formed structures. General stress states may be characterized by two independent parameters; the stress triaxiality ratio and the Lode angle. When both parameters remain constant throughout the strain history, the loading is said to be proportional. In this work, the mechanical and damage behavior of ductile metal was captured using an anisotropic time-dependent continuum damage model coupled plasticity. The model was implemented in a finite element simulation code using an implicit time integration scheme. A hybrid method combining experimental (proportional loading) and finite element simulations was used for the model calibration. The predictive capability of the model with embedded cumulative damage law was validated on proportional loading tests conducted on a 6xxx series aluminum alloy sheets.

Keywords Continuum damage mechanics · Anisotropic damage · Anisotropic plasticity · Proportional loading

Introduction

Stamping operations are used for producing a large number of structural components for the automotive, aerospace, electronics, and telecommunications industries. More specifically, sheet metal forming is of high interest for the automotive industry prompted by the need to produce fuel-efficient vehicles and therefore manufacture intricate shape structural parts at higher rate and lower cost. Furthermore, with the increasing use of lightweight materials for stamping processes new challenges emerged. Aluminum alloys are high specific strength structural metals widely used

M. Makki · G. Ayoub (✉) · G. Kridli
Industrial and Manufacturing Systems Engineering Department, University of Michigan
Dearborn, Dearborn, MI 48128, USA
e-mail: gayoub@umich.edu

A. Ilinich
Ford Motor Company, Dearborn, MI 48124, USA

by the aerospace and automotive industries. The fracture is an important failure mode limiting the design space feasible for manufacturing and in-service use. Aluminum alloy sheets generally exhibit an anisotropic plastic and fracture behaviors. In this work we propose a novel fracture prediction model that can be used in stamping feasibility assessment.

A considerable number of models were proposed to capture the ductile behavior of metals associated with their mechanical properties degradation. The ductile fracture behavior is characterized by a sequence of degradation mechanisms induced by the plastic deformation, namely; void nucleation, growth, and coalescence [1, 2]. In the literature, we can differentiate among three different types of fracture models. First, the “Gurson type” models explicitly formulate macroscopic yield criterion based on homogenization theories for spherical and cylindrical voids [3–7]. The second type is the phenomenological “uncoupled damage” fracture models formulated without accounting for the damage evolution directly in the elastic and plastic properties [8]. These models make use of damage indicator functions to accumulate damage. The damage increment is proportional to the increment of the effective plastic strain weighted by severity of the stress state. The weighting is a function of two stress state parameters; the stress triaxiality (ratio of the hydrostatic stress to von Mises stress) and Lode angle (third stress invariant) [9–14]. Finally, the “continuum damage mechanics/coupled damage” models are derived from a thermodynamic dissipation potential and account for the damage evolution directly in the elastic and plastic properties [15]. Kachanov first introduced the formulation of the damage variable to predict creep induced fracture in metals [16]. Originally, the effect of damage was quantified using a continuity scalar variable ranging from zero for defect free material to unity for a failed material. Later, the loss of the material’s load bearing capability was explained by defining the damage parameter as the ratio between the material’s damaged surface and the total surface [17]. Based on that definition, the concept of effective stress linking the damage configuration to a fictitious defect free configuration was proposed [18, 19]. Initially, the continuum damage mechanics model assumed metal to be isotropic [20–22]. After, a multitude of experimental investigations on the ductile fracture of metallic materials reported that the damage is anisotropic, an anisotropic model was developed in which damage is a tensorial variable [23]. The theoretical formulation of the coupled anisotropic damage with plasticity was achieved by replacing the nominal stress with its effective value in the plastic potential function [24].

In this work, the mechanical and damage behavior of a 6xxx aluminum alloy is captured using an anisotropic time-dependent continuum damage-coupled plasticity model. The model was implemented in Abaqus/Standard as a user subroutine, and the parameters were calibrated on the experimental data. A hybrid method combining experimental and FEM simulations was used for the model calibration. The predictive capability of the model with embedded damage cumulative law was validated on proportional loading tests.

Experiments

In this section, the experimental procedure is detailed. Notched tensile specimens with a notch radius of 10 mm (NR10) were tested using a uniaxial tensile testing machine combined with a digital image correlation system (DIC). The material used in this study is a 6xxx aluminum alloy sheet of 1 mm thickness, widely used for stamping outer vehicle body panels. The nominal chemical composition of the studied 6xxx series aluminum alloy is given in Table 1. The material was studied in T4 temper after a substantial amount of natural aging.

An MTS servo-hydraulic machine was used to conduct the experimental tests. The test specimens were machined from a 1 mm Al 6xxx sheet using a wire electrical discharge machine (EDM). The specimens were extracted with their major axis being aligned with either of the rolling direction (RD), diagonal direction (DD), or transverse direction (TD) as shown in Fig. 1.

The test was repeated three times in each direction and the average force vs. displacement is presented in Fig. 1. It was observed that the tested specimens exhibited the same elastic, yield (1.38 kN) and hardening behavior. However, the fracture point was different for the different tested directions. The DD direction exhibited the highest displacement to fracture (2.18 mm).

Table 1 Chemical composition

Element	Si	Mg	Fe	Cu	Mn	Cr	Zn	Ti	Other
Wt%	0.5–1	0.4–0.8	0.3	0.2	0.15	0.1	0.1	0.1	0.15

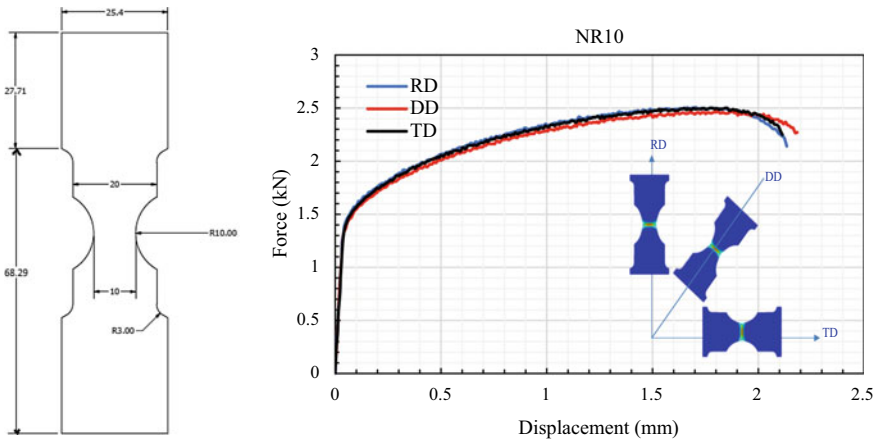


Fig. 1 NR10 specimen geometry and dimensions (in mm), force versus displacement response of specimens extracted from three different material orientations, the inset shows the test specimens' directions: Rolling Direction (RD), Diagonal Direction (DD), and Transversal Direction (TD)

Constitutive Model

In this section, the framework of the anisotropic time-dependent continuum damage-coupled plasticity model is presented. The framework of finite strains was used for developing the model. A detailed description of the model was provided by Kassab et al. [25]. The current work builds upon the previously developed model and proposes the use of damage effect tensor described in the local material coordinate system and not in the principal coordinate system of the damage. We start by providing a brief description of the kinematic variables. The deformation gradient is defined as $\mathbf{F} = \nabla \mathbf{x}(\mathbf{X}, t)$, with \mathbf{x} is the coordinates of a material point in the deformed configuration while \mathbf{X} is the coordinate of the material point in the undeformed configuration. The deformation gradient can be written as $\mathbf{F} = \mathbf{F}^e \mathbf{F}^p$ with \mathbf{F}^e is the elastic part and \mathbf{F}^p is the plastic part. The velocity gradient can be written as $\mathbf{L} = \dot{\mathbf{F}} \mathbf{F}^{-1} = \mathbf{D} + \mathbf{W}$, where \mathbf{W} is the spin component (skew-symmetric part) and \mathbf{D} is the total rate of deformation (symmetric part). The total rate of deformation can be additively decomposed into elastic and plastic rate for finite deformation $\mathbf{D} = \mathbf{D}^e + \mathbf{D}^p$.

The physical nature of damage induced by the initiation, growth, and coalescence of micro-cracks was quantified by measuring the geometric deterioration of the material's microstructure [26, 27]. For an isotropic case, the damage variable $D = (A - \tilde{A})/A$ is expressed as function of A is the material's total area, and \tilde{A} is the material's total area excluding micro-voids. For the anisotropic case, the effective stress is described as $\tilde{\sigma} = \mathbf{M} : \sigma$, where $\mathbf{M}(\mathbf{D})$ is the fourth-rank linear operator termed damage effect tensor. The damage effect tensor links the damaged material configuration to its fictitious undamaged configuration. For the present investigation, the damage effect tensor was expressed in the local material coordinate system [28]. The elastic energy for a representative volume element under applied stress is expressed as

$$W^e(S) = \frac{1}{2} \sigma_{ij} C_{ijkl}^{-1} \sigma_{kl} \quad (1)$$

where C_{ijkl}^{-1} is the elastic compliance tensor. The elastic energy of the damaged material can be determined by substituting the stress with the effective stress such that $W^e(\sigma, \mathbf{D} \neq 0) = W^e(\tilde{\sigma}, \mathbf{D} = 0)$. Hence, the expression of the effective elastic compliance tensor is defined as

$$\tilde{C}_{ijop}^{-1} = M_{ijkl} C_{klmn}^{-1} M_{mnop} \quad (2)$$

The visco-plastic constitutive coupled damage equations were developed by replacing the stress tensor with the effective stress tensor in the plastic potential of the undamaged material [29]. Accordingly, the effective Hill equivalent plastic stress is expressed as follows:

$$\tilde{\sigma}_{eq} = \left(\frac{1}{2} \tilde{\sigma} : H : \tilde{\sigma} \right)^{1/2} \quad (3)$$

where the stress σ is integrated from the following stress rate expression $\dot{\sigma} = \tilde{C} [D - D^p]$ And $\tilde{C}_{ijop} = M_{ijkl}^{-1} C_{klmn} M_{mnop}^{-1}$, and H is the symmetric fourth-order Hill tensor [30]. The plastic rate of deformation D^p is expressed as follows:

$$D_{ij}^p = \frac{\lambda^p}{2\tilde{S}_{eq}} H_{ijkl} \tilde{S}_{kl} \quad (4)$$

where λ^p is the plastic multiplier approximated by the cumulative plastic strain rate \dot{p} quantified using a visco-plastic strain sensitive power law:

$$\dot{p} = \gamma^p \left(\frac{\tilde{S}_{eq}}{s} \right)^{\frac{1}{m}} \quad (5)$$

where γ^p is the initial plastic rate, m is the strain rate sensitivity parameter and s is the shear strength resistance evolving according to [31].

The damage evolution rate was developed by assuming a dissipative damage potential f^d :

$$\dot{D}_{ij}^d = -\frac{\lambda^d}{2Y_{eq}^d} L_{ijkl}^d Y_{kl} \quad (6)$$

where λ^d is the Lagrange multiplier term approximated by the cumulative plastic damage rate \dot{q} . L^d is a fourth-order plastic damage characteristic tensor. The cumulative plastic damage rate is

$$\lambda^d \approx \dot{q} = \gamma^d \left(\frac{Y_{eq}}{Y^0} \right)^{\frac{1}{n}} \quad (7)$$

where γ^d is the initial damage rate, Y^0 is a damage strengthening resistance, and n is a rate sensitive parameter. The damage strain energy rate is defined as

$$Y_{ij} = -S_{ij} \left\{ C_{ijkl}^{-1} M_{klmn} \frac{\partial M_{mnop}}{\partial D_{qr}} \right\}^s S_{qr} \quad (8)$$

where “s” denotes taking the symmetric part within the curly brackets. Finally, the effective equivalent energy release rate is defined as

$$Y^{eq} = \left(\frac{1}{2} Y_{ij} L_{ijkl}^p Y_{kl} \right)^{\frac{1}{2}} \quad (9)$$

An implicit time integration algorithm using the backward Euler scheme was proposed to integrate the constitutive equations and compute the six components of the symmetric stress tensor and the six components of the symmetric damage tensor. Recall that the damage tensor was not expressed in the principal directions (three components) but in the local material coordinate system. The state variable vector was expressed by combining the six stress and six damage components as follows:

$$[X]^T = [\sigma_{11} \sigma_{22} \sigma_{33} \sigma_{23} \sigma_{13} \sigma_{12} D_{11} D_{22} D_{33} D_{23} D_{13} D_{12}] \quad (10)$$

The residual function is defined as the difference between the rate equation and the ratio [of the difference between the previous and current increment with the time step Δt], for the state variable X_i at a time $t + 1$ the residual function was explicitly expressed as follows:

$$R_{X_i}^{t+1} = \frac{X_i^{t+1} - X_i^t}{\Delta t} - \dot{X}_i^{t+1} \quad (11)$$

The 12 residual functions were collected in the residual vector:

$$[R]^T = [R_{S_{11}} R_{S_{22}} R_{S_{33}} R_{S_{23}} R_{S_{13}} R_{S_{12}} R_{D_{11}} R_{D_{22}} R_{D_{33}} R_{D_{23}} R_{D_{13}} R_{D_{12}}] \quad (12)$$

A Newton–Raphson scheme was used to minimize the residual vector and to update the current values of the state variables. For that purpose the inverse of a 12×12 Jacobian matrix was calculated. The constitutive model was implemented in a commercial finite element model ABAQUS as a user subroutine (UMAT). The consistent tangent matrix \mathcal{L} was calculated by the UMAT and was supplied to ABAQUS to ensure numerical convergence.

Model Predictions

In this section, the model's ability to capture the mechanical and fracture behavior of Al 6xxx series specimens extracted along different directions is examined. One eighth of the specimen geometry was modeled in ABAQUS by applying adequate symmetry and boundary conditions. The constitutive model parameters were calibrated on the NR10RD experimental data. The calibrated model was used to predict the mechanical and fracture behavior of the NR10 DD and TD. An isotropic stiffness tensor was used where $E = 69000\text{MPa}$ and $\nu = 0.34$. The Hill yield criterion was calibrated using the yielding properties and the Lankford coefficient of dog-bone specimens extracted along different sheet directions (the results of those test were not presented as a standard calibration of the Hill matrix was used). The identified Hill parameters

are as follow $F = 1$, $G = 1$, $H = 1$, $L = 2$, $M = 2$, and $N = 2$. The parameter η value was assumed to be 0.25 [29]. The list and value of the eight constitutive model parameters are given in Table 2.

The comparison between the NR10 RD experimental and simulated load vs displacement curves is shown in Fig. 2. It was observed that the model is able to fit the experimental results. The damage evolution along the three material directions was also plotted. The damage 11 was computed along the loading direction, Damage 22 was computed along the width direction of the specimen, and Damage 33 was computed along the thickness direction of the specimen.

Figure 2 shows non-linear damage accumulation. The maximum damage stayed relatively low (below 0.01) up until the maximum load and rapidly increased thereafter. The damage along the loading direction presented the highest values, as expected. Fracture occurred for a damage in the loading direction equal to 0.045.

The model capability to predict the mechanical and fracture behavior of 6xxx aluminum alloys along different material directions was assessed with Fig. 3. In Fig. 3, the predicted and the experimental NR10 DD and TD load vs displacement curves were compared. The damage evolution along the three material directions was also plotted. Figure 3 shows that the model is able to predict the mechanical and the fracture behavior of NR10 DD and TD specimens. Furthermore, fracture occurred at a level of damage 11 similar to the one reached at fracture by the NR10 RD specimen.

Conclusion

In this work, the mechanical and damage behavior of ductile metal was captured using an anisotropic time-dependent continuum damage-coupled plasticity. The mechanical properties degradation with increasing crack density was accounted for in the model formulation using an anisotropic damage tensor as internal variable. Both

Table 2 Model parameters

Material Constants		
<i>Plasticity Constants</i>		
Shear resistance	s^0	100 MPa
Hardening saturation limit	s^s	400 MPa
Fitted hardening coefficient	n^h	4.8 s^{-1}
Strain sensitivity parameter	m	0.01
Initial plastic rate	γ^p	1000
<i>Damage Constants</i>		
Initial damage rate	γ^d	$2\text{e-}7$
Damage strengthening resistance	Y^0	0.032
Rate sensitivity parameter	n	0.2

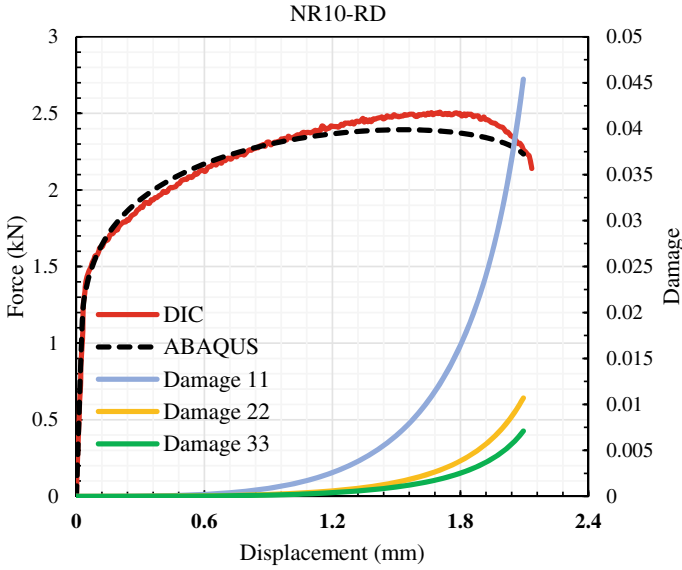


Fig. 2 Load–displacement and damage–displacement results

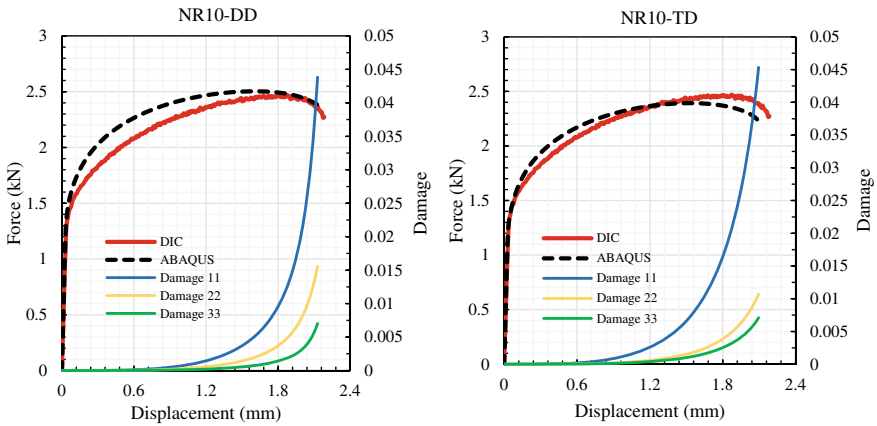


Fig. 3 DIC and ABAQUS results for Notch Specimen with R = 10 mm in the Diagonal Direction (Left), and Transversal Direction (Right)

the damage and the elastoviscoplastic formulations were developed in an arbitrary coordinate space to accommodate multiaxial loadings, both proportional and non-proportional. An implicit implementation of the constitutive equation as user subroutine in a finite element method code was achieved. A hybrid method combining experimental (proportional loading) and FEM simulations was used for the model

calibration. The predictive capability of the model with embedded damage cumulative law was validated on proportional loading tests conducted on a 6xxx series aluminum sheets. The proposed model capability and limitation in predicting for anisotropic materials the fracture properties for proportional and non-proportional loadings will be explored in future work.

References

1. Murakami S (1987) Anisotropic aspects of material damage and application of continuum damage mechanics. In: Continuum damage mechanics theory and application, vol 295. Springer, Vienna, pp 91–133
2. Benzerga AA (2002) Micromechanics of coalescence in ductile fracture. *J Mech Phys Solids* 50:1331–1362
3. Gurson AL (1977) Continuum theory of ductile rupture by void nucleation and growth: Part I—yield criteria and flow rules for porous ductile media. *J Eng Mater Technol* 99:2
4. Tvergaard V, Needleman A (1984) Analysis of the cup-cone round tensile fracture. *Acta Metall* 32:157–169
5. Leblond J-B, Perrin G, Devaux J (1995) An improved Gurson-type model for hardenable ductile metals *Eur J Mech A Solids* 14:499–527
6. Chu CC, Needleman A (1980) Void nucleation effects in biaxially stretched sheets, pp 249–256
7. Mear ME, Hutchinson JW (1985) Influence of yield surface curvature on flow localization in dilatant plasticity *Mech Mater* 4:395–407
8. Gu G, Mohr D (2015) Anisotropic Hosford-Coulomb fracture initiation model: theory and application. *Eng Fract Mech* 147:480–497
9. Wierzbicki T, Bao Y, Lee Y-W, Bai Y (2005) Calibration and evaluation of seven fracture models. *Int J Mech Sci* 47:719–743
10. Bai Y, Wierzbicki T (2009) Application of extended Mohr-Coulomb criterion to ductile fracture. *Int J Fract* 161:1
11. Bao Y, Wierzbicki T (2004) A comparative study on various ductile crack formation criteria. *J Eng Mater Technol* 126:314–324
12. Bao Y, Wierzbicki T (2004) On fracture locus in the equivalent strain and stress triaxiality space. *Int J Mech Sci* 46:81–98
13. Xue L (2007) Ductile fracture modeling: theory, experimental investigation and numerical verification. Doctoral dissertation, Massachusetts Institute of Technology
14. Bai Y, Wierzbicki T (2008) A new model of metal plasticity and fracture with pressure and Lode dependence. *J Int J Plast* 24:1071–1096
15. Lemaitre J (1992) A course on damage mechanics. Springer, New York
16. Kachanov LM (1958) Time of the rupture process under creep conditions. *Izy Akad Nank SSR Otd Tech Nauk* 8:26–31
17. Backhaus G (1971) Yu. N. Rabotnov, creep problems in structural members. North-Holland series in applied mathematics and mechanics, IX + 822 S. m. 255 Fig. Amsterdam/London 1969. North-Holland Publishing Company. Preis geb. Hfl. 120. –. *Z. angew. Math. Mech.*, vol 51, pp 575–576. <https://doi.org/10.1002/zamm.19710510726>
18. Lemaitre J (1971) Evaluation of dissipation and damage in metals submitted to dynamic loading. In: Proceedings. I. C. M. I Kyoto, Japan
19. Lemaitre J, Chaboche JL (1978) Aspects phénoménologiques de la rupture par endommagement. *J Mécanique Appliquée* 2:317–365
20. Lemaitre J, Doghri I (1994) Damage 90: a post processor for crack initiation. *Comput Methods Appl Mech Eng* 115(3–4):197–232. ISSN 0045-7825. [https://doi.org/10.1016/0045-7825\(94\)90060-4](https://doi.org/10.1016/0045-7825(94)90060-4). <https://www.sciencedirect.com/science/article/pii/0045782594900604>

21. Chaboche J (1997) Application to the viscoplasticity and. *J Int J Solids Struct* 34:2239–2254
22. Lemaitre J (1985) A continuous damage mechanics model for ductile fracture. *ASME J Eng Mater Technol* 107(1):83–89. <https://doi.org/10.1115/1.3225775>
23. Cordebois JP, Sidoroff F (1982) Damage induced elastic anisotropy. In: *Mechanical behavior of anisotropic solids/comportment mécanique des solides anisotropes*. Springer, Netherlands, Dordrecht, pp 761–774. https://link.springer.com/chapter/10.1007/978-94-009-6827-1_44
24. Hao L, Ke P, June W (1985) An anisotropic damage criterion for deformation instability and its application to forming limit analysis of metal plates. *Fract Eng Fract Mech* 21:1031–1054
25. Kassar S, Ayoub G, Kridli G (2019) Anisotropic time dependent and continuum damage coupled plasticity model: an application for Mg AZ31B. *Int J Solids Struct* 178–179:199–211
26. Cordebois JP, Sidoroff F (1982) Damage induced elastic anisotropy BT. In: *Boehler JP (ed) Mechanical behavior of anisotropic solids/comportment mécanique des solides anisotropes*. Springer Netherlands, Dordrecht, pp 761–774
27. Cordebois JP, Sidoroff F (1982) Endommagement anisotrope en élasticité et plasticité. *J Mécanique Théorique Appliquée*, 45–60
28. Voyiadjis GZ, Kattan PI (1999) Damage and plasticity in metals. In: *Advances in damage mechanics: metals and metal matrix composites*, pp 109–157
29. Chow CL, Yu LG, Demeri MY (1997) A unified damage approach for predicting forming limit diagrams. *J Eng Mater Technol* 119:346
30. Hill R (1948) A theory of the yielding and plastic flow of anisotropic metals. *R Proc Soc Lond Ser A Math Phys Sci* 193:281–297
31. Stringfellow RG, Parks DM, Olson GB (1992) A constitutive model for transformation plasticity accompanying strain-induced martensitic transformations in metastable austenitic steels. *Acta Metall Mater* 40:1703–1716

Characterization of Impurities in Nanomaterials



Kemi Y. Adewale and Mathew O. Aibinu

Abstract Nanomaterials have been known for varieties of applications. Interest in mixed metal-oxide nanoparticles stems mainly due to their unusual optical, electric, and magnetic properties. There are reports on the investigation of nanoferrous alloys for unique applications in medical imaging, hyperthermia, and drug targeting. In the last decade, considerable attention has been paid to overcome the miniaturization challenges facing the industries in the synthesis of magnetic and electronic devices such as ferrites. This study will set the phase for numerical characterization of the nonmagnetic ions whose dilution with nanoferrites improves the magnetic properties of the nanomaterials. The substitution of impurities into the different ferrite systems to improve their basic properties are presented. This research will help in the technological development that will further increase the understanding of researchers in physical and biological sciences.

Keywords Nanomaterials · Nanoparticles · Ferrite · Magnetic

K. Y. Adewale

School of Chemistry and Physics, University of KwaZulu-Natal, Westville Campus,
Durban 4000, South Africa

e-mail: kemiadewale2@gmail.com; 217078608@stu.ukzn.ac.za

M. O. Aibinu (✉)

Institute for Systems Science & KZN E-Skill CoLab, Durban University of Technology,
Durban 4000, South Africa

e-mail: moaibinu@yahoo.com; mathewa@dut.ac.za

DSI-NRF Centre of Excellence in Mathematical and Statistical Sciences (CoE-MaSS),
Johannesburg, South Africa

National Institute for Theoretical and Computational Sciences (NITheCS),
Stellenbosch, South Africa

© The Minerals, Metals & Materials Society 2022

K. Inal et al. (eds.), *NUMISHEET 2022*, The Minerals, Metals & Materials Series,
https://doi.org/10.1007/978-3-031-06212-4_3

Introduction

The technological importance of superparamagnetic ferrite materials has increased significantly over the last few decades [17, 29]. Progress in synthesis techniques has generated more interest in ferrites in order to improve their properties and expand their applications. Ferrites are ceramic magnetic materials with general chemical formula $M\text{Fe}_2\text{O}_4$, where M represents one or a mixture of divalent transition metals such as Mn, Zn, Ni, Co, Cu, Fe, Mg, or Ca. Zinc ferrite (ZnFe_2O_4) possesses normal spinel structure and contains two different cationic sites; eight tetrahedral A-sites and sixteen octahedral B-sites. Zinc ions occupy exclusively the tetrahedral A sites while iron ions are only at the octahedral B sites. The distribution of cations determines the magnetic properties of spinel ferrites. Magnetic coupling in spinel ferrite occurs via super-exchange interactions. Super-exchange between two metal cations can occur via intermediate oxygen ions in the spinel structure through A-O-A, B-O-B, and A-O-B coupling. The magnetic behavior of ferrites is strongly influenced by the particle size, the preparation method, and structure [7]. Nanoparticles have sizes in the range from 1 to 100 nm and exhibit unique physical and chemical properties due to their high surface area and nanoscale size [21]. The size reduction of a magnetic material leads to novel properties like super-paramagnetism due to small volume compared to the corresponding bulk material. The optical properties of nanoparticles are reported to be dependent on the size, which imparts different colors due to absorption in the visible region. Other properties such as their reactivity and toughness also depend on their unique size, shape, and structure. These characteristics make the magnetic nanoparticles useful for various commercial and domestic applications, which include catalysis, magnetic resonance imaging, medical applications, energy-based research, and environmental applications.

Zinc substitution influences the magnetic properties of a nanoscale system [35]. There is a recent outline on the analysis of Mg-doped ZnFe_2O_4 [4]. Calcium and iron-based compounds have also been explored in the bulk form for optical memory devices, steel making industry (as deoxidizer, desulfuration, and dephosphorization) [19], as pigment [31], and as absorbent of hydrogen sulfide (H_2S) [18]. In comparison with other ferrites such as MnFe_2O_4 , NiFe_2O_4 , CoFe_2O_4 and CuFe_2O_4 , CaFe_2O_4 has significant advantages. It is biocompatible and eco-friendly due to the presence of Ca^{2+} instead of the heavy metals. The synthesis and formation mechanism and magnetic properties in bulk form have also been considered [11, 20]. CaFe_2O_4 does not have the spinel structure due to the large size of the calcium ion which tends to be 8 or 9-fold coordinated [37]. Its structure is made of distorted FeO_6 octahedra calcium atoms and the phase transition is due to Fe^{3+} high spin/low spin transition [25]. There are few reports on the morphology, structure and magnetic properties of Ca-ferrites in the nano-regime (See e.g., [8]). A report on hematite-like structure of CaFe_2O_4 is given in [5].

Samples produced from different laboratories and by different techniques can show differences in their properties. The aim of this work is to determine the effects

of Ca^{2+} on the phase stability of ZnFe_2O_4 , without any additional calcination and reduction steps. The reports on the synthesis, structural, magnetic, and morphological properties of Ca-doped ZnFe_2O_4 nanoparticles are given.

Experimental Details

Nanoferrites and nanocomposites of $\text{Ca}_x\text{Zn}_{1-x}\text{Fe}_2\text{O}_4$ ($x = 0, 0.02, 0.06, 0.08, 0.2, 0.5, 0.6, 0.8, \text{ and } 1$) were prepared by the glycol-thermal method. The chemical reagents used were calcium chloride $\text{CaCl}_2 \cdot 2\text{H}_2\text{O}$, zinc chloride ZnCl_2 , and iron (III) chloride hexa-hydrate $\text{FeCl}_3 \cdot 6\text{H}_2\text{O}$. All chemicals were of analytical grades. These were weighed in required proportions, then dissolved in about 50 ml of de-ionized water and magnetically stirred. Ammonia solution (NH_3) was slowly added to the mixture of chloride solutions under rapid stirring for about 10 min in order to initiate precipitation until a $\text{pH} \approx 10$. The solution was further stirred for 40 min. The precipitate was mixed with 100 ml of ethylene glycol. The mixture was then placed in a 600 ml stainless steel pressure vessel (Watlow series model PARR 4843 reactor). The reactor was heated to a soak temperature of 200°C and the gauge pressure was allowed to gradually rise to about 170 psi and angular speed of 300 rpm. These conditions were held for 6 h. The cooled reacted products were filtered and washed several times with de-ionized water and finally with ethanol over a Whatman filter in a Büchner flask in order to remove the chlorides. The absence of chlorides was confirmed by the addition of a standard solution of silver nitrate (AgNO_3) to the filtrate. The recovered synthesized samples were left to dry on the filter paper for 24 hrs under a 200 W infrared light. The dried products were then homogenized using an agate mortar and pestle. The samples were characterized at room temperature by X-ray diffraction (XRD) using a monochromatic beam of Co-K_α radiation ($\lambda = 1.7903 \text{ \AA}$), high-resolution transmission and scanning electron microscopy (HRTEM and HRSEM), ^{57}Fe Mössbauer spectroscopy and a vibrating sample magnetometer.

Results and Discussion

X-ray Diffraction

The XRD patterns of $\text{Ca}_x\text{Zn}_{1-x}\text{Fe}_2\text{O}_4$ ($x = 0, 0.02, 0.06, 0.08, 0.2, 0.5, 0.6, 0.8, \text{ and } 1$) are given in Fig. 1. The calculated values of crystallite sizes D , lattice parameter a , and the X-ray density ρ are presented in Table 1. The peaks were correctly indexed and matched with documented XRD patterns and no impurity phase was detected in all the samples [22, 23]. The peaks in $x=0, 0.02$ and 0.06 correspond to a single phase cubic spinel structure. A mixed phase of a spinel and a hematite-like structure started to evolve at $x = 0.08$. A nanocomposite of a spinel and a hematite-like structure is

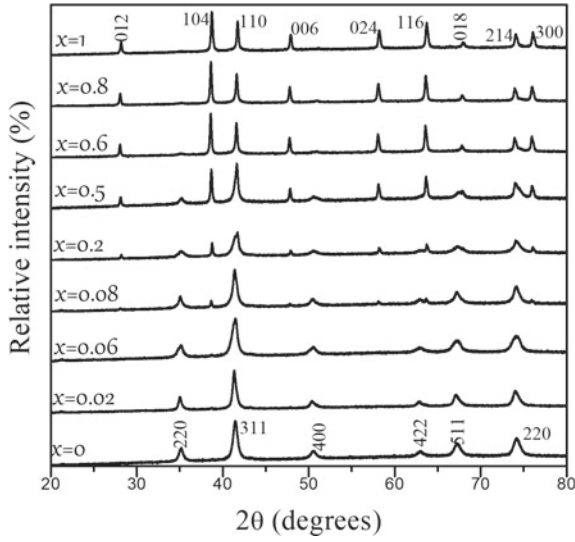


Fig. 1 XRD patterns of $\text{Ca}_x\text{Zn}_{1-x}\text{Fe}_2\text{O}_4$, **a** $x = 0, 0.02, 0.06, 0.08, 0.2, 0.5, 0.6, 0.8$ and 1

Table 1 Crystallite size (D), lattice parameters (a) and X-ray densities ρ_{XRD} for prepared samples of $\text{Ca}_x\text{Zn}_{1-x}\text{Fe}_2\text{O}_4$ ($x = 0, 0.02, 0.06, 0.08, 0.2, 0.5, 0.6, 0.8,$ and 1)

Sample x	Composition	Spinel			Hematite		
		D (nm) ± 0.4	a (Å) ± 0.006	ρ_{XRD} (g/cm^3) ± 0.28	D (nm) ± 0.94	a (Å) ± 0.01	ρ_{XRD} (g/cm^3) ± 0.48
0	ZnFe_2O_4	18.6	8.386	5.43	–	–	–
0.02	$\text{Ca}_{0.02}\text{Zn}_{0.98}\text{Fe}_2\text{O}_4$	23.1	8.407	5.38	–	–	–
0.06	$\text{Ca}_{0.06}\text{Zn}_{0.94}\text{Fe}_2\text{O}_4$	16.0	8.399	5.37	–	–	–
0.08	$\text{Ca}_{0.08}\text{Zn}_{0.92}\text{Fe}_2\text{O}_4$	23.4	8.401	5.36	63.40	11.15	2.29
0.2	$\text{Ca}_{0.2}\text{Zn}_{0.8}\text{Fe}_2\text{O}_4$	17.0	8.375	5.34	63.44	11.12	2.28
0.5	$\text{Ca}_{0.5}\text{Zn}_{0.5}\text{Fe}_2\text{O}_4$	24.2	8.376	5.16	54.62	11.14	2.19
0.6	$\text{Ca}_{0.6}\text{Zn}_{0.4}\text{Fe}_2\text{O}_4$	–	–	–	52.48	11.17	2.15
0.8	$\text{Ca}_{0.8}\text{Zn}_{0.2}\text{Fe}_2\text{O}_4$	–	–	–	54.41	11.16	2.11
1	CaFe_2O_4	–	–	–	45.42	11.13	2.08

formed at $x = 0.2$ and 0.5 . Complete hematite-like structures were observed at $x = 0.6$, $x = 0.8$ and 1 . The increase in the addition of Ca^{2+} ion concentration makes the diffraction peaks sharper and narrower [9]. This is a one-step technique for the synthesis of CaFe_2O_4 and it gives clear and sharp diffraction peaks. This is an interesting result compared to other reports where CaFe_2O_4 was synthesized by more than one-step or at a much-elevated temperature [13, 33]. Using the Debye-Scherrer formula,

$$D = \frac{K \lambda}{W_{hkl} \cos \theta}, \quad (1)$$

where K is a constant associated with the shape factor usually taken to be 0.9 for particles of unknown shape, 0.89 for particles with spherical shape and 0.94 for cubic particles. The wavelength for the monochromatic X-ray beam is $\lambda = 1.7903 \text{ \AA}$ and W_{hkl} is the full width at half maximum (FWHM) of the broadening line diffraction peak of the most prominent peak and θ is the Bragg angle. The crystallite sizes (D) for the pure cubic spinel phases were calculated from the most intense 311 peak, while for the mixed phase, 220 peak was used for the spinel and 104 peak for the hematite phases. The lattice parameters were obtained using

$$a = \frac{\lambda}{2 \sin \theta} \sqrt{h^2 + k^2 + l^2}, \quad (2)$$

where h , k and l are known as the Miller indices for the diffracting planes and the X-ray density using

$$\rho_{xRD} = \frac{8M}{N_A a^3}, \quad (3)$$

where 8 is the number of molecules per unit, M is the molecular weight, N_A is the Avogadro's constant and a is the size of the lattice parameter that defines the size of the unit cell [3].

The strong and sharp diffraction peaks indicate good crystallinity of the samples [9]. This suggests an increase in particle size. The present results indicate that at $x = 0, 0.02, 0.06, 0.08, 0.2$, and 0.5 , the lattice parameter a and crystallite size D of the cubic spinel structures varies. The lattice parameters a and crystallite size D of the hematite phase increased for $x = 0.08, 0.2$, and 0.5 . However, at $x = 0.6, 0.8$, and 1 , the lattice parameter a decreased while the crystallite size D varies for the hematite phase as the Ca^{2+} ion concentration increases. The variation of the size of the obtained particles is between 19 nm and 63 nm.

Morphology Study

The morphology and micro-structure of the nanoparticles were investigated by HRSEM and HRTEM measurements. Figures 2 and 3 show the HRSEM and HRTEM micrographs of the samples. The particles are almost spherical in shape as seen in

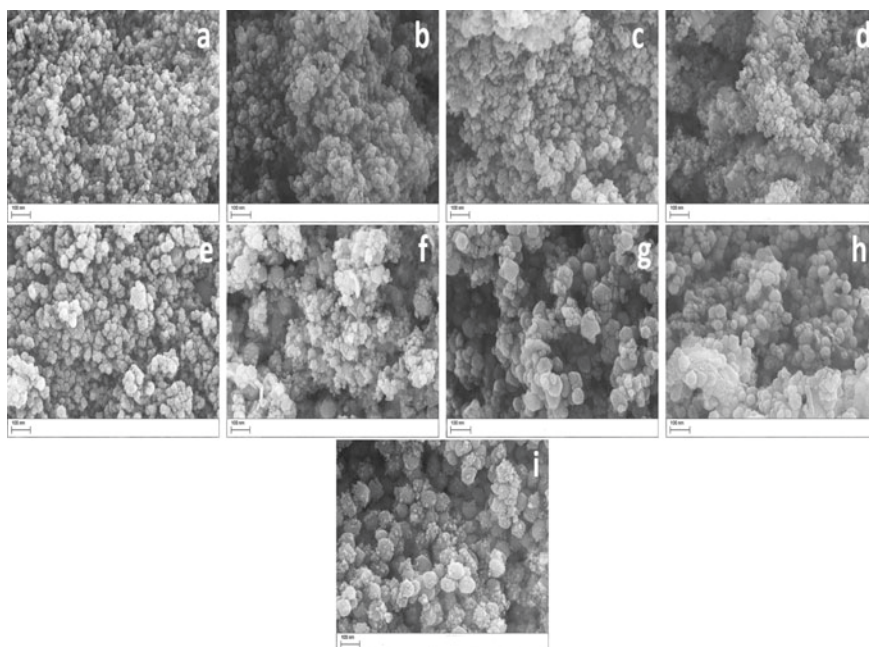


Fig. 2 HRSEM images of $\text{Ca}_x\text{Zn}_{1-x}\text{Fe}_2\text{O}_4$, **a** $x = 0$, **b** $x = 0.02$, **c** $x = 0.06$, **d** $x = 0.08$, **e** $x = 0.2$, **f** $x = 0.5$, **g** $x = 0.6$, **h** $x = 0.8$, and **i** $x = 1$

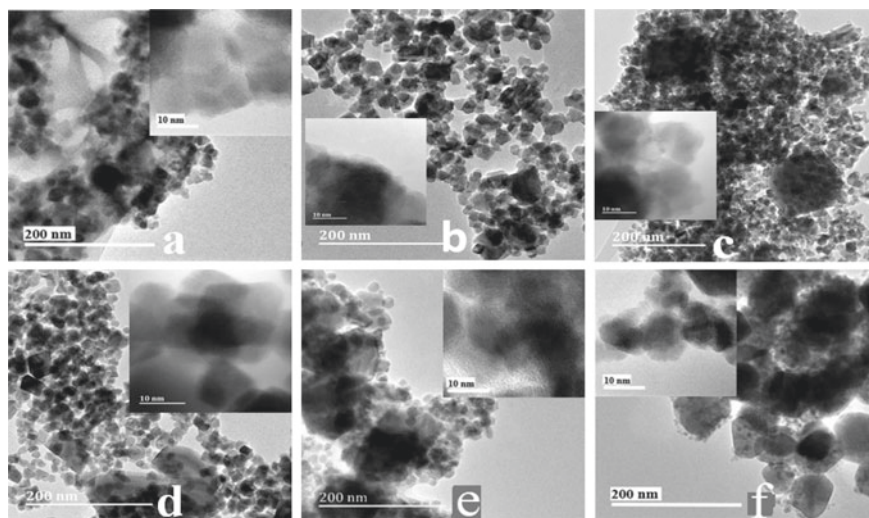


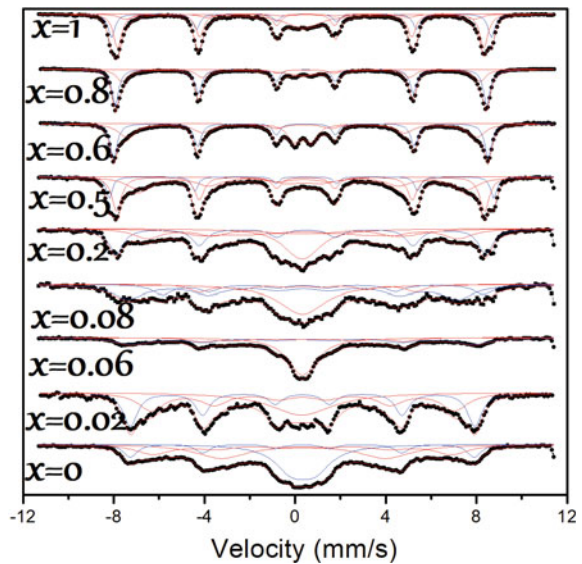
Fig. 3 Selected HRTEM images of $\text{Ca}_x\text{Zn}_{1-x}\text{Fe}_2\text{O}_4$, **a** $x = 0$, **b** $x = 0.02$, **c** $x = 0.06$, **d** $x = 0.2$, **e** $x = 0.5$, and **f** $x = 1$

the images. The particle size increased significantly as the Ca^{2+} ion concentration increases. This is due to the replacement of Zn^{2+} which has a smaller ionic radius of 0.74 \AA , [1], with Ca^{2+} which has larger ionic radius of 0.99 \AA , [27]. This is in good agreement with the results obtained from the XRD measurements. The pure samples are ZnFe_2O_4 and CaFe_2O_4 in Fig. 2 of HRSEM. In the figure, the 3d and 3e show a mixed phase of cubic spinel and a hematite-like structure for $\text{Ca}_{0.2}\text{Zn}_{0.8}\text{Fe}_2\text{O}_4$ and $\text{Ca}_{0.5}\text{Zn}_{0.5}\text{Fe}_2\text{O}_4$. These show a clear distinction of the nanocomposite for mixed phases as compared to pure cubic spinel structure of doped samples $\text{Ca}_{0.02}\text{Zn}_{0.8}\text{Fe}_2\text{O}_4$ and $\text{Ca}_{0.06}\text{Zn}_{0.5}\text{Fe}_2\text{O}_4$ [10].

Mössbauer Measurements

The room temperature ^{57}Fe Mössbauer spectroscopy is presented in Fig. 4. The calibration was done using $\alpha\text{-Fe}$ foil at a constant acceleration. The magnetic components of the spectra were fitted using the Lorentzian site analysis. The spectrum for $x = 0$ was best fitted with two sextets and two doublets. Two sextets and one doublet were used to fit $x = 0.02, 0.06, 0.6,$ and 0.8 . The spectra for $x = 0.2, 0.5,$ and 1 exhibit three sextets and one doublet. The two sextets for the samples $x = 0, 0.02,$ and 0.06 are associated with the coordination of Fe^{3+} ions at tetrahedral A and octahedral B sites of the spinel crystal structure [16]. The sextets having large hyperfine magnetic field are assigned to the hematite-like structure of the materials [24]. The other two sextets are attributed to Fe^{3+} at tetrahedral A and octahedral B sites, based on the nature of their hyperfine magnetic field values (hyperfine magnetic field at B sites

Fig. 4 Fitted room temperature ^{57}Fe Mössbauer spectra of $\text{Ca}_x\text{Zn}_{1-x}\text{Fe}_2\text{O}_4$ ($x = 0, 0.02, 0.06, 0.08, 0.2, 0.5, 0.6, 0.8,$ and 1) nanoferrites



is greater than the hyperfine field at A sites) [28]. The doublets are associated with small nanoparticles in paramagnetic states. It was observed that the obtained isomer shift values are less than 0.6 mm/s. This leads to the deduction that only Fe^{3+} is present and ruling out the detectable presence of Fe^{2+} ions [34]. The higher values of quadrupole splitting indicate that the ions are embedded in noncubic surroundings [12, 14], while the relatively small values of the quadrupole splitting indicate that A and B sites have nearly cubic symmetry [12]. The larger line width on the A - and B -sites are attributed to the magnetic dipolar effects [26, 36]. The hyperfine magnetic field reported here are in the range of the reported values for $\alpha\text{-Fe}_2\text{O}_3$ [5, 23].

Magnetization Measurements

The hysteresis loops measured at room temperature performed in a magnetic field of up to 14 kOe are shown in Fig. 5. The values of coercive fields (H_C), saturation magnetizations (M_S), residual magnetizations (M_R), and squareness of the loops (M_R/M_S) are calculated from the hysteresis loops and the results are presented in Table 2. Figures 6, 7 and 8, respectively, display the variation of H_C , M_S , and M_R with respect to x . We obtained the coercive field from

$$H_C = \left| \frac{H_{C1} + H_{C2}}{2} \right| \quad (4)$$

For the pure spinel and mixed phase samples, it was observed that there is variation in the coercive fields as x increases. However, as for the pure hematite structure samples, there is decrease in values of the coercive fields as x increases. This observation compares well with the Mössbauer results which can be attributed to fewer magnetic

Fig. 5 Room temperature hysteresis loops of $\text{Ca}_x\text{Zn}_{1-x}\text{Fe}_2\text{O}_4$ ($x = 0, 0.02, 0.06, 0.08, 0.2, 0.5, 0.6, 0.8, \text{ and } 1$) nanoferrites

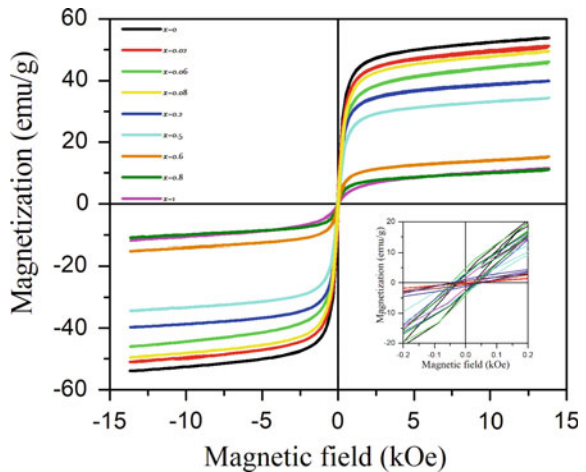
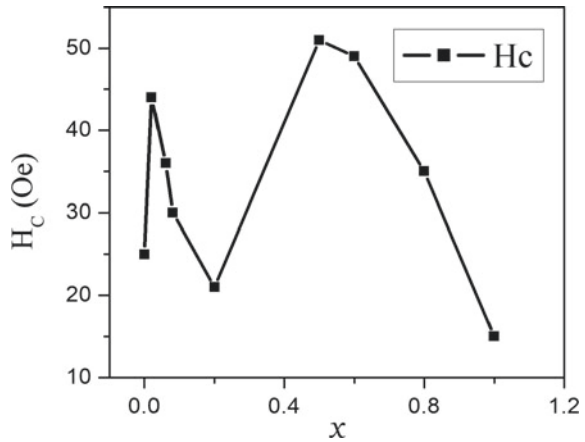


Table 2 Coercivity H_C , saturation magnetization M_S , remanence magnetization M_R and squareness ratio (M_R/M_S) obtained at room temperatures in applied field of 14 kOe for $\text{Ca}_x\text{Zn}_{1-x}\text{Fe}_2\text{O}_4$ ($x = 0, 0.02, 0.06, 0.08, 0.2, 0.5, 0.6, 0.8, \text{ and } 1$)

x	H_C (Oe) ± 1	M_S (emu/g) ± 0.5	M_R (emu/g) ± 0.5	M_R/M_S ± 0.03	K (emu kOe/g) ± 0.03	p (psi)
0	25	49.1	2.9	0.05	1.28	170
0.02	44	46.87	4.5	0.09	2.15	170
0.06	36	41.52	3.1	0.08	1.56	170
0.08	30	45.93	0.6	0.01	1.44	180
0.2	21	38.3	1.7	0.04	0.84	180
0.5	51	31.15	3.2	0.10	1.66	170
0.6	49	8.28	1.2	0.14	0.42	170
0.8	36	6.61	0.6	0.09	0.25	180
1	15	7.92	0.1	0.01	0.12	180

Fig. 6 Variation of coercive field H_C with x .



neighbours as a result of substitution of Zn^{2+} by Ca^{2+} ions. The M_S were estimated using the equation for the law of approach to saturation magnetization

$$M(H) = M_S \left(1 - \frac{a}{H} - \frac{b^2}{H^2} \right) + \chi H, \quad (5)$$

where M_S , a , b and χ are the best fit parameters to the data. The low squareness (M_R/M_S ratios) and the small H_C values reflected the superparamagnetic behavior of the samples [2, 38]. The obtained magnetic squareness values for $x = 0, 0.02, 0.06, 0.08, 0.2, 0.5, 0.6, 0.8$ and 1 , are $0.05, 0.09, 0.08, 0.01, 0.04, 0.10, 0.14, 0.09, 0.10$, and 0.01 , respectively. Since the values are in the range of 0.1 for superparamagnetic materials [15], this supports the superparamagnetic nature of the samples. It was

Fig. 7 Variation of saturation magnetization M_S with x .

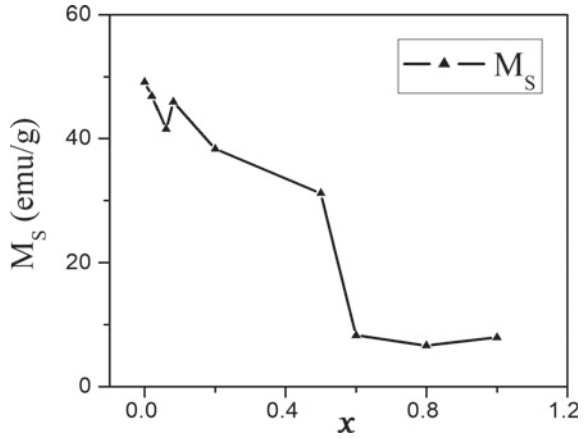
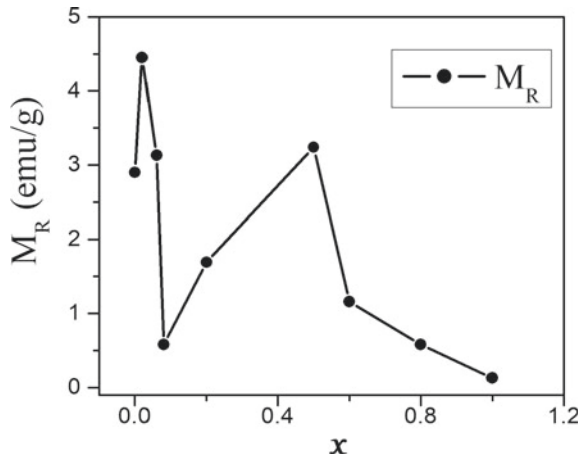


Fig. 8 Variation of remanent magnetization M_R with x .



observed that the saturation magnetization decreases as the Ca^{2+} ion concentration increases. This observation agrees with the reports in the literature [32]. The decrease in M_S can be attributed to the formation of hematite-like phase [6].

Conclusion

$\text{Ca}_x\text{Zn}_{1-x}\text{Fe}_2\text{O}_4$ nanoferrites were synthesized via glycol-thermal method. The prepared samples were characterized by XRD, HRTEM, HRSEM, Mössbauer spectroscopy, and magnetization measurements. XRD results show single phase cubic spinel structure for $x = 0, 0.02, \text{ and } 0.06$. For $x = 0.08, 0.2, \text{ and } 0.5$, the XRD results show mixed phases of cubic spinel and hematite-like structures, while for

$x=0.6, 0.8,$ and $1,$ the observed phase is a pure hematite-like structure. Crystallite sizes were obtained in the range $19\text{--}63$ nm, which appear to be influenced by the increasing value of $x.$ The substitution of Zn^{2+} for larger amounts of Ca^{2+} increased the crystallite size of the sample. A gradual increase in the lattice parameter was also observed with increasing Ca content. Results also show a strong correlation between the XRD density with Ca concentration $x,$ that is, as x increases the XRD density decreases. The HRTEM and HRSEM images show clearly nanocrystalline nature of the samples. HRTEM reveals the clear differences in the morphologies of the samples. ^{57}Fe Mössbauer spectroscopy results which were measured at room temperature show transformation to higher magnetic hyperfine fields for the samples with pure hematite-like structural phase. The magnetization measurements at room temperature show evidence of superparamagnetic behaviour of the compounds. It is interesting to note that there is variation in the saturation magnetization of the samples with mixed phase, while the saturation magnetization for the pure hematite phase reduced drastically with increasing amount of $x.$ The decrease in magnetization is attributed to the formation of the hematite-like phase or cation distribution in A- and B-sites.

Acknowledgements The second author acknowledges with thanks the postdoctoral fellowship and financial support from the DSI-NRF Center of Excellence in Mathematical and Statistical Sciences (CoE-MaSS). Opinions and conclusions are those of the authors and are not necessarily to be attributed to the CoE-MaSS.

References

1. Abdallah HMI, Moyo T (2013) Structural and magnetic studies of $(\text{Mg}, \text{Sr})_{0.2}\text{Mn}_{0.1}\text{Co}_{0.7}\text{Fe}_2\text{O}_4$ nanoferrites. *J Alloys Comput* 562:156–163. <https://doi.org/10.1016/j.jallcom.2013.02.056>
2. Abdallah HMI, Moyo T (2012) The influence of annealing temperature on the magnetic properties of $\text{Mn}_{0.5}\text{Co}_{0.5}\text{Fe}_2\text{O}_4$ nanoferrites synthesized via mechanical milling method. *J Supercond Nov Magn* 26:1361–1367
3. Abdallah HMI, Moyo T, Msomi JZ (2011) Mössbauer and electrical studies of $\text{Mn}_x\text{Co}_{1-x}\text{Fe}_2\text{O}_4$ compounds prepared via glycothermal route. *J Supercond Nov Magn* 24:669
4. Adewale KY, Ezekiel IP, (2020) Synthesis and characterization of Mg doped ZnFe_2O_4 . research and reviews. *J Phys* 9(1):57–65
5. Adewale ky, Ezekiel IP, (2019) Magnetic and Mössbauer studies of $\text{Ca}_x\text{Zn}_{1-x}\text{Fe}_2\text{O}_4$ nanoferrites. *Int J Solid State Mater* 5(2):23–28
6. Airimioaei M, Ciomaga CE, Apostolescu N, Leontie L, Iordan AR, Mitoseriu L, Palamaru MN (2011) Synthesis and functional properties of the $\text{Ni}_{1-x}\text{Mn}_x\text{Fe}_2\text{O}_4$ ferrites. *J Alloy Compd* 509:8065–8072. <https://doi.org/10.1016/j.jallcom.2011.05.034>
7. Aisida SO, Akpa PA, Ishaq Ahmad M, Maaza Ezema FI (2019) Influence of PVA, PVP and PEG doping on the optical, structural, morphological and magnetic properties of zinc ferrite nanoparticles produced by thermal method. *Physica B: Condensed Matter* 571:130–136. <https://doi.org/10.1016/j.physb.2019.07.001>
8. Almessiere MA, Slimani Y, Auwal IA, Shirsath SE, Gondal MA, Sertkol M, Baykal A (2021) Biosynthesis effect of Moringa oleifera leaf extract on structural and magnetic properties of Zn doped Ca-Mg nano-spinel ferrites. *Arab J Chem* 14(8):103261. <https://doi.org/10.1016/j.arabjc.2021.103261>

9. Barsoum MW (2019) Fundamentals of ceramics, 2nd edn. CRC Press. <https://doi.org/10.1201/9781498708166>
10. Bertaut F, Blum P, Magnano G (1955) Structure of the monocalcium vanadate, chromite and ferrite. *Compt Rend Acad Sci Paris* 241:757–759
11. Candeia RA, Bernardi MIB, Longo E, Santos IMG, Souza AG (2004) Synthesis and characterization of spinel pigment CaFe_2O_4 obtained by the polymeric precursor method. *Mater Lett* 58:569–572
12. Birchall T, Greenwood NN, Reid AF (1969) Mössbauer, electron resonance, optical, and magnetic studies of iron(III) in oxide host lattices. *J Chem Soc A* 2382–2398
13. Das AK, Govindaraj R, Srinivasan A (2018) Structural and magnetic properties of sol-gel derived CaFe_2O_4 nanoparticles. *J Magn Magn Mater* 451:526–531, 103261. <https://doi.org/10.1016/j.jmmm.2017.11.102>
14. DeBenedetti S, Lang G, Ingalls R (1961) Electric quadrupole splitting and the nuclear volume effect in the ions of Fe^{57} . *Phys Rev Lett* 6:60. <https://doi.org/10.1103/PhysRevLett.6.60>
15. Debnath A, Bera A, Chattopadhyay KK, Saha B (2016) Studies on magnetic properties of chemically synthesized crystalline calcium ferrite nanoparticles. *AIP Conf Proc* 1731:050103. <https://doi.org/10.1063/1.4947757>
16. Gismelseed AM, Mohammed HM, Widatallah HM, Al-Rawas AD, Elzain ME, Yousif A (2010) Structure and magnetic properties of the $\text{Zn}_x\text{Mg}_{1-x}\text{Fe}_2\text{O}_4$ ferrites. *J Phys: Conf Ser* 217:012138
17. Hirabayashi D, Sakai Y, Yoshikawa T, Mochizuki K, Kojima Y, Suzuki K, Ohshita K, Watanabe Y (2006) Mössbauer characterization of calcium-ferrite oxides prepared by calcining Fe_2O_3 and CaO . *Hyperfine Interact* 167:809–813
18. Jain TK, Morales MA, Sahoo SK, Leslie-Pelecky DL, Labhasetwar V (2005) Ironoxide nanoparticles for sustained delivery of anticancer agents. *Mol Pharm* 2:194–205
19. Jalil RA, Zhang Y (2008) Biocompatibility of silica coated NaYF_4 upconversion fluorescent nanocrystals. *Biomaterials* 29:4122–4128
20. Jeon JW, Jung SM, Sasaki Y (2010) Formation of calcium ferrites under controlled oxygen potentials at 1273 K. *ISIJ Int* 50(8):1064–1070
21. Khan I, Saeed K, Khan I (2019) Nanoparticles: Properties, applications and toxicities. *Arab J Chem* 12(7):908–931. <https://doi.org/10.1016/j.arabjc.2017.05.011>
22. Khanna L, Verma NK (2013) Size-dependent magnetic properties of calcium ferrite nanoparticles. *J Magn Magn Mater* 336:1–7, 012138
23. Hirabayashi D, Sakai Y, Yoshikawa T, Mochizuki K, Kojima Y, Suzuki K, Ohshita K, Watanabe Y (2006) Mössbauer characterization of calcium-ferrite oxides prepared by calcining Fe_2O_3 and CaO . *Hyperfine Interact* 167:809. <https://doi.org/10.1007/s10751-006-9362-x>
24. Lavela P, Tirado JL (2007) CoFe_2O_4 and NiFe_2O_4 synthesized by sol-gel procedures for their use as anode materials for Li ion batteries. *J Power Sour* 172:379–387. <https://doi.org/10.1016/j.jpowsour.2007.07.055>
25. Li X, Chen C, Zhang F, Fang H, Huang X, Yi Z (2021) Photostriction of ferrites under visible light. *ACS Appl Electron Mater* 3(6):2534–2542, 012138. <https://doi.org/10.1021/acsaelm.1c00077>
26. Lu SP, Evan BJ (1976) High temperature electronic structure of Fe_3O_4 . *AIP Conf Proc* 34:181. <https://doi.org/10.1063/1.2946059>
27. McBride MB, Frenchmeyer M, Kelch SE, Aristilde L (2017) Solubility, structure, and morphology in the co-precipitation of cadmium and zinc with calcium-oxalate. *J Colloid Interface Sci* 486:309–315. <https://doi.org/10.1016/j.jcis.2016.09.079>
28. Meena SS, Srinivas Ch, Sudarsan V, Tirupanyam BV, Rao KR, Sastry DL, Yusuf SM (2012) Mössbauer spectroscopic study of heat-treated $(\text{Ni}_{0.5}\text{Zn}_{0.5})\text{Fe}_2\text{O}_4$ nanoparticles. *AIP Conf Proc* 1447:231–245, 012138. <https://doi.org/10.1063/1.4710463>
29. Pandey B, Litterst FJ, Baggio-Saitovitch EM (2015) Preferential spin canting in nanosize zinc ferrite. *J Magn Magn Mater* 385:412–417
30. Pettit GA, Forester DW (1971) Mössbauer study of cobalt-zinc ferrites. *Phys Rev B* 4:3912

31. Ruan J, Wang K, Song H, Xu X, Ji JJ, Cui DX (2011) Biocompatibility of hydrophilic silica-coated CdTe quantum dots and magnetic nanoparticles. *Nanoscale Res Lett* 6(299):1–13
32. Shobana MK, Sankar S (2009) Structural, thermal and magnetic properties of $\text{Ni}_{1-x}\text{Mn}_x\text{Fe}_2\text{O}_4$ nanoferrites. *J Magn Magn Mater* 321:2125–2128
33. Sulaiman NH, Ghazali MJ, Majlis BY, Yunus J, Razali M (2015) Superparamagnetic calcium ferrite nanoparticles synthesized using a simple sol-gel method for targeted drug delivery. *Bio-Med Mater Eng* 26:S103–S110. <https://doi.org/10.3233/BME-151295>
34. Sorescu M, Diamandesu L, Pelemedu R, Roy R, Yadiji P (2004) Structural and magnetic properties of NiZn ferrites prepared by microwave sintering. *J Magn Magn Mater* 279:195–201. <https://doi.org/10.1016/j.jmmm.2004.01.079>
35. Tiwari P, Verma R, Kane SN, Tatarchuk T, Mazaleyrat F (2019) Effect of Zn addition on structural, magnetic properties and anti-structural modeling of magnesium-nickel nano ferrites. *Mater Chem Phys* 229:78–86. <https://doi.org/10.1016/j.matchemphys.2019.02.030>
36. Van D (1977) Magnetic and structural phase transitions in sodium intercalates Na_xVS_2 and Na_xVSe_2 . *Physica* 955:86-88B. [https://doi.org/10.1016/0378-4363\(77\)90782-3](https://doi.org/10.1016/0378-4363(77)90782-3)
37. Vigneswari T, Raji P (2017) Structural and magnetic properties of calcium doped nickel ferrite nanoparticles by co-precipitation method. *J Mol Struct* 1127:515–521. <https://doi.org/10.1016/j.molstruc.2016.07.116>
38. Zheng W, Gao F, Gu H (2005) Magnetic polymer nanospheres with high and uniform magnetite content. *J Magn Magn Mater* 288:403–410, 012138

Constructing Exact Solutions to Modelling Problems



Mathew O. Aibinu, Surendra C. Thakur, and Sibusiso Moyo

Abstract Modelling of several processes and phenomena, which occur in sciences and engineering, often lead to Nonlinear Partial Differential Equations (NPDEs). Reaction–diffusion systems are members of NPDEs which can be described as mathematical models with applications in diverse physical phenomena. Obtaining the solutions of modelling problems is often a big challenge due to several conditions and parameters which are involved. This study demonstrates how to construct the solutions of modelling problems. A modified method of functional constraints is proposed for constructing exact solutions to nonlinear equations of reaction–diffusion type with delay and which are associated with variable coefficients. Arbitrary functions are present in the solutions, and they also contain free parameters, which make them suitable for usage in solving certain modelling problems, testing numerical, and approximate analytical methods. Specific examples of nonlinear equations of reaction–diffusion type with delay are given and their exact solutions are presented.

Keywords Exact solutions · Generalized traveling-wave · Heat and wave equations · Reaction–diffusion

M. O. Aibinu (✉)

Institute for Systems Science & KZN E-Skill CoLab, Durban University of Technology, Durban 4000, South Africa

e-mail: moaibinu@yahoo.com; mathewa@dut.ac.za

DSI-NRF Centre of Excellence in Mathematical and Statistical Sciences (CoE-MaSS), Johannesburg, South Africa

National Institute for Theoretical and Computational Sciences (NITheCS), Johannesburg, South Africa

S. C. Thakur

KZN E-Skill CoLab, Durban University of Technology, Durban 4000, South Africa

S. Moyo

Institute for Systems Science & Office of the DVC Research, Innovation & Engagement Milena Court, Durban University of Technology, Durban 4000, South Africa

© The Minerals, Metals & Materials Society 2022

K. Inal et al. (eds.), *NUMISHEET 2022*, The Minerals, Metals & Materials Series, https://doi.org/10.1007/978-3-031-06212-4_4

Abbreviations

NPDEs	Nonlinear Partial Differential Equations
ODEs	Ordinary Differential Equations
RDEs	Reaction–Diffusion Equations

Introduction

The roles which Nonlinear Partial Differential Equations (NPDEs) play are prominent in the description and analysis of the real-life processes and phenomena. Therefore, it is pivotal to seek the ways of obtaining the exact solutions of NPDEs for a proper and accurate analysis. Several processes and phenomena which occur in sciences and engineering lead to NPDEs as there are several conditions and parameters to be considered in the modeling of such systems. Reaction–Diffusion Equations (RDEs) are members of NPDEs. Reaction–diffusion systems can be described as mathematical models which find applications in diverse physical phenomena. In its simplest form in one spatial dimension, RDE has the form

$$u_t = Du_{xx} + H(u), \quad (1)$$

where $u(x, t)$ denotes the unknown function, H accounts for all local reactions, and D is a diffusion coefficient (which is a constant) (See e.g., [1]). RDEs are pervading in the mathematical modeling of the systems which occur in biology, chemistry, complex physics phenomena, engineering, and mechanics [2]. RDEs delineate the chemical reactions and diffusion processes. Basically, many real-life processes do not only depend on the present state but also on past occurrences. Also, the dynamical systems are constituted by the time delay. The study of nonlinear delay RDEs provides a fundamental tool for the quantitative and qualitative analyses of various dynamical systems such as infections. For RDEs with delay, the kinetic function H which denotes the chemical reactions rates is a function of both $u = u(x, t)$ and $w = u(x, t - \tau)$, which represent the sought concentration function and delayed argument, respectively. Two special cases which can arise are $H(u, w) = H(w)$ and $H(u, w) = H(u)$. A system with local non-equilibrium media is described by $H(u, w) = H(w)$. These are systems which possess inertial properties and reactions will always begin after a time τ . $H(u, w) = H(u)$ represents the classical local equilibrium case [3].

NPDEs are universal in nature and for finding their solutions, several methods have been employed which include spectral collocation and waveform relaxation [4–6], adomian decomposition [7, 8], Tan-Cot [9], residual power series [10], and perturbation [11, 12]. However, there are disadvantages which are commonly associated with these methods. There are conditions which make the universal application of these listed methods and others to be impossible. The objects are different in

their geometric shapes. The reaction kinetics and type of fluid flow are erratic. The worthlessness in the presence of singular points is indisputable. Obtaining the exact solutions is imperative for proper analysis of the processes which are under consideration (localization, nonuniqueness, blowup regimes, spatial, etc.).

Subsequently, the term “exact solution” in relating to NPDEs will refer to where the solution can be expressed in:

- (i) terms of elementary functions;
- (ii) closed form with definite or/and indefinite integrals;
- (iii) terms of solutions to Ordinary Differential Equations (ODEs) or systems of such equations.

Accepted form for exact solutions also includes the combinations of cases listed above (See e.g., [3, 13–17]).

Let $H(u, w)$ denote an arbitrary function which takes two arguments u and w . Consider reaction–diffusion problems of the form

$$c(x)u_t = [a(x)u_x]_x + b(x)H(u, w)u_x, \quad w = u(x, t - \tau), \tag{2}$$

where $a = a(x)$, $b = b(x)$, $c = c(x)$ are appropriate functions with precise roles in the equation. Namely, $a > 0$ casts the diffusion of the second-order divergence form operator, b models the reaction term, c represents a time weight factor (both b and c also casting nonlinearities on the unknown), and $\tau > 0$ is the time delay. We construct the exact solutions of (2) in the form of generalized traveling-wave equations. We apply our results to obtain the solutions of certain essential modelling problems which are peculiar to metal forming processes.

Solutions of Generalized RDEs with Delay

The exact solutions of (2) will be constructed in the form

$$u = U(y), \quad y = t + \int h(x)dx, \tag{3}$$

which is the generalized traveling-wave equations. Substitute (3) into (2) to obtain

$$a(x)h^2U''_{yy} + ([a(x)h]'_x - c(x))U'_y + b(x)hH(U, W)U'_y = 0, \tag{4}$$

where $W = U(y - \tau)$ and $h = h(x)$. The coefficients of the equation are chosen such that they conform to the relations

$$b(x) = a(x)h(x), \tag{5}$$

$$[a(x)h]'_x = -ka(x)h^2(x) + c(x), \tag{6}$$

where k is a constant. The relations reduce (4) to

$$U''_{yy} + [H(U, W) - k] U'_y = 0, \quad W = U(y - \tau), \tag{7}$$

which is a delay ODE. Equation (6) can be written in standard form as

$$a(x)h'_x + ka(x)h^2 + a'(x)h - c(x) = 0. \tag{8}$$

Constructing Exact Solutions When the Function $h(x)$ Is not Given

The relation (8) forms a Riccati ODE for $h = h(x)$ when the functions $a(x)$ and $c(x)$ are given. Degenerate and nondegenerate cases will be considered for the Riccati ODE (8).

Degenerate case. For $k = 0$, the general solution for the degenerate form of Riccati equation (8) has the solution which is given by

$$h(x) = \frac{\int a(x)c(x)dx + q}{a(x)}, \tag{9}$$

where q signifies an arbitrary constant.

Example 1 Let $0 < x < \pi$, consider the case where $a(x) = \cos(x)$ and $c(x) = 1$. By (8), $h(x) = \tan(x)$, where it has been taken that $q = 0$. Equation (5) is applied to obtain that $b(x) = \sin(x)$. Thus, for arbitrary functions $H(u, w)$, the nonlinear RDE

$$u_t = [\cos(x)u_x]_x + \sin(x)H(u, w)u_x, \quad w = u(x, t - \tau),$$

admits the generalized traveling-wave equations

$$u = U(y), \quad y = t + \tan(x),$$

as its exact solution, where $U(y)$ is determined by

$$U''_{yy} + H(U, W) U'_y = 0, \quad W = U(y - \tau). \tag{10}$$

Nondegenerate case. When $k \neq 0$, let

$$h = \frac{1}{k} \frac{\varphi'_x}{\varphi}. \tag{11}$$

Substitution (11) into (9) gives

$$\frac{a(x)}{k} \left(\frac{\varphi''_{xx}}{\varphi} - \left(\frac{\varphi'_x}{\varphi} \right)^2 \right) + ka(x) \left(\frac{1}{k} \frac{\varphi'_x}{\varphi} \right)^2 + \frac{a'(x)}{k} \frac{\varphi'_x}{\varphi} - c(x) = 0. \quad (12)$$

Simplified form of (12) is

$$a(x)\varphi''_{xx} + a'(x)\varphi'_x - kc(x)\varphi = 0, \quad (13)$$

which is a linear second-order ODE. For the exact solutions of (13) with various functions $a(x)$ and $q(x)$, interested readers are referred to [18, 19].

Example 2 Taking $a = c = 1$ in (13) gives its general solution as

$$\varphi = \begin{cases} A_1 \cosh(\phi x) + A_2 \sinh(\phi x), & \text{if } k = \phi^2 > 0, \\ A_1 \cos(\phi x) + A_2 \sin(\phi x), & \text{if } k = -\phi^2 < 0, \end{cases} \quad (14)$$

where the arbitrary constants are A_1 and A_2 . By using (11), it can be obtained from (14) when $A_1 = 1, A_2 = 0$, and $k = \phi^2 (> 0)$ that

$$h(x) = \coth(\phi x). \quad (15)$$

Substitute (15) into (5) to obtain

$$b(x) = \coth(\phi x).$$

Thus, for arbitrary $H(u, w)$,

$$u_t = u_{xx} + \coth(\phi x)G(u, w)u_x,$$

admits the generalized traveling-wave equations

$$u = U(y), y = t + \ln |\sinh(\phi x)|,$$

as its exact solution, where $U(y)$ is determined by the delay ODE

$$U''_{yy} + [H(U, W) - \phi^2]U'_y = 0, \quad W = U(y - \tau).$$

Constructing Exact Solutions When the Function $h(x)$ Is Given

Given $h = h(x)$ in (8), the derived generalized traveling-wave equations (3) solves certain RDEs with delay of the form (2) provided (5) and (3) are satisfied. Such derived generalized traveling-wave equations are said to be the exact solutions of

the corresponding RDEs. Solving the Riccati ODE (8) is not required as h has been given. An algebraic equation is required to be solved if h in (8) is already given.

Example 3 Degenerate and nondegenerate cases will be considered for arbitrary given functions $a(x)$ and $h = h(x)$.

(I) Degenerate case $k = 0$. Apply (5) to obtain

$$b(x) = a(x)h,$$

and by (8)

$$c(x) = a(x)h'_x + a'(x)h.$$

Thus, for arbitrary function $H(u, w)$,

$$[a(x)h'_x + a'(x)h]u_t = [a(x)u_x]_x + a(x)hH(u, w)u_x,$$

admits the generalized traveling-wave equations

$$u = U(y), \quad y = t + \int h dx, \tag{16}$$

as its exact solution, where $U(y)$ is determined by (10).

(II) Nondegenerate case $k \neq 0$. By (8),

$$c(x) = a(x)h'_x + ka(x)h^2 + a'(x)h.$$

Thus, for arbitrary function $H(u, w)$,

$$[a(x)h'_x + ka(x)h^2 + a'(x)hh]u_t = [a(x)u_x]_x + a(x)hH(u, w)u_x,$$

admits the generalized traveling-wave equations (16) as its exact solution, where $U(y)$ is determined by (7).

Application to Metal Forming Processes

The metal forming processes are broad. The results which have been obtained will be applied to an essential metal forming process which is the heating of a uniform metal rod of length L and thermal diffusivity K_0 .

Derivation of Heat and Wave Equations in 3D

The derivation of heat and wave equations in 3D is presented in this section to make this study a complete paper. For a full account of the derivation steps, the readers are referred to consult [20, 21]. Let V be an arbitrary 3D subregion of \mathbb{R}^3 (i.e. $V \subset \mathbb{R}^3$) and temperature $u = u(x, t)$ be defined for all points $\mathbf{x} = (x, y, z) \in V$. The heat energy in the subregion V is given by

$$\text{heat energy} = \int \int_V \alpha \rho u \, dV,$$

where ρ is the density of the rod, α is the specific heat, which is the energy required to raise a unit mass of the substance by 1 unit in temperature. In this study, we shall use these basic units: M mass, L length, T time, U temperature, and $[\alpha] = L^2 T^{-2} U^{-1}$. Let S denote the boundary of V and $\hat{\mathbf{n}}$ be the outward unit normal at the boundary S . We seek the heat flux through S which is the normal component of the heat flux vector ϕ , $\phi \cdot \hat{\mathbf{n}}$. Notice that $\phi \cdot \hat{\mathbf{n}} < 0$ if ϕ is directed inward and the outward flow of heat is negative. The sum $\phi \cdot \hat{\mathbf{n}}$ is taking over the entire closed surface S to get the total heat energy flowing across S . The total heat energy flowing across is denoted by $\int \int_S dS$. It can be recalled from the conservation of energy principle that

$$\begin{array}{l} \text{rate of change} \\ \text{of heat energy} \end{array} = \begin{array}{l} \text{heat energy into } V \text{ from} \\ \text{boundaries per unit time} \end{array} + \begin{array}{l} \text{heat energy generated} \\ \text{in solid per unit time} \end{array}$$

Applying the conservation of energy principle gives

$$\frac{d}{dt} \int \int \int_V \alpha \rho u \, dV = - \int \int_S \phi \cdot \hat{\mathbf{n}} dS + \int \int \int_V Q dV. \tag{17}$$

According to divergence theorem (also known as Gauss’s Theorem), for any volume V with closed smooth surface S ,

$$\int \int \int_V \nabla \cdot \mathbf{A} dV = - \int \int_S \mathbf{A} \cdot \hat{\mathbf{n}} dS, \tag{18}$$

where \mathbf{A} is any function that is smooth (i.e. continuously differentiable) for $\mathbf{x} \in V$ and

$$\nabla = \left(\frac{\partial}{\partial x}, \frac{\partial}{\partial y}, \frac{\partial}{\partial z} \right).$$

Applying divergence theorem to (17) leads to

$$\int \int \int_V \left(\alpha \rho \frac{\partial u}{\partial t} + \nabla \cdot \phi - Q \right) dV = 0. \tag{19}$$

It is clear that the integrand must be everywhere zero since $V \subset \mathbb{R}^3$ and the integrand is assumed continuous. Thus,

$$\alpha\rho \frac{\partial u}{\partial t} + \nabla \cdot \phi - Q = 0. \quad (20)$$

By Fourier's law of heat conduction (for 3D),

$$\phi = -K_0 \nabla u, \quad (21)$$

where K_0 is called the thermal diffusivity. Substitute (21) into (20) to obtain 3D Heat Equation

$$\frac{\partial u}{\partial t} = a \nabla^2 u + \frac{Q}{\alpha\rho}, \quad (22)$$

where $a = K_0/(\alpha\rho)$ and

$$\nabla^2 = \left(\frac{\partial^2}{\partial x^2}, \frac{\partial^2}{\partial y^2}, \frac{\partial^2}{\partial z^2} \right).$$

Normalizing with

$$\tilde{x} = \frac{x}{l}, \quad \tilde{t} = \frac{a}{l^2} t,$$

to obtain a non-dimensional Heat Equation

$$\frac{\partial u}{\partial t} = \nabla^2 u + H, \quad (23)$$

where $H = l^2 Q/K_0$.

Construction of Solution of Heat and Wave Equations

We seek for the exact solution of (23) in the form of the generalized traveling-wave equations (3). Substitute (3) into (23) to obtain

$$h^2 U''_{yy} - U'_y + H = 0, \quad (24)$$

where $H = H(U)$ and $h \equiv 1$. Consequently, it can be deduced that (23) (for 1D Heat Equation) admits the generalized traveling-wave equations

$$u = U(y), \quad y = t + x, \quad (25)$$

as its exact solution, where $U(y)$ is determined by

$$U''_{yy} - U'_y + H = 0.$$

Conclusion: Recently, exact solutions of RDEs and reaction–diffusion systems have attracted great attention. In this paper, exact solutions are presented for RDEs with delay and variable coefficients. The presence of arbitrary functions and free parameters in the solutions vouches for their feasible application in solving certain modeling problems such as diffusion of pollutants and population models, where the population is spatially distributed. It also makes the obtained solutions to be suitable for usage in testing the numerical and approximate analytical methods. The obtained results also find applications in finding the exact solutions of other forms of partial differential equations which are more complex. Our results are specifically applied as an illustration to obtain the solutions of certain essential modelling problems which are peculiar to metal forming processes.

Acknowledgements The first author acknowledges with thanks the postdoctoral fellowship and financial support from the DSI-NRF Center of Excellence in Mathematical and Statistical Sciences (CoE-MaSS). Opinions and conclusions are those of the authors and are not necessarily to be attributed to the CoE-MaSS.

References

1. Kolmogorov A, Petrovskii I, Piskunov N (1937) Study of a diffusion equation that is related to the growth of a quality of matter and its application to a biological problem. *Mosc Univ Math Bull* 1(6):1–25
2. Murray JD (1989) *Mathematical biology*. Springer, Berlin
3. Sorokin VG, Vyazmin A, Zhurov AI, Reznik V, Polyanin AD (2017) The heat and mass transfer modeling with time delay. *Chem Eng Trans* 57:1465–1470. <https://doi.org/10.3303/CET1757245>
4. Jackiewicz Z, Zubik-Kowal B (2006) Spectral collocation and waveform relaxation methods for nonlinear delay partial differential equations. *Appl Numer Math* 56(3–4):433–443
5. Kumbinaraiah S (2019) Numerical solution of partial differential equations using Laguerre wavelets collocation method. *Int J Manage Technol Eng* 9(1):3635–3639
6. Aziz I, Siraj-ul-Islam I, Asif M (2017) Haar wavelet collocation method for three-dimensional elliptic partial differential equations. *Comput Math Appl* 73(9):2023–2034
7. Alderemy AA, Elzaki TM, Chamekh M (2019) Modified Adomian decomposition method to solve generalized Emden–Fowler systems for singular IVP. *Math Probl Eng* 2019:6, Article ID 6097095. <https://doi.org/10.1155/2019/6097095>
8. Elzaki TM, Chamekh M (2018) Solving nonlinear fractional differential equations using a new decomposition method. *Univ J Appl Math Comput* 6:27–35
9. Al-Shaer M (2013) Solutions to nonlinear partial differential equations by Tan-Cot method. *IOSR J Math* 5(3):6–11
10. Rajarama J, Chakraverty S (2018) Residual power series method for solving time-fractional model of vibration equation of large membranes. *J Appl Comput Mech* 5(4):603–615
11. Bilidik N (2017) General convergence analysis for the perturbation iteration technique. *Turk J Math Comput Sci* 6:1–9
12. Jena RM, Chakraverty S (2019) A new iterative method based solution for fractional Black-Scholes option pricing equations (BSOPE). *SN Appl Sci* 1(1):95. <https://doi.org/10.1007/s42452-018-0106-8>
13. Polyanin AD (2019) Generalized traveling-wave solutions of nonlinear reaction-diffusion equations with delay and variable coefficients. *Appl Math Lett* 90:49–53. <https://doi.org/10.1016/j.aml.2018.10.012>

14. Polyanin AD (2019) Functional separable solutions of nonlinear reaction-diffusion equations with variable coefficients. *Appl Math Comput* 347:282–292. <https://doi.org/10.1016/j.amc.2018.10.092>
15. Polyanin AD, Sorokin VG (2020) New exact solutions of nonlinear wave type PDEs with delay. *Appl Math Lett* 108:106512. <https://doi.org/10.1016/j.aml.2020.106512>
16. Polyanin AD, Sorokin VG (2021) A method for constructing exact solutions of nonlinear delay PDEs. *J Math Anal Appl* 494(2):124619. <https://doi.org/10.1016/j.jmaa.2020.124619>
17. Aibinu MO, Thakur SC, Moyo S (2021) Exact solutions of nonlinear delay reaction-diffusion equations with variable coefficients. *PartL Differ Equ Appl Math* 4:100170. <https://doi.org/10.1016/j.padiff.2021.100170>
18. Polyanin AD, Zaitsev VF (2003) *Handbook of ordinary differential equations: exact solutions, methods, and problems*, 2nd edn. Chapman & Hall/CRC Press, Boca Raton, pp 93–192
19. Polyanin AD, Zaitsev VF (2018) *Handbook of ordinary differential equations: exact solutions, methods, and problems*, 3rd edn. CRC Press, Boca Raton, 1496 p
20. Guenther RB, Lee JW (1996) *Partial differential equations of mathematical Physics and integral equations*, 1st edn. Dover Publications Inc., New York, pp 19–187
21. Hancock MJ (2006) *Linear partial differential equations: the heat and wave equations in 2D and 3D*. MIT OpenCourseWare 1–39. <https://ocw.mit.edu/courses/mathematics/18-303-linear-partial-differential-equations-fall-2006/lecture-notes/pde3d.pdf>. Accessed 30 March 2022

Crystal Plasticity Modelling of Localization in Precipitation Hardened AA6060



Y. Larry Li, Christopher P. Kohar, Raja K. Mishra, and Kaan Inal

Abstract Precipitation hardened aluminum alloys are used extensively in the construction of vehicle components and demand high fidelity models in order to simulate their complex precipitate mechanics. In this work, a crystal plasticity approach utilizing an Eshelby homogenization scheme is proposed to capture the single crystal response of age-hardened AA6060. The constitutive framework uses the precipitate's morphology and orientation for the direct simulation of the alloy's mechanical behaviour. A numerical study is conducted with the developed model to investigate the effects of different precipitate properties on the material's formability. The model utilizes a full-field finite element framework in combination with a plastic instability criterion to simulate the alloy's localization response. Results of this study highlight the significance of incorporating precipitates into constitutive models for the prediction of formability in age-hardened materials.

Keywords Crystal plasticity finite element method · Precipitation hardening · Homogenization · Formability

Introduction

Reducing overall vehicle weight is an effective strategy for controlling carbon emissions in the automotive industry. To satisfy regulatory demands imposed by the government, automakers have started to integrate new generations of advanced lightweight alloys to make passenger vehicles even lighter. 6000-series aluminum alloys are particularly favourable for these initiatives as they have relatively high specific strengths that allow them to be used for various applications across the vehicle. These aluminum alloys derive their strength from the growth of a second phase of precipitates, which impede against dislocation movement during large plastic deformation. Over the last two decades, significant efforts have been made towards the characterization of precipitates in age-hardened materials [1, 2]. The

Y. L. Li (✉) · C. P. Kohar · R. K. Mishra · K. Inal
Department of Mechanical and Mechatronics Engineering, University of Waterloo, Waterloo N2L 3G1, Canada
e-mail: y493li@uwaterloo.ca

improvements in experimental techniques and the discovery of new characteristics have enabled the development of advanced and more accurate physics-based models to capture precipitate-induced effects [2–4].

An area of study that has been relatively neglected is the effect of ageing on the formability of aluminum alloys. Formability is especially important for these lightweight materials as they tend to be less formable than the steels that they are expected to replace. The formability of metals is most commonly described by the forming limit diagram (FLD), which was first introduced by Keeler and Goodwin [5, 6]. An FLD shows a plot of major and minor strains corresponding to the onset of localized necking for various strain paths. Unfortunately, the experimental procedure to obtain a single FLD is time-consuming and expensive; thus, a considerable amount of effort has been made towards the development of formability models from theoretical means [7, 8]. Existing studies have shown that the simulation of an FLD can depend on the integrity of the underlying constitutive model [9, 10]. Since the properties of age-hardened materials are strongly influenced by their precipitate distribution, constitutive models should include information about the precipitates for better predictions of their properties. Incorporating advanced constitutive models that capture precipitate mechanics will allow for more accurate characterization of the alloy's formability for a given ageing condition.

In the present work, the previously developed crystal plasticity-based constitutive model for precipitation-hardenable alloys by Li et al. [11] is employed within a finite element framework to simulate the formability of AA6060. The approach taken in this work uses key microstructural components, such as precipitate size and quantity, as direct parameters for the simulation of the mechanical response. These parameters can be obtained experimentally from transmission electron microscopy (TEM) of the underlying precipitate distribution. The constitutive model uses a micromechanics framework that directly incorporates the loading and unloading of precipitates that is associated with age-hardened materials. Finally, an imperfection-less method of generating FLDs is proposed to calculate the localized necking response. The framework uses an instability criterion to capture the ratio of plastic strain rates between the localized and un-localized regions of the crystal plasticity finite element (CPFE) model.

Constitutive Model

This work utilizes the constitutive framework presented in Li et al. [11]. This model includes a hardening model and an elastic-viscoplastic homogenization scheme to capture the mechanics of the precipitate.

Crystal Plasticity Constitutive Framework

A rate-dependent crystal plasticity framework based on the formulation by Peirce et al. [12] is used in this work. The overall deformation gradient, \mathbf{F} , is decomposed into

$$\mathbf{F} = \mathbf{F}^* \mathbf{F}^P \quad (1)$$

where \mathbf{F}^P is the plastic component and \mathbf{F}^* is the elastic component of deformation. The rate-sensitive constitutive law is defined by

$$\hat{\boldsymbol{\sigma}} = \mathcal{L}^e : \mathbf{D} - \dot{\boldsymbol{\sigma}}^0 - \boldsymbol{\sigma} \text{tr}(\mathbf{D}) \quad (2)$$

where $\hat{\boldsymbol{\sigma}}$ is the Jaumann rate of Cauchy stress, \mathcal{L}^e is the elastic modulus, $\dot{\boldsymbol{\sigma}}^0$ is the viscoplastic stress rate, and \mathbf{D} is the strain rate tensor. The plastic slip rate on each slip system, $\dot{\gamma}^{(\alpha)}$, is defined as

$$\dot{\gamma}^{(\alpha)} = \dot{\gamma}_0 \frac{\tau^{(\alpha)}}{g^{(\alpha)}} \left| \frac{\tau^{(\alpha)}}{g^{(\alpha)}} \right|^{\frac{1}{m}-1} \quad (3)$$

and is used to calculate $\dot{\boldsymbol{\sigma}}^0$. Here, $\dot{\gamma}_0$ is a reference shear strain, m is the rate sensitivity exponent, $\tau^{(\alpha)}$ is the resolved shear stress, and $g^{(\alpha)}$ represents the hardening on slip system α . Further details of this formulation can be found in Inal et al. [13].

Hardening Model

The hardening term, $g^{(\alpha)}$, is defined according to

$$g^{(\alpha)} = \tau_0 + \tau_d + \tau_p \quad (4)$$

where τ_0 is the initial yield stress of the matrix material, τ_d is a forest hardening term due to internal dislocation content, and τ_p is the hardness contribution from precipitation hardening. τ_d is captured using a standard dislocation density hardening law

$$\tau_d = \kappa \mu b \sqrt{\sum_{\alpha} \rho^{(\alpha)}} \quad (5)$$

where κ is the obstacle strength of dislocation–dislocation interactions, μ is the shear modulus of the crystal, b is the magnitude of the Burgers vector, and $\rho^{(\alpha)}$ is the dislocation density on slip system α . The dislocation content evolution is described by a Kocks–Mecking-type equation [14]

$$d\rho^{(\alpha)} = 1/(k_1 * b) \sqrt{\sum_{\alpha} \rho^{(\alpha)} d\gamma^{(\alpha)}} - k_2 \rho^{(\alpha)} d\Gamma \quad (6)$$

where k_1 and k_2 are constants related to the multiplication and recovery of dislocations, respectively, and $d\Gamma = \sum_{\alpha} |d\gamma^{(\alpha)}|$ is the accumulated shear increment on all slip systems.

The precipitate hardening term, τ_p , is incorporated following the approach by Esmaeili et al. [3]. The effect of needle-like precipitates on the alloy's strength is given by

$$\tau_p = \frac{F}{L_f b} \quad (7)$$

where F is the obstacle strength and L_f is the effective mean spacing of precipitates. The precipitates are classified into two regimes based on the radius of the smallest cross section

$$\begin{aligned} F &= 2\beta\mu b^2 \left(\frac{r}{r_c}\right) \quad \text{for } r < r_c \\ F &= 2\beta\mu b^2 \quad \text{for } r \geq r_c \end{aligned} \quad (8)$$

where β is a constant associated with the tension of a dislocation line, μ is the shear modulus of the matrix, r is the mean radius of the precipitates, and r_c is the critical radius of the shearable–non-shearable transition. The effective mean spacing of precipitate obstacles, L_f , is defined as

$$\begin{aligned} L_f &= \sqrt{\frac{\sqrt{3}\pi r_c}{f} r} - 2r \quad \text{for } r < \frac{\sqrt{3}}{2} * r_c \\ L_f &= \sqrt{\frac{2\pi}{f} r} - 2r \quad \text{for } r \geq \frac{\sqrt{3}}{2} * r_c \end{aligned} \quad (9)$$

where f is the volume fraction of the precipitate phase.

Homogenization Scheme

The elastic–viscoplastic homogenization scheme by Mercier and Molinari [15] is used to model the precipitate phase. This homogenization is accomplished at the

single crystal level. The precipitates are assumed to be spheroidal and their constitutive behaviour defined using crystal elasticity. Under a Mori–Tanaka assumption, the following interaction law can be obtained

$$\mathbf{D}_i - \mathbf{D}_0 = \left(\mathcal{L}_0^e - (\mathbf{P}_i^e)^{-1} \right) : (\hat{\boldsymbol{\sigma}}_i - \hat{\boldsymbol{\sigma}}_0) + \mathbf{n}^e \left(\mathcal{L}_0^{vp} - (\mathbf{P}_i^{vp})^{-1} \right) : (\boldsymbol{\sigma}_i - \boldsymbol{\sigma}_0) \quad (10)$$

where \mathbf{D}_i is the strain rate in phase i ; \mathbf{D}_0 is the strain rate in the matrix phase; \mathcal{L}_0^e and \mathcal{L}_0^{vp} are the elastic and viscoplastic moduli of the matrix phase; \mathbf{P}_i^e and \mathbf{P}_i^{vp} are fourth-order tensors calculated with the use of Green functions for the elastic and viscoplastic moduli, respectively; and \mathbf{n}^e is a parameter used to adjust the interaction strength. The current framework assumes that three separate precipitate phases exist within the matrix. The longitudinal axis of each phase is aligned to one of the $\langle 100 \rangle$ lattice directions, as observed experimentally in artificially aged 6000-series alloys [16, 17]. Finally, the macroscopic properties of each single crystal are found by volume averaging the properties within each phase such that: $\bar{\boldsymbol{\sigma}} = \sum_i^N f_i \boldsymbol{\sigma}_i$ and $\bar{\mathbf{D}} = \sum_i^N f_i \mathbf{D}_i$, where f_i is the volume fraction of phase i .

Finite Element Model

The crystal plasticity constitutive model is implemented into a user-defined subroutine (UMAT) using the commercial finite element software, LS-DYNA, following the methodology outlined by Rossiter et al. [18]. The implementation uses the orientations and morphologies obtained from electron backscattered diffraction (EBSD) imaging as an input into the finite element model. The representative volume element (RVE) used in this work is shown in Fig. 1a, which was reconstructed from three orthogonal EBSD scans of an AA6060 alloy [19].

Determining the Forming Limit

The forming limit curve is generated by performing multiple simulations with various principal strain ratios, $\rho = \frac{\epsilon_{22}}{\epsilon_{11}}$. Each ρ corresponds to a loading condition under a different proportional strain path. The strain ratios are enforced using velocity boundary conditions at the surface nodes of the RVE, as illustrated in Fig. 1b. It should be noted that the surface nodes normal to the X- and Y-axes remain parallel throughout deformation, which guarantees periodicity in the X- and Y-directions. The velocities are also prescribed incrementally to ensure that the major and minor strain rates, $\dot{\epsilon}_{11}$ and $\dot{\epsilon}_{22}$, are constant throughout the simulations.

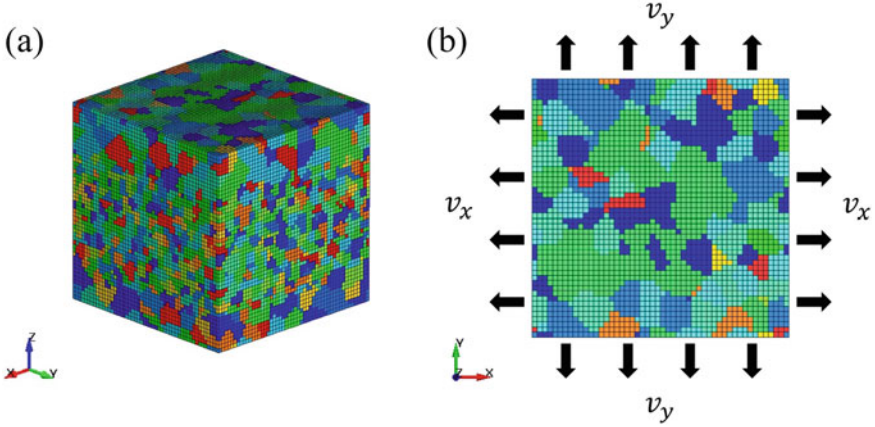


Fig. 1 **a** Initial 3D RVE used in CPFE simulations (125,000 elements). **b** Top view of RVE showing applied velocity boundary conditions. Surface nodes on the Z-axis are left unconstrained

The primary advantage of the proposed formability framework is that localization appears naturally within the RVE without the need for the predefined band or imperfection utilized in Marciniak and Kuczynski (MK)-based frameworks [7, 9, 10, 20, 21]. The microstructural heterogeneities from the distribution and morphology of grains are directly responsible for the resulting localization pattern. Furthermore, force equilibrium is automatically implied across the developed neck since the deformed geometry is directly computed from the solution of the finite element problem. Normally, a criterion exists that relates the strain rate within the developed neck to the strain rate outside of the neck to determine the forming limits [8]. In this work, a new criterion is introduced to determine the elements in the simulation that belong to the necked region. This is accomplished by looking at the top n percentage of elements with the highest plastic strain rates and comparing their volume-averaged plastic strain rate value to the bottom n percentage. This criterion is applicable because the elements with the highest plastic strain rates are most likely to be a part of the necked region, and the opposite is true for the elements with the lowest plastic strain rates. If the average plastic strain rate in the top straining elements, $\dot{\epsilon}_{high}^p$, is higher than the average plastic strain rate of the lowest straining elements, $\dot{\epsilon}_{low}^p$, by some order of magnitude, then the material is deemed to have localized. The plastic strain rate ratio, q , between $\dot{\epsilon}_{high}^p$ and $\dot{\epsilon}_{low}^p$ is defined as

$$q = \frac{\dot{\epsilon}_{high}^p}{\dot{\epsilon}_{low}^p} \quad (11)$$

Plastic instability is said to have occurred when $q > \lambda$, where λ is a predetermined constant to determine the onset of necking. This constant, λ , is determined by measuring the plastic strain rate ratio of an RVE that undergoes in-plane tension

($\rho = 0.0$) at a major strain level that corresponds to the onset of localization from experimental measurements of in-plane tension. Once λ is determined, it is used as a criterion for all other strain paths. The major and minor strains at the boundary of the RVE are then used to characterize the forming limit.

Results and Discussion

Three ageing conditions that generate different precipitate structures are selected to explore the effect of precipitation hardening on formability. These are representative of peak-aged, under-aged, and over-aged conditions. The precipitate distribution at each temper is informed from literature using experimental studies of 6000-series alloys with similar compositions [16, 17]. Table 1 presents the parameters selected for each ageing condition that is used in the forming simulations.

This study assumes that the crystalline microstructure and the constitutive model parameters for the matrix and precipitate remain constant across the various ageing conditions. The constitutive model parameters are identified following the procedure outlined in Li et al. [11], using a cyclic shear experiment to fit both the micromechanics framework and the strain hardening rate for a peak-aged AA6060 alloy. Table 2 presents the calibrated coefficients for the crystal plasticity constitutive model. Table 3 presents the elastic constants for the matrix and precipitate phases. The simulated uniaxial stress–strain curves for the materials listed in Table 1 are shown in Fig. 2.

With a complete set of modelling parameters, the RVE was simulated within the range $-0.5 < \rho < 1$ in increments of 0.25. The calibration process for determining

Table 1 Precipitate microstructure parameters for under-aged, peak-aged, and over-aged conditions

Ageing condition	Mean length (nm)	Mean radius (nm)	Number density (μm^{-3})
Peak-age [16]	50	1.78	11,500
Under-age [16]	35	2.26	2000
Over-age [17]	270	4.41	425

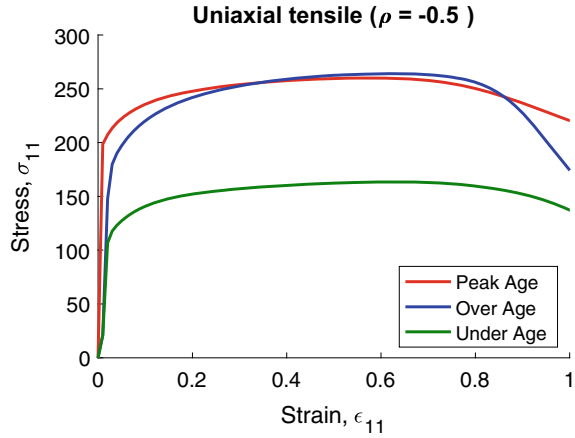
Table 2 Crystal plasticity parameters used in CPFE simulations

$\dot{\gamma}_0$ (s^{-1})	m	τ_0 (MPa)	κ	k_1 (m^{-1})	k_2	n^e	r_c (nm)	β	b (nm)
0.001	0.02	17	0.3	60	12	10	3.0	0.5	0.286

Table 3 Elastic constants for the matrix (m) and precipitate (p) phases. All values in GPa

C_{11}^m	C_{12}^m	C_{44}^m	C_{11}^p	C_{22}^p	C_{33}^p	C_{44}^p	C_{55}^p	C_{66}^p	$C_{12}^p = C_{13}^p = C_{23}^p$
103.3	51.7	25.8	101.0	80.0	80.0	30.0	30.0	16.0	50.0

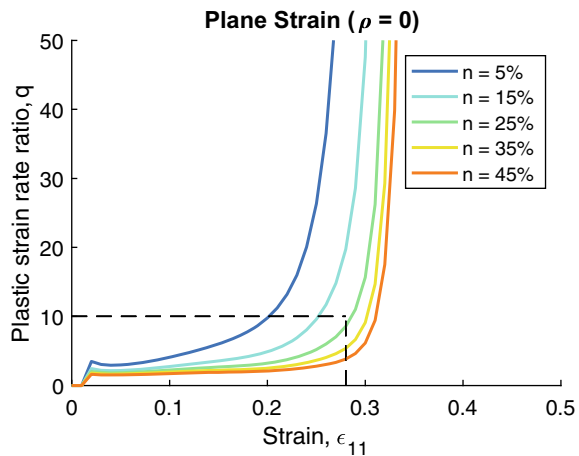
Fig. 2 Uniaxial tensile stress–strain behaviours for under-aged, peak-aged, and over-aged alloys defined in Table 1



the onset of localization with the RVE for the FLD is illustrated in Fig. 3, which shows the volume-averaged plastic strain rate ratio, q , for various values of n . In this work, $n = 25\%$ is the percentage of elements and $\lambda = 10$ is the plastic strain rate ratio that was used in the instability criterion, which was found to accurately capture the experimental plane strain localization point of $\epsilon_{11} = 0.28$. The experimental in-plane strain localization point was obtained using stereo digital image correlation of a notch tensile specimen [19].

Figure 4 shows the simulation sequence from start to finish for the equi-biaxial strain path ($\rho = 1$). During the early stages of deformation (Fig. 4a, b), the material behaves rather uniformly as the surface of the RVE is initially smooth and distortion-free. As the material is deformed further (Fig. 4c), the surface of the RVE develops significant patterning as a consequence of crystallographic and morphological heterogeneities between individual grains. These surface undulations are precursors to the

Fig. 3 Plastic strain rate ratio versus major strain for varying values of n . n is calibrated to a plane strain tension experiment with a failure strain of $\epsilon_{11} = 0.28$. A good fit to the data is obtained using $n = 25\%$ for $\lambda = 10$



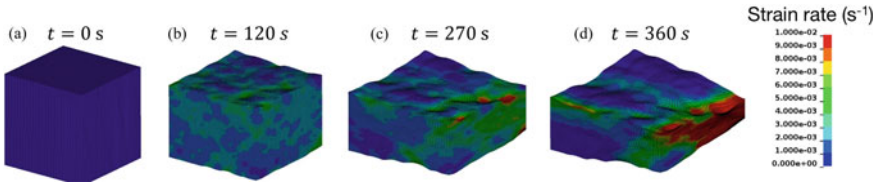
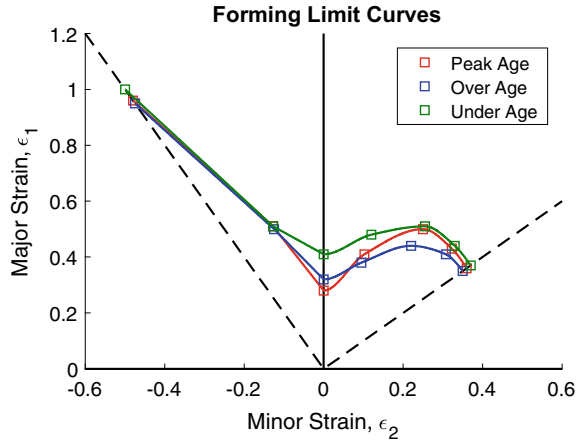


Fig. 4 Finite element simulation for equi-biaxial stretching. Colours illustrate the strain rates within each element

Fig. 5 Simulated forming limit curves for under-aged, peak-aged, and over-aged alloys using the proposed numerical framework



subsequent formation of shear bands and are responsible for the onset of localization by concentrating high amounts of plastic strain. Eventually, a defined neck forms within the material (Fig. 4d), which satisfies the plastic instability criterion in Eq. (11) for the calculation of limit strains. This process is repeated for each strain path, ρ , in order to generate a forming limit curve.

Figure 5 presents the predicted forming limit curves for each ageing condition. It is shown that the under-aged alloy consistently has higher formability for all strain paths studied, while the over-aged and peak-aged alloys show comparable results to one another. Analyzing the uniaxial tensile response of the three alloys from Fig. 2, the over-aged and peak-aged conditions exhibit similar stress–strain responses with minor differences in the hardening rate. From this observation, it is expected that the two would perform similarly in terms of formability because the ductility of metals can be approximated from the stress–strain curve using the Considère law: $d\sigma/d\epsilon = \sigma$.

The significance of these simulations is that the numerical framework is able to capture the changes in formability between different ageing states without recalibration for each condition. These changes are captured uniquely from the differences in precipitate microstructure at each temper. Figure 5 shows that formability is generally

reduced at longer ageing times, which is in close agreement with findings from literature for 6000-series aluminum materials [17, 22, 23]. Most importantly, the model is able to predict the significant improvement in formability at the under-aged state, which is expected since these alloys are normally formed at this state and hardened later in the assembly process, such as during a paint bake cycle.

Conclusions

This work presented a precipitation hardening crystal plasticity model that was implemented into a finite element framework to predict the formability of age-hardened aluminum alloys at different ageing conditions. The constitutive model relies on measurements that can be obtained from TEM for the accurate prediction of precipitate-induced properties. A plastic instability criterion was introduced into the finite element framework to determine the onset of localization for evaluating formability limits. Good agreement with experimental localization strains was obtained by comparing 25% of elements with the highest plastic strain rates to 25% of elements with the lowest plastic strain rates. It was shown that the proposed model was capable of capturing the large differences in behaviour expected from the various heat treatment processes. Initial simulations showed a general reduction in formability as the material is aged longer. This is expected for precipitation-hardenable alloys where sacrifices to ductility are made to obtain higher strengths. For slightly over-aged materials, the interplay between a lower yield stress but higher hardening rate allows it to perform similarly to the peak-aged forming limit. These results are, however, highly dependent on the state of over-ageing as well as the initial solute composition. It should be noted that the parameters selected for this study are based on experimental characterizations of different 6000-series alloys, but with similar chemical compositions. The results from the numerical model are in line with observations from literature and demonstrate the correct trends for a theoretical alloy with the defined precipitate distributions. The study highlights the importance of incorporating precipitate information into constitutive models, as it has large effects on localization as well as the alloy's formability limits.

Acknowledgements This work was supported by the Natural Sciences and Engineering Research Council—Industrial Research Chair (NSERC-IRC) under grant no. IRCPJ-503185-2016, and General Motors of Canada. The first author would like to acknowledge the Queen Elizabeth II Graduate Scholarship in Science and Technology and Ontario Graduate Scholarship for their financial support that was provided.

References

1. Andersen SJ, Marioara CD, Friis J et al (2018) Precipitates in aluminium alloys. *Adv Phys X* 3:1479984. <https://doi.org/10.1080/23746149.2018.1479984>
2. Sigli C, De Geuser F, Deschamps A et al (2018) Recent advances in the metallurgy of aluminum alloys. Part II: age hardening. *Comptes Rendus Phys* 19:688–709. <https://doi.org/10.1016/j.crhy.2018.10.012>
3. Esmaeili S, Lloyd DJ, Poole WJ (2003) A yield strength model for the Al–Mg–Si–Cu alloy AA6111. *Acta Mater* 51:2243–2257. [https://doi.org/10.1016/S1359-6454\(03\)00028-4](https://doi.org/10.1016/S1359-6454(03)00028-4)
4. Bhattacharyya JJ, Bittmann B, Agnew SR (2019) The effect of precipitate-induced backstresses on plastic anisotropy: demonstrated by modeling the behavior of aluminum alloy, 7085. *Int J Plast* 117:3–20. <https://doi.org/10.1016/j.ijplas.2018.04.011>
5. Keeler SP (1965) Determination of forming limits in automotive stampings. SAE Tech Pap 650535. <https://doi.org/10.4271/650535>
6. Goodwin GM (1968) Application of strain analysis to sheet metal forming problems in the press Shop. SAE Tech Pap 680093. <https://doi.org/10.4271/680093>
7. Marciniak Z, Kuczyński K (1967) Limit strains in the processes of stretch-forming sheet metal. *Int J Mech Sci* 9:609–620. [https://doi.org/10.1016/0020-7403\(67\)90066-5](https://doi.org/10.1016/0020-7403(67)90066-5)
8. Hutchinson JW, Neale KW (1978) Sheet Necking-II. Time-Independent Behavior. *Mech Sheet Met Form Mater Behav Deform Anal* 127–153. https://doi.org/10.1007/978-1-4613-2880-3_6
9. Wu P, Neale K, Van der Giessen E (1997) On crystal plasticity FLD analysis. *Proc R Soc Lond Ser Math Phys Eng Sci* 453:1831–1848
10. Inal K, Neale KW, Aboutajeddine A (2005) Forming limit comparisons for FCC and BCC sheets. *Int J Plast* 21:1255–1266. <https://doi.org/10.1016/j.ijplas.2004.08.001>
11. Li YL, Kohar CP, Mishra RK, Inal K (2020) A new crystal plasticity constitutive model for simulating precipitation-hardenable aluminum alloys. <https://doi.org/10.1016/j.ijplas.2020.102759>
12. Peirce D, Asaro RJ, Needleman A (1983) Material rate dependence and localized deformation in crystalline solids. *Acta Metall* 31:1951–1976. [https://doi.org/10.1016/0001-6160\(83\)90014-7](https://doi.org/10.1016/0001-6160(83)90014-7)
13. Inal K, Wu PD, Neale KW (2002) Finite element analysis of localization in FCC polycrystalline sheets under plane stress tension. *Int J Solids Struct* 39:3469–3486. [https://doi.org/10.1016/S0020-7683\(02\)00162-2](https://doi.org/10.1016/S0020-7683(02)00162-2)
14. Kitayama K, Tomé CN, Rauch EF et al (2013) A crystallographic dislocation model for describing hardening of polycrystals during strain path changes. application to low carbon steels. *Int J Plast* 46:54–69. <https://doi.org/10.1016/j.ijplas.2012.09.004>
15. Mercier S, Molinari A (2009) Homogenization of elastic–viscoplastic heterogeneous materials: self-consistent and Mori-Tanaka schemes. *Int J Plast* 25:1024–1048. <https://doi.org/10.1016/j.ijplas.2008.08.006>
16. Teichmann K, Marioara CD, Pedersen KO, Marthinsen K (2013) The effect of simultaneous deformation and annealing on the precipitation behaviour and mechanical properties of an Al–Mg–Si alloy. *Mater Sci Eng A* 565:228–235. <https://doi.org/10.1016/j.msea.2012.12.042>
17. Khadyko M, Marioara CD, Dumoulin S et al (2017) Effects of heat-treatment on the plastic anisotropy of extruded aluminium alloy AA6063. *Mater Sci Eng A* 708:208–221. <https://doi.org/10.1016/j.msea.2017.09.133>
18. Rossiter J, Brahme A, Simha MH et al (2010) A new crystal plasticity scheme for explicit time integration codes to simulate deformation in 3D microstructures: Effects of strain path, strain rate and thermal softening on localized deformation in the aluminum alloy 5754 during simple shear. *Int J Plast* 26:1702–1725. <https://doi.org/10.1016/j.ijplas.2010.02.007>
19. Kohar CP, Brahme A, Hekmat F et al (2019) A computational mechanics engineering framework for predicting the axial crush response of Aluminum extrusions. *Thin-Walled Struct* 140:516–532. <https://doi.org/10.1016/j.tws.2019.02.007>

20. Zhang P, Kohar CP, Brahme AP et al (2019) A crystal plasticity formulation for simulating the formability of a transformation induced plasticity steel. *J Mater Process Technol* 116493. <https://doi.org/10.1016/j.jmatprotec.2019.116493>
21. Mohammadi M, Brahme AP, Mishra RK, Inal K (2014) Effects of post-necking hardening behavior and equivalent stress–strain curves on the accuracy of M-K based forming limit diagrams. *Comput Mater Sci* 85:316–323. <https://doi.org/10.1016/j.commatsci.2014.01.017>
22. Poole WJ, Lloyd DJ (2004) Modelling the stress-strain behaviour for aluminum alloy AA611. In: *International conference on aluminum alloys*, p 6
23. Ryen Ø, Holmedal B, Marthinsen K, Furu T (2015) Precipitation, strength and work hardening of age hardened aluminium alloys. *IOP Conf Ser Mater Sci Eng* 89:012013. <https://doi.org/10.1088/1757-899X/89/1/012013>

Deformation and Fracture in Micro-stamping Process



Peng Zhang, Michael P. Pereira, Buddhika Abeyrathna, Bernard F. Rolfe, Daniel E. Wilkosz, Peter Hodgson, and Matthias Weiss

Abstract Hydrogen fuel cells could be used to power vehicles with zero emissions. An essential component in the fuel cell is the bipolar plate, which conducts electricity, distributes gas, and removes heat. The metallic bipolar plate that is micro-formed from an ultra-thin stainless-steel sheet is more cost-effective for mass production and more lightweight than the conventional carbon bipolar plates. The scope of this work is to understand the material deformation and ductile fracture behaviour in the micro-stamping process, which is a prototype process that may be used to manufacture bipolar plates. The hardening and fracture models of the ultra-thin stainless-steel sheet were calibrated in the authors' previous work [1] and are implemented in the current process. The accuracy of the FE model is assessed by comparison with experimental trials with regard to material thinning, profile shape, and point of fracture initiation.

Keywords Micro-stamping · Ultra-thin sheet · Bipolar plate · Ductile fracture · FEA

Introduction

The innovation of fuel cells provides a cleaner and more efficient electricity generation technique for future electrification of vehicles. Among all the different types of fuel cells, Proton Exchange Membrane Fuel Cells (PEMFCs) have been successfully commercialised [2] due to their outstanding performance. The Bipolar Plate (BPP) is

P. Zhang (✉) · B. Abeyrathna · P. Hodgson · M. Weiss
Institute for Frontier Materials, Deakin University, Waurn Ponds, Pigdons Rd., Geelong, VIC 3216, Australia
e-mail: pen@deakin.edu.au

M. P. Pereira · B. F. Rolfe
School of Engineering, Deakin University, Waurn Ponds, Pigdons Rd., Geelong, VIC 3216, Australia

D. E. Wilkosz
Ford Motor Company, Research and Innovation Center, 2101 Village Rd., Dearborn, MI 48121, USA

a key component in a PEMFC. The common shape of the bipolar plate is designed so that it consists of multi-rows of close-spaced micro-channels to maximise the power density of the PEMFC [3]. These micro-channels are necessary to provide reaction sites for the hydrogen and the oxygen. Historically, the material used for the bipolar plate has been graphite [4]. The conventional graphite plate, however, is brittle, expensive, and has high permeability to gas thus requiring additional processing steps; therefore, it is not highly suitable for mass production. The bipolar plate made from stainless steel offers a substitute solution to using its conventional graphite counterpart [4]. Recently, micro-roll forming [3, 5] and micro-stamping [6] have been identified as two potential approaches to produce the bipolar plate using thin stainless steel. The scope of this work is to experimentally and numerically evaluate the material thinning and fracture in micro-stamping conditions that are representative of those used for bipolar plate production.

Material and Methods

Experimental Procedure

The target dimension of one single corrugation of the micro-stamping sample is specified in Fig. 1a and a formed sample is shown in Fig. 1b. This cross-section geometry was chosen based on anticipated forming challenges. The 2D geometry of the experimental tooling used was measured with a non-contact profilometer (Alicona, Austria) for implementation in the FEA in Sect. 2.2.

Industry standard 0.1-mm-thick 316L stainless-steel sheet is stamped between a punch and die to produce seven identical channels that are parallel to each other, as shown in Fig. 1b. The load is applied on the punch using an Instron 500 kN universal tensile machine, the test setup, and schematics of the stamping tools are shown in Fig. 2a. The load frame moves with 5 N/s and is controlled in Bluehill®

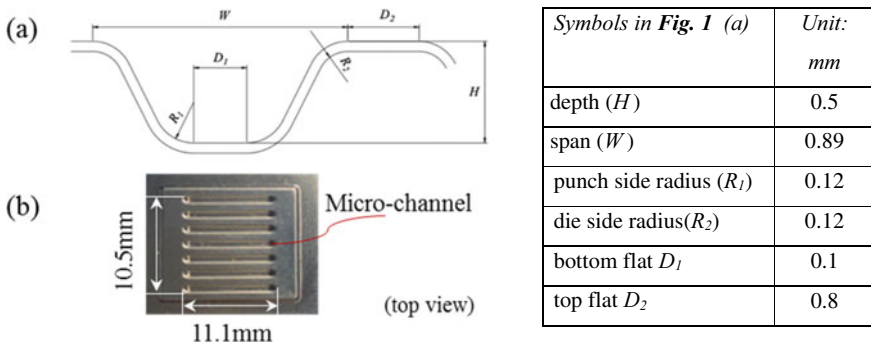


Fig. 1 a Schematic and dimensions of the target corrugation profile b a micro-stamped sample

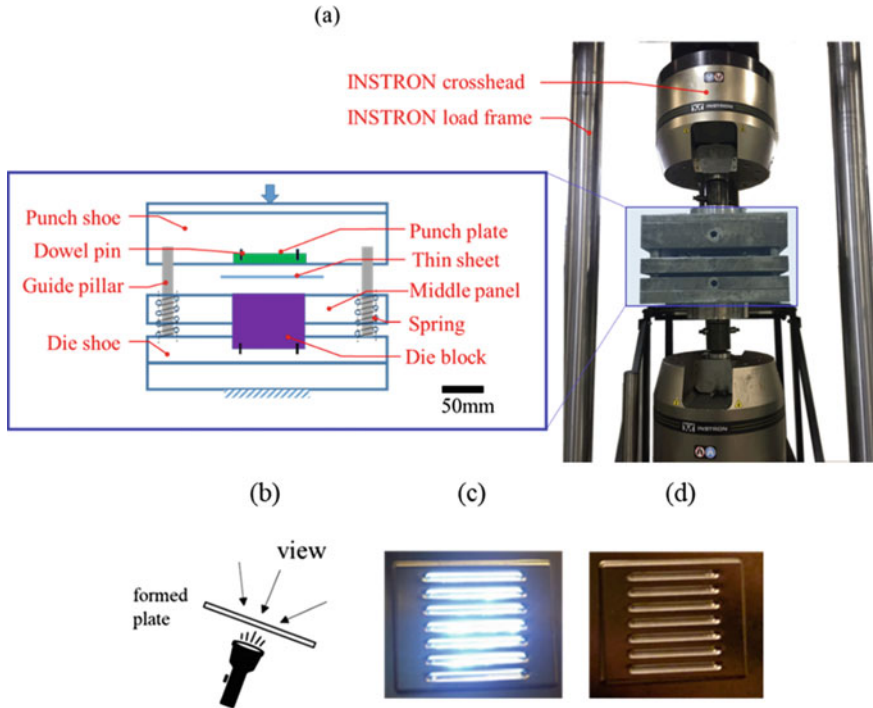


Fig. 2 a Stamping tool schematics and the test setup. b White light method used to identify cracks and pin holes. Examples of channel patterns formed: c failed and d successful

(Instron, Ill., USA). After forming, a white light apparatus was used to illuminate the back surface of formed samples, as schematically shown in Fig. 2b. If cracks or pin holes were present the back-side surface light would diffuse through the voids and be visible from the top surface. Examples of a cracked sample and a successfully formed sample are shown in Fig. 2c, d, respectively. The profile shape achievable before fracture initiation is measured with the profilometer on the top surface.

Subsequently, the formed part is cut out from the formed sheet with scissors. The surface of the specimen was cleaned using ethanol, mounted using epoxy resin and cut in sections with an Accutom 50–1 (Struers, Australia). Two section cuts were performed at 1/3 and 2/3 of the corrugation length, as schematically shown in Fig. 3a. The measurement of material thinning is conducted in Image J in the same way as it was previously done for micro-roll formed specimens in [5]. The direction of the microscope observation is schematically shown in Fig. 3b.

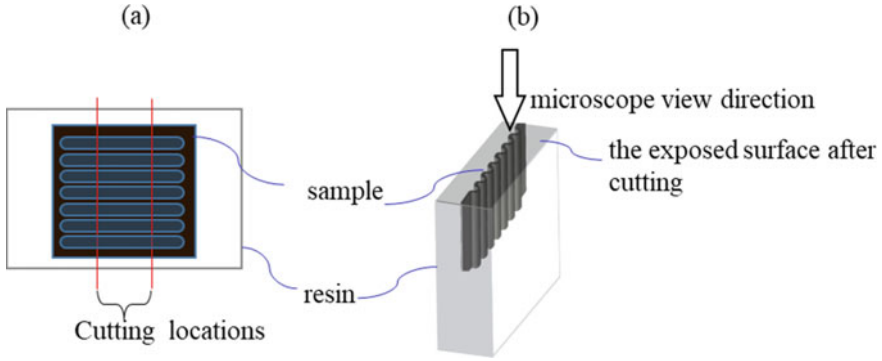


Fig. 3 a Schematics of the mounted sample and the cutting locations (in top view) and b the exposed surface after the cutting process for microscope examinations

Micro-stamping FEA Model

In all channels, the crack did not initiate from the cavities at two ends (half-spherical shapes), where three-dimensional forming would be presented. In addition, the shape of all corrugations is the same and the major deformation is stretching along the transverse direction. For this reason, the deformation of the sheet metal was simplified as plane strain and the FEA model reduced to a two-dimensional (2D) problem. In lieu of no available CAD information, the 2D geometry of the experimental tool's profile was measured with the profilometer and imported to ABAQUS. For this, a 2D middle cross section on the 3D shape was created to represent the shape of the forming region, as it is shown in Fig. 4. The punch and the die have a periodical geometry, and thus the dimensions of one channel are representable for all seven channels. An approximation of the tool radii was made to build the sketches in ABAQUS so that an analytical rigid model could be used to represent the forming tools. For this, the real geometry was smoothed by a combination of straight lines and regular radii to match the measured tool profile as close as possible. This avoids penetration of the sheet by very small sharp tool features in the FEA.

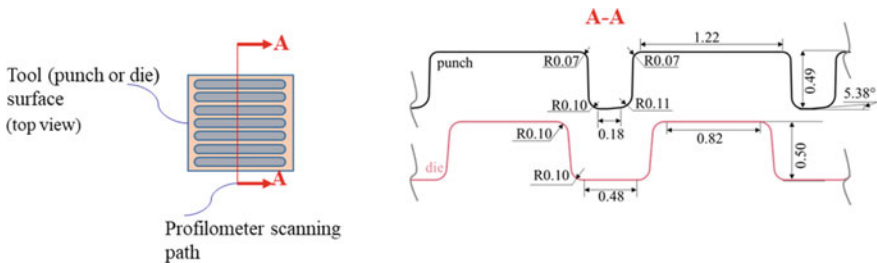


Fig. 4 Schematics of the profilometer scanning path on tools surfaces and the obtained contour of the punch and the die used for simulation

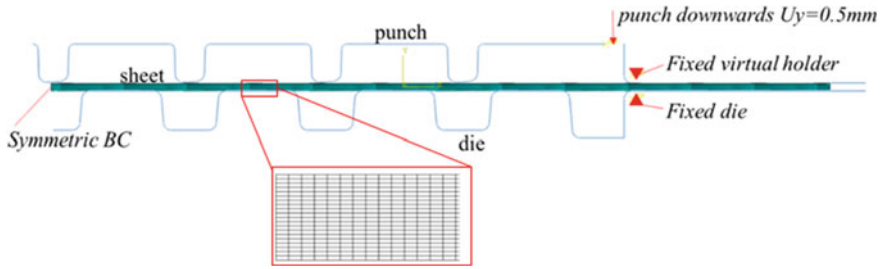


Fig. 5 Model of the micro-stamping process

Due to the symmetry of the load and geometry, half of the pattern was simulated, that is, the punch and die were reduced to 3.5 corrugations. The sheet was meshed with CPE8R elements, which are plane-strain continuum elements with reduced integration, and 20 elements in the thickness direction were used. Previous studies have indicated that in micro-forming, the coefficient of friction (COF) is higher compared to that in conventional forming [7] and a COF = 0.4 was used here. The “surface-to-surface” contact was applied to define the interaction between the sheet and tools. In the forming step, a vertical displacement was applied to the punch while the die and the blank holder remained fixed. The left end of the sheet was constrained by a symmetry boundary condition (BC) while the right end remained free to move, as shown in Fig. 5.

Fracture Model

The plastic hardening behaviour of the sheet material is expressed in Eq. 1, with $\bar{\sigma}$ being the true stress and $\bar{\epsilon}$ the equivalent plastic strain. The Gurson–Tvergaard–Needleman (GTN) model [8], with its yield function expressed in Eq. 2, is used for the analysis of fracture initiation.

$$\bar{\sigma} = S_0 \bar{\epsilon} + H \quad (1)$$

$$\phi = \left(\frac{\sigma_v}{\bar{\sigma}}\right)^2 + 2q_1 f \cosh\left(\frac{3}{2}q_2 \frac{P}{\bar{\sigma}}\right) - (1 + q_3 f^2) = 0 \quad (2)$$

where S_0 and H are the linear hardening parameters; σ_v is von Mises stress; P is the hydrostatic stress; q_1, q_2, q_3 are material parameters; f is the void volume fraction, the rate of which (\dot{f}) can be determined with the void growth term (\dot{f}_{gr}); and void nucleation term (\dot{f}_{nucl}) described in Eq. 3.

$$\dot{f} = \dot{f}_{gr} + \dot{f}_{nucl} \quad (3)$$

Table 1 Parameters used for the simulation

S_N	ε_N	f_N	q_1	q_2	q_3	S_0	H
0.1	0.27	0.05	1.8	1	3.24	2204.2	325.6

The rate of growth based on the law is expressed in Eq. 4, where $\dot{\boldsymbol{\varepsilon}}$ is the plastic strain rate tensor and \mathbf{I} is the identity tensor.

$$\dot{f}_{gr} = (1 - f)\dot{\boldsymbol{\varepsilon}} : \mathbf{I} \quad (4)$$

The nucleation of voids is given by a strain-controlled intensity index A , as expressed in Eq. 5:

$$\dot{f}_{nucl} = A\dot{\boldsymbol{\varepsilon}}; \quad A = \frac{f_N}{S_N\sqrt{2\pi}} \exp\left(-\frac{1}{2}\left[\frac{\varepsilon - \varepsilon_N}{S_N}\right]^2\right) \quad (5)$$

where f_N , S_N , and ε_N are the parameters related to void nucleation. The contribution of void volume fraction due to void coalescence is included in the conventional GTN model; however, the coalescence term is neglected here. This is because a sudden load drop (fracture) was found in the thin sheet samples during the calibration test, and thus the gradual degradation of the material's load bearing capacity due to void coalescence can be neglected. The models were calibrated in [1] and the calibrated parameters are listed in Table 1. Fracture is deemed to occur when the void volume fraction f reaches the critical value f_c , which is dependent on the stress triaxiality. The stress triaxiality and the f_c are expressed in Eqs. 6 and 7, respectively.

In general, the stress triaxiality of all the samples varies until fracture occurs. Therefore, the stress triaxiality η was averaged in a range between 0.1 and 0.5 of equivalent plastic strain $\bar{\varepsilon}$. The average triaxiality η_{avg} is calculated with Eq. 6. It is assumed that the computed void volume fraction f (in Eq. 2) of the thin sheet reaches the critical volume fraction f_c when fracture initiates. The relation between f_c and η_{avg} was determined by fitting the various pair data of (η_{avg}, f_c) determined by tensile tests with notched thin sheet samples and biaxial stretch forming tests during the calibration process [1].

$$\eta_{avg} = 2.5 \int_{0.1}^{0.5} \eta d\bar{\varepsilon} \quad (6)$$

$$f_c = 4.34\eta_{avg}^2 - 3.76 + 0.88 \quad (7)$$

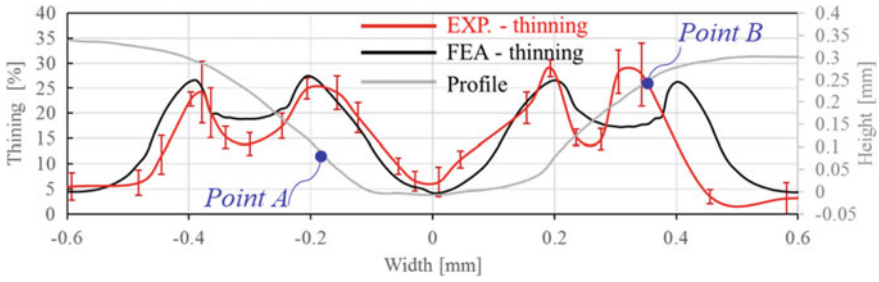


Fig. 6 Thinning prediction for the micro-stamped profile compared to the experimental results (maximum achievable profile)

Results and Discussion

Material Thinning Prediction

The FEA model was used to analyse material thinning at the final punch stroke before fracture. The experimental and the FEA results are illustrated in Fig. 6. The results are overlaid with the maximum achievable profile shape of the top surface before fracture obtained from the experiments (see grey curve in Fig. 6). It is evident that the FEA model captures well the general trends of material thinning, except for some area near the 0.2–0.3 mm region width. The localised thinning observed in this area appears in every row of channels and, therefore, may be due to misalignment between the punch and die which was not captured by the FEA model.

Fracture Model Implementation

The location of the peak equivalent plastic strain changes as the punch moves down, until it begins to stabilise at the left corner of the bottom radius at an equivalent plastic strain of 0.5. When the void volume fraction f at this point reaches the critical constant f_c (Eq. 7) fracture is considered to initiate. This node is located at the left bottom radius in *point A* shown in Figs. 6 and 7. It is noted that this node does not coincide with the fracture initiation *point B* found in the micro-stamping experiments which is located on the right top radius with scattered thinning (*point B* shown in Fig. 6). This may be due to tool misalignment as explained earlier. The average stress triaxiality in *point A* is numerically determined first to enable the use of the parabolic coalescence law (Eq. 5). The stress triaxiality versus the equivalent plastic strain is shown in Fig. 7. Using Eq. 6, the average stress triaxiality is calculated to be $\eta_{avg} = 0.54$. Implementing $\eta_{avg} = 0.54$ in the parabolic law of Eq. 7 gives $f_c = 0.12$.

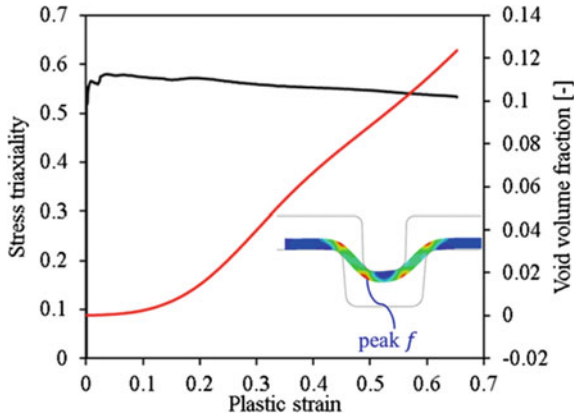


Fig. 7 The stress triaxiality (black line) and the void volume fraction (red) versus the equivalent plastic strain at the critical node (point A)

Using $f_c = 0.12$ in the numerical model of the micro-stamping process suggests safe forming for the full punch stroke of 0.5 mm, as shown in Fig. 8. However, in the experimental trials, fracture initiated at a punch stroke of 0.3 mm (indicated by the blue line in Fig. 8). This discrepancy may be due to a combination of the tool shape inaccuracy, tool misalignment, and the resolution of the model predictions, which need to be further explored. Nevertheless, one attribution is the potential misalignment of the punch and the die in the experimental scenario, which is not included in the numerical model. The experimental thinning results in Fig. 6 suggest that unsymmetrical thinning exists which indicates tool misalignment. However, the FEA model predicts symmetrical thinning because a perfect (i.e. symmetric) alignment of the punch and die is assumed. This represents a less severe forming condition and may explain why fracture is predicted to occur at a lower punch stroke than observed in the experiments.

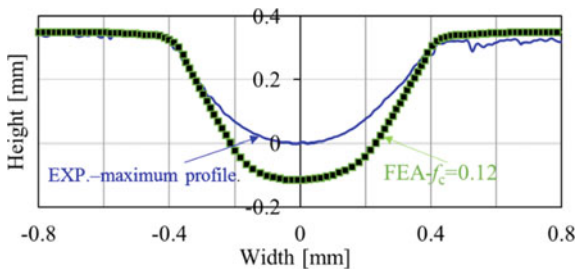


Fig. 8 Comparison of the formed profile at fracture predicted by the FEA and shown by the experimental results (EXP. plot in blue is the profile at fracture initiation). FEA with $f_c = 0.12$ suggests successful forming for the full punch stroke

Conclusion

The micro-stamping process is numerically analysed using a calibrated GTN model. The implementation of a parabolic coalescence model, which estimates the critical volume fraction, f_c , gives a reasonable thinning prediction that correlates well with the experiments. The FEA fracture initiation is defined to initiate on a critical node that shows a critical void volume fraction. However, it was found that the critical node predicted by the model does not correlate with the fracture initiation location found in the experiments. This discrepancy may be due to a combination of tool shape inaccuracy and tool misalignment that was not captured in the FEA model. In addition, the maximum depth of the channel that can be safely formed is overestimated. Future study will investigate the effect of the tool radius and alignment on the thinning and the level of void volume fraction in the micro-stamping process, to further improve the fracture model.

References

1. Zhang P, Pereira M, Rolfe B, Wilkosz D, Abeyrathna B, Hodgson P, Weiss M (2020) Plastic instability and fracture of ultra-thin stainless-steel sheet. *Int J Solids Struct* 202:699–716
2. Gerbec M, Jovan V, Petrovčič J (2008) Operational and safety analyses of a commercial PEMFC system. *Int J Hydrogen Energy* 33:4147–4160. <https://doi.org/10.1016/j.ijhydene.2008.04.063>
3. Zhang P, Pereira M, Rolfe B, Daniel W, Weiss M (2017) Deformation in Micro Roll Forming of Bipolar Plate. *J Phys Conf Ser* 896:012115. <https://doi.org/10.1088/1742-6596/896/1/012115>
4. Hermann A, Chaudhuri T, Spagnol P (2005) Bipolar plates for PEM fuel cells: a review. *Int J Hydrogen Energy* 30:1297–1302. <https://doi.org/10.1016/J.IJHYDENE.2005.04.016>
5. Abeyrathna B, Zhang P, Pereira MP, Wilkosz D, Weiss M (2019) Micro-roll forming of stainless steel bipolar plates for fuel cells. *Int J Hydrogen Energy* 44:3861–3875. <https://doi.org/10.1016/J.IJHYDENE.2018.12.013>
6. Leng Y, Ming P, Yang D, Zhang C (2020) Stainless steel bipolar plates for proton exchange membrane fuel cells: materials, flow channel design and forming processes. *J Power Sour* 451:227783. <https://doi.org/10.1016/j.jpowsour.2020.227783>
7. Geiger M, Kleiner M, Eckstein R, Tiesler N, Engel U (2001) Microforming. *CIRP Ann Manuf Technol* 50:445–462. [https://doi.org/10.1016/S0007-8506\(07\)62991-6](https://doi.org/10.1016/S0007-8506(07)62991-6)
8. Dassault Systèmes (2014) Porous metal plasticity. In: Abaqus 6.14-Abaqus theory guid. Dassault Systèmes Simulia Corp., Providence, RI

Die Design for Flashless Forging of a Polymer Insulator Fitting



Pedram Khazaie and Sajjad Moein

Abstract In conventional hot forging of Tongue, which is a fitting for polymer insulator, the material wasted to flash accounts for 20–30% of workpiece. In order to reduce the cost of forged products, this waste material must be minimized. In this study, a flashless forging die is designed and simulated using the finite element method (FEM). A solution to avoid overloading the die is also presented. In addition, since in flashless forging, a thin flash is created in the gap between die and punch, a controlled flash forging method is proposed to solve this problem. The simulation results have been validated by experiments, achieving close agreement between simulated and experimental data. It was shown that numerical modelling is helpful in reducing cost and time in manufacturing process.

Keywords Die design · FEM · Flashless forging · Thin flash

Introduction

The growing worldwide competition in the processing industries leads to a constant rise of cost pressure. Research and technological development in manufacturing technologies are the basic prerequisites to meet cost and quality requirements to assert on market. Forging has enjoyed an eminent position among various methods of manufacturing because forged products, for good reason, have been looked upon as offering maximum reliability and superior properties [1].

Approximately half the cost of the forging is comprised of the cost of purchased material. If by flashless forging, a 15% material savings can be achieved (a reasonable goal), the cost of forging can be reduced by 7.5% [2].

In flashless precision forging processes of steel and aluminum as well, the forging tools include die gravures that almost completely enclose the workpiece. Punches move into the dies and carry out the forming of the work piece [3]. The elimination of flash forming in the forging process reduces the consumption of material, energy

P. Khazaie (✉) · S. Moein
R&D Department, Kaveh Forging Co., Bozorge Isfahan Industrial Zone, Kar Afarinan 14,
Esfahan, Iran
e-mail: Pedram.khazaie1@gmail.com

(used for heating the billet in hot forging), and time (spent on flash trimming). In addition, flashless forging preserves the continuity of metal fibers, increasing in this way the strength of parts [4].

The disadvantage of this process is its inherent inflexibility on billet volume fluctuations, which can either lead to an overload of the dies and the press or, conversely, incomplete die filling [5]. Another is that due to geometrical tolerances and complex thermal expansions of these tool elements small gaps must exist between punch and die. In hot forging processes material flows into these gaps unintendedly and the so-called thin flash is generated [3]. The generation of thin flash in a forging process leads to post-process operations.

Tongue, which is an electrical polymer insulator end fittings, has high amount of production and can be forged by flashless method. Its forged schematic is shown in Fig. 1.

In this study, the forging process has been simulated using finite element method (FEM). Two dies are designed for mass production of Tongue. The first die is designed in such a way that the production process does not require preform and trimming, and also the volume of the original billet does not have to be accurate. However, the generation of thin flash leads to post-process operations.

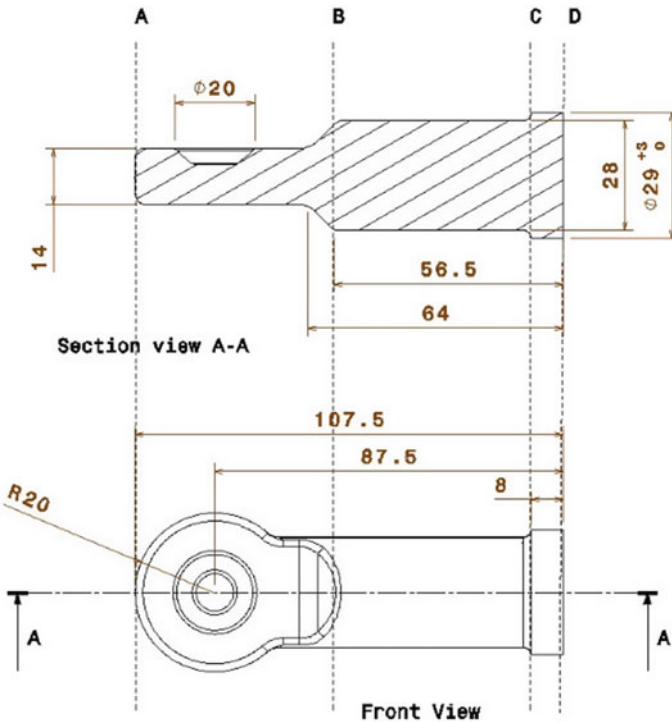


Fig. 1 Schematic of forged Tongue. Workpiece is divided into three sections: large end section (a, b), shank section (b, c), and small end section (c, d)

Table 1 Input data for DEFORM-3D simulations

Parameter	Value	Value
Material (characteristics taken from DEFORM database)	AISI-1045	Al 7075
Punch speed	50 mm/s	30 mm/s
Workpiece temperature	1200 C	420 C
Die temperature	120 C	200 C
Friction method	Shear	Shear
Friction factor	0.3	0.4
Heat transfer coefficient	5 N/s/mm/C	5 N/s/mm/C
Maximum element size	2 mm	2 mm
Minimum element size	1 mm	1 mm

In the second die, the production process does not require a preform, a controlled flash, in the amount of 3% of the weight of the initial billet, is created in the piece, which must be removed during trimming, but no thin flash is created on the workpiece.

Tool and Process Design for Flashless Forging of Tongue

The FEM for elastic–plastic material properties is considered to be the most accurate method available at present [6]. Instead of using traditional design methods based on experiments, experience, and trial and error, the use of computers in the design of metal forming operations has become widespread to reduce both development time and cost [1]. A number of commercial FE codes are available in the market for simulation of bulk forming processes, viz. DEFORM, FORGE, QFORM, etc. [8]. The capabilities of DEFORM-3D have been evaluated and validated by applying it to several applications [9, 10].

This paper uses Deform-3D to simulate forging processes. Input data is shown in Table 1. In order to save computation time, all of the processes are modeled in 3D using 1/2 symmetry for the billet and the dies and it is assumed that dies are rigid.

Conventional Forging of Tongue

Figure 2 shows the conventional forged Tongue. In the conventional forging process, the formation of flash restricts the lateral flow of material and thus facilitates the filling of the die cavity, the excess material of the flash being trimmed upon the completion of the forging process [11].

This method results in 25% of material to be waste as flash. A major advantage of this method is that the press does not need to have any ejector.



Fig. 2 Conventional forging of Tongue. 25% of the material is wasted in the flash form

Simulation of Flashless Forging of Tongue

Figure 3 shows tool concept for flashless forging of Tongue.

As shown in Figs. 1 and 3, the workpiece is divided into three sections: large end section (a, b), shank section (b, c), and small end section (c, d).

At the large end section, die gravures completely enclose the workpiece. Punches move into the dies and carry out the forming of the workpiece.

In the shank section, due to the formation of a sharp edge in the upper punch, the die gravures cannot enclose the workpiece. In this section, the materials do not tend to move laterally and this section is designed like conventional closed-die tooling.

The material flow is shown in Fig. 4. The upper punch squeezes the material at the large end section and extrudes it toward wall D. The wall D upsets the material. The small end section is designed as an open die. This prevents overloading of the die.

Figure 5 compares experimental test with simulation result. There is a good agreement between FEM calculation and experimental results. It can be seen that a thin flash is formed at the large end section of the workpiece. Removing this thin flash is expensive.

FE Simulation of Controlled Flash Forging of Tongue

Controlled flash forging of Tongue design is very similar to the flashless forging die design. The difference is that instead of the die gravures completely enclosing the workpiece, the parting line is raised as high as possible. In this design, the depth of top die cavity is only 2.8 mm.

Figure 6 shows tool concept for controlled flash forging of Tongue.

Considering that the Tongue produced from AISI 1015 must be hot-dip galvanized and machined, Kaveh Forging Company concluded that the production of this part

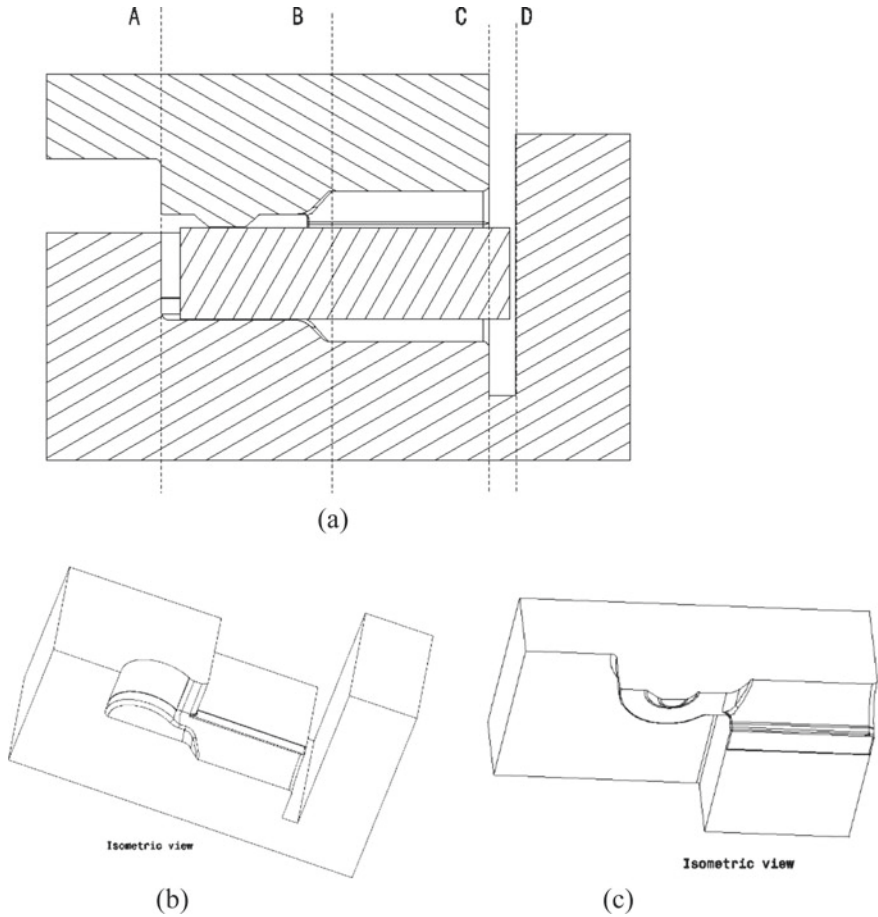


Fig. 3 a Cross section of bottom die, upper die, and billet initial situation, in flashless forging of Tongue, b bottom die cross section, in 3D view, c top die cross section, in 3D view

from aluminum 7075 is more profitable and more than 400,000 parts have been produced with this design. Figure 7 compares industrial test with simulation result.

Conclusion

In this paper, a study on conventional flash forging, flashless forging and controlled flash forging of Tongue is performed by DEFORM-3D and by experiment. Comparison of the final shape of the Tongue in flashless and controlled flash forging shows a good agreement between the experimental and simulation results obtained in the FEM calculation.

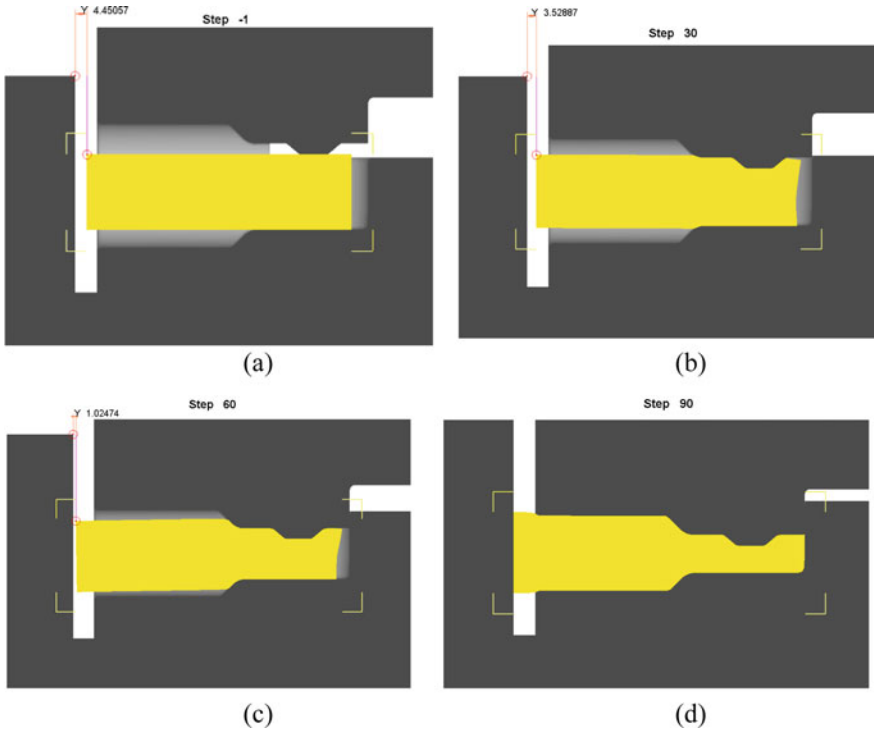
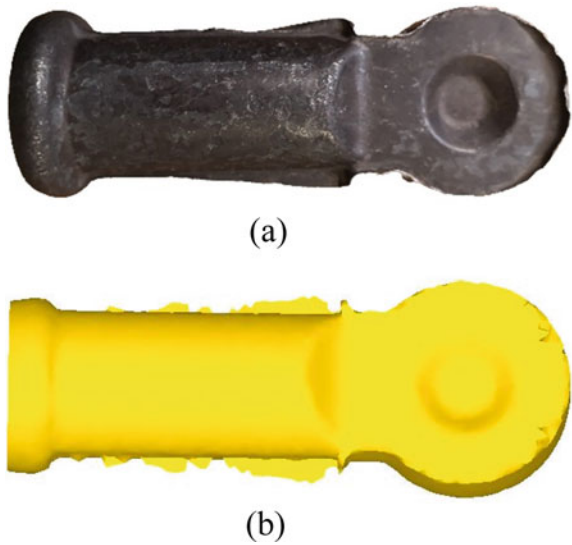


Fig. 4 The material flow of the Tongue in flashless forging. The distances between the billet and the wall in (a), (b), (c), and (d) are 4.6 mm, 3.5 mm, 1 mm, and 0 mm, respectively

Fig. 5 Comparison of experimental test with simulation result of Tongue flashless forging. AISI 1015
a experimental result
b simulation result



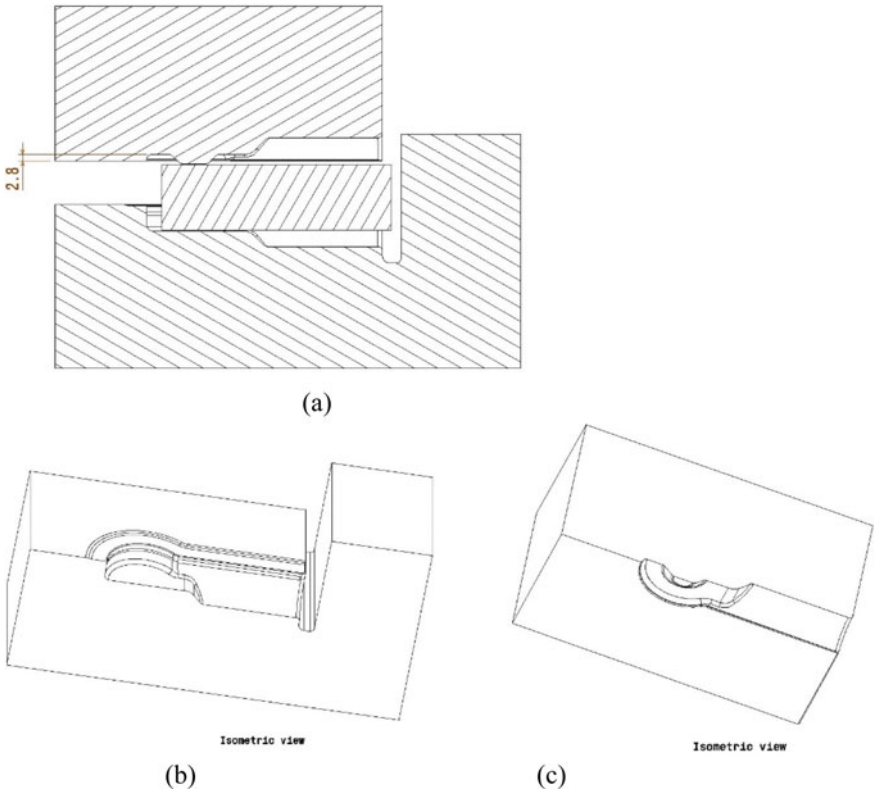


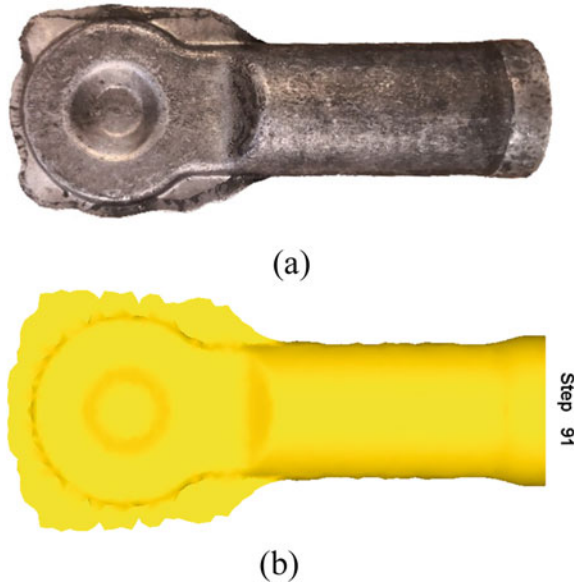
Fig. 6 a Cross section of bottom die, upper die, and billet initial situation, in controlled flash forging of Tongue, b bottom die cross section, in 3D view, c top die cross section

Flashless forging can lead to significant material savings, eliminates the trimming process, and at the same time does not require strict control of the billet volume. However, causes a thin flash to appear on the edge of workpiece and the process of removing the thin flash is expensive.

Controlled flash forging concept allows a small amount of flash (3%) compared to conventional flash forging, and unlike flashless forging, thin flash does not appear.

In the case study presented in this paper, it is shown that numerical modeling is a helpful technique, and it is cheaper than performing tryout with actual die and equipment, and it gives more information about the process.

Fig. 7 Comparison of experimental test with simulation result of Tongue controlled flash forging. Al 7075 **a** industrial result **b** simulation result



References

1. Khazaie P et al (2012) Die design for flashless forging of connecting rod cap. Steel Research International. In: Paper presented at the 14th international conference on metal forming. Poland. 199–202
2. Douglas R, Kuhlmann D (2000) Guidelines for precision hot forging with applications. J Mater Process Technol 98:182–188
3. Richter J et al (2017) Quality optimization for aluminum precision forging processes in completely enclosed dies of long forging parts by prediction and avoidance of thin flash generation. In: Paper presented at the international conference on the technology of plasticity. Cambridge, United Kingdom. 484–489
4. Bulzak T, Tomczak J, Pater Z (2021) A comparative analysis of hot and cold flashless forging of a stepped shaft using vertically-parted dies. Int J Adv Manuf Technol 116:2521–2530
5. Behrens B, Stonis M., R  ther T, Langner J, Guzey G (2015) In: Closing mechanisms for forging flashless closed-die preforms. FORGE Magazine. <https://www.forgemag.com/articles/84432-closing-mechanisms-for-forging-flashless-closed-die-preforms>. Accessed 20 March 2022
6. Metha BV, Al-Zkeri I, Gunasekera JS, Buijk A (2001) 3D flow analysis inside shear and streamlined extrusion dies for feeder plate design. J Mater Process Technol 113:93–97
7. Behrens BA, Odening D (2009) Process and tool design for precision forging of geared components. Int J Mater Form 2:125–128
8. Altan T (2005) Methods of analysis for forging operations. In: Cold and hot forging fundamentals and applications. American Society of Metals (ASM), Ohio, p 104
9. Altan T, Wu W, Li G, Tang J (1994) Finite element analysis of three dimensional metal flow in cold and hot forming processes. CIRP Ann 43(1994):235–239

10. Wu W, Li G, Arvind A, Tang J (1996) Development of a three dimensional finite element method based process simulation tool for the metal forming industry. In: Third biennial joint conference on engineering systems design and analysis. A.B. Sabir, Montpellier, France, pp 143–150
11. Kang BS, Lee JH, Kim BM, Choi JC (1995) Process design in flashless forging of rib/web-shaped plane-strain components by the finite element method. *J Mater Process Technol* 47:291–309

DP1180 Material Calibration Between Sheet Metal Simulation and Prototype



L. I. U. Rongfeng and L. I. Dayong

Abstract One of the advanced high-strength steel materials, DP1180, is widely used in the automobile industry so as to satisfy lightweight demands in China mainland market in recent years. Formability and springback problems are very serious in manufacturing. To shorten die development lead time for hard material in mass production, sheet metal forming simulation and its accuracy are becoming essential. After conducting uniaxial tension, compression–tension experiment and fitting a database for real sheet, using Yoshida–Uemori material model in integrated sheet metal simulation system JSTAMP/NV, the springback evaluation result is improved to close with prototype result of one typical frame part. Through this study, it is found that proper material model and real material database have much influence on the simulation accuracy for DP1180 material.

Keywords Sheet metal simulation · Material model · Material database

Introduction

Advanced High-Strength Steel (AHSS) with ultra-high strength up to 1180 MPa by cold forming has been increasingly employed in automotive bodies so as to reduce the white bodies' weight and improve crashworthiness as well. The strong requirements from industries pushed the development of material makers to deliver more strong materials. On the other hand, it is a really big challenge for die shop and part suppliers because it is much difficult to design and make parts than usual. Simulation needs for AHSS are coming up and the problem is accuracy improving for formability and springback prediction. Generally, the material property and material model are important factors to improve simulation accuracy if not considering much

L. I. U. Rongfeng (✉)
JSOL Corporation, 2-18-25 Marunouchi, Naka-ku, Nagoya 460-0002, Japan
e-mail: rongfeng.liu@jsol.co.jp

L. I. Dayong
Shanghai Jiaotong University, Shanghai, China
e-mail: sjtukbe@126.com

of real manufacturing conditions. In this paper, there was a calibration between simulation and prototype focus on DP1180 material database and material models. First, there was an investigation in China mainland market. It was found that Bao Steel's DP1180 was a major AHSS material in mass production during the past 3 years. Then uniaxial tension and Compression–Tension (CT) experimental tests occurred in a particular test method. Based on those raw test data, a Yoshida–Uemori (YU) material database was fit for integrated simulation system named JSTAMP/NV. Simulation result compares between YU material model and scanned prototype panel. It was found that about 20% springback accuracy came up after material database and model calibration.

AHSS Questionnaire and DP1180 Material Test

In July 2019, a questionnaire survey occurred so as to find out the majority of AHSS makers and the most widely used AHSS materials in China market. Survey targets are OEM makers and major stamping part suppliers in mainland. There were 11 valuable feedbacks from 12 companies. It was found that 68% of OEM makers or suppliers had the experience to use AHSS during the past 3 years. For 980 and 1180 MPa grades, the survey shows that there are totally 24 kinds of AHSS materials and the thickness varies from 1.0 mm to 2.3 mm. Nineteen materials, about 85% of AHSS in current mass production, are come from Bao Steel and the others are imported from Japanese or American steelmaker outside mainland. In future, using local AHSS is a trend and the percentage is expected to be higher due to cost performance.

Considering most widely used AHSS material during past years, DP1180 steel from Bao Steel is studied. Test was conducted in professor Dayong Li's lab, located at Shanghai Jiaotong University. In order to measure the mechanical properties for material modeling, uniaxial tensile test, CT test, and Loading–Unloading–Loading (LUL) test are performed, respectively.

All CT test samples are machined along RD (rolling direction), and all tests are performed at the strain rate of 10^{-4} . The CT tests are conducted with the assistance of an anti-buckling device, which is shown in Fig. 2. The side support is provided by two plates, against which the springs act. In order to enlarge the compression range before buckling, an optimal specimen is utilized [1], as shown in Fig. 2. A 0.2 mm thick Teflon film is utilized on each side of the specimen to reduce friction force. A non-contact EIR laser extensometer (LE-05) is used to measure strain in the CT test, as shown in Fig. 1. The measurement of sample deformation over the gage length is realized by receiving the reflected signals from the two parallel tapes bonded to the edge of specimen. In the CT test, the specimens are compressed to a pre-strain and then reloaded reversely until fracture. The friction compensation of CT test procedure has been described in details [1].

Fig. 1 CT test device



Fig. 2 CT specimen and jig

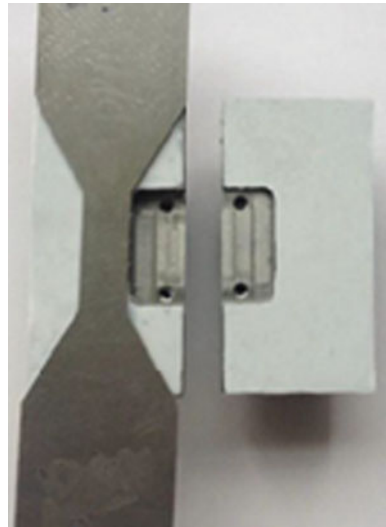


Figure 3 shows test uniaxial tension results. For three directions as RD, Transfer Direction (TD), and 45-degree (45°) direction, all curves show the different specimens and the fracture occurred at about 8% level. The 45° specimens seem to crack a litter earlier than RD and TD direction. The reproducibility of uniaxial test is pretty well.

In Fig. 4, the experimental curves for a typical LUL scheme of DP1180 are shown. Starting from 0, then loading to 2, 4, 6, and 8% engineering strain, each followed by an unloading–reloading loop. Due to nonlinearity of the unloading and reloading, significant hysteresis loops exist, corresponding to the variation of elastic modulus.

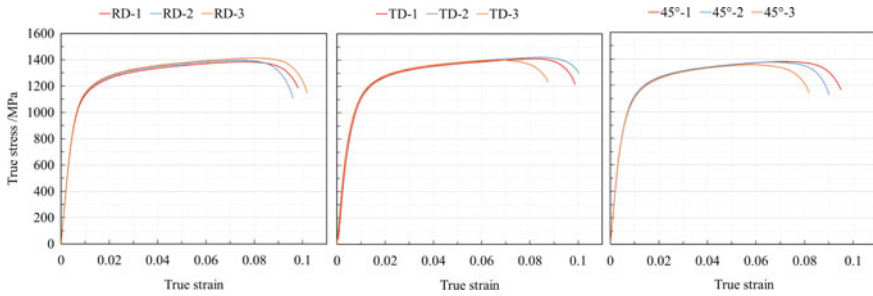


Fig. 3 True stain true stress curves of RD, TD, 45°

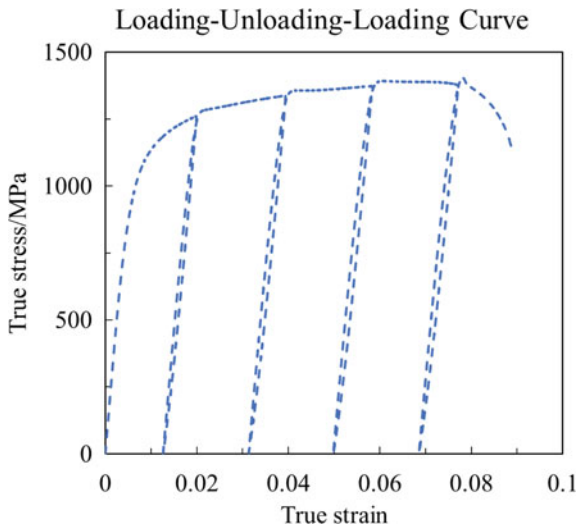


Fig. 4 True stain true stress curves of LUL test

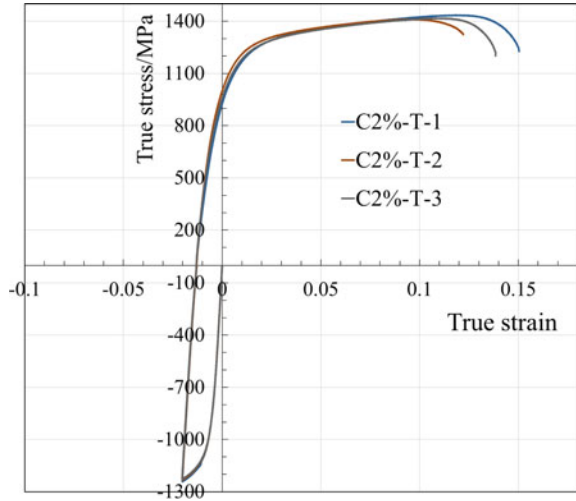
CT experimental curves are shown in Fig. 5. Two percent pre-strain at compression at first and then unloading to 0, continuously tension until to fracture. It should be noted that bulking is occurred during compression because DP1180 is a very hard material. For the same reason, there are no other pre-stain levels in CT experiment in this paper.

In Fig. 5, CT test occurred at 2 % pre-strain, and crack strain became 10% which is higher than uniaxial test in RD, 45° and TD. The reason for this phenomenon is not clear and is going to be studied through more material tests in future.

The Lankford value of R is 0.592, 0.796, and 0.840 for RD, 45° and TD, respectively. All values are measured at 4% engineering strain using separate specimens from uniaxial and CT specimens.

The plastic strain-dependent Young’s modulus was measured from the sequential LUL experiment (see Fig. 4). The variation of Young’s modulus (slope of unloading

Fig. 5 True stain true stress curves of CT test at 2% pre-strain



stress–strain curve) is expressed by the following Eq. (1) which is suggested by Yoshida [2]:

$$E = E_0 - (E_0 - E_\alpha)(1 - \exp(-\xi \varepsilon)) \tag{1}$$

where E_0 denotes Young’s modulus for a virgin material and E_α is its asymptotic value at an infinitely large plastic strain. It is a material parameter representing the variation of Young’s modulus with increasing the effective plastic strain ε . Material constants in Eq. (1) were determined from E versus ε diagram (see Fig. 6) and they are listed in Table 1.

Fig. 6 Plastic strain-dependent Young’s modulus

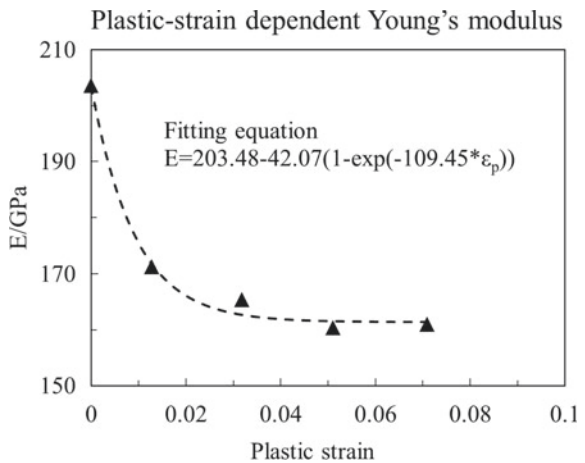


Table 1 Plastic strain-dependent Young's modulus

$E0$ (GPa)	Ea (GPa)	ξ
203.5	160.8	109.45

Table 2 YU material model parameters of DP1180

Y (yield stress) (MPa)	$a0$ (initial value of a = $B-Y$) (MPa)	$C1$	$C2$	$bsat$ (MPa)	m	$Rsat$ (MPa)	h
800	429.0	420	180	95.0	15.0	50.0	0.2

Material parameters of plastic strain-dependent Young's modulus.

Material parameters identification was conducted by the fitting tools MATPARA which is able to easily fit YU material model parameters for DP1180 as shown in Table 2.

Simulation in JSTAMP/NV Using YU Material Model

Material Model

Yoshida and Uemori proposed a model of large strain cyclic plasticity that well describes the stress-strain responses in reverse deformation [2, 3, 4], as well as cyclic hardening characteristics. The key capability of YU model is the transient Bauschinger deformation characterized by early re-yielding and smooth elastic-plastic transition with a rapid change of work hardening rate. The permanent softening is characterized by stress offset observed in a region after the transient period. In addition, plastic strain-dependent Young's modulus and work hardening stagnation appear at a certain range of reverse deformation. Strain-range and mean-strain dependency of cyclic hardening, e.g., the larger the cyclic strain range the larger the saturated stress amplitudes.

It is noted that YU material model has been integrated into JSTAMP/NV. For JSTAMP users, a standard solution is recommended for AHSS springback simulation in sheet metal manufacturing field.

Simulation Result

A typical frame part using DP1180 was studied in this paper as shown in Fig. 7. Two material models are compared in sheet metal simulation. One is one of the common material models Hill'48. The other is YU model. Both of them use Hill's function as yield function and work hardening model is isotropic hardening in Hill'48



Fig. 7 Frame part of DP1180 by cold forming

and nonlinear kinematic hardening in YU model, respectively. Simulation model information is listed in Table 3.

Three stages to make the part are Bending, Flanging, and Cut/Restrike sequentially. To compare sheet simulation with scanned panel, geometry evaluation contour is used which shows the geometry coincidence percentage. Figs. 8, 9 and 10 show the geometry evaluation contour results between Hill’48 model and prototype panels as well as YU material model with scanned prototype panels. As a common springback evaluation method in industry, the area percentage of the part under ± 1.0 mm comes up to 79.6% in Bending stage, 73.7% in Flanging stage, and 83.2% in Cut/Restrike stage. However, in Hill’ 48, the same value under ± 1.0 mm remains at 69.6% in Bending, 38.7% in Flanging, and 44.7% in Cut/Restrike stages, respectively.

The Hill’48 model overestimated that springback and YU model result is closer to prototype panel. Using the experimental data and fitting the material database, YU material model is able to realize bending and reverse-bending behavior during the Bending, Flanging, and Cut/Restrike stage processing. This is the main reason that YU model simulation result is closer to the prototype panel.

From this study, the geometry evaluation result shows 10 ~ 30% springback accuracy up during Bending, Flanging, and Cut/Restrike stages just by changing the

Table 3 Simulation model information

FEM code	JSTAMP/NV2.17 (Solver: LS-DYNA R10)
Basic formulations	Forming: Dynamic Explicit (LS-DYNA); Springback: Static implicit (LS-DYNA)
Element/Mesh technology	Full integrated Sheet Element
Contact property model	Penalty Method: Node to Surface
Friction formulation	Coulomb’s friction law, friction coefficient 0.13

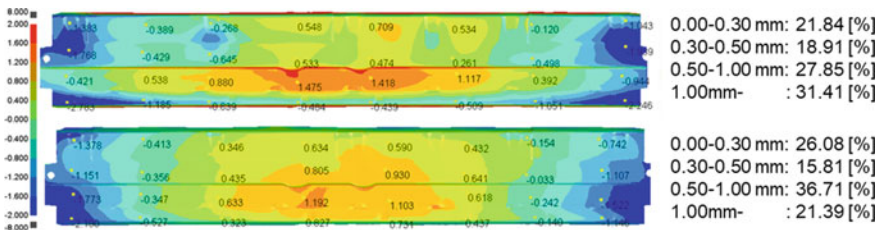


Fig. 8 Geometry evaluation contour of Bending stage by Hill’48 (upper) and YU model (lower)

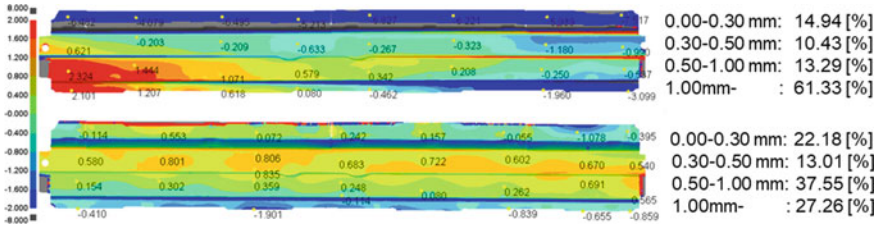


Fig. 9 Geometry evaluation contour of Flanging stage by Hill'48 (upper) and YU model (lower)

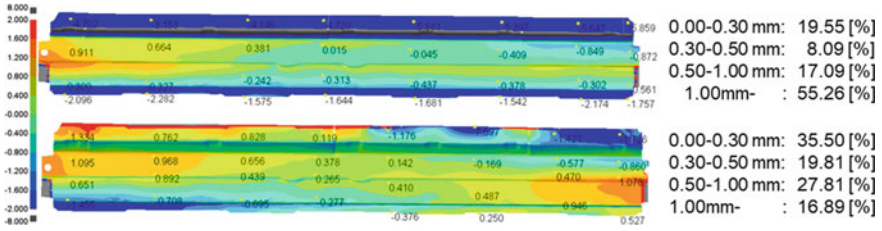


Fig. 10 Geometry evaluation contour of Cut/Restrike stage by Hill'48 and YU model (lower)

material model and material database. It is a practical way to improve sheet metal simulation accuracy for AHSS material. Considering the cost of uniaxial and CT experiments may not be acceptable for most of the industrial users, stimulating more AHSS material databases of mass production material in software will be one option.

Conclusions and Next Step

To perform calibration of sheet metal simulation for DP1180 steel, uniaxial tension, CT, and LUL experiments were performed. After fitting a YU database, it was used in JSTAMP/NV. The simulation result of springback shows that YU model and YU database are helpful to improve sheet metal simulation accuracy even for the current ultra-high-strength material DP1180. On the other hand, there is still left about 20–30% deviation between simulation and prototype. Tool deflection coupling effect is supposed to take much influence. That is going to be studied on the same model next.

Acknowledgements It is noted that GH Auto Parts Industries Inc. provided DP1180 material for uniaxial and CT experiments in this paper. The prototype panel data are also delivered from them. The author would like to acknowledge many thanks and respect to GH Auto Parts Industries.

References

1. Boger RK, Wagoner RH, Barlat F, Lee MG, Chung K (2005) Continuous, large strain, tension/compression testing of sheet material. *Int J Plast* 21(12):2319–2343
2. Yoshida F, Uemori T (2002) A model of large-strain cyclic plasticity describing the Bauschinger effect and workhardening stagnation. *Int J Plast* 18:661–686
3. Yoshida F, Uemori T, Fujiwara K (2002) Elastic-plastic behavior of steel sheets under in-plane cyclic tension-compression at large strain. *Int J Plast* 18:633–660
4. Yoshida F, Uemori T (2003) A model of large-strain cyclic plasticity and its application to springback simulation. *Int J Mech Sci* 45:1687–1702

Evolution of the R-value and Its Determination Based on Reverse Fitting for Sheet Metal



Jun Zhao, Zhenkai Mu, Qingdang Meng, and Haoran Wang

Abstract The plastic anisotropy R-value is an important material parameter for constitutive models, and the fact that the R-value varies with deformation has been recognized. However, there is not a unified method so far to determine the variable R-value. Therefore, based on the initial definition of the R-value, this paper proposes a reverse fitting model to determine the evolution of the R-value for sheet metal. Meanwhile, the limitations of the existing calculation methods for the R-value have been compared and analyzed in detail. The results show that although the longitudinal plastic strain–transverse plastic strain curve is close to a straight line, the R-value changes greatly. With the increase in the uniaxial tensile plastic strain, the evolution of the R-value is generally decreased and the curves' form can be divided into two types: up convex and down concave. In addition, the reason why there are significant differences in the R-value calculated by different methods is clarified. The proposed reverse fitting model can greatly simplify the secondary development of constitutive model considering the evolution of anisotropy and enhance the accuracy of numerical simulation.

Keywords Anisotropic coefficient · Tensile test · Reverse fitting · Sheet metal · R-value

Introduction

The mechanical properties of sheet metals generally show obvious anisotropy when they undergo severe plastic deformation during manufacturing processes such as cold rolling. The macroscopic characteristics of anisotropy mainly reflect the variation of the yield stress and R-value with direction. Various phenomenological yield models have been proposed to describe the initial anisotropy for sheet metals [1–6]. In fact,

J. Zhao (✉) · Z. Mu · Q. Meng · H. Wang
School of Mechanical Engineering, Yanshan University, Qinhuangdao, People's Republic of China
e-mail: zhaojun@ysu.edu.cn

Z. Mu
e-mail: mzk@stumail.ysu.edu.cn

during the plastic deformation process of the anisotropic sheet metal, the hardening as well as the deformation behavior is actually evolving. The hardening-induced anisotropy strongly affects the plastic deformation behavior, which has been observed experimentally [7], especially in the use of high-strength steel and aluminum alloy.

The R-value is an important material parameter for constitutive model, and it is defined as the ratio of the transverse plastic strain-increments to thickness plastic strain-increments in uniaxial tensile tests [8]. The evolution of texture will lead to the variation of the R-value in plastic deformation [9]. Consequently, the yield surface and flow potential need to be updated with the development of plastic strain [10]. However, the R-value is usually calculated based on measured strains in a certain strain range and is assumed to be a constant. Most anisotropic plasticity models also still use the initial yield stress and invariable R-value to determine the parameters of the yield function, only a few models consider the evaluation of the R-value [11–17]. In order to characterize the change law of the R-value during the plastic deformation, it is usually described as a function of the longitudinal plastic strain. Choi et al. [18] proposed an experimental method for the anisotropic evolution based on DIC and analyzed the evolution of the R-value in the deformation process. Rossi et al. [19] studied the planar anisotropy of sheet metals at large strains based on DIC. Safaei et al. [20] presented a phenomenological approach to describe the evolution of anisotropy during the plastic deformation based on the non-associated flow rule, and the curves of the R-value varying with longitudinal strain were obtained by fitting the longitudinal plastic strain–transverse plastic strain curves with a linear function and a third-order polynomial function, respectively. Yoshida et al. [21] made an interpolation between two yield surfaces at two different levels of the equivalent plastic strain to describe the evolution of the yield surface and gave the changes of the R-value for 3003-O aluminum sheet based on interpolation functions. Lian et al. [22] described the variation of the R-value with longitudinal strain for AISI 439 material. Based on the principle of work equivalence, the relationship between the R-value and equivalent strain was deduced, and the anisotropic behavior was predicted with the non-correlated flow criterion. However, it is not reasonable to regard the rolling direction strain as the equivalent strain.

Although some methods have been proposed to calculate the variable R-value, however, the application conditions and problems of these methods are not been analyzed in detail. In addition, there is no unified method so far to determine the relationship between the R-value and longitudinal plastic strain during deformation. Therefore, based on the initial definition of the R-value, this paper presents a reverse fitting method to characterize the evolution of the R-value with deformation. The proposed reverse fitting model can greatly simplify the secondary development of the phenomenological yield model considering the evolution of anisotropy and enhance the accuracy of FEM.

Experiments

The experimental materials are DC01, DC04, and DC06. Specimens for the standard uniaxial tensile tests are cut along the rolling direction. The size of a specimen is shown in Fig. 1. The standard uniaxial tensile tests are carried out with an Inspekt 100 kN electronic universal material testing machine imported from Germany. The gauge elongation and width reduction of the specimen are measured by the axial extensometer and transverse extensometer, respectively. Then, the transverse–longitudinal plastic strain curves during the uniform deformation stage can be obtained, as shown in Fig. 2. The load–gauge elongation curves are shown in Fig. 3.

Fig. 1 Size of the specimen

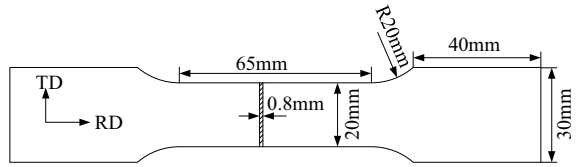


Fig. 2 Longitudinal plastic strain–transverse plastic strain curves in the RD

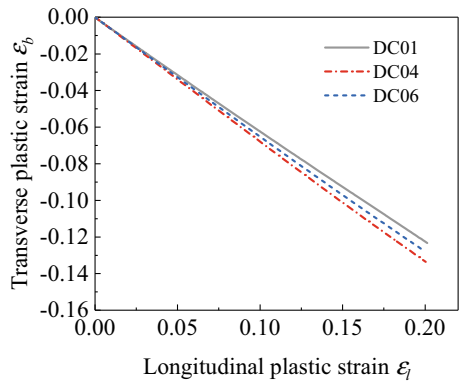
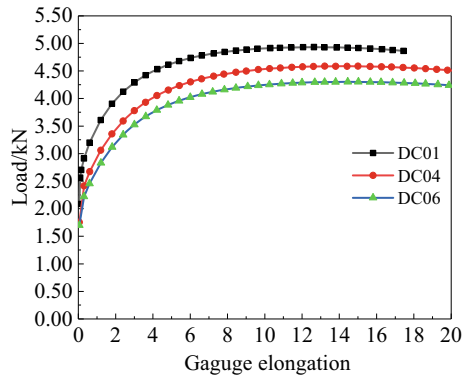


Fig. 3 Load–gauge elongation curves



The plastic anisotropy R-value is defined as

$$R = d\varepsilon_b/d\varepsilon_t \quad (1)$$

where $d\varepsilon_b$ and $d\varepsilon_t$ are the transverse plastic strain-increment and thickness plastic strain-increment, respectively. It is difficult to measure the thickness of plastic strain. Therefore, Eq. (1) is usually translated to the following formula according to the incompressibility constraint.

$$R = -\frac{d\varepsilon_b}{d\varepsilon_t + d\varepsilon_b} \quad (2)$$

Equation (2) can be further transformed as

$$R = -\frac{d\varepsilon_b/d\varepsilon_t}{1 + d\varepsilon_b/d\varepsilon_t} = -\frac{k(\varepsilon_t)}{1 + k(\varepsilon_t)} \quad (3)$$

where $k(\varepsilon_t)$ is the slope of the transverse plastic strain–longitudinal plastic strain curve, and it can be assumed to be a function of the longitudinal plastic strain. According to Eq. (3), the solution of the R-value is essentially the determination of the slope of the plastic strain curve.

Current Research Methods

Point Slope Method (PS Method)

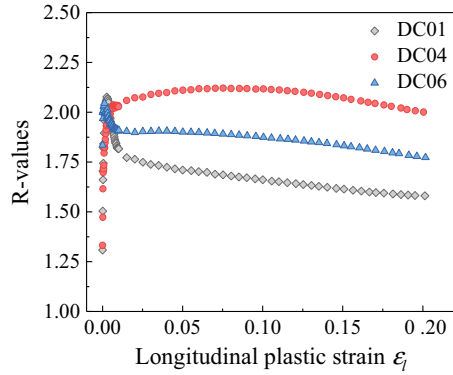
According to standard ISO 10113 [23], the total strain is usually used instead of the strain-increments in the calculation of R-value.

$$R = -\frac{\varepsilon_b}{\varepsilon_t + \varepsilon_b} \quad (4)$$

where ε_t and ε_b are the longitudinal plastic strain and transverse plastic strain at a certain time during the tensile process, respectively. They can be calculated by Eq. (5).

$$\begin{cases} \varepsilon_t = \ln\left(\frac{L_0 + \Delta L}{L_0}\right) - \varepsilon_s \\ \varepsilon_b = \ln\left(\frac{B_0 - \Delta B}{B_0}\right) + \nu\varepsilon_s \end{cases} \quad (5)$$

Fig. 4 R-values obtained based on PS method



where L_0 and B_0 are the initial gauge length and width of the specimen, respectively. ΔL and ΔB are the gauge elongation and width reduction of the specimen, respectively. ϵ_s is the initial yield strain and ν is Poisson’s ratio. Then, the R-values during the uniform plastic deformation stage can be calculated according to Eqs. (4) and (5). In this paper, this method is referred to as Point Slope method (PS method).

In Fig. 4, the R-values significantly increase in the initial deformation stage and then tends to change smoothly. This is because the transition curve from elasticity to plasticity is approximately an arc, and the starting point of plasticity is approximately located in the middle of this arc curve. In fact, Eq. (4) is reasonable only when the deformation of the longitudinal and transverse of the specimen satisfies a certain proportion in the uniaxial tensile test. That is, the longitudinal plastic strain–transverse plastic strain curve is a straight line.

Piecewise Linear Regression Method (PLR Method)

In accordance with standard ISO 10113, the linear regression of the transverse versus longitudinal plastic strain curve within a certain plastic strain is used to calculate the R-value. On this basis, in order to characterize, the R-value varies with the longitudinal strain. An et al. [24] proposed a new piecewise linear regression method. The transverse and longitudinal plastic strain discrete data are divided into i partitions, as shown in Fig. 5. The slope k_i of each interval can be fitted according to Eq. (6) and then the R_i -value of each interval can be calculated by Eq. (7). In this paper, this method is referred to as Piecewise Linear Regression method (PLR method). A comparison of the R-value calculated based on different partition sizes is in Fig. 6.

$$\epsilon_b = k_i \epsilon_l + c_i \tag{6}$$

$$R_i = -\frac{k_i}{1 + k_i} \tag{7}$$

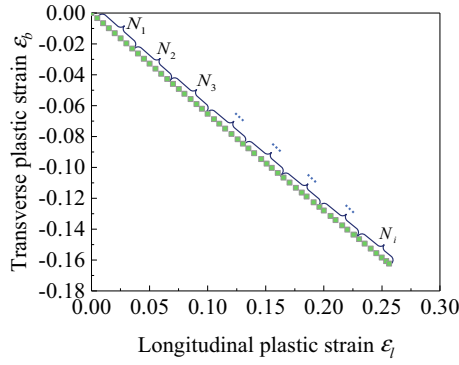


Fig. 5 Schematic diagram of piecewise linear regression method

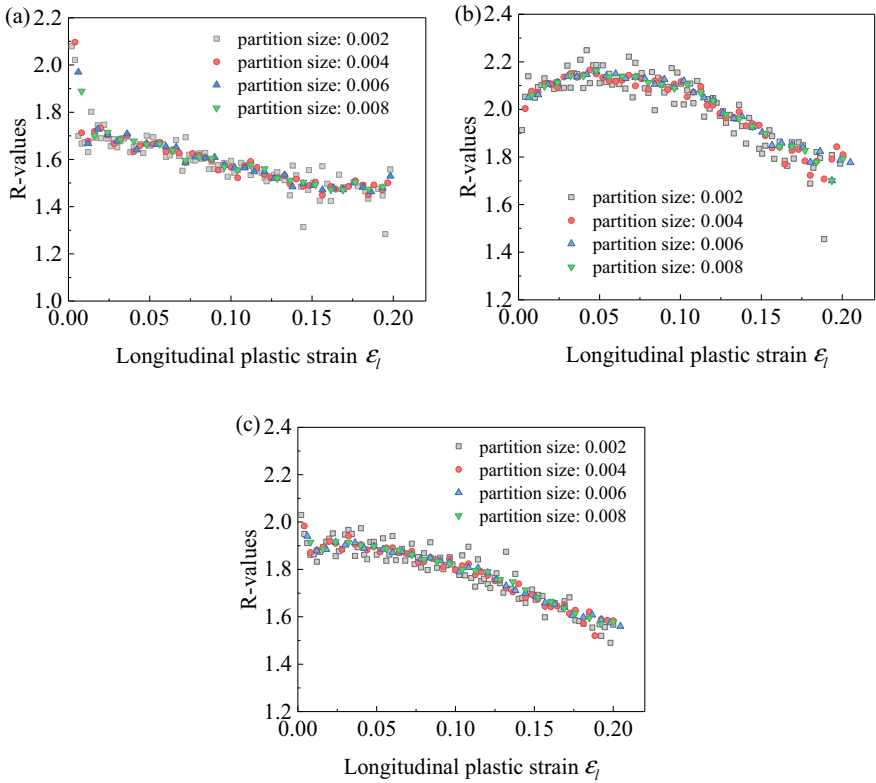


Fig. 6 Comparison of the R-values obtained with different partition sizes according to PLR method: a DC01, b DC04, c DC06

The results show that PLR method is very sensitive to the partition size. The R-values are relatively dispersive when the partition size is too small, and the fitting distortion is easy to occur under this condition. Conversely, few discrete data points can be obtained when the interval size is too large, which cannot reflect the real change law of the R-value. Furthermore, only fitting these discrete points can get the relationship function between the R-value and longitudinal strain, but it will create a new fitting error. Nevertheless, to a certain extent, the results obtained with PLR method can reflect the change law of the R-value with the deformation when a suitable partition size is chosen. Therefore, it can be used to analyze the function form of the relationship between the R-value and longitudinal plastic strain.

Polynomial Fitting Method (Polynomial Method)

Only the discrete data points of R-value can be obtained in the above method. For this reason, relevant scholars proposed to use polynomial function to fit the discrete data of the longitudinal plastic strain and transverse plastic strain [20]. It is assumed that the relationship between the transverse plastic strain and longitudinal plastic strain satisfies

$$\varepsilon_b = c_0 + c_1\varepsilon_l + c_1\varepsilon_l^2 + c_2\varepsilon_l^3 + \cdots + c_n\varepsilon_l^n \quad (8)$$

where c_0, c_1, \dots, c_n are the undetermined coefficients. By deriving on both sides of Eq. (8), the following relationship can be obtained:

$$\frac{d\varepsilon_b}{d\varepsilon_l} = c_1 + 2c_2\varepsilon_l + 3c_3\varepsilon_l^2 + \cdots + nc_n\varepsilon_l^{n-1} \quad (9)$$

According to Eqs. (2) and (9), there is

$$R = -\frac{c_1 + 2c_2\varepsilon_l + 3c_3\varepsilon_l^2 + \cdots + nc_n\varepsilon_l^{n-1}}{1 + c_1 + 2c_2\varepsilon_l + 3c_3\varepsilon_l^2 + \cdots + nc_n\varepsilon_l^{n-1}} \quad (10)$$

In theory, the higher the polynomial order, the higher the fitting accuracy for the relationship between the transverse plastic strain and longitudinal plastic strain. However, the R-value varies with longitudinal strain will be more complex, even the change law is different as shown in Fig. 7. The function form of the R-value obtained with the polynomial method is also complicated, and there is no basis for choosing the polynomial order.

The principle of the above calculation methods is consistent. That is, fitting the data of the transverse plastic strain and longitudinal plastic strain by a function with some undetermined coefficients. Then, the slope of the plastic strain curve can be calculated by deriving these functions. In this paper, the methods based on this

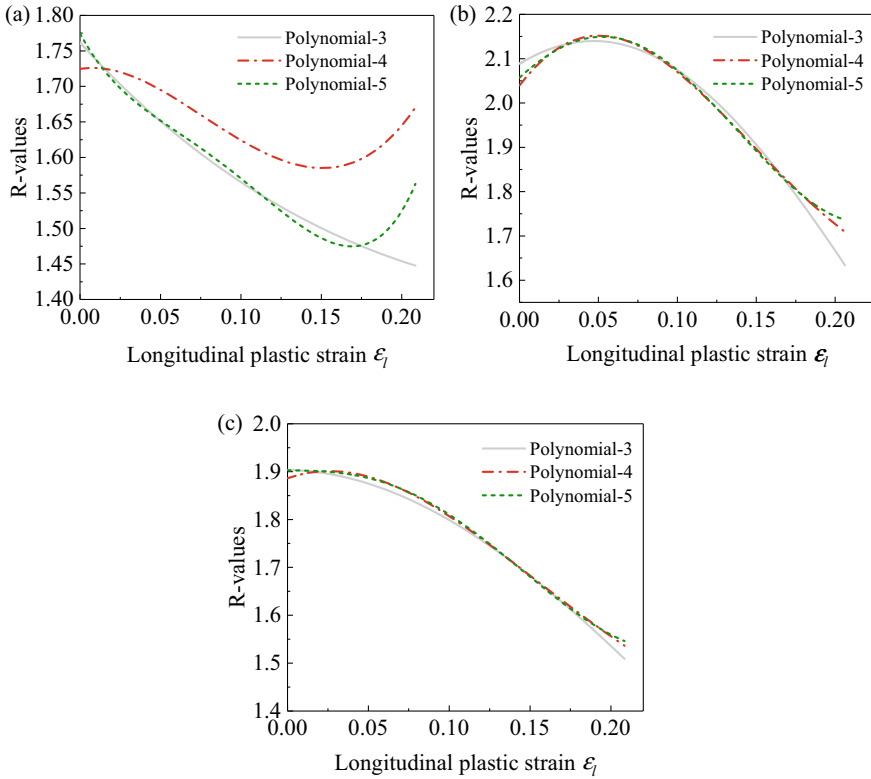


Fig. 7 Comparison of the R-values obtained with different polynomial order: **a** DC01, **b** DC04, **c** DC06

principle are named the forward solution method. However, there is no basis for selecting a suitable fitting function, and the change law of R-value obtained with different fitting functions is vary greatly. In view of the shortcomings of the above calculation methods, a reverse fitting model of the R-value is proposed.

Establishment of the Reverse Fitting Model

Assume that the relationship between the R-value and longitudinal plastic strain satisfies:

$$R = f(\varepsilon_l, a, b, c...) \tag{11}$$

where a , b , and c are the undetermined coefficients. According to Eq. (2), there is

$$-\frac{d\varepsilon_b}{d\varepsilon_l + d\varepsilon_b} = f(\varepsilon_l, a, b, c...) \quad (12)$$

Equation (12) can be further simplified as

$$\frac{d\varepsilon_b}{d\varepsilon_l} = -1 + \frac{1}{f(\varepsilon_l, a, b, c...) + 1} \quad (13)$$

Then, the relationship between the transverse plastic strain and longitudinal plastic strain can be obtained by integrating Eq. (13).

$$\varepsilon_b = -\varepsilon_l + \int \frac{1}{f(\varepsilon_l, a, b, c...) + 1} d\varepsilon_l + C \quad (14)$$

where C is the integral constant which can be calculated according to the boundary condition $\varepsilon_b = \varepsilon_l = 0$ in the initial plastic deformation time. The undetermined coefficients can be determined by fitting the transverse plastic strain and longitudinal plastic strain data based on Eq. (14). Then, Eq. (11) can be determined.

According to the calculation results of the R-value based on PLR method in Sect. “Experiments”, and the previous research results in literatures [20–22, 24], the curves of the R-value vary with longitudinal strain and can be approximately divided into two types: linear function and quadratic function. Linear function is a special form of quadratic function. It is assumed that the relationship function between the R-value and longitudinal plastic strain is a quadratic function:

$$R = a\varepsilon_l^2 + b\varepsilon_l + c \quad (15)$$

where a , b , and c are the undetermined coefficients. According to Eqs. (12), (13), and (15), the following relationship can be derived:

$$\begin{cases} \varepsilon_b = -\varepsilon_l + \frac{2}{\sqrt{4a(1+c) - b^2}} \arctan\left(\frac{2a\varepsilon_l + b}{\sqrt{4a(1+c) - b^2}}\right) + C_1 & b^2 < 4a(1+c) \\ \varepsilon_b = -\varepsilon_l + \frac{1}{\sqrt{b^2 - 4a(1+c)}} \left[\ln \left| \frac{2a\varepsilon_l + b - \sqrt{b^2 - 4a(1+c)}}{2a\varepsilon_l + b + \sqrt{b^2 - 4a(1+c)}} \right| \right] + C_2 & b^2 > 4a(1+c) \end{cases} \quad (16)$$

where

$$\begin{cases} C_1 = -\frac{2}{\sqrt{4a(1+c) - b^2}} \arctan\left(\frac{b}{\sqrt{4a(1+c) - b^2}}\right) \\ C_2 = -\frac{1}{\sqrt{b^2 - 4a(1+c)}} \ln \left| \frac{b - \sqrt{b^2 - 4a(1+c)}}{b + \sqrt{b^2 - 4a(1+c)}} \right| \end{cases} \quad (17)$$

When the R-value varies with the longitudinal strain is approximately a straight line, the value of a obtained by fitting will be approximately zero.

Results and Discussion

According to uniaxial tensile tests, the specimens will undergo elastic deformation, uniform plastic deformation, diffuse instability deformation, located instability deformation, and fracture in turn. However, only the plastic strain data during the uniform plastic deformation stage can be obtained from the standard uniaxial tensile test. The installation position of the transverse extensometer is generally not on the narrowest cross-section. Therefore, the data closed to the necking should be removed to ensure the reliability of the plastic strain data. The longitudinal strain and transverse strain data within an interval of 0%–90% longitudinal strain during the uniform deformation stage are used to fit the undetermined coefficients. A comparison of the R-values based on different methods is shown in Fig. 8.

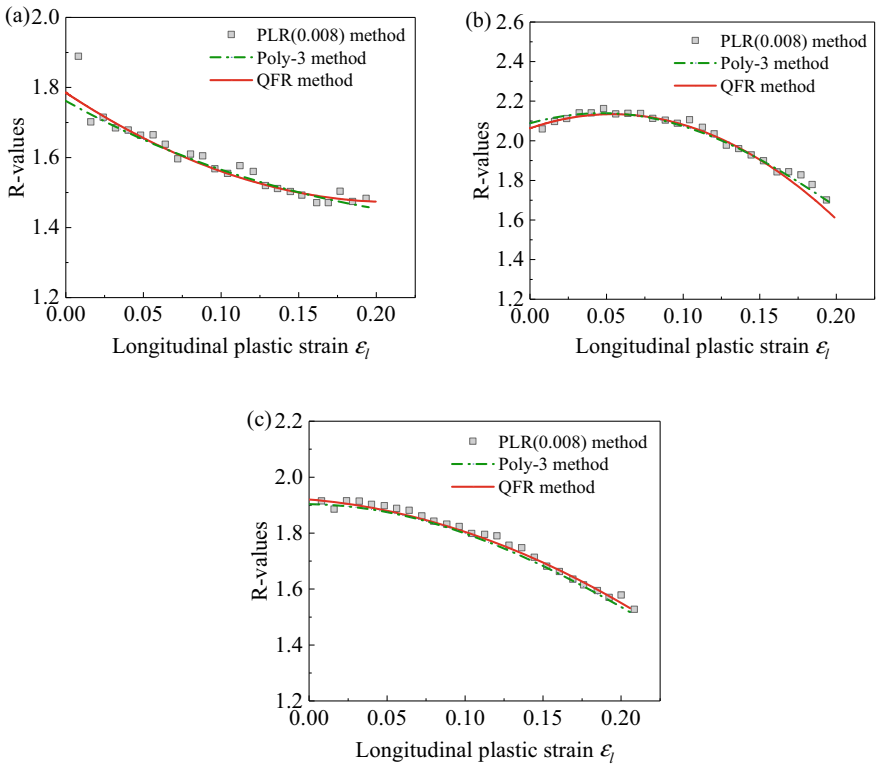
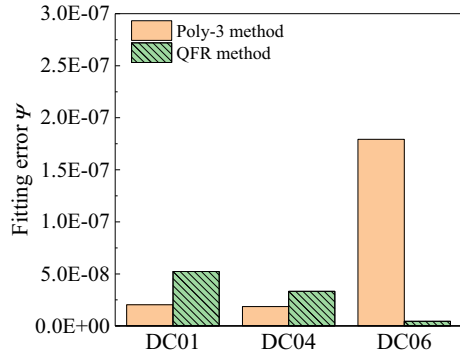


Fig. 8 Comparison of the R-values based on different methods: **a** DC01, **b** DC04, **c** DC06

Fig. 9 Comparison of the fitting error based on different methods



The prediction curves of the R-value based on reverse fitting model agree well with the discrete data points obtained with the PLR method. In order to evaluate the fitting accuracy of different methods, the following error evaluation formulas are established:

$$\psi = \frac{\sum (\varepsilon_b^{pre} - \varepsilon_b^{exp})^2}{\sum |\varepsilon_b^{exp}|} \tag{18}$$

where ε_b^{pre} is the predictive value of the transverse plastic strain and ε_b^{exp} is the experimental value of the transverse plastic strain. Figure 9 shows that the fitting error based on different methods. The reverse fitting model based on quadratic function has relatively high fitting accuracy, and the function form of the R-value obtained with QFR method is simpler than the polynomial method. It is easier to be applied in the secondary development of the constitutive model considering hardening anisotropy. In addition, the reverse fitting model proposed in this paper is not limited to the quadratic function. Therefore, the model has strong flexibility, which provides a valuable reference for the investigation of the R-value with complex variation law.

In order to clarify the effect of the strain curve slope on the calculation results of the R-value, according to Eq. (3), there is

$$dR = \frac{-1}{[1 + k(\varepsilon_l)]^2} dk \tag{19}$$

By Eqs. (3) and (19), the following relationship can be derived:

$$\frac{dR}{R} = \frac{1}{1 + k(\varepsilon_l)} \frac{dk}{k} \tag{20}$$

The above results show that the R-values approximately locate in $1 < R < 2.5$ for most deep drawing sheet metals. Then, the change range of the strain curve slope is $-0.5 < k(\varepsilon_l) < -0.71$. Therefore, according to Eq. (20), the calculation error of

the slope will enlarge the prediction error of the R-value approximately by 2 ~ 3.5 times. Therefore, the significant differences in the R-value calculated by different methods are caused by the calculation error of the strain curve slope. In the future, the methods for determining the plastic strain curve slope should be studied to improve the accuracy of R-values.

Conclusions

- (1) According to R.Hill's orthotropic plasticity theory, the R-value is a function of the derivative of the transverse plastic strain to longitudinal plastic strain. The R-value is a constant only when the relationship of the above two strains is a linear function. Under this condition, the experimental results of the R-value can be obtained with the total strain of uniaxial tension.
- (2) The relationship between the transverse strain and longitudinal strain is approximately a straight line, but the slight change in its slope will lead to a great change in the R-value. In order to obtain high-precision anisotropic constitutive model for sheet metal, the evolution of R-value must be considered.
- (3) The piecewise linear regression method can give the evolution trend of the R-value, but the difference in the partition size will result in the fluctuation of the R-value. The results obtained with this method are relatively discrete and the second fitting will introduce new fitting errors.
- (4) The polynomial forward fitting method can ensure the fitting accuracy of the relationship between the transverse strain and longitudinal strain, but it cannot guarantee the accuracy of its derivative function. Because of the different orders of polynomial, the evolution of the R-value is diverse and the function form of the R-value is very complex.
- (5) The proposed reverse fitting model of quadratic function with three undetermined coefficients can not only ensure the fitting accuracy of the uniaxial tensile strain relationship but also show a high degree of consistency in the evolution law of the R-value. Its function form is simple and the undetermined coefficients are few, which provides great convenience for the establishment of the high-precision anisotropic constitutive model for sheet metal.
- (6) With the increase in the uniaxial tensile plastic strain, the evolution of the R-value is generally downward, and the curve form can be divided into two types: up convex and down concave.

References

1. Hill R (1948) A theory of the yielding and plastic flow of anisotropic metals. *Proc R Soc Lond Ser A Math Phys Sci* 193:281–297
2. Barlat F, Lege DJ, Brem JC (1991) A six-component yield function for anisotropic materials. *Int J Plast* 7:693–712
3. Barlat F, Lian K (1989) Plastic behavior and stretchability of sheet metals. Part I: a yield function for orthotropic sheets under plane stress conditions. *Int J Plast* 5:51–66
4. Barlat F, Maeda Y, Chung K, Yanagawa M, Brem JC, Hayashida Y, Lege DJ, Matsui K, Murtha SJ, Hattori S, Becker RC, Makosey S (1997) Yield function development for aluminum alloy sheets. *J Mech Phys Solids* 45:1727–1763
5. Hu W (2003) Characterized behaviors and corresponding yield criterion of anisotropic sheet metals. *Mat Sci Eng A* 345:139–144
6. Aretz H (2005) A non-quadratic plane stress yield function for orthotropic sheet metals. *J Mater Process Technol* 168:1–9
7. Ohashi Y, Kawashima K, Yokochi T (1975) Anisotropy due to plastic deformation of initially isotropic mild steel and its analytical formulation. *J Mech Phys Solids* 23:277–294
8. Lankford WT, Snyder SC, Bauscher JA (1950) New criteria for predicting the press performance of deep drawing sheets. *Trans Am Soc Metals* 42:1197–1225
9. Savoie J, Jonas JJ, Macewen SR, Perrin R (1995) Evolution of r-value during the tensile deformation of aluminium. *Textures Microstruct* 23:149–171
10. Choi Y, Han C, Lee JK, Wagoner RH (2006) Modeling multi-axial deformation of planar anisotropic elasto-plastic materials, part I: theory. *Int J Plast* 22:1745–1764
11. Barlat F, Gracio JJ, Lee M, Rauch EF, Vincze G (2011) An alternative to kinematic hardening in classical plasticity. *Int J Plast* 27:1309–1327
12. Hu H (1975) The strain-dependence of plastic strain ratio (r value) of deep drawing sheet steels determined by simple tension test. *Metall Trans A* 6:945–947
13. Hu W (2007) Constitutive modeling of orthotropic sheet metals by presenting hardening-induced anisotropy. *Int J Plast* 23:620–639
14. Stoughton TB, Yoon JW (2009) Anisotropic hardening and non-associated flow in proportional loading of sheet metals. *Int J Plast* 25:1777–1817
15. Truszkowski W (1976) Influence of strain on the plastic strain ratio in cubic metals. *Metall Trans A* 7:327–329
16. Xie Q, Van Bael A, An YG, Lian J, Sidor JJ (2018) Effects of the isotropic and anisotropic hardening within each grain on the evolution of the flow stress, the r-value and the deformation texture of tensile tests for AA6016 sheets. *Mater Sci Eng A-Struct Mater Prop Microstruct Process* 721:154–164
17. Zamiri A, Pourboghra F (2007) Characterization and development of an evolutionary yield function for the superconducting niobium sheet. *Int J Solids Struct* 44:8627–8647
18. Choi Y, Walter M, Lee J, Han C (2006) Observations of anisotropy evolution and identification of plastic spin parameters by uniaxial tensile tests. *J Mech Mater Struct* 1:301–323
19. Rossi M, Broggiato GB, Papani S (2008) Application of digital image correlation to the study of planar anisotropy of sheet metals at large strains. *Meccanica* 43:185–199
20. Safaei M, Lee M, Zang S, De Waele W (2014) An evolutionary anisotropic model for sheet metals based on non-associated flow rule approach. *Comput Mater Sci* 81:15–29
21. Yoshida F, Hamasaki H, Uemori T (2015) Modeling of anisotropic hardening of sheet metals including description of the Bauschinger effect. *Int J Plast* 75:170–188
22. Lian J, Shen F, Jia X, Ahn D, Chae D, Münstermann S, Bleck W (2018) An evolving non-associated Hill48 plasticity model accounting for anisotropic hardening and r-value evolution and its application to forming limit prediction. *Int J Solids Struct* 151:20–44
23. ISO 10113 (2006) Metallic materials-sheet and strip-determination of plastic strain ratio
24. An YG, Vegter H, Melzer S, Triguero P R (2013) Evolution of the plastic anisotropy with straining and its implication on formability for sheet metals. *J Mater Process Technol* 213:1419–1425

Modelling Transient Mechanical Behavior of Aluminum Alloy During Electric-Assisted Forming



Jai Tiwari, Hariharan Krishnaswamy, and Murugaiyan Amirthalingam

Abstract Electric-assisted forming is a promising technique in which the mechanical behavior of the materials is altered by the application of electric current during deformation. Advantages of electric-assisted forming include improved ductility, reduction of flow stress, and springback. The alteration in the mechanical behavior is in general linked to Joule's heating due to the lack of comprehensive understanding of the mechanism of electric-assisted deformation. Significant efforts are being made in the field of electroplasticity to propose the existence of additional mechanisms through which the electrical effects on deformation could be better explained by experimental and numerical approaches. However, a consensus is lacking on the governing mechanism and a generalized constitutive model for electroplastic deformation therefore is not yet established. In the present work, two models, namely, Joule's heating-based and dislocation density-based are used to predict the mechanical behavior of aluminium alloy samples subjected to pulsed electric current. The dislocation density-based model superposes the thermal and athermal mechanical behavior independent of the underlying mechanism. Results indicate that an attempt to model the electroplastic behavior purely through Joule's heating produces inconsistent results. It is shown that the Joule's heating model can accurately predict either the temperature history or the mechanical behavior and not concurrently.

Keywords Electric-assisted forming · Constitutive model · Joule's heating · Dislocation density

J. Tiwari (✉) · H. Krishnaswamy
Department of Mechanical Engineering, IIT Madras, Chennai 600036, India
e-mail: me18d006@smail.iitm.ac.in

M. Amirthalingam
Department of Metallurgical and Materials Engineering, Indian Institute of Technology Madras,
Chennai 600036, India

Introduction

Electric-assisted forming involves the application of electric current during the deformation process. The interaction between the applied current and plastic deformation on the mechanical behaviour is generally referred to as electro-plastic effect. Application of electric current leads to significant improvement in formability [1, 2]. Other advantages of electric-assisted forming include reduction of springback [3] and anisotropy effects [4]. The alteration in the mechanical behavior is in general linked to Joule's heating [5]. However, subsequent efforts in the field have proposed the existence of additional mechanisms. These mechanisms include electron wind effect [6], magnetoplasticity [7], and charge imbalance around the defects [8]. The exact rate-controlling mechanism of the observed behavior is still debatable. Therefore, a comprehensive constitutive model to explain the electroplastic effect is not yet established.

Several efforts in the past have been made to systematically analyze the changes in the mechanical behavior under electric-assisted (EA) deformation. These modelling attempts were focused primarily on the Joule's heating due to the lack of complete understanding of the electroplasticity mechanism. In one such attempt, Kroneberger et al. [9] modelled the electric-assisted upsetting process assuming Joule's heating only. The predicted results were found to be deviating from the experimental results. Subsequent efforts were made to modify the heat transfer parameters [10, 11]. Although they were successful in predicting the temperature profile, none of the above could predict the flow stress softening due to EA deformation. This approach completely ignores the microstructural changes such as dislocation density during EA deformation. Any model [12, 13] that considers only the temperature effect on the mechanical behavior is not sufficient to accurately predict the electroplastic behaviour. Therefore, a model capable of incorporating the changes in mechanical behavior under EA deformation will enable us to understand the mechanisms behind it.

In the present work, two models are considered to evaluate the efficacy of a coupled model to predict the electroplastic behavior. For this purpose, a finite element framework is developed for a coupled electrical–thermal–structural analysis in a commercial software ABAQUS. Firstly, the traditional Joule's heating model is implemented into the framework using the electric–thermal parameters. In the same framework, the dislocation density-based constitutive model coupled with Joule's heating effect is implemented using user material (UMAT) subroutines. In order to estimate the extent of error, the results predicted using the dislocation density model are compared with that predicted assuming traditional Joule's heating.

Modelling the Electroplastic Effect

Joule's Heating Model

In case of electric-assisted deformation, temperature of the specimen increases due to Joule's heating effect. Simultaneously, heat loss to the ambient environment takes place from the specimen. The thermal balance of the specimen can be given as

$$mc_p\Delta T = \zeta I^2 Rt - hA_s(T - T_A), \quad (1)$$

where m , c_p , ΔT , A_s , and T represent mass, specific heat capacity, increase in specimen temperature, surface area, and instantaneous temperature of the specimen, respectively. In the Eq. 1, ζ , h , and T_A represent Joule's heating fraction, overall heat transfer coefficient, and ambient temperature, respectively. From the temperature change (ΔT), the resulting drop in flow stress ($\Delta\sigma$) can be predicted using the high-temperature properties of the specimen, as shown in the literature [14].

Dislocation Density-Based Model

A dislocation density-based constitutive model [15, 16] is used to model the electroplastic behaviour. This model is a simplified form of Kocks–Mecking–Estrin model [17], according to which the flow stress is a function of averaged dislocation density ρ as

$$\sigma = M\alpha Gb\sqrt{\rho} \left(\frac{\dot{\epsilon}}{\dot{\epsilon}_0} \right)^{\frac{1}{m}}, \quad (2)$$

where M , G , b , and m are Taylor factor, shear modulus, Burger's vector, and strain rate exponent, respectively. $\dot{\epsilon}_0$ corresponds to a critical strain rate at which the thermal component of the flow stress reaches to zero. The material constant, α is obtained by curve fitting the experimental stress–strain data. The evolution of dislocation density (ρ) with respect to strain (ϵ) is given as

$$\frac{d\rho}{d\epsilon} = M(K_1\sqrt{\rho} - K_2\rho), \quad (3)$$

where K_1 and K_2 represent the coefficients of stage-II and stage-III strain hardening, respectively. The parameter K_1 is treated as constant, as the stage-II hardening is athermal in nature. State-III hardening relates to the recovery or annihilation of dislocations. Therefore, the coefficient K_2 relies on temperature and strain rate. It can be represented [17] as

$$K_2 = (K_2)_0 \left(\frac{\dot{\varepsilon}}{\dot{\varepsilon}_0} \right)^{-\frac{1}{n}}, \quad (4)$$

where $(K_2)_0$ is a material constant and the exponent n depends on temperature.

In Eq. 2, m and α and $\dot{\varepsilon}$ depend on the temperature and strain rate. Similarly, n in Eq. 4 depends on temperature. In order to avoid complexity, the rate dependency of m and $\dot{\varepsilon}_0$ is coupled with that of α [16]. Therefore, α and n can be modelled as

$$\alpha = \alpha_0 \beta_1 \{ \dot{\varepsilon}^{\beta_2} T^{\beta_3} \}, \quad (5)$$

$$n = \beta_6 \{ T^{\beta_7} \}, \quad (6)$$

where α_0 , β_1 , β_2 , β_3 , β_6 , and β_7 are material constants.

The rate-dependent parameters (α and n) can be further modified to include the effect of electric current. The following relation, which was originally proposed in [15], is utilized in the present work.

$$\alpha = \alpha_0 \beta_1 \left\{ \dot{\varepsilon}^{\beta_2} T^{\beta_3} + \frac{\beta_4}{\beta_1} J^{\beta_5} \right\}, \quad (7)$$

$$n = \beta_6 \left\{ T^{\beta_7} + \frac{\beta_8}{\beta_6} J^{\beta_9} \right\}, \quad (8)$$

where the constants β_4 , β_5 , β_8 , and β_9 are used to describe the electroplastic effect for a current density J . The procedure to obtain the above-mentioned parameters is explained in our recent work [18].

A two-parameter dislocation–density model was proposed to account for the recovery in pulsed mode. In that case, the total dislocation density is decomposed to forward (ρ_f) and reverse (ρ_r) components [16]. In the present work, if $\overset{\circ}{\rho}_f$ is the total dislocation density at a given strain corresponding to the application of electric pulse, the ρ_f and ρ_r are given by

$$\rho_f = (1 - p) \overset{\circ}{\rho}_f, \quad (9)$$

$$\rho_r = p \overset{\circ}{\rho}_f, \quad (10)$$

where ‘ p ’ is a scalar indicating the fraction of reverse dislocation split from the total dislocation density during the reduction of electric current density. ρ_r decreases with strain and its evolution is given by

$$\frac{d\rho_r}{d\varepsilon} = -q M K_1 \sqrt{\rho_f} \frac{\rho_r}{\overset{\circ}{\rho}_f} \quad (11)$$

where the scalar ‘ q ’ corresponds to the rate of evolution of reverse dislocation.

The flow stress in Eq. 2 is modified as

$$\sigma = M\alpha Gb \left(\frac{\dot{\epsilon}}{\dot{\epsilon}_{\text{ref}}} \right)^{1/m} \sqrt{\rho_f - \rho_r} \quad (12)$$

When scalars p and q become zero, $\rho_r = 0$ and the governing equations return to the continuous current application case.

The model superposes the thermal and athermal mechanical behavior independent of the underlying mechanism by modifying the variables n and α .

Finite Element Framework

Steps followed in the finite element modelling of electric-assisted deformation are described below:

1. A real scale model of the cylindrical specimen was created with a length of 15 mm and diameter of 10.2 mm. Specimen, upper platen, and lower platen were modelled to simulate the experimental setup, as shown in Fig. 1.
2. Eight-node general-purpose linear brick element (C3D8) is used to carry out the FE analysis. A suitable mesh size (0.5 mm) for the modeled specimen is chosen after a detailed mesh convergence study.
3. A fully coupled thermal–electrical–structural analysis is performed due to the necessity of coupling between the displacement, temperature, and electric fields to obtain solutions for all three fields simultaneously.
4. Fixed boundary condition (displacements and rotations are restricted) is imposed on the lower platen and the boundary condition of the upper platen is given in such a way that the specimen could move only in the axial direction. The cross-head speed was maintained at 2 mm/min during the simulation.
5. The specimen and the platens are bonded using the TIE constraint option. The TIE constraint bonds surfaces together so that there is no relative motion between them. Also, the contact between the platens and specimen is considered to be perfect in the present analysis.
6. The electric current amplitude is converted to the instantaneous current density and applied as electrical load at the top of the specimen. The bottom side of the specimen is grounded to ensure the flow of the electric current in die–specimen assembly.
7. Temperature evolution during EA deformation was measured using a non-contact type FLIR-T621 infrared camera.
8. High-temperature stress–strain behavior of the material is taken from the reference [19]. The thermophysical properties of the material and overall heat transfer coefficient used in the present framework are given in Table 1.

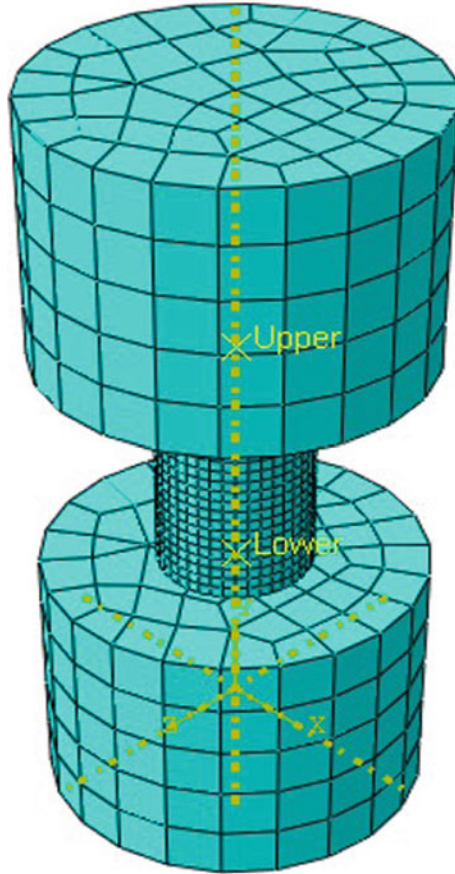


Fig. 1 Setup assembly of platen and specimen used in the finite element analysis is shown

Table 1 Properties used in the present framework

Specific heat (C_p) ($\text{J kg}^{-1} \text{K}^{-1}$)	Thermal conductivity (k) ($\text{W m}^{-2} \text{K}^{-1}$)
$929 - 0.627 * T$	$25.2 + 0.398 * T$
Joule heating fraction (ζ)	Overall heat transfer coefficient (h) ($*10^3, \text{W m}^{-1} \text{K}^{-1}$)
0.9	0.765

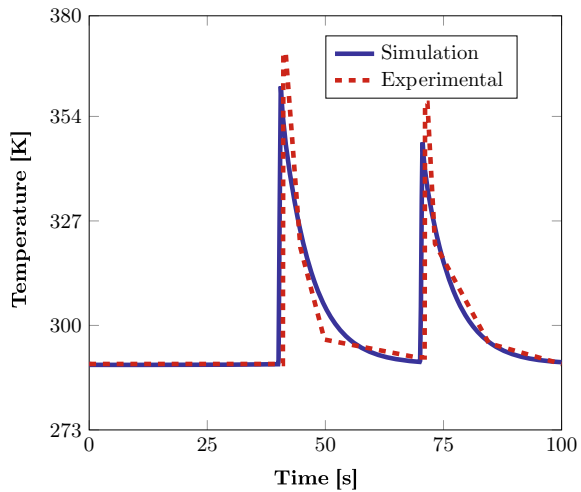
Results and Discussion

In the present work, Joule's heating model and the dislocation density model are evaluated using the pulsed current-assisted results of AA 60661-T6 alloy published in the literature [20]. The present analysis is performed till a strain of 0.2 to avoid any potential fracture. As mentioned in literature [20], nominal electric current densities of 75 and 90 A/mm² are applied for a duration of 0.5 s with a background time of 29.5 s for the pulsed current-assisted tests.

In order to obtain the Joule's heating fraction and overall heat transfer coefficient, iterative FE simulations were performed to match the experimentally observed temperature history. Predicted temperature history in case of current density, $J = 90 \text{ A/mm}^2$; fits satisfactorily with the experimental profile as shown in Fig. 2. Subsequently, the FE simulation is carried out at a nominal current density of 75 A/mm² with the same modelling parameters. The resulting stress–strain behavior along with the experimental results are shown in Fig. 3. It is clear from Fig. 3 that Joule heating model produces inconsistent results while describing stress–strain behavior under electric-assisted deformation.

In the same FE framework, the dislocation density-based constitutive model is implemented using user material (UMAT) subroutines. The fitting constants used in the model are tabulated in Table 2. The predicted stress–strain behavior is presented along with the experimental results in Fig. 4.

Fig. 2 FE simulation result of temperature profile is plotted with the experimentally recorded temperature history



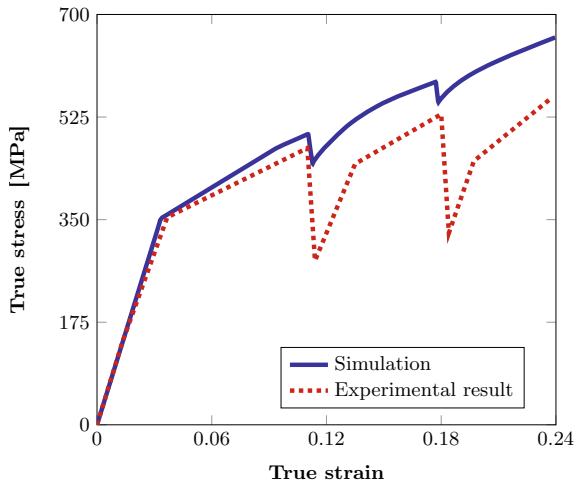
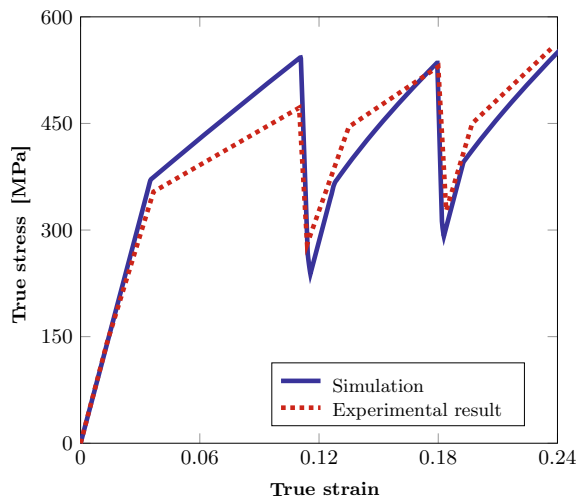


Fig. 3 FE simulation result of temperature profile is plotted with the experimentally recorded temperature history

Table 2 Parameters used in the dislocation density model [21]

M	α_0	G (MPa)	b (mm)	K_1	K_{20}	m	ϵ_0 (S^{-1})	ρ_0 (mm^{-2})	β_1
3.5	0.45	27,000	$2.86 \cdot 10^{-7}$	5000	55	2.2	$1.5 \cdot 10^{-7}$	$7.67 \cdot 10^5$	1
β_2	β_3	β_4	β_5	β_6	β_7	β_8	β_9	p	q
-0.33	-0.5	-0.065	0.31	0.22	0.42	0.35	0.1	0.3	1

Fig. 4 FE simulation result of temperature profile is plotted with the experimentally recorded temperature history



Conclusion

In the present work, two models to predict the electroplastic behaviour have been examined in the same finite element framework. It is observed that the Joule heating model could not accurately predict the temperature profile and stress–strain behavior concurrently. The limitation of Joule’s heating model is overcome by the use of modified dislocation density model. This constitutive model in conjunction with Joule’s heating effect predicts the mechanical behavior of aluminum alloys under electric-assisted deformation satisfactorily.

Acknowledgements Authors would like to acknowledge the financial support from the Science and Engineering Research Board (Project reference: CRG/2019/0D3539), Department of Science and Technology (DST), India.

References

1. Roth JT, Loker I, Mauck D, Warner M, Golovashchenko SF, Krause A (2008) In: Transactions of the North American manufacturing research institution of SME, pp 405–412
2. McNeff PS, Paul BK (2020) *J Alloy Compd* 829:154438
3. Lee J, Bong HJ, Lee YS, Kim D, Lee MG (2019) *Metall Mater Trans A* 50(6):2720
4. Pleta AD, Krugh MC, Nihhare C, Roth JT (2013) In: ASME 2013 international manufacturing science and engineering conference collocated with the 41st North American manufacturing research conference, p V001T01A018
5. Goldman P, Motowidlo L, Galligan J (1981) *Scripta Metallurgica* 15(4):353
6. Conrad H (2000) *Mater Sci Eng: A* 287(2):276
7. Molotskii M, Fleurov V (1995) *Phys Rev B* 52(22):15829
8. Kim MJ, Yoon S, Park S, Jeong HJ, Park JW, Kim K, Jo J, Heo T, Hong ST, Cho SH et al (2020) *Appl Mater Today* 21:100874
9. Kronenberger TJ, Johnson DH, Roth JT (2009) *J Manuf Sci Eng* 131(3):031003
10. Hariharan K, Lee MG, Kim MJ, Han HN, Kim D, Choi S (2015) *Metall Mater Trans A* 46(7):3043
11. Ruzskiewicz BJ, Mears L, Roth JT (2018) *J Manuf Sci Eng* 140(9)
12. Salandro WA, Bunget C, Mears L (2010) In: ASME 2010 international manufacturing science and engineering conference. American Society of Mechanical Engineers, pp 581–590
13. Magargee J, Fan R, Cao J (2013) *J Manuf Sci Eng* 135(6)
14. Salandro WA, Bunget CJ, Mears L (2012) Proceedings of the institution of mechanical engineers. Part B: *J Eng Manuf* 226(5):775, 031003
15. Kim MJ, Lee MG, Hariharan K, Hong ST, Choi IS, Kim D, Oh KH, Han HN (2017) *Int J Plast* 94:148
16. Krishnaswamy H, Kim MJ, Hong ST, Kim D, Song JH, Lee MG, Han HN (2017) *Mater Des* 124:131
17. Estrin Y (1996) Unified constitutive laws of plastic deformation 1:69
18. Tiwari J, Pratheesh P, Bembalge O, Krishnaswamy H, Amirthalingam M, Panigrahi S (2021) *J Mater Res Technol* 12:2185
19. Dorbane A, Ayoub G, Mansoor B, Hamade R, Kridli G, Imad A (2015) *Mater Sci Eng: A* 624:239
20. Hong ST, Jeong YH, Chowdhury MN, Chun DM, Kim MJ, Han HN (2015) *CIRP Ann* 64(1):277
21. Tiwari J, Balaji V, Krishnaswamy H, Amirthalingam M (2022) *International Journal of Mechanical Sciences*, p 107433

Numerical Prediction of Failure in Single Point Incremental Forming Using a New Yield Criterion for Sheet Metal



H. Quach, X. Xiao, J. J. Kim, and Y. S. Kim

Abstract A new yield function depends on the second stress invariant J_2 and the third stress invariant J_3 is proposed to describe the elastoplastic behavior of sheet metals. Additionally, a series of basic fracture testing covering a wide range of stress state and different material orientations for aluminum alloy is carried out. The ductile fracture of the aluminum alloy is investigated using a hybrid experimental–numerical approach. Besides, a new uncoupled ductile fracture that is concerned with the micro-mechanisms of voids is introduced to predict the failure of material. The new yield criterion and fracture model are implemented into the ABAQUS/Explicit code to predict the fracture in different stress states. The incremental sheet-forming tests are performed to verify the efficiency of the proposed yield criterion and fracture criterion. The proposed yield criterion and fracture model can be utilized for predicting plastic deformation and initial fracture in sheet metal forming.

Introduction

Incremental sheet forming (ISF) is a flexible sheet-forming process that has gained significant interest since the pioneering work of Iseki et al. [1]. ISF is a highly localized deformation process in which a tool is programmed to move along to a certain path to create the desired part geometry. A simple incremental sheet-forming process to manufacture a truncated cone is depicted in Fig. 1 [2]. Without complex tools and dies, the process can form various part geometries directly from computer-aided design models and computer numerical control codes. The process has great potential for rapid parts prototyping requiring small quantities.

H. Quach · X. Xiao · J. J. Kim

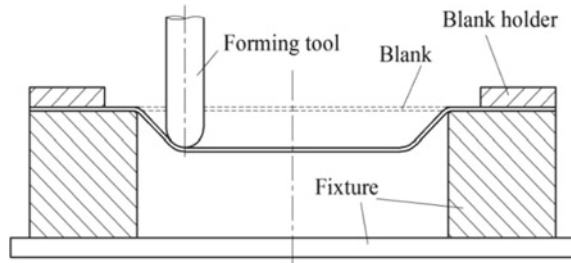
Graduate School of Mechanical Engineering, Kyungpook National University, 80, Daehakro, Bukgu, Daegu 41566, Korea

Y. S. Kim (✉)

School of Mechanical Engineering, Kyungpook National University, 80, Daehakro, Bukgu, Daegu 41566, Korea

e-mail: caekim@knu.ac.kr

Fig. 1 Single point incremental forming for truncated cone



Aluminum sheets are well known to develop considerable plastic anisotropy on the mechanical properties due to the extrusion and rolling processes. The anisotropy properties have strong effect on the plastic deformation and the fracture initiation in several manufacturing processes especially in automotive industry. The prediction of anisotropic plastic deformation of metals is critical for the design of lightweight structure. Although there are a lot of efforts in prediction of anisotropic plastic deformation and fracture initiation in sheet metal forming, these works still remain significant issues. In this paper, a new yield function named Kim-Van equation describes the elastoplastic behavior of sheet metals. This yield function depends not only on the second stress invariant J_2 for the yield but also on the third stress invariant J_3 , both may effect on the shape of the yield surface. The extension of this criterion is developed using generalized invariants of the stress deviator for anisotropy. The proposed yield function greatly enhances the flexibility of describing the strong anisotropic materials. Besides, a uncoupled ductile fracture which is concerned with the micro-mechanisms of void nucleation, void growth, and evolution of void coalescence is used to predict the failure of material. These two models are implemented into Abaqus/Explicit using a user subroutine to predict fracture in ISF. Compared with the experiment results, the proposed yield criterion and ductile fracture criterion can be utilized for predicting plastic deformation and initial fracture in single point incremental sheet metal forming.

Anisotropic Yield Function

Kim-Van Yield Function

In the present study, the proposed yield function represents a symmetric yield function, which is applied to materials such as aluminum and steel, and it is expressed as follows:

$$f \equiv J_2^6 + \alpha J_3^4 + \beta (J_2^3 \times J_3^2) = k^{12} \quad (1)$$

where J_2 and J_3 are the invariants discussed in the introduction, k denotes the yield stress in pure shear, and α and β_j are material constants.

Anisotropic generalizations of the second and third invariants are expressed as follows:

$$J_2^0 = \frac{a_1}{6}(\sigma_{xx} - \sigma_{yy})^2 + \frac{a_2}{6}(\sigma_{yy} - \sigma_{zz})^2 + \frac{a_3}{6}(\sigma_{xx} - \sigma_{zz})^2 + a_4\sigma_{xy}^2 + a_5\sigma_{xz}^2 + a_6\sigma_{yz}^2 \quad (2)$$

$$\begin{aligned} J_3^0 = & \frac{1}{27}(b_1 + b_2)\sigma_{xx}^3 + \frac{1}{27}(b_3 + b_4)\sigma_{yy}^3 + \frac{1}{27}[2(b_1 + b_4) - b_2 - b_3]\sigma_{zz}^3 \\ & - \frac{1}{9}(b_1\sigma_{yy} + b_2\sigma_{zz})\sigma_{xx}^2 - \frac{1}{9}(b_3\sigma_{zz} + b_4\sigma_{xx})\sigma_{yy}^2 \\ & - \frac{1}{9}[(b_1 - b_2 + b_4)\sigma_{xx} + (b_1 - b_3 + b_4)\sigma_{yy}]\sigma_{zz}^2 + \frac{2}{9}(b_1 + b_4)\sigma_{xx}\sigma_{yy}\sigma_{zz} \\ & - \frac{\sigma_{xz}^2}{3}[2b_9\sigma_{yy} - b_8\sigma_{zz} - (2b_9 - b_8)\sigma_{xx}] \\ & - \frac{\sigma_{xy}^2}{3}[2b_{10}\sigma_{zz} - b_5\sigma_{yy} - (2b_{10} - b_5)\sigma_{xx}] \\ & - \frac{\sigma_{yz}^2}{3}[2b_7\sigma_{xx} - b_6\sigma_{yy} - (2b_7 - b_6)\sigma_{zz}] + 2b_{11}\sigma_{xy}\sigma_{xz}\sigma_{yz} \end{aligned} \quad (3)$$

In the above expressions, a_i ($i = 1 \dots 6$) and b_j ($j = 1 \dots 11$) are coefficients that describe anisotropy. If $a_i = b_j = 1$, it becomes isotropic yield functions.

Calibrate Plastic Model

The strain hardening behavior of aluminum 5052-H32 (AA5052-H32) is determined from uniaxial tension results at rolling direction (Fig. 2). The stress–strain relation is modeled by Kim-Tuan hardening equation [3] as follows:

$$\sigma = \sigma_0 + K(\varepsilon + \varepsilon_0)^h(1 - \exp^{-t\varepsilon}) \quad (4)$$

where σ represents the equivalent stress, σ_0 denotes the initial yield stress, K denotes a material constant to control the expansion of hardening stress, t and h denote parameters of the hardening model, ε_0 denotes the initiation of plastic deformation, and $\varepsilon_0 = 0.002$.

Several dog-bone specimens were cut from the sheet along 0° , 15° , 30° , 45° , 60° , 75° , and 90° with respect to the rolling direction to identify the Lankford r -value and the yield stress at these directions. Besides, the cruciform specimens were prepared

Fig. 2 Stress–strain curve fitted by Kim-Tuan hardening equation

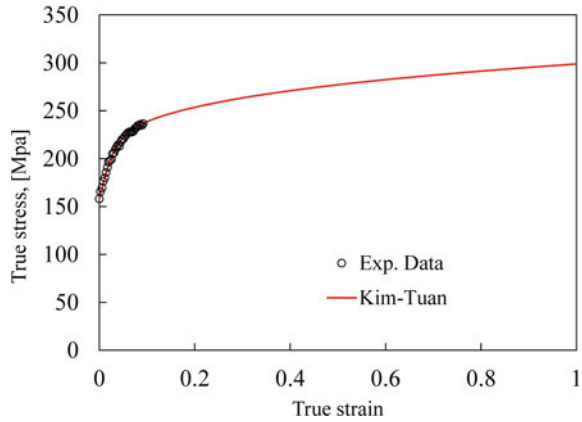
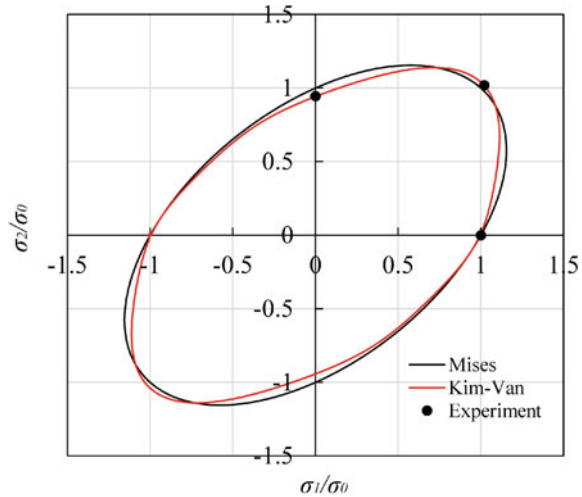


Fig. 3 Yield locus fitted by Kim-Van yield function for aluminum alloy 5052-H32



to determine the biaxial yield stress. The Lankford r-values and yield stress were utilized to calibrate the Kim-Van yield function as shown in Fig. 3.

Ductile Fracture in ISF

Single point incremental sheet forming has some limitations and encounters the challenges in application of some lightweight alloys, especially for failure and fracture during forming the desired geometric components. As a microscopic crack, ductile fracture occurs with damage accumulation and the material softening after large plastic deformation stage, including the nucleation of voids, the growth of voids

and eventually the coalescence of voids. So the study for prediction initiation and propagation of failure and fracture in SPIF is necessary and promising. Because the prediction of failure and fracture in SPIF can reveal the deformation mechanics and failure evolution, and provide some reference for practical SPIF process. Mirnia et al. [4] have incorporated ductile fracture models into SPIF to simulate damage accumulation and propagation of fracture. It is noted that the fracture forming limit diagram (FFLD) in SPIF is different in shape and value from conventional forming process and other findings. Li et al. [5] utilized the Gurson–Tvergaard–Needleman (GTN) damage model in order to analyze the fracture prediction in ISF. Jin et al. [6] combined the Lemaitre damage model into a modified constitutive model and implemented the model to FE simulations of ISF.

In efforts to predict the anisotropic ductile fracture behaviors in ISF, an extent of ductile fracture criterion of Quach et al. [7] work for anisotropic material is introduced as

$$\bar{\epsilon}_f = \frac{C_1}{\left(\eta + \frac{3-\mu}{3*\sqrt{\mu^2+3}} + \frac{1}{\sqrt{\mu^2+3}} \right)^{C_2} \left(\frac{3+\sqrt{3}C_3}{\sqrt{\mu^2+3}} - C_3 \right)} \tag{5}$$

where

$$\eta = \frac{\sigma_{xx} + \sigma_{yy} + \sigma_{zz}}{3 * \tilde{\sigma}} \tag{6}$$

$$\mu = \frac{2\sigma_{yy} - \sigma_{xx} - \sigma_{zz}}{\sigma_{xx} - \sigma_{zz}} - 1 \leq \mu \leq 1, \text{ with } \sigma_{xx} \geq \sigma_{yy} \geq \sigma_{zz} \tag{7}$$

$\bar{\epsilon}_f^p$ is equivalent plastic strain at the failure; η is stress triaxiality; μ is Lode stress parameter; $C_1, C_2,$ and C_3 are material parameters which are calibrated from fracture experiments testing. $\tilde{\sigma}$ is effective stress presented by Kim-Van yield function.

ISF Experiments

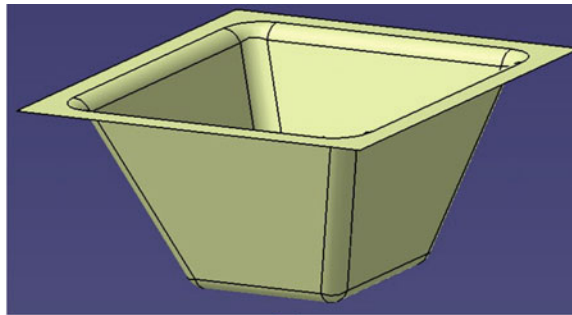
In the ISF experiments, an AA5052 specimen with a size of 130 mm × 130 mm was cut to be formed using CNC machine as shown in Fig. 4. Two types of incremental sheet-forming test with pyramid and varying wall-angle conical frustums (VWACF) specimens are performed in order to verify the efficiency of the proposed yield criterion and fracture criterion in predicting fracture behavior (Fig. 5).

In these tests, forming angle of the pyramid model is 70°, and for VWACF model, the forming angle is from 40° to 90°. While the forming parameter is shown in Table 1. And in each cases, liquid lubricant was used. After fracture happened, record the final forming depth. The results of each experiments are shown in Fig. 6a, b.



Fig. 4 The CNC machine used in this study

Fig. 5 The shape of pyramid model (a) and VWAF model (b)



(a)



(b)

Table 1 Forming parameter in ISF experiment

Parameter	Tool diameter (mm)	Step depth (mm)	Feed rate (mm/min)
Value	10	0.5	500

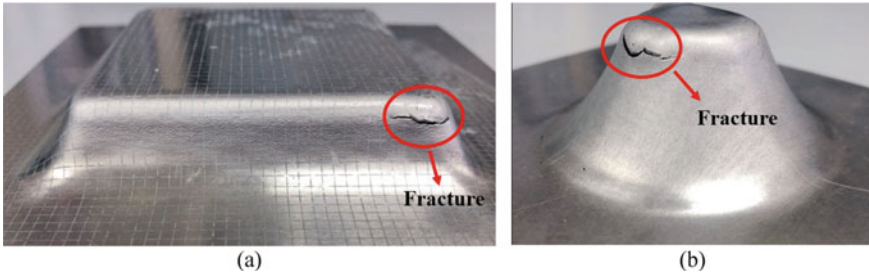


Fig. 6 Forming result of **a** pyramid model and **b** VWAFC model

Conclusion

A new anisotropic yield function and an extended ductile fracture for anisotropic material are utilized in considering effect of anisotropy property for incremental sheet metal forming applications. The yield locus constructed by Kim-Van yield function fitted well with experimental data. The proposed yield function greatly enhances the flexibility of describing the strong anisotropic effect in metal sheet.

Acknowledgements This work was supported by the Ministry of Education of the Republic of Korea and the National Research Foundation of Korea (NRF-2019R1A2C1011224).

References

1. Iseki H, Kato K, Sakamoto S (1992) Flexible and incremental sheet metal bulging using a path-controlled spherical roller. *Trans Japan Soc Mech Eng Ser C* 504(58):3147–3155
2. Ham M, Jeswiet J (2006) Single point incremental forming and forming criteria for AA3003. *CIRP Ann Manuf Technol* 55(1):241–244
3. Pham QT, Kim YS (2017) *Met Mater Int* 23(2):254–263
4. Mirmia MJ, Vahdani M, Shamsari M (2018) Ductile damage and deformation mechanics in multistage single point incremental forming. *Int J Mech Sci* 136:396–412
5. Li J, Li S, Xie Z, Wang W (2015) Numerical simulation of incremental sheet forming based on GTN damage model. *Int J Adv Manuf Technol* 81:2053–2065
6. Jin K, Guo X, Tao J, Wang H, Kim N, Gu Y (2016) A model of one-surface cyclic plasticity with Lemaitre damage criterion for plastic instability prediction in the incremental forming process. *Int J Mech Sci* 114:88–97
7. Quach H, Kim JJ, Nguyen DT, Kim YS (2020). *J Mech Sci* 169(1)

Part II
Modeling of Sheet Metal Forming:
In Memory of Prof. Jean-Claude Gelin

3D-Swivel-Bending—A Flexible and Scalable Forming Technology



Michael Schiller, Peter Frohn-Sörensen, and Bernd Engel

Abstract Established forming processes in the automotive industry are used for series with annual production runs of more than 100,000 units. Until now, there has been a lack of forming technologies for the economical production of batch sizes below 100,000 units. This trend is also changing production. Swivel-bending is suitable as a flexible and low-tool process to produce variable cross-section geometries. The manufacturing technology developed for 3D-swivel-bending significantly expands the application possibilities of the basic process by enabling the production of non-linear, three-dimensional bending edges, to manufacture cross-section variable and load-adapted components. The process is designed to be scalable and thus adjustable for processing variable workpiece thicknesses, materials, and spring-back behavior. With additively manufactured joint structures, the effective surfaces of the tools can be adapted to individual requirements. The joint structures can also be manufactured as a print-in-place solution within a significantly shorter product development process.

Keywords 3D-swivel-bending · Additive manufacturing · Bending · Lightweight design · Cross section adapted · Load adapted · Forming · Flexibility · Scalability

Introduction

Many products show the way from mass production to the manufacture of individualized products. This trend is also fundamentally changing production which requires the ability of production techniques to meet the demand for flexibility. This can only be fulfilled economically if the main techniques (forming processes) also perform a change in extension to construction. The requirements for manufacturing processes, in particular, for forming processes, are flexible tool production, fast setup, and fast product changeover. Scalability must be achieved in terms of component geometry, machinable materials, and batch sizes to meet market requirements.

M. Schiller (✉) · P. Frohn-Sörensen · B. Engel
Chair of Forming Technology, Institute of Production Technologies, University of Siegen, Breite
Strasse 11, 57076 Siegen, Germany
e-mail: Michael.Schiller@Uni-Siegen.de

In the automotive industry, body components are manufactured using production techniques designed for mass production. Medium and smaller batch sizes can often only be produced uneconomically by automotive suppliers using rigid manufacturing techniques and production systems with inflexible capacities. The use of new technologies often fails because of the investment required for new machine technologies, which discourage SMEs in particular.

A survey the authors conducted specifically for sheet metal parts suppliers in 2021 indicates a critical number of units at an annual batch size <100,000 components, cf. Figure 1. Of the nine companies surveyed, 60% are SMEs with a size of less than 250 employees. On average, an annual quantity of 100,000 components per article is produced today. On average, companies have <500 “living” components. The “ideal” annual quantity is already above 100,000 components today. The companies surveyed can hardly produce economically below 50,000 components. Limiting factors for the economic production of smaller quantities are the setup and the tooling costs. The analysis shows that sheet metal component suppliers stick to high-volume processes even if the critical cost-covering number of units is not reached. Compensation takes place through the production and supply of order packages with low and high quantities. Majority of SME parts suppliers use progressive manufacturing.

Established forming processes in the automotive industry are used for series with annual production runs of more than 100,000 units. Until now, there has been a lack of forming technologies for the economical production of batch sizes below

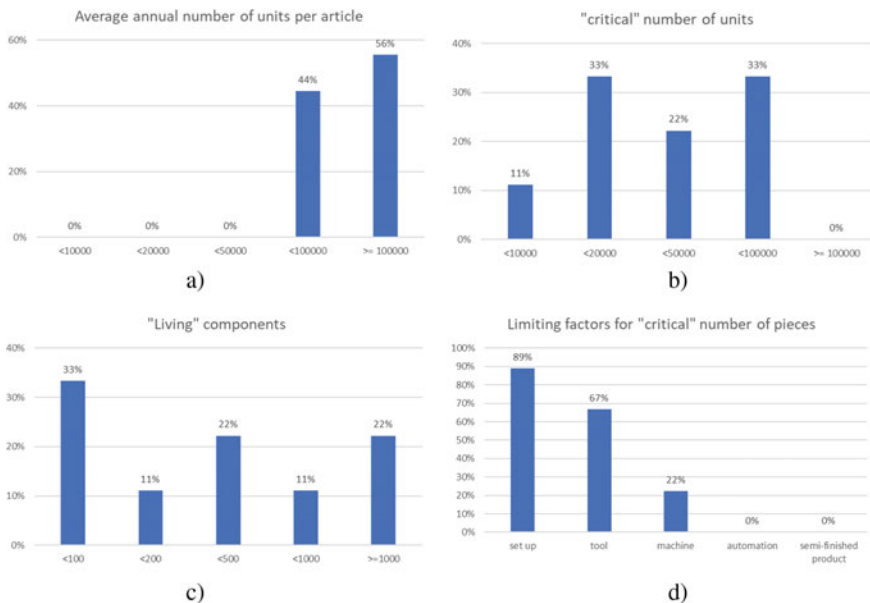


Fig. 1 Analysis of critical batch size survey. **a** Average annual number of units per article in the company portfolio, **b** “critical” number of units, **c** “living” components, **d** limiting factors for “critical” number of pieces

100,000 units. In the past decade, additive manufacturing has become established to produce quantity 1. Incremental forming processes are used for 10–100 pieces per year. However, no forming processes have been established for the critical range between 100 and 100,000 units per year. Accordingly, there is a lack of scalable and low-tooling processes that can also be used to manufacture economically in this quantity. Conventional swivel-bending can be used economically here. Swivel-bending is suitable as a flexible and low-tool process to produce variable cross-section geometries. However, the component complexity required by automotive components cannot be guaranteed by the restriction to bending only straight bending edges.

The manufacturing technology developed for 3D-swivel-bending significantly expands the application possibilities of the basic process by enabling the production of non-linear, three-dimensional bending edges, to manufacture cross-section variable and load-adapted components. Such components are often found in developments for body and structural components, e.g., in the automotive and aerospace industries. Due to the possibility of manufacturing non-linear bending edges and bending surfaces, 3D-swivel-bending can be used to produce many required geometries for the automotive industry and close the gap of the critical quantity range. The process is designed to be scalable and thus adjustable for processing variable workpiece thicknesses, materials, and springback behavior. With additively manufactured joint structures, the effective surfaces of the tools can be adapted to individual requirements. The joint structures can also be manufactured as a print-in-place solution within a significantly shorter product development process.

State of the Art

Swivel-bending is bending with rotating tool movement. The tool structure essentially consists of the three basic tools: upper, lower, and swivel or bending beam. The sheet to be bent is clamped between the upper and lower beams. The bending beam is placed against the part of the sheet metal protruding over the upper and lower beams and swiveled with it around the bending edge, with a generally circular rotation, around a bending axis which is usually stationary. In Fig. 2, the schematic structure of a swivel-bending machine and the associated kinematics of swivel-bending are shown.

A wide variety of cross-sectional geometries can be produced with standard tools. Incremental operation or special tools can also be used to produce roundings, cf. Figure 3. The bending is still carried out via linear bending edges. To increase process speed, swivel-bending machines are equipped, for example, with automated tool change systems and 3D graphic controls with automated program generation and learning material-dependent databases. To ensure product quality, angle measurements are carried out by laser and crowning of the bending beam by means of dynamic systems [1]. In addition, swivel-bending is characterized by high flexibility and good automation capability.

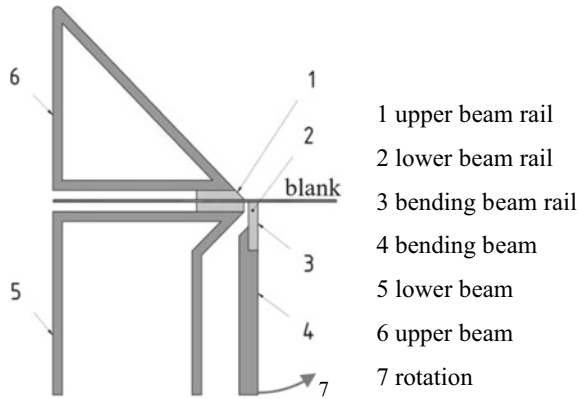


Fig. 2 Principle of the swivel-bending process



Fig. 3 Geometric manufacturing range of CNC swivel-bending machines (center image) according to [2]

The following is a presentation of manufacturing processes with which it is possible to realize non-linear bending edges. In the state of the art, these are in comparison with the 3D-swivel-bending developed.

Incremental swivel-bending has been developed over the last decade. The profile bending process allows a pronounced manufacturing flexibility due to the incremental process sequence and its indistinct tooling [3]. The major application use cases of this technique have been suggested for automotive structural parts where

high variances are demanded, for instance, length, bending radii, and angles. In particular, longitudinal members were focused due to their strong substitution potential for profile intense structural body layouts [4]. As a swivel-bending technique, ISB transmits the forming forces by clamping. In contrast to the aforementioned standard procedure of swivel bending, a blank or profile working piece is clamped on both sides in ISB, the stationary and rotatory sides. Moreover, while the conventional process achieves bends out of the blank plane, in-plane bent geometries result from ISB [5]. Because the bending force is transmitted by friction in ISB, unlubricated forming conditions are preferred due to their higher friction coefficients, and thus higher efficiency of force transmission. For a purposeful layout of ISB, it was proven crucial to apply pressure-dependent functions of static friction coefficients [6]. Due to its continuous process sequence, the herein presented manufacturing technology 3D-swivel-bending might on the one hand substitute parts preferred for ISB. On the other hand, both processes could be combined to drastically increase the specific complexity limitations in terms of manufacturable geometries.

Deep Drawing of automotive body parts is used to produce irregular components. Within this process, deep drawing, stretch forming and bending sections can be found. During the linear movement of the punch, bending sections also occur around concave or convex edges, cf. [7].

With flexible roll forming, load-optimized profiles with adapted cross sections can be produced. Using an NC-controlled forming stand, component families of cross-sectionally variable profiles can be realized by simply modifying the control system. Separate halves of the stand each have a translational and a rotational degree of freedom, thus enabling the production of variable profile shapes cf. [8, 9].

In slide draw bending, sheet metal strips or coils are bent by drawing through a forming tool. By changing the cross-sectional geometry of the drawing gap, variable cross-sectional geometries can be produced in flexible slide draw bending with a split and adjustable fixture, cf. [10]. Here, the use of multi-stage tool concepts is also possible in order to produce more complex geometries.

Motivation

In the development of the production structure in automotive engineering and the development of alternative drive systems, a large variety of models are produced in decreasing time-to-market, including in some cases smaller batch sizes. Despite increasing complexity and variety, development times are shortened [11, 12].

In the specially conducted study indicated above, it was found that no forming processes have been established for the critical range between 100 and 100,000 units per year in automotive production.

With the invention of 3D-swivel-bending, the swivel-bending manufacturing process, which is well suited for this range of units, is enabled to produce cross-section variable and load-adapted geometries that can also be used in automotive production.

Table 1 Material parameters determined in the tensile test

R _{p0,2} (MPa)	R _m (MPa)	A _g [%]
233	342	19,1

3D-swivel-bending is intended to meet the requirements of bending non-linear bending edges, technically favorable design and manufacture of tools, low-tool production of sheet metal components, fast setup, and fast possible product changes.

The stated goal is to develop and design a flexible manufacturing process that can also be used to economically produce smaller batch sizes in order to close the existing gap of the lack of a suitable forming process.

Material

For the experimental investigations as well as the associated FE simulations, the material used was 1.0038, which is suitable for steel and mechanical engineering. To characterize the material, tensile tests were carried out according to [13] on a universal testing machine of the type Zwick/Roell Z250. The determined material properties can be taken from Table 1. For input to the FE simulation, the yield curve was calculated according to the Swift-Krukowski approach [14], see Eq. (1).

$$k_f = b \cdot (c + \varphi_v)^d \quad (1)$$

Process Development of 3D-Swivel-Bending

Following on from the demand defined in the introduction for the further development of standardized production processes, the development of 3D-swivel-bending was taken up [15].

3D-swivel-bending extends the swivel-bending process in so far as cross-sectional changes in the form of non-linear bending edges can already be introduced into the sheet metal to be formed on longitudinally oriented components during production. The bending tools have a curved bending edge and complementary bending surfaces that correspond to the desired shape on the component. In this way, 3D-swivel-bending can be used to produce cross-section variable and load-adapted components. The process and application limits of the established manufacturing process, which was previously limited to the production of straight bending edges, are significantly extended. Compared to deep drawing, progressive, and transfer presses, the developed process is characterized by low required machine and tool investments, low-tooling requirements, short start-up and setup times, and the associated fast possible product changes. This favors the production of smaller batches and enables

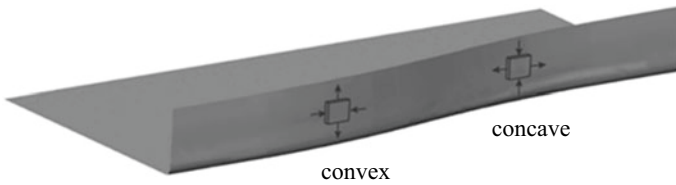


Fig. 4 Characteristic plastic longitudinal and transverse strains in the sheet metal leg of the s-shape

high production flexibility with regard to variable component geometries. Above all, it is thus possible to use 3D-swivel-bending economically in the automotive industry for the market demand for production quantities <100,000 components p.a.

In conventional swivel bending, pure bending stresses occur. In 3D-swivel-bending, the bending stresses are superimposed by tensile and compressive stresses and thus also strains depending on the geometry, which are critical for failure. In Fig. 4, the resulting characteristic plastic longitudinal and transverse strains are shown on an S-beat component with inwardly directed concave circular arcs and outwardly directed convex circular arcs.

Figure 5 on the left shows an example of the characteristic longitudinal plastic strains occurring in the longitudinal direction of the sheet, which increase in magnitude with the height of the sheet leg. The longitudinal plastic strains form a compression region in the convex part (blue) and a tension region in the tapered concave part (red). Figure 5 on the right shows an example of the characteristic transverse plastic strains occurring in the sheet height direction, which increase in magnitude with the height of the sheet leg. The transverse plastic strains form a tensile region in the convex part (red) and a compressive region in the tapered concave part (blue).

At the forming limits, this consequently leads to wrinkle failure for both concave and convex geometries before crack criteria set in. The limiting geometric factor is the height of the bent sheet leg, cf. Figure 6.

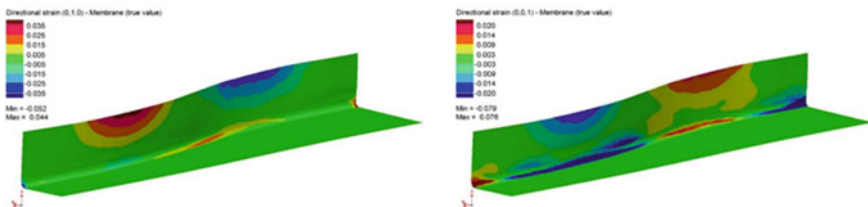


Fig. 5 Characteristic plastic strains—longitudinal direction (left), height direction (right)

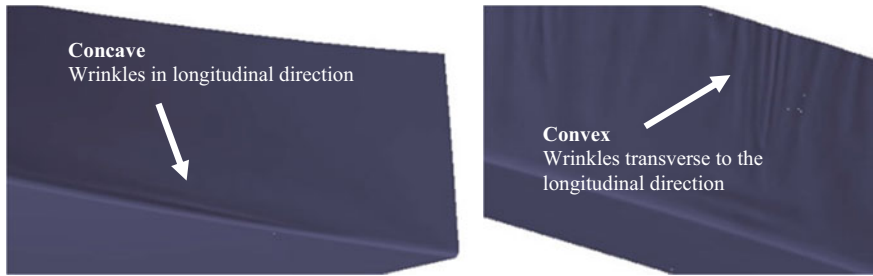


Fig. 6 Wrinkling as a case of failure—concave (left), convex (right)

Process Design of 3D-Swivel-Bending

To design the process limits, a sensitivity analysis was first performed using FE simulations to determine the process-critical geometric parameters. Simplified elemental geometries were derived from the geometric features cataloged as characteristic of 3D-swivel-bent products. To simplify the analysis, circular, concave, and convex bending edges were selected as elementary geometries. Starting from a flat sheet blank, a sheet metal leg is bent to produce an L-shaped component. Calculation models were set up for these elementary bends in the finite element simulation with PAM-STAMP 2019.0 with shell elements. The geometrical variables—radius, plate thickness, chord length, plate leg height, and resulting geometrical properties such as circular arc angle and cross-section offset were systematically varied in the sensitivity analysis. In Table 2, the variation parameters are listed.

The definition of the geometry parameters is shown in Fig. 7 using a concave cross-section geometry.

The investigation shows that the process limits are dependent on the geometric parameters' radius R , sheet metal thickness s , and sheet metal leg height h . The circular arc angle α has no influence on the achievement of a process limit, so that

Table 2 Variation parameters for the sensitivity analysis

Variation parameter	Value
Radius R (mm)	400; 800; 900; 1200; 1600; 2000; 2400; 3200; 4000; 6000
Sheet thickness s (mm)	1, 2, 3
Arc angle α ($^{\circ}$)	28, 96; 43, 43; 57, 91
Sheet metal leg height h (mm)	Indirect
Circular chord length S (mm)	Indirect
Cross-section offset Q (mm)	Indirect
Radius bending edge r (neutral fiber) (mm)	3

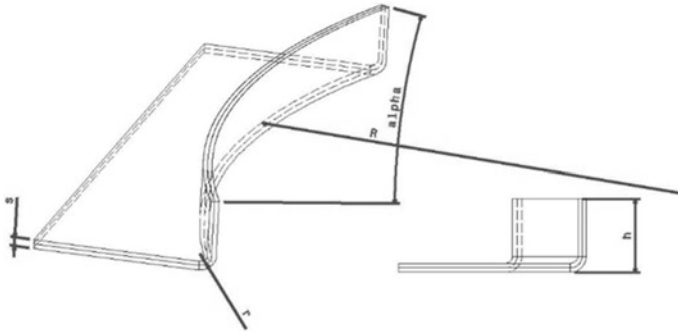


Fig. 7 3D-swivel-bending—geometric parameter definitions

semi-circular bending geometries with a circular arc angle of 180° can also be bent, see Fig. 8.

Model experiments were carried out to validate the results on the possible working field of 3D-swivel-bending. Likewise, a corresponding wrinkling failure for concave and convex bending geometries could be determined here when exceeding a critical sheet metal leg height, cf. Figure 9. The failure limits also depend on the radius of the non-linear bending edge and the sheet metal thickness.



Fig. 8 Semi-circular concave cross-section geometry



Fig. 9 Wrinkling as a case of failure—concave (left), convex (right)

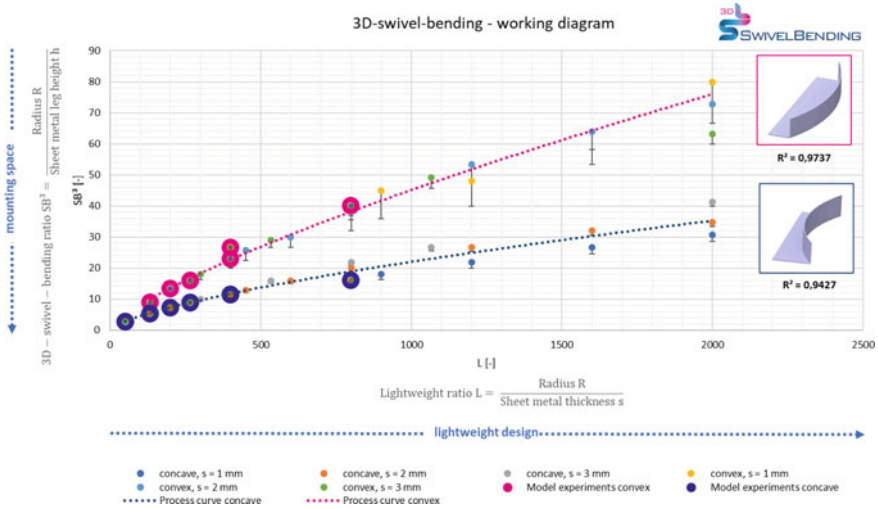


Fig. 10 Working diagram for 3D-swivel-bending

The working diagram for 3D-swivel-bending is shown in Fig. 10. Here, concave and convex geometries are shown simultaneously. Each point in the process window represents a parameter setting in the FEM model as well as the model experiments of the sensitivity analysis. The investigation and evaluation of the sheet metal leg heights were carried out in a step size of 5 mm.

Compared to the process boundary points designed using the FE simulation, those validated with the model experiments are shown as larger blue (concave)- and pink (convex)-colored points.

Bending below the respective limit curve for concave or convex geometries is not possible. For the concave process curve, it can be seen that it extends further to the left. With a lightweight ratio $L = 50$ and a 3D-swivel-bending ratio $SB^3 = 2.5$, the concave 180° bend is noted. With the bending of a 180° circular arc angle, a theoretical process limit is reached than then an undercut would be present.

Figure 10 R^2 denotes the coefficient of determination and thus the quality with which the measured values fit the model formed. The model for the coefficient of determination was empirically fitted in Microsoft Excel.

A significant result is that higher sheet metal leg heights can be achieved when bending concave geometries than when bending convex geometries. The reason for this lies in the stress ratios present and the resulting failure modes. For concave geometries, tensile stresses in the bent sheet metal leg along the bending edge have a favorable effect. In comparison, convex geometries are subject to corresponding compressive stresses. It can also be seen that with increasing sheet thickness, it is also possible to shape greater sheet metal leg heights.

Overall, the practical model experiments meet the process limits determined in the simulation without any further anomalies.

The following dimensionless key indicators (2) and (3) were derived to represent a working diagram for 3D-swivel-bending:

$$\text{Lightweight ratio } L = \frac{\text{Radius } R}{\text{Sheet metal thickness } s} \tag{2}$$

$$\text{3Dswivel bending ratio } SB^3 = \frac{\text{Radius } R}{\text{Sheet metal leg height } h} \tag{3}$$

Demonstration of 3D-Swivel-Bending

A demonstrator was developed to represent 3D-swivel-bending in a proof-of-concept. For the design of a demonstrator, a geometry was chosen that contains a variable progression along the bending edge and is not represented by a single circular arc, as is the case with the model test parts. The course of a straight bending edge is also linked with a non-linear one. The special feature in the design of the bent sheet metal leg, in addition to the variable curvature progression, is that starting from a 110° bend, i.e., >90°, there is a bend opening with the longitudinal progression down to a 70° bending angle. This is intended to demonstrate the potential of 3D-swivel-bending to reproduce such variable curves and to realize bends >90°. This would lead to considerable additional tooling costs in the case of substitution processes. In principle, the demonstrator design is based on bulkhead parts, wheel housing elements, cover plates, and taillight mounts used in automotive engineering in order to demonstrate realistic application potential. When looking at potentially manufacturable components using 3D-swivel-bending, it was recognized that secondary forming elements such as embossing are often introduced into components. This was also included in the design of a pocket which could be used as a tethering surface, for example, cf. Figure 11.

The demonstration component can be manufactured in variable lengths and sheet metal leg heights with little tooling effort, see Fig. 12. For example, the component

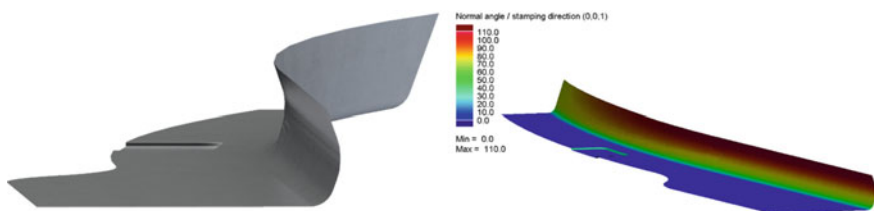
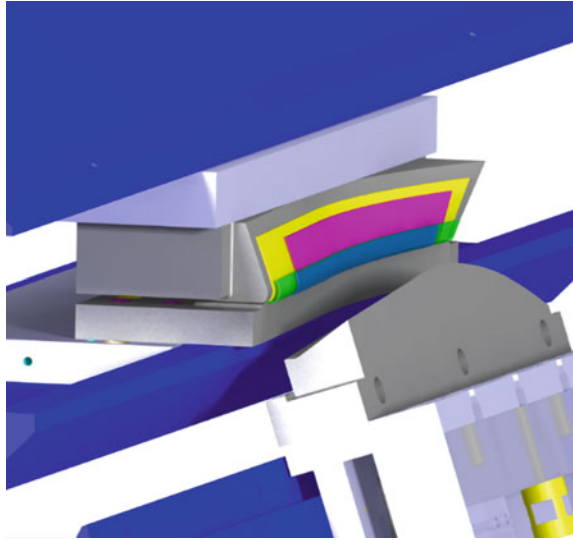


Fig. 11 Demonstration component 3D-swivel-bending (left), bending angle course (right)

Fig. 12 Scalable demonstrators in a single tooling design



shown in green and yellow was manufactured from material 1.0933. The parameters, which are relevant for bending, are listed in Table 3.

The proof-of-concept shows successful bending results in Fig. 13.

Table 3 Geometric properties scaled demonstrator

Bending parameter	Unit	Demo 1	Demo 2
Sheet metal length l	mm	600,00	600,00
Sheet metal leg height h	mm	20,00	60,00
Sheet thickness s	mm	1,50	1,50
Radius r	mm	5,00	5,00
Min. radius bending edge R	mm	1537,96	1537,96
Min. radius sheet metal leg R	mm	1307,92	833,03
Lightweight ratio L bending edge	–	1025,31	1024,93
Min. lightweight ratio L	–	871,95	555,35
3D-swivel-bending ratio SB^3	–	76,90	26,62
Min. 3D-swivel-bending ratio SB^3	–	65,40	13,88



Fig. 13 Bending results 3D-swivel-bending

Increasing Manufacturing Flexibility Through Adjustable Tooling Technology

For 3D-swivel-bending, as according to the presented state of research, adjustable die faces might enhance manufacturing possibilities of the process. A spring loaded, displaceable upper die could, for instance, help to flexibly compensate springback influences of material variations. Moreover, adjustable faces would help to compensate variations in sheet metal thickness, both in terms of product variations, as well as using tailored blanks. Moving one step further, segmented tool faces would allow to change the whole bending geometry by tool surface adjustments.

In order to make tool surfaces adjustable for a wide geometrical variety, its segmentation is required, as known from multipoint forming processes [16]. For the controlled movement of the segments, actuators such as hydraulic pistons are needed, but these systems require a large amount of space. However, for some process adjustments, a finer segmentation might be necessary, leading to a conflict of objective. At this point, other tool structures behind the segments could be useful, e.g., single and multiple connected joint structures. A conventional manufacturing method of such joint structures is to assemble several standardized pieces. Generative technologies, in particular, additive manufacturing have paved the way to manufacture complex structures in one single process sequence without assembly, including joint structures [17–21]. With additively manufactured joint structures, the effective surfaces of the tools can be adapted to individual requirements. The joint structures can also be manufactured as a print-in-place solution within a significantly shorter product development process.

In future work, it will be focused, if additively manufactured joint structures are applicable to allow to adjust tool surfaces in order to increase manufacturing flexibility in terms of scalability. The principal idea is to design the upper die of 3D-swivel-bending as adjustable structure to allow for compensating variable sheet thicknesses and springback effects during bending.

When using articulated structures to adjust the tool contact surface, low forces must be absorbed compared to the required bending force and calibration force. The calibration force during bending should be absorbed by an end stop so that the joints can be used with as little space as possible.

Conclusions

3D-swivel-bending was developed to produce cross-section and load-adapted components. Such components are used in lightweight structures, which are often found in developments for car bodies and structural components, for example, in the automotive and aerospace industries. In 3D-swivel-bending, characteristic plastic longitudinal strains occur in the bent sheet leg in the form of a tensile region in the inwardly curved part of the sheet and a compression region in the outwardly curved part of the sheet. The opposite is the case in the transverse direction. The failure criterion for both cases is wrinkling. With a validated working diagram determined via FE simulations and model experiments, the feasibility of components can be evaluated depending on the material and geometric features. Following a proof-of-concept, the developed process for 3D-swivel-bending demonstrates the applicability of the invention. Due to the high process flexibility compared to deep drawing, faster product changes are possible due to shorter development times, lower tool volumes, and quicker setup. Investment requirements in machinery and tooling are also low compared to forming presses. The possible near net shape manufacturing also enables sustainable resource conservation. 3D-swivel-bending which is characterized by low-tool manufacturing, a high degree of flexibility and good automation, so that rapid product changes are possible and previously used manufacturing processes can be substituted. Longitudinally oriented components with L-, Z-, U-, and O-shaped cross sections and non-linear bending edges can be produced in variable sheet thicknesses and materials for a wide range of applications. With the help of the developed working diagram, the manufacturability of desired components can be evaluated in advance and without further simulation effort. For variable materials, an adaptation of the limit curves is required. Due to the possibility of manufacturing non-linear bending edges and bending surfaces, many required geometries can be produced by means of 3D-swivel-bending and the gap described at the beginning of the critical quantity range for the production of automotive components <100,000 components/year could be closed or at least supported.

Acknowledgments This project is supported by the Federal Ministry for Economic Affairs and Climate Action (BMWK) on the basis of a decision by the German Bundestag.

References

1. Hochstrate G-A, Hochstrate W (2001) Folding machine. DE19735793C2. 12 July 2001
2. Hochstrate W, Engel B, Schiller M, Frohn-Sörensen P (2019) Extended production variety of folding/swivel-bending. *Produktionsvielfalt des Schwenkbiegens erweitert*. 1(2019):20–21. <https://doi.org/10.1177/0954405420982227>
3. Frohn-Sörensen P, Hochstrate W, Schneider D et al (2021) Incremental bending of conic profiles on CNC hydraulic bending machines. *Proc Inst Mech Eng Part B J Eng Manuf* 235:1248–1268
4. Engel B, Frohn P, Hillebrecht M, Knappe A (2017) Incremental swivel bending for scalable lightweight structures. *ATZ Worldw* 119:26–31. <https://doi.org/10.1007/s38311-017-0023-2>

5. Frohn-Sörensen P, Borchmann L, Engel B (2020) Modelling the forming zone of force fitted bending processes. *Proc Manuf* 50:411–417. <https://doi.org/10.1016/j.promfg.2020.08.075>
6. Frohn-Sörensen P, Cislo C, Paschke H et al (2021) Dry friction under pressure variation of PACVD TiN surfaces on selected automotive sheet metals for the application in unlubricated metal forming. *Wear* 476:203750. <https://doi.org/10.1016/j.wear.2021.203750>
7. Birkert A, Haage S, Straub M (2013) Umformtechnische Herstellung komplexer Karosserieteile: Auslegung von Ziehanlagen. Springer-Verlag
8. Groche P, Istrate A (2001) Verfahren und Vorrichtung zum Herstellen von Bauteilen mit über der Längsachse veränderlichen Querschnitten. DE2000111755. 20 September 2001
9. Groche P, Istrate A (2005) Verfahren und Vorrichtung zur Herstellung eines Profils mit über der Längsachse veränderlichem Querschnitt mittels Walzprofilieren. DE2000111755. 25 May 2005
10. Dröder K, Martin V, Mütze S et al (2007) Vorrichtung zum Umformen eines bandförmigen Werkstücks. DE102006008237A1 23 August 2007
11. Lichtblau K, Kempermann H, Bähr C et al Zukunft der Automobilwirtschaft in Nordrhein-Westfalen Status quo, Trends, Szenarien. 181
12. Seiffert U, Rainer G (2008) Virtuelle Produktentstehung für Fahrzeug und Antrieb im Kfz: Prozesse, Komponenten. Springer, Beispiele aus der Praxis
13. DIN EN ISO 6892-1:2020-06, Metallic materials - Tensile testing - Part 1: Method of test at room temperature (ISO 6892-1:2019); German version EN ISO 6892-1:2019. Beuth Verlag GmbH
14. Swift H (1952) Plastic instability under plane stress. *J Mech Phys Solids* 1:1–18
15. Engel B, Frohn P, Schiller M (2019) Vorrichtung zum Schwenkbiegen eines Bleches. DE102018104776A1. 05 September 2019
16. Walczyk DF, Hardt DE (1998) Design and analysis of reconfigurable discrete dies for sheet metal forming. *J Manuf Syst* 17:436–454. [https://doi.org/10.1016/S0278-6125\(99\)80003-X](https://doi.org/10.1016/S0278-6125(99)80003-X)
17. Cuellar JS, Smit G, Plettenburg D, Zadpoor A (2018) Additive manufacturing of non-assembly mechanisms. *Addit Manuf* 21:150–158. <https://doi.org/10.1016/j.addma.2018.02.004>
18. Mavroidis C, DeLaurentis KJ, Won J, Alam M (2000) Fabrication of non-assembly mechanisms and robotic systems using rapid prototyping. *J Mech Des* 123:516–524. <https://doi.org/10.1115/1.1415034>
19. Cuellar JS, Smit G, Zadpoor AA, Breedveld P (2018) Ten guidelines for the design of non-assembly mechanisms: the case of 3D-printed prosthetic hands. *Proc Inst Mech Eng [H]* 232:962–971. <https://doi.org/10.1177/0954411918794734>
20. Scarcia U, Berselli G, Melchiorri C et al (2016) Optimal design of 3D printed spiral torsion springs. American Society of Mechanical Engineers Digital Collection
21. Hu Y, Zhang L, Li W, Yang G-Z (2019) Design and fabrication of a 3-d printed metallic flexible joint for snake-like surgical robot. *IEEE Robot Autom Lett* 4:1557–1563. <https://doi.org/10.1109/LRA.2019.2896475>

A Comparative Study of Incremental Sheet Forming Process to Achieve Optimal Accuracy



Jaekwang Shin, Dohyun Leem, Newell Moser, Ankush Bansal,
Randy Cheng, Kornel Ehmann, Jian Cao, Alan Taub, and Mihaela Banu

Abstract The use of finite element modeling for metal forming processes allows the reduction of trial and error of the manufacturing process and thus contributes to achieve high precision of the part geometries. However, the localized deformation and the long process time observed in Incremental Sheet Forming (ISF) provide a challenge in the selection of finite element modeling tools and process parameters (e.g., FEA software, constitutive material model, mesh type, element size) and in obtaining accurate results with acceptable computational costs. In this work, a comparative study is conducted for a truncated 45° cone of AA7075-O manufactured by the two-point incremental forming (TPIF) process. The cone is modeled using two different commercially available software, Abaqus, and LS-Dyna, which hold different combinations of constitutive material models and numerical parameters. The simulation results were compared with the experimental measurements of the geometric profile, thickness distribution, and forming forces to give a best practice guideline in modeling ISF that achieves accuracies within desired computational costs.

Introduction

In finite element models, many factors contribute to the accuracy of the model where the major components are the constitutive material model and element formulation. The constitutive material model generally consists of a yield function and a hardening

J. Shin · A. Bansal · M. Banu (✉)

Department of Mechanical Engineering, University of Michigan, 2350 Hayward St., Ann Arbor, MI 48109, USA

e-mail: mabanu@umich.edu

R. Cheng · A. Taub

Department of Material Science and Engineering, University of Michigan, 2300 Hayward St., Ann Arbor, MI 48109, USA

D. Leem · N. Moser · K. Ehmann · J. Cao

Department of Mechanical Engineering, Northwestern University, 2145 Sheridan Rd., Evanston, IL 60208, USA

© The Minerals, Metals & Materials Society 2022

K. Inal et al. (eds.), *NUMISHEET 2022*, The Minerals, Metals & Materials Series,
https://doi.org/10.1007/978-3-031-06212-4_13

curve. The simplest combinations are the combination of isotropic hardening law and von Mises yield criteria as shown in Li et al. [1] and Robert et al. [2] which resulted in a prediction of the result with acceptable error. Flores et al. [3] highlighted the importance of the material parameter identification which can impact the result of the prediction. A biaxial tensile testing machine was utilized to obtain the coefficients of the constitutive material models where isotropic Swift type hardening law and kinematic Teodosiu and Hu hardening model was used to predict the forming forces. Eyckens et al. [4] compared isotropic yield criteria and anisotropic yield criteria in combination with isotropic hardening and kinematic hardening where the result of the simulation was validated against the measurement from the DIC. The effect of the different 3D yield functions in a single point incremental forming (SPIF) process was examined by Esmaeilpour et al. [5]. In his study, von Mises, Hill48 and Yld 2004–18p yield functions were investigated using Abaqus/explicit. The forming force, thickness, strain, and stress components were compared, respectively.

The element formulation plays a key part in achieving high accuracy in prediction. Due to the high nonlinearity and local deformation that occur during the incremental forming process, the difference in the element formulation results in different computation time and accuracy. Bambach et al. [6] investigated the influence of the different types of elements along with a different combination of basic constitutive models on accuracy and computation utilizing Abaqus. In many cases, the solid elements have been utilized to capture the change in thickness as shown by [1, 5, 7–9] others have turned to shell element which generally resulted in lower computational cost [4, 10, 11] and in some cases better force prediction [12]. Due to the limitation of the solid element having high computation cost and the shell element not being able to predict the deformation accurately enough to satisfy the needs, some have turned to solid-shell elements. The solid-shell elements were able to provide an accurate prediction of the thickness and forces [13] and with the use of adaptive remeshing showed a significant decrease in the computational cost [9].

In this research, the impact of various TPIF process parameters and numerical simulation parameters on the accuracy and the computational time of the model is investigated for a truncated 45° cone with aluminum alloy AA 7075-O, an aerospace-grade material. Three different models created by the University of Michigan and Northwestern University are considered as follows:

- (1) *Compliant-Isotropic Hardening* model with the following characteristics: von Mises yield criterion, isotropic hardening, and tool compliance.
- (2) *Rigid-Isotropic Hardening (Mises)* model with the following characteristics: von Mises yield criterion, isotropic hardening, and no tool compliance.
- (3) *Rigid-Isotropic Hardening (Hill)* model with the following characteristics: Hill 48 yield criterion, isotropic hardening, and no tool compliance.
- (4) *Rigid-Kinematic Hardening (Mises)* model with the following characteristics: von Mises yield criterion, kinematic hardening, and no tool compliance.
- (5) *Rigid-Kinematic Hardening (Hill)* model with the following characteristics: Hill 48 yield criterion, kinematic hardening, and no tool compliance.

The details of these models are presented in the following sections.

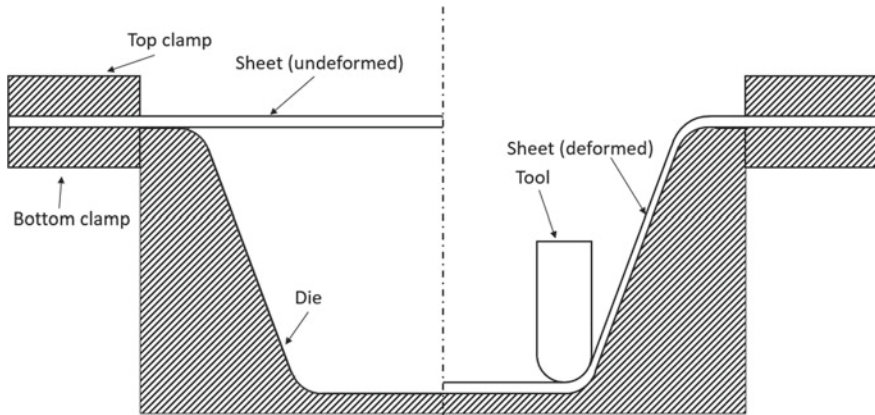


Fig. 1 Two-point incremental forming (TPIF) scheme showing the sheet clamped between the die and the clamp while the tool does forming

Experimental Setup

A TPIF setup was established on a Cincinnati HMC 400-EP CNC milling machine. A hemispherical tool with a diameter of 8 mm was used to form the AA7075-O sheet. The sheet was clamped to a female partial die. The helical toolpath was designed using a MATLAB script where the incremental depth was chosen to be 0.5 mm with no squeeze factor. The feed rate was set to 42 mm/sec and the sheet was well lubricated using AP-5™ grease. The test was conducted three times and compared to ensure the reproducibility of the result. The formed cones were laser-scanned afterward using Romer Absolute Arm (Hexagon-7525SI) in order to digitize the geometry for comparison purposes with the models (Fig. 1).

Finite Element Modeling

ISF exhibits stress and strain distribution which is far more complicated than that of its conventional counterparts (e.g., deep drawing) where there exists an analytical solution for stress distribution. This is due to the localized nature of the deformation occurring in ISF processes where only the material near the vicinity of the tool is deformed. This allows the ISF to possess its unique formability which is higher than that of the conventional forming process [ref needed]. In order to accurately capture the local deformation around the tool, there has been an emphasis on the material model and the use of element formulation that suits the ISF deformation characteristics. This research looks closely at the influence of the yield function and hardening law with the combination of commercial FEA software to give information

Table 1 Elastic properties of AA5754-O and material parameters for the Voce hardening law

Modulus	Yield strength	Density	Poisson's ratio	k_0	Q	β
69.74 GPa	89 MPa	2810 kg/m ³	0.33	91.30 MPa	149.34 MPa	-26.71

to the users to what would be the outcome of the process with given input for the aerospace-grade aluminum AA 7075-O.

Material Characterization

The behavior of material to the tensile loading is the most well-known way of characterizing the behavior of the materials. Most FEA software allows input of its material card in this form along with some modifications and also for more sophisticated material models start off with calibrating its coefficient from this test. To this end, tensile tests were conducted on the MTS Insight 10 Mechanical Tester with sheet metal samples created based on the ASTM B557M standard. The samples were taken every 15° relative to the rolling direction. The strains were measured with both a 50 mm extensometer and a correlation solution's DIC. The tests were repeated three times per each direction and the results were converted to true stress and true strain. To describe the isotropic hardening properties of the aluminum alloy, the stress-strain diagram was fitted with a Voce-type hardening law as described in Eq. (1)

$$\bar{\sigma} = k_0 + Q(1 - e^{\beta \varepsilon^p}) \quad (1)$$

where $\tilde{\sigma}$ is the effective stress; ε^p is the effective plastic strain; and k_0 , Q , and β . The basic material parameters and exact value for the parameters for the hardening law are defined in Table 1.

Defining Kinematic Hardening Parameter

The kinematic hardening was modeled with a nonlinear kinematic hardening model provided in the Abaqus 6.14-1 which is based on the associated flow rule. The back stress of the kinematic hardening law is described by the following equations given in the Abaqus 6.14 manual [14].

$$\alpha_i = \sigma_i - \sigma_i^0 \quad (2)$$

$$\alpha = \frac{C}{\gamma} (1 - e^{-\gamma \varepsilon^p}) \quad (3)$$

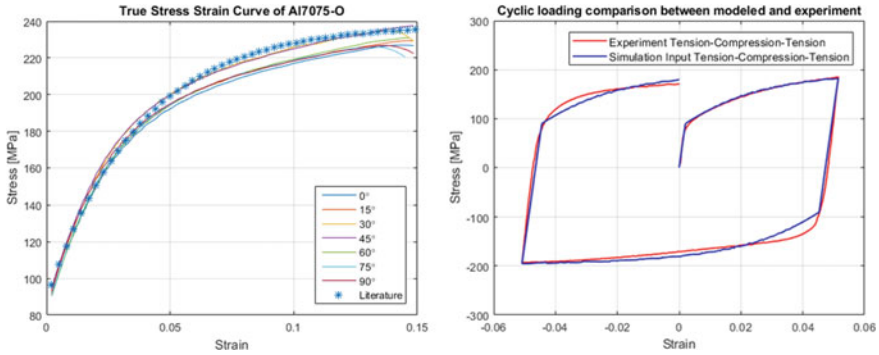


Fig. 2 Result of the tensile test (left) and the comparison result (right) of the calibration of the kinematic hardening model with the TCT test

where the parameters C and γ are the hardening modulus and rate at which the kinematic hardening modulus decrease with increasing plastic deformation, respectively. These coefficients are calculated from back stress α using the equation which calculates for a given set of half-cycle data (σ_i, ϵ_i^p) .

The kinematic hardening law was fitted based on the half-cycle data of the tensile stress–strain curve and thus it was later compared with the experimental tension–compression–tension curve in Fig. 2. The result shows sign of Bauschinger effect when going through compression after tension. However, the difference between the two curves can be considered small enough to conclude that it would not result in a significant difference in the outcome of the finite element model.

Material Yield Function

The yield function plays a vital role in determining whether the material that is being subjected to deformation has undergone strains that would induce plastic deformation. von Mises yield criteria is one of the most widely used yield criteria for its ease of implementation in which it does not require determination of coefficient like in other yield functions. This has made von Mises yield function a popular yield function for material that does not exhibit strong anisotropy. The von Mises yield function is described as

$$\sigma_{Mises} = \frac{1}{2} [(\sigma_{11} - \sigma_{22})^2 + (\sigma_{22} - \sigma_{33})^2 + (\sigma_{33} - \sigma_{11})^2 + 6(\sigma_{12}^2 + \sigma_{23}^2 + \sigma_{31}^2)] \tag{4}$$

where σ_{Mises} denotes the equivalent von Mises yield stress; σ_{11} the stress component (MPa) in the circumferential direction; σ_{22} the stress component (MPa) in the

Table 2 Anisotropy coefficients for the Hill'48 model

F	G	H	N	L	M
0.4486	0.5799	0.4201	0.9700	-	-

meridional direction, σ_{33} the stress component (MPa) in through-thickness direction; and σ_{12} , σ_{23} , and σ_{13} their respective shear stress components (MPa). The material coordinate system is defined as such that orientation is kept consistent.

While the AA 7075-O does not exhibit strong anisotropy, the Hill 48 yield criteria is used to describe the basic anisotropy of the material. The Hill 48 yield function is described as in Eq. (5) [15].

$$f_{Hill}(\sigma) = \sqrt{F(\sigma_{22} - \sigma_{33})^2 + G(\sigma_{33} - \sigma_{11})^2 + H(\sigma_{11} - \sigma_{22})^2 + 2L\sigma_{23}^2 + 2M\sigma_{31}^2 + 2N\sigma_{12}^2} \quad (5)$$

where F, G, H, L, M, and N are constants obtained by the test of the material in the different orientations. The σ_{11} is the stress component (MPa) in the rolling direction; σ_{22} the stress component (MPa) in the transverse direction; σ_{33} the stress component (MPa) in the through-thickness direction; and σ_{12} , σ_{23} , and σ_{13} their respective shear stress components (MPa). F, G, H, L, M, and N can further be defined as a function of R_{ij} where R_{11} , R_{22} , and R_{33} denote the anisotropic yield stress ratios in circumferential, meridional, and through-thickness direction, respectively, and R_{12} , R_{23} , and R_{31} their respective shear components [15]. Table 2. summarizes the coefficients of the Hill 48 yield criteria. These quantities can be calculated from the Lankford coefficients r_0 , r_{45} , and r_{90} which are the ratio of in-plane strain and through-thickness strain and the calculated values are $r_0 = 0.7244$, $r_{45} = 0.4327$, and $r_{90} = 0.9364$.

Model Setup

The five different TPIF models were created using Abaqus 6.14-1 and LS-Dyna R10.1. The baseline simulation package containing toolpath, tool-mesh, and die-mesh has been provided so as to have the same input mesh settings. For all of the models, the sheet was meshed with 3D solid elements with reduced integration and hourglass controls.

Rigid Models

The Rigid-Isotropic Hardening and Rigid-Kinematic Hardening models consisted of a meshed sheet that was secured in place between a (rigid) circular clamp—which applied a force of 50 kN to the sheet—and a conical die surface that was defined using rigid shell elements. The in-plane width and length of the sheet were set to 200 mm

by 200 mm, and the domain was modeled (in Abaqus) with C3D8R solid elements. The mesh was refined in a circular pattern within the forming area, where the characteristic, in-plane element size was specified to be 0.5 mm by $1.0 \text{ mm} \pm 0.5$; the sheet's thickness direction was discretized with five elements resulting in a total of 291,700 elements. Stiffness-based hourglass controls were used to alleviate hourglassing and no damping factor. A mass scaling factor of 10^7 was used to accelerate the explicit simulation where the values were optimized in the previous study [16]. No velocity scaling of the feed rate was utilized. The penalty method was used to enforce contact, and the Coulomb (static and dynamic) friction coefficients were defined to be 0.1. The friction coefficient value of 0.1 was determined after completing a sensitivity study that varied the friction coefficient values from 0.01 to 0.8. The result of the study demonstrated that the friction coefficient has a negligible impact on axial forces, but the friction coefficient has a significant effect on the in-plane forces; larger friction coefficients increase the in-plane forces. However, the difference in the in-plane forces between 0.01 and 0.1 was less than 10% and thus the value of 0.1 was utilized. A future study is needed regarding the tribological nature of incremental forming to determine the exact friction coefficient and its impact on forming (Fig. 3).

The Rigid-Isotropic Hardening model utilized solely isotropic strain hardening (see Table 1) with the von Mises yield criterion, whereas the Rigid-Kinematic Hardening model utilized kinematic strain hardening model and the Hill'48 anisotropic yield criterion. The kinematic hardening components were calibrated using a tension-compression-tension (TCT) test (see Fig. 2).

For the Rigid-Isotropic Hardening and Rigid-Kinematic Hardening models, the total number of time steps was 9,597,231, which required a total time of an average of 22.4 h. Simulations were completed using 120 cores, each specified to be 2.8 GHz Intel Xeon E5-2780v2 processors.

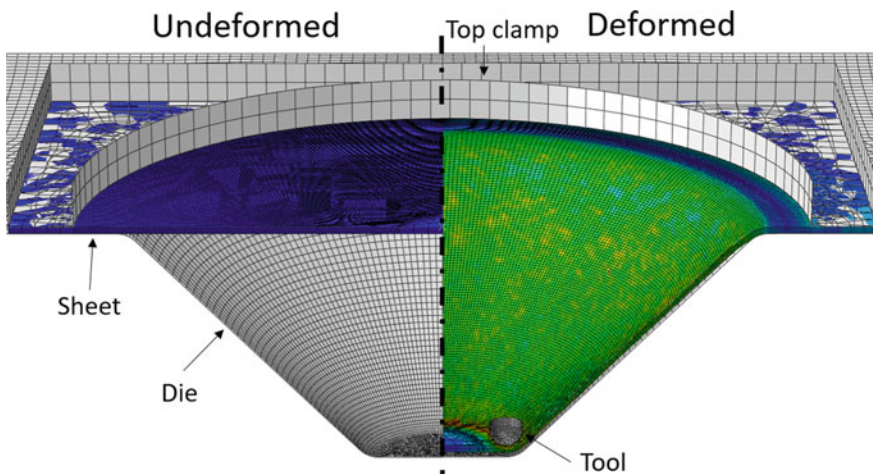


Fig. 3 The Abaqus model of a cone of 45° for the Rigid-Isotropic and Kinematic Hardening models

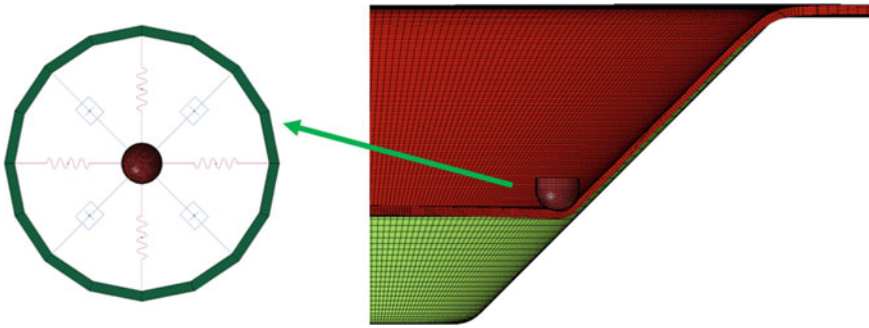


Fig. 4 LS-Dyna model of the 45° cone for Compliant-Isotropic Hardening model showing the tool compliance setup

Compliant Models

In the Compliant-Isotropic Hardening model, the sheet's in-plane width and the length were set to 250 mm by 250 mm and were meshed with LS-Dyna's linear brick elements with reduced integration (and stiffness-based hourglass control). Using six elements through the thickness, the total number of elements in the model was 352,500. The sheet's periphery nodes along the bottom edge were constrained to support the sheet vertically but allow small sliding during the forming process. The sheet's density was scaled up by a factor of 10^4 and the velocity of the tool was set to be 500 mm/s, which is approximately 10 times faster than that of the original tool speed. The conical toolpath took 22,474,559 explicit time steps, which necessitated a computational time of 32.24 h on 48 cores (Intel Xeon Silver 4110 CPUs operating at 2.10 GHz).

The Compliant-Isotropic Hardening model utilized isotropic strain hardening and the von Mises yield criterion, based on the parameters described in Table 1. In real TPIF processes, the tool position deviates from the original toolpath due to the compliance of the tool and the machine. The compliance of the tool was taken into account by utilizing a tool model that captures the aggregate compliance based on springs and dashpots (see Fig. 4). The stiffness of the springs was calibrated to 2575 N/mm (based on the real machine), and the dashpots were set to critically damped.

Results and Discussion

Force Prediction

In order to understand the effects of various process parameters and material models on the simulation accuracy, the models were validated against the experimentally

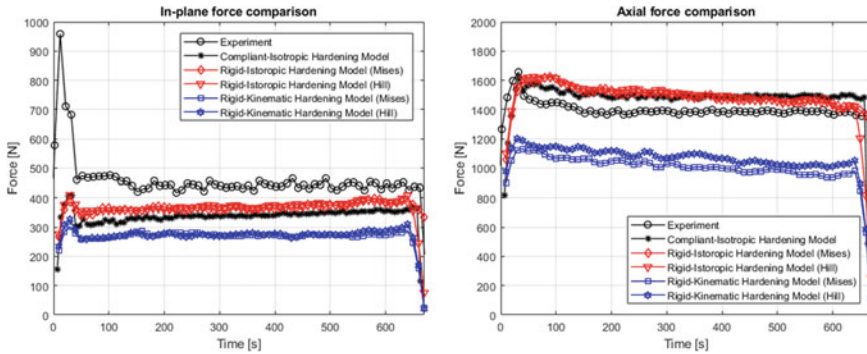


Fig. 5 In-plane contact force comparison (left) and axial force comparison (right) between the experiment and the simulation

measured forming forces and geometry. In the experiment, the forces were measured with a Kistler transducer system which measured the forces in x-, y-, and z-directions relative to the machine coordinate system. The model coordinate system was matched with that of the experiment and forces in the x-, y-, and z-directions were outputted. The forces were divided into two components, the axial force (i.e., z-direction) and the in-plane force (i.e., $\sqrt{x^2 + y^2}$). The compared forces are shown in Fig. 5, with the time scale adjusted for the compliant models to match with the experimental forming time.

There was not a significant difference between the Compliant-Isotropic Hardening model and Rigid-Isotropic Hardening model (Mises, Hill) in terms of the force levels, leading to the conclusion that all three models were able to predict the forces with similar errors where the errors of force curves were calculated at the steady-state region of the force as shown in Fig. 8. The use of isotropic hardening resulted in over-predicting the axial forces by 7%, which is about 100 N. While in the case of the in-plane forces, the model under-predicted the experimental result by around 20%. The Rigid-Kinematic Hardening models (Mises, Hill), on the other hand, under-predicted both axial and in-plane forces by quite a margin. Since in-plane forces are influenced by the friction coefficient, the use of different friction values could have led to a more accurate result. The Compliant-Isotropic Hardening was able to capture the intrinsic oscillations that occurred in the forces during forming, though differences in the amplitude were present.

Thickness Prediction

The thickness distributions, as shown in Fig. 6, were well captured by all of the models with a small margin of error. Little difference in the geometry was seen

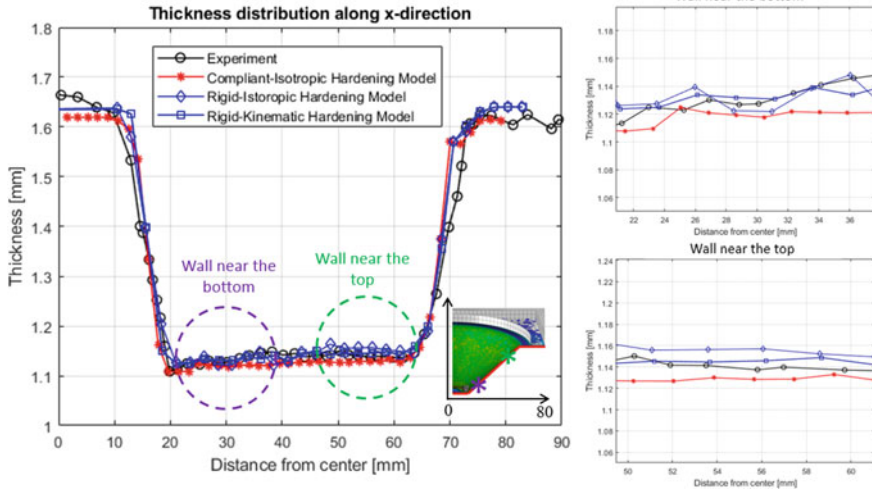


Fig. 6 Thickness distribution comparison between experiment and simulation

between the models that share the same hardening law such as Rigid-Isotropic Hardening (von Mises) and Rigid-Isotropic Hardening (Hill), thus for the thickness and geometry comparison, the three models, namely, the Compliant-Isotropic Hardening model, Rigid-Isotropic Hardening (Mises), and Rigid-Kinematic Hardening model (Mises) were compared. The Rigid-Isotropic Hardening and Rigid-Kinematic Hardening models appear to have a slight over-prediction of the thickness while the Compliant-Isotropic Hardening model under-predicted the thickness.

A geometry comparison was also performed between the experiments and the simulation models, and the result is exhibited in Fig. 7. The deviation from the experimental result is shown in the right plot of Fig. 8. The level of deviation was smallest for the Compliant-Isotropic model, followed by the Rigid-Isotropic Hardening model and Rigid-Kinematic Hardening model which had a common trend in all the sections of the cone. Also, it can be seen that in all cases, the models predicted a small bulge in the middle, the unformed region, and the level of the bulge was slightly higher for rigid models compared to the compliant model. This lesser bulge is due to the fact that the compliant model squeezes the material less than the rigid models (due to the compliance), thus the buildup of the material is less than that of the rigid models, which coincides with the earlier findings in Shin et al. [17].

The differences in the three models’ predictions of the forces, thicknesses, and geometries can be explained through considering two different attributes between the models: (1) Abaqus and LS-Dyna implement the finite element method differently (e.g., contact, integration scheme, element implementation, etc.) and (2) the different yield loci and hardening laws. By comparing the Compliant-Isotropic Hardening model and Rigid-Isotropic Hardening model, with the same material input, the Abaqus and LS-Dyna formulations were able to predict similar results. Comparing

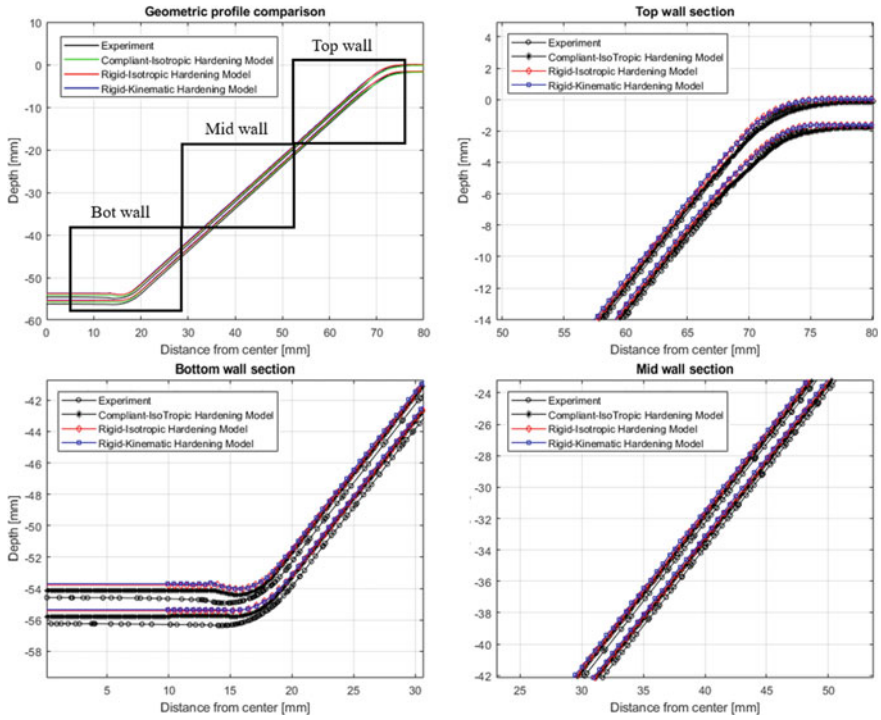


Fig. 7 Geometrical profile comparison between the experiment and the simulation for overall geometry, bending (top wall), steady state (mid-wall), and end tool contact (bottom wall)

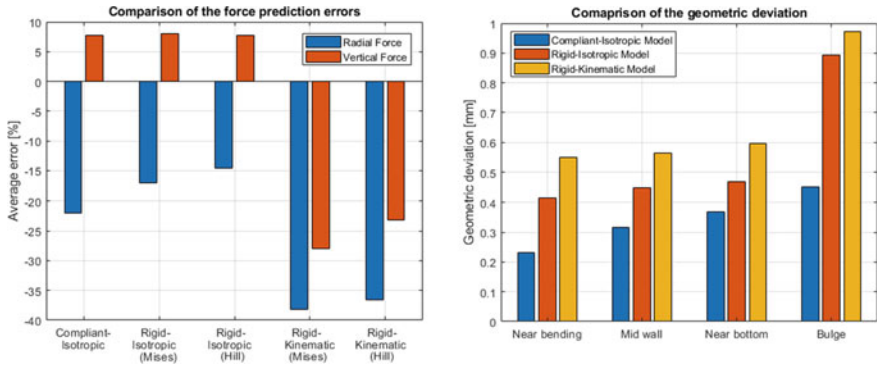


Fig. 8 Comparison of the errors and deviation of the force predictions (left) and the geometry (right)

the Rigid-Isotropic Hardening model to the Rigid-Kinematic Hardening model, the material model has a significant influence on the results, particularly for the force predictions.

In prior work [1], it was reported that kinematic hardening was able to improve the predictions of the forming forces in incremental forming. However, in the case of TPIF of the truncated cone (45° wall) for AA 7075-O, the opposite was observed; the inclusion of kinematic hardening led to under-predicted forces relative to the experiment and other models. This suggests that kinematic hardening does not always result in the increase in the accuracy of the prediction, though further studies are needed to determine what specifically led to these observed differences. Also worth noting, the use of kinematic hardening requires TCT tests in order to calibrate the material parameters. These tests require a dedicated setup that prevents the specimen from buckling in reverse-loading. Compliance modeling enables to capture the fine oscillation in the forces better, and further improvements in the predictions may be observed upon consideration of additional squeezing between the tools. However, the compliance model requires additional measurements and calibration with the physical machine.

In terms of computational costs, the Compliant-Isotropic Hardening model was run on 48 cores and took 32.24 h to complete, while Rigid-Isotropic Hardening and Rigid-Kinematic Hardening models were run on 120 cores and each took about 22.4 h to complete. The organized table containing a list of parameters and its respective predicted errors are shown in Table 3.

Conclusion

The truncated cone with a wall angle of 45° was investigated for a Two-Point Incremental Forming (TPIF) with several ways to simulate the process, including using different FEM software, mesh schemes, material hardening, and yield criteria. A model using Abaqus and a solid element with the combination of von Mises/Hill 48 and isotropic/kinematic hardening was created and compared with a model created with LS-Dyna and solid element utilizing only von Mises and isotropic hardening. The results of the simulations were compared to the experiment. Between the LS-Dyna and Abaqus models utilizing the von Mises yield criterion and isotropic hardening, the results were very similar regarding the forces, thickness distribution, and geometrical profile. The combination of Hill 48 and kinematic hardening under-predicted the forces while the geometry was similar to the other models. If one is looking to model the incremental forming process, it can be concluded that both LS-Dyna and Abaqus can be used to accurately predict the outcome of the process. Various material models should be carefully trialed to find one that can predict the result with sufficient accuracy. However, if limited resources are available, using isotropic hardening with the von Mises yield criterion is a pragmatic solution that

Table 3 Table of process parameters and its respective predicted errors

Approach	Software	Yield Function	Hardening Law	Geometry error (mm)				Force error (%)		CPU Cost
				Bend	Mid	Bot	Bulge	Radial	Vertical	
Compliant-Isotropic Hardening	LS-Dyna	von Mises	Isotropic	0.23	0.32	0.37	0.45	-22.0	7.7	48 cores 32.24 h
Rigid-Isotropic (Mises)	Abaqus	von Mises	Isotropic	0.41	0.45	0.47	0.89	-17.0	8.0	120 cores 21 h
Rigid-Isotropic (Hill)	Abaqus	Hill 48	Isotropic					-14.6	7.7	120 cores 22.4 h
Rigid-Kinematic (Mises)	Abaqus	von Mises	Kinematic	0.55	0.56	0.60	0.97	-38.2	-28	120 cores 23 h
Rigid-Kinematic (Hill)	Abaqus	Hill 48	Kinematic					-36.6	23.2	120 cores 23.2 h

yields excellent predictions in the geometry with a deviation of less than 100 μm and force prediction of around 7% over-prediction in axial forces. The radial force which can be influenced by friction coefficient requires further study to come up with an exact percentage of error.

References

1. Li Y, Daniel W, Meehan P (2017) Deformation analysis in single-point incremental forming through finite element simulation. *Int J Adv Manuf Technol* 88(1–4):255–267
2. Robert C, Dal Santo P, Delamézière A, Potiron A, Batoz J (2008) On some computational aspects for incremental sheet metal forming simulations. *Int J Mater Form* 1(1):1195–1198
3. Flores P, Duchene L, Bouffieux C, Lelotte T, Henrard C, Pernin N, Habraken A (2007) Model identification and FE simulations: effect of different yield loci and hardening laws in sheet forming. *Int J Plast* 23(3):420–449
4. Eyckens P, Belkassam B, Henrard C, Gu J, Sol H, Habraken A, Van Houtte P (2011) Strain evolution in the single point incremental forming process: digital image correlation measurement and finite element prediction. *Int J Mater Form* 4(1):55–71
5. Esmailpour R, Kim H, Park T, Pourboghra F, Mohammed B (2017) Comparison of 3D yield functions for finite element simulation of single point incremental forming (SPIF) of aluminum 7075. *Int J Mech Sci* 133:544–554
6. Bambach M, Hirt G (2005) Performance assessment of element formulations and constitutive laws for the simulation of incremental sheet forming (ISF). In: VIII International conference on computational plasticity
7. Hirt G, Ames J, Bambach M, Kopp R (2004) Forming strategies and process modelling for CNC incremental sheet forming. *CIRP Ann* 53(1):203–206
8. Li Y, Liu Z, Daniel W, Meehan P (2014) Simulation and experimental observations of effect of different contact interfaces on the incremental sheet forming process. *Mater Manuf Process* 29(2):121–128
9. De Sena J, Guzmán C, Duchêne L, Habraken A, Behera A, Dufloy J, de Sousa R (2016) Simulation of a two-slope pyramid made by SPIF using an adaptive remeshing method with solid-shell finite element. *Int J Mater Form* 9(3):383–394
10. Bouffieux C, Lequesne C, Vanhove H, Dufloy J, Pouteau P, Duchêne L, Habraken A (2011) Experimental and numerical study of an AlMgSc sheet formed by an incremental process. *J Mater Process Technol* 211(11):1684–1693
11. Henrard C, Bouffieux C, Eyckens P, Sol H, Dufloy J, Van Houtte P, Habraken A (2011) Forming forces in single point incremental forming: prediction by finite element simulations, validation and sensitivity. *Comput Mech* 47(5):573–590
12. Malhotra R, Huang Y, Xue L, Cao J, Belytschko T (2010) An investigation on the accuracy of numerical simulations for single point incremental forming with continuum elements. *AIP Conf Proc* 1252(1):221–227. AIP
13. Duchêne L, Guzmán C, Behera A, Dufloy J, Habraken A (2013) Numerical simulation of a pyramid steel sheet formed by single point incremental forming using solid-shell finite elements. *Key Eng Mater* 549:180–188. Trans Tech Publications
14. Abaqus 6.14 manual/18.2.2 Models for metals subjected to cyclic loading
15. Abaqus 6.14 manual/8.2.6 Anisotropic yield/creep
16. Salem E, Shin J, Nath M, Banu M, Taub A (2016) Investigation of thickness variation in single point incremental forming. *Proc Manuf* 5:828–837
17. Shin J, Bansal A, Nath M, Cheng R, Banu M, Taub A, Martinek B (2018) Prediction of negative bulge in two point incremental forming of an asymmetric shape part. *J Phys Conf Ser* 1063(1):012057. IOP Publishing

A Virtual Laboratory Based on Full-Field Crystal Plasticity Simulations to Predict the Anisotropic Mechanical Properties of Advanced High Strength Steels



Haiming Zhang, Qian Li, Dongkai Xu, and Zhenshan Cui

Abstract Advanced high strength steels are of growing interest in automotive industry for their superior strength-to-weight ratio. The heterogeneous microstructure renders their complex anisotropic properties. In this work, a series of uniaxial tension (combining with the 3D digital image correlation technique) were employed to capture the plastic anisotropy of a DP980 sheet. Postmortem EBSD characterizations and the state-of-the-art full-field crystal plasticity simulations were performed to explore the effect of texture evolution and heterogeneous microstructure on its anisotropic behavior. The results indicate that the r -value of the DP980 sheet is significantly affected by the deformation level; it increases initially, and then falls continuously after localization. Specially, the r -value of the studied steel is much smaller compared to that of single-phase steels. The inhomogeneous deformation and interactions between the ferrite and martensite phases are demonstrated to account for the anisotropic behaviors of the studied material.

Keywords Anisotropy · r -value · Crystal plasticity

Introduction

Due to their excellent strength-to-weight ratio, advanced high strength steels (AHSSs) have been in great demand in automotive industry. Among them, dual-phase (DP) steel is of significant interest for its simultaneous good formability and high strength and used to produce critical parts like B-pillar and engine cradle, etc. [1] Nevertheless, the heterogeneous multi-phase microstructure of AHSSs also leads to their complex mechanical properties [2]. AHSSs sheets essentially show

H. Zhang (✉) · Q. Li · Z. Cui

School of Materials Science and Engineering, Shanghai Jiao Tong University, 1954 Huashan Road, Shanghai 200030, PR China
e-mail: hm.zhang@sjtu.edu.cn

D. Xu

Research Institute, Baoshan Iron and Steel Co., Ltd., State Key Laboratory of Development and Application Technology of Automotive Steels (BaoSteel), Fujin Road 655, Shanghai 201900, China

distinct mechanical anisotropy due to the preferential orientation (i.e., crystallographic texture) developed in the proceeding thermomechanical operations. The typical texture component γ fiber ($\langle 111 \rangle \parallel \text{ND}$, with ND represents the normal direction of sheet) of body-centered cubic (BCC) metals generally improves the deep drawing ability; while the α fiber ($\langle 110 \rangle \parallel \text{RD}$, with RD represents the rolling direction) does the opposite.

A critical parameter used to characterize the plastic anisotropy is the Lankford coefficient (r -value) from uniaxial tension of metal sheets. Since the deep drawing ability of metal sheets generally relates to r -values which are easily accessible through uniaxial tension, r -values therefore are frequently used for calibration of yield functions, for instance, Hill48 [3] and Yld2004 [4] criteria, etc. As a first-hand and important parameter of polycrystalline sheets, r -values of single-phase BCC steels have been extensively investigated by many researchers, for instance, 1.64–2.43 for IF steel [5], 1.4–1.8 for low-carbon steel [6] and 1.2–1.8 for ferrite stainless steel [7]. For AHSSs, however, r -values were announced to be 0.85–1.1 [8, 9], i.e., much smaller than those of single-phase steels. Unlike the single-phase body-centered cubic (BCC) steels, the anisotropic behavior of multi-phases steels is not well understood yet.

Crystal plasticity (CP) modeling is an effective and commonly used approach for studying the anisotropic behaviors and underneath micro-mechanisms of polycrystalline metals. Using a CPFEM scheme, Woo et al. [10] verified that the crystal orientations of ferrite phase have a great influence on the strain localization and void initiation in the ferrite matrix near the phase boundaries for a DP980 steel sheet. Based on a full-field CPFEM framework, Pagenkopf et al. [11] revealed the relation between the martensite morphology and the flow stress as well as the r -values. Zhang et al. [12] developed a virtual laboratory based on high-resolved CP modeling to predicted the anisotropy of aluminum alloys, and the predicted yield stress points were adopted to identify advanced yield functions successfully.

In this work, we adopt microstructure-based full-field crystal plasticity (CP) simulations as a virtual laboratory to predict the plasticity anisotropy of a cold-rolled AHSS (DP980), and further to probe the micromechanical behaviors due to the heterogeneous microstructure. The results are verified and explained complementally via a series of uniaxial tension (combining with the 3D digital image correlation technique) as well as postmortem EBSD characterizations.

Experiments and Full-Field Crystal Plasticity Modelling

Uniaxial Tensile Tests and Post-Mortem EBSD Characterizations

The studied material is a commercial cold-rolled DP980 sheet of 1.2 mm thickness (provided by Baosteel). To explore the mechanical anisotropy of the sheet, uniaxial

tensile tests along seven directions (i.e., 0° , 15° , 30° , 45° , 60° , 75° , and 90° to the RD) were performed on the specimens via an electronic testing machine (Instron Model 8080 with a load cell of 100KN). The crosshead velocity is 3 mm/min. The gauge length and width of the dog-bone specimens are 50 mm and 12.5 mm, respectively. A 3D DIC system (Aramis) was used to capture the strain field evolution up to fracture.

To investigate the influence of texture evolution on mechanical anisotropy, the microstructures before and after uniaxial tensile tests were characterized using a VEGA 3 field emission SEM equipped with an Oxford EBSD detector at 20 kV. The initial and deformed specimens were ground with 100, 240, 320, and 600 grit SiC papers respectively, and then polished with $9\ \mu\text{m}$ and $3\ \mu\text{m}$ diamond suspensions, followed by $0.05\ \mu\text{m}$ alumina suspension. Finally, the specimens were vibratory polished with $0.02\ \mu\text{m}$ silica suspension for two hours. For the deformed specimens, the region of interest is on the RD-TD plane and close to the fracture surface, where the material has undergone larger deformation.

Microstructure-Based Full-Field Crystal Plasticity Modelling

To investigate the influence of the heterogeneous microstructure on the anisotropic behaviors, microstructure-based full-field CP simulations were performed on the DP980 sheet. The plastic velocity gradient resulted from dislocation slip is written as

$$\mathbf{L}^P = \sum_{\alpha} \dot{\gamma}^{\alpha} \mathbf{S}^{\alpha} \quad (1)$$

Here, \mathbf{S}^{α} and $\dot{\gamma}^{\alpha}$ are the Schmid tensor and the slip rate of the α slip system respectively.

A phenomenological rate-dependent constitutive model was adopted to describe the slip rate resulting from dislocation slip. It is expressed as

$$\dot{\gamma}^{\alpha} = \dot{\gamma}_0 \left| \frac{\tau^{\alpha}}{g^{\alpha}} \right|^{1/m} \text{sign}(\tau^{\alpha}) \quad (2)$$

Here, $\dot{\gamma}_0$ denotes the reference slip rate, m refers to the rate sensitivity coefficient, and g^{α} refers to the slip resistance. The evolution of g^{α} is formulated as

$$\begin{cases} \dot{g}^{\alpha} = \sum_{\beta} h_{\alpha\beta} \dot{\gamma}^{\beta} \\ h_{\alpha\beta} = h_0 [q + (1 - q) \delta^{\alpha\beta}] \left| 1 - \frac{g^{\beta}}{g_{\infty}^{\beta}} \right|^a \end{cases} \quad (3)$$

Here, h_0 is the initial hardening modulus of slip systems, g_{∞} is the saturated slip resistance, a is an estimated constant, and q refers to the hardening coefficient describing

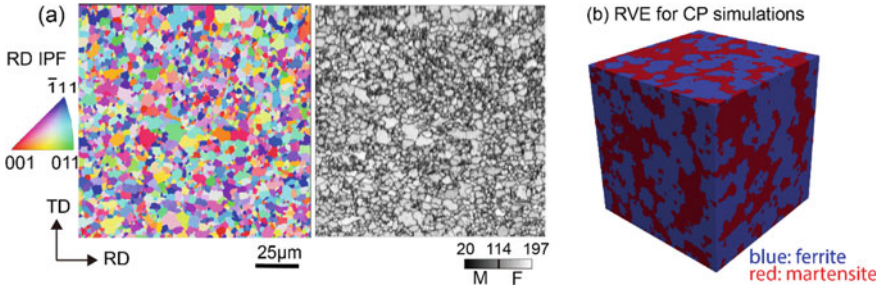


Fig. 1 a Microstructure of the as-received DP980 sheet: orientation imaging microscopy and band contrast maps obtained by EBSD; the 3D-RVE reconstructed by DREAM. 3D based on the EBSD data

the interaction between slip systems. $q = 1.0$ for coplanar interaction and 1.4 for non-coplanar interaction.

In this work, the CP constitutive model considers $\{\bar{1}10\}\langle 111\rangle$ and $\{\bar{2}11\}\langle 111\rangle$ slip for both ferrite and martensite phases. As shown in Fig. 1a, EBSD data of the initial microstructure was used to separate the ferrite and martensite phases based on the band contrast (BC) value. After that, 3D representative volume elements were reconstructed via an open-source software DREAM.3D with emphasizing of matching phase constituent and orientations; the RVE is exemplified in Fig. 1b. A genetic algorithm-based inverse method then was adopted to identify the CP material parameters for both ferrite and martensite phases. The constitutive parameters for the studied DP980 sheet are listed in Table 1. The methodology was validated by comparing the predicted flow stress curves with the experimental ones from uniaxial tensile tests. The full-field CP simulations were conducted in the open-source spectral method solver DAMASK. Periodic boundary condition was applied on the RVEs to simulate uniaxial tension along different directions. More details can be found in Li et al. [13].

Results and Discussion

Figure 2 displays the contour maps of the equivalent plastic strain $\bar{\epsilon}^p$ for uniaxial tensile specimens at different stages. As can be seen from Fig. 2a, the strains of the specimens are well distributed at the stage of $\bar{\epsilon}^p = 5.5\%$ except for 60° and 75° specimens, which manifest moderate strain localizations. With deformation, the strain localizations get more obvious. At the stage before fracture shown in Fig. 2b, shear bands with angle of 50° – 55° to the loading direction can be observed in all the specimens. The results demonstrate that the DIC technique used in this work provides a high-fidelity strain field during the entire uniaxial tension process.

The Lankford coefficient (r -value), defined as the ratio of the width to thickness plastic strain rates ($\dot{\epsilon}_w^p/\dot{\epsilon}_t^p$), is a critical parameter for characterizing the plastic

Table 1 The constitutive parameters of the CP model for the DP980 steel

Phase	System	g_0/MPa	g_∞/MPa	h_0/GPa	a	m	$\dot{\gamma}_0/s^{-1}$	C_{11}/GPa	C_{12}/GPa	C_{44}/GPa
Ferrite	$\{\bar{1}10\}\langle 111 \rangle$	150.8	223.4	2.0	1.9	0.05	0.001	233.3	135.5	118.0
	$\{\bar{2}11\}\langle 111 \rangle$	154.0	614.3							
Martensite	$\{\bar{1}10\}\langle 111 \rangle$	644.3	917.8	1.12	1.9	0.05	0.001	417.4	242.4	211.1
	$\{\bar{2}11\}\langle 111 \rangle$	725.2	1021.2							

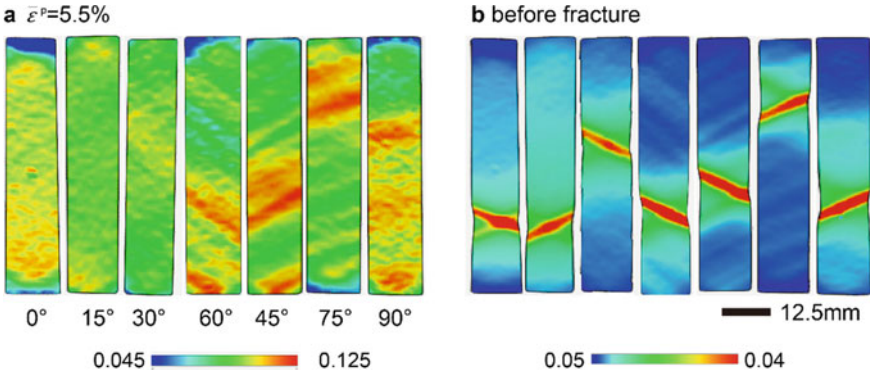


Fig. 2 The contour maps of equivalent plastic strain $\bar{\epsilon}^p$: **a** at global $\bar{\epsilon}^p = 5.5\%$, **b** at global $\bar{\epsilon}^p = 9\%$

anisotropy of metal sheets. Figure 3 presents the evolution of r -value for the specimens tensioned along the seven directions. As can be seen, the r -value of the studied DP980 sheet is highly sensitive to the loading directions. For instance, the large value appears in the diagonal direction (DD) specimen and the lowest one in the RD specimen. Different from the traditional low-carbon steels whose r -values generally exceeding 2.0, in most cases the r -values of the studied DP980 sheet are below 1.0. This suggests that the DP980 sheet is more vulnerable to reduction in thickness than width. As illustrated in Fig. 3, the r -value also relies on the strain level. For all the specimens, the r -values ascends gradually with deformation initially and then decrease until failure. The inflection point arises near global $\bar{\epsilon}^p = 0.055$, taking the smallest value for 75° specimen and largest for 0° and 15° specimen. Associated with the strain distribution at $\bar{\epsilon}^p = 5.5\%$ shown in Fig. 2a, it is concluded that the heterogeneous deformation resulting from strain localization mainly accounts for the transition of r -values. Furthermore, the results suggest that the traditional practice

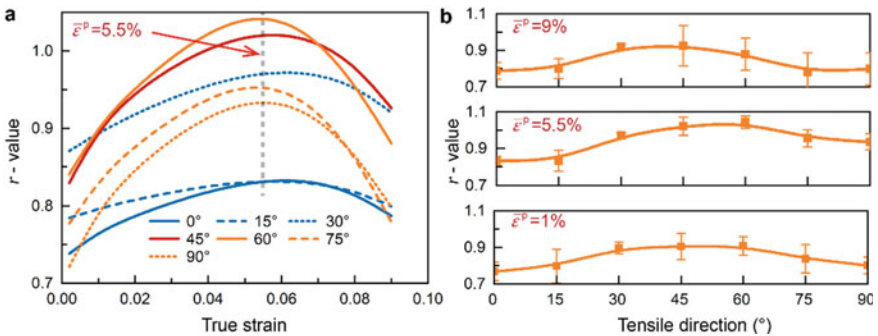


Fig. 3 **a** The evolution of r -values with deformation, **b** the variation of r -values with respect to the loading directions at strain levels of $\bar{\epsilon}^p = 1\%$, 5.5% and 9%

of using the r -values at a specific stage to characterizing the plastic anisotropy and calibrating yield functions simplifies the anisotropy evolution of AHSS sheets.

Figure 4 shows the ND IPF and RD IPF reconstructed with the MATLAB toolbox MTEX for specimens tensioned along RD, DD, and TD. Significant texture change from main component $\{111\}\langle 11\bar{2}\rangle$ to $\{111\}\langle 011\rangle$ is clearly observed in all the specimens, especially for the DD specimen, which agrees with the uniaxial tensile experiments as the DD specimen has the largest r -value in all the three specimens. After deformation, the orientations spread from $[011]$ to $[\bar{1}12]$ and gather at the pole $[\bar{1}11]$, leading to the preservation of γ fiber and weakening of α fiber. This texture evolution is inferred to account for the gradual ascent for r -values of the studied DP980 sheet before strain localization since the γ fiber generally improves r -values of polycrystalline sheets while the α fiber does the opposite.

Figure 5 presents the comparison between the predicted and experimental r -values of the studied DP980 sheet with respect to loading directions obtained from CP simulations. Despite the mild deviation, the evolution of r -values suggests that the CP modeling successfully forecasts the in-plane anisotropy of r -values. Furthermore, referring to the 0° and 90° specimens whose simulated r -values matched very well with the experimental ones. It is verified that the CP modeling is more precise when the principal axes of stress coincide with that of the material. Previous work of Zhang et al. [12] on an AA3104 aluminum sheet demonstrated the nice dependability of full-field CP based virtual laboratory in modeling the plastic anisotropy of single-phase metals. Figure 5 further proves that the CP modeling with high-resolution is promising in predicting the anisotropy of multi-phase polycrystalline metals.

To investigate the influence of heterogeneous microstructure on anisotropic properties, contour maps of equivalent strain and r -value at the stage of global $\bar{\epsilon}^p = 0.09$

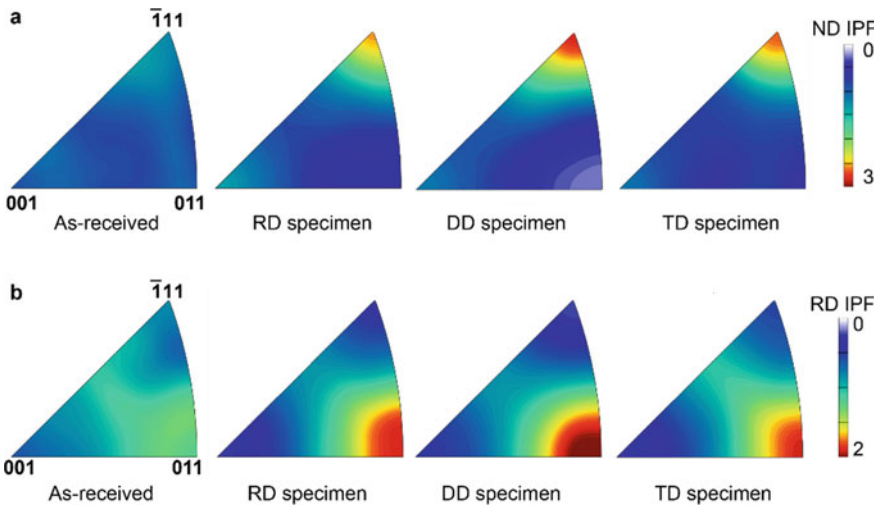
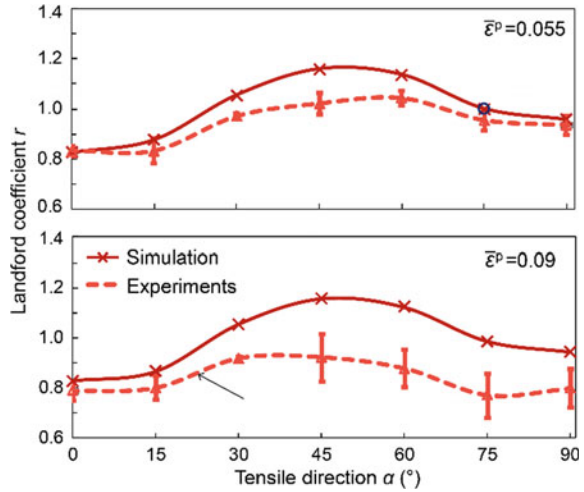


Fig. 4 a The ND IPF; b the RD IPF of specimens tensioned along RD, DD, and TD

Fig. 5 a The in-plane anisotropy of r -values predicted by CP simulations at strain levels of $\bar{\epsilon}^p=5.5\%$ and 9%



are studied for the RD, DD, and TD specimens, as shown in Fig. 6. As anticipated, the grain-level strain distributions of all the specimens are strongly inhomogeneous; strain localizations mainly occur in the phase boundaries (PBs) and in the necklaces of the martensite islands. The soft ferrite matrix underwent a larger deformation than the hard martensite islands, and local shear bands with direction consistent to the macroscopic shear bands shown in Fig. 2b are clearly observed near the PBs. That is, the soft ferrite matrix accommodates the imposed deformation while the hard martensite phase maintains deformation compatibility. The deformation constraint resulting from the PBs of the heterogeneous microstructure dominates the strain distribution of the specimens and could reduce the overall r -values of the DP steels [13]. Figure 6a further demonstrates that the three RVEs show a quite similar distribution of strain, i.e., the grain-level deformation partition is more influenced by the heterogeneous microstructure while less by the loading direction.

Regarding the contour map of r -values, as shown in Fig. 6b, the distributions are also highly inhomogeneous. For RVEs tensioned along different directions, they all have r -values smaller than 0.5 for most areas, especially for the RVEs tensioned in RD and TD. According to the statistics, the proportion of material points with r -value below 0.45 is 36.9% for the RD RVE and 33.9% for the TD RVE, which is much larger than that of the DD RVE (26.2%). The result is consistent with Fig. 3b, as the DD specimen has a higher r -value compared to the RD and TD specimens, which further proves the reliability of CP simulation in modeling multi-phase polycrystalline. Unlike the distribution of strain, Fig. 6b shows that the grain-level r -value is more affected by the loading direction.

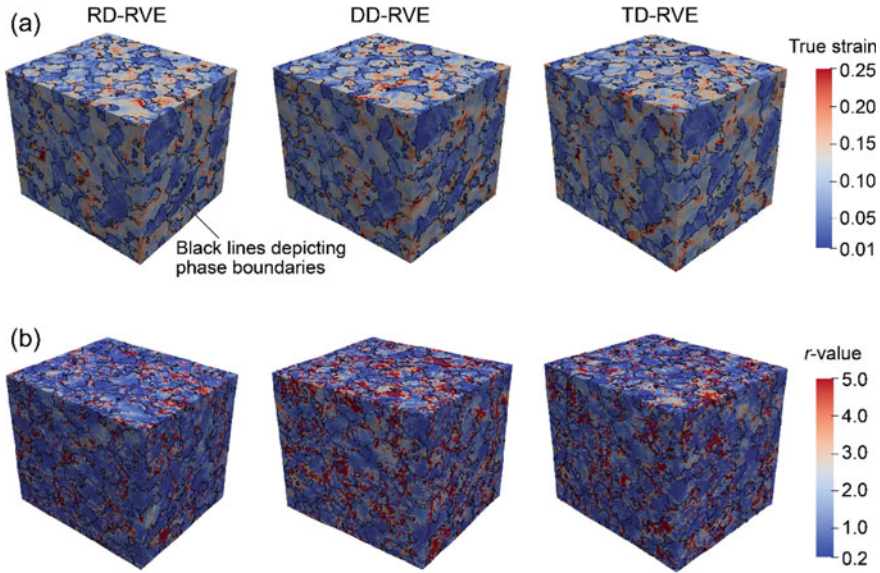


Fig. 6 The contour maps of **a** true strain and **b** r -values at the stage of global $\bar{\epsilon}^p = 0.09$ simulated by full-field CP-based virtual laboratory for the RD, DD, and TD specimens

Conclusions

A series of uniaxial tensile tests and postmortem EBSD characterizations combining with the full-field CP simulations were conducted to explore the anisotropic behaviors of the DP980 steel sheet and the influence of the heterogeneous microstructure. The mechanical anisotropy and the evolution of r -value were evidenced with the 3D DIC technique. The results indicate that the texture evolution, strain localization, and plastic heterogeneity resulting from the dual-phase heterogeneous microstructure dominates the r -values jointly. The texture evolution from $\{111\}\langle 11\bar{2}\rangle$ to $\{111\}\langle 011\rangle$ intensifies the γ fiber and weakens the α fiber, leading to the gradual ascent of r -values at the beginning. Afterwards, the strain localization brings down the thinning resistance of the sheet and brings about the continuous fall of r -values. The high-resolved CP simulations successfully reproduce the evolution of r -values with respect to tensile directions and demonstrate the influence of the heterogeneous microstructure on r -values. The heterogeneous deformation between the ferrite and martensite phases results in strain partition and deformation constraint. Such deformation constraint is confirmed to reduce the overall r -values of the DP980 sheet. The grain-level distributions of strain and r -values show that the strain partition is more affected by the heterogeneous microstructure, while r -values show strongly dependence on loading directions.

Acknowledgements The authors acknowledge the funding support from the National Natural Science Foundation of China with the project No. 52075329 and Shanghai Rising-Star Program (20QA1405300).

References

1. Stuart K, Menachem K (2014) Advanced high-strength steels: application guidelines version 5.0, WorldAutoSteel
2. Cai Z, Diao K, Wu X, Wan M (2016) Constitutive modeling of evolving plasticity in high strength steel sheets. *Int J Mech Sci* 43–57
3. Hill R, Orowan E (1948) Mathematical and physical sciences. *Math Phys Sci* 193:281–297
4. Barlat F, Aretz H, Yoon JW, Karabin ME, Brem JC, Dick RE (2005) Linear transformation based anisotropic yield functions. *Int J Plast* 5:1009–1039
5. Oh GJ, Lee KM, Huh MY, Park JE, Park SH, Engler O (2017) Effect of r-value and texture on plastic deformation and necking behavior in interstitial-free steel sheets. *Met Mater Int* 1:26–34
6. Tada M, Nakagawa Y, Kojima K (2018) Effect of annealing temperature and coiling temperature on r-value of Nb and B-added extra low-carbon steel. *ISI J Int* 5:970–977
7. Yazawa Y, Muraki M, Kato Y, Furukimi O (2003) Effect of chromium content on relationship between r-value and 111 recrystallization texture in ferritic steel. *ISI J Int* 10:1647–1651
8. Panich S, Barlat F, Uthaisangsuk V, Suranuntchai S, Jirathearanat S (2013) Experimental and theoretical formability analysis using strain and stress based forming limit diagram for advanced high strength steels. *Mater Des* 756–766
9. Huh J, Huh H, Lee CS (2013) Effect of strain rate on plastic anisotropy of advanced high strength steel sheets. *Int J Plast* 23–46
10. Woo W, Em V, Kim EY, Han SH, Han YS, Choi SH (2012) Stress–strain relationship between ferrite and martensite in a dual-phase steel studied by in situ neutron diffraction and crystal plasticity theories. *Acta Mater* 20:6972–6981
11. Pagenkopf J, Butz A, Wenk M, Helm D (2016) Virtual testing of dual-phase steels: Effect of martensite morphology on plastic flow behavior. *Mater Sci Eng A* 672–686
12. Zhang H, Diehl M, Roters F, Raabe D (2016) A virtual laboratory using high resolution crystal plasticity simulations to determine the initial yield surface for sheet metal forming operations. *Int J Plast* 111–138
13. Li Q, Zhang H, Chen F, Xu D, Sui D, Cui Z. Study on the plastic anisotropy of advanced high strength steel sheet: experiments and microstructure-based crystal plasticity modelling. *Int J Mech Sci*

Development of a Numerical 3D Model for Analyzing Clinched Joints in Versatile Process Chains



C. R. Bielak, M. Böhnke, M. Bobbert, and G. Meschut

Abstract The application of the mechanical joining process clinching enables the joining of sheet metals with a wide range of material-thickness configurations, which is of interest in lightweight construction of multi-material structures. Each material-thickness combination results in a joint with its own property profile that is affected differently by variations. Manufacturing process-related effects from preforming steps influence the geometric shape of a clinched joint as well as its load-bearing capacity. During the clinching process high degrees of plastic strain, increased temperatures and high strain rates occur. In this context, a 3D numerical model was developed which can represent the material-specific behaviour during the process chain steps sheet metal forming, joining, and loading phase in order to achieve a high predictive accuracy of the simulation. Besides to the investigation of the prediction accuracy, the extent of the influence of individual modelling aspects such as temperature and strain rate dependency is examined.

Keywords Mechanical joining · Numerical simulation · Strain rate · Temperature

Introduction

Clinching is a common mechanical joining technology for sheet metal materials, in which the joint is based solely on cold forming of the parts to be joined and no auxiliary joining elements are required. It has proven particularly effective for the

C. R. Bielak (✉) · M. Böhnke · M. Bobbert · G. Meschut
Laboratory for Material and Joining Technology (LWF), Paderborn University, Pohlweg 47-49,
33098 Paderborn, Germany
e-mail: christian.bielak@lwf.upb.de

M. Böhnke
e-mail: max.boehnke@lwf.upb.de

M. Bobbert
e-mail: mathias.bobbert@lwf.upb.de

G. Meschut
e-mail: meschut@lwf.upb.de

implementation of multi-material construction methods, which has become important in the context of lightweight design in the automotive industry [1]. With tools like a punch, blankholder, and a die, a force and form fit joint in two or more overlapping sheet metal parts is produced. During the process the punch is penetrating and radially expanding the sheet metal parts. Thus, the induced material flow of both sheets into the die creates a mechanical interlock [2]. From a quality point of view, different geometrical parameters (bottom thickness, neck thickness, and interlock) are considered to be particularly relevant for the connection.

Simulation of the clinching process has already been studied in [3]. Further developments in the simulation of the clinching process are summarized in [4]. The mechanical properties of the joint depend on the geometrical characteristics of the joining zone, which is influenced by the material, the tools used, and the process parameters. For this reason, simulation is used to design an efficient development process.

In [5] a numerical study based on a 2D axisymmetric FE- model was shown to investigate the influence of the pre-strain of sheet metal components on the characteristic properties of clinched joints. It was shown that FE simulation is suitable to investigate and quantify clinching in the context of a manufacturing process chain. Furthermore, the influence of the pre-straining on the loading was also investigated numerically, for which a model was shown in [6]. Therein, the influence on the maximum transferable shear load depending on the preforming of the sheet metal parts was investigated. It has been shown that the pre-strain of the materials before joining has an influence on the level of the transferable tensile shear load. This pre-deformation influences the joinability depending on the formability of the materials and must be taken into account in the design of joints. The influence of the forming history on clinched joints is described experimentally in [7] for steel and in [8] for aluminium sheet metal materials. It has been reported that the preforming of the punch-side material has a greater influence on the load-bearing behaviour of the clinched joints than the die-side material. This was related to a decreasing neck thickness at the clinched joint with increasing strain hardening of the material, which in turn caused earlier failure in shear tensile tests. In [9], the static and dynamic behavior and failure modes of SPR and clinched joints were characterized by experiments. The influence of strain rate dependent mechanical behavior of the materials on the joints was investigated. It has been observed that the strength of clinched joints under overlap shear conditions increases with increasing loading rate. In [10], an experimental and numerical study of the rate-dependent mechanical behavior of a hybrid clinched joints was presented. Experiments were presented in the form of lap shear and peel tests, where the joint specimens were investigated under quasi-static and dynamic loads. Numerical simulations were performed using a detailed 3D FE model that considers the influence of process-induced strain hardening. It was found that the dynamic hardening effect of the hybrid clinched joint varies with the loading modes. The present experimental and numerical study shows that the strain hardening in peel is almost negligible compared to lap shear. In [11], the heat development during the flat-clinching process was investigated. Using a validated simulation model, temperature increases in the forming zone of up to 203 K were

determined. Due to the temperature dependence of the mechanical properties of sheet materials, this must be taken into account in the numerical simulation of the clinching process.

In this study, the influence of strain rate and temperature on clinch joining will be investigated along the process chain (pre-strain, joining, loading). For this purpose, three different FE models are presented and investigated.

Materials and Method

The dual phase steel HCT590x ($t = 1.5$ mm), which is widely used in the automotive industry, with a two-phase microstructure was selected for the numerical investigation of the material-specific strain rate and temperature dependence in the clinch process chain. The mechanical properties of HCT590x are given in Table 1. according to experimental material investigations.

In order to determine the material properties and generate flow curves, experimental material characterization tests were performed in [12], which included different sample geometries and various strain hardening laws for extrapolation methods. The quasi-static flow curve used in this work was generated with a layer compression test (LCT) [13], which allows the experimental investigation of material plasticity up to true strains of $\varphi = 0.5$. The obtained experimental data were extrapolated with the Hockett-Sherby approach. In addition, the clinching process simulation with the flow curves obtained from the LCT showed very good results in direct comparison with the experimental data. For the identification of material-specific strain rate and temperature effects, standard tensile specimens according to SEP1230 [14] are used and the tensile tests were performed according to the guideline from [15]. With the tensile tests hardening or softening parameters are identified and used to scale the quasi-static flow curve from the LCT test accordingly. The resulting scaled flow curves depending on different strain rates and temperatures are shown in Fig. 1.

The flow curves shown were tabulated according to the strain rate or temperature in a visco-elastic-plastic material model (MAT224_MAT_TABULATED_JOHNSON_COOK) [16]. Due to the lack of a failure model, a neck crack during joining or a failure during loading cannot be predicted. The parameterized material model was used consistently along the simulated process chain. The process chain to be investigated in this paper consists of three stages. The pre-strain of the materials, the joining process, and the loading phase. Figure 2 shows an overview of the models in chronological order. The

Table 1 Mechanical properties of HCT590X

$R_{p0.2}$ (MPa)	390 ± 5
R_m (MPa)	620 ± 5
Elongation at break (A_{80})	$\geq 20\%$

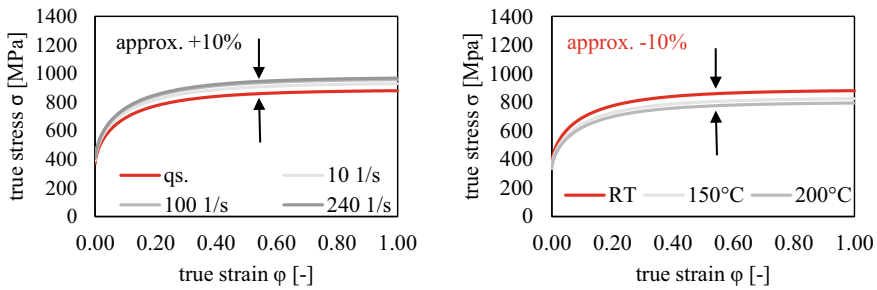


Fig. 1 Quasistatic flow curve from LCT scaled according to the strain rates and temperature tensile tests

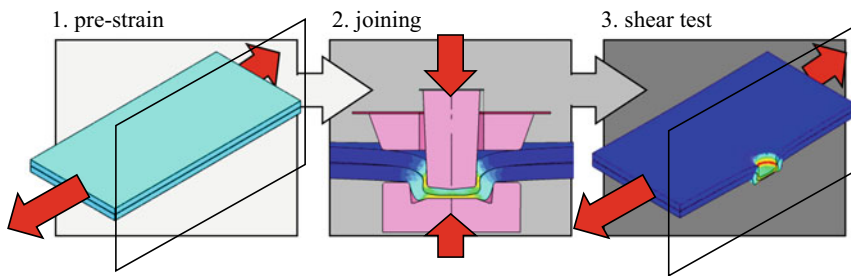


Fig. 2 Simulated three-step process chain of clinch joining

stage in each step is calculated in a separate FE model and the result, with internal stresses and strains, is transferred to the subsequent stage. For model development the simulation software LS-Dyna is used. All models have been calculated with the LS-DYNA Solver `ls-dyna_smp_d_R11_1_0` in implicit for mechanical solution. The strain rate effects were activated by the control card `_IMPLICIT_DYNAMIC`. As the process is limited to a short time period, temperature effects have been considered in a very simplified way in this study. On the one hand, the heat generation is only taken into account from the transformation energy. Heat generated by friction is not considered. Furthermore, there is no heat conduction in the materials and no heat transfer between the sheets or to the tools. For the investigation of the different influences of strain rates and temperature dependence of the implemented material model, various models are calculated. Table 2 presents settings for the material

Table 2 Simulation setup according to the strain rate/temperature dependence of the material model

No.	1	2	3	4
Pre-strain	$\varphi = 0.0$	$\varphi = 0.1$	$\varphi = 0.0$	$\varphi = 0.1$
Strain rate	Yes	Yes	No	No
Temperature	Yes	Yes	No	No

model for the FE models studied in this work. The material settings with respect to strain rate and temperature dependence are valid for the process chain (pre-strain, joining, shear test).

Prior to the joining process, the sheet pre-strain is calculated in a separate model. The top sheet as well as the base sheet is formed to a homogeneous effective plastic strain of 0.1 by means of a unidirectional pre-strain. The model of the 3D joining process was in principle already used in earlier studies, but only with quasi-static flow curves. It was evaluated with regard to the contact pressures in [17]. It was adapted for the investigations in this paper as a half model. This is due to the subsequent non-axisymmetric design of the lap shear test.

Results and Discussion

The first evaluation, shown in Figs. 3 and 4, refers to Model 1 and 3 for the process and shear load. Model 2 was evaluated for the pre-strain. The process chain was evaluated with (1, 2) and without (3) consideration of the strain rate and temperature effect. The strain rates and temperatures that can occur during the simulation are determined in Fig. 4. For this purpose, the maximum local element temperature over time was determined. The location of this local temperature changes during the process and is strongly influenced by the location of the highest plastic deformation.

Figure 3 shows the maximum local stress (related to left ordinate) and the maximum local plastic strain (related to right ordinate) over the course of the process chain (pre-straining, joining, and shear test). The finite element with the maximum value was evaluated in the FE model. The maximum effective stress is shown as a dashed line in the diagram. The max. stress exceeds the elastic region at the beginning of the process in order to induce the plastic deformation (pre-strain) of the top and base sheet. After the pre-strain operation, the stress decreases due to the unloading

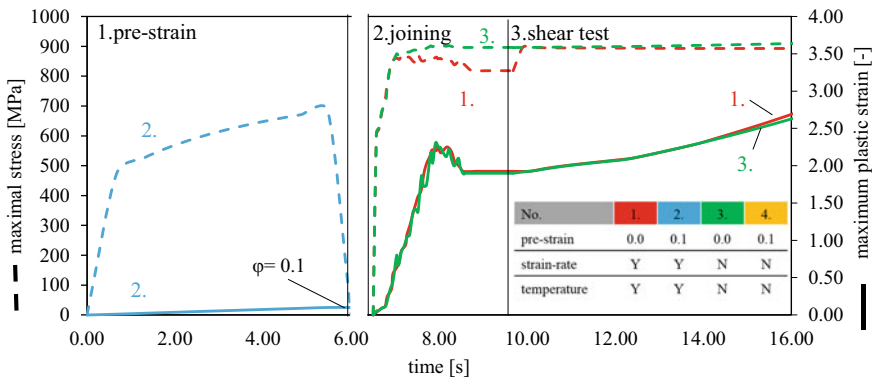


Fig. 3 Local maximum stress and plastic strain along a three-step process chain

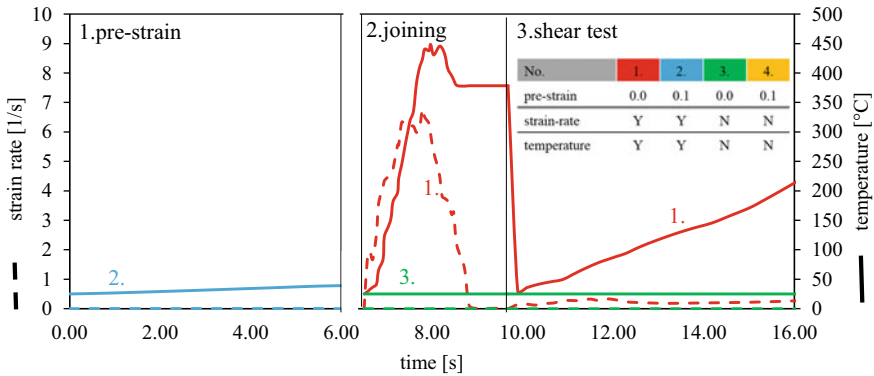


Fig. 4 Local maximum strain rate and temperature along the three-step process chain

and increases again due to the forming process of the clinch joining operation. In the third sector, the stress is maintained due to the residual stresses. A further increase in the stress is not possible due to the limitation of the flow curve. Between the models (1) in red (with consideration of the strain rate and temperature effects) and (3) in green (without consideration), there is a difference in the progression of the stress during joining. Model (1) has a lower stress curve, this is caused by the high local temperature development and the resulting softening. The plastic strain is very similar for both models over the process.

Figure 4 shows the strain rate and the temperature response for models (1) and (3), as well as (2) for the preforming process. The dashed line shows the development of the highest local strain rate over the process chain. Since the pre-strain and shear loading is quasi-static, only very low strain rates are achieved. During the joining process, strain rates of up to 7.0 s^{-1} are achieved. The local temperature development during the joining process reaches maximum values of $450 \text{ }^\circ\text{C}$. During shear loading, maximum temperatures of $250 \text{ }^\circ\text{C}$ can be reached. These temperatures are very local and it is assumed that they are dissipated in the real experiment by the heat conduction. For a more accurate determination of the local maximum temperature, the FE model shall be calculated to some extent thermal coupling. Since model (3) does not consider temperature and strain rates, these values do not change over the process.

Furthermore, the process forces during joining and the transferable shear force were evaluated. The results are summarised in Fig. 5. On the left side of the figure, four process forces of the models (1–4) are shown. These are all in a comparable range, but effects caused by the local high temperatures can be observed. For the models with (2, 4) and without pre-straining (1, 3), the curves with consideration of the temperature and strain rate are below the models without consideration.

The same tendencies can be seen for the courses of the maximum shear force on the right of Fig. 5. The differences can be explained by the high local temperatures occurring during the shear load, as the strain rates are negligible low.

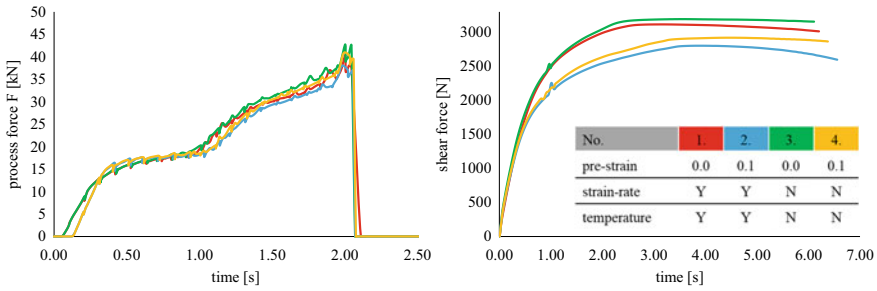


Fig. 5 Influence of the consideration of the strain rate and temperature-dependent material model on the process force and the shear force curve

Summary

A 3D FEM process chain (half model) was developed and presented in this study for clinching with pre-strain of the sheet metal materials followed by a shear test. A material model has been experimentally developed which reproduces the strain rates and temperature effects. This was used in the calculation of the FE models.

Stress, strain, strain rate and temperature were evaluated along the process chain for the local maximum. It could be seen that due to the low velocities, a maximum local strain rate of 7 s^{-1} occurs. Two local maximum values were observed for the temperature curve, $450 \text{ }^\circ\text{C}$ for joining, and $250 \text{ }^\circ\text{C}$ for the shear test. These temperatures occur locally and are excessive due to the lack of thermal coupling. The high temperatures lead to a softening of the material, resulting in lower process and shear forces. This effect was seen in both pre-strained and non-pre-strained materials.

Outlook

This first preliminary investigation of the strain rate and temperature effect on a 3D FE-model process chain has shown that it is difficult to estimate the effective temperature without a thermo-mechanically coupled solver. The local maximum temperature during joining is overestimated. To be able to make a more precise statement, a more accurate temperature calculation must be made. The strain rate effect, on the other hand, could be neglected due to the slow process velocities for the three stages of the process chain presented here. The further study will examine the thermomechanical coupling and the impact loading of the shear tests in order to describe the influence of the strain rate and temperature dependence in more detail.

Acknowledgements This research was funded by the Deutsche Forschungsgemeinschaft, DFG, TRR 285—project number 418701707. Responsibility for the content of the report lies with the authors.

References

1. Meschut G, Janzen V, Olfermann T (2014) Innovative and highly productive joining technologies for multi-material lightweight car body structures. *J Mater Eng Perform* 23:1515–1523. <https://doi.org/10.1007/s11665-014-0962-3>
2. Deutscher Verband für Schweißen und Verwandte Verfahren (2009) Taschenbuch DVS-Merkblätter und -Richtlinien, Mechanisches Fügen. Fachbuchreihe Schweißtechnik, vol 153. DVS-Verl., Düsseldorf
3. Varis JP, Lepistö J (2003) A simple testing-based procedure and simulation of the clinching process using finite element analysis for establishing clinching parameters. *Thin-Walled Struct* 41:691–709. [https://doi.org/10.1016/S0263-8231\(03\)00026-0](https://doi.org/10.1016/S0263-8231(03)00026-0)
4. Coppieters S, Lava P, Baes S et al (2012) Analytical method to predict the pull-out strength of clinched connections. *Thin-Walled Struct* 52:42–52. <https://doi.org/10.1016/j.tws.2011.12.002>
5. Bielak CR, Böhnke M, Beck R et al (2021) Numerical analysis of the robustness of clinching process considering the pre-forming of the parts. *J Adv Join Process* 3:100038. <https://doi.org/10.1016/j.jajp.2020.100038>
6. Bielak CR, Böhnke M, Bobbert M et al (2021) Further development of a numerical method for analyzing the load capacity of clinched joints in versatile process chains. ESAFORM 2021. <https://doi.org/10.25518/esaform21.4298>
7. Hahn O, Kurzok JR (1998) Umformtechnisches Fügen vorverformter Halbzeuge, Als Ms. gedr. Berichte aus dem Laboratorium für Werkstoff- und Fügetechnik, vol 37. Shaker, Aachen
8. Hahn O, Kurzok JR (1998) Umformtechnisches Fügen vorverformter Halbzeuge, Als Ms. gedr. Berichte aus dem Laboratorium für Werkstoff- und Fügetechnik, vol 38. Shaker, Aachen
9. Ge Y, Xia Y (2019) Dynamic behavior of self-piercing riveted and mechanical clinched joints of dissimilar materials: an experimental comparative investigation. *Adv Mater Sci Eng* 2019:1–12. <https://doi.org/10.1155/2019/6463576>
10. Ge Y, Xia Y (2020) Mechanical characterization of a steel-aluminum clinched joint under impact loading. *Thin-Walled Struct* 151:106759. <https://doi.org/10.1016/j.tws.2020.106759>
11. Härtel S, Graf M, Gerstmann T et al (2017) Heat generation during mechanical joining processes—by the example of flat-clinching. *Proc Eng* 184:251–265. <https://doi.org/10.1016/j.proeng.2017.04.093>
12. Böhnke M, Kappe F, Bobbert M et al (2021) Influence of various procedures for the determination of flow curves on the predictive accuracy of numerical simulations for mechanical joining processes. *Mater Test* 63:493–500. <https://doi.org/10.1515/mt-2020-0082>
13. DIN EN ISO 50106: Testing of Metallic materials—compression test at room temperature
14. The determination of the mechanical properties of sheet metal at high strain rates in high-speed tensile tests (2006) Stahlinstitut VDEh - Unterausschuss Prüftechnik
15. Böhme W, Luke M, Blauel JG, Dong-Zhi S, Rohr I, Harwick W (2007) Dynamic material characteristics for crash simulation. FAT-Publications 211
16. Livermore Software Technology Corporation (2019) LS_DYNA manual II
17. Böhnke M, Rossel M, Bielak CR et al (2022) Concept development of a method for identifying friction coefficients for the numerical simulation of clinching processes. *Int J Adv Manuf Technol* 118:1627–1639. <https://doi.org/10.1007/s00170-021-07986-4>

Experimental and Finite Element-Based Analyses of FLCs for AA5052 and AA5083 Alloys



Shahin Ahmad, Vilas Tathavadkar, Alankar Alankar, and K. Narasimhan

Abstract Higher strength and superior corrosion resistance of Al-Mg alloys classify them as the most widely used aluminum alloys for various forming applications in automotive and marine domain. However, the increasing Mg content causes a deteriorating effect on the formability of Al-Mg alloys. The Nakajima test was conducted on AA5052 and AA5083 alloy sheets at room temperature using ARAMIS-GOM™ system for dynamic measurements of 3D displacements and 3D surface strain to understand the impact of varying Mg content on formability of Al-Mg alloys. The test result showed higher formability in AA5052 alloy with 2.55 wt. % Mg as compared to AA5083 with 4.42 wt. % Mg. The distribution of second phase particles/intermetallics was also quantified using optical microscopy for both the alloy samples. Finite element analyses (FEA) of FLC (Forming Limit Curve) prediction were also performed where various necking criteria were implemented and compared with the experimental results.

Keywords Formability · Al-Mg alloys · AA5052 · AA5083 · FLC · Nakajima · PAM-STAMP™

Introduction

Aluminum alloys have always been the material of choice for automotive, packaging, marine, cryogenic, and construction applications due to its light weight, excellent corrosion resistance in alkaline environment, and superior formability. Among all

S. Ahmad (✉) · K. Narasimhan

Department of Metallurgical Engineering and Materials Science, Indian Institute of Technology Bombay, Powai, Mumbai 400076, India

e-mail: shahin.ahmad@adityabirla.com; 164117002@iitb.ac.in

S. Ahmad · V. Tathavadkar

Aditya Birla Science and Technology Company Private Limited, Navi Mumbai 410208, India

A. Alankar

Department of Mechanical Engineering, Indian Institute of Technology Bombay, Powai, Mumbai 400076, India

the aluminum alloys Al–Mg alloys (AA5XXX) provide one of the best combinations of strength and formability. The Mg content in these alloys varies from ~0.5 to 5 wt. % providing the improved strength but with increasing Mg content, the formability decreases due to intergranular precipitation of secondary β -phase (Al_3Mg_2). This precipitation occurs via heterogeneous nucleation and growth [1, 2]. Traditionally, Nakajima type tests were used to estimate the formability of sheet metals. However, with recent advancements in computation technology, numerical simulation-based virtual testing has not only improved the product quality but also has considerably reduced the production lead time and number of required experiments [3, 4].

The prediction accuracy of these sheet metal forming simulations strongly depends on the yield criterion and associated plastic flow rules used for the analysis. The applicability of various yield criteria for different materials and work history has been the area of interests for the research community over the years. The von Mises and Tresca criteria have been most widely used for describing the plastic behaviour of isotropic materials for experiments as well as commercial FEM software packages. But in real life, most of the engineering materials show anisotropic behaviour due to its processing history. The first orthotropic yield criterion was proposed by a British mathematician Rodney Hill in 1948 [5] which was further updated in 1979 [6] and 1993 [7]. Due to its simplicity, Hill's criterion and its modifications have been widely used in numerical and analytical analysis of various forming processes. For aluminum alloys, the most widely accepted family of yield criteria was proposed by Frédéric Barlat in 1989–2004 [8–12].

In the present work, the effect of Mg on the formability of Al–Mg alloys was investigated by comparing the forming Limit Diagrams (FLDs) of AA5052 (~2.5 wt. % Mg) and AA5083 (~4.5 wt. % Mg) alloys using a Nakajima experimental setup and DIC (Digital Image Correlation) at Metal Forming Lab, IIT Bombay. The secondary β -phase (Al_3Mg_2) was also quantified for both the alloys using optical microscopy and image analysis software. The numerical simulation of the Nakajima experiment was performed using PAM-STAMP™ commercial package for predicting the FLD of both the alloys. Tensile test data was used to describe the hardening behavior of the alloys whereas, Barlat 2000-2d yield criterion [11] with 8-parameters was used to predict the yielding in the simulation model. The maximum force [13] and 0.92 thickness gradient necking criteria [14] were used to define the necking for each simulation.

Experimental Details

In the present work, commercial grade AA5052 and AA5083 alloy sheets of 1 mm thickness in fully annealed (O-temper) condition were used. The chemical compositions of the test materials estimated using ICP-OES (Inductively coupled plasma—optical emission spectrometry) method have been presented in Table 1.

Table 1 Chemical composition of AA5052 and AA5083 test samples

Alloy		Mg	Si	Fe	Cu	Mn	Zn	Cr	Ti	Al
AA5052	Standard	2.2–2.8	<0.25	<0.4	<0.10	<0.10	< 0.1	0.15–0.35	–	–
	Actual	2.55	0.067	0.295	0.005	0.074	0.002	0.233	0.033	Balance
AA5083	Standard	4–4.9	<0.4	<0.4	<0.1	0.4–1	<0.25	0.05–0.25	<0.15	Balance
	Actual	4.42	0.07	0.22	0.02	0.64	0.03	0.10	0.02	Balance

Nakajima Experiment

The forming limit curves for AA5052 and AA5083 samples were estimated using a Nakajima experimental setup shown in Fig. 1a. The detailed schematic of the die-punch-holder assembly has been presented in Fig. 1b.

Eight different samples representing 8 different strain paths as per ASTM E2218-02 were prepared using water jet cutting technique. The various specimen dimensions have been illustrated in Fig. 2a. Lubricant (grease) was applied onto the back of the samples with multiple layers of varying thickness PVC (Poly Vinyl Chloride) sheets to eliminate any stress concentration apart from the central gauge position of the sample which is in contact with the punch.

To generate a stochastic pattern, the upper surface of the sample was cleaned with acetone and a matt white paint was applied uniformly to provide a white background. Subsequently, black paint was then sprayed uniformly to let small black droplets distribute on a white background as can be seen in Fig. 2b. The dried sample was then mounted on the bottom holder in central symmetric position with stochastic pattern side on top. During the experiment, the bottom holder moves up and holds

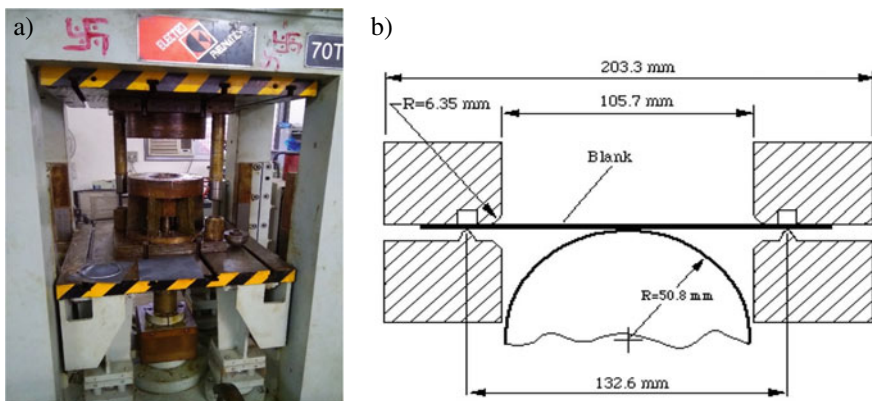


Fig. 1 a Nakajima experimental setup at IIT Bombay and b the schematic of die-punch arrangement

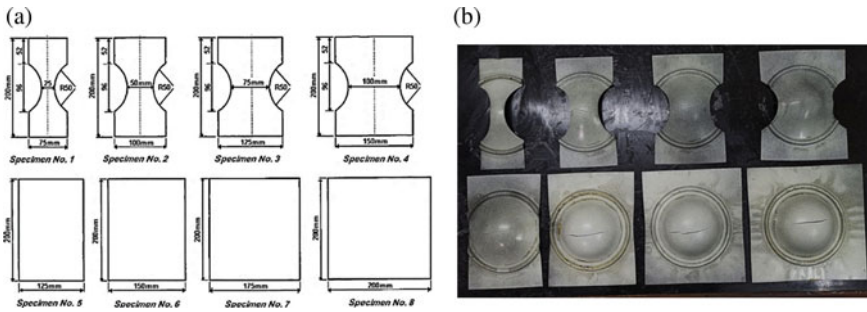


Fig. 2 a Specimen dimensions for Nakajima test as per ASTM E2218-02; b failed AA5052 samples after the test

the blank firmly with top blank holder and the punch moves upward from bottom through die with a speed of 1 mm/s to deform the blank. The punch retracts as soon as the neck has been observed by the sensor represented by a sudden decrease in punch load.

Strain Estimation Using Digital Image Correlation

The strain values at each stage were quantified using the attached high-speed camera with DIC capabilities. The camera captured snapshots of the complete deformation process and stored them using the GOM-ARAMIS software. The stochastic pattern on the blank helped the software in generating user defined facets on them using the black droplet's size and distances. With increase in deformation, the shape and distance of each black droplet changes which was analyzed by the software to calculate the major and minor strain at each location of the sample.

At the stage where necking is observed, a section was drawn across it in the perpendicular direction and the major and minor strain data was generated by the software. The major and minor strain data at the neck was then collected into excel sheet and plotted together to evaluate the major and minor strain value for the sample. A sample case of the analysis has been presented in Fig. 3.

Optical Microscopy

AA5052 and AA5083 sheet samples were cut using a Silicon Carbide cutter and molded in epoxy-based molds followed by polishing to mirror finish by successively decreasing the polishing particle size. The polishing paper # 220 (coarse) to 2000 (fine) were used followed by diamond paste polishing and finally OPS (Colloidal Silica Abrasive Solution) were used to reach a mirror finish. The polished samples

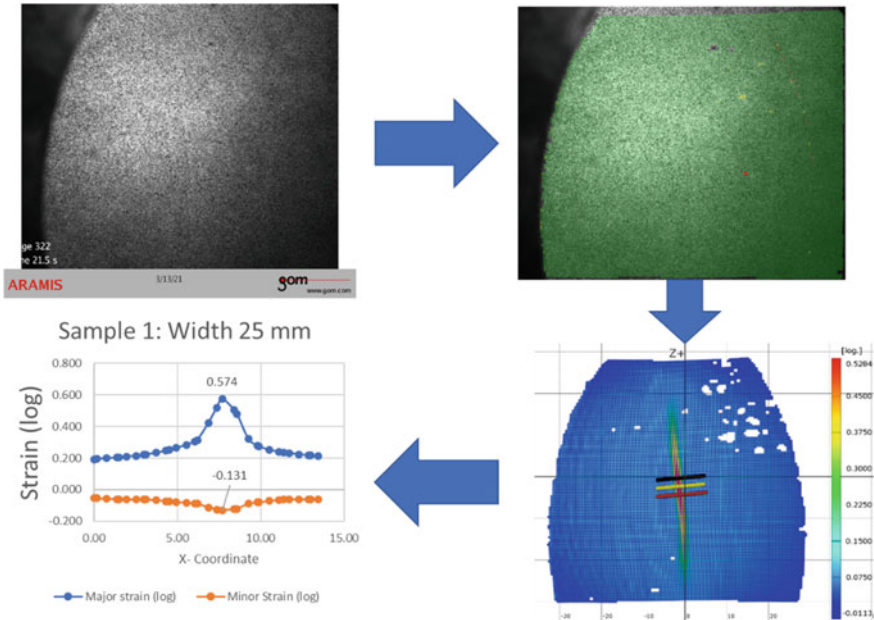


Fig. 3 Steps illustrating the strain analysis for a Nakajima sample using DIC

were analyzed under the optical microscope using a bright field in reflective mode and 12 images were captured at 100 X magnification for each sample to cover the whole sample area and eliminate any human bias. These images were then analyzed using Carl-Zeiss image analyzer software, where, once the contrast of the particle has been defined, the system automatically captures all the particles on the micrograph and measures its diameter, area, perimeter, and other features. These raw data were exported in excel sheet and analyzed further to find out the particle size and area % distribution. A representative micrograph and corresponding capturing of particles by image analyzer software for AA5083 sample have been presented in Fig. 4.

Forming Limit Diagram

Using the above methodology major and minor strain values were calculated for all the 8 specimens and plotted on major and minor strain axis to generate the FLC for AA5052 and AA5083 alloys. The FLC for AA5052 and AA5083 is presented in Fig. 5. It is evident from the FLD that the formability of AA5052 alloy is much higher than AA5083 alloy, which can be attributed to the relatively lower concentration of Mg concentration.

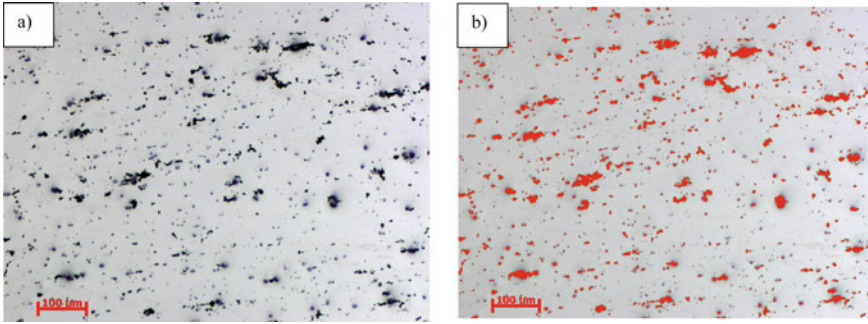


Fig. 4 Second phase capturing by image analyzer software. **a** Original micrograph, **b** macrograph with captured particles by the software

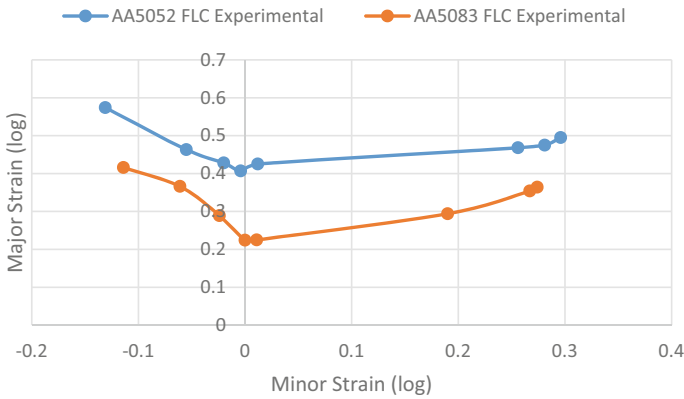


Fig. 5 Experimental FLC for AA5052 and AA5083 alloys

Secondary β -phase Quantification

The optical micrographs of both AA5052 and AA5083 alloys were captured and analysed using image analyzer software. A representative micrograph taken at 100X magnification has been presented in Fig. 6. It can be clearly observed that the concentration and size of the second phase particles were higher in case of AA5083 alloy sample due to higher wt. % of Mg content as compared to AA5052 alloy sample.

The particle and area data obtained from the image analysis was plotted for understanding the effect of increasing Mg content. Figure 7a, c present the histogram showing the area % distribution of second phase particles with increasing particle sizes for AA5052 and AA5083 respectively. The total area % for AA5052 was found to be 2.32% whereas it was 3.12% for AA5083 sample. Similarly, Fig. 7b depicts the distribution of number of particles with increasing particle sizes for AA5052

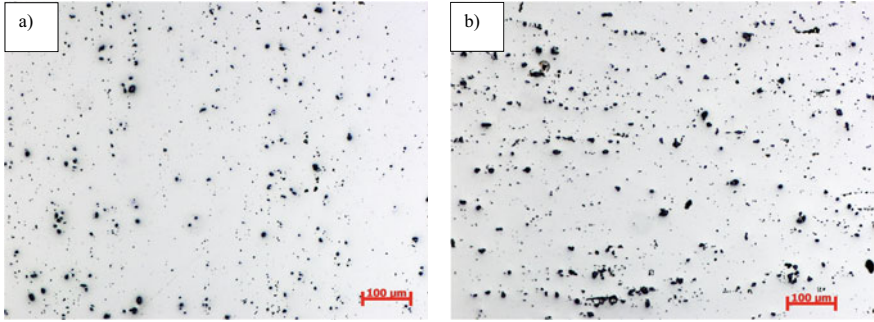


Fig. 6 Optical macrographs showing second phase particles in **a** AA5052 and **b** AA5083

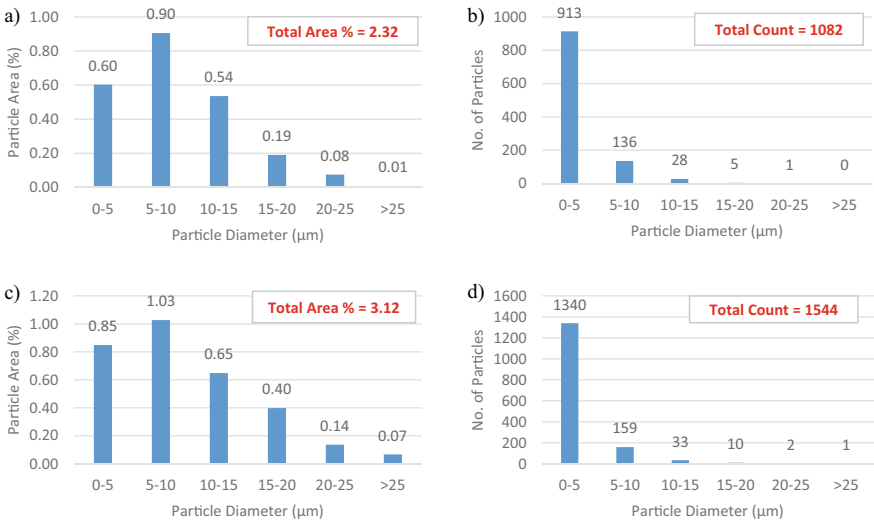


Fig. 7 Distribution of second phase particles by area % (left) and number (right) **a, b** AA5052 **c, d** AA5083

and AA5083 samples respectively. The number of particles was also found to be increased from 1082 to 1544 in case of AA5052 and AA5083 respectively.

Numerical Model

FEM model to simulate the Nakajima experiment was developed using PAM-STAMP™. The material properties for AA5052 and AA5083 are taken from the metals handbook. The dimensions of various components are kept same as the experimental setup dimensions at Metal Forming Lab (IIT Bombay).

Five boundary conditions were employed to simulate the experimental process. An encastre BC was employed on the die whereas a vertical displacement and blank holding force was applied on blank holder. A Y-displacement with a vertical velocity of 1 mm/s was applied to the punch. The basic components of the Nakajima setup assembly made using PAM-STAMP™ are depicted in Fig. 8. The hardening behavior of the material was captured by incorporating the plastic data of uniaxial tensile test for AA5052 and AA5083 alloys at 0.01 s^{-1} .

The Barlat 2000-2d yield criteria [11] were considered for describing the yielding phenomenon. The 2000-2d yield parameters for AA5052 were taken from Esmailpour et al. [15] and parameters for AA5083 were taken from Prakash et al. [16] as presented in Table 2. The value of parameter m was considered as “8” for all the cases as the material was aluminum alloy.

The simulations were run for six different specimen geometry with mesh size 1. The necking stage was identified by two different criterions, viz. maximum force criteria and 0.92 thickness gradient criteria. The maximum force criteria state that diffuse necking is initiated in a tensile test of a bar when the maximum force is reached [13]. Thus, the contact load was plotted against the progression and the peak point was taken as the necking stage from which stage the load decreases suddenly. In 0.92 thickness gradient criteria, the ratio of neck element thickness and its adjacent element thickness is checked. The ratio 0.92 is considered as the critical ratio below which the necking has occurred [14]. The contour plot of major strain and thickness

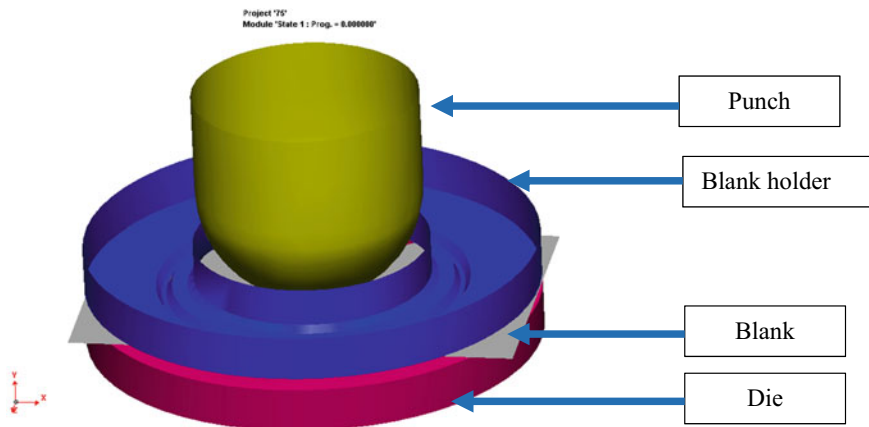


Fig. 8 Various components in the Nakajima assembly of the FEM model in PAM-STAMP™

Table 2 Barlat 2000-2d yield criterion parameters for AA5052 and AA5083 taken from literature

Material	α_1	α_2	α_3	α_4	α_5	α_6	α_7	α_8	References
AA5052	0.934	1.092	0.870	1.044	1.012	1.013	1.009	1.169	[15]
AA5083	0.9508	1.020	1.037	1.029	1.022	1.023	1.009	1.018	[16]

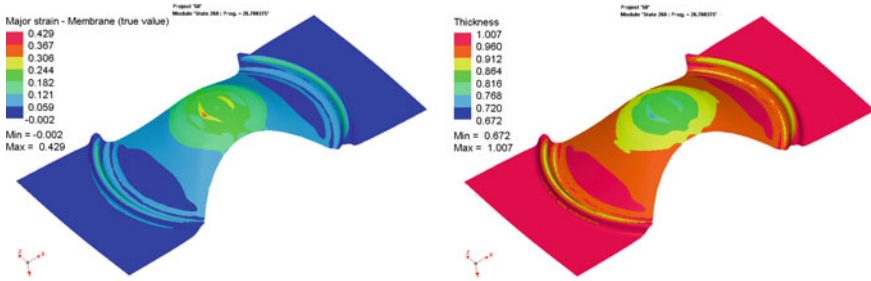


Fig. 9 Major strain (left) and thickness (right) distribution in AA5052 blank-50 at the time step before necking



Fig. 10 Comparison of model predicted FLD with punch load and 0.92 thickness gradient criterion with experimental FLD for **a** AA5052, **b** AA5083

distribution of AA5052 blank-50 has been presented in Fig. 9 at the necking stage. The major and minor strain was then estimated by taking the average value along the neck elements for each sample. All the strain values were then plotted to get the model predicted FLD for both AA5052 and AA5083 alloys. The comparison of experimental and simulated FLDs is presented in Fig. 10.

Results and Discussion

The forming limit diagrams were obtained for AA 5052 and AA5083 alloys in O-temper using Nakajima experimental setup. It was clearly observed in Fig. 5 that AA5052 alloy has relatively higher formability as compared to AA5083 alloy. The difference in formability can be attributed to the lower Mg content in AA5052 alloy (2.5 wt. %) as compared to AA5083 (4.6 wt. %). The presence of lower precipitation of secondary β -phase will result into a relatively lower impediment of the dislocation movement during deformation and thus lower peak stress will generate while solute-dislocation interaction. This was also confirmed by the optical microscopy results obtained by image analyzer software. As depicted in Fig. 7, the total area % of second

phase particles was found to be 2.32% in AA5052 alloy sample as compared to 3.12% for AA5083 alloy sample whereas the number of second phase particles was found to be 1082 in AA5052 alloy sample as compared to 1544 number of second phase particles found in AA5083 alloy sample.

The finite element simulation model of the Nakajima experiment was also developed using PAM-STAMP™ software for both the alloys. As clearly seen in Fig. 10, both necking criteria predictions were in good agreement with the experimental results but the prediction of FLC (Forming Limit Curve) with 0.92 thickness gradient necking criteria was in relatively better agreement as compared to maximum force necking criteria for both AA5052 and AA5083 alloys. This can be attributed to the fact that the necking process has different stages, namely, the diffuse necking and localized necking [17] and in most cases the maximum force is not a single point rather a curve leading to incorrect selection of necking stage.

Conclusions

The Nakajima test was conducted on AA5052 and AA5083 alloy sheets at room temperature using ARAMIS-GOM™ system for dynamic measurements of 3D displacements and 3D surface strain to understand the impact of varying Mg content on formability of Al-Mg alloys. The distribution of second phase particles was also quantified using optical microscopy and image analyzer software for both the alloy samples. Finite element analyses of FLC prediction were also performed where maximum force and 0.92 thickness gradient necking criteria were implemented and compared with the experimental results. The results of the study can be concluded as follows:

- i. The Nakajima test result showed higher formability in AA5052 alloy with 2.55 wt. % Mg as compared to AA5083 with 4.42 wt. % Mg.
- ii. The optical microscopy analysis showed lower concentration of second phase particles in AA5052 alloy as compared to AA5083 (2.32 and 3.12 area % respectively), due to relatively lower Mg content.
- iii. FEM model for FLC predictions depicted a better prediction with thickness gradient criteria as compared to maximum force criteria for both AA5052 and AA5083 alloys.

References

1. Bumiller E (2011) Intergranular corrosion in AA5XXX aluminum alloys with discontinuous precipitation at the grain boundaries. PhDT
2. Lim MLC, Kelly RG, Scully JR (2016) Overview of intergranular corrosion mechanisms, phenomenological observations, and modeling of AA5083. Corrosion 72(2):198–220

3. Gantar G, Pepelnjak T, Kuzman K (2002) Optimization of sheet metal forming processes by the use of numerical simulations. *J Mater Process Technol* 130:54–59
4. Yang H, Fan X, Sun Z, Guo L, Zhan M (2011) Recent developments in plastic forming technology of titanium alloys. *Sci China Technol Sci* 54(2):490–501
5. Hill R (1948) A theory of the yielding and plastic flow of anisotropic metals. *Proc R Soc Lond Ser A Math Phys Sci* 193(1033):281–297
6. Hill R (1979) Theoretical plasticity of textured aggregates. In: *Mathematical proceedings of the cambridge philosophical society*, vol 85, no 1, pp 179–191. Cambridge University Press
7. Hill R (1993) A user-friendly theory of orthotropic plasticity in sheet metals. *Int J Mech Sci* 35(1):19–25
8. Barlat F, Lian K (1989) Plastic behavior and stretchability of sheet metals. Part I: A yield function for orthotropic sheets under plane stress conditions. *Int J Plast* 5(1):51–66
9. Barlat F, Lege DJ, Brem JC (1991) A six-component yield function for anisotropic materials. *Int J Plast* 7(7):693–712
10. Barlat F, Maeda Y, Chung K, Yanagawa M, Brem JC, Hayashida Y, Lege DJ, Matsui K, Murtha SJ, Hattori S, Becker RC (1997) Yield function development for aluminum alloy sheets. *J Mech Phys Solids* 45(11–12):1727–1763
11. Barlat F, Brem JC, Yoon JW, Chung K, Dick RE, Lege DJ, Pourboghraat F, Choi SH, Chu E (2003) Plane stress yield function for aluminum alloy sheets—part 1: theory. *Int J Plast* 19(9):1297–1319
12. Barlat F, Aretz H, Yoon JW, Karabin M, Brem JC, Dick R (2005) Linear transformation-based anisotropic yield functions. *Int J Plast* 21(5):1009–1039
13. Hora P, Tong L, Reissner J (1996) A prediction method for ductile sheet metal failure in FE-simulation. In: *Proceedings of NUMISHEET*, vol 96, pp 252–256
14. Narasimhan K (2004) A novel criterion for predicting forming limit strains. In: *AIP Conference Proceedings*, vol 712, no 1, pp 850–855. American Institute of Physics
15. Esmailpour R, Tiji SN, Kim H, Park T, Pourboghraat F, Mohammed B (2019) Stamping of a cross-shaped part with 5052, 5754 and 6016 aluminum alloy sheets—experimental and finite element analysis comparison. *IOP Conf Ser Mater Sci Eng* 521(1):012002. IOP Publishing
16. Prakash V, Kumar DR, Horn A, Hagenah H, Merklein M (2020) Modeling material behavior of AA5083 aluminum alloy sheet using biaxial tensile tests and its application in numerical simulation of deep drawing. *Int J Adv Manuf Technol* 106(3):1133–1148
17. Hora P, Tong L, Berisha B (2013) Modified maximum force criterion, a model for the theoretical prediction of forming limit curves. *Int J Mater Form* 6(2):267–279

Finite Element and Experimental Investigation of Multi-stage Deep Drawing of Stainless Steel 304 Sheets at Elevated Temperature



Vipin Yadav, Kanhu Nayak, and Prashant Date

Abstract In this study, multi-stage hot deep drawing of an SS304 sheet of 0.5 mm thick at elevated temperatures (600, 700 and 900 °C) has been investigated numerically. Initially, uniaxial tensile properties and the plastic strain ratio of the SS304 sheet was evaluated at different temperatures. These experimental values were then used in a finite element (FE) simulation to simulate the multi-stage hot deep drawing process. The results obtained from the simulation, such as blank holding force, peak deep drawing force, and distribution of strain, were discussed. A strain non-uniformity index (SNI) was used to predict failure of the deep drawn cup during deformation at elevated temperatures. In addition, the effect of blank holding force and temperature on wrinkling, earing, and thinning of the deep drawn cup were analyzed. Finally, the required deep drawn cup can be manufactured based on the outcomes of the numerical simulation of deformation of the SS304 sheet.

Keywords FE simulation · Hot deep drawing · Plastic strain ratio · SNI

Introduction

Nowadays, the products with higher drawing depth are found to be more in use. Hence there has been extensive research going in finding out the material with higher formability. Austenitic stainless steel SS304 is significantly used in aerospace, electronics, and automobile industries. Hence there are many researches are going on to improve the drawability of SS304 to make deep drawn part. One such technique for improving the formability is hot forming.

Deep drawing is a complex forming process in which there is tension (cup wall), bending (die and punch corners), and compression (flange of cup). Both high tensile strength and better ductility in compression are required for the deep drawing material

V. Yadav · K. Nayak (✉) · P. Date
Indian Institute of Technology Bombay, Mumbai 400076, India
e-mail: nayakkanhu83@gmail.com; 183100079@iitb.ac.in

P. Date
e-mail: ppdate@iitb.ac.in

[1]. Although the deep drawing process of high strength/low formability metals has an extensive industrial application area, deep drawing at room temperature has serious difficulties because of the large amount of deformations and high flow stresses of the material [2]. The higher temperature allows for the decrease in the flow stress of the material and also the residual stresses are removed, which makes it possible for an increase in the formability and hence deformation is easier.

Kaya et al. [3] have simulated and also conducted experiments on the non-isothermal warm deep drawing of SS304 between room temperature and 125 °C in which the thinning at the bottom of the cup along the transverse and rolling direction is found to be between 20 and 30%. Jayahari et al. [4] have conducted experiments on SS304 temperature of 300 °C temperature and found an increase in limiting drawing ratio (LDR) of 2.46 but also found that LDR decreases after 350 °C temperature due to dynamic strain regime. Ethiraj et al. [5] have conducted experiments and simulations at different temperatures from 30 to 300 °C with an increment of 100 °C and found that the maximum reduction in thickness increases with the increase in temperature. Also, hoop strain is more at the top portion of the drawn cup wall and the reason for that is due to bending, straightening, and tension. Shingawa et al. [6] simulated plastic deformation and temperature distribution in deep drawing of stainless steel sheets with deformation-induced martensitic transformation using the rigid-plastic finite element method and the finite element method for heat conduction. Jayahari et al. [7] observed in the study that in order to achieve better formability the temperature and punch speed should be selected so that the martensite formation and grain refinement are minimum. Takuda et al. [8] showed that the LDR increased from 2 at room temperature to 2.8 at 150 °C temperature. The forming limit and fracture initiation site are predicted by combinations of rigid-plastic and heat conduction finite element method. Bong et.al has showed through experiment and simulation that the LDR can be increased by using temperature gradient between the punch and the die/holder. The total and uniform elongation is decreased as the temperature is increasing in case of SS304 [9]. Seri et al. [10] conducted the numerical simulations and showed that SS304 has poor drawability at room temperature which is due to strain induced martensite transformation taking place in flange and along the radius of the die.

SS 304 has the highest percentage of elongation about 70%. SS304 is in austenitic form at room temperature and is also metastable and hence it turns into martensite during cold forming. Also, it will be impossible for the manufacturer to do annealing after every stage of redrawing and hence hot forming is used to reduce the strain induced martensitic transformation. In the present research, the formability of SS304 was studied at 600, 700, and 900 °C temperature. Simulation is also carried out for three stages of drawing.

Material Testing and Finite Element Simulation

SS 304 was tested at 600, 700, and 900 °C temperature in Gleeble at a strain rate of 0.001 s⁻¹. The specimen for the tensile test are as shown in Fig. 1 for 600,700 and 900 °C temperature in various directions, i.e., 0°, 45°, and 90°.

Nowadays, finite element simulation is finding wide applications in the manufacturing processes. Previously the manufacturer used to do trial and error method while designing components. The job was too tedious that it was taking more time to come out on some conclusions and now, due to the development in the finite element code, it has become possible to simulate the process and the required change in dimension can be done at the development stage.

Assumptions are taken for finite element simulation:

- (1) The plastic strain ratio value, i.e., R is taken as 1
- (2) The material is assumed to obey the Hollomon equation, i.e., $\sigma = K\epsilon^n$.
- (3) The mechanical interaction between the contacting surfaces is assumed to be frictional contact with a coefficient of friction 0.12.

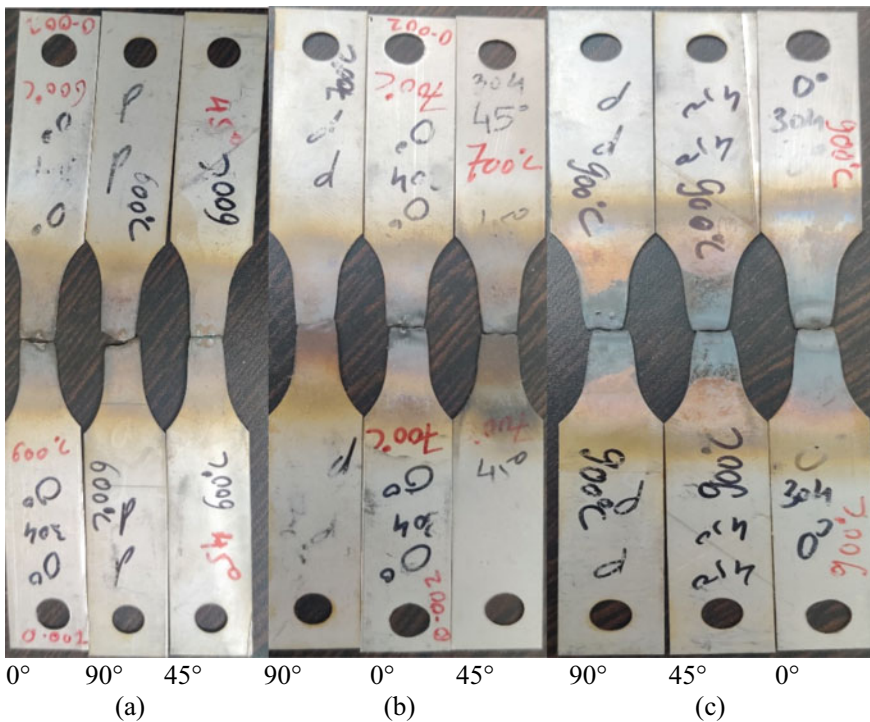


Fig. 1 Tensile sample for a 600, b 700, and c 900 °C temperature in various directions of 0°, 45°, and 90°

- (4) Deforming material was assumed to be incompressible, i.e., volume constancy was used.
- (5) Baushinger effect is neglected, and only isotropic hardening is assumed.

The required blank dimension for the present purpose is 60 mm diameter and 0.5 mm thickness. Finite element software PAMSTAMP was used for the simulation. The material properties of the blank were obtained from the results of the tensile tests at 600 °C, 700 °C, and 900 °C. A coupled temperature displacement four-noded quadrilateral element C3D4T of 0.5 mm size was used with adaptive meshing to refine the mesh up to the third level during forming whenever necessary. FLC (forming limit curve) is calculated by the software automatically using Keeler FLC.

Parameters for Various Stages of Drawing

The schematic setup in Fig. 2 shows the punch, blank, blank holder, and die used in the three stages of drawing. Die, blank holder, and punch are modeled as the rigid body. Blank is only modeled as a deformable body. Geometrical parameters and blank holding force for three stages of drawing are as shown in Table 1.

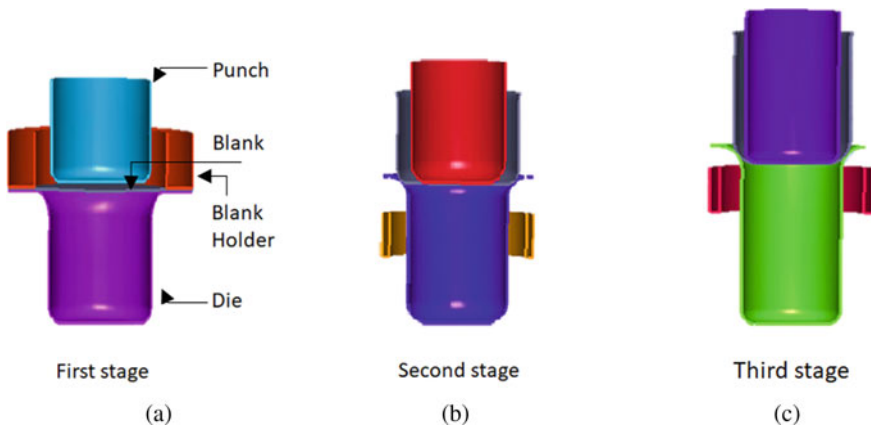


Fig. 2 Schematic view of punch, blank, blank holder, and die

Table 1 Different input parameters for simulation

First stage		Second stage	Third stage
Die	Internal dia = 33.1 mm External dia = 60 mm	Internal dia = 26.7 mm External dia = 33 mm	Internal dia = 22.4 mm External dia = 26.4 mm
Punch (mm)	Dia = 33	Dia = 26.4	Dia = 22
Die entry radius (mm)	5	5	5
Punch nose radius (mm)	3	3.5	3
Clearance (mm)	0.05	0.15	0.2
Height (mm)	19	27.5	35.4
Blank holder force (N)	6000	1500	1000

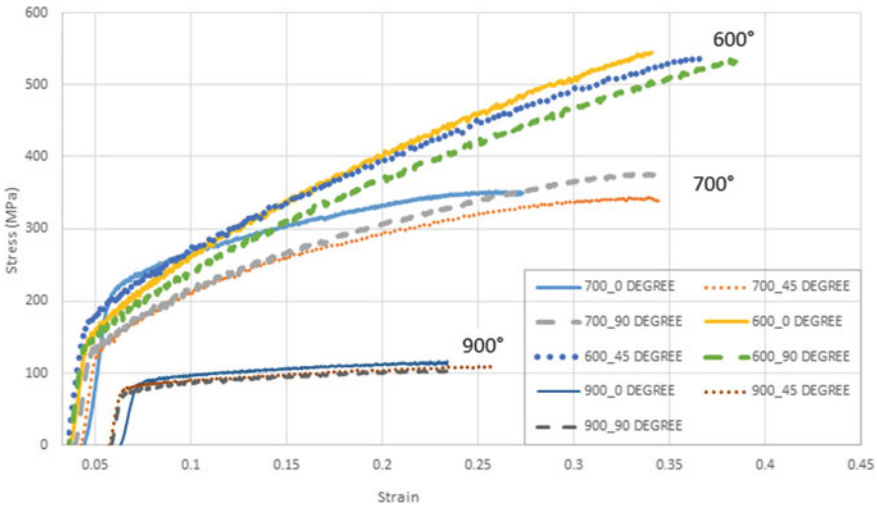


Fig. 3 Stress-strain curve for 600 °C, 700 °C and 900 °C temperature

Results and Discussion

Tensile Properties of SS304 at Elevated Temperature

Strain hardening exponent (n) is a measure of good formability of the material. A material with a higher value of n can stretch more before necking because of its increased strength due to strain hardening. It can be seen from Table 2 and Fig. 3 that the average yield strength and n value for the material at 600 °C are more as

Table 2 Results of stress-strain data

Temperature (°C)	Direction	Yield stress (MPa)	K (MPa)	n
600	0° (Rolling)	160.27	950.4	0.55
	45° (Transverse)	164.7	948.32	0.545
	90°(Perpendicular)	153.65	971.65	0.6
		$\sigma_y(\text{avg}) = 159.54$	$K_{\text{avg}} = 956.79$	$n_{\text{avg}} = 0.565$
700	0° (Rolling)	139.4	546.53	0.3129
	45° (Transverse)	137.23	572.26	0.4206
	90°(Perpendicular)	130.14	679.52	0.5
		$\sigma_y(\text{avg}) = 135.59$	$K_{\text{avg}} = 599.43$	$n_{\text{avg}} = 0.411$
900	0° (Rolling)	85.73	158.17	0.2104
	45° (Transverse)	78.43	149.29	0.2223
	90°(Perpendicular)	70.12	147.51	0.2312
		$\sigma_y(\text{avg}) = 78.09$	$K_{\text{avg}} = 151.65$	$n_{\text{avg}} = 0.2213$

compared with 700 and 900 °C temperature. With the increase in temperature, the yield strength of material decreases, which shows softening takes place. Stress-strain data also reveals that the material has more yield strength in rolling direction, i.e., 0° as compared with other directions (Fig. 3). The present research deals with redrawing of the cup in three stages and hence it will be more beneficial if we select the material with a high value of n. Therefore, results from stress-strain data of SS304 at 600 °C are the input for simulation (Table 2).

Thickness Contour

As it can be seen from Fig. 4 that after every stage of drawing the thickness of the cup goes on decreasing at the punch nose radius. Hence it becomes necessary to see that the thinning in the cup after every stage of redrawing must not go beyond 25 percent. The main reason for thinning is due to the tensile stresses that are generated when the punch corner radius comes in contact with the blank. Thickening takes place at the top of cup due to circumferential compressive stress generated while drawing. The reduction taking place in first stage of drawing is 45%, whereas it is only 20% for the second and third stages of drawing. Proper clearance between die and punch and correct die entry and nose radius can reduce the effect of thickening and thinning. In case of first stage of drawing usually (10–20% of sheet thickness + sheet thickness) is given as clearance, whereas for second and third stage the measured values of thickness at various height from the top of cup are used for giving clearance.

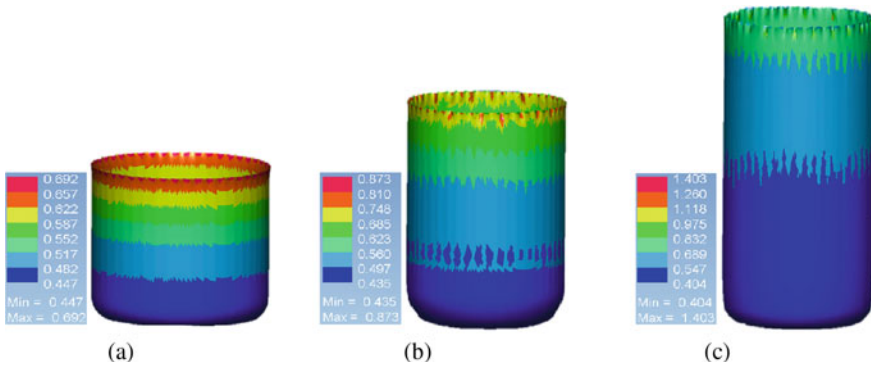


Fig. 4 Thickness contour for **a** first stage, **b** second stage, and **c** third stage drawing

Thickness Strain

In order to obtain thickness strain, half section of the cup is cut and measuring major and minor strain from the centre till the end of punch nose region. Using the volume constancy condition ($\epsilon_1 + \epsilon_2 + \epsilon_3 = 0$) thickness strain, i.e., ϵ_3 can be obtained. As can be seen from Fig. 5 the thickness strain is negative in the bottom of cup for all stages of drawing, which as a result shows the effect of thinning. It is positive for the top of the cup, which shows the effect of thickening as the height of cup is increasing. The value of thickness strain is more for the 3rd stage of drawing as compared to first and second stages.

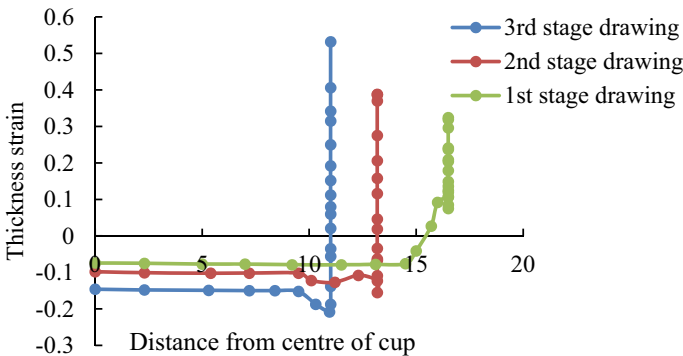


Fig. 5 Thickness strain vs distance from centre of cup

Minor and Major Stress Contours

At the start of the deep drawing process, the biaxial stresses are produced in the plane of the blank. The portion in contact with the punch remains under tensile stress and the portion under blank holder experiences compressive stress. It is due to this reason only blank holding force is applied to limit this stress; otherwise wrinkling takes place. This can be seen from Figs. 6 and 7 as when the height of cup is increasing the effect of minor stress is increasing at the top of cup. Tensile stress is predominant in the cup wall and the punch nose radius region. The stresses that are generated are much below the ultimate tensile stress. Different yielding theories are used to simulate the deep drawing process. Pamstamp v 2018.01 uses Hills 48' yield criterion. The stress in thickness direction is assumed to be negligible and hence plane stress condition exists.

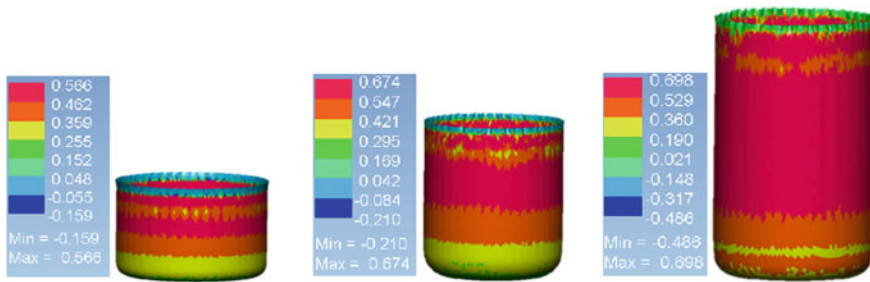


Fig. 6 Major stress contour

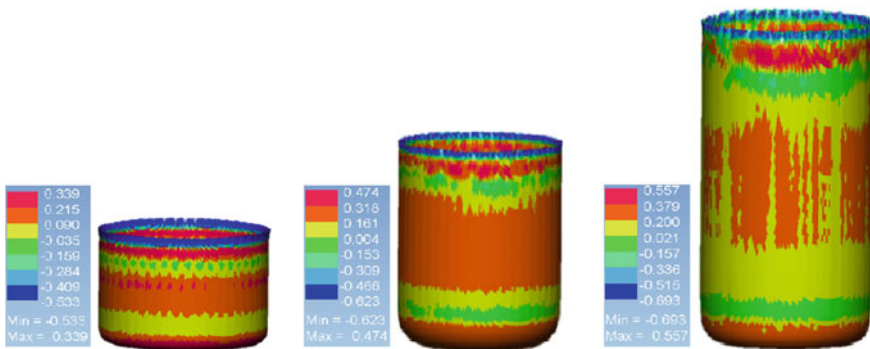


Fig. 7 Minor stress contour

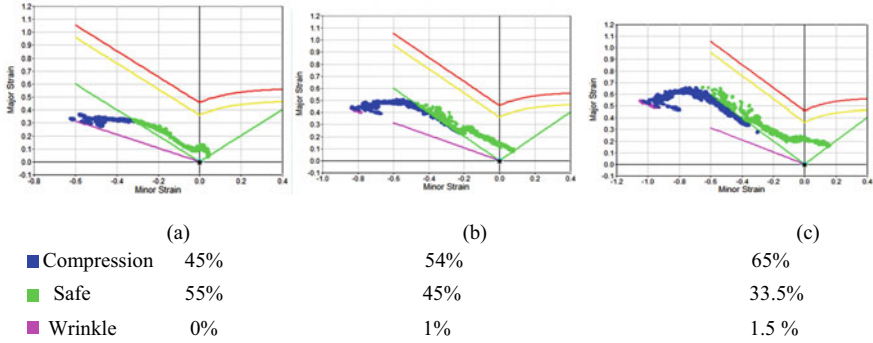


Fig. 8 Forming limit diagram for **a** first stage, **b** second stage, **c** third stage

Forming Limit Diagram (FLD)

It can be observed from Fig. 8 that as the drawing stage increases, the values of major strain and minor strain on the right side of the major strain axis line increases. This shows the effect of biaxial stretching and it can be seen in the bottom region of the cup, including the nose radius. As we go on increasing the height from the bottom of the cup, major strain is predominant up to a certain height. This predominance of major strain can be seen more in first stage of drawing and it goes on decreasing during second and third stages of drawing. As discussed in 3.4 that the effect of compressive stress goes on increasing as we move up and hence the effect of minor strain also goes on increasing. In order to have no wrinkling to take place, the strain path must not go below the pink line. Normally wrinkling takes place in the flange region of the cup as well as at the top. The main cause of wrinkling is due to low blank holding force and a more die entry radius. The blank holding force is equal to one-third of the punch force. Also, it is recommended to take die entry radius to be in between 4 and 10t (where t = thickness) to have no wrinkling effect. All the three stages of drawing are considered as safe as it is much below the yellow line and also only 1% and 1.5% wrinkling takes place during second and third stage of drawing. This wrinkled part can be easily trimmed off.

Strain Non-uniformity Index

Strain non-uniformity index (SNI) represents the degree of magnitude of non-uniformity in the strain distribution and is given by the maximum deviation of the strain from the ideally expected uniform strain distribution [11]. It is the difference between peak thickness strain of the formed part and the average thickness as shown

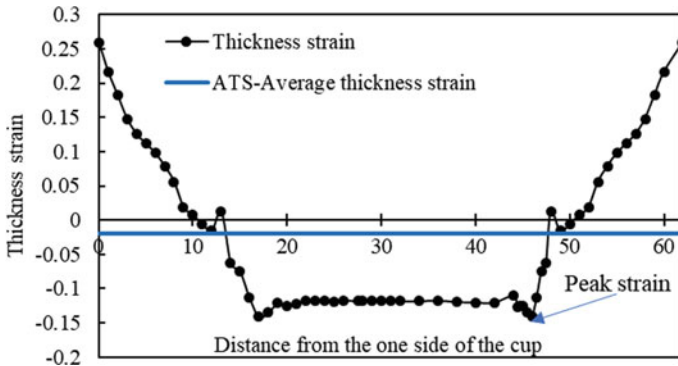


Fig. 9 Thickness strain distribution along the maximum thinning section

in Fig. 9. The failure strain non-uniformity index (critical SNI) is 0.1496. SNI calculated for first stage of deep drawn cup is 0.1202 which is less than the critical SNI (Fig. 9).

Conclusions

- (1) Forming limit diagram shows no effect of failure and hence the design of punch, die, and blank holder is safe.
- (2) h/d ratio of 1.61 has been successfully achieved in three stages of drawing.
- (3) As the value of n (strain hardening exponent) is more at 600°C temperature as compared to 700 and 900°C , it shows better formability.
- (4) The reduction in thickness at the punch nose region is much within limits.
- (5) It can be seen from tensile stress-strain data as the temperature increases the flow stress and the yield strength decreases.
- (6) SNI value for first stage of drawing is less than the critical value.

References

1. Jiang J, Collado C, Keeley D, Dodd B (1995) Room temperature formability of particle-reinforced metal matrix composites: forging, extrusion and deep drawing. *Composites* 26(11):785–789
2. Bolt PJ, Lamboo NAPM, Rozier PJCM (2001) Feasibility of warm drawing of aluminium products. *J Mater Process Technol* 115(1):118–121
3. Kaya S (2016) Nonisothermal warm deep drawing of SS304: FE modeling and experiments using servo press. *Int J Adv Manuf Technol* 83(5–8):1047–1056

4. Jayahari L, Sasidhar PVR, BaluNaik PP, Gupta B, AK, Singh (2014) Formability studies of ASS 304 and evaluation of friction for Al in deep drawing setup at elevated temperatures using LS-DYNA. *J King Saud Univ Eng Sci* 26(1):21–31
5. Ethiraj N, Kumar VS (2012) Finite element method based simulation on warm deep drawing of AISI 304 steel circular cups. *Proc Eng* 38:1836–1851
6. Shinagawa K, Mori KI, Osakada K (1991) Finite element simulation of deep drawing of stainless steel sheet with deformation-induced transformation. *J Mater Process Technol* 27(1–3):301–310
7. Jayahari L, Naik BB, Singh SK (2014) Effect of process parameters and metallographic studies of ASS-304 stainless steel at various temperatures under warm deep drawing. *Proc Mater Sci* 6:115–122
8. Takuda H, Mori K, Masachika T, Yamazaki E, Watanabe Y (2003) Finite element analysis of the formability of an austenitic stainless steel sheet in warm deep drawing. *J Mater Process Technol* 143:242–248
9. Bong HJ, Barlat F, Ahn DC, Kim HY, Lee MG (2013) Formability of austenitic and ferritic stainless steels at warm forming temperature. *Int J Mech Sci* 75:94–109
10. Serri J, Martiny M, Ferron G (2005) A numerical analysis of the formability of unstable austenitic steels. *J Mater Process Technol* 164:1241–1247
11. Desai SG, Date PP (2006) On the quantification of strain distribution in drawn sheet metal products. *J Mater Process Technol* 177:439–443

Formability Analysis of Metal–Polymer Sandwich Composites Made of Al and PE Sheets Using Numerical Simulations



Tsegaye Bekele, Perumalla Janaki Ramulu, Habtamu Beri, Amrela Siraji,
and P. Praveen Kumar Reddy

Abstract Metal/polymer/metal (MPM) sandwiched composites are in the class of capable engineering materials which give outstanding strength-to-weight ratios because of their comparatively low density. These materials are vital constituents within the automobile, aerospace, marine, and civil construction industries as substitutes for sheet metals that considerably reduce weight while not compromising practicality such as load bearing capacity stiffness and flexibility. For these materials to be utilised within the aforesaid industries, they need to bear numerous forming processes. This paper investigates the formability of metal-polymer sandwich composites made of AA-PE-AA (APA) and Galvanised Steel-PE-Galvanised Steel (GPG) considering the adhesion strength via numerical simulation. For evaluating the formability, the actual limit dome height (LDH)—bi-axial strain path—test setup is simulated using FEM. The results analysed are forming limit diagram (FLD), punch force distribution, and dome height at diverse conditions of punch velocity and friction. All the numerical simulations were performed using Altair Hyperworks with various blank sizes. The results are noted as FLD and dome height at varied conditions. A comparison is made to represent the best combinations for formability of the sandwich composites. Maximum formability and dome height are attained at low friction conditions and forming speed.

Keywords MPM sandwich · Formability · Adhesion · Dome height · Limit dome height

T. Bekele · H. Beri · A. Siraji

Program of Mechanical Engineering, School of Mechanical, Chemical and Materials Engineering, Adama Science and Technology University, Adama, Ethiopia

P. Janaki Ramulu (✉)

Centre of Excellence for Advanced Manufacturing Engineering, School of Mechanical, Chemical and Materials Engineering, Adama Science and Technology University, Adama, Ethiopia

e-mail: perumalla.janaki@astu.edu.et

P. Praveen Kumar Reddy

School of Technology, Gitam Deemed to Be University and Mahaveer Institute of Science and Technology, Hyderabad, India

Introduction

In manufacturing engineering, it is common to specify and select suitable and reliable materials that can fulfil the product's requirements. Sometimes, already existing materials are able to accomplish these demands with or without necessary modifications. Otherwise, new materials are designed and manufactured according to necessities of the product being manufactured. The need for contemporary materials, hence, arises to deal with the requirements of recent and economical engineering innovations. Handiness of engineering materials that meet design necessities is the major issue that influences engineering design flexibility.

Composite materials play an important role in achieving the aforesaid development. One of the ways to create composite materials is by the formation of Metal–Polymer–Metal (MPM) sandwiches joined together to create composite sheets. It consists of two metal skin sheets and a low-density polymeric core material as shown in Fig. 1.

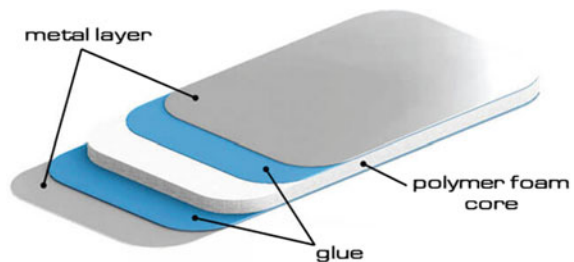
Nowadays, MPM sandwich composite materials pulled in noteworthy attention for their prevalent properties which don't have any of the layers alone. Metallic sandwich sheets have better strength-to-weight proportion, vibrational damping, and sound-stifling properties than monometallic layers [1, 2].

Sandwich composites are broadly utilized in the auto and aviation industries [3, 4]. Sandwich structures are made out of a high strength metallic sheet as the skin layer and thermoplastic or thermosetting polymers as the middle layer.

These MPM laminates can be created by various cycles like roll bonding, layup technique, and hot pressing [5, 6]. Because of the inhomogeneous behavior of the complex sandwich materials over their thickness, a few exploration needs have been concerned about describing their forming behavior. Underlying elements, for example, face to core sheet thickness proportion, physical and mechanical properties of the face and core materials, and bonding between the layers and the interfacial properties are the principal boundaries influencing the physical (for example, sound and vibration damping) and mechanical (for example, strength and formability) properties of the sandwich sheets.

Numerous sorts of aluminum–plastic sandwich sheets have been created with various aluminum alloy as skin sheet and distinctive plastic as core layer, for example, AA5182-polypropylene-AA5182 sandwich sheet, AA5005-polypropylene-AA5005

Fig. 1 MPM sandwich composite



sandwich sheet, and AA3105-polypropylene-AA3105 sandwich sheets. Among these sandwich sheets, AA5182-polypropylene-A5182 sandwich sheet have been produced for possible use of these materials for car body boards in future superior automobiles with critical weight decrease [7].

Albeit the metal–plastic sandwich sheets have numerous benefits, in any case, the forming of these materials is exceptionally complicated because of the very huge distinction in mechanical properties and in the measures of polymer core and the metal skins. The forming of the sandwich sheets is not the same as those of homogenous metallic sheets. Forming processes of MPM sandwiches typically include issues, for example, wrinkling, delamination, and shearing, identified with the deficient interlayer metal–polymer bondage. The adhesive strength at the metal–polymer interfaces is a critical factor for MPM sandwich composites since the interfacial collaboration produces a framework that can emphatically influence the sheets to either act autonomously, feebly, or as unequivocally coupled. A frail polymer core can go about as an oil between the metal skins; such behavior can cause the event of debonding at interfaces among sheet and plastic core, prompting a sliding of metal skins and an untimely failure during forming activities. Then again, a too solid attachment power between polymer core and metal sheet can adversely influence formability since the ceaseless smooth sliding between layers is prevented [4, 8].

Some overlaid metal/polymer materials have been proven to show a satisfactory or even great formability. For example, Hylite, an Al/PP/Al sandwich [9], shows a decent forming behavior under profound drawing or bending conditions. Although many researches have been done in the characterization of MPM sandwich composites, very few combine the effects of process parameters in addition to material properties in the analysis of their formability. This research work will examine the effects of process parameters—lubrication condition and forming speed—in amalgamation with the composites' mechanical properties, which will be taken from experimentation, to study their forming behavior with the help of LDH simulation.

In this investigation, the metallic components of the sandwich composites are aluminum (AA5052) and galvanised steel sheets. The polymeric core, for both, is Polyethylene (PE). LDH Simulation results, attempted by means of Altair Hyperworks software, are examined thoroughly. The obtained information is utilized to forming analysis of 'AA5052-PE- AA5052 (APA)' and 'Galvanized steel-PE-Galvanized steel (GPG)' sandwich plates and henceforth its forming capability is resolved.

Methodology

The strategy followed for the prediction of the formability of the APA and GPG sandwich plates started with the characterization of the skin sheet layers and core (PE) material properties. Polyethylene (PE) is a member of the important family of polyolefin resins [10]. It has a high strength-to-weight ratio and is a good electrical and thermal insulator. PE is also self-extinguishing per UL flammability tests. PE

Table 1 Material properties

Materials	AS	GSS	PE	APA	GPG	Epoxy adhesive
Density (g/cm^3)	2.68	7.874	0.952	2.19	7.3	1.24
Young's modulus, E (GPa)	70	211	1.07	63.8	197.2	1.4
Ultimate tensile strength, UTS (MPa)	208.6	474.56	28.5	186.4	459.57	34
Yield strength, σ (MPa)	160.49	287.7	–	147.5	268.13	–
Strength coefficient, K (MPa)	423.9	555.1	–	392.7	512.04	–
Hardening exponent, n	0.27	0.22	–	0.25	0.2	–
Lankford's coefficient, R	0.69	1.6	–	1.12	1.65	–

may be used to temperatures of 140°F (60 °C) and is readily available in sheets, rods, and tubing. A two-component structural epoxy adhesive, which cures at room temperature, is utilized in preparation of samples for experiments undertaken for this research.

The polymers, metallic skin sheets—galvanized steel sheet (GSS) and aluminium sheet (AS)—and MPM sandwich composites made from these substrates have undergone various testing procedures in order to obtain their properties as tabularized in Table 1.

FEA Simulation

The considered APA and GPG sandwich composite materials for the examination comprises three layers each: two layers of metallic sheets and a PE core, with structural epoxy adhesive layer at their interfaces. To replicate the composite material's real behaviour, the empirically tested material properties, tabulated in Table 1, were allotted to the numerical model. The coefficient of friction between the surfaces has been assigned to the model [11] as indicated in Table 2.

Radioss-Incremental Solver, which is one of the solvers in Altair Hyperworks software, is utilized to perform the LDH simulations. The input process parameters and geometrical specifications of the components—punch (dome shaped), binder, blank, and die—are reproduced in the FEA software so as to simulate the experimental LDH test first proposed by Hecker and Ghosh [12] (see Fig. 2). Table 2 indicates these specifications.

Among the four components, the punch, binder and die are made rigid components (meshed with R-mesh) while the blank (MPM sandwich sheets) are deformable with their mechanical properties fed into the model. For the non-deformable bodies (R-meshed) the software decides the element size so as to provide the optimum mesh density. The deformable blanks (Q-meshed), however, have a uniform element size of 1 mm, which will generate fine mesh density for the sake of better accuracy.

Table 2 Input process parameters and geometrical specifications

Sandwich plates		
	GPG	APA
Thickness of sandwich plate, t (mm)	1.5	2.5
Die diameter (mm)	105.7	105.7
Punch dome diameter (mm)	101.6	101.6
Die corner radius (mm)	6.35	6.35
Friction coefficient (lubricated, dry)	(0.029, 0.42) [11]	(0.04, 0.47) [11]
Binder—by keeping gap (mm)	1.5	2.5
Punch velocity (mm/s)	80 and 150	5000 and 10,000

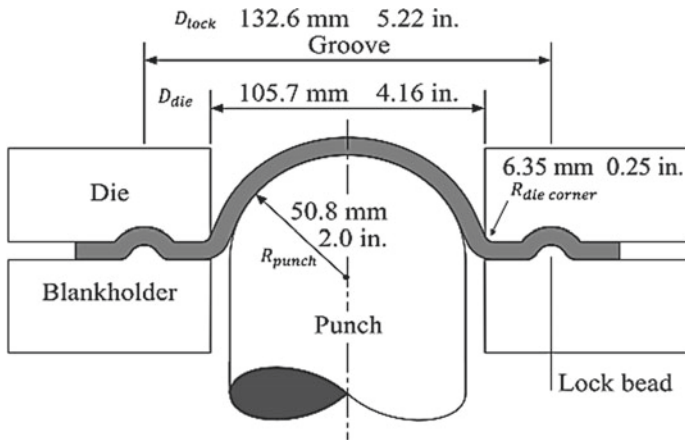


Fig. 2 Schematic of LDH experiment tooling [12]

In LDH experiment, there is lock-bead mounted between die-flange and binder to hold the blank in place while the stretching takes place [12]. This lock-bead is imitated, on the FEA analysis, by a fixed edge constraint applied on the MPM sheet such that it can't be drawn into the die-cavity (pure stretching takes place).

Modelling for Limit Dome Height (LDH) Simulation

For the geometrical modelling of the components, Solidworks CAD software has been used. The finite element software utilized in the present work is Hyperworks to simulate (limit dome height) test on bi-axial strain path. Blank dimensions are

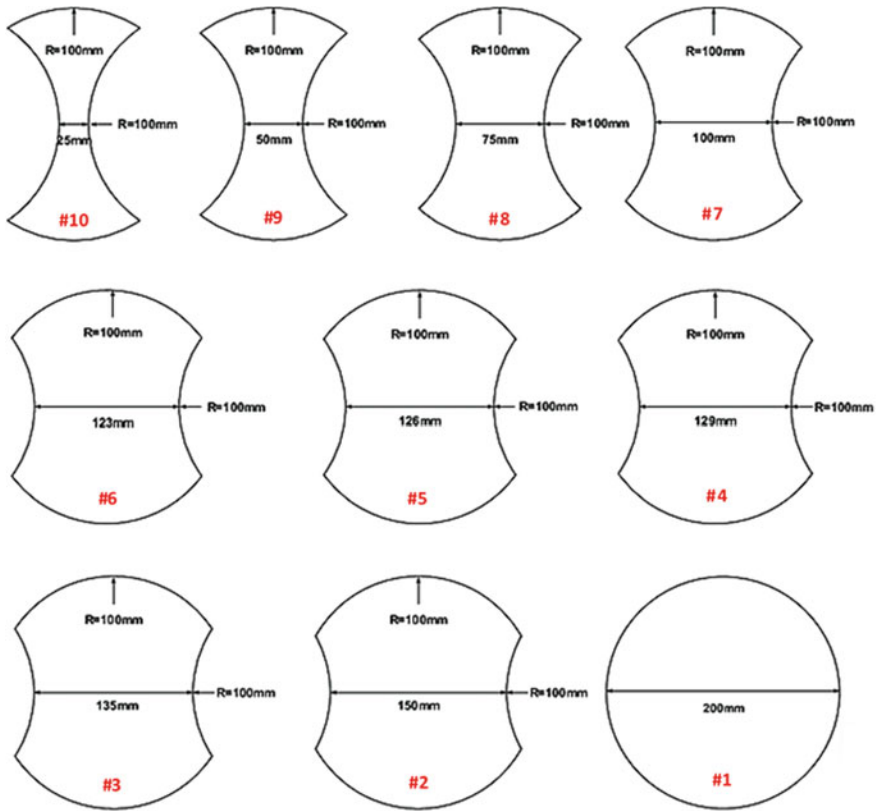


Fig. 3 Blank geometry with numbering [12]

shown in Fig. 3. These blanks model the GPG and APA sandwiches' properties with a thickness of 1.5 and 2.5 mm respectively. Process parameters are indicated in Table 2.

The simulations are allowed to run until failure starts in the blank, and the dome height was taken just before failure. From the data obtained, forming limit diagram (FLD) and dome height graphs are plotted and analyzed thoroughly.

Meshing and Process Setup

The LDH simulation components and APA and GPG sandwich composite blanks are meshed using the Hypermesh tool. The four noded rigid quadrilateral element (R-mesh) is used for the dome test tools—punch, binder, and die, whereas the eight noded linear brick tetrahedron element was used for the blanks. The surface-to-surface explicit contacts are defined by using penalty function, and the coefficient of

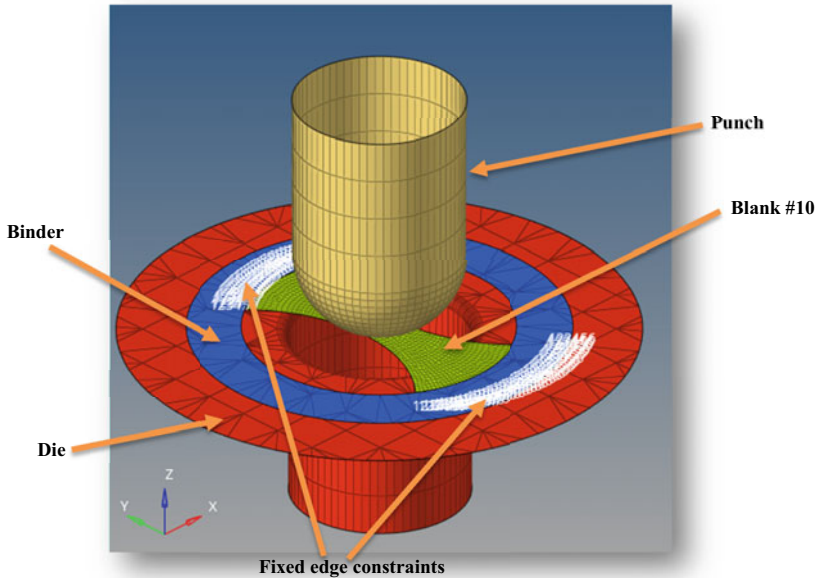


Fig. 4 LDH simulation setup

friction is assigned between tools and sample. The adhesive layer's contacts between skin Al, Galvanized steel sheets, and PE core are defined by using ply laminates.

The generated mesh model is further utilised for the explicit analysis, which is carried out in two different stages. In the first stage, the sandwich composite blank is pressed over the die by applying force using the blank holder whereas in the second stage, the pressed blank is further formed by applying force using the dome shaped punch.

The type of process used in the simulation is Double Action Draw. The setup window is utilized to incorporate the process parameters—blank thickness and material properties, punch speed, and binding mechanism. The obtained mechanical properties were fed into custom materials before they were assigned for the blanks.

The simulation setup (pre-processing) in the graphics area after meshing is shown in Fig. 4.

Yield Criterion

When a material is subjected to large plastic deformations the grain sizes and orientations change in the direction of deformation. As a result, the plastic yield behaviour of

the material shows directional dependency. Under such circumstances, the isotropic yield criteria such as the von Mises yield criterion are unable to predict the yield behaviour accurately. Several anisotropic yield criteria have been developed to deal with such situations. For this research work Hill 1948 yield criterion has been applied in the LDH simulations since it accounts for anisotropic plastic deformations of composite materials.

Results and Discussion

The main objective of this work is to observe the composite sandwich sheets' forming behaviors by applying punch velocities and frictional conditions specified in the process parameters table. The blank holding force is fixed to a constant value that prevents the blank from being drawn into the die-cavity (pure stretching is required). Simulations with various combinations of geometry and process parameters are performed using the Hyperworks software.

The properties of the APA and GPG sandwich sheets that have been obtained through empirical testing are replicated with FE models in Hyperworks and simulations are conducted using Radioss-Incremental solver.

Forming limit diagrams (FLDs) which encompass forming limit curves (FLCs) have been generated for each simulation. The FLC is a failure limiting criterion for sheet material forming. The entire diagram is known as FLD—which indicates thinning, wrinkling tendency, insufficient stretch, and safe forming zones in addition to FLC. FLC illustrates the onset of localized necking in linear straining paths in a diagram of major and minor strains (i.e., in-plane minimum and maximum principal strains). Figure 5 shows the sandwich deformation along with the failure zones, which shows the preliminary stage of failure zone in the sheets. Figure 6 indicates the FLC of both materials.

The colour coding helps to visualise the different zones—failure, marginal, safe, compression, loose, and high wrinkle tendency—which exists in contour plots.

FE simulations for the LDH test indicate that the test is very sensitive to friction and it affects the test measurements. Friction at tool-workpiece interface (in this case, mainly at punch-blank interface) has an effect on formability and thinning distribution. It can be expected that maximum thinning when friction is zero occurs at the apex of the dome. Some simulations have been conducted with zero interface frictional value (between punch and blank), and the failure did in fact occur at the tip of the dome—Fig. 7 indicates this condition for APA blank #1. Generally, location of maximum thinning moves away from the apex of the dome (moves toward die corner radius) as interface friction increases, and punch force also increases as interface friction increases.

From Fig. 5, it is clear that failure zones are in the side wall of sandwich dome, which means more thinning has happened in the side wall of sandwich sheet along with punch travel. From all the simulations in the bi-axial sandwich sheets, almost similar failure phenomenon is noticed.

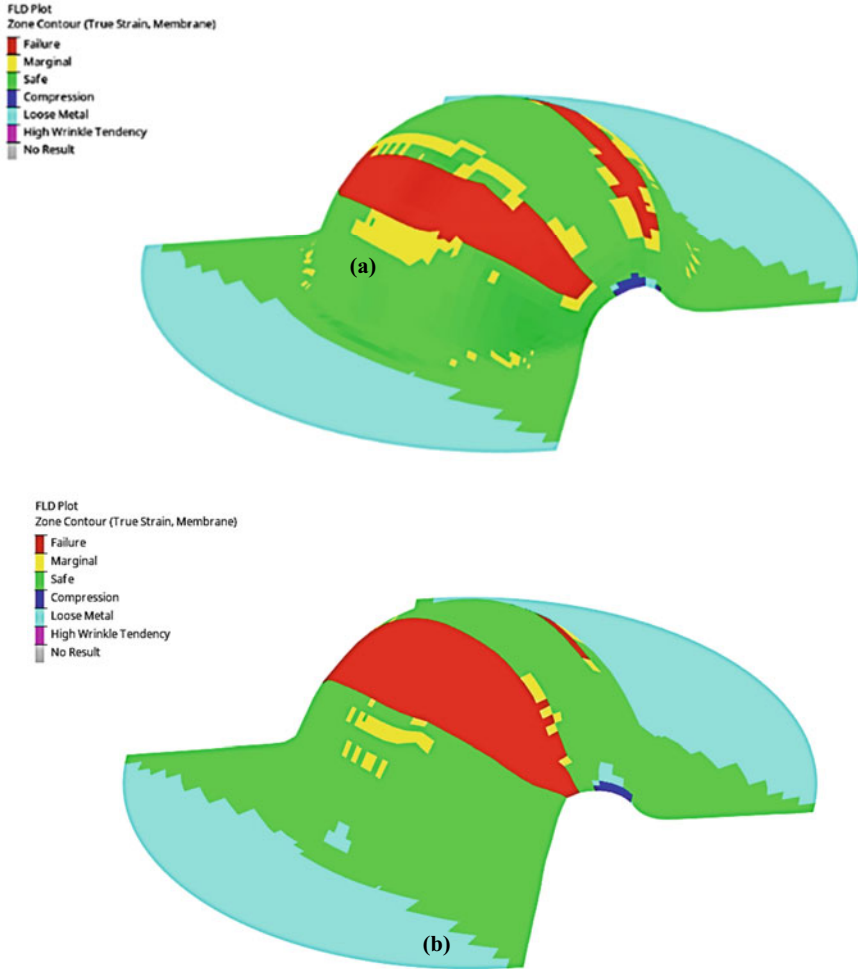


Fig. 5 Contour plot of: **a** APA blank #6, **b** APA blank #10, **c** GPG blank #6, **d** GPG blank #10

Along with FLD, dome height till (just before) failure—also known as LDH—graphs have been extracted from the simulations. From all the simulation conditions, maximum dome height have been recorded at blank #4 for APA (0.015 friction coefficient) and at blank #2 for GPG (0.005 friction coefficient). This indicates that better formability is achieved when friction is decreased to a minimum possible value. For illustration, graphs for all blank geometry and process parameters are shown in Fig. 8.

Another crucial process parameter being studied is the punch velocity, which has a direct correlation with forming speed. Two punch velocities (80 and 150 mm/s) have been applied—with considerable gap between the two—to see the effects clearly.

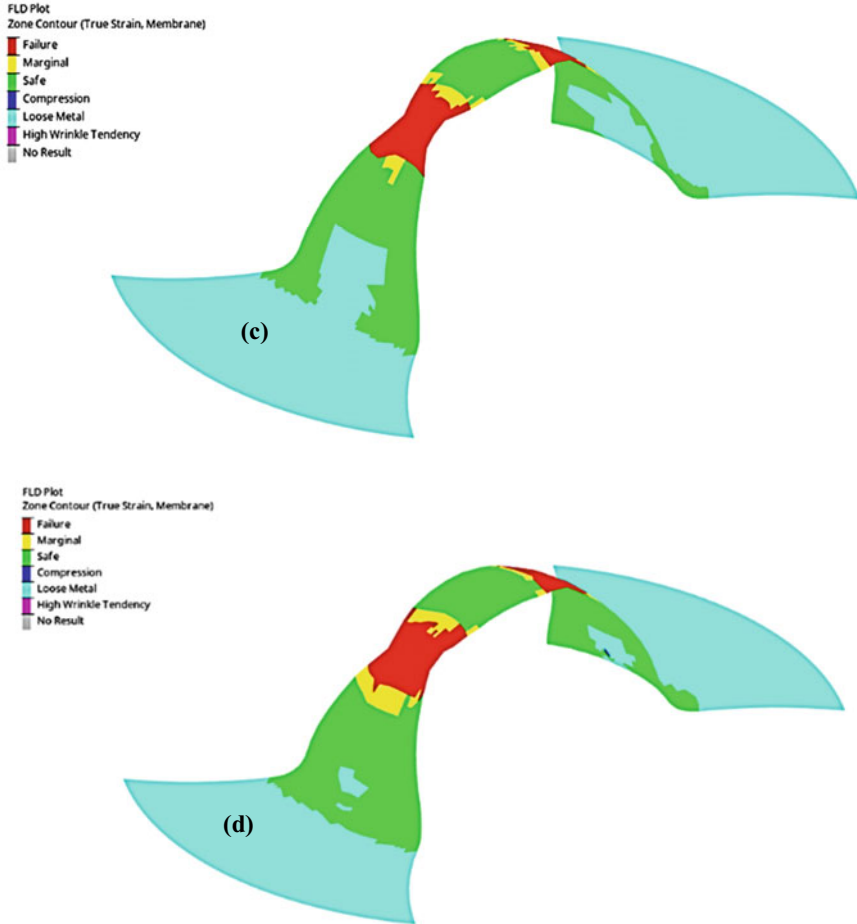


Fig. 5 (continued)

Maximum LDH for both APA and GPG is attained with 80 mm/s punch velocity. For the larger value of punch velocity, however, poor formability is observed, with the blank material being rapidly drawn into failure. For instance, blank #8 is formed with 150 mm/s punch velocity, and it can be observed that small LDH is attained for both blank materials (Fig. 8).

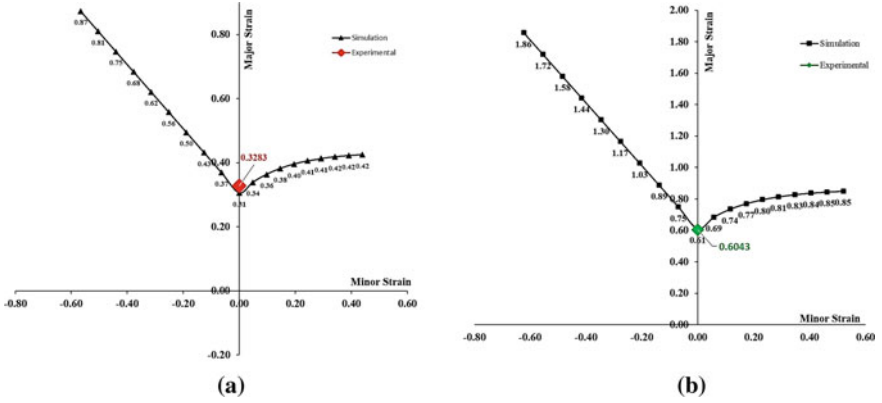


Fig. 6 FLC of: a APA, b GPG

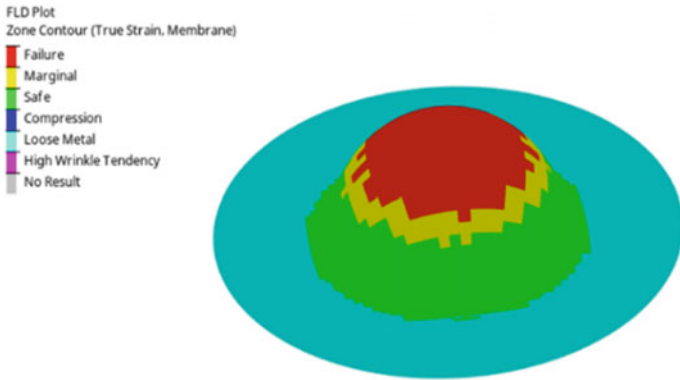


Fig. 7 Contour plot of APA blank #1 with zero friction coefficient between punch and blank

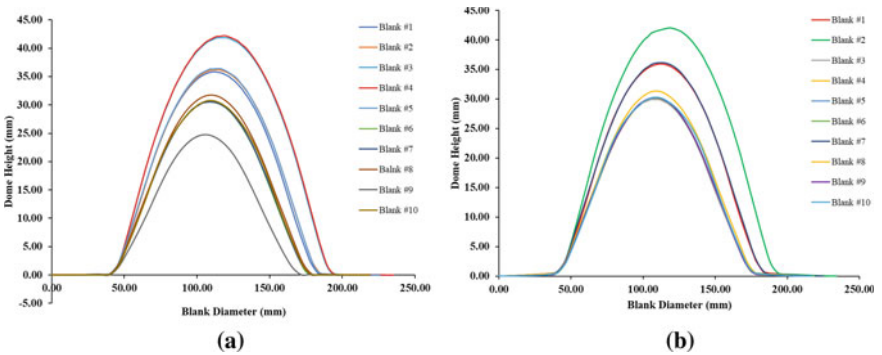


Fig. 8 Dome height comparison— a APA, b GPG

Conclusions

In the present work, limit dome height (LDH) simulation for bi-axial stretching conditions has been performed using Hyperworks FEA software to study the formability of sandwich sheets made up of aluminium (AA5052) and galvanized steel sheets with PE—and structural epoxy adhesive as a binding agent. The simulations are conducted under two levels of punch velocities (80 and 150 mm/s), and many levels of frictional conditions—starting from zero. The data extracted from all of the simulations are FLD and maximum dome height. It is observed that the maximum dome height is seen at blank #4 for APA (0.015 friction coefficient) and at blank #2 for GPG (0.005 friction coefficient). In both cases, the punch velocity is 80 mm/s.

It has also been observed that LDH simulations are very sensitive to friction and have influence on the test outputs. Friction at tool-blank interface has considerable effect on formability and thinning distribution. When friction is zero (imaginary and can only be achieved via simulation), the maximum thinning occurs at the tip of the dome. Generally, location of maximum thinning moves away from the apex of the dome (moves toward die corner radius) as interface friction increases, and punch force also increases as interface friction increases. Hence, applying suitable lubricant should improve the formability of the sheets.

References

1. Gholamzadeh Babaki M, Shakouri M (2021) Free and forced vibration of sandwich plates with electrorheological core and functionally graded face layers. *Mech Based Des Struct Mach* 49(5):689–706
2. Kee JK, Rhee HM, Choi BI, Kim CW, Sung CW, Han CP, et al (2009) Development of application technique of aluminum sandwich sheets for automotive hood. *Int J Precis Eng Manuf* 10:71–5
3. Sokolova OA, Carrado A, Palkowski H (2011) Metal–polymer–metal sandwiches with local metal reinforcements: a study on formability by deep drawing and bending. *Compos Struct* 94(1):1–7
4. Stachowiak G, Batchelor AW (2014) *Engineering tribology*, 4th edn. Elsevier Inc., Oxford
5. Engel B, Buhl J (2011) Metal forming of vibration-damping composite sheets. *Steel Res Int* 82(6):626–631
6. Ruokolainen RB, Sigler DR (2008) The effect of adhesion and tensile properties on the formability of laminated steels. *J Mater Eng Perform* 17:330–339
7. Mousa S, Kim GY (2017) A direct adhesion of metal–polymer–metal sandwich composites by warm roll bonding. *J Mater Process Technol* 239:133–139
8. Safaei B, Moradi-Dastjerdi R, Behdinin K, Qin Z, Chu F (2019) Thermoelastic behavior of sandwich plates with porous polymeric core and CNT clusters/polymer nanocomposite layers. *Compos Struct* 226:111209
9. Carrado A, Sokolova O, G Ziegmann, Palkowski H (2010) Press joining rolling process for hybrid systems. *Key Eng Mater* 425:271–281
10. Titow WV (1990) *Pe plastics, properties, processing, and applications*
11. Friction factors—coefficients of friction. Archived from the original
12. Hecker and Ghosh (1975) Failure in thin sheets stretched over rigid punches. *Metall Trans A* 6:1065–1074

Numerical Modeling and Optimization of Fiber Metal Laminates



Sheng Sijia and Lang Lihui

Abstract Fiber metal laminates (FMLs) are functional and structural composite materials. The major advantage of these materials is a combination of low weight and high mechanical strength, which is crucial for modern aerospace and automotive industries. This paper mainly introduces the modeling and simulating method of the flexible medium forming process of fiber metal laminates. Subroutines have been developed for the input of interlayer prepreg material parameters and definitions of damage evolution and failure criteria. A thin layer of resin is set between the metal layer and the prepreg layer. And the cohesive element based on traction-separation is applied to characterize the adhesion between the layers through which interlayer failure process can be obtained. In the respect of flexible media forming, the setting and optimization of boundary conditions have been discussed in detail. Finally through experimental verification the numerical simulation results can effectively predict the defects of the laminates.

Keywords Fiber metal laminates · Subroutines · Cohesive element · Boundary condition

Introduction

Fiber Metal Laminates (FMLs) are essentially an interlayer hybrid composite, consisting of thin aluminum sheets and prepreg layers. It combines the good toughness of the metal with the high strength ratio of the fiber and also improves the environmental corrosion resistance to a certain extent. At present, after half a century of development, four generations of FMLs have come out. They are Aramid Reinforced Aluminum Laminates (ARALL), Glass Reinforced Aluminum Laminates (GLARE), Carbon Reinforced Aluminum Laminates (CARE), and Titanium-Graphite hybrid Laminates (TiGr) [1]. Due to its high strength, low density, good fatigue resistance,

S. Sijia · L. Lihui (✉)

School of Mechanical Engineering and Automation, Beihang University, Beijing 100191, China
e-mail: lang@buaa.edu.cn

good toughness, and corrosion resistance [2], Fiber Metal Laminates have received widespread attention and applications in a variety of fields such as aerospace and automotive.

At present, the traditional forming methods of FMLs mainly include self-forming technology, roll forming technology, shot peening, etc. The above forming method can form single and double curvature members with small curvatures, and it is difficult to apply to complex parts with small rounded corners and large curvatures. Luke Moss [3] and RAJABI [4] et al. explored the stamping technology of laminates. Zafar [5] proposed a 3A forming method to obtain composite laminates with complex shapes. Sherkatghanad [6] used hydroforming technology to form semi-cured composite laminates. According to the experimental results, it was found that the deformation depth of the laminates was greater in the semi-cured state. Liu [7–9] and others used hydroforming technology to form a semi-cured FMLs, and successfully obtained a variety of complex shapes and good quality parts.

There are few scholars studying the innovative forming method at home and abroad at present. The process optimization method is not mature enough, so a large number of experiments are needed to obtain the deformation characteristics of the FMLs under this forming method. Finite element analysis is undoubtedly the best way to reduce workload. Linde [10] deals with a microscopic model based on the finite element method for simulating the damage behaviour of FMLs. Each of the layers is modelled by solid elements, and the interlaminar behaviour is modelled by an interface model. Each physical damage mechanism is modelled separately. This article focuses on accurate modeling of the hydroforming process of semi-cured FMLs by ABAQUS software, which will be used to predict defects during forming.

Establishment of Material Model

The definition of the FMLs model is mainly divided into three parts, namely metal layers, fiber reinforced resin-based prepreg layers, and adhesive layers.

Metal Layers

The metal layer adopts an isotropic elastoplastic model, and strain strengthening is defined by the measured true stress-strain data. Since most of the FMLs are made of ductile metals such as aluminum, magnesium, and titanium, the ductile damage rule is used to determine the initial failure. According to the damage rule, the material undergoes plastic deformation during loading, which causes the initiation, expansion, and aggregation of micropores and microcracks inside the material. As a result, the stiffness of the material decreases and its performance deteriorates.

Prepreg Layers

The fiber failure and matrix cracking in the glass fiber reinforced prepreg layer are treated by the user material subroutine VUMAT. Taking plain woven fiber prepreg as an example, it is assumed that the elastic stress-strain relations are given by orthotropic damaged elasticity. The stress-strain relationship is given by Eq. (1). And material stiffness degradation can be calculated by introducing damage variables d . Referred to a local coordinate system aligned with the fiber directions (Fig. 1) the elastic relations take the form [11]:

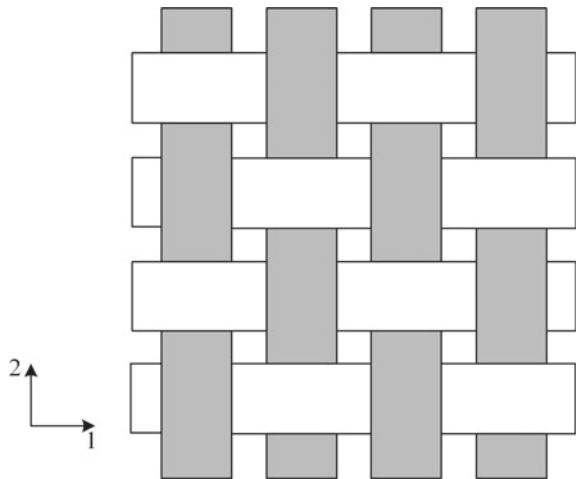
$$\begin{pmatrix} \varepsilon_1 \\ \varepsilon_2 \\ \varepsilon_{12}^{el} \end{pmatrix} = \begin{pmatrix} \frac{1}{(1-d_1)E_1} & \frac{-\nu_{12}}{E_1} & 0 \\ \frac{-\nu_{21}}{E_2} & \frac{1}{(1-d_2)E_2} & 0 \\ 0 & 0 & \frac{1}{(1-d_{12})2G_{12}} \end{pmatrix} \begin{pmatrix} \sigma_{11} \\ \sigma_{22} \\ \sigma_{12} \end{pmatrix} \quad (1)$$

The damage variables d_1 and d_2 are associated with fiber fracture along the 1 and 2 directions respectively, whereas d_{12} is related to matrix micro-cracking due to shear deformation. The tensile strength and compressive strength in the 1 and 2 directions and the shear strength we input are the initial parameters of fiber damage. The evolution of the damage variables is given by the equation [11]:

$$d_\alpha = 1 - \frac{1}{r_\alpha} \exp(-A_\alpha(r_\alpha - 1)); \quad \dot{d}_\alpha \geq 0$$

where $A_\alpha = \frac{2g_0^\alpha L_c}{G_j^\alpha - g_0^\alpha L_c}$.

Fig. 1 Schematic representation of woven fiber



Here, the damage thresholds, r_α are initially set to one. L_c is the characteristic length of the element, G_f^α is the fracture energy per unit area under uniaxial tensile/compressive loading, and g_0^α is the elastic energy density.

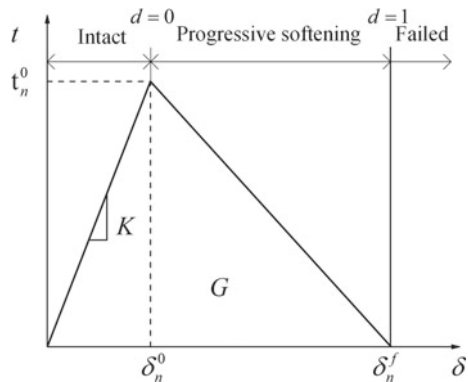
The subroutine can implement the delete function of the mesh. When the variable in a certain direction of the mesh unit reaches the maximum set value, the unit will be deleted, indicating that it has become invalid. The damage status of the fiber and resin matrix along the 1 and 2 directions can be obtained.

Adhesive Layers

The bonding effect can be treated with a special interface adhesive layers. Between the metal layer and the prepreg layer, an adhesive layer is inserted to define the bonding effect between the layers. The thickness of the adhesive layer is usually small and can be given 0.01 mm. In the layer the cohesive element based on traction-separation description used to simulate composite failure.

In the method described based on traction-separation, the most commonly used constitutive model is the bilinear constitutive model shown in Fig. 2. It gives the linear elastic segment before the material reaches the strength limit and the falling section of that represents the stiffness decay and failure process. Note that the ordinate t is stress and the abscissa δ is displacement. So the slope K of the linear elastic segment actually represents the stiffness of the cohesive element. What's more, the area under the curve is the energy release rate G when the material breaks. Therefore, when defining the mechanical properties of cohesive, the actual form of the above constitutive model is to be determined including stiffness, ultimate strength, and critical energy release rate, or the displacement of the element in the event of failure. Cohesive element can be understood as a quasi-two-dimensional element, which can be considered as two faces separated by a thickness layer. And these two faces are connected to other solid elements respectively. About the cohesive element, only

Fig. 2 Traction-separation constitutive relationship of cohesive model



out-of-plane forces are considered, including normal stresses and shear stresses in both XZ and YZ directions.

The initial damage corresponds to the material’s beginning to degrade. When the stress or strain meets the defined initial critical damage criteria, then the degradation begins. About the FMLs, common damage for traction-separation laws include Quade Damage, Maxe Damage, Quads Damage, and Maxs Damage. And in the process of damage evolution, energy is generally used to control the degradation of the unit. It is worth noting that the mesh size of the cohesive element cannot be too large. Usually a finer mesh is required, otherwise convergence problems are likely to occur, and even the calculation cannot be continued. In addition, the sweep method must be used, and the sweep direction is perpendicular to the cohesive surface.

Simulation of the Forming Process

Hydroforming Technology

Hydroforming technology is a manufacturing technology that uses liquid as a force transmission medium instead of a rigid die (or punch) to transfer loads. It can cause the sheet to abut against the punch (or die) under the pressure of the force-transmitting medium to realize the forming of the part. Hydroforming is divided into active hydroforming and passive hydroforming, as shown in Fig. 3. The medium pressure is controlled within a certain range, so that the sheet can complete the forming process under the designed loading path. The sheet sticks to the surface of the punch during forming process which causes the contact area between the sheet and tool increase. The useful friction force is created. At the same time, the increase of cavity pressure

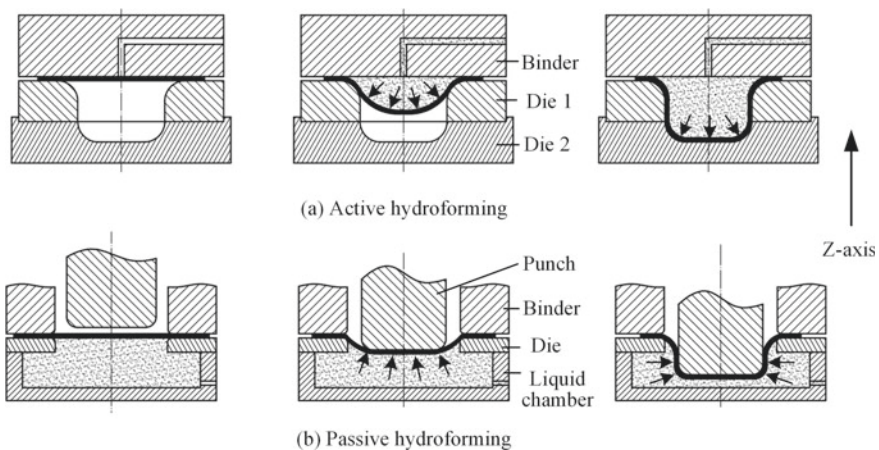
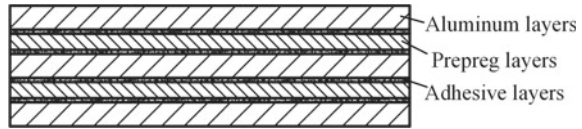


Fig. 3 Schematic of hydroforming technology

Fig. 4 Schematic diagram of layer structure



can make the parts produce the effect of soft drawbead. The above two reasons can effectively increase the deformation of the material and improve the forming limit.

Establishment of the Forming Process

The paper takes 3+2 structure fiber metal laminate as an example. In the numerical simulation, the laminate includes 3 layers of aluminum 2024-T3, 2 layers of prepreg and 4 layers of adhesive, as shown in Fig. 4. The thickness of aluminum layer is 0.3 mm and that of prepreg layer is 0.2 mm. The properties are assigned to the corresponding layer respectively. And the laying direction of the fibers deserves special attention. When we use glass fiber as the reinforcing phase, such a laminate is called Glass Fiber Metal Laminate (GLARE). Laminates can be divided into 2+1, 3+2, and other structures FMLs according to different paving methods.

The die, punch, and binder are modeled as rigid bodies. Penalty contact interfaces are used to enforce the intermittent contact and sliding boundary conditions are applied for contacts between the sheet metal and the tooling elements. The die is completely constrained and the punch and binder are able to move in the Z-axis direction. In the active hydroforming technology, the binder goes down firstly and the mould is closed. And then the pressure in the liquid chamber increases gradually. The blank holder force (BHF) loading curve and cavity pressure loading curve are very important the forming quality of the part. While in the passive hydroforming process, the downward movement of the punch and the loading of the cavity pressure is performed simultaneously. Therefore, it is a huge challenge to match the BHF, the downward curve of the punch, and the cavity pressure loading curve and obtain the perfect part.

Numerical Simulation Results

Take a certain part as an example, the comparison between simulation results and experimental results is shown in Fig. 5. It can be seen from Fig. 5 that the simulation results are basically consistent with the experimental results. This modeling method can accurately simulate the wrinkle defects of the sheet, and provides a strong basis for analyzing the deformation of the FMLs.

What's more, when we choose laminates with different structures and different process loading methods, the test results will obviously be different, as shown in

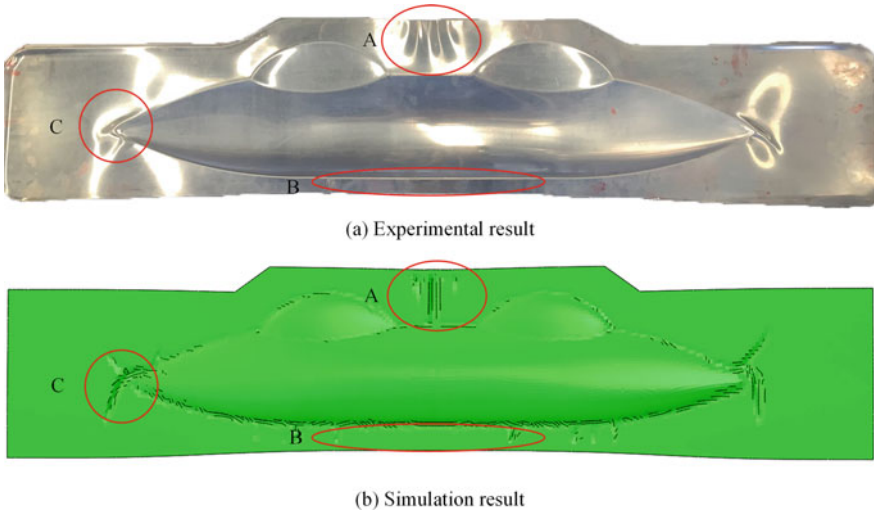
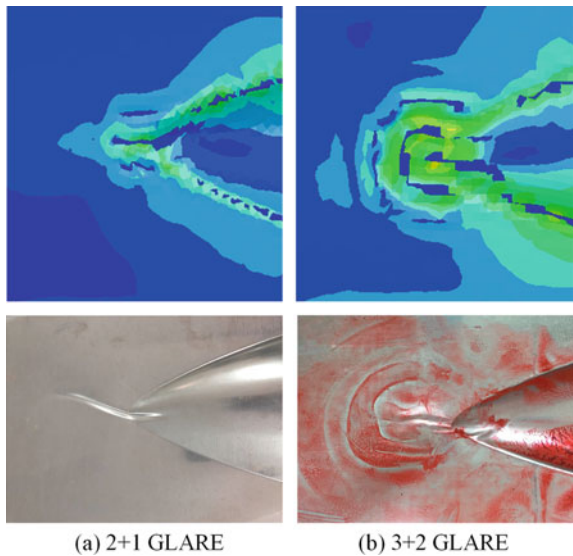


Fig. 5 Comparison of simulation results and experiment results

Fig. 6. We find that the simulation results are basically consistent with the experimental results, which further validates the reliability of modeling method. Similarly, the simulation method has a wide reference meaning and can be used for modeling and analysis of other types of FMLs forming processes.

Fig. 6 Comparison of simulation results and experiment results of different laminate structures (2+1 GLARE and 3+2 GLARE)



Conclusion

In this paper, the numerical simulation modeling process of an innovative technology named hydroforming technology of FMLs is introduced in detail based on ABAQUS software. And a few conclusions are obtained as follows:

- (1) The material modeling of FMLs is to model the metal layers and the prepreg layers separately, and connect them with cohesive layers to simulate the bonding effect between layers.
- (2) The user material subroutine VUMAT is used to define the stress-strain relationship of woven fiber and its damage law through the constitutive. And for adhesive layers the cohesive element based on traction-separation description is utilized. The constitutive relationship of the adhesive layers and its stiffness degradation process can be set according to user needs.
- (3) Hydroforming can increase the forming limit of FMLs and can be used to form parts with complex shapes. Optimizing the relationship between the cavity pressure loading, the blank holder force, and the downward movement of the punch is the key point.
- (4) Through comparison of numerical simulation and experimental results, the above modeling method is reliable and can accurately simulate the defects of FMLs.

References

1. Sinmazçelik T, Avcu E, Bora MÖ, Çoban O (2011) A review: fibre metal laminates, background, bonding types and applied test methods. *Mater Des* 32:3671–3685
2. Moussavi- SE, Dariushi S, Sadighi M, Safarpour P (2010) A study on tensile properties of a novel fiber/metal laminates. *Mater Sci Eng A* 527:4920–4925
3. Mosse L, Compston P, Cantwell WJ, Cardew-Hall M, Kalyanasundaram S (2005) The effect of process temperature on the formability of polypropylene based fibre-metal laminates. *Compos Part A Appl Sci Manuf* 36:1158–1166
4. Rajabi A, Kadkhodayan M, Manoochehri M, Farjadfar R (2015) Deep-drawing of thermoplastic metal-composite structures: experimental investigations, statistical analyses and finite element modeling. *J Mater Process Technol* 215:159–170
5. Zafar R, Lang L, Zhang R (2016) Experimental and numerical evaluation of multilayer sheet forming process parameters for light weight structures using innovative methodology. *Int J Mater Form* 9:35–47
6. Sherkatghanad E, Lang L, Liu S, Wang Y (2018) Innovative approach to mass production of fiber metal laminate sheets. *Mater Manuf Process* 33:552–563
7. Liu S, Lang L, Guan S, Alexandrov S, Zeng Y (2019) Investigation into composites property effect on the forming limits of multi-layer hybrid sheets using hydroforming technology. *Appl Compos Mater* 26:205–217
8. Shichen L, Lihui L, Shiwei G (2019) An investigation into the formability and processes of GLARE materials using hydro-bulging test. *Int J Precis Eng Manuf* 20:121–128
9. Liu S, Lang L, Sherkatghanad E, Wang Y, Xu W (2018) Investigation into the fiber orientation effect on the formability of GLARE materials in the stamp forming process. *Appl Compos Mater* 25:255–267

10. Macura P, Petruska J (1996) Numerical and experimental simulation of pass rolling. *J Mater Process Technol* 60:55–60
11. User AA (2008) VUMAT for fabric reinforced composites. Dassault Syst 1–10

Investigation of the Effect of Blank Holding Force on Earing Defect During Circular Deep Drawing Process Through Finite Element Analysis and Experimentation Using AA6061 and Low-Carbon Steel Sheets



Amirela Siraji, Tsegaye Bekele, Perumalla Janaki Ramulu, Habtamu Beri, and P. Venkateswar Reddy

Abstract Earing is defined as the formation of waviness on uppermost portion of deep drawn cup. It is one of the major defects observed during deep drawing process. The objective of the present study aims to investigate the influence of the blank holding force (BHF) on Earing defect in the deep drawing process of cylindrical cups through finite element analysis. For this purpose, mechanical properties of AA6061 and low-carbon steel sheets along with deep drawing tool design parameters were incorporated in the finite element modeling of deep drawing process. The finite element software (Pam-Stamp 2G) was utilized to carry out the numerical simulation of the deep drawing process. Different BHF's were applied during the deep drawing process. The simulation results showed that the best earing is observed when the BHF is 9kN for the AA6061 alloy and 20kN for the low-carbon steel sheet. The earing tendency and deep drawability of the low-carbon steel sheets is higher than AA6061.

Keywords Blank holding force · Deep drawing · PAMSTAMP

A. Siraji · T. Bekele · H. Beri

Department of Mechanical Engineering, School of Mechanical, Chemical and Materials Engineering, Adama Science and Technology University, Adama, Ethiopia

P. Janaki Ramulu (✉)

Department of Mechanical Engineering and Centre of Excellence for Advanced Manufacturing Engineering, School of Mechanical, Chemical and Materials Engineering, Adama Science and Technology University, Adama, Ethiopia

e-mail: perumalla.janaki@astu.edu.et

P. Venkateswar Reddy

Department of Mechanical Engineering, Vardhaman College of Engineering, Kacharam, Shamshabad, Hyderabad 501218, Telangana, India

Introduction

Sheet metal forming is one of the most widely used manufacturing processes for making different kind of products in many industries. It is due to the ease with which metal may be formed into useful shapes through plastic deformation processes in which the volume and mass of the metal are conserved and the thickness is substantially the same as that of the original material. Deep drawing is one of the most important processes for forming sheet metal parts. It is mainly used for mass production of cup shapes in automobile, aerospace, and packaging industries. In deep drawing operation, a sheet metal (blank) converted to cylindrical parts by using a process in which sheet is drawn into cavity of die to convert the blank into desired [1]. The deformation of a sheet metal in deep drawing was estimated quantitatively [2–4] using draw ratio (DR), which is defined as ratio of initial blank diameter to the diameter of the cup drawn from the blank (approximately equal to the punch diameter). For a given material, there is a limiting draw ratio (LDR), representing the largest blank that can be drawn through a die without tearing [4, 5]. Maximizing drawability in deep drawing operations directly reduces the manufacturing cost and time associated with these operations [4, 6]. Furthermore, a prior knowledge of the limits of drawability can also be useful in avoiding the development of infeasible designs early on thereby decreasing the total product design cycle time. Drawability can be increased by delaying the onset of process failures. Towards this end, process parameters which influence the drawing operation need to be properly selected. Blank shape is one of the most important process parameters that strongly influence drawability, i.e., by altering the blank design considerable improvement in the drawability may be obtained [4]. The quality of the product is influenced by many of the process parameters like blank holder force, coefficient of friction, strain rate, thickness, and temperature, punch force and punch speed, etc. So, a good knowledge is required to produce good quality of deep drawing products by minimizing the defects [7]. One of the major defects [8] which affects the quality of the deep drawn cups is the occurrence of a wavy edge at the top, commonly referred to as the earing defect. Earing is a result of non-uniform flow of material into the die cavity from different anisotropy directions of the sheet. The blank is anisotropic due to the directionality of plastic properties produced by rolling and other primary working process [4, 9]. In practice, a significant amount of material is lost as this wavy edge of the cup needs to be trimmed. It is undesirable because it requires additional processing [2]. Information concerned formation of ears in deep drawing operation permits a pervious alteration of operation, which results in production of final cup with defect less/minimized and financial saving and time [3, 4, 10–12]. Some research works have been conducted to explain the relationships between earing defect and the parameters of the deep drawing process. For example, the effect of blank shape on earing defect [2–4, 13], the effect of tool geometry on earing defect [14], the effect of anisotropic nature of blank material on earing defect [15, 16], the effect of temperature on earing defect [17] (Seo et al. 2018), etc. However, the aim of removing earing defect from the final product is not fully achieved, which means there are other process parameters

which effects on earing defect. Hence, the objective of this work is to investigate the relationship between earing defect and varying blank holding force to reduce earing through numerical simulation.

Methodology and Simulation

Modeling and Design of Deep Drawing Tools

The finite element analysis is carried out with explicit elasto-plastic finite element software, PAMSTAMP 2G. The tool models punch, blank holder, and die are assumed to be perfectly rigid. The blank material is meshed with size two. The material properties are determined using tensile testing which is given as input material for simulation as shown in Table 1. Yielding of the material is assumed to be described by quadratic Hill's yield criteria. The constant friction condition is assumed at all tool interfaces. The coefficient of friction at the interfaces among the blank, the punch, blank holder, and die is assumed to be 0.15. A better earing results were observed by using circular blank from the literatures [2–4, 12, 13]. So, in this paper, circular blank was selected. To determine the size of the blank and the steps of deep drawing, the three rules presented by [18] were considered. The drawing setup designed using SolidWorks and imported into the PAMSTAM 2G. The dimensions of the setups are shown in Fig. 1.

Table 1 Geometric dimension and process parameters

Tool dimensions	Values
Punch velocity (mm/s)	0.5
Punch displacement (mm)	50
Friction	0.15
Punch diameter (mm)	48
Punch radius (mm)	6
Die diameter (mm)	51.1
Die radius (mm)	8
Sheet metal thickness (mm)	1
Initial blank diameter (mm)	90
Drawing ratio	1.67
Clearance (mm)	1.1

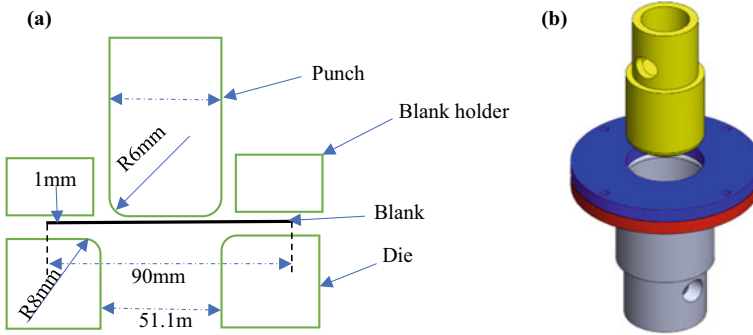


Fig. 1 a Schematic illustration and b surface model assembly of deep drawing setup

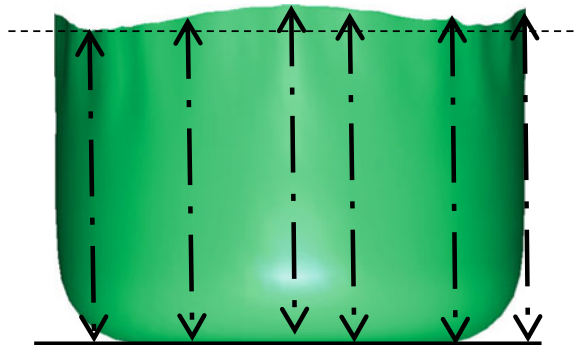
Tensile Testing

To define the properties of the sheet metal (blank), specimens were designed and prepared according to ISO (International Standard Organization) standard ISO 6892-1 2016 specification. The dogbone and rectangular shape specimens were prepared from AA6061 alloy and low-carbon steel metal sheets at different orientations with respect to the rolling direction: 0°, 45°, and 90°, and for each rolling direction, three specimens were prepared for tensile testing and one for plastic strain ratio testing.

Cup Height and % Earing Height

The cup heights were measured at different points with respect to width as shown in Fig. 2. Variation of cup height is better observed in terms % ear height where % ear height is calculated using Eq. (1) as given by [4] below:

Fig. 2 Simulated cup showing variation of height



$$\% \text{ ear height} = \frac{\text{maximum cup height} - \text{minimum cup height}}{\text{minimum cup height}} \times 100 \tag{1}$$

Results and Discussion

In order to study blank holding force effect, two different sheets materials, AA6061 and low-carbon steel sheets with 1 mm thickness, are used. The chemical compositions and the mechanical properties of Al 6061 alloy and low-carbon steel are shown in Tables 2 and 3.

Using the r-values in the three directions (0°, 45°, and 90° to the rolling direction), two other important parameters—planar anisotropy parameter (Δr) and normal anisotropy parameter (r_m)—are also calculated. Planar anisotropy parameter (Δr) is an indicator of the ability of a material to demonstrate a non-earring behavior and it is preferred to be as small as possible. On the other hand, normal anisotropy parameter (r_m) is an indicator of the ability of a material to be deep drawn and it is preferred to be as high as possible. Table 3 shows these values for AA6061 and low-carbon steel sheet materials.

Table 2 Chemical compositions of AA6061 and low-carbon steel

	Al	Mg	Si	Fe	Cu	Cr	Zn	Ti	Mn	K	C	Others
AA6061	96.8	0.9	0.7	0.6	0.3	0.25	0.2	0.1	0.05			0.05
Low-carbon steel			0.28	98					1.03	0.04	0.25	

Table 3 Mechanical properties of the AA 6061 alloy and low-carbon steel sheet metal

Material	AA6061	Low-carbon steel
Young’s modulus (E) (GPa)	70	
Yield stress MPa	92	267
Ultimate tensile strength (MPa)	158	289
Strength of coeff. (K) MPa	147	534.5
Strain hardening exp (n)	0.3564	0.2357
Blank holder force (kN)	1–50	1–50
Coeff. of friction (μ)	0.15	0.15
Punch velocity mm/s	0.5	0.5
r_0	0.871	1.780
r_{45}	0.840	1.600
r_{90}	0.792	1.860

From the results tabulated in Table 3, it is observed that low-carbon steel sheet has high earing tendency and deep drawability than that of AA6061 sheet metal as the planar and normal anisotropy values are higher for low-carbon steel sheet.

Simulation of Deep Drawing Process

The FE simulations of deep drawing were conducted using BHF's of 1kN and 50kN, respectively, for both AA6061 and low-carbon steel. It is observed that wrinkling occurred when the BHF is not enough to prevent the buckling of the blank sheet, and tearing appeared due to the insufficient material flow when the BHF is excessive. Next, the predictions of earing in deep drawing using various uniform BHF's of 1 kN, 5 kN, 10 kN, 15 kN, 20 kN, 25 kN, 30 kN, 35 kN, 40 kN, 45 kN, and 50 kN are carried out, after the simulations, for the low-carbon steel, it is observed that wrinkling occurred when the blank holder forces are below 20 kN and as the BHF goes above 20 kN, it generates challenges for the blank material to flow into the die, the earing profile graphs for 15 kN, 20 kN, and 25 kN are shown in Fig. 4. And for the AA6061, it is observed that wrinkling which occurred at BHF's is below 9kN and as the BHF goes above 9kN, it produces challenges for the blank material to flow into the die, and the earing profile graphs for 6 kN, 9 kN, and 14 kN are shown in Fig. 3. The present FEA showed that the height of the deep drawn cup monotonically increases from 15 to 25 kN for low-carbon steel and 6–14 kN for the AA6061 alloy material. The results revealed that the height of earing, the peaks of the waves shown in Figs. 5 and 6, increased when the BHF increased. A significant increase of earing height was observed at high BHF.

The number of the blank holding force required is selected to be three BHF's for both materials. However, many more analyses were conducted by varying the blank holding forces which reduces wrinkling first and then earing phenomenon then tearing. The range 1–50 kN is inspected thoroughly for both materials and wrinkling is observed at blank holder force lower than 9 kN for AA6061 alloy and 20 kN for low-carbon steel and failures occurred above BHF of 9 kN for AA6061 alloy and 20 kN for low-carbon steel due to tearing, cracking, and others. This is the effect of wrinkling (due to insufficient blank holding) on the final shape. For AA6061 alloy, in the 9 kN case, almost no wrinkling is observable, whereas the 1 and 6kN show wrinkles. The wrinkling waves of the low force case are visually observable without argument, and the same phenomenon has happened for low-carbon steel; in the 20 kN case, no wrinkling is observed and wrinkling is observed for BHFS of 1 and 15 kN. First, the FE simulations of deep drawing were conducted using BHF's of 1 kN and 50 kN, respectively. It was observed that wrinkling occurred when the BHF was not enough to prevent the buckling of the blank sheet, and tearing appeared due to the insufficient material flow when the BHF was excessive [10]. Next, the determination of earing in deep drawing using various uniform BHF's of 6kN, 9kN, and 14kN for AA6061 alloy and 15 kN, 20 kN, and 25 kN for low-carbon steel sheets was carried out. The present FEA showed that the height of the deep drawn cup monotonically

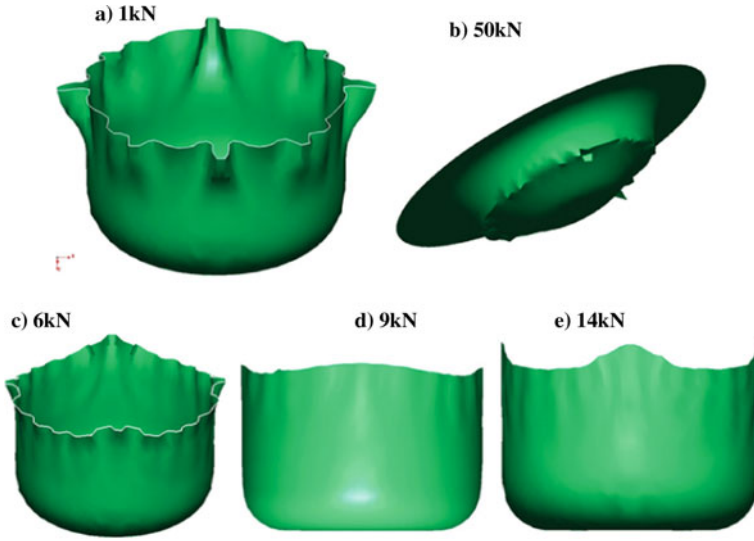


Fig. 3 FE simulation of the deep drawn cup of AA6061 using uniform BHF's of **a** 1 kN, **b** 50 kN, **c** 6 kN, **d** 9 kN, and **e** 14 kN

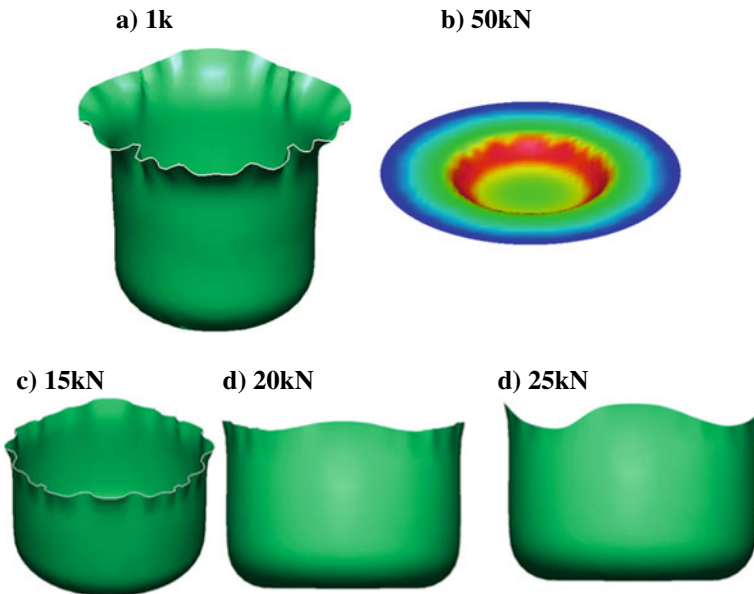


Fig. 4 FE simulation of the deep drawn cup of low-carbon steel using uniform BHF's of **a** 1 kN, **b** 50 kN, **c** 15 kN, **d** 20 kN, and **e** 25 kN

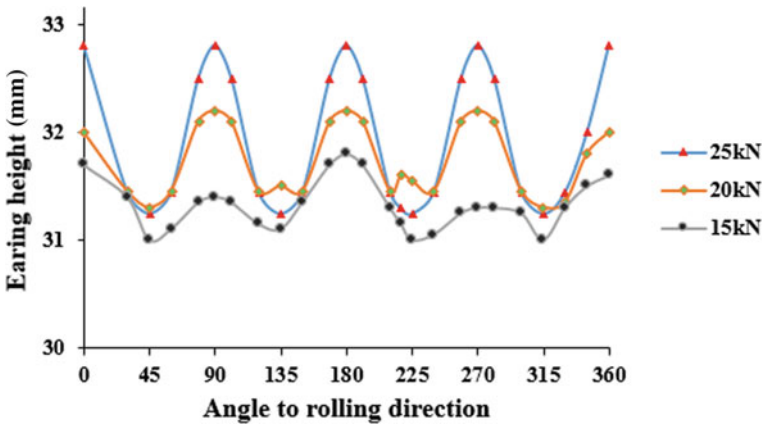


Fig. 5 Earing height profiles of low-carbon steel using the present finite element analysis (FEA) with uniform BHF of 15 kN, 20 kN, and 25 kN

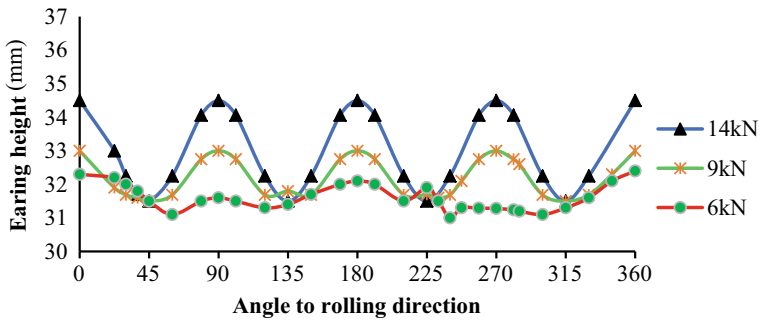


Fig. 6 Results of the earing height profiles of AA6061 using the present finite element analysis (FEA) with uniform BHF of 6 kN, 9 kN, and 14 kN

decreases from 0° to 45° to the RD and monotonically increases from 45° to 90° to the RD. This is due to the contribution of the yield stress directionality [15]. As the planar anisotropy was positive (for AA6061, $\Delta r = 0.01$ and for low-carbon steel, $\Delta r = 0.22$), the formation of earing was observed at 0° and 90° to the RD, which well correlated with the theoretical analysis [19]. It can be seen that four main ears formed at 0° , 90° , 180° , and 270° in the cup deep drawing process. This is partially attributed to the slower flow of sheet metal into the die cavity in these regions than in the other ones. The results show that the uniform BHF of 9 kN and 14 kN for AA6061 alloy, and 20 kN and 25 kN for low-carbon steel exhibited bigger ears at 0° and continues to show with 90° gaps. Meanwhile, the uniform BHF of 6 kN for AA6061 and 15 kN for low-carbon steel exhibited very small earing profile at 0° , 90° , 180° , and 270° . The results revealed that the height of earing, the peaks of the waves increased when the BHF increased. A significant increase of earing height

was observed at 0° , 90° , 180° , and 270° with the larger BHF. By using Eq. (1), the % ear height variation is determined. This result illustrates that the ΔH also increased with the increase in BHF.

Cup Height and % Earing Height

The cup heights were measured at different points with respect to width. Variation of cup height is better observed in terms % ear height where % ear height is calculated using Eq. (1). The percentage of earing with respect to the selected blank holding force is shown in Table 4.

For the AA6061 alloy, among all the three blank holding forces, the smallest cup height is found under blank holder force of 6 kN. Although, BHF of 6kN shows good result of earing, it also shows high or observable amount of wrinkling. When the BHF is 14 kN, the earing is increased by 2.44%. However, when the BHF is 9 kN, optimized earing is observed and wrinkling is reduced. For the low-carbon steel, BHF of 15 kN shows 4.52% earing which is the smallest among others and also shows high wrinkling defect. BHF of 25 kN shows 9.52% earing which is the highest among others and BHF of 20 kN provides with intermediate value of earing and reduced wrinkling (Table 5).

From Table 4, the low-carbon steel shows high amount of earing when it is compared with the AA6061 alloy. This is due to the plastic anisotropic properties of the low-carbon steel as shown in Table 3. It was, thus, observed that blank holder force significantly affects the cup height and quality of the deep drawn cup of both AA6061 and low-carbon steel. This result illustrates that the earing height also increased with the increase in BHF.

Table 4 Planar anisotropy parameter (Δr) and normal anisotropy parameter (r_m) values

Material	Planar anisotropy parameter (Δr)	Normal anisotropy parameter (r_m)
AA6061	0.01	0.836
Low-carbon steel	0.22	1.71

Table 5 Variation of earing of AA6061 and low-carbon steel cups with varying blank holding force (other parameters kept constant)

Material	Blank holding force (kN)	Earing %
AA6061 alloy	6	2.52
	9	2.88
	14	4.96
Low-carbon steel	15	4.52
	20	6.45
	25	9.52

Conclusion

In the present study, investigating the effect of blank holding force (BHF) on earing defect by using finite element analysis was proposed to the circular deep drawing process of AA6061 and low-carbon steel sheets. The following conclusions are drawn:

- Circular blank with diameter of 90 mm was designed.
- Tensile testing is conducted to determine the mechanical properties of the materials.
- Numerical simulation of deep drawing process is done with blank holder force of 1–50 kN using PAMSTAMP 2G software.
- Drawing setups are designed and manufactured.
- Deep drawing experiment is conducted with varying blank holder force.
- The present study revealed that the blank holding force of 9 and 20 kN for AA6061 and low-carbon steel sheets, respectively, have showed a noticeable earing height reduction by 2.08% and 3.07%. The simulated result also showed when the blank holder force is below 9 and 20 kN, the wrinkling is increased and when it is above 9 and 20 kN, tearing phenomenon is increased for both AA6061 and low-carbon steel sheet, respectively.
- The tensile experimental result showed higher tendency of earing for low-carbon steel than AA6061 as the planar anisotropy (AA6061, $\Delta r = 0.11$, and $\Delta r = 0.22$) and the deep drawability of low-carbon steel are greater than AA6061 as it is given by the normal anisotropy (AA6061, $r_m = 0.836$ and low-carbon steel, $r_m = 0.836$).

References

1. Ghosh A, Mallik AK (2011) Manufacturing science, 2nd edn. Affiliated East West Press
2. Das P, Panda SK, Pratihari DK (2013) Modification of initial blank shape to minimize earing in deep drawing process. *Int J Adv Mater Manuf Charact* 3(1):99–104
3. Nagda PS, Bhatt PS, Shah MK (2017) Finite element simulation of deep drawing process to minimize earing. *World Acad Sci Eng Technol Int J Mech Mechatron Eng* 11(2):413–416
4. Patel R, Dave H, Raval H (2015) Study of earing defect during deep drawing process with finite element simulation. *Key Eng Mater* 639(3):91–98
5. Ahmetoglu MA, Altan T, Kinzel GL (1992) Improvement of part quality in stamping by controlling blank-holder force and pressure. *J Mater Process Tech* 33(1–2):195–214
6. Reddy PV, Ramulu PJ, Madhuri GS, Govardhan D, Prasad PVS (2016) Design and analysis of deep drawing process on angular deep drawing dies for different anisotropic materials. *IOP Conf Ser Mater Sci Eng* 149(1)
7. Joshi AR, Kothari KD, Jhala RL (2013) Effects of different parameters on deep drawing process: review. *Int J Eng Res Technol (IJERT)* 2
8. Singh A, Basak S, Lin LP, Roy GG, Jha MN, Mascarenhas M, Panda SK (2018) Prediction of earing defect and deep drawing behavior of commercially pure titanium sheets using CPB06 anisotropy yield theory. *J Manuf Process* 33(September):256–267

9. Srirat J, Kitayama S, Yamazaki K (2012) Optimization of initial blank shape with a variable blank holder force in deep-drawing via sequential approximate optimization. *J Adv Mech Des Syst Manuf* 6(7):1093–1106
10. Han J, Yamazaki K, Makino S, Shirasawa T (2013) Optimization of deep drawing process for circular cup forming. In: 10th World congress on structural and multidisciplinary optimization May, vol 19, p 24
11. Muhsin Younis DK, Shbeeb Jaber A (2011) Experimental and theoretical study of interaction. *Eng Tech J* 29(12):1143–1152
12. Dixit PM, Saxena RK (2009) Finite element simulation of earing defect in deep drawing. *Int J Adv Manuf Technol* 45:219–233
13. Desai SG, Pardeshi RH, Date PP (2005) Study of various initial blank shapes to minimize the earing in the different shaped formed parts using finite element analysis. *AIP Conf Proc* 778 A:855–860
14. Gürün H, Karaağaç I (2015) The experimental investigation of effects of multiple parameters on the formability of the DC01 sheet metal. *Strojnicki Vestnik/J Mech Eng* 61(11):651–662. <https://doi.org/10.5545/sv-jme.2015.2562>
15. Yoon JW, Dick RE, Barlat F (2011) A new analytical theory for earing generated from anisotropic plasticity. *Int J Plast* 27(8):1165–1184
16. Trzepieciński T, Gelgele HL (2010) Investigation of anisotropy problems in sheet metal forming using finite element method. *Int J Mater Form* 4:357–369
17. Athale M, Gupta AK, Singh SK, Vaidyanathan A (2017) Analytical and finite element simulation studies on earing profile of Ti-6Al-4V deep drawn cups at elevated temperatures. *Int J Mater Form* 11:479–490
18. Groover MP (2010) *Fundamentals of modern manufacturing*, 4th edn. John Wiley & Sons, Inc. 10:987654321
19. Hu P, Liu Y, Wang J (2001) Numerical study of the flange earing of deep-drawing sheets with stronger anisotropy. *Int J Mech Sci* 43:279–296

On the Generalized Plane-Strain Constraints for Orthotropic Plasticity Modeling of Sheet Metals



Jie Sheng, Seung-Yong Yang, and Wei Tong

Abstract Generalized plane-strain constraints have recently been proposed in the literature as a rather general restriction on admissible anisotropic plastic potentials for modeling all FCC or BCC sheet metals. In addition to the early proposed shear constraint, a set of seven constraints have been advocated to be physically necessary for plane-strain tension and compression of those sheet metals as well. This study examines first the implication of such constraints on Gotoh's 1977 non-quadratic yield criterion. These new constraints are then investigated in the context of crystal plasticity modeling of FCC crystals. Finally, the experimental evidence that is used to support these constraints is re-assessed upon the study of Gotoh's 1977 fourth-order yield criterion and crystal plasticity modeling. The applicability of newly proposed generalized plane-strain constraints for sheet metal plasticity modeling in general is discussed in the end.

Introduction

Due to its independence on hydro-static pressure and incompressibility, plasticity of a metal piece under a Cauchy stress $\boldsymbol{\sigma}$ with its ordered principal stresses $\sigma_1 \geq \sigma_2 \geq \sigma_3$ may be modeled in terms of the deviatoric stress \boldsymbol{s} [1–3], where its ordered principal stresses $s_1 \geq s_2 \geq s_3$ are given as

$$3s_1 = 2\sigma_1 - \sigma_2 - \sigma_3, \quad 3s_2 = 2\sigma_2 - \sigma_3 - \sigma_1, \quad 3s_3 = 2\sigma_3 - \sigma_1 - \sigma_2. \quad (1)$$

J. Sheng (✉) · W. Tong
Southern Methodist University, Dallas, TX 75275, USA
e-mail: sheng@mail.smu.edu

W. Tong
e-mail: wtong@smu.edu

S.-Y. Yang
Korea University of Technology and Education, Chungnam 31253, Korea
e-mail: ysy@koreatech.ac.kr

Its three invariants can also be readily computed as

$$J_1(\mathbf{s}) = s_1 + s_2 + s_3 = 0, \quad 2J_2(\mathbf{s}) = s_1^2 + s_2^2 + s_3^2, \quad J_3(\mathbf{s}) = s_1 s_2 s_3. \quad (2)$$

It has been proposed recently [4, 5] that an anisotropic plastic potential function for modeling sheet metal plasticity $g(\sigma_1, \sigma_2, \sigma_3)$ must satisfy the generalized plane strain constraint (noting $\dot{\varepsilon}_1^p + \dot{\varepsilon}_2^p + \dot{\varepsilon}_3^p = 0$ so $\dot{\varepsilon}_2^p = 0$ is equivalent to $\dot{\varepsilon}_3^p = -\dot{\varepsilon}_1^p$)

$$\dot{\varepsilon}_2^p = \dot{\lambda} \frac{\partial g}{\partial \sigma_2} = 0 \quad \text{or} \quad \frac{\dot{\varepsilon}_3^p}{\dot{\varepsilon}_1^p} = \frac{\partial g}{\partial \sigma_3} / \frac{\partial g}{\partial \sigma_1} = -1 \quad (3)$$

under the critical deviatoric loading (where $\partial J_2 / \partial s_2 = 0$) as defined in [5]

$$s_2 = J_3(\mathbf{s}) = 0, \quad s_3 = -s_1, \quad J_2(\mathbf{s}) = s_1^2. \quad (4)$$

For a sheet metal under plane stress $\boldsymbol{\sigma} = (\sigma_x, \sigma_y, \tau_{xy})$ where xy -axes are rolling and transverse directions, respectively, two special cases of the critical deviatoric loading have been considered, namely, in-plane shear [4, 5] and biaxial tension [5]. Assuming on-axis loading $\tau_{xy} = 0$ for simplicity, the new plastic flow constraint per Eq. (3) under in-plane shear per Eq. (4) are given as (also called the shear constraint in [4])

$$\begin{aligned} \dot{\varepsilon}_z^p = 0 \quad \text{or} \quad \dot{\varepsilon}_y^p / \dot{\varepsilon}_x^p = -1 : \quad \sigma_1 = \sigma_x > 0, \quad \sigma_2 = \sigma_z = 0, \quad \sigma_3 = \sigma_y = -\sigma_x, \\ \dot{\varepsilon}_z^p = 0 \quad \text{or} \quad \dot{\varepsilon}_x^p / \dot{\varepsilon}_y^p = -1 : \quad \sigma_1 = \sigma_y > 0, \quad \sigma_2 = \sigma_z = 0, \quad \sigma_3 = \sigma_x = -\sigma_y. \end{aligned} \quad (5)$$

Similarly, the new plastic flow constraint per Eq. (3) under biaxial tension per Eq. (4) are given as [5]

$$\begin{aligned} \dot{\varepsilon}_y^p = 0 \quad \text{or} \quad \dot{\varepsilon}_z^p / \dot{\varepsilon}_x^p = -1 : \quad \sigma_1 = \sigma_x > 0, \quad 2\sigma_2 = 2\sigma_y = \sigma_x, \quad \sigma_3 = \sigma_z = 0, \\ \dot{\varepsilon}_x^p = 0 \quad \text{or} \quad \dot{\varepsilon}_z^p / \dot{\varepsilon}_y^p = -1 : \quad \sigma_1 = \sigma_y > 0, \quad 2\sigma_2 = 2\sigma_x = \sigma_y, \quad \sigma_3 = \sigma_z = 0. \end{aligned} \quad (6)$$

The implication and applicability of the shear constraint Eq. (5) have already been examined by Tong et al. [6] in the context of Gotoh's 1977 non-quadratic yield criterion [7]. In this study, the same approach is applied to examine the implication of the new plane-strain constraint Eq. (6) on Gotoh's 1977 fourth-order homogeneous polynomial stress function. The new shear and plane-strain constraints are then investigated in the context of crystal plasticity modeling of cubic crystals. Finally, the experimental evidence that is used to support these constraints is re-assessed upon the study of Gotoh's 1977 fourth-order stress function and crystal plasticity modeling. The general applicability of newly proposed two constraints for sheet metal plasticity modeling is discussed in the end.

Gotoh’s Fourth-Order Flow Potential Under the Plane-Strain Tension Constraint

Gotoh’s non-quadratic or quartic yield stress function has the following form [7]:

$$\begin{aligned} \Phi_4(\sigma_x, \sigma_y, \tau_{xy}) = & A_1\sigma_x^4 + A_2\sigma_x^3\sigma_y + A_3\sigma_x^2\sigma_y^2 + A_4\sigma_x\sigma_y^3 \\ & + A_5\sigma_y^4 + A_6\sigma_x^2\tau_{xy}^2 + A_7\sigma_x\sigma_y\tau_{xy}^2 + A_8\sigma_y^2\tau_{xy}^2 + A_9\tau_{xy}^4, \end{aligned} \tag{7}$$

where $A_1, A_2, \dots,$ and A_9 are its nine material constants. The corresponding flow potential of homogeneous degree one in stress $g(\boldsymbol{\sigma})$ is given as $g^4(\boldsymbol{\sigma}) = \Phi_4(\boldsymbol{\sigma})$. Under only on-axis biaxial plane stress $\boldsymbol{\sigma} = (\sigma_x, \sigma_y, 0)$, plastic axial strain increments per the flow rule are

$$\begin{aligned} \dot{\epsilon}_x = \lambda \partial g / \partial \sigma_x \propto & 4A_1\sigma_x^3 + 3A_2\sigma_x^2\sigma_y + 2A_3\sigma_x\sigma_y^2 + A_4\sigma_y^3, \\ \dot{\epsilon}_y = \lambda \partial g / \partial \sigma_y \propto & A_2\sigma_x^3 + 2A_3\sigma_x^2\sigma_y + 3A_4\sigma_x\sigma_y^2 + 4A_5\sigma_y^3. \end{aligned} \tag{8}$$

So, the new constraints in biaxial tension with a zero axial strain in either transverse or rolling direction imply

$$\begin{aligned} 2\sigma_y = \sigma_x > 0, \quad \dot{\epsilon}_y = 0 : & A_2\sigma_x^3 + 2A_3\sigma_x^2\sigma_y + 3A_4\sigma_x\sigma_y^2 + 4A_5\sigma_y^3 = 0, \\ 2\sigma_x = \sigma_y > 0, \quad \dot{\epsilon}_x = 0 : & 4A_1\sigma_x^3 + 3A_2\sigma_x^2\sigma_y + 2A_3\sigma_x\sigma_y^2 + A_4\sigma_y^3 = 0. \end{aligned} \tag{9}$$

That is, there exist two additional conditions imposed on the five polynomial coefficients

$$4A_2 + 4A_3 + 3A_4 + 2A_5 = 0, \quad 2A_1 + 3A_2 + 4A_3 + 4A_4 = 0. \tag{10}$$

It is noted that there are only four independent material constants in Gotoh’s biaxial plastic flow potential. Assuming $A_1 = 1$ per convention and using the plastic strain ratios under uniaxial tension in rolling and transverse directions [7, 8]

$$R_0 = -\frac{A_2}{4A_1 + A_2}, \quad R_{90} = -\frac{A_4}{A_4 + 4A_5}, \tag{11}$$

one can readily obtain the remaining four polynomial coefficients from Eqs.(10)–(11). The resulting Gotoh’s plastic potential is applicable for on-axis biaxial tension from uniaxial tension in the rolling direction to uniaxial tension in the transverse direction ($\sigma_x \geq 0$ and $\sigma_y \geq 0$).

Recall that the restrictive condition imposed by the shear constraint of Eq.(5) on the polynomial coefficients has been derived in [6] as

$$2A_1 - A_2 = 2A_5 - A_4. \tag{12}$$

This can be seen from Eq. (5)₁ and Eq. (8) as

$$-\dot{\varepsilon}_z = \dot{\varepsilon}_x + \dot{\varepsilon}_y = 0, \quad \sigma_y = -\sigma_x > 0: \quad 2A_1 - A_2 + A_4 - 2A_5 = 0. \quad (13)$$

It turns out that Eq. (12) can also be obtained from two equations in Eq. (10) by eliminating A_3 . That is, under on-axis biaxial loading, the plane-strain tension constraints of Eq. (10) imply automatically the shear constraint of Eq. (12) for Gotoh's flow potential.

Crystal Plasticity Modeling Under the Generalized Plane-Strain Constraints

Flow Potential for FCC Crystals

According to [5], the generalized plane-strain constraints for shear and plane-strain tension Eqs. (3)–(6) are deemed applicable to all FCC and BCC metals, where plastic deformation is slip-dominated but not to HCP metals at all where twinning plays a significant role in their plastic deformation. We thus consider here the implication of those constraints on plasticity modeling of FCC crystals.

A single crystal may be modeled by a microscopic yield stress function or its dual plastic strain-rate function just like any continuum material element [9–14]. For example, a slip potential for an FCC single crystal may have the following form per the regularized Schmid law:

$$\phi_b(\tau^{(1)}, \dots, \tau^{(12)}) = w_1|\tau^{(1)}|^b + w_2|\tau^{(2)}|^b + \dots = \sum_{\alpha=1}^{12} w_\alpha|\tau^{(\alpha)}|^b, \quad (14)$$

where $(\tau^{(1)}, \dots, \tau^{(12)})$ are resolved shear stresses, (w_1, \dots, w_{12}) are non-negative weights related to the relative slip resistance of twelve slip systems in the FCC crystal, and $b > 1$ is the stress exponent. The resolved shear stress on α th slip system of the FCC crystal can be directly computed via $\tau^{(\alpha)} = \boldsymbol{\sigma}^* \mathbf{m}^{(\alpha)} \cdot \mathbf{s}^{(\alpha)}$, where $\boldsymbol{\sigma}^* = (\sigma_{11}, \sigma_{22}, \sigma_{33}, \tau_{12}, \tau_{23}, \tau_{31})$ is the Cauchy stress in terms of cubic 123-axes and $(\mathbf{m}^{(\alpha)}, \mathbf{s}^{(\alpha)})$ are the unit slip plane normal and slip direction of the 12 slip systems as shown in Table 1 (including the corresponding resolved shear stresses). The names for incremental slips are similar but slightly different from those originally used by Bishop and Hill [15].

For simplicity, we consider the quadratic slip potential ($b = 2$) with an orthotropic symmetry along the cubic axes for modeling an FCC single crystal under plane stress $\boldsymbol{\sigma}^* = (\sigma_{11}, \sigma_{22}, 0, \tau_{12}, 0, 0)$, namely

$$\phi_{2o} = a_1\sigma_{11}^2 + a_2\sigma_{11}\sigma_{22} + a_3\sigma_{22}^2 + (a_1 + a_2 + a_3)\tau_{12}^2, \quad (15)$$

Table 1 Slip systems in FCC crystals

Number α	Incremental slip	Normal $\mathbf{m}^{(\alpha)}$	Direction $\mathbf{s}^{(\alpha)}$	Resolved shear stress $\sqrt{6}\tau^{(\alpha)}$
1	$\dot{\gamma}_{a1}$		$[01\bar{1}]$	$\sigma_{22} - \sigma_{33} + \tau_{12} - \tau_{31}$
2	$\dot{\gamma}_{a2}$	(111)	$[\bar{1}01]$	$\sigma_{33} - \sigma_{11} - \tau_{12} + \tau_{23}$
3	$\dot{\gamma}_{a3}$		$[1\bar{1}0]$	$\sigma_{11} - \sigma_{22} + \tau_{13} - \tau_{23}$
4	$\dot{\gamma}_{b1}$		$[0\bar{1}\bar{1}]$	$\sigma_{22} - \sigma_{33} + \tau_{12} + \tau_{31}$
5	$\dot{\gamma}_{b2}$	($\bar{1}\bar{1}1$)	$[101]$	$\sigma_{33} - \sigma_{11} - \tau_{12} - \tau_{23}$
6	$\dot{\gamma}_{b3}$		$[\bar{1}10]$	$\sigma_{11} - \sigma_{22} - \tau_{13} + \tau_{23}$
7	$\dot{\gamma}_{c1}$		$[01\bar{1}]$	$\sigma_{22} - \sigma_{33} - \tau_{12} + \tau_{13}$
8	$\dot{\gamma}_{c2}$	($\bar{1}11$)	$[101]$	$\sigma_{33} - \sigma_{11} + \tau_{12} + \tau_{23}$
9	$\dot{\gamma}_{c3}$		$[\bar{1}\bar{1}0]$	$\sigma_{11} - \sigma_{22} - \tau_{13} - \tau_{23}$
10	$\dot{\gamma}_{d1}$		$[0\bar{1}\bar{1}]$	$\sigma_{22} - \sigma_{33} - \tau_{12} - \tau_{13}$
11	$\dot{\gamma}_{d2}$	($1\bar{1}1$)	$[\bar{1}01]$	$\sigma_{33} - \sigma_{11} + \tau_{12} - \tau_{23}$
12	$\dot{\gamma}_{d3}$		$[110]$	$\sigma_{11} - \sigma_{22} + \tau_{13} + \tau_{23}$

where one can show that [16]

$$\begin{aligned}
 a_1 &= (w_2 + w_3 + w_5 + w_6 + w_8 + w_9 + w_{11} + w_{12})/6, \\
 a_2 &= -(w_3 + w_6 + w_9 + w_{12})/3, \quad a_7 = (w_2 + w_5 - w_8 - w_{11})/3, \\
 a_3 &= (w_1 + w_3 + w_4 + w_6 + w_7 + w_9 + w_{10} + w_{12})/6.
 \end{aligned}
 \tag{16}$$

By applying the slip rule to the slip potential above (analogous to the flow rule and flow potential in macroscopic plasticity), one obtains plastic strain increments of the single crystal as

$$\dot{\epsilon}_{11} \propto 2a_1\sigma_{11} + a_2\sigma_{22}, \quad \dot{\epsilon}_{22} \propto a_2\sigma_{11} + 2a_3\sigma_{22}, \quad \dot{\gamma}_{12} \propto (a_1 + a_2 + a_3)\tau_{12}. \tag{17}$$

Effects of New Shear and Plane-Strain Tension Constraints

If $\tau_{12} = 0$, then the new shear and plane-strain constraints of Eq.(5) and Eq.(6) apply to the orthotropic FCC single crystal as well with $(\sigma_x, \sigma_y) = (\sigma_{11}, \sigma_{22})$ and $(\dot{\epsilon}_x, \dot{\epsilon}_y) = (\dot{\epsilon}_{11}, \dot{\epsilon}_{22})$, namely

$$\text{in-plane shear : } \frac{a_2 - 2a_3}{2a_1 - a_2} = -1, \quad \frac{a_2 - 2a_1}{2a_3 - a_2} = -1, \quad \text{or } a_3 = a_1; \tag{18}$$

$$\text{biaxial tension : } a_2 + a_3 = 0, \quad a_2 + a_1 = 0, \quad \text{or } a_2 = -a_1 = -a_3. \tag{19}$$

That is, the quadratic slip potential of Eq. (15) becomes

$$\phi_{2c} = a_1(\sigma_{11}^2 - \sigma_{11}\sigma_{22} + \sigma_{22}^2 + \tau_{12}^2), \quad (20)$$

which models an FCC single crystal with the highest or cubic symmetry [16].

Discussion and Conclusions

As pointed out in [6], there are typically three types (levels) of constraints (conditions) imposed on an anisotropic yield function/flow potential in the mathematical theory of metal plasticity. Positivity and convexity are the first-level or most basic ones and thus are universal. Independence of hydro-static pressure (at least on its magnitude if not on its sign as well) and plastic incompressibility are also commonly imposed conditions for modeling metals. These can be regarded as the second type of general constraints in metal plasticity.

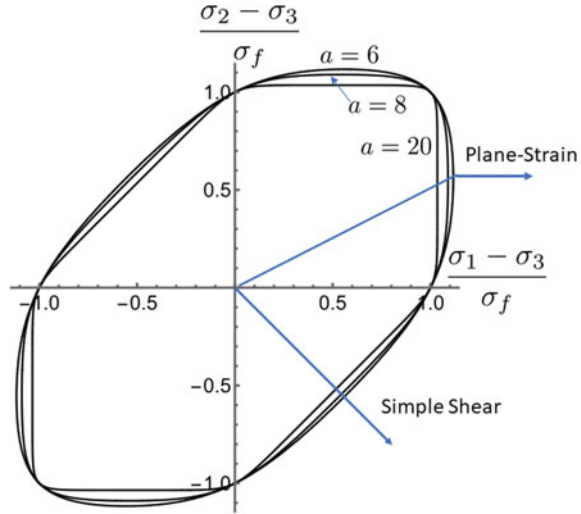
Third type of conditions are mostly heuristic, widely varying, and empirical in nature and they depend on the specific modeling flexibility and complexity requirements. For example, convex stress functions of different forms with various numbers of independent material constants may be considered depending on the availability of experimental inputs. Broadly speaking, these types of conditions are amounted to make various assumptions about the nature or degree of plastic anisotropy for a given sheet metal under study. Using only lower order stress functions, yield stress function, and a non-associated flow potential may be adapted to model highly anisotropic metals with many experimental inputs. On the other hand, when the measurement data are rather limited, one can impose various heuristic conditions for a given stress function with reduced anisotropy [8, 17] and thus a smaller number of independent material constants.

The newly proposed constraints for pure shear and plane-strain tension [4, 5] are of the third type imposed on an anisotropic flow potential for modeling sheet metal plasticity [6]. As presented in this study, they effectively reduce two polynomial coefficients from the biaxial Gotoh's fourth-order function so only R_0 and R_{90} are needed to fully calibrate the flow potential. It is well known that non-quadratic flow potentials with a large stress exponent are required for modeling even isotropic FCC and BCC sheet metals [18, 19]. For such sheet metals, the surface curvatures around the stress states under in-plane shear and plane-strain tension are rather flat (see Fig. 1). Any experimental evidence based on the plastic strain ratio measurements in supporting these constraints would be inconclusive with unavoidable uncertainties for both isotropic and anisotropic (textured) sheet metals.

Using $(R_0, R_{90}) = (0.93, 0.66)$ for an AA6111-T4 sheet studied in [6] as an example, the five polynomial coefficients of biaxial Gotoh's fourth-order flow potential under two plane-strain tension constraints are found to be (per Eq. (10) and (11)):

$$(A_1, A_2, A_3, A_4, A_5) = (1., -1.92746, 2.68528, -1.73968, 1.09389). \quad (21)$$

Fig. 1 Biaxial flow surfaces given by Hershy–Hosford non-quadratic isotropic flow potential [18, 19] with a stress exponent $a = 6, 8$ and 20 . The two vectors normal to the flow surface ($a = 6$) are at the stress states corresponding to the in-plane and out-of-plane plane-strain plastic flows, respectively



The corresponding plastic strain ratio under equal biaxial tension R_b is found to be 1.406 where [7, 8]

$$R_b = \frac{A_2 + 2A_3 + 3A_4 + 4A_5}{4A_1 + 3A_2 + 2A_3 + A_4}. \tag{22}$$

If Gotoh’s fourth-order stress function is used as both yield function and flow potential in an associated plasticity model, its five polynomial coefficients may be obtained using $(\sigma_0/\sigma_f, R_0, \sigma_{90}/\sigma_f, R_{90}, R_b) = (1, 0.93, 0.9575, 0.66, 1.406)$ as [8]

$$(A_1, A_2, A_3, A_4, A_5) = (1., -1.92746, 2.85891, -1.89205, 1.18970). \tag{23}$$

However, if the normalized shear strength $\sigma_{s0}/\sigma_f = 0.5819$ is used instead of $R_b = 1.406$, the corresponding polynomial coefficients are [6]

$$(A_1, A_2, A_3, A_4, A_5) = (1., -1.92746, 2.71259, -1.89205, 1.18970). \tag{24}$$

Furthermore, the three flow potentials with their coefficients given by Eqs. (21), (23) and (24) are certified to be strictly positive and convex per the necessary and sufficient algebraic condition [20, 21]

$$3A_1 + A_3 + 3A_5 \geq 0, \tag{25}$$

$$24A_1A_3 + 72A_1A_5 + 24A_3A_5 - 9A_2^2 - 2A_3^2 - 9A_4^2 \geq 0, \tag{26}$$

$$72A_1A_3A_5 + 9A_2A_3A_4 - 2A_3^3 - 27A_1A_4^2 - 27A_2^2A_5 \geq 0. \tag{27}$$

It is interesting to note that under pure shear ($\sigma_y = -\sigma_x > 0, \sigma_x = -\sigma_y > 0$) or other two critical deviatoric loading cases ($\sigma_x = 2\sigma_y > 0, \sigma_y = 2\sigma_x > 0$), the

plane-strain conditions are not strictly satisfied by the flow potentials of Eqs. (23) and (24). Nevertheless, the related strain ratios are all very close to -1. For the flow potential given by Eq. (23), one has (see Eqs. (5) and (6))

$$\dot{\epsilon}_y^p / \dot{\epsilon}_x^p = -1.0397, \quad \dot{\epsilon}_x^p / \dot{\epsilon}_y^p = -0.9619, \quad \dot{\epsilon}_x^p / \dot{\epsilon}_x^p = -1.0466, \quad \dot{\epsilon}_z^p / \dot{\epsilon}_y^p = -1.0068. \tag{28}$$

For the flow potential given by Eq. (24), those strain ratios are

$$\dot{\epsilon}_y^p / \dot{\epsilon}_x^p = -1.0402, \quad \dot{\epsilon}_x^p / \dot{\epsilon}_y^p = -0.9613, \quad \dot{\epsilon}_x^p / \dot{\epsilon}_x^p = -0.9825, \quad \dot{\epsilon}_z^p / \dot{\epsilon}_y^p = -0.9588. \tag{29}$$

That is, they are approximately near the plane-strain conditions under those loading cases. This fact can be seen more clearly from biaxial flow surfaces defined by these three Gotoh’s flow potentials shown in Fig. 2 in both stress (a) and strain-rate (b) spaces. Within the experimental uncertainties, those three flow potentials may be regarded as equivalent but the flow potential given by Eq. (21) is more restrictive than the other two potentials given by either Eq. (23) or Eq. (24).

In conclusion, it is found that the two plane-strain tension constraints proposed in [5] also imply the shear constraint proposed in [4] for biaxial Gotoh’s quartic stress function. When applying those constraints to a quadratic slip potential for an FCC single crystal, it reduces its plastic anisotropy to the cubic symmetry. These constraints limit the capability of a given flow potential by reducing its number of independent material constants, so it can only model a reduced degree of anisotropy in a sheet metal.

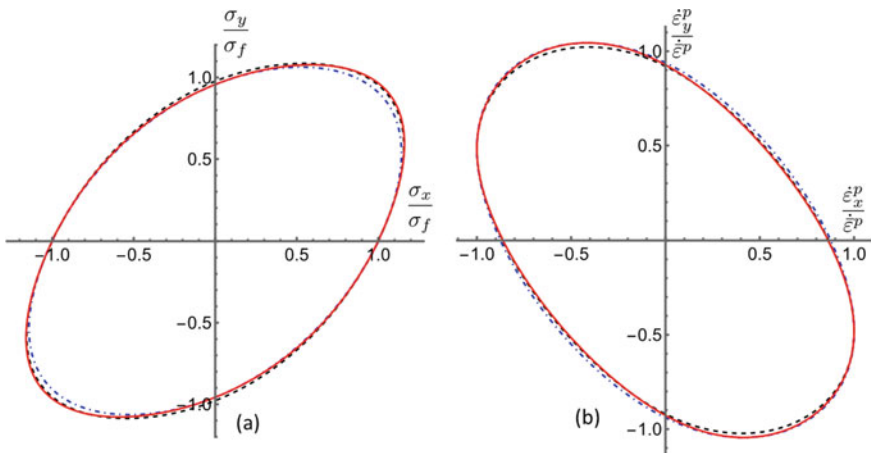


Fig. 2 Biaxial Gotoh’s flow surfaces in **a** stress and **b** strain-rate spaces based on polynomial coefficients from Eq. (21) (dashed lines), Eq. (23) (dotted-dashed lines) and Eq. (24) (solid lines)

References

1. Hill R (1950) *The mathematical theory of plasticity*. Oxford University Press, London
2. Lubliner J (1990) *Plastic theory*. Macmillan, New York
3. Maugin GA (1992) *The thermomechanics of plasticity and fracture*. Cambridge University Press, Cambridge
4. Abedini A, Butcher C, Rahmaan T, Worswick MJ (2018) Evaluation and calibration of anisotropic yield criteria in shear Loading: constraints to eliminate numerical artefacts. *Int J Solids Struct* 151:118–134
5. Butcher C, Abedini A (2019) On anisotropic plasticity models using linear transformations on the deviatoric stress: physical constraints on plastic flow in generalized plane strain. *Int J Mech Sci* 161–162:105044
6. Tong W, Alharbi M, Sheng J (2020) On the new shear constraint for plane-stress orthotropic plasticity modeling of sheet metals. *Exp Mech* 60:889–905
7. Gotoh M (1977) A theory of plastic anisotropy based on a yield function of fourth order (plane stress state). *Int J Mech Sci* 19:505–520
8. Tong W (2018) An improved method of determining Gotoh's nine material constants for a sheet metal with only seven or less experimental inputs. *Int J Mech Sci* 140:394–406
9. Hill R (1987) Constitutive dual potentials in classical plasticity. *J Mech Phys Solids* 31(1):23–33
10. Montheillet F, Gilormini P, Jonas JJ (1985) Relation between axial stresses and texture development during torsion testing: a simplified theory. *Acta Metall* 33:4705
11. Arminjon M, Bacroix B (1990) On plastic potentials for anisotropic metals and their derivation from texture function. *Acta Mech* 88:219
12. Arminjon M (1991) A regular form of the Schmid law, application to the ambiguity problem. *Textures and Microstruct* 14–18:1121–1128
13. Darrieulat M, Piot D (1996) A method of generating analytical yield surfaces of polycrystalline materials. *Int J Plast* 12:575–610
14. Darrieulat M, Montheillet F (2003) A texture based continuum approach for predicting the plastic behaviour of rolled sheet. *Int J Plast* 19:517–546
15. Bishop JFW, Hill R (1951) A theoretical derivation of the plastic properties of a polycrystalline face centered metal. *Philos Mag* 42:1298–1307
16. Sheng J, Yang S-Y, Tong W On the quadratic yield criterion for FCC single crystals (in preparation)
17. Tong W (2018) Calibration of a complete homogeneous polynomial yield function of six degrees for modeling orthotropic steel sheets. *Acta Mech* 229:2495–2519
18. Hershey AV (1954) The plasticity of an isotropic aggregate of anisotropic face centered cubic crystals. *J Appl Mech* 21:241–249
19. Hosford WF (1972) A generalized isotropic yield criterion. *J Appl Mech* 39:607–609
20. Tong W (2018) Algebraic convexity conditions for Gotoh's nonquadratic yield function. *ASME J Appl Mech* 85:074501–1
21. Tong W (2018) On the certification of positive and convex Gotoh's fourth-order yield function. *J Phys: Conf Ser* 1063:012093

Springback Investigation of Advanced Path-Dependent Constitutive Models for Sheet Metal Forming



Yanfeng Yang, Hocine Chalal, Cyrille Baudouin, Gabriela Vincze, and Tudor Balan

Abstract Sheet forming processes generally induce complex loading conditions, including monotonic, reversal, and orthogonal strain paths. Complex work hardening behavior of the sheet metal is revealed when the deformation path involves several steps. In order to investigate the forming conditions that require more advanced hardening models, a specific tension bend under tension (BUT) test configuration has been implemented. The test bench allows to characterize the springback after drawing-like forming processes for different values of tool radius and tension in the sheet. Isotropic and combined isotropic-kinematic hardening models are compared in the framework of refined FE simulations of the experiment. Test configurations are identified where one, the other, or none of the tested models is sufficiently accurate to predict springback. For a few configurations, the need for advanced hardening models is clearly demonstrated.

Introduction

Nowadays, the advanced high-strength steel (AHSS) is widely used in automobile industry with the increasing demands of energy saving and emission reduction. Springback is main defect for AHSS during sheet metal forming processes, especially involving complex loading path changes, e.g., in [1–3]. In this paper, in order to investigate the forming conditions that require more advanced hardening models, a specific tension bend under tension (BUT) test configuration has been implemented. A series BUT tests for DP600 with different loading conditions are performed and

Y. Yang · C. Baudouin · T. Balan (✉)

Arts et Metiers Institute of Technology, Université de Lorraine, LCFC, F-57000 Metz, France
e-mail: tudor.balan@ensam.eu

H. Chalal

Arts et Metiers Institute of Technology, Université de Lorraine, LEM3, F-57000 Metz, France

G. Vincze

Center for Mechanical Technology and Automation, Department of Mechanical Engineering, University of Aveiro, Campus Universitário de Santiago, 3810193 Santiago, Portugal

analyzed. Moreover, two hardening models: isotropic hardening Swift-Voce (IH) and modified Chaboche hardening (mod IKH) are employed to predict springback. Compared with experimental results, such two hardening models are discriminated.

The BUT test configuration used for this research and experimental results is described in Sect. 2, while Sect. 3 describes the numerical simulations of BUT and the results. Finally, the confrontations between simulations and experiments of BUT lead to the conclusions in Sect. 4.

BUT Test Configuration and Experimental Results

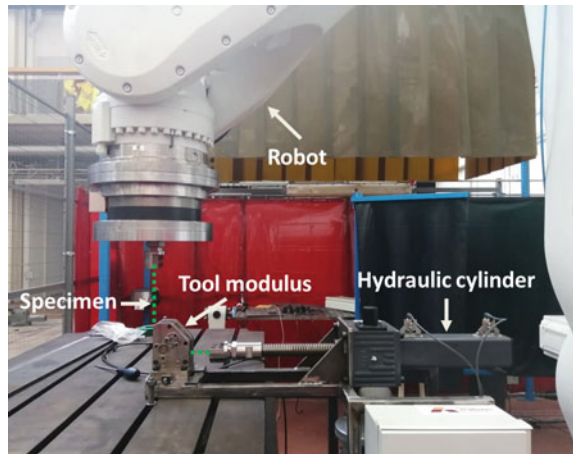
The bending under tension test configuration used in springback investigation is designed and built in LCFC, as illustrated in Fig. 1. The test bench allows characterizing the springback after drawing-like forming processes for different values of tool radius and tension in the sheet. This test bench includes three parts as given below:

1. Robot, providing a constant backforce.
2. Three different tool radii modulus.
3. Hydraulic cylinder, piloting the displacement in bending under tension processes.

For bending under tension springback investigation, two factors were studied: backforce factor k and the ratio of tools radius and thickness of sheet metal (R/t). The backforce factor can be defined by

$$k = \frac{F_b}{\sigma_0 \cdot w \cdot t} \quad (1)$$

Fig. 1 Bending under tension test configuration developed in LCFC



where F_b is the back force applied in bending under tension test, σ_0 is flow stress corresponding the strain at 0.02%, and w and t are width and thickness of specimen. Table 1 gives backforce factors and tools radii investigated in bending under tension test.

Figure 2 shows springback experimental investigation results of DP600 with applying different R/t and backforce factors k . From these experimental results, springback shows its obvious difference which validates the sensibility of investigated factors (R/t and k).

In order to describe and quantify springback after BUT test, here two indicators are employed: springback angle θ and curvature C . Figure 3 illustrates the definition of springback angle and its curvature. Figure 4 shows BUT experimental results of springback angle θ for DP600. Generally, the springback angle decreases with the increasing of backforce factor k for both two materials. For DP600, the experimental results in rolling direction (RD) and traverse direction (TD) don't show obvious dispersion. The maximum springback angle's gap between RD and TD is not more

Table 1 Influence factors of springback in bending under tension test

Configuration	Tools radius (R)	R/t	Backforce factor (k)					
			0.29	0.48	0.67	0.86	1.04	1.25
DP600	3 mm	2.46	0.29	0.48	0.67	0.86	1.04	1.25
	6 mm	4.92	0.29	0.48	0.67	0.86	1.05	1.24
	10 mm	8.2	0.29	0.48	0.67	0.85	1.05	1.25

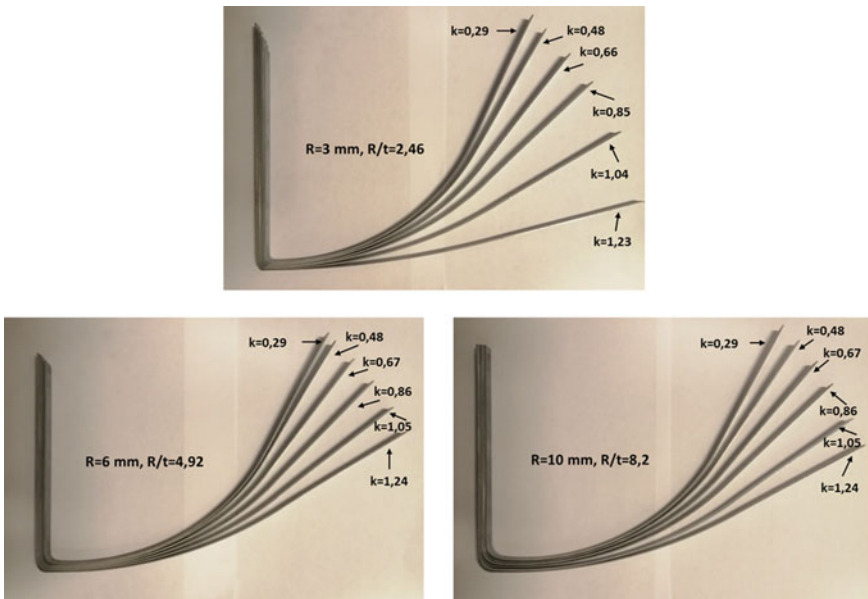


Fig. 2 BUT springback experimental investigation results of DP600

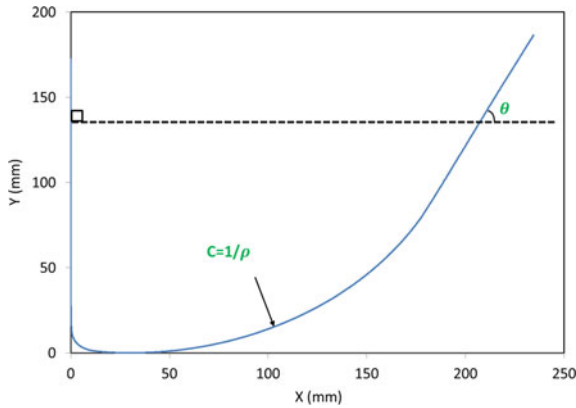


Fig. 3 Illustration measurement of springback angle θ and curvature C

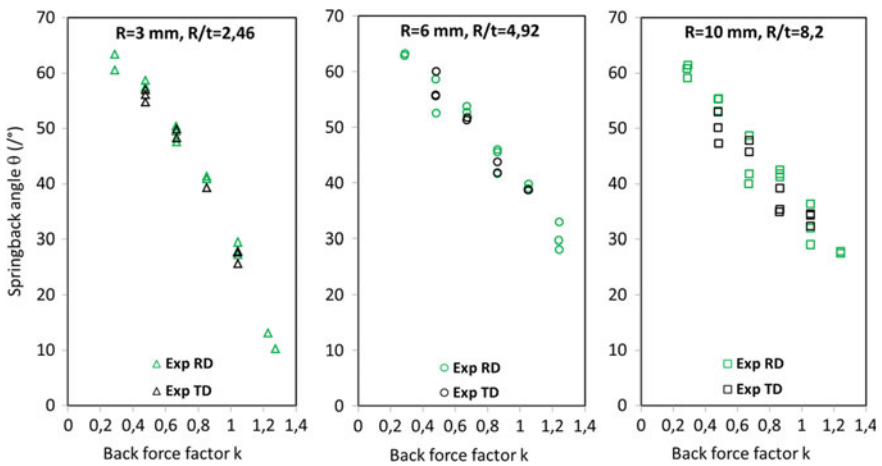


Fig. 4 Experimental results of springback angle θ of DP600

than 15° , which strengthens the use of von Mises in finite element simulation. And for local curvature shown in Fig. 5, the same influences trend caused by R/t and k are observed as well.

Numerical Simulations

The numerical simulation of BUT test is realized in Abaqus. In literature review [4–8], the predictions of simulation results are depended on hardening model, element type, number of elements through the thickness, etc. The hardening model considering the

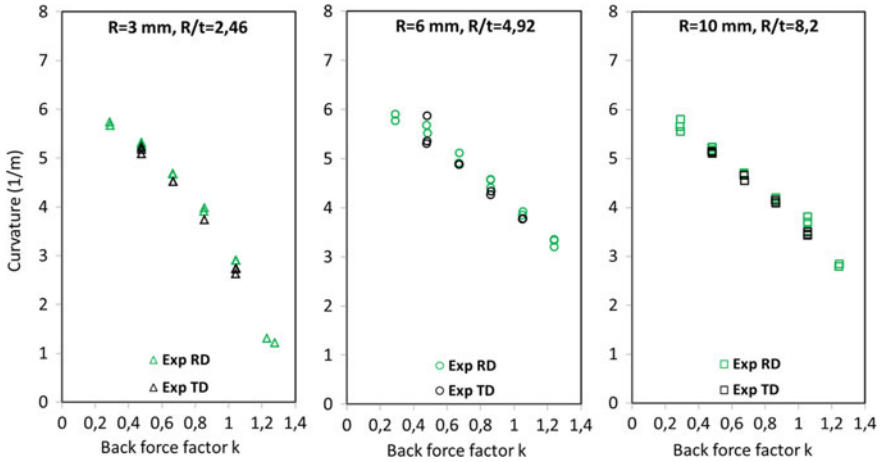


Fig. 5 Experimental results of local curvature of DP600

effect of different strain paths has strong influence on the simulation results. In this section, we investigate two types of hardening models: (a) IH: isotropic hardening model; (b) IKH mod: modified isotropic-kinematic hardening model.

Due to the isotropy of DP600, elasto-plastic material models are considered, defined by the following equations:

$$f(\boldsymbol{\sigma}, \mathbf{X}, R) = \tilde{\sigma}(\boldsymbol{\sigma}' - \mathbf{X}) - Y, \text{ yield function} \quad (2)$$

where $\boldsymbol{\sigma}$ is the Cauchy stress tensor, $\boldsymbol{\sigma}'$ denotes its deviatoric part, \mathbf{X} is an internal variable describing the current position of the yield surface, Y is the size of the yield surface, which can be decomposed into Y_0 (initial size of the yield surface), and R (isotropic hardening). In this work, von Mises isotropic yield function is considered. The total strain rate tensor $\dot{\boldsymbol{\epsilon}}$ can be decomposed in elastic strain rate $\dot{\boldsymbol{\epsilon}}^e$ and plastic strain rate $\dot{\boldsymbol{\epsilon}}^p$. The hypo-elastic law is expressed as

$$\dot{\boldsymbol{\sigma}} = \mathbf{C} : \dot{\boldsymbol{\epsilon}}^e = \mathbf{C} : (\dot{\boldsymbol{\epsilon}} - \dot{\boldsymbol{\epsilon}}^p), \quad (3)$$

where \mathbf{C} is the fourth-order tensor of elastic constants. The plastic strain rate tensor $\dot{\boldsymbol{\epsilon}}^p$ is given by the associated flow rule

$$\dot{\boldsymbol{\epsilon}}^p = \dot{\lambda} \cdot \mathbf{V} = \dot{\lambda} \cdot \frac{\partial f}{\partial \boldsymbol{\sigma}}, \quad (4)$$

where \mathbf{V} is the flow direction defined by the normality rule.

The hardening models used in this work include Swift-Voce isotropic hardening (IH) and modified Chaboche hardening (mod IKH). The so-called Swift-Voce isotropic hardening model is adopted, which is a classical combination of a power law and a saturating law:

$$\dot{R}_v = H_{R_v} \cdot \dot{\lambda} = C_R \cdot (R_{sat} - R_v) \cdot \dot{\lambda}, \quad (5)$$

$$\dot{R}_s = H_{R_s} \cdot \dot{\lambda} = n \cdot K^{1/n} (K \varepsilon_0^n)^{1/n} \cdot \dot{\lambda} \quad (6)$$

where C_R and R_{sat} are the parameters of Voce isotropic hardening described by variable R_v , and K , ε_0 , and n are the parameters of Swift isotropic hardening R_s . The resulting isotropic hardening is given by

$$\dot{Y} = \dot{R} = \dot{R}_v + \dot{R}_s, \text{ with } Y_0 = K \varepsilon_0^n, \quad (7)$$

$$H_Y = H_{R_v} + H_{R_s}. \quad (8)$$

When only isotropic hardening is used to simulate a monotonic loading mode, say uniaxial tension, then variable Y describes the evolution of the tensile stress σ_T component,

$$Y \equiv \sigma_T \text{ for isotropic hardening} \quad (9)$$

However, when kinematic hardening is taken into account, this equality does not hold anymore: one obtains $\sigma_T = Y + X^*$, where X^* is a scalar quantity corresponding to the tensile component of X under monotonic tensile loading, e.g., in [9, 10]. An alternative to overcome this drawback consists in explicitly modelling σ_T and calculate the size of the yield surface as

$$Y = \sigma_T - X^* \quad (10)$$

In the proposed approach, the isotropic part of the hardening model describes the yield stress under monotonic loading by the Swift-Voce rate equation

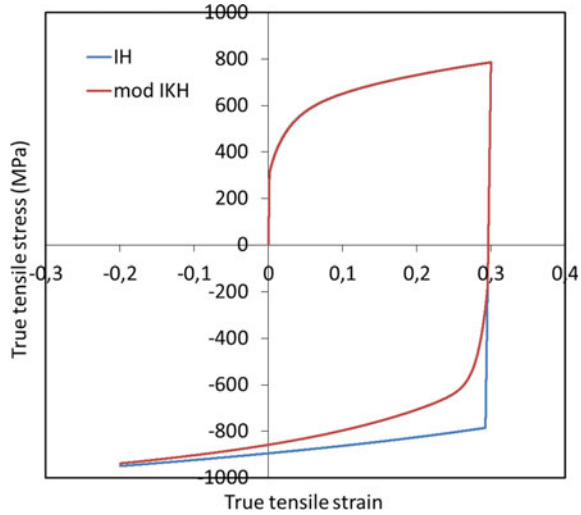
$$\dot{\sigma}_T = H_{\sigma_T} \cdot \dot{\lambda}, H_{\sigma_T} = H_{R_v} + H_{R_s} \quad (11)$$

The size Y of the yield surface is determined by Eq. (10), where X^* is also described by rate equations, corresponding to the tensile component of X under monotonic tensile loading:

$$\dot{X}_1 = H_{X1} \cdot \dot{\lambda}, H_{X1} = C_{X1}(X_{sat1} - X_1), \quad (12)$$

$$\dot{X}_2 = H_{X2} \cdot \dot{\lambda}, H_{X2} = C_{X2}(X_{sat2} - X_2), \quad (13)$$

Fig. 6 Uniaxial tension–compression simulations with using IH and mod IKH models



$$\dot{X}^* = \dot{X}_1 + \dot{X}_2, H_X^* = H_{X1} + H_{X2} \quad (14)$$

The rate of Eq. (10) becomes

$$H_Y = H_{\sigma_T} - H_X^* \quad (15)$$

In this modified method, the monotonic flow curve is described independently of the kinematic hardening model and its parameters, which makes it more robust and especially convenient for model comparison. Figure 6 shows uniaxial tension–compression simulations with using IH and mod IKH models. Compared with the simulation results from isotropic hardening (IH), the modified combined hardening model (mod IKH) can predict the identical simulation results in monotonic loading. Application of modified hardening model has advantage over the comparison for different hardening models which become more robust, especially for springback.

Confrontations and Discussions

In Fig. 7, IH and mod IKH models predict nearly the same springback angle when R/t is larger than 4. However, the trend of simulation results using IH is strange when R/t is smaller than 4, which need to be further studied. Moreover, at larger value of $R/t > 4$, both of two hardening models (IH, mod IKH) can predict springback at different backforce factor k very well. The developed BUT test configuration is not discriminant to clarify selected hardening models. However, at smaller value of $R/t < 4$, the predictions from IH and mod IKH are not the same at smaller k (0.29; 0.48)

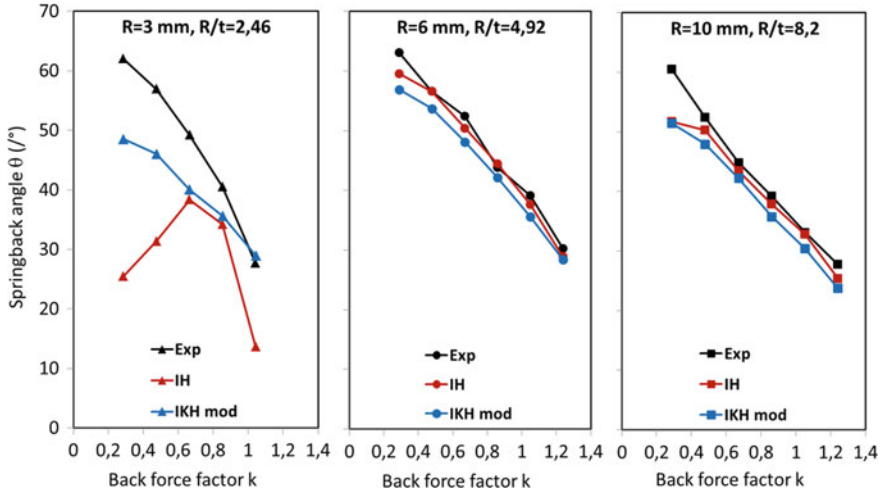


Fig. 7 Springback angle θ comparisons between experiment and simulation of DP600

and larger k (1.25). Compared with IH model, although mod IKH model improves predictions of springback angle, it still needs to enhance the springback prediction at $R/t = 2.46$ and $k = 0.29, 0.48, \text{ and } 1.25$.

Acknowledgements Gabriela Vincze acknowledges support from COMPETE 2020, in its FEDER/FNR component and the Portuguese Foundation of Science and Technology (FCT), in its State Budget component (OE) through projects POCI-01-0145-FEDER-032466. The authors thank Dr. Leopold Wagner in Voestalpine Stahl GmbH, Austria for the fruitful discussions and for providing the DP600 material.

References

1. Haddag B, Balan T, Abed-Meraim F (2007) Investigation of advanced strain-path dependent material models for sheet metal forming simulations. *Int J Plastic* 23:951–979
2. Qin J, Holmedal B, Hopperstad OS (2019) Experimental characterization and modeling of aluminum alloy AA3103 for complex single and double strain-path changes. *Int J Plasticity* 112:158–171
3. Wang J, Levkovitch V, Reusch F, Svendsen B, Huetink J, Van Riel M (2008) On the modeling of hardening in metals during non-proportional loading. *Int J Plasticity* 24:1039–1070
4. Carden WD, Geng LM, Matlock DK, Wagoner RH (2002) Measurement of springback. *Int J Mech Sci* 44:79–101
5. Li KP, Carden WP, Wagoner RH (2002) Simulation of springback. *Int J Mech Sci* 44:103–122
6. Wang JF, Wagoner RH, Matlock DK, Barlat F (2005) Anticlastic curvature in draw-bend springback. *J Solids Struct* 42:1287–1307
7. Wagoner RH, Li M (2007) Simulation of springback: through-thickness integration. *Int J Plast* 23:345–360
8. Chalal H, Racz S-G, Balan T (2012) Springback of thick sheet AHSS subject to bending under tension *Int J Mech Sci* 59:104–114

9. Yang Y, Balan T (2019) Prediction of the yield surface evolution and some apparent non-normality effects after abrupt strain-path change using classical plasticity. *Int J Plasticity* 119:331–343
10. Carbonniere J, Thuillier S, Sabourin F, Brunet M, Manach BY (2009) Comparison of the work hardening of metallic sheets in bending–unbending and simple shear. *Int J Mech Sci* 51:122–130

Stretch-Flanging Behavior of Dual-Phase Steel Using Single-Point Incremental Forming Process



Sandeep Pandre, Ayush Morchhale, Nitin Kotkunde, Kurra Suresh, and Swadesh Kumar Singh

Abstract Dual-Phase (DP) steel alloy is one of the mostly used in manufacturing of various automotive parts due to its good blend of mechanical properties. High strength and low formability make it difficult to form complex shapes and flanges, leading to fracture or higher springback. In this work, the conventional method of making the flanges is replaced with the incremental flanging operation. The flanging behavior of the DP steel is investigated by performing an incremental stretch-flanging operation on the rectangular blanks of different widths (25, 30, 40, and 50 mm) and lengths (20 and 30 mm). The Finite Element (FE) simulations are also performed, and the results are validated for one experimental condition for fixing the optimum mesh size. The various quality parameters, namely; strain path, thickness distribution, geometrical accuracy and surface roughness are analyzed using FE simulations, and the results are validated with the experimental findings. The critical elements considered near the edge region have experienced uniaxial tensile deformation, whereas the bend center has experienced plane strain compression. The average thickness variation for all the flange widths is approximately 8.1%. The DP steel has experienced low stiffness at the bottom of the flange, due to which the springback is more, and it increases with an increase in the flange length. The surface roughness of the flanges formed using incremental forming is higher than that on the as-received sheet, which is due to the continuous movement of the tool over the surface of the blank.

Keywords DP steel · Stretch-flanging · Incremental forming · Strain path · Geometrical accuracy · Surface roughness

S. Pandre · N. Kotkunde (✉) · K. Suresh
Department of Mechanical Engineering, BITS Pilani, Hyderabad, Telangana, India
e-mail: nitink@hyderabad.bits-pilani.ac.in

A. Morchhale
Department of Mechanical and Aerospace Engineering, The Ohio State University, Columbus, OH, USA

S. Kumar Singh
Department of Mechanical Engineering, GRIET, Hyderabad, Telangana, India

Adjunct Professor, Institute for Sustainable Industries & Livable Cities, Victoria University, 14428, Melbourne, VIC 8001, Australia

Introduction

The demand for advanced high-strength steels (AHSS) in the automotive industry is increasing day by day as they possess excellent blend mechanical properties. The AHSS has several benefits, such as, high strength, improved crash safety, mass reduction and lower CO₂ emissions [1]. Dual-Phase (DP) steels are the second-generation AHSS. They have two distinct microstructural phases: martensite and ferrite, which provide high strength, ductility, and considerable formability [4]. The DP steel is used to make various parts of the automotive. The flanges are generally used in the manufacturing of household utensils, aerospace, and automotive components [4]. The flanging process provides smooth round edges in the form of fillets for increasing the structural stiffness and easy matting of different specimens in an assembly [5]. Usually, the flanging process is classified into three types: stretch-flanging, shrink flanging, and straight flanging. In the flanging process [6], one end of the sheet is bent at an angle while the other is held firmly between the blank holder and die. Finally, the force is applied at the free end of the sheet using the punch till the sheet bends to an angle. The sheet metal resists the shear edge cracking phenomenon while undergoing deformation [7]. The tooling setup for flanging operation is limited to one kind of flange only. Producing flanges with different dimensions require developing a new tooling setup, which requires high capital investment.

Many researchers in the past have worked on the various aspects of the sheet metal flanging process. Kumar et al. [4] studied the stretch-flanging behavior of AA5052 alloy using a conventional punch and die setup. Six different punch designs are used and found the least radial strain, circumferential strain, and deformation load using a hemispherical punch. In another study, Kumar et al. [8] analyzed the effect of die radius and width on the deformation behavior of AA5052 sheet using experimental and numerical simulation techniques. They found the edge crack propagation to be directly proportional to the sheet width and inversely proportional to the die radius. Additionally, the die radius has a significant effect on the thinning of the sheet along the bend region of the flange.

Further, they recommended using a die radius to be nearly equal to the width of the flange for better stretch flangeability. Dewang et al. [9] investigated the change in stretch-flanging behavior of AA5052 alloy under different process parameters, namely, initial flange length, punch-die clearance, and blank-holding force. They found that the blank-holding force and initial flange length are directly proportional, while the clearance between punch and die is inversely proportional to radial and circumferential strains.

In the studies mentioned above, the influence of process parameters on stretch-flanging has been investigated and optimizing the process parameters is an effective method to control the edge cracking phenomenon. However, this method could not essentially eliminate the high stresses and large strains around the flanged neck area during the stretch-flanging of advanced high-strength steel. The incremental sheet metal forming (ISF) [10] process is used as an alternative to the conventional stretch-flanging for improving the flangeability of material. However, low working speed,

the requirement of skilled technicians, and intelligent machinery have limited its industrial applications only to rapid prototyping and low batch productions [11]. Voswinckel et al. [12] adopted an incremental forming process for the first time in history to perform the stretch-flanging operation and analyzed the effect of flange radius, flange length, and tool path. The stretch-flanged specimen formed using the incremental forming process displayed better form accuracy compared to the one formed using the conventional drawing process. Additionally, they proposed a new blank-holding plate design to reduce the excessive deformation occurring outside the major forming zone. Centeno et al. [13] used the ISF process for enhancing the fracture limits of cylindrical and conical hole flanges made using AISI 304 sheets. They further analyzed the effect of parameters such as the spindle speed, tool diameter, and step downsize, among which the tool diameter majorly affected the fracture limit of flanges. Han et al. [14] stretch formed and analyzed the deformation mechanism of the AA2024-O sheet using the ISF process. They concluded that the flanges are deformed in the uniaxial and the plain strain regions.

Based on the literature review, it has been found that sufficient literature is available on the conventional flanging operation. Although few literature is reported on the incremental flanging process, it is limited to low-strength materials like aluminum alloys. In the present work, the stretch-flanging behavior of high-strength DP steel sheet has been analyzed using the incremental forming process. The effect of different flange widths and lengths on the stretch-flanging behavior is analyzed. Various parameters that affect the specimen's quality, like thickness distribution, form accuracy and surface roughness are studied using FE analysis. The results have been validated with the experimental findings.

Experimental Details

The DP steel alloy sheet of 1 mm thickness was used to perform the experiments in this work. The major alloying elements revealed after the analysis were C 0.075, Si 0.25%, Mn 2.29%, Cr 0.45%, Mo 0.3%, and the balance is Fe. Uniaxial tensile tests were conducted on a ZwickRoell which make the tensile testing machine at a strain rate of 0.00033 S^{-1} and room temperature. The basic nomenclature of the stretch-flanged specimen is shown in Fig. 1a. Based on the design of the stretch-flanged specimen, a tool path is generated for flanging operation using Master CAM software as shown in Fig. 1b. All the single-point incremental forming (SPIF) experiments were performed on a three-axis CNC machining center (Make: Bridgeport), whose experimental setup and the schematic of the working process are shown in Fig. 1c, d. The experimental setup consists of a backing plate to which the specimen was fastened tightly using a nut and bolt during the experimentation. A single-point hemispherical tool made of high-speed steel material was used to form the sheet. The different process parameters used in the study are mentioned in Table 1. The thickness, geometrical accuracy and the local surface roughness of stretch-flanged specimens are measured using a pointed anvil micrometer (Make: Mitutoyo), Coordinate Measuring Machine (CMM) (Make:

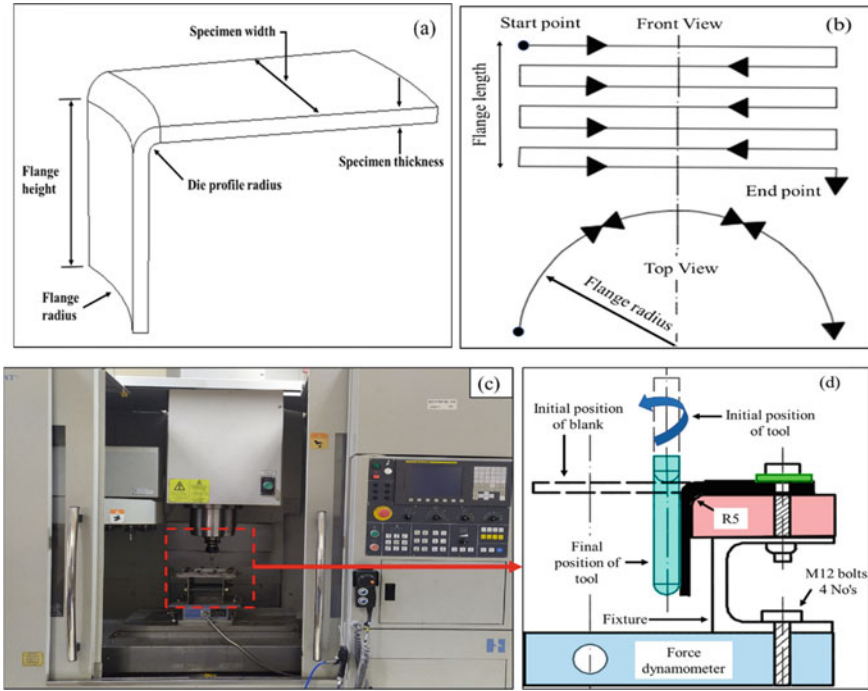


Fig. 1 a Nomenclature, b tool path generated of stretch-flanged specimen, c experimental CNC machining center, d schematic representation of the incremental sheet flanging process

Table 1 Process parameters considered for experimental and numerical analysis during stretch-flanging process

S. No	Process parameters	Value
1	Backing plate radius (mm)	26
2	Single-point tool radius (mm)	5
3	Temperature	Room temperature
4	Specimen dimensions (mm)	Flange widths: 25, 30, 40, and 50 Flange lengths: 20 and 30
5	Spindle speed (rpm)	200
6	Feed rate (mm/min)	1000
7	Step depth (mm)	0.5

Accurate), and 2D surface profilometer (Make: Bruker). All the tests are repeated three times at different locations on the sample, and the average values are reported for the repeatability of the measurement.

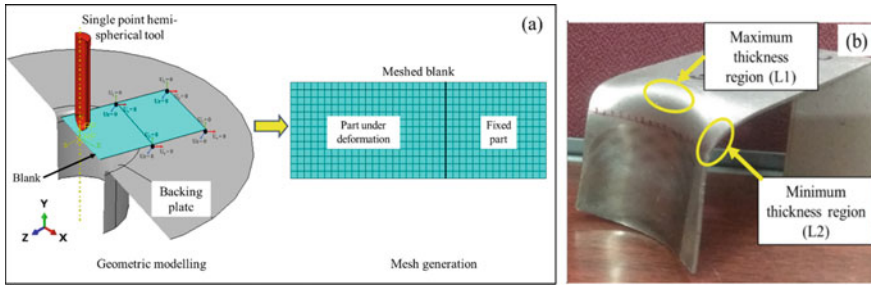


Fig. 2 The representation of **a** part instances created in FE model with boundary conditions, **b** experimental flanged specimen

The FE simulations of the stretch-flanging process are performed in ABAQUS 6.13 software using an explicit approach. The tool path generated for experimental flanging operation was converted into time versus position data using MATLAB software and used as an input during the FE simulations. Figure 2a represents the geometrical model and mesh generated for the FE simulations. The blank is segregated into two parts: part under deformation and fixed. The part under deformation only makes contact with the tool and deforms during the experimentation, while the fixed part was used for constraining the blank. During the FE simulations, the blank was considered deformable and modelled using S4R shell elements with reduced integration for fast computation, reduced hourglass effect and improved robustness. The instances like punch or tool, die and supporting plate are all considered rigid bodies and modelled using analytically rigid elements where no deformation is expected. The contact between tool-blank and blank-backing plate is modelled using a hard surface to surface contact algorithm. Coulomb’s law of friction was applied between different contacting surfaces. As lubrication is applied between the contacting surfaces during experimentation, a low coefficient of friction of 0.01 is considered. An optimum mesh size for the stretch-flanging is selected based on the lowest percent of error between the experimental and FE-simulated thickness considered at the locations, as shown in Fig. 2b. Finally, based on the least error in thickness and computational time listed in Table 2, to flange the specimen, an optimum mesh size of 2 mm × 2 mm is selected. Thus, all the FE simulations were performed using the optimal mesh size for efficient and accurate results.

Results and Discussion

Figure 3a shows the representation of both the stretch-flanged specimens formed by experimental and FE simulations. It is observed that the plastic strain is observed to be more at the edge compared to other locations in the flanges. Figure 3b shows the deformation path of the critical elements considered at the center of the bend region and edge (L2) of the flange. The critical elements during numerical simulations

Table 2 Results of mesh sensitivity analysis for ISF

Mesh size (mm ²)	Simulation results					
	Maximum thickness (mm)	%Error of maximum thickness	Minimum thickness (mm)	%Error of minimum thickness	% Error of average thickness	CPU run time (sec)
6 × 6	1.037	0.679	0.977	1.770	1.224	4272
4 × 4	1.037	0.679	0.977	1.770	1.224	4675.5
2 × 2	1.031	0.097	0.955	0.520	0.308	24,808.1
1 × 1	1.035	0.485	0.937	2.395	0.711	229,346.1

Considered case: 25 W-30L

Experimental thickness:

Maximum: 1.03 mm; Minimum: 0.96 mm

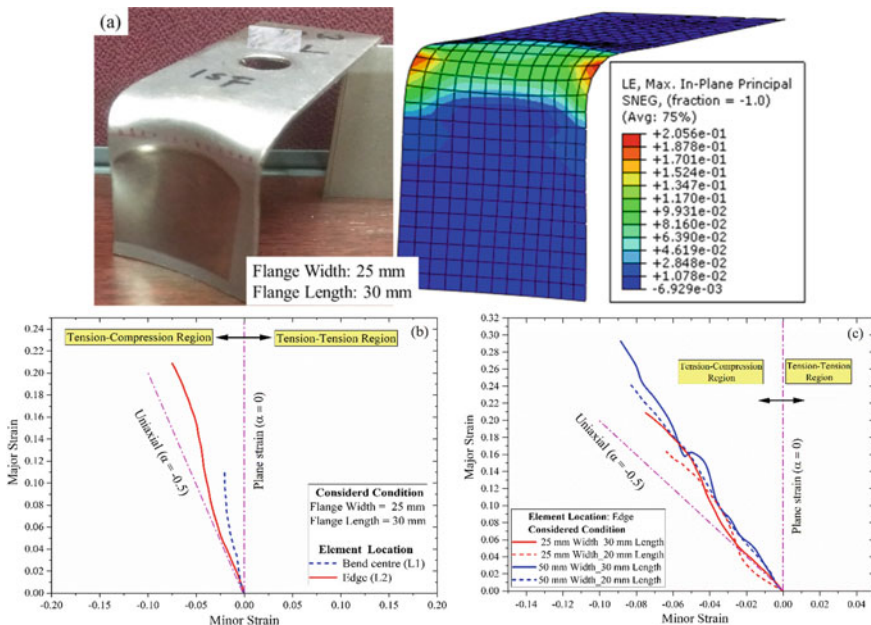


Fig. 3 a Representation of stretch-flanged specimens formed using experimental and FE simulations, b and c comparative plots showing the strain paths of the critical elements considered at different locations

are identified based on the element thinning. The deformation path of these critical elements is tracked at different time steps until the whole movement of the tool during flanging. Different regions of stretch-flanged specimens displayed different characteristics while undergoing the deformation. The whole space for representing the deformation region can be distributed into the tension–tension (T-T) region, plane

strain, and the tension–compression (T-C) region. The deformation in the plane strain region represents that the strain along the minor strain axis is negligible or zero. The deformation of the critical elements at the edge falls in the T-C region, i.e., they experienced uniaxial tension whose strain ratio (α) is near to -0.5. The dotted lines show the strain path of the elements in the center of the bend region (L1), which moves approximately in a vertical straight path indicating the deformation of ‘L1’ region under the plane strain condition whose strain ratio (α) is near to zero.

Figure 3c shows the strain path of the elements for two different flange widths and lengths. With an increase in the width of the specimen, the strains at the corner region have increased. The specimen with larger flange widths (50 mm) has experienced a higher amount of strains compared to the lower (25 mm) represented with solid lines. This can be due to the large strain experienced by the flanges of higher widths near the edge region during the flanging operation. Also, the flanges with higher lengths have shown more strain compared to that of lower ones. It can be due to the more length of material under deformation zone of the tool during the flanging operation. A similar trend of deformation path has been observed for 30 mm, 40 mm, and 50 mm width specimens.

Thickness Distribution

Figure 4a shows the representative images of thickness distribution in the stretch-flanged specimens formed using ISF processes. From Fig. 4a, it is observed that the thickness is more at the ‘L1’ of flange shown in red colour compared to the edge part represented in blue colour. This variation in the thickness distribution can be due to the circumferential stresses acting along the periphery of the flange. At the ‘L1’ region, due to the curvature of the die, compressive stresses are acted upon it during the deformation process, which leads to the flow of material towards the central region. The flow of material towards the central part has ultimately led to

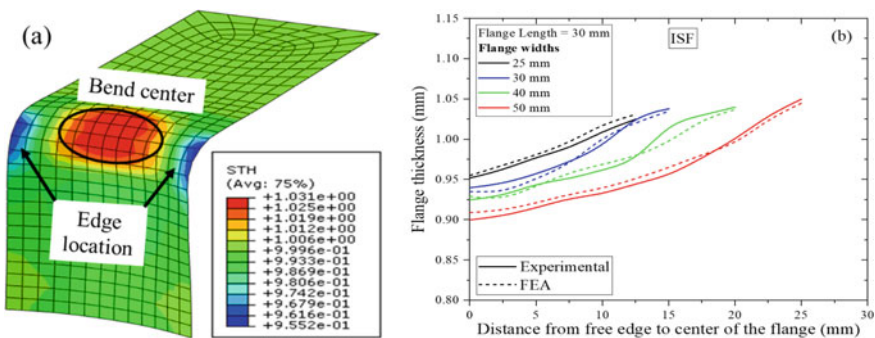


Fig. 4 a Representative image of the FE-simulated thickness distribution, b comparison of experimental and FE-simulated thickness

the increase in the thickness in that region, thereby leaving the edge region with minimal thickness [15]. Figure 4b shows the comparison of the experimental and FE simulations of thickness variation from ‘L2’ to ‘L1’ region. A similar trend in the thickness variation is seen for all the flanges of different dimensions. Moreover, it can be seen that with the increase in the flange width, the minimum thickness is also reduced. In the case of the flanges with different flange lengths, there is not much variation in minimum thickness observed, which indicates the insignificant effect of flange length on the thickness variation along the bend region. The FE-simulated thickness and the experimental thickness agree with each other, with an average absolute error percentage less than 4.5% for all the flange dimensions.

Springback

The geometrical deviation of the experimentally formed flanges is measured using CMM, as shown in Fig. 5a. The formed flanges are observed to have bending, bulge, and springback region on the flanges, as shown in Fig. 5b. The bulge seen at the

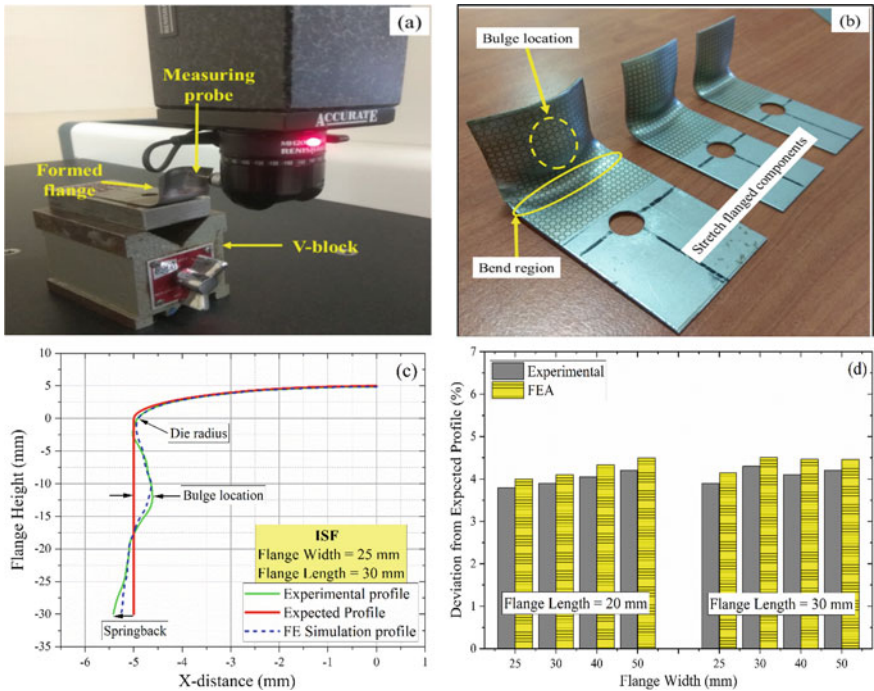


Fig. 5 a Experimental measurement of coordinates on the flanged specimen, b flanged specimens, c comparative plot of geometrical deviation, and d percentage deviation in formed flanges with the expected profile

'L1' can be due to the stretching of the flange during flanging operation. The bottom end of the flange has moved in the reverse direction, which can be due to the less stiffness exhibited by the specimen during the flanging operation helped in the elastic recovery of the material. This can affect the accuracy of the final flanged specimen. The results of the experimental and FE-simulated profiles are compared with the expected profile to calculate the percentage of deviation, as shown in Fig. 5c. It is observed that the obtained profiles are deviating from the expected profiles at the bulge location and bottom of the flange with a maximum deviation percentage of 4.12 and 4.07% for 20 mm and 30 mm flange lengths as shown in Fig. 5d. Finally, the experimental and FE-simulated profiles are in good agreement when compared with each other, with an average error percentage of less than 3%.

Surface Roughness

The quality of the flanged specimen is affected by the surface roughness produced during the flanging operation. If the surface roughness increases beyond an optimum level, its applications are limited. The surface roughness of the flanged specimen is measured at different locations using a 2D surface roughness profilometer. Figure 6a, b shows the surface roughness plots of the as-received and flanged specimen. The average surface roughness values measured on the flanged specimen are compared with the as-received sheet. The 'Ra' value of 1.4635 μm is obtained for the stretch-flanged specimen which is 100.3% higher than that obtained on the undeformed (as-received) sheet (0.7306 μm). The higher value of 'Ra' in the ISF process is due to the continuous movement of the single-pointed hemispherical tool over the sheet's surface.

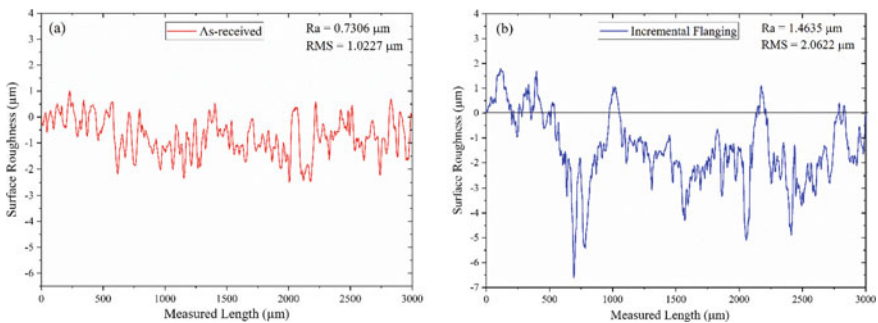


Fig. 6 Surface roughness profiles obtained from the **a** as-received specimen, **b** stretch-flanged specimen

Conclusions

In the current work, experimental and numerical analysis of flanging behavior of high-strength DP steel has been carried out using the ISF process and some of the significant conclusions are listed below:

- The stretch-flanged specimens of different flange widths (25, 30, 40, and 50 mm) and lengths (20 and 30 mm) have formed to analyze the flanging behavior of the DP steel. The strain distribution has revealed that the bent edge (L2) of the sheet during the flanging operation has experienced uniaxial strain. At the same time, the center of the bend (L1) region is deformed under the plane strain condition.
- In all the flanged specimens, the 'L1' is thicker and 'L2' region is thinner due to the compressive stresses acting upon the material along the circumference of the flange during the flanging operation. Moreover, a reduction in minimum thickness has been observed with the increase in flange width.
- Due to low stiffness in the bottom of the flange, the springback of the material is more for higher flange lengths. The percentage deviation of the experimental and FE-simulated profiles with the expected profile has been found to be 4.12 and 4.07% for 20 mm and 30 mm flange lengths. Finally, the experimental and FE-simulated profiles are in good agreement when compared with an average error percentage of less than 3%.
- The 'Ra' value has increased by 100.3% compared to the 'Ra' value of the as-received sheet, which can be due to the movement of the tool over the flange surface.

References

1. Prasad K, Venkatesh B, Krishnaswamy H, Banerjee DK, Chakkingal U (2021) On the interplay of friction and stress relaxation to improve stretch-flangeability of dual phase (DP600) steel. *CIRP J Manuf Sci Technol* 32:154–169. <https://doi.org/10.1016/j.cirpj.2020.11.014>
2. Pandre S, Kotkunde N, Takalkar P, Morchhale A, Sujith R, Singh SK (Dec. 2019) Flow Stress Behavior, Constitutive Modeling, and Microstructural Characteristics of DP 590 Steel at Elevated Temperatures. *J. of Materi Eng and Perform* 28(12):7565–7581. <https://doi.org/10.1007/s11665-019-04497-y>
3. Pandre S, Morchhale A, Kotkunde N, Singh SK, Ravindran S (2021) Prediction of forming limits and microstructural evolution during warm stretch forming of DP590 steel. *Archiv Civ Mech Eng* 21(3):1–23. <https://doi.org/10.1007/s43452-021-00262-y>
4. Kumar S, Ahmed M, Panthi SK (2020) Effect of punch profile on deformation behavior of AA5052 sheet in stretch flanging process. *Archiv Civ Mech Eng* 20(1):18. <https://doi.org/10.1007/s43452-020-00016-2>
5. Yu X, Chen J, Chen J (2016) Influence of curvature variation on edge stretchability in hole expansion and stretch flanging of advanced high-strength steel. *Int J Adv Manuf Technol* 86(1):1083–1094. <https://doi.org/10.1007/s00170-015-8251-3>
6. Hu P, Li DY, Li YX (2003) Analytical models of stretch and shrink flanging. *Int J Mach Tools Manuf* 43(13):1367–1373. [https://doi.org/10.1016/S0890-6955\(03\)00150-0](https://doi.org/10.1016/S0890-6955(03)00150-0)

7. Chatterjee S, Bhadeshia HKDH (2007) Stretch-flangeability of strong multiphase steels. *Mater Sci Technol* 23(5):606–609. <https://doi.org/10.1179/174328407X179511>
8. Kumar S, Ahmed M, Panthi SK (2020) Investigation on the crack and thinning behavior of aluminum alloy 5052 sheet in stretch flanging process. *J Fail. Anal. and Preven.* 20(4):1212–1228. <https://doi.org/10.1007/s11668-020-00922-w>
9. Dewang Y, Hora MS, Panthi S (2017) Effect of process parameters on deformation behavior of AA 5052 sheets in stretch flanging process. *Materials Today: Proceedings* 4:9316–9326. <https://doi.org/10.1016/J.MATPR.2017.07.291>
10. Pandre S, Morchhale A, Kotkunde N, Kurra S (2021) Processing of DP590 steel using single point incremental forming for automotive applications. *Mater Manuf Processes* 36:1–9. <https://doi.org/10.1080/10426914.2021.1942903>
11. Martins PAF, Bay N, Skjoedt M, Silva MB (2008) Theory of single point incremental forming. *CIRP Ann* 57(1):247–252. <https://doi.org/10.1016/j.cirp.2008.03.047>
12. Voswinckel H, Bambach M, Hirt G (2015) Improving geometrical accuracy for flanging by incremental sheet metal forming. *Int J Mater Form* 8(3):391–399. <https://doi.org/10.1007/s12289-014-1182-y>
13. Centeno G, Bagudanch I, Martínez-Donaire AJ, García-Romeu ML, Vallellano C (2014) Critical analysis of necking and fracture limit strains and forming forces in single-point incremental forming. *Mater Des* 63:20–29. <https://doi.org/10.1016/j.matdes.2014.05.066>
14. Han K et al (2019) Experimental and numerical study on the deformation mechanism of straight flanging by incremental sheet forming. *Int J Mech Sci* 160:75–89. <https://doi.org/10.1016/j.ijmecsci.2019.06.024>
15. Kumar S, Ahmed M, Panthi SK (2020) Investigation on the Crack and Thinning Behavior of Aluminum Alloy 5052 Sheet in Stretch Flanging Process. *J Fail Anal Prev* 20(4):1212–1228

Three-Dimensional Control Point Based Surface Description for Data Reduction, Reverse Engineering and Springback Compensation in Sheet Metal Forming



L. Maier, C. Hartmann, B. Ünver, and W. Volk

Abstract A common process for automotive body component manufacturing is deep drawing. Launching and reworking of deep drawing tools is known as tryout process. In order to distinguish between stochastic changes and deterministic deviations already during the tool tryout, both simulated and measured data sets are required. However, especially with measured components, large data sets are generated. These often make a comparison difficult due to high computation times. In this paper, a method for reverse engineering is introduced, which allows representing complex three-dimensional component surfaces using B-Splines. The advantage here is a reduction of memory required and straightforward processing. The approach enables the comparison of numerous data sets, a springback compensation for measured, simulated or even combined data sets, as well as a separation of deterministic and stochastic deviations. Since this surface description is widely spread in the CAD world, the approach further enables a direct derivation of a new tool geometry.

Keywords Springback compensation · Data reduction · Deep drawing · Sheet metal forming · Reverse engineering

Introduction

In production of automotive body components deep drawing is a widely spread process [1, 2]. Although deep drawing is a common process, e.g. for structural parts such as floor assemblies, outer skin part or even more complex chassis parts for decades, industry is facing problems when Advanced High Strength Steel (AHSS) needs to be formed and assembled [3]. Driven by lightweight concepts to reduce carbon-footprint and to raise the range of electric vehicles those AHSSs progressively replace common ordinary steels [2]. By using these materials, manufacturers are confronted with complex springback predictions and compensations. Springback

L. Maier (✉) · C. Hartmann · B. Ünver · W. Volk
Chair of Metal Forming and Casting, Technical University of Munich, Walther-Meißner-Straße 4,
85748 Garching, Germany
e-mail: lorenz.maier@utg.de

compensation is one of the most relevant fields of deep drawing research with high industrial relevance, especially in the field of forming AHSS, aluminum alloys or components with a high drawing depth [4]. To solve this problem, finite element (FE) analyses is used to support the launching and the reworking process of deep drawing tools [1]. This experience-based process is time- and cost consuming [5]. It can, for example, affect the start of production, which is why minimizing the time required is desirable for industry. In addition to simulated data from FE analyses, measurement data are also provided during this process [1, 4]. Optical measurement systems generate point clouds and enable a 3D visualization and analysis of the first falling parts [3, 6]. What is missing is a tool that enables the user to compare the deviations for a large number of components between on one hand simulated and on the other hand measured data to the target geometry. To realize this, the amount of data has to be reduced. Reverse engineering (RE) is an established but complex procedure to achieve this [6, 7]. Another side effect is that including larger data sets allows the separation of stochastic and deterministic deviations [5, 8].

In order to be able to manufacture deep-drawn components within a defined tolerance, first springback prediction is required. Initially, empirical predictions were made for this purpose, primarily in two-dimensional space [9]. However, predicting springback is far more complex. Springback is massively dependent on the material behavior, the strain path and the part geometry. The state of the art is the calculation of springback by FE method considering these influencing factors. Predicting springback is one aspect, but compensating for its effects is another. With the development of FE simulations, the compensation of these predicted springback was also investigated in more detail. The results of these investigations were two compensation approaches widely used in industry and research, namely springforward [10] and displacement adjustment (DA) [3].

This investigation focuses on the springback compensation after reducing data using an RE approach for deep drawn components. Our RE approach is based on B-Spline surfaces as already investigated by e.g. Greco et al. and Weiss et al. [11, 12]. After the RE returns the surface description in a mathematical way, we introduce a springback compensation approach similar to DA, which adapts the tool geometry by shifting the surface control points (CP). To investigate whether the compensation factor is independent of the material properties, we performed several compensation iterations with three different Young's moduli.

Reverse Engineering and Data Reduction

To reduce the amount of data, the simulated and measured, as well as the target geometry are represented by a RE approach based on B-Splines. Using a bidirectional set of CP, two independent non-decreasing knot vectors and the B-Spline function

$$S(u, v) = \sum_{i=0}^n \sum_{j=0}^m N_{i,p}(u)N_{j,q}(v)P_{i,j} \tag{1}$$

a surface can be described. The knot vectors u and v are vectors in the parameter space and written e.g. $u = \{u_0, u_1, \dots, u_{n+p+1}\}$, where u_i is the i -th knot, n the number of basis functions and p is the polynomial degree. $N_{i,p}(u)$ is the i -th basis function of degree p , written as is defined recursively as follows: beginning with the basis function

$$N_{i,0}(u) = \begin{cases} 1 & \text{if } u_i \leq u < u_{i+1} \\ 0 & \text{otherwise} \end{cases} \tag{2}$$

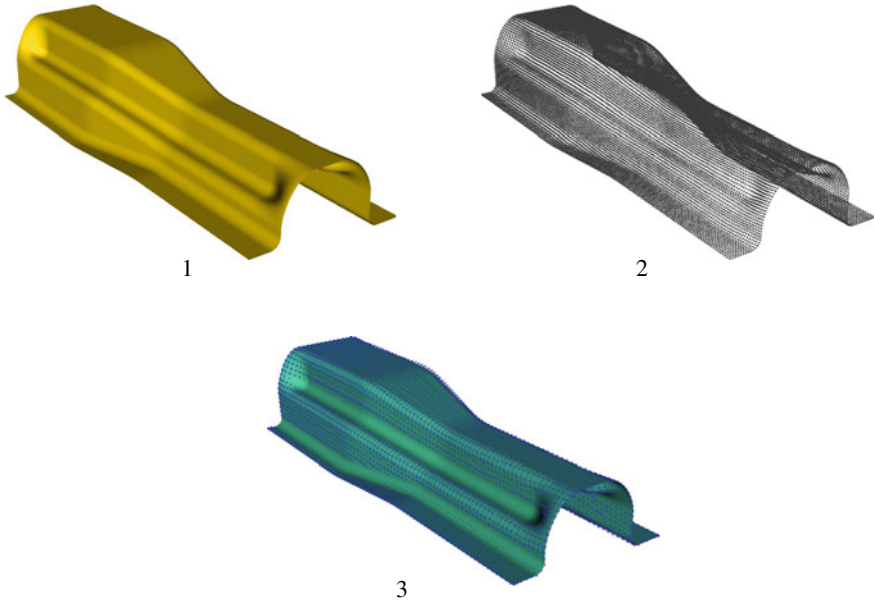
for $p = 0$ and followed for $p > 0$ the Cox-de Boor recursion defines the B-Spline basis function:

$$N_{i,p}(u) = \frac{u - u_i}{u_{i+p} - u_i} N_{i,p-1}(u) + \frac{u_{i+p+1} - u}{u_{i+p+1} - u_{i+1}} N_{i+1,p-1}(u) \tag{3}$$

As shown for $N_{i,p}(u)$ the structure for the Cox-de Boor recursion with the B-Spline functions $N_{j,q}(v)$ along the knot vector v and a degree of q is similar [12]. We applied this surface reconstruction to describe the components surface generated by point clouds as followed.

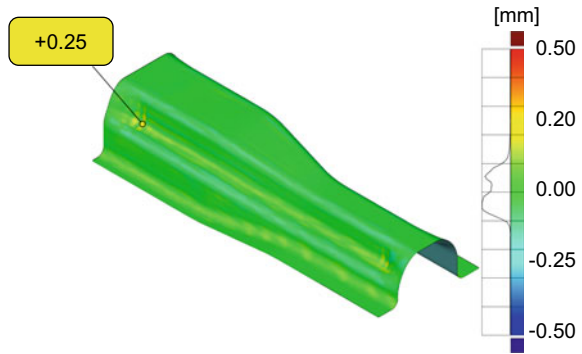
First, we loaded the point clouds from the .stl or .xyz file. In order to be able to apply the surface reconstruction, the point clouds must be transformed in an organized structure. For this, we used the approach of Krishnamurthy. Krishnamurthy and Levoy utilizes an automatic coarse-to-fine sampling, which creates a regular grid that lies on the polygonal surface [13]. The resulting grid structure then is transformed into the B-Spline representation by a least-squared error approximation according to Piegl [7]. In this paper, we use a scaled tunnel reinforcement to introduce the approach. The dimensions of the component shown are $400 \times 150 \times 75$ mm. The transition from a polygonized irregular point cloud to the B-Spline representation is shown in Figs. 1, 2, and 3. The raw data of the scanned component required a memory of approx. 119 MB. This RE approach reduces the data required to 441 KB per component.

This data set is the result of the stored control point location in three-dimensional space and the two knot vectors. The accuracy of the RE with its B-Spline surface is not only dependent from the number of CP, but also from the curve degree. To determine the degree of the curves, the curvatures at the individual points are considered. For numerical stability reasons, we limited the maximum degree of the curve to three. For the tunnel reinforcement the number of CP was set to $n = 54$ in and $m = 84$. The curve's degree in u -direction (p) is three and two in v -direction (q). In Fig. 4, a false color plot shows the deviation between RE and the target geometry in normal direction. The mean deviation between the target's sample points and the RE surface is 0.0221 mm with a maximal deviation of 0.25 mm. For this calculation, we rendered



Figs. 1–3 (1) Polygonized point cloud. (2) Organized point cloud. (3) B-Spline surface

Fig. 4 Distance between target point cloud and RE in normal direction according to the defined B-Spline parameters presented in a false color diagram



the mathematical B-Spline surface description with 160.000 evaluation points. By rendering the geometric surface description in higher resolution, the RE represents e.g. radii more accurately. This leads to a minimization of the chord error. Focus should be on the small deviation with a standard deviation of 0.030 between RE and target geometry. This shows that the RE approach is suitable for the representation of deep-drawn components, since there are usually no discontinuities in the component due to the forming process. Furthermore, the rendering has no influence on the subsequent compensation, since the rendering only serves as visualization for the user. Due to the mathematical surface description, in principle, an infinite resolution rendering is possible.

Springback Compensation

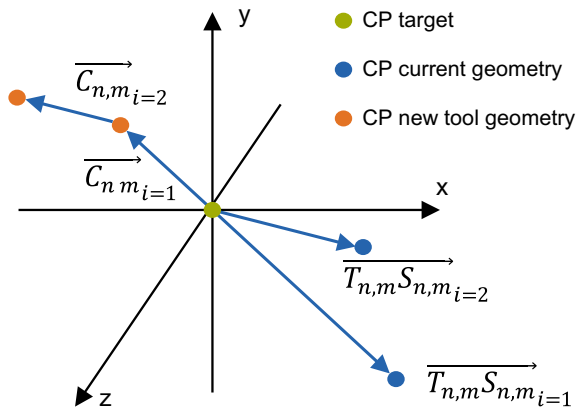
It is possible to use both measured and simulated components to perform the subsequent springback compensation. For this purpose, we load the data and reconstruct it according to the above described RE approach. In contrast to the initial RE of the target geometry from Fig. 4, the approximation algorithm is changed. For these data sets, we reuse the target’s knot vectors of for the approximation. Accordingly, the number of CP and the degrees of the curves are equal to the RE of the objective function (1). Thus, the knot vector does not have to be stored again for each component. This reduces the memory requirement and computational effort again. Only the position of the CP in x, y and z direction changes by the approximation of the individual data sets.

After the initial RE of the target geometry has defined two knot vectors and the location of the target CP and the data sets have been brought into the same representation by the RE approach, a new compensation approach can be performed. By definition, when all current part’s CP are superimposed with the target CP, the component surface represented by B-Splines is identical to the target geometry. In order to be able to calculate the new position of these CP, we considered the CP with the same indices. Control point compensation (CPC) follows a similar procedure to DA. However, since DA does not directly generate an effective tool geometry, but a polygonized mesh, and it is not possible to perform a DA compensation with measured data sets, we improved the compensation method CPC accordingly. The RE generates a smooth B-Spline surface. In the approach presented, we utilize the CP to compensate the springback. Figure 5 illustrates the shift of the CPC schematically for one CP and two iterations.

The following term is introduced for the CPC:

$$\vec{C}_{n,m} = -\alpha \cdot \vec{T}_{n,m} S_{n,m} \tag{4}$$

Fig. 5 Schematic diagram of the shift for a CP covering two iterations (*i*)



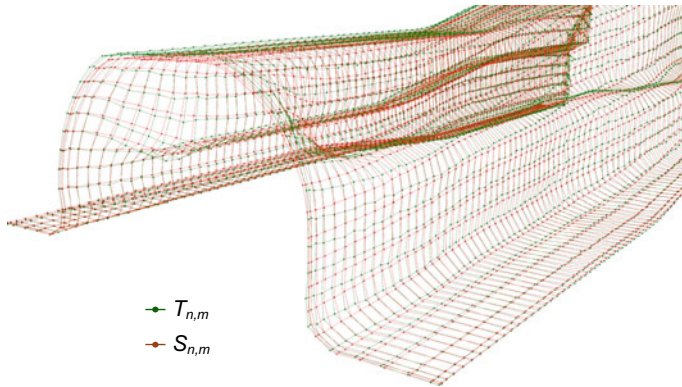


Fig. 6 CP grid of T_k and S_k of the scaled tunnel reinforcement for the calculation of the control point shift in three dimensions

First, we move the component into the position of the target geometry. For this purpose, we aligned the component by a global iterative closest point (icp) algorithm. After that, the component is realigned by another icp, which considers significant component characteristics the user can define, e.g. assembly joining or operative surfaces. Then, we calculated the vector $\overrightarrow{T_{n,m}S_{n,m}}$ between the target CP $T_{n,m}$ and the current CP $S_{n,m}$ for each individual CP. The compensation factor α inverse and reduce this vector. α is a constant value between zero and one. Since compensation is an iterative process, the CP of the tool T_{i-1} is shifted by the vector $\overrightarrow{C_{c,m}}$ from formula (4) in every i th iteration. This step calculates the new position of the CP and creates a new tool geometry $S(u, v)$ according to formula (1). Figure 6 shows the CP grid of the surface for the tool and a component after springback represented through the RE approach. According to these grids, the vectors and the new tool surface is calculated and exported as a .stp-file, which is a common standard in the computer aided design (CAD) world. With this new tool geometry, we can simulate the next iteration of the deep drawing process or derivate a tool reworking strategy.

Results

The proposed approach is applied using simulations in this paper for three different Young's moduli and three compensation factors. Hereby we want to examine whether the compensation depends significantly on the material parameters or the choice of the compensation factor. We performed the simulations with the FE software *AutoForm R8*, which is widely used in industry. The simulations are utilizing a BBC material model for a deep drawing steel DC04. To investigate the iterative CPC approach, we analyzed each compensation factor for each Young's modulus over five iterations. By simulating these different Young's moduli, we depict a stochastic

deviation. Compared to measured components, the user can utilize this variation to calculate the deterministic deviation. We calculated the deviations for each point of the point cloud in normal direction to the target geometry and thereby computed the mean deviation.

Figures 7, 9, and 11 show the mean deviation of the 48 simulations after the local best fit according to the icp algorithm graphically. Figures 8, 10, and 12 represent the maximum surface bulges of the combination of compensation factor, Young’s modulus and number of iteration with the minimal mean deviation. Initially, the tunnel reinforcement with an increasing Young’s modulus has a lower mean deviation, which we compensated afterwards. For $E = 190$ GPa the uncompensated mean deviation is 0.257 mm. Increasing the Young’s modulus to $E = 205$ GPa leads to a deviation of 0.236 mm. The third test sequence with a Young’s modulus of $E = 220$ GPa has a deviation of 0.218 mm.

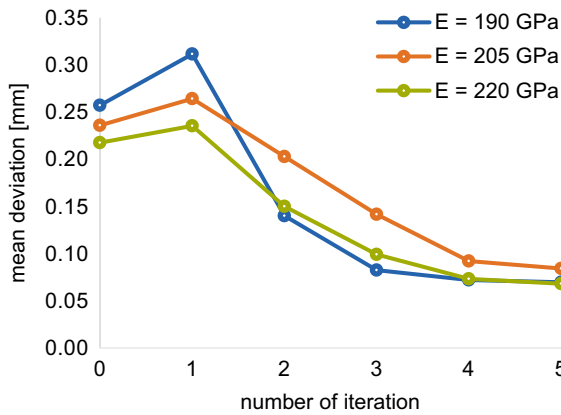


Fig. 7 Mean deviation for the compensation factor of $\alpha = 0.3$ over five iterations for three individual Young’s moduli

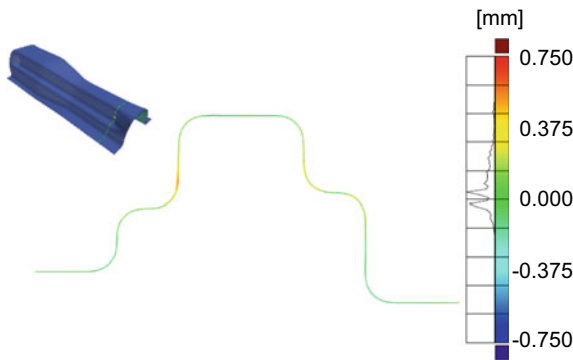


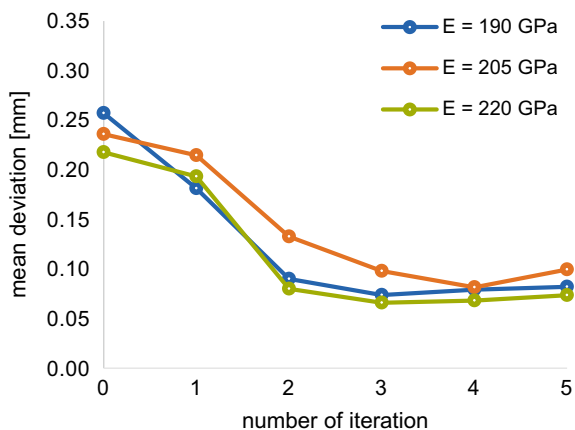
Fig. 8 Maximum surface defect with minimum mean deviation for $\alpha = 0.3$, $E = 190$ GPa and $i = 5$

Figure 7 shows the compensation for an α -value of $\alpha = 0.3$. Here it can be seen that for all three simulation series the mean deviation, depending on the first deviation, increases in the first iteration. In the following iterations, the averaged deviation decreases until it reaches a saturation. On the right side in Fig. 8, the component part with the maximal surface bulges is illustrated. For this compensation factor, we generated a smooth tool surface over the iterations. This can also be seen from the deviations in the false color diagram in Fig. 13. After the five iterations, we achieved a deviation in the range of 0.068 to 0.084 mm. This corresponds to a minimization of the deviation between 64.3 and 72.9%.

The aim of a tool redesign process is to achieve the desired target geometry in as few iterations as possible, thus reducing costs and saving time. In order to get a better understanding of the iterative process, we increased the compensation factor for the next series of experiments. Figure 9 shows the development of the mean deviation with $\alpha = 0.5$ for the three Young's moduli examined over the five CPC iterations. In contrast to the previous series of tests, the mean deviation falls from the first iteration until it reaches a minimum after three or four iterations. This can save computing time or tool reworking time. Subsequently, the mean deviation increases again. Here, we achieved a reduction of the initial average deviation in the range between 65.5 and 71.3%. If we look at the smoothness of the tool surfaces, we can see that local balancing occurs. In Fig. 10 we can see, that this effect is significantly higher with this compensation factor compared to Fig. 8. This becomes more pronounced over the course of the iterations, which leads to an increasing mean deviation.

With a compensation factor of $\alpha = 0.8$, the mean deviation between initial simulation and iteration one falls most sharply for all investigated α -values, as can be seen in Fig. 11. We reached a minimum of the average deviation already after two or three iterations. After only a few iterations, we can observe local flaws, which lead to a deterioration of the component quality in terms of dimensional stability. Figure 12 shows this effect. Nevertheless, the error is halved within one iteration. After two to

Fig. 9 Mean deviation for the compensation factor of $\alpha = 0.5$ over five iterations for three individual Young's moduli



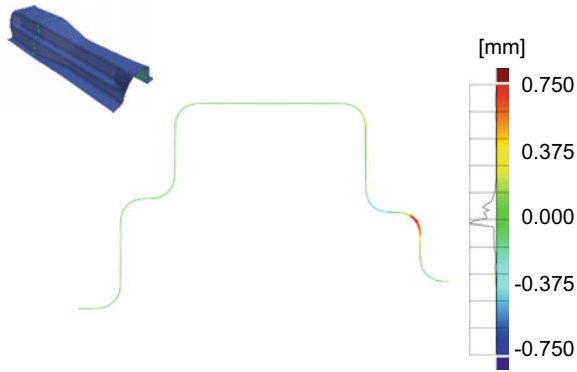


Fig. 10 Maximum surface defect with minimum mean deviation for $\alpha = 0.5, E = 220$ GPa and $i = 3$

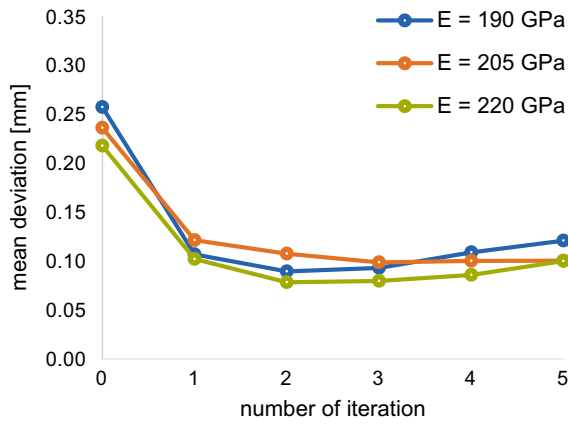


Fig. 11 Mean deviation for the compensation factor of $\alpha = 0.8$ over five iterations for three individual Young's moduli

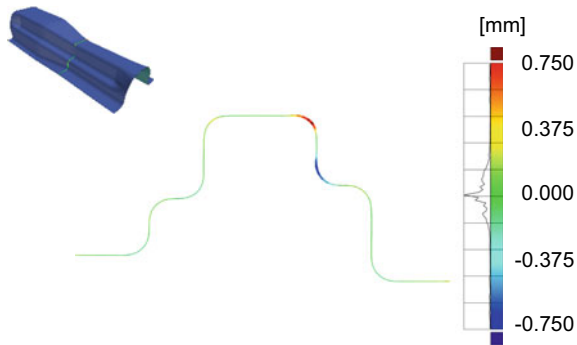


Fig. 12 Maximum surface defect with minimum mean deviation for $\alpha = 0.8, E = 220$ GPa and $i = 2$

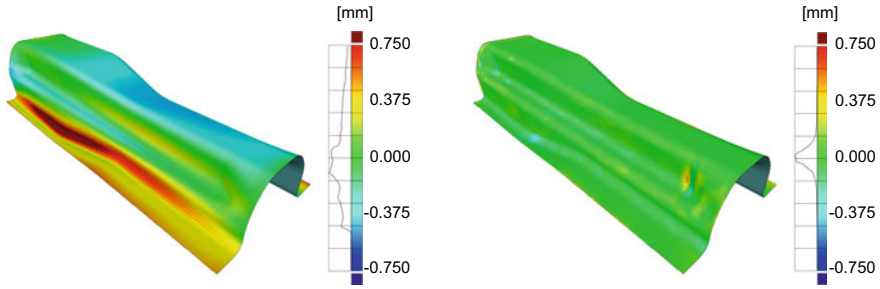


Fig. 13 False color plot of the initial deviation in normal direction for a Young's modulus of 190 GPa (left) and the compensated component after five iterations with a compensation factor of $\alpha = 0.3$ (right)

three iterations, the mean deviation relative to the initial one falls between 58.2 and 65.2%.

Figure 13 shows the deviation of the initial simulation for a Young's modulus of 190 GPa on the left and the CPC compensated component with a compensation factor of $\alpha = 0.3$ after five iterations on the right in a false color diagram. With this compensation factor, the maximum reduction of the average deviation was achieved over the five iterations. The histogram of the deviation can also be seen in the false color diagram. Here we can see that the icp algorithm aligns the component uniformly. The maximum component deviation is in the trough at the end of the reinforcement bead. Figure 8 shows this deviation in a plane section in more detail.

Discussion

The simulative investigations show that the iterative CPC approach is suitable to compensate for the deviations of a deep-drawn component but rise some questions about the local unevenness when using a larger compensation factor. With regard to the amount of data required for this, a significant saving could be achieved by the RE approach shown in Fig. 4. The mathematical description of formula (1) for the surface via B-Spline reduced the amount of data from 119 MB to 441 KB. This corresponds to a reduction in memory requirements by a factor of 270 and the mathematical description of curvatures also prevents a chord error. This data reduction has an essential role, especially for the in-line measurement of components, where storage and computing time is a significant factor. In addition, this RE approach results in an average deviation of only 0.0221 mm between the input point cloud and the approximated surface.

With this work, we demonstrated the transfer of our CPC from two to three dimensions. With an appropriate choice of compensation factor α corresponding to formula (4), deviation of an industry-related component could systematically be

minimized. An advantage of this CPC approach is that a .stp file is generated directly by the compensation, which can be used for the tool's rework strategy.

During the iterative process, we reduced the initial deviation from 0.257 mm by 72.9% to 0.070 mm with a small compensation factor, as shown in Fig. 13. This is due to the geometry and is not directly related to the Young's modulus used, as can be seen in Figs. 7, 9 and 11. If, on the other hand, one chooses a larger compensation factor, we saw that the mean deviation is halved within one iteration. Nevertheless, a larger compensation factor has also an influence on the resulting tool's surface smoothness. This we pointed out with the Figs. 8, 10 and 12. Accordingly, it is important to achieve a systematic choice of the compensation factor and thereby minimize the number of iterations required until the deviations are within a desired tolerance.

Conclusion and Outlook

The RE process reproduces the examined component with a high degree of accuracy. Nevertheless, there is an increased deviation in the area of high curvatures. An optimizer, which adjusts the degrees of freedom of the B-spline representation, could improve this and thus support the highly experience-based process.

This investigation on the three-dimensional CPC has shown that the approach produces more than acceptable results and reduces the amount of memory required significantly. However, a local balancing problem occurs, especially with a higher compensation factor. We could observe that this effect mostly occurred in radii. Therefore, we concluded that the CP run out of the radius here and the CPC algorithm must be further adjusted here. If further investigations solve the local balancing problem of the CPC method with a larger compensation factor, we assume that the number of iterations required will also decrease. This is what we conclude from the studies with a compensation factor of $\alpha = 0.8$ and $\alpha = 0.5$. The functionality of this approach to measured data show the achievable possibilities by this compensation method. We can use purely measurement components for compensation without running further simulations and the experience-based, industry-related tool tryout process can be supported significantly. In this process, we can distinguish between stochastic variations and deterministic deviations by a stochastic distribution of the location of the control points. In addition, finally yet importantly, the output file with its .stp-format is well known in the CAD world and a tool reworking strategy can directly deviated from the CPC, which reduces both time and memory requirements.

Acknowledgements The authors would like to thank the European Research Association for Sheet Metal Processing (Europäische Forschungsgesellschaft für Blechverarbeitung e.V.) for supporting this research by funding the research project IGF 21467N-EFB 10/218.

References

1. Meinders T, Burchitz IA, Bonte MHA, Lingbeek RA (2008) Numerical product design: springback prediction, compensation and optimization. *Int J Mach Tools Manuf* 48:499–514
2. Wagoner RH, Lim H, Lee M-G (2013) Advanced issues in springback. *Int J Plast* 45:3–20
3. Gan W, Wagoner RH (2004) Die design method for sheet springback. *Int J Mech Sci* 46:1097–1113
4. Wang H, Zhou J, Zhao T, Tao Y (2016) Springback compensation of automotive panel based on three-dimensional scanning and reverse engineering. *Int J Adv Manuf Technol* 85:1187–1193
5. Maier L, Hartmann C, Volk W (2021) Parameterized data handling for forming tool tryout: reverse engineering, data consolidation and springback compensation. *IOP Conf Ser: Mater Sci Eng* 1157:12035
6. Mao Q, Liu S, Wang S, Ma X (2018) Surface fitting for quasi scattered data from coordinate measuring systems. *Sensors* 18:214
7. Piegel L (1997) *The NURBS book*. Springer Berlin/Heidelberg, Berlin, Heidelberg
8. Hartmann C, Maier L, Volk W (2021) Springback and compensation in sheet metal forming reconsidered as an ill-posed problem. *IOP Conf Ser: Mater Sci Eng* 1157:12044
9. Wenner ML (1983) On work hardening and springback in plane strain draw forming. *J Appl Metalwork* 2:277–287
10. Karafillis AP, Boyce MC (1992) Tooling design in sheet metal forming using springback calculations. *Int J Mech Sci* 34:113–131
11. Greco F, Coox L, Maurin F, Balla VK, Deckers E, Desmet W (2018) Reverse engineering of deep drawn components with an isogeometric framework. *Comput Struct* 201:15–25
12. Weiss V, Andor L, Renner G, Várady T (2002) Advanced surface fitting techniques. *Comput Aided Geom Des* 19:19–42
13. Krishnamurthy V, Levoy M (1996) Fitting smooth surfaces to dense polygon meshes. In: Fujii J (ed) *Proceedings of the 23rd annual conference on computer graphics and interactive techniques*. ACM, New York, pp 313–324

Time-Dependent Method for the Inverse Evaluation of Yield Locus Using Nakazima Experiments



K. Barth, B. Berisha, and P. Hora

Abstract The position of the plane strain (PS) point in the stress space depends on the choice of the yield locus. Using non-quadratic yield loci the curvature and therefore the location of PS are determined by the yield locus exponent. On the contrary, the Vegter yield locus offers the opportunity to define exactly the position of PS. Currently, to use this freedom cost-expensive experiments have to be conducted or the position is roughly approximated. In this work, a new method is described to determine the two stress components of the plane strain point for the aluminum alloy AA6016-T4. The time-dependent strain distributions of Nakazima experiments recorded by an optical measurement system are used to conduct a reverse fitting of the PS point. Different strategies of determining the PS point using this new method are compared.

Keywords Plane strain · Yield locus · Strain distribution · Nakazima experiments · Aluminum alloy · Vegter yield locus · DIC · Inverse fitting · Time dependent

Introduction

The complexity of yield locus models increased over the past decades. For Hill'48, only three input parameters (uniaxial tension and R-values in 0° , and 90°) are necessary. Nowadays, yield loci Barlat'89 and YLD2000 are mainly used in the automotive industry. The YLD2000 yield locus already needs nine input parameters to be calibrated [1]. Accordingly, uniaxial tension test in 0° , 45° , and 90° and a biaxial experiment have to be conducted for yield strength and R-values to fit this yield locus. The exponent $M = 6$ is suggested for BCC and an exponent of $M = 8$ for FCC crystal structures [2]. However, recent research based on advanced crystal plasticity simulations showed that an exponent of $M = 8$ is not optimal for aluminum

K. Barth (✉) · P. Hora
Institute of Virtual Manufacturing, ETH Zürich, Tannenstr. 3, 8092 Zürich, Switzerland
e-mail: barth@ivp.mavt.ethz.ch

K. Barth · B. Berisha
Inspire - Ivp, Inspire AG, Technoparkstrasse 1, 8005 Zürich, Switzerland

alloys [3, 4]. Across all the yield loci, the plane strain point in the stress space is only indirectly specified due to the curvature of the yield locus. However, in most of the automotive simulations, this point has a direct influence on the critical forming limit.

Newer yield locus models are coming up with a more flexible curvature description [5, 6]. The yield locus of Vegter and van den Boogaard are able to describe exactly the uniaxial tension, biaxial tension, plane strain as well as the shear point in the different directions depending on the rolling direction [5]. 14 input parameters and therefore the corresponding experiments are necessary to calibrate the Vegter yield locus with data points in 0°, 45°, 90°, and biaxial direction. To overcome this huge experimental effort, the Vegter Lite yield locus has been developed [7]. A weight factor is used to determine the plane strain and shear stress points. Vegter et al. propose general weight factors for aluminum and steel materials [7].

To describe a complete material behavior, besides uniaxial and biaxial experiments to determine the yield locus also the forming limit is investigated. Using the Nakazima experiment set, enough experimental data are present to fit the plane strain point with an inverse fitting method.

In this study, Nakazima experiments of an aluminum AA6016-T4 recorded by DIC are used to find the plane strain parameters for the Vegter yield locus. The strain distribution of Nakazima simulations is compared with the results of experiments depending on time and evaluation area. Different possibilities of comparing settings are tested. In addition, the performance of the Vegter yield locus is compared to the BBC yield locus as implemented in AutoForm R8.

Material AA6016-T4

Experimental data presented in this chapter are taken from [8]. The investigated aluminum AA6016-T4 has a blank thickness of 1.02 mm. The flow curve is approximated using Hockett-Sherby (see Table 1). Tensile tests in 0°, 45°, and 90° as well as in biaxial direction have been performed to determine yield stresses and Lankford coefficients. The corresponding parameters are listed in Table 2. Shear stress is fixed at $\sigma_{shear}/\sigma_{uni} = 0.6052$ for this study.

Table 1 Hockett-Sherby parameters for AA6016-T4

A [MPa]	B [MPa]	m [-]	n [-]
123.7	352.355	5.62	0.865

Table 2 Yield strength and Lankford coefficients in 0°, 45°, 90°, and biaxial direction

σ_0	σ_{45}	σ_{90}	σ_b	r_0	r_{45}	r_{90}	r_b
123.7 MPa	119.4 MPa	120.3 MPa	122.0 MPa	0.686	0.500	0.666	1.000

In [8], the YLD2000 yield locus has been fitted with those values including a typical exponent of $M = 8$ for aluminum. With this exponent, the strain distribution of a Nakazima experiment with width 200 mm cannot be reproduced. Earlier investigation has shown that an exponent of $M = 4.5$ results in a better plane strain as well as biaxial representation. Figure 1 shows the deviation in the strain distribution for both M-values depending on the drawing depth. As AutoForm is used in this study, the mathematically equal yield locus BBC is applied instead of YLD2000. The difference in the yield locus shape and therefore in the position of PS can be seen in the right figure.

All seven Nakazima specimens have been tested with DIC recording to determine the forming limit of the AA6016-T4 in [8]. The corresponding forming limit curve (FLC) is shown in Fig. 2. With these data, the time-dependent strain distribution from $\beta = \Delta\varepsilon_{22} / \Delta\varepsilon_{11} = -0.5$ (uniaxial tension) until $\beta = 1.0$ (biaxial tension) is known. The corresponding stress states are located within the 45° angle from uniaxial to biaxial stress as shown in Fig. 2.

As those Nakazima strain distributions are given and the Vegter yield locus is used, the investigation of this paper focuses on the position of plane strain case.

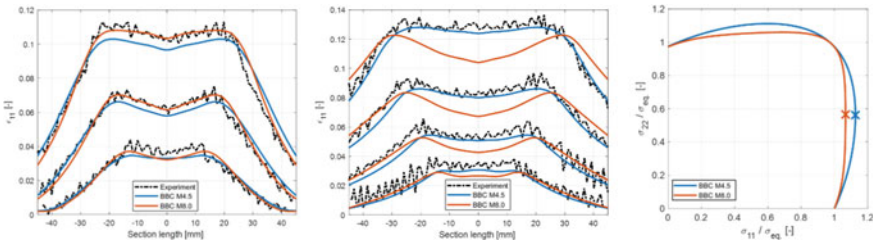


Fig. 1 Strain distribution of a 100 mm (left) and 200 mm (middle) Nakazima specimen at different drawing heights; Right: Comparison of the yield locus shape and position of PS

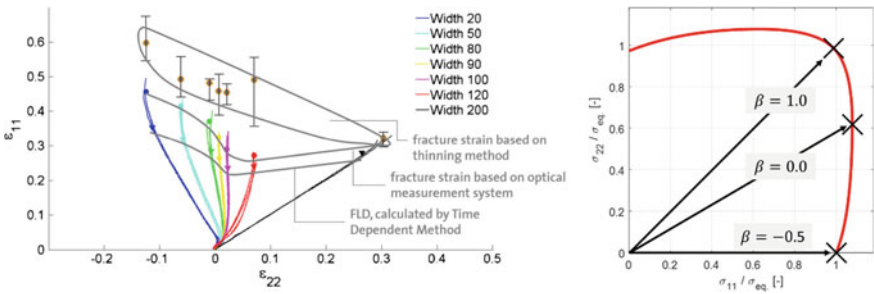


Fig. 2 Strain paths of a FLC (left) [8] and stress distribution on a yield locus (right) for Nakazima experiments

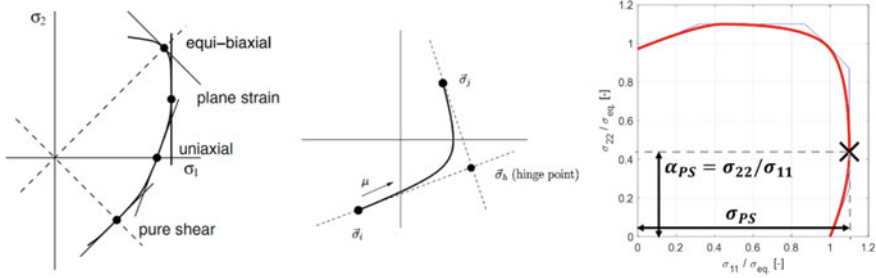


Fig. 3 Stress points and their tangential directions of a Vegter yield locus [5]; Right: Definition of α_{PS}

Vegter Yield Locus

The Vegter yield locus is build up out of second-order Bezier curves which are positioned between the four input stress points: shear, uniaxial, plane strain, and biaxial. Figure 3 shows these points and their corresponding tangential directions. The intersection between two neighboring tangents is the hinge point of their Bezier curve.

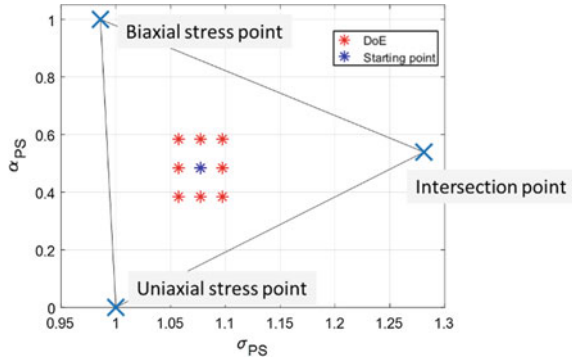
Besides the combination of $(\sigma_{11}|\sigma_{22})$, the position of the plane strain point in the stress space can be also specified by $\sigma_{PS} = \sigma_{11}$ and $\alpha_{PS} = \sigma_{22}/\sigma_{11}$. Due to the convexity of a yield locus, the PS point has the largest σ_{11} -value.

Method

For the used aluminum material, the standard material parameters have been measured (see Table 2) and the shear point is taken from the calibrated yield locus. Only the plane strain point is missing to set up the Vegter yield locus. Due to the available Nakazima DIC data, the PS point is determined using the inverse procedure ‘time-dependent cross-sectional optimization method’ [9]. A simulation of the Nakazima experiment is set up with a certain parameter set and afterwards the strain distribution at different drawing depths is compared. The Nakazima experiments with a width of 50 mm (between uniaxial tension and PS, B50), 100 mm (close to plane strain, B100), and 200 mm (biaxial tension, B200) are used in this study to find the best PS parameters. B50 and B200 are included in the investigation to ensure an overall good yield locus shape from $\beta = -0.5$ until $\beta = 1.0$.

The PS point derived out of the Vegter Lite yield locus is used as the starting point. It is determined at $\sigma_{PS_Start} = 1.0773$ and $\alpha_{PS_Start} = 0.4842$ using the weight factor proposal of $w_{PS} = 0.4125$ for aluminum [7]. A first DoE is designed by varying σ_{PS} by $\sigma_{PS_Start} \pm 0.02$ and α_{PS} by $\alpha_{PS_Start} \pm 0.1$. The resulting DoE can be seen in Fig. 4. The possible combination of σ_{PS} and α_{PS} is bounded within a triangle.

Fig. 4 Starting DoE with bounding triangle



The convex curvature of the yield locus would be violated outside of this triangle. The yield strength points in uniaxial and biaxial direction define two vertices of the triangle. The third point is the intersection point between the tangential lines (slope of R-values) of those two points (Fig. 4).

Various methods of evaluating the strain deviation between experiment and simulation are possible. In this study, the evaluation is done using the strain distribution along the central cross-sectional line. The strain distribution is also evaluated at different drawing depths. It is worth to mention that a full field comparison is possible as well. The error is measured as the deviation between experimental and simulated strains along the cross section.

$$res = \varepsilon_{Exp}(x) - \varepsilon_{Sim}(x) \tag{1}$$

Besides the complete cross-sectional length, the central 40 mm and the maximal strain deviation are investigated separately. To ensure that larger deviations are more weighted and therefore count for more, the root mean square error (RMSE) is used to evaluate the error of the parameter set.

$$RMSE = \sqrt{\frac{\int_{x_{min}}^{x_{max}} res^2 dx}{x_{max} - x_{min}}} \tag{2}$$

A polynomial 2×2 meta-model is calibrated with the RMSE deviations using linear least square method. After the evaluation of this meta-model, a new plane strain parameter set can be derived at the global minimum of the meta-model within the DoE-triangle. New simulations are started with those parameters and evaluated with the same procedure as described before. Updating the meta-model with the new results leads to a new minimum and therefore to a new parameter set. This procedure can be repeated until the error is satisfactory small enough.

Results

The first optimization strategy uses the entire cross-sectional length to calculate the deviation. The Nakazima experiments with a width of 50 mm, 100 mm, and 200 mm are considered at the drawing depths of 10 mm, 15 mm, 20 mm, and 25 mm. The height of 25 mm is only available for the B200 specimen. It is not recommended to use lower drawing depths as the strain state has to evolve and the relative measurement inaccuracy is too large. To ensure a good representation of the strains, all strains in all three directions are considered in the optimization process.

Figure 5 shows the resulting meta-model. It can be seen that the tendency for a minimal error shows in the direction of higher σ_{PS} and higher α_{PS} compared to the starting point. The sensitivity of σ_{PS} is higher than for α_{PS} which has only a small influence on the performance of the yield locus.

The best parameter set for the description of the plane strain point is $\sigma_{PS_opt} = 1.1$ and $\alpha_{PS_opt} = 0.6$. Figure 6 shows the corresponding strain distribution in comparison to the BBC yield locus with $M = 8$ and $M = 4.5$. The optimal parameter set fits very well on all three Nakazima experiments over all drawing depths. In comparison to BBC $M = 4.5$ and BBC $M = 8.0$, the Vegter yield locus performs much better, especially to $M = 8.0$ which is not a good assumption for the used aluminum alloy.

The error value can also be specifically calculated for the single Nakazima specimens or the individual drawing depths. Figure 7 shows the meta-models for B50, B100, and B200 considering all drawing depths in comparison to the overall meta-model. The meta-model is plotted within the DoE triangular boundaries, which are shown in Fig. 4. The red curve represents the Vegter yield locus with the best PS parameter set. It can be clearly seen that the sensitivities for σ_{PS} and α_{PS} vary between

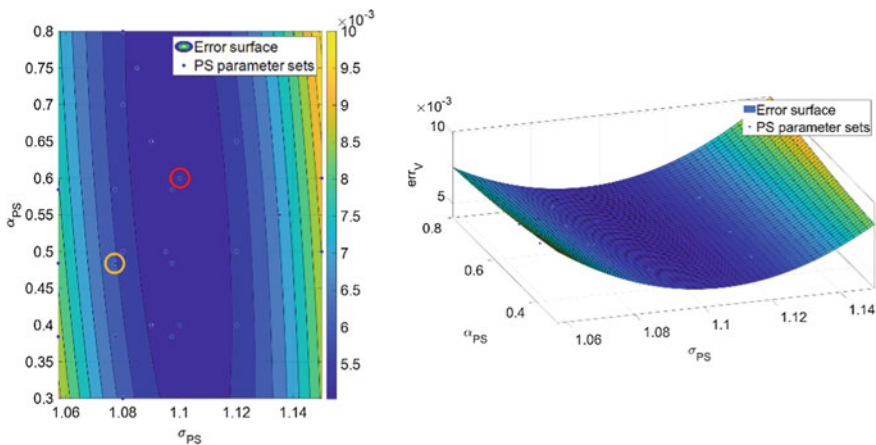


Fig. 5 Error meta-model including all parameters in 2D (left) and 3D (right). The optimal parameter set is marked in red and the starting point in orange

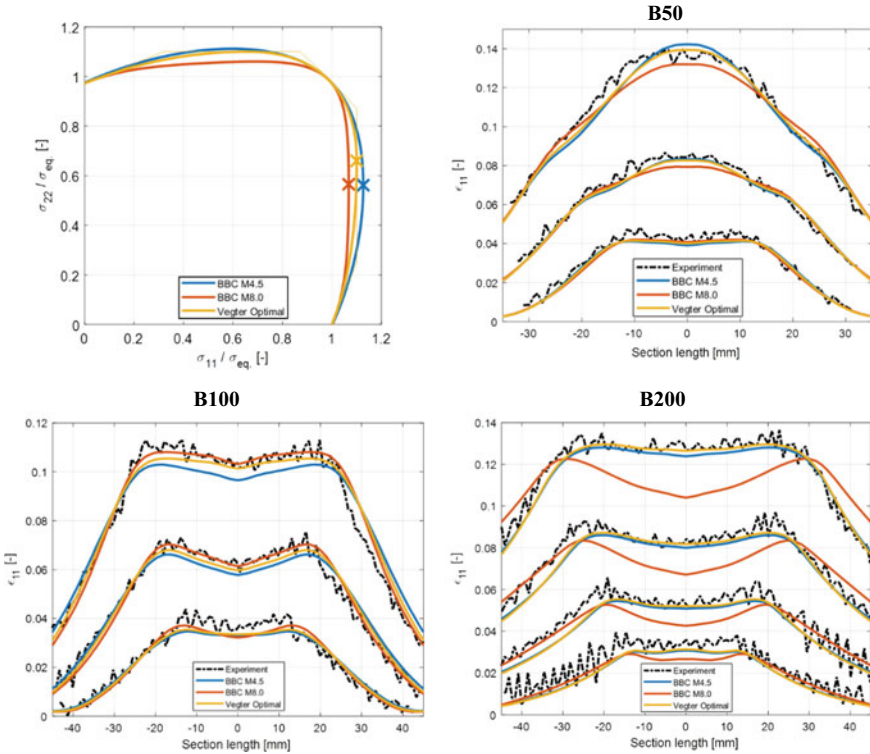


Fig. 6 Yield locus shape and strain distributions of the optimal Vegter PS parameter set in comparison to BBC

the specimens. For B100 Nakazima specimen, the influence of α_{PS} is much higher and the error is lower than for B50 and B200. The reason for this behavior is that the PS point is the optimization parameter in this paper. The resulting strain distributions of B50 and B200 are influenced by the plane strain point definition too. Figure 8 shows the stresses of the three Nakazima specimens along the cross section at a depth of 20 mm. Besides the desired strain state in the center of the specimen, different strain states result on the path from the center towards the edges due to the specimen geometry. These strain states lead via the associated flow rule and therefore via the curvature of the yield locus to the stresses shown in Fig. 8.

Looking at the meta-model in dependency of the depth in Fig. 9, the sensitivities for σ_{PS} and α_{PS} are very similar. Accordingly, the evaluation depth has a low influence on the PS point determination. The higher the depth the larger the error values as the strains increases as well. Hence, the absolute deviation gets larger which can be seen in Fig. 6.

Using the central section length of 40 mm for the error calculation, the tendency for an optimal PS set tends towards higher α_{PS} -values and the sensitivity for σ_{PS} stays similar (see Fig. 10). However, the optimal parameter set is the same as for the

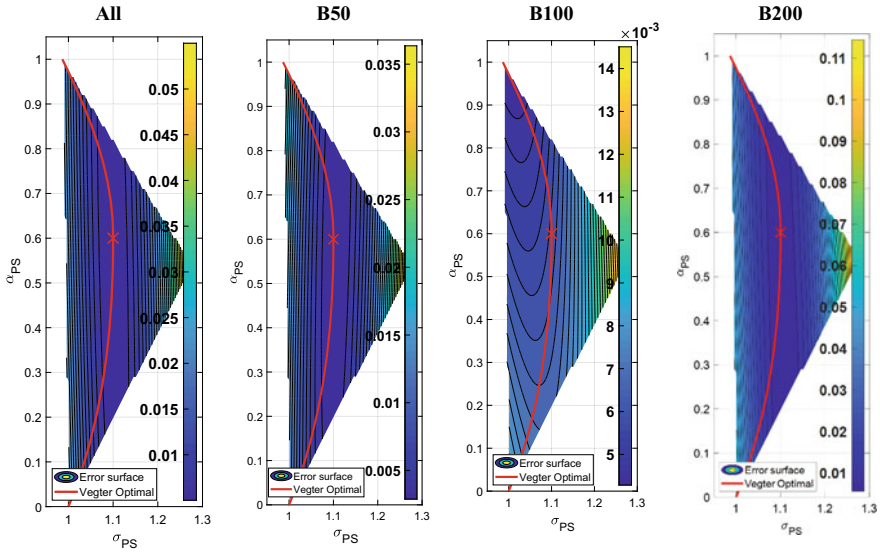


Fig. 7 Different sensitivities for σ_{PS} and α_{PS} depending on the Nakazima specimen considering all drawing depths

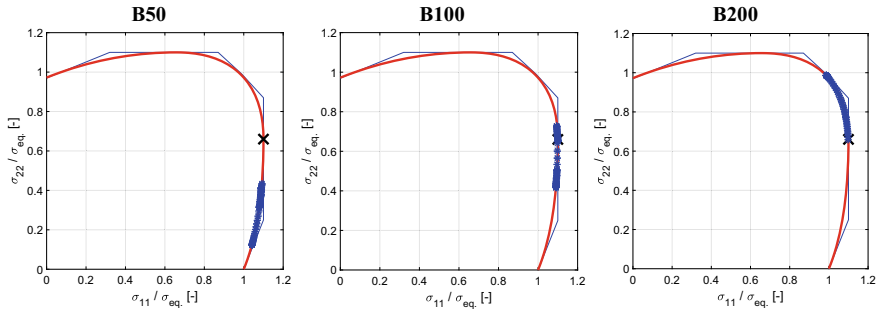


Fig. 8 Stress distribution along the cross section for B50, B100, and B200 at a depth of 20 mm; black crosses mark the plane strain point in the stress space

entire section length. Using the maximal deviation strategy, the meta-model shows a tendency to higher α_{PS} and smaller σ_{PS} -values although the optimal parameter set ($\sigma_{PS_Opt_Max} = 1.097$ and $\alpha_{PS_Opt_Max} = 0.584$) is located very close to the other optimal PS point. The absolute error of the maximal deviation strategy is greater than for the other two. Using this evaluation strategy a single measurement peak or error can influence the entire result. Therefore, one of the first two strategies should be used.

The overall best PS parameter set ($\sigma_{PS_opt} = 1.1$ and $\alpha_{PS_opt} = 0.6$) is compared to the BBC yield loci ($M = 4.5$ and $M = 8.0$) in Table 3 according to the RMSE

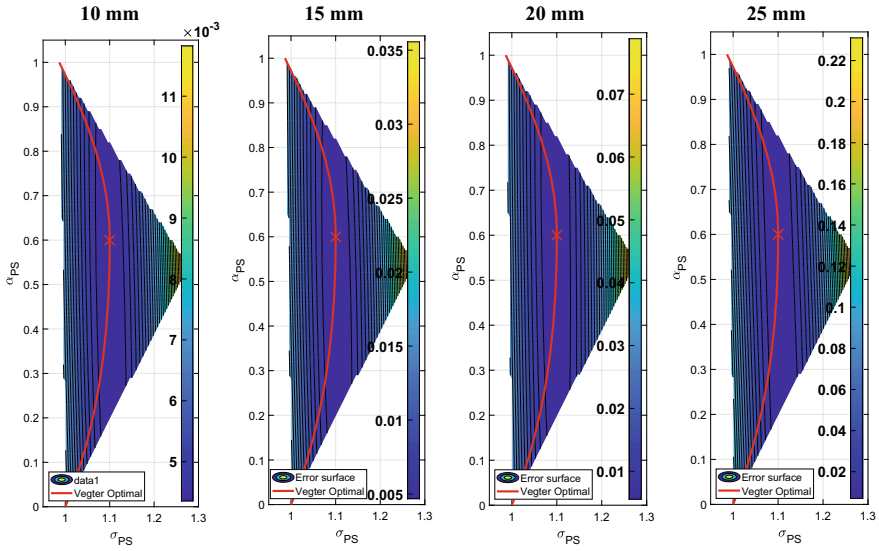


Fig. 9 Sensitivities of σ_{PS} and α_{PS} for the investigated drawing depths; the three Nakazima specimens have been considered for all meta-models

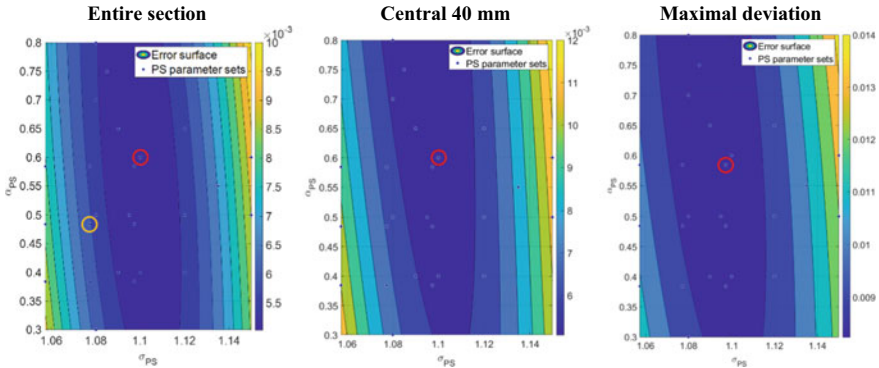


Fig. 10 Meta-model and the optimal point for the three evaluation methods

Table 3 Comparison of the error calculated with the entire cross-sectional strategy

	Vegter Optimal	BBC M = 4.5	BBC M = 8.0
Error	4.723×10^{-3}	5.021×10^{-3}	7.539×10^{-3}

error. The three Nakazima specimens at all drawing depths are used to calculate the error with the entire cross-sectional strategy. The accuracy of the strain distribution representation can be improved using the introduced optimization strategy.

Conclusion

The new ‘time-dependent cross-sectional optimization method’ has been used to determine the position of plane strain of a Vegter yield locus. It is possible to find the optimal parameter set using optical recorded Nakazima experiments B50, B100, and B200 doing reverse fitting. The method showed that σ_{PS} is more sensitive on the strain deviation and therefore influences the overall performance of the yield locus more than α_{PS} .

All three optimization methods deliver nearly the same optimal plane strain point. It is recommended to use either the central section or the entire cross-sectional length as the maximum value error comparison strongly depends on the measurement quality of the experiment. It has been shown that the Vegter yield locus can be calibrated very precisely directly from the Nakazima experiments without using additional experiments.

The validation of the Vegter yield locus using the optimal PS parameter set with a cross-die experiment is part of ongoing work.

References

1. Barlat F et al (2003) Plane stress yield function for aluminum alloy sheets - part 1: theory. *Int J Plast* 19(9):1297–1319
2. Logan RW, Hosford WF (1980) Upper-bound anisotropic yield locus calculations assuming (111)-pencil glide. *Int J Mech Sci* 22(7):419–430
3. Hippke H, Hirsiger S, Rudow F, Berisha B, Hora P (2019) Optimized prediction of strain distribution with crystal plasticity supported definition of yielding direction. In: 12th Forming Technology Forum, Herrsching am Ammersee, Germany. <https://doi.org/10.3929/ethz-b-00377565>
4. Hirsiger S, Berisha B, Hippke H, Hora P (2019) Predicting plastic strain anisotropy of AA6016-T4 and DC05 by multiobjective parameter calibration of crystal plasticity models and coupling strategies with macroscopic models. In: Proceedings of COMPLAS 2019. <https://doi.org/10.3929/ethz-b-000386362>
5. Vegter H, Van Den Boogaard AH (2006) A plane stress yield function for anisotropic sheet material by interpolation of biaxial stress states. *Int J Plast* 22(3):557–580
6. Raemy C (2018) Novel constitutive models for capturing anisotropy, tension-compression asymmetry, and anisotropic hardening of titanium. PhD thesis, ETH Zurich
7. Vegter H, ten Horn C, Abspoel M (2009) The Corus-Vegter Lite material model: simplifying advanced material modelling. *Int J Mater Form* 2(SUPPL. 1):511–514
8. Gorji M, Berisha B, Hora P, Barlat F (2016) Modeling of localization and fracture phenomena in strain and stress space for sheet metal forming. *Int J Mater Form* 9(5):573–584
9. Hora P, Barth K (2019) Impact of advanced measurement methods on the development and setup of new (complex) constitutive models. In: 12th Forming Technology Forum, Herrsching am Ammersee, Germany

Part III
Mechanics and Materials of Sheet Forming:
In Honor of Thomas B. Stoughton

A Novel Testing Methodology for In Situ Microstructural Characterisation During Continuous Strain Path Change



Sisir Dhara, Scott Taylor, Łukasz Figiel, Darren Hughes, Barbara Shollock, and Sumit Hazra

Abstract Change of strain path is a familiar phenomenon during continuous stamping operations of sheet metal for several applications, including automotive body parts. Strain path transition can potentially alter the forming limit of the material. Controlling the strain path change in a single deformation stage is a key challenge in elucidating this strain path-dependent deformation. In this work, a novel testing rig and specimen geometry that is capable of changing the strain path of a sample continuously without unloading the specimen were conceptualised, modelled, and subsequently manufactured. The size of this mechanical test rig permits it to be placed inside a scanning electron microscope (SEM) chamber in order to study strain path transition in situ to highlight strain localisation and related microstructural changes in real time. Using this apparatus, the effect of strain path change on material microstructure was investigated by carrying out in situ SEM and electron back-scattered diffraction (EBSD) analysis.

Keywords Strain path change · Microstructure characterisation · In situ SEM and EBSD · Finite element modelling

Introduction

Automotive stamping is a multi-stage deformation process. In the first stage, a metal sheet is drawn into a definite shape and in the subsequent stages; the drawn component is redrawn, flanged or pierced. During various stamping stages, a material can undergo two different types of strain path change. These are continuous and discontinuous strain path changes. A material undergoes a continuous strain path change at the first draw stage of the stamping, where a draw tool with typically complex geometry draws and stretches the material. On the other hand, a discontinuous strain

S. Dhara (✉) · S. Taylor · Ł. Figiel · D. Hughes · S. Hazra
WMG, University of Warwick, Coventry CV4 7AL, UK
e-mail: Sisir.Dhara@warwick.ac.uk

B. Shollock
Department of Engineering, King's College London, London WC2R 2LS, UK

path is induced in the material when the drawn shell from the first stage of stamping is unloaded from the draw tool and subsequently redrawn, flanged, or pierced along a different strain path. The study of strain path change has been a hot topic in metal forming for a long time. Graf and Hosford [1, 2] studied the discontinuous strain path change phenomenon and examined the effect of uniaxial, biaxial and plain strain pre-strain on the forming limit of AA 2008 T4 and AA 6111 T4 aluminium alloy. They found that the biaxial pre-strain lowered the forming limits, whereas uniaxial pre-strain raised the forming limit when the pre-strain direction was transverse direction (normal to the rolling direction of the sheet). The pre-straining near plain strain increased the forming limits slightly when the direction of pre-strain was transverse direction. Dhara et al. [3] further investigated the effect of discontinuous strain path change on forming limits of AA5754-O aluminium alloy by pre-straining the samples in uniaxial tension in a Zwick tensile machine and thereafter re-loaded the samples in the biaxial strain path by using a 50 mm diameter punch in a Nakajima test. They reported that the pre-straining along the transverse direction increased the forming limit strains while the pre-straining along the rolling direction decreased the forming limits. Similarly, Collins et al. [4] uniaxially pre-strained low carbon ferritic steel samples by stretching along one direction and then re-loaded the samples along a biaxial strain path by using a purpose-built biaxial stretching equipment. They found that a uniaxial pre-strain followed by biaxial stretching resulted in a significant gain in the limiting strains. During these discontinuous strain path change experiments, a common characteristic emerges as the two stages of deformation were carried out on different experimental set-ups and the samples may have experienced dissimilar strain rates during both the stages.

It is thought that the changing strain path affects the formability as it changes the texture and work-hardening behaviour of the material [5, 6]. To investigate the effect of material deformation on microstructure, Ghadbeigi et al. [7] and Celotto et al. [8] applied a recently developed technique where mechanical deformation of a material was performed inside a scanning electron microscope (SEM) chamber using a miniaturised test rig, and the SEM images were captured from the sample surface while the elongation process was going on in situ. They elongated the samples along the uniaxial strain path and post-processed the periodically captured SEM images using the digital image correlation (DIC) technique to examine the strain field induced on the sample surface at the mesoscale. At this scale, they analysed the effect of elongation on the strain distribution in the ferritic and martensitic phases of the dual-phase 1000 (DP1000) steel and transformation-induced plasticity 800 (TRIP800) steel samples, respectively. In addition, they observed the micro-void nucleation and fracture mechanism of these materials. Caër and Pesci [9] contributed to the design of the sample for the in situ deformation technique by designing a cruciform sample that ensured the strain localisation at the centre of the sample while elongating the sample along both the directions using a micromechanical rig. They studied the grain rotation and misorientation development in an annealed AISI 304 stainless steel in situ during the biaxial loading inside an SEM chamber. In addition, they measured the texture evolution by tracking the captured electron back-scattered diffraction (EBSD) data in situ from the centre of the biaxial specimen

periodically during the entire elongation process. They concluded that the loading path had the potential to orient the grains along a particular direction. Kubo et al. [10] proposed an innovative design of cruciform specimen by introducing a notch at each of the corners of the central part of the specimen for in situ deformation technique. They performed the biaxial tensile test of the specimen made of interstitial free (IF) steel in an SEM chamber and examined the inverse pole figure (IPF) maps, grain average misorientation (GAM) maps, and Taylor factor (TF) maps to characterise microstructural changes during the biaxial elongation. In brief, the in situ deformation technique is a vital tool to understand the effect of plastic deformation induced by strain path change on the evolution of strain, microstructure and texture revealing the changes in formability of the material. However, the work so far has focussed on the effect of discontinuous strain path changes, which are typically observed when a material is reloaded between stamping stages. As a result, there is a research gap in the understanding of material behaviour under continuous strain path condition that occurs in the draw process. Addressing this gap will enable formability to be quantified more accurately, thereby increasing the confidence of designers in utilising high-strength materials that have low formability.

In this work, the gap was addressed by developing an experimental method to investigate the effect of the continuous strain path transition that occurs in the drawing stage. The method was then used to investigate the effect of continuous loading on the evolution of material strain, microstructure and texture. A novel cruciform sample was designed based on the design of Caër and Pesci [9]. The sample was elongated in a Micromecha biaxial testing rig to enable the continuous strain path change to occur at a set point during the experiment. The strain evolution of the samples was observed at the macroscopic and microscopic scales termed as macro-strain and micro-strain using DIC while the texture evolution was observed with EBSD. The macro-strain evolution at the centre of the specimen confirmed the occurrence of continuous strain path transition. The micro-strain evolution showed a rotation of strain bands while the texture evolution conveyed grain rotation during continuous strain path change.

Development of Continuous Strain Path Change Mechanism

The development of the continuous strain path change mechanism was carried out in two stages. In the first stage, finite element (FE) modelling of the strain path change specimen with the testing rig was performed. This optimised the sample geometry and the overall design of the rig and the specimen assembly. In the second stage, the actual physical testing of the strain path change mechanism was performed and the macro-strain evolution at the centre of the specimen was evaluated to confirm the occurrence of continuous strain path change.

FE Modelling of Continuous Strain Path Change Mechanism

The experimental set-up consisting of the Micromecha rig and the cruciform specimen is presented in Fig. 1. The inline grips and transverse grips of the rig were connected through a 45° wedge (Fig. 1). A motor drove one end of the inline grip 1, while the inline grip 2 was securely fastened to the body of the rig. When the motor moved the inline grip 1, its motion was translated into a vertical motion of the transverse grips via the wedge, thus loading the sample vertically at the same time. The inline grip 1 was moved along the X-axis and the transverse grips were moved along the Y-axis during the experiments. To change the strain path during testing, the cruciform specimen geometry proposed by Caër and Pesci [9] was modified to include slotted holes in the vertical arms (Fig. 2). The external dimension of the strain path change sample was 30.4 mm by 30 mm and its thickness was 1 mm (Fig. 2a). The central region was reduced in thickness (0.3 mm) to concentrate the strain in that

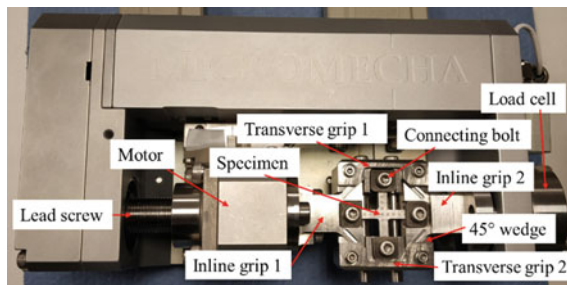


Fig. 1 Experimental set-up consisting of the Micromecha rig and the cruciform specimen

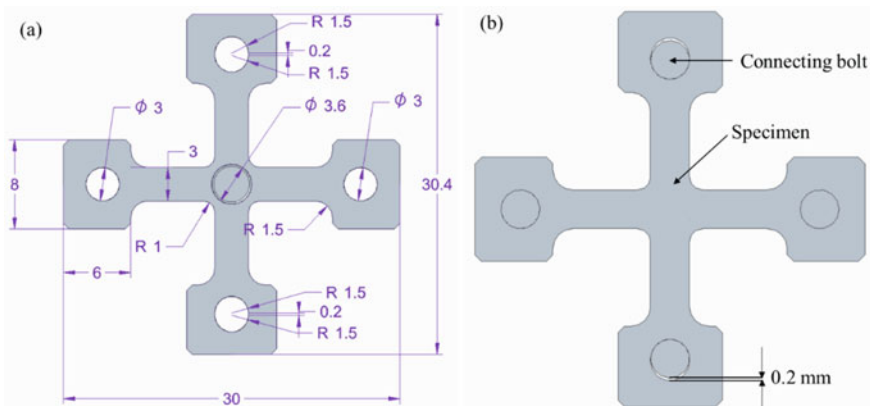


Fig. 2 **a** Design of strain path change specimen and **b** assembly design of connecting bolts and the strain path change specimen showing 0.2 mm travel of connecting bolts in the vertical arms during strain path change

Table 1 Material properties of DX54 steel used in this work

Material	DX54	
Gauge (mm)	1	
Young's modulus (GPa)	213	
Yield strength (MPa)	225	
Ultimate tensile strength (MPa)	329	
% Elongation	43	
Anisotropy parameters	r_0	1.53
	r_{45}	1.08
	r_{90}	2.16
Hardening parameters according to Hollomon law	Strength coefficient, K (MPa)	555
	Hardening exponent, n	0.20
Density (g/cm^3)	7.87	
Poisson's ratio	0.3	

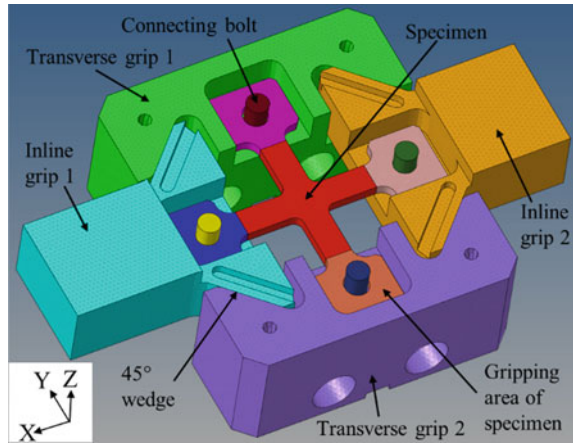
Table 2 Chemical composition (wt %) of DX54 steel used in this work

Material	C	Mn	Si	Ti	S	P	Fe
DX54	0.12	0.60	0.50	0.30	0.045	0.10	Balance

region and to prevent overloading the load cell of the rig. DX54 steel was chosen for the specimen material, as it is a deep drawing quality steel with a higher amount of elongation commonly used in automotive applications. The material properties and chemical compositions are detailed in Tables 1 and 2, respectively. At the start of the continuous strain path change experiment, the slots allowed the bolts of the transverse grips to translate without loading the sample. After a specified elongation that was determined by the length of the slots (0.2 mm), the transverse grips engaged and the specimen was deformed biaxially. Hence, the material was deformed uniaxially at the start of the test before the strain path changed to a biaxial strain path resulting in a continuous strain path transition.

The rig and specimen were modelled using the finite element (FE) method. The validated model was used to optimise the design of the sample and experimental apparatus. The model consisted of the horizontal grips, vertical grips and the specimen (Fig. 3). The grips and the gripping areas of the sample were modelled as rigid bodies while the specimen was modelled as a deformable body. All bodies were meshed with solid elements of an appropriate size that optimised speed and accuracy. For simplicity, yielding was modelled with the von Mises model and power-law hardening was assumed. A more advanced material model, such as crystal plasticity-based model with anisotropic behaviour, and hardening law were beyond the scope of current research and will be studied in future. To model the clamping of the sample to the grips, the nodes in the connecting bolts were joined to the nodes of the grips as constrained rigid bodies while the connecting bolts were making surface contact with

Fig. 3 FE model of the assembly consisting of the grips, connecting bolts and the specimen



the gripping areas of the specimen. Displacement (2.5 mm) was applied to in-line grip 1 along the X-axis (Fig. 3) to represent the motor in the physical rig. Inline grip 2 was fixed. The motion of transverse grips 1 and 2 was restricted to the Y-axis, to reflect the physical rig. The model was solved using LS-Dyna explicit v.10.1.0.

Experimental Trials of Continuous Strain Path Change Mechanism

The FE model of continuous strain path change mechanism was validated against physical trials. During trial experiments with the rig and the sample, the strain evolution at the centre of the specimen was calculated to confirm the occurrence of continuous strain path change. During the experiments, it was ensured that the specimen was loosely held in the transverse grips to allow the connecting pins to travel freely in the 0.2 mm slot in the first stage of the travel (Fig. 2b). The strain evolution of the sample during the experiments was measured with the GOM 12 M macro-DIC system. The DIC system consisted of two 12MP cameras fitted with lenses to capture the strains in the arms and the central region of the specimen. The measurement frame rate was 1 frame/second and samples were loaded at 0.3 mm/min.

Measuring Technique of Micro-Strain and Texture Evolution During Continuous Strain Path Change

The specimens for strain path change were prepared from a DX54 steel sheet and were polished by using silicon carbide (SiC) paper, diamond suspension solutions, and finally 0.05 μm colloidal silica solution. Samples for micro-strain evaluation

were etched with Kalling's No. 2 reagent for 10 s. To carry out the microstructural measurements, the polished sample was loaded into the rig and the rig was placed in the chamber of a ZEISS SIGMA field emission gun scanning electron microscope (FEG-SEM). The rig was controlled by using the POROS 2 software supplied with the Micromechea rig. The inline grip 1 was elongated at a rate of 5 $\mu\text{m}/\text{sec}$. The elongation was arrested after every 0.2 mm travel to perform SEM and EBSD scans for micro-strain and texture analysis, respectively. For micro-strain observation, an etched sample was used. The micro-strain analysis was performed using the micro (grain level) DIC analysis and texture analysis was carried out using EBSD analysis. For micro DIC analysis, the SEM scans were done by using secondary electrons (SE2) with 20 keV voltage. The captured SEM images were post-processed with Lavision's DIC software (Davis 10) to obtain the micro-strain distribution. The subset size was used as 25 μm and the step size was used as 8 μm during the micro DIC analysis. For texture analysis, the test was repeated to obtain EBSD scans by using the SEM's EBSD detector. During EBSD scanning, the step size was kept at 0.5 μm . The EBSD results were analysed in HKL Channel 5 software.

Results and Discussion

Strain Evolution During Continuous Strain Path Change

Simulation Versus Experimental Macro-Strain Evolution

The simulated X-axis and Y-axis macro-strain (ϵ_x and ϵ_y , respectively) contour of the specimen were computed before and after the strain path change and are presented in Fig. 4.

The experimental ϵ_x and ϵ_y macro-strain contour of the specimen before and after the strain path transition was evaluated and is presented in Fig. 5.

The macro-strain contours showed the strain concentration and uniformity of the strain distribution in the central region. The behaviour and level of the simulated macro-strain contours were reasonably close to the experimental macro-strain contours.

The strain path evolution at the centre of the specimen was evaluated from both simulation and experiment and it is presented in Fig. 6. It can be noted that the sample was deformed along the uniaxial strain path initially and then it was deformed along a biaxial strain path towards the end of the test. The slope of the uniaxial strain path was found to be -0.85 , which was in between uniaxial tension (slope = -0.5) and pure shear deformation (slope = -1.0). The slope obtained in the biaxial strain path was 1.2 which was a little higher than the slope of the equibiaxial strain path (slope = 1). There was a good similarity between the simulated and experimental strain path transition curves. The difference in the length of the uniaxial deformation between the experiment and simulated curves was likely to be due to the machining

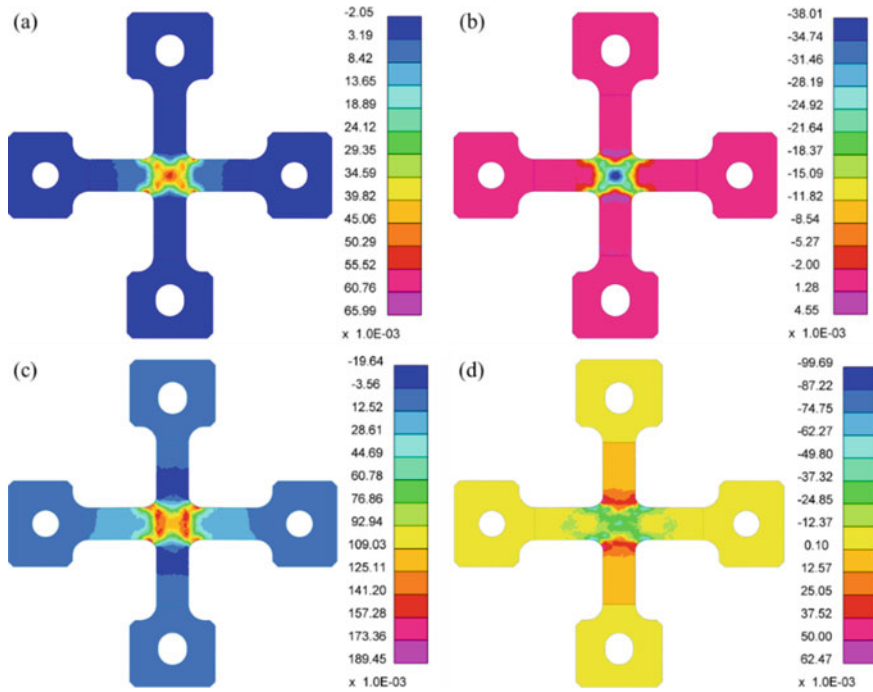


Fig. 4 Simulated macro-strain contour of DX54 specimen during continuous strain path change: **a** ϵ_x and **b** ϵ_y contour before the strain path change and **c** ϵ_x and (d) ϵ_y contour after the strain path change

tolerance for the slot and thickness of the central region during the manufacturing of the specimen for the experimental trial. Hence, the developed strain path change mechanism performed continuous strain path transition.

Micro-strain Evolution

The X-axis and Y-axis micro-strain (ϵ_x and ϵ_y , respectively) distributions calculated from the micro-DIC analysis showed that the strain distributions were heterogeneous with a wide spread of strains (Figs. 7 and 8). This is because the grains of the DX54 steel samples were not uniformly deformed. This may be the intrinsic property of the material behaviours at the micro level. However, what we had seen at macro level was the summation of these by considering the suitable homogenization rule. During the initial stage of the experiment when the sample was loaded uniaxially, ϵ_x increased while ϵ_y decreased. The average strains in the data were reasonably matching with the macro-strain values at the centre of the specimen. At the starting of the biaxial strain path, ϵ_y started to increase confirming that the strain path change (uniaxial to biaxial) started. The banding of ϵ_x and ϵ_y micro-strains (indicated by the black line

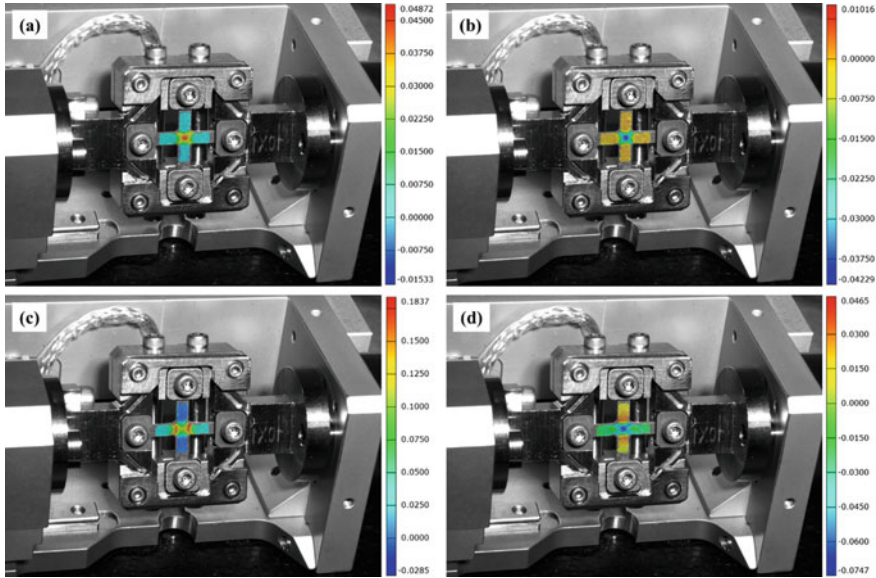


Fig. 5 Experimental macro-strain contour of DX54 specimen during continuous strain path change: **a** ϵ_x and **b** ϵ_y contour before the strain path change and **c** ϵ_x and **d** ϵ_y contour after the strain path change

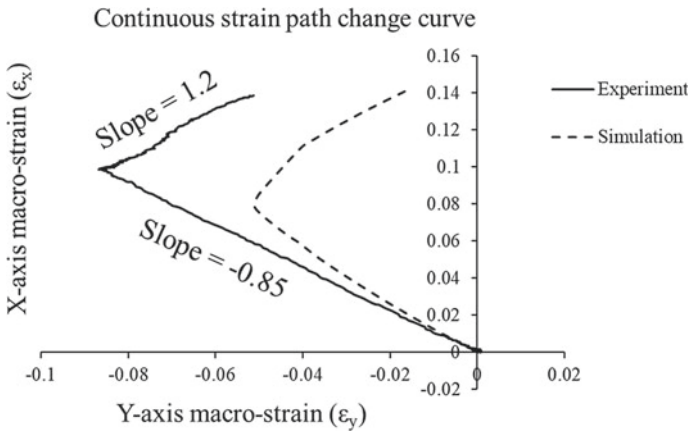


Fig. 6 Experiment versus simulation continuous strain path change curve of DX54 sample

in Figs. 7 and 8) were found to be approximately 74° and 78° , respectively, at the end of the uniaxial strain path. When the strain path change occurred and the sample underwent subsequent elongation along the biaxial strain path, the angle of these lines appeared to rotate. However, the rotation was minute. The rotation was slightly more prominent in the ϵ_y strain distribution than in the ϵ_x strain distribution.

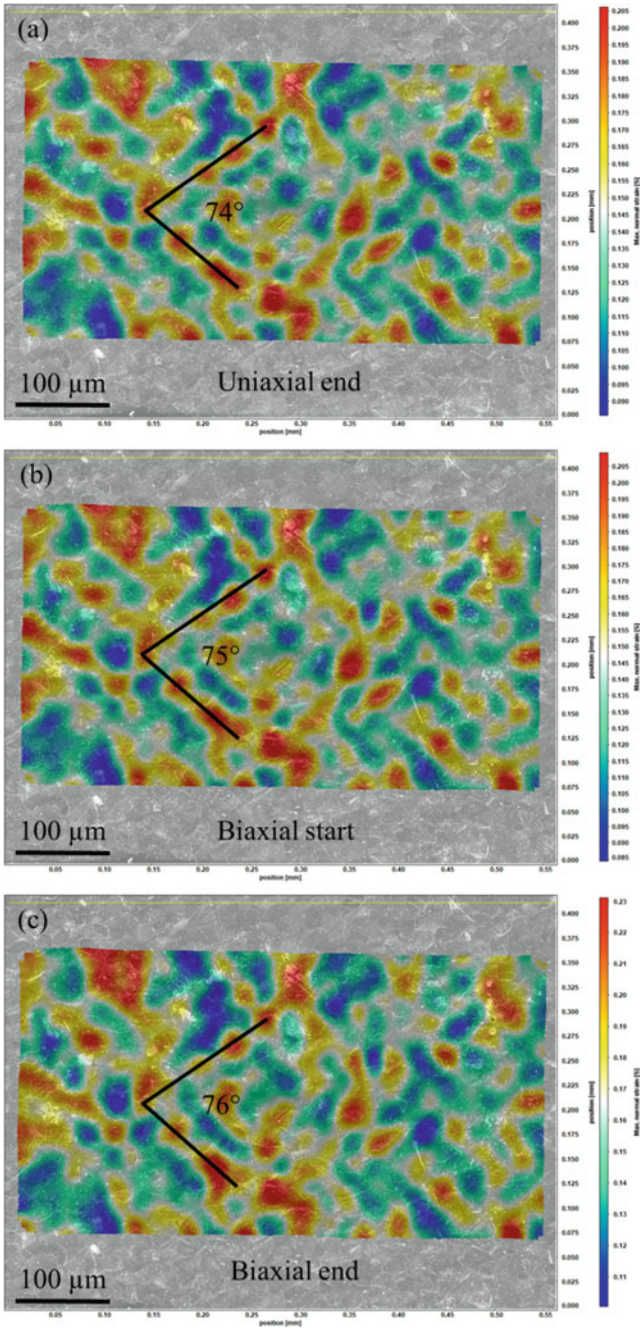


Fig. 7 X-axis micro-strain (e_x) distribution at the centre of the specimen calculated from micro DIC analysis after **a** uniaxial end, **b** biaxial start, and **c** biaxial end during the continuous strain path change

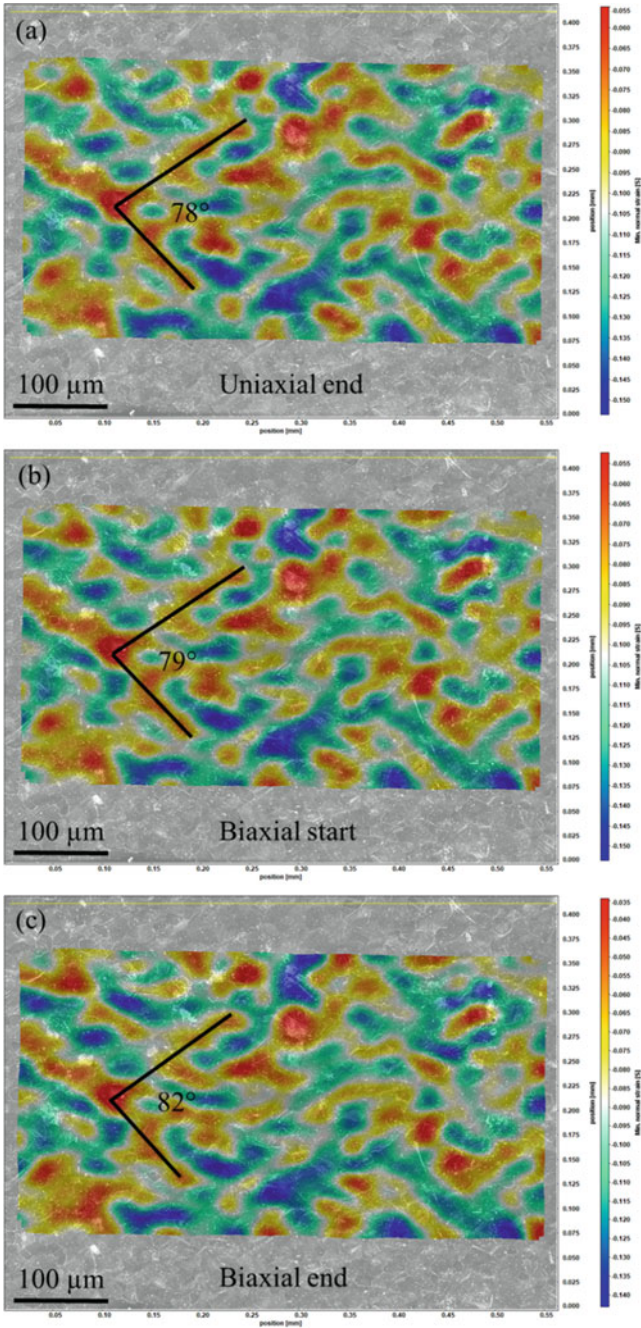


Fig. 8 Y-axis micro-strain (ϵ_y) distribution at the centre of the specimen calculated from micro DIC analysis after **a** uniaxial end, **b** biaxial start, and **c** biaxial end during the continuous strain path change

Texture Evolution During Continuous Strain Path Change

Further analysis of microstructural changes was performed by carrying out texture analysis using EBSD mapping of around 400 grains at the centre of the specimen. The EBSD X maps, SEM images, and inverse pole figure (IPF) X maps are shown in Fig. 9. Evidence of deformation was clear within the grain structure, with grain elongation and rotation occurring with increased elongation of the sample. Grains with orientations of [111] (indicated by black circles) and [001] (indicated by black dotted circles) underwent rotation differently. The [111] grains underwent rotation from the crystallographic direction [111] towards [101] during the entire deformation

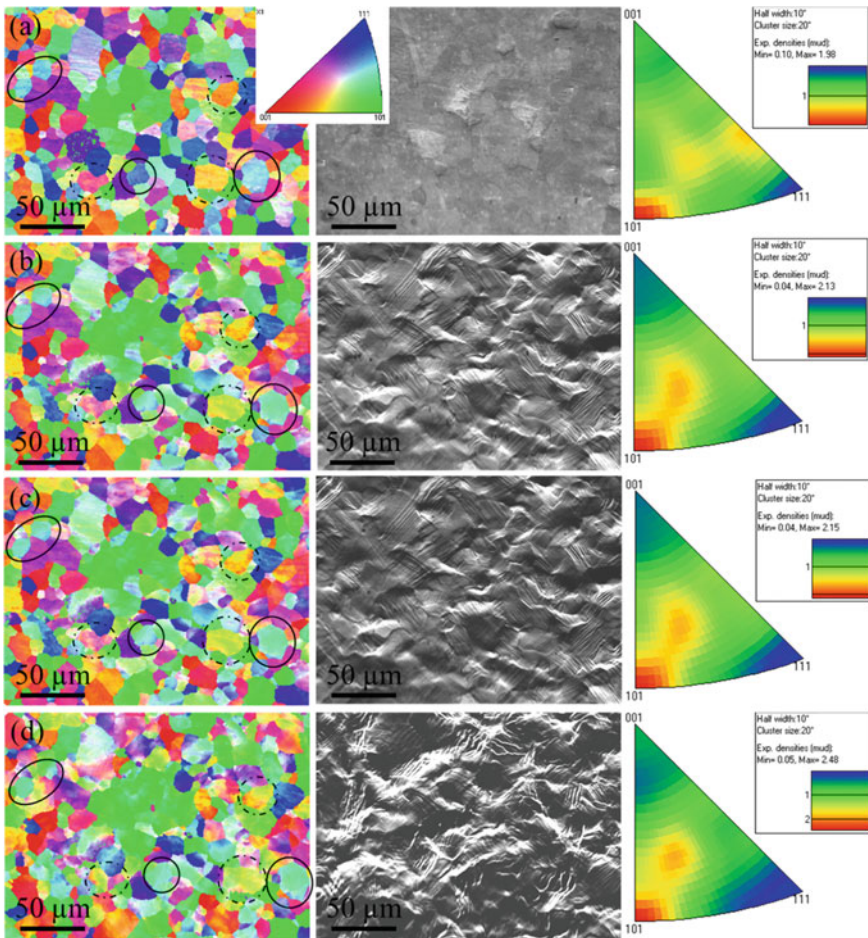


Fig. 9 On the left: EBSD X mappings, in the middle: SEM images and on the right: inverse pole figure (IPF) X of the centre of the specimen at **a** uniaxial start, **b** uniaxial end, **c** biaxial start and **d** biaxial end during continuous strain path change

process. On the other hand, the [001] grains underwent rotation from the crystallographic direction [001] towards [101] during the strain path change. The extensive deformation of the sample surface was shown by the increase in slip bands in SEM images captured during the deformation process. IPF X maps showed the gradual increase of multiples of uniform distribution (MUD) values and the sample showed [101] X texture with a maximum intensity factor of 2.48 at the end of the biaxial strain path.

The grain rotation was further studied with the help of pole figures as shown in Fig. 10. There was a difference in colour contour in the pole figures in the {100} and {111} planes. The MUD value increased in the uniaxial strain path and it decreased in the biaxial strain path in the {100} plane. On the contrary, the MUD value increased

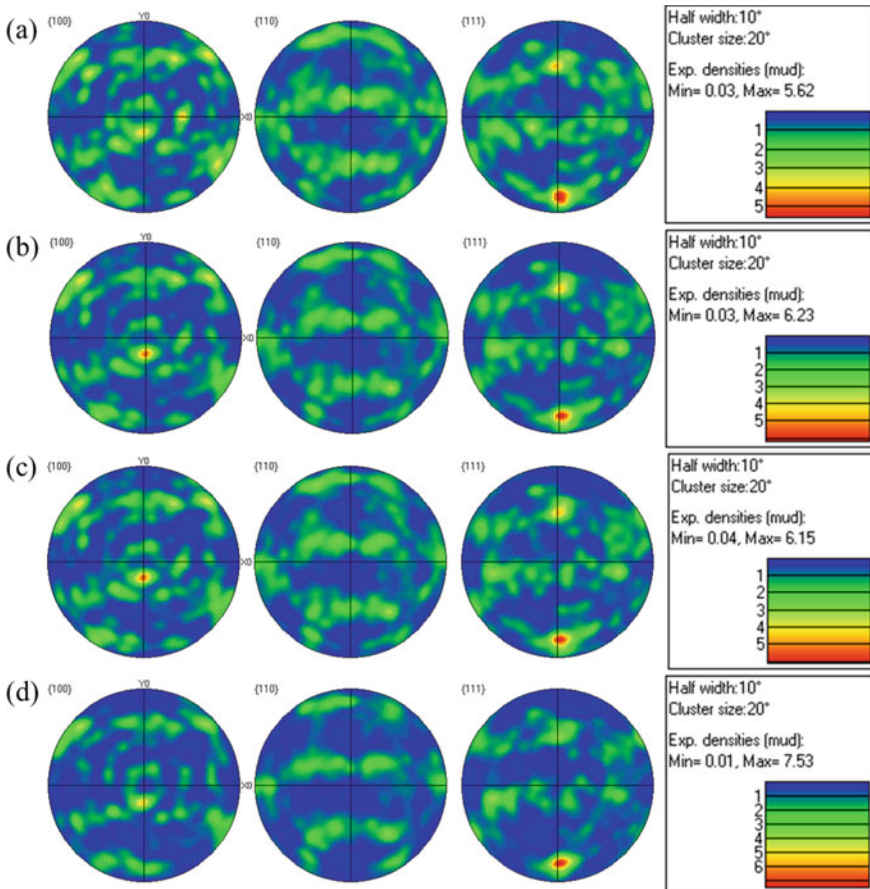


Fig. 10 Pole figures of the grains at the centre of the specimen at **a** uniaxial start, **b** uniaxial end, **c** biaxial start, and **d** biaxial end during continuous strain path change

and concentrated in a particular location in the $\{111\}$ plane after the strain path change.

Conclusions

An experimental technique was developed to perform continuous strain path change without the withdrawal of the applied load from the specimen. The developed FE model of the rig and the suitable sample geometry were capable enough to mimic the strain path transition during the experiment. The macro-strain evolution captured at the centre of the specimen by using the DIC analysis confirmed that the DX54 steel specimen underwent uniaxial to biaxial continuous strain path transition. The microstructural analysis was performed by placing the overall set-up inside an SEM chamber. The micro-strain distribution analysed by micro DIC analysis revealed the heterogeneous strain banding on the sample surface and the angle of the bands was rotated during the strain path transition and subsequent deformation. The EBSD and pole figure results confirmed the evidence of grain rotation during strain path change. Thus, DX54 steel is susceptible to grain rotation during strain path transition.

References

1. Graf AF, Hosford WF (1993) Calculations of forming limit. *Metall Trans A* 24:2497–2501
2. Graf A, Hosford W (1994) The influence of strain-path changes on forming limit diagrams of A1 6111 T4. *Int J Mech Sci* 36:897–910
3. Dhara S, Basak S, Panda SK et al (2016) Formability analysis of pre-strained AA5754-O sheet metal using Yld96 plasticity theory: role of amount and direction of uni-axial pre-strain. *J Manuf Process* 24:270–282
4. Collins DM, Erinoshio T, Dunne FPE et al (2017) A synchrotron X-ray diffraction study of non-proportional strain-path effects. *Acta Mater* 124:290–304
5. Erinoshio TO, Cocks ACF, Dunne FPE (2013) Coupled effects of texture, hardening and non-proportionality of strain on ductility in ferritic steel. *Comput Mater Sci* 80:113–122
6. Erinoshio TO, Cocks ACF, Dunne FPE (2013) Texture, hardening and non-proportionality of strain in BCC polycrystal deformation. *Int J Plast* 50:170–192
7. Ghadbeigi H, Pinna C, Celotto S et al (2010) Local plastic strain evolution in a high strength dual-phase steel. *Mater Sci Eng A* 527:5026–5032
8. Celotto S, Ghadbeigi H, Pinna C et al (2018) Deformation-induced microstructural banding in TRIP steels. *Metall Mater Trans A* 49:2893–2906
9. Caër C, Pesci R (2017) Local behavior of an AISI 304 stainless steel submitted to in situ biaxial loading in SEM. *Mater Sci Eng A* 690:44–51
10. Kubo M, Yoshida H, Uenishi A et al (2016) Development of biaxial tensile test system for *in-situ* scanning electron microscope and electron backscatter diffraction analysis. *ISIJ Int* 56:669–677

Comparison of Experimental and Finite Element Analysis Results of a Car Body Part with the Optimization of Material Parameters



M. E. Tamer, S. Bortucen, and U. Sahinoglu

Abstract Sheet metal forming operations in an automotive industry depend on the deformation degrees in which the mechanical characterization is crucial, and the geometry dependence is important. Numerical simulations in the deep drawing process predict the possible cracks depending on material behavior and the complexity of the part. With the aim of improving the reliability of sheet forming simulations from the perspective of material behavior, finite element analysis of a car body component is performed in this study. Tensile and stack compression tests have been performed to acquire the material data for sheet metal simulations. For accurate deformation results, the parameters of material equations are optimized. Finally, the finite element results are compared with experimental results for the validation and a good consistency is shown.

Keywords Sheet metal · Forming · Mechanical characterization

Introduction

In cold forming operations the accuracy and efficiency of deep drawing simulations have a challenging task due to shape effects, springback, and anisotropy. Thus, finite element modeling has a significant role in cold forming simulations in industrial areas. An integral part of numerical modelling in sheet metal forming is proper material characterization. In fact, the predictive capabilities of the numerical models are largely dictated by the quality of the material and interface (friction) characterization. The demand for the reliability of the numerical simulations on formability in the deep drawing process increasingly promoted the application of low carbon mild

M. E. Tamer (✉)

Borcelik Celik Sanayi Ticaret A.S, R&D Center, 16601 Gemlik, Bursa, Turkey

e-mail: emint@borcelik.com

S. Bortucen

Tofas Turk Otomobil Fabrikasi, Bursa, Turkey

U. Sahinoglu

ArcelorMittal Europe, 16601 Gemlik, Bursa, Turkey

© The Minerals, Metals & Materials Society 2022

K. Inal et al. (eds.), *NUMISHEET 2022*, The Minerals, Metals & Materials Series,

https://doi.org/10.1007/978-3-031-06212-4_27

steels to automotive body components. The strength levels of major body parts have already reached 320 MPa for cold forming.

In order to obtain higher strain values, both tensile and stack compression tests were performed. The stack compression test, as well as hydraulic-bulge testing and in-plane stretch-bend testing, has the advantage to measure the evolution of flow stress at large strains [1].

In cold forming operations of mild steels, major problems are tearing and unexpected dimensional problems, whereas the tool and die design has a major role in crack propagation, as well as the improvement of productivity. The aim of the study is to investigate different material models with mechanical characterization tests. A new algorithm BORMech is used to optimize these material parameters, in which the mechanical modelling affects the deformation results. BORMech is developed by Borçelik R&D in 2019 and as a steel manufacturer, the authors focused on material and tool-related issues, including the basic understanding of the relationship between the mechanical test results and the deformation behavior of tested materials.

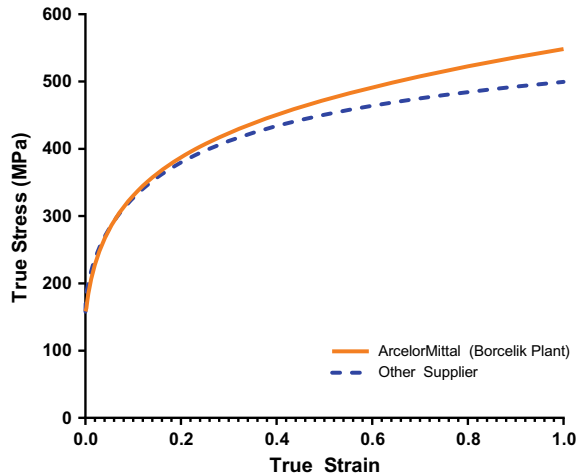
Experiments and Numerical Modeling

The competency in performance of sheet metal forming simulations is notably dependent on the chosen materials' constitutive relationships. Thus, material modelling is a field of study which gains increased attention of the scientific community, especially in the case of sheet metal forming, where pronounced anisotropy is expected [2].

Experiments

To obtain the mechanical properties such as Young's modulus, Poisson's ratio, anisotropy, yield strength, and ultimate tensile strength, a uniaxial tensile test has been performed. This test is superior due to its simplicity and well-defined testing standard [3]. Despite the fact that the most commonly used characterization test for sheet metals is the uniaxial tension test, the maximum strain level reached up to 0.21, which is low as compared to strain levels reached in cold forming operations. The stress and strain curves in the strain range larger than uniform elongation in uniaxial tensile testing are required because the strain gradient in the deep drawing process delays the onset of necking and the strains at some certain regions reach such high values. Moreover, the biaxial flow curve and anisotropy parameter were acquired by means of stack compression and compression tests. The stack compression test was first proposed by Pawelski [4], which is an alternative experiment for acquiring a flow curve in a wide range of strain values due to its deformation state. The stack compression test made use of multi-layer cylinder-like specimens that were assembled by gathering up circular discs cut from the same material by electric discharge machine. The preparation of the circular flat specimens was critical for ensuring

Fig. 1 Average true stress and strain curves obtained by tensile and stack compression tests



that all the layers were concentric and had identical cross-sectional areas provided with frictionless conditions along the contact interface. The tests were performed as three repetitions for each sample including five circular discs each. Both, tensile and compression tests were performed at ZwickRoell 250 kN tension-compression testing device. True stress and true strain curves of mechanical characterization tests are illustrated in Fig. 1.

As seen in Fig. 1, the results are limited and are not optimized with the material models. To obtain material parameters with BORMech, three material equations Swift, Hockett-Sherby, and combined were used as a material hardening model. The material DX56D + Z obtained from different suppliers was conducted in this study. The mechanical properties of the considered material can be found in Table 1. BORMech found out that the combined material model flow curve approximation for the best match, whereas it has been used for the hardening behavior with the parameters given in Table 2.

Moreover, to predict the formability limits of a sheet metal Nakazima specimens were used. This test is significant in a sheet metal forming industry. Although alternative approaches are increasingly investigated in the academic community, the forming limit curve (FLC) is still the main instrument for the quantitative description of sheet metal formability [5]. In this context, the standard Nakazima geometry was utilized in the FLC experiments and limit strain values, plotted in Fig. 2, include the average for all the three repetitions.

Numerical Modeling

In this study, the lower rear side of the inner door panel for FIAT Tipo Sedan/HB/SW has been used for the case study (Fig. 3). The deep drawing analyses were performed

Table 1 Mechanical properties of DX56D + Z

Mechanical properties	E (GPa)	n	σ_0 (MPa)	σ_{45} (MPa)	σ_{90} (MPa)	σ_b (MPa)	r_0	r_{45}	r_{90}	r_b
ArceorMittal Borcelik Plant	208	0.23	158	174	163	201	1.98	1.69	2.51	0.84
Diferent Supplier	205	0.21	158.5	161	161	205	2	1.65	2.52	0.82

Table 2 Combined model hardening curve parameters of DX56D + Z

Mechanical Parameters	C (MPa)	n	ϵ_0	σ_i (MPa)	σ_{sat} (MPa)	a	p	α
ArcelorMittal Borcelik Plant	525.2	0.24	0.0053	158.2	945	9.11	0.795	0.1
Different Supplier	548.5	0.24	0.0068	157.9	456	3.87	0.71	0.5

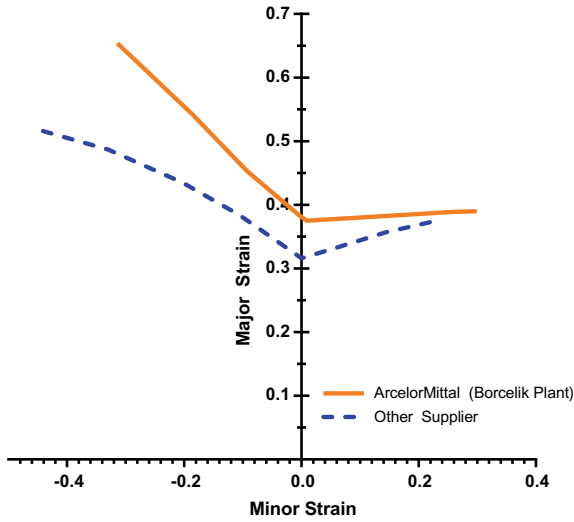


Fig. 2 Average forming limit curves obtained by digital image correlation method with Aramis optical measurement system

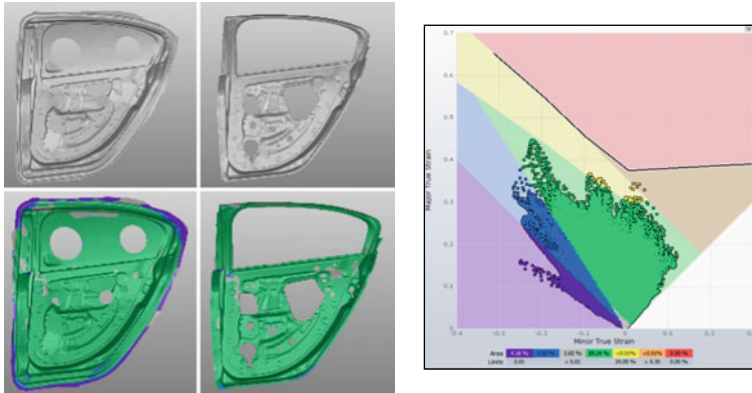


Fig. 3 The formability analyses of rear door inner panel in AutoForm simulation software and forming limit curve with deformation results

in AutoForm environment. The finite element analyses were conducted with two different steel suppliers. The initial mesh size was 12 mm, with 11 layers and 6 refinement levels. BBC material model in Autoform was used to model the sheet materials. The Coulomb friction model is applied with a constant friction coefficient of 0.15 (Figs. 4 and 5).

The trustworthiness of the forming analysis depends on some of the key factors such as material model, layers (integration points through thickness), contact between tools, and sheet nesting. These factors such as drawbead model, blankholder model, mesh size, friction, refinement level, spacer, pilot usage and certainly clamping

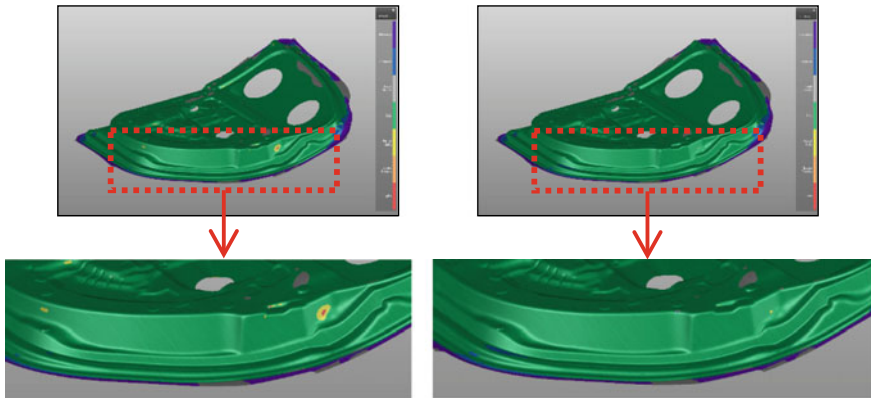


Fig. 4 BORMech material library gives better formability results as compared to FIAT simulation result

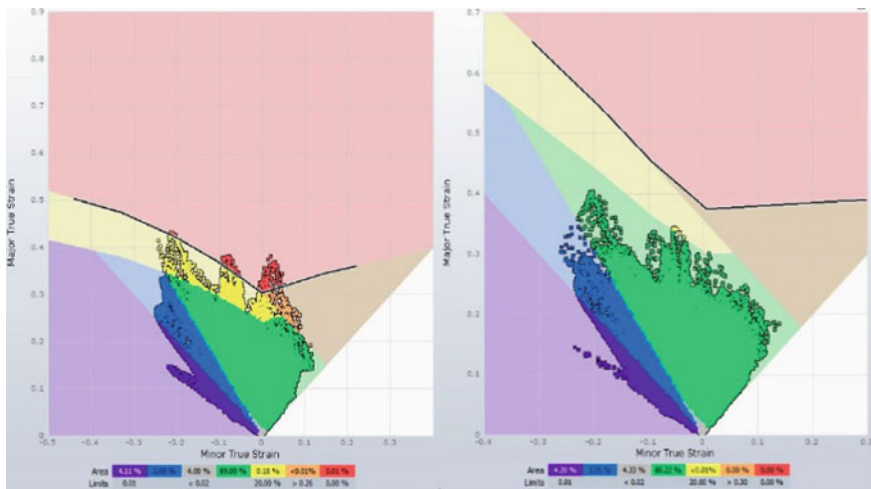


Fig. 5 The difference between forming limit curves depending on material models

concept are input parameters for numerical modelling which are dependently on the user choices.

Validation

The validity of the numerical modeling is assessed through comparison with the measurements of manufactured parts. According to this, GOM-ARGUS 3D optical deformation measurement system was used. The difference between the real part and the virtual tryout is shown in Fig. 6.

It is illustrated in Fig. 6a that the surface deviation of real part measurement differs maximum of 4 mm at the edge of the right side of the door panel. On the contrary, almost all surface deviation results are consistent. Additionally, major and minor strain results have been compared. The real part measurement and simulation results agree well with a maximum deviation of 2%. As can be seen in Fig. 6b, some regions have excessive difference, however, these regions will be trimmed after the drawing operation. Minor strain results' comparison is given in Fig. 6c. It must be noted that minor strains are much smaller than the major ones in magnitude. Although the predictions of the numerical models are of the same order as the optical measurements, at certain locations, the details of the measurement profile could not be captured. The simulation results deviate from optical measurement results with the strain value of 0.06. Moreover, the thickness distribution has been investigated (Fig. 6d). As it was described before, the initial thickness of the sheet material was 0.6 mm. The results of optical measurement and simulation are generally consistent. In some certain regions, the difference is not exceeding the value of 10%. These

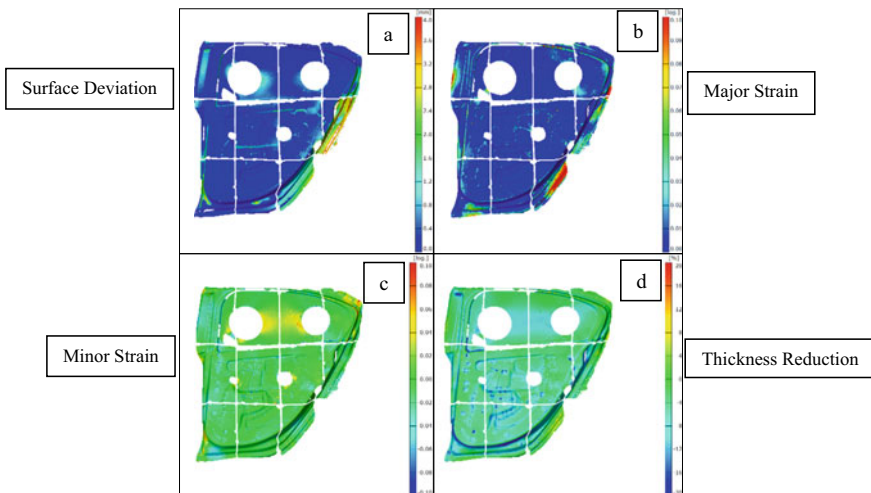


Fig. 6 The difference between the real part and simulation results

discrepancies can be considered acceptable due to manufacturing tolerances in the automotive industry.

Conclusion

In this study, it is aimed to improve the reliability of sheet forming simulations from the perspective of material behavior. The deep-drawn car body component has been investigated with finite element analysis and optical measurements. As mentioned before, sheet metal forming operations in the automotive industry depend on the deformation degrees in which the mechanical characterization is significant. A new material parameter optimizer, BORMech, is used to optimize material hardening equation parameters. In this context, mechanical characterization tests have been performed to acquire the material data for sheet metal simulations. For accurate deformation results, the parameters of material equations are optimized. After numerical and experimental studies, the FEA and experiments are compared in terms of geometrical accuracy, major–minor strain, and thickness distribution. The results are consistent with each other. The conclusions are given below:

- Owing to validation of the results, it is concluded that the simulation results are almost identical to the experiments in terms of geometry, deformation behavior, and thickness distribution.
- Steel strip manufactured by ArcelorMittal's Borcelik plant shows better deformation behavior as compared to another supplier.
- BORMech algorithm gives a good opportunity to optimize the material parameters in which the deformation and thickness results are close to real part measurement.

References

1. Hiwatashi S, Yoshida T (2018) Simulation-aided application of advanced sheet steels to automotive parts, IOP Conf Ser: J Phys: Conf Ser 1063:012006
2. Manopulo N, Raemy C, Hora P (2018) A discussion of the associated rule based on the FAY model and Nakajima tests. IOP Conf Ser: J Phys: Conf Ser 1063:012090
3. Lange K (1985) Handbook of metal forming, 1st edn, vol part 4.1. Society of Manufacturing Engineers, McGraw-Hill Inc, pp 40–56
4. Pawelski O (1967) Über das stauchen von holzylindern und seine eignung zur bestimmung der formänderungsfestigkeit dünner bleche. Arch Eisenhüttenwes 38:437–442
5. Karadogan K, Tamer ME (2015) Development of a new and simplified procedure for the experimental determination of forming limit curves. CIRP Ann-Manuf Technol 64:265–268

Draw Die Development to Maximize Aluminum Formability Potential for Making Styling Featured Outer Panels



Zhi Deng, Anil K. Sachdev, and Raj Dasu

Abstract The 6000 series aluminum alloys have been increasingly used to make the autobody outer panels. Since the 6000 series alloys are typically less formable than mild steel, it is often a very challenging task to make aluminum outer panels with the sharpness that can be obtained with steel. With the development of the next-generation 6000 series alloys, making aluminum outer panels with distinguishing sharper features becomes realistic. This paper demonstrates an advanced practice in draw die development, material modeling, simulation approach, and part formability assessment. The unique technology developed enables the desired aluminum part geometry formed with the critical styling features which were thought impossible. By means of the FEA simulations, the tooling geometric features, draw bead configurations, and lubricant effect were thoroughly investigated and optimized. It ensured that the optimal balance of material flow and desired amount of plastic deformation were achieved. The simulation-based draw die development was completely adapted to the prototype tool. The tryout results showed an excellent match between the simulation results and physical measurements. The key findings and technical advances from this investigation would be beneficial to improving the current industrial practice.

Introduction

The aesthetic appearance of the autobody exterior styling is highly desired and is largely realized by stylish panels with distinguished sharp features. These sharp features are characterized by very small curvatures and radii in the needed local areas and provide a great challenge to part formability during stamping. Since aluminum alloys are typically less formable than mild steel, it has been seen that aluminum exposed panels show a much less attractive appearance than expected. With the

Z. Deng (✉) · R. Dasu

Commonwealth Rolled Products, Madison Heights, MI, USA

e-mail: Zhi.Deng@commonwealthrolledproducts.com

A. K. Sachdev

General Motors Research and Development, Detroit, MI, USA

© The Minerals, Metals & Materials Society 2022

K. Inal et al. (eds.), *NUMISHEET 2022*, The Minerals, Metals & Materials Series,

https://doi.org/10.1007/978-3-031-06212-4_28

increasing use of aluminum alloys in today's automotive industry, making aluminum outer panels with steel-like sharper features is still a big challenge.

To address this challenge, more formable aluminum 6000 series alloys with significantly improved formability have been developed. To demonstrate the potential applications of this new 6000 alloy, a desirable autobody outer panel with very aggressive styling and sharper features was identified for the case study. Targeting the mass production applications with this new alloy, this case study investigated all the aspects from product engineering to production requirements. This paper summarizes the key advances from the case study in draw die development, material modeling, simulation approach, and part formability assessment. The unique technology developed enables the desired aluminum part geometry formed with the critical styling features which were thought impossible. By means of FEA simulations, the tooling geometric features, draw bead configurations, and lubricant effect were thoroughly investigated and optimized. It ensured that the optimal balance of material flow and desired plastic deformation were reached without scarifying the class-A panel surface quality requirements.

Part Geometry and Forming Challenges

An example of aggressively styled part geometry identified for the current outer panel study is shown in Fig. 1a. This panel was targeted to be made with 6000 series aluminum alloy with a thickness of 1.2 mm. The critical forming area is highlighted in Fig. 1b, where the local features are characterized by extremely small radii along its two-directional curvatures. The forming of these centralized sharper features requires the material to be stretched from the beginning of the stamping process. The remaining areas of the part should be deformed with a minimum amount of plastic strain to meet the class-A surface quality requirements. The combination of these formability and surface quality requirements drives challenges for overcoming either split in the critical forming area or wrinkling into its nearby areas.

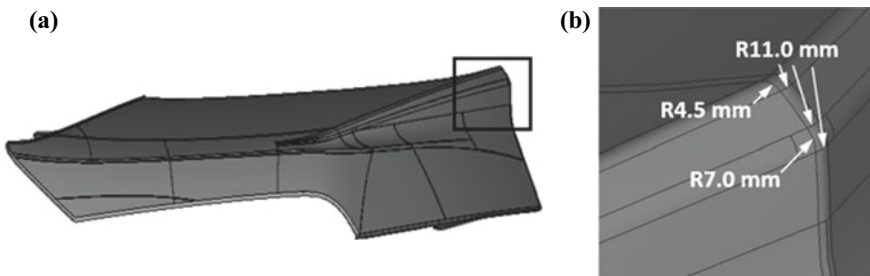


Fig. 1 **a** The panel geometry for the current study and **b** the local details of the studied panel

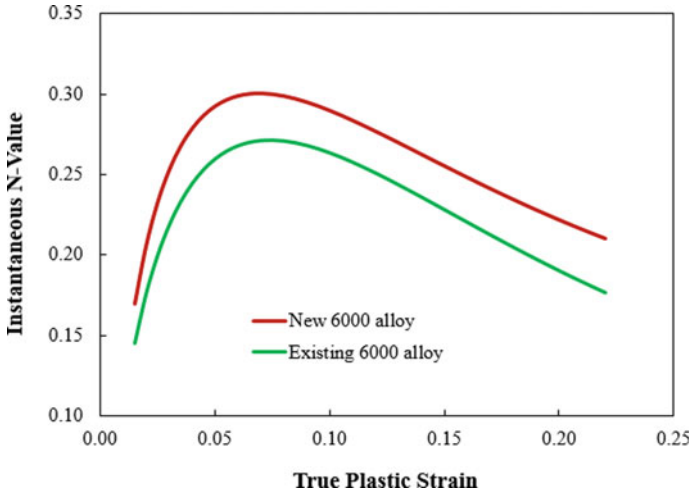


Fig. 2 Comparison of the instantaneous *n*-value between the new and existing 6000 alloys

New 6000 Alloy Development

The earlier part feasibility study revealed that this panel could not be formed with the existing 6000 series aluminum alloys. In order to meet the increasing challenges in making stylish outer panels, a new formable 6000 alloy has recently been developed. This new alloy targets the application of both the autobody outer and inner panels, having not only enhanced stretchability over the existing 6000 alloys but also improved the drawability compared with the current AA5182 alloy. Figure 2 compares the material instantaneous strain hardening between the newly developed and existing 6000 alloys. It is well known that the instantaneous strain hardening exponent has a good correlation to material stretchability [1]. It can be seen from Fig. 2 that the new 6000 alloy increases the material strain hardening by about 16% in the strain range of over 5%. The improvement in the forming limits of the new 6000 alloy over the current AA5182 alloy is clearly demonstrated in Fig. 3, where the forming limit curves (FLC) for both alloys for the thickness of 1.1 mm are compared. The lowest major strain value on the FLC of the new 6000 alloy is 4% higher than that of the AA5182 alloy. In the highlighted strain region where most of the panel splits occur, the new 6000 alloy shows a 7% increase in forming limit compared with the AA5182 alloy.

Material Modelling and Stamping Simulation Accuracy

In today’s automotive industry, stamping die design and engineering rely heavily on stamping simulations for guidance. Simulation accuracy is governed mainly by

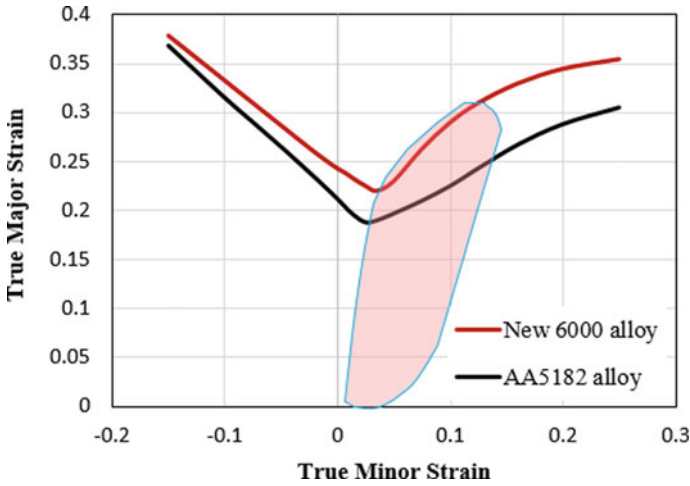


Fig. 3 FLC comparison of the new 6000 alloy and the AA5182 alloy

the level of material details that can be incorporated into material models. The previous investigation associated with AutoForm software [2] has verified that for aluminum stamping simulations, the BBC2005 yield criterion provided the most accurate strain calculations and forming force predictions. It was also validated that the combined Swift/Hockett-Sherby model was most suitable to describe aluminum strain-hardening characteristics. This best practice in aluminum material modeling has been exclusively used in the current case study, which ensures the simulation accuracy to guide the steps between stamping die design and process development.

In order to take full advantage of the BBC2005 model, it is necessary to do the bulge test for determining the material property parameters. Figure 4 compares the

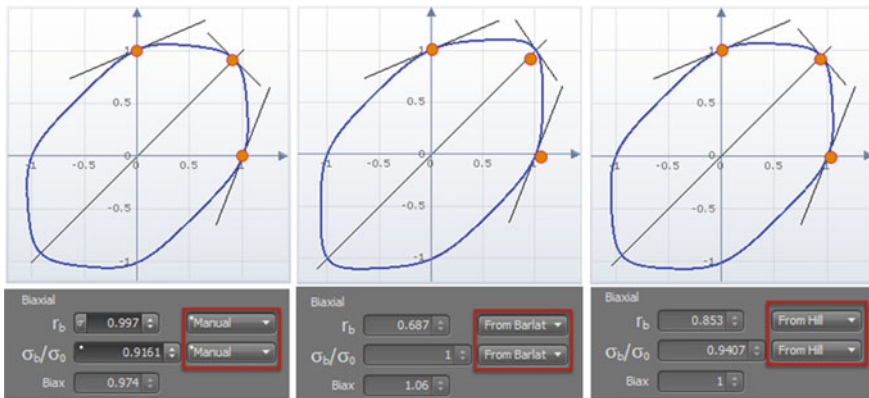


Fig. 4 Influence of the r_b value on the yield locus

difference in the yield loci derived from the r_b value measured from the bulge test and calculated from the Barlat89 and Hill48 models, where r_b is the coefficient of plastic anisotropy in the biaxial stress state. Even though the yield strength ratio (σ_b/σ_0) in the biaxial stress state (σ_b) and in the uniaxial stress state (σ_0) seems close to each other, the r_b values are significantly different. Compared to the measured r_b value, the calculated r_b value using the Barlat89 model is 31% less and the r_b value using the Hill48 model is 14% less. These differences would dramatically change the yield loci in the stretch–stretch quarter, especially in the area near the equibiaxial stress state as shown in Fig. 4. For one of the calibration investigations, the influence of the r_b value on plastic strain predictions was examined for the deep elliptical punch test with a circular blank 160 mm in diameter, mill oil at the lubricant, and a binder holding force of 14 kN [2]. Figure 5 compares the true major strain distributions along the 90° section of the deep ellipse sample between the measurement and the simulation results using the three different r_b values. The comparative results shown in Fig. 5 validate that the experimentally determined r_b value gives the most accurate strain prediction.

Another important material parameter when using the BBC2005 model is the M value. For a good representation of aluminum behavior, the M value is typically set to be 8 [1]. However, several investigations have been conducted on how to calibrate the M value for aluminum alloys and other materials [3]. By using a series of elliptical punch tests [4], the M value can be calibrated for different stress states. The hemisphere punch testing case, as shown in Fig. 6, truly validates the influence of the M value on simulation accuracy in which the circular blank of 190 mm in

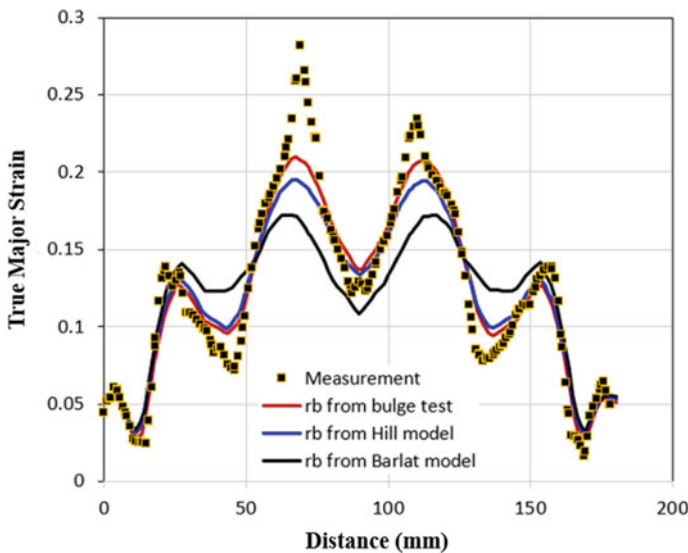


Fig. 5 Comparison between the simulation and experimental results of the major strains for the deep ellipse sample along the 90° section

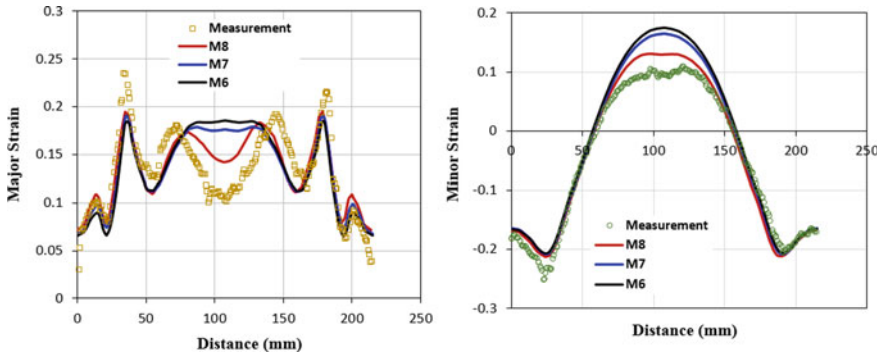


Fig. 6 Comparison between the simulation/experimental results of the major/minor strains for the hemisphere sample along the 45° section

diameter was deformed with mill oil lubrication and a binder holding force of 32.4 kN. By comparing the predicted major and minor strain distributions along the 45° section of the sample, it has been proven that 8 is the best M value for using the associated BBC2005 model.

Draw Die Design and Process Development

Autobody outer panels are mainly formed in the first draw operation. For the draw die design of the current panel, the formability must be ensured in the critical area together with surface quality requirements for other relatively flat areas. The recipe to solve the challenges is to maximize the material flow into the most needed critical area, while also maintaining a high amount of material stretch deformation in other areas. In order to achieve the optimum material flow at the different locations, the draw die geometry was designed in such a way that the central contact between the punch and the blank material was initialized after binder closing, and the draw depth was made uniform as much as possible along the styling feature lines. The double-bead layout was optimized to maintain a balanced material flow along all directions and to have enough material stretch ($\geq 4\%$ thinning) over the flat area for good surface quality.

The stochastic analysis with AutoForm Sigma module revealed that the most influential factors in controlling the panel formability in the critical area are the drawbead (DBA) and the friction effect, as illustrated in Fig. 7. The drawbead effect includes the drawbead geometry and layout. Figure 8 shows how the formability of the critical area is sensitive to the variation of the drawbead force factor. Good part formability can be realized without scarifying the part surface quality by optimizing the variable drawbead geometries and layout. The optimized drawbead geometries

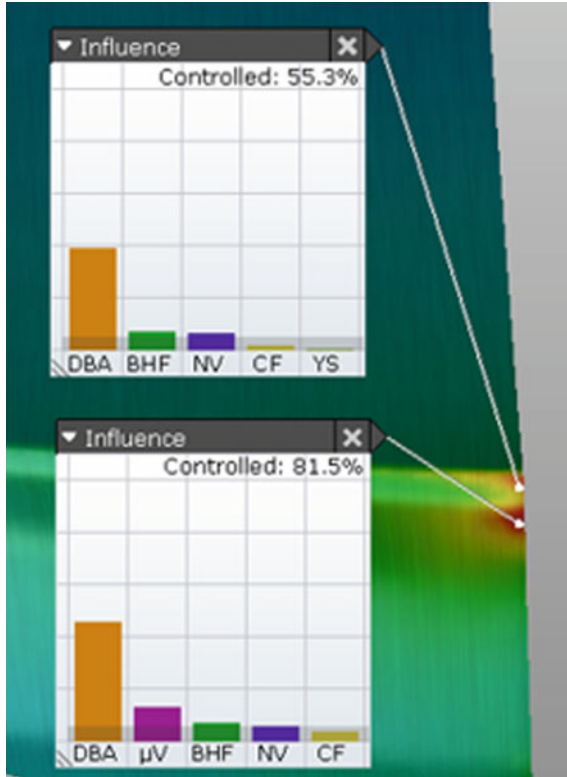


Fig. 7 Influence of the drawbead and frictional coefficient on material formability in the critical area

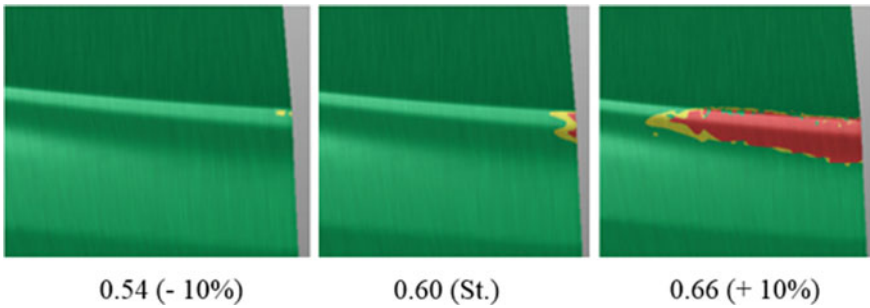


Fig. 8 Sensitivity study of drawbead effect on material formability in the critical area

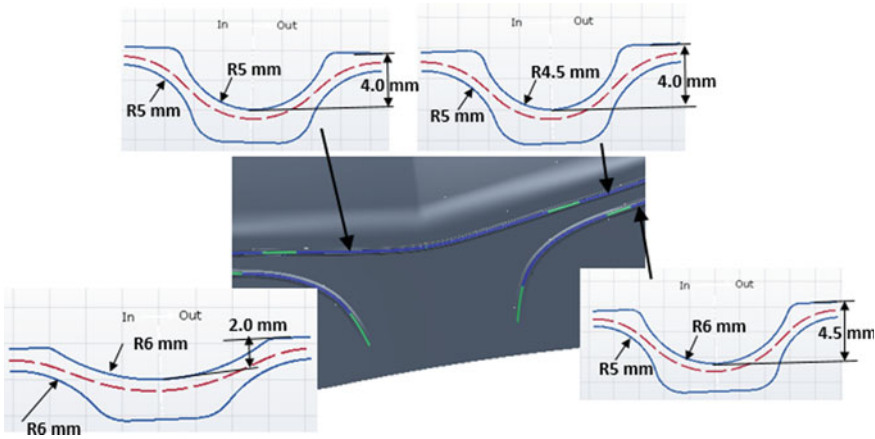


Fig. 9 Development of drawbead geometry and layout

and layout nearby the critical area are illustrated in Fig. 9, which have been directly transformed into the physical draw die for the tryout.

Lubrication is beneficial to promote material flow in stamping operations. For the current case, however, extensive simulation studies found that minimizing lubrication in the critical area is necessary to control material thinning to the allowed amounts. Figure 10 demonstrates the influence of friction coefficient on local thinning in the critical area of the panel. It can be seen from Fig. 10 that material thinning increases dramatically with decreasing friction coefficient. Compared to the local maximum thinning value of 24.6% for a friction coefficient of 0.15, the thinning value at the same location jumps to 32.4% for a friction coefficient of 0.03. During the drawing

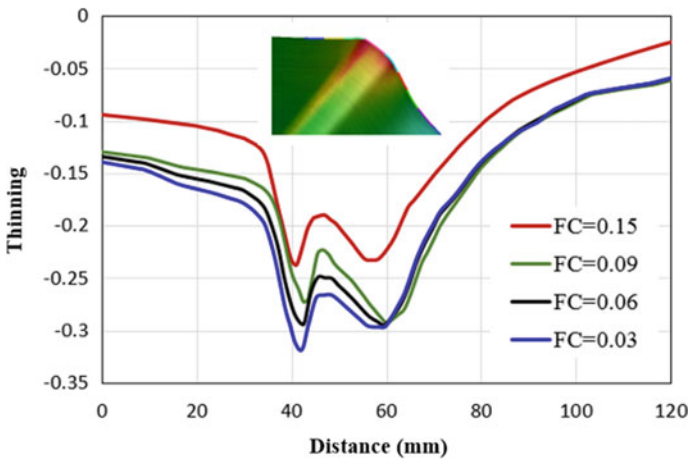


Fig. 10 Frictional effect on local material thinning

operation, the material in the critical area initiates the first contact with the lower punch from the beginning of die closure. Because of its centralized location, local material stretching would be largely controlled by the interfacial contact condition. Higher interfacial friction applies more restriction to the local material movement, and thus reduces material thinning. This finding was valuable in a successful physical die tryout.

Physical Die Tryout and Validation

Based on the simulation results in terms of the panel formability and surface quality requirements, the draw die design was optimized together with blank geometry and other drawing process parameters. The developed draw die geometric surfaces were exported from AutoForm software, and directly transformed to the die shop for building the prototype die without any further modifications. The blank outline, position, and draw-in values, together with binder tonnage and travel predicted from the AutoForm simulations, were provided to guide the die tryout. This would ensure that the material deformation on the tryout panels matched the simulation predictions. The die tryout was carried out on both the hydraulic press and the mechanical press to compare the material formability performance under the prototype and production conditions. Figures 11 and 12 show the drawn panels out of the die tryout with the newly developed 6000 alloy with a thickness of 1.2 mm. It is worthy to emphasize that Fig. 11 depicts the drawn panel made from a 6-month aged material, and Fig. 12 shows the drawn panels made from the 16-month aged material. This success clearly demonstrated the superior forming performance of the newly developed 6000 series alloy and the technical innovations in draw die development.

Fig. 11 Drawn panel made with the 6-month aged 6000 alloy

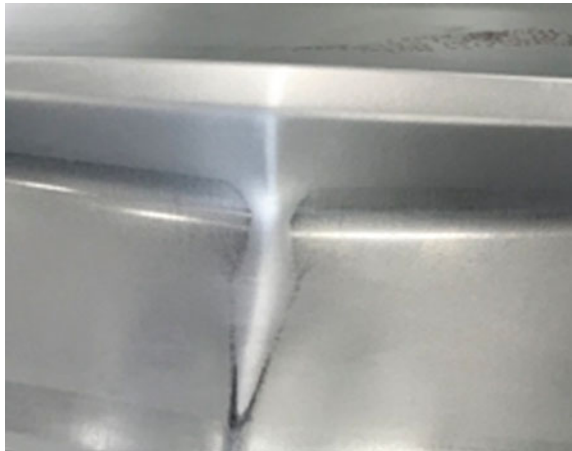
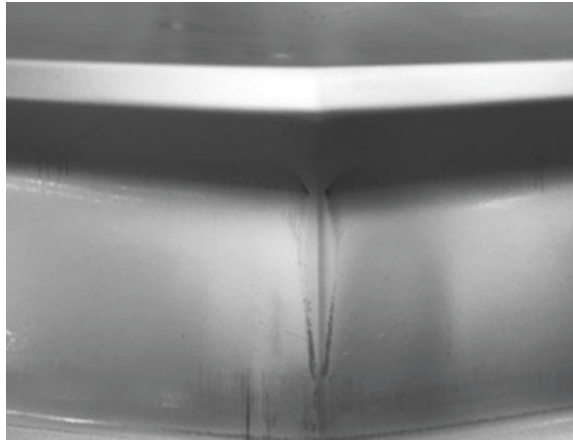


Fig. 12 Drawn panel made with the 16-month aged 6000 alloy



To further verify the methodology applied in the current draw die development, a panel formability correlation study was conducted. This study aimed to rerun the simulations with the physical draw die geometries and to compare the simulation results with measurements on the tryout panels. Blue-light scanning was used to capture the physical draw die geometries, which were then adapted for the simulation setup. By using the ARGUS technique, the material major and minor strain distributions on the drawn panels after the drawing process were measured with two repeats. The ARGUS measurements were done for the blanks orientated at 0° and 45° to the coil rolling directions, respectively. The blank draw-in values of the tryout panels were also measured at the different locations, which serves as a guideline to compare the simulation results with the measurements.

Figure 13 illustrates the comparison of the major and minor strain distributions along the symmetric section of the panel between the simulation results and the two repeated Argus measurements for the blank cut along the coil rolling direction. The displayed distance on the figure is the projected distance inside the physical draw-beads. It can be found from Fig. 13 that the simulation results match the measurements very well over the entire sectional profile. For the major strains, the maximum derivation of the predicted values to the measurements is less than 2%. The maximum deviation of the calculated minor strains to the measurements is about 4%. Figure 14 compares the thinning distribution along the symmetric section of the panel between the simulation results and the two repeated Argus measurements for the blank cut 45° to the coil rolling direction. The thinning values from the Argus measurements are the calculated ones from the measured major and minor strains on the surfaces. It is evident from Fig. 14 that the thinning values predicted from the simulations are in good agreement with the Argus measurements, with the maximum deviation being about 4%. Figures 13 and 14 further verify that a higher simulation accuracy has been achieved with the currently developed methodology.

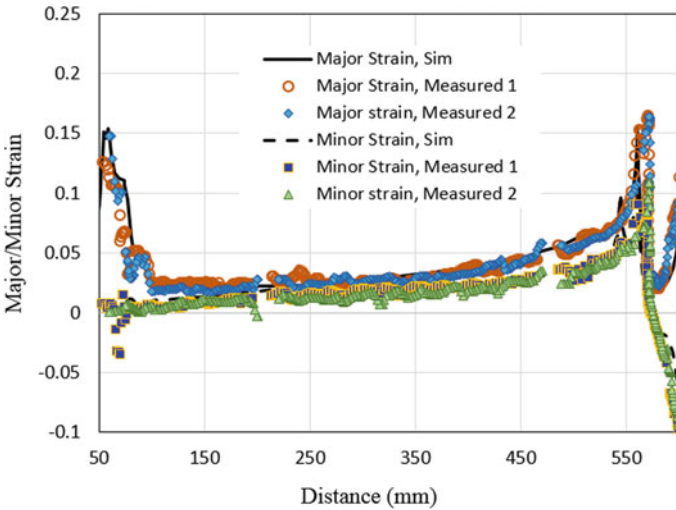


Fig. 13 Comparison of the major and minor strain distributions between the simulation results and the Argus measurements for the 0° blank

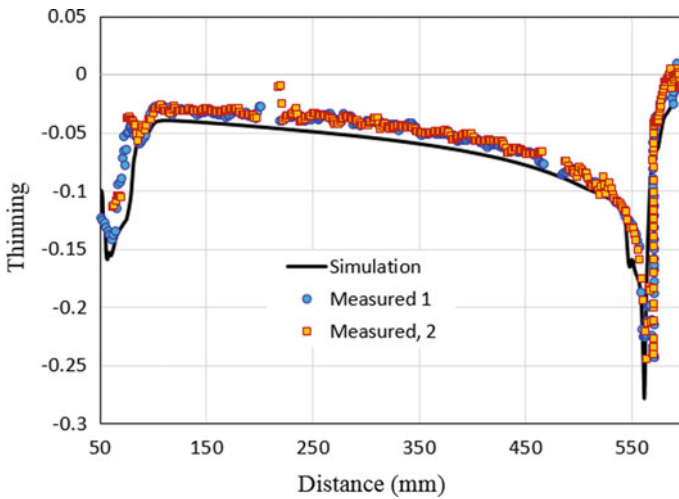


Fig. 14 Comparison of the thinning distribution between the simulation results and Argus measurements for the 45° blank

Conclusions

A newly developed 6000 series alloy has demonstrated superior formability to make the challenged outer panel even when aged for 16 months. The current case study has confirmed the need for a systematic approach to maximizing aluminum formability

potential. This approach consists of the best practice in stamping die design, process optimization, lubrication, material modeling, and simulation techniques. The results from the prototype tryout and the part formability correlation study verified that the developed approach paves the way to make aluminum outer panels with steel-like sharp features.

Acknowledgements The authors thank Krishna Murali of General Motors for discussions during the simulation and prototype tryout.

References

1. Banabic D (2010) Sheet metal forming processes. Springer, New York
2. Deng Z, Hennig R (2017) Influence of material modeling on simulation accuracy of aluminum stampings. *J Phys: Conf Ser* 896:012025
3. Hora P et al (2020) Modeling of the anisotropic behavior and failure initiation based on DIC data collection and crystal plasticity models. Paper presented at the international conference on plasticity, damage and fracture, Rivera Maya, Mexico, 3–9 January 2020
4. Hennig R, Deng Z (2016) Advanced formability testing method for sheet metal materials by combining stretch forming with deep drawing. Paper presented at the 9th forming technology forum, Ohlstadt, Germany, 12–13 September 2016

Hydroforming Behaviour of TIG-Welded Tubes of Austenitic Stainless Steel



M. Krishnamraju, Sandeep Sahu, Amarjeet Kumar Singh,
and K. Narasimhan

Abstract Tube hydroforming is an emerging manufacturing technique that uses pressurized fluid to deform the metal tubes into the desired shape. It is carried out by keeping tubular blank in the die, then deforming it into the final shape by applying fluid pressure using axial punches. Hollow components from TIG welded tubes of Austenitic stainless steels, AISI304 find automobile applications, particularly exhaust systems. The microstructure has strong effect on formability of AISI 304 tubes and therefore the effect of microstructure on the formability of tube is required to understand the correlation between microstructure and formability. Hence, in the present study, TIG weld tubes of AISI304 deformed and deformation behaviour is studied in comparison with bulge ratio and grain size effect. It was noticed that bulge height (deformation) decreased with increased bulge width and fracture surface observed was ductile nature along with fine grains.

Keywords AISI 304 · TIG welding · Tube hydroforming · Formability · Ductile fracture · Grain size

Introduction

Tube hydroforming [1–3] is an emerging manufacturing technique in which tubular blank is placed inside the die cavity and plastically deformed with the application of internal fluid pressure. Then tube undergoes plastic deformation, once the internal fluid pressure crosses the yield strength of the tube material, then takes the shape of die cavity. Similarly, axial compressive forces provided by the axial cylinder to simultaneously feed the material at the tube end to the critical bulging zone.

Tube hydroforming having the advantage like, less spring back, increased strength of the component, greater part consolidation compared to conventional stamping operation. Thus in hydroforming, long, complex shapes having reduced number of welds can be formed which reduces the secondary operations and improves the

M. Krishnamraju · S. Sahu · A. K. Singh · K. Narasimhan (✉)
Department of Metallurgical Engineering and Materials Science, IIT Bombay, Mumbai, India
e-mail: nara@iitb.ac.in

reliability of the formed components. This also leads to part consolidation and thus increases the productivity. But hydroforming has relatively longer cycle time which lowers production rates and needs highly polished dies to achieve greater dimensional stability.

Carleer et al. [4] investigated the effect of material properties like plastic anisotropy (R), strain hardening exponent (n), and coefficient of friction (μ) and concluded that higher R , n and lower μ favor larger deformations. Omar et al. [5] studied the effect of bulge ratio on the deformation behaviour and concluded that formability decreases with increase of bulge ratio. Koc [6] investigated experimentally the effect of loading path on hydroforming process and noted loading path which is function of fluid pressure, axial feed with respect to time has significant effect on part formation. That is slightly lower internal pressure during initial stages, with higher axial feed resulted higher bulge height. Park et al. [7] established that advanced sealing system consists of die spring, cylindrical sleeve, and punch with end filler results better sealing system than conventional rubber ring fastening over the axial punch, which finally resulted increased axial pressure with increased axial feeding. Sorine et al. [8] studied the effect of end feeding rate and confirmed that higher end feed loads enhance the formability of the tube because of the action of the internal pressure and axial compressive loads. Pavlina et al. [9] confirmed that novel processing route for dual phase steel, which consists of normalizing at 900 C followed by cooling to room temperature, then induction heating to 770 C followed by water sparing resulted tubes bursting pressure of 600 MPa without weld line effect due to phase distribution from weld region to non-weld region. Liu et al. [10] studied the effect of phase transformation during hydroforming on TRIP (Transformation Induced Plasticity) steel and observed that due to phase transformation average local misorientation was increased.

Hence the formability of TG weld Austenitic stainless steel with the effect of microstructure on formability, is not focused much. Thus, in this study the effect of grain size and grain orientation on formability of SS304 tubes is studied, along with fracture behavior during tube hydroforming.

Experimental Process

Material used: Cold rolled annealed Austenitic stainless-steel AISI 304L with thickness of 1.2 mm, provided by Bhandari Foils and Tubes Ltd (BFTL), Indore India is used for this work. Roll formed of same material with Tungsten Inert Gas (TIG) weld having Outer Diameter (OD) of 35 mm was used. Chemical composition and mechanical properties of received sheet material are given in Tables 1 and 2 respectively whereas tube mechanical properties are given in Table 3.

Experimental process: As received tubes of SS304 of OD 35 mm, thickness 1.2 mm cut by manual hack saw into various lengths say 248, 283, and 318 mm as per L/D ratio = 1, 2, 3. Selection of tube length is based on bulge length and clamping length,

Table 1 Chemical composition of received sheet material (by weight percentage)

C	Cr	Ni	Si	Mn	P	S	Mo	N	Fe
0.029	18.66	8.06	0.33	1.44	0.038	0.011	0.12	0.005	71.301

Table 2 Mechanical properties of received sheet material

Hardness (HRB)	YS (MPa)	TS (MPa)	K (GPa)	Elongation (%)	n	R
69.9	259.4	638.9	1.28	59.48	0.381	1.09

Table 3 Mechanical properties of received tube material

Material	YS (MPa)	TS (MPa)	K (GPa)	Elongation (%)	n
Base metal	420.1	706.1	1.247	47.42	0.260
Weld zone	407.2	681.2	1.199	45.49	0.251

and boundary condition as shown in Fig. 1 and Table 4 respectively. These tubes were deburred at the edges to get smooth surface, then kept in the bottom die of die set, in such a way that weld region of the tube is in opposite region of the LVDT sensor. Once tube placed in the die, then die is closed by lowering the upper die then blank holding

Fig. 1 Die dimensions

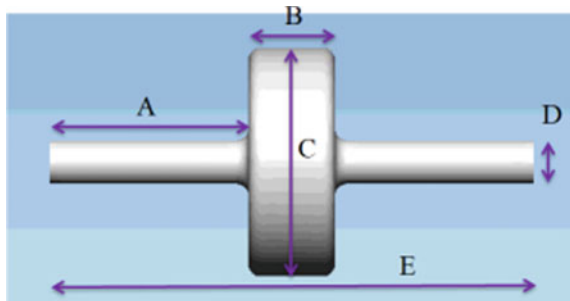


Table 4 Tube dimensions (in mm) for different boundary conditions

	Axial feed			Fixed end		
	Die-1	Die-2	Die-3	Die-1	Die-2	Die-3
	L/D = 1	L/D = 2	L/D = 3	L/D = 1	L/D = 2	L/D = 3
A	106.5	106.5	106.5	161.5	161.5	146.5
B	35	70	105	35	70	105
C	135	180	180	135	180	180
D	35.3	35.3	35.3	35.3	35.3	35.3
E	248	283	318	358	393	398

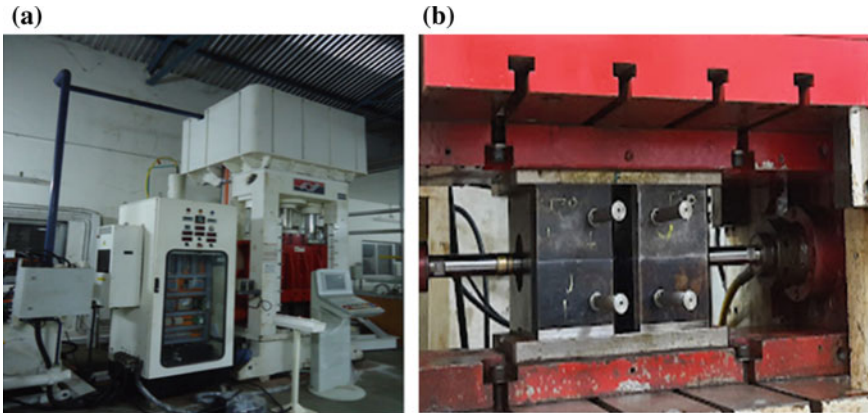


Fig. 2 **a** Hydroforming setup (250 T hydraulic press) and **b** die setup for 35 mm OD tube

force is applied as shown in Fig. 2a, b respectively. Then both sides of the tube are closed by axial punches then water pressure is applied through water intensifier and then deformed into die shape. Loading path (program) should be selected in such a way that no wrinkling occurs. The internal pressures may vary from 530 to 540 MPa. Then bursting pressure is recorded from digital display of the machine and bulge height recorded by LVDT sensor as given in Table 5. Experiment is conducted for three tube of each size to get reliable information. Once the hydroforming is complete the liquid is evacuated and the formed tube is removed. Tubes before hydroforming and after hydroforming are shown in Fig. 3a, b respectively.

For microstructural analyses of deformed tubes, samples of size 10×10 mm cut by wire Electric Discharge Machining technique from locations close to neck as shown in Fig. 3b. These samples were polished mechanically to get flat scratch free surface, then electro polished by using electrolyte (20% per chloric acid and 80% ethyl alcohol) at 20 V for 20 s to get mirror-like surface. Then EBSD scans were taken with a step size of 0.4 at magnification of $500\times$ on the area of 300×300 mm using Scanning electron microscope GEMINI FE-SEM, with Electron back scattered diffraction detector, EBSD. Electron microscope uses, Primary Electron as a source to

Table 5 Bulge height and bursting pressure of hydroformed tubes

S. No	Tube length	Bulge height	Bursting pressure (MPa)	Fracture location
01	248	12.2	535–538	In weld region
02	283	10.3	535–538	In weld region
03	318	8.4	535–538	In weld region
04	358	6.1	535–538	In weld region
05	393	5.8	535–538	In weld region
06	398	5.4	535–538	In weld region

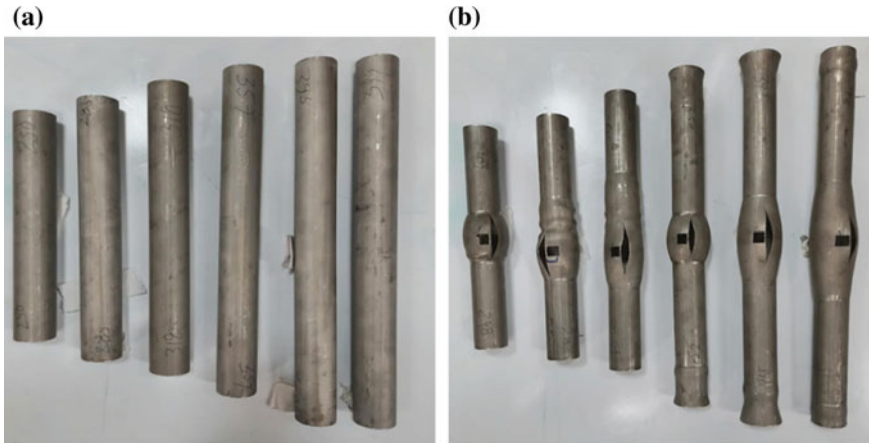


Fig. 3 a Undeformed tubes and b deformed (hydroformed) tubes

detect the structural character of the material. Once primary electron incidents on the metal surface, secondary electron and back scattered electron diffracts from the metal surface. This back scattered diffracted electrons are taken for the characterization of deformed samples particularly for grain morphology. Then analysis of EBSD images is done using HKL software to determine inverse pole figure IPF, Excel graph for grain size distribution.

Results and Discussion

Tube bulge test was performed on 250 T hydraulic press with die of 35 mm OD on TIG welded tubes of SS304 having different lengths say 248, 283, 318, 358, 393, and 398 mm by using axial punches. Bulge height for each tube is measured with LVDT and bursting pressure for each tube is measured from digital display. It is noted that bursting pressure is more or less same for all tubes, but bulge height is decreased from 12.2 to 5.4 mm with increase in bulge width as shown in Table 5.

- i. Similarly, fracture took place on the weld line along the weld for all tubes irrespective of tube geometry (L/D ratio) as shown in Fig. 4.
- ii. Type of fracture is ductile in both base metal and weld zone as it shows voids and micro voids as shown in Fig. 5a, b respectively.
- iii. Sample of size 10×10 mm cut by EDM technique from necked region and EBSD scan were taken for the study of grain morphology in the deformed tubes at magnification of $500\times$. It has been found that grain size for undeformed tube is $35 \mu\text{m}$ as shown in Fig. 6a. The grain size was high in deformed tube of size 248 mm compared to 283 and 318 length tubes as shown in Fig. 6b–d respectively (Fig. 7).



Fig. 4 Fracture location in deformed tubes

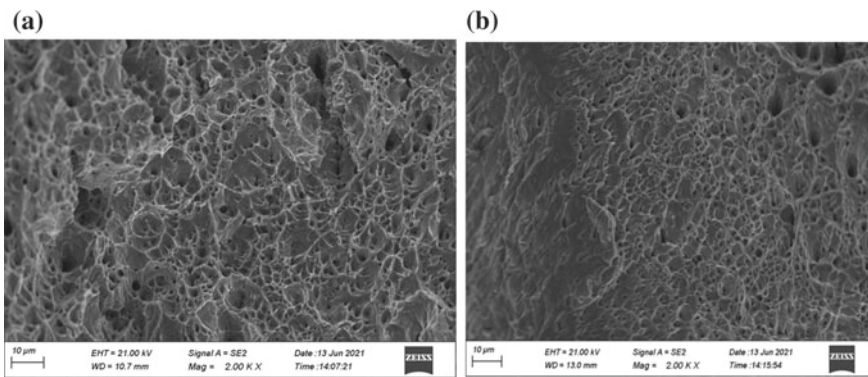


Fig. 5 a Fracture in tube base metal and b fracture in tube weld zone

Conclusions

In this work the hydroforming behavior of TIG weld tubes of SS304 of OD 35 mm was studied along with microstructure. The following conclusions were drawn.

- Yield strength, Tensile strength of tube base metal are greater than as received sheet, but elongation percent was lower, due to induced stresses during bending operation.
- Bursting pressure is more or less same for all tubes, but bulge height is geometry sensitive and decreasing with bulge width for axial feed and fixed feed condition.
- Fracture location is in weld region, along weld line for all bulge widths, and nature of fracture is ductile for both tube base metal and weld region.

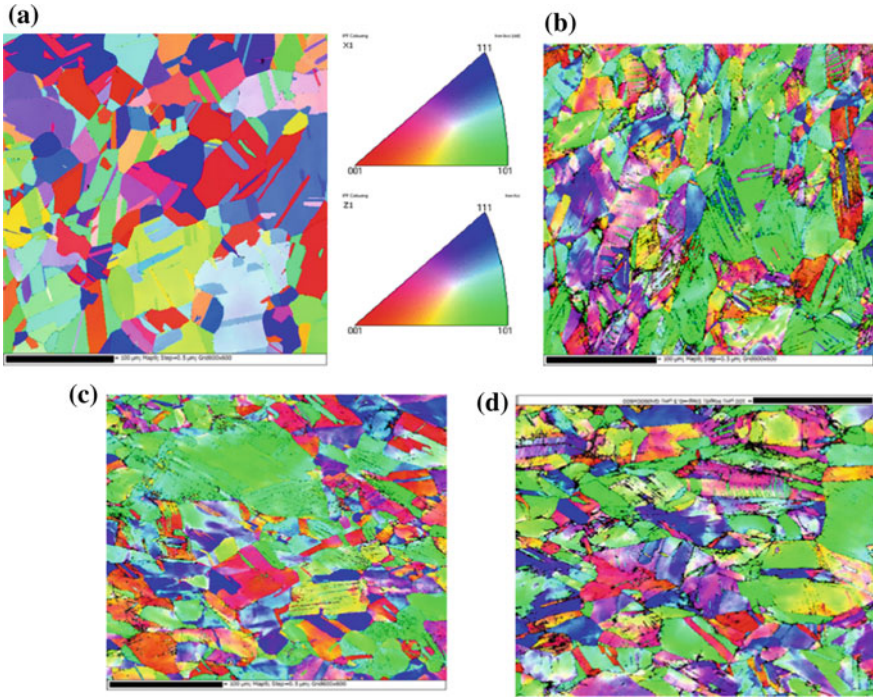


Fig. 6 **a** As received sheet grains, **b** grains in 248 mm tube, **c** grains in 283 mm tube, and **d** grains in 318 mm tube

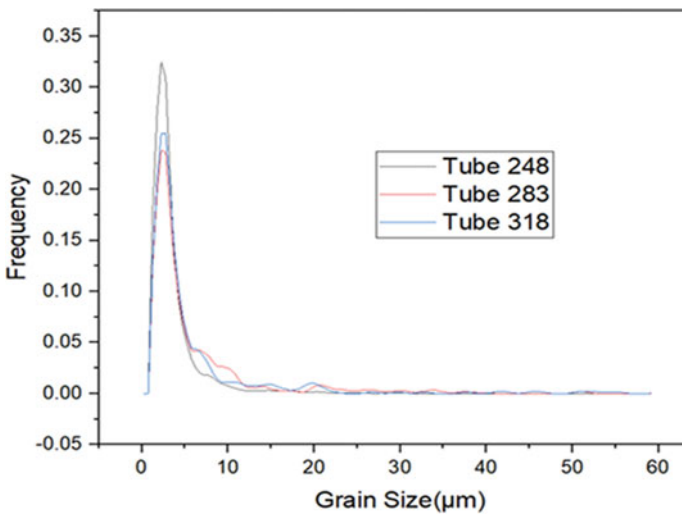


Fig. 7 Grain size for deformed tube samples

- Grain size distribution in hydroformed tube of length 248 mm ($L/D = 1$) is uniform compared to 283 and 318 mm for axial feed condition based on EBSD study.
- Grain size of as received sheet (un deformed) is 35 μm .

Acknowledgements The author thanks Center of Excellence in Steel Technology (CoEST), Indian Institute of Technology Bombay India, for providing support in procuring tooling to conduct experiments and Electro Pneumatics Pune India for providing the tool (die). The author also thanks Bhandari Foils & Tubes Ltd. (BFTL), Indore India, for providing material for experiments.

Declaration of Conflicting Interests The author(s) confirms no potential interest of conflict with respect to authorship, research in publication of this article.

References

1. Alaswad A, Benyounis KY, Olabi AG (2012) Tube hydroforming process: a reference guide. *Mater Des* 33(1):328–339
2. Ahmetoglu M, Sutter K, Li XJ, Altan T (2000) Tube hydroforming: current research, applications and need for training. *J Mater Process Technol* 98(2):224–231
3. Lang LH et al (2004) Hydroforming highlights: sheet hydroforming and tube hydroforming. *J Mater Process Technol* 151(1–3 SPEC. ISS.):165–177
4. Carleer B, Van Der Kevie G, De Winter L, Van Veldhuizen B (2000) Analysis of the effect of material properties on the hydroforming process of tubes. *J Mater Process Technol* 104(1):158–166
5. Omar A, Tewari A, Narasimhan K (2020) Effect of bulge ratio on the deformation behaviour and fracture location during welded steel tube hydroforming process. *Results Mater* 6:100096
6. Koc M (2003) Investigation of the effect of loading path and variation in material properties on robustness of the tube hydroforming process. *J Mater Process Technol* 133:276–281
7. Park JY, Han SW, Jeong HS, Cho JR, Moon YH (2017) Advanced sealing system to prevent leakage in hydroforming. *J Mater Process Technol* 247:103–110
8. Sorine M, Simha CHM, Van Riemsdijk I, Worswick MJ (2008) Prediction of necking of high strength steel tubes during hydroforming - multi-axial loading. *Int J Mech Sci* 50(9):1411–1422
9. Pavlina EJ, Van Tyne CJ, Hertel K (2008) Hydraulic bulge testing of dual phase steel tubes produced using a novel processing route. *J Mater Process Technol* 201(1–3):242–246
10. Liu J, Zhang Z, Manabe KI, Li Y, Misra RDK (2014) Microstructure evolution in TRIP-aided seamless steel tube during T-shape hydroforming process. *Mater Charact* 94:149–160

Influence of Kinematic Hardening on Clinch Joining of Dual-Phase Steel HCT590X Sheet Metal



Johannes Friedlein, Julia Mergheim, and Paul Steinmann

Abstract Nowadays, clinching is a widely used joining technique, where sheets are joined by pure deformation to create an interlock without the need for auxiliary parts. This leads to advantages such as reduced joining time and manufacturing costs. On the other hand, the joint strength solely relies on directed material deformation, which renders an accurate material modelling essential to reliably predict the joint forming. The formation of the joint locally involves large plastic strains and possibly complex non-proportional loading paths, as typical of many metal forming applications. Consequently, a finite plasticity formulation is utilised incorporating a Chaboche–Rousselier kinematic hardening law to capture the Bauschinger effect. Material parameters are identified from tension–compression tests on miniature specimens for the dual-phase steel HCT590X. The resulting material model is implemented in LS-Dyna to study the locally diverse loading paths and give a quantitative statement on the importance of kinematic hardening for clinching. It turns out that the Bauschinger effect mainly affects the springback of the sheets and has a smaller effect on the joint forming itself.

Keywords Clinching · Material modelling · Kinematic hardening · Parameter identification · Bauschinger effect

J. Friedlein (✉) · J. Mergheim · P. Steinmann
Institute of Applied Mechanics, Friedrich-Alexander-Universität Erlangen-Nürnberg,
Egerlandstrasse 5, 91058 Erlangen, Germany
e-mail: Johannes.Friedlein@fau.de

J. Mergheim
e-mail: Julia.Mergheim@fau.de

P. Steinmann
e-mail: Paul.Steinmann@fau.de

Introduction

Clinching can be used to join sheet metal by pure deformation and eliminate the need for auxiliary joining parts, such as rivets or bolts. Consequently, the joint takes its strength purely from controlled local deformations leading to an interlock of both sheets. The formation of this interlock is relevant to predict the joint strength [1] and is related to severe plastic strains requiring reliable finite strain material models for finite element analyses. These constitutive models need to incorporate plastic hardening, where a distinction between isotropic and kinematic hardening is only important if non-proportional loading paths are present during the forming. Such loading paths can occur due to changing material flow directions as experienced by the successively oriented material flow during clinch joining. To quantitatively study the influence of kinematic hardening on clinch joining, we subsequently investigate two decisive factors as research questions (RQ): the material (RQ1) and the loading paths during the clinching process (RQ2).

Exemplarily, a *dual-phase steel HCT590X* is considered, which is often used in the automotive industry. It is well known that especially dual-phase steel can exhibit an early re-plastification and pronounced transition region at load reversal named Bauschinger effect [2, 3]. Due to the higher strength of dual-phase steel, it shows a stronger tendency for springback, which together with the microstructure combining soft and hard phases leads to larger Bauschinger effects compared to conventional steel [4, 5]. This has for instance been shown in [6] for the congeneric DP600 and similarly in [3, 5, 7]. By a sensitivity analysis for dual-phase steel [8], the most influential aspects of the Bauschinger effect have been identified as the transient hardening and yield stress at load reversal. Material modelling can capture the Bauschinger effect by kinematic hardening, which causes the yield surface to shift rather than increase in size as for isotropic hardening. To quantify the Bauschinger effect, cyclic tests can be conducted. This can be realised for instance by cyclic shearing [3], cyclic bending [7], or by tension–compression tests [7, 9]. Especially usually thin sheet metal is susceptible to buckling under compressive loading [7, 9]. Therefore, either special anti-buckling devices must be used [10] or miniature specimen are utilised as presented in [9] for tension–compression tests. Herein, the experiments are conducted at lower strains motivated by the observed stagnation of the Bauschinger effect towards larger strains [5]. Studies at various strain levels and pre-strain have been examined in [5, 6]. Herein, miniature tension–compression tests for sheet metal are conducted to investigate whether the steel HCT590X shows a Bauschinger effect (RQ1).

It has already been shown for several metal forming processes that kinematic hardening can have a significant influence on the final product. In deep drawing, for instance, the sheet is drawn over the intake radii causing an alternating plastification [2, 9], which is relevant for an accurate prediction of the springback. In addition to the springback at unloading, kinematic hardening might also affect the formation of

the interlock during the *clinch joining process*. This leads to the second research question to be addressed: Does clinch joining contain such non-proportional loading paths in the plastic region and is consequently influenced by kinematic hardening? (RQ2).

Material Modelling

The continuum mechanics framework is briefly presented in the following. It is important to note that the kinematics and the in LS-Dyna underlying balance equations are formulated in the geometrically nonlinear (finite strain) setup, whereas the herein used logarithmic strain space enables the material model to be formulated similarly as in the geometrically linear case.

Kinematics

A body in the reference (undeformed) configuration is described by its material points with coordinates \mathbf{X} . The spatial (deformed) configuration contains the deformed body and its spatial coordinates \mathbf{x} . Deformations of the body are captured by the nonlinear deformation map \mathbf{y} as $\mathbf{x} = \mathbf{y}(\mathbf{X}, t)$ and its gradient $\mathbf{F} = \nabla_{\mathbf{X}} \mathbf{y}$.

Logarithmic Strain Space

The logarithmic strain space [11] is a hyperelastic-based approach that easily extends material models to the geometrically nonlinear setting. It has been successfully applied in various field, such as thermo-elastic-plastic solids [12] or additive manufacturing [13]. It is based on a modular geometric pre- and post-processing utilising the logarithmic Hencky strain.

The logarithmic Hencky strain \mathbf{H} is part of Seth–Hill’s family of generalised strain measures and can be computed from the right Cauchy–Green tensor $\mathbf{C} = \mathbf{F}^T \cdot \mathbf{F}$ as

$$\mathbf{H} = \frac{1}{2} \ln(\mathbf{C}) = \sum_{a=1}^3 \ln(\sqrt{\eta_a}) \mathbf{n}_a \otimes \mathbf{n}_a \tag{1}$$

and the three eigenvalues η_a and eigenvectors \mathbf{n}_a of \mathbf{C} [11].

Due to the properties of the tensor logarithm $\ln(\blacksquare)$, the Hencky strain is interpretable as a geometrically linear strain that can be handled as a small strain measure and applied as such. This enables material models to subsist inside the logarithmic strain space and be encompassed by the pre-processing of the strains in Eq. (1) and

a post-processing of the resulting logarithmic stress \mathbf{T} and tangent(s) \mathcal{C} back into the “real world”. The latter concerns the (spatial) Cauchy stress $\boldsymbol{\sigma}$ and the Eulerian tangent \mathbf{E} as

$$\boldsymbol{\sigma} = \mathbf{T} : \mathcal{P}^E; \mathbf{E} = [\mathcal{P}^E]^T : \mathcal{C} : \mathcal{P}^E + \mathbf{T} : \mathcal{L}^E, \quad (2)$$

derivable from the strain energy density with the Eulerian projection tensors \mathcal{P}^E and \mathcal{L}^E as stated for instance in [11]. The Fortran source code for the geometric pre- and post-processing is available online [14]. A Fortran tensor toolbox [15] is utilised for the implementation of the logarithmic strain space and the material model.

The benefits of the logarithmic strain space include its easy usability and wide applicability, whereas some limitations have recently been summarised [16].

Additive Plasticity with Combined Isotropic-Kinematic Hardening

The plastic material behaviour of the sheet metal is modelled by combined isotropic and kinematic hardening. This is described by an isotropic von Mises yield surface with classical isotropic hardening and a Chaboche–Rousselier type kinematic hardening [17]. Due to the use of the logarithmic strain space, the following material model is formulated similarly as a geometrically linear model.

The logarithmic stress \mathbf{T} for additive plasticity can directly be computed from the total Hencky strain \mathbf{H} with the bulk modulus κ , shear modulus μ , and symmetric plastic strain tensor \mathbf{H}^P . The superscript dev denotes the deviatoric part of the tensor.

$$\mathbf{T}(\mathbf{H}) = \kappa \text{trace}(\mathbf{H})\mathbf{I} + 2\mu[\mathbf{H}^{\text{dev}} - \mathbf{H}^P] \quad (3)$$

Isotropic von Mises (J2-) plasticity with isotropic and kinematic hardening is assumed by the following yield condition and described by the scalar flow stress σ_{flow} and the second-order back stress tensor \mathbf{B} , respectively.

$$\Phi^P = \|\mathbf{T}^{\text{dev}} + \mathbf{B}\| - \sqrt{2/3}\sigma_{\text{flow}}(\mathbf{H}_{\text{acc}}^P) \leq 0 \quad (4)$$

The additive framework can directly be extended to anisotropic plasticity, see for instance [11].

Isotropic hardening is introduced in the flow stress $\sigma_{\text{flow}}(\mathbf{H}_{\text{acc}}^P)$ either by a tabular true stress–strain curve or by an analytical hardening law as stated in Eq. (8).

The effect of kinematic hardening is incorporated into the yield function by the total back stress tensor \mathbf{B} . Herein a Chaboche–Rousselier type kinematic hardening

model with multiple back stresses is chosen, which is expected to be well suited to describe the dual-phase steel [3, 6].

Starting from the yield function, the evolution equations for the internal variables, namely, the second-order plastic strain tensor \mathbf{H}^p , the accumulated plastic strain H_{acc}^p , and the back stress tensors \mathbf{B}_i are stated as

$$\dot{\mathbf{H}}^p = \dot{\gamma} \mathbf{N}; \dot{H}_{acc}^p = \sqrt{2/3} \|\dot{\mathbf{H}}^p\| = \sqrt{2/3} \dot{\gamma}; \dot{\mathbf{B}}_i = k_{1,i} \dot{\gamma} \mathbf{N} - k_{2,i} \dot{\gamma} \mathbf{B}_{n,i} \quad (5)$$

with the Lagrange multiplier $\dot{\gamma}$ and the evolution direction $\mathbf{N} = [\mathbf{T}^{dev} + \mathbf{B}]/\|\mathbf{T}^{dev} + \mathbf{B}\|$. The evolution equations are integrated by an implicit Euler-Backward scheme

$$\mathbf{H}_{n+1}^p = \mathbf{H}_n^p + \gamma_{n+1} \mathbf{N}; H_{accn+1}^p = H_{accn}^p + \sqrt{2/3} \gamma_{n+1} \quad (6)$$

and solved by a cutting-plane algorithm from [18]. The latter is chosen for simplicity and was found to fit well to the default BFGS solver in LS-Dyna. With the concept shown in [19] an arbitrary number of back stresses n_B can easily be introduced by summations resulting in the discrete incremental equation for the total back stress

$$\mathbf{B}_{n+1} = \sum_{i=1}^{n_B} \mathbf{B}_{n+1,i} = \sum_{i=1}^{n_B} [1 + k_{2,i} \gamma_{n+1}]^{-1} \mathbf{B}_{n,i} + \gamma_{n+1} \mathbf{N} \sum_{i=1}^{n_B} \frac{k_{1,i}}{[1 + k_{2,i} \gamma_{n+1}]} \quad (7)$$

Experiments and Parameter Identification

To study the Bauschinger effect and describe the combined isotropic-kinematic hardening behaviour, tension–compression tests are conducted. Together with uniaxial stress–strain curves, the material parameters are inversely identified.

Experimental Setup

Layer compression tests are conducted to determine the uniaxial stress–strain curve as outlined in [20, 21]. To distinguish between isotropic and kinematic hardening, tension–compression tests are utilised. For that purpose, miniature specimens are advantageous for sheet metal to avoid buckling under the compressive loading and thus eliminate the need for special anti-buckling devices [9]. The miniature specimen shown in Fig. 1a is clamped in a universal testing machine in Fig. 1b and loaded in a tension–compression-tension cycle (measured strain path in Fig. 2). At each load path change, the influence of the Bauschinger effect can be observed and used to distinguish between isotropic and kinematic hardening. The resulting force on the

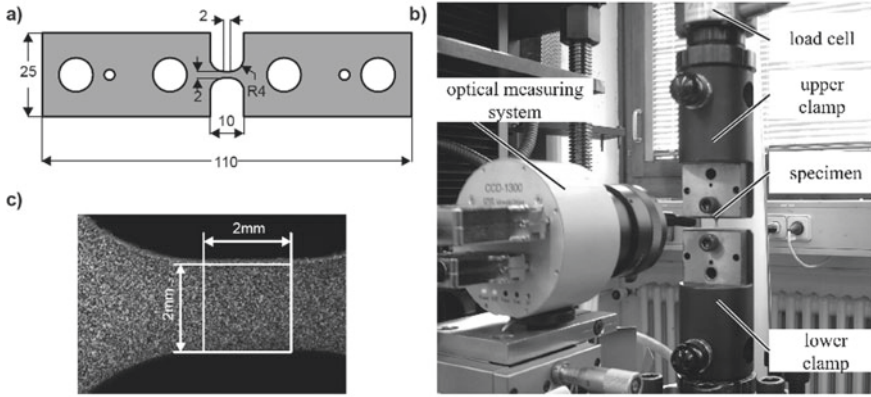
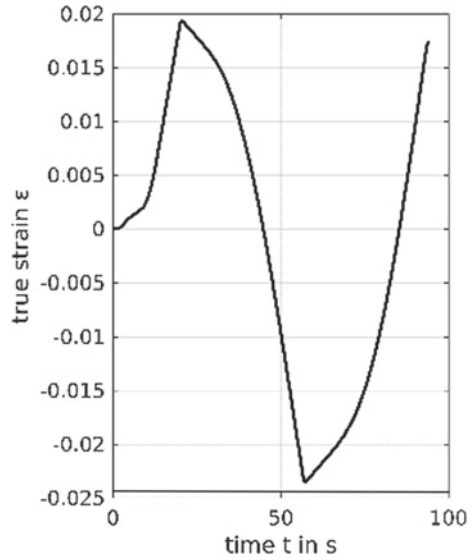


Fig. 1 Experimental setup of the tension–compression test. **a** specimen geometry and dimensions with sheet thickness of 1.5 mm. **b** experimental setup. **c** 2×2 mm measuring range (based on [9])

Fig. 2 Tension–compression-tension loading cycle. Optically measured true strain versus time response



specimen is recorded by a load cell, whereas the deformation and the resulting strains in the measuring range (Fig. 1c) are determined optically.

Parameter Identification

For the steel HCT590X Young’s modulus $E = 205800\text{MPa}$ and Poisson’s ratio $\nu = 0.3$ are chosen. In the following, the isotropic and kinematic hardening parameters are identified from layer compression tests and tension–compression tests.

Layer Compression Test

The flow curve of the considered steel HCT590X has already been identified from layer compression tests in [20], where this test method has been shown to be well suited for the subsequent application to clinching. The experimental results are plotted as true stress–strain data in Fig. 3 (red). This uniaxial flow curve is sufficient to either fit pure isotropic (IH) or pure kinematic hardening (KH).

For the description of *isotropic hardening*, particular points of the flow curve in Fig. 3 (red) could directly be used to describe the flow stress σ_{flow} in Eq. (4) by means of tabulated values. However, to be able to compare a pure isotropic and pure kinematic hardening model with the exact same uniaxial flow curve, the behaviour is described by an analytical ansatz

$$\sigma = \sigma_y + \sum_{i=1}^{n_Q} Q_i [1 - \exp(-b_i \cdot H_{\text{acc}}^p)] \tag{8}$$

which can exactly be matched by a Chaboche–Rousselier model with n_Q back stresses in Eq. (9) under monotonic uniaxial loading. By minimising the difference

Fig. 3 Uniaxial flow stress. Experimental results (red) determined from layer compression tests [20]. Isotropic (dashed), kinematic (dotted) and combined isotropic-kinematic (solid) are fitted to match the experimental results (red). Isotropic and kinematic hardening models are designed to exactly coincide under uniaxial loading

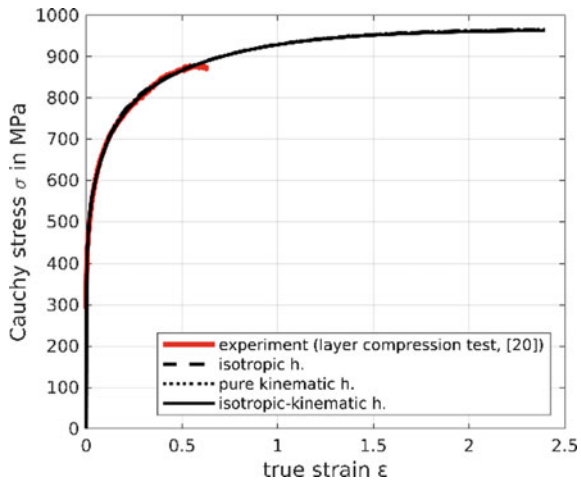


Table 1 Plastic material parameters for isotropic and kinematic hardening

Behaviour	Symbol	Pure isotropic hardening (IH)	Pure kinematic hardening (KH)	Combined isotropic-kinematic hardening (IKH)	Unit
Yield stress	σ_y	371.32	371.32	337.91	MPa
Isotropic hardening	Q_1	257.42	–	260.55	MPa
	b_1	1.9030	–	1.9569	–
	Q_2	230.27	–	–	MPa
	b_2	12.020	–	–	–
	Q_3	111.22	–	–	MPa
	b_3	123.59	–	–	–
Kinematic hardening	$k_{1,1}$	–	326.58	33,333	MPa
	$k_{2,1}$	–	1.5538	1144.9	–
	$k_{1,2}$	–	1845.3	10,894	MPa
	$k_{2,2}$	–	9.8143	104.82	–
	$k_{1,3}$	–	9164.3	1490.3	MPa
	$k_{2,3}$	–	100.91	8.8490	–

between the experimental and numerical results, the material parameters are identified as stated in Table 1 considering an extrapolation to higher strains as suggested in [20]. As shown in Fig. 3, three summands ($n_Q = 3$) in Eq. (8) are sufficient to match the experimental flow curve (red).

On the other hand, the stress in loading direction for a pure *kinematic hardening* (KH) Chaboche–Rousselier model can be computed as

$$\sigma = \sigma_y + \sqrt{\frac{3}{2}} \sum_{i=1}^{n_B} \frac{k_{1,i}}{k_{2,i}} \left[1 - \exp\left(-\sqrt{\frac{3}{2}} k_{2,i} \cdot H_{acc}^p\right) \right] \quad (9)$$

From the comparison of Eq. (8) and (9), the parameters for KH, namely $k_{1,i}$ and $k_{2,i}$, can be determined from IH as

$$k_{1,i} = 2/3 \cdot Q_i \cdot b_i; k_{2,i} = \sqrt{2/3} b_i \quad (10)$$

if the same stress–strain curve is to be modelled with either pure isotropic or pure kinematic hardening. This ensures that all differences visible in the results between IH and KH can solely be attributed to load path changes and the fundamental difference between both hardening types.

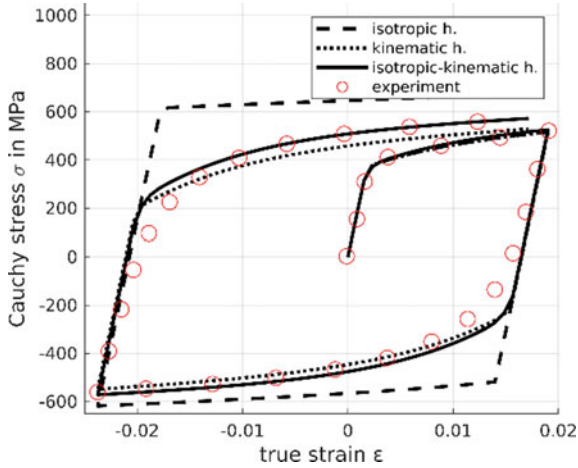


Fig. 4 True stress–strain results from tension–compression tests (red circles). Isotropic hardening (dashed) overestimates the yield stress at both load reversals. Pure kinematic hardening (dotted) underestimates the stress. Combined isotropic-kinematic hardening (solid) can model the response well

Tension–Compression Test

The tension–compression tests need to be considered to distinguish between isotropic and kinematic hardening. True stress–strain results from the former are depicted in Fig. 4. At each load reversal a distinctly earlier yielding and a transient area is visible that cannot be described by classical isotropic hardening (IH). On the other hand, pure kinematic hardening (KH) slightly underestimates the yield stress after each load reversal. Interestingly, even the KH model is not able to capture the extremely early re-yielding after the load reversal. This could, for instance, indicate an initial back stress from the previous manufacturing of the sheet metal included in [22].

Because of the (almost) uniaxial stress state in the tension–compression test, a 1D analytical model can be used to identify the parameters of the combined isotropic-kinematic hardening model (IKH) from the cyclic loading as listed in Table 1.

To sum up, Fig. 4 shows that the present HCT590X exhibits a pronounced Bauschinger effect (RQ1) and that the material model represents the experimental results for the layer compression test and tension–compression test sufficiently well.

Numerical Analysis of Clinch Joining

To analyse the influence of the Bauschinger effect on clinching, we firstly study the loading paths during the joining process. Only if non-proportional loading is present,

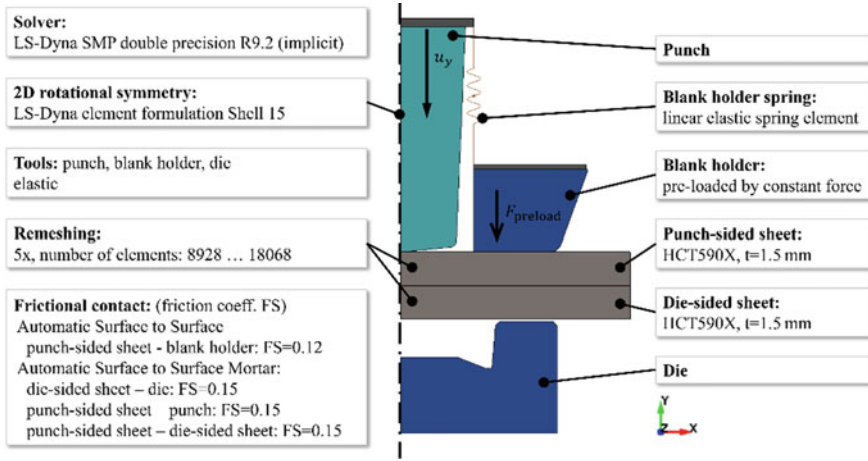


Fig. 5 Overview of the clinch joining process simulation in LS-Dyna (based on [23])

the different hardening types will be influential. Secondly, the results of clinching simulations with the hardening models from Table 1 are compared.

The clinch joining process is simulated in LS-Dyna (Solver: SMP, double precision, R9.2) as depicted in Fig. 5 with an implicit time integration. Rotational symmetry of the joint is utilised to reduce the model to 2D (axial symmetry, LS-Dyna element formulation Shell 15). The sheets are remeshed at predefined time intervals during the forming to avoid strong mesh distortion.

Loading Paths During Clinching

We propose to analyse the evolution of the Lode angle as a simple criterion to study the existence of non-proportional loading paths. The Lode angle parameter is defined in LS-Dyna as the normalised third deviatoric stress invariant [24]

$$\xi = \frac{27 \det(\text{dev}(\boldsymbol{\sigma}))}{2 \sigma^3} = (-1 \dots 1) \quad \text{with} \quad \sigma_{\text{VM}} = \sqrt{\frac{3}{2}} \|\boldsymbol{\sigma}^{\text{dev}}\| \quad (11)$$

Proportional loading requires a constant Lode angle parameter ξ . However, a constant ξ does not guarantee a proportional loading, compare Fig. 6 where for instance up to 6 points on the initial yield surface (red circle) can possess the same ξ . But without erratic changes in the principal stress direction, the Lode angle parameter can be used to detect changes in the direction of the loading path. The latter can help to quantify the need for kinematic hardening during the process.

Figure 7 shows the evolution of the Lode angle parameter for three points in the sheets (points marked in Fig. 7d, at each remeshing the element that contains the tracer

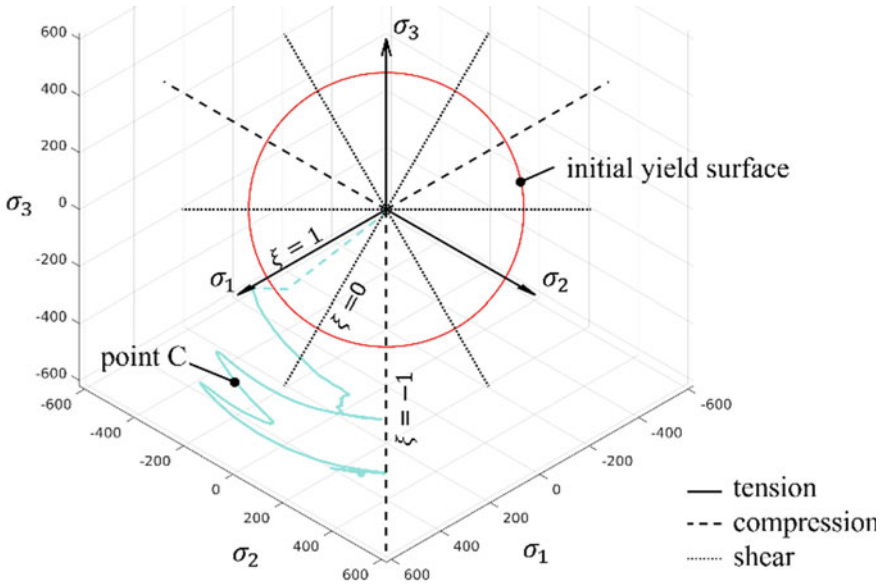


Fig. 6 Principal stress space viewed in the deviatoric plane. Along the positive principal directions (solid black lines) tension occurs ($\xi = 1$) and in negative direction compression (dashed black, $\xi = -1$). Pure shear ($\xi = 0$) is present along the bisectrices (dotted black). The principal deviatoric stress evolution for point C from Fig. 7c is exemplarily added (cyan)

point is selected). A finer discretisation with more remeshing steps than in Fig. 5 has been chosen for the stress analysis to improve the accuracy. Point A between the punch and the bottom of the die shows an almost constant evolution of the Lode angle parameter indicating a proportional loading at $\xi = -1$ (compression). In such areas, no differences between isotropic and kinematic hardening would be observed during loading. Points B and C detect changes in the Lode angle parameter indicating non-proportional loading paths. This is also visible for point C in Fig. 6 (cyan), where the stress state evolves radially due to the plastic hardening but also significantly shifts in tangential direction.

Consequently, we can summarise that the clinch joining process contains non-proportional loading paths (RQ2).

Influence of Kinematic Hardening

The three material parameter sets IH, KH and IKH listed in Table 1 are applied to the clinch joining simulation outlined previously. Figure 8 depicts the final geometry of the clinched joint for each model.

At first, Fig. 8 shows only larger differences in the springback of the two sheets on the right end. This is measured by the displacement of the upper-right corner (point

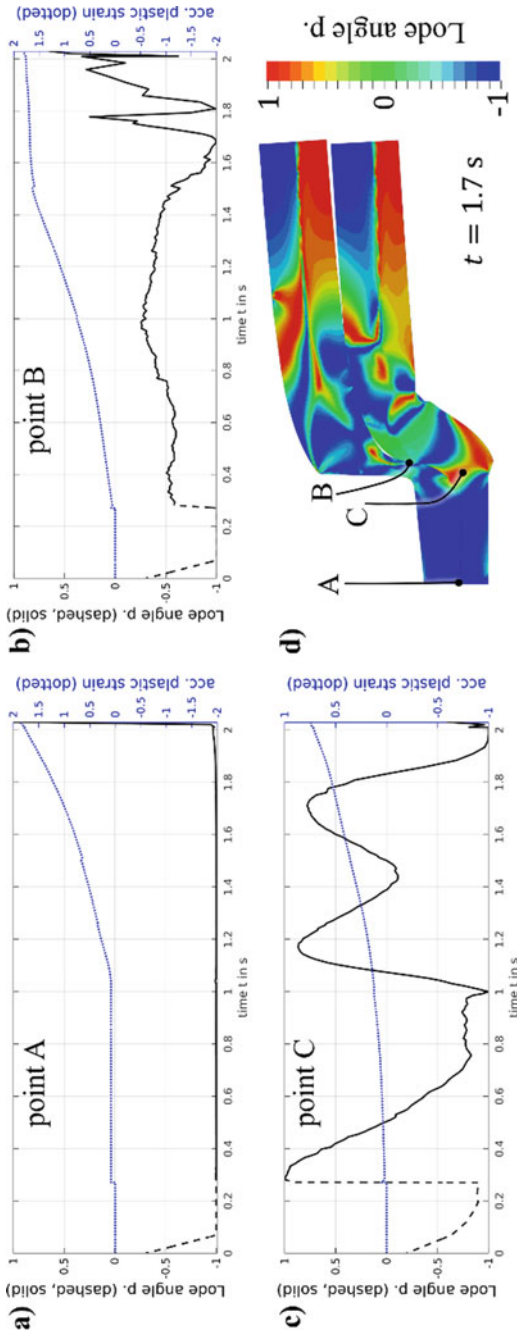


Fig. 7 Lode angle parameter ξ -evolution for different points (A, B, C) in the sheets shown in (d) with their traces. **a** Point A resides between the punch and the bottom of the die. Thus, it undergoes compression ($\xi = -1$) remaining constant in the plastic region due to proportional loading. **b** Point B in the neck shows mainly a combination of compression and shear with some non-proportional evolution. **c** Point C undergoes substantial non-proportional loading including tension, shear and compression. Additionally, each figure shows the evolution of the accumulated plastic strain (H_{acc}^p , dotted blue). Only the ξ -evolution in the active plastic region (plastic strain rate $\dot{H}_{acc}^p > 0$) is relevant to trigger differences between isotropic and kinematic hardening, thus the elastic parts are marked by a dashed line. **d** Deformation of the sheets during the process at $t = 1.7$ s with the Lode angle parameter as colour map and the location and trace (black line) of the points A, B, and C

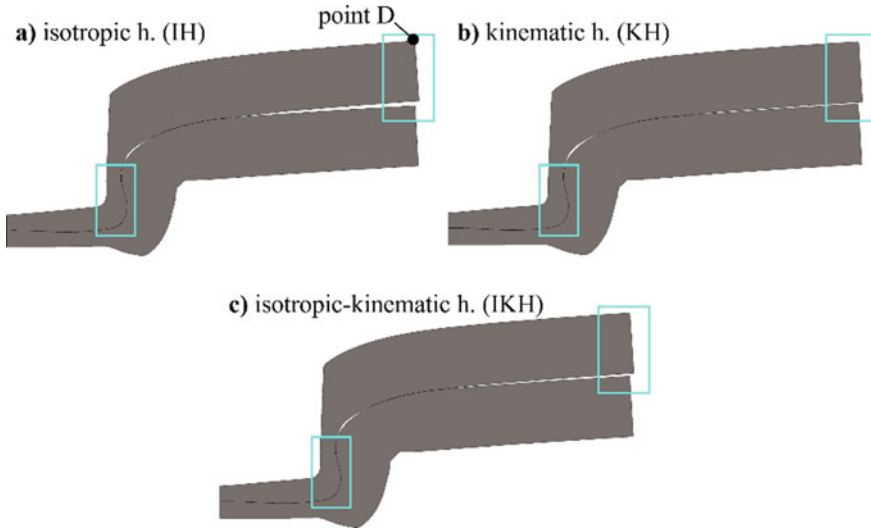


Fig. 8 Final geometry of the clinched joint for the different hardening models. Main differences are visible in the springback of the sheets on the right end and in the interlock region, as marked by the two rectangles and magnified in Fig. 11

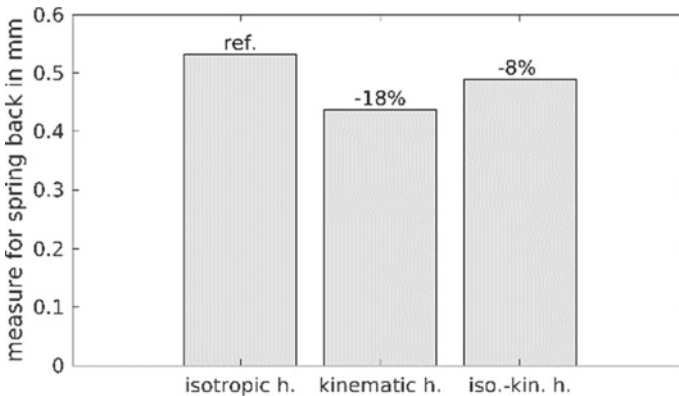


Fig. 9 Comparing the displacement of point D marked in Fig. 8a that can be used as a measure for the springback. With pure kinematic hardening the springback is reduced by about 18%

D marked in Fig. 8a) and compared in Fig. 9. By using a pure kinematic hardening model (KH), the final vertical deformation of point D is 18% lower than for the reference model with pure isotropic hardening (IH).

Secondly, changes in the interlock, as compared in Fig. 10, and neck shape are visible as depicted in Fig. 11. The interlock (defined in Fig. 11) is of high relevance for the joint strength [1] and appears to be also influenced by the hardening law.

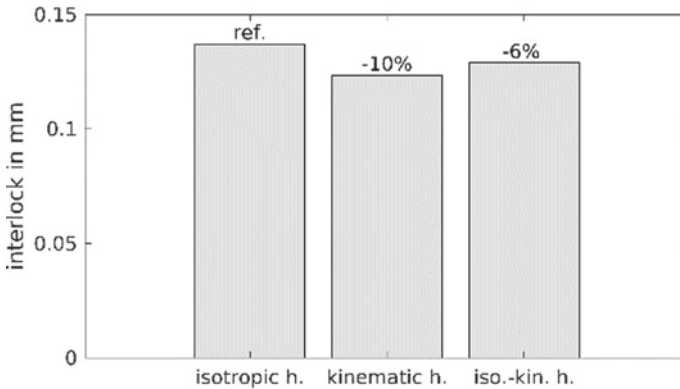


Fig. 10 Comparing the interlock for different hardening models. Kinematic hardening appears to reduce the formation of the interlock

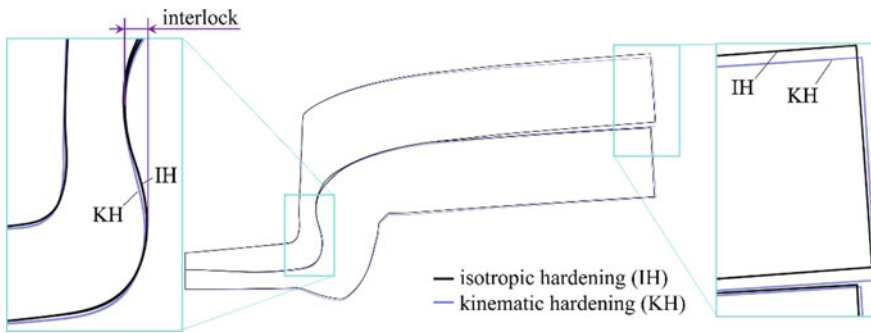


Fig. 11 Comparing the deformation of the clinched joint with isotropic (black, IH) and kinematic hardening (blue, KH). The right end of the sheet clearly shows a lower springback of the KH model. The zoom also reveals detectable differences in the formation of the neck and interlock

For both geometric quantities, the combined isotropic-kinematic hardening model settles in between IH and KH with differences of (6...8)%.

Lastly, the process force, measured as the force on the punch, is compared for the three models in Fig. 12. Up to around $t = 1$ s, the process forces between the three models are comparable. Once the die-sided sheet comes into contact with the bottom of the die to initiate the radial material flow that forms the interlock, differences in the process forces between the models become visible. In the end, isotropic hardening requires the highest punch force, whereas the pure kinematic hardening model remains approximately 6% lower. Exemplary experimental results for the punch force are added in grey in Fig. 12. Between $t = (0.4 \dots 1)$ s the force is underestimated for each hardening model possibly due to deviations in the yielding or frictional behaviour, which is apparently not influenced by the hardening type.

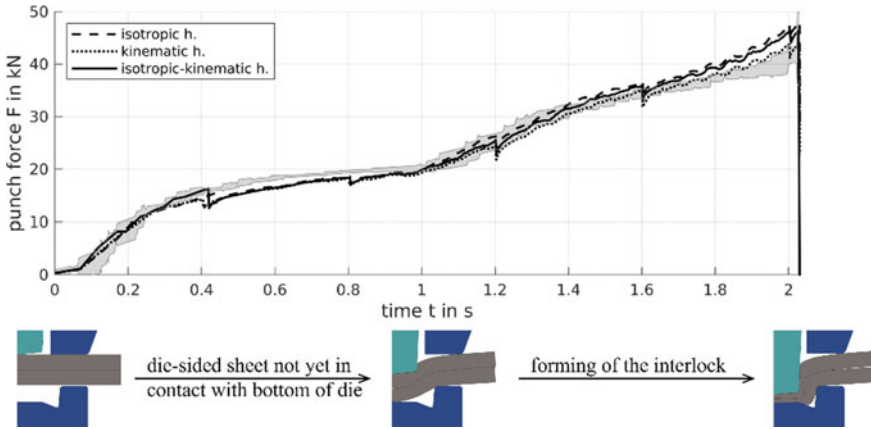


Fig. 12 Comparing the punch force during the joint forming. The three different hardening models (line styles) show mainly differences during the secondary phase, namely the forming of the interlock, where kinematic hardening leads to lower process forces

Summary and Outlook

We have studied the plastification of dual-phase steel HCT590X sheet metal by miniature tension–compression tests. The resulting tension–compression–tension cycle enabled a distinction between isotropic and kinematic hardening completing the material model initially only defined by uniaxial flow curves from layer compression tests. Results indicate a pronounced Bauschinger effect (RQ1) as expected for the dual-phase steel. A Chaboche–Rousselier kinematic hardening model with multiple back stresses was implemented in LS-Dyna and equipped with the identified hardening parameters. Moreover, the loading paths during the clinch joining have been analysed. The evolution of the Lode angle parameter reveals that locally distinct non-proportional loading occurs (RQ2). Finally, the different hardening models have been applied to clinching simulations and their results compared. Kinematic hardening appears to primarily affect the final springback and only secondarily the joint forming and process force (RQ2). Future work could quantify the effect of kinematic hardening on the joint strength, for instance, by pull-out and shear tests. Even though the current material model was sufficient to study the fundamental influence of the Bauschinger effect on clinching, also more advanced kinematic hardening models could be utilised. The latter might be able to capture the observed early re-plastification that cannot be reproduced by a Chaboche–Rousselier model [2].

Acknowledgements The funding by the Deutsche Forschungsgemeinschaft (DFG, German Research Foundation)—Project-ID 418701707—TRR 285, subproject A05 is gratefully acknowledged. Moreover, we want to thank our colleagues in the TRR285 Christian Bielak (A01) for providing the LS-Dyna clinching model and David Römisch (C01) for conducting the tension–compression tests.

References

1. Roux E, Bouchard PO (2013) Kriging metamodel global optimization of clinching joining processes accounting for ductile damage. *J Mater Process Technol* 213(7):1038–1047
2. Banabic D (2010) Sheet metal forming processes: constitutive modelling and numerical simulation. Springer Science & Business Media, Berlin, Heidelberg
3. Yin Q et al (2012) A cyclic twin bridge shear test for the identification of kinematic hardening parameters. *Int J Mech Sci* 59(1):31–43
4. Zhonghua L, Haicheng G (1990) Bauschinger effect and residual phase stresses in two ductile-phase steels: Part I The influence of phase stresses on the Bauschinger effect. *Metall Trans A* 21(2):717–724
5. Weiss M et al (2015) On the Bauschinger effect in dual phase steel at high levels of strain. *Mater Sci Eng A* 643:127–136
6. Biallas A, Merklein M (2021) Material model for the production of steel fibers by notch rolling and fulling. *Key Eng Mater* 883:277–284
7. Eggertsen P, Mattiasson K (2011) On the identification of kinematic hardening material parameters for accurate springback predictions. *Int J Mater Form* 4(2):103–120
8. Zang S, Lee M, Kim JH (2013) Evaluating the significance of hardening behavior and unloading modulus under strain reversal in sheet springback prediction. *Int J Mech Sci* 77:194–204
9. Staud D (2010) Effiziente Prozesskettenauslegung für das Umformen lokal wärmebehandelter und geschweißter Aluminiumbleche. Ph.D. thesis, Friedrich-Alexander-Universität Erlangen-Nürnberg
10. Choi JS et al (2015) Measurement and modeling of simple shear deformation under load reversal: application to advanced high strength steels. *Int J Mech Sci* 98:144–156
11. Miehe C, Apel N, Lambrecht M (2002) Anisotropic additive plasticity in the logarithmic strain space: Modular kinematic formulation and implementation based on incremental minimization principles for standard materials. *Comput Methods Appl Mech Eng* 191(47–48):5383–5425
12. Aldakheel F (2017) Micromorphic approach for gradient-extended thermo-elastic-plastic solids in the logarithmic strain space. *Contin Mech Thermodyn* 29(6):1207–1217
13. Burkhardt C, Soldner D, Mergheim J (2020) A comparison of material models for the simulation of selective beam melting processes. *Procedia CIRP* 94:52–57
14. Friedlein J. Logarithmic_Strain_Space-Fortran. GITHUB. https://github.com/jfriedlein/Logarithmic_Strain_Space-Fortran. Accessed 1 March 2022
15. Dutzler A (2020) Tensor toolbox for modern Fortran - high-level tensor manipulation in Fortran. <https://doi.org/10.5281/zenodo.4077378>
16. Friedlein J, Mergheim J, Steinmann P (2022) Observations on additive plasticity in the logarithmic strain space at excessive strains. *Int J Solids Struct* 239–240:111416
17. Chaboche JL, Rousselier G (1983) On the plastic and viscoplastic constitutive equations—Part I: Rules developed with internal variable concept. *J Pressure Vessel Technol* 105(2):153–158
18. Simo JC, Hughes TJR (1998) Computational inelasticity. Springer Science & Business Media, New York
19. Wali M et al (2015) One-equation integration algorithm of a generalized quadratic yield function with Chaboche non-linear isotropic/kinematic hardening. *Int J Mech Sci* 92:223–232
20. Böhnke M et al (2021) Influence of various procedures for the determination of flow curves on the predictive accuracy of numerical simulations for mechanical joining processes. *Mater Test* 63(6):493–500
21. Friedlein J et al (2021) Inverse parameter identification of an anisotropic plasticity model for sheet metal. In: IOP Conf Ser: Mater Sci Eng 1157:012004
22. Marcadet SJ, Mohr D (2015) Effect of compression–tension loading reversal on the strain to fracture of dual phase steel sheets. *Int J Plast* 72:21–43
23. Bielak CR et al (2021) Numerical analysis of the robustness of clinching process considering the pre-forming of the parts. *J Adv Join Proces* 3:100038
24. Hallquist JO (2020) LS-DYNA Keyword User’s Manual - vol II. Livermore Software Technology Corporation

Lightweighting Through Stiffening Dart Formation and Its Rigidity Evaluation



Dohyun Leem, Lu Huang, Joshua Solomon, Hui-ping Wang, and Jian Cao

Abstract Stiffening darts are commonly added in angle brackets to enhance the bending stiffness of the components such that a thinner gauge can be used for lightweighting. It also helps to reduce springback in a press brake operation. This study investigates the plastic material deformation in stiffening dart formation in a press brake bending process by means of a combined numerical and experimental approach. The forming process is simulated with the finite element (FE) method and the simulation result is compared with an actual forming result to validate the accuracy of the simulation model. In addition, methods of systematically evaluating dart stiffening effect in an angle bracket are proposed, where flattening and folding tests are described. Example rigidity test results for dart designs are provided to discuss the relationship between dart geometry and its stiffening effect.

Keywords Press brake · Angle bracket · Stiffening dart · Finite element simulation · Rigidity evaluation

Introduction

Lightweighting of automotive vehicles has been a core interest for automakers due to its impact on the fuel efficiency, in conjunction with the concerns of environmental issues. However, it is important that lightweighting practices for auto vehicles do not weaken the vehicle performance and passenger safety. That is, the lightweight bodies need to maintain satisfactory body rigidity and crashworthiness levels. For enhancing the stiffness of auto body components without increasing their total masses, stiffening darts shown in Fig. 1 are commonly used in angle brackets. In addition to the structural enhancement, the stiffening darts also have several manufacturing advantages including: (1) the feature can be formed simultaneously while the initial blank

D. Leem · J. Cao (✉)

Department of Mechanical Engineering, Northwestern University, Evanston, IL 60208, USA
e-mail: jcao@northwestern.edu

L. Huang · J. Solomon · H. Wang
General Motors Company, Warren, MI, USA

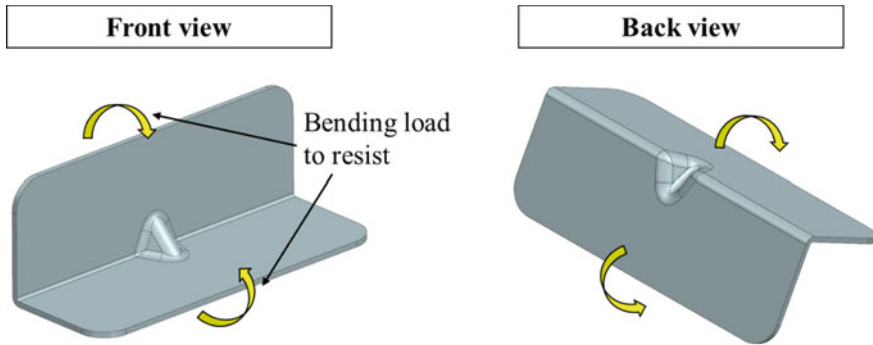


Fig. 1 Stiffening dart of an angle bracket component

is being bent to form an angle bracket in a press brake; (2) adding a stiffening dart can reduce the overall springback angle in the bending process; and (3) no additional materials are needed other than the initial blank itself to form the stiffening dart.

Although popularly used via trial and error, the fundamental dart formation mechanics in the press brake has not been well understood among engineers. For the regular press brake operations which do not involve stiffening dart formation, there have been a wide range of studies. For instance, Pancheco and Santos [1] investigated the effect of punch nose radius on the final bending geometry using a finite element (FE) simulation approach. Wang et al. [2] proposed an incremental press brake bending process for controlling springback of structural steel sheets based on an analytic calculation for predicting the springback angle. More recently, Miranda et al. [3] developed a combined FE simulation and neural network approach for predicting springback in the press brake bending of two different types of steel. As for the press brake operation involving stiffening dart formations, some manufacturing guidelines are available such as: (1) the width and depth of a 45 degree dart should be directly proportional to the bend radius and material thickness; and (2) the minimum distance between a dart and the edge of a hole in a parallel plane should be at least eight times the material thickness [4, 5]. These guidelines are likely from empirically accumulated knowledges and do not provide an idea of the fundamental characteristics of the stiffening dart formation process. In addition, while it is commonly accepted that the stiffening darts are helpful for enhancing the rigidity of angle brackets, a systematic way of evaluating how much rigidity improvements can be made by the darts has not been established.

The presented work studies the mechanics of stiffening dart formation in a press brake operation in details and develops a systematic way of evaluating the rigidity improvements by the stiffening darts. To understand the stiffening dart formation mechanics, a combined simulation-experiment approach is used to investigate the material deformation caused by the press brake operation. For the rigidity evaluation, novel experimental test is designed and example test data is explained.

Analysis of Stiffening Dart Formation

A FE simulation model shown in Fig. 2a is built in Abaqus/Standard 2019 for simulating the press brake operation. The blank has a dimension of 120 mm × 40 mm and a rectangular hole generated for a post-forming measurement purpose. The tooling adopted for stiffening dart formation is exhibited in Fig. 2b with the die and dart insert variables noted in Fig. 2c and punch variables noted in Fig. 2d.

A 2 mm thick 340 high-strength low-alloy (HSLA) steel is used for the blank material in the study. All the tools are modeled as discrete rigid bodies. The blank is meshed with a combination of C3D8S linear brick elements with improved surface visualization function in the critical forming area, and C3D8R linear brick elements with reduced integration outside the critical forming area to accelerate the computation time while maintaining the overall simulation accuracy. Note that the element dimension in the critical forming area is 0.28 mm × 0.28 mm × 0.29 mm, resulting in seven brick elements through the blank thickness. The critical forming area is the area where bending and dart formation occur. For meshing the discrete rigid tools, the element sizes are controlled to be ranged from 0.25 mm × 0.25 mm to 1 mm × 1 mm in the regions interacting with the blank, while having larger element sizes in the regions not making any contacts with the blank. The interaction between the blank and the tools are characterized with the surface-to-surface contact modeling in Abaqus/Standard, and an assumed Coulomb friction coefficient of 0.15.

To validate the simulation accuracy by comparing it with the actual forming process, a 340 HSLA steel angle bracket with a stiffening dart is formed using TruBend 5320 press brake with the tooling configuration shown in Table 1. A punch

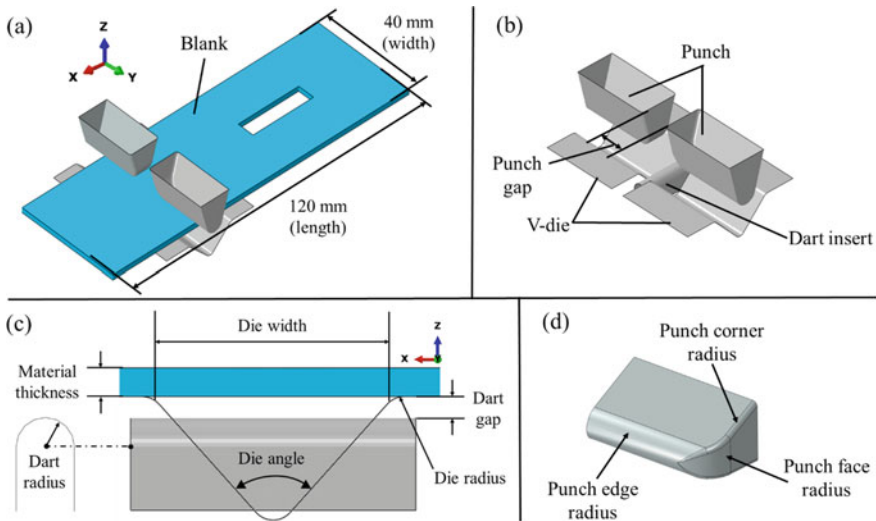


Fig. 2 a FE simulation setup of the press brake operation; b tooling for the stiffening dart formation; c die and dart insert variables; and d punch variables

Table 1 Tooling configuration adopted for comparing the simulated and actual formed darts

Die		Punch	
Die width	16 mm	Punch edge radius	3 mm
Die radius	1.6 mm	Punch face radius	6 mm
Die angle	84 deg	Punch corner radius	0.8 mm
Dart radius	2 mm	Punch gap	8 mm
Dart gap	1 mm		

displacement of 6.09 mm is applied to deform the blank. The corresponding Abaqus forming simulation is shown in Fig. 3.

The formed geometries of the actual and simulated 340 HSLA brackets after springback are compared by measuring the dart profiles on the inner surfaces of the brackets using Keyence VR-3200 system. Both horizontal and vertical profiles are measured and compared as shown in Fig. 4. A good profile agreement between the actual formed part (experiment) and simulated part (Abaqus) is observed with the maximum error measured being less than 0.2 mm from both horizontals and vertical profiles.

In addition to the dart profile, the final bend angle between the actual and simulated brackets was also compared by measuring the bend angle after springback on the outer surface of the brackets. The measurement results are shown in Fig. 5, and the

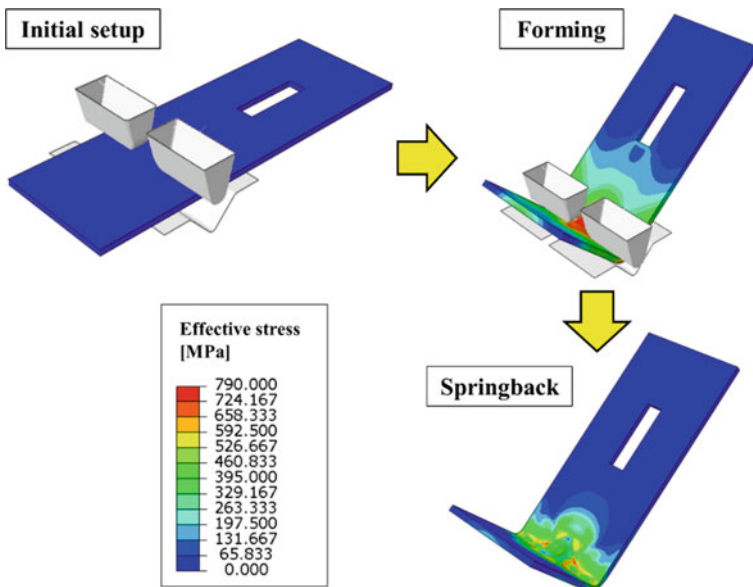


Fig. 3 Abaqus simulation of the press brake operation for manufacturing the angle bracket with the stiffening dart

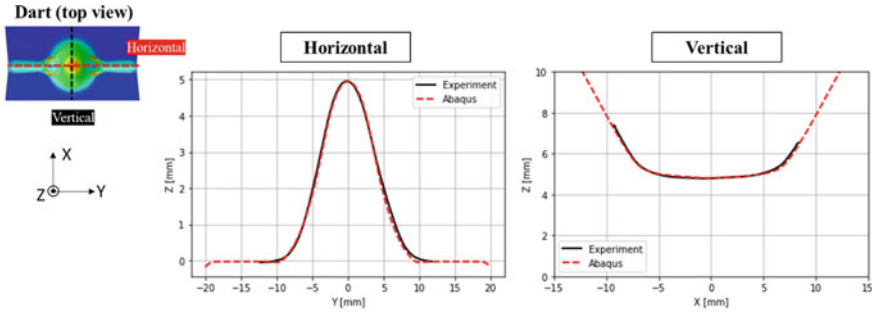


Fig. 4 Dart profile comparison between the actual formed bracket and simulated bracket

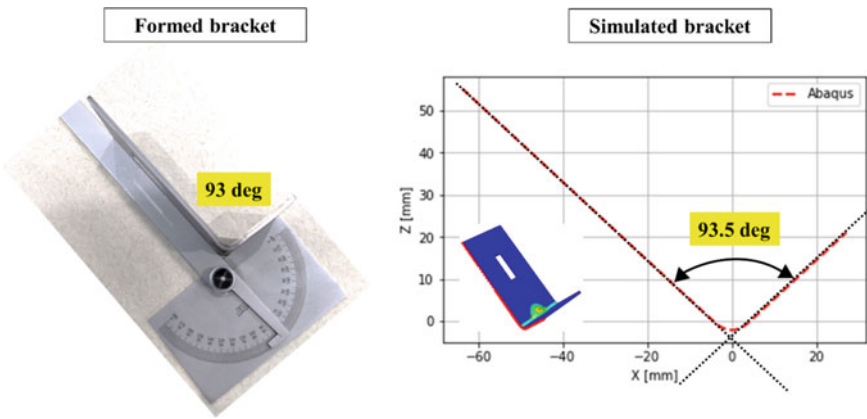


Fig. 5 Final bend angle comparison between the actual formed bracket and simulated bracket

angle difference between the actual and simulated brackets is 0.5 deg, implying a good match between the simulation and the actual forming process.

Now that the accuracy of the FE model has been validated, the FE model is used to investigate the dart formation mechanics of a 340 HSLA blank size of 80 mm × 40 mm × 2 mm where the dart is formed in the center of the blank during press brake bending. The same tooling configuration in Table 1 is used while a punch displacement of 6.41 mm is applied for the forming simulation. Once the forming simulation is completed, three axial strains (length, width, and thickness strains) values are investigated to study the deformation mechanics of stiffening dart formation. The contours of these three strain components are plotted in Fig. 6.

Based on the strain contours of Fig. 6, the following observations can be made:

- (1) Length strain (ϵ_{LL}): a clear concentration of high compression strains is detected on the inner surface of the dart, suggesting that the concurrent occurrence of wall bending and dart formation squeezed the materials in this area.

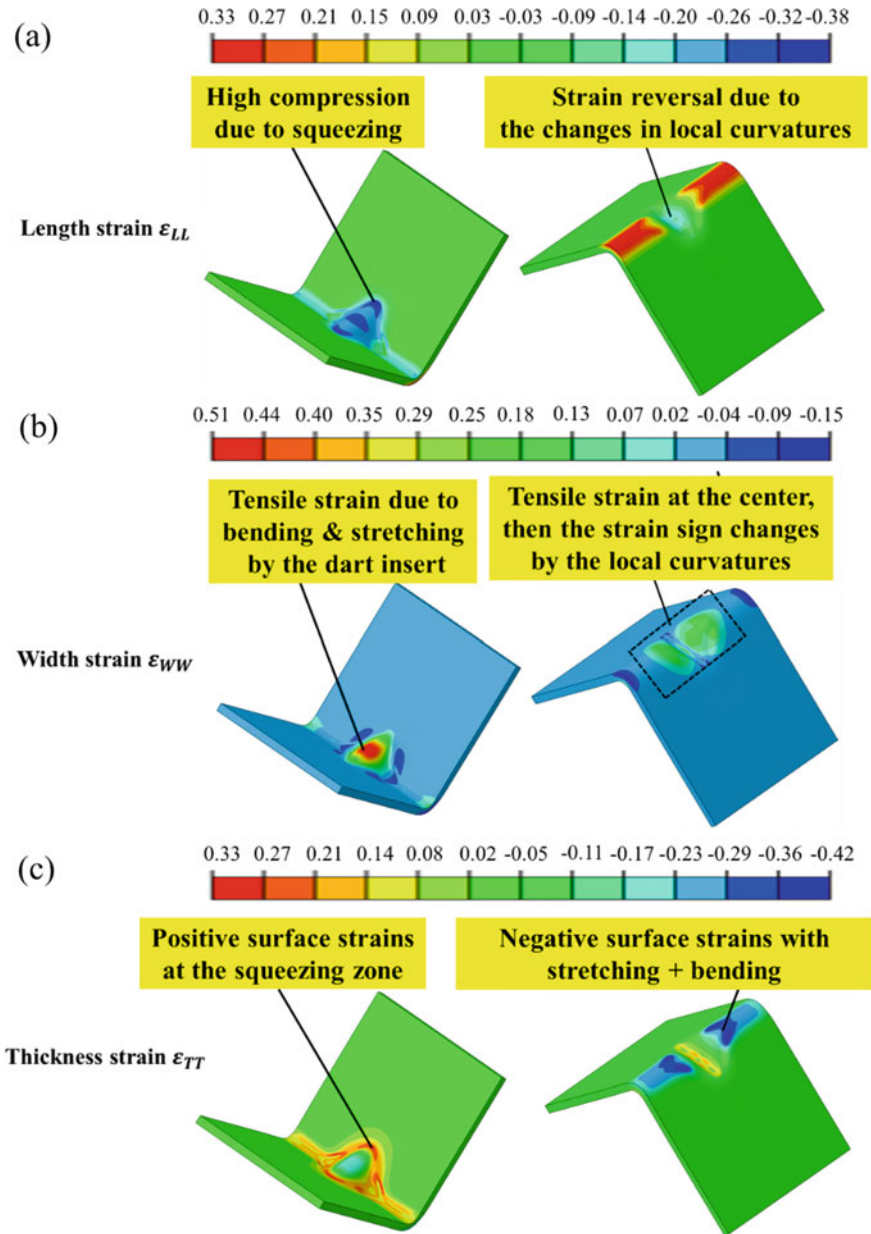


Fig. 6 Contours of three axial strain components: **a** length strain; **b** width strain; and **c** thickness strain

These squeezed areas are speculated as the main “docking station” between the dart and bracket walls, providing higher mechanical resistance to external loads for the bracket and causing less springback. For the bottom surface, a strain reversal at the dart center is detected. That is, large tensile strains at the bottom of the bending surface change to compression strains when coming into the center of the dart area. This strain reversal is caused by the reverse curvature change induced when the dart shape is formed as the blank is bent.

- (2) Width strain (ε_{WW}): the cylindrical surface of the dart insert tool caused bending-like deformations at the center of the dart, generating noticeable tensile strain developments at the dart center on the inner surface. In addition, more tensile strains are added to the dart because of the punches pushed down the material around the dart insert. The outer surface of the dart shows a mixed strain state of both tensile and compression. More specifically, the compression strains near the center of the dart are likely due to the bending-like deformation by the dart insert tool, but the tensile strains detected at the center are thought to be strongly affected by the material stretching by the punches.
- (3) Thickness strain (ε_{TT}): the contours of this strain component can be indirectly predicted from the other two axial strain components by the incompressibility of metallic materials (i.e., $\varepsilon_{LL} + \varepsilon_{WW} + \varepsilon_{TT} = 0$), acknowledging that the plastic portion of the strains is far more dominant than the elastic portion. Nevertheless, it can be still confirmed from Fig. 6c that positive thickness strains are developed where the other two normal strains are compression-dominant, while negative strains are induced in the areas where the other normal strain components are mostly in tensile states.

The above analysis shows us the manufacturability of stiffening dart is limited by the tensile strain on the back of the bended bracket caused by the punch and the tensile strain on the back of the dart caused by the reverse movement of the dart tool. The strain levels are affected by both the bending radius and height of the formed dart.

Rigidity Evaluation of Darded Brackets

FE simulation results presented in the previous section provides an explanation of the basic dart formation mechanics, but evaluating the rigidity improvements by adding stiffening darts needs a post-bending procedure where clampable flanges are formed at the two side walls of the bracket. The brackets can then be clamped for testing the rigidity using a generic material testing machine as shown in Fig. 7a. Figure 7b and c shows two proposed testing methods with the clampable bracket design—the flattening test for evaluating the bracket rigidity under a loading condition to open the bracket angle (Fig. 7b) and the folding test for evaluating the bracket rigidity under a loading condition to close the bracket angle (Fig. 7c).

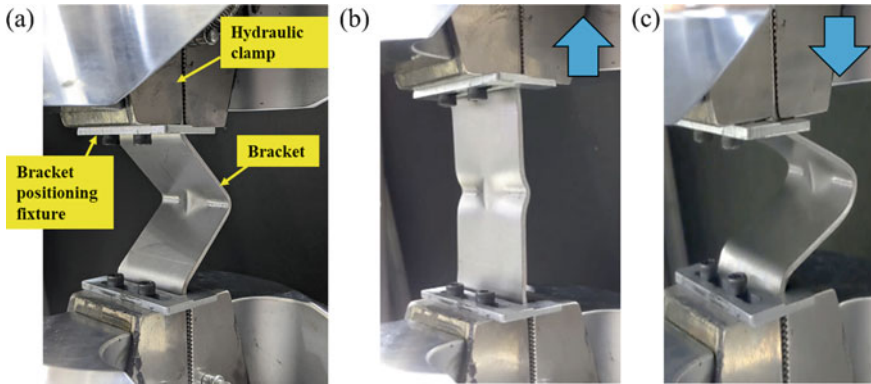


Fig. 7 a Darted bracket clamped for the rigidity test, b flattening test, and c folding test

For evaluating the changes in bracket rigidity with different stiffening dart geometries, a set of angle brackets are manufactured with a 2 mm thick 340LA steel sheet and initial blank size of 160 mm × 40 mm. Same tooling configurations as that of Table 1 are used for manufacturing the testing brackets, with variations in the dart gap and punch displacements to generate different formed dart heights in the brackets as shown in Table 2.

The brackets presented in Table 2 are tested using MTS Model E45 universal testing machine to evaluate their rigidities under the flattening and folding conditions shown in Fig. 7. The force–displacement curves obtained from each test are plotted in Fig. 8, and it is rather clear that the overall bracket rigidity is improved with a stiffening dart, and a higher rigidity is achieved with a deeper dart geometry.

While the curves shown in Fig. 8 provide experimental evidence of the rigidity improvements with the stiffening dart, the typical rigidity evaluation of auto body components is done within the small deformation region of the materials (usually within the elastic deformation region of the materials). For this reason, the representative value of each bracket’s rigidity is calculated by computing the slope of the initial region that resembles a linear line of each curve in Fig. 8, and the calculated representative values are shown in Fig. 9. The values shown in Fig. 9 prove that adding a stiffening dart can enhance the initial bracket rigidity as much as 44.9% under the flattening condition, and 35.1% under the folding condition. The proposed rigidity evaluation method enables quantification of dart design for different loading conditions, which can be used for designing optimal dart geometry for given bracket

Table 2 Three different testing brackets manufactured for the rigidity tests

Testing brackets	Bracket 1	Bracket 2	Bracket 3
Bracket type	Not darted	Darted	
Dart gap	N/A	3 mm	1 mm
Formed dart height	N/A	3.05 mm	5.1 mm

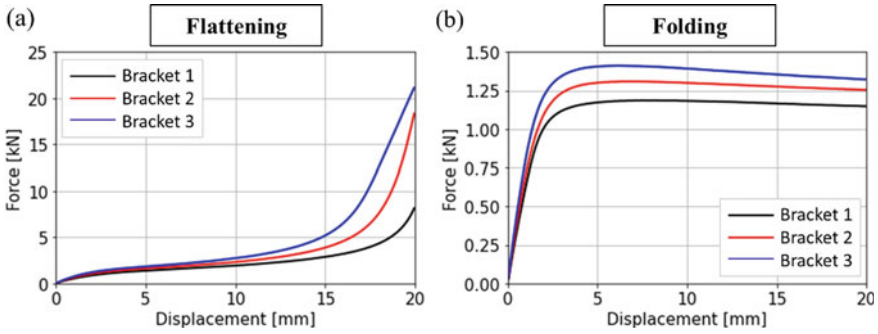


Fig. 8 Force–displacement curves from the rigidity tests: **a** flattening test and **b** folding test

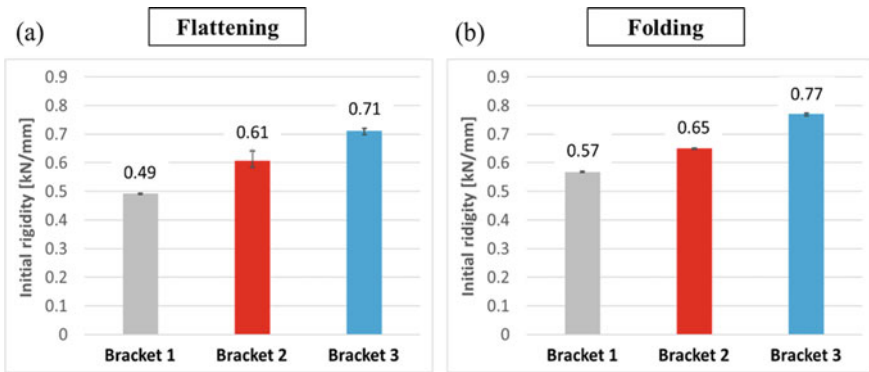


Fig. 9 Initial rigidities evaluated for the testing brackets from: **a** flattening test and **b** folding test

dimensions while considering the materials formability for the purpose of effectively maximizing the product rigidities.

Conclusion

The current study revealed the fundamental material deformation mechanics of darted bracket manufacturing based on a press brake operation, by using a combined simulation-experiment approach. A set of FE simulation results revealed how the stiffening dart can enhance the bracket rigidity while reducing the springback angle in the forming process. Moreover, a set of mechanical tests utilizing a bracket design with clampable flanges are proposed to systematically evaluate the rigidity improvements induced by the stiffening dart designs. The test results show that adding a stiffening dart can enhance the bracket rigidity as much as 44.9% under the flattening condition and 35.1% under the folding condition for the bracket design adopted in

this study. The proposed rigidity evaluation method enables designing optimal dart geometry for given bracket dimensions while considering the materials formability, helping to effectively maximize the product rigidities.

References

1. Pacheco BJ, Santos A (2013) A study on the Nose Radius influence in Press brake bending operations by finite element analysis. *Key Eng Mater* 554:1432–1442. <https://doi.org/10.4028/www.scientific.net/KEM.554-557.1432>
2. Wang J, Verma S, Alexander R, Gau JT (2008) Springback control of sheet metal air bending process. *J Manuf Process* 10(1):21–27. <https://doi.org/10.1016/j.manpro.2007.09.001>
3. Miranda SS, Barbosa MR, Santos AD, Pacheco JB, Amaral R (2018) Forming and springback prediction in press brake air bending combining finite element analysis and neural networks. *J Strain Anal Eng Des* 53(8):584–601. <https://doi.org/10.1177/0309324718798222>
4. Geometric Limited (2015) Sheet metal design guidelines. In: Form feature design guidelines issue IX. https://dfmpro.com/wp-content/uploads/2015/04/A-Definitive-Guide-to-DFM-success_Sheet-Metal_Form-Features-guidelines_Issue_IX_April2015.pdf Accessed 14 Dec 2021
5. NPD Solutions (2019) Design for manufacturability guidelines – sheetmetal. <https://www.npd-solutions.com/sheetmetal.html>. Accessed 14 Dec 2021

Modeling of the Anisotropic Evolution of Yield Surface Based on Non-associated Flow Rule



Namsu Park, Gihyun Bae, Jung Han Song, Jong Sup Lee,
Thomas B. Stoughton, and Jeong Whan Yoon

Abstract This work is concerned with a new approach for modeling of a yield function that is able to describe the anisotropic hardening considering general loading directions. A new model explicitly integrates eight flow stress curves including the strain hardening response under balanced-biaxial stress state into the yield criterion in a closed-form solution, which makes it possible to deal with the anisotropy-induced distortional yielding behavior as implied in experimental tests. The new approach accordingly induces relatively small systemic errors in stresses in different loading directions compared to conventional hardening models considering the low and high levels of plastic deformation, which will lead to a significant improvement in the accuracy of numerical analyses for sheet metal forming processes.

Keywords Anisotropic hardening · Yield surface evolution · Non-associated flow rule · Sheet metal forming

Introduction

Each material point in a product during forming processes experiences certain loading states in conjunction with the variation of loading directions, which is normally investigated by means of numerical analysis. Especially for the sheet metal forming, the

N. Park (✉) · G. Bae · J. H. Song · J. S. Lee
Metal Forming Technology R&D Group, Korea Institute of Industrial Technology, 156
Gaetbeol-ro, Yeonsu-gu, Incheon 21999, Republic of Korea
e-mail: nspark@kitech.re.kr

T. B. Stoughton
Manufacturing Systems Research Lab, General Motors R&D Center, Warren, MI, USA

T. B. Stoughton · J. W. Yoon
School of Engineering, Deakin University, Geelong Waurn Ponds, VIC 3220, Australia

J. W. Yoon
School of Mechanical, Aerospace and Systems Engineering, KAIST, 291 Daehak-ro, Yuseong-gu,
Daejeon 34141, Republic of Korea

material generally shows the anisotropic response on both hardening and deformation behaviors so that the changes in stress and strain states during the deformation should be well described based on the numerical formulation of anisotropic constitutive laws for the trustworthy evaluation of the deformed component via finite element simulation. At an early stage in the modeling of the anisotropic yielding behavior, a shape of the yield surface is fixed by initial yield stresses at certain loading directions, and thereafter the normalized shape of it is not allowed to vary with the plastic deformation. The adoption of the isotropic expansion of the yield surface in numerical analysis shows the suitable predictability for cases, especially when the evolution of anisotropic quantities is moderate: i.e., variations in normalized yield stress ratios and r -values during forming processes are small enough, which gives rise to a reasonable assumption of neglecting the influence of potential errors cumulated through the stress update process on the numerical accuracy taking into account the uncertainty of the mechanical properties [1]. This assumption, however, leads to the erroneous prediction of stress and strain states in the deformed component particularly when the material hardening and deformation behaviors evolve in a different manner with the respect to the loading direction as the plastic deformation goes on [2–5]. Besides, the numerical error propagation becomes more inevitable considering the intrinsic nature of mechanical properties that can be influenced by changes in the plastic strain rate and temperature which are normally subjected to during sheet metal forming processes [6–8]. It is, therefore, of great importance to accurately model the strain rate- and temperature-dependent anisotropic distortion of subsequent yield surface for the reliable prediction of the material behavior.

In this paper, a new model proposed by Park et al. [9] is reviewed in order for an accurate description of the yield surface evolution of metal sheets considering general stress states under proportional loading. The proposed approach allows to directly include directional flow stress curves obtained from the experiments into the yield formulation so that it provides unmatched flexibility in predicting the anisotropic evolution of yield surface in the framework of the non-associated flow plasticity. The model performance is verified from applications of the proposed approach to various metal sheets by representing the 3D yield surface evolution with the plastic deformation.

Modeling of a Directional Evolution of Yield Surface

The model proposed by Park et al. [9] is developed on the basis of the Stoughton and Yoon (2009) yield function [1], given in Eq. (1), which is able to describe the evolution of yield surface considering the directional hardening responses along the RD, DD, and TD including the non-directional hardening under equi-biaxial tension.

$$f = \left[\frac{\sigma_{11}(\sigma_{11} - \sigma_{22})}{\sigma_0^2(\bar{\epsilon}^p)} + \frac{\sigma_{22}(\sigma_{22} - \sigma_{11})}{\sigma_{90}^2(\bar{\epsilon}^p)} + \frac{4\sigma_{12}^2}{\sigma_{45}^2(\bar{\epsilon}^p)} + \frac{\sigma_{11}\sigma_{22} - \sigma_{12}^2}{\sigma_{EB}^2(\bar{\epsilon}^p)} \right]^{\frac{1}{2}} = 1 \quad (1)$$

In order to consider a non-quadratic curvature of the overall yield surface for description of the yielding behavior especially for metal sheets having a relatively flat yield locus near plane strain state, a shape-dependent term in the Park et al. [7] is employed in the model development:

$$f = \left[\frac{\sigma_{11}(\sigma_{11} - \sigma_{22})}{\sigma_0^2(\bar{\epsilon}^p)} + \frac{\sigma_{22}(\sigma_{22} - \sigma_{11})}{\sigma_{90}^2(\bar{\epsilon}^p)} + \frac{4\sigma_{12}^2}{\sigma_{45}^2(\bar{\epsilon}^p)} + \frac{\sigma_{11}\sigma_{22} - \sigma_{12}^2}{\sigma_{EB}^2(\bar{\epsilon}^p)} \right]^{\frac{1}{2}} \cdot [X]^k = 1 \quad (2)$$

where

$$X = (C_0 - 1)[D(\theta_L)]^4 - 2(C_0 - 1)[D(\theta_L)]^2 + C_0 \text{ with } D(\theta_L) = \frac{2}{\sqrt{3}}\sin\left(\theta_L + \frac{\pi}{3}\right) \quad (3)$$

Here, θ_L denotes the Lode angle parameter defined as $\theta_L = \frac{1}{3}\cos^{-1}\left(\frac{3\sqrt{3}J_3}{2J_2^{3/2}}\right)$ where J_2 and J_3 are the second and third invariants of the stress deviator, respectively. $\sigma_0(\bar{\epsilon}^p)$, $\sigma_{45}(\bar{\epsilon}^p)$, $\sigma_{90}(\bar{\epsilon}^p)$, and $\sigma_{EB}(\bar{\epsilon}^p)$ denote the flow stress curves at three different loading directions and the one under equi-biaxial tension. It is worthwhile to note that the evolution of yield surface can be successfully modeled by Eq. (2) in the case that the mathematical form of yield function that employs the flow stress curves for the RD, DD, and TD produces an acceptable degree of accuracy in describing the anisotropic hardening responses at angles other than 0° , 45° , and 90° to the RD. However, the arising concern here is that the previous anisotropic modeling of the yield surface evolution may not provide a suitable model performance in the directional hardening response of the metal sheets that shows the complicated anisotropic behavior over the variation in loading directions. In an effort not only to improve the model performance but also to enhance the model flexibility, Park et al. [9] came up with a new approach to scaling the shear component of the previous model as below:

$$f = \left[\frac{\sigma_{11}(\sigma_{11} - \sigma_{22})}{\sigma_0^2(\bar{\epsilon}^p)} + \frac{\sigma_{22}(\sigma_{22} - \sigma_{11})}{\sigma_{90}^2(\bar{\epsilon}^p)} + \frac{4\alpha\sigma_{12}^2}{\sigma_{45}^2(\bar{\epsilon}^p)} + \frac{\sigma_{11}\sigma_{22} - \alpha\sigma_{12}^2}{\sigma_{EB}^2(\bar{\epsilon}^p)} \right]^{\frac{1}{2}} \cdot [X]^k = 1 \quad (4)$$

where

$$\alpha = \frac{\left[\frac{\cos^2\theta_P(\cos^2\theta_P - \sin^2\theta_P)}{\sigma_0^2(\bar{\epsilon}^p)} + \frac{\sin^2\theta_P(\sin^2\theta_P - \cos^2\theta_P)}{\sigma_{90}^2(\bar{\epsilon}^p)} + \frac{\cos^2\theta_P\sin^2\theta_P}{\sigma_{EB}^2(\bar{\epsilon}^p)} \right] - \left[\frac{1}{g(\theta_P, \bar{\epsilon}^p)} \right]^2}{\frac{\cos^2\theta_P\sin^2\theta_P}{\sigma_{EB}^2(\bar{\epsilon}^p)} - \frac{4\cos^2\theta_P\sin^2\theta_P}{\sigma_{45}^2(\bar{\epsilon}^p)}} \in \left(0, \frac{\pi}{2}\right)$$

with $\alpha\left(0, \bar{\epsilon}^p\right) = \alpha\left(\frac{\pi}{2}, \bar{\epsilon}^p\right) = 1$

(5)

$$g(\theta_P, \bar{\varepsilon}^P) = \sum_i N_i(\theta_P) \sigma_i(\bar{\varepsilon}^P) \text{ with } N_i(\theta) = \prod_{j=1(j \neq i)}^m \frac{\theta - \theta_j}{\theta_i - \theta_j} \quad (6)$$

The sub-function g is devised with the use of the Lagrangian interpolation function N_i defined in the domain of $\theta_P \in [0, \frac{\pi}{2}]$ where θ_P is a direction of the maximum principal stress. Here, $\sigma_i(\bar{\varepsilon}^P)$ represents the flow stress curve for a certain loading direction, e.g., $i = 1, 2, 3$ for the RD, DD, and TD, and any set of $\sigma_i(\bar{\varepsilon}^P)$ can be simply considered in modeling the sub-function g . The main characteristic of the proposed approach is that the scaling term α does not affect the yielding behavior at the stress states where there is no shear stress under the plane stress condition, yet produces additional flexibility in controlling the level of shear stress related to the directional yielding at loading angles other than the RD and TD. The basic characteristic of the anisotropic yield function given in Eq. (2) can be maintained by forcing the sub-function g to include the flow stress curves at the loading directions of the RD, DD, and TD in modeling the scaling term α , which consequently leads to the scaling value of unity at the reference loading directions of the RD, DD, and TD with employment of the Lagrangian formulation N_i that satisfies the delta function property: i.e.,

$$N_i(\theta_P^j) = \delta_{ij} = \begin{cases} 1 & \text{for } i = j \\ 0 & \text{for } i \neq j \end{cases} \quad (7)$$

The unmatched flexibility in predicting the directional hardening behavior can be simply guaranteed by including additional flow stress curves at loading directions other than the reference ones in the modeling of the sub-function g .

Verification of the Model Performance

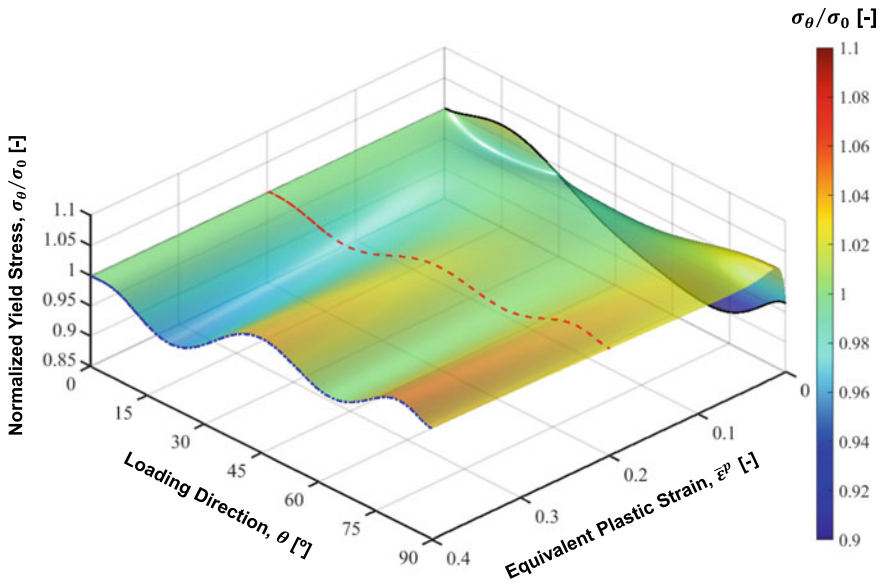
For verification of the model performance in predicting the directional yielding and hardening behaviors, the experimental data reported by Stoughton and Yoon [1] were revisited in this study. The flow stress curves in 15° increments to the rolling direction of the steel sheet were considered especially for two different types of metal sheets of MP980 and AA5182-O. The material constants of the modified Hockett–Sherby strain hardening model, defined as $\bar{\sigma} = A - B \exp[-C(\bar{\varepsilon}^P)^n] + D\bar{\varepsilon}^P$, for both materials are listed in Table 1. Each material shows noticeable changes in the dynamic hardening behavior as the plastic deformation goes on, which evidently reveals the need of a way for accurate description of not only the initial yielding but also the consecutive variation in the strain hardening rate with respect to the loading direction. Figure 1 represents the evolution of normalized flow stress according to the loading direction with the plastic deformation.

Table 1 Materials constants of the modified Hockett–Sherby strain hardening model for MP980 and AA5182-O

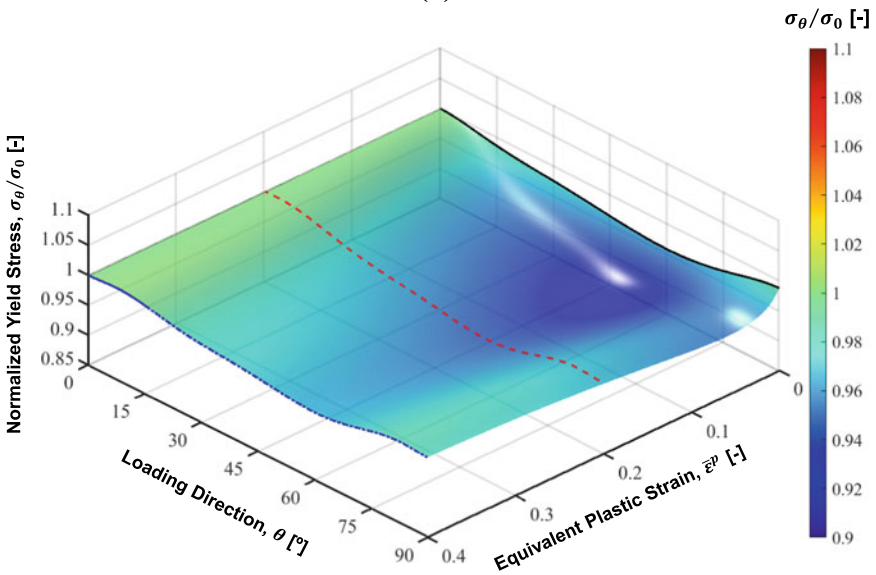
Material	Loading direction [°]	Material constants				
		A [MPa]	B [MPa]	C [-]	n [-]	D [MPa]
MP980	0	1011.98	371.15	52.99	0.79	1114.29
	15	1013.52	359.96	39.06	0.75	985.80
	30	1014.61	383.36	43.39	0.76	1040.53
	45	999.57	400.75	61.88	0.81	1290.46
	60	1015.62	435.71	55.28	0.79	1118.85
	75	1026.57	448.85	62.96	0.80	1211.60
	90	1028.35	411.03	77.22	0.84	1197.45
	Equi-Biaxial	1090.72	507.75	18.77	0.64	435.47
AA5180-O	0	366.75	250.97	11.18	1.00	0.23
	15	366.87	252.76	10.46	1.00	0.00
	30	361.10	248.21	10.08	1.00	0.43
	45	358.44	246.79	9.74	1.00	0.67
	60	355.56	244.73	9.64	1.00	0.00
	75	360.75	248.59	9.99	1.00	0.35
	90	362.39	248.11	9.98	1.00	0.00
	Equi-Biaxial	432.33	307.11	6.32	1.00	8.36

At an early stage of the material yielding, both materials exhibit the rapid changes in directional strain hardening behaviors due to their strong anisotropic characteristics: however, it gradually stabilizes to certain levels of anisotropy after the re-orientation of microstructures towards the loading direction. The new approach is able to accurately describe the aforementioned complicated anisotropic yielding behavior, which is not able to be successfully modeled by the previous approach as represented in Figs. 2 and 3. The noticeable superiority of the new approach is that it has no additional optimization procedure not only for the calibration of the yield surface but also for description of the yield surface evolution with the plastic deformation since the model directly employs the directional flow stress curves required for the reliable prediction of material yielding behavior. Figures 2b and 3b show the initial yield loci with an interval of 10% level of the maximum shear stress. It is worthwhile to note that both previous and new approaches have the same value of maximum shear stress as they are developed based on the Stoughton and Yoon (2009) yield function [1] with a special feature of the new model that the scale factor α becomes unity at the shear stress state of $\sigma = (\sigma_{xx}, \sigma_{yy}, \sigma_{xy}) = (0, 0, \sigma_{xy})$ which mathematically yields the maximum principal stress direction of $\frac{\pi}{4}$ to the rolling direction: i.e., $\alpha(\frac{\pi}{4}, \bar{\epsilon}^P) = 1$ for any given level of the equivalent plastic strain.

In addition to the accurate description of the initial anisotropic yield surface, the new approach is able to further provide the sufficient accuracy in predicting the distortional evolution of yield surface in such a way that the yield surface envelope



(a)



(b)

Fig. 1 Normalized yield stress envelope according to the plastic deformation: **a** MP980; **b** AA5182-O

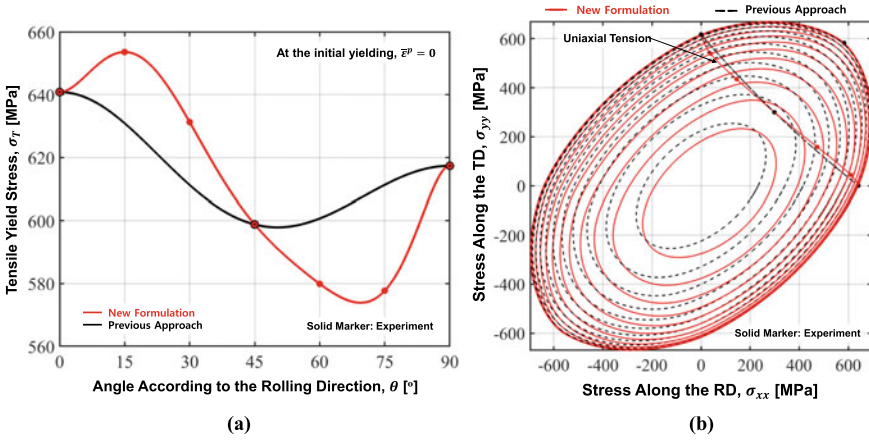


Fig. 2 Prediction of the material yielding behavior for MP980: **a** Directional yield stress; **b** Initial yield surface on the normal plane with an interval of 10% level to the maximum shear stress (after Park et al. [9])

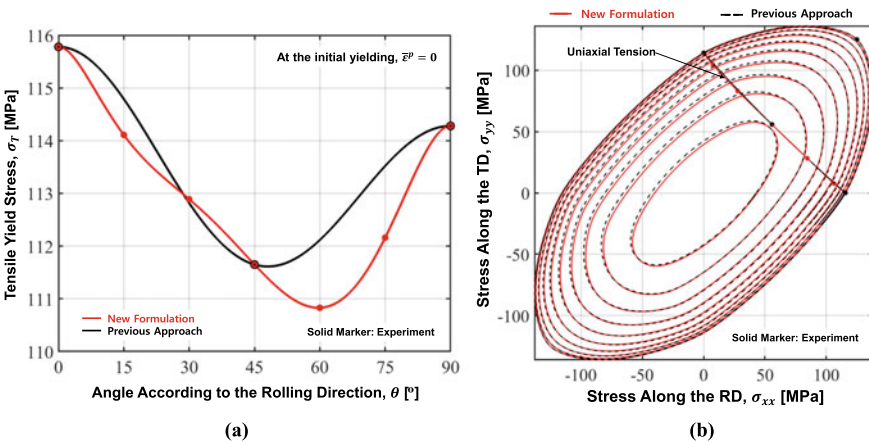


Fig. 3 Prediction of the material yielding behavior for AA5182-O: **a** Directional yield stress; **b** Initial yield surface on the normal plane with an interval of 10% level to the maximum shear stress (after Park et al. [9])

is continuously updated by the flow stresses determined from each directional hardening curve employed in the model so that the yield surface exactly passes through the experimental data of tensile stress evaluated at each loading direction in 15° increments to the RD including equi-biaxial tensile stress as shown in Figs. 4 and 5. In this study, the exponent value k of the model is set to 0.01 and 0.02 for MP980 and AA5182-O, respectively, as suggested by Park et al. [7]. Note that the loading direction θ_p corresponding to the certain stress state is calculated by using the components of the Cauchy stress tensor under the plane stress condition as follows:

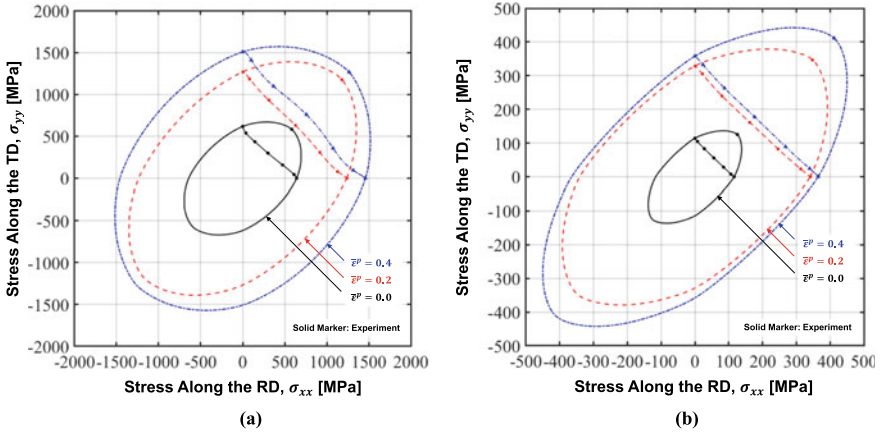


Fig. 4 Evolution of the yield locus with respect to the plastic deformation: **a** MP980; **b** AA5182-O (after Park et al. [9])

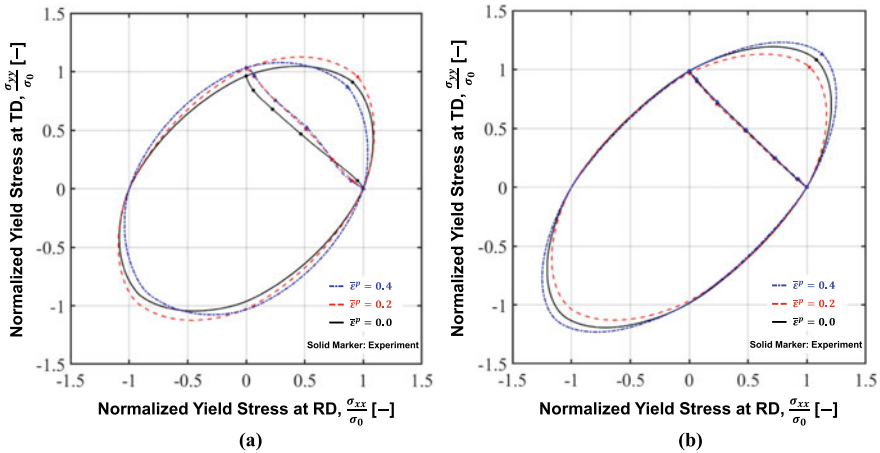


Fig. 5 Distortion of the normalized yield locus with respect to the plastic deformation: **a** MP980; **b** AA5182-O (after Park et al. [9])

$$\theta_P = \frac{1}{2} \cos^{-1} \left(\frac{\sigma_{xx} - \sigma_{yy}}{\sigma_1 - \sigma_2} \right) = \frac{1}{2} \cos^{-1} \left(\frac{\sigma_{xx} - \sigma_{yy}}{2 \sqrt{\left(\frac{\sigma_{xx} - \sigma_{yy}}{2} \right)^2 + \sigma_{xy}^2}} \right) \quad (8)$$

For the comprehensive understanding of the model performance in describing the anisotropic evolution of the yield surface, the yield surface envelope is represented in the space of $(\sigma_{xx}, \sigma_{yy}, \sigma_{xy})$ with discrete level of the equivalent plastic strain as shown in Fig. 6. From the graphical representation of the 3D yield surface, the

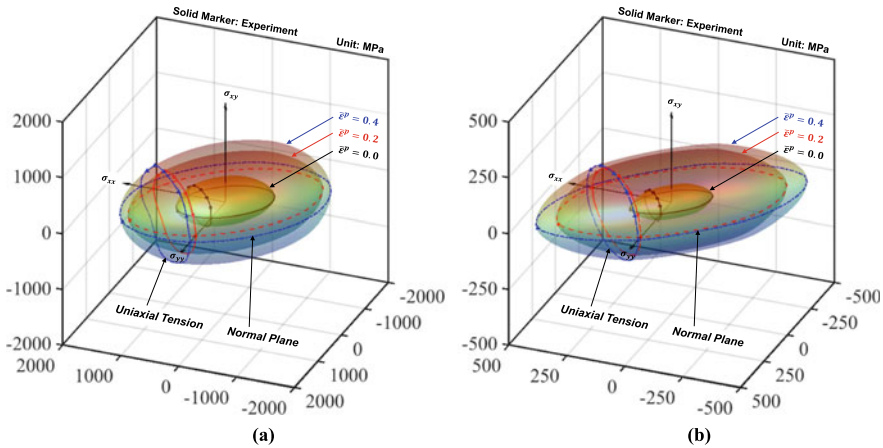


Fig. 6 Evolution of the anisotropic yield surface with respect to the plastic deformation: **a** MP980; **b** AA5182-O (after Park et al. [9])

convexity of the yield surface is simply confirmed over the general stress state under the plane stress condition. It should be noted that the plastic potential is necessary in order to determine the increments of plastic strains as the new approach features non-associated flow plasticity.

Comparison of the experimental results with predictions from the new approach effectively reveals that the new approach has not only a strong potential to deal with anisotropic yielding behaviors of various metallic materials but also the noticeable flexibility in describing the consecutive evolution of distortional yield surface using neither any interpolation nor optimization processes for the calibration of yield surface according to the level of plastic deformation.

Conclusion

A novel way of accurately modeling the anisotropic evolution of yield surface has been discussed. The new model has a special mathematical characteristic of producing the unmatched flexibility for description of directional hardening behaviors of various metallic materials by scaling the level of shear stress in the model according to the loading direction with the use of directional flow stress curves. Applications of the proposed approach to various metallic materials lead to the conclusion that the proposed way of advanced modeling can potentially produce remarkable accuracy of numerical solutions for sheet metal forming processes with the material having strong anisotropy in their yielding and deformation behaviors.

References

1. Stoughton TB, Yoon JW (2009) Anisotropic hardening and non-associated flow in proportional loading of sheet metals. *Int J Plast* 25:1777–1817
2. Khan AS, Yu S (2012) Deformation induced anisotropic responses of Ti–6Al–4V alloy. Part I: Exp *Int J Plast* 38:1–13
3. Park N, Huh H, Lim SJ, Lou Y, Kang YS, Seo MH (2017) Fracture-based forming limit criteria for anisotropic materials in sheet metal forming. *Int J Plast* 96:1–35
4. Park N, Huh H, Yoon JW (2018) Anisotropic fracture forming limit diagram considering non-directionality of the equi-biaxial fracture strain. *Int J Solids Struct* 151:181–194
5. Park N, Park M, Kwon J, Huh H (2018) Material properties of the nugget zone in resistance spot-welded DP980 steel joint at various strain rates. *Sci Technol Weld Join* 23(1):7–12
6. Huh J, Huh H, Lee CS (2013) Effect of strain rate on plastic anisotropy of advanced high strength steel sheets. *Int J Plast* 44:23–46
7. Park N, Stoughton TB, Yoon JW (2019) A criterion for general description of anisotropic hardening considering strength differential effect with non-associated flow rule. *Int J Plast* 121:76–100
8. Park N, Stoughton TB, Yoon JW (2019) A new approach for fracture prediction considering general anisotropy of metal sheets. *Int J Plast* 124:199–225
9. Park N, Stoughton TB, Yoon JW (2020) A novel approach for modeling the anisotropic evolution of yield surface considering the general stress state in arbitrary loading directions. *Int J Plast* (Submitted)

On Strain Hardening Modeling in Associated and Non-Associated Orthotropic Plasticity



Jie Sheng, Mohammed Alharbi, Seung-Yong Yang, and Wei Tong

Abstract In rate-independent associated plasticity, the flow surface in stress space is identical to the yield surface given by a yield stress function. Two distinct stress functions are however needed in non-associated plasticity to specify the yield surface and the flow surface separately. In this study, we explore the possibility of modeling strain hardening in metal plasticity by a new equivalent stress function that may be different from both yield and flow stress functions. As an initial effort, we consider all stress functions to be quadratic and orthotropic to describe either isotropic or differential strain hardening behaviors of rolled sheet metals under plane stress. The advantages and limitations of using an independent equivalent stress function for strain hardening modeling in sheet metal plasticity are discussed.

Introduction

A mathematical theory of rate-independent plasticity consists typically of a yield condition, a flow rule, and the material flow strength σ_f with strain hardening in terms of an equivalent plastic strain $\bar{\epsilon}^p$ [1–3], namely

J. Sheng · W. Tong (✉)
Southern Methodist University, Dallas, TX 75275, USA
e-mail: wtong@smu.edu

J. Sheng
e-mail: sheng@mail.smu.edu

M. Alharbi
Unizah, Qassim University, Unizah, Qassim, Saudi Arabia
e-mail: maalharbi@mail.smu.edu

S.-Y. Yang
Korea University of Technology and Education, Chungnam 31253, Korea
e-mail: ysy@koreatech.ac.kr

$$\text{yield condition : } f(\boldsymbol{\sigma}) - \sigma_f(\bar{\boldsymbol{\varepsilon}}^p) = 0, \quad (1)$$

$$\text{flow rule : } \dot{\boldsymbol{\varepsilon}}^p = \dot{\lambda} \frac{\partial g(\boldsymbol{\sigma})}{\partial \boldsymbol{\sigma}}, \quad (2)$$

$$\text{plastic work rate equivalency : } \bar{\sigma}(\boldsymbol{\sigma}) \dot{\bar{\boldsymbol{\varepsilon}}}^p = \boldsymbol{\sigma} : \dot{\boldsymbol{\varepsilon}}^p, \quad (3)$$

where $f(\boldsymbol{\sigma})$, $g(\boldsymbol{\sigma})$, and $\bar{\sigma}(\boldsymbol{\sigma})$ are scalar-valued functions of the Cauchy stress $\boldsymbol{\sigma}$ with a number of material parameters, and $\dot{\lambda} > 0$ is the proportionality parameter in the flow rule for computing the plastic strain increments $\dot{\boldsymbol{\varepsilon}}^p$ when the yield condition holds. The proportionality parameter of incremental plastic flow (also being called plastic multiplier, consistency parameter, compliance factor, etc.) is related to the equivalent plastic strain increment as

$$\dot{\lambda} = \frac{\bar{\sigma}(\boldsymbol{\sigma})}{g(\boldsymbol{\sigma})} \dot{\bar{\boldsymbol{\varepsilon}}}^p. \quad (4)$$

The classical Hill's 1948 quadratic anisotropic plasticity theory [4, 5] assumes the associated flow rule $g(\boldsymbol{\sigma}) = f(\boldsymbol{\sigma})$ and the plastic work equivalent stress as the same as the equivalent yield stress $\bar{\sigma}(\boldsymbol{\sigma}) = f(\boldsymbol{\sigma})$, namely

$$\Phi_h(\sigma_x, \sigma_y, \tau_{xy}) = f^2(\boldsymbol{\sigma}) = F\sigma_y^2 + G\sigma_x^2 + H(\sigma_x - \sigma_y)^2 + 3N\tau_{xy}^2, \quad (5)$$

where $\boldsymbol{\sigma} = (\sigma_x, \sigma_y, \tau_{xy})$ are three plane stress components and F , G , H , and N are four material parameters to be determined from mechanical test data for a given orthotropic sheet. This greatly simplifies the theory but limits somewhat its capability of modeling plastic anisotropy of a sheet metal in plane stress with only four polynomial coefficients in the single quadratic yield stress function.

A *non-quadratic* yield function such as Gotoh's 1977 quartic yield function with nine polynomial coefficients [6] or YLD2000-2D with eight material parameters [7] in associated plasticity can be used to overcome such a limitation of Hill's 1948 anisotropic plasticity. Alternatively, *non-associated* quadratic plasticity may also be used for better modeling sheet metals using two separate quadratic stress functions [8], namely, a yield stress function Φ_{2y} and a stress-based flow potential Φ_{2p} in a compact polynomial form as [9]

$$\begin{aligned} \Phi_{2y} = f^2(\boldsymbol{\sigma}) &= Y_1\sigma_x^2 + Y_2\sigma_x\sigma_y + Y_3\sigma_y^2 + Y_4\tau_{xy}^2, \\ \Phi_{2p} = g^2(\boldsymbol{\sigma}) &= P_1\sigma_x^2 + P_2\sigma_x\sigma_y + P_3\sigma_y^2 + P_4\tau_{xy}^2, \end{aligned} \quad (6)$$

where Y_1 , Y_2 , Y_3 , and Y_4 are the four materials parameters in the yield function and P_1 , P_2 , P_3 , and P_4 are the four material parameters in the flow potential (only three of them are independent). The plastic work equivalent stress has been defined as either $\bar{\sigma}(\boldsymbol{\sigma}) = f(\boldsymbol{\sigma})$ or $\bar{\sigma}(\boldsymbol{\sigma}) = g(\boldsymbol{\sigma})$ in the applications of non-associated anisotropic plasticity [10–12].

We point out here that in general one can define a third independent stress function as the plastic work equivalent stress $\bar{\sigma}(\boldsymbol{\sigma})$ [13, 14] and for the case of a quadratic function as

$$\Phi_{2q} = \bar{\sigma}^2(\boldsymbol{\sigma}) = Q_1\sigma_x^2 + Q_2\sigma_x\sigma_y + Q_3\sigma_y^2 + Q_4\tau_{xy}^2, \tag{7}$$

where $Q_1, Q_2, Q_3,$ and Q_4 are the four additional material parameters.

In the following, the identification of material parameters of these three stress functions are first given. The new anisotropic plasticity modeling approach is then applied to two rolled sheet metals that have been modeled previously by non-associated quadratic anisotropic plasticity in the literature [11]. The difference and connection among the yield, flow and equivalent strength surfaces are pointed out for those sheet metals. The similarities and differences between the new and previous strain hardening modeling approaches are compared. The advantages and limitations of using an independent equivalent stress function for strain hardening modeling in sheet metal plasticity are summarized in the end.

Calibration of Three Quadratic Polynomials of Stresses

Before the quadratic anisotropic plasticity theory with the new strain hardening modeling approach can be used in a sheet metal forming analysis, its material parameters in three quadratic polynomials have to be identified using experimental measurements. Seven inputs from three uniaxial tension and one equal biaxial tension tests are often used to calibrate these material parameters [9–12]. They are four yield/flow stresses ($\sigma_0, \sigma_{45}, \sigma_{90}, \sigma_b$) and three plastic strain ratios (r_0, r_{45}, r_{90}).

Parameter Identification for Yield Stress and Flow Functions

A total of seven material parameters in Hill’s quadratic yield stress function Φ_{2y} and flow potential Φ_{2p} are readily obtained as [8, 10, 11]

$$Y_1 = \left(\frac{\sigma_f}{\sigma_0}\right)^2, \quad Y_2 = -\left(\frac{\sigma_f}{\sigma_0}\right)^2 - \left(\frac{\sigma_f}{\sigma_{90}}\right)^2 + \left(\frac{\sigma_f}{\sigma_b}\right)^2, \tag{8}$$

$$Y_3 = \left(\frac{\sigma_f}{\sigma_{90}}\right)^2, \quad Y_4 = 4\left(\frac{\sigma_f}{\sigma_{45}}\right)^2 - \left(\frac{\sigma_f}{\sigma_b}\right)^2,$$

$$\frac{P_2}{P_1} = -\frac{2R_0}{R_0 + 1}, \quad \frac{P_3}{P_1} = \frac{R_0R_{90} + R_0}{R_0R_{90} + R_{90}}, \tag{9}$$

$$\frac{P_4}{P_1} = \frac{(2R_{45} + 1)(R_0 + R_{90})}{(R_0 + 1)R_{90}}, \quad P_1 = \left(\frac{\sigma_f}{\sigma_0}\right)^2.$$

where the yield and flow surfaces are defined as $f(\boldsymbol{\sigma}) = \sigma_f(\bar{\epsilon}^p)$ and $g(\boldsymbol{\sigma}^*) = \sigma_f(\bar{\epsilon}^p)$, respectively (where $\boldsymbol{\sigma}^* \neq \boldsymbol{\sigma}$ in general except at uniaxial tension in RD). By common

practice, one often sets $\bar{\varepsilon}^p = \varepsilon_0^p$ and $\sigma_f(\bar{\varepsilon}^p) = \sigma_0(\varepsilon_0^p)$, so $Y_1 = P_1 = 1$ and P_2 to P_4 depend only on three plastic strain ratios (which themselves are constants to first approximation for most sheet metals). On the other hand, Y_2 to Y_4 are in general not completely determined yet without specifying $\varepsilon_{45}^p(\bar{\varepsilon}^p)$, $\varepsilon_{90}^p(\bar{\varepsilon}^p)$, and $\varepsilon_b^p(\bar{\varepsilon}^p)$.

Parameter Identification for the Equivalent Stress Function

Instead of assuming either $\bar{\sigma}(\boldsymbol{\sigma}) = f(\boldsymbol{\sigma})$ or $\bar{\sigma}(\boldsymbol{\sigma}) = g(\boldsymbol{\sigma})$ as in [8, 10–12], the four material parameters Q_1 to Q_4 in the quadratic stress function Φ_{2q} may be prescribed separately. Considering the plastic work rate equivalency of Eq. (3) for three uniaxial tension tests and one equal biaxial tension test, one has (Q_1 to Q_4 are not constant in general and $\bar{\varepsilon}_i^p$ is the initial value of $\bar{\varepsilon}^p$ of the sheet metal)

$$\begin{aligned} \sqrt{Q_1} \dot{\bar{\varepsilon}}^p &= \dot{\varepsilon}_0^p, \quad \varepsilon_0^p(\bar{\varepsilon}^p) = e_0 + \int_{\bar{\varepsilon}_i^p}^{\bar{\varepsilon}^p} \sqrt{Q_1} \, d\bar{\varepsilon}^p, \\ \sqrt{Q_1 + Q_2 + Q_3 + Q_4} \dot{\bar{\varepsilon}}^p &= 2\dot{\varepsilon}_{45}^p, \quad \varepsilon_{45}^p(\bar{\varepsilon}^p) = e_{45} + \int_{\bar{\varepsilon}_i^p}^{\bar{\varepsilon}^p} \frac{\sqrt{Q_1 + Q_2 + Q_3 + Q_4}}{2} \, d\bar{\varepsilon}^p, \\ \sqrt{Q_3} \dot{\bar{\varepsilon}}^p &= \dot{\varepsilon}_{90}^p, \quad \varepsilon_{90}^p(\bar{\varepsilon}^p) = e_{90} + \int_{\bar{\varepsilon}_i^p}^{\bar{\varepsilon}^p} \sqrt{Q_3} \, d\bar{\varepsilon}^p, \\ \sqrt{Q_1 + Q_2 + Q_3} \dot{\bar{\varepsilon}}^p &= \dot{\varepsilon}_b^p, \quad \varepsilon_b^p(\bar{\varepsilon}^p) = e_b + \int_{\bar{\varepsilon}_i^p}^{\bar{\varepsilon}^p} \sqrt{Q_1 + Q_2 + Q_3} \, d\bar{\varepsilon}^p, \end{aligned} \tag{10}$$

where (e_0, e_{45}, e_{90}, e_b) are initial strain offset values.

On the other hand, if the four plastic strain functions $\varepsilon_0^p(\bar{\varepsilon}^p)$, $\varepsilon_{45}^p(\bar{\varepsilon}^p)$, $\varepsilon_{90}^p(\bar{\varepsilon}^p)$, $\varepsilon_b^p(\bar{\varepsilon}^p)$ are known, the four material parameters Q_1 to Q_4 are simply related to the first derivatives of these four plastic strains

$$\begin{aligned} Q_1(\bar{\varepsilon}^p) &= (\varepsilon_0'(\bar{\varepsilon}^p))^2, \quad Q_2(\bar{\varepsilon}^p) = -(\varepsilon_0'(\bar{\varepsilon}^p))^2 - (\varepsilon_{90}'(\bar{\varepsilon}^p))^2 + (\varepsilon_b'(\bar{\varepsilon}^p))^2, \\ Q_3(\bar{\varepsilon}^p) &= (\varepsilon_{90}'(\bar{\varepsilon}^p))^2, \quad Q_4(\bar{\varepsilon}^p) = 4(\varepsilon_{45}'(\bar{\varepsilon}^p))^2 - (\varepsilon_b'(\bar{\varepsilon}^p))^2. \end{aligned} \tag{11}$$

One way to obtain those plastic strain functions is from four experimentally measured stress–strain relationships $\sigma_0^{exp}(\varepsilon_0^p)$, $\sigma_{45}^{exp}(\varepsilon_{45}^p)$, $\sigma_{90}^{exp}(\varepsilon_{90}^p)$, and $\sigma_b^{exp}(\varepsilon_b^p)$ per three uniaxial and one equal biaxial tension tests if material parameters Y_1 to Y_4 of the yield stress function Φ_{2y} are known. In fact, their inverted form as plastic strain–stress relations, $\varepsilon_0^{exp}(\sigma_0)$, $\varepsilon_{45}^{exp}(\sigma_{45})$, $\varepsilon_{90}^{exp}(\sigma_{90})$, and $\varepsilon_b^{exp}(\sigma_b)$, are what needed (the superscript p of strains is omitted for simplicity). According to the yield condi-

tion of Eq. (1) under three uniaxial tension and one equal biaxial tension tests, one can obtain the analytical expressions for these four plastic strains in terms of the equivalent plastic strain as

$$\begin{aligned}
 \sigma_0(\varepsilon_0^p) &= \frac{\sigma_f(\bar{\varepsilon}^p)}{\sqrt{Y_1}}, \quad \varepsilon_0(\bar{\varepsilon}^p) = \varepsilon_0^{exp}(\sigma_0(\bar{\varepsilon}^p)) = \varepsilon_0^{exp}\left(\frac{\sigma_f(\bar{\varepsilon}^p)}{\sqrt{Y_1}}\right), \\
 \sigma_{45}(\varepsilon_{45}^p) &= \frac{2\sigma_f(\bar{\varepsilon}^p)}{\sqrt{Y_1 + Y_2 + Y_3 + Y_4}}, \quad \varepsilon_{45}(\bar{\varepsilon}^p) = \varepsilon_{45}^{exp}\left(\frac{2\sigma_f(\bar{\varepsilon}^p)}{\sqrt{Y_1 + Y_2 + Y_3 + Y_4}}\right), \\
 \sigma_{90}(\varepsilon_{90}^p) &= \frac{\sigma_f(\bar{\varepsilon}^p)}{\sqrt{Y_3}}, \quad \varepsilon_{90}(\bar{\varepsilon}^p) = \varepsilon_{90}^{exp}(\sigma_{90}(\bar{\varepsilon}^p)) = \varepsilon_{90}^{exp}\left(\frac{\sigma_f(\bar{\varepsilon}^p)}{\sqrt{Y_3}}\right), \\
 \sigma_b(\varepsilon_{45}^p) &= \frac{\sigma_f(\bar{\varepsilon}^p)}{\sqrt{Y_1 + Y_2 + Y_3}}, \quad \varepsilon_b(\bar{\varepsilon}^p) = \varepsilon_b^{exp}\left(\frac{\sigma_f(\bar{\varepsilon}^p)}{\sqrt{Y_1 + Y_2 + Y_3}}\right).
 \end{aligned}
 \tag{12}$$

Per convention $\bar{\varepsilon}^p = \varepsilon_0^p$, $\sigma_f(\bar{\varepsilon}^p) = \sigma_0(\varepsilon_0^p)$ and $Y_1 = 1$ so $Q_1 = 1$.

Application to Selected Sheet Metals

We are now ready to apply the new strain hardening model to two sheet metals that have been previously modeled via conventional non-associated quadratic anisotropic models [11], where the Voce strain hardening law with three material constants (A, B, C) is adapted for the sheet metals

$$\sigma_f(\bar{\varepsilon}^p) = A - B e^{-C\bar{\varepsilon}^p}.
 \tag{13}$$

For the convenience of readers here, the relevant experimental data for the two sheet metals (aluminum alloy AA5182-O and stainless steel 718-AT) are relisted in Table 1. As shown in Fig. 1, the four stress–strain curves for each of these two sheet

Table 1 Voce model parameters and plastic strain ratios for two sheet metals [11]

Material	Test	A	B	C	R_θ
AA5182-O	0	366.84	251.07	11.166	0.957
	45	358.74	247.11	9.719	0.934
	90	362.39	248.11	9.981	1.058
	EB	437.28	312.26	6.179	
SS718-AT	0	532.38	321.50	9.592	1.830
	45	520.70	301.30	10.149	2.294
	90	516.28	299.79	10.412	2.517
	EB	709.54	471.79	9.980	

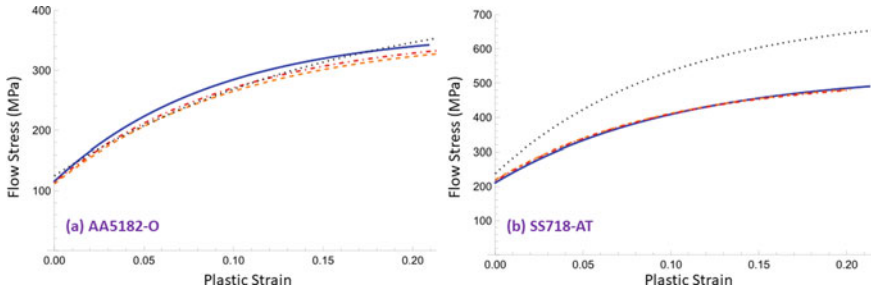


Fig. 1 Stress–strain curves for **a** AA5182-O and **b** SS718-AT sheet metals under uniaxial tension along rolling (solid lines), cross (dashed lines), and transverse (dot-dashed lines) directions and under equal biaxial tension (dotted lines)

Table 2 Material constants in yield function Φ_{2y} and flow potential Φ_{2p}

	$Y_2(0)$	$Y_3(0)$	$Y_4(0)$	P_2	P_3	P_4
AA5182-O	-1.16875	1.02625	3.44470	-0.97803	0.95122	2.79111
SS718-AT	-1.16211	0.94885	2.90863	-1.29329	0.90355	3.41017

metals are not completely self-similar, especially for AA5182-O, indicating clearly the differential strain hardening behavior. Table 2 lists the materials parameters for Y_2 to Y_4 based on the initial yield stresses ($\bar{\epsilon}^p = 0$) and P_2 to P_4 based on (R_0, R_{45}, R_{90}) for each material (noting $Y_1 = P_1 = 1$).

von Mises Isotropic Equivalent Stress Function

As an initial effort, one may simply assume that the equivalent stress function to be isotropic von Mises type with $(Q_1, Q_2, Q_3, Q_4) = (1, -1, 1, 3)$. From Eq. (10), one has (letting $\bar{\epsilon}_i^p = 0$)

$$\epsilon_0^p(\bar{\epsilon}^p) = e_0 + \bar{\epsilon}^p, \epsilon_{45}^p(\bar{\epsilon}^p) = e_{45} + \bar{\epsilon}^p, \epsilon_{90}^p(\bar{\epsilon}^p) = e_{90} + \bar{\epsilon}^p, \epsilon_b^p(\bar{\epsilon}^p) = e_b + \bar{\epsilon}^p. \tag{14}$$

So the material parameters Y_2 to Y_4 from Eq. (8) are (recalling $\sigma_f(\bar{\epsilon}^p) = \sigma_0(\epsilon_0^p)$)

$$\begin{aligned} Y_2(\bar{\epsilon}^p) &= -1 - \left(\frac{A_0 - B_0 e^{-C_0 \bar{\epsilon}^p}}{A_{90} - B_{90} e^{-C_{90} \bar{\epsilon}^p}} \right)^2 + \left(\frac{A_0 - B_0 e^{-C_0 \bar{\epsilon}^p}}{A_{eb} - B_{eb} e^{-C_{eb} \bar{\epsilon}^p}} \right)^2, \\ Y_3(\bar{\epsilon}^p) &= \left(\frac{A_0 - B_0 e^{-C_0 \bar{\epsilon}^p}}{A_{90} - B_{90} e^{-C_{90} \bar{\epsilon}^p}} \right)^2, \\ Y_4(\bar{\epsilon}^p) &= 4 \left(\frac{A_0 - B_0 e^{-C_0 \bar{\epsilon}^p}}{A_{45} - B_{45} e^{-C_{45} \bar{\epsilon}^p}} \right)^2 - \left(\frac{A_0 - B_0 e^{-C_0 \bar{\epsilon}^p}}{A_{eb} - B_{eb} e^{-C_{eb} \bar{\epsilon}^p}} \right)^2, \end{aligned} \tag{15}$$

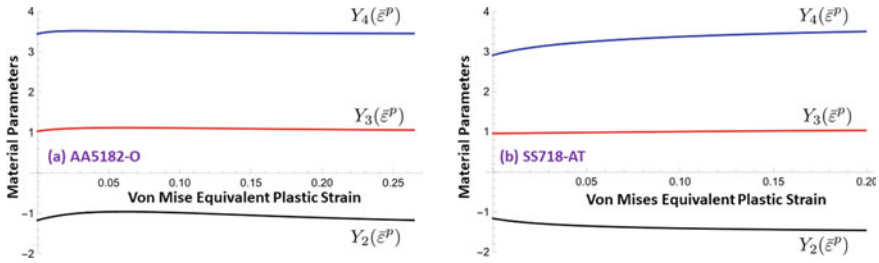


Fig. 2 Variation of three material parameters of the yield function Φ_{2y} with von Mises equivalent plastic strain for **a** AA5182-O and **b** SS718-AT sheet metals

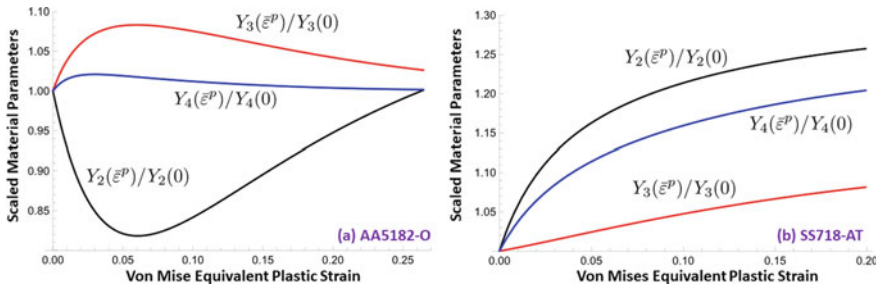


Fig. 3 Variation of scaled material parameters of the yield function Φ_{2y} with von Mises equivalent plastic strain for **a** AA5182-O and **b** SS718-AT sheet metals

where $e_0 = e_{45} = e_{90} = e_b = 0$ are assumed. Variations of these three material parameters with von Mises equivalent plastic strain are shown in Fig. 2 for AA5182-O and SS718-AT sheet metals. The strain dependence of these material parameters are better illustrated using the normalized values as shown in Fig. 3. Again, AA5182-O exhibits a stronger differential strain hardening behavior (i.e., its dissimilar strain-dependence of Y_2 , Y_3 , and Y_4).

Differential Hardening Equivalent Stress Function

Alternatively, one may use the constant material parameters $Y_2 = Y_2(0)$, $Y_3 = Y_3(0)$, and $Y_4 = Y_4(0)$ to define the yield stress function first and the differential strain hardening behavior of a sheet metal is modeled instead via the strain dependence of material parameters Q_2 , Q_3 , and Q_4 in the equivalent stress function Φ_{2q} .

From Eq. (12), one has the experimental Voce hardening parameters as given in Table 1

$$\begin{aligned}
 A_{45} - B_{45} e^{-C_{45}\varepsilon_{45}^p} &= \alpha_{45}A_0 - \alpha_{45}B_0 e^{-C_0\bar{\varepsilon}^p}, \\
 A_{90} - B_{90} e^{-C_{90}\varepsilon_{90}^p} &= \alpha_{90}A_0 - \alpha_{90}B_0 e^{-C_0\bar{\varepsilon}^p}, \\
 A_{eb} - B_{eb} e^{-C_{eb}\varepsilon_b^p} &= \alpha_{eb}A_0 - \alpha_{eb}B_0 e^{-C_0\bar{\varepsilon}^p}.
 \end{aligned}
 \tag{16}$$

where $\alpha_{45} = 2/\sqrt{Y_1 + Y_2 + Y_3 + Y_4}$, $\alpha_{90} = 1/\sqrt{Y_3}$ and $\alpha_{eb} = 1/\sqrt{Y_1 + Y_2 + Y_3}$. After solving the above equations to obtain $\varepsilon_{45}^p(\bar{\varepsilon}^p)$, $\varepsilon_{90}^p(\bar{\varepsilon}^p)$, and $\varepsilon_b^p(\bar{\varepsilon}^p)$, one can then compute their first derivatives as

$$\begin{aligned}
 \varepsilon'_{45}(\bar{\varepsilon}^p) &= \frac{1}{C_{45}} \frac{\alpha_{45}B_0C_0 e^{-C_0\bar{\varepsilon}^p}}{A_{45} - \alpha_{45}A_0 + \alpha_{45}B_0 e^{-C_0\bar{\varepsilon}^p}}, \\
 \varepsilon'_{90}(\bar{\varepsilon}^p) &= \frac{1}{C_{90}} \frac{\alpha_{90}B_0C_0 e^{-C_0\bar{\varepsilon}^p}}{A_{90} - \alpha_{90}A_0 + \alpha_{90}B_0 e^{-C_0\bar{\varepsilon}^p}}, \\
 \varepsilon'_b(\bar{\varepsilon}^p) &= \frac{1}{C_{eb}} \frac{\alpha_{eb}B_0C_0 e^{-C_0\bar{\varepsilon}^p}}{A_{eb} - \alpha_{eb}A_0 + \alpha_{eb}B_0 e^{-C_0\bar{\varepsilon}^p}}.
 \end{aligned}
 \tag{17}$$

Variations of these derivatives (strain increment ratios) with the equivalent plastic strain are shown in Fig. 4 for AA5182-O and SS718-AT sheet metals. Finally, material parameters $Q_2(\bar{\varepsilon}^p)$, $Q_3(\bar{\varepsilon}^p)$, and $Q_4(\bar{\varepsilon}^p)$ of the equivalent stress function Φ_{2q} can be obtained from Eq. (11) and their strain dependence is shown in Fig. 5.

Discussion

By equivalency of the plastic work rate, an equivalent stress function $\bar{\sigma}(\sigma)$ and its corresponding plastic strain increment $\dot{\bar{\varepsilon}}^p$ can be introduced independent of either the yield stress function or plastic flow potential. Like the previous works [10–12], the accumulated equivalent plastic strain $\bar{\varepsilon}^p$ may be used as a scalar state variable to model strain hardening behavior of a sheet metal under proportional loading only.

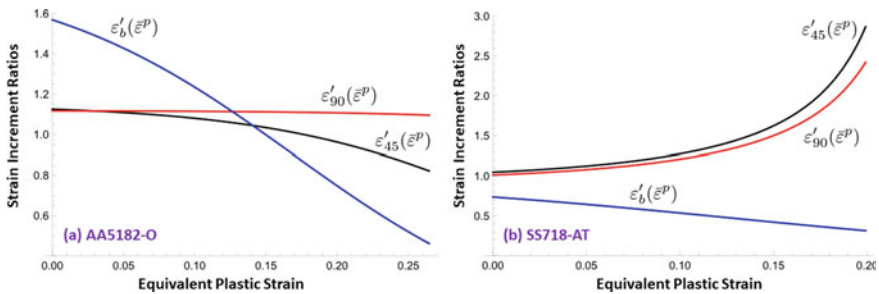


Fig. 4 Variation of three material parameters of the yield function Φ_{2y} with von Mises equivalent plastic strain for **a** AA5182-O and **b** SS718-AT sheet metals

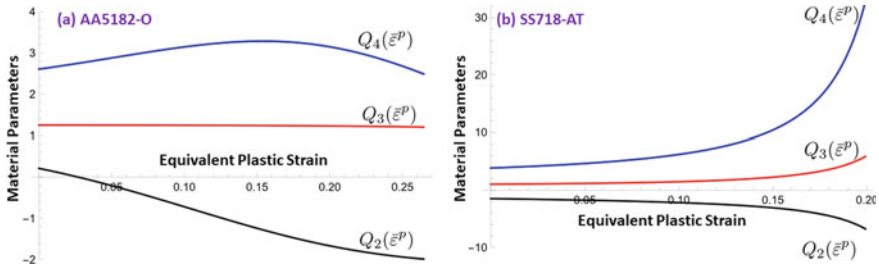


Fig. 5 Variation of scaled material parameters of the yield function Φ_{2y} with von Mises equivalent plastic strain for **a** AA5182-O and **b** SS718-AT sheet metals

As shown in this study, when the von Mises stress function is used as the equivalent stress function, the non-constant material parameters $Y_2(\bar{\epsilon}^p)$ to $Y_4(\bar{\epsilon}^p)$ of the quadratic yield stress function can model the differential strain hardening of the two sheet metals under consideration. Both the size and shape of the yield surface $\Phi_{2y}(\sigma, \bar{\epsilon}^p) = \sigma_f(\bar{\epsilon}^p)$ evolve with the plastic deformation. This is similar to the use of the flow potential with constant parameters P_2 to P_4 as the equivalent stress function $\Phi_{2q}(\sigma) = \Phi_{2p}(\sigma)$ [11]. It is however simpler especially when plastic strain ratios of a sheet metal also evolve with plastic deformation (i.e., when the sheet metal exhibits a more general anisotropic strain hardening behavior).

On the other hand, our study has also shown that it is still possible to only use constant material parameters (the initial values $Y_2(0)$ to $Y_4(0)$) in the yield stress function for modeling a sheet metal with a differential strain hardening behavior. Its corresponding quadratic equivalent stress function $\Phi_{2q}(\sigma, \bar{\epsilon}^p)$ will have non-constant material parameters $Q_2(\bar{\epsilon}^p)$ to $Q_4(\bar{\epsilon}^p)$ instead. In this case, only the size of its yield surface $\Phi_{2y}(\sigma) = \sigma_f(\bar{\epsilon}^p)$ increases with strain hardening and its shape remains fixed. This particular strain hardening model may be called the *generalized* or *enhanced* isotropic strain-hardening type.

Just like the yield stress function Φ_{2y} and plastic flow potential Φ_{2p} , the equivalent stress function Φ_{2q} is also required to be positive and convex for sheet metal plasticity modeling. Strict positivity and convexity of these three quadratic polynomial stress functions calibrated for both AA5182-O and SS-718-AT sheet metals have been numerically certified up to the necking strain level as per the following necessary and sufficient conditions [5, 8–10]

$$\begin{aligned}
 &Y_1 > 0, \quad Y_3 > 0, \quad Y_4 > 0, \quad 4Y_1Y_3 - Y_2^2 > 0, \\
 &P_1 > 0, \quad P_3 > 0, \quad P_4 > 0, \quad 4P_1P_3 - P_2^2 > 0, \\
 &Q_1 > 0, \quad Q_3 > 0, \quad Q_4 > 0, \quad 4Q_1Q_3 - Q_2^2 > 0.
 \end{aligned}
 \tag{18}$$

References

1. Hill R (1950) *The mathematical theory of plasticity*. Oxford University Press, London
2. Lubliner J (1990) *Plastic theory*. Macmillan, New York
3. Maugin GA (1992) *The thermomechanics of plasticity and fracture*. Cambridge University Press, Cambridge
4. Hill R (1948) A theory of yielding and plastic flow of anisotropic metals. *Proc Royal Soc* 193A:281–297
5. Hill R (1990) Constitutive modeling of orthotropic plasticity in sheet metals. *J Mech Phys Solids* 38:403–417
6. Gotoh M (1977) A theory of plastic anisotropy based on a yield function of fourth order (plane stress state). *Int J Mech Sci* 19:505–520
7. Barlat F, Yoon JW, Cazacu O (2007) On linear transformations of stress tensors for the description of plastic anisotropy. *Int J Plast* 23:876–896
8. Stoughton TS (2002) A non-associated flow rule for sheet metal forming. *Int J Plast* 18:687–714
9. Tong W, Alharbi M (2017) Comparative evaluation of non-associated quadratic and associated quartic plasticity models for orthotropic sheet metals. *Int J Solids Struct* 128:133–48
10. Cvitanic V, Vlcek F, Lozina Z (2008) A finite element formulation based on non-associated plasticity for sheet metal forming. *Int J Plast* 24:646–687
11. Stoughton TB, Yoon JW (2009) Anisotropic hardening and non-associated flow in proportional loading of sheet metals. *Int J Plast* 25:1777–1817
12. Safaei M, Yoon JW, Waele WD (2014) Study on the definition of equivalent plastic strain under non-associated flow rule for finite element formulation. *Int J Plast* 58:219–238
13. Tong W (2005) A planar plastic flow theory of orthotropic sheets and the experimental procedure for its evaluations. *Proc R Soc Lond A* 461:1775–1809
14. Tong W (2006) A plane stress anisotropic plastic flow theory for orthotropic sheet metals. *Int J Plast* 22:497–535

Prediction of Ductile Fracture in Bainitic Steel with Dependence on Stress States and Loading Orientation



Fuhui Shen, Sebastian Münstermann, and Junhe Lian

Abstract The influence of stress states and loading direction on ductile fracture of high-strength steels is investigated through a hybrid experimental and numerical approach. The experimental characterization of ductile fracture is carried out by performing tensile tests at room temperature along three different directions on flat specimens with features, including central-hole, notched dog-bone, plane-strain, and shear. In addition, the fracture behavior under the equibiaxial tension state is captured by the bulge test. The anisotropic plastic flow behavior is described by an evolving non-associated plasticity model, capable of representing the anisotropic hardening and evolution of Lankford coefficients. The evolving anisotropy is integrated into a damage mechanics model and further used for the numerical prediction of the stress state and loading orientation dependence of ductile fracture behavior. Different strategies, such as linear transformation and scaling approach, have been adopted to formulate a unified ductile fracture criterion independent of loading orientations.

Keywords Anisotropy · Flow rule · Stress state · Damage · Fracture

Introduction

Mechanical properties of metallic materials produced in the form of thin sheets or heavy plates after the rolling process always show anisotropy with different levels of intensity. The effects of anisotropy on the plasticity and ductile damage and fracture properties have been recognized in many different materials [1–4]. Numerous

F. Shen · S. Münstermann
Integrity of Materials and Structures, Steel Institute, RWTH Aachen University, Intzestraße 1,
52072 Aachen, Germany

J. Lian (✉)
Advanced Manufacturing and Materials, Department of Mechanical Engineering, Aalto
University, Otakaari 4, 02150 Espoo, Finland
e-mail: lianjh@mit.edu; junhe.lian@aalto.fi

Impact and Crashworthiness Laboratory, Department of Mechanical Engineering, Massachusetts
Institute of Technology, Cambridge, MA 02139, USA

phenomenological anisotropic constitutive models have been proposed to describe the anisotropic plastic flow behavior of various materials with distinct crystallographic structures, i.e., body-centered cubic (bcc), face-centered cubic (fcc), and hexagonal close-packed (hcp). In order to enhance the efficiency and flexibility of these models in the description of anisotropy, tremendous efforts have been made from different aspects. One significant aspect is the formulation of advanced expressions of anisotropic equivalent stress in the yield function, starting from the first quadratic anisotropic Hill48 model to the recent non-quadratic ones based on different linear transformation methods [5, 6]. Another significant progress is the development of the non-associated flow rule, which increases the accuracy and efficiency of constitutive models without requiring more experiments [7, 8]. The consideration of evolving anisotropy is also an important perspective in the recent developments of anisotropic plasticity models [9–11]. The evolving anisotropic plasticity model based on the quadratic Hill48 formulation coupled with the non-associated flow rule proposed by Lian et al. [12] leads to improved accuracy in the plasticity, localization, and fracture description of different materials [12–14].

The ductile damage and fracture behavior of many metallic materials can be captured using either coupled or uncoupled damage mechanics models [15]. In the coupled groups of damage mechanics models, the influence of damage-induced softening on plasticity is taken into consideration, such as in these Curson-Tvergaard-Needleman (GTN) [16–18] and continuum damage mechanics (CDM) [19] models. In contrast, damage effects are separated from plasticity in the uncoupled damage models by formulating an expression of the critical plastic strain that depends on the stress states. An essential aspect of the recent development of damage mechanics concepts is the recognition of the Lode angle dependence of ductile fracture in various metallic materials over a wide range of loading conditions. Several uncoupled failure criteria considering the effects of the stress triaxiality and the Lode angle have been proposed and successfully applied to the prediction of ductile failure in many aluminium alloys and steels [20–25]. In order to establish an effective link between load-carrying capacities with material degradation caused by damage initiation, Lian et al. [26] have proposed the modified Bai-Wierzbicki (MBW) model, which is a hybrid damage model capable of describing the damage initiation, evolution and final fracture of various steels subjected to different loading conditions.

Simulation and prediction of anisotropic ductile damage and fracture have been an important topic, which is of particular significance in the metal forming and mechanics committee. The consideration of anisotropy effects in coupled damage mechanics models is typically accomplished by using either vectorial or tensorial damage variables. In the uncoupled damage mechanics models, different approaches have been adopted to include the influence of loading orientation. A prevalent method in formulating a unified anisotropic ductile fracture criterion is to apply a linear transformation to either the plastic strain tensor or the stress tensor at the fracture moment, which has been adopted for several different alloys [1, 3, 27]. Another alternative approach is introducing anisotropic parameters in the weight function, as proposed by Lou and Yoon [28] for the anisotropic fracture description of AA6082 alloy. An empirical scaling approach has been proposed by Park et al. [29] by modifying the

definition of the stress triaxiality and making damage parameters as continuous functions of loading orientation. In general, these methods have provided sufficient accuracy for specific materials; however, their applicability to other materials under more loading conditions needs further validation. In this study, the anisotropic damage and fracture properties of high-strength steel are investigated using a combination of experiments and numerical simulation. Different approaches have been adopted and compared in the description of anisotropic ductile fracture of the investigated material.

Material and Experiments

The anisotropic plasticity at room temperature of the investigated material, X70 steel with a mainly bainitic microstructure, is characterized by performing tensile tests on smooth dog-bone (SDB) specimens along seven different directions (every 15°) with respect to the rolling direction as well as the through-thickness compression test using cylindrical specimens. During the tensile tests, both the engineering strain vs. strain curves and the evolution of r -value have been measured along these directions to characterize the evolution of anisotropy. The flow behavior under the equibiaxial tension state is obtained from the through-thickness compression tests by assuming the negligible strength differential effects in compression and tension of the investigated material. All the plasticity tests have been performed with three repeating experiments under the quasi-static loading conditions. Detailed information regarding the experimental setup and procedures are available in the previous studies [30, 31]. The experimental results provide strong evidence of the pronounced evolution of anisotropy in the plasticity of the investigated bainitic steel at room temperature.

In order to investigate the influence of loading orientation and stress states, in particular, the triaxiality and Lode angle, on the ductile fracture properties of the high-strength steel, a comprehensive experimental characterization program is carried out to describe the fracture behavior over a broad stress state spectrum. The adopted sample geometries are composed of mainly five different categories, i.e., one central hole (CH-R3), three notched dog-bone with different notch radii (NDB-R30, NDB-R10, and NDB-R6), two side-grooved plane-strain with different notch radii (PS-R16 and PS-R2), one shear (SH) and one bulge test to characterize the fracture behavior under equibiaxial tension. The effects of anisotropy on the ductile fracture of the investigated material are studied by varying the longitudinal loading direction in all experiments except the bulge tests parallel to three different directions with respect to the rolling direction, e.g., rolling (0°), diagonal (45°), and transverse (90°) direction. An extensometer with an initial distance of 40 mm has been used to measure the elongation during all the tensile tests under quasi-static loading rates. During the hydraulic bulge tests, the quasi-static loading condition has been assured as well. Three parallel tests have been performed for each loading condition. An overview of all specimens used for the characterization of plasticity and fracture behavior of the

material is provided in Fig. 1. The experimental results show good repeatability in terms of fracture displacement and force in all specimens. More detailed information on the experimental program is provided in our previous study [30, 31]. Based on the experimental results, clear anisotropic ductile fracture behavior with apparent stress state dependence is observed in the high-strength steel.

Models

The anisotropic plasticity is described by an evolving non-associated Hill48 (enHill48) plasticity model proposed by Lian et al. [12]. The non-associated flow rule is adopted in order to overcome the well-known drawback of the conventional Hill48 model, in which limited accuracy can be achieved in the simultaneous prediction of stress and r-value. A scalar damage variable D is introduced in both the yield function f and flow potential g to describe the damage induced softening effects, which are expressed as

$$f = \tilde{\sigma}_\sigma(\sigma | F_\sigma, G_\sigma, H_\sigma, L_\sigma, M_\sigma, N_\sigma) - (1 - D) \cdot \sigma_Y(\bar{\epsilon}^p) \leq 0 \tag{1}$$

$$g = \tilde{\sigma}_r(\sigma | F_r, G_r, H_r, L_r, M_r, N_r) - (1 - D) \cdot \sigma_Y(\bar{\epsilon}^p) \leq 0 \tag{2}$$

$$\tilde{\sigma}(\sigma) =$$

$$\left\{ \frac{1}{2} [F(\sigma_{22} - \sigma_{33})^2 + G(\sigma_{33} - \sigma_{11})^2 + H(\sigma_{11} - \sigma_{22})^2] + L\sigma_{23}^2 + M\sigma_{13}^2 + N\sigma_{12}^2 \right\}^{\frac{1}{2}} \tag{3}$$

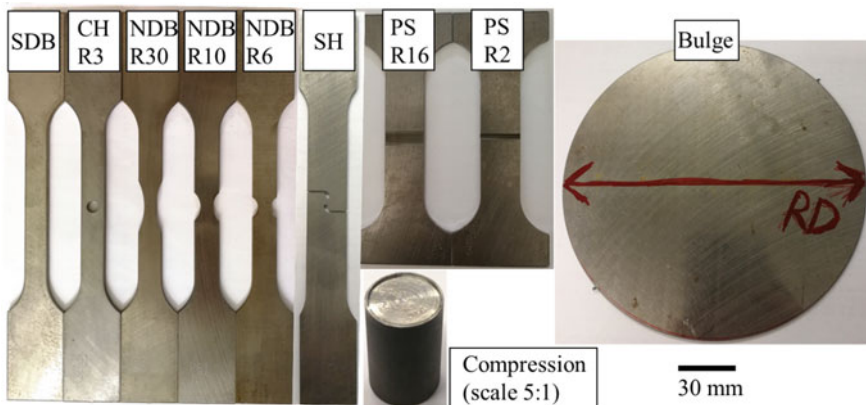


Fig. 1 Overview of specimen geometries for plasticity and fracture characterization

The yield function and the flow potential share the identical expression of the quadratic equivalent stress $\tilde{\sigma}(\sigma)$ with six different anisotropic parameters. According to the concept of non-associated flow rule, whether plastic deformation takes place is determined by the value of yield function, while the update of strain components is controlled by the flow potential:

$$\dot{\tilde{\epsilon}}^p = \dot{\lambda} \cdot \frac{\tilde{\sigma}_r}{\tilde{\sigma}_\sigma} \tag{4}$$

A critical step in successful finite-element-based numerical simulation is finding the solution of the equivalent plastic strain rate $\dot{\tilde{\epsilon}}^p$, which is defined in Eq. 4 with the assistance of the non-negative plastic multiplier $\dot{\lambda}$. A major advantage of the quadratic anisotropic plasticity model belonging to the Hill48’s family is the existence of several analytical expressions for the determination of anisotropic parameters. In non-evolving plasticity models, these six anisotropic parameters can be obtained by the yield strength of uniaxial tensile tests along different directions and the yield strength under the equibiaxial tension state. Other methods can also be used to determine these parameters based on the yield strength along the rolling direction and r-value along other directions. A summary of these analytical equations is available in [32]. Omitting the effects of out-of-plane anisotropy, it is typically assumed that $L = M = 3$. For the description of evolving characteristics of anisotropy, a straightforward modification has been made by Lian et al. [12] to calculate anisotropic parameters as continuous functions of the equivalent plastic strain by using complete flow curves and evolution functions of r-value along different loading directions as inputs.

A ductile damage initiation (DDI) criterion is defined in the MBW model [26] as a critical value of the equivalent plastic strain $\bar{\epsilon}_{ddi}$, which is a weigh function of the stress triaxiality η and the Lode angle parameter $\bar{\theta}$. In the MBW model under proportional loading conditions, ductile damage initiates once the damage initiation locus (DIL) is reached, which is represented by the symmetric surface with respect to the Lode angle parameter in the space of the equivalent plastic strain, triaxiality, and Lode angle parameter.

$$\bar{\epsilon}_{ddi}(\eta, \bar{\theta}) = (D_1^\alpha \cdot e^{-D_2^\alpha \cdot \eta} - D_3^\alpha \cdot e^{-D_4^\alpha \cdot \eta}) \cdot \bar{\theta}^2 + D_3^\alpha \cdot e^{-D_4^\alpha \cdot \eta} \tag{5}$$

Due to the change of sample geometry and the strain hardening that occurs during the deformation process, the critical elements in different specimens experience non-proportional loading history due to the change of stress states. Therefore, the proper design of specimen geometry based on the hardening properties of the material to achieve a more or less constant stress state is an important approach to minimize the effects on non-proportionality. An alternative method to consider the effects of stress state evolution is to use the average stress state variables until the damage initiation, i.e., the average values of the stress triaxiality η_{avg} and the Lode angle parameter $\bar{\theta}_{avg}$ are used to represent the overall stress state during the complete loading history. In

this case, an indicator of ductile damage I_{dd} has been used as an initiation criterion to evaluate the accumulative effects of damage and damage initiation takes place once $I_{dd} = 1$.

$$\eta_{\text{avg}} = \frac{1}{\bar{\varepsilon}_{\text{ddi}}} \int_0^{\bar{\varepsilon}_{\text{ddi}}} \eta d\bar{\varepsilon}^{\text{P}}, \bar{\theta}_{\text{avg}} = \frac{1}{\bar{\varepsilon}_{\text{ddi}}} \int_0^{\bar{\varepsilon}_{\text{ddi}}} \bar{\theta} d\bar{\varepsilon}^{\text{P}} \quad (6)$$

$$I_{\text{dd}} = \int_0^{\bar{\varepsilon}^{\text{P}}} \frac{1}{\bar{\varepsilon}_{\text{ddi}}(\eta_{\text{avg}}, \bar{\theta}_{\text{avg}})} d\bar{\varepsilon}^{\text{P}} \quad (7)$$

$$\dot{D} = \frac{\tilde{\sigma}_{\text{ddi}}}{G_f} \cdot \dot{\bar{\varepsilon}}^{\text{P}} \quad (8)$$

In the coupled MBW model, a simple linear damage accumulation law is assumed. The damage evolution rate \dot{D} is formulated as a linear function of the equivalent plastic strain rate $\dot{\bar{\varepsilon}}^{\text{P}}$ by introducing two additional parameters, i.e., the stress at ductile damage initiation $\tilde{\sigma}_{\text{ddi}}$ and the energy dissipation rate G_f . By modifying these two parameters, the damage evolution rate can be adjusted according to the experimental results. Similar to the damage initiation locus, a ductile fracture criterion is also proposed as a critical value of the damage variable D_c , that is, a weight function of the stress triaxiality and the Lode angle parameter. For the reason of simplicity, the critical damage variable is assumed to be unity ($D_c = 1$) in this study. This anisotropic damage mechanics model has been written as a VUMAT user subroutine, and the ABAQUS/EXPLICIT simulation software has been used to perform all these simulations.

Simulation Results

The numerical prediction of the final anisotropic ductile fracture relies on the accurate description of the plastic deformation of the investigated material. Therefore, the accuracy of the applied evolving plasticity model needs to be verified prior to the simulation of damage and fracture. The difference in the yield function and the flow potential of the enHill48 model is attributed to the distinct methods used for the determination of anisotropic parameters. The anisotropic parameters in the yield function are calculated using the flow stress obtained from uniaxial tensile tests along three different directions (σ_0 , σ_{45} , and σ_{90}) and the flow stress of equibiaxial tension σ_b . The anisotropic parameters in the flow potential are calculated using the evolution functions of the r-value obtained from uniaxial tensile tests along three different directions (r_0 , r_{45} , and r_{90}) and the flow stress of the reference direction σ_0 . Explicit equations are available for the calibration of these parameters. With the calibrated parameters at different levels of plastic strain, the predicted distribution of

the normalized stress (σ_α/σ_0) and the r-value using the enHill48 model is compared with experimental results in Fig. 2. From the experimental results, it is evident that the anisotropy patterns in terms of the distribution of normalized stress and r-value are changing with increasing plastic deformation, indicating the non-negligible effects of evolving anisotropy. Besides the accurate prediction of the stress and r-value along 0° , 45° , and 90° directions, which are used in the calibration procedure, the normalized stress and r-value along the other four additional directions are generally captured with acceptable accuracy as well. The evolution in the anisotropy distribution is predicted by the enHill48 model at different strain levels. The corresponding yield locus and flow potential in the enHill48 model at different strain values are plotted in Fig. 2 as well, where the yield locus of the isotropic Mises plasticity model is also

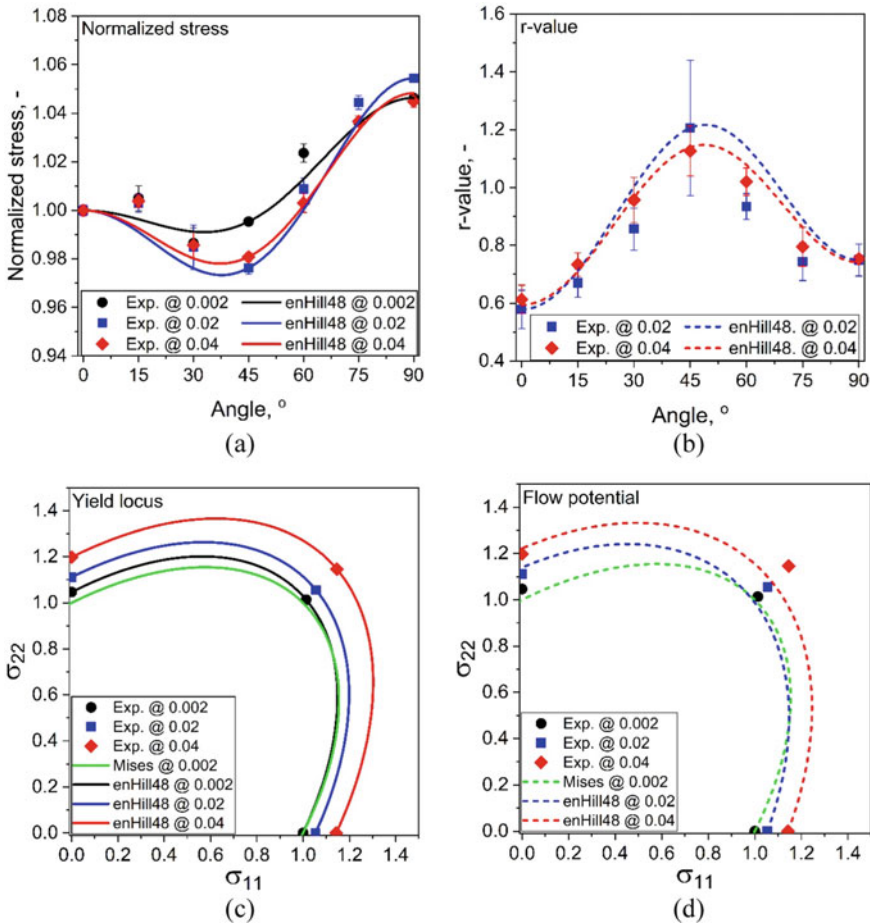


Fig. 2 Evolution of anisotropy of X70 steel obtained from uniaxial tensile tests and compression tests: **a** normalized stress, **b** r-value, **c** yield locus, and **d** flow potential

shown for comparison. At the yield point, the difference between the yield locus of the enHill48 model and the Mises model is quite obvious, especially in the transverse uniaxial tension and equibiaxial tension state. The experimental results of the stress obtained from uniaxial tensile tests along 0° and 90° directions and the equibiaxial tension state are located on the yield locus of the enHill48 model. However, an apparent deviation is noticed between the flow potential and the experimental results at different strain levels, which indicates the significant difference between the yield locus and the flow potential. In addition, the evolution of both yield locus and the flow potential is accurately captured by the evolving enHill48 plasticity model, which is accomplished by the adoption of the non-associated flow rule and the consideration of strain dependence of anisotropic parameters.

After verifying the accuracy of the enHill48 model in the description of stress and r -value at discrete points of plastic strain, it is necessary to calibrate the flow curves and evolution functions of r -value along different loading directions. The parameters in the Swift hardening law have been calibrated individually for three uniaxial tensile tests and the equibiaxial tension state to describe the anisotropic hardening behavior of the material. In addition, the evolution of the r -value along three loading directions is also described using a continuous exponential equation with three sets of individually calibrated parameters. The validation of plasticity parameters in the description of the evolution of the yield locus and flow potential is assessed based on the accurate prediction results of the force–displacement curves obtained from tensile tests of CH-R3 specimens along three loading directions.

With all calibrated plasticity parameters, the finite element simulations have been performed for all specimens along the corresponding loading directions. Concerning the global response of the force–displacement curves in different samples, a generally good agreement is achieved by using the enHill48 plasticity model. The local stress state variables have been extracted from the critical elements in these samples, which are assumed to be the symmetry center of the specimen as ductile damage typically initiates from the inside of the material. With the collection of these local variables for all tested geometries, i.e., the equivalent plastic strain at damage initiation, the average stress triaxiality, and the average Lode angle parameter, the four parameters in the symmetric damage initiation locus function have been calibrated independently for three specific loading directions. The damage evolution parameter G_f has also been inversely calibrated and the same value has been assumed in three different directions for the reason of simplicity. Damage initiation occurs at a very late stage of deformation in the investigated material, therefore, the hybrid MBW model has been used in the uncoupled manner, where the damage initiation is assumed to be identical to the ductile fracture initiation in this study. The stress state dependence of the critical damage variable is omitted by assuming $D_c = 1$ for all loading cases. This simple assumption has not caused any significant loss of accuracy in the prediction capacity of the anisotropic damage mechanics models. The simulation results on the force–displacement curves of two representative geometries, i.e., CH-R3 and NDB-R30, have been shown in Fig. 3 for three loading directions. In comparison with corresponding experimental results, the anisotropic ductile fracture behavior under the influence of stress states is accurately predicted by the proposed

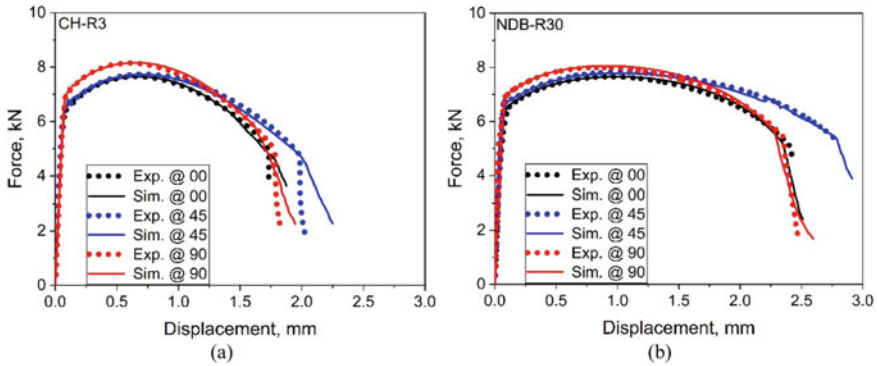


Fig. 3 Simulation results of the anisotropic global response of force–displacement curves obtained from tensile tests of different specimens along three loading directions: **a** CH-R3 and **b** NDB-R30

anisotropic damage mechanics models. In both specimens, the force is the highest along the transverse direction in the early stage of plastic deformation and that along the other two directions has similar values, which is consistent with the two flow stress distribution in Fig. 2. With the increase of displacement, the force decreases most rapidly along the transverse direction, which indicates the significance of anisotropic hardening in the investigated material. The fracture displacement along the diagonal direction is the largest in both geometries and that along transverse and rolling directions has similar values. This pattern of anisotropy in the distribution of fracture displacements depends on the corresponding stress states in different geometries, which is not completely shown here due to the limitation of space. With all these independently calibrated damage parameters for three individual loading directions, the force–displacement curves until the fracture point have been accurately predicted by the anisotropic damage models all specimens, which provides strong evidence of the efficiency and accuracy of the proposed damage mechanics model.

Though a very good agreement is achieved in the prediction of anisotropic global force–displacement curves over a wide range of stress states, however, it is also of significant importance to formulate one anisotropic damage and fracture criterion which considers the influence of stress state but is independent of the loading direction. As mentioned in the previous section, several different approaches are available for the formulation of one unified anisotropic damage model, among which the empirical scaling function and the linear transformation approach are two promising methods with a good balance of accuracy and simplicity. Therefore, these two approaches have been applied to the collected results in this study.

In the first empirical approach, a straightforward phenomenological modification has been adopted by establishing an empirical relationship between these calibrated damage parameters and loading directions. The individually calibrated damage initiation curves explained in the previous part under the plane stress condition ($\sigma_3 = 0$) have been plotted as dotted curves with different colors in Fig. 4. Taking the damage initiation curves along the rolling direction as the reference, normalization has been

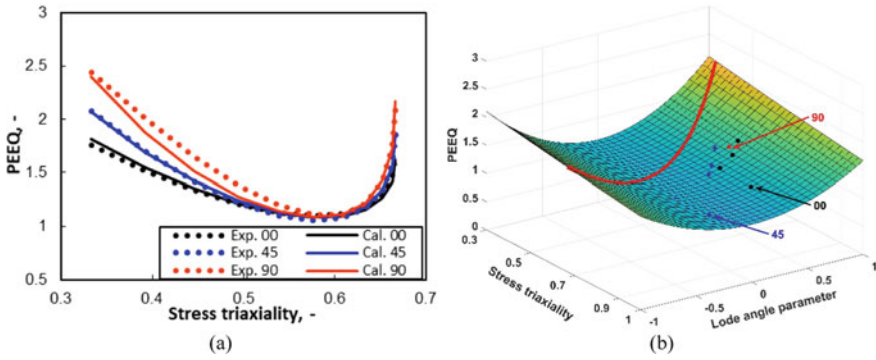


Fig. 4 Anisotropic damage initiation locus for X70 steel based on **a** scaling approach and **b** linear transformation approach

performed on the damage initiation strain with respect to the local stress state variables for the transverse and diagonal directions. A combination of polynomial and trigonometric functions has been used to determine the loading orientation dependence of damage parameters in the investigated material. The adopted approach is similar to the method proposed by Park et al. [29]. With all these calibrated parameters in the scaling function, the damage initiation curves under plane stress conditions are reproduced for all three loading directions, which are compared with experimental ones determined based on the hybrid experimental and numerical approach. It is evident that the calculated results using the empirical scaling method are in line with the experimental results under the plane stress condition.

$$\boldsymbol{\varepsilon}^d = \begin{bmatrix} \varepsilon_{11}^d \\ \varepsilon_{22}^d \\ \varepsilon_{33}^d \\ \varepsilon_{23}^d \\ \varepsilon_{13}^d \\ \varepsilon_{12}^d \end{bmatrix} = \mathbf{D} \cdot \boldsymbol{\varepsilon}^p = \begin{bmatrix} 0 & -d_{12} & -d_{13} & 0 & 0 & 0 \\ -d_{21} & 0 & -d_{23} & 0 & 0 & 0 \\ -d_{31} & -d_{32} & 0 & 0 & 0 & 0 \\ 0 & 0 & 0 & d_{44} & 0 & 0 \\ 0 & 0 & 0 & 0 & d_{55} & 0 \\ 0 & 0 & 0 & 0 & 0 & d_{66} \end{bmatrix} \cdot \begin{bmatrix} \varepsilon_{11}^p \\ \varepsilon_{22}^p \\ \varepsilon_{33}^p \\ \varepsilon_{23}^p \\ \varepsilon_{13}^p \\ \varepsilon_{12}^p \end{bmatrix} \quad (9)$$

In the second linear transformation approach, the plastic strain tensor at the damage initiation moment has been collected for different geometries along three loading directions. The anisotropy effects are considered by introducing a four order transformation tensor \mathbf{D} , as shown in Eq. 9, which is identical to the matrix applied by Lou and Yoon [3]. As many geometries are considered in this study and necking phenomena are observed at the late stage of plastic deformation, therefore, the full plastic strain tensor with six components $\boldsymbol{\varepsilon}^p$ and nine anisotropic parameters in the transformation matrix \mathbf{D} have been used to recalculate the damage strain tensor $\boldsymbol{\varepsilon}^d$. The calibration of damage parameters in the damage initiation locus $D_{1\sim4}^\alpha$ and those in the transformation matrix d_{ij} is performed using the optimization method to minimize the deviation with experimental results. The equivalent plastic strain (PEEQ)

of the damage strain tensor is calibrated as a function of the stress triaxiality and the Lode angle parameter, as demonstrated in Fig. 4. The symbols with different colors represent the local variables obtained from three distinct orientations. Though a unified anisotropic damage initiation locus is calibrated using the linear transformation matrix; however, it is still challenging to make all data points from experimental results locate the single surface.

Due to the fact that a large dataset covering a wide range of stress states is considered in this study, not all experimental results are located on the anisotropic damage initiation locus. In order to minimize the deviation between experimental and numerical results on the anisotropic damage initiation locus, further developments are necessary to provide more efficient and accurate approaches for the establishment of one anisotropic damage and fracture criterion that is valid for a wide range of loading conditions.

Conclusions

The anisotropic ductile damage and fracture properties of high-strength bainitic steel have been investigated using experimental mechanical characterization on a comprehensive category of specimens and numerical prediction based on the damage mechanics model. The damage parameters have been calibrated for three individual loading directions. Based on these experimental and numerical results, the applicability of the evolving anisotropic plasticity and the damage mechanics models has been validated over a broad range of loading conditions, in which the significance of evolving characteristics of anisotropy and stress state has been revealed as well. Two different approaches have been adopted and compared to establish the relationship between damage initiation criterion and loading orientation considering the influence of stress states. Both methods are efficient in the formulation of one unified anisotropic damage and fracture criterion, however, a certain deviation is also noticed, which requires further developments in the modeling strategies.

References

1. Gu G, Mohr D (2015) Anisotropic Hosford-Coulomb fracture initiation model: theory and application. *Eng Fract Mech* 147:480–497
2. Jia Y, Bai Y (2015) Experimental study on the mechanical properties of AZ31B-H24 magnesium alloy sheets under various loading conditions. *Int J Fract* 197:25–48
3. Lou Y, Yoon JW (2017) Anisotropic ductile fracture criterion based on linear transformation. *Int J Plast* 93:3–25
4. Park N, Huh H, Lim SJ, Lou Y, Kang YS, Seo MH (2017) Fracture-based forming limit criteria for anisotropic materials in sheet metal forming. *Int J Plast* 96:1–35
5. Barlat F, Brem JC, Yoon JW, Chung K, Dick RE, Lege DJ, Pourgoghrat F, Choi SH, Chu E (2003) Plane stress yield function for aluminum alloy sheets—part I: theory. *Int J Plast* 19:1297–1319

6. Hill R (1948) A theory of the yielding and plastic flow of anisotropic metals. *Proc R Soc Lond Ser-A* 193:281–297
7. Stoughton TB, Yoon JW (2009) Anisotropic hardening and non-associated flow in proportional loading of sheet metals. *Int J Plast* 25:1777–1817
8. Stoughton TB (2002) A non-associated flow rule for sheet metal forming. *Int J Plast* 18:687–714
9. Kondori B, Madi Y, Besson J, Benzerga AA (2019) Evolution of the 3D plastic anisotropy of HCP metals: experiments and modeling. *Int J Plast* 117:71–92
10. Lee E-H, Stoughton TB, Yoon JW (2017) A yield criterion through coupling of quadratic and non-quadratic functions for anisotropic hardening with non-associated flow rule. *Int J Plast* 99:120–143
11. Lian J, Shen F, Münstermann S (2018) Evolution of plastic anisotropy and strain rate sensitivity. *J Phys: Conf Ser* 1063(3):012063. <https://doi.org/10.1088/1742-6596/1063/1/012063>
12. Lian J, Shen F, Jia X, Ahn D-C, Chae D-C, Münstermann S, Bleck W (2018) An evolving non-associated Hill48 plasticity model accounting for anisotropic hardening and r-value evolution and its application to forming limit prediction. *Int J Solids Struct* 151:20–44
13. Lian J, Shen F, Liu W, Münstermann S (2018) Forming limit prediction by an evolving non-quadratic yield criterion considering the anisotropic hardening and r-value evolution. *AIP Conf Proc* 1960:150008
14. Shen F, Münstermann S, Lian J (2019) Forming limit prediction by the Marciniak–Kuczynski model coupled with the evolving non-associated Hill48 plasticity model. *J Mater Process Technol* 287:116384. <https://doi.org/10.1016/j.jmatprotec.2019.116384>
15. Besson J (2009) Continuum models of ductile fracture: a review. *Int J Damage Mech* 19:3–52
16. Gurson AL (1977) Continuum theory of ductile rupture by void nucleation and growth: part I—yield criteria and flow rules for porous ductile media. *J Eng Mater Technol* 99:2–15
17. Tvergaard V (1982) On localization in ductile materials containing spherical voids. *Int J Fract* 18:237–252
18. Tvergaard V, Needleman A (1984) Analysis of the cup-cone fracture in a round tensile bar. *Acta Metall* 32:157–169
19. Lemaitre J (1985) A continuous damage mechanics model for ductile fracture. *J Eng Mater Technol-Trans ASME* 107:83–89
20. Bai Y, Wierzbicki T (2008) A new model of metal plasticity and fracture with pressure and Lode dependence. *Int J Plast* 24:1071–1096
21. Mu L, Zang Y, Wang Y, Li XL, Stemler PMA (2018) Phenomenological uncoupled ductile fracture model considering different void deformation modes for sheet metal forming. *Int J Mech Sci* 141:408–423
22. Bai Y, Wierzbicki T (2010) Application of extended Mohr-Coulomb criterion to ductile fracture. *Int J Fract* 161:1–20
23. Mu L, Jia Z, Ma Z, Shen F, Sun Y, Zang Y (2020) A theoretical prediction framework for the construction of a fracture forming limit curve accounting for fracture pattern transition. *Int J Plast* 129:102706
24. Lou Y, Huh H (2013) Prediction of ductile fracture for advanced high strength steel with a new criterion: experiments and simulation. *J Mater Process Technol* 213:1284–1302
25. Mohr D, Marcadet SJ (2015) Micromechanically-motivated phenomenological Hosford-Coulomb model for predicting ductile fracture initiation at low stress triaxialities. *Int J Solids Struct* 67–68:40–55
26. Lian J, Sharaf M, Archie F, Münstermann S (2013) A hybrid approach for modelling of plasticity and failure behaviour of advanced high-strength steel sheets. *Int J Damage Mech* 22:188–218
27. Jia Y, Bai Y (2016) Ductile fracture prediction for metal sheets using all-strain-based anisotropic eMMC model. *Int J Mech Sci* 115–116:516–531
28. Lou Y, Yoon JW (2019) Alternative approach to model ductile fracture by incorporating anisotropic yield function. *Int J Solids Struct* 164:12–24
29. Park N, Huh H, Yoon JW (2018) Anisotropic fracture forming limit diagram considering non-directionality of the equi-biaxial fracture strain. *Int J Solids Struct* 151:181–194

30. Shen F, Lian J, Münstermann S, Kokotin V, Pretorius T (2018) An experimental and numerical investigation of the anisotropic plasticity and fracture properties of high strength steels from laboratory to component scales. *Procedia Struct Integr* 13:1312–1317
31. Shen F, Münstermann S, Lian J (2020) Investigation on the ductile fracture of high-strength pipeline steels using a partial anisotropic damage mechanics model. *Eng Fract Mech* 227:106900
32. Aretz H (2007) Numerical analysis of diffuse and localized necking in orthotropic sheet metals. *Int J Plast* 23:798–840

Shape Optimization of a Cruciform-Like Specimen for Combined Tension and Shear Loading



Minki Kim, Jinjin Ha, and Yannis P. Korkolis

Abstract The present work is concerned with the optimization of cruciform-like specimen shape under combined tension and shear loading. A novel shape of a cruciform-like specimen is proposed, to measure flow stresses under combined tension and shear. The overall concept of the cruciform-like specimen is the combination of general cruciform specimen and simple shear specimen. The proposed cruciform-like specimen has four arms, two of which are used to apply the tension and the other two arms the shear. The dimensions of the gage-section were then optimized to minimize the variation of axial and shear stresses from uniformity, as well as to find the difference with the average stresses, i.e., force divided by current area, so that measured forces can be used to calculate the stresses in experiments. The optimized specimen design was tested by FE simulations with various force ratios to confirm its performance.

Keywords Shape optimization · Specimen design · Cruciform specimen · Combined tension-shear · Stress state

Introduction

Multi-axial material properties are being required to design complex structures for an auto-body. To predict the deformation of the complex structures, finite element simulations must be conducted with accurate yield function and hardening curve considering combined loading conditions, such as tension-the multi-axial stress states. Many types of specimen design, for example tube [1], notch [2], cruciform-like [3], and butterfly [4] specimens, have been developed to measure the material behavior under combined loading conditions. For constitutive identification, using a bi-axial tensile testing machine with a cruciform specimen [5] makes it easy to realize various

M. Kim (✉) · J. Ha · Y. P. Korkolis
Integrated Systems Engineering, The Ohio State University, Columbus, OH 43210, USA
e-mail: kim.7834@osu.edu

J. Ha
Mechanical Engineering, University of New Hampshire, Durham, NH 03824, USA

stress states by controlling the force ratio. In this work, to measure flow stresses for complex stress states a novel shape of a cruciform-like specimen that allows combined tension and shear is suggested. The specimen dimensions are then optimized for the minimum variation of both stress fields for tension and shear from forces divided by current area in the gage sections. Finite element (FE) simulations are performed with the optimized specimen design for various force ratios to confirm its performance.

A Novel Cruciform-Like Specimen

The overall concept of the novel cruciform-like specimen is the combination of general cruciform specimen [6, 7] and the smiley shear specimen [8] as shown in Fig. 1. The proposed specimen has four arms; two arms for tension and the other two arms for shear, so the horizontal force (F_1) and the vertical force (F_2) induce tension and shear on the gage sections, respectively. With the grip width (D) of 30 mm, which is a constraint coming from the grips of the cruciform testing machine, the design parameters are the gage length (L), the gage width (G), the leg width (A), and the neck width (B) as shown in Fig. 1, which are optimized by FE simulations in the next section.

Shape Optimization

To optimize the specimen dimensions, some geometrical constraints are determined such as to avoid the plastic deformation on other parts of the specimen except gage section, for loading in 22-direction.

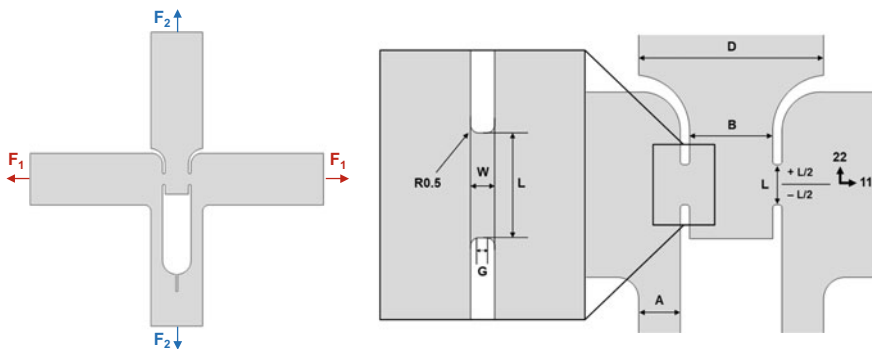


Fig. 1 A novel cruciform-like specimen and design parameters

$$\sigma_{A,yield} \geq \frac{F_2}{2At} \tag{1}$$

$$\sigma_{B,yield} \geq \frac{F_2}{Bt} \tag{2}$$

$$\tau_{L,max} \leq \frac{F_2}{2Lt} \tag{3}$$

The constraints for gage-length can be expressed with letting the $\sigma_{A,yield}$, $\sigma_{B,yield}$ and $\tau_{L,max}$ be determined by the yield stress (σ_y) and the UTS (σ_{UTS}) from uniaxial tensile data along the RD [9], i.e., $\sigma_{A,yield} = \sigma_{B,yield} = \sigma_y$, $\sqrt{3}\tau_{L,max} = \sigma_{UTS}$.

$$L \leq \frac{\sqrt{3}\sigma_y}{\sigma_{UTS}} A \tag{4}$$

$$L \leq \frac{\sqrt{3}\sigma_y}{2\sigma_{UTS}} B \tag{5}$$

For simplicity, the leg width is assumed to be the same with the half of the neck width. The minimum gage length and the gage width are set to 5 mm and 0.5 mm, respectively. Among them, the maximum leg width is determined to be 6.75 mm. The constraint for the gage section can be described as in Eq. (6) for shear deformation, where the gage width is related to widths of other parts except the gage section. The fillet radius (R) can be described as in Eq. (7).

$$G \leq L \tag{6}$$

$$G = \frac{D}{2} - \left(A + \frac{B}{2} \right) - 2R \tag{7}$$

From Eqs. (4–7), the feasible design region is determined as the triangular region as shown in Fig. 2a. Then, 16 design candidates were selected to test the performance for the shape optimization as depicted in Fig. 2b.

The design candidates are examined by FEA to observe the stress distribution in the gage section under the combined tension and shear. All analyses are performed with the ABAQUS 2019 implicit. The applied stress–strain curve is determined by Swift fitting of uniaxial tensile data of AA6013-T4 2.0t [9] and is listed in Table 1. The material property is assumed to be isotropic hardening. The symmetric design of the specimen with respect to the 22-axis allows all FEAs to be performed on the half FE model with boundary conditions shown in Fig. 3. The mesh configuration of the gage section consists of plane stress, quadratic, reduced integration elements (CPS8R), with the element size of 0.1 mm. The force ratio ($F_1 : F_2$) was set to (1:2) corresponding to the ratio of axial stress to shear stress of (1:1).

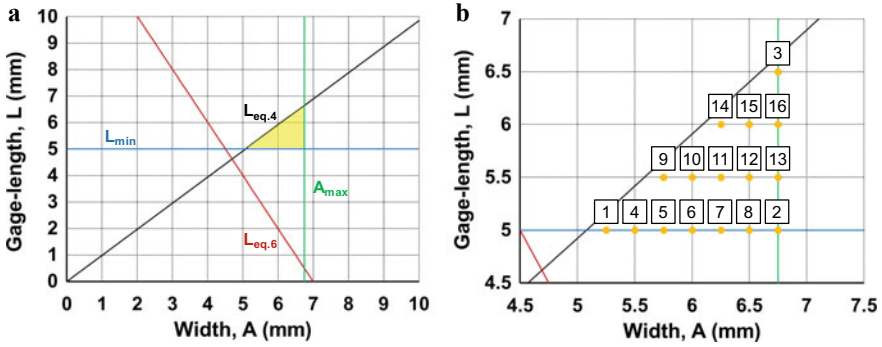


Fig. 2 Feasible design: a region, b candidates

Table 1 Coefficient of Swift fitting

Swift fit $\bar{\sigma} = k(\epsilon_0 + \bar{\epsilon})^n$		
k	ϵ_0	N
628.5	0.02396	0.2785

Fig. 3 Boundary conditions and mesh configuration on gage section

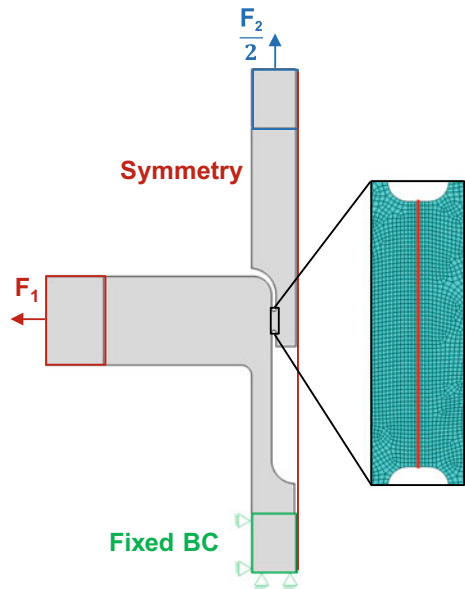


Figure 4 shows an example of the distribution of the equivalent plastic strain with respect to the displacement in 22-direction (U_2) for the design option 3 (see Fig. 2b). Stress or strain concentration occurs at the fillet region because of the geometrical characteristics. This concentration becomes larger and larger during the deformation

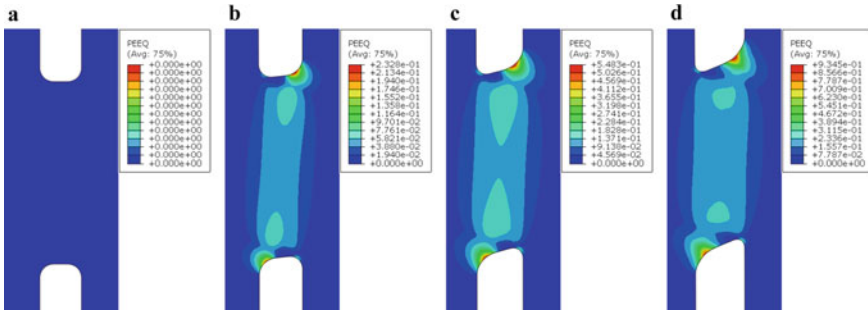


Fig. 4 Equivalent plastic strain distribution at U_2 of: **a** 0 mm, **b** 0.4 mm, **c** 0.8 mm, **d** 1.2 mm. Note that each color bar is on a different scale

due to tension and shear loading, so that the level of equivalent plastic strain is the largest at the fillet region.

To evaluate the distributions of the axial stress (σ_{11}) and shear stress (σ_{12}) on the gage section, the stresses were extracted from the centerline on the gage section for all design candidates. Designs 1, 2, and 3 were selected first to confirm the stress uniformity on the gage section for extreme cases of the feasible design region. Figure 5 shows the axial stress and shear stress distribution according to the displacement in 22-direction. Each dashed line describes the force divided by current area (A) corresponding to experimental stress calculation, $\frac{F_1}{A}$ for axial and $\frac{F_2}{2A}$ for shear. The current area at each displacement U_2 is calculated by summation of the current area for each node, see Eq. (8), where N is the number of nodes along the centerline of the gage section. The axial and shear stress distribution come closer to the dashed line and the uniform region increases when the design number increases from 1 to 3, meaning that a longer gage length and a shorter gage width are preferable.

The cost function (f) is defined by Eq. (9) as the sum of the variation of axial and shear stresses from the forces divided by the current area, i.e., the average stresses.

$$A = \sum_{i=1}^N l^i t^i \tag{8}$$

$$f = \frac{1}{N} \sum_{i=1}^N \sqrt{\left(\sigma_{11,FEA}^i - \frac{F_1}{A}\right)^2} + \frac{1}{N} \sum_{i=1}^N \sqrt{\left(\sigma_{12,FEA}^i - \frac{F_2}{2A}\right)^2} \tag{9}$$

For shape optimization, the cost function values of the design candidates are evaluated to find out the optimized solution that has the minimum cost function value as shown in Fig. 6. The design 3 has the minimum values regarding the U_2 except 0.2 mm meaning the early part of the deformation. The total summation of the cost function values is still the smallest for design 3. The final design, therefore, is determined with the design 3 that has the gage length of 6.5 mm, the gage width of 0.5 mm, the leg width of 6.75 mm, and the neck width of 13.5 mm.

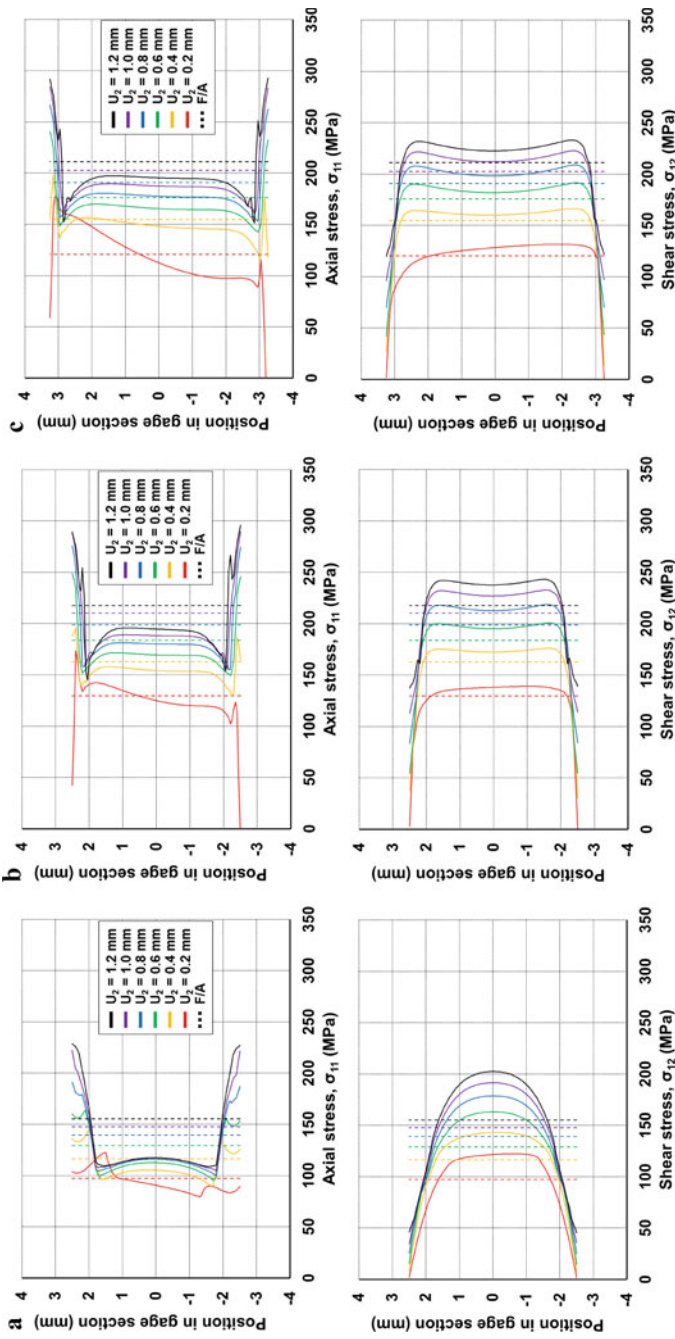
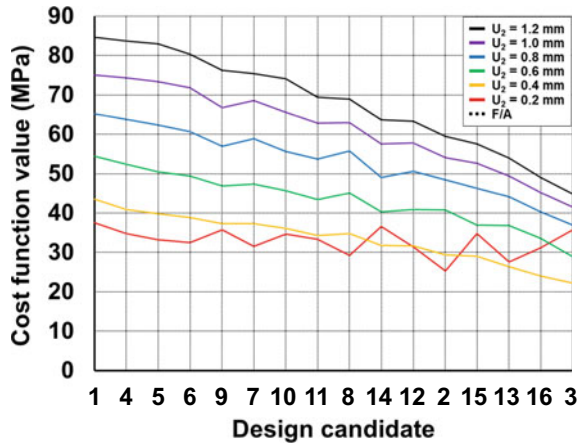


Fig. 5 Axial and shear stress distribution during deformation: **a** Design 1, **b** Design 2, **c** Design 3

Fig. 6 Cost function value



In order to confirm the performance of the optimized specimen design, FEA is conducted with the different force ratios of (1:8) and (2:1). The former force ratio indicates combined tension and shear but most deformation is induced by shear, while in the latter force ratio, the most deformation is induced by tension. Figure 7 shows the

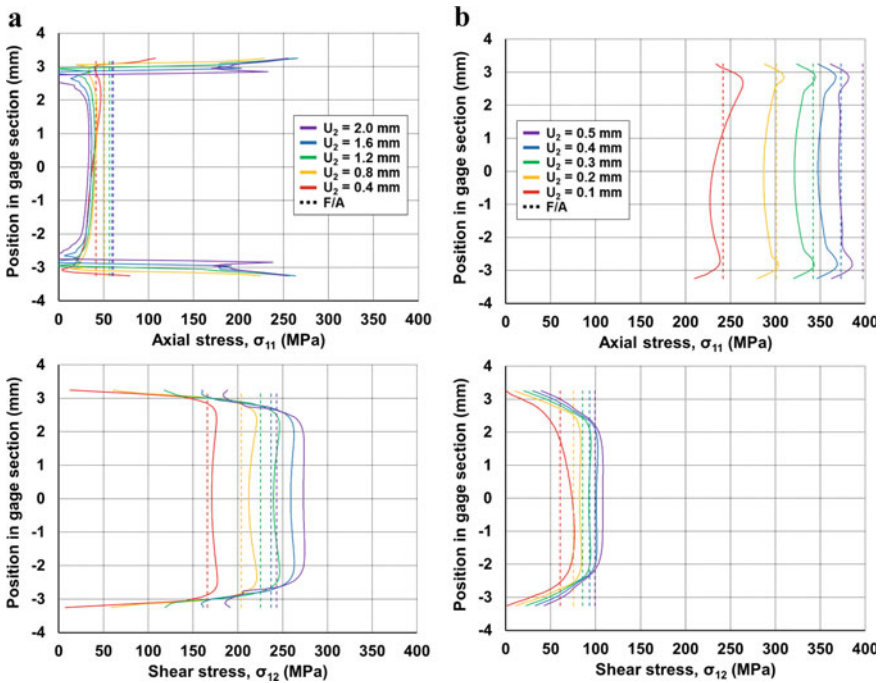


Fig. 7 Stress distribution with force ratio of: a 1:8, b 2:1

axial and shear stress distribution with regard to U_2 . The overall stress distributions for both force ratios are showing a good uniformity, but the difference between the stresses and the force divided by the current area is not small when the deformation amount is high. The optimized design can be utilized to measure the multi-axial properties with the correction of measured stress levels by a comparison between the stress level in FEA and experiments [9, 10]. For experimentally measuring the axial and shear stresses without the correction, further study for shape optimization will be performed with an extended feasible region to find out a dimension set showing a good stress uniformity and stress levels closer to the force divided by the current area.

Conclusion and Future Works

In this work, a novel cruciform-like specimen with four arms was proposed to obtain multi-axial material properties under combined tension and shear. Specimen dimensions were optimized by FEA with various design candidates in the feasible design region. The final design was determined with the optimized dimension set, which has the minimum value of the cost function. The performance of the final design was confirmed by FEAs with various force ratios. In future work, the optimization will be performed with an extended feasible design region so that various design candidates will be examined to determine the one showing a good uniformity of stress distribution, and proximity to the force divided by the area.

Acknowledgements This work was performed under awards CMMI-1563216 and -1929873 from the U.S. National Science Foundation. This support is acknowledged with thanks. We also thank Samantha Bonica for early work on this project.

References

1. Korkolis YP, Kyriakides S (2009) Path-dependent failure of inflated aluminum tubes. *Int J Plast* 25(11):2059–2080
2. Mohr D, Dunand M, Kim KH (2010) Evaluation of associated and non-associated quadratic plasticity models for advanced high strength steel sheets under multi-axial loading. *Int J Plast* 26(7):939–956
3. Gerke S, Adulyasak P, Brünig M (2017) New biaxially loaded specimens for the analysis of damage and fracture in sheet metals. *Int J Solids Struct* 110–111:209–218
4. Dunand M, Mohr D (2011) On the predictive capabilities of the shear modified Gurson and the modified Mohr-Coulomb fracture models over a wide range of stress triaxialities and Lode angles. *J Mech Phys Solids* 59(11):1374–1394
5. Kuwabara T (2007) Advances in experiments on metal sheets and tubes in support of constitutive modeling and forming simulations. *Int J Plast* 23(3):385–419
6. Deng N, Kuwabara T, Korkolis YP (2018) On the non-linear unloading behavior of a biaxially loaded dual-phase steel sheet. *Int J Mech Sci* 138–139:383–397

7. Deng N, Kuwabara T, Korkolis YP (2015) Cruciform specimen design and verification for constitutive identification of anisotropic sheets. *Exp Mech* 55:1005–1022
8. Roth CC, Mohr D (2016) Ductile fracture experiments with locally proportional loading histories. *Int J Plast* 79:328–354
9. Ha J, Baral M, Korkolis YP (2018) Plastic anisotropy and ductile fracture of bake-hardened AA6013 aluminum sheet. *Int J Solids Struct* 155:123–139
10. Tian H, Brownell B, Baral M, Korkolis YP (2017) Earing in cup-drawing of anisotropic Al-6022-T4 sheets. *Int J Mater Form* 10:329–343

Part IV
Machine Learning and Big Data

Data-Based Prediction Model for an Efficient Matching Process in the Body Shop



Arndt Birkert, Johannes Weber, Moritz Nowack, Christian Schwarz,
Benjamin Hartmann, and Philipp Zimmermann

Abstract Achieving the optimal dimensional quality for automotive body parts today is a time and cost-intensive process still often based on trial-and-error approaches. There are two ways to improve the accuracy in the production process: Early modification of the tools in the press shop is one way to significantly manipulate the dimensional quality of parts, although resulting in high costs. The other—much more time and cost-effective—way is trying to change the geometry in the body shop, although providing a lesser adjustment range. Definition of a reasonable parameter adjustment in a single joining stage needs expert knowledge because the adjustment of a single fixture component can have a complex impact on the final assembly. In this publication, a new approach based on finite element simulation and statistical methods is presented being able to characterize the interactions between clamp settings and assembly geometry and to identify the main impact factors on the dimensional accuracy of assembled body parts. The surrogate model is based on smart data, gathered from FEM simulations.

Keywords Body manufacturing process · Body shop · Body-in-white · Matching process · Assembly simulation · Smart data · Coupled process analysis · CPA · Machine learning · FEM simulation

Introduction

Considering the customers' increasing expectations of vehicle quality in terms of design, appearance, and functionality, the manufacture of dimensionally accurate and robust car bodies represents a fundamental aspect of automotive production. Typically, even slight variations in gaps between body assemblies, such as side panel

A. Birkert (✉) · M. Nowack · B. Hartmann · P. Zimmermann
Inigence Gmbh, Bernbachstr. 36, 74626 Bretzfeld, Germany
e-mail: arndt.birkert@inigence-gmbh.de

J. Weber · C. Schwarz
Fraunhofer Institut Für Werkzeugmaschinen Und Umformtechnik, Reichenhainer Straße 88,
09126 Chemnitz, Germany

frames and doors, can have a significant impact on the visual appearance of a vehicle. Throughout the body manufacturing process, many process influences affect the quality of the body assemblies (e.g. geometry variations of the individual parts) potentially resulting, in the geometry lie far outside the required tolerances [1]. This means that the ramp-up phase until the start of production (SOP) is characterized by time-consuming and cost-intensive adjustment loops. The shortening of these trial and error processes is an essential criterion for achieving competitive advantages in automotive manufacturing.

To achieve the highest possible degree of process capability, the numerical validation of individual process steps in car body production based on the finite element method (FEM) is part of the industrial standard [2]. The springback and gravity simulations performed are the prerequisite that enables a valid analysis of the dimensional quality of individual parts and assemblies at an early stage of development. In the automotive production process, the application of simulation methods based on the finite elements has been state of the art since decades [3]. The simulation results can then be used during the planning phase as well as at the start of the series production process in order to save time-consuming and cost-intensive quality loops [2]. Frequently used simulation engines are the commercial packages *AutoForm*, *PAM-STAMP*, *ANSYS*, or *LS-DYNA*.

Due to the large number of adjustment options along the automotive process chain, the identification of complex interactions based on trial and error approaches is not very target-oriented, so simulation is increasingly supplemented by parameter studies. Especially in the field of sheet metal forming and assembly simulation, Machine Learning (ML) methods are used to predict and optimize the effects of undesired process variations on the quality of parts and assemblies [4].

Through the integration of statistical methods into the virtual production process, it is possible to perform systematic variant calculations in the form of parameter studies. In automotive industry, studies are frequently employed to support, among others, the following tasks:

- springback compensation in sheet metal forming [5–7].
- robustness evaluation and optimization of the manufacturability of drawn parts during deep drawing to identify critical areas [8].
- optimization of the dimensional accuracy of assemblies [9].
- 3D representation of statistical measures on the surface of discretized scan or FE meshes by data reduction methods [10–12].
- identification of typical hemming defects [13, 14].
- sensitivity analysis to identify quality-relevant process parameters along the automotive process chain [11, 15].

An important approach for systematic use of parameter studies in the automotive environment is the method called Coupled Process Analysis (CPA) presented in [15]. The main advantage is the shape-based (elementwise) visualization of statistical quantities on the surface of FE and scan meshes in sheet metal forming and assembly processes. The procedure is shown in Fig. 1.

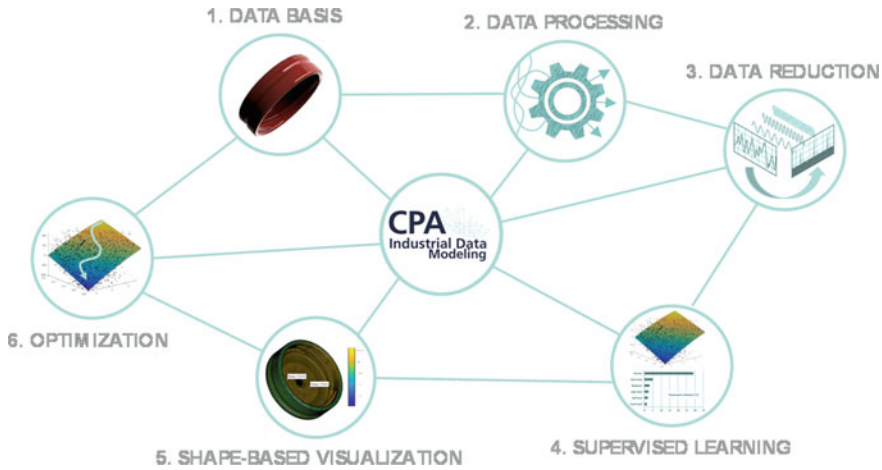


Fig. 1 CPA algorithm [15]

The method can be divided into five steps: In the first step, simulation variants are calculated by varying defined input parameters (e.g., variations of clamp and pin positions in fixture). The second step is to standardize the inconsistent simulation data. In the next step, the mesh-based simulation results (deviations from CAD target) are transformed into a low-dimensional feature space. The idea is a feature map of large data sets into a new coordinate system so that the input data can be described using a small number of geometric error modes. In the fourth step, surrogate modeling is performed in the low-dimensional feature space. Here, the input parameters are functionally linked with the error modes by linear and quadratic regression models. The models can also be used to estimate the sensitivities of the parameters in the feature space by variance-based methods. Through the possibility of inverting the feature mapping, a functional connection can be made between the surrogate models and the real space domain. This connection enables the shape-based visualization of sensitivities on the part geometry (step 5) and the optimization of the input parameters in the sixth step.

From these observations, it can be concluded that it is highly relevant to study how FE simulations and machine learning methods can be integrated more tightly, in particular, to find process-relevant parameters, which influence the dimensional quality of parts and assemblies. Therefore, within the present publication, a concept is presented that allows the identification of relevant process parameters affecting the dimensional accuracy of assemblies based on FEM simulations. The CPA algorithm presented in [15] is used for the statistical analysis of the correlations.

Overview of the Developed Concept

The developed concept is presented in the following with the corresponding workflow shown in Fig. 2.

1. Forming simulation with *AutoForm*

The scatter of springback of the stamped part is strongly influenced by the variation of the sheet thickness, by the process forces of the press (e.g. blankholder force), the blank position in the die, the friction and material properties (yield stress and anisotropy of the material) [1]. Therefore, in a first step, the geometric variations of body parts are obtained by simulating the stamping process with varying parameters in *AutoForm*. The individual parts (subject to springback) are used as input data for the subsequent assembly simulations done with *ANSYS*. The idea is to take the individual part variation into account in the assembly simulation, the variation of the individual part geometry realistic, simulated deformations.

2. Assembly simulation with *ANSYS*

The second step is the assembly simulation with *ANSYS*. With the chosen simulation model, it is possible to account for the sheet thickness distribution, a provided stress state and the (deviating) geometry of each individual part. In addition, it is possible to map the current configuration of the fixture. This includes the kinematics of the fixture units, clamping and joining sequence as well as the position of the clamps in the fixture. The assembly simulation process can be divided into several steps: First, the individual parts are inserted into the fixture, then the clamps are closed, the individual parts are joined by connecting nodes, the clamps are released and finally the joined assembly

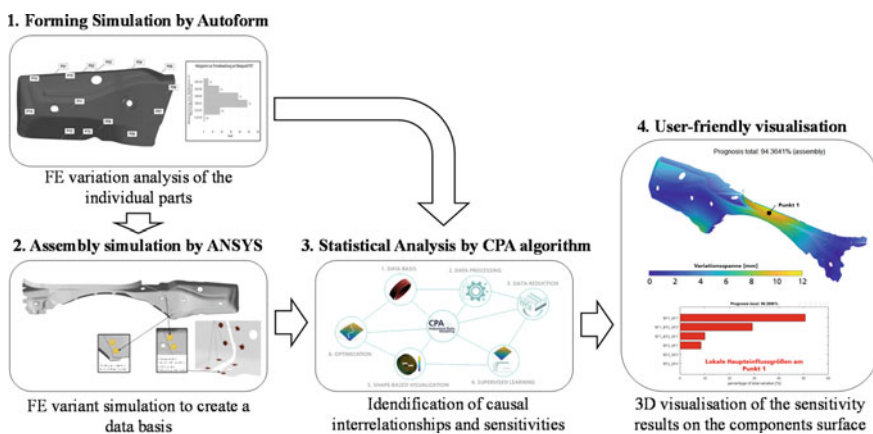


Fig. 2 Developed concept to identify process relevant parameter

(positioned according to RPS) is measured to determine the deviation between measurement and reference geometry (CAD).

The primary objective of the study is to identify changes in the dimensional quality of the assembly as a consequence of a defined adjusting of the clamps of the fixture. In order to systematically generate input data for the CPA algorithm, a design of experiments (DOE) plan is created with various settings of the clamps of the fixture. In the context of the investigation, the simulation model has been extended so that various settings of the clamps of the fixture can be implemented and corresponding simulations are calculated automatically.

3. Statistical analysis by CPA algorithm

Based on the *ANSYS* simulation data, CPA is used to identify how the clamps of the fixture varied in step 2 and influence the dimensional accuracy of the assembly. For this purpose, a surrogate model is built, which approximates the relationship between clamps settings and part geometry.

4. User-friendly visualization

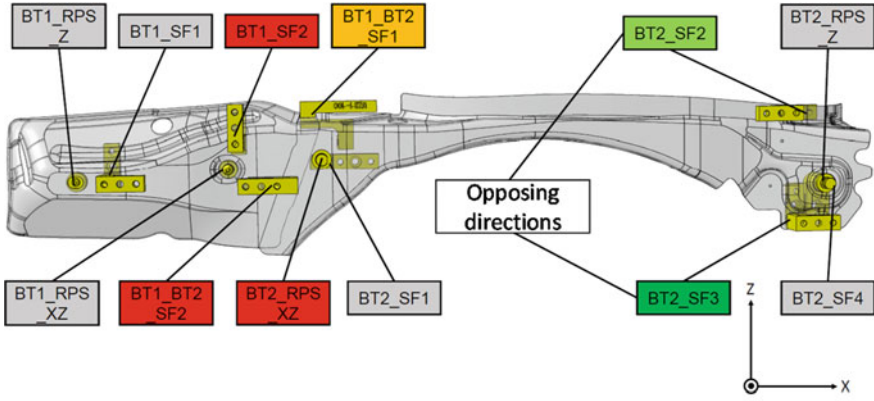
With the CPA algorithm, the calculated sensitivities of the clamps can be visualized node-based on the FE mesh surface in the last step.

Sensitivity Analysis of a Wheelhouse Sub-Assembly

In the first case study, the presented concept is applied to a two-piece sub-assembly of a wheelhouse. The aim is to identify the influence of six clamps of the fixture on the dimensional quality of the sub-assembly. Figure 3 shows the varied input parameters within the simulation model.

Based on the input parameters, ten samples are generated using a random-based sampling strategy (Latin hypercube), and the final dimensional accuracy is calculated for each test variant using the *ANSYS* simulation engine. The resulting FE meshes are standardized as an input for the CPA algorithm, where they are linked to the input parameters by statistical models. For analyzing the sensitivity effects of the clamp parameters, a *MATLAB*-based graphical user interface (GUI) was designed, with which the user is able to apply the CPA algorithm independently and menu-driven. The mesh-based results of the CPA method for identifying cause–effect relationships can be seen in Fig. 4.

The results show that the prognosis quality of the CPA model is very high. A total prognosis of approx. 94% (coefficient of determination) can be achieved. The upper bar chart in Fig. 4 on the left shows that the clamp parameter “BT1_SF1” has the greatest influence on the dimensional accuracy with almost 50%, followed by the clamp parameter “BT1_BT2_SF2” with 27%. Likewise, the local sensitivity on each FE-node of the entire *ANSYS* mesh can be determined by the CPA model. The lower bar chart in Fig. 4 shows the impact of the different clamp parameters on a single point 1 (position is indicated on the right-hand side of Fig. 4). The point lies in an area



Sample	Variation of clamp parameters [mm]					
	BT1_SF1	BT1_BT2_SF2	BT1_BT2_SF1	BT2_SF1	BT2_SF2	BT2_SF4
0	0	0	0,0	0	0	0
1	0,7	1,6	0,3	5	0,6	-1,9
2	-5	-5	0,8	0	-0,7	1,1
3	2,7	4,7	0,1	-5	-2,5	-1,8
4	5	3,3	0,6	1,4	-1,7	2,2
5	-0,7	3,5	0,4	3,9	-1,1	-0,3
6	-2	1,7	0,9	-3,8	-0,5	2,5
7	-3,1	3,1	0,7	1,1	2,2	1,9
8	-2,1	5	0,1	-2,7	2,5	-2,5
9	-3,2	-5	0,2	0,7	1,4	1,6
10	2,3	3,8	0,5	1,6	2,4	-0,8

Fig. 3 Varied input parameters within the simulation model

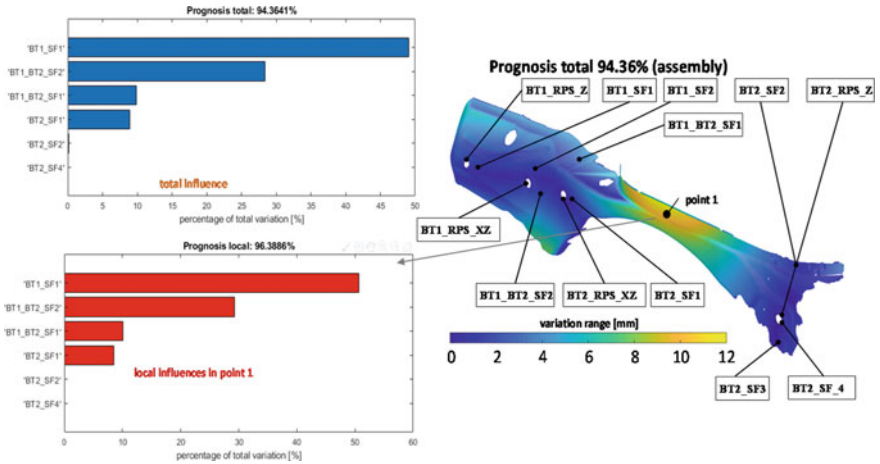


Fig. 4 CPA results of the wheelhouse sub-assembly

with a very high variation range of about 8 mm (Fig. 4—right). A local prognosis value of approx. 96% can be obtained here. Due to the high prediction quality of the model, it can be stated that the CPA model works well for this multi-part body assemblies.

Sensitivity Analysis of a Structural Side Panel

With the developed procedure, it is also possible to simulate the manufacturing process of more complex assemblies; such as the structural side panel shown in Fig. 5. The assembly, which is produced in four (sub)-assembly stages, consists of nine individual parts. One simulation result with a modification of the clamping settings in the last assembly stage is shown as an example. The so-called *shim task* causes the *b-pillar* to rotate transverse to the driving direction (around the y-axis). Figure 5 visualizes the clamp and pin positions in fixture (P_n). The rotation of the *b-pillar* by approx. 5 degrees is achieved by adjusting the P4, P10, P13, P24, P44, and P45. In addition, the *b-pillar* is displaced by 0.1 mm in opposite driving direction. Figure 5 includes the quantitative adjustments of the clamps and pins (P_n).

Figure 6 shows the simulation result with rotated *b-pillar*. The maximum deviation to the reference at the assembly amounts to 3.7 mm in the transition area to the *roof rail* (*M3* in Fig. 6). This simulation result—as one among many ($n > 10$)—is used

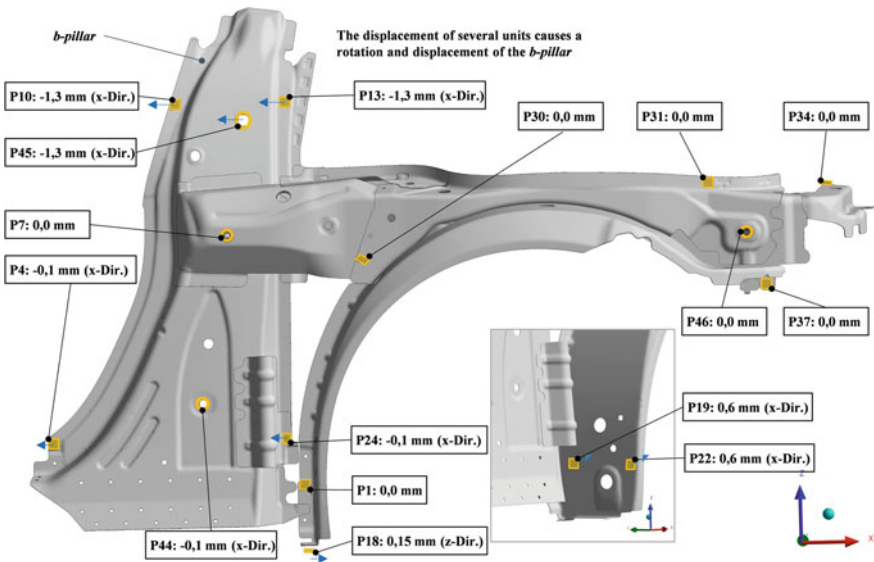


Fig. 5 Clamp and pin positions in structural side panel fixture (P_n) and the belonging adjustment value

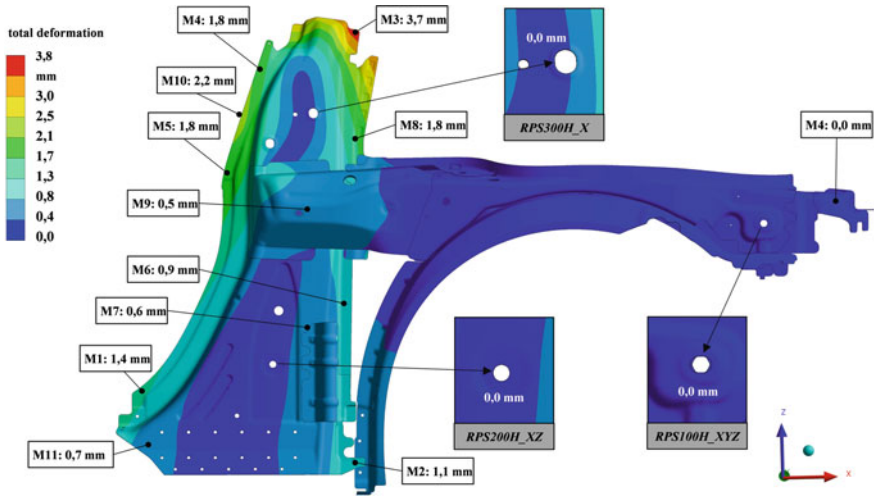


Fig. 6 Simulation result; *total deformation* as a measure of deviation from the reference geometry

by the CPA algorithm to create a surrogate model for predicting the influence of a *shim task* on dimensional accuracy of the assembly (Fig. 7).

Again, a high prognoses quality of approx. 91% is achieved. The clamp group 1, located at the bottom of the *b-pillar*, has major influence on the dimensional accuracy. Further validation with practical test series is pending.

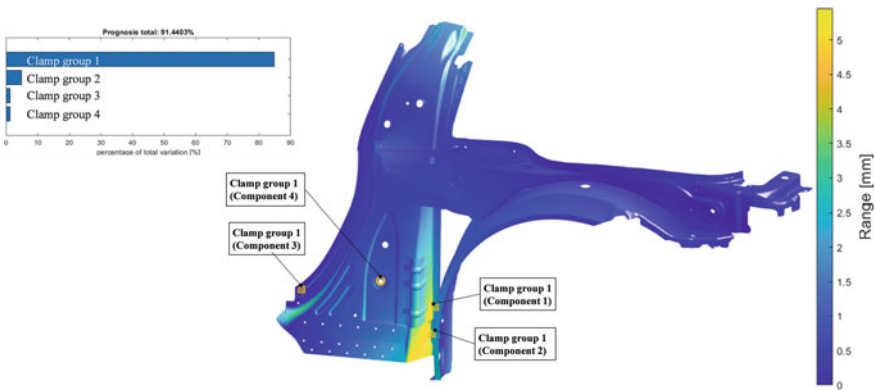


Fig. 7 CPA results of the structural side panel assembly

Conclusion

The construction of dimensionally accurate car body assemblies is a huge challenge in automotive industry. Complex multi-step joining procedures, involving diverse process uncertainties, do not admit simple cause–effect relationships between clamp parameter adjustments and resulting geometrical deviations in the joined assembly. The present paper suggests a new approach based on simulation and statistics, which is able to approximate these interactions to a large extend.

It is possible to map the manufacturing process, involving the stamping process, the assembly and the measurement, completely virtually (*AutoForm*, *ANSYS*). The resulting assembly geometries for varying process input parameters (stamping parameters as well as clamp settings) are given as input to a prediction model based on Coupled Process Analysis (CPA). Here, also measurement data can be provided. Based on the input data, CPA is used to identify how the clamps of the fixture varied in the step before influence the dimensional accuracy of the assembly. For this purpose, a surrogate model is built, which approximates the relationship between clamps settings and part geometry. The results show that the effect of the clamp settings can be predicted with a high accuracy via statistical models even for complex assemblies.

Acknowledgement This research is supported by Federal Ministry of Education and Research (Bundesministerium für Bildung und Forschung BMBF) in context of the collaborative research “KMU-innovativ -Verbundprojekt MoKomp: Modellbasierte Kompensation von Fehlern in der Operationsfolge von Fertigungsprozessen”.

References

1. Birkert A, Haage S, Straub M (2013) Umformtechnische Herstellung komplexer Karosserieteile. Springer, Berlin. <https://doi.org/10.1007/978-3-642-34670-5>
2. Wahl M, Schulz F, Altermann T et al (2011) Die Prozesskettensimulation – Ein Beitrag zum virtuellen Karosseriebau. Reports from the IWU 59: Verlag Wissenschaftliche Scripten, pp 259–269
3. Hofmann M, Neukart F, Bäck T Artificial intelligence and data science in the automotive industry. CoRR 2017; abs/1709.01989
4. Poelmeyer J, Breme M, Wahl M (2015) Process chain simulation at audi tool shop. Reports from the IWU 88: Verlag Wissenschaftliche Scripten, pp 377–384
5. Kakandikar G, Nandedkar V (2018) Springback optimization in automotive shock absorber cup with genetic algorithm. Manuf Rev 5. <https://doi.org/10.1051/mfreview/2017013>
6. Asgari SA, Pereira M, Rolfe BF et al (2008) Statistical analysis of finite element modeling in sheet metal forming and springback analysis. J Mater Process Technol 203(1–3):129–136. <https://doi.org/10.1016/j.jmatprotec.2007.09.073>
7. Wei L, Yuying Y, Zhongwen X et al (2009) Springback control of sheet metal forming based on the response-surface method and multi-objective genetic algorithm. Mater Sci Eng A 499(1–2):325–328. <https://doi.org/10.1016/j.msea.2007.11.121>
8. Wolff S (2015) Robustness analysis of metal forming simulation – state of the art in practice. Reports from the IWU 88: Verlag Wissenschaftliche Scripten, pp 319–334

9. Konrad T, Gasco V, Wiegand K et al. (2015) Sensitivity analysis of forming process parameters regarding the shape accuracy of single and assembled parts. 12th Annual Weimar Optimization and Stochastic Days, Weimar
10. Schwarz C, Ackert P, Mauermann R (2018) Principal component analysis and singular value decomposition used for a numerical sensitivity analysis of a complex drawn part. *Int J Adv Manuf Technol* 94(5–8):2255–2265. <https://doi.org/10.1007/s00170-017-0980-z>
11. Schmadalla V, Schwarz C (2019) Virtual identification of significant parameters regarding the quality of assemblies. In:Bad Nauheim: virtualcarbody conference, pp 22–23
12. Das A, Franciosa P, Pesce A, Gerbino S (2017) Parametric effect analysis of free-form shape error during sheet metal forming. *Int J Eng Sci Technol* 9(09S):117–124
13. Lin G, Iyer K, Hu SJ et al (2005) A computational design-of-experiments study of hemming processes for automotive aluminium alloys. *Proc Inst Mech Eng Part B: J Eng Manuf* 219(10):711–722. <https://doi.org/10.1243/095440505X32661>
14. Gürgen S (2013) A parametric investigation of roller hemming operation on a curved edge part. *Arch Civil Mech Eng* 19(1):11–19. <https://doi.org/10.1016/j.acme.2018.07.009>
15. Schwarz C et al (2022) Model-based joining process design for the body shop process chain international conference on advanced joining processes (AJP 2022). *Proceedings in engineering mechanics* https://doi.org/10.1007/978-3-030-95463-5_2

Deep Learning-Based Defect Inspection in Sheet Metal Stamping Parts



Aru Ranjan Singh, Thomas Bashford-Rogers, Sumit Hazra,
and Kurt Debattista

Abstract Defect inspection is a crucial step in sheet metal stamping manufacturing. However, current inspection methods largely consist of visual inspection by trained operatives but are unreliable and prone to error. Computer vision techniques have the potential advantage of utilising low cost hardware to enable accurate classification of defects particularly through using techniques such as deep learning. Currently, the use of convolutional neural networks (CNN) is one of the best methods in the field of computer vision for classification tasks. Despite the advantages, vision-based deep learning models for detecting defects in sheet material are currently limited to flat sheet materials and certain classes of surface defects such as scratches and delamination. This research proposes a practical deep learning approach for classification of cracks in realistically formed sheet metal stamping components and suggests a route towards reliable and automated inspections in sheet metal stamping. This study used ResNet18, a state-of-the-art deep learning model to classify split defects in “Nakajima” stamped components. The model was able to achieve a 99.9% accuracy on validation set, which implies that this technique could be suitable for automated defect detection on stamped metal parts.

Keywords Deep learning · Sheet metal stamping · Industrial inspection · Image classification

Introduction

Sheet metal stamping components are widely used in every major industrial product from automobiles and aerospace to home appliances. Stamping is used extensively due to its low cost of production compared to other manufacturing processes such as casting and machining. Stamping also has a high production rate and the ability to

A. R. Singh (✉) · S. Hazra · K. Debattista
The University of Warwick, Coventry CV4 7AL, UK
e-mail: aru-ranjan.singh@warwick.ac.uk

T. Bashford-Rogers
University of West of England, Frenchay Campus, Bristol BS16 1QY, UK

© The Minerals, Metals & Materials Society 2022
K. Inal et al. (eds.), *NUMISHEET 2022*, The Minerals, Metals & Materials Series,
https://doi.org/10.1007/978-3-031-06212-4_38

manufacture complex shapes without going through further mechanical processing. Despite all these advantages, defects are the main concern of the stamping process. During stamping, sheet metal is deformed into its net shape with the help of a die and punch set. Ideally, this deformation should be done without causing any local instability. However, in practice, a large amount of force is applied for a small amount of time which adds a number of uncertainties to the process and means that it is impossible to completely avoid unacceptable defects such as splits.

As splits cannot be avoided in practice, they instead must be detected, and the part removed from the production process. The most effective current inspection technique used for defect detection after stamping operations is human vision inspection [9]. This inspection method is costly, time-consuming, and tedious, especially in the case of mass production. Additionally, this technique also suffers from human error, commonly caused by fatigue. Furthermore, the time available to detect defects in between the manufacturing line is limited. Any misclassification, particularly a false negative (not detecting a defect) can continue along the manufacturing line and will likely assemble into sub-assembly or final product. Scrapping a product later in the production process incurs a substantial cost. Therefore, finding a reliable and robust inspection method that occurs immediately after the sheet metal stamping process is necessary.

An alternative to human inspection is to use computer vision-based approaches. These have the potential to be fast, easy to implement and cost-effective solutions to visual inspection. In defect detection on complicated surfaces, conventional computer vision (CV) techniques such as ICA, [6] Gabor filter, [1], and co-occurrence [7] matrices have been studied. However, recent developments in Artificial Intelligence (AI) and Machine Learning (ML) especially in the field of Deep Learning (DL) have changed the way data can be used to produce higher accuracy classifiers. Most modern DL methods for imaging are based on Convolutional Neural Networks (CNN) [5], which automatically learn features for classification without being explicitly programmed.

In spite of the accuracy of CNN models, they have not been widely adopted by industries for sheet metal inspection. In particular to the best of our knowledge, with the exception of [2], no CNN-based studies have been made on sheet metal stamping defects.

This research studies the usefulness and practicality of using CNN- based techniques in sheet metal stamping defect inspections and proposes a practical deep learning approach for defect classification. Since splits are the most common type of defect in stamping parts, in this study a dataset of “nakajima” samples with and without split defects were manufactured and a state-of-the-art CNN model was implemented to classify the defective samples from good samples. Results show that this type of system is able to reliably classify split defects using DL methods.

Defect Inspection Based on Deep Learning

Yang et al. [13] implemented a pre-trained CNN model to detect defects in safety vents for the power battery and achieved up to 99.56% accuracy at a 0.33% false positive (FP) rate. Further model performance was evaluated on a Raspberry Pi to indicate the framework can be implemented in an industrial setup. A improved faster R-CNN-based network is proposed to tackle small size steel defects [14]. For the smaller features and complex shape, they implemented multiscale fusion training and deformable convolutional network (DCN), respectively. They implemented on NEU-DET dataset and achieved a 12.1% improvement in mean average precision (mAP) compared with other state-of-the-art networks. Wang et al. [11] used similar DCN-based faster R-CNN model to identify defect on a real dataset collected from industry. However, they used a ResNet as a base model and DCN-based faster R-CNN in a conditional basis for difficult to classify data. Their method is able to achieve 98.2% accuracy with a low average running time compared to state-of-the-art models.

In the context of industrial surface defect detection, Božič et al. [3] experimented on various open source datasets containing images of defects such as DAGM [12], KolektorSDD [10], and the Severstal steel defect dataset [8]. However, the images in these open source datasets include either artificially created images or only consider flat surface defects like delamination, scratch, casting surface defects. With the exception of [2], no CNN based studies for stamping defects inspection were found in the literature. Therefore, this study proposes a practical CNN approach for classification of realistically formed sheet metal stamping components and suggests a route towards reliable and automated inspections in sheet metal stamping.

Method

Datasets

In this work, 60 defective and 35 non-defective Nakajima samples (Fig. 1 top row) were manufactured. More defective samples were created to capture a wider range of defects than the non-defective samples, which all had a similar appearance. The aluminium samples were manufactured from a flat sheet using a Datron CNC milling machine. A variety of sample widths were manufactured to train the algorithm to detect cracks independent of sample width. As this work is interested in the detection of splits, this method did not follow the full set of samples required for forming limit curve (FLC) evaluation, instead hemispherical samples of different sizes were randomly generated for testing. Then using an Interlaken 225 press, samples were pressed to their final shape. In order to generate cracked samples, the material is deformed until the load cell in the press detects the characteristic load drop associated with the formation of a crack. During the defective sample preparation, average forming height was calculated and used as limit to deformation to generate parts

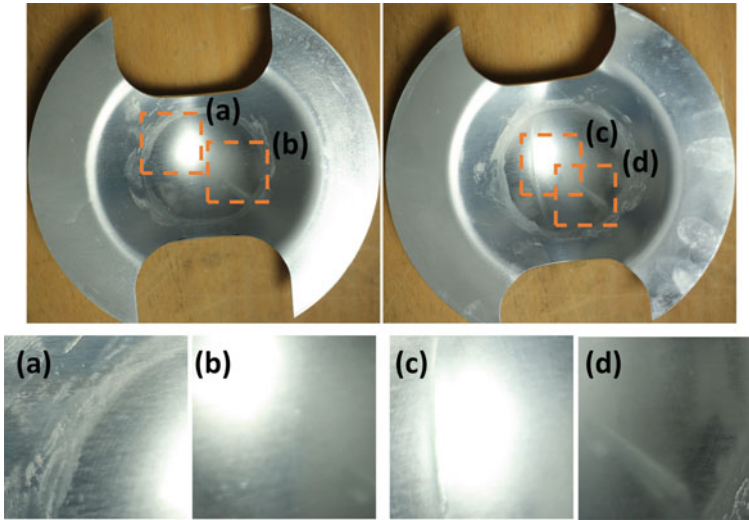


Fig. 1 Top row shows the full manufactured samples, where left top is a good sample and right top is defective sample. **a**, and **b** tile of images extracted from non-defective sample. **c**, and **d** tile of images extracted from defective sample. The tiles without defect, extracted from a defective sample are removed from the dataset manually

without splits. The manufactured samples were placed on a flat surface (concave surface facing up) and photographed with a Canon (MARK III) from a height of 1m.

In order to ensure that the machine learning approach developed in this work learns information about how to classify the presence of a crack from images, it is essential to ensure no confounding factors are present in the dataset. These include features from the background, or from shadows, that may be mistakenly modelled and associated with the split defect.

Therefore, considering the fact defects were present only near the centre of the samples, the images were cropped to the central area as shown in Fig. 1 where the defects would have occurred. Then data set containing 600 defective and 700 non-defective samples was created by augmenting the initial dataset of cropped samples of size $512 * 512 * 3$ with random rotation and flipping of the samples where all the defective and non-defective samples were given equal weight. The cropped images extracted from defective sample without a crack (see Fig. 1d) were removed manually.

ResNet-18

Since this task involves detecting the similar type of cracks from parts with a similar shape, a shallow network can work well for this type of dataset, and we observed this in a pilot study. However, the higher number of layers in DL can generalise more and

can learn better, although this comes with a cost of being difficult to optimise. As a result, the training and testing accuracy can reduce on smaller and simple datasets when the number of layers increases after a limit. Residual networks (ResNet) allows for deeper models without losing performance. ResNet was built on the philosophy that “considering a shallow network as a solution and its deeper counterpart, there exists a solution where it can copy the learnt shallow model and identity function for the extra added model” [4]. This uses a residual connection (by connecting the input to layer, to the output from the layer), which ultimately made the layer to learn the deviation from the input to the layer rather than learning a function from scratch. This also implies that even when a model doesn’t learn anything then also it can keep the input as it is rather than making it to zero as the model weights generally initialised by sampling a zero-mean Gaussian function. Therefore, ResNet gives a freedom of using larger DL models without losing performance.

This kind of model is particularly helpful for our study, since it contains a relatively small set with two classes of data (‘split’ and ‘not split’) and single type of geometry. This experiment used a deep residual network (ResNet-18) [4] with and without pre-trained weights. Fig. 2 shows the architecture of ResNet-18. Originally the network ends with 1000 fully connected outputs and a softmax layer. To apply the ResNet to this experiment a new layer of 2 classes replaced the previous 1000 fully connected layer at the end of the network, then the model was trained using a cross-entropy loss function, and Adam was used as the optimiser with a learning rate 0.001 for 150 epochs.

Results and Discussion

Since there are a relatively small number of samples used in this study, we used fivefold cross-validation for the evaluation of the model to reduce bias in the results. In this technique, the dataset was first divided into five equal subsets, and the model is trained and tested five times on each subset. Each time one subset was used as validation set and the rest as training set.

The metrics used are based on four variables, which can be computed from the output of the classifier: TP (True Positive) means the number defective sample, which are predicted correctly, TN (True Negative) is the number of non-defective samples predicted correctly, FP (False Positive) is the number of good sample predicted as defects and FN (False Negative) is the number of samples containing defects predicted to be good.

Recall is the most important evaluation metric in quality control due to high cost associated with any false prediction of defective samples. Whereas, precision is important when the cost for a false positive is high. Therefore, a trade-off between precision and recall is necessary, which can be accomplished by the ‘F1’ score (defined below). We also include the commonly used metric of accuracy in our results. The metrics are calculated as follows:

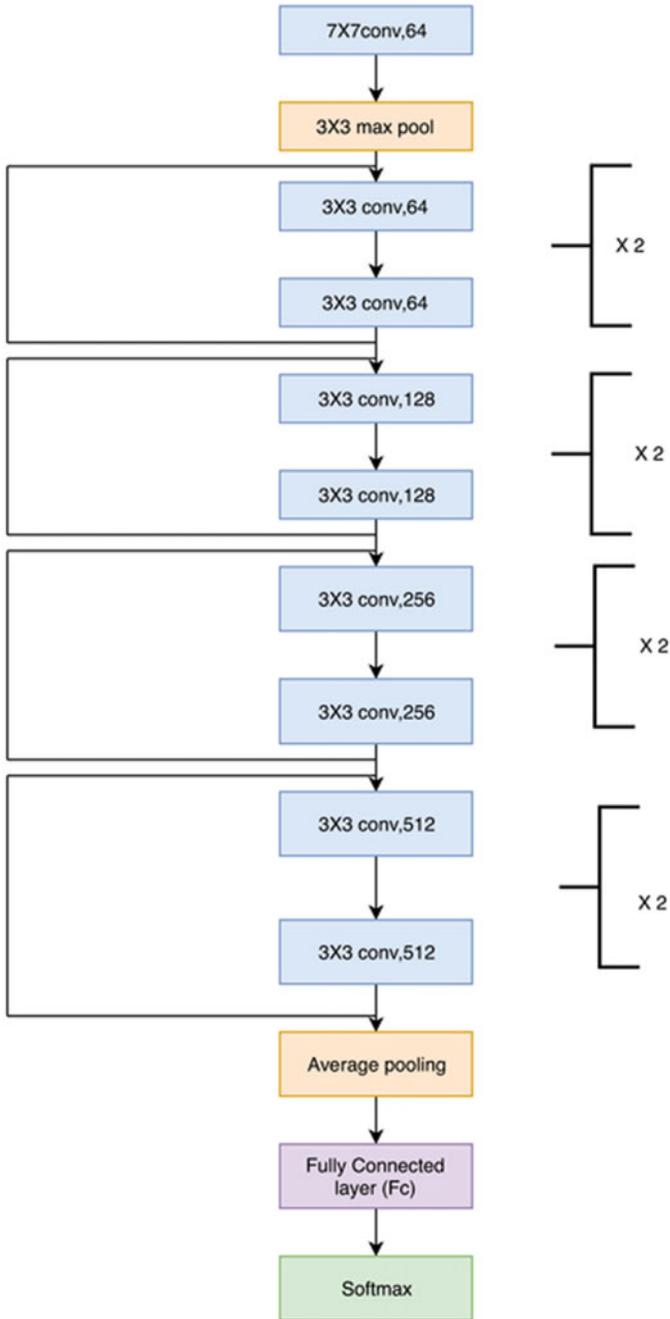


Fig. 2 ResNet-18 architecture [4]

$$accuracy = \frac{TP + TN}{TP + TN + FP + FN}$$

$$precision = \frac{TP}{TP + FP}$$

$$recall = \frac{TP}{TP + FN}$$

$$F1Score = 2 * recall * precision / (recall + precision)$$

The obtained recall precision, F1 score, and accuracy for each K-fold are shown in Table 1. This level of performance may be attributed to the relatively simple part design (made up of single geometry type) and a single defect type. As a result, the defect could be extracted reliably using few convolutions in a manner similar to classical image processing filters, which the CNN is known to be particularly effective. However, the use of multiple layers in DL models allows for multiple features extracted by learnt convolutional kernel to be combined in a non-linear fashion, which is similar to results observed in image processing [5], lead to large improvements over simple edge detection methods.

This can be seen visually in Fig. 3, which shows the types of images used for classification and the results of our method. The top row shows samples without defects, and the bottom row shows samples with defects. All defect-free samples are classified correctly, and almost all samples with defects are detected. However, as is shown in Fig. 3f, the classifier occasionally misclassifies defects, although in this case, it is likely due to limitations of the camera and the lighting in the scene.

Although the results shown in Table 1 are promising and defect detection is indeed possible using DL based models, there are several limitations to the current framework.

This study considered only splits and a simple stamping part, i.e. a FLC sample. In practice, there are more than 25 types of defects with various shapes and sizes found in stamping parts. In addition, different shapes and sizes of stamping parts are used in various industries. Therefore, for the generalisation of the model, the data set should contain more varied examples of both crack and part geometries to further explore the performance of the DL approach. More complicated samples could be chosen iteratively to select those which are harder to classify, this would allow training to

Table 1 Results showing different metrics across multiple folds when testing our method

Matrices	Fold1	Fold2	Fold3	Fold4	Fold5	Avg
Accuracy	1	1	0.996	1	1	0.999
Precision	1	1	1	1	1	1
Recall	1	1	0.991	1	1	0.998
F1-Score	1	1	0.995	1	1	0.999

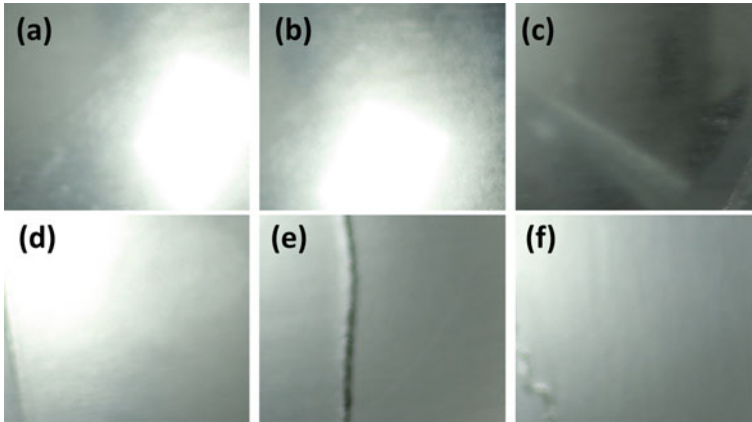


Fig. 3 Example classified samples. **a–c** non-defective samples, and **d–f** are defective samples. From which **f** is the only sample incorrectly classified

better focus on difficult to detect defects. However, creating defective stamping parts is costly due to the parts being scrapped after the dataset preparation. Therefore, in our future work, we will explore to creating a realistic-looking artificial stamping dataset.

The neural network used in this study has high classification accuracy. However, as future developments in machine learning occur the method proposed in this paper can easily be switched to use future network architectures, which may provide higher classification accuracy.

Summary

This paper has proposed an automated defect detection system for stamped metal parts using Deep Learning. This system is based on a state-of-the-art deep learning based model and was trained on and validated with a dataset of real parts. This dataset was created by manufacturing a series of Nakajima samples, which contained parts with and without defects, and used data augmentation to generate a sufficiently large dataset for training. This system achieved high classification accuracy, recall and precision, which indicates that the proposed method can reliably detect defects. These results indicate that computer vision-based defect classification is viable in sheet metal stamping processes.

References

1. Ashour MW, Khalid F, Abdul Halin A, Abdullah LN, Darwish SH (2019) Surface defects classification of hot-rolled steel strips using multi-directional shearlet features. *Arab J Sci Eng* 44(4):2925–2932
2. Block SB, da Silva RD, Dorini LB, Minetto R (2020) Inspection of imprint defects in stamped metal surfaces using deep learning and tracking. *IEEE Trans Ind Electron* 68(5):4498–4507
3. Božič J, Tabernik D, Skočaj D (2021) Mixed supervision for surface-defect detection: from weakly to fully supervised learning. *Comput Ind* 129:103459
4. He K, Zhang X, Ren S, Sun J (2016) Deep residual learning for image recognition. In: *Proceedings of the IEEE conference on computer vision and pattern recognition*, pp 770–778
5. Krizhevsky A, Sutskever I, Hinton GE (2012) Imagenet classification with deep convolutional neural networks. In: *Advances in neural information processing systems*, vol 25
6. Leng Q, Zhang H, Fan C, Deng D (2014) Fabric defect detection using independent component analysis and phase congruency. *Wuhan Univ J Nat Sci* 19(4):328–334
7. Sasaki T, Takada H, Tomura Y (2007) Automatic surface inspection system for tin mill black plate(TMBP) 1. *JFE Tech Rep* 9:60–63
8. Severstal: Severstal: Steel defect detection. Kaggle (2018) <https://www.kaggle.com/c/severstal-steel-defect-detection>
9. Shen Y, Sun H, Xu X, Zhou J (2019) Detection and positioning of surface defects on galvanized sheet based on improved mobilenet v2. In: *2019 chinese control conference (CCC)*, IEEE, pp 8450–8454
10. Tabernik D, Šela S, Skvarč J, Skočaj D (2020) Segmentation-based deep-learning approach for surface-defect detection. *J Intell Manuf* 31(3):759–776
11. Wang S, Xia X, Ye L, Yang B (2021) Automatic detection and classification of steel surface defect using deep convolutional neural networks. *Metals* 11(3):388
12. Weimer D, Scholz-Reiter B, Shpitalni M (2016) Design of deep convolutional neural network architectures for automated feature extraction in industrial inspection. *CIRP Ann* 65(1):417–420
13. Yang Y, Yang R, Pan L, Ma J, Zhu Y, Diao T, Zhang L (2020) A lightweight deep learning algorithm for inspection of laser welding defects on safety vent of power battery. *Comput Ind* 123:103306
14. Zhao W, Chen F, Huang H, Li D, Cheng W (2021) A new steel defect detection algorithm based on deep learning. *Comput Intell Neurosci*

Part V
Multiscale Modeling of Deformation
and Fracture Behavior of Metallic
Materials

Analysis of Damage and Fracture Mechanisms in Steel Sheets: Biaxial Experiments and Numerical Simulations



Michael Brüinig, Moritz Zistl, and Steffen Gerke

Abstract The paper discusses new experiments and corresponding numerical simulations to analyze the effect of proportional and non-proportional loading paths on damage and fracture behavior of steel sheets. An anisotropic continuum damage model is presented based on criteria corresponding to various stress state-dependent damage and failure processes on the micro-level. Experiments with biaxially loaded specimens and corresponding numerical simulations have been performed. Results for proportional and corresponding non-proportional loading histories are discussed. During the experiments, strain fields in critical regions of the specimens are analyzed by digital image correlation technique while the fracture surfaces are examined by scanning electron microscopy. Numerical simulations reveal stress distributions leading to different failure modes. The results demonstrate the efficiency of the experimental program covering a wide range of stress states, the accuracy of the proposed continuum model as well as the effect of loading history on damage and fracture behavior in steel sheets.

Keywords Ductile metals · Biaxial experiments · Damage · Fracture · Non-proportional loading

Introduction

Requests on reduction in energy consumption as well as improvement in cost efficiency, in safety and in lifetime of engineering products, have led to increased research activities to develop high-quality metals during the last decades. Mate-

M. Brüinig (✉) · M. Zistl · S. Gerke
Institute for Mechanics and Structural Analysis, Bundeswehr University Munich,
Werner-Heisenberg-Weg 39, 85577 Neubiberg, Germany
e-mail: michael.bruenig@unibw.de

M. Zistl
e-mail: moritz.zistl@unibw.de

S. Gerke
e-mail: steffen.gerke@unibw.de

© The Minerals, Metals & Materials Society 2022
K. Inal et al. (eds.), *NUMISHEET 2022*, The Minerals, Metals & Materials Series,
https://doi.org/10.1007/978-3-031-06212-4_39

rial strengths have to be enhanced to reduce localization of irreversible strains and to avoid damage and fracture of structural elements under different loading conditions and loading histories. Thus, modeling of constitutive behavior as well as numerical simulation of deformation, damage mechanisms and fracture modes of metals are important aspects of engineering applications.

Characteristics of the damage and fracture mechanisms on the micro-scale depend on stress states and on loading histories. Thus, development of accurate continuum models must be based on detailed investigations of the stress state-dependent and loading path-dependent phenomena. In this context, results of experiments with various specimens have been presented in the literature. For example, stress state-dependent damage and fracture processes have been examined by uniaxial tests with unnotched and differently notched specimens and corresponding numerical simulations [1, 2, 6, 9, 10, 16]. Since these uniaxially loaded specimens only cover a small range of stress triaxialities biaxial experiments with different cruciform specimens have been performed taking into account proportional and non-proportional loading paths [5, 7, 8, 13–15]. The results clearly demonstrate that formation of damage and fracture processes remarkably depend on the loading history and have to be analyzed in further detail.

Therefore, new biaxial experiments and corresponding numerical simulations with the X0-specimen [11] taken from aluminum alloy sheets undergoing different non-proportional loading histories have been performed [12]. They also showed remarkably different damage and fracture processes compared to proportional loading paths. Therefore, further experiments and numerical investigations with steel sheets are presented in this paper. In this context, a continuum damage model is discussed with special focus on different stress states and loading histories. In the experiments, digital image correlation (DIC) technique is applied to monitor formation of strain fields in critical regions of the specimens. After the tests, fracture mechanisms are visualized by scanning electron microscopy (SEM) of the fracture surfaces. Numerical simulation of the experiments reveals stress distributions leading to different damage processes and fracture modes.

Continuum Damage Model

Analysis of damage and fracture behavior in ductile metals is based on the continuum damage model proposed by Brünig [3]. Consideration of damaged and fictitious undamaged configurations is the basis of the kinematic approach introducing elastic, plastic, and damage strain rate tensors.

Plastic behavior is characterized by the yield criterion

$$f^{pl} = a\bar{I}_1 + \sqrt{\bar{J}_2} - c = 0 \quad (1)$$

with the first and second invariants, \bar{I}_1 and \bar{J}_2 , of the effective Kirchhoff stress tensor with respect to the undamaged configurations, a denotes the hydrostatic stress sensitivity parameter and c represents the current yield stress. The isochoric effective plastic strain rate

$$\dot{\mathbf{H}}^{pl} = \dot{\gamma} \bar{\mathbf{N}} \tag{2}$$

predicts the evolution of plastic deformations where $\bar{\mathbf{N}} = 1/(\sqrt{2\bar{J}_2}) \text{dev}\bar{\mathbf{T}}$ is the normalized effective deviatoric stress tensor and γ represents the equivalent plastic strain measure.

In addition, the damage criterion

$$f^{da} = \alpha I_1 + \beta \sqrt{J_2} - \sigma = 0 \tag{3}$$

models onset and continuation of damage. Assuming isotropic initial elastic and plastic behavior the damage criterion (3) is written in terms of the first and second deviatoric stress invariants I_1 and J_2 of the Kirchhoff stress tensor with respect to the damaged configurations and σ denotes material toughness to micro-defect propagation. In Eq. (3), the parameters α and β are damage mode variables taking into account different damage mechanisms acting on the micro-level depending on the stress triaxiality

$$\eta = \frac{\sigma_m}{\sigma_{eq}} = \frac{I_1}{3\sqrt{3}J_2} \tag{4}$$

defined as the ratio of the mean stress $\sigma_m = I_1/3$ and the von Mises equivalent stress $\sigma_{eq} = \sqrt{3}J_2$ as well as on the Lode parameter

$$\omega = \frac{2T_2 - T_1 - T_3}{T_1 - T_3} \quad \text{with } T_1 \geq T_2 \geq T_3 \tag{5}$$

expressed in terms of the principal values T_1, T_2 and T_3 of the Kirchhoff stress tensor.

Furthermore, the damage strain rate tensor

$$\dot{\mathbf{H}}^{da} = \dot{\mu} \left(\bar{\alpha} \frac{1}{\sqrt{3}} \mathbf{1} + \frac{\bar{\beta}}{\sqrt{2}} \mathbf{N} \right) \tag{6}$$

predicts evolution of inelastic strains caused by damage where μ represents the equivalent damage strain measure. In Eq. (6), the stress-related deviatoric tensor $\mathbf{N} = 1/(\sqrt{2J_2}) \text{dev}\bar{\mathbf{T}}$ has been used. The stress state-dependent parameters $\bar{\alpha}$ and $\bar{\beta}$ are kinematic variables denoting the portion of volumetric and isochoric damage-induced strain rates. These variables also correspond to various damage and fracture mechanisms on the micro-level.

It is worthy to note that since the proposed phenomenological continuum model will be used in different engineering applications, its validation must be based on a

number of multiaxial experiments with proportional and non-proportional loading paths, which are discussed for the investigated steel in the present paper.

Experiments and Corresponding Numerical Simulations

Experimental Equipment and Specimen

The experiments are performed with the biaxial test machine shown in Fig. 1a. It contains four electro-mechanically driven cylinders with loads up to ± 20 kN located in perpendicular axes. The specimens are fixed in the heads of the cylinders with clamped boundary conditions. During the experiments, three-dimensional displacement fields in selected parts of the specimens are monitored by digital image correlation (DIC) technique. The stereo setting contains four 6.0 Mpx cameras with corresponding lighting system shown in Fig. 1b.

The investigated material is the steel X5CrNi18-10 (EN 10088-3) and specimens are cut out from thin sheets with 4 mm thickness. The biaxial X0-specimen shown in Fig. 2a has a central opening and four notched regions inclined by 45° . This is the region where displacement fields will be analyzed by DIC. The specimens dimensions are 240 mm in each axis and the depth of the notches is 1 mm reducing the thickness in these parts from 4 mm to 2 mm at the thinnest points. During the tests, the specimen is biaxially loaded by F_1 and F_2 and the movements of the red points, $u_{1,1}$ and $u_{1,2}$ in 1-direction and $u_{2,1}$ and $u_{2,2}$ in 2-direction, shown in Fig. 2b are recorded by DIC. This leads to the relative displacements $\Delta u_{ref,1} = u_{1,1} - u_{1,2}$ and $\Delta u_{ref,2} = u_{2,1} - u_{2,2}$, respectively, used in the load-displacement curves. The different loading paths can be seen in Fig. 2c. In the proportional one, the specimen is biaxially loaded by $F_1 : F_2 = 1$ with the load maximum $F_1 = F_2 = 12.0$ kN. In

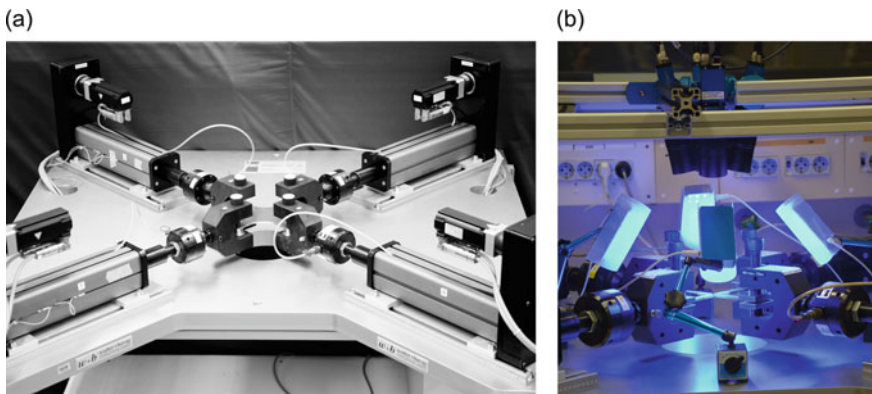


Fig. 1 a Biaxial test machine, b Lighting system and camera equipment

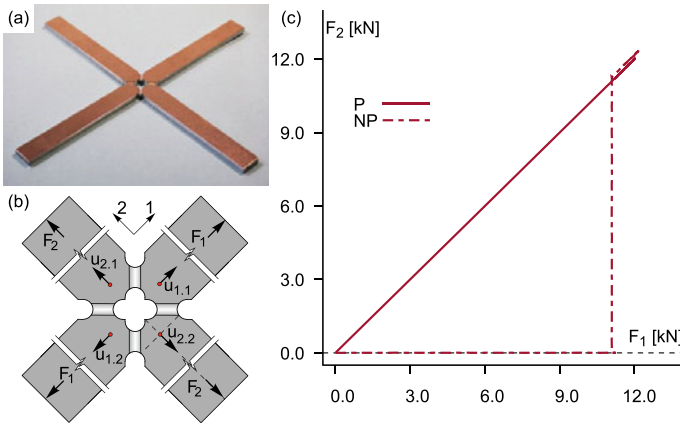


Fig. 2 X0-specimen: a photo, b forces and displacements, c loading path

the non-proportional case, the specimen is first loaded by F_1 only up to $F_1 = 11.0$ kN, then F_1 is kept constant and in axis 2 the additional load F_2 increases up to $F_2 = 11.0$ kN and in the final step the specimen is proportionally loaded up to final fracture.

Numerical Aspects

The numerical simulations have been carried out using the finite element program ANSYS enhanced by a user-defined material subroutine based on the constitutive equations of the proposed continuum damage model. Integration of the constitutive rate Eqs. (2) and (6) is performed by the inelastic predictor–elastic corrector method [4]. In the simulations, eight-node elements of type Solid185 have been used to predict strains and stresses in the specimen.

Results of Biaxial Experiments and Corresponding Numerical Simulations

Load-displacement curves related to axis 1 (a1) and axis 2 (a2), respectively, for the proportional (Fig. 3a) and the non-proportional case (Fig. 3b) show good agreement between experiments (Exp) and the corresponding numerical simulations (Sim). In addition, comparison of the first principal strain fields in the notched region of the X0-specimen is shown in Fig. 4. In particular, at the end of the proportional loading path (P 1/+1 end), high principal strains up to 85% can be seen in the experiment (Exp)

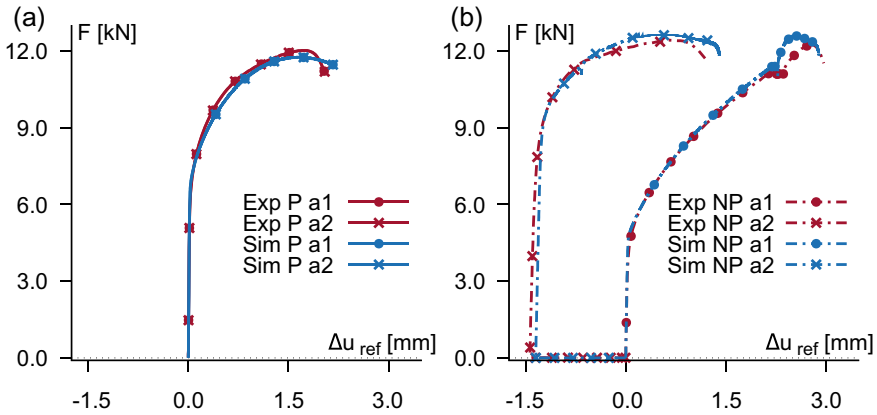


Fig. 3 Load-displacement curves

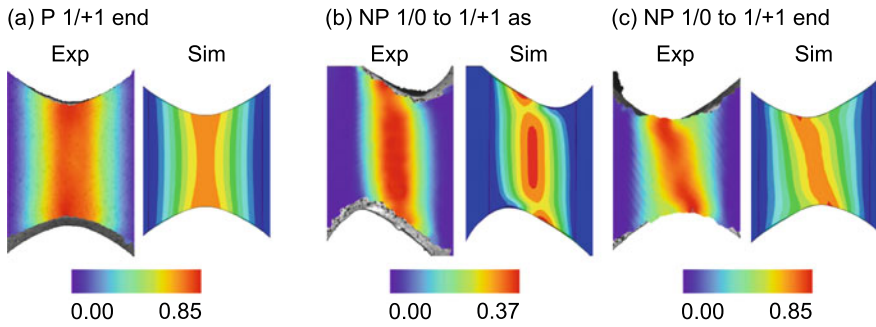


Fig. 4 Principal strain fields

in a widespread vertical band. This behavior is also predicted by the corresponding numerical simulation (Sim) where only slightly smaller strain maxima occur. For the non-proportional loading path, on the other hand, a more localized band of the first principal strain with slightly diagonal orientation after the first load step (NP 1/0 to 1/+1 as) can be seen in the experiment (Exp) with maxima of 37%. At the end of the non-proportional path (NP 1/0 to 1/+1 end), the strains reach values up to 85% localized in a band with diagonal orientation from top left to bottom right. This diagonal band is also predicted by the numerical simulation (Sim) with slightly smaller maxima. The strain fields in Fig. 4 clearly show that the loading history remarkably affects the deformation and localization behavior of the investigated steel.

Based on the numerical simulations, the stress state in the notched regions can be predicted, see Fig. 5. For example, after the proportional loading path, the stress triaxiality reaches the maximum of $\eta = 0.7$ in the center of the notch which decreases to $\eta = 0.5$ at the boundaries (Fig. 5a). The corresponding Lode parameter is $\omega =$

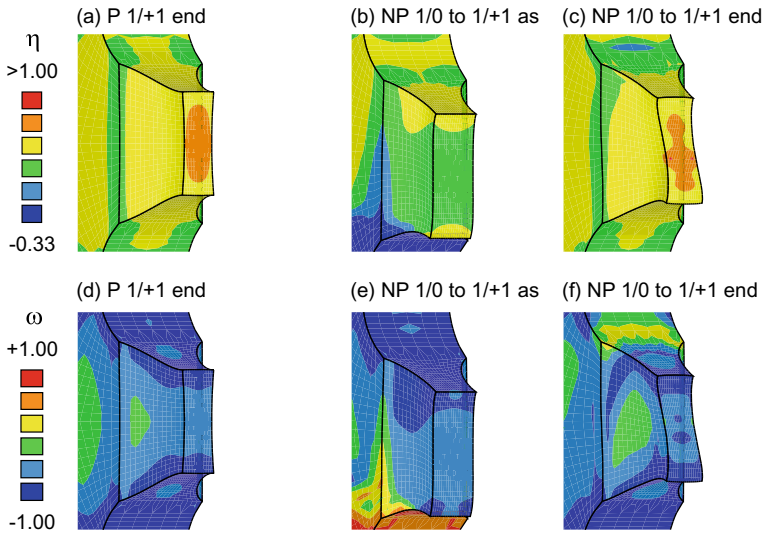


Fig. 5 Stress triaxiality and Lode parameter

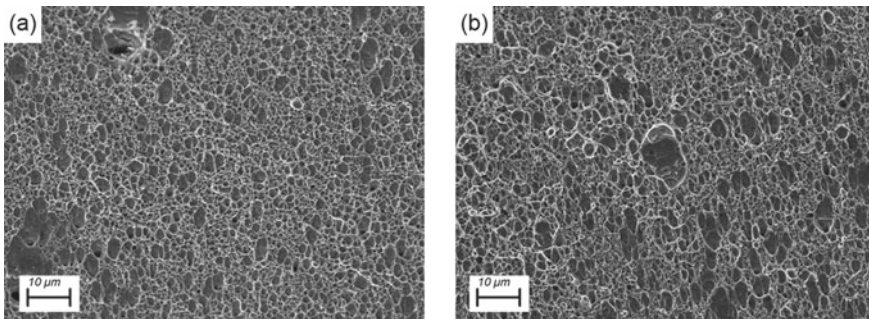


Fig. 6 Pictures from scanning electron microscopy

-0.6 in the center and $\omega = -1$ at the boundaries of the notched region (Fig. 5d). This stress state is characteristic for tensile loading conditions. In the case of the non-proportional loading path the stress triaxiality after the first load step reaches $\eta = 0.3$ in the center of the notch and $\eta = 0.5$ at its boundaries (Fig. 5b). The corresponding Lode parameter is $\omega = -0.6$ in the center and $\omega = -1.0$ in the boundaries (Fig. 5e). After further non-proportional loading the stress triaxiality at the end of the test (shortly before fracture occurs) is $\eta = 0.8$ in the center and $\eta = 0.5$ at the boundaries of the notch (Fig. 5c) whereas the Lode parameter is more inhomogeneous with values between $-1.0 \leq \omega \leq -0.3$ (Fig. 5f). Thus, the final stress state is only marginally influenced by the loading history.

Furthermore, Fig. 6 shows pictures from the fracture surfaces taken by scanning electron microscopy. After the proportional loading path, a regular distribution of

voids can be seen (Fig. 6a) caused by the high-stress triaxiality predicted by the numerical simulation. During the non-proportional loading path, the first loading step leads to growth of voids with superimposed shear mechanisms caused by the predicted moderate stress triaxiality. During the following load steps (see Fig. 2c), the stress triaxiality remarkably increases leading to further growth of voids (Fig. 6b), which are larger compared to the proportional case (Fig. 6a), and the initial superimposed shear mechanisms are still visible. Therefore, the damage and failure processes on the micro-level are affected by the loading history.

Conclusions

The paper discussed a continuum framework to model damage of ductile materials. The phenomenological model takes into account different branches in the damage criteria and damage rule corresponding to different stress state-dependent damage and failure processes on the micro-scale. Evolution of plastic and damage strains is modeled by rate equations, which are numerically integrated by the inelastic predictor–elastic corrector method. Validation of the continuum damage model has been performed by new experiments with the biaxially loaded X0-specimen, and results have been compared with those taken from corresponding numerical simulations. Focus was on biaxial loading conditions and on different loading paths with the same final loading ratio. The analysis revealed the effect of non-proportional loading histories on the damage and fracture behavior in ductile steels compared to proportional ones. In the critical notched regions of the specimen, different stress states have been predicted leading to different stress state-dependent damage processes on the micro level, which were visualized by scanning electron microscopy of fractured surfaces. Thus, evolution of damage and fracture mechanisms is remarkably affected by the loading conditions and the loading histories and have to be considered in validation of accurate material models predicting failure and lifetime of engineering structures.

Acknowledgements The project has been funded by the Deutsche Forschungsgemeinschaft (DFG, German Research Foundation)—project number 322157331, this financial support is gratefully acknowledged. The SEM images of the fracture surfaces presented in this paper were performed at the Institut für Werkstoffe im Bauwesen, Bundeswehr University Munich, and the support of Wolfgang Saur is gratefully acknowledged.

References

1. Bao Y, Wierzbicki T (2004) On the fracture locus in the equivalent strain and stress triaxiality space. *Int J Mech Sci* 46:81–98
2. Bonora N, Gentile D, Pirondi A, Newaz G (2005) Ductile damage evolution under triaxial state of stress: theory and experiments. *Int J Plast* 21:981–1007

3. Brünig M (2003) An anisotropic ductile damage model based on irreversible thermodynamics. *Int J Plast* 19:1679–1713
4. Brünig M (2003) Numerical analysis of anisotropic ductile continuum damage. *Comput Methods Appl Mech Eng* 192:2949–2976
5. Brünig M, Brenner D, Gerke S (2015) Stress state dependence of ductile damage and fracture behavior: experiments and numerical simulations. *Eng Fract Mech* 141:152–169
6. Brünig M, Chyra O, Albrecht D, Driemeier L, Alves M (2008) A ductile damage criterion at various stress triaxialities. *Int J Plast* 24:1731–1755
7. Brünig M, Gerke S, Schmidt M (2018) Damage and failure at negative stress triaxialities: experiments, modeling and numerical simulations. *Int J Plast* 102:70–82
8. Chow C, Lu T (1992) An analytical and experimental study of mixed-mode ductile fracture under nonproportional loading. *Int J Damage Mech* 1:191–236
9. Driemeier L, Brünig M, Micheli G, Alves M (2010) Experiments on stress-triaxiality dependence of material behavior of aluminum alloys. *Mech Mater* 42:207–217
10. Gao X, Zhang G, Roe C (2010) A study on the effect of the stress state on ductile fracture. *Int J Damage Mech* 19:75–94
11. Gerke S, Adulyasak P, Brünig M (2017) New biaxially loaded specimens for analysis of damage and fracture in sheet metals. *Int J Solids Struct* 110:209–218
12. Gerke S, Zistl M, Bhardwaj A, Brünig M (2019) Experiments with the X0-specimen on the effect of non-proportional loading paths on damage and fracture mechanisms in aluminum alloys. *Int J Solids Struct* 163:157–169
13. Green D, Neale K, MacEwen S, Makinde A, Perrin R (2004) Experimental investigation of the biaxial behaviour of an aluminum sheet. *Int J Plast* 20:1677–1706
14. Kulawinski D, Nagel K, Henkel S, Hübner P, Fischer H, Kuna M, Biermann H (2011) Characterization of stress-strain behavior of a cast trip steel under different biaxial planar load ratios. *Eng Fract Mech* 78:1684–1695
15. Kuwabara T (2007) Advances in experiments on metal sheet and tubes in support of constitutive modeling and forming simulations. *Int J Plast* 23:385–419
16. Roth C, Mohr D (2016) Ductile fracture experiments with local proportional loading histories. *Int J Plast* 79:328–354

Damage Evolution in DP600 Sheets Using a Combined Finite Element—Cellular Automata Model



Iman Sari Sarraf, Daniel E. Green, Yang Song, and Javad Samei

Abstract Modelling the damage and fracture behaviour of engineering materials with composite microstructures such as dual phase (DP) steels requires a thorough understanding of not only macro-scale mechanical properties but also microstructural features and characteristics. Quasi-static and high strain rate uniaxial tension tests were carried out to determine the flow curves of DP600 steel sheets and calibrate the constitutive models. Then, electrohydraulic forming test data were used to validate the numerical results. In addition, metallographic examinations were conducted to quantify the material microstructural properties. Subsequently, the Rousselier damage model with a modified Johnson-Cook hardening function was used to determine macro-scale strain, and the ductile and brittle cell arrays were used to determine if each element still has load bearing capacity. The proposed model can be effectively used to evaluate the effect of process parameters and microstructural features such as ferrite grain size on the onset of localisation and fracture of DP steel sheets.

Keywords Dual phase steel · Finite element · Rousselier model · Cellular automata · Ductile damage · Brittle damage

Introduction

Dual phase steels (DP), being low carbon steels, belong to a family of high strength strip grades, which consist of hard second phase islands (usually martensite) distributed across a ductile ferritic matrix [1, 2]. The application of dual phase steels is rapidly growing in the automotive sheet metal forming industry. New high strain-

I. S. Sarraf (✉) · D. E. Green · Y. Song · J. Samei
University of Windsor, 401 Sunset Ave., Windsor, ON N9B 3P4, Canada
e-mail: sarisa@uwindsor.ca

D. E. Green
e-mail: dgreen@uwindsor.ca

Y. Song
e-mail: songw@uwindsor.ca

J. Samei
e-mail: sameij@uwindsor.ca

© The Minerals, Metals & Materials Society 2022
K. Inal et al. (eds.), *NUMISHEET 2022*, The Minerals, Metals & Materials Series,
https://doi.org/10.1007/978-3-031-06212-4_40

rate forming techniques such as electro-hydraulic forming (EHF), which can increase metal formability and uniform strain distribution and decrease usual forming defects [3], are generating a great interest in the automotive industry. Experimental research has shown remarkable improvement in the formability of DP500, DP600, DP780, and DP980 steel sheets that were formed using an electrohydraulic deformation process [4]. Maris et al. [5] derived the high strain rate FLC of DP600 using electrohydraulic free forming (EHFF), and Samei et al. [6] studied the effect of strain path on the damage evolution in terms of the void density, void area fraction, void aspect ratio and mean void size. It has been shown by several researchers that the predominant damage mechanism and failure in DP steels depends on the ferrite and martensite grain sizes and their morphology, and can change from a mixture of cleavage and dimples to a completely ductile failure mechanism, which consists of nucleation, growth, and coalescence of voids during the forming process [2].

The complexity of the microstructural properties of DP steels and their alternating dominant damage mechanisms clearly indicates the importance of multi-scale modelling [7]. As described by Shterenlikht [8, 9], the main problem in conventional finite element analysis software is that an FE is both a material and a structural unit simultaneously. Therefore, they fail to address the micro-scale microstructural features and properties in evaluating the damage mechanisms in non-homogeneous materials. Although the combination of cellular automata and FE has been used for solidification or recrystallisation of materials, Beynon et al. [10] and Shterenlikht [11] were the first to utilise it for evaluating forming and damage behaviour of steels. In this model, the microstructural properties of the material are moved from the finite elements to an appropriate number of cells in two independent cell arrays, responsible for ductile and brittle fracture mechanisms, i.e. embedded cellular automata arrays contain a detailed description of microstructural features and properties. Therefore, the FE mesh is employed to represent the macro-level strain, and stress tensors and damage variables, and the cellular automata arrays with independent and desired size scales are utilised to analyse the microstructural response of the material.

This paper investigates the performance of a combined FE + CA model to predict the dominant damage mechanism of DP600 sheet specimens deformed in uniaxial tension tests at various strain rates and in electrohydraulic free forming.

Theoretical Framework

The Rousselier damage model [12, 13] is a thermodynamically consistent constitutive pressure-dependent plasticity model, which is used to predict the onset of the yielding of materials based on the presence of a certain void volume fraction.

The Rousselier plastic potential (Φ) is:

$$\Phi = \frac{\sigma_{eq}}{(1-f)} - H(\varepsilon_p, \dot{\varepsilon}_p) + D\sigma_k f \exp\left(\frac{\sigma_m}{(1-f)\sigma_k}\right) \quad (1)$$

where σ_{eq} , σ_m , D , and σ_k are the von Mises equivalent stress, hydrostatic stress, and two material parameters that represent the resistance of the void growth, respectively. β is an internal scalar damage variable and f is the current void volume fraction. $H(\varepsilon_p, \dot{\varepsilon}_p)$ describes the hardening behaviour of the material as a function of strain (ε_p) and strain-rate ($\dot{\varepsilon}_p$). In this research, a 5-parameter modified version of the Johnson-Cook [14, 15] hardening function was also utilised to describe the rate-dependent hardening behaviour of DP600 sheet specimens:

$$H(\varepsilon_p, \dot{\varepsilon}_p) = (C_1 + C_2 \varepsilon_p^{C_3}) \left[1 + C_4 \left(\ln \frac{\dot{\varepsilon}_p}{\dot{\varepsilon}_0} \right)^{C_5} \right] \quad (2)$$

In order to make a link between the cell arrays in the cellular automata framework and each element in the FE model, two 3D-cubic cell arrays are used to partition the space for each Gauss point; one array representing the ductile damage behaviour and the other representing the brittle fracture mechanism. The total number of cells in each array can be calculated based on the number of brittle cells per linear FE (c_d and c_b for ductile and brittle CA) and the total number of cells in the ductile and brittle cell arrays are $D_d = c_d^3$ and $D_b = c_b^3$, respectively. Similar to Shterenlikht's work [8], the cells in both cell arrays are neither deformable nor time-dependent. The cell sizes in the ductile and brittle arrays are independent of each other but depend on the micromechanical size scale, as described Faleskog et al. [16] who introduced the concept of "damage cell" or "computational cell". The damage cell size for ductile and brittle fracture is reported to be 0.1–0.5 mm and 0.005–0.05 mm (or 10–20 times larger than the median grain size), respectively [8]. These sizes are related to the observed cleavage facet size, and the spacing between large voids on the fractured surface [11, 17]. Due to the nature of brittle mode of fracture, its damage cell size should be significantly smaller than that of ductile damage mode. A three-dimensional 26-cell Moore neighbourhood was used for each individual cell.

In a CA array, each cell, regardless of the array size and position of the cell, should have a 26-cell neighbourhood. This implies the concept of "self-closing boundary condition" which means that for a cell lying at the edge of a CA the corresponding cells of the opposite edge are considered adjacent. Therefore, for a cell on the edge of a CA array, its 26 neighbouring cells are located at the opposite edge. It is worth noting that to assign the properties of each cell in either a ductile or brittle CA array, a sophisticated random number generator, which is a combination of subtractive Fibonacci generator with a Marsaglia shift sequence along with an additional (different) Marsaglia shift sequence is employed to ensure that perfectly random numbers are generated. Either a uniform, normal, or Weibull distribution function can be selected to be used along with the random number generator. In the ductile cell array, the Rousselier damage model was employed to evaluate the ductile damage behaviour of a dual phase (DP) steel. For each cell in the ductile cell array, only one property is assigned, which is the critical Rousselier damage variable at failure (β_F) based on the initial volume fraction of the material (f_0) that was obtained using X-Ray tomography analysis [18]. A normal distribution random number generator is

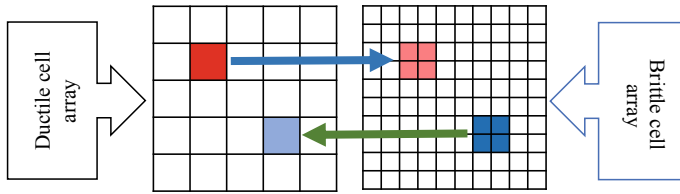


Fig. 1 Illustration of the mapping operation

used to generate f_0 in each cell at the beginning of the simulation. Each ductile cell m can take one of two possible states as “alive” or “dead” based on the comparison between their current β (calculating through the simulations) and β_F . Similar to the ductile cell array, each cell in the brittle CA array carries one property which is the fracture stress σ_f calculated using Smith’s relation [19] based on a Weibull distribution random number generator assigning a grain size value to each cell as described below:

$$\sigma_f = \left[\frac{\pi E \gamma_e}{2(1 - \nu^2) d_p} \right]^{1/2} \quad (3)$$

where E , γ_e , ν , and d_p are Young’s modulus, the effective surface energy of a ferrite-martensite interface, Poisson’s ratio, and the grain size, respectively.

The cells in each array follow rules and criteria that are independent of each other; however, since these two arrays represent the same physical space, the state of a cell in one array would be dependent on the state of a group of cells in the other array. It means that if a cell status changes from *alive* to *dead* in either the ductile or brittle CA array, it should be reflected in the other array in order to take the loss of integrity into account for both CA arrays. This procedure is done using a mapping function and is illustrated in Fig. 1.

Material and Method

Mechanical and Microstructural Properties

The sheet material used in this research was DP600 steel with nominal thickness of 1.5 mm. It has 92.0, 4.7, and 3.3 vol% of ferrite, martensite, and bainite content, respectively [6].

Uniaxial tension tests were carried out on the DP600 sheet specimens in a broad range of strain rates from quasi-static conditions (0.001 and 0.1 s^{-1}) to high strain rates (1000 s^{-1}) using ASTM E8M and miniature “dog-bone” specimens, respectively. A detailed description of the uniaxial testing procedure, specimen geometries, and tools are published by Rahmaan et al. [20].

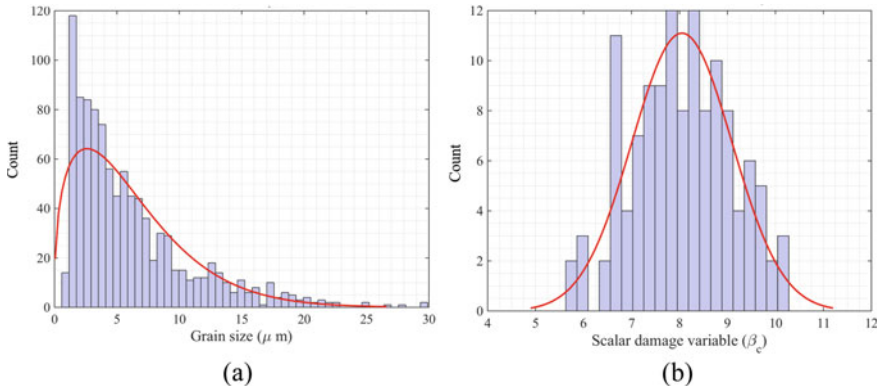


Fig. 2 **a** Distribution of ferrite grain size in DP600 sheet specimens and **b** overall distribution of β_f calculated based on f_0

For each cell in the ductile CA array, the critical scalar damage variable based on the initial void volume fraction, obtained by X-Ray tomography analysis using SkyScan 1172 at 100 kV using Cu/Al filter at resolution $1 \mu\text{m}$ pixel, was determined as the only cell property. Other properties such as the fracture stress as a function of ferrite grain size were defined for each cell in the brittle CA array using optical microscopy. These properties are assigned to each cell in the CA arrays based on three different distribution functions, namely, uniform distribution, normal distribution, and Weibull distribution. The distribution of the ferrite grain size and the Rousselier scalar damage variable are shown in Fig. 2b.

Finite Element Model

The uniaxial tension test is modelled using the modified Rousselier constitutive damage model for the FE-scale part and the hybrid FE+CA model for predicting the evolution of ductile and brittle damage mechanisms. Tensile specimens were meshed using 8-node reduced integration elements (C3D8R) and symmetric boundary conditions on the X and Z planes were applied to both symmetry planes. To evaluate the performance of the proposed model, a parametric study was conducted to investigate the effect of ferrite grain size and strain rate on the failure behaviour of the miniature dog-bone tensile specimens. The simulations were carried out for strain rates of 1 and 1000 s^{-1} . Different ferrite grain sizes ranging from ultra-fine-grained to coarse-grained were considered as the microstructural properties of the materials.

According to the conventional finite element simulation method, only a quarter of the cross-section (1/8 of specimen) was modelled to reduce the computational cost due to the symmetries associated with the material and test geometry. In this approach, the uniform and post-uniform deformation of the specimen would be sym-

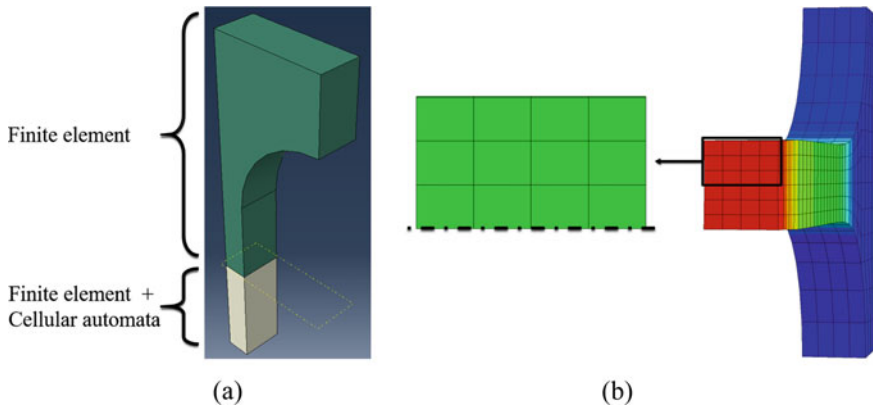


Fig. 3 Miniature dog-bone model used for parametric study

Table 1 Material properties, hardening, and damage parameters for DP600

ρ	E	ν	C_1	C_2	C_3	C_4	C_5	D	σ_k
7800 kg/m ³	210 GPa	0.3	225.35	850.16	0.3194	0.0037	1.5715	2.5	425 MPa

metric and even the predicted fracture surface would not show any asymmetry since no microstructural properties or material heterogeneity is associated with the FE properties. However, in the following examples, half of the cross-sectional area (or a quarter of the specimen) was modelled to see if the proposed model was capable of predicting any non-symmetry of the final fracture surface. The FE model of the miniature tensile specimen is shown in Fig. 3. It should be noted that to reduce computational cost, the hybrid FE+CA model was employed just in a specific part of the gauge area where the damage is more probable to develop, as shown in Fig. 3a. The 12 elements on the cross-section of the specimen that are shown above the symmetry line in Fig. 3b will be reproduced in Fig. 4 so as to display the results predicted by the FE+CA hybrid model. In order to simulate the EHFF process, one quarter of the sheet material was modelled and meshed using reduced integration three-dimensional Lagrangian solid elements (C3D8R in the ABAQUS element library) and the water pressure was defined using a pressure profile as an exponentially decaying function of time [15, 21]. The material properties, hardening function coefficients, and the Rousselier damage model constants can be found in Table 1.

Results and Discussion

The effect of grain size and strain rate on the fracture surface of DP600 sheet specimens in uniaxial tension is shown in Fig. 4. It should be mentioned at the onset that the predicted percentage of brittle fracture ($\%F_b$) in the following examples is

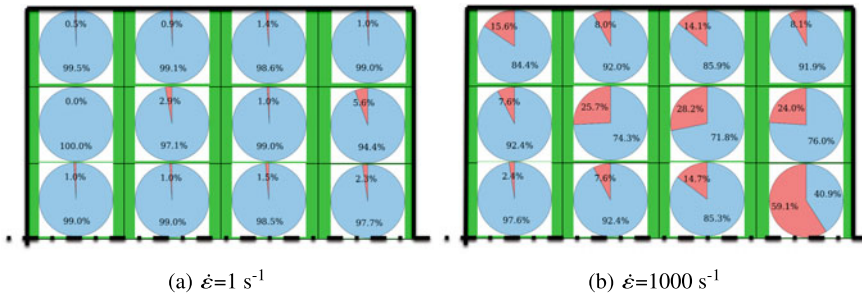


Fig. 4 Fraction of brittle fracture in **a** fine-grained ($d_g = 3 \mu\text{m}$) and **b** coarse grained ($d_g = 6.5 \mu\text{m}$) DP600 specimens

provided for qualitative comparison, and further detailed investigation is required for quantitative evaluation of ductile and brittle fracture on the fracture surface. It can be seen in Fig. 4 that the fraction of brittle fracture ($\%F_b$) for both fine- and coarse-grained DP600 is negligible when the test is carried out at low strain rate, although, a slight increase in $\%F_b$ can be observed when the ferrite grain size increases. The brittle fracture percentage also increases with an increase in strain rate. Nevertheless, with a martensite volume percentage as low as 4.7% in DP600 and a fine ferrite grain size, the $\%F_b$ remains very low and the dominant fracture mechanism is ductile. This is in very good agreement with the experimental results shown in Fig. 5. Quasi-cleavage fracture is distinct from cleavage fracture since dimples and tear ridges can be observed around the periphery of the facets [6]. However, the amount of brittle fracture observed in low- and high-strain rate deformation of DP600 sheet specimens is not significant compared to the percentage of ductile fracture where the dominant presence of dimples on the fracture surface indicates that ductile fracture is predominant.

Figure 6 shows the comparison between the average percentage of brittle fracture in fine- and coarse-grained DP600 subjected to low- and high-strain rate uniaxial tension. It can be clearly seen that an increase in either the ferrite grain size or the strain rate lead to an increase in the percentage of brittle fracture. Several researchers have stated that the coarse-grained dual phase structures have much lower elongation (ductility) and higher tendency to experience brittle fracture due to the initiation of cleavage cracks in the ferrite matrix [22]. It has also been shown that dual phase steels exhibit relatively less ductile damage failure and more brittle fracture as the volume percentage of martensite increases. Therefore, the combination of higher martensite volume content with coarse-grained ferrite and high-strain rate deformation can contribute to increased brittle fracture.

Figure 7 shows the experimental and predicted damage accumulation and final damage geometry of fine-grained DP600 sheet specimen in a failed EHFF specimen deformed with 13.6 kJ energy input. Severe fracture and tearing starting from the apex of the specimen were observed due to the absence of a die and the high energy input released from the electrodes, as shown in Fig. 7a. The model predicted the damage

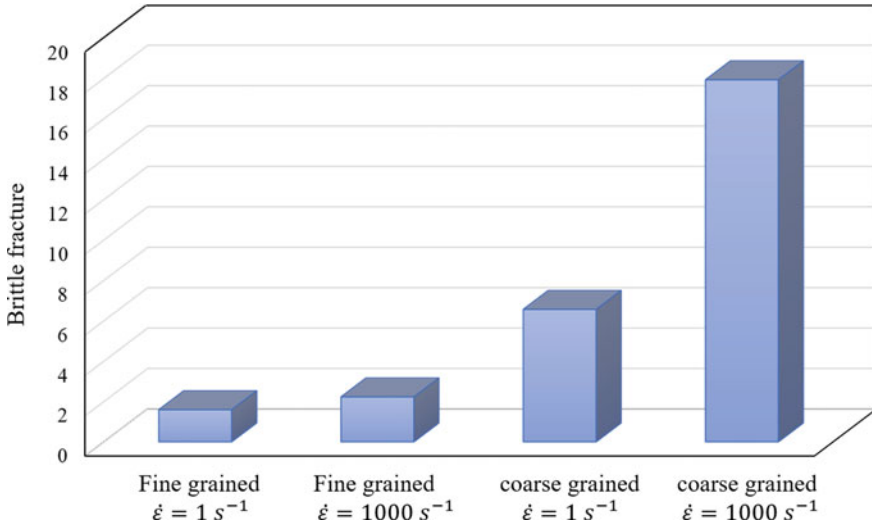
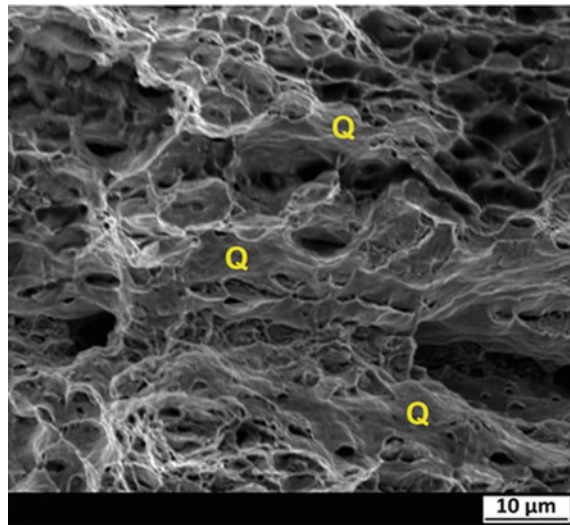


Fig. 5 Quasi-cleavage (Q) fracture on the fracture surface of DP600 tested under quasi-static condition

Fig. 6 Total fraction of brittle fracture predicted in fine-grained and coarse-grained DP600 at low- and high-strain rates



to initiate from the apex and propagate radially toward the edge of the specimen. It can be seen that there is good agreement between the experimental and predicted geometry of damage for fine-grained DP600. Figure 8 shows the total percentage of brittle fracture in damaged elements in fine- and coarse-grained DP600 sheets deformed by EHFF. It can be seen that only around 6.5% of the fracture is predicted to be brittle fracture so it can be concluded that the dominant failure mode in this

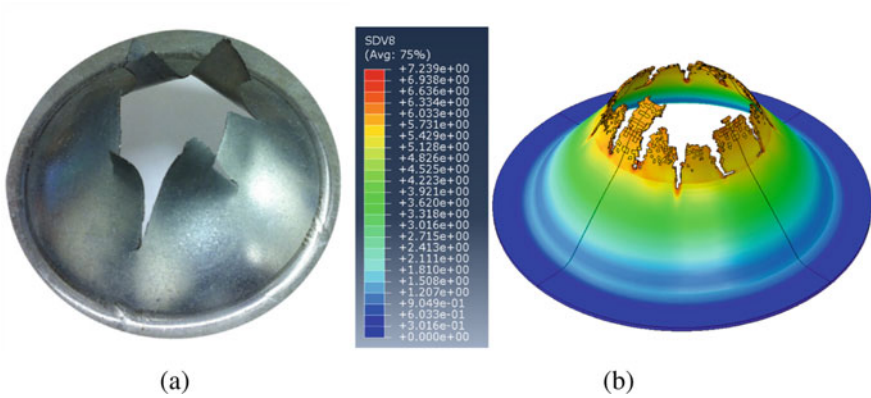


Fig. 7 Final fracture geometry in the EHFF specimens deformed with 13.6 kJ energy **a** experiment and **b** FE model

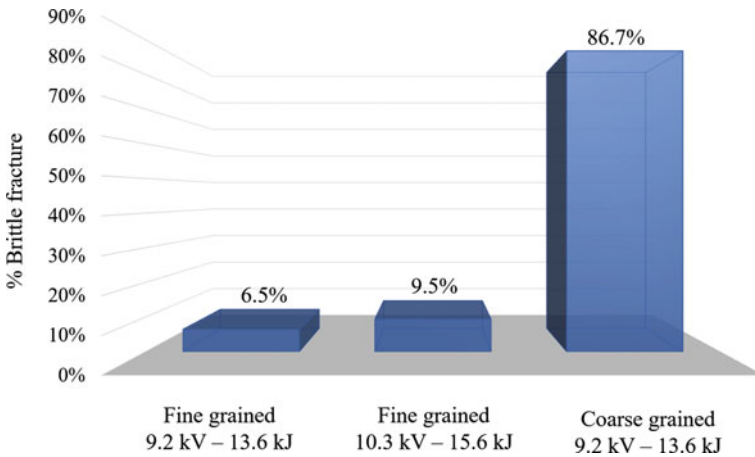


Fig. 8 Total predicted fraction of brittle fracture in fine-grained and coarse-grained DP600 subjected to EHFF with different applied energy values

case was ductile fracture. A thorough fractography analysis of the fracture surfaces was carried out by Samei [6] and revealed that ductile fracture was the dominant type of fracture in all EHFF specimens, although he observed a limited amount of quasi-cleavage fractures in DP780 sheet specimens deformed under EHFF. The effect of increasing the input energy and the ferrite grain size on the dominant damage mechanism in DP600 specimens subjected to EHFF is shown in Fig. 8. It can be seen that the fraction of brittle fracture remains less than 0.1, which indicates that the major fracture mode is ductile. On the other hand, the dominant failure mechanism, when using lower energy for a coarse-grained DP600 specimen, was predicted to be brittle since less than 15% of cells were predicted to be *dead* due to ductile fracture.

Therefore, it can be seen that increasing the input energy of the EHFF process or the ferrite grain size results in a significant change in the dominant damage mechanism from ductile to brittle mode.

Conclusions

- Numerical simulations using the hybrid FE+CA model showed that greater ferrite grain sizes and higher strain rates would result in a considerable increase in the fraction of brittle fracture.
- The FE+CA model is able to predict the occurrence of quasi-cleavage fracture in ultra-fine and fine-grained DP600, as evidenced by a few brittle “dead” cells surrounded by ductile “dead” cells.
- The damage geometry and fracture morphology were predicted accurately by the hybrid FE+CA model for the fine-grained DP600 sheet specimens deformed under 13.6 kJ energy EHFF. Similar to the experiments, a negligible amount of brittle fracture was predicted. Increasing the ferrite grain size to 12 μm leads to a considerable increase in the percentage of brittle fracture. Thus, the ferrite grain size has a dominant influence on the fracture mechanism.

One of the most important advantages of the proposed model is that it is a combination of a finite element constitutive model (to calculate macro-level strains, stresses, and damage variables) and cellular automata (responsible for evaluating the fracture mode). Therefore, it is now possible to run parametric studies based on process parameters (such as strain path, strain rate, and temperature) and microstructural properties (such as grain size distribution, volume fraction, and distribution of martensite), which can be very beneficial for steel producers.

References

1. Ramazani A, Abbasi M, Prah U, Bleck W (2012) Failure analysis of DP600 steel during the cross-die test. *Comput Mater Sci* 64:101–105
2. Calcagnotto M, Ponge D, Raabe D (2010) Effect of grain refinement to 1 μm on strength and toughness of dual-phase steels. *Mater Sci Eng: A* 527(29–30):7832–7840
3. Hassannejadasl A, Green DE, Golovashchenko SF, Samei J, Maris C (2014) Numerical modelling of electrohydraulic free-forming and die-forming of DP590 steel. *J Manuf Process* 16(3):391–404
4. Samei J, Green DE, Golovashchenko S, Hassannejadasl A (2013) Quantitative microstructural analysis of formability enhancement in dual phase steels subject to electrohydraulic forming. *J Mater Eng Perform* 22:2080–2088 Dec
5. Maris C, Hassannejadasl A, Green DE, Cheng J, Golovashchenko SF, Gillard AJ, Liang Y (2016) Comparison of quasi-static and electrohydraulic free forming limits for DP600 and AA5182 sheets. *J Mater Process Technol* 235:206–219
6. Samei J, Green DE, Cheng J, de Carvalho Lima MS (2016) Influence of strain path on nucleation and growth of voids in dual phase steel sheets. *Mater Design* 92:1028–1037

7. Saucedo-Mora L, James Marrow T (2015) Method for the explicit insertion of microstructure in Cellular Automata Finite Element (CAFE) models based on an irregular tetrahedral Finite Element mesh: application in a multi-scale Finite Element Microstructure Meshfree framework (FEMME). *Finite Elem Anal Design* 105:56–62
8. Shterenlikht A (2003) 3D CAFE modelling of transitional ductile-brittle fracture in steels. PhD thesis, University of Sheffield
9. Sari Sarraf I (2017) Meso-scale modelling of deformation, damage and failure in dual phase steels. PhD thesis, PhD Dissertation, University of Windsor
10. Beynon JH, Das S, Howard IC, Palmier EJ, Shterenlikht A (2000) The combination of cellular automata and finite elements for the study of fracture; the CAFE model of fracture. In: *Proceedings of Conferences, ECF14*, pp 241–248
11. Shterenlikht A, Howard IC (2006) The CAFE model of fracture-application to a TMCR steel. *Fatigue Fract Eng Mater Struct* 29:770–787
12. Rousselier G, Quilici S (2015) Combining porous plasticity with Coulomb and Portevin-Le Chatelier models for ductile fracture analyses. *Int J Plast* 69:118–133
13. Ahmad M, Curiel-Sosa J, Arun S, Rongong J (2019) An enhanced void-crack-based Rousselier damage model for ductile fracture with the XFEM. *Int J Damage Mech* 28:943–969
14. Sarraf IS, Jenab A, Boyle KP, Green DE (2017) Effect of rate-dependent constitutive equations on the tensile flow behaviour of DP600 using Rousselier damage model. *Mater Design* 117:267–279 Mar
15. Sarraf IS, Green DE (2018) Simulation of electrohydraulic free forming of DP600 sheets using a modified Rousselier damage model. *J Phys: Conf Ser* 1063:012111 Jul
16. Faleskog J, Shih CF (1997) Micromechanics of coalescence-I. Synergistic effects of elasticity, plastic yielding and multi-size-scale voids. *J Mech Phys Solids* 45(1):2127–2550
17. Wu SJ, Davis CL, Shterenlikht A, Howard IC (2005) Modeling the ductile-brittle transition behavior in thermomechanically controlled rolled steels. *Metall Mater Trans A* 36:989–997, 012111
18. Sari Sarraf I, Green DE, Jenab A (2018) Damage evolution and void coalescence in finite-element modelling of DP600 using a modified Rousselier model. *Eng Fract Mech* 196:168–190
19. Nohava J, Hausild P, Karlik M, Bompard P (2002) Electron backscattering diffraction analysis of secondary cleavage cracks in a reactor pressure vessel steel. *Mater Charact* 49:211–217, 012111
20. Rahmaan T, Bardelcik A, Imbert J, Butcher C, Worswick MJ (2016) Effect of strain rate on flow stress and anisotropy of DP600, TRIP780, and AA5182-O sheet metal alloys. *Int J Impact Eng* 88:72–90
21. Golovashchenko SF, Mamutov VS (2005) Electrohydraulic forming of automotive panels. In: *MPMD sixth global innovations proceedings - trends in materials and manufacturing technologies for transportation industries and powder metall. research and development in the transportation industry*, (Warrendale, PA), pp 65–70
22. Hwang B-C, Cao T-Y, Shin S, Kim S-H, Lee S-H, Kim S-J (2005) Effects of ferrite grain size and martensite volume fraction on dynamic deformation behaviour of 0.15c–2.0mn-0.2si dual phase steels. *Mater Sci Technol* 21(8):967–975

Deformation and Failure Behavior of Steel Under High Strain Rate and Multiaxial Loading



Chongyang Zeng and Xiangfan Fang

Abstract In order to model a vehicle crash event using the finite element method (FEM), accurate material properties at high strain rates are required. However, high-speed loading always results in structural vibration, which deteriorates the quality of the force measurement in a conventional tensile testing machine. Therefore, it has been a challenge for long to produce reliable experimental data under high strain rates for both deformation and failure description of engineering materials. In this work, a newly proposed high-speed testing approach with a specific specimen geometry and an oscillation-free force measurement method is applied to study the mechanical properties of a steel sheet. In addition to the plasticity behavior description by regular tensile tests, fracture specimens with various geometries, such as the central hole, notched dog bone, plane-strain, and shear specimens, are designed and tested from quasi-static to 1000/s. The deformation fields and local strains at failure are measured using digital image correlation (DIC) method. The influences of stress states and strain rates on deformation and failure behavior of the investigated steel are presented and discussed.

Keywords High-speed tensile test · Specimen geometry · Oscillation-free force measurement · Strain rate · Stress state

Introduction

Lightweight construction plays an important role in automotive development. More and more lightweight metallic materials, such as high strength steels, advanced high strength steels, and some aluminum or magnesium alloys, come to application in automotive structural components. During a vehicle crash event, large multiaxial deformation occurs at the strain rate ranging from quasi-static up to 1000/s. To improve the predictive capability of crash simulation, accurate characterization of

C. Zeng (✉) · X. Fang

Institute of Automotive Lightweight Design, University of Siegen, Breite Straße 11, 57076 Siegen, Germany

e-mail: chongyang.zeng@uni-siegen.de

© The Minerals, Metals & Materials Society 2022

K. Inal et al. (eds.), *NUMISHEET 2022*, The Minerals, Metals & Materials Series, https://doi.org/10.1007/978-3-031-06212-4_41

445

material deformation and failure behavior under different stress states, strain rates, and temperatures is necessary.

Different test machines have been utilized to characterize the strain rate dependency of material mechanical behavior in the strain rate range of $10^{-4} - 10^3/s$. Conventional load frame such as that of the universal test machine is used to conduct tensile tests for strain rate between quasi-static and 0.1/s [1, 2]. The servo-hydraulic system can cover the strain rate range of 0.1–200/s [1–3]. For higher strain rates (up to $10^3 - 10^4/s$), a split Hopkinson bar is normally used [1–4]. However, the measured behaviors of material might vary on different test machines. Therefore, the influences of test systems, specimen sizes, and geometries should be considered.

Since system ringing deteriorates the quality of force measurement, many efforts have been made to improve data quality with the servo-hydraulic high-speed machine [5–7]. However, the accurate measurement of the force signal on a servo-hydraulic machine under high-speed loading is still problematic. Fang et al. [8] developed a new specimen geometry (Generation III specimen) and a corresponding oscillation-free force measurement method to solve the system ringing effect. The results show that it is possible to determine material properties in a servo-hydraulic machine at strain rates up to 1000/s. Since the influence of strain rate on failure strain might vary for different stress states, high-speed multiaxial tensile tests are necessary to describe the influence of strain rate on the whole failure curve.

In this work, uniform fracture specimens (shear, central hole, notched, and plane-strain) are designed for multiaxial tensile tests at strain rate from quasi-static to nominal 1000/s. A unique minor plastic deformation area (MinDA) is created in each specimen, which allows for the measurement of oscillation-free force under high-speed loading with a servo-hydraulic machine. The size of the MinDA for each specimen is optimized with finite element (FE) simulation. Subsequently, the low and high-speed tensile tests of a micro-alloy HX340LAD are performed for validation of the fracture specimens. The influences of stress state and strain rate on deformation and failure behavior of HX340LAD are also investigated.

Experimental Techniques

The quasi-static tests are executed on a 100 kN testing machine (Z100) manufactured by Zwick, while the high-speed tensile test is conducted with a servo-hydraulic tensile machine HTM 5020. The maximum loading velocity of HTM 5020 is 20 m/s, which corresponds to a nominal strain rate of 1000/s with the generation III specimen shown in Fig. 1 (gauge length = 20 mm).

Strain field and local strain at failure are measured using the digital image correlation (DIC) method. In quasi-static tests, the strains are measured using two Aramis 5 M CCD cameras (maximum frame rate: 29 Hz, maximum resolution $2,448 \times 2,050$ pixels). For high-speed tests, two SA5 PHOTRON high-speed cameras (maximum frame rate: 1 MHz; maximum resolution: $1,024 \times 1,024$ pixels) are used. The calculation of the strain is also carried out using the DIC software Aramis.

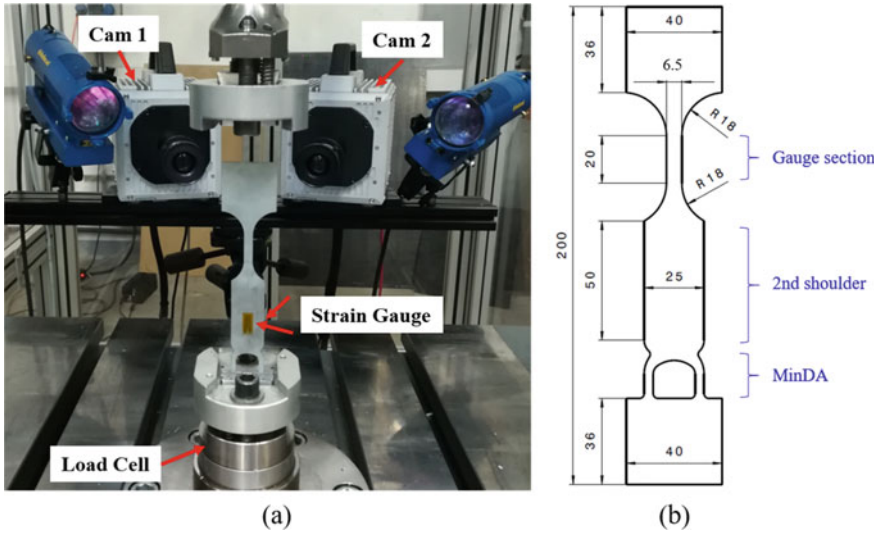


Fig. 1 Experimental setup. **a** Servo-hydraulic machine, high-speed camera, and GEN III specimen, **b** geometry of GEN III specimen

For tensile tests at low and intermediate strain rates, test force is directly measured by the load cell. At a high strain rate, the test force is measured in the elastic measurement area (EMA) of the specimen shoulder with a strain gauge, as shown in Fig. 1. The force can be calculated according to Eq. (1):

$$F = \epsilon_{zz} \cdot E \cdot A \tag{1}$$

where ϵ_{zz} is the elastic strain in the tensile direction, E is Young’s modulus, and A is the cross-section of the specimen in the area where strain gauge sensor measurements take place. A more detailed set-up of high-speed tests and the design of generation III specimen geometry is found in [8].

Geometry Design for Fracture Specimens

Geometry Design for Fracture

To cover a wide range of stress states, different fracture specimens are designed for high-speed tests using the principle for GEN III specimen [8], as shown in Fig. 2.

- Shear specimen (SH): This specimen is designed with a radius of 1 mm, an eccentricity of 1 mm, and a vertical interval of 5 mm according to the previous

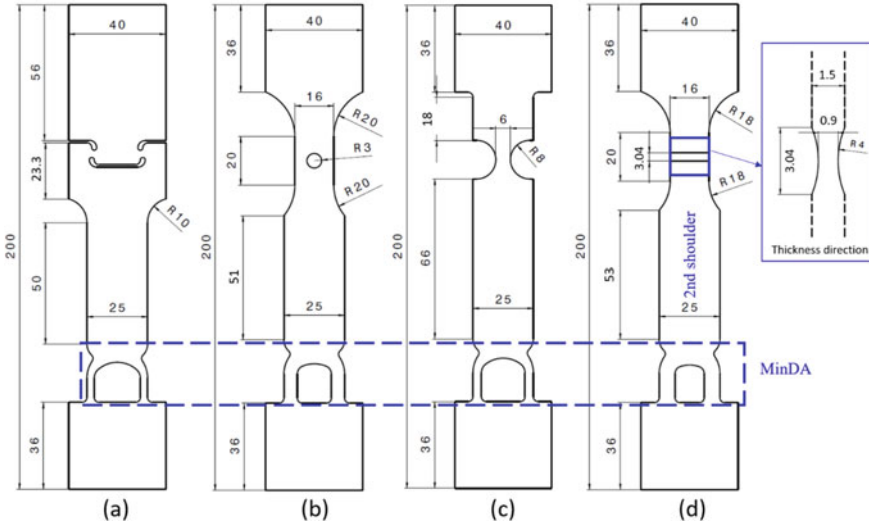


Fig. 2 Geometry and dimensions of fracture specimens. **a** SH, **b** CH, **c** NT, **d** PS

study by Peirs et al. [9]. In this work, a symmetry geometry with two same local notches is used to get a homogenous stress/strain distribution in the EMA, as shown in Fig. 2a.

- Central hole specimen (CH): The CH specimen is designed with a hole diameter of 6 mm and 16 mm wide-gauge section, which is slightly different from the initial design by Liu et al. [10], as shown in Fig. 2b.
- Notched dog-bone specimen (NDB): Fig. 2c shows the NDB specimen, which is designed with a 25 mm wide-gauge section and two symmetrical notches. The notch radius is 8 mm and the minimum gauge section is 6 mm in the center of the notches.
- Plane-strain (PS) specimen: The PS specimen (Fig. 2d) is designed with a 16 mm wide-gauge section. Two symmetrical notches with a radius of 4 mm are manufactured through the width direction of the specimen. The thickness of sheet metal is 1.5 mm, while the minimum thickness is 0.9 mm according to Liu et al. [10].

Geometry Design for Oscillation-Free Force Measurement

As shown in Fig. 2, a second only elastic deformable shoulder and a MinDA are designed for each specimen. The novel design can significantly reduce the system ringing effect resulting from high-speed impact loading. In addition, a homogenous stress/strain distribution can be obtained due to the special design of MinDA. Therefore, the test force can be determined without oscillation at high strain rate tensile tests. To optimize the actual size of MinDA, FE simulation is carried out

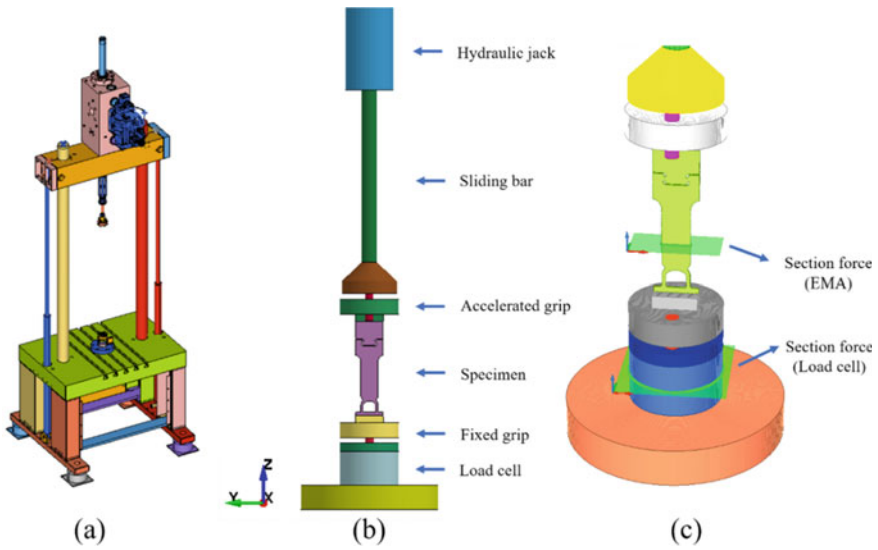


Fig. 3 **a** CAD model of the servo-hydraulic system, **b** simplified FE model, **c** cross-sections for extraction of simulated force

using LS-DYNA explicit solver. Considering the stress wave propagation through the servo-hydraulic system, a simplified FE model of a servo-hydraulic system is used to evaluate the effects of stress wave, as shown in Fig. 3b. The details including boundary conditions of the FE model are shown in previous studies [7, 8].

The investigated material is a 1.5 mm thick micro-alloyed steel (HX340LAD) sheet. The tabulated material law *MAT_024 (*MAT_PIECEWISE_LINEAR_PLASTICITY) is used to describe the elastoplastic behavior of the material. The hardening curves of HX340LAD are determined from smooth tensile tests under different strain rates at room temperature. The GEN III specimen (see in Fig. 1b) is used to determine true stress–strain curves until strain rates of 1000/s. The experimental hardening curves are plotted until material necking. To obtain a flow curve with a large range of strain for simulation, a combined Swift-Voce law is used to fit the hardening curves under different strain rates, as shown in Fig. 4. To obtain the strain rate of over 1000/s in the failure location of fracture specimens, the initial velocity of impact is set as 10 m/s.

In the simulation, the strain distribution on the second shoulder is investigated. It is found that the strain pattern does not change during the entire test. Figure 5 shows the strain distribution on the second shoulder of the specimen before the onset of fracture. A homogenous strain distribution is obtained for each specimen. The black solid square on the second shoulder shows the position where a strain gauge can take place for force measurement under high-speed loading. The actual optimized geometry of MinDA for each fracture specimen is shown in the black dash square.

To verify the positive effect of the new geometries on the reduction of the system ringing effect during force measurement, the section force in EMA (in the center of

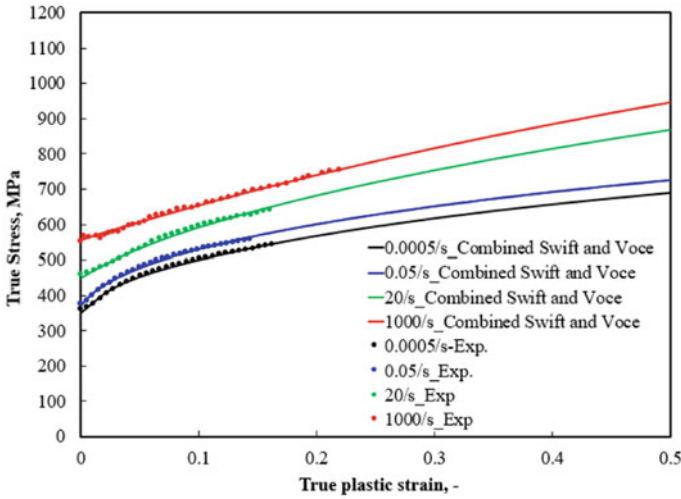


Fig. 4 Flow curves of HX340LAD used in FE simulation

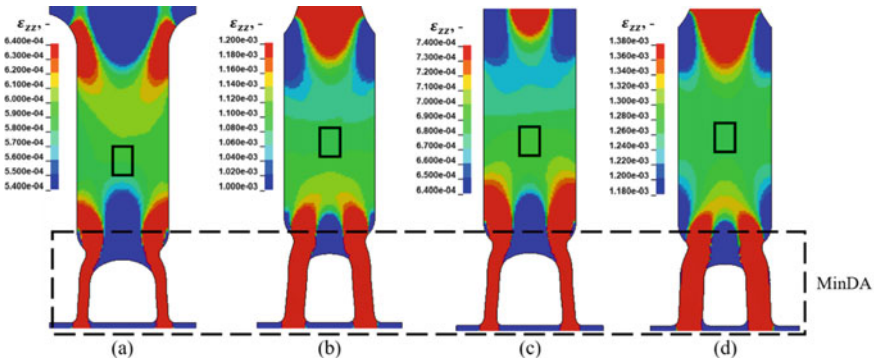


Fig. 5 Strain distribution pattern of the specimen before the onset of fracture. **a** SH, **b** CH, **c** NT, **d** PS

the black solid square) and load cell are plotted in Fig. 6. Figure 3c shows the position of the cross-section of EMA and load cell in the FE model. Under the high-speed loading of 10 m/s, severe oscillation is found for the force measured by a load cell, while the force measured in EMA is much smoother. Slight oscillation is still found for section force at EMA, but it is already acceptable compared to the force at the load cell.

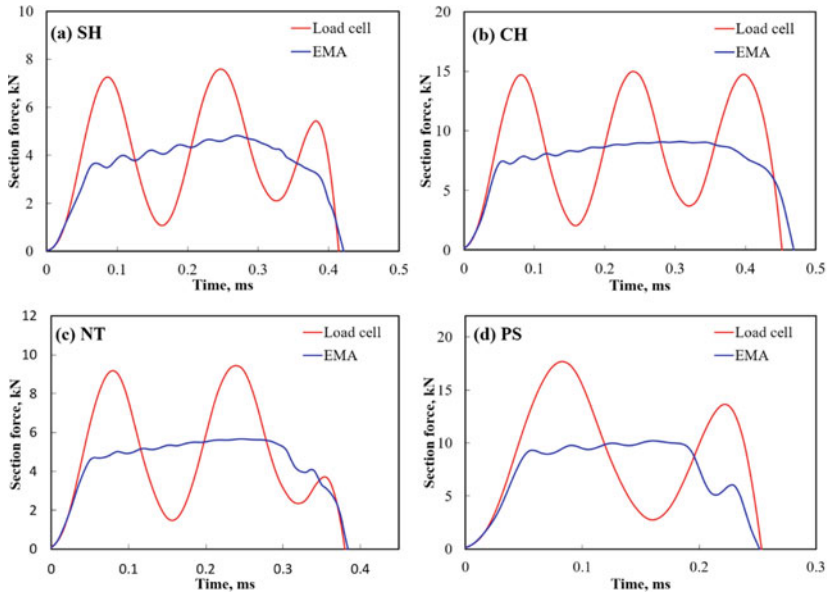


Fig. 6 Simulated section force versus time curves at load cell and EMA (impact velocity is 10 m/s)

Results

Validation of Geometries with Experiments

Figure 7 shows the force versus time curves measured by a load cell and strain gauge under a loading speed of 10 m/s with the servo-hydraulic tensile machine HTM 5020. It is found that the quality of the force signal by strain gauge is much higher than the data measured by the load cell. The geometries of fracture specimens are validated with the experimental data.

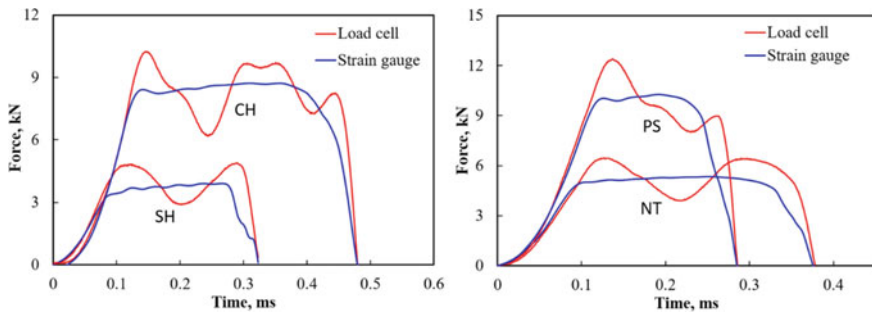


Fig. 7 Experimental force signal measured by the load cell and strain gauge under 10 m/s

Influence of Strain Rates on Deformation

Figure 8 shows the force–displacement curves for SH, CH, NT, and PS experiments under various test velocities. The loading direction is 90° to the rolling direction. For test speeds of 0.005 mm/s, 0.05 mm/s, and 0.5 m/s, the test force is measured directly by the load cell. However, the test force under loading speeds of 2 m/s and 10 m/s is measured with a strain gauge. The deformation up to fracture is evaluated with DIC. A gauge length of 10 mm is used to calculate the displacement.

With increasing loading speed, the force–displacement curves exhibit a significantly higher force level, especially at the beginning. For shear and plane-strain specimens, shorter fracture displacements are observed with increasing loading speeds. The results of 0.5 mm/s for shear specimen are excluded from this. However, the displacement up to fracture for notched dog-bone and central-hole specimens is almost independent of the loading speed. The reasons for the results can be multiple and one of them is related to the adiabatic heating induced local softening of the sample [11].

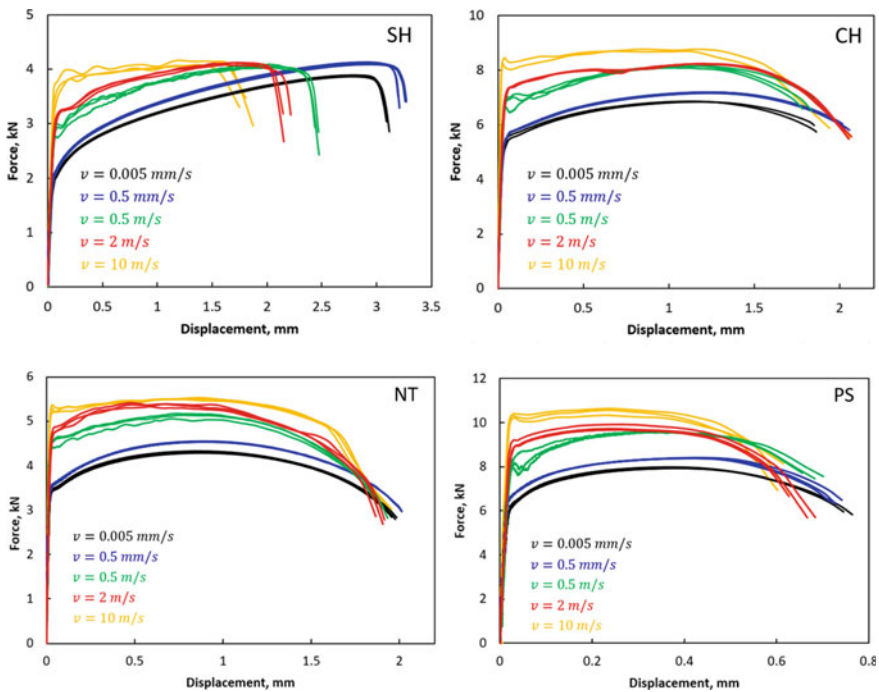


Fig. 8 Force–displacement curve of HX340ALD with different loading speeds

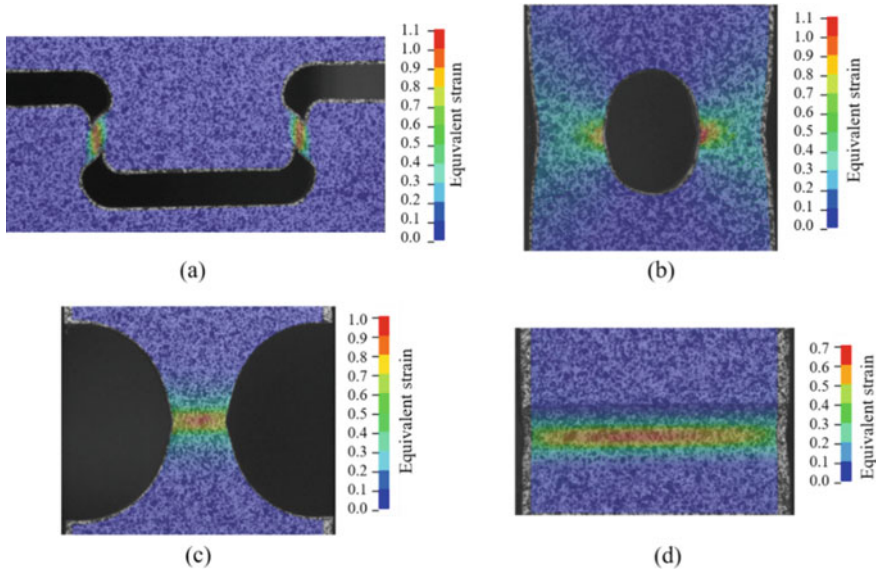


Fig. 9 DIC-based equivalent strain field before the onset of fracture. a SH, b CH, c NT, d PS

Influence of Strain Rates and Stress States on Failure Behavior

Local failure strain is determined with DIC as the equivalent strain before the appearance of the first visible crack on the specimen surface. A uniform reference length of 0.2 mm is used for local strain measurement. As shown in Fig. 9, failure for notched dog-bone and plane-strain specimens occurs in the middle of the fracture gauge sections. The maximal equivalent strain for the central-hole specimen appears on the inner side of the hole. However, for the shear specimen, it is difficult to determine the accurate position of failure initiation. In this work, the center of the shear zone is chosen to be the position of onset of fracture.

The failure strain of HX340LAD under different loading speeds and types is shown in Fig. 10a. For a better comparison of the failure strain under different loading speeds, a slight interval is used between different loading speeds on the x-axis. From shear loading to plane-strain tension, the failure strain exhibits an obvious decreasing trend. For shear and plane-strain tensile tests, the failure strain decreases with increasing loading speeds. But for notched tension, there is no big influence of strain rate on failure strain observed. Currently, the x-axis in Fig. 10a shows the types of fracture specimens since only DIC results are available. For future work, the failure strain versus stress triaxiality or Lode angle curves has to be plotted from FEM. Figure 10b shows the evolution of equivalent strain in failure location as a function of strain rate under different loading speeds. The equivalent strain is plotted until the onset of fracture. A spline approximation is used to show the continuous development of the local strain rate. It is noted that the local strain rates under

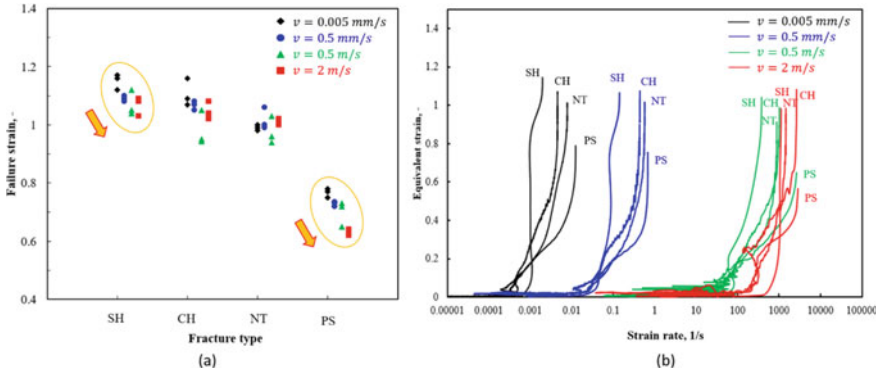


Fig. 10 Local equivalent strain evaluated by DIC under different loading speeds: **a** failure strain, **b** evolution of equivalent strain as a function of strain rate

multiaxial loading increase significantly during the entire test. One can also notice that the local strain rate already reaches over 1000/s under a loading speed of 2 m/s. For a better investigation of the influence of strain rate on failure behavior, a tensile test with a local constant strain rate is necessary.

Summary and Conclusion

In this work, the uniform fracture specimens are designed for multiaxial tensile tests at the strain rate from quasi-static to nominal 1000/s. The geometries of new fracture specimens are validated by both numerical and experimental results. Almost oscillation-free forces have been measured with a strain gauge for all four fracture specimens under a loading speed of 10 m/s. With the new fracture specimens, the effects of strain rates and stress states on the deformation and failure behavior of HX340LAD are investigated. For shear loading and plane-strain tension, a decrease in failure strain is observed with increasing loading speeds. But for the central-hole and notched dog-bone specimens, no big influence of strain rate on failure strain is observed. This trend can also be seen in force–displacement curves under different loading speeds.

In the present work, the failure strains under various loading speeds and types are only evaluated on the failure local surface by DIC. With force–displacement curves and surface local equivalent strain evolution curves, the failure strain of material can be calibrated in FE simulation. For a better investigation of the influence of strain rate on deformation and failure behavior, a tensile test with a constant local strain rate shall be developed.

Acknowledgements This work was supported by the German Research Foundation (Deutsche Forschungsgemeinschaft, grant No.: FA 1024/5-1) to which we are indebted.

References

1. Borsutzki M, Cornette D, Kuriyama Y, Uenishi A, Yan B, Oprobek E (2005) Recommendations for dynamic tensile testing of sheet steels. International Iron and Steel Institute, 30
2. Xia Y, Zhu J, Wang K, Zhou Q (2016) Design and verification of a strain gauge based load sensor for medium-speed dynamic tests with a hydraulic test machine. *Int J Impact Eng* 88:139–152
3. Yang X, Hector LG, Wang J (2014) A combined theoretical/experimental approach for reducing ringing artifacts in low dynamic testing with servo-hydraulic load frames. *Exp Mech* 54(5):775–789
4. Roth CC, Mohr D (2014) Effect of strain rate on ductile fracture initiation in advanced high strength steel sheets: experiments and modeling. *Int J Plast* 56:19–44
5. Xiao X (2008) Analysis of dynamic tensile testing. In: Proceedings of the XIth international congress and exposition, Orlando, Florida USA, Society for Experimental Mechanics Inc. Bethel, CT, pp 06801–1405
6. Zhu D, Rajan SD, Mobasher B, Peled A, Mignolet M (2011) Modal analysis of a servo-hydraulic high speed machine and its application to dynamic tensile testing at an intermediate strain rate. *Exp Mech* 51(8):1347–1363
7. Li J, Fang XF (2014) Stress wave analysis and optical force measurement of servo-hydraulic machine for high strain rate testing. *Exp Mech* 54(8):1497–1501
8. Fang XF, Grams R (2019) A novel oscillation-free force measurement for the determination of material properties during high-speed tests. *J Test Eval* 49(3):1389–1411
9. Peirs J, Verleysen P, Degrieck J (2012) Novel technique for static and dynamic shear testing of Ti6Al4V sheet. *Exp Mech* 52(7):729–741
10. Liu W, Lian J, Münstermann S (2019) Damage mechanism analysis of a high-strength dual-phase steel sheet with optimized fracture samples for various stress states and loading rates. *Eng Fail Anal* 106:104138
11. Liu W, Lian J, Münstermann S, Zeng C, Fang X (2020) Prediction of crack formation in the progressive folding of square tubes during dynamic axial crushing. *Int J Mech Sci* 105534

Forming–Structural-Coupled Analysis: The Method to Predict Die Deformation Using Quick Simulations



K. H. Yun, S. H. Jun, M. S. Moon, J. S. Kim, and H. S. Kim

Abstract This research analyzed die deformation caused by sheet metal forming stress. The stress results in elastic deformation on the die as well as plastic deformation on the panels. To predict the exact amount of the die deformation, forming–structural-coupled analysis was implemented. In the analysis, two simulations were used: AutoForm and midas MeshFree which are known as advantageous software for reliable results and quick-solving. As a sequel to the coupled analysis, we could figure out the exact deformation more precisely and quickly, compared to the previous methods that had consumed much time. The numerical results were significantly analogous to the measured results. Ultimately, this research proposes a widely applicable, accessible, and time-effective process to assess die deformability. Through this practical methodology, it is expected that die design departments would be able to predict die deformation without spending much time.

Keywords Coupled analysis · Die deformation · Die compensation · Quick method · AutoForm · midas MeshFree

Introduction

Recently, customer preferences for automobiles are dramatically changing. Consumer behaviors are showing some meaningful signals that they crave for optimized and flexible models for their personal purposes [1]. These trends are likely to accelerate a shift to the production of diversified car models that meet customer needs. For these reasons, most automotive engineers are continuously asked to develop new technologies to reduce the lead time for new models and customized

K. H. Yun (✉) · S. H. Jun · H. S. Kim
KIA, Seoul, Korea
e-mail: kihoon.yun@kia.com

M. S. Moon
AutoForm Korea, Seoul, Korea

J. S. Kim
MIDAS IT, Seongnam, Korea

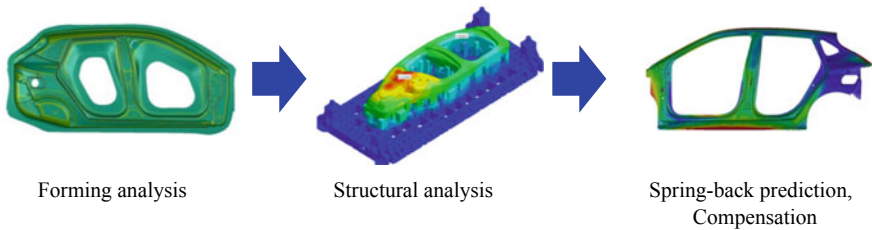


Fig. 1 Deformation analysis process

production. Accordingly, the engineers desire to bring concurrent engineering into the development processes for new models.

Stamping tool engineers have been attempting to reduce the lead time producing dies, especially by eliminating additional compensation processes. Normally in structural analyses of dies, the stamping tools are considered rigid bodies to simplify mechanical difficulties [2]. But in reality, panel forming force triggers contact pressure on the surfaces of the stamping tools and the pressure induces elastic deformation on the dies [2]. This is the primary cause restricting the engineers from predicting die deformability. Due to the deformation, additional spring back analyses and manual rework would be essentially required after the die constructions. To curtail these additional processes, how much and where it deforms should be predicted accurately. Through a deformation analysis like Fig. 1, the exact amount of compensation should be applied to the 3D model drawings at the stage of the die design. Previous studies have proposed diverse approaches to estimate the deformation and substantiated the effects of a forming–structural-coupled analysis. Integrated forming and structural simulations were conducted to cut down die cost and enhance stamping productivity, with fine mesh generated by ICEM CFD [3]. Spring-back on automotive fender panels was accurately predicted by coupling structural simulations with forming analysis [4]. Haufe et al. and Pilthammar et al. conducted a forming–structural-coupled analysis by generating a high-density shell mesh and interpolating between coarse solid mesh and fine surface mesh [5, 6].

Despite these advanced researches, the processes of the simulations seem to take fairly much time that die designers may have big difficulties in analyzing the die deformability. It is widely accepted that a time-effective approach is necessary. To enable die designers to predict the deformation quickly and easily, the present research intends to build a quick analysis process using AutoForm and midas MeshFree.

Validity of Implicit Boundary Method

In this part, it is theoretically validated whether using the implicit boundary method (IBM), a type of mesh-free method, is appropriate for a die deformation analysis. Several numerical methods such as finite element method (FEM), finite volume method (FVM), and finite difference method (FDM) have been developed strikingly. But basically, those approaches are limited to modifying every low-quality mesh into a high-quality mesh because the mesh can be distorted depending on a given geometry [7]. The mesh those methods use is called a conforming mesh, which means that the entire mesh should completely fit in the shape of the domain. This type of mesh requires additional work to make the geometry simplified, which is called a cleanup or preprocessing. Moreover, refining a mesh is required to adjust the mesh to the shape of the domain. These steps are highly labor-intensive and need much computational cost. But these are too indispensable to be taken out of an analysis process. As the scale and the complexity of the given shape of the domain increases, the difficulty of generating the mesh tends to increase exponentially. A surface of an automotive stamping die consists of various radial dimensions, and the curvature of the surface varies with the automotive design. These are the major reasons that many difficulties arise in analyzing a die structure.

IBM can make these problems evitable. This method has a similar approach to traditional FEM with respect to approximate results. But there is a notable difference between those methods. The former method utilizes a shape-independent grid, which fully encloses the given domain, whereas the latter method uses a shape-dependent grid. By using IBM, generating and refining a mesh could be skipped. According to the experiments we have tried, it takes no more than 30 min to create a structured grid for a set of stamping tools. IBM can be considered an appropriate methodology for any die design.

The structural analysis tool used in this study, midas MeshFree, utilizes the concept of IBM mentioned above. IBM computes a result by interpolating boundary equations and assigning essential boundary conditions to the interpolated nodes [8, 9]. This method can be meaningfully used in a case when the boundary does not have nodes on it [10]. Since the boundary of the domain does not completely correspond to the node, one may have a question of whether IBM is possible to get a reliable result. Kumar et al. proved the effectiveness of IBM and investigated computational time and error occurrences in several linear static cases [8]. The authors substantiated that the results of IBM are analogous to those of traditional FEM [8].

Data Compatibility

Data compatibility needed to be checked to couple AutoForm with midas Mesh-Free. As in the following, contact stress and reference system from AutoForm were converted to those of midas MeshFree. To convert these, mathematical operations are

needed as many as the number of nodes involved in the analysis. We could develop a data converter to do plenty of calculations.

Contact Stress

AutoForm and midas MeshFree deal with distinct types of meshes. The former uses a tetrahedral mesh, whereas the latter does a regular hexahedral grid. In principle, one might raise the question of whether each node of AutoForm completely corresponds to those of midas MeshFree. To interpolate each nodal information from one to the other, additional data converting is needed. Several steps for the compatibility of both data were simply described in Fig. 2. The first step is to divide the representative stress of each element in AutoForm equally into each node. And the total stress on each node can be obtained by adding other stress which was split from the adjacent shells. In the next step, the total nodal stress should be transformed with respect to a global coordinate system. Afterward, each nodal information extracted from AutoForm is interpolated by the nearest neighbor method and matched with each node of the nearest background grid (square dashed line in Fig. 2) of midas MeshFree. As a final step, each nodal stress is mapped on midas MeshFree.

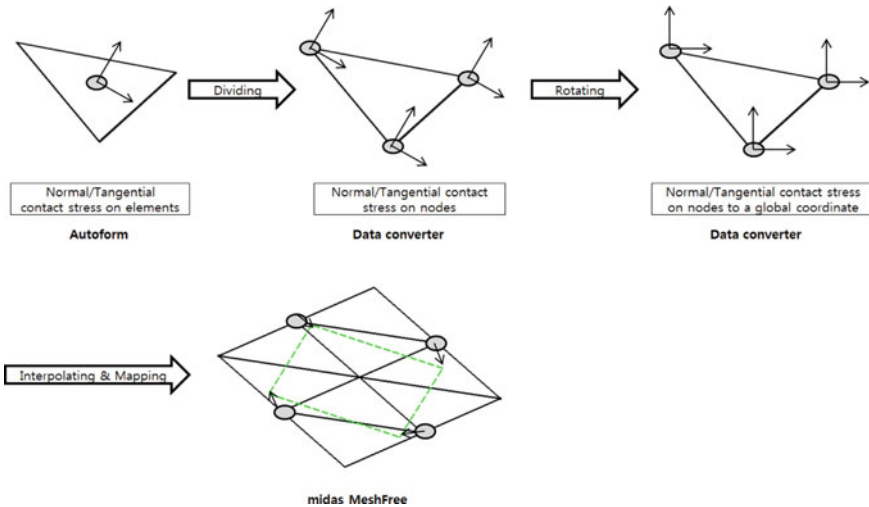


Fig. 2 Data converting from AutoForm to midas MeshFree

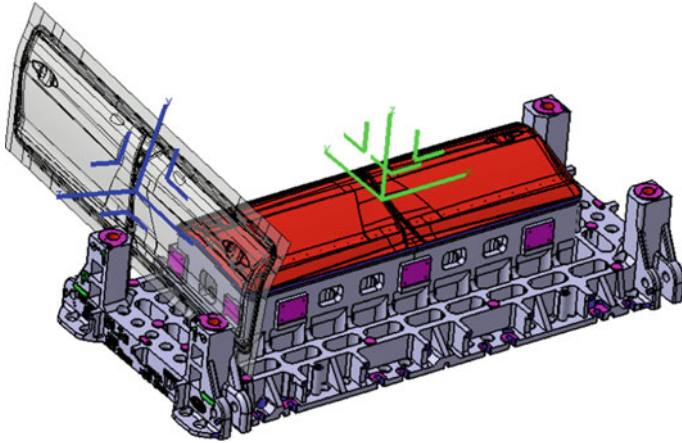


Fig. 3 Non-identical coordinate systems

Coordinate System

To carry out the coupled simulations, the coordinate systems of each simulation should be identical. But as illustrated in Fig. 3, both coordinate systems are completely different. The forming simulation is performed based on a car-line which means a reference axis of an assembled car body; otherwise, the structural simulation is based on a coordinate of a press centerline. The coordinate of the car-line was transformed to the reference of the press center in this study.

Deformation Analysis of Front Door Outer Draw Lower

The simulation conditions that affect the result are stated in Tables 1 and 2.

Forming Analysis Conditions and Material Properties

See Tables 1 and 2.

Table 1 Forming analysis condition of front door outer draw

Blank	Material	35 kgf/mm ²
	Thickness [mm]	0.65
	BLK size [mm × mm]	(2650 + 2560)/2 × 920
Force	Press type	Single action
	BLK holding force [Ton]	200
	Forming force [Ton]	540.3
Mesh	Initiative mesh size [mm]	0.1
	Radius penetration [mm]	0.1
	Max. element angle [Deg]	15

Table 2 Material properties of front door outer draw

Part name	Material	Young’s modulus	Poisson’s ratio	Density
Die	Ductile cast iron	175 GPa	0.3	7.30e-006 kg/mm ³

Contact Pressure and Boundary Conditions

Each node of the die surface is subjected to the contact pressure obtained from the data converting process. In addition, the bottom of the die was considered to be completely fixed to a press bolster as shown in Fig. 4. This structural analysis was conducted in linear static mode. A 20 mm-sized shape-independent grid was used as presented in Fig. 5. This analysis took into account the lower part of the die only, with the exception of the upper die, in order to simplify the process of the analysis. As

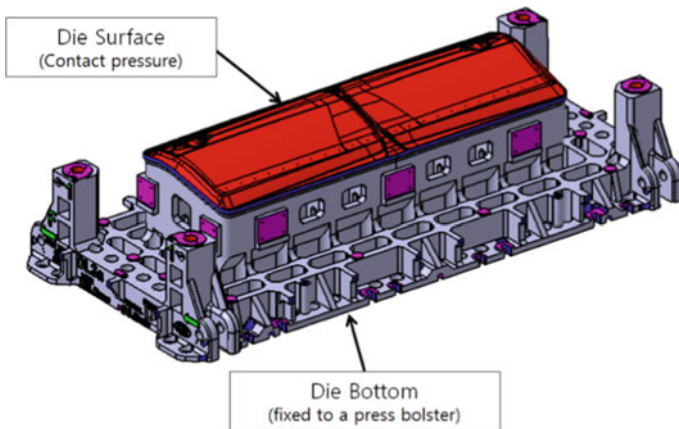


Fig. 4 Boundary conditions

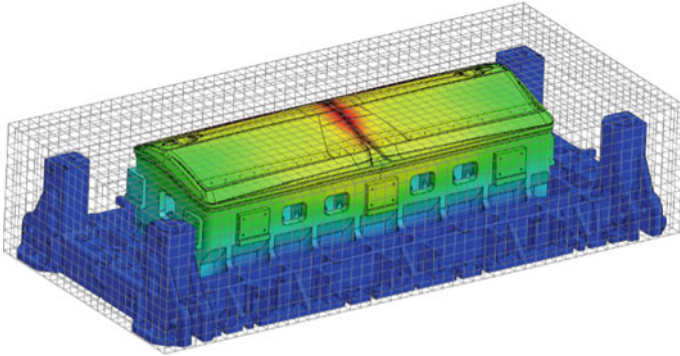


Fig. 5 Shape-independent background grid

the die components were not expected to affect the result of the analysis, all of those components were excluded to simplify the contact conditions in this CAD model.

Deformation Analysis of Side Outer Draw with Press Machine Structures

The simulation conditions that affect the result are stated in Tables 3 and 4.

Forming Analysis Conditions and Material Properties

See Tables 3 and 4.

Table 3 Forming analysis condition of side outer draw

Blank	Material	28 kgf/mm ²
	Thickness [mm]	0.65
	BLK size [mm × mm]	3615 × 1672
Force	Press type	Single action
	BLK holding force [Ton]	170
	Forming force [Ton]	1289
Mesh	Initiative mesh size [mm]	0.5
	Radius penetration [mm]	0.22
	Max. element angle [Deg]	30

Table 4 Material properties of side outer draw

Part name	Material	Young's modulus (GPa)	Poisson's ratio	Density
Die	Ductile cast iron	175	0.3	7.30e-006 kg/mm ³
Bolster/slide	Stainless steel	200	0.3	7.85e-006 kg/mm ³

Contact Pressure and Boundary Conditions

Each node of the die surfaces is subjected to the contact pressure obtained from the data converting process. Particularly in this analysis, two main parts of the press machine were contemplated to affect the deformation of the side outer draw die. In addition, the bottom surface of the die was considered to be under general contact with the press bolster and slide. On top of that, clamping conditions on given positions were taken into consideration. In most cases, general contact in midas MeshFree takes into account that involved objects can slide horizontally and move vertically to contact surfaces as a form of micro-displacement movement. Each bottom surface of the bolster and slide was contemplated to be fixed to the ground as presented in Fig. 6. Both the bolster and slide of the press machine came in contact with other parts of the press structures, which are considered to be rigid bodies in this analysis, only at the surfaces of the edge areas as shown in Fig. 7. Accordingly, only edge areas of the bottom surfaces of the bolster and slide were considered to be fixed to the ground as shown in Fig. 8. This structural analysis was conducted in linear static mode. 20 mm-sized shape-independent grid was used as presented in Fig. 5. As the die components were not expected to affect the result of the analysis, all the components were excluded to simplify the contact conditions in this CAD model.

Fig. 6 Contact conditions

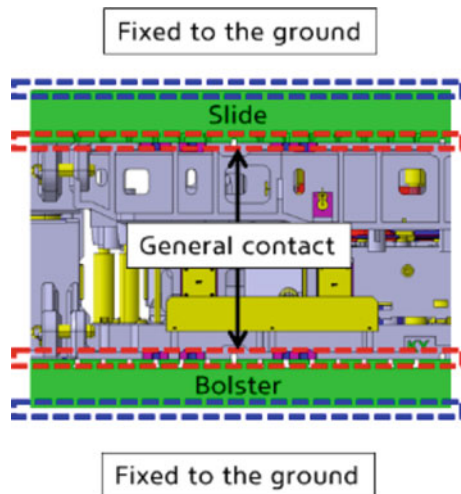


Fig. 7 Cross-section of the die and press machines

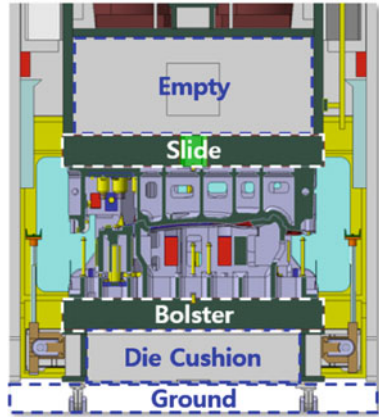
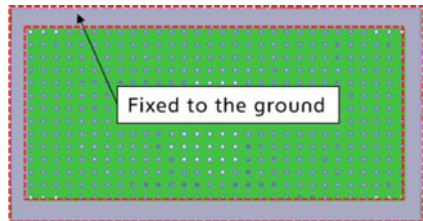


Fig. 8 Contact condition of bottom surfaces of the bolster and slide



Result

The Result of the Analysis on the Front Door Outer Draw (Lower Die)

Figure 9 shows the result of the deformation analysis on the front door outer die. The middle of the punch surface seemed to be deformed maximum of 0.2 mm and the deformation of the rest part ranges from 0.1 mm to 0.15 mm. The result obtained from this analysis was analogous to what could be measured in a real die. In most of the cases in the field, the die engineers used to decide the amount of the compensation depending on trial and error. The used-to-be compensation on a front door outer was usually from 0.2 mm up to 0.3 mm. That is approximate to what we gained through this analysis. If iterative analyses are carried out, it will be possible to gain higher accuracy of the result.

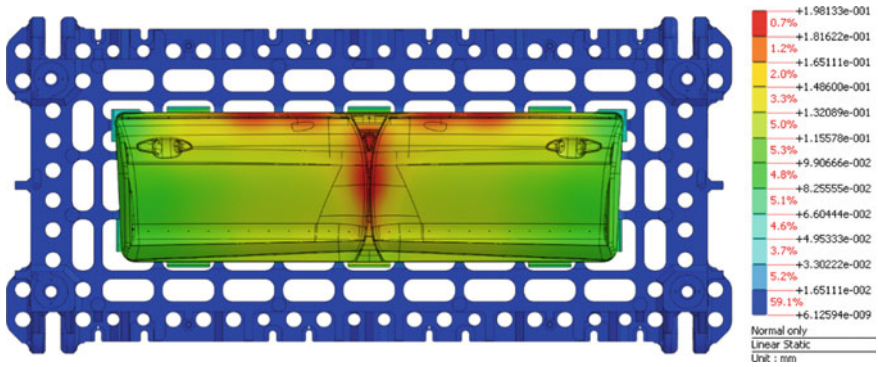


Fig. 9 The result of the deformation analysis on the front door outer draw (lower die)

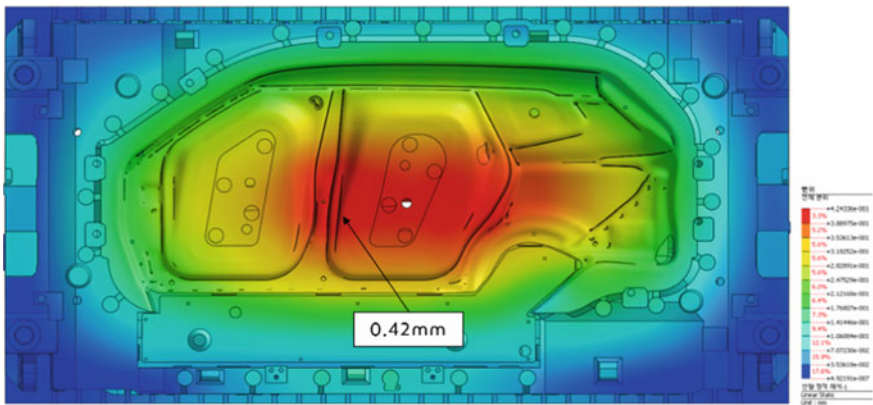


Fig. 10 The result of the deformation analysis on the side outer draw (upper die)

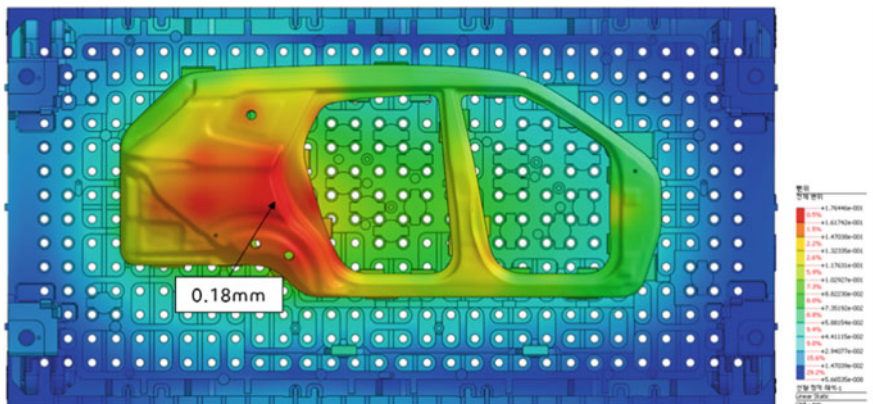
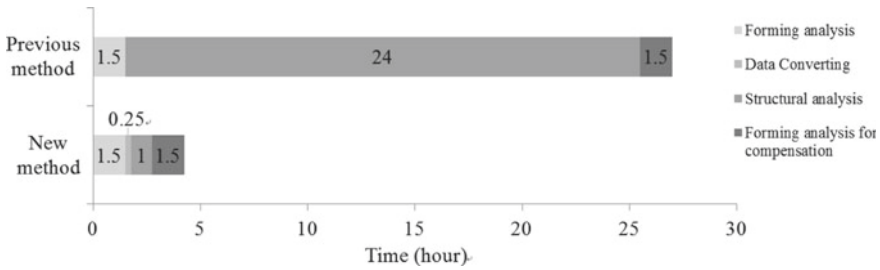


Fig. 11 The result of the deformation analysis on the side outer draw (lower die)



Graph 1 Total time for the deformation analysis

The Result of the Analysis on the Side Outer Draw

Figures 10 and 11 show the result of the deformation analysis on the side outer panel. The B-pillar side of the upper die surface seemed to be deformed maximum 0.42 mm. The rear skin of the side outer on the lower die seemed to be deformed maximum of 0.18 through this analysis. It slightly differed from what was measured in a real die. The used-to-be compensation applied to a B-pillar surface was largely up to 0.3 mm. However, the previous compensation used to lead to unsatisfying consequences that needed a multitude of manual rework. According to the result of this analysis, we altered our compensation standards for a side outer draw die and we could cut down on man-hour for manual rework.

The Time Required for the Analysis

The process of deformation analysis is composed of four steps. It took 4 h and 15 min to conduct the whole process as shown in Graph 1. By using a shape-independent background grid like in Fig. 5, the time to preprocess and generate the mesh was reduced up to 95%. In total, we could cut down on the time required in this analysis up to 85% compared to the previous method.

Deformation Analysis Process

The past process as shown in Fig. 12 has been improved like the process presented in Fig. 13. In the past process, the stage of ‘Deformation analysis’ was needed separately and took fairly much time (light gray colored in Fig. 12). In the new process as presented in Fig. 13, it is highly possible to improve the accuracy of the prediction by eliminating distorted meshes and considerably reducing the time needed for the analysis. As shown in Fig. 13, contact pressure would be gained at the stage of ‘Forming analysis’ and be sent to the ‘Die design part’. Afterward, the

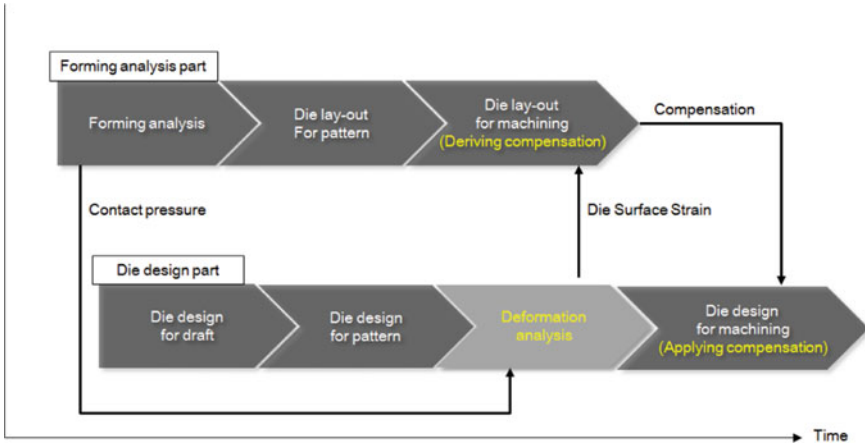


Fig. 12 Deformation analysis process (as is)

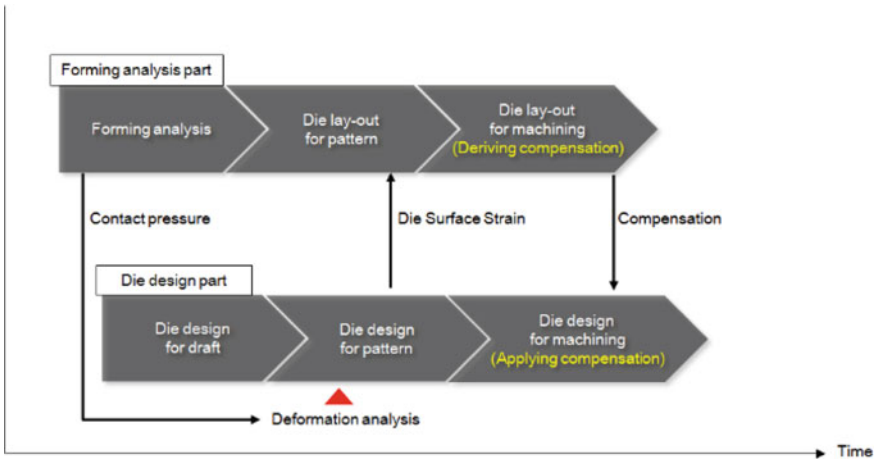


Fig. 13 Deformation analysis process (to be)

deformation analysis would be conducted at the stage of ‘Die design for pattern’. And the distribution of the die deformation obtained from the stage would be applied to compensation analysis at the stage of ‘Die layout for machining’. The purpose of the stage is to derive the compensation for the die surfaces. In the end, the compensation is applied to the 3D modeling of the die at the stage of ‘Die design for machining’.

Conclusion and Future Study

In this research, forming–structural-coupled analyses were carried out on stamping tools, and the distribution of the die deformation was obtained as the final results. The results seemed to correspond to what we have measured on actual dies. As a consequence of the analyses, we built the process to implement both die design and deformation analysis concurrently. Furthermore, it was substantiated that the presented methodology brought a remarkable time reduction in the analyses. The improved process could be used practically in the die design field, without particular expertise and labor-intensive work in the finite element method. It is quick to solve, easy to handle, and appropriate to assist the die designers who are not experts in a simulation. This methodology seems to be cost-effective, especially in the case that a die manufacturer would not be affordable to employ simulation specialists but need to see quick and accurate verifications. The future study will focus on expanding the presented analysis process into every stamping tool, especially every die of an exterior part like a hood outer, roof, etc. We will continuously attempt to figure out proper compensation for each item, to completely innovate the conventional method based on manual rework and trial and error.

Acknowledgements We would like to express a deep sense of gratitude to AutoForm Korea and MIDAS IT. This research could not have been completed without their support.

References

1. Gao P, Kaas HW, Mohr D, Wee D (2016) mckinsey.com: disruptive trends that will transform the auto industry. <https://www.mckinsey.com/industries/automotive-and-assembly/our-insights/disruptive-trends-that-will-transform-the-auto-industry>. Accessed 17 Feb 2020
2. Neto DM, Coër J, Oliveira M, Alves JL, Manach PY, Menezes L (2016) Numerical analysis on the elastic deformation of the tools in sheet metal forming processes. *Int J Solids Struct* 100. <https://doi.org/10.1016/j.ijsolstr.2016.08.023>
3. Aitharaju V, Liu M, Dong J, Zhang J, Wang C (2005) Integrated forming simulations and die structural analysis for optimal die designs. *AIP Conference Proceedings* 778:96–100. <https://doi.org/10.1063/1.2011200>
4. Keum Y, Ahn IH, Lee I, Song M, Kwon S, Park J (2005) Simulation of stamping process of automotive panel considering die deformation. *AIP Conference Proceedings* 778:90–95. <https://doi.org/10.1063/1.2011199>
5. Haufe A, Roll K, Bogon P (2008) Sheet metal forming with elastic tools in LS-DYNA, Numisheet 2008
6. Pilthammar J, Schill M, Sigvant M, Sjöblom V, Lind M (2019) Simulation of sheet metal forming using elastic stamping dies. In: 12th European LS-DYNA conference 2019, May
7. Garg S, Pant M (2018) Meshfree methods: a comprehensive review of applications. *Int J Comput Methods* 15(4):1830001. <https://doi.org/10.1142/S0219876218300015>
8. Kumar A, Padmanabhan S, Burla R (2008) Implicit boundary method for finite element analysis using non-conforming mesh or grid. *Int J Numer Methods Eng* 74:1421–1447. <https://doi.org/10.1002/nme.2216>

9. Chen H, Kumar A (2013) Implicit boundary approach for Reissner-Mindlin plates. In: Proceedings of the ASME design engineering technical conference (Vol. 2). <https://doi.org/10.1115/DETC2013-12714>
10. Burla R, Kumar A (2008) Implicit boundary method for analysis using uniform B-spline basis and structured grid. *Int J Numer Methods Eng* 76:1993–2028. <https://doi.org/10.1002/nme.2390>

Investigating the Formability and Failure Mechanism of an Advanced High Strength Steel by a Microstructure-Based Hierarchy Modeling Approach



Haiming Zhang, Shuai Luo, Jiaru Liu, and Zhenshan Cui

Abstract A reliable prediction of sheet formability is especially necessary for designing the lightweight components made of advanced high strength steels (AHSSs) with complex microstructure. In this work, a hierarchy modeling approach based on FEM and crystal plasticity (CP) was proposed to investigate the deformation and failure of a hot-rolled AHSS subjected to hole expansion (HE) operations. At the engineering scale, the HE simulation was performed by a commercial FEM software. The deformation history of critical elements was used as the boundary conditions for grain-level CP simulations. Microstructural data including phase morphology, grain size, and orientation obtained from EBSD characterizations were used to build high-fidelity representative volume elements for the CP simulations. The simulated results were compared with high-resolution SEM data in terms of damage initiation sites. Plasticity heterogeneities and micromechanical interactions predicted by the hierarchy modeling sheds light on understanding the failure mechanism of AHSSs under complex deformation paths.

Keywords Hole expansion · Crystal plasticity · Hierarchy modeling approach · AHSS

Introduction

As environmental and climate change concerns escalate, the automotive industry is receiving increasing pressure to reduce its environmental impact while maintaining safety and affordability. To address this requirement, advanced high strength steels (AHSS) with excellent strength–ductility balance have been widely adopted by the automobile industry for reducing the weight while improving the safety of up-to-date

H. Zhang (✉) · J. Liu · Z. Cui

School of Materials Science and Engineering, Shanghai Jiao Tong University, 1954 Huashan Road, Shanghai 200030, PR China

e-mail: hm.zhang@sjtu.edu.cn

S. Luo

Research Institute, Baoshan Iron and Steel Co., Ltd, Fujin Road 655, Shanghai 201900, China

© The Minerals, Metals & Materials Society 2022

K. Inal et al. (eds.), *NUMISHEET 2022*, The Minerals, Metals & Materials Series, https://doi.org/10.1007/978-3-031-06212-4_43

471

vehicles and devices. However, the stretch-frangibility (the ability to be formed into a complex shape) is still one of the major obstacles of AHSS sheets for application in complex stamping operations [1].

The hole expansion (HE) test is a common method to characterize the formability edge crack resistance of metal sheets. Park et al. [2] used a dual-scale finite element model to predict the failure initiation and location near the hole edge in the hole expansion of a hyper-burring steel sheet. The central hole was fabricated through a wire cut which neglected the influence of initial defects. However, few experimental results can be used to compare with the results of simulation for explaining the actual failure mechanism. Kamibayashi et al. [3] investigated the strength–ductility–HE ratios of two ferrites steel with added Ti and Nb, respectively; the author inferred that the inferior strength–ductility–HE ratio balance of Nb steel was mainly caused by the formation of large textural colonies and MnS.

The microstructural characteristics have immense influences on strain localization [4], voids nucleation and growth [5], and crack propagation [3, 5, 6], so the evaluation of stretch-flangeability of AHSS involves the analysis of micromechanical and failure behaviors of the AHSS sheet's microstructure with initial defects. However, only a few micromechanical-based modeling techniques have been used to investigate the HER recently. Kim et al. [7] analyzed the stretch-flangeability of two DP steels with different microstructures carried out by a realistic microstructure-based model, but this model was constructed by the SEM graph which has neglected the crystal orientations. Park et al. [2] used a dual-scale finite element model for predicting the failure initiation and location near the hole edge in the hole expansion of a hyper-burring steel sheet. Choi et al. [8] used the crystal plasticity finite element method (CPFEM) by directly mapping the microstructure into finite element meshes and capturing the effect of microstructural heterogeneity on hot spots for the void formation and micro-crack propagation. Nevertheless, the direct mapping method neglected the difference in deformation characteristics at different positions in the thickness direction, which can be the potential fracture initiation sites.

In this article, the effect of microstructural characteristics on the deformation and failure mechanisms of AHSS during the HE operations were investigated using a hierarchy modeling approach based on FEM and CP modeling. The engineering scale simulation of the HE process was completed using the isotropic elastoplastic FEM. Microstructural data including phase morphology, grain size, and crystal orientation obtained from EBSD characterizations were used to build high-fidelity representative volume elements for the CP simulation. The deformation paths of critical elements (potential crack initiation points) at the hole edge that were acquired by macroscopic FEM were used as the periodic boundary conditions for CP simulation. The macro fractography, void nucleation and growth mechanisms, micro-crack propagation as well as plastic deformation heterogeneity were analyzed through an optical microscope (OM) and field-emission scanning electron microscope (FE-SEM) observations at the hole edge.

Experimental and Modeling Procedures

The studied material is a martensitic (MS 1150/1400) steel sheet with a thickness of 3.0 mm. It consists of a martensitic matrix with smaller amounts of bainite. For its superior strength, it is commonly used to manufacture side intrusion beams, bumper beams, bumper reinforcements, etc. [9].

Microstructure Characterization

The initial microstructure and texture of the sheet were characterized by electron-backscattered diffraction (EBSD) on the RD-TD plane. The experimental system is a VEGA 3 XMU (LaB6) FE-SEM (TESCAN) equipped with an Oxford/Nordlys EBSD detector. The specimens were mechanically polished with SiC papers of grit size 100, 240, 320, and 600 first, then followed by fine polishing operations with 9 and 3 μm diamond suspensions, as well as 0.05 μm alumina suspension. After the mechanical polishing, each specimen went through a vibratory polishing operation with 0.02 μm silica suspension for two hours. The SEM-EBSD system was operated at an acceleration voltage of 20 kV and a working distance of 20 mm; it scanned an area with the size of 40 μm \times 40 μm and the step size of 0.1 μm , i.e., collected high-resolved microstructure maps with 160,000 data points totally. The data was processed by the AZtec[®] system (Oxford Inst.).

Figure 1 shows the EBSD characterized microstructure of the as-received sheet. Figure 1a corresponds to the orientation imaging microscopy (OIM) which evidences that the as-received steel sheet has an equiaxial microstructure. The band contrast (BC) map shown in Fig. 1b demonstrates the martensitic microstructure of the steel is in general homogeneous. Figure 1c shows the grain boundary (GB) structure, in

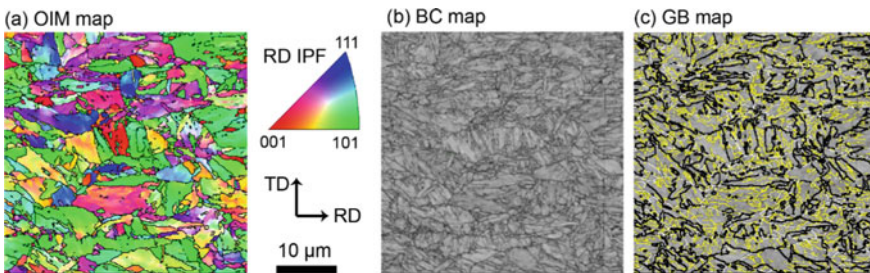


Fig. 1 The EBSD characterized microstructure of the as-received martensitic steel; **a** orientation imaging microscopy coloring with the RD inverse pole figure; **b** band contrast map; **c** grain boundaries with black lines representing HAGB and yellow lines LAGB

which the black lines represent the high angle GBs (HAGBs) identified with a mis-orientation angle above 15° , and the yellow lines for the low angle GBs (LAGBs) identified with a mis-orientation angle below 15° . It shows clearly that the LAGBs fill in the grains.

Hole Expansion Experiments

An in-house HE tester following the ISO standard 16630 was employed to perform the HE experiments. The tester is composed of a 60° conical punch, a die, and a blank holder that avoids the draw-in of material during the HE processes. The specimens for the HE test are square plates with a size of $100\text{ mm} \times 100\text{ mm}$ and a 10 mm diameter center hole; the center hole was fabricated by punching. A video recorder camera was used to capture the HE process and photograph cracks online. The tests were stopped when a crack completely penetrated through the sheet thickness. The macro fractography of the fracture surface at the hole edge was observed by optical microscope subsequently. The cross-section in the vicinity of the hole surface was cut along the diagonal line for the analyses of micro-failure mechanisms and plastic heterogeneity by field-emission scanning electron microscopy (FE-SEM).

Uniaxial Tensile Tests

Uniaxial tensile tests at room temperature were conducted for the as-received sheet in both the RD and TD; three tests were repeated for each direction. According to the Chinese standard GB/T 228.1-2010 (ISO 6892-1:2009, MOD), dog-bone specimens with a gauge length of 50 mm and width of 12.5 mm were machined via electrical discharge machining. The tensile tests were carried out quasi-statically on an electronic testing machine (Instron Model 8080 with a load cell of 100 kN capacity) at a constant crosshead speed of 0.05 mm/s, corresponding to a nominal strain rate of 0.001/s. A DIC system (Aramis) was employed to measure the deformation and strain field. Prior to the tensile tests, all specimens were sprayed with random speckle patterns. The 3D position change of the speckles was photographed with two high-resolution cameras at a frequency of 2 Hz; the strain field of the deformed specimens then was computed by the commercial DIC software GOM.

Hierarchical Modeling Methodology

In this work, we proposed a hierarchy modeling methodology to capture the influence of microstructure on the stress/strain partition and damage initiation in the material during the HE operation. At the macroscopic engineering scale, traditional

FEM simulations of the HE process were carried out in the commercial FEM solver ABAQUS/Explicit to track the evolution of deformation and stress state in the sheet; the deformation gradient (\mathbf{F}) and stress state in the region of interest (critical elements or integration points) were extracted in a prescribed frequency. The data of \mathbf{F} and stress state through the entire HE process were then organized into a group of periodic boundary conditions (PBCs) for the full-field CP simulations at the microscopic scale. The PBCs were applied on the microstructure-based representative element volume (RVE) which uses the EBSD map (shown in Fig. 1) as the input directly. Therefore, the CP modeling is capable of considering both the complex boundary conditions of the critical elements and the realistic microstructure-like grain morphology and orientation.

It is noted that the material model used in the FEM simulation is the classic J2 constitutive model. Since the build-in J2 model of ABAQUS does not support the output of deformation gradient and the first Piola–Kirchhoff stress tensor \mathbf{P} , a VUMAT identical to the build-in J2 model was developed designedly. In the VUMAT, the deformation gradient and the stress tensor are stored in the user-defined state variables and written to the result data file. A python script was then used to extract the data of \mathbf{F} and \mathbf{P} of the critical element. Figure 3 shows the evolution of the components of \mathbf{F} and \mathbf{P} at the critical element (as shown in Fig. 2) in the HE process. The subscript ‘2’ is the working direction of the punch, and also the thickness direction of the sheet; the subscripts ‘1’ and ‘3’ are the other two in-plane orthogonal directions, i.e., the RD and TD. According to the evolution of the components of the deformation gradient shown in Fig. 3a, one can see that the critical element undergoes a jointly in-plane biaxial stretching deformation and in-plane shear deformation; all the out-of-plane shear deformation are well suppressed as anticipated, while in-plane shear deformation F_{31} and F_{13} are noticeably up to -0.5 . Figure 3b shows the evolutions of the components of the first Piola–Kirchhoff stress. The stress evolutions substantially correlate with those of the deformation gradient, i.e., in-plane tensile stresses, out-of-plane compressive stress, noticeable in-plane shear stresses, and small out-of-plane shear stresses. However, the evolutions of the stress components are rather irregular and show obvious oscillation. This is mainly because of the complicated contact between the tools and the material.

The results of both \mathbf{F} and \mathbf{P} were then organized into the PBCs for the CP simulations. A mixed PBCs, i.e., the components F_{21} , F_{22} , F_{31} , F_{32} , and F_{33} of \mathbf{F} and the components P_{11} , P_{12} , P_{13} , and P_{23} of \mathbf{P} were prescribed based on the macroscopic data shown in Fig. 3, while the other components were relaxed. More details about the assigning of the PBCs can be found in the work of Zhang et al. [10].

As stated, the studied steel sheet is made of a martensitic matrix with a small amount of bainite. Without loss of generality, we treat the material as a single-phase martensite when performing the full-field CP simulation, and the martensite was assumed to have a BCC crystal structure like the ferrite [11]. For BCC metals, the potential slip systems at room temperature generally include the slip families $\{\bar{1}10\}\langle 111 \rangle$ and $\{\bar{2}11\}\langle 111 \rangle$; both contain 12 slip systems. Given the frequently reported $\langle 111 \rangle$ glide mechanism of BCC metals, we adopted the same material parameter for both slip families $\{\bar{1}10\}\langle 111 \rangle$ and $\{\bar{2}11\}\langle 111 \rangle$. First of all, the elastic constants

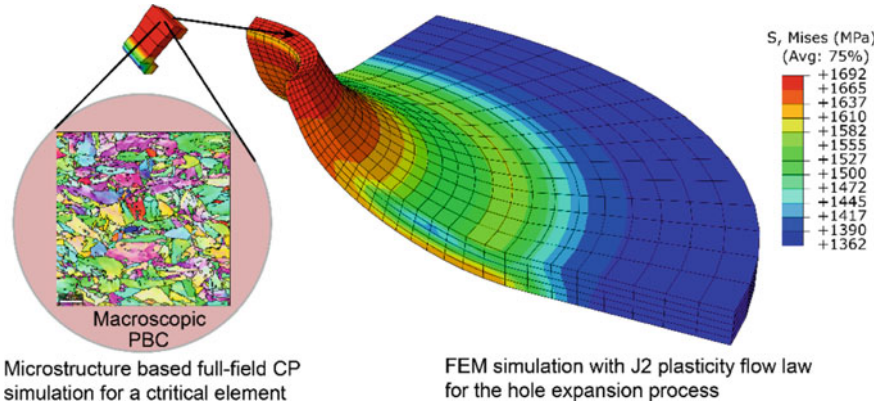


Fig. 2 The methodology of the proposed hierarchy modeling approach. FEM simulation provides the history of deformation and stress state of the specimen during the HE operation. The FEM predicted the time-dependent deformation gradient and stress state of the critical element were imported to a full-field CP modeling which incorporates the authentic microstructure of the material

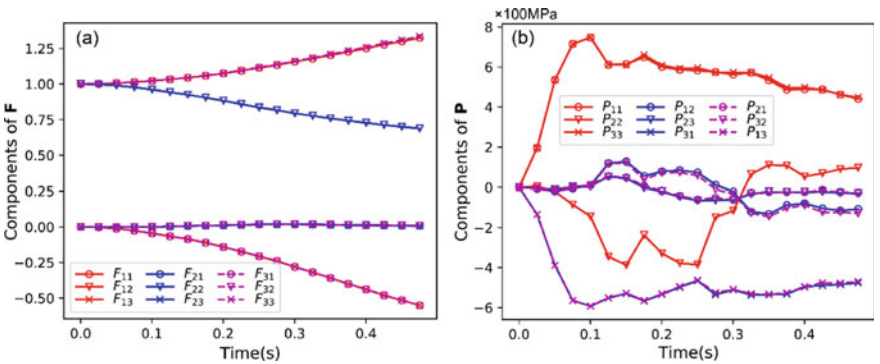


Fig. 3 The evolution of the components of the deformation gradient and the first Piola–Kirchhoff stress tensor at the critical element is shown in Fig. 2. The results were predicted by FEM simulation with the J2 plasticity model

C_{11} , C_{12} , and C_{44} , the reference slip rate $\dot{\gamma}_0$, and the rate sensitivity coefficient m are well documented and referred to in the work of Tasan et al. [12]. The parameters g_0 , g_∞ , h_0 , and a , which describe the evolution of slip resistance, were determined from the experimental data via an in-house inverse method [11] (Fig. 4).

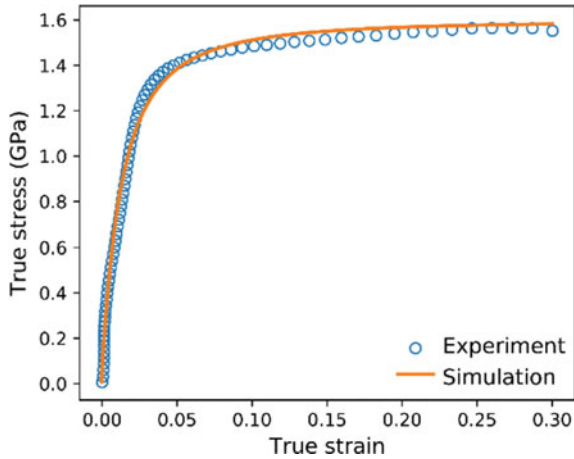


Fig. 4 The stress–strain curves of the studied martensitic AHSS, one of the experiment data versus the predicted one by CP model with constitutive parameters listed in Table 1.

Table 1 The CP constitutive parameters for the martensitic steel sheet

g_0 (MPa)	g_∞ (MPa)	h_0 (GPa)	a	$\dot{\gamma}_0$ (s ⁻¹)	m	C_{11} (GPa)	C_{12} (GPa)	C_{44} (GPa)
30.8	761	26.9	1.57	0.001	0.05	417.4	242.4	211.1

g_0 , g_∞ , h_0 , and a were identified according to the experimental data; other parameters are taken from Tasan et al. [12]

Results and Discussion

Macro and Micro-failure Mechanisms

We have tested three specimens for the HE operation. The HE rates are 46, 42, and 32%, i.e., the average HE rate is about 40%. The MS steel essentially shows high strength and considerable stretch formability. Figure 5a shows the macro fractography in the hole's edge region of one HET specimen. Small diffused cracks (marked with the dashed ellipse) distribute uniformly in the hole's inner edge and propagate less than a quarter of the sheet thickness. This is primarily because the crack growth is suppressed by the compressive stress developed in the hole's inner edge due to the direct contact with the conical punch. Moreover, on the exposed cross-section there are also some large cracks that transverse the thick, as marked with solid ellipses. These cracks initiated in the hole's outer edge and propagated along a direction orienting with an angle of about 45° to the circumferential direction.

Figure 5b, c shows the SEM micrographs with magnification 2000× and 5000× of the regions close to the crack-tips. Figure 5b shows that the material near the crack-tips was significantly distorted which provides the channel for the propagation

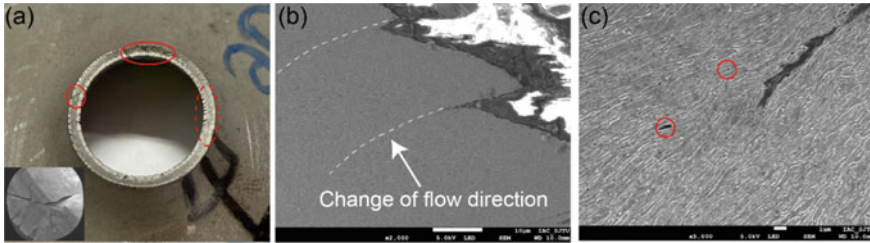


Fig. 5 Failure mechanisms of the martensitic material; **a** macroscopic fractography of the hole expansion specimen; SEM micrographs with magnification, **b** 2000 \times and **c** 5000 \times of the regions close to the crack-tips

of cracks, as marked with the dash lines. It implies that the high-stress concentration near the crack-tips renders strong strain localization to maintain deformation compatibility. From the high magnification image shown in Fig. 5c, one can see that the voids of various sizes (as exemplified with the solid circles) distribute in the studied region. Besides, the near-equiaxial microstructure was obviously elongated during the HE process.

We further characterized the microstructure in the region away from the hole edge, as shown in Fig. 6. Clusters of micro-voids, highlighted with boxes, can be clearly seen in Fig. 6a, which means that damage was initiated early in the sheet. The microstructure was also elongated, but not too significant like that shown in Fig. 5c. From the high-magnified image of Fig. 6b, it is found that the micro-voids distribute along the boundaries of the microstructure. The aggregation of the micro-voids shows a strong correlation with the microstructural morphology of the martensite. Moreover, although the microstructure was elongated, micro-voids are essentially equiaxial. That is, in the region away from the hole edge, the growth of voids is not evident.

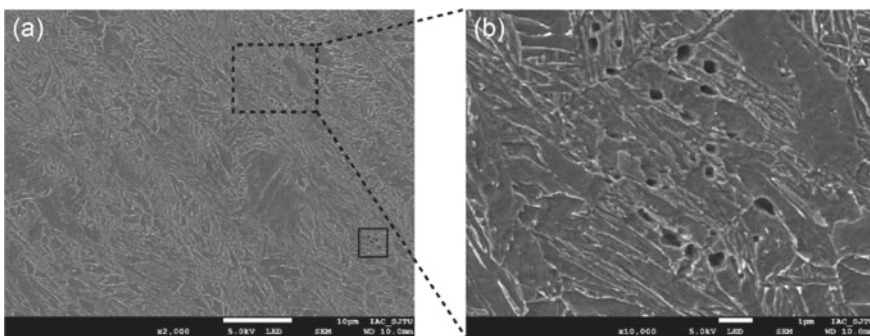


Fig. 6 SEM characterized microstructure in the region apart from the hole edge: **a** with a magnification of 2000 \times ; **b** with a magnification 5000 \times

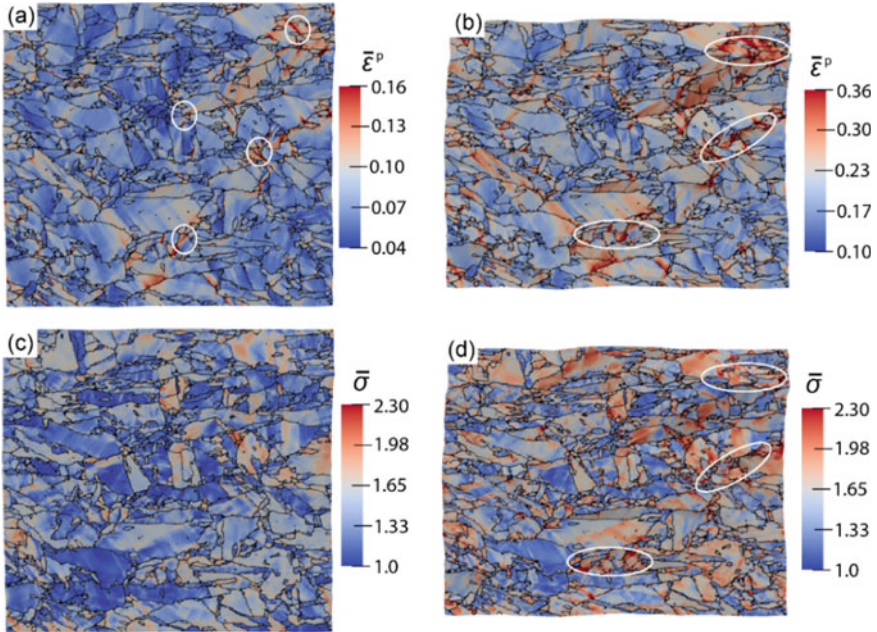


Fig. 7 Contour maps of the grain-level strain and stress distributions; **a** and **b** the strain distributions of the RVE deformed at 11% and 37% HE ratios, respectively; **c** and **d** the stress distributions at 11% and 37% HE ratios, respectively

Grain-Level Strain/Stress Partitions

Full-field CP simulations are further used to explore the effect of microstructure on stress and strain partition during the HE process. Figure 7 shows the counter maps of the grain-level stress and strain distributions; Fig. 7a, b corresponds to the strain maps of the RVE at the deformation stage with the HE ratio of 11% and 37%, respectively; and Fig. 7c, d corresponds to the stress maps. The results clearly show that both the stress and strain distributions are strongly inhomogeneous, strain localizations occur early at GBs, particularly in the region with fine-size microstructure, as highlighted by the circles in Fig. 7a. These regions primarily serve as the nucleation sites of micro-voids, which agrees well with the experimental result shown in Fig. 5. The hot spots of the stress distribution, in contrast, do not distribute at GBs but appear in some particular grains, i.e., the grains with hard orientation. As a result, the heterogeneous microstructure renders the strong inhomogeneous distributions of stress and strain; and the deformation compatibility requires large deformation in the fine size microstructures and GBs. With the increase of the HE ratio, as shown in Fig. 7b, d, the strain localizations become more obvious, and shear bands are clearly seen. These shear bands propagate through regions with GBs and fine size microstructures, which provide the channel for the growth of cracks.

Conclusion

In this work, we developed a hierarchy modeling approach for the multiscale simulation of the hole-expansion (HE) of advanced high-strength steel sheets. The FEM simulation was adopted to obtain the complex deformation path and stress state of the critical elements during the whole HE process. The predicted deformation gradient and stress state were then imported to a full-field crystal plasticity (CP) modeling which uses the realistic microstructure of the material as the input. A martensitic AHSS sheet was used as the case study. The postmortem examination of the HE specimen evidences that the damage nucleation and crack propagation show a strong correlation with the microstructural morphology of the martensite. The grain-level strain and stress fields obtained by the hierarchy modeling technical are strongly inhomogeneous and closely related to the microstructure; strain localizations occur early at grain boundaries, particularly in the region with fine-size microstructure. The predicted hot spots and shear bands of the strain field can be correlated well with the SEM micrographs.

Acknowledgements The authors acknowledge the funding support from the National Natural Science Foundation of China with the projects of No. 52075329, and Shanghai Rising-Star Program (20QA1405300).

Appendix: Finite Strain CP Theory

The CP model was implemented in a finite strain framework via the multiplication decomposition of deformation gradient, i.e., $\mathbf{F} = \mathbf{F}^e \mathbf{F}^p$ where \mathbf{F}^e denotes the elastic deformation gradient and \mathbf{F}^p the plastic one. The plastic velocity gradient due to dislocation slip is expressed as

$$\mathbf{L}^p = \sum_{\alpha} \dot{\gamma}^{\alpha} \mathbf{S}^{\alpha}, \text{ with } \mathbf{S}^{\alpha} = \mathbf{m}^{\alpha} \otimes \mathbf{n}^{\alpha} \quad (1)$$

with \mathbf{S}^{α} the Schmid tensor of the α slip system, $\dot{\gamma}^{\alpha}$ the plastic shear rate, and \mathbf{m}^{α} and \mathbf{n}^{α} the slip direction and the normal of the slip system. A rate-dependent flow law was used to describe the plastic shear rate $\dot{\gamma}^{\alpha}$, i.e.,

$$\dot{\gamma}^{\alpha} = \dot{\gamma}_0 \left| \frac{\tau^{\alpha}}{g^{\alpha}} \right|^{1/m} \text{sign}(\tau^{\alpha}), \text{ with } \tau^{\alpha} = (\mathbf{F}^{eT} \mathbf{F}^e \cdot \mathbf{T}^e) : \mathbf{S}^{\alpha} \quad (2)$$

with $\dot{\gamma}_0$ the reference slip rate, m the rate sensitivity coefficient, and g^{α} the slip resistance. \mathbf{T}^e is the second-order Piola–Kirchhoff stress tensor expressed on the intermediate stress-free configuration.

The evolution of g^α is described as follows:

$$\dot{g}^\alpha = \sum_{\beta} h_{\alpha\beta} \dot{\gamma}^\beta \text{ with } h_{\alpha\beta} = h_0 [q + (1 - q) \delta^{\alpha\beta}] \left| 1 - \frac{g^\beta}{g_\infty} \right|^a \quad (3)$$

Here, h_0 denotes the hardening modulus of slip systems, g_∞ the saturated slip resistance, and a an estimated constant. q describes the interaction among slip systems. It is assumed to be 1.0 for coplanar slip systems and 1.4 for non-coplanar slip systems.

For most metals, \mathbf{T}^e is formulated by Hooke’s law as

$$\mathbf{T}^e = \mathbf{C}:\mathbf{E}^e \text{ with } \mathbf{E}^e = \frac{1}{2}(\mathbf{F}^{eT}\mathbf{F}^e - \mathbf{I}) \quad (4)$$

where \mathbf{E}^e is the elastic Green–Lagrange strain tensor, and \mathbf{C} is the fourth-order elastic tensor. For cubic crystals, \mathbf{C} can be specified with three elastic constants C_{11} , C_{12} , and C_{44} .

References

1. Kuziak R, Kawalla R, Waengler S (2008) Advanced high strength steels for automotive industry: a review. *Archiv Civil Mech Eng* 8(2):103–117
2. Park S et al (2019) Practical microstructure-informed dual-scale simulation for predicting hole expansion failure of hyper-burring steel. *Int J Mech Sci* 156:297–311
3. Kamibayashi K, Tanabe Y, Takemoto Y, Shimizu I, Senuma T (2012) Influence of Ti and Nb on the strength-ductility-hole expansion ratio balance of hot-rolled low-carbon high-strength steel sheets. *ISIJ Int* 52:151–157
4. Panich S et al (2014) Investigation of anisotropic plastic deformation of advanced high strength steel. *Mater Sci Eng A* 592:207–220
5. Teng ZK, Chen XM (2014) Edge cracking mechanism in two dual-phase advanced high strength steels. *Mater Sci Eng A* 618:645–653
6. Kim JH et al (2019) Effect of prior austenite grain size on hole expansion ratio of quenching and partitioning processed medium-Mn steel. *JOM* 71(4):1366–1374
7. Kim JH et al (2010) Hole-expansion formability of dual-phase steels using representative volume element approach with boundary-smoothing technique. *Mater Sci Eng A* 527(27–28):7353–7363
8. Choi SH, Kim EY, Kim SI (2014) The micromechanical deformation behaviors of hot-rolled 590FB steel during hole-expansion test. *Int J Plast* 58:184–200
9. Keeler S, Kimchi M, Mooney PJ (2017) Advanced high-strength steels: application guidelines version 6.0. *WorldAutoSteel*
10. Zhang H, Diehl M, Roters F, Raabe D (2016) A virtual laboratory using high resolution crystal plasticity simulations to determine the initial yield surface for sheet metal forming operations. *Int J Plast* 80:111–138

11. Li Q, Zhang H, Chen F, Xu D, Sui D, Cui Z (2020) Study on the plastic anisotropy of advanced high strength steel sheet: experiments and microstructure-based crystal plasticity modelling. *Int J Mech Sci* 176:105569
12. Tasan CC, Diehl M, Yan D, Zambaldi C, Shanthraj P, Roters F, Raabe D (2014) Integrated experimental–simulation analysis of stress and strain partitioning in multiphase alloys. *Acta Materialia* 81:386–400

Investigation on the High Strain Rate Formability of Al-Cu-Mg Alloy by Solid–Liquid Coupling Simulation



Shi-Hong Zhang and Da-Yong Chen

Abstract The formability of the sheet is getting more attention these several years for the impact hydroforming (IHF). Investigation on the formability is complicated for the IHF because of the limited forming time and testing space. The finite element modeling is no doubt a high-efficient and low-cost method to evaluate the high strain rate formability. The Al-Cu-Mg sheet specimen was tested by tensile test under different strain rates. The stress–strain curve characterizes with S-shape when the strain rates are on the level of $10^3/s$. A modified Johnson–Cook model was established in LS-DYNA software to precisely describe the stress–strain response. The fluid structure interaction algorithm was employed to realize the solid–liquid coupling. The formability improvement owns to fluctuating feeding when the strain rates are 1000/s–2000/s. Fluctuating loading helps the material feeding, meanwhile the resistance of necking is improved when the strain rates change from 3000/s to 5000/s.

Keywords Al-Cu-Mg alloy · Impact hydroforming · Modified Johnson–Cook model · Fluid structure interaction · High strain rate formability

Introduction

Impact hydroforming (IHF) represents the process of utilizing the energy produced by the projectile with high speed to form the sheet or tube blank to the final part, in which the liquid is selected to be the medium to transfer the impact energy from the projectile to the blank [1]. The energy characterized with wave loading of inhomogeneous distribution in both axial and radial directions. The typical feature is that the process combines the advantages of impact loading from high speed hammer and flexible effect from the liquid. The energy transfer and propagation were systematically

S.-H. Zhang (✉) · D.-Y. Chen
Institute of Metal Research, Chinese Academy of Sciences, Shenyang 110016, People's Republic of China
e-mail: shzhang@imr.ac.cn

investigated using the equipment of impact hydroforming (the IHF press) which was designed and manufactured based on the relative study according to the work of Ma et al. [2].

According to the previous results, IHF could increase the formability of low-plasticity material such as aluminum and titanium alloy, et al. Several typical parts had been developed by using this technology which included the complicated double-frame aircraft aluminum sheet part, cup part with deep cavity [3, 4]. Furthermore, the recent investigated testing demonstrated that one kind of dynamic recovery emerged and contributed to plasticity increase for some Al-Cu-Mg alloy under impact loading.

However, IHF characterized with high speed and high energy which increased the difficulty of elaborate investigation on the measurement of strain rates and forming pressure, and analysis of pressure distribution in narrow space and limited time. Apparently, the finite element modeling (FEM) was a useful method for this kind of investigation. Especially, the solid–liquid coupling FEM was effective to deal with the procedure including the interaction of the projectile and the liquid, as well as the liquid and the blank to be formed [5, 6]. In this study, what was interested including the variation of part outline with time, the stress and strain state in a different area, also including the thickness distribution. Meanwhile, the contribution of the impact loading to the formability was investigated by the method of coupling FEM.

Establishment of Modeling

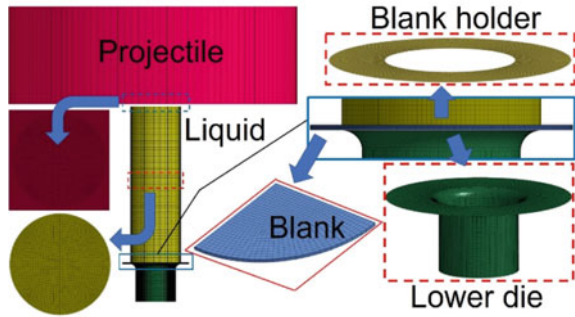
The Basis of Fluid Structure Interaction

The Fluid Structure Interaction (FSI) was chosen to tackle with the coupling interaction between the projectile and the liquid, as well as the liquid and the blank. It mainly involved the keyword of “CONSTRAINED_LARGRANGE_IN_SOLID” in LS-DYNA [7]. Meanwhile, the ALE algorithm was utilized to treat with the problem of convergence for the liquid under large deformation which would initiate the distortion [8]. It considered the problem of element motion and material node which could effectively deal with the simulation of IHF occurred in a very short time and large deformation [6].

Geometrical Models

A cup part was designed to investigate the feature of forming, stress and strain state, the wall thickness distribution under both quasi-static hydroforming and impact hydroforming. The forming height was set as 16.86 mm and 18.82 mm, respectively, according to the corresponding experiment. The blank initial thickness was 1.2 mm, the diameter of die, and radius of corner was 38.5 mm and 5 mm, respectively.

Fig. 1 Geometrical model and meshing



The geometrical model was discrete to be solid and shell elements according to its function on the solid–liquid coupling FEM as illustrated in Fig. 1. The projectile, liquid, and blank were discrete to be eight-node hexahedron elements with same size from the axial projection to guarantee the coupling calculation. And the drawing die and blank holder were treated as shell elements of four-node quadrilateral to consider the efficiency of calculation and precision comprehensively [6].

Equation of State

The Gruneisen equation was an ideal option to describe the behavior of liquid during the impact hydroforming. The pressure was listed as follows for both compressed and expanded material according to the Gruneisen equation of state:

$$P = \frac{\rho_0 C^2 \mu [1 + (1 - \frac{\gamma_0}{2})\mu - \frac{a}{2}\mu^2]}{[1 - (S_1 - 1)\mu - S_2 \frac{\mu^2}{\mu + 1} - S_3 \frac{\mu^3}{(\mu + 1)^2}]^2} + (\gamma_0 + a\mu)E \tag{1}$$

and

$$P = \rho_0 C^2 \mu + (\gamma_0 + a\mu)E \tag{2}$$

And the relative density was used to present the compression as follows:

$$\mu = \frac{\rho}{\rho_0} - 1$$

where ρ_0 stands for the water density in the beginning, C is the speed of sound transferring in the water with room temperature, E represents the internal energy in the unit volume, γ_0 and a stands for Gruneisen gamma and its volume correction in the first order.

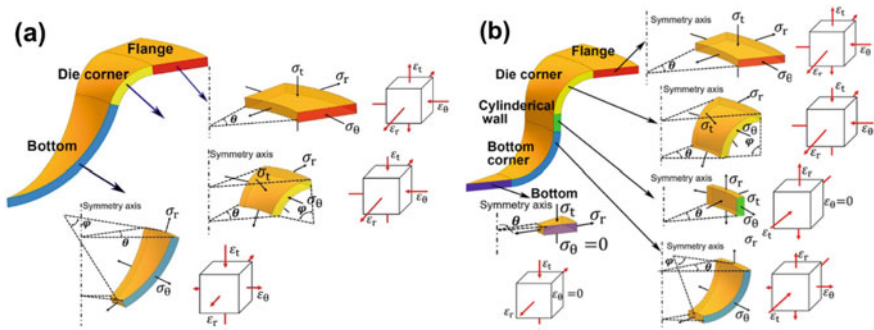


Fig. 2 Stress–strain state for cup part subjected to impact hydroforming: **a** Before the bottom touch the die; **b** After the bottom touch the die

Results and Discussion

Stress and Strain State Analysis Under IHF

The stress and strain states were analyzed for the forming procedure of cup part under IHF as illustrated in Fig. 2a, b which represented the stage of uncompleted and completed forming. It was illustrated in Fig. 2a that the specimen experienced identical state of stress and strain with conventional sheet hydroforming. Furthermore, the specimen possessed the area of cylindrical wall after contacting with the die bottom which characterized with deep drawing. It was also found that the area of bottom and bottom corner endured more deformation under the double stretching. Hence, a better forming process should be designed for the part with large forming height although IHF could increase the formability of hard-to-form material.

The Variation of Outline with Time

The outline under different time was illustrated in Fig. 3a, b for both quasi-static and impact hydroforming. The constant time step was chosen for both forming methods which was 5s and 6×10^{-5} s, respectively, according to the whole forming time. It was found that IHF differentiated with the quasi-static hydroforming at the beginning forming stage but it was identical with quasi-static one at the middle stage from the aspect of part outline. The specimen characterized with flat bottom in the first two steps because the special loading effect exerted by IHF. The pressure characterized with radial gradient distribution in the beginning. Hence, a special loading was achieved which had the similar effect to the deep drawing with rigid punch. It had advantage of easy material feeding to the die cavity which would contribute in the central area of the part. In the final stage, the specimen contacted with the die

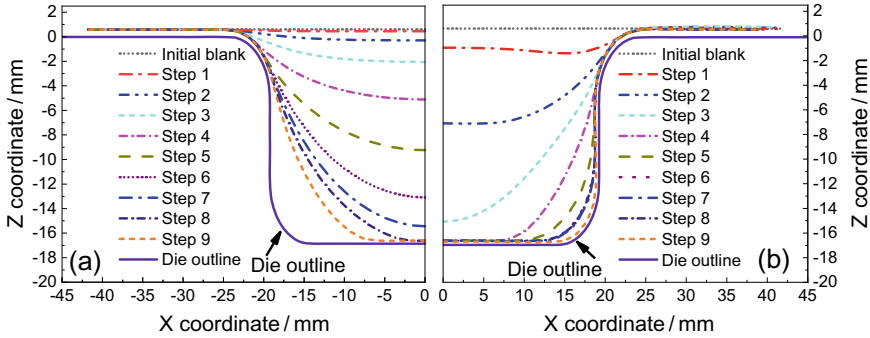


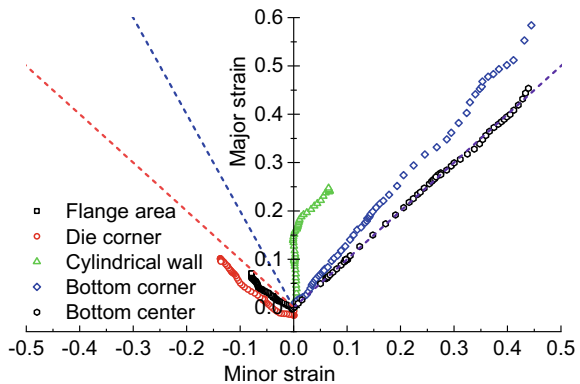
Fig. 3 The variation of outline with time: **a** Under quasi-static hydroforming; **b** Under impact hydroforming

especially at the area of bottom corner. But the specimen failed before contacted with the die corner under the quasi-static hydroforming.

The Strain Path Analysis

The forming depth increased gradually when the depth of the die cavity was increased step by step. The forming depth of 18.82 mm was achieved without the defects of wrinkle and crack using IHF. The strain paths were listed in Fig. 4 to illustrate the variation of strain in several typical areas. As for the areas of flange and die corner, the major strain increased gradually and the minor strain decreased almost along with the line of pure shear. The strain of die corner was larger than the one of flange owing to the effect of wave loading with high energy and the bending effect from die corner. The area of bottom center characterized with equal double stretching and the major and minor strains were on the level of 0.45. Furthermore, the area

Fig. 4 The strain paths evolution of several classical forming areas



of bottom corner characterized with near equal double stretching and the strains were on the level of 0.6. It was found that the bottom corner was the area of largest strain which became the most dangerous area under tension strain. These two areas were different from the conventional deep drawing with punch from the aspect of strain path. Initially, the cylindrical wall characterized with plane strain and finally converted to tension state in two directions. The feature of deep drawing was found from the above analysis. Hence, it was verified that the impact hydroforming was a procedure of hybrid process combining both deep drawing and hydro-bulging.

The Wall Thickness Distribution and Comparison

The largest forming height was 16.86 mm and 18.82 mm for quasi-static hydroforming and impact hydroforming, respectively, from the series of investigation. Therefore, the wall thickness and thinning ratio were investigated under the situation of 16.86 mm forming height for both processes. Firstly, the outline and wall thickness were measured as it was illustrated in Figs. 5 and 6, respectively. It was found that the wall thickness decreased gradually from the area of flange to bottom center. The thinning ratios of area I and II were in the range of 30–50% which stood for the vulnerable areas under hydroforming process. And the flange area retained thickening because of the circumferential-compressive stress.

The quasi-static hydroforming and IHF were compared in the aspect of thinning distribution along with radial direction. The similar state was selected for IHF to compare with the quasi-static hydroforming before crack. It was illustrated in Fig. 7 to describe the variation of thinning ratio with arc length and the relative parts obtained from experimentation. The specimen hadn't the area III under both forming means before it contacted with die corner. Furthermore, the thinning ratio was on the level of 60% and 40% for quasi-static hydroforming and impact hydroforming, respectively.

Fig. 5 The outline of the cup part at the final step using impact hydroforming

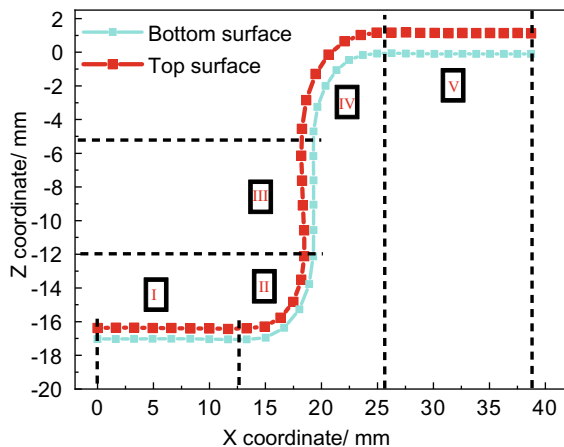


Fig. 6 The variation of wall thickness, thinning ratio with arc length along with the radial direction

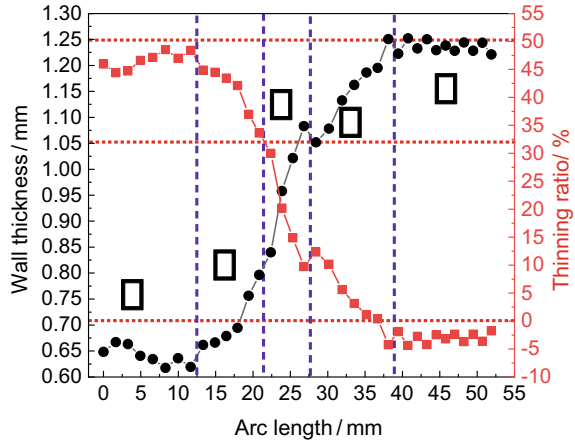
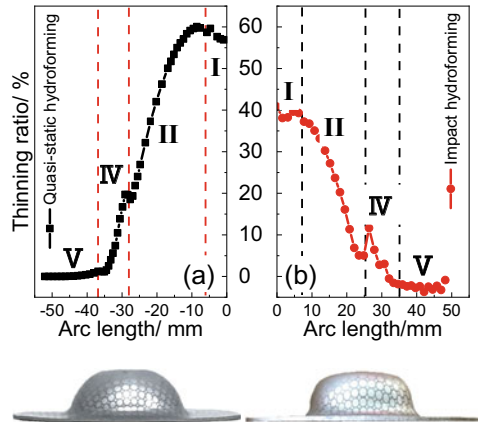


Fig. 7 The variation of thinning ratio versus arc length and corresponding parts under: **a** Quasi-static hydroforming; **b** Impact hydroforming



The larger thickening ratio was found in the part manufactured by IHF than the quasi-static one. It was attributed to the enough material feeding at the beginning stage for IHF specimen, however, the specimen experienced with almost pure bulging for quasi-static owing to the large enough holding force to satisfy the strict requirement of liquid sealing. It was concluded that the IHF increased the formability of sheet part from the aspect of helping material feeding.

Conclusions

- (1) The solid-liquid coupling FEM was an effective method to investigate the procedure of impact hydroforming based on the algorithm of FSI and ALE;

- (2) The IHF could altered the strain path in a certain range which would contribute to the material feeding into the die cavity to prevent the local thinning at the end of forming;
- (3) The maximum of thinning ratio decreased from 60 to 40% when the specimen produced by quasi-static hydroforming compared with the one by impact hydroforming.

Acknowledgements All authors appreciate the funding support from National Natural Science Foundation of China (No. 51875548), Natural Science Foundation of Liaoning Province of China (Grand No. 20180550851), Project for transfer and transformation of scientific and technological achievements, Chinese Academy of Sciences, Henan Province (No. 2020204).

References

1. Kosing OE, Skews BW (1998) An investigation of high-speed forming of circular plates in a liquid shock tube. *Int J Impact Eng* 21(9):801–816
2. Ma Y, Xu Y, Zhang SH, Banabic D, El-Aty AA, Chen DY, Cheng M, Song HW, Pokrovsky AI, Chen GQ (2018) Investigation on formability enhancement of 5A06 aluminum sheet by impact hydroforming. *CIRP Ann-Manuf Technol* 67:281–284
3. Azaryan NS, Shirkov GD, Zhuravskiy AY, Petrakovskiy VS, Batouritskiy MA (2016) Manufacture of superconducting niobium cavity parts by hydropercussion punching. *Part Nuclei Lett* 13(2):218–223
4. Abd El-Aty A, Xu Y, Zhang SH, Ha S, Ma Y, Chen DY (2019) Impact of high strain rate deformation on the mechanical behavior, fracture mechanisms and anisotropic response of 2060 Al-Cu-Li alloy. *J Adv Res* 18:19–37
5. Khodko O, Zaytsev V, Sukaylo V, Verezub N, Scicluna S (2015) Experimental and numerical investigation of processes that occur during high velocity hydroforming technologies: an example of tubular blank free bulging during hydrodynamic forming. *J Mater Process Technol* 20:304–313
6. Chen DY, Xu Y, Zhang SH, Ma Y, AbdEl-Aty A, Banabic D, Pokrovsky AI, Bakinovskaya AA (2019) A novel method to evaluate the high strain rate formability of sheet metals under impact hydroforming. *J Mater Process Technol* 116553. <https://doi.org/10.1016/j.jmatprotec>
7. LS-DYNA (2007) Keyword user's manual, version 971. Livermore Software Technology Corporation (LSTC), Livermore, CA
8. Noh WF (1964) CEL: A time-dependent two-space-dimensional coupled Eulerian-lagrangian code. In: Alder B, Fernbach S, Rotenberg M (eds) *Methods in computational physics* 3, Academic Press, New York

Neutron Diffraction and Crystal Plasticity Analysis on Q&P Steel in Deformation



Hao Yang, Dayong Li, Huamiao Wang, Yinghong Peng, and Peidong Wu

Abstract The individual phases' responses of commercial Q&P1180 steel during uniaxial tension are investigated by using the in situ neutron diffraction technique and elastic-visco-plastic self-consistent crystal plasticity method coupled with martensitic transformation crystallography theory. Stress, phase transformation, lattice strains, diffraction intensities, and textures of the constituent phases are calculated and good agreement with experimental results is obtained. The phase transformation considerably enhances the flow stress and weakens diffraction intensities of the residual austenite. The orientation dependency of transformation behavior is found to be related with the transformation potency for austenite grains with different orientations. The transformation has little effect on texture evolutions for both phases.

Keywords Q&P steel · Crystal plasticity · Neutron diffraction

Introduction

As a representative of the third generation advanced high strength steels (3G-AHSS), Q&P steels possess good combination of strength and ductility and offer great potential in forming light-weight vehicle structures [1]. The Q&P concept was originally proposed by Speer et al. [2] and has been explored for years [3]. The Q&P980 steel has been commercialized for fabrication of automotive structural and safety parts such as cross members, longitudinal beams, B-pillar reinforcements, sills, and bumper reinforcements [4]. Recently, a higher strength level 3G-AHSS steel, Q&P1180, with

H. Yang · D. Li (✉) · H. Wang · Y. Peng

State Key Laboratory of Mechanical System and Vibration, Shanghai Jiao Tong University, Shanghai 200240, China

e-mail: dyli@sjtu.edu.cn

D. Li

Materials Genome Initiative Center, Shanghai Jiao Tong University, Shanghai 200240, China

P. Wu

Department of Mechanical Engineering, McMaster University, Hamilton, ON L8S 4G7, Canada

almost the same chemical composition as Q&P980 steel, was successfully developed by BAOSTEEL.

To investigate the macroscopic mechanical behavior as well as microstructure evolution of the Q&P1180 steel during deformation, in situ neutron diffraction technique was carried out during uniaxial tension process. Stress, phase transformation, lattice strains, diffraction intensities, and textures of the constituent phases are experimentally analyzed. A dislocation density-based elastic-visco-plastic self-consistent (EVPSC) model incorporating the transformation kinetics model is established to study the effect of phase transformation on the macroscopic mechanical properties as well as microstructure evolution of the Q&P1180 steel. Good agreement with experimental results is obtained and the orientation dependency of transformation is found.

Experiment

A commercial cold rolled Q&P1180 steel sheet of 1.4 mm thickness from BAOSTEEL is used in this study.

In situ neutron diffraction measurements are performed on the sample of rolling direction (RD) during tensile deformation by an angle dispersion method on a neutron diffractometer equipped with a tensile tester at Key Laboratory of Neutron Physics of China Academy of Engineering Physics. The wavelength of the monochromatic neutron beam used in this study is 1.594 Å, and the scattering volume is ~140 mm³. The diffraction geometry is aligned such that the diffraction vector is parallel to the loading direction (LD), as shown in Fig. 1a. Namely, average information about the grains, whose {hkl} normal is parallel to the LD, is reflected in each {hkl} diffraction profile. The patterns (Fig. 1b) are recorded as binary codes and transformed by software StressTexCalculator into diffraction profiles. Diffraction profiles are obtained during temporary stops during the tensile test. Seven reflections, the α {110}, α {200}, and α {211} of the bcc crystal structure and γ {111}, γ {200}, γ {220}, and γ {311} of the fcc crystal structure, are monitored before and during loading process. Neutron diffraction profiles are measured at a total of thirteen static strain-holding stages.

There are two kinds of crystal structure in the steel, body-centered cubic (bcc or α) and face-centered cubic (fcc or γ) retained austenite (RA). The texture of each

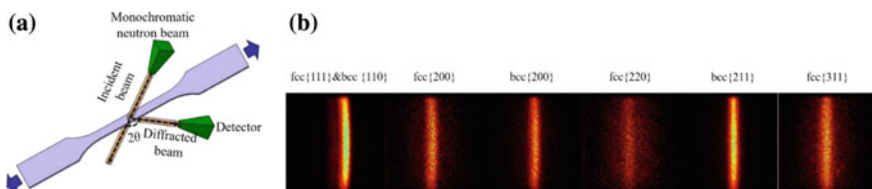


Fig. 1 a A schematic diagram for in situ neutron diffraction technique, b Diffraction patterns of crystal planes for each phase

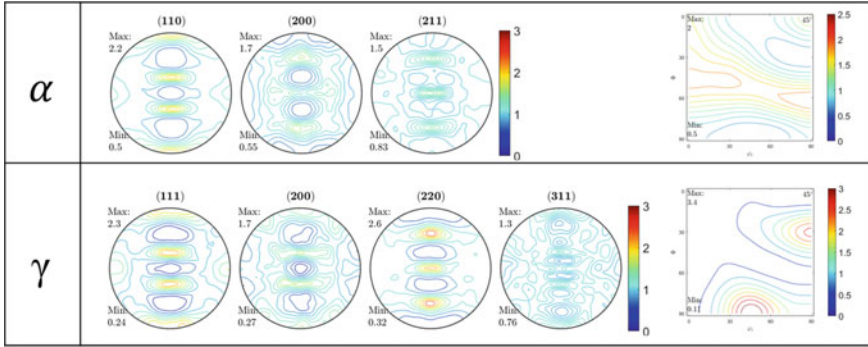


Fig. 2 Pole figures and reconstructed ODF section ($\varphi_2 = 45^\circ$) of each phase

phase before and after loading is measured by neutron diffraction method. Slices with 5 mm length and 5 mm width are cut from the samples and then glued to a cube-like shape for pole figure measurement. The orientation distribution function (ODF) of the bcc phase is remodeled by the measured $\alpha\{110\}$, $\alpha\{200\}$ and $\alpha\{211\}$ pole figures. The ODF of the fcc phase is reconstructed by using the $\gamma\{111\}$, $\gamma\{200\}$, $\gamma\{220\}$, and $\gamma\{311\}$ pole figures. The initial texture of each phase is shown in Fig. 2.

Numerical Model

The elastic-visco-plastic self-consistent crystal plasticity method [5, 6] is used here for numerical analysis. For each crystal, the total strain rate is divided by elastic strain ($\dot{\varepsilon}^e$) and plastic strain. The plastic strain consists of crystal slip ($\dot{\varepsilon}^p$) and transformation strain ($\dot{\varepsilon}^{pt}$).

$$\dot{\varepsilon}^p = \dot{\gamma}_0 \sum_{\alpha} \mathbf{P}^{\alpha} \left| \frac{\tau^{\alpha}}{\tau_{cr}^{\alpha}} \right|^{\frac{1}{m}-1} \frac{\tau^{\alpha}}{\tau_{cr}^{\alpha}} \quad (1)$$

where $\dot{\gamma}_0$ is the reference value for the slip rate; m the rate sensitivity, \mathbf{P}^{α} the Schmid tensor, τ^{α} and τ_{cr}^{α} are the resolved shear stress (RSS), and the critical resolved shear stress (CRSS), respectively. The CRSS $\tau_{cr}^{\alpha} = \tau_0^{\alpha} + \tau_{forest}^{\alpha} + \tau_{HP}^{\alpha}$ consists of initial slip resistance (τ_0^{α}) due to solid solution, the forest dislocation term (τ_{forest}^{α}), and grain boundary resistance (τ_{HP}^{α}). The forest dislocation resistance can be obtained by $\tau_{forest}^{\alpha} = \chi b^{\alpha} \mu \sqrt{\rho^{\alpha}}$ [7]. Here, χ is the dislocation interaction coefficient, b^{α} the magnitude of the Burgers vector, and μ the modulus. The dislocation densities of each slip system (ρ^{α}) are calculated by the K-M model [8]:

$$\frac{\partial \rho^{\alpha}}{\partial \gamma^{\alpha}} = k_1^{\alpha} \sqrt{\rho^{\alpha}} - k_2^{\alpha} \hat{\rho}^{\alpha}, \quad \hat{\rho}^{\alpha} = h^{\alpha \alpha'} \rho^{\alpha'} \quad (2)$$

where k_1^α and k_2^α are material parameters, respectively, $h^{\alpha\alpha'}$ the latent hardening parameters. τ_{HP}^α is defined as $\tau_{HP}^\alpha = \chi' u \sqrt{b^\alpha/d_g}$ [7], where χ' is Hall–Petch coefficient, d_g the grain size.

For the primary bcc phase and newly formed martensite (NM) grains, there is no transformation strain ($\epsilon^{Pl} = 0$). For the austenite grains, phase transformation can occur and induce transformation strain when the dislocation densities exceed a critical value. The orientation relationship matrix ARG and transformation strain ϵ^{PT} are calculated according to classical phenomenological theory of martensite crystallography (PTMC) [9]. The orientation relationship matrix $ARGs$ and transformation strain tensors of other variants are calculated by multiplication with associated crystal symmetry operation matrices. The transformation energy potential is chosen as the variant selection criteria [10]. A modified phenomenological transformation kinetics equation [11] is used to describe the volumetric evolution of an austenite grain.

$$f = 1 - \exp(-C(\rho/\rho_c - 1)) \quad (3)$$

where C is the transformation governing parameter; ρ and ρ_c are the current dislocation density and critical dislocation density of the austenite grain, respectively.

The calibrated model parameters of each phase are listed in Table 1. k_1 , k_2 , χ' , τ_0 , C and ρ_{cr} are fitting parameters and the rest are constants. k_1 , k_2 , and χ' are determined by fitting the macroscopic stress-strain curve and lattice strains of each phase; τ_0 is determined by fitting the initial yielding strength of each phase; C and ρ_{cr} are determined by fitting the volumetric evolution of the RA.

Table 1 Model parameters

Material parameters	RA	primary bcc phase	NM
Reference strain rate, $\dot{\gamma}_0/s^{-1}$	0.001	0.001	0.001
Shear modulus, μ/GPa	64.23	80	80
Burgers vector, b/nm	0.254	0.254	0.254
Interaction parameter, χ	0.35	0.35	0.35
Initial volume fraction, V_f	0.145	0.855	0
Grain size, $d_g/\mu m$	0.358	0.46	0.038
HP factor, χ'	0.063	0.063	0.063
Initial dislocation densities, ρ/m^{-2}	$1.0e^{13}$	$6.0e^{14}$	$9.0e^{14}$
Latent hardening parameter, $h^{\alpha\alpha'}$	1	1	1
k_1/m^{-1}	$6.0e^8$	$1.6e^8$	$1.6e^8$
k_2	0.01	0.0	0.0
Solid solution strength, τ_0/MPa	250	105	400
Transformation parameter, C	0.2	–	–
Critical dislocation densities, ρ_c/m^{-2}	$1.224e^{14}$	–	–

Results and Discussion

The experimental and simulated macroscopic true stress-strain curves are presented in Fig. 3a. The calculated flow stress without considering martensitic transformation is also included in the figure, indicating that martensitic transformation exerts considerable effect on the flow stress. The experimental and simulated volumetric evolutions of the RA are presented comparatively in Fig. 3b. Phase transformation is initiated when the austenite grains yield, and thereafter the volume fraction of RA decreases exponentially from the initial 14.5–5.06% at the necking.

At 10% strain, the experimental and simulated ODF sections ($\varphi_2 = 45^\circ$) of each phase are presented in Fig. 4. For the RA, the $\{112\} \langle 111 \rangle$ and $\{011\} \langle 112 \rangle$ texture components are two preferred orientations, since the $\gamma\{111\}$ families rotate toward LD (or RD) during uniaxial tension deformation. For the bcc phase, the $\alpha\{110\}$ families rotate toward LD after tension, resulting in the preferred $\{112\} \langle 110 \rangle$ and $\{111\} \langle 112 \rangle$ texture components. The simulation reasonably reproduces these texture evolutions, with only slight deviation in maximum intensity values. Furthermore, according to simulation results, phase transformation exerts little effect on texture evolution of the RA, similar to the conclusion for the stainless steel [12].

Figure 5 compares the experimental and simulated lattice strains along LD as a function of macroscopic strain. Both the RA (γ) and bcc (α) lattice strains during uniaxial tension are successfully reproduced. All the lattice strains increase linearly and rapidly at first, and then moderately after strain exceeds $\sim 0.5\%$, corresponding to ~ 1038 MPa of applied stress, and yielding for all the reflections. After yielding, the lattice strains of γ increase faster than those of α , which implies higher hardening rate of the RA. The $\gamma\{200\}$ lattice strain is the highest in the RA and $\alpha\{200\}$ is the highest in the bcc phase, indicating the lowest stiffness of the two reflections.

Figure 6a compares the simulated and measured diffraction intensities of each crystal plane as a function of macroscopic strain. The diffraction intensities of $\alpha\{211\}$ reflection are the strongest while $\gamma\{220\}$ reflection is the weakest. The diffraction

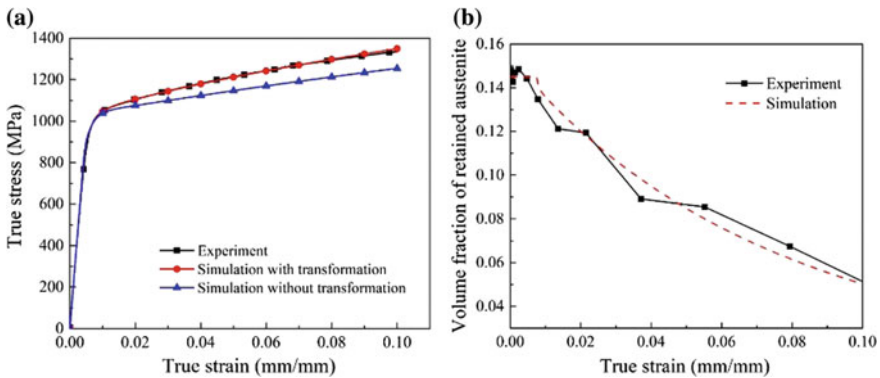


Fig. 3 a Measured and simulated stress, b Measured and simulated volume fraction of the RA

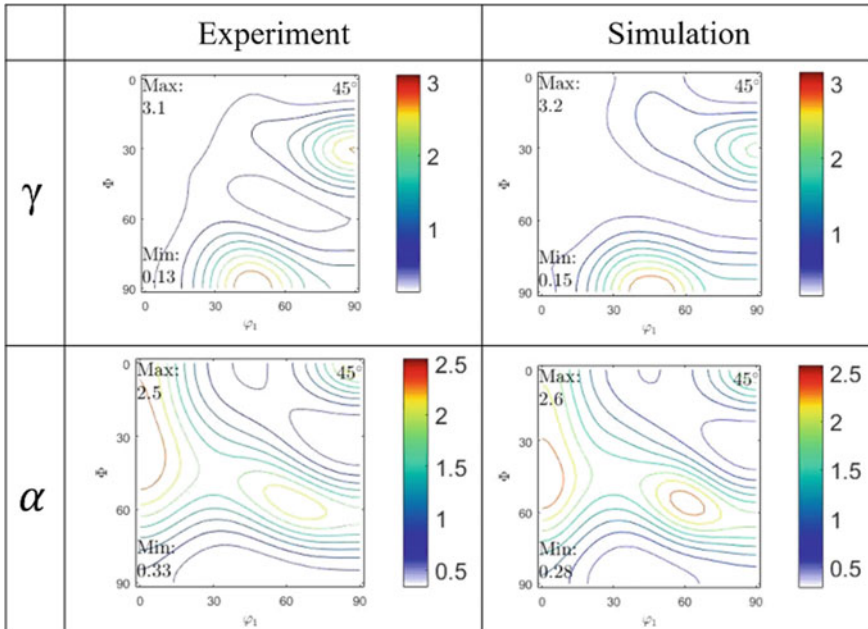


Fig. 4 Measured and simulated textures of the RA and bcc phase after loading

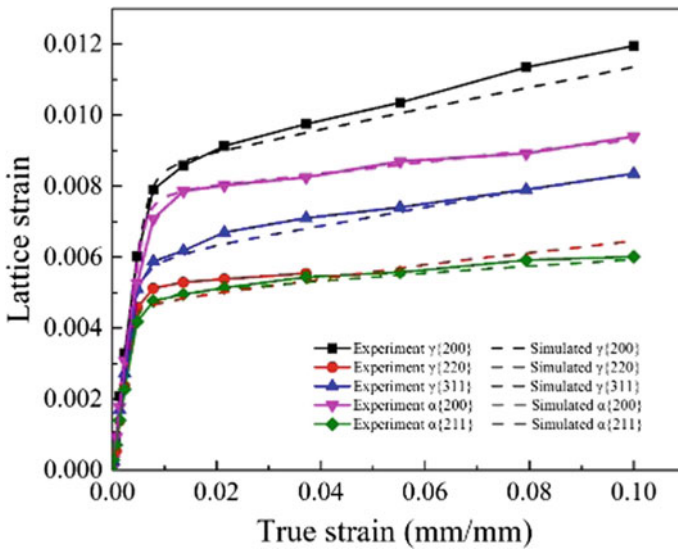


Fig. 5 Measured and simulated lattice strains

intensities of all the crystal planes decrease with increasing strain. For the α phase, the variation of the diffraction intensities is mainly caused by grain rotation. For the γ phase, the diffraction intensities are affected by both grain rotation and phase transformation. The diffraction intensities of each crystal plane with macroscopic strain are also simulated without considering transformation, and the results are shown in Fig. 6b. Since phase transformation has little effect on the diffraction intensities of the α phase, the results are not shown in the figure. The diffraction intensities of $\gamma\{200\}$ keep increasing; the diffraction intensities of $\gamma\{311\}$ almost do not change; the diffraction intensities of $\gamma\{220\}$ decrease with increasing strain. The comparison between Fig. 6a, b shows that the stability of the RA in Q&P1180 steel is orientation-dependent and the austenite grains with $\gamma\{200\}$ orientation along tensile direction have preferential transformation tendency. To study why the $\gamma\{200\}$ has preferential transformation tendency, we put three austenite grains with ideal $\gamma\{200\}$ ($\varphi_1 = 90^\circ, \phi = 90^\circ, \varphi_2 = 90^\circ$), $\gamma\{220\}$ ($\varphi_1 = 180^\circ, \phi = 90^\circ, \varphi_2 = 45^\circ$) and $\gamma\{311\}$ ($\varphi_1 = 228^\circ, \phi = 72^\circ, \varphi_2 = 72^\circ$) orientation along the tensile direction into the aggregate and perform the same simulation. It was found that when transformation occurs, the largest transformation energy potential of the 24 variants in $\gamma\{200\}$ grain is twice as those in $\gamma\{220\}$ and $\gamma\{311\}$ grains. In this sense, the orientation-dependent martensitic transformation is found to be related with the transformation energy potential.

Conclusion

In this paper, in situ neutron diffraction coupled with crystal plasticity method was carried out to study the macroscopic mechanical behavior as well as microstructure evolution of the Q&P1180 steel. Stress, phase transformation, lattice strains, diffraction intensities, and textures of the constituent phases are numerically analyzed

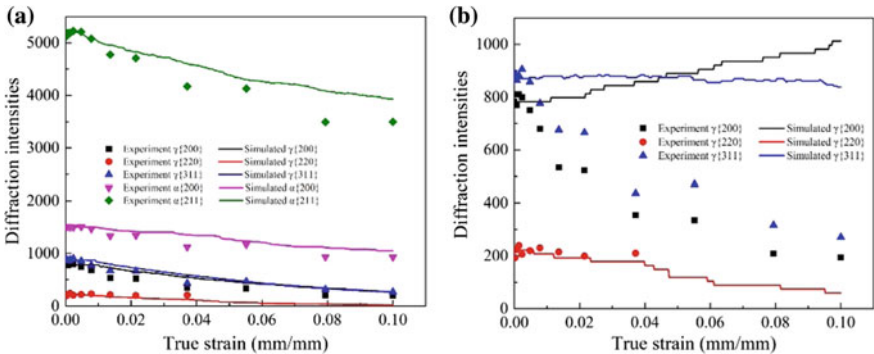


Fig. 6 a Measured and simulated diffraction intensities considering phase transformation, b measured and simulated diffraction intensities of the RA without considering phase transformation

and good agreement with experimental results is obtained. The phase transformation considerably enhances the flow stress and weakens diffraction intensities of the residual austenite. The orientation dependency of transformation is found to be related with the transformation potency for austenite grains with different orientations.

Acknowledgements DL acknowledges the support by NSFC [Grant number U1860110]. The assistance of the Key Laboratory of Neutron Physics and Institute of Nuclear Physics and Chemistry of China Academy of Engineering Physics in the neutron diffraction experiment is gratefully acknowledged.

References

1. Matlock DK, Speer JG (2009) Third generation of AHSS: microstructure design concepts, microstructure and texture in steels
2. Speer JG, Matlock DK, De Cooman BC, Schroth JG (2003) Carbon partitioning into austenite after martensite transformation. *Acta Mater* 51(9):2611–2622
3. Wang L, Feng W (2011) Development and application of Q&P sheet steels
4. Wang L, Speer JG (2013) Quenching and partitioning steel heat treatment. *Metallogr Microstruct Anal* 2(4):268–281
5. Wang H, Wu PD, Tomé CN, Huang Y (2010) A finite strain elastic–viscoplastic self-consistent model for polycrystalline materials. *J Mech Phys Solids* 58(4):594–612
6. Lebensohn RA, Tomé CN (1993) A self-consistent anisotropic approach for the simulation of plastic deformation and texture development of polycrystals: application to zirconium alloys. *Acta Metall Mater* 41(9):2611–2624
7. Beyerlein IJ, Tomé CN (2008) A dislocation-based constitutive law for pure Zr including temperature effects. *Int J Plast* 24(5):867–895
8. Mecking H, Kocks UF (1981) Kinetics of flow and strain-hardening. *Acta Metall* 29(11):1865–1875
9. Bhadeshia H (2001) Geometry of crystals
10. De Knijf D, Nguyen-Minh T, Petrov RH, Kestens LAI, Jonas JJ (2014) Orientation dependence of the martensite transformation in a quenched and partitioned steel subjected to uniaxial tension. *J Appl Crystallogr* 47(4):1261–1266
11. Olson GB, Cohen M (1975) Kinetics of strain-induced martensitic nucleation. *Metall Trans A* 6(4):791
12. Wang H, Jeong Y, Clausen B, Liu Y, McCabe RJ, Barlat F, Tomé CN (2016) Effect of martensitic phase transformation on the behavior of 304 austenitic stainless steel under tension. *Mater Sci Eng A* 649:174–183

Predicting the Flow and Failure Properties of Dual-Phase Steel Using Phenomenological Models



Arshdeepsingh Sardar, Amin L. Vanjani, A. Bardelcik, and C. H. M. Simha

Abstract Owing to the complexity of the mechanical response of Dual-Phase (DP) steels, steel makers rely largely on experiments and trial-and-error approaches to develop new lines with higher strength and ductility in order to enable lightweighting of automotive parts. Crucially, the flow and failure behaviors are intimately linked to the morphology of the microstructure. This paper presents an approach that uses morphological features to predict the flow and failure behavior of DP Steels. We exploit phenomenological models to connect the deformation and failure at the microscopic level to the average mechanical response. Using basic microstructural features and flow behavior of the ferrite and martensite phases, the flow and failure behavior of DP Steels is estimated. Comparisons with macroscopic stress–strain response and in situ tensile data for a DP steel show that the model estimates local as well as global flow and failure properties and is an emergent microstructure design tool.

Introduction

Among the Advanced High-Strength Steel (AHSS), DP steels have become increasingly popular on account of passenger safety demands and vehicle lightweighting (to reduce fuel consumption). The Ultimate Tensile Strength (UTS) of DP steel varies from 450 to 1200 MPa with better formability when compared to HSLA steels with a similar strength [9]. Additionally, the higher limit of uniform elongation combined with the strength allows the DP steel structure to absorb more load in case of an impact. Fundamentally, DP steel is a hard particle phase surrounded by a softer matrix. The harder phase (martensite) is reinforcing the softer (ferrite) matrix which lends better formability properties to the material, although the proportion of hard phase (martensite) fraction might be higher depending on higher strength demands.

A. Sardar · A. L. Vanjani · A. Bardelcik · C. H. M. Simha (✉)
School of Engineering, University of Guelph, 50 Stone Road, East, ON N1G 2W1, Canada
e-mail: csimha@uoguelph.ca

Currently, the research for designing DP steels is largely a trial-and-error or heuristic approach. Admittedly, the availability of a model to determine the properties of DP steel would help in reducing the cumbersome procedures to procure data. The macroscopic properties of DP steel depend on the microstructural parameters such as grain morphology (diameter), composition of phases, and alloy content [11]. Accordingly, this study presents a phenomenological model that predicts the average mechanical properties based on the plastic flow and failure behavior of the individual phases.

Modelling of the Flow Curve of Individual Phases

The initial step in the phenomenological modelling of DP Steel involves the prediction of flow stress for individual phases. For an accurate representation of DP steel, it is necessary that the effect of microstructural parameters is acutely addressed. The model used for determining the flow stress was presented by [2].

Ferrite Model

The flow model for ferrite is based on a combination of empirical models and physically motivated models; the latter is based on the theory of dislocations [8]. The flow stress comprises of three components, namely, friction stress (σ_f^0), isotropic stress (σ_f^I), and kinematic stress (σ_f^K).

$$\sigma_f(\epsilon_p^f) = \sigma_f^0 + \sigma_f^I + \sigma_f^K \quad (1)$$

$$\sigma_f^0 = 52 + 0.33\text{Mn} + 0.80\text{Si} + 0.60\text{Cr} + 0.80\text{Mo} \quad (2)$$

The friction stress component incorporates the effect of the alloy composition (Eq. 2). The isotropic component of the flow stress accommodates the hardening effect caused by the total dislocations collected with an increase in effective plastic strain (Eq. 3).

$$\sigma_f^I = \alpha M \mu b_{111} \sqrt{\rho} \quad (3)$$

$$\sigma_f^K = \frac{M \mu b_{111}}{d_f} n \quad (4)$$

where M is the Taylor factor, μ the shear modulus, b_{111} the Burgers parameter, ρ the dislocation density, d_f the ferrite grain size, α the hardening coefficient, and n represents mean grain-boundary dislocations. The kinematic component (σ_f^K) accounts for the dislocations stored at the grain boundary (Eq. 4). The equations for calculating the density of the dislocations are based on the modification of theory dislocations (Eqs. 5 and 6) provided by the [10]. The model accurately predicts the flow stress for fully ferritic steels over a wide range of grain diameters.

$$\frac{d\rho}{d\varepsilon_p^f} = M \left(\frac{\left(1 - \frac{n}{n_s}\right)}{b_{111}d_f} + k_f\sqrt{\rho} - f_f\rho \right) \tag{5}$$

$$\frac{dn}{d\varepsilon_p^f} = \frac{\lambda_f}{b_{111}} \left(1 - \frac{n}{n_s}\right) \tag{6}$$

In Eq. (6), n_s is the maximum dislocations that can pile up on the grain boundary and λ_f is the mean distance between the slip bands.

Martensite Model

Traditionally, martensite was always modelled as an elastic phase, especially for the DP Steels with a low martensite fraction. However, various researchers have confirmed the significant plasticization of martensite even at lower strains [7]. Another common observation made while examining martensite is the non-uniformity of carbon distribution [6]. Since local carbon content is the primary factor contributing to strength, adjacent martensite grains can have varying yield strength. Owing to the varying strength, the plasticization of martensite is gradual. Therefore, the grains with higher yield strength contribute to the initial high hardening rate. As the dislocation theory does not explain the initial high hardening rate, Allain et al. addressed the peculiar behaviour of martensite by modelling it using a Continuum Composite Approach (CCA) [1].

In CCA, martensite is modelled as a composite with a different local yield strength (due to non-uniform carbon content). Since the phase is modelled as an elastic–perfectly plastic, the stress–strain curve can be predicted using just young’s modulus (Y) and the local yield strength (σ_L). The probability function ($F(\sigma_L)$) in the Eq. (7) determines the proportion of martensite that has a yield strength of σ_L .

$$\frac{d\sigma_m}{d\varepsilon_m} = \frac{1}{\frac{1}{Y} + \frac{F(\sigma_L)}{\beta}} (1 - F(\sigma_L)), \text{ where, } \sigma_m = \frac{\sigma_m + \beta\varepsilon_m}{1 + \frac{\beta}{Y}} \tag{7}$$

In the above equation, β is the fitting parameter to calculate composite stress for martensite (σ_m) at composite martensite strain (ε_m).

The probability function with respect to σ_m is done based on the following conditions:

$$\text{If } \sigma < \sigma_{\min} + \sigma_m^{\text{fric}}, \text{ then } F(\sigma) = 0 \quad (8)$$

else,

$$F(\sigma) = 1 - \exp\left(-\left(\frac{\sigma - (\sigma_{\min} + \sigma_m^{\text{fric}})^n}{\sigma^0}\right)\right) \quad (9)$$

$$\sigma_m^{\text{fric}} = 60 + 0.33\text{Mn} + 0.81\text{Si} + 0.48\text{Cr} + 0.48\text{Mo} \quad (10)$$

The σ^0 describes the distribution of the yield strength for martensite composite based on the carbon content.

$$\sigma^0 = 645 + 5053(C_m/100)^{1.34} \quad (11)$$

The CCA effectively captures the hardening of martensite over a wide range of carbon content. Additionally, it accurately simulates the initial high hardening rate.

Mixture Law

Once the individual curves have been determined the macroscopic stress is calculated by the Iso-Work law [5]. As per the Iso-Work law, both the phases must do equal amount of work for unit increment in the strain.

$$\sigma_{\text{DP}} = F_m \sigma_m(\varepsilon_m) + (1 - F_m) \sigma_f(\varepsilon_f) \quad (12)$$

$$\varepsilon_{\text{DP}} = F_m \varepsilon_m + (1 - F_m) \varepsilon_f \quad (13)$$

Mathematically, the Iso-Work law can be described as

$$\sigma_f d\varepsilon_f = \sigma_m d\varepsilon_m \quad (14)$$

In addition to the dislocations owing to effective plastic strain, there are Geometrically Necessary dislocations (GNDs) due to the non-uniformity of phases and the dislocations due to pre-stress present in DP steels.

$$\rho_{\text{GND}} = F_m \frac{1}{b_{111} L_f} \frac{(1 - \exp(-\beta_{\text{GND}}(\varepsilon_f - \varepsilon_m + \varepsilon_0)))}{\beta_{\text{GND}}} \quad (15)$$

$$\rho_f^0 = F_m \frac{M}{b_{111} L_f} \varepsilon_0 \quad (16)$$

Table 1 Approaches to determine the limit of uniform elongation

Approach	Flow curve equation	Criterion for necking
Considere Criterion	$\sigma = k\varepsilon^n$	$\frac{d\sigma}{d\varepsilon} = \sigma(\text{Orn} = \varepsilon_u)$
Crussard Jaoul Analysis	$\sigma = \sigma_0 + c\varepsilon_p^m$	$\ln\left(\frac{d\sigma}{d\varepsilon}\right) = (m - 1)\ln\varepsilon + \ln(c * m)$
Modified CJ Analysis	$\varepsilon_p = \varepsilon_{p0} + c\sigma^m$	$\ln\left(\frac{d\sigma}{d\varepsilon}\right) = (1 - m)\ln\sigma - \ln(c * m)$

In the above equations, β_{GND} is the relaxation parameter for the GNDs that occur due to strain partitioning between the phases, L_f denotes the region affected by the strain partitioning, and ε_0 stands for the pre-stress caused by martensitic transformation. Equations (15) and (16) calculate the density of GNDs and pre-stress dislocations. While calculating the composite stress, Eqs. (3) and (4) are modified to include the effect of GNDs.

$$\frac{d\rho}{d\varepsilon_p^f} = M\left(\frac{1 - \frac{n}{n_s}}{b_{111}d_f} + k_f\sqrt{\rho + \rho_{\text{GND}}} - f_f\rho\right) \tag{17}$$

$$\sigma_f^I = \alpha M\mu b_{111}\sqrt{\rho + \rho_{\text{GND}}} \tag{18}$$

Prediction of Necking

In a uniaxial tensile test, the stress required to elongate the test-piece increase with strain accompanied by a reduction in the gauge area. This strain hardening competes with the decrease in the load-bearing capacity caused by the reduced area. Until the limit of uniform elongation, the deformation is uniform across the gauge area of the sample. However, once the sample reaches maximum load the specimen starts necking. Beyond this limit, the deformation is restricted to the necked area of the sample.

Based on the predicted true stress–strain,, there are several approaches that can be applied for determining the limit of uniform elongation. The results of Considere criterion, Crussard Jaoul (CJ) analysis, and Modified CJ analysis are compared in the study (Table 1).

Prediction of Failure Strain

The non-homogeneity of individual phases in DP steels leads to complex interactions between the hard and soft phases and finally failure owing to the interactions

of voids in the soft phase. Several factors contribute to the nucleation of voids in DP microstructure. With the increasing strain, the nucleated voids grow and coalesce which ultimately leads to fracture. The strain partitioning between ferrite and martensite plays a crucial role in void nucleation. The difference in their individual properties leads to the collection of dislocations at the ferrite/martensite interface. Smith-Barnby addressed the decohesion that occurs at the ferrite/martensite interface by formulating critical stress [4]. Based on the microstructural parameters, critical stress (Eq. 19) calculates the failure stress when added to the other components. The critical stress considers the microstructural parameters like effective grain diameter (d_{eff}) and mean spacing between islands (L_{ms}).

$$\sigma_{\text{critical}} = \frac{1}{L_{\text{ms}}^{1/2}} \left(\frac{d_{\text{eff}}}{d_{\text{eff}} + L_{\text{ms}}} \right)^{1/2} \left(\frac{2\gamma G}{\pi(1 - \nu)} \right) \quad (19)$$

Here, G is the shear modulus, ν is the Poisson ratio, and γ is the surface energy.

$$\sigma_{\text{F}} = \sigma_{\text{critical}} + \sigma_{\text{B}} + \sigma_{\text{fric}} + \sigma_{\text{g+c}} \quad (20)$$

In their research, Balliger et al. [3] suggested a model that determines failure strain using Smith-Barnby critical stress. The back stress (σ_{B}) and friction stress (σ_{fric}) were empirically approximated to be 720 MPa.

$$\sigma_{\text{F}}(\text{MPa}) = \frac{1}{L_{\text{ms}}^{1/2}} \left(\frac{d_{\text{eff}}}{d_{\text{eff}} + L_{\text{ms}}} \right)^{1/2} \left(\frac{2\gamma G}{\pi(1 - \nu)} \right) + 720 \quad (21)$$

For calculating the failure strain in DP Steels, the true stress–strain curve was approximated to be a straight line with a constant slope (hardening rate) beyond 20% strain. Equation (23) determines the failure strain for DP steels.

$$\left(\frac{d\sigma}{d\varepsilon} \right)_{0.2} = \frac{\sigma_{\text{F}} - \sigma_{0.2}}{\varepsilon_{\text{f}} - 0.2} \quad (22)$$

$$\sigma_{\text{F}} = \sigma_{0.2} + \left(\frac{d\sigma}{d\varepsilon} \right)_{0.2} (\varepsilon_{\text{f}} - 0.2) \quad (23)$$

Balliger et al. (1981) used Eqs. (24) and (25) for determining $\sigma_{0.2}$ and strain hardening at 20% strain.

$$\sigma_{0.2}(\text{MPa}) = 1420(F_{\text{m}}) + 500 \quad (24)$$

$$\left(\frac{d\sigma}{d\varepsilon} \right)_{0.2} (\text{MPa}) = 40 \sqrt{\left(\frac{F_{\text{m}}}{d_{\text{m}}} \right)} + 75 \quad (25)$$

Results and Discussion

Several approaches were investigated to determine the limit of uniform elongation (ϵ_u) and Ultimate tensile strength (UTS). Graphically, both CJ and modified CJ approach need a certain delineate the transition strain to determine ϵ_u . As martensite transformation from elastic to plastic is gradual, both the approaches were not viable. Although the Considere criterion is convenient to apply, the accuracy was poor for microstructures with larger grain diameter ($D > 10 \mu\text{m}$) or high martensite fraction ($F_m > 0.8$). For improving the accuracy, the stress–strain data was fit to the polynomial curve (with a degree 5) instead of power-law and then differentiated (Fig. 1).

We first predict the flow curve value for the annealed and tempered DP steels used by [7] to load mini dog-bone specimens in an SEM. Predicted stress–strain curves are compared with experimental values of stress and strain in Fig. 2. Additionally, the onset of necking is predicted by intersection with the derivative of the stress–strain curve (blue curve in the figure). The predicted necking strain agrees with the experimental value to be within 10%.

As discussed earlier, the approach used to determine the failure stress involves empirical approximation of back stress and friction stress components. However, the phenomenological model offers a comprehensive alternative that incorporates the effect of grain diameters and phase compositions. Therefore, both the stress components and hardening rate were calculated using the phenomenological model. In mini dog-bone specimens loaded in situ in an SEM, [7] have reported both the average *global* strains at the onset of necking and the corresponding *local* strains in the neck. The latter strains are 3–4 times the value of the global strain and were obtained using the Digital Image Correlation method (Table 2).

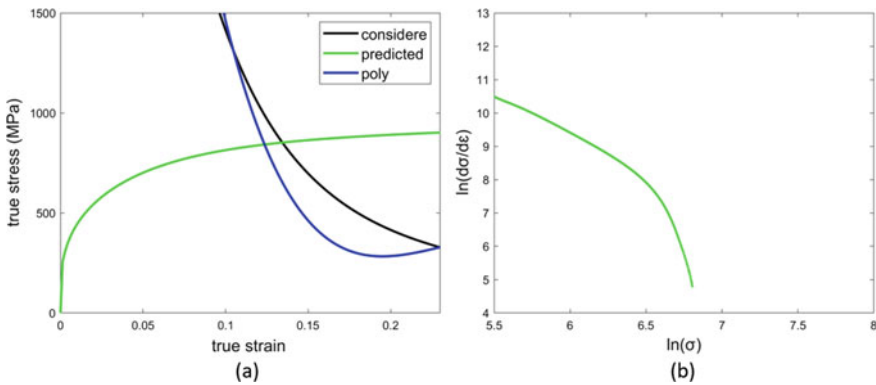


Fig. 1 **a** Phenomenological model with the Considere criterion and polynomial **b** The modified CJ analysis does not show transition strain when applied to the model

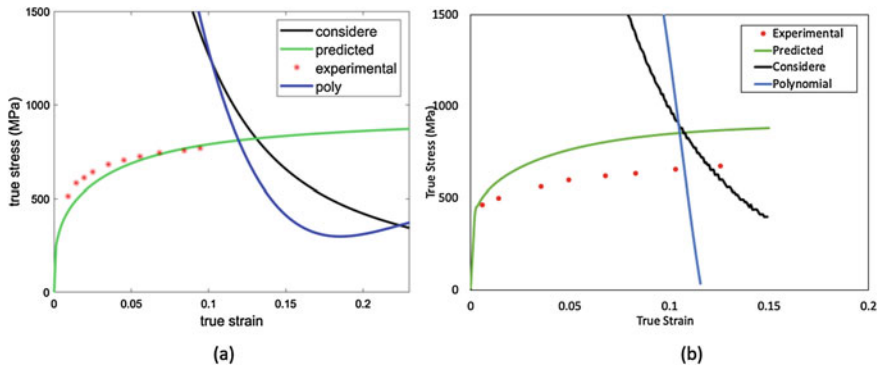


Fig. 2 **a** Intercritically annealed DP steel sample and **b** Tempered DP steel sample by [7]. The graphs compare the experimental data with the phenomenological model along with the approach for determining the limit of uniform elongation and UTS

Table 2 Comparing the experimental failure strain with predicted values

	Failure strain	
	Experimental	Predicted
IA sample [7]	0.40	0.43
Tempered sample [7]	0.59	0.43

Conclusion

The study presents a phenomenological model that assists in designing microstructure in DP steels by predicting the average tensile behaviour based on a knowledge of the volume fraction of phases and a few microstructural parameters. The predicted flow behaviour, the limit of uniform elongation, and the corresponding average failure strain between martensite phases are predicted and found to be in good agreement with stress–strain curves and strain values reported in the literature. However, for tempered steels, the method under predicts the flow and failure behavior.

References

- Allain S, Bouaziz O, Takahashi M (2012) Toward a new interpretation of the mechanical behaviour of asquenched low alloyed martensitic steels. *ISIJ Int* 52(4):717–722. <https://doi.org/10.2355/isijinternational.52.717>
- Allain SYP, Bouaziz O, Pushkareva I, Scott CP (2015) Towards the microstructure design of DP steels: a generic size-sensitive mean-field mechanical model. *Mater Sci Eng A* 637:222–234. <https://doi.org/10.1016/j.msea.2015.04.017>
- Balliger NK (1981) Ductile fracture of dual phase steels. In: *Advances in the physical metallurgy and applications of steels*, pp 73–83

4. Barnby JT (1967) The initiation of ductile failure by fractured carbides in an austenitic stainless steel. *Acta Metall* 15(5):903–909. [https://doi.org/10.1016/0001-6160\(67\)90372-0](https://doi.org/10.1016/0001-6160(67)90372-0)
5. Bouaziz O, Buessler P (2002) Mechanical behaviour of multiphase materials: an intermediate mixture law without fitting parameter. *Revue de Métallurgie*. <https://doi.org/10.1051/metal:2002182>
6. He BB, Zhu K, Huang MX (2014) On the nanoindentation behaviour of complex ferritic phases. *Philos Mag Lett* 94(7):439–446. <https://doi.org/10.1080/09500839.2014.921348>
7. Kang J, Ososkov Y, Embury JD, Wilkinson DS (2007) Digital image correlation studies for microscopic strain distribution and damage in dual phase steels. *Scripta Mater* 56(11):999–1002. <https://doi.org/10.1016/j.scriptamat.2007.01.031>
8. Mecking H, Kocks UF (1981) Kinetics of flow and strain-hardening. *Acta Metall* 29(11):1865–1875. [https://doi.org/10.1016/0001-6160\(81\)90112-7](https://doi.org/10.1016/0001-6160(81)90112-7)
9. Rashid MS (1981) Dual phase steels. *Annu Rev Mater Sci* 11(1):245–266. <https://doi.org/10.1146/annurev.ms.11.080181.001333>
10. Sinclair CW, Poole WJ, Bréchet Y (2006) A model for the grain size dependent work hardening of copper. *Scripta Mater* 55(8):739–742. <https://doi.org/10.1016/j.scriptamat.2006.05.018>
11. Tasan CC, Bechtold M, Schemmann L, Tsuzaki K, Raabe D, Diehl M, Zheng C, Koyama M, Roters F, Ponge D, Peranio N, Yan D (2015) An overview of dual-phase steels: advances in microstructure-oriented processing and micromechanically guided design. *Annu Rev Mater Res* 45(1):391–431. <https://doi.org/10.1146/annurev-matsci-070214-021103>

Part VI
Modelling of Thermo-Mechanical Sheet
Forming

Development of a Hot Cutting Process for Functional Parts by Stress State-Dependent Damage Modeling



C. Löbbe, J. Martschin, D. Putschkat, H. Sulaiman, A. Jäger,
and A. E. Tekkaya

Abstract Trimming by forming is the method of choice for the production of complex components with functional surfaces. With increasing strength, this method is no longer applicable due to the high tool load and risk of production stop. Hot cutting and quenching of boron-manganese grades is a solution to meet the part requirements out of geometry, mechanical properties, and surface condition. This approach requires an immediate sequence of austenitization, hot cutting, and quenching and has multiple thermal and mechanical adjustment screws. Hence, the design principles for the thermomechanical cutting process are revealed, which are obtained by a load path-dependent damage simulation. The basis for this is a fracture characterization at elevated temperatures. Building on this, the process and cutting parameters are simulated by variation, and optimal process execution is found. The method is validated on a component that has to satisfy a requirement collective of geometric and mechanical characteristics.

Keywords Hot stamping · Shear cutting · Trimming · GISSMO

Introduction

Hot stamping is an established process to manufacture structural components for lightweight automotive design [1]. For this purpose, the indirect or direct press hardening is used, in which the forming process is conducted before the annealing process or takes place simultaneously. In addition, process variants are known today which are used to produce components with functional surfaces for mechanical drives.

C. Löbbe · J. Martschin (✉) · A. E. Tekkaya

Institute of Forming Technology and Lightweight Components (IUL), TU Dortmund University,
Baroper Str. 303, 44227 Dortmund, Germany
e-mail: juri.martschin@iul.tu-dortmund.de

D. Putschkat · A. Jäger

KODA Stanz- Und Biegetechnik GmbH, August-Borsig Str. 20-28, 59439 Holzwickede, Germany

H. Sulaiman

Faurecia Autositze GmbH, Nordsehler Str. 38, 31655 Stadthagen, Germany

Besides the multi-stage forming [2], shear cutting is a key to the success of the process chain application. The trimming by shearing instead of laser cutting has already been examined under various conditions. This includes conventional shear cutting at room temperature, at higher temperatures [3], or the adiabatic high-speed cutting [4]. While the tool durability limits the process at room temperature, the adiabatic cutting efforts a simple trimming geometry in order to avoid tool cracks. Therefore, the hot shear cutting is a promising option so that the shearing leads to a relatively low-yield stress and a subsequent annealing is possible through an additional tool stage. Against this background, the production of straight cuts has already been studied by So [5]. The shear cutting process in the warm state could be modeled according to the Brozzo fracture criterion. As a result, the cutting force and the geometry of the cut surface can be predicted. In general, the edge geometry consists of a high proportion of smooth-sheared length, a small amount of edge draw-in, and little or no fracture and burr proportion. At this point, the process of cutting components with functional surfaces with non-straight cuts such as round cutouts or any curvature remains open. Due to the multi-axis strain state and the relatively high fracture strain in the austenite condition, the strain path changes so that higher triaxialities are triggered and the material is separated under these conditions. As a result, the smooth-sheared length decreases due to the large edge indentation. For this purpose, the GISSMO model is applied to reflect the complex strain and stress states and to cover the trimmed geometry.

Within the new multi-stage hot forming process, the material is shaped through multiple forming and heat treatment steps. The typical stages include contouring, cold forming, heating, hot forming, quenching, and separation operations (Fig. 1a). Depending on the thickness of the sheet, the heat is provided by means of pure inductive heating or conductive-inductive heating [2]. Through the electrical heating, the heating rate could be relatively high so that the heat removal by conductance is prevailing at the clock rate. For a given tool cooling rate and the required number of strokes, the cooling is divided into several tool stages [6]. For this study, a Schuler servo press MSD2-400 is used in combination with an induction generator TRUMPF MF7040 combined with a coaxial transformer. The stroke rates for the three-stage cooling are around 4–10 strokes/min. Figure 1b shows exemplary components with strong requirements for dimensional accuracy and lightweight design.

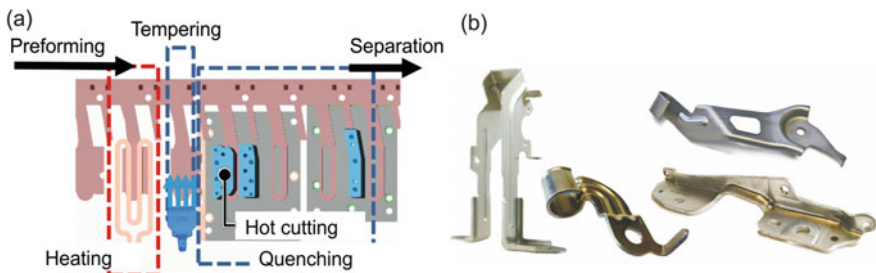


Fig. 1 Heat-assisted stamping in progressive dies: **a** Strip and tool layout, **b** Exemplary components

Components with functional surfaces produced by shear cutting such as bearings or gears are particularly demanding because the cut edges require precise shape, hardness, toughness, and residual stresses. Since an indirect hot stamping process would lead to oxidation of the surface in terms of scale, the direct process with a warm cut is one possible solution. Correspondingly, Fig. 2a shows surfaces resulting

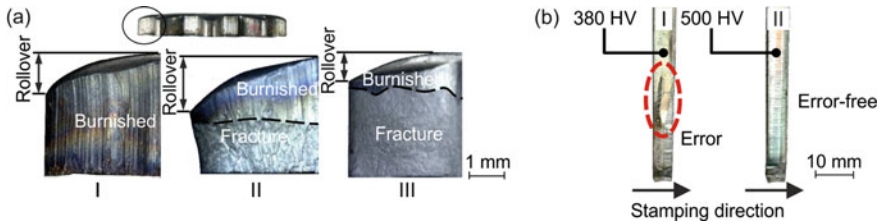


Fig. 2 Heat-assisted shear cutting of functional parts: **a** Geometrical aspect of gearing part (I: hot, 1% clearance, II: hot, 10% clearance, III: cold, 10% clearance) [3], **b** Surface and mechanical properties of straight cut (I: Stamping at room temperature, ferrite–pearlite microstructure, II: Stamping at elevated temperatures after austenitization)

from varying clearances so that under certain conditions an acceptable proportion of smooth-sheared area occurs. Furthermore, the ductility of the material in the mild state with a relatively soft ferrite–pearlite microstructure is not suitable for producing a high proportion of smooth-sheared cuts (Fig. 2b). The material 34MnB5 is shown, which manifests a large edge indentation after austenitization, but has no defects such as surface disruptions. The hardness after the thermomechanical process chain is higher than 500 HV.

Taking these results into mind, the successful application of the heat-assisted shear cutting process requires a profound process model in order to select a suitable tool set-up and matching process parameters. Hence, the objective is to evaluate the outcome of a continuous simulation of ductile damage and failure in the process chain. For this target, the mapping of the strain and stress state and further mechanical properties as a function of the thermomechanical boundary conditions is essential to estimate the evolution of the microstructure. At this point, a tabular yield stress in relation to the strain rate and the temperature is considered. Nevertheless, a more physical approach taking into account the changing phases and the ongoing recrystallization would be a more comprehensive base for broader transferability. Against this background, the applicability of the GISSMO model known from conventional stamping processes should be proved. This framework is suitable for mapping both hard and soft material conditions. The goal is to consider the triaxiality, the strain path, and the changing flow direction so that in addition to simple forming steps, more complex geometries and processes can be mapped in one consistent environment.

The triaxiality η is defined by the hydrostatic stress σ_m and the equivalent flow stress according to von Mises σ_{vM} :

$$\eta = \frac{\sigma_m}{\sigma_{vM}} = \frac{I_1}{3\sigma_{vM}} \quad (1)$$

The Lode parameter ξ for characterizing the load direction is defined by the third stress invariant and the flow stress von Mises:

$$\xi = \frac{27}{2} \frac{J_3}{\sigma_{vM}^3}, \text{ with } J_3 = \det(\boldsymbol{\sigma}') \quad (2)$$

The damage variable D_f evolves in relation to the plastic strain rate $\dot{\varepsilon}_p$ considering a non-linear behavior, described by the exponent n :

$$D_f = \frac{n}{\varepsilon_f} D_f^{1-1/n} \dot{\varepsilon}_p \quad (3)$$

The transition to the failure is modeled through the calculation of the effective stress σ^* in relation to the unaffected stress σ by the fading exponent m :

$$\sigma^* = \sigma \left(1 - \left(\frac{D - D_{\text{crit}}}{1 - D_{\text{crit}}} \right)^m \right) \quad (4)$$

Furthermore, depending on the given boundary conditions, regularization is necessary, which takes place through the fading exponent and another empirical compensation variable [7].

The first objective is parameter identification based on elementary tests with comparable thermomechanical treatment. On this basis, the next goal is the modelling of the shear cutting process of components with functional surfaces. The possibility of optimization by checking the strain path should also be analyzed. Furthermore, the effect of a counter pressure comparable to fine blanking is possible so that a higher geometrical accuracy is reached. Finally, the results will be reflected to evaluate the usability of a stress-dependent damage and failure model to realize complex heat-assisted stamping processes for functional parts with tailored properties.

Parameter Identification

The calibration of the model parameters is carried out by elementary tests under comparable thermomechanical conditions. The evolution of the damage variable D , the non-linear damage growth exponent n , the fading exponent m , and other values for regularization have to be determined. Different stress and strain states have to be captured. The basic tests deliver the onset of instability, which finally crosses over into the scalar value for the damage prediction. Due to the consistent formulation, a damage value $D = 1$ is equal to the failure and leads to element erosion. The problem in this context is the complex influence of the strain- and temperature-dependent flow stress. For this reason, in the experimental characterization, isothermal states

and uniform strain paths are aspired at a comparable strain rate. The simplified characterization also requires a stable load direction without significant changes during the plastic deformation. Sample shapes are used with a plane strain state as depicted in Fig. 3. In a preliminary study, these have already been used for the

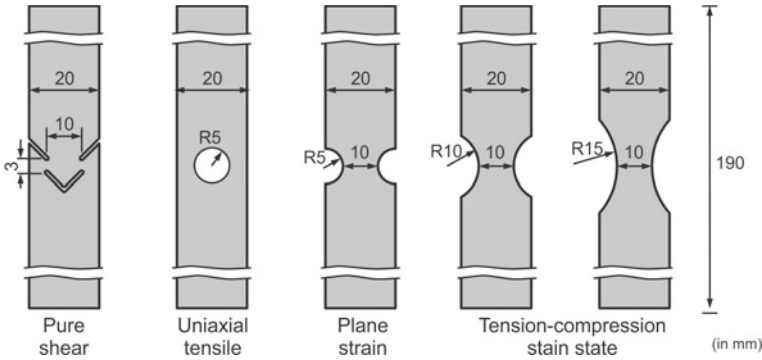


Fig. 3 Specimen shapes for parameter identification based on Chen [8]

determination of a conventional FLC at elevated temperatures [8].

A major limitation of experimental calibration is the measurability of the strains by means of digital image correlation (DIC) using the Aramis 5 M system from GOM. For this purpose, sample preparation was adapted to enhance the stability of the speckle pattern. The surfaces are cleaned from oxides by grinding. Then a white painting base coat is applied. The second layer is a stochastic pattern in black. Here, spray paints Flameproof of the company VHT are used. Figure 4 shows a representative result. The painting decreases its contrast when the localization initiates and high strain values occur. In consequence, the pattern recognition is not more possible and the pattern tracking stops. Hence, in the following the estimation of the displacement is based on point-to-point distances of the plastically undeformed region.

Representative force–displacement results of the basic tests are shown in Fig. 5. According to the hot forming characteristics, the force is dependent on temperature and stroke rate. The depicted temperatures are kept approx. constant during deformation, while previous treatment is selected with respect to full austenitization (950 °C, 20 s) and transport time under an ambient condition (25 °C). The forming temperature is controlled via PID for at least 10 s to an isothermal state. To neglect the influence of specimen clamping, in this set-up a laser speckle detection is used to track the distance above the notched area. The initial length is selected to 15 mm. According to the strain states, the lowest displacement is achieved in the uniaxial loading. Within the case of biaxial tension, the deformability increases while the highest value is achieved at the pure shear condition. Because of the imperfect specimen geometry, the shear type is transforming into a uniaxial tensile load before fracture so that the final stress state is not representative of the desired condition.

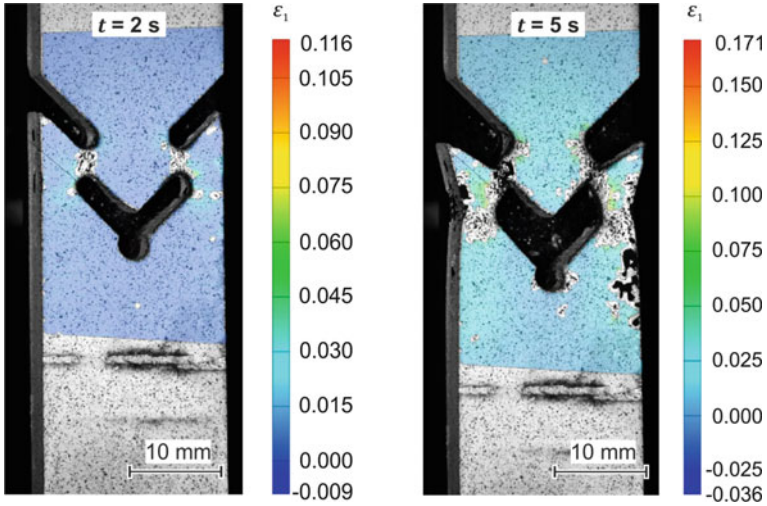


Fig. 4 Restrictions of high-temperature DIC strain detection due to brittle coating with spalling during plastic deformation (600 °C, pure shear type, $v = 1 \text{ mm/s}$)

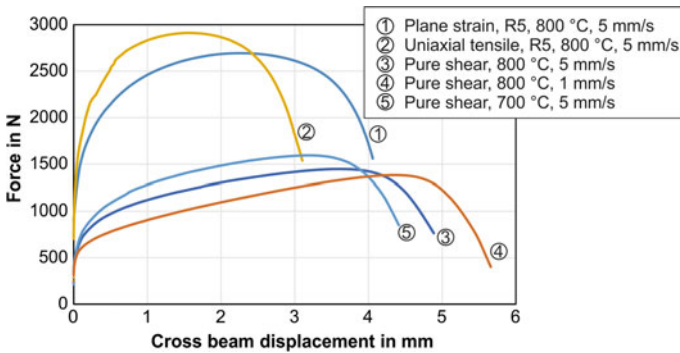


Fig. 5 Results of tensile tests under different load conditions (Material 22MnB5, $t = 1.5 \text{ mm}$)

The calibration of the model is conducted by the tool Ls-Opt of the company LSTC. The optimization is achieved by a metamodel-based approach with a sequential domain reduction (SRSM). This approach leads to the desired result after four iterations with eight permutations in each step so that the force response of the experiment is fulfilled. Figure 6 shows the triaxiality of the three different samples for plane strain, uniaxial tensile, and pure shear condition. During the initial deformation, the plastic strain field is relatively uniform. After a certain displacement, the triaxiality increases in the uniaxial and notched tensile specimen, while the shear type leads to lower values. Before the final fracture occurs, also the shear test leads to a rising stress level because of the tilting bridge between the center and the sides (comp. Fig. 4).

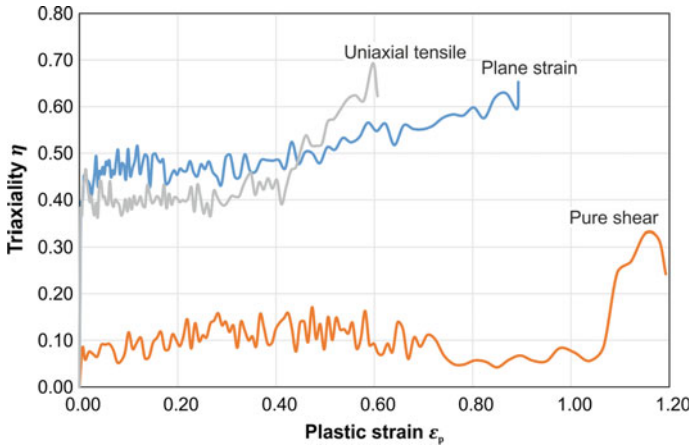


Fig. 6 Determined triaxiality evolution in three different characterization tests (800 °C, 5 mm/s)

The experiments were finally mapped using parameter identification with regard to the strain distribution and the resulting force. Accordingly, Fig. 7a shows the results from the simulation and experiment for the shear test. While the softening is predicted relatively well, there is a slight deviation of the model in the elastic range. In addition to the elasticity behavior, the measurement inaccuracy of the Zwick laser extensometer can also be responsible for this. The elongation at fracture results from the parameter identification as a function of the triaxiality (see Fig. 7b). To handle the numerous model parameters, the curve was discretized within the parameter identification by 4 points with a constant distance of $|\Delta\eta| = 0.33$.

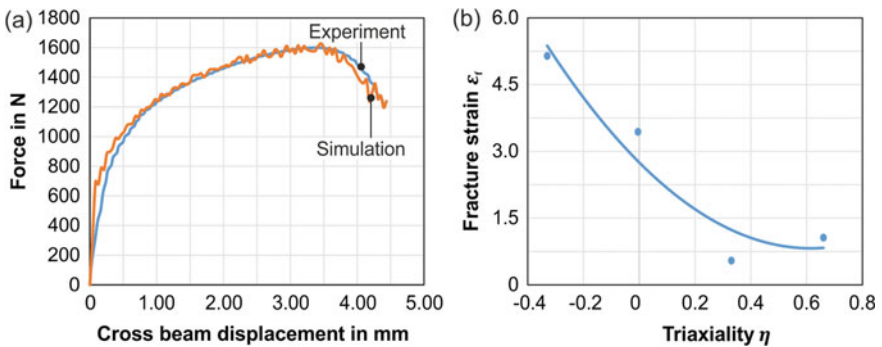


Fig. 7 **a** Force results of experiment and simulation (shear-type specimen); **b** Determined fracture strain versus triaxiality determined by parameter identification

Shear Cutting Process

Essential requirements of sheared components with functional surfaces are the geometry, the surface, and the mechanical properties. The surface should be as smooth as possible and free of oxides. The microstructure of the cutting edge should in turn be recovered so that the edge crack sensitivity is not adversely affected after trimming. Various approaches cover these issues by means of thermal treatment to relax and recover the highly stressed cutting surface [9]. Comparable to So [5], this solution contains a simultaneous heat treatment. Thereby, also the unique opportunity to set the microstructure and hardness is given. In order to avoid scaling, the cutting temperature after austenitization is reduced by a cooling period through free or forced convection. The strength and the hard martensitic microstructure are achieved by quenching, which finishes the multi-stage process. The edge should have a high proportion of smooth-sheared area, minimum roll-over, fracture zone, and burr. This ensures that the functionality is proposed in the best possible way. Conventional shear cutting is therefore not suitable for the production of components with functional surfaces with high demands on the cutting edge for the transfer of static and dynamic loads.

Figure 8 shows the resulting sheared edge height for the cutting speed of 5 mm/s.

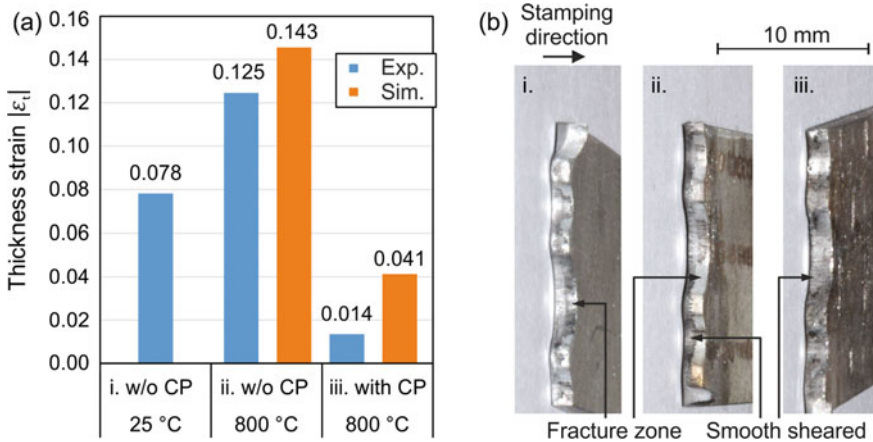


Fig. 8 Results of blanking operation with non-straight edges at different temperatures, with and without counter-punch (CP): **a** Thickness strain; **b** Surface of sheared workpiece

The cutting at room temperature is accompanied by a high fracture zone because the microstructure consists of ferrite and pearlite. As a result of the austenitization, the trimming behavior changes completely. Under this condition, the high roll-over with a decreasing smooth-sheared zone is problematic. On the other side, the edge thinning increases. In consequence, the load-carrying surface area vanishes and the

functionality suffers from the hot shearing process. The best shape accuracy is generated through an additional counter-punch. Under this condition, the thickness strain decreases to a minimum, because the roll-over is comparatively small and the fracture zone vanishes completely (Fig. 8a).

The result of a decreasing roll-over is reproduced by the numerical simulation with the stress-dependent damage model. The simulation indicates the influence of triaxiality, which has the lowest value when an additional counter-punch is used (see Fig. 9b). Due to the better clamping, the fracture strain is reached at a relatively low hydrostatic stress so that the plastic strain concentrates on a narrow band (Fig. 9a). This effect goes hand in hand with the fact that the edge filling has a higher proportion.

Nevertheless, the experimental result is not precisely modelled for the given application. One reason is the necessary regularization, which eliminates the effect of element size. Against this background, the modeling of complex three-dimensional geometries remains pending. If a correspondingly high resolution is required, the computing time actually increases disproportionately. In addition, the separation of the material without damage and failure is not covered by the GISSMO model. Particularly in the case of high pressures and recovering material at elevated temperatures, it can be assumed that separation occurs due to dislocation slip. This event leads to a pure smooth-shear zone without fracture. In the experiments, this result was characterized, which strengthens the assumed relationship. This requires finally new models that take into account also the grid independency.

On the experimental side, it could be noted that the thermomechanical process control for the production of high-strength components with special demands on the geometry, the mechanical parameters, and the surface is possible. At this point, it remains to be clarified to what extent the high strain at fracture influences the phase transformation to martensite when the counter-punch is used to concentrate the shearing zone. A stronger separation of carbides has to be expected due to the high dislocation density so that the diffusion of carbon and formation of carbides accelerates [10]. This is opposed by the hardening mechanism due to grain refinement so that a compensation of this effect with a moderate decrease in hardness can be expected.

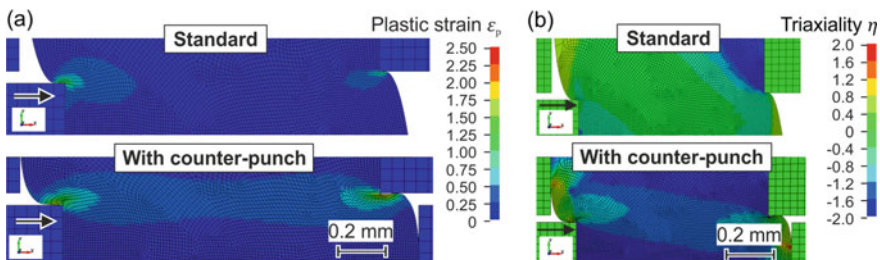


Fig. 9 Numerical results of simulation without and with counter-punch: **a** Plastic strain; **b** triaxiality

Conclusion

The investigation showed that the sheared edge in terms of the roll-over and remaining load-carrying surface can be simulated by using the stress-dependent GISSMO model. The austenitization for hot forming is generally accompanied by a high strain at fracture, which causes a high fraction of smooth-sheared area with a reduced edge height due to the increasing roll-over. The failure case converts to a tensile stress state due to the mechanical boundary conditions so that the determination of fracture strain at different hydrostatic pressures is required. By parameter identification, the force response can be described sufficiently well, the deformation of the material being consistent with the experimental observations. When the model is applied to the shearing process, the simulation predicts a ductile behavior with a relatively high roll-over. In consequence, the estimated load-carrying zone decreases due to the large thickness strain. By adapting the stress state, the shear failure is ultimately triggered and a shape results that meets the requirements for a high proportion of smooth-shear cut.

At this point, it remains open which experiments are relevant for the parameter identification if more complex load paths should be associated to the observed phenomena. Due to the additional thermal and timing influences, tests have to be found that provide information about several parameters in an integral way. Furthermore, it was found that the separation of the components with functional surfaces is dependent on more effects than the ductile damage and subsequent failure. Accordingly, an extended model is needed that reflects the generation of arising surfaces when the lattice perfectly dislocates without rupture of the material. In order to map product properties, the history of the temperature and plastic deformation must be considered, which influences the final microstructure. A determination of the grain size, the phase fractions, and the chemical composition is important so that a connection to the hardness and the other mechanical properties is obtained.

Acknowledgements The authors thank the support from the German Research Foundation (DFG) for the TE 508/59-1 project, the support from Faurecia Autositze GmbH and KODA Stanz- und Biegetechnik GmbH.

References

1. Karbasian H, Tekkaya AE (2010) A review on hot stamping. *J Mater Process Technol* 210:2103–2118
2. Löbbbe C (2019) Temperaturunterstütztes Biegen und Wärmebehandeln in mehrstufigen Werkzeugen. Dr.-Ing. Dissertation, Shaker Verlag, Aachen
3. Mori K, Maeno T, Yamada H, Matsumoto H (2015) 1-Shot hot stamping of ultra-high strength steel parts consisting of resistance heating, forming, shearing and die quenching. *Int J Mach Tools Manuf* 89:124–131
4. Schmitz F, Winter S, Wagner MF-X, Clausmeyer T, Tekkaya AE (2020) Adiabatic blanking of advanced high strength-steels. *CIRP Ann Manuf Technol* 69 (in Press)

5. So H (2015) Scherschneiden von Mangan-Bor-Stählen unter Temperatureinfluss. Dr.-Ing.-Dissertation, Shaker Verlag
6. Löbbbe C, Hater S, Kamaliev M, Tekkaya AE (2017) Sheet metal forming in progressive dies assisted by rapid induction heating: setting of springback and product properties. In: Oldenburg M, Prakash B (eds) 6th international conference hot sheet metal forming of high performance steel. Verlag Wissenschaftliche Scripten, Atlanta, USA, pp 649–661
7. Andrade F, Feucht M, Haufe A (2014) On the prediction of material failure in LS-DYNA: a comparison between GISSMO and DIEM. In: 13th international LS-DYNA users conference
8. Chen H (2017) Granular medium-based tube press hardening. Dr.-Ing.-Dissertation, Shaker Verlag, Aachen
9. Denks I, Mütze S (2017) Method for producing a component by subjecting a sheet bar of steel to a forming process. US. Patent 20170333971A1
10. Löbbbe C, Hering O, Hiegemann L, Tekkaya AE (2016) Setting mechanical properties of high strength steels for rapid hot forming processes. *Materials (Basel)* 9:229

Impact of Thermal Conditions on Predicted Formability of TRIP Steels



Daniel S. Connolly, Christopher P. Kohar, Raja K. Mishra, and Kaan Inal

Abstract To improve vehicle fuel economy and improve safety, automakers have focussed on substituting low-carbon steel for advanced high-strength steel (AHSS) alloys. A common grade of AHSS is the transformation-induced plasticity (TRIP) steels, which undergo a phase transformation from austenite to martensitic that enhances the ductility and strength. This work employs a phenomenological constitutive model for TRIP 800 steel to study the thermomechanical behaviour over large strains. This formulation is implemented into the recently developed fully coupled thermomechanical Marciniak–Kuczynski (MK) framework by Connolly et al. (2018). These are employed to analyze formability of a TRIP 800 alloy under a range of thermal conditions expected in realistic stamping operations. This work demonstrates that control of the initial blank temperature, die temperature, and die conduction coefficient can produce improvements in uniaxial and plane strain formability of up to 44% and 41% relative to room temperature formability. In contrast, the presented study shows that poor control of these parameters can reduce uniaxial and plane strain formability by up to 35% and 41%. Additionally, the conditions for optimal formability are shown to be strain path dependent, suggesting that tightly coupling component, process, and die design could improve final component designs.

Keywords TRIP steel · M–K-based forming limit diagrams · Thermomechanical modelling

D. S. Connolly (✉) · C. P. Kohar · K. Inal
Department of Mechanical and Mechatronics Engineering, University of Waterloo, Waterloo N2L 3G1, Canada
e-mail: dconnol@uwaterloo.ca

R. K. Mishra
General Motors Research & Development Center, Warren, MI 48090, USA

Introduction

Structural lightweighting through the novel design technology development [1] and advanced material substitution [2–4] has been a focus for automakers to address vehicle fuel economy regulations [5]. For formability components, particular focus has been directed to the development of novel advanced high-strength steel (AHSS) alloys due to their high strength and ductility. These desirable characteristics result from advanced chemical compositions and heat treatment processes allowing fine control of phase properties with these multiphase alloys. In addition, AHSS alloys commonly exhibit the transformation-induced plasticity (TRIP) effect, wherein metastable retained austenite (γ) transforms into martensite (α'). This effect depends on temperature [6], stress state [7], and strain rate [8], and can induce tension–compression asymmetry in yield behaviour [9]. This results in substantial increase in material hardening, improving ductility, strength, and fracture resistance [10]. The most industrially applicable steels exhibiting this behaviour are TRIP steels, wherein the retained austenite (RA) and martensite exist within a matrix of ferrite (α) and bainite (β) [11].

To enable rapid and cost-effective design iteration, vehicles are designed primarily in a virtual environment, with experiments used as calibration and validation. Component design is then limited by a combination of formability, weight, energy absorption, and strength (i.e., anti-penetration). One formability measure is the forming limit diagram (FLD) [12, 13], which is defined as a set of limit strains below which a sheet metal deformed under a constant strain path is unlikely to fail through localized necking. A common approach for numerically predicting an FLD is the Marciniak–Kuczynski (MK) analysis [14], wherein analytical equations are used to model the evolution of a diffuse neck.

Connolly et al. [15] recently extended MK analysis to include a fully coupled thermal model. This was coupled with an advanced constitutive model to analyze the effects of transformation deformation kinematics and thermal conditions on the formability of a TRIP 800 steel alloy. Their results showed that control of the thermal boundary conditions and initial blank temperature could be used to improve formability by up to 35% in uniaxial tension and 25% in plane strain tension. This work builds upon these results by analyzing formability under a realistic forming process, controlling initial blank temperature, stamping die temperature, and the stamping die to blank conduction coefficient to suggest specific avenues of exploration for improving formability in existing TRIP steel alloys.

Model Formulation

Constitutive Modeling

This work employs the phenomenological model previously used in Kohar et al. [16] and Connolly et al. [15]. This model is summarized below with full details in the aforementioned paper.

Strain-Rate Decomposition

The total strain rate, $\dot{\epsilon}_{ij}$, is decomposed into elastic ($\dot{\epsilon}_{ij}^{elast}$), inelastic ($\dot{\epsilon}_{ij}^p$), and thermal ($\dot{\epsilon}_{ij}^{therm}$) terms:

$$\dot{\epsilon}_{ij} = \dot{\epsilon}_{ij}^{elast} + \dot{\epsilon}_{ij}^p + \dot{\epsilon}_{ij}^{therm} \quad (1)$$

The thermal strain rate can be modelled using isotropic thermal expansion, given by

$$\dot{\epsilon}_{ij}^{therm} = \alpha_L \delta_{ij} \dot{T} \quad (2)$$

where α_L is the linear thermal expansion coefficient, δ_{ij} is the Kronecker delta, and \dot{T} is the temperature rate. The inelastic deformation is further decomposed into plastic slip strain ($\dot{\epsilon}_{ij}^{pslip}$) and both a dilational ($\dot{\epsilon}_{ij}^{pdilat}$) and shape change ($\dot{\epsilon}_{ij}^{pshape}$) component of transformation strain:

$$\dot{\epsilon}_{ij}^p = \dot{\epsilon}_{ij}^{pslip} + \dot{\epsilon}_{ij}^{pdilat} + \dot{\epsilon}_{ij}^{pshape} \quad (3)$$

The plastic slip strain is given by the associative flow rule

$$\dot{\epsilon}_{ij}^{pslip} = \dot{\bar{\epsilon}}^{pslip} \frac{\partial \Phi}{\partial \sigma_{ij}} \quad (4)$$

where $\dot{\bar{\epsilon}}^{pslip}$ is the effective plastic slip rate and Φ is the yield function. The dilational and shape change transformation strains are given by

$$\dot{\epsilon}_{ij}^{pdilat} = \frac{1}{3} \Delta V \dot{f}_{\alpha'} \delta_{ij} \quad (5)$$

$$\dot{\epsilon}_{ij}^{pshape} = \left[R_0 + R_1 \left(\frac{\tilde{\sigma}_{eff}}{\sigma_{0,\gamma}} \right) \right] \dot{f}_{\alpha'} \frac{\partial \Phi}{\partial \sigma_{ij}} \quad (6)$$

where $\Delta V = 0.02$ is the austenite to martensite volume change, $R_0 = 0.02$ and $R_1 = 0.02$ are fitted parameters, $\tilde{\sigma}_{eff}$ is the effective flow stress, $\sigma_{0,\gamma}$ is the austenite initial yield stress, and $\dot{f}_{\alpha'}$ is the rate of transformation of martensite.

Kinetics of Transformation

Martensite transformation rate is assumed to occur as a result of the formation of new martensitic units at potent nucleation sites at shear band intersections [6, 17]. The transformation rate is given by

$$\dot{f}_{\alpha'} = f_{\gamma} [p \dot{f}_{sb}^i + f_{sb}^i \dot{p} \theta(\dot{p})] \quad (7)$$

where f_{γ} is the austenite volume fraction, p is the probability of a shear band intersection site transforming, f_{sb}^i is the volume fraction of shear band intersection sites, and $\theta(\star)$ is a Heaviside function. The shear band intersection volume fraction, shear band volume fraction (f_{sb}), and effective slip rate in the austenite ($\dot{\bar{\epsilon}}_{\gamma}^{pslip}$) are related using

$$f_{sb}^i = \eta (f_{sb})^{n_s} \quad (8)$$

$$\dot{f}_{sb} = a_m (1 - f_{sb}) \dot{\bar{\epsilon}}_{\gamma}^{pslip} \quad (9)$$

where η and n_s are calibration constants and a_m is given by

$$a_m = (a_{m,1} + a_{m,2}T + a_{m,3}T^2 - a_{m,4}\Sigma) \left(1 - a_{m,5} \left(\frac{\dot{\bar{\epsilon}}}{\dot{\bar{\epsilon}}_0} \right)^{a_{m,6}} \right) \quad (10)$$

$$\Sigma = \frac{\text{tr}(\sigma)}{3\tilde{\sigma}} \quad (11)$$

where $a_{m,1}$ - $a_{m,6}$ are calibration parameters, T is temperature, Σ is stress triaxiality, $\dot{\bar{\epsilon}}$ is an effective strain rate, $\dot{\bar{\epsilon}}_0$ is a normalization factor, and $\tilde{\sigma}$ is the von Mises equivalent stress. The probability of transformation is given by

$$p = \frac{1}{\sqrt{2\pi}\sigma_s} \int_{-\infty}^g \exp\left(-\frac{(g' - g_0)^2}{2\sigma_s^2}\right) dg' \quad (12)$$

$$g = -T + g_1 \Sigma \quad (13)$$

where g_0 and σ_s are the mean and standard deviation of the distribution of critical driving forces required to cause transformation at a shear band intersection site, g is the transformation driving force, and g_1 is the dependence of the driving force triaxiality.

Effective Flow Stress

It is assumed that the average effective flow stress ($\bar{\sigma}_{ave}$) is given by a rule of mixtures such that

$$\bar{\sigma}_{ave} = f_\gamma \tilde{\sigma}_\gamma + f_\beta \tilde{\sigma}_\beta + f_\alpha \tilde{\sigma}_\alpha + f_{\alpha'} \tilde{\sigma}_{\alpha'} \quad (14)$$

where f_i and $\tilde{\sigma}_i$ are the volume fraction and effective stress of each phase as denoted by $= \{\gamma, \beta, \alpha, \alpha'\}$. The effective stress of each phase i is given using a Holloman hardening law:

$$\tilde{\sigma}_i = K_i (\varepsilon_{0,i} + \bar{\varepsilon}^{pslip})^{n_i} \quad (15)$$

$$\varepsilon_{0,i} = \left(\frac{E_i}{K_i} \right)^{\frac{1}{n_i-1}} \quad (16)$$

where K_i and n_i are calibrated constants, $\varepsilon_{0,i}$ is the yield strain, and E_i is Young's modulus. The Johnson–Cook [18] model is used to incorporate temperature sensitivity and the Cowper–Symonds [19] model is used to incorporate strain-rate sensitivity, such that the total flow stress, $\bar{\sigma}$, is given by

$$\bar{\sigma} = \bar{\sigma}_{ave} \left(1 + \left(\frac{\dot{\varepsilon}}{C} \right)^{1/P} \right) \left(1 - \left(\frac{T - T^*}{T_{melt} - T^*} \right)^m \right) \quad (17)$$

where C and P are Cowper–Symonds rate sensitivity parameters, $\dot{\varepsilon}$ is the total effective strain rate, T^* is a reference temperature, T_{melt} is the material melting point, and m is a temperature sensitivity exponent.

Evolving Anisotropic Yield Function

The yield surface is given by a modified Yld2000 function [20] with an evolving asymmetry term [9]:

$$\Phi = \phi(\sigma_{ij})^{\frac{1}{3}} + 3^{\frac{7}{6}} k \frac{J_3(\sigma_{ij})}{\phi(\sigma_{ij})^{1/6}} - \bar{\sigma}(\bar{\varepsilon}^{pslip}, T, \dot{\varepsilon})^2 = 0 \quad (18)$$

$$\dot{k} = C_k(1 - k)\dot{\bar{\epsilon}}^{pslip} \tag{19}$$

where $\phi(\sigma_{ij})$ is the Yld2000 function, J_3 is the third deviatoric stress tensor invariant, k is a parameter defining the evolving yield surface asymmetry, and $C_k = 0.49$ [21] governs the asymmetry increase rate. A maximum limit is enforced for k such that yield surface convexity is maintained [15]. The overall constitutive equation for stress is given by a hypo-elastic formulation with a modified Jaumann co-rotational framework such that

$$\dot{\sigma}_{ij}^{\nabla J} = \mathcal{L}_{ijkl}^{el} \dot{\epsilon}_{kl}^{elast} \tag{20}$$

$$\dot{\sigma}_{ij} = \dot{\sigma}_{ij}^{\nabla J} + \sigma_{ik} W_{kj} - W_{ik} \sigma_{kj} + \sigma_{ij} \dot{\epsilon}_{kk} \tag{21}$$

where \mathcal{L}_{ijkl}^{el} is the isotropic elasticity tensor and W_{ij} is the antisymmetric component of the velocity gradient.

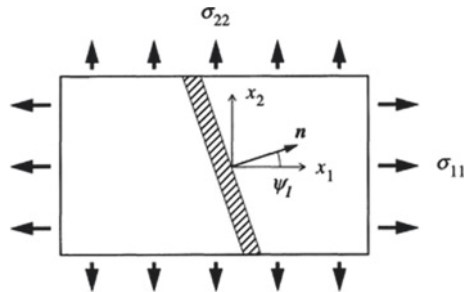
Coupled Thermomechanical Marciniak–Kuczynski Analysis

This work uses the fully coupled thermal MK model outlined in Connolly et al. [15] which is utilized for this work. A brief description of the model is given here. Figure 1 [15] shows a schematic of an infinite sheet with axes x_1 and x_2 and an infinite band related by an initial angle ψ_I to the x_1 -axis. A superscript B and no superscript are used to denote in-band and out-of-band properties, respectively. The band ($H^B(t)$) and sheet ($H(t)$) thicknesses are initially related through an imperfection parameter (f):

$$f = \frac{H^B(0)}{H(0)} \tag{22}$$

The MK formulation assumes plane stress sheet deformation such that

Fig. 1 Sheet with initial band inclined at angle ψ_I



$$\dot{\varepsilon}_{22} = P\dot{\varepsilon}_{11}, W_{12} = \dot{\varepsilon}_{12} = 0 \quad (23)$$

where P is a proportionality constant. The band angle (ψ) is updated by

$$\tan \psi = \exp[(1 - P)\varepsilon_{11}]\tan \psi_I \quad (24)$$

The in-band and out-of-band velocity gradients are related by [22]

$$L_{\alpha\beta}^B = L_{\alpha\beta} + \dot{g}_\alpha n_\beta \quad \alpha, \beta = 1, 2 \quad (25)$$

Force equilibrium requires that in-band and out-of-band stresses are related by

$$n_\alpha \sigma_{\alpha\beta}^B H^B = n_\alpha \sigma_{\alpha\beta} H \quad (26)$$

The numerical results are updated by solving algebraic equations for \dot{g}_α and D_{33}^B created by combing the constitutive law, force equilibrium, and boundary conditions. Necking localization failure occurs when the in-band thickness strain rate (D_{33}^B) is tenfold larger than the out-of-band thickness strain rate (D_{33}). Temperature evolution in band and out of band is considered independently and is described by

$$\rho C_p T = \frac{2[R_f(1 - s_f)(T_{ext} - T) + s_f h_c(T_\infty - T) + s_f \sigma_b \epsilon_r (T_\infty^4 - T_4)]}{H} + (\chi \bar{\sigma} \dot{\varepsilon}^{pslip} + Q_{tr} f_{\alpha'}) \quad (27)$$

where R_f is a conductive heat transfer constant, T_{ext} is conductive boundary temperature, s_f is the surface fraction exposed to air, h_c is a convective heat transfer coefficient, T_∞ is the air temperature, $\sigma_b = 5.67 \times 10^{-8} W/m^2 K$ is the Stefan–Boltzmann constant, ϵ_r is a coefficient of emissivity, $\chi = 0.9$ is the plastic work fraction converted into heat, and Q_{tr} is the specific latent heat of austenite to martensite transformation.

Material Characterization and Calibration

This work uses coefficients presented in Connolly et al. [15] as summarized here. Table 1 presents the elastic and plastic parameters for each phase and Table 2 presents the TRIP 800 steel thermal properties.

Table 3 lists the yield function coefficients as calibrated to experimental Lankford coefficients and normalized yield stress variation with $k = 0$ and with the coefficient ranges restricted to $\alpha_i \in [0.8, 1.2]$. The maximum asymmetry coefficient with these parameters was determined to be $k_{lim} = 0.762$.

Table 1 Elasticity and hardening parameters for TRIP800 [15]

	f_i [%]	E_i [GPa]	ν_i	K_i [MPa]	n_i	$\epsilon_0 (\times 10^{-3})$
Austenite, γ	16.5	190	0.30	1300	0.114	3.602
Bainite, β	13.5	210	0.30	2930	0.201	4.776
Ferrite, F	70.0	210	0.30	720	0.135	1.416
Martensite, α'	0.0	210	0.30	3470	0.126	9.133

Table 2 Thermal properties of TRIP 800 steel

	TRIP 800
Density, ρ [gm^{-3}]	7800
Specific heat capacity, C_p [$Jkg^{-1}K^{-1}$]	519
Thermal expansion, α_L [K^{-1}]	12×10^{-6}
Thermal resistance, R_f'' [$Wm^{-2}K^{-1}$]	22
Coefficient of convection, h'' [$Wm^{-2}K^{-1}$]	15
Emissivity coefficient, ϵ''	0.80
Fraction of exposed surface to air, s_f	0.50

Table 3 Yld2000 yield function parameters for TRIP 800

α_1	α_2	α_3	α_4	α_5	α_6	α_7	α_8	a
0.9719	0.9882	1.1051	0.9634	0.9882	0.8918	1.0214	0.8980	6.00

Tables 4 and 5 present the calibrated parameters for martensite transformation, Johnson–Cook thermal sensitivity, and Cowper–Symonds strain rate sensitivity. These were determined via simultaneous calibration to flow stress for several temperatures and strain rates, martensite evolution for several strain rates and strain paths, and temperature rise under uniaxial tension at an elevated strain rate.

Table 4 Flow stress strain rate and temperature sensitivity parameters for TRIP 800

C [s^{-1}]	P	$\dot{\epsilon}_0$ [s^{-1}]	m	T^* [K]	T_{meli} [K]	χ	Q_{tr} [Wm^{-3}]
9.938×10^4	5.2554	1.0×10^{-4}	1.274	293	1643	0.90	4.981×10^9

Table 5 Martensite generation parameters for TRIP 800

$a_{m,1}$	$a_{m,2}$	$a_{m,3}$	$a_{m,4}$	$a_{m,5}$	$a_{m,6}$	σ_g	g_0	g_1	η	n_s
1.698	5.865×10^{-2}	-1.137×10^{-4}	-4.320	0.09864	0.153	335.12	0.0071	76.8	9.626	4.058

Results and Discussion

The purpose of this work is to study the influence of thermal processing parameters on formability of TRIP 800 steel during a forming operation. In forming processes where the blank is typically constrained in a fixture that is not exposed to the surroundings, conduction to the forming dies is the main heat transfer mechanism. In practice, the conduction coefficient can be modified through selective lubricants and die design. It should be stressed that the conduction coefficient used here is meant to represent the overall heat transfer between the blank surface and a thermal boundary (e.g., coolant) and will therefore be much lower than the conduction between the blank and the die surface.

In this study, the thermal conductivity coefficient is varied to explore the effect on formability through modification of the martensite generation rate in the sheet. It is assumed that the entire surface of the sheet is in contact with the dies, such that convective and radiative heat transfer can be neglected ($s_f = 0$). The conduction coefficients used are $R_f = \{10, 20, 40, 80\} \text{ Wm}^{-2}\text{K}^{-1}$. The initial temperature of the blank, $T(0)$, and external thermal BCs varied between 400K and 700K with $\Delta T(0) = \Delta T_{ext} = 100\text{K}$ and compared to formability with a blank initially at room temperature ($T(0) = 293\text{K}$) and with room temperature dies ($T_{ext} = 293\text{K}$). The independent variables of this study are the initial blank temperature ($T(0)$), the external boundary temperature (T_{ext}), and the conduction coefficient (R_f). Each formability study was conducted with a macroscopic strain rate, $D_{11} = 1.0 \times 10^{-3}\text{s}^{-1}$, an imperfection parameter, $f = 0.996$ [23], proportionality constant of $-0.5 \leq P \leq 1.0$ with $\Delta P = 0.1$, and initial band angle of $0^\circ \leq \psi_I \leq 40^\circ$ with $\Delta\psi_I = 5^\circ$.

Figure 2 presents the FLD for an effective conduction coefficient of $R_f = 10\text{Wm}^{-2}\text{K}^{-1}$ for different initial temperature conditions. The percentage improvement in formability for a given initial blank temperature, thermal boundary condition, and strain path for the same strain path for an initial blank temperature and boundary temperature of 293K and conduction coefficient of 10Wm^{-2} is presented in Fig. 3. Raising the initial blank temperature for a constant die temperature results in two possible effects depending on the die temperature. For room temperature external BCs, increasing the initial blank temperature primarily had the effect of delaying martensite generation, while also resulting in minor reductions in the final volume fraction of martensite generated. This yielded a net improvement in formability, up until the critical temperature discussed in Connolly et al. [15], where the blank does not chill sufficiently for transformation to initiate. Throughout this work, this point will be referred to as the critical blank temperature. However, at elevated die temperatures, raising the initial blank temperature resulted in a major reduction in the final volume fraction of martensite. This yielded a net reduction in formability.

Figures 4, 5, 6 present the percentage improvement in formability for a given initial blank temperature, die temperature, and strain path with $R_f = \{20, 40, 80\} \text{ Wm}^{-2}\text{K}^{-1}$ relative to the formability with boundary and die temperatures of 293K

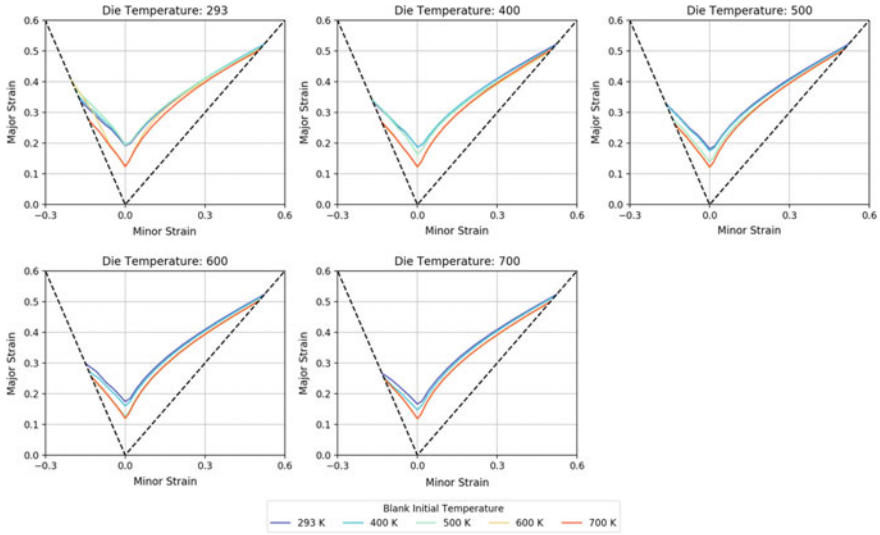


Fig. 2 Predicted forming limit diagrams for an effective conduction coefficient of $10 \text{ W m}^{-2} \text{ K}^{-1}$ for a variety of boundary temperatures and initial blank temperatures

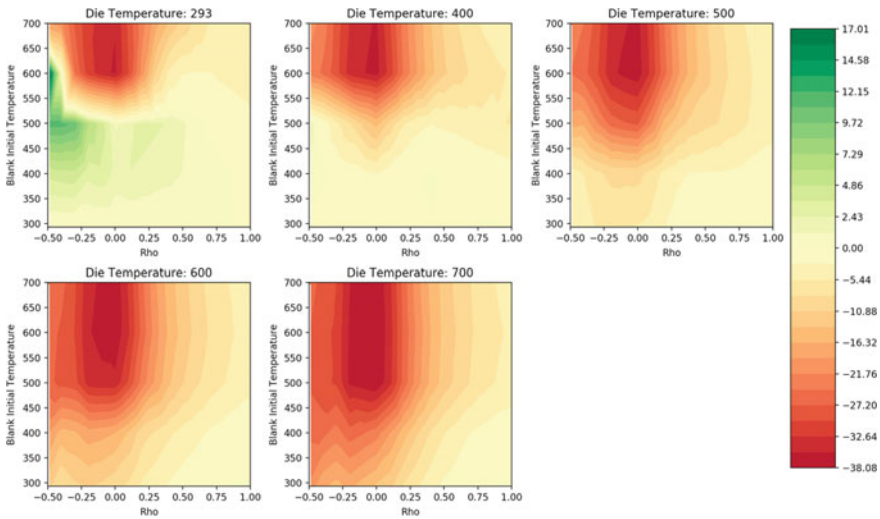


Fig. 3 Predicted percentage improvement in forming limit strain comparing an effective conduction coefficient of $10 \text{ W m}^{-2} \text{ K}^{-1}$ for a variety of boundary temperatures and initial blank temperatures to an effective conduction coefficient of $10 \text{ W m}^{-2} \text{ K}^{-1}$ with boundary temperature 293 K and initial blank temperature 293 K

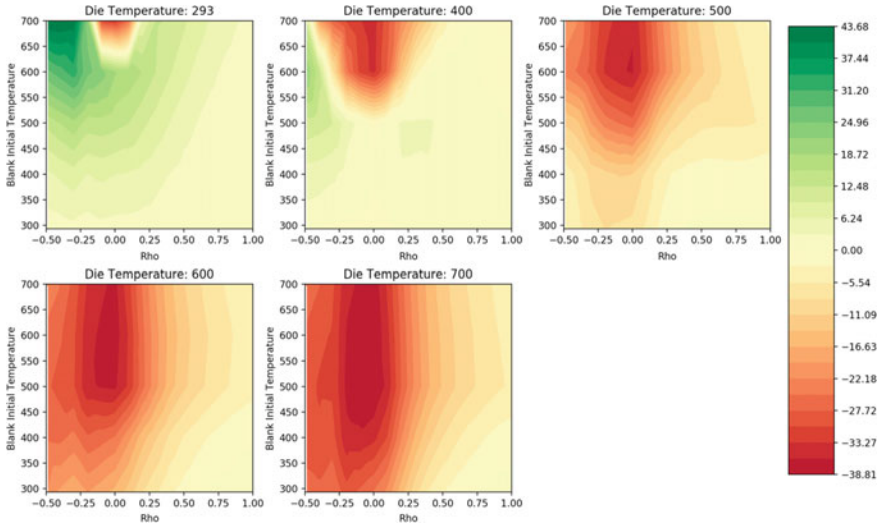


Fig. 4 Predicted percentage improvement in forming limit strain comparing an effective conduction coefficient of $20 \text{ Wm}^{-2} \text{ K}^{-1}$ for a variety of boundary temperatures and initial blank temperatures to an effective conduction coefficient of $10 \text{ Wm}^{-2} \text{ K}^{-1}$ with boundary temperature 293 K and initial blank temperature 293 K

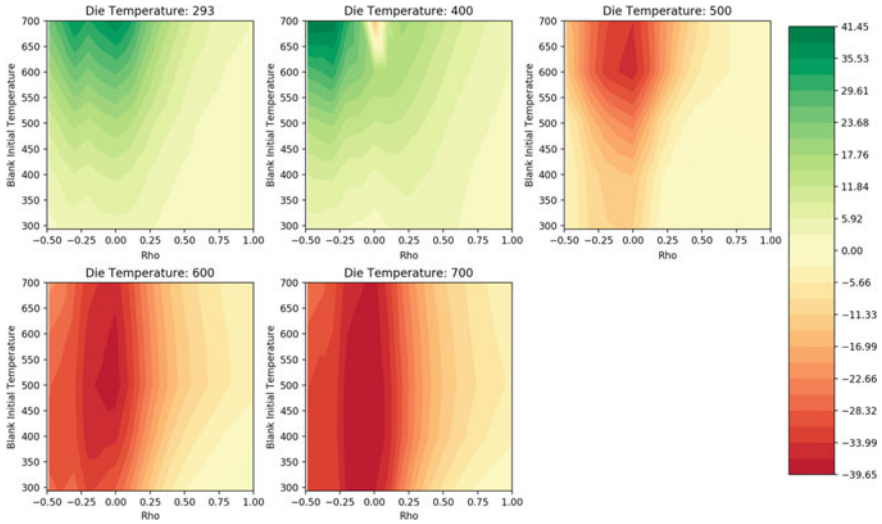


Fig. 5 Predicted percentage improvement in forming limit strain comparing an effective conduction coefficient of $40 \text{ Wm}^{-2} \text{ K}^{-1}$ for a variety of boundary temperatures and initial blank temperatures to an effective conduction coefficient of $10 \text{ Wm}^{-2} \text{ K}^{-1}$ with boundary temperature 293 K and initial blank temperature 293 K

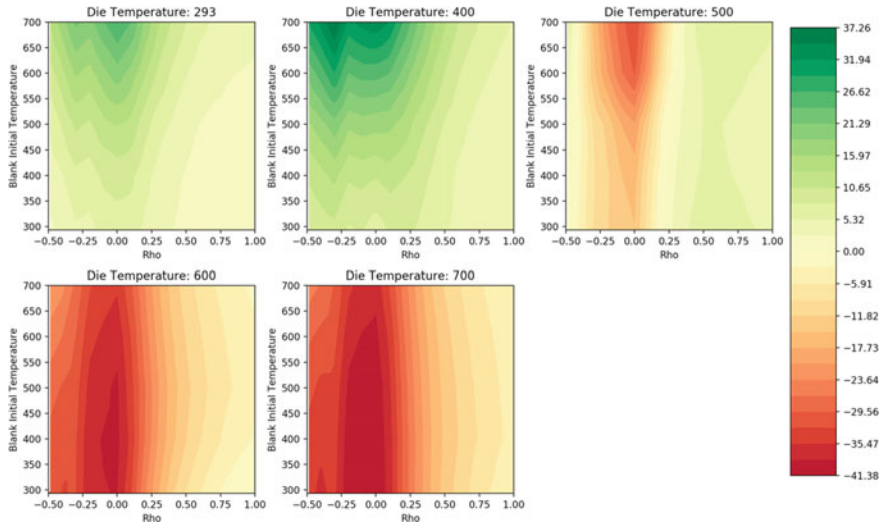


Fig. 6 Predicted percentage improvement in forming limit strain comparing an effective conduction coefficient of $80 \text{ W m}^{-2} \text{ K}^{-1}$ for a variety of boundary temperatures and initial blank temperatures to an effective conduction coefficient of $10 \text{ W m}^{-2} \text{ K}^{-1}$ with boundary temperature 293 K and initial blank temperature 293 K

and a conduction coefficient of 10 W m^{-2} . The effect of increased blank temperature with room temperature dies and elevated conduction coefficients is similar to the low conduction case: increasing blank temperature leads to an increase in formability until reaching the critical blank temperature. However, unlike the low condition case, simultaneously increasing blank and die temperatures can result in a net improvement in formability for moderate die temperatures (400 K and 500 K). This is because the elevated die conduction coefficient allows cooling to occur faster, allowing martensite formation to begin earlier and continue longer. Despite an increase in the conduction coefficient, the high die temperature cases (600 K and 700 K) did not result in an increase in formability. This is because transformation is almost completely suppressed at these temperatures, where little transformation occurs despite the blank reaching the die temperature.

It is important to understand the overall sensitivity of formability to initial blank temperature, die temperature, and conduction coefficient to optimize the thermal parameters. Considering only cases with room temperature or moderate die temperature and a blank temperature beneath the critical blank temperature, formability is improved with decreasing die coefficient, increasing initial blank temperature, and increasing die temperature. Conversely, the value of the critical blank temperature itself increases with increasing die coefficient and decreasing die temperature. In a forming process, the critical blank temperature limits the maximum formability of a process. Improving formability requires finding the correct process parameters to simultaneously increase the critical blank temperature while improving formability

below the critical blank temperature. Since the critical blank temperature is dependent on the strain path of deformation, the optimal choice of process parameters will likely be dependent on the expected strain paths of the specific component being formed.

In this study, the maximum uniaxial tension formability was predicted to occur with a boundary temperature of 293 K, a conduction coefficient of 20 W m^{-2} , and an initial blank temperature of 700 K. These conditions resulted in a uniaxial tension formability improvement from 0.33 to 0.48 strain (+44%), but also caused a reduction in plane strain formability from 0.19 to 0.14 (−27%). The maximum plane strain formability occurred with a boundary temperature of 293 K, a conduction coefficient of 40 W m^{-2} , and an initial blank temperature of 700 K. With these conditions, plane strain formability improved from 0.19 to 0.26 (41%) and uniaxial formability improved from 0.33 to 0.41 (26%). As in Connolly et al. [15], there are only minor effects on the equibiaxial side because the yield surface changes are decoupled from the martensite generation, and the martensite generation is saturated and therefore has minimal effect on hardening at the localization strain. In this study, the blank temperature, die temperature, and conduction coefficient. In an unbounded optimization, larger improvements could likely be obtained. Additionally, it is crucial to recognize that poor control of thermal process parameters may also result in significant reductions in formability. The worst case obtained in the study had an initial blank temperature of 293 K, die temperature of 700 K, and a conduction coefficient of 80 W m^{-2} . In this case, uniaxial formability reduced from 0.33 to 0.21 (−35%), plane strain formability reduced from 0.19 to 0.11 (−41%), and equibiaxial formability is unchanged.

Conclusion

In this paper, the formability behaviour of a TRIP 800 steel subject to realistic thermal conditions for forming processes was analyzed. It employed the constitutive model and fully coupled thermomechanical MK analysis presented in Connolly et al. [15]. This study varied the effective conduction coefficient, blank temperature, and die temperature to obtain the following specific conclusions:

- Hot forming of TRIP steels using in-die cooling can result in improvements in predicted formability of up to 44% under uniaxial tension and 41% under plane strain tension were observed.
- Excessive blank and die heating can result in reductions in predicted formability of up to 35% under uniaxial tension and 41% under plane strain tension were observed
- Optimal thermal process parameters depend on strain path, suggesting that the ideal formability curve is tightly coupled to die and component design

Acknowledgements This work was supported by the Natural Sciences and Engineering Research Council-Automotive Partnership Collaboration (NSERC-APC) under grant no. APCJ 441668-12, Natural Sciences and Engineering Research Council-Industrial Research Chair (NSERC-IRC) under grant no. IRCPJ-503185-2016, and General Motors of Canada. The first author (D.S.C.) would like to acknowledge the Natural Sciences and Engineering Research Council-Undergraduate Student Research Award for financial support that was provided. The second author (C.P.K.) would like to acknowledge the Ontario Graduate Scholarship for their financial support that was provided.

References

1. Kohar CP, Zhumagulov A, Brahme A, Worswick MJ, Mishra RK, Inal K (2016) Development of high crush efficient, extrudable aluminium front rails for vehicle lightweighting. *Int J Impact Eng* 95:17–34
2. Kohar CP, Bassani JL, Brahme A, Muhammad W, Mishra RK, Inal K (2019) A new multi-scale framework to incorporate microstructure evolution in phenomenological plasticity: theory, explicit finite element formulation, implementation and validation. *Int J Plast* 117:122–156
3. Zhang P, Kohar CP, Brahme AP, Choi S-H, Mishra RK, Inal K (2019) A crystal plasticity formulation for simulating the formability of a transformation induced plasticity steel. *J Mater Process Technol*:116493
4. Connolly D, Kohar C, Muhammad W, Hector LG, Mishra RK, Inal K (2020) A coupled thermomechanical crystal plasticity model applied to quenched and partitioned steel. *Int J Plast*. Under Review
5. U.S.E.P.A. (2016) Draft technical assessment report: midterm evaluation of light-duty vehicle greenhouse gas emission standards and corporate average fuel economy standards for model years 2022–2025. U.S. Environmental Protection Agency, Washington, D.C.
6. Olson GB, Cohen M (1975) Kinetics of strain-induced martensitic nucleation. *MTA* 6(4):791
7. Iwamoto T, Tsuta T, Tomita Y (1998) Investigation on deformation mode dependence of strain-induced martensitic transformation in trip steels and modelling of transformation kinetics. *Int J Mech Sci* 40(2):173–182
8. Tomita Y, Iwamoto T (1995) Constitutive modeling of trip steel and its application to the improvement of mechanical properties. *Int J Mech Sci* 37(12):1295–1305
9. Miller MP, McDowell DL (1996) Modeling large strain multiaxial effects in FCC polycrystals. *Int J Plast* 12(7):875–902
10. Wu R, Li W, Zhou S, Zhong Y, Wang L, Jin X (2014) Effect of retained austenite on the fracture toughness of quenching and partitioning (Q&P)-treated sheet steels. *Metall Mater Trans A* 45(4):1892–1902
11. Bhandarkar D, Zackay VF, Parker ER (1972) Stability and mechanical properties of some metastable austenitic steels. *MT* 3(10):2619–2631
12. Keeler S, Backofen W (1963) Plastic instability and fracture in sheets stretched over rigid punches. *ASM Trans Q* 56(1):25–48
13. Goodwin GM (1968) Application of strain analysis to sheet metal forming problems in the press shop. *SAE Papers*
14. Marciniak Z, Kuczyński K (1967) Limit strains in the processes of stretch-forming sheet metal. *Int J Mech Sci* 9(9):609–620
15. Connolly DS, Kohar CP, Mishra RK, Inal K (2018) A new coupled thermomechanical framework for modeling formability in transformation induced plasticity steels. *Int J Plast* 103:39–66
16. Kohar CP, Cherkaoui M, El Kadiri H, Inal K (2016) Numerical modeling of TRIP steel in axial crashworthiness. *Int J Plast* 84:224–254

17. Stringfellow RG, Parks DM, Olson GB (1992) A constitutive model for transformation plasticity accompanying strain-induced martensitic transformations in metastable austenitic steels. *Acta Metall Mater* 40(7):1703–1716
18. Johnson GR, Cook H (1983) A constitutive model and data for metals subjected to large strains, high strain rates and high temperatures. In: *Proceedings of the 7th international symposium on ballistics*, The Hague, Netherlands, pp 541–547
19. Cowper G, Symonds P (1957) *Strain-hardening and strain-rate effects in the impact loading of cantilever beams*. Brown University Division of Applied Mathematics, Providence, Rhode Island, USA
20. Barlat F, Brem JC, Yoon JW, Chung K, Dick RE, Lege DJ et al (2003) Plane stress yield function for aluminum alloy sheets—part 1: theory. *Int J Plast* 19(9):1297–1319
21. Dan WJ, Zhang WG, Li SH, Lin ZQ (2007) Finite element simulation on strain-induced martensitic transformation effects in TRIP steel sheet forming. *Comput Mater Sci* 39(3):593–599
22. Hutchinson JW, Neale KW (1978) Sheet necking. II. Time independent behaviour. III. Strain-rate effects. In: Koistinen D, Wang N-M (eds) *Mechanics of sheet metal forming*. Plenum Publishing Corporation, New York, pp 269–285
23. Barlat F, Richmond O (2003) Modelling macroscopic imperfections for the prediction of flow localization and fracture. *Fatigue Fract Eng Mater Struct* 26(4):311–321

Local Heat Treatment for Springback Reduction in Deep Drawing of Advanced High-Strength Steel



Josef Domitner, Vladimir Boskovic, Iris Baumgartner, Florian Grünbart, Christof Sommitsch, and Mustafa Kičin

Abstract The concept of a novel hybrid process which includes local heat treatment for springback reduction in deep drawing of AHSS is presented. In order to demonstrate the feasibility of this process a prototype tool for deep drawing of U-profiles was designed and optimized for integrating an inductive heating coil. Both, cold forming as well as local heat treatment, were performed within a single process step, as the radius zones of the deep-drawn U-profile were heated immediately after completing the forming stroke. To quantify the influence of the local heat treatment on the internal stresses inside the U-profile, a two-dimensional model of the hybrid forming–heating process was built using the Abaqus finite element (FE) software package. The flow curves required for this model were determined by tensile testing of dual-phase (DP) steel sheets at temperatures between 25 °C and 1000 °C. Both, the experimental and the numerical results, confirm that local heat treatment can significantly reduce the local internal stresses and the springback without decreasing the overall strength of the component.

Keywords Advanced high-strength steel · AHSS · Springback · Deep drawing · Local heat treatment · Hybrid forming–heating process

J. Domitner (✉) · V. Boskovic · F. Grünbart · C. Sommitsch
Graz University of Technology, Institute of Materials Science, Joining and Forming, Research Group of Lightweight and Forming Technologies, Inffeldgasse 11/I, 8010 Graz, Austria
e-mail: josef.domitner@tugraz.at

I. Baumgartner
Austrian Institute of Technology (AIT), Light Metals Technologies Ranshofen GmbH (LKR), P.O. Box 26, 5282 Ranshofen, Austria

M. Kičin
Cosma Engineering Europe GmbH, Puchberger Straße 267, 2722 Weikersdorf, Austria

Introduction

In recent years, the use of high-strength steel (HSS) and advanced high-strength steel (AHSS) sheets for deep drawing of automotive components has been steadily increasing, because these steel types show great potential for producing lightweight structures with improved crash resistance [1]. However, elastic springback is considered a serious problem which makes controlling the dimensional specifications of components quite challenging [2]. Springback can be mainly considered as elastic deformation which occurs when the formed component is released from the forming tool. Hence, it would be highly effective to focus on measures aiming to minimize elastic stresses directly in forming operations. Different technological concepts were proposed for reducing springback in sheet forming of HSS or AHSS, respectively: variation of the blankholder force [3] or inductive heating of the flange region [4] in deep drawing, as well as local heat treatments using infrared [5–7] or laser [8, 9] heat sources, or using a counterpunch [10] in sheet bending.

This work presents the concept of a hybrid forming–heating process. The designed tool enables local heat treatment of deep-drawn components immediately after completing the forming stroke, i.e. before releasing the formed component from the tool. The feasibility of this concept for springback reduction was already proven at a lab scale [11], but the present work investigates the feasibility at semi-industrial scale using a prototype tool. The results of the forming–heating experiment are discussed and analyzed in detail with the help of finite element (FE) simulation.

Tool and Process Concept

Figure 1 shows the design of the hybrid forming–heating tool. The main components are the upper and the lower base plates, the central plate, the four guiding pillars, the drawing die, the blankholder, the clamping bar, the drawing punch, and the inductor next to the drawing edges of the punch. A straight cooling channel is located parallel to each drawing edge, because water cooling is mandatory to prevent excessive local heating of the punch. The lower base plate with the drawing punch and the blankholder are fixed to the table of a Schuler 400-tons hydraulic press, whereas the upper base plate with the drawing die is fixed to the ram of the press.

The hybrid forming–heating process which is schematically illustrated in Fig. 2 works as follows: (a) After the blank has been positioned on the blankholder, the ram of the hydraulic press moves downward and clamps the blank with a predefined cushion force between the blankholder and the drawing die. (b) With the downward movement of the ram and, therefore, of the die, the clamped blank is drawn over the fixed punch until the lower end position is reached. (c) The formed blank is fixed at the end position, while its radius zones are locally heated to the predefined peak temperature using the inductor. The blank is also fixed during the subsequent cooling

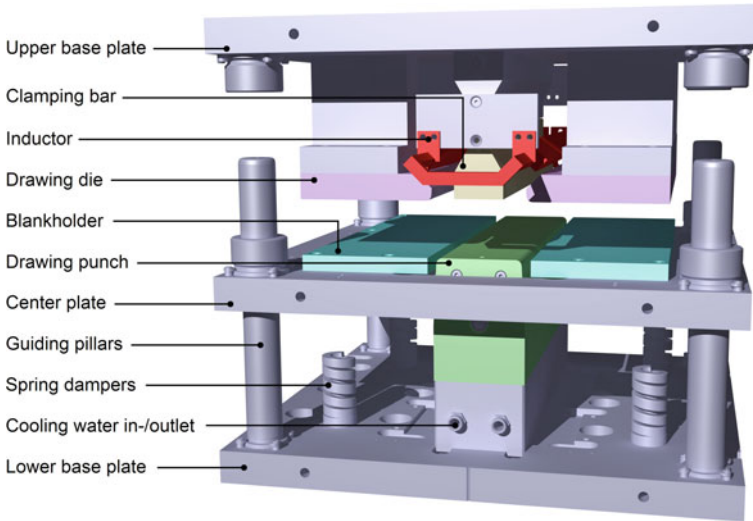


Fig. 1 Main components of the hybrid forming–heating tool

period. (d) Finally, the ram of the press and, therefore, the die moves upward to the upper-end position and the formed blank is released.

Deep Drawing Experiments

In order to prove the feasibility of the presented hybrid concept for reducing springback at semi-industrial scale, a prototype tool was manufactured at the Research Group of Lightweight and Forming Technologies at the Graz University of Technology, Austria. U-profiles were formed from blanks of galvanized dual-phase (DP) steel CR700Y980T-DP (YS 700–850 MPa, UTS 980–1130 MPa, [12]) using the process conditions of Table 1. The blank dimensions were 500 mm × 400 mm × 1.6 mm. For lubrication 0.4 ml of Wisura FMO 5010 forming oil for fine blanking was applied to both sides of the blank.

As shown in Fig. 3, local inductive heating of the radius zones of the U-profile was performed immediately after the forming step had been completed. In order to achieve different peak temperatures, the inductive heating system was switched off after heating times of 2.5 s or 5.5 s, resulting in peak temperatures of about 525 °C or 925 °C, respectively. Subsequent cooling was achieved by natural convection. For both experiments, the die was opened and the U-profile was released after the total heat treatment time of 15 s.

After hybrid forming–heating, the entire geometries of the U-profiles produced with and without heat treatment of the radius zones were captured using the GOM

Fig. 2 Schematic illustration of the hybrid forming–heating process

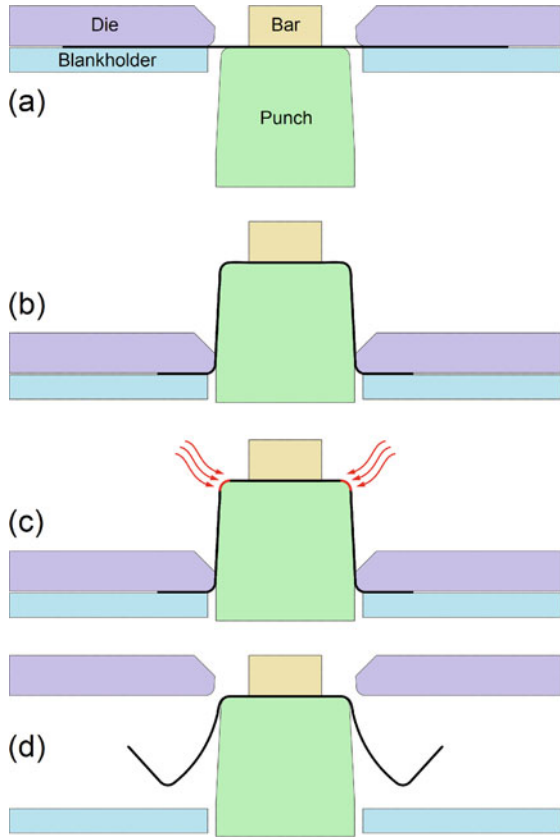
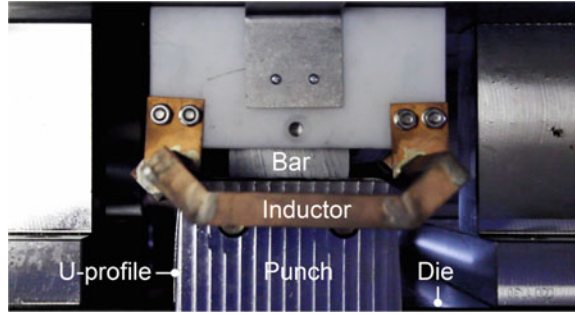


Table 1 Process conditions

Drawing speed	80 mm/s
Drawing depth (ideal height of U-profile)	100 mm
Blankholder force	300 kN
Peak temperatures for inductive heating	525 °C / 925 °C
Heating time	2.5 s / 5.5 s
Cooling time	12.5 s / 9.5 s
Total heat treatment time (heating and cooling)	15 s

ATOS III Triple Scan [13] measurement system. The measured geometry data were then used for validating the results of the numerical simulation of the process.

Fig. 3 Inductive heating of the radius zones of the U-profile



Numerical Model

Geometry and Mesh

The strain in length direction of the formed U-profile is negligible since the length of the profile is several times greater than the overall height and width of the profile. Furthermore, the cross section of the U-profile is de facto constant. Hence, for the finite element simulation, the “real” three-dimensional (3D) process setup can be simplified as symmetric two-dimensional (2D) model shown in Fig. 4. The 2D model was built using the Abaqus software package [14]. It consists of one deformable component (blank) and four rigid components (die, blankholder, clamping bar, punch). Only the blank was meshed with “4-node bilinear plane strain quadrilateral, hybrid, constant pressure, reduced integration, hourglass control” (CPE4RH)

Fig. 4 Symmetric 2D model with rigid (grey) and with deformable (green) components for the finite element simulation of the process

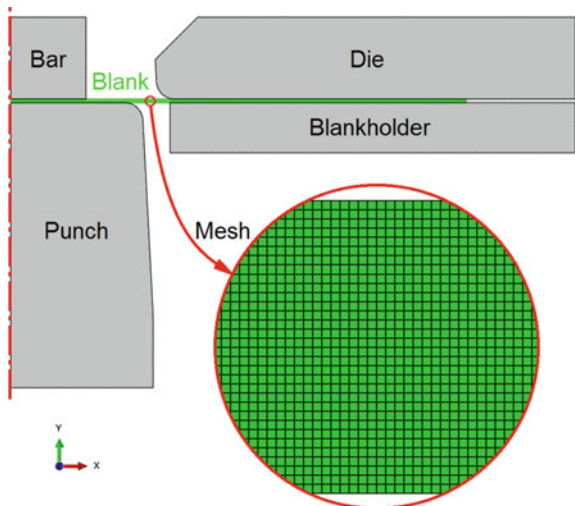
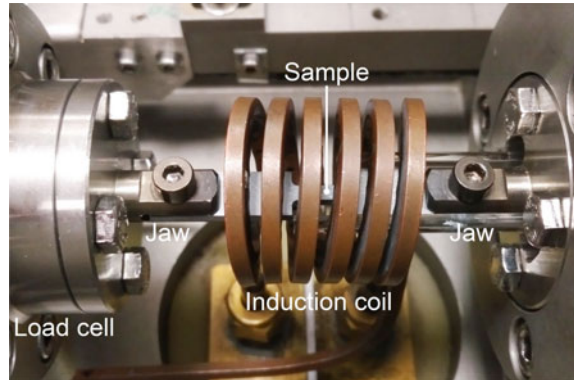


Fig. 5 Tensile testing of samples using the dilatometer



elements of $0.05 \text{ mm} \times 0.05 \text{ mm}$. Hence, the rectangular cross section of the 1.6-mm-thick and 200-mm-wide blank half illustrated in Fig. 4 was meshed with 128,000 elements aligned in 4,000 columns and 32 rows.

Material Properties

The temperature-dependent elastoplastic properties including Young's modulus and flow curves of the DP steel were determined using a Bähr DIL 805 D/T dilatometer equipped with an inductive heating system. The tensile samples were centred inside the induction coil and clamped by the jaws of the dilatometer as shown in Fig. 5. Before testing, the samples were inductively heated to different temperatures between room temperature and $1,000 \text{ }^\circ\text{C}$. Three samples were tested at each of these temperatures.

During testing, both tensile force and elongation of the sample were monitored. Based on these data, true stress–strain curves were calculated. The temperature-dependent flow curves shown in Fig. 6a were extrapolated from the true stress–strain curves using Hollomon's equation [15]. Furthermore, the temperature dependence of Young's modulus as shown in Fig. 6b was determined. Note that the factor f_E represents the ratio between Young's modulus at elevated temperature and Young's modulus of 204 GPa at room temperature ($25 \text{ }^\circ\text{C}$). Poisson's number of 0.3 was assumed as constant.

Process Conditions

The hybrid process was modeled in four steps as illustrated in Fig. 2. The positions of the punch and of the clamping bar were fixed. Movement of the drawing die was only allowed in the vertical direction. The blankholder force was applied against the movement direction of the die. The process conditions listed in Table 1 were

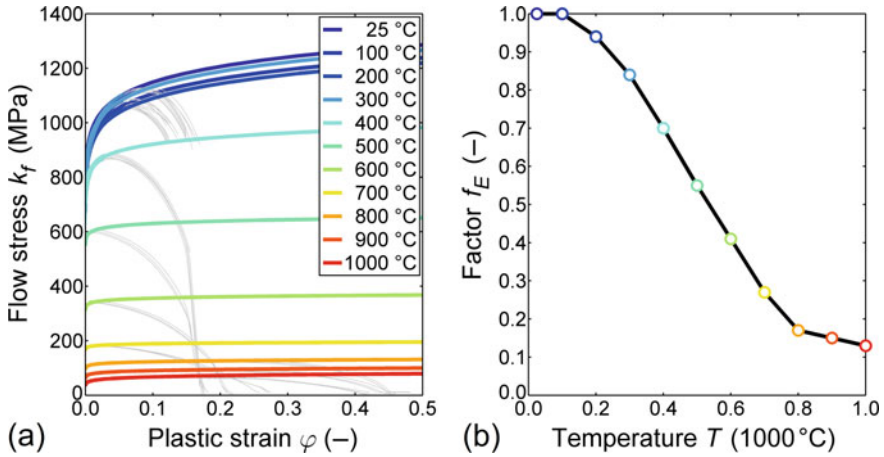


Fig. 6 **a** Temperature-dependent flow curves and **b** temperature dependence of Young’s modulus of the DP steel

also used in the numerical model. However, local inductive heating was not directly modeled. Instead of, the actual peak temperature–time curve measured during the deep drawing experiment at the radius zone was specified. As shown in Fig. 7a, two curves with different peak temperatures of $T_{peak} = 525 \text{ °C}$ and $T_{peak} = 925 \text{ °C}$ were used. To consider local heating only at the radius zone, each of the two curves shown in Fig. 7a was multiplied with the corresponding trapezoidal function shown in Fig. 7b. Note that the temperature factor f_T is zero outside the radius zone. In the present model, allocating the temperature was based on the width coordinate of the plain undeformed blank. Constant temperature in thickness direction of the blank was assumed. Constant Coulomb’s friction coefficient of 0.1 was defined for each contact interface.

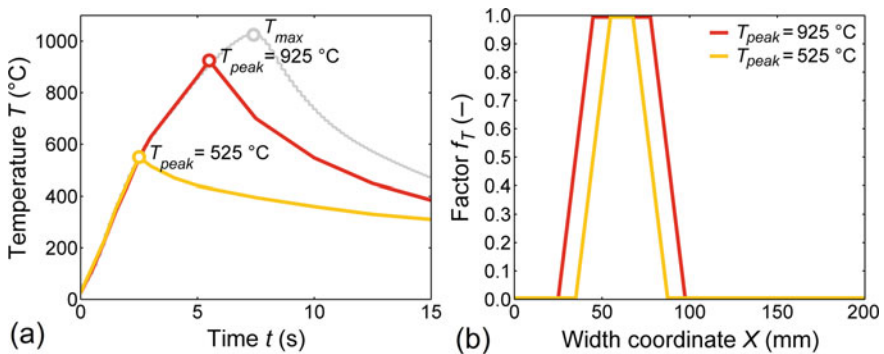


Fig. 7 **a** Peak temperature–time curve and **b** trapezoidal temperature distribution

Results and Discussion

Microstructure

Figures 8 and 9 show etched microstructures and local hardness curves of the DP steel investigated for different processing conditions: (a) as-bent without any heat treatment, (b) bent and heat-treated with the peak temperature of 525 °C, and (c) bent and heat-treated with the peak temperature of 925 °C. As shown in Fig. 8a, b, the fractions of both ferrite (light grey) and martensite (dark grey) are almost equal. Hence, heat treatment with the peak temperature of 525 °C did not influence the microstructure significantly. In comparison, the microstructure shown in Fig. 8c contains a higher fraction of ferrite, which indicates that martensite decomposed partially due to the heat treatment with the peak temperature of 925 °C. This change

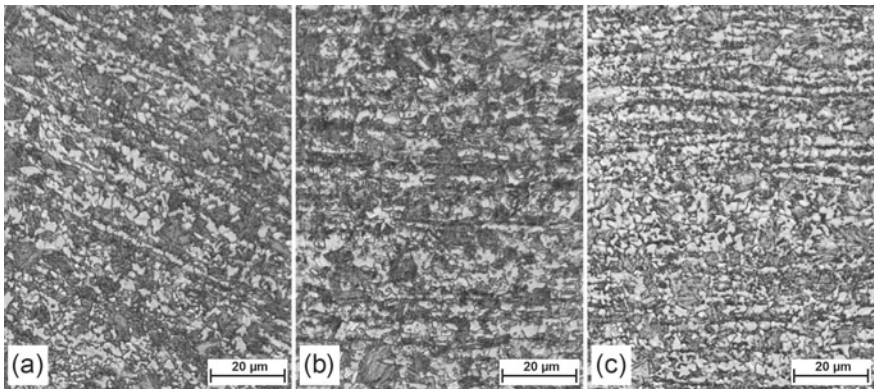


Fig. 8 Microstructures of the DP steel **a** without heat treatment and heat-treated with peak temperatures of **b** 525 °C and **c** 925 °C

Fig. 9 Local hardness of the DP steel at the radius zone of the U-profile with and without heat treatment (HT)

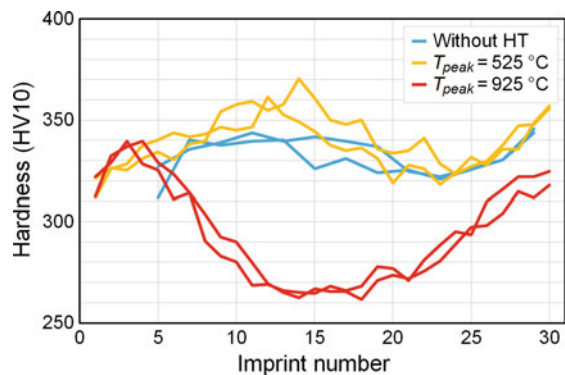
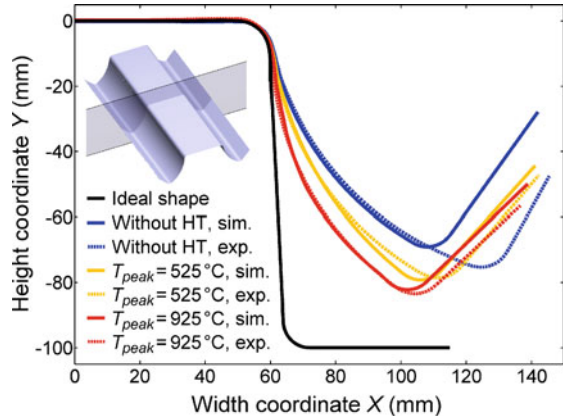


Fig. 10 Comparison of springback with and without heat treatment (HT) at the radius zone of the U-profile (continuous lines: simulations, dashed lines: experiments)



in the microstructure decreased the local hardness at the radius zone of the U-profile, as illustrated in Fig. 9.

Springback

Figure 10 compares the cross sections of U-profiles produced with and without local heat treatment of the radius zone. As illustrated, the cross sections were measured at the middle of the deep-drawn U-profiles. It is evident that the springback angle decreased significantly with increasing peak temperature. Small variations of the drawing depth in the experiments caused different lengths of the profile legs. However, this length difference influenced the springback angle just slightly. Figure 10 illustrates that the simulation model was able to estimate the springback angle and, therefore, to predict the influence of heat treatment quite well.

Summary and Conclusions

This work presents the concept of a hybrid forming–heating process to reduce springback in deep drawing of AHSS. Both experimental and numerical investigations demonstrated the feasibility of the concept for deep drawing of U-profiles from DP steel using a prototype tool at semi-industrial scale. Based on the results of these investigations, the following conclusions can be drawn:

- Local inductive heating before opening the tool decreases internal stresses and, therefore, may reduce significantly the springback. Increasing the peak temperature of the heating process decreases the springback angle.

- Heat treatment with peak temperatures of 925 °C combined with convective air cooling causes partial decomposition of martensite and loss of hardness, but heat treatment with peak temperatures of 525 °C does not significantly influence the initial microstructure.
- The FE model of the hybrid forming-heating process is able to predict the spring-back tendency based on the peak temperature–time curve measured during heat treatment.

Acknowledgements The authors would like to thank Thomas Stern for his assistance with the design of the deep drawing tool. Many thanks also go to Heinz Karl Fasching and to Nino Müllner for manufacturing and assembling the tool, and for supporting the deep drawing experiments.

References

1. Lesch C, Kwiaton N, Klose FB (2017) Advanced High Strength Steels (AHSS) for automotive applications—Tailored properties by smart microstructural adjustments. *Steel Res Int* 88(10):1700210
2. Ul Hassan H, Traphöner H, Güner A, Erman Tekkaya A (2016) Accurate springback prediction in deep drawing using pre-strain based multiple cyclic stress-strain curves in finite element simulation. *Int J Mech Sci* 110:229–241
3. Ul Hassan H, Maqbool F, Güner A, Hartmaier A, Ben Khalifa N, Erman Tekkaya A (2016) Springback prediction and reduction in deep drawing under influence of unloading modulus degradation. *Int J Mater Form* 9:619–633
4. Kayhan E, Kaftanoglu B (2018) Experimental investigation of non-isothermal deep drawing of DP600 steel. *Int J Adv Manuf Technol* 99:695–706
5. Lee E-H, Hwang J-S, Lee C-W, Yang D-Y, Yang W-H (2014) A local heating method by near-infrared rays for forming of nonquenchable advanced high-strength steels. *J Mater Process Technol* 214(4):784–793
6. Lee E-H, Yang D-Y, Yoon JW, Yang W-H (2015) Numerical modeling and analysis for forming process of dual-phase 980 steel exposed to infrared local heating. *Int J Solids Struct* 75–76:211–224
7. Lee E-H, Yang D-Y, Yoon JW, Yang W-H (2017) A manufacturing process using the infrared ray local heating method for seat cross members. *Int J Adv Manuf Technol* 89:3299–3305
8. Mäntyjärvi K, Keskitalo M, Karjalainen JA, Leiviskä A, Heikkala J, Mäkikangas J (2007) Laser-assisted bending. *Key Eng Mater* 344:235–241
9. Järvenpää A, Jaskari M, Hietala M, Mäntyjärvi K (2015) Local laser heat treatments of steel sheets. *Phys Procedia* 78:296–304
10. Komgrit L, Hamasaki H, Hino R, Yoshida F (2016) Elimination of springback of high-strength steel sheet by using additional bending with counter punch. *J Mater Process Technol* 229:199–206
11. Boskovic V, Sommitsch C, Kičín M (2017) Development of a hybrid deep drawing process to reduce springback of AHSS. *J Phys: Conf Ser* 896:012084
12. Voestalpine Stahl GmbH, Linz, Austria, Data sheet dual-phase steels (2019)
13. GOM GmbH (2019) Braunschweig, Germany. <https://www.gom.com/de/3d-software/gom-inspect.html>
14. Dassault Systèmes SE (2019) Vélizy-Villacoublay, France. <https://www.3ds.com/products-services/simulia/products/abaqus/>
15. Hollomon JH (1945) Tensile deformation. *Metals Technol* 12(4):268–289

Strain and Stress-Based Forming Limit Diagrams for Inconel 718 Alloy



Gauri Mahalle, Prathamesh Takalkar, Nitin Kotkunde, Amit Kumar Gupta, and Swadesh Kumar Singh

Abstract Study of material forming limits plays a crucial role in producing complex shape components without failure for high-strength and limited ductility materials. The accurate determination of forming limits is also crucial for trustworthy finite element analysis and development of the reliable tool setup. The present study mainly focused on forming limit diagrams (FLDs) of thin precipitate-hardenable Inconel 718 (IN718) sheet using Nakazima test at different temperatures (400–700 °C). Limiting strains are evaluated to plot strain-based forming limit diagram (ϵ -FLD) from deformed specimens in three different strain paths, viz. equi-biaxial, plane, and uniaxial strains. Further, stress-based forming limit diagram (σ -FLD) was estimated using Barlat'89 anisotropic yield criteria coupled with Swift power hardening law. It was found that test temperature influences limiting strain and stresses in FLD.

Keywords IN718 alloy · Nakazima test · Barlat'89 yield criteria · Strains · Swift power hardening law · Forming limit diagram (FLD)

Introduction

Inconel 718 (IN718), among all the Ni–Cr–Fe-based super-alloys, is having excellent material properties and is able to withstand extreme temperature conditions (up to 705 °C). IN718 holds superior material properties, for example, high ultimate (950–1650 MPa) and yield (700–1250 MPa) tensile strengths, good rupture and creep strengths, high corrosion, and fatigue resistance at elevated temperatures [1, 2]. This indispensable alloy is used for high performance required applications like nuclear reactors, rocket engines, gas turbines, marine applications, and high-pressure vessels [3]. Especially outer casings of Ni–H₂ battery and high pressure-O₂ gas cylinders

G. Mahalle · P. Takalkar · N. Kotkunde (✉) · A. Kumar Gupta
Department of Mechanical Engineering, Birla Institute of Technology and Science, Pilani,
Hyderabad Campus, Hyderabad, India
e-mail: p20160415@hyderabad.bits-pilani.ac.in

S. Kumar Singh
Department of Mechanical Engineering, GRIET, Hyderabad, Telangana 500072, India

are facing challenges while manufacturing (mainly manufactured by deep drawing) as critical space components in space mission [4, 5].

Sheet Metal Forming processes (SMF) are predominantly used for the production of a variety of complex and crucial components in nuclear and gas turbine sectors. Formability of sheet metal is generally evaluated based on various lab-scale tests such as limiting drawing ratio (LDR), stretching, forming limit diagram (FLD) and hole expansion ratio (HER) [6]. FLD is a significant performance index which describes the limiting strain capacity of a material. Commonly, stretching process, especially Nakazima test is used to determine the limiting strains. FLD is plotted based on the major (ϵ_2) and minor strains (ϵ_1) obtained for various loading paths/strain paths (equibiaxial, biaxial, uniaxial, etc.) [7]. Different width rectangular specimens were stretched using a hemispherical punch to determine limiting strains for each strain path. Simplicity in tool design and shape of the specimen are the key features of this test. It is reported that maximum permissible limiting strain is strongly depends on numerous physical factors such as work-hardening, strain rate sensitivity, and induced plastic anisotropy (only in cold rolling process) [8, 9].

However, Prasad et al. [10] reported strain-based FLD at room temperature for solution-treated IN718 alloy. The author described that failure in stretched specimens followed without any prior hint of the localized necking. Hence, it is very much important to predict material failure. To avoid dependency on forming limit over strain paths, effective plastic strain vs. triaxiality (EPS vs. η), and stress-based FLD (σ -FLD) are used to predict damage [11, 12]. Bai et al. [13] evaluated 16 different fracture models for η -EPS space and compared their accuracy on the basis of various statistical parameters for different aluminum and steel alloys.

Hence, formability studies of Inconel alloy are extremely necessary for above-discussed reasons. The main objective of the present work is to estimate limiting and fractured strains of IN718 alloy at warm temperatures by Nakazima test. Further, limiting stress has been reported by stress-based FLD.

Materials and Methods

Commercially available IN718 alloy sheet, thickness 1 mm, is used for the present study. Some of the major alloying elements by % wt are Ni (51.5%), Fe (20%), Cr (18.4%), Nb (5%), and Mo (3%) with balanced other alloying elements (Each $\leq 0.05\%$ and Total $\leq 0.17\%$). The authors in their previous work discussed the uniaxial tensile flow stress behavior and DSA phenomenon that occurred within 500–700 °C temperature range [14, 15]. Tensile strength was calculated using a series of uniaxial tensile test experiments. Various material properties, namely, % elongation (% elong.), tensile yield (σ_{ys}) and ultimate (σ_{uts}) strengths, and anisotropic properties, mainly Lankford coefficient (r_0, r_{45}, r_{90}), planer(r) and normal (Δr) anisotropy, have also been evaluated and are shown in Table 1.

Swift hardening law is used to calculate strain hardening coefficient (K) and exponent (n) of IN718 alloy, expressed as in Eq. 1.

Table 1 Tensile properties of IN718 alloy

Temp (°C)	Material properties			Anisotropic properties				
	YS (MPa)	UTS (MPa)	Elong (%)	R ₀	R ₄₅	R ₉₀	\bar{R}	ΔR
400	394.66 ± 4%	819.73 ± 6%	49.22 ± 0.7	1.0869	0.6612	0.7043	0.7784	0.5650
700	343.58 ± 5%	753.22 ± 6%	54.6% ± 0.7	1.0642	0.9176	0.9639	0.9658	0.5552

YS—yield strength, UTS—ultimate tensile strength, Elng—% elongation, R_{0, 45, 90}—Lanford coefficients in 0°, 45°, & 90° orientation, R—normal anisotropy, and ΔR—planer anisotropy

$$\sigma = (\epsilon + k_s(\epsilon_0)^{n_s}) \tag{1}$$

Warm stretching experiments are conducted on a 40-Ton double-acting hydraulic press with an induction heating setup and working pressure up to 100 bar, schematically shown in Fig. 1a. The temperature during test was measured using the K-type thermocouple. Three different specimens geometries as per ASTM E2218-15 standard were prepared to induce three distinct strain paths (uniaxial strain, biaxial region, and plane strain) in FLD, mentioned in Fig. 1b. All experiments are performed by applying graphene-based moly-spray as lubricant. All the stretch-formed specimens were laser-etched using a 2.5 mm diameter circular grid for measuring the minor and major strains as suggested in standard. The stretch forming test was conducted at 400 °C and 700 °C to understand the effect of temperature over forming limits of material at a fixed BHP (25 bar) and punch speed (2 mm/min).

Further, high-resolution stereo microscope with an image analyzing software is used to measure minor and major diameters of stretched/deformed grid (ellipses) in the stretched blanks to estimate the engineering minor (e_2) and major (e_1) strains using the Eq. 2, Then transferred into the corresponding true strains (ϵ_1 & ϵ_2) as in Eq. 3.

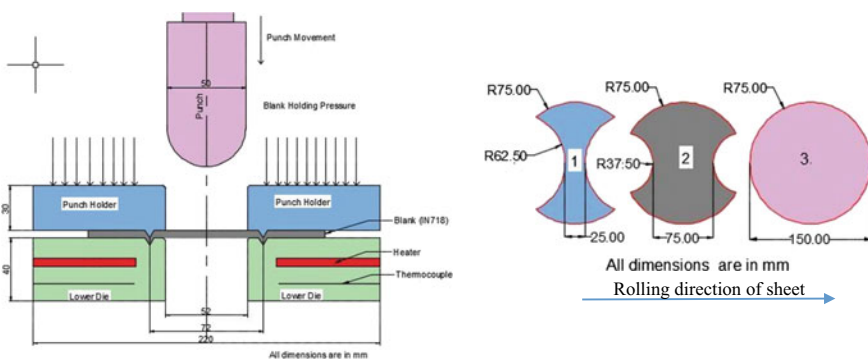


Fig. 1 a Stretch forming setup schematic diagram, b Specimen geometry considered for plotting FLDs

$$e1 = \frac{\text{major axis of stretched/deformed ellipse} - \text{grid diameter}}{\text{major axis of Stretched/deformed ellipse}}, \tag{1}$$

$$e2 = \frac{\text{minor axis of stretched/deformed ellipse} - \text{grid diameter}}{\text{minor axis of Stretched/deformed ellipse}}, \tag{2}$$

$$\varepsilon_{1,2} = \ln(1 + e_{1,2}) \tag{3}$$

The equivalent stress function according to r-based Barlat’89 stress function is defined as

$$\sigma_{\text{Barlat}} = \bar{\sigma} = \left[\frac{1}{2} \{ a + a|h\rho|^m + c|1 - h\rho|^m \} \right]^{\frac{1}{m}} \tag{4}$$

where stress ratio (minor to major stress) $\rho = \frac{\sigma_2}{\sigma_1}$ and strain ratio (minor to major strain), $\alpha = \frac{\varepsilon_2}{\varepsilon_1}$. Anisotropy ratio functions a, c, and h can be shown in terms of the Lankford coefficient as

$$h = \sqrt{\frac{r_0}{1 + r_0} \times \frac{1 + r_{90}}{r_{90}}} \tag{5}$$

$$c = 2 \times \sqrt{\frac{r_0}{1 + r_0} \times \frac{r_{90}}{1 + r_{90}}} \tag{6}$$

$$a = 2 - c \tag{7}$$

Associative flow law ($d\varepsilon_{ij} = d\lambda \frac{\partial \bar{\sigma}}{\partial \sigma_{ij}}$) is used to find the relationship between α and ρ , given as

$$\alpha = \frac{a|h\rho|^{m-1} - ch|1 - h\rho|^{m-1}}{a + c|1 - h\rho|^{m-1}} \tag{8}$$

Further, parameter χ according to Barlat’89 criteria is evaluated as a ratio of major principle stress (σ_1) and effective stress ($\bar{\sigma}$) as

$$\chi = \frac{\sigma_1}{\bar{\sigma}} = \frac{1}{\left[\frac{1}{2} \{ a + a|h\rho|^m + c|1 - h\rho|^m \} \right]^{\frac{1}{m}}} \tag{9}$$

Stress triaxiality (η) as per Barlat’89 criteria is further calculated as

$$\eta = \frac{\sigma_m}{\bar{\sigma}} = \frac{\sigma_1 + \sigma_2}{3\sigma_{\text{Barlat}}} = \frac{1}{3} \times \frac{(1 + \rho)}{\left[\frac{1}{2} \{ a + a|h\rho|^m + c|1 - h\rho|^m \} \right]^{\frac{1}{m}}} \tag{10}$$

Results and Discussion

Strain-Based Forming Limit Diagram (ϵ -FLD)

Minor and major true surface strains are measured from deformed ellipse in the necking region. FLD using corrected true major and minor strains is shown in Fig. 2. As these corrected strain data are scattered throughout the region, distinct color is assigned to differentiate between safe and fractured ellipses. It is observed from Fig. 2 that very few ellipses represented on necking as IN718 has very high-strength. It fails suddenly without any visible localized necking. As a result, very few major–minor strains were observed in the region of necking which is evident from plotted FLD at different temperatures. Limiting strains are separated by drawing a line between maximum safe ellipses and failed ellipses to plot FLD. At 400 °C, the highest major limiting strains in T-C and T-T regions (equi-biaxial tension) are 0.5526 and 0.469, respectively. FLD_o , an important FLD indicator, is observed as 0.4642. Limiting true strains are increasing with the increase in test temperature in all the deformation regions (T-T, plane strain, T-C), as shown in Fig. 2b. Limiting true strains at 700 °C temperature are improved by 20–25% compared to that at 400 °C, due to further rise in thermal softening which improves the ductility of the material. It is also observed that the slope of FLD at 700 °C increases significantly on both sides. High strain hardening exponent (n) and anisotropic coefficient (r -values) have significantly influenced on experimental FLDs. It is reported that a higher n -value delays the onset of instability in metal which enhances the limiting true strains [16]. This result is more pronounced in forming studies.

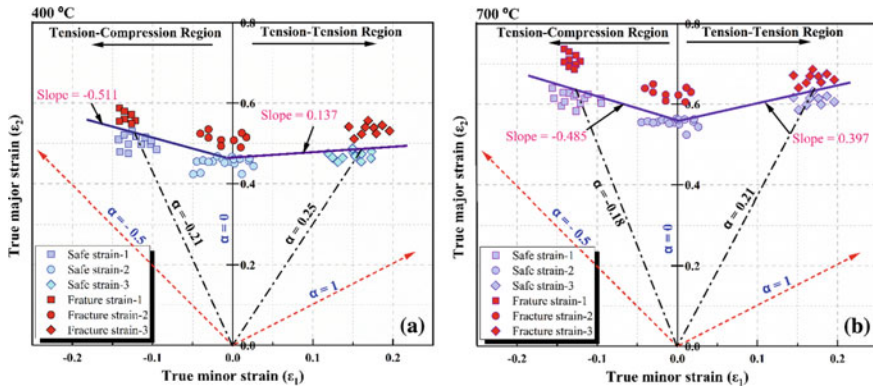


Fig. 2 ϵ -FLD of IN718 alloy at a 400 °C and b 700 °C

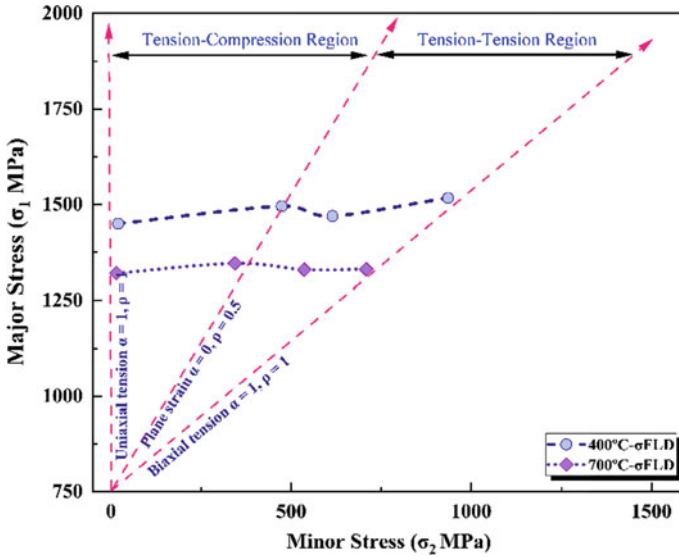


Fig. 3 σ -based FLD for IN718 alloy at warm temperature

Stress-Based Forming Limit Diagram (σ -FLD)

To avoid dependency of limiting strains on strain paths, σ -FLD is used by the transformation of limiting strains. To calculate the stress values and triaxiality, Barlat’89 quadratic yield function (Eqs. 4–9) has been used to transfer experimental strain values of FLD [10, 12]. From experimental minor and major limiting strains, strain ratio is used to calculate stress ratio (ρ) by Eq. 8. Minor and major (σ_2 σ_1) stress components are calculated by Eq. 9 and stress ratio (ρ). Calculated stress values from limiting strains of FLD have been used to calculate σ -FLD, as shown in Fig. 3, in-plane strain, T-C and T-T deformation paths. It is noticed from Fig. 3, σ -FLD curve shows a gradual increase till plane strain ($\alpha = 0$); afterward, there is a marginal stress increase till the end of T-T region. Similar nature of σ -FLD is observed for 700 °C. There is a drop by 22–33% approximately in major limiting stress with the rise in temperature. Maximum difference is observed in major limiting stress at T-T strain condition.

Conclusion

The following important conclusions are made:

1. Forming limits of Inconel 718 alloy are significantly affected by test temperatures. Limiting true strains at 700 °C temperature are improved by 20–25%

compared to that at 400 °C, which might be due to the thermal softening and improved ductility at high temperatures.

2. Stress-based FLD (σ -FLD) by the transformation of limiting strains shows a tendency to move towards plane strain conditions. σ -FLD curve shows increased nature till plane strain ($\alpha = 0$); afterward, there is a marginal stress increase till the end of T-T region. A decrease in major limiting stress is observed with the rise in test temperature.

References

1. Thomas A, El-Wahabi M, Cabrera JM, Prado JM (2006) High temperature deformation of Inconel 718. *J Mater Process Technol* 177(1–3):469–472. <https://doi.org/10.1016/j.jmatprotec.2006.04.072>
2. Mahalle G, Kotkunde N, Shah R, Gupta AK, Singh SK (2018) Analysis of flow stress behaviour of inconel alloys at elevated temperatures using constitutive model. *J Phys Conf Series* 1063. <https://doi.org/10.1088/1742-6596/1063/1/012037>
3. Schafrik RE, Ward DD, Groh JR (2001) Application of alloy 718 in GE aircraft engines: past, present and next five years. In: *Superalloys 718, 625, 706 and various derivatives*, pp. 1–11.
4. Patel MR (2004) *Spacecraft power systems*. Boca Raton, CRC Press
5. Lawrence H, Thaller AHZ (2003) Overview of the design, development, and application of nickel-hydrogen batteries. In: *NASA Tech., NGR Center (ed) National Aeronautics and Space Administration, Glenn Research Center*
6. Banabic D, Carleer B, Comsa DS, Kam E, Krasovskyy A, Mattiasson K, Sester M, Sigvant M, Zhang X (2010) *Sheet metal forming processes: constitutive modelling and numerical simulation*. Springer, Berlin, Heidelberg
7. Nakazima K, Kikuma T, Hasuka K (1968) Study on the formability of steel sheets. *Yawata Tech Rep* 264:8414–8442
8. Kotkunde N, Krishna G, Shenoy SK, Gupta AK, Singh SK (2017) Experimental and theoretical investigation of forming limit diagram for Ti-6Al-4 V alloy at warm condition. *Int J Mater Form* 10(2):255–266. <https://doi.org/10.1007/s12289-015-1274-3>
9. Venkateswarlu G, Singh AK, Davidson J, Tagore GR (2013) Effect of microstructure and texture on forming limits in friction stir processed AZ31B Mg alloy. *J Mater Res Technol* 2(2):135–140. <https://doi.org/10.1016/j.jmrt.2013.01.003>
10. Prasad KS, Panda SK, Kar SK, Murty SVSN, Sharma SC (2018) Prediction of fracture and deep drawing behavior of solution treated Inconel-718 sheets: numerical modeling and experimental validation. *Mater Sci Eng A* 733:393–407. <https://doi.org/10.1016/j.msea.2018.07.007>
11. Bao Y, Wierzbicki T (2004) On fracture locus in the equivalent strain and stress triaxiality space. *Int J Mech Sci* 46:81–98. <https://doi.org/10.1016/j.ijmecsci.2004.02.006>
12. Basak S, Panda SK, Zhou YN (2015) Formability assessment of prestrained automotive grade steel sheets using stress based and polar effective plastic strain-forming limit diagram. *J Eng Mater Technol Trans ASME* 137:1–12. <https://doi.org/10.1115/1.4030786>
13. Bai Y, Wierzbicki T (2015) A comparative study of three groups of ductile fracture loci in the 3D space. *Eng Fract Mech* 135:147–167. <https://doi.org/10.1016/j.engfracmech.2014.12.023>
14. Mahalle G, Kotkunde N, Gupta AK, Sujith R, Singh SK, Lin YC (2019) Microstructure characteristics and comparative analysis of constitutive models for flow stress prediction of inconel 718 alloy. *J Mater Eng Perform* 28(6):3321–3321. <https://doi.org/10.1007/s11665-019-04116-w>

15. Mahalle G, Salunke O, Kotkunde N, Gupta AK, Singh SK (2019) Neural network modeling for anisotropic mechanical properties and work hardening behavior of Inconel 718 alloy at elevated temperatures. *J Mater Res Technol* 8(2):2130–2140. <https://doi.org/10.1016/j.jmrt.2019.01.019>
16. Dieter GE (1961) *Mechanical metallurgy*, 3rd Edition. McGraw-Hill, New York

Validation of Comprehensive Material and Friction Models for Simulation of Thermo-Mechanical Forming of High-Strength Aluminium Alloys Using HFQ Technology



Damian Szegda, Mohamed Mohamed, Yogendra Joshi, and Mustapha Ziane

Abstract Advanced thermo-viscoplastic material model coupled with continuous integration of damage parameter was combined with dedicated friction model in a thermo-mechanical FE simulation of HFQ(R) forming of high-strength aluminium alloy. The friction model was set up to capture the complex tribologic response of hot and dry aluminium sheets formed on cold and lubricated tools. Friction was assumed as a function of temperature, contact pressure, and sliding distance. This paper presents the results of correlation of the simulation results with experimental measurements of thermo-mechanically HFQ[®] formed door inner. Thickness and shape measurements were then correlated to finite element simulation performed in PAM-STAMP 2019 with friction and material models implemented in HFQ[®] Module.

Keywords Friction · Aluminium alloy · Heat treatment/quenching · Simulation/modelling

Introduction

Strict EU regulations on vehicle emissions drive the automotive industry towards building more efficient lightweight vehicles. Aluminium alloys offer excellent lightweighting opportunities at a progressively more affordable cost. New manufacturing technologies allowing forming of high- and ultrahigh-strength aluminium alloys have emerged recently. One such technology is HFQ[®]—solution heat treatment, forming and in-die quenching which is typically followed by artificial ageing. The process combines material tempering with mechanical deformation.

D. Szegda (✉) · M. Mohamed · Y. Joshi
Impression Technologies Limited, 46 Sayer Drive, Unit E, Lyons Park, Coventry CV5 9PF, UK
e-mail: d.szegda@impression-technologies.com

M. Ziane
ESI Group, 100-102 Avenue de Suffren, 75015 Paris, France
e-mail: Mustapha.Ziane@esi-group.com

In this paper, the authors will discuss the capability of an advanced friction model coupled with thermo-viscoplastic continuum damage-based material model in application to simulation of the HFQ[®] process. First, integration and verification of both the models into commercially available FE software—PAM-STAMP is discussed. Several basic test cases are shown highlighting the models' accuracy and capability to capture the effect of strain rate history on the flow curve and material ductility. Then a thorough validation of the model based on HFQ[®] formed a complex high-strength deep-drawn door inner is presented. Forming simulations for failed and successfully formed panels are shown and used for validation of the simulation capability. A study of the effect of the apparent coefficient of friction is also discussed. It is concluded that an accurate simulation of HFQ[®] process requires not only a sophisticated material model but also should be supplemented by a more advanced model for the coefficient of friction.

The HFQ[®] Process in a Nutshell

A process which combines high formability with virtually no springback for (ultra) high-strength aluminium alloys was developed and patented by a team of researchers based at Imperial College London [1] and commercialised by a spin-out company—Impression Technologies Ltd (ITL) [2]. The process is called Solution Heat Treatment, Forming, and in-Die Quenching, or HFQ^{®1} for short. It consists of heating an Al-alloy blank sheet to its Solution Heat Treatment (SHT) temperature to produce a homogeneous solid solution with high ductility and hence good formability. The blank is then transferred to the press where a high forming speed is set to take advantage of strain rate hardening of the material. The formed part is held in the tool for a few seconds to quench in order to avoid the formation of precipitates in the microstructure. The process schematics together with temperature and micromechanics evolution is shown in Fig. 1. This is a hot forming technology which combines mechanical deformation with alloy tempering where forming and in-die quenching are done in one step. This doesn't only reduce production steps but also facilitates the production of high-strength, high-precision, and complex-shaped lightweight Al-alloy panels in an efficient and cost-effective way.

Friction Characterisation

The tribological experiments were carried out at the Technical University of Lulea using the hot strip drawing tribometer. A flat die linear strip draw test was used to obtain the coefficient of friction for a range of contact pressures and forming temperatures. In this set-up, two flat pins apply contact force, one on either side

¹ HFQ[®] is a registered trademark owned by Impression Technologies Ltd.

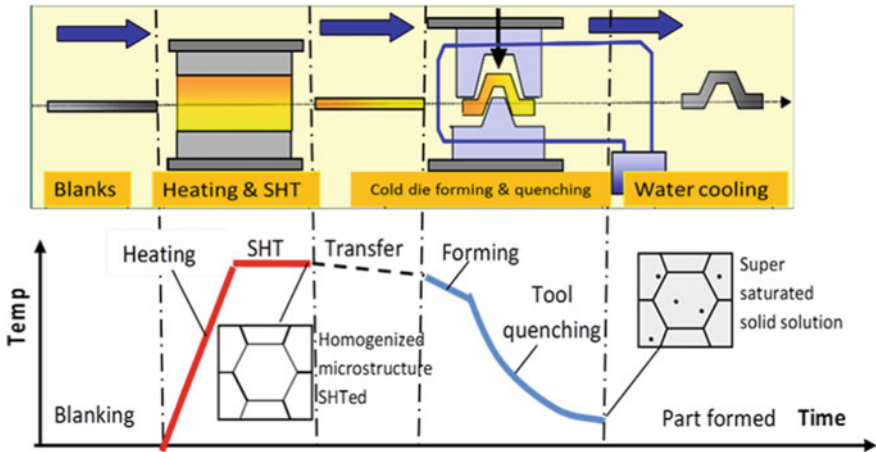


Fig. 1 The HFQ process in a nutshell

of the stationary strip, and slide along the length at a prescribed sliding velocity and distance. To represent the HFQ[®] conditions, the pins were maintained at room temperature, whereas the strip was heated to the desired temperature by Joule’s heating. The principle of operation of the strip draw set-up is illustrated in Fig. 2.

The test pins were made of GGG70L cast iron, nitride to 52 HRC and polished to Sa 0.1 μm. Firstly, a measured quantity HFQ[®] ITL WBD 001 lubricant was carefully applied on a heated pair of test pins to allow deposition of a dried layer. The pins were then mounted on the tribometer. Next, the strip was heated to the SHT temperature, held for a certain period. Then the heating was turned off to allow the strip to cool down to the desired forming temperature. The test pins immediately engaged thereafter under stipulated contact force and slid along the strip at a specific sliding velocity and distance.

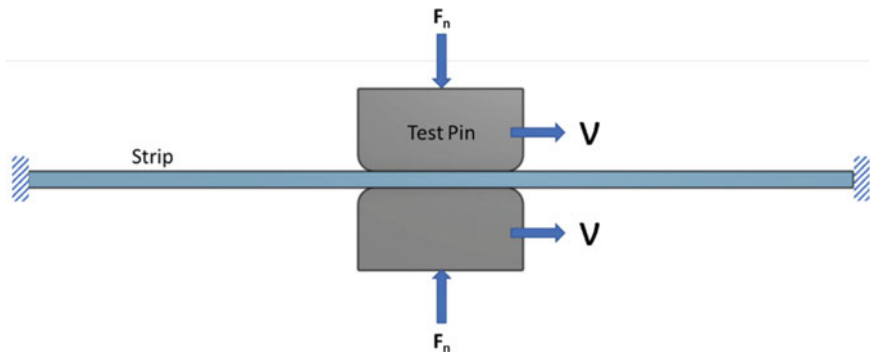


Fig. 2 Illustration of strip draw test’s working principle

A few selected preliminary experiments were carried out to establish the strip draw test method that subsequently led to the selection of the range of parameters to obtain the coefficient of friction for the development of the numerical friction model. In these experiments, it was observed that contact pressure lower than 3 MPa led to significant noise in the acquired frictional forces. Contact pressures higher than 15 MPa resulted in stretching and eventually necking of the strip. The test temperature range appropriately represents the blank temperature during the forming stage in HFQ® process. Owing to the “dry” lubricant layer, the tests showed negligible dependence of sliding velocity. Hence, the velocity was fixed at 0.25 m s^{-1} . The actual test conditions are given in Table 1.

Experimental Results

The coefficient of friction behaviour against normalised sliding distance for 15 MPa and $350 \text{ }^\circ\text{C}$ is shown in Fig. 3. This response was typical of the tests carried out and could be divided into three zones, namely, Zones I, II, and III. These zones are a consequence of the diminishing presence of the lubricant in the pin–strip–pin contact. A low steady coefficient of friction in Zone I is due to the presence of the lubricant layer over the entire contact area. The lubricant layer completely deteriorates eventually as sliding continues in Zone 3 simultaneously causing a transfer of aluminium onto the cast iron pins. The coefficient of friction can saturate eventually (red dashed line) or continue rising depending on contact pressure and max sliding distance as the transferred aluminium exacerbates ploughing into the test strip until the end of the test.

Figure 4 shows the coefficient of friction obtained at a sliding distance of 50 mm as the frictional behaviour was relatively consistent and stable up to 50 mm at least. Generally, it was observed that the contact pressure significantly influenced the coefficient of friction as compared to the test temperature. Apart from $250 \text{ }^\circ\text{C}$, the coefficient of friction reduced with increasing contact pressures. Except for 15 MPa, the coefficient of friction increased with increasing test temperature. This discrepancy could be attributed to the frictional behaviour, which was found to be significantly sensitive to the uniformity of the lubricant film thickness and planarity of the test pins with the strip. The reduction in coefficient of friction with increased contact pressures could arise from the formation of boundary film with the aluminium due to the generation of low shear strength interface. On the other hand, a partial breakdown

Table 1 Test parameters

Test parameter	Value
Nominal contact pressure	3, 10, 15 MPa
Contact force	210, 700, 1050 N
Sliding speed	0.25 m/s
Test temperatures	250, 350 and $450 \text{ }^\circ\text{C}$

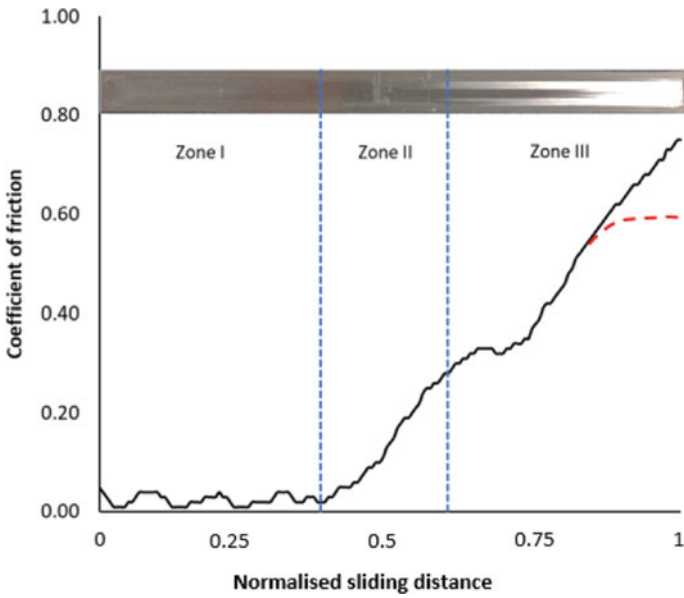


Fig. 3 A typical coefficient of friction plot against sliding distance also comparing frictional behaviour with corresponding surface change on the aluminium strip

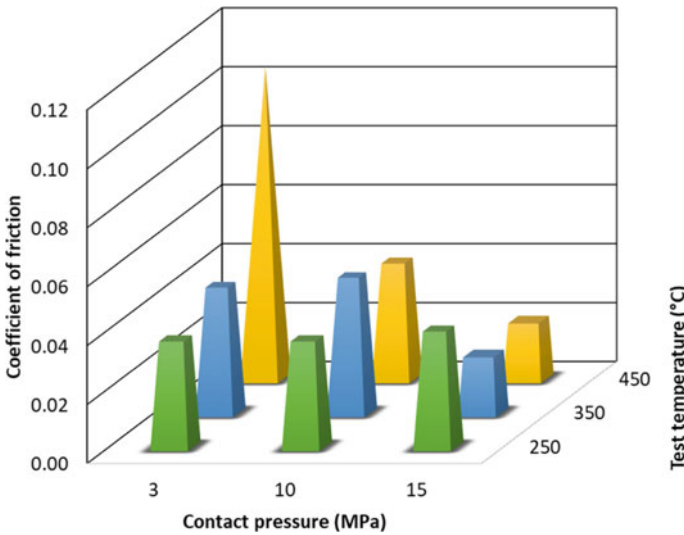


Fig. 4 Coefficient of friction at 50 mm sliding distance for the range of contact pressures and test temperatures

of lubricant can explain the relative increase in the coefficient of friction at higher test temperatures. Similar findings were also reported by [3] after conducting hot strip draw testing of boron steel.

Description of Sliding Velocity-Dependent Friction Model for HFQ[®] Process

The HFQ[®] Friction Model is used to predict the apparent coefficient of friction between the tool surface and the hot aluminium alloy blank. The model presented in this paper was established based on the work by Hu et al. [4]. The overall coefficient of friction, μ , stems from two mechanisms (Eq. (1)), namely, the coefficient of friction at the full film lubrication condition, μ_L , and the dry coefficient of friction, μ_d . The contribution of these two components is governed by a lubricated area ratio, β , which varies from 0 (the initial full lubricated state) to about 1 (dry sliding state).

$$\mu = (1 - \beta)\mu_L + \beta\mu_D \quad (1)$$

Hence, as shown in Fig. 4, the contact evolves from the initial full film lubrication to eventual dry sliding during the sliding process. Therefore, the initial full lubricated and final dry sliding coefficient of friction can be established from experimental testing for any given tribologic system for a sufficiently long sliding track. The transition from full lubricated to dry friction depends on the evolution of lubricant film thickness. According to Hu et al., the lubricated area ratio, β , depends exponentially on the film thickness, $h(t)$, as shown in Eq. (2), where $h(t)$ is the instantaneous film thickness of the lubricant and λ_1 and λ_2 are the breakdown distance parameters for the lubricant.

$$\beta = \exp[-(\lambda_1 h(t))^{\lambda_2}] \quad (2)$$

During HFQ[®] forming process, the thickness of the lubricant film, $h(t)$, is primarily influenced by the transportation of lubricant during sliding, entrapped lubricant quantity, lubricant squeeze out, sliding speed, lubricant properties, and contact geometry. For model purposes, $h(t)$ was assumed to be a function of contact pressure, velocity, and temperature; hence, $h(t) = f(P, v, T, t)$. In the formulae proposed by Hu et. al. for lubricant film, thickness is given by Eq. (3)

$$h(t) = h(0)\exp[-cP^{k_1}v^{k_2}t] \quad (3)$$

Authors propose a modification of the model outlined by Hu et al. to incorporate the dependence on temperature of the lubricant film thickness, $h(t)$, and the lubricated area ratio, β , by making the power law exponents $k_1 = f_1(T)$, $\lambda_1 = f_2(T)$ and $\lambda_2 = f_3(T)$ temperature-dependent using the form shown in Eq. (4),

where for $i = 1, 2, 3$ we have

$$f_i(T) = a_i + \frac{(b_i - a_i)}{1 + \left(\frac{T}{c_i}\right)^{d_i}} \tag{4}$$

Calibrated model performance as a function of normalised sliding distance for temperatures 250, 350, and 450 °C and contact pressures of 3, 10, and 15 MPa at a single sliding velocity of 250 mm/s is shown in Fig. 5.

The above equations of the sliding distance-dependent friction model were implemented into a subroutine for PAM-STAMP 2019. To integrate the model equations given above numerically, we proceed iteratively throughout time following the below steps.

For simulation time $t + \Delta t$, let: $P(t + \Delta t)$ be the contact pressure, $v(t + \Delta t)$ be the sliding velocity, $T(t + \Delta t)$ be the temperature, and Δt be the time step. Then we have the following algorithm:

Step 1 Computation of the lubricant film thickness:

$$h(t + \Delta t) = h(t)\exp[-cP^{k_1(T)}v^{k_2}\Delta t]$$

Step 2 Computation of the lubricated area ratio:

$$\beta(t + \Delta t) = \exp[-(\lambda_1(T)h(t + \Delta t))^{\lambda_2(T)}]$$

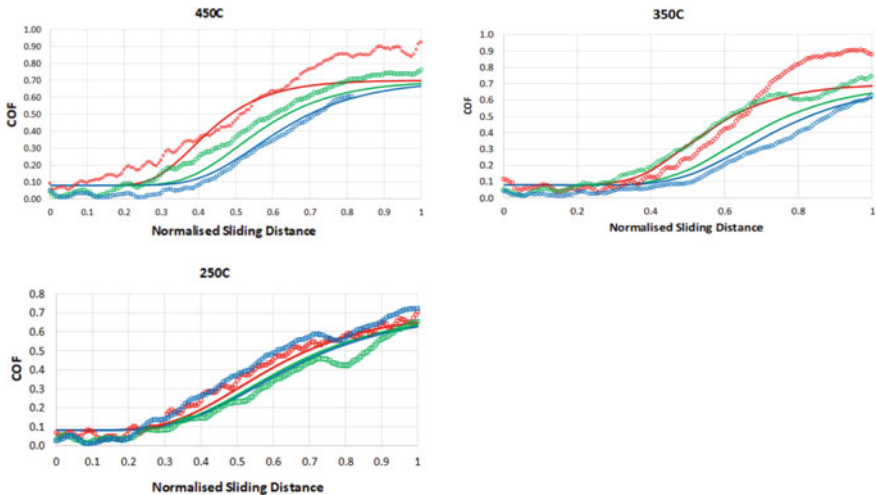


Fig. 5 Model predictions (solid) correlated against experimental tests data (dots) for apparent coefficient of friction at 450 °C, 350 °C, 250 °C and contact pressures of 3, 10, and 15 MPa depicted by blue, green and red curves, respectively

Step 3 Computation of the apparent coefficient of friction:

$$\mu(t + \Delta t) = (1 - \beta(t + \Delta t))\mu_L + \beta(t + \Delta t)\mu_D$$

Description of Material Mechanical Model for HFQ[®] Process

Description of Viscoplastic Damage Model

Over the last couple of years, the viscoplastic damage CDM model has been extended to account for the effect of stress state on damage accumulation and failure. Different shapes of forming limit diagrams (FLCs) under HFQ[®] hot stamping conditions could be predicted with different temperatures and strain rates. Integrating those viscoplastic damage constitutive equations into the FE code, such as PAM-STAMP, allows the formability for any process conditions, cold or hot and low or high forming speeds, to be predicted by the FE simulation. A viscoplastic damage constitutive model has been developed that takes the mechanisms of dislocation-driven evolution processes such as hardening, dynamic and static recovery, and damage into account [5, 7]. An example of such a model is presented below.

A stress–elastic strain relation is given by

$$\tilde{\sigma}_{ij} = \frac{\sigma_{ij}}{(1 - \omega)} = D_{ijkl} \varepsilon_{kl}^e \quad (5)$$

where ω is the damage variable, D is the elasticity tensor in which the Young modulus is assumed to depend on temperature.

The total strain can be written as a sum of elastic, viscoplastic, and thermal strains:

$$\varepsilon_{ij} = \varepsilon_{ij}^e + \varepsilon_{ij}^p + \varepsilon_{ij}^{th} \quad (6)$$

where the viscoplastic strain can be obtained from the integration of the viscoplastic strain rate given by the following:

$$\dot{\varepsilon}_{ij}^p = \dot{p} \frac{3}{2f} s_{ij} \quad (7)$$

$$\dot{p} = \left(\frac{2}{3} \dot{\varepsilon}_{ij}^p \dot{\varepsilon}_{ij}^p \right)^{1/2} \quad (8)$$

where p is the equivalent viscoplastic strain, which could be also written ε_{eq}^{vp} , f is the equivalent von Mises stress, (also written σ_e), s_{ij} is the deviatoric stress tensor.

Taken the isotropic hardening as a function of dislocation density ρ , we write:

$$R = B\rho^{n_1} \quad (9)$$

where dislocation density is integrated from:

$$\dot{\rho} = A(1 - \rho)\dot{p} - C\rho^{n_2} \quad (10)$$

Evolution of dislocation density ρ is related to the equivalent viscoplastic strain rate, it includes the dynamic recovery and the static recovery which appear at high temperatures. Parameters A , B , and C are the functions of temperature.

The viscous stress:

$$F = \tilde{f} - R - k \quad (11)$$

where $\tilde{f} = f(\tilde{\sigma})$, k is the initial yield stress which is a function of temperature in our case, if $F > 0$ irreversible viscoplastic strain occurs.

Assuming power law function for the equivalent viscoplastic strain rate, we write:

$$\dot{p} = \left(\frac{F}{K}\right)^n \quad (12)$$

or

$$F = k\dot{p}^{\frac{1}{n}} \quad (13)$$

where parameters K and n are functions of temperature.

The damage criterion is a combination of the three invariants of stress tensor $J_0(\sigma)$, $J_1(\sigma)$, $J_2(\sigma)$, which are, respectively, the maximum principle stress: $J_0(\sigma) = \sigma_1$, the first invariant: $J_1(\sigma) = tr(\sigma) = 3\sigma_H$, the second invariant: equivalent stress $J_2(\sigma) = f = \sigma_e$.

$$X(\sigma) = \frac{\alpha_1 J_0(\sigma) + \alpha_2 J_1(\sigma) + \alpha_3 J_2(\sigma)}{(\alpha_1 + \alpha_2 + \alpha_3) J_2(\sigma)} \quad (14)$$

or

$$X(\tilde{\sigma}) = \frac{\alpha_1 J_0(\tilde{\sigma}) + \alpha_2 J_1(\tilde{\sigma}) + \alpha_3 J_2(\tilde{\sigma})}{(\alpha_1 + \alpha_2 + \alpha_3) J_2(\tilde{\sigma})} \quad (15)$$

where the parameters α_1 , α_2 , and α_3 are temperature-independent [7].

The three invariants allow representing two different damage mechanisms, namely, the grain boundary damage and the ductile damage. Irreversible damage occurs if $X > 0$.

Finally, the rate of damage accumulation is given by

$$\dot{\omega} = \Delta X^\phi \eta_1 \dot{p}^{\eta_2} \frac{1}{(1 - \omega)^{\eta_3}} \tag{16}$$

where parameters η_1, η_2 are assumed to be functions of temperature and parameters η_3, ϕ, Δ are assumed to be temperature-independent.

In the scope of the explicit solver PAM-STAMP, the equilibrium equations are solved based on an explicit numerical integration scheme for which each cycle corresponds to a very small time step. However, at each cycle, the equations of the material model itself are solved based on an implicit scheme.

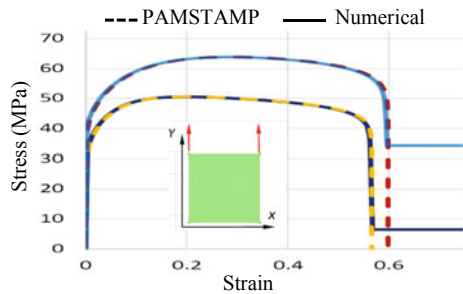
Numerical Stability and Initial Testing

In order to test the numerical stability and carry out verification of the integration of the viscoplastic damage model discussed above, fundamental test cases were set up. The model was tested in single- and multi-element uniaxial and biaxial simulations at various temperatures and rates of deformation. In this paper, only two simple different cases are presented. First is a single-element case under uniaxial tension at 500 °C and two different strain rates, 0.1 and 4 s⁻¹. The second test is a single-element uniaxial tension at 450 °C with a change in strain rate.

Figure 6 shows the one-element tensile model with a comparison between flow curves at 500 °C and strain rates of 0.1 and 4 s⁻¹ obtained from an external numerical integration in MATLAB and PAM-STAMP. A very good correlation was found between the two different algorithms.

The second simple case was performed to test the viscoplastic damage model implementation into PAM-STAMP via user-defined subroutine was a strain rate “transition” test where strain rate was accelerated from 0.1 to 10 s⁻¹ and from 0.3 to 0.4 strain, respectively, at 450 °C. The complete strain rate curve and the resultant

Fig. 6 One element tensile model result from the viscoplastic damage model integrated into PAM-STAMP at 500 °C and strain rate of 0.1 and 4 s⁻¹



material flow curve are shown in Fig. 7a, b. The corresponding damage accumulation together with damage curves for constant strain rate tests at 0.1 and 10 s⁻¹ are shown in Fig. 8.

The variable strain rate test is an example highlighting the capability of the viscoplastic damage model to capture the effect of the history of deformation on the material ductility. This is a major benefit of the material model to simulate HFQ[®] process over a look-up table-based material model. Another benefit is the ability to take into account material softening prior to failure. Moreover, the viscoplastic damage model can capture changes in mode, or path, of deformation and reflect those on material ductility and ultimately failure during stamping process [7].

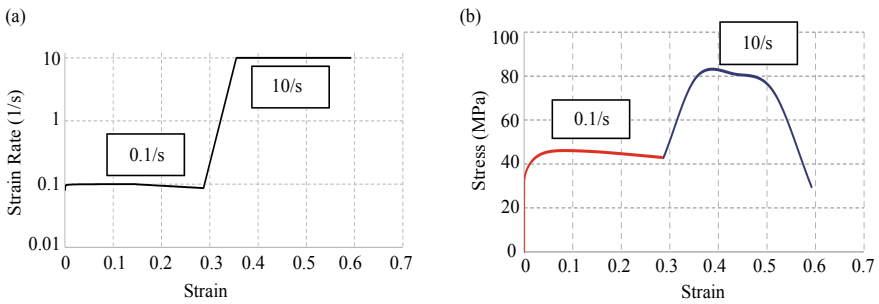


Fig. 7 Variable strain rate test case. Plot **a** shows the transition in strain rate from 0.1 to 10 s⁻¹ and plot, **b** the resultant stress–strain response at a temperature of 450 °C

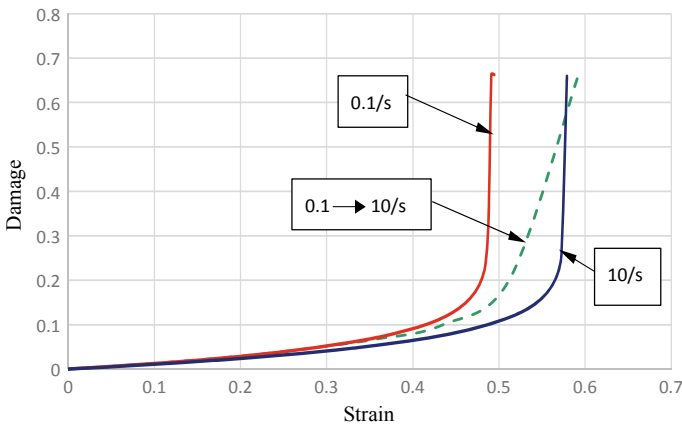


Fig. 8 Predicted damage curves showing the effect of variation of strain rate from 0.1 to 10/s at 450 °C

Industrial Application Based on Door Inner

HFQ[®] Forming Trials for Door Inner

Having verified the integration of the viscoplastic damage CDM model against simple test cases we can move on to validation against a large industrial case. A validation based on complex deep-drawn high-strength door inner was selected for this purpose. The HFQ[®] stamping trials started from an oversized blank shape which induced splits in the panel. Following the failures, a blank shape optimisation was carried out during the trials and a successful panel was produced by removing material in critical areas of the blank. The difference between initial and final blanks is shown in Fig. 9. In all the trial cases, lubrication was applied to the punch and the die. The hot aluminium blanks were dry, non-lubricated, on delivery to the tool.

A successful pressing of the door inner is shown in Fig. 10. The panels were cut into several sections and thickness was measured using Vernier callipers. Overall, approximately 40 measurements were taken in critical locations along selected cut planes. Similarly, the results of the simulation were sectioned along the corresponding planes. An example of cutup panel can be seen in Fig. 11.

HFQ[®] Forming Simulation of Door Inner

An HFQ[®] simulation was performed using ESI's PAM-STAMP. The finite element model set up in PAM-STAMP was composed of three stages: gravity, holding, and stamping. The gravity stage was simulated using the implicit solver in PAM-STAMP,

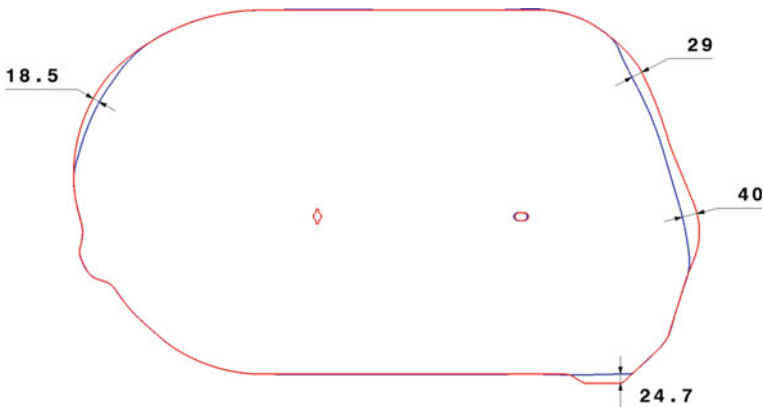


Fig. 9 Blank shape comparison. Red is the initial blank shape and blue is the final optimised blank which yielded successful panels



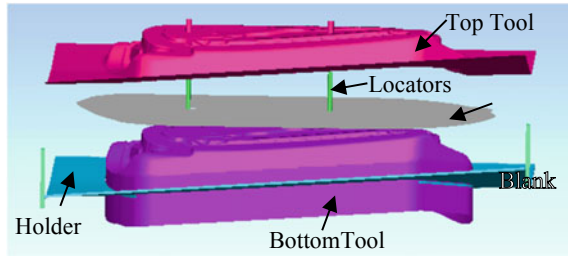
Fig. 10 A successful door inner pressing



Fig. 11 Door inner sections cut for thickness evaluation

while the explicit solver was used for both holding and stamping stages. First, simulations were run with the apparent friction coefficient between the blank and the tool assumed to be constant and independent of contact pressure, temperature, velocity, or sliding distance. Simulations were performed with the friction coefficients of 0.5 and 0.8 for both blank shapes. The die and blank holder velocity were set to 0.2 m/s with no velocity scaling. A ramp curve was used to accelerate the velocity to the set speed of over 1 ms. The tool setup for the door inner simulation can be seen in Fig. 12. Both blank shapes were used in simulation of this case—the first one was the initial blank shape designed prior to the stamping trials. As mentioned above, this blank shape was not successful, and the blank shape was optimised during the trials which yielded successful panels. Simulations with the use of subroutine were run with a fixed element size of 5.8 mm for the blank. This yielded a total of approximately 42 k elements for the blanks.

Fig. 12 Door inner simulation setup in PAM-STAMP



The correlation between the simulation and the actual measurements for the failed panel run with friction coefficient of 0.5 and 0.8 is shown in Fig. 13a, b, respectively. The boxes marked with red outline on the figures highlight areas where the deviation between the model prediction and the actual measurement was greater than the acceptance target of 5%. As can be expected friction plays a significant role in the accuracy of model predictions. Simulations run with the lower friction coefficient of 0.5 with a minor exception failed to predict splits in the panel, see Fig. 13a. Increasing friction coefficient to 0.8 allowed prediction of all the splits but at the same time highlighted areas where splits did not occur, as is shown in Fig. 13b. Looking at thickness prediction for the simulation run with friction coefficient of 0.5, we can notice that the deep-drawn side wall was predicted to be thicker as shown in Fig. 14a.

(a) Fixed COF of 0.5

(b) Fixed COF of 0.8

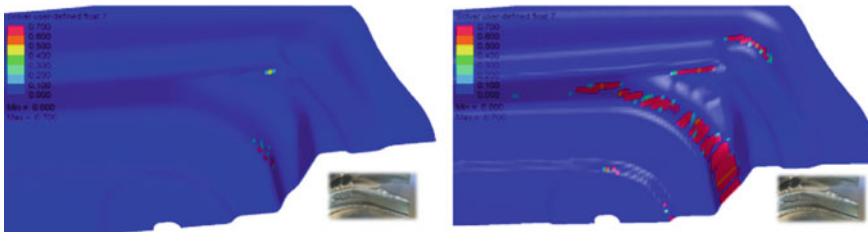


Fig. 13 Predicted values of damage for different values of COF

(a) Fixed COF of 0.5

(b) Fixed COF of 0.8

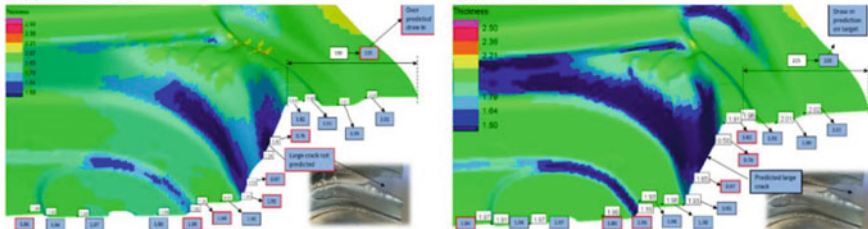


Fig. 14 Predicted versus measured thickness comparison for failed panel. Deviations higher than 5% difference highlighted by red outline

A better result in that area was achieved for simulation with a higher friction coefficient of 0.8 which is shown in Fig. 14b. On the other hand, on the shallow bottom features of the panel, the side walls tended to be thinner in both simulation cases. This suggests that friction coefficient assumed in simulation for those areas was too high. This confirms that the apparent coefficient of friction for the HFQ[®] process depends, amongst others, on the draw distance. That is thought to be due to lubricant removal from the draw fillets as the dry blank is drawn against the lubricated tools as was observed in the strip draw friction tests.

Taken the findings from simulation of the failed panels simulations for the successful panel were set up sliding distance-dependent friction model. The resultant distribution of thickness and its correlation to measurements is shown in Fig. 15. Although there is still room for improvement, as can be seen, a much closer correlation was found. On average, the model met the target of less than 5% deviation at over 90% of the measurement points.

Conclusion

The work summarised in this paper shows that simulation of HFQ[®] process is very sensitive to the apparent coefficient of friction which proves to be more complex than a single value Columbian assumption. Simulative studies based on the door inner indicated a strong dependence of the friction value on the depth of draw and using a sliding distance-dependent friction model produced significant improvement in correlation to experimental measurements. We have shown the combined predictive capability of simulations run with advanced friction model and viscoplastic damage CDM material model in application to the HFQ[®] process. The viscoplastic damage

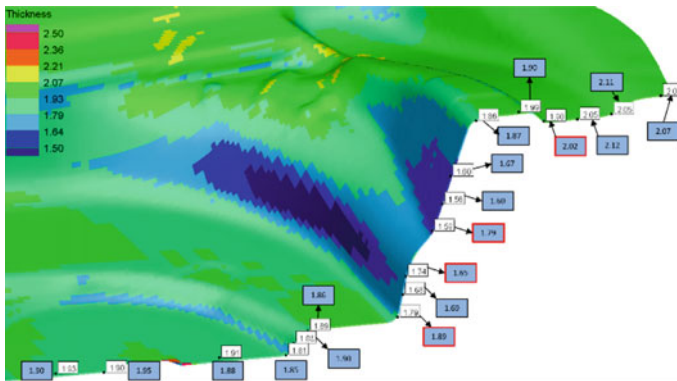


Fig. 15 Predicted versus measured thickness comparison for successful panels. Deviations higher than 5% difference highlighted by red outline

model allows to capture the effects of path and history of deformation on flow curves and ductility. This should be particularly useful for complex applications like the presented deep-drawn door inner. Integration of both models into PAM-STAMP was also discussed.

Further work is being carried out on sensitivity studies of the advanced friction model which will be published in the future.

Acknowledgements The work described in this article is supported by the European Commission (Grant no: 604240 under FP7) for the LoCoLite project (Low-Cost forming of Lightweight structures for transportation industries). <http://www.locolite.net/>. The authors would like to thank all LoCoLite Partners for their support during the project and in particular the team of researchers and engineers at ESI (Jean-Luc Babeau, Daniel Vieilledent, Patrick Saillard, and Vladimir Cerny), ICL (Liliang Wang and Nan Li), and ITL (Alistair Foster) for their contribution to this article.

References

1. Lin J, Dean T, Foster A, A method of forming a component of complex shape from aluminium alloy sheet, UK Patent (GB2473298), European (09785115.8) and International (WO2010/032002)
2. <http://www.impression-technologies.com/>
3. Ghiotti A, Sgarabotto F, Bruschi S (2013) A novel approach to wear testing in hot stamping of high strength boron steel sheets. *Wear Wear Mater* 302(1–2):1319–1326. <https://doi.org/10.1016/j.wear.2012.12.051>
4. Hu Y, Wang L, Politis DJ, Masen MA (2017) Development of an interactive friction model for the prediction of lubricant breakdown behaviour during sliding wear. *Tribol Int* 110:370–377
5. Mohamed M, Foster A, Lin J, Balint D, Dean T (2012) Investigation of deformation and failure features in hot stamping of AA6082: experimentation and modelling. *Int J Mach Tools Manuf* 53(1):27–38
6. Foster A, Mohamed M, Lin J, Dean T (2008) An investigation of lubrication and heat transfer for a sheet aluminium heat, form-quench (HFQ) process. *Steel Res Int* 79-11-VII(2):133–140
7. Lin J, Mohamed M, Balint D, Dean TA (2014) The development of CDM-based theories for predicting FLD for hot stamping applications. *Int J Damage Mech* 23(5):684–701

Part VII
Modelling of Failure

Development of a Modified Punch Test for Investigating the Failure Behavior in Sheet Metal Materials



M. Böhnke, Ch.R. Bielak, M. Bobbert, and G. Meschut

Abstract In the numerical simulation of mechanical joining technologies, the material modeling of the joining parts is of major importance. This includes modelling the damage and failure behavior of the materials in accordance with varying occurring stress states. For the experimental determination of the material-related damage parameters the punch test has proven to be suitable, as it enables to generate different stress states. However, the exact determination of the failure time or location has been problematic due to the lack of optical accessibility. Therefore, a modified, half-sectioned test rig for a punch test was developed, which enables a precise detection of failure initiation time, location, and failure evolution under defined stress states in sheet metal by means of local optical measurements of the specimen. This study presents the proof of functionality of the testing method by experiments in automotive relevant sheet metal material and the verification of related simulations.

Keywords Mechanical joining · Numerical simulation · Damage · Punch test

Introduction

Driven by legal regulations and growing customer requirements, the automotive industry is forced to reduce the greenhouse emissions of new vehicle concepts. One of the most suitable approaches, in order to fulfil these emission-oriented goals, is the application of various multi-material designs, which enable optimal material

M. Böhnke (✉) · Ch.R. Bielak · M. Bobbert · G. Meschut
Laboratory for Material and Joining Technology (LWF), Paderborn University, Pohlweg 47-49,
33098 Paderborn, Germany
e-mail: max.boehnke@lwf.upb.de

Ch.R. Bielak
e-mail: christian.bielak@lwf.upb.de

M. Bobbert
e-mail: mathias.bobbert@lwf.upb.de

G. Meschut
e-mail: meschut@lwf.upb.de

utilization and thus the highest possible weight reduction [1]. Based on this, the ongoing search for lightweight materials and innovative construction methods puts high demands on joining technology. An efficient joining process for assembling different sheet metal materials is clinching. Unlike traditional riveting techniques, clinching does not use any auxiliary elements and the joint is created by solely cold forming the material [2].

In modern product development processes, numerical simulations can be used to reduce experimental effort and thus the product development cycles. In this context, accurate material modeling is of decisive importance. In addition to the plasticity and frictional behavior, the description of the damage and the failure behavior of material must also be taken into account. During the clinching process, the punch partially penetrates the sheet metal and causes a local metal flow of the material into the die. This generates a three-dimensional stress state in the parts to be joined [3].

In forming technology, the limits of formability are often described by means of a forming limit curve. In this case, the principal strains are defined as a limit value curve and a plane stress condition is taken as a basis. However, this is not sufficient for an explicit description of the three-dimensional stress conditions that occur in clinching processes. The damage is accumulated in the process chain of part production, joining process, and operation under different stress conditions so that this effect can become relevant. The three-dimensional stress condition is unambiguously described by the stress triaxiality η and the Lode angle parameter ξ .

Stress triaxiality is a dimensionless ratio expressed by the following equation:

$$\eta = \frac{\sigma_m}{\sigma_{vM}} \quad (1)$$

Therein, σ_m is the hydrostatic stress:

$$\sigma_m = \frac{I_1}{3} = \frac{\sigma_1 + \sigma_2 + \sigma_3}{3} \quad (2)$$

In addition, σ_{vM} is the von Mises equivalent stress:

$$\sigma_{vM} = \sqrt{\frac{1}{2}[(\sigma_1 - \sigma_2)^2 + (\sigma_2 - \sigma_3)^2 + (\sigma_3 - \sigma_1)^2]} = \sqrt{3J_2} \quad (3)$$

With σ_1 , σ_2 , and σ_3 are the principal stresses with the assumption: $\sigma_1 \geq \sigma_2 \geq \sigma_3$.

Derived from Eqs. (1)–(3), stress triaxiality can be expressed as a function of the first and second stress invariants I_1 and J_2 , as follows:

$$\eta = \frac{I_1}{3\sqrt{3}J_2} = \frac{\sigma_1 + \sigma_2 + \sigma_3}{3\sqrt{\frac{1}{2}[(\sigma_1 - \sigma_2)^2 + (\sigma_2 - \sigma_3)^2 + (\sigma_3 - \sigma_1)^2]}} \quad (4)$$

Developments and experimental observations in damage plasticity theory showed that the effect of stress state on fracture behaviour could not be fully reflected by

stress triaxiality alone [4]. Therefore, in addition to stress triaxiality η , the Lode angle parameter ξ must also be considered, which can be related to the third deviatoric stress invariant J_3 in following equation [5]:

$$\xi = \frac{27}{2} \frac{J_3}{\sigma_{vM}^3} = \frac{3\sqrt{3}}{2} \frac{J_3}{J_2^{3/2}} \quad (5)$$

In [3], the stress states occurring during the clinching process of DC04 sheet materials were investigated numerically. It was shown that in the bottom area of the clinched joint, pressure superimposed stress states occur according to the process kinematics with values for stress triaxiality of $\eta < 0$ and Lode angle parameter around $\xi = -1$. However, this is not the critical area with regard to material failure during the joining process, but the necking area. At this point, stress triaxiality of $\eta = 0.3-0.7$ can occur and Lode angle parameter $\xi = 0-1$.

In order to numerically represent the failure behavior of sheet metal materials under different stress conditions, these have to be generated experimentally. Therefore, a wide range of tests (e.g. shear tests, various shear tensile tests as well as tensile tests with notched and un-notched specimens) is proposed [6]. These specimen geometries are well suited to cover and experimentally investigate a wide range of stress states and are considered in stress state-dependent damage models for mechanical joining technologies [7]. However, tests with notched tensile specimens are associated with increased effort, since the fabrication of the notches must be carried out very precisely in order to achieve the required stress state during the test. A series of tests with several specimens and different notch geometries are associated with high preparation efforts. In addition, the stress state may change during the test due to the necking of the specimen in the failure area.

For the experimental investigation of different stress states with respect to the specific adjustment of stress triaxiality and lode angle parameter, [8] proposes various punch tests. Thus, equibiaxial as well as pure shear stress states were investigated. The experimental setup shows similarities to the clinching process, as it also consists of punch and die acting orthogonally to the sheet plane. Different alternative punch test methodologies exist depending on the shape of the punch and specimen geometry such as Marciniak [9], Nakazima [10], and Keeler [11]. Nakazima tests require variable specimen geometries, whilst in the Keeler test the sheet metal specimen geometry is kept the same and the geometry of the punch is varying. Punch tests can be used for failure prediction studies in metallic materials for quasi-static [12] as well as for impact loads [13].

In order to record the deformation behavior of the specimen surface during the tests, optical measurement methods can be used. For this purpose, the samples can be provided with paint patterns and captured images can be evaluated by means of DIC [14] or systems are used, that work with structured light [15]. This works well for biaxial stress conditions such as in Nakazima tests, where the crack also develops on the outside and the failure time and location can be accurately determined. However, when it comes to shear stress states like in [8], crack initiation can occur on the inner

side of the punch. As a result, an exact determination of the crack initiation time and location is not possible and damage parameters have to be determined inversely on the basis of the force–displacement curve.

For this reason, this paper presents a test that essentially consists of a half-sectioned punch test and enables the punch to penetrate the sheet material directly on the edge. With the help of DIC, the deformation behavior of the sheet plane as well as the exact crack initiation time and location should be determined. The design requirements and their implementation are explained. Furthermore, a corresponding simulation model is presented. Finally, a proof of functionality will be provided by comparing experimental results with simulated data.

Constructive Design

First, specific requirements that arise for the test setup will be explained. A sectioned punch test is to be constructed to allow optical accessibility to the sheet plane. Since the punch is pressing directly on the sheet edge with its tip, increased transverse forces can arise during the test, which must be absorbed by a punch bearing that is as stiff as possible. However, a type of bearing with as little friction as possible must be used, in order not to influence the force measurement in the axial direction. Furthermore, it should be possible to use different punch geometries as well as a concept for simple exchange of the dies. This enables further adjustment possibilities to influence the stress state, in particular through the variation of the die diameter as well as the edge radius of the die. In addition, variable positioning of the punch to the die should be possible in order to be able to carry out the exact alignment of the two components in the tests. For not affecting the stress state during the test, it is necessary to prevent the specimens from slipping.

Figure 1 shows the constructive implementation of the explained requirements. The assembly of the modified punch test can be seen in the center of the illustration (Fig. 1c). It consists of a base plate that can be flanged to any universal testing machine. A solid support plate is mounted vertically on it, to which a U-bracket is screwed. This bracket serves as a mounting for the linear ball bearing system, which is capable of absorbing large lateral forces with low friction at the same time. The pick-up shaft for the punches is guided in it. A sectional view is shown in Fig. 1a. Figure 1b shows the inserter for holding the die and fixing the sheet specimens. It is manufactured in such a way that the dies can simply be clamped in. The specimens are inserted into a milled pocket. The blank holder is screwed to the insert and thus clamps the sheet specimens in a non-slip manner. The surface of the blank holder, made of 42CrMo4 steel, is also knurled and subsequently hardened. The inserter, including the clamped specimen, can be easily removed from the set-up and inserted. It is guided by a precisely fitting groove in the base of the base plate. Distance screws are provided in the support plate for exact alignment. Once the punch is aligned with the specimen, the insert is fixed to the support plate via two screws.

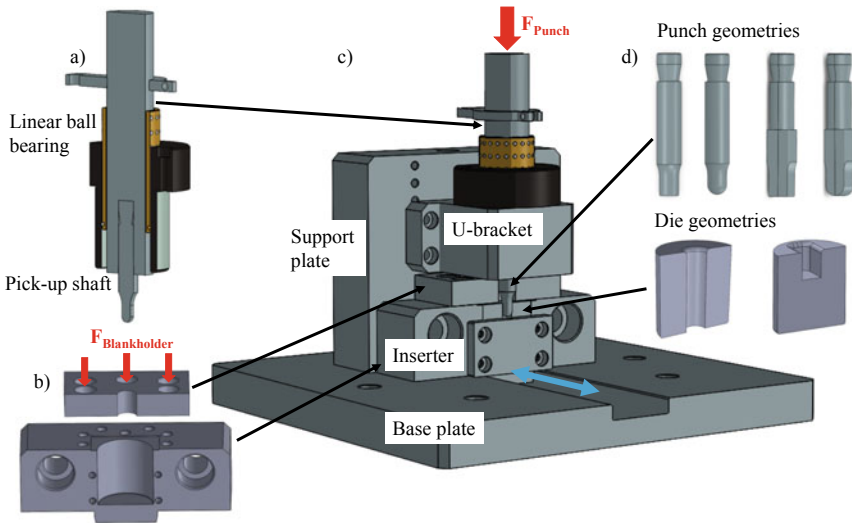


Fig. 1 Constructive design implementation of the modified punch test

The modified punch test can be used to examine different types of punches, see Fig. 1d. On the one hand, conventional cylindrical punches can be used, which are either blunt nose or hemispherical. For this purpose, a conventional die is used half-sectioned. Furthermore, bar-shaped punches can also be used, which do not induce any stress in the sheet in the spatial direction and produce shear-cutting-like deformation conditions. For this purpose, a long pocket is made in the die, over which a strip of sheet metal is clamped that corresponds to the width of the punches.

Numerical Modeling

For the numerical investigation of the sheet deformation and, finally, for the evaluation of the stress states at the time of failure, a 3D model has been created and analyzed using the FEM software LS-DYNA. Due to the symmetrical test setup, the geometry of the model is simulated half-sectioned in order to reduce calculation time. According to the half-sectioned punch test, a quarter die is shown in Fig. 2, as well as a half punch, blank holder, and sheet specimen. The punch, blank holder, and die are modeled elastic, which allows the force to be evaluated by cross sections. The sheet specimen is modeled using the MAT_224 tabulated Johnson–Cook material model. The aluminum alloy EN AW-6014 in condition T4 was selected for the tests. The characterization of the material properties and extrapolation of the yield curve with the Hockett–Sherby hardening law can be taken from [16]. The sheet sample was meshed with tetrahedral elements ELFORM 13. For this purpose, an element edge length of 0.05 mm is used in the area of influence of the punch. The punch

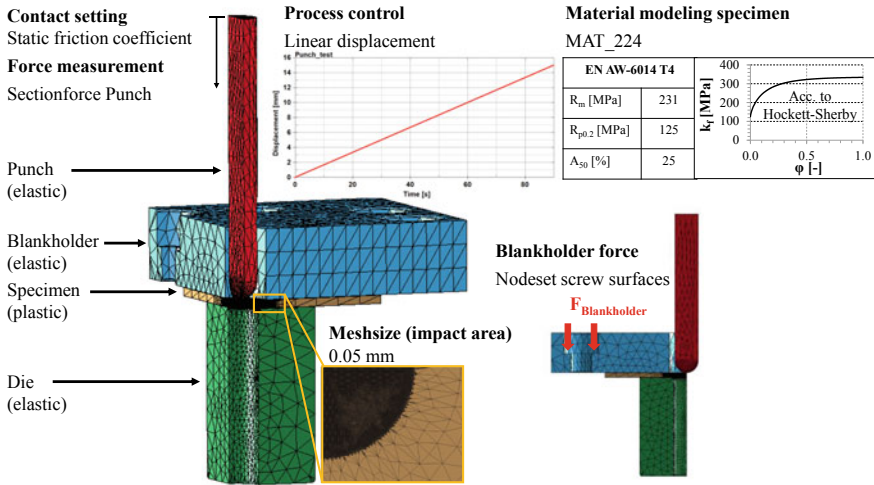


Fig. 2 Numerical model of the modified punch test

tip and die edges are also finely meshed with a maximum edge length of 0.5 mm. All remaining areas are coarsely meshed to save computing time. A defined force is applied to the blank holder via a node set on the surfaces for the screw heads in order to clamp the sheet. In this way, any slippage can be modelled realistically. For contact settings, static friction coefficients at the various contacts were defined. The process is controlled by displacement of the punch at a defined speed of 10 mm/min. The numerical model is calculated implicitly. The occurring punch force is measured via section force (punch).

Experimental

The fabricated modified punch test as well as the test setup with DIC can be seen in Fig. 3a. For proof of functionality, the test rig was implemented in a Zwick Z1484 universal testing machine with a maximum test load of 200 kN. The axial force is applied by moving the system traverse. The pick-up shaft of the punch test is pressed against an adapter of the test machine on which the load cell is located. According to the simulation, a testing speed of 10 mm/min is chosen. A GOM ARAMIS system was used to optically capture the deformation of the sheet edge and the crack initiation. In addition, the calibrated 3D DIC system is used to position the inserter in spatial direction so that the punch tip is aligned exactly above the sheet edge. In doing so, the distance between the front of the punch and the sprayed sheet is measured in a captured DIC photo and the distance is adjusted accordingly using the distance screws. The sheet edge was provided with a fine stochastic pattern. As

already described, the aluminum alloy EN AW-6014 was investigated in condition T4. The sheet thickness was 2.0 mm. Figure 3b shows the setup with cylindrical punch, which can be hemispherical or blunt nose as well as the associated die and blank holder. Figure 3c shows a bar-shaped punch with corresponding die and two-part blank holder. In this setup, there is an increased risk of specimen slippage. The screws of the blank holder have therefore all been tightened to a defined 15 Nm.

Results and Discussion

In all experimental investigations, it has been shown that the location of crack initiation is in the optical pickup area and not on the underside of the sheet or behind the punch. This makes the test suitable for determining damage parameters experimentally. For the cylindrical punches, it was observed that the sheet specimen bends backwards during the test due to circumferential clamping. However, this deformation behavior is numerically simulated in the same way. No slippage of the specimens was observed.

Figure 4a shows a DIC image with cylindrical hemispherical punch and speckled sheet edge shortly before the time of crack initiation. Using the DIC software, the degree of deformation on the sheet edge was evaluated. The experimental deformation behavior of the specimen is compared with the numerical simulation in Fig. 4c

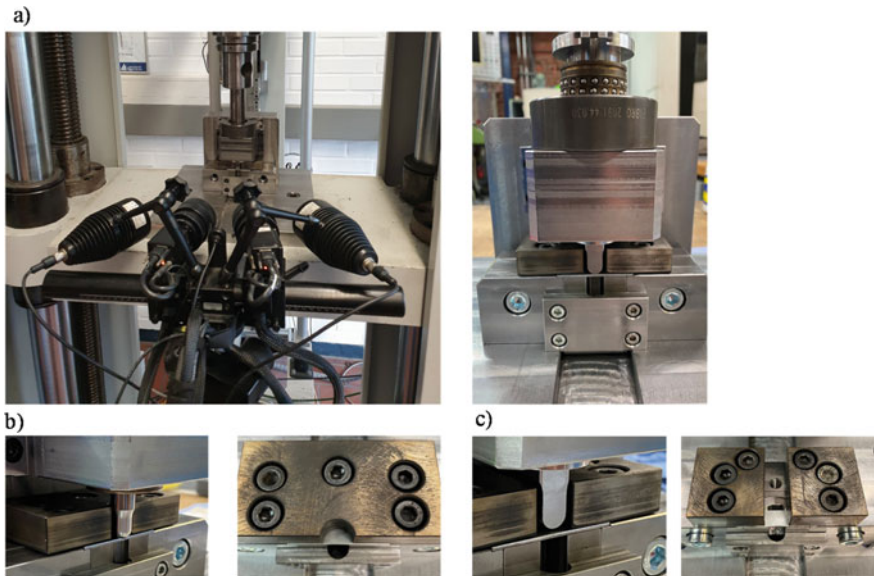


Fig. 3 Experimental test setup of the modified punch test (a) with varying punch and die geometries (b, c)

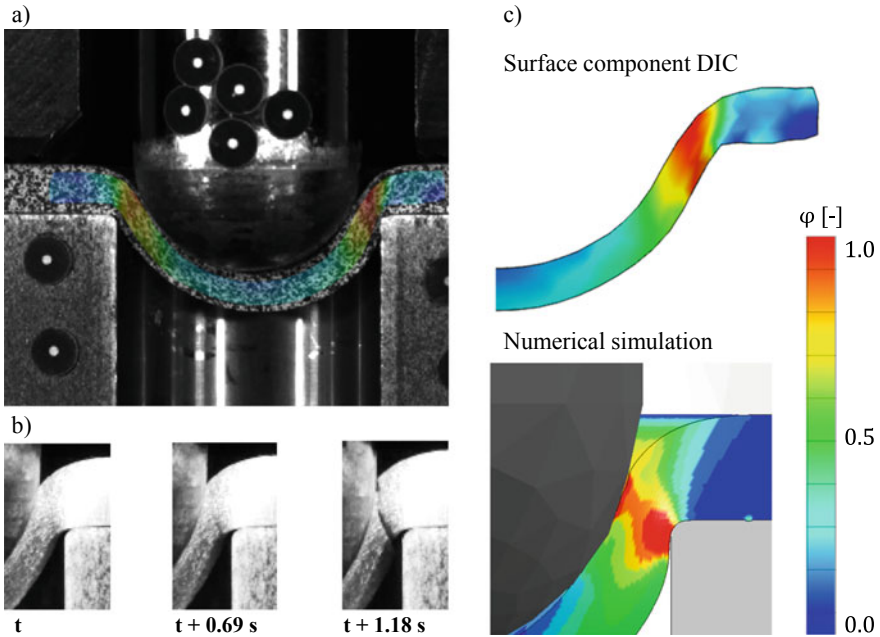


Fig. 4 Comparison of plastic deformation in captured DIC images and numerical simulation

at the same time and displacement of the punch. The deformation states show good agreement in the magnitude and location of the maximum strain. Another specimen was tested without a spray pattern to better detect the location of crack initiation. Figure 4b shows three deformation stages at the location of crack initiation. It is clear to observe where the crack initiates and how it develops.

Figure 5a shows force–time curves from the experiments as well as from the numerical simulation. The experimental curves show good reproducibility. In

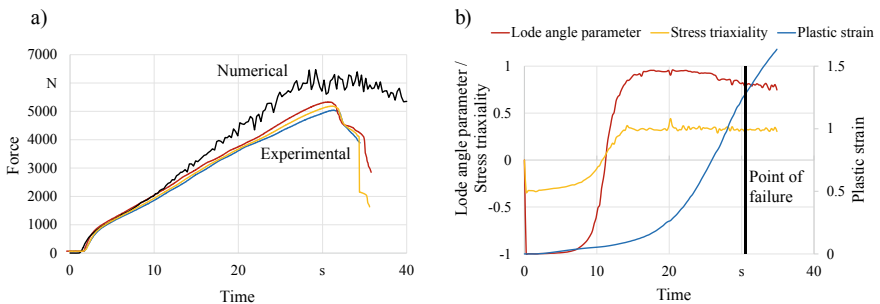


Fig. 5 Force–time diagram of numerical and experimental data (a) and evaluated parameters at the point of failure (b)

comparison with the simulative results, the curves agree well in the specimen stiffness and in the first part of the progression. In the further course, the simulative curve overestimates the experimental results. This is due to the fact that no damage criterion is implemented in the simulation. However, the force level of the simulation is stagnating from the time when the experiment fails.

From the agreements of the deformation states as well as the force–time curves compared to the experimental results, the validation of the numerical model can be confirmed.

The model can be used to evaluate the stress states present at the experimentally determined location of crack initiation. This has been done exemplarily for the cylindrical hemispherical punch on the aluminum sheet material EN AW-6014 T4 in sheet thickness 2.0 mm. Figure 5b shows the course of the stress triaxiality η and the load angle parameter ξ , they refer to the left ordinate. The plastic strain at the same location is also shown and referred to as the right ordinate. Corresponding to the tensile superimposed stress state on the sheet edge, the Lode angle parameter is $\xi = 1$, but decreases slightly during the test and is 0.8 at the point of failure. The stress triaxiality is $\eta = 1/3$ at the time of failure. The plastic failure strain is evaluated at $\varphi_f = 1.35$.

Summary and Outlook

In this paper, the development and functional proof of a modified punching test has been presented. Design requirements have been outlined and implemented with appropriate concepts. A corresponding numerical model has been explained and validated by comparison with experimental data. The test rig allows the application of defined stress conditions in different sheet materials using varying punch and die geometries. Due to the sectioned design, the crack initiation location and timing can be precisely determined. An exemplary evaluation was carried out for the sheet material EN AW-6014 in state T4 using a cylindrical hemispherical punch.

In future investigations, different punch and die geometries will be implemented to represent a wide range of stress states and derive a damage model. With the implemented damage model, the simulation will be recalculated and a comparison of the failure time and location with experimental data will be performed. The technical setup of the test rig can be optimized by using cameras with a higher recording frequency and a higher resolution in order to be able to track the crack development even more precisely.

Acknowledgements Funded by the Deutsche Forschungsgemeinschaft (DFG, German Research Foundation)—TRR 285—Project-ID 418701707.

References

1. Ostermann F (2014) Anwendungstechnologie Aluminium, 3., neu bearb. Aufl. VDI-Buch. Springer, Berlin, Heidelberg
2. DVS - Deutscher Verband für Schweißen und verwandte Verfahren e.V. (2018) Merkblatt DVS/EFB 3420: Clinching - basics
3. Jäckel M, Coppieters S, Vandermeiren N et al (2020) Process-oriented flow curve determination at mechanical joining. *Procedia Manuf* 47:368–374. <https://doi.org/10.1016/j.promfg.2020.04.289>
4. Wierzbicki T, Bao Y, Lee Y-W et al (2005) Calibration and evaluation of seven fracture models. *Int J Mech Sci* 47:719–743. <https://doi.org/10.1016/j.ijmecsci.2005.03.003>
5. Carlos Felipe Guzmán (2014) About the Lode angle influence in ductile fracture. University of Liège
6. Basaran M (2011) Stress state dependent damage modeling with a focus on the lode angle influence. Zugl.: Aachen, Techn. Hochsch., Diss., Berichte aus dem Maschinenbau. Shaker, Aachen
7. Otroshi M, Rossel M, Meschut G (2020) Stress state dependent damage modeling of self-pierce riveting process simulation using GISSMO damage model. *J Adv Join Process* 1:100015. <https://doi.org/10.1016/j.jajp.2020.100015>
8. Buyuk M (2013) Development of a tabulated thermo-viscoplastic material model with regularized failure for dynamic ductile failure prediction of structures under impact loading: thesis
9. Marciniak Z, Kuczyński K (1967) Limit strains in the processes of stretch-forming sheet metal. *Int J Mech Sci* 9:609–620. [https://doi.org/10.1016/0020-7403\(67\)90066-5](https://doi.org/10.1016/0020-7403(67)90066-5)
10. Nakazima K, Kikuma T, Hasuka K (1968) Study on the formability of steel sheets. Yamata Tech Rep 264:8517–8530
11. Keeler SP (1961) Plastic instability and fracture in sheets stretched over rigid punches. Massachusetts Institute of Technology
12. Lee Y-W (2005) Fracture prediction in metal sheets: thesis
13. Seidt JD (2010) Plastic deformation and ductile fracture of 2024-T351 aluminum under various loading conditions. Ph.D. thesis
14. Gruben G, Morin D, Langseth M et al (2017) Strain localization and ductile fracture in advanced high-strength steel sheets. *Eur J Mech A Solids* 61:315–329. <https://doi.org/10.1016/j.euromechsol.2016.09.014>
15. Grytten F, Fagerholt E, Auestad T et al (2007) Out-of-plane deformation measurements of an aluminium plate during quasi-static perforation using structured light and close-range photogrammetry. *Int J Solids Struct* 44:5752–5773. <https://doi.org/10.1016/j.ijsolstr.2007.01.026>
16. Böhnke M, Kappe F, Bobbert M et al (2021) Influence of various procedures for the determination of flow curves on the predictive accuracy of numerical simulations for mechanical joining processes. *Mater Test* 63:493–500. <https://doi.org/10.1515/mt-2020-0082>

Effect of Width/Thickness Effect of Sheet Metals on Bendability



M. M. Shahzamanian, D. J. Lloyd, and P. D. Wu

Abstract The effect of width/thickness ratio on the bendability of sheet metal is investigated using the finite element method (FEM) employing the Gurson–Tvergaard–Needleman (GTN) model. Strain path changes in the sheet with a change in width/thickness ratio. It is shown that bendability and fracture strain increase significantly by a decrease in width/thickness ratio. The stress state is almost uniaxial when the stress ratio (α) is close to zero for narrow sheets. This delays the growth and coalescence of microvoids as the volumetric strain and stress triaxiality decrease. On the other hand, ductility decreases with an increase in α for wider sheets. Fracture bending strain is calculated and, as expected, it increases with the decrease in width/thickness ratio. Numerical results are found to be in good agreement with experimental observations.

Keywords Bendability · Fracture · Width to thickness ratio · Finite element method (FEM)

Introduction

Bending is an important property in sheet metal as bending occurs as a part of several forming operations such as in deep drawing and auto industry [1–3]. In [4–6], the bending properties of various materials have been studied, and in [7, 8], the mechanical performance of materials is studied using the three-point bend test.

It is explained in [1] that bendability of sheet metals is dependent on the width to thickness ratio of sheet metals. For narrow sheets, the stress state is almost uniaxial when stress ratio (α) is close to zero and the ductility decreases with an increase in α for wider sheets. The maximum achievable α is 0.5 for the plane strain state where the ductility is a minimum. Kao et al. in [9] investigated the effect of superimposed

M. M. Shahzamanian (✉) · P. D. Wu

Department of Mechanical Engineering, McMaster University, Hamilton, ON L8S 4L7, Canada
e-mail: shahzamm@mcmaster.ca

D. J. Lloyd

Aluminum Materials Consultants, 106 Nicholsons Road, Bath, ON, Canada

© The Minerals, Metals & Materials Society 2022

K. Inal et al. (eds.), *NUMISHEET 2022*, The Minerals, Metals & Materials Series,
https://doi.org/10.1007/978-3-031-06212-4_53

585

hydrostatic pressure on workability and ductility of 1045 spheroidized steel in three-point bending with various width/thickness ratios. They presented the forming limit diagrams for sheets under various hydrostatic pressures and it was found that fracture under bending increased with an increase in hydrostatic pressure and caused the forming limit diagram to increase, which was attributed to the suppression of void growth.

The aim of this study is to perform a numerical study of the effect of the width/thickness ratio on fracture in sheet metal under three-point bending. All the simulations presented in this study are performed using ABAQUS/Explicit [10] based on the GTN model. The effect of the width/thickness on three-point bending is explained in detail. To the best of our knowledge, the effect of width/thickness ratio of sheet metals on bendability has not been considered numerically in detail elsewhere.

Constitutive Model

The Gurson–Tvergaard–Needleman (GTN) model [11–13] is used in this study which is on the basis of damage growth in metals due to nucleation, void growth, and coalescence, and this model was originally developed by Gurson [14]. The void growth is a function of the plastic strain rate \mathbf{D}^P :

$$(\dot{f})_{\text{growth}} = (1 - f)\mathbf{I} : \mathbf{D}^P \quad (1)$$

and the void nucleation in ABAQUS is assumed to be strain-controlled as follows:

$$\dot{f} = \bar{A} \bar{\varepsilon}^P \quad (2)$$

where $\bar{\varepsilon}^P$ is the effective plastic strain rate and the parameter \bar{A} is chosen so that nucleation follows a normal distribution as suggested by Chu and Needleman [15]:

$$\bar{A} = \frac{f_N}{S_N \sqrt{2\pi}} \exp \left[-\frac{1}{2} \left(\frac{\bar{\varepsilon}^P - \varepsilon_N}{S_N} \right)^2 \right] \quad (3)$$

where ε_N is the average void nucleating strain, f_N is the volume fraction of void nucleating particles, and S_N is the standard deviation of void nucleating strain.

The growth of existing voids and the nucleation of new voids are considered in the evolution of void volume fraction as follows:

$$\dot{f} = (\dot{f})_{\text{growth}} + (\dot{f})_{\text{nucleation}} \quad (4)$$

and the function of void volume fraction ($f^*(f)$) is defined to consider coalescence as follows:

$$f^* = \begin{cases} f & \text{for } f \leq f_c \\ f_c + \frac{f_u^* - f_c}{f_f - f_c} (f - f_c) & \text{for } f > f_c \end{cases} \quad (5)$$

where f_c is the critical void volume fraction when coalescence happens and f_f is the void volume fraction at failure. Lastly, the parameter $f_u^* = \frac{1}{q_1}$ is defined. It should be mentioned that void growth and nucleation do not happen when the stress state of an element is compressive in ABAQUS and void growth and nucleation only happen in tension.

Finally, the approximate yield function to be used in which f^* is distributed randomly is as follows:

$$\Phi(\sigma, \tilde{\sigma}, f) = \frac{\sigma_e^2}{\tilde{\sigma}^2} + 2f^*q_1 \cosh\left(\frac{3q_2\sigma_H}{2\tilde{\sigma}}\right) - \left[1.0 + (q_2f^*)^2\right] = 0 \quad (6)$$

where σ is the macroscopic Cauchy stress tensor, and σ_e , σ_H , and $\tilde{\sigma}$ are equivalent stress, hydrostatic stress, and matrix stress, respectively. Also, q_1 and q_2 are the calibrated parameters.

The uniaxial elastic–plastic undamaged stress–strain curve for the matrix material is provided by the following power-law form:

$$\bar{\epsilon} = \begin{cases} \frac{\tilde{\sigma}}{E}, & \text{for } \tilde{\sigma} \leq \sigma_y \\ \frac{\sigma_y}{E} \left(\frac{\tilde{\sigma}}{\sigma_y}\right)^n, & \text{for } \tilde{\sigma} > \sigma_y \end{cases} \quad (7)$$

Problem Formulation and Method of Solution

A three-dimensional (3D) bending test simulation using ABAQUS software is performed in this study. However, the two-dimensional (2D) schematic presentation of a metal sheet with length “2L” and thickness “t” is shown in Fig. 1. Rigid bodies are considered for both punch and mandrel with radii R_p and R_m , respectively. The mandrel is stationary with a length span of L_m when the punch applies a force in the middle section of the sheet. The sheet rests on the two mandrels and punch motion deforms the sheet.

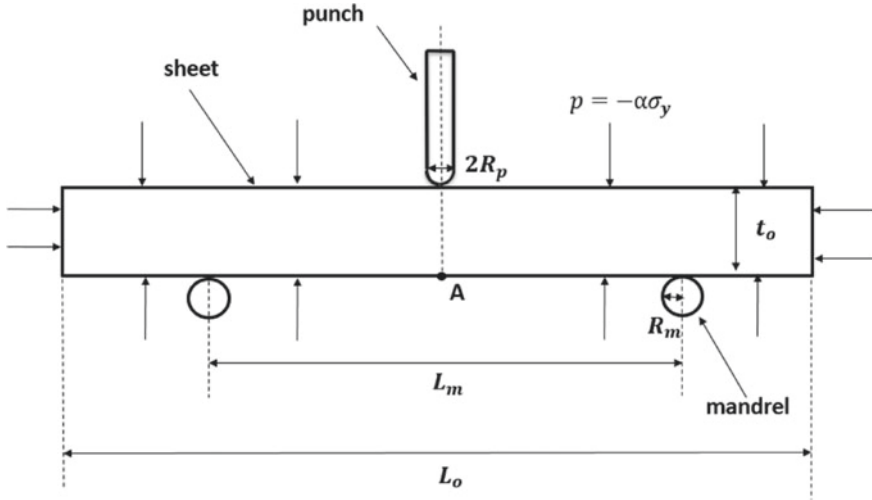


Fig. 1 2D Schematic of three-point bending test

Results and Discussion

The elastic–plastic properties of the matrix material are specified by $\sigma_y/E = 0.0033$, $\nu = 0.3$, and $n = 10$. It is assumed that the initial void volume fraction is zero and the fit parameters in GTN model (Eq. (6)) are $q_1 = 1.0$ and $q_2 = 1.5$. Void nucleation is assumed to be plastic strain-controlled with the volume fraction $f_N = 0.04$ of void nucleating particles, the mean strain for nucleation $\varepsilon_N = 0.3$, and the corresponding standard deviation $S_N = 0.1$. The final failure is taken to be characterized by the parameters $f_c = 0.15$ and $f_f = 0.25$. These values of mechanical properties are taken from Tvergaard and Needleman [11]. Three-dimensional fully reduced integration element C3D8R in ABAQUS/Explicit is considered, and length of sheet (L) and thickness (t) are 20 mm and 2.5 mm, respectively. Also, R_m , R_p , and L_m are 0.25 mm, 0.2 mm, and 5.5 mm, respectively.

It should be mentioned that although the three-point bending test is a static analysis, ABAQUS/Explicit is used in this study as ABAQUS/Standard is not able to provide the failure in the GTN model. However, a mass scaling method with a sufficient low target time increment is used to minimize the dynamic effect of the sample.

The finite element (FE) configuration of the 3D three-point bending test in ABAQUS is shown in Fig. 2. Due to the symmetry, only half of the sheet is investigated. $60 \times 110 \times 12$ C3D8R elements (60 elements in Y direction, 110 elements in X direction, and 12 elements in Z direction) in ABAQUS/Explicit is used. Mesh sensitivity on prediction of fracture strain in tensile tests simulation using FEM is reported in [16–19]. The effect of mesh sensitivity on the force–displacement curve

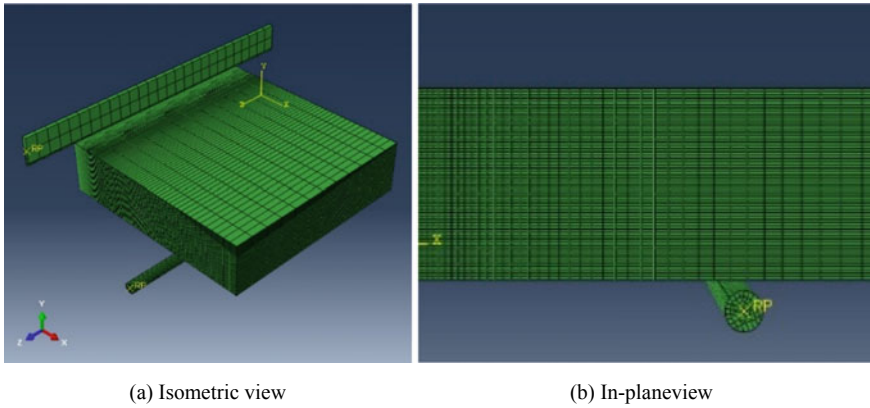


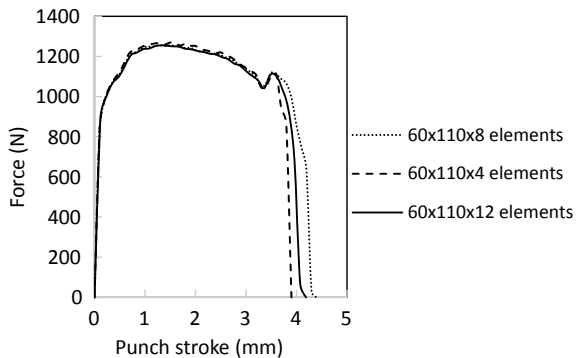
Fig. 2 A typical mesh with $60 \times 110 \times 12$ 3D elements (C3D8R in ABAQUS/Explicit)

is shown in Fig. 3 for three different meshes. It is found that the size of elements has an insignificant effect on the fracture initiation.

The effect of specimen width on the force–displacement curve and bendability is shown in Fig. 4 while the thickness is constant for all cases. It is found that the force–displacement curve rises with increasing width because the volume of material increases, and it takes more force to bend the specimen. However, the ductility decreases with an increase in width as the stress ratio increases and the stress state changes from uniaxial tensile to in-plane plane strain.

The stress ratio at the outer surface in the middle section of a sheet metal changes with a change in width/thickness ratio. For wide specimens, the stress ratio is close to 0.5 corresponding to in-plane plane strain state and, for a narrow specimen, the stress ratio is close to zero corresponding to a uniaxial tensile state [1]. The major and minor strains for five different sheets with different widths are shown in Fig. 5 with the same thickness value. Figure 6 shows the volumetric strain ($\epsilon_{11} + \epsilon_{22} + \epsilon_{33}$) for these five cases and it is found that this value decreases with decreasing width/thickness ratio

Fig. 3 Effect of mesh sensitivity on force–displacement curve



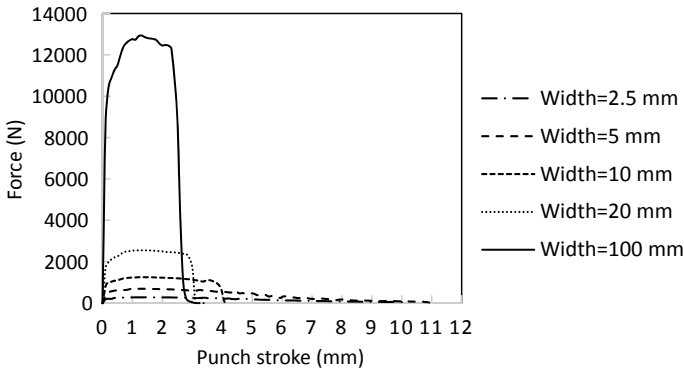


Fig. 4 Force–displacement curves in metal sheets with various widths

as shown in Fig. 6. This helps decrease the void growth following Eq. (1) and it leads to higher bendability. It is to be noted that fracture does not occur for the sheet with a width of 2.5 mm and this is the reason that volumetric strain increases and then decreases when it only slides over the mandrel with less force.

Figure 7 presents the hydrostatic pressure $\sigma_H = (1/3)(\sigma_{xx} + \sigma_{yy} + \sigma_{zz})$ and stress triaxiality $\frac{\sigma_H}{\sigma}$ at point A (see Fig. 1), where fracture initiates as a function of punch stroke under various widths. It is found that stress-triaxiality and hydrostatic pressure decrease with decreasing width and this helps delay void growth following Eq. (6).

Figure 8 shows the total void volume fraction (f) and it demonstrates that the growth of f decreases with a decrease in specimen width. As mentioned previously, the change in strain path as well as the decrease in stress triaxiality are the main reasons for the decreased void growth.

The ductility of the sheet is measured in terms of the fracture strain $\left(\varepsilon_c = \ln\left(\frac{t_o}{t_f}\right)\right)$, where t_o and t_f are the initial and final thicknesses of sheet in the middle section of specimen. Figure 9 shows the fracture strain of specimen with various widths and it is observed that the fracture strain decreases with an increase in width. The decrease in fracture strain can be explained by considering the variation in void volume fraction of specimens with various widths. Void volume fraction decreases with decreasing width and this causes an increase in ductility. It is to be noted that fracture does not occur for the sheet with a width of 2.5 mm.

Conclusion

In this study, an FE analysis of the three-point bend test for sheet metal with various width/thickness ratios is carried out. It is found that a lower width/thickness ratio improves bendability significantly as the stress state in the sheet changes and it

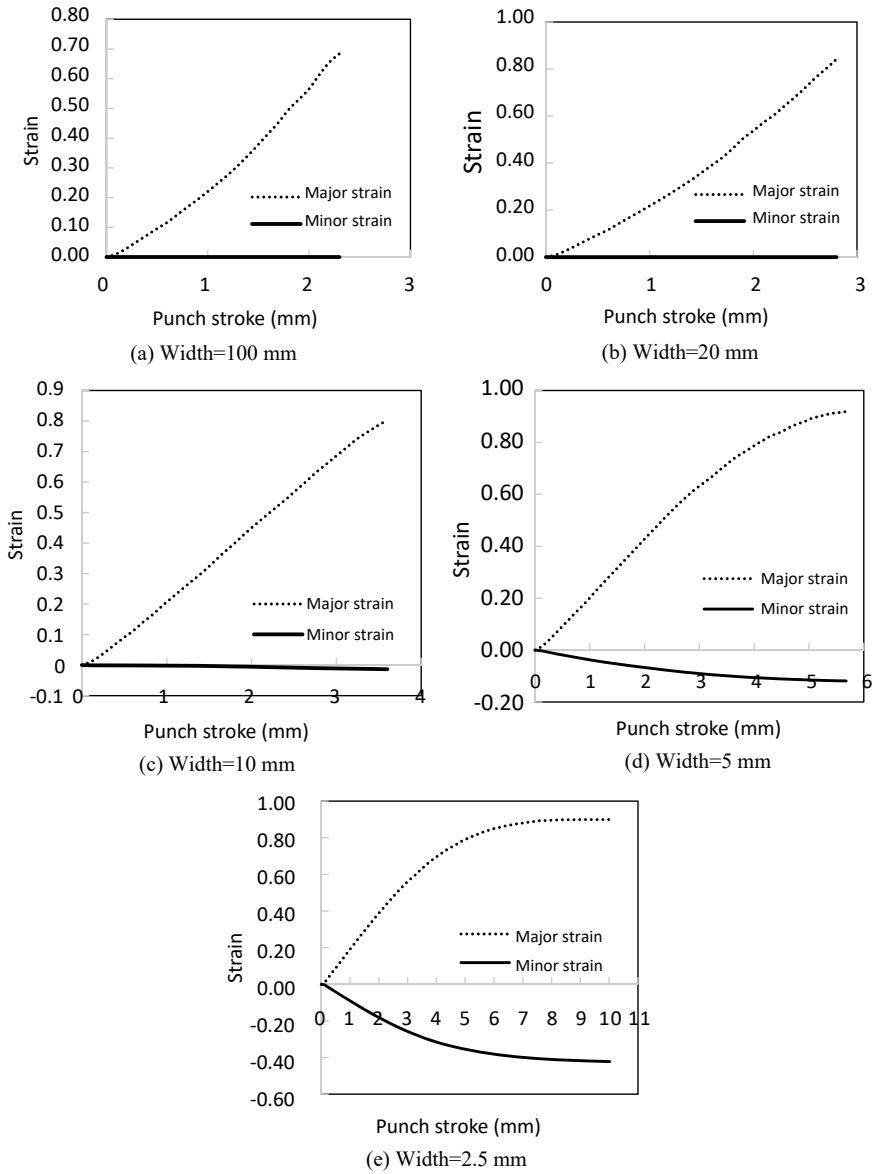


Fig. 5 Major and minor strains in metal sheets with various width/thickness ratios

Fig. 6 Volumetric strain in metal sheets with various widths

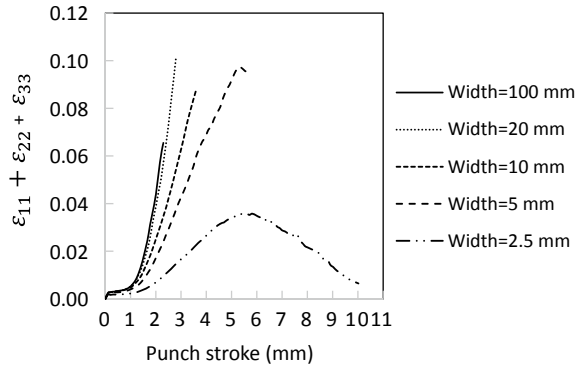
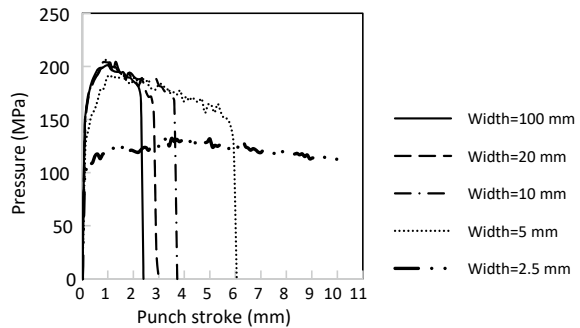
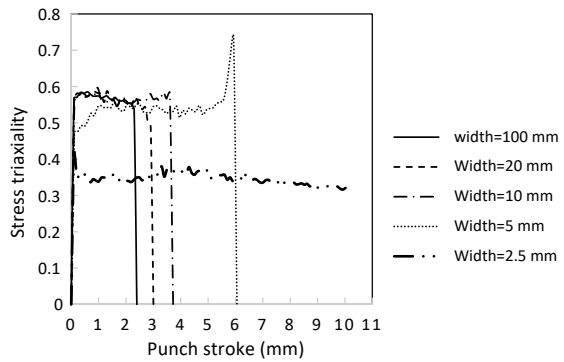


Fig. 7 Effect of width on **a** hydrostatic pressure and **b** stress triaxiality at point A



(a)



(b)

becomes closer to a tensile stress state. The volumetric strain and stress triaxiality decrease with a decrease in width/thickness ratio and this delays void growth and coalescence. Thus, the fracture strain decreases with decreasing width/thickness ratio.

Fig. 8 Void volume fractions in metal sheets with various widths

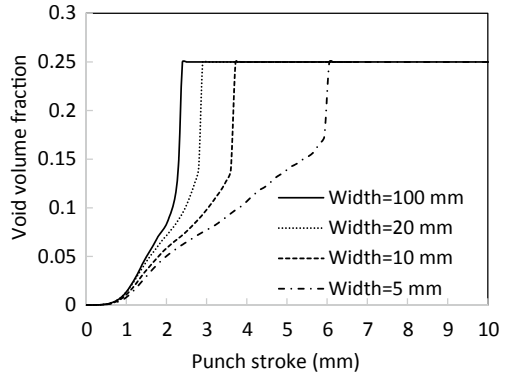
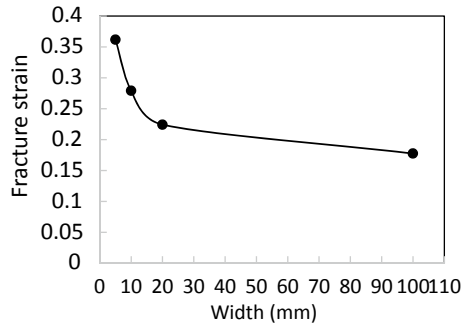


Fig. 9 Fracture bending strain in metal sheets with various widths



References

1. Ragab AR, Saleh CA (2005) Evaluation of bendability of sheet metals using void coalescence models. *Mater Sci Eng A* 395(1–2):102–109
2. Lloyd DJ, Gallerneault M, Wagstaff RB (2010) The deformation of clad aluminum sheet produced by direct chill casting. *Metall Mater Trans A* 41(8):2093–2103
3. Shi Y, Zhao PZ, Jin H, Wu PD, Lloyd DJ (2016) Analysis of surface roughening in AA6111 automotive sheet under pure bending. *Metall Mater Trans A* 47(2):949–960
4. Lloyd DJ, Evans D, Pelow C, Nolan P, Jain M (2002) Bending in aluminium alloys AA 6111 and AA 5754 using the cantilever bend test. *Mater Sci Technol* 18(6):621–628
5. Sarkar J, Kutty TRG, Conlon KT, Wilkinson DS, Embury JD, Lloyd DJ (2001) Tensile and bending properties of AA5754 aluminum alloys. *Mater Sci Eng A* 316(1–2):52–59
6. Sarkar J, Kutty TRG, Wilkinson DS, Embury JD, Lloyd DJ (2004) Tensile properties and bendability of T4 treated AA6111 aluminum alloys. *Mater Sci Eng A* 369(1–2):258–266
7. Hou P, Zhao H, Ma Z, Zhang S, Li J, Dong X, Sun Y, Zhu Z (2016) Influence of punch radius on elastic modulus of three-point bending test. *Adv Mech Eng* 8(5):1687814016649116
8. Datsko J, Yang CT (1960) Correlation of bendability of materials with their tensile properties. *J Manuf Sci Eng* 82(4):309–313
9. Kao AS, Kuhn HA, Richmond O, Spitzig WA (1989) Workability of 1045 spheroidized steel under superimposed hydrostatic pressure. *Metall Trans A* 20(9):1735–1741
10. Abaqus/CAE User’s Manual (2014) ABAQUS Inc., Waltham
11. Tvergaard V, Needleman A (1984) Analysis of the cup-cone fracture in a round tensile bar. *Acta Metall* 32(1):157–169

12. Tvergaard V (1981) Influence of voids on shear band instabilities under plane strain conditions. *Int J Fract* 17(4):389–407
13. Tvergaard V (1982) On localization in ductile materials containing spherical voids. *Int J Fract* 18(4):237–252
14. Gurson AL (1977) Continuum theory of ductile rupture by void nucleation and growth: part I—Yield criteria and flow rules for porous ductile media. *J Eng Mater Technol* 99(1):2–15
15. Chu C, Needleman A (1980) Void nucleation effects in biaxially stretched sheets. *J Eng Mater Technol* 102(3):249–256
16. Wu PD, Chen XX, Lloyd DJ, Embury JD (2010) Effects of superimposed hydrostatic pressure on fracture in sheet metals under tension. *Int J Mech Sci* 52(2):236–244
17. Chen XX, Wu PD, Lloyd DJ, Embury JD, Huang Y (2010) Enhanced ductility in sheet metals produced by cladding a ductile layer. *J Appl Mech* 77(4):041015
18. Peng J, Wu PD, Huang Y, Chen XX, Lloyd DJ, Embury JD, Neale KW (2009) Effects of superimposed hydrostatic pressure on fracture in round bars under tension. *Int Solids Struct* 46(20):3741–3749
19. Chen XX, Wu PD, Embury JD, Huang Y (2010) Enhanced ductility in round tensile bars produced by cladding a ductile ring. *Modell Simul Mater Sci Eng* 18(2):025005

Investigation of a Pre-strain-Specific Edge Crack Sensitivity Factor and Its Implementation in FEM



Alexander Kindsmueller, Roman Norz, Niko Manopulo, and Wolfram Volk

Abstract The shear cutting process can significantly reduce the formability of a shear cut edge, which can lead to edge cracking. This problem occurs especially when processing high-strength and ultra-high-strength sheet materials such as dual-phase steels. In practice, component manufacture often takes place as a sequence of several deep drawing and shear cutting operations. However, the influence of prior sheet forming on edge crack sensitivity has not yet been sufficiently investigated and has not been considered in simulations so far. In this work, an experimentally determined model is presented that describes the edge crack sensitivity as a function of pre-forming for a selected cutting strategy for the sheet material HCT580X. Here, a reduced edge crack sensitivity is found with all three uniaxial, plane strain, and biaxial pre-strain modes compared to the undeformed sheet material. This model is implemented into the FEM simulation to study the manufacturability of deep-drawn collars in a previously formed sheet. Finally, the simulation results are validated by means of collar-forming experiments.

Keywords Edge crack · Pre-forming · Shear cutting · Collar-forming · FEM

Introduction

Shear cutting is the most commonly used process for material separation in the mass production of formed sheet metal components. This is due to its high cost-effectiveness and high output with good integrability in multi-stage tools [1]. The cutting process and the cutting parameters have a significant influence on the properties of the shear-cut edge. The edge crack sensitivity of a material also depends largely on these cutting parameters. Edge cracking describes the problem that the

A. Kindsmueller (✉) · R. Norz · W. Volk
Institute of Metal Forming and Casting, Technical University of Munich, Walther-Meißner-Str. 4,
85748 Garching, Germany
e-mail: alexander.kindsmueller@utg.de

N. Manopulo
AutoForm Development GmbH, Technoparkstrasse 1, Zurich, Switzerland

forming capacity of a component edge can be significantly reduced compared to the original material due to strains and micro-damages introduced during the shear cutting process [2]. This problem occurs, for example, in the processing of high-strength and ultra-high-strength sheet materials such as dual-phase steels, which are frequently used in vehicle construction due to lightweighting aspects (Fig. 1).

In practice, the manufacturing process of complex components usually consists of a sequence of shear cutting, deep drawing, trimming, post-forming, or collar-forming operations. This means that shear cutting operations often also take place in areas that have already been formed and when the newly created component edges are subjected to further forming operations. However, the influence of prior sheet forming on edge crack sensitivity has not yet been sufficiently investigated and has not yet been taken into account in simulations. Research by [3] suggests that pre-forming may have an effect on edge crack sensitivity depending on the strain gradients at the edges. In investigations by [4], it has been shown that increasing pre-forming causes a reduction of edge crack sensitivity. However, both studies have in common that only a few discrete pre-forming states were investigated and thus not enough data are available for a model that can be integrated into an FEM simulation.

In this work, the edge crack sensitivity for the dual-phase steel HCT580X with a sheet thickness of 1 mm is investigated depending on the path and amount of pre-straining and is then transferred to a model. This model is implemented in the FEM simulation of a collar-forming operation in pre-formed sheet with shear cut edges using the AutoForm Forming R10 software in combination with the R&D plugin. Finally, the simulation results and the model are validated by means of collar-forming experiments.

Fig. 1 Edge crack on a shear cut collar edge



Methodology for Determining Edge Crack Sensitivity with Pre-formed Sheets

Experimental Procedure

The sheet metal pre-forming is performed using a modified Marciniak tool (Fig. 2a), whereby a homogeneously pre-strained area can be generated [5]. The type and amount of pre-forming are set by the initial blank geometry and the drawing depth. To examine the pre-strain state, a uniform pattern is applied to the initial blank and analyzed after the drawing process using the GOM Argus optical forming analysis system (Fig. 2b, c). The pre-forming is performed transversely to the rolling direction.

The specimens for the *Edge-Fracture-Tensile-Test (EFTT)* are taken from the homogeneously pre-formed area, whereby both reference specimens, milled on both sides and half-sided shear-cut specimens, are produced (Fig. 3a). The selected cutting parameters for the shear-cut specimens can be obtained from Table 1.

For the *EFTT* according to [6], the specimens are stretched on a universal tensile testing machine until failure. Here, the deformation of the specimens is recorded during the tensile tests using the GOM Aramis deformation analysis system. The major strain at the beginning of local necking is determined using the time-dependent evaluation method according to [7]. While local necking for the both-sided milled reference specimens usually starts in the center of the specimen (Fig. 3b), local necking for half-sided shear-cut specimens may start at the shear-cut edge if there is sensitivity to edge cracking (Fig. 3c). One measure of edge crack sensitivity is the *Edge Crack-Sensitivity-Factor K_{ec}* according to [4]. It is calculated by the quotient of the major strains at the beginning of local necking of the shear cut specimens and the milled reference specimens (Formula 1).

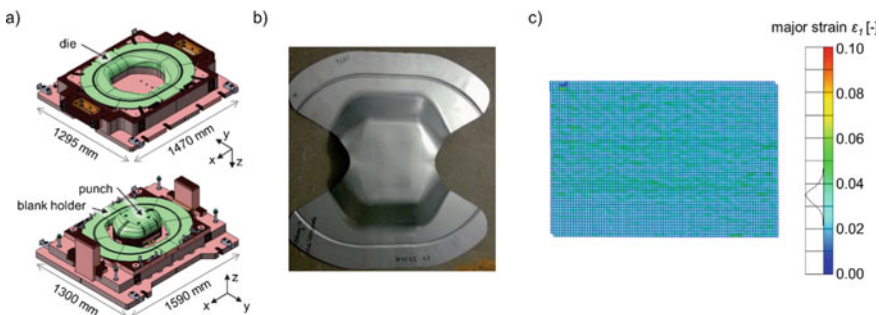


Fig. 2 a Modified Marciniak tool [5]; b pre-formed sheet [5]; c result of a GOM Argus measurement of the homogeneously formed sheet area

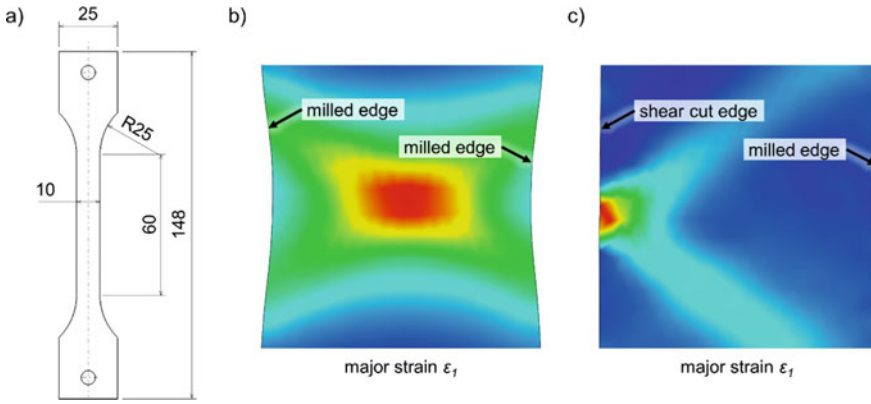


Fig. 3 a Geometry of an *EFTT* sample; b start of necking in the center for a both-sided milled specimen; c start of necking at the edge for a half-sided shear cut specimen

Table 1 Investigated shear cutting parameters

Shear cutting parameter	Value
Die clearance u	0.1 mm
Punch edge radius	200 μm
Die edge radius	20 μm
Cutting line	Open
Rolling direction of the specimen	90°

$$K_{ec} = \frac{\varepsilon_{1,loc,Sheared}}{\varepsilon_{1,loc,Ref}} \tag{1}$$

K_{ec} *Edge Crack-Sensitivity-Factor* without pre-forming

$\varepsilon_{1,loc,Sheared}$ Logarithmic major strain at the beginning of local necking, half-sided shear cut specimen.

$\varepsilon_{1,loc,Ref}$ Logarithmic major strain at the beginning of local necking, both-sided milled reference specimen.

Principle of Equivalent Pre-forming

The calculation of the *Edge Crack-Sensitivity-Factor* K_{ec} according to Formula 1 is only valid if non-pre-formed specimens are examined. For arbitrarily pre-formed specimens, the pre-forming must be transformed into an equivalent uniaxial pre-strain state. This is done using the principle of equivalent pre-forming according to [8]. This principle implies that every deformation state built up of two linear strain

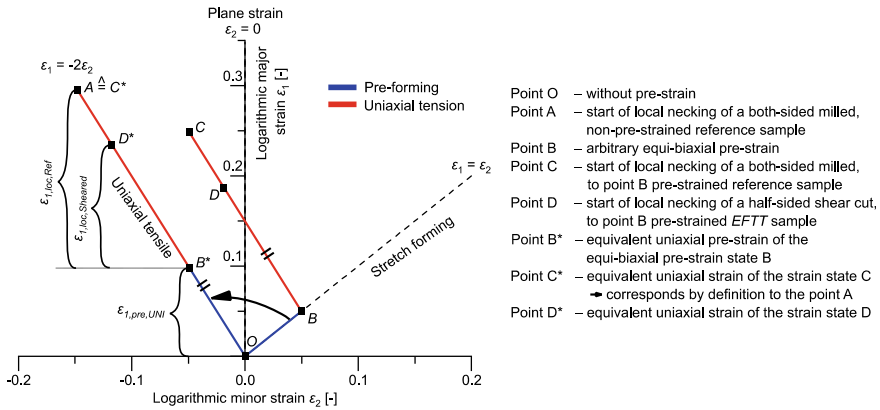


Fig. 4 Transformation of an equi-biaxial pre-strain with a following uniaxial *EFTT* into an equivalent uniaxial strain state based on the principle of the equivalent pre-forming

increments can be transformed into a linear strain path with the same formability of the material. To illustrate this principle, the transformation of a biaxial pre-formed point B into an equivalent uniaxial forming state B* is explained in Fig. 4.

Considering equivalent uniaxial pre-forming, the *Edge Crack-Sensitivity-Factor* K_{ec} for pre-formed specimens can be calculated according to Formula 2:

$$K_{ec} = \frac{\varepsilon_{1,pre,UNI} + \varepsilon_{1,loc,Sheared}}{\varepsilon_{1,pre,UNI} + \varepsilon_{1,loc,Ref}} \tag{2}$$

K_{ec} *Edge Crack-Sensitivity-Factor with pre-forming*

- $\varepsilon_{1,pre,UNI}$ Logarithmic major strain of an equivalent uniaxial pre-formed state.
- $\varepsilon_{1,loc,Sheared}$ Logarithmic major strain at the beginning of local necking, half-sided shear cut, pre-formed specimen.
- $\varepsilon_{1,loc,Ref}$ Logarithmic major strain at the beginning of local necking, both-sided milled, pre-formed reference specimen.

Modeling of a Pre-strain-Dependent Edge Crack Sensitivity Factor

In addition to non-pre-formed specimens, 46 different pre-forming conditions are investigated for model generation, with these lying on the three uniaxial, plane-strain, and biaxial strain paths. An overview of the different pre-strain states is given in Fig. 5, where each point corresponds to one pre-formed sheet. From each sheet, usually, one reference specimen milled on both-sided and one half-sided shear cut specimen are produced for the *EFTT*. The condition without pre-forming is examined

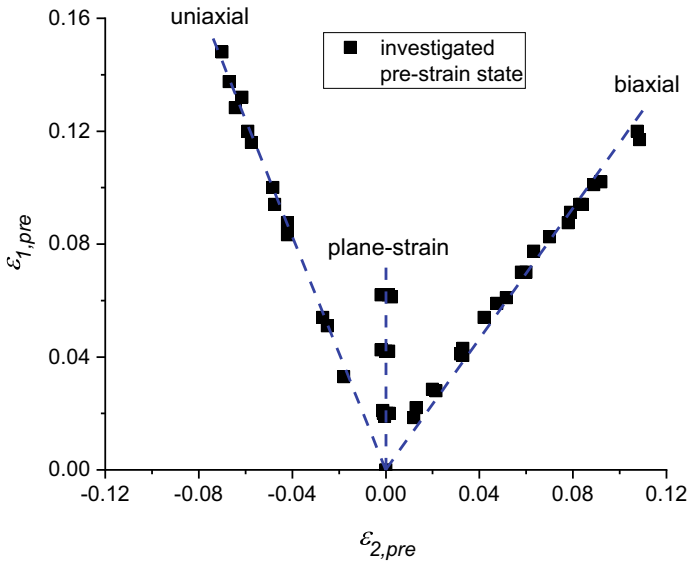


Fig. 5 Overview of the investigated pre-strain states

on five reference specimens milled on both sides and on eight half-sided shear-cut specimens.

The $\varepsilon_{I,loc,Sheared}$ and $\varepsilon_{I,loc,Ref}$ residual major strains at the beginning of local necking are plotted in Fig. 6 for each strain path as a function of the major strain of the pre-forming. Each black dot corresponds to the residual formability of a milled reference specimen, and each red dot to the residual formability of a shear-cut specimen. For further analysis, the measuring points are fitted with suitable linear or cubic polynomial functions, with the aim of minimizing the sum of the error squares. Since a larger number of specimens statistically secures the measuring point without pre-strain, the mean value of all non-pre-strained specimens is assumed the same for all three investigated pre-forming types and is taken into account accordingly in the fitting.

For the milled specimens, it is found that residual formability decreases with increasing pre-forming for all three pre-strain paths. For the shear-cut specimens, no effect of pre-strain on the residual formability can be detected at low degrees of pre-strain, and the fitted curves are nearly horizontal. Only when the curves of the shear-cut and the milled reference specimens intersect, the residual formability of the shear-cut specimens decreases to a similar extent as the reference specimens. Therefore, the fitted curves of the shear cut specimens approach the curves of the both-sided milled reference specimens with increasing pre-forming, which means that the influence of shear cutting on formability decreases. For the uniaxial and biaxial strain paths, both curves intersect slightly. However, the overlap is only marginal and can be attributed to statistical scattering in the test execution and the method of curve fitting.

The residual formability shown in Fig. 6 can be converted into a pre-strain-dependent *Edge Crack Sensitivity Factor* K_{ec} for each pre-strain path according to the procedure presented in section “*Principle of Equivalent Pre-forming*” (see Formula 2). The results are illustrated in Fig. 7 for the three pre-strain paths investigated as functions of the major strain of pre-forming. While the *Edge Crack Sensitivity Factor* without pre-forming is $K_{ec} = 0.69$, it increases with pre-formed material. This means that pre-strained and subsequently shear cut edges exhibit a reduced sensitivity to edge cracking. In the case of uniaxial and biaxial pre-strain, the *Edge Crack Sensitivity Factor* K_{ec} exceeds the value of 1.0 due to the reasons described above. In this case, K_{ec} is set as 1.0. This means that no edge damage is expected due to shear cutting and the residual formability of the edge is described by the material’s formability.

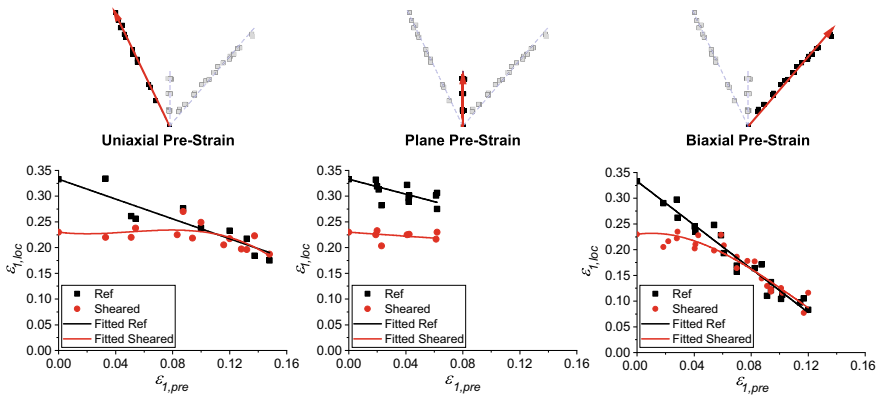


Fig. 6 Residual major strains ϵ_1 at the beginning of local necking of half-sided shear cut and both-sided milled pre-formed specimens

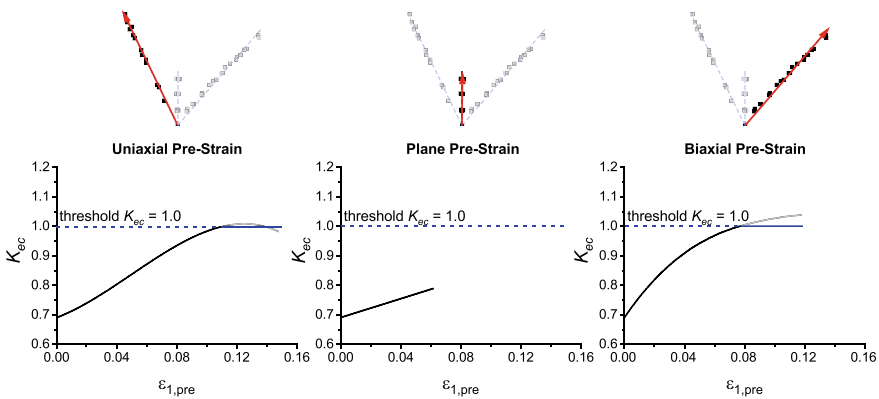


Fig. 7 Pre-strain-dependent *Edge Crack Sensitivity Factor* K_{ec}

Due to the fitting by linear and cubic functions and the resulting possible inflection points of the K_{ec} -curve, the model presented above is only valid for the investigated pre-forming range and should not be extrapolated for larger pre-forming states. However, an interpolation between the three strain paths is feasible and was considered when implementing the model into the FEM.

Implementation of the Pre-strain-Dependent Edge Crack Sensitivity Factor into FEM

The implementation of a pre-strain-dependent Edge Crack Sensitivity Factor into the FEM simulation is realized with the AutoForm Forming R10 simulation software in combination with the R&D plugin. This plugin enables the application of self-programmed evaluation routines using the C programming language, whereby custom history variables can be created and evaluated.

First, a deep-drawing process with a flat-bottom die is simulated, that generates a homogeneously formed flat area depending on the initial blank geometry and the drawing depth. A hole with a diameter of 50.0 mm is then cut in the center of the homogeneous area and a blank with external dimensions of 160×160 mm is cut out. Finally, a collar is drawn by plunging a conical punch through the hole. Here, the inner diameter of the collar \varnothing_i depends on the diameter of the selected punch. A schematic overview of the simulated process chain is illustrated in Fig. 8.

In the programmed evaluation routine, the major and minor strains ε_1 and ε_2 are calculated for each element. Subsequently, the strain states are parameterized by calculating the strain ratio $\beta = \varepsilon_2/\varepsilon_1$ and the strain path length ratio

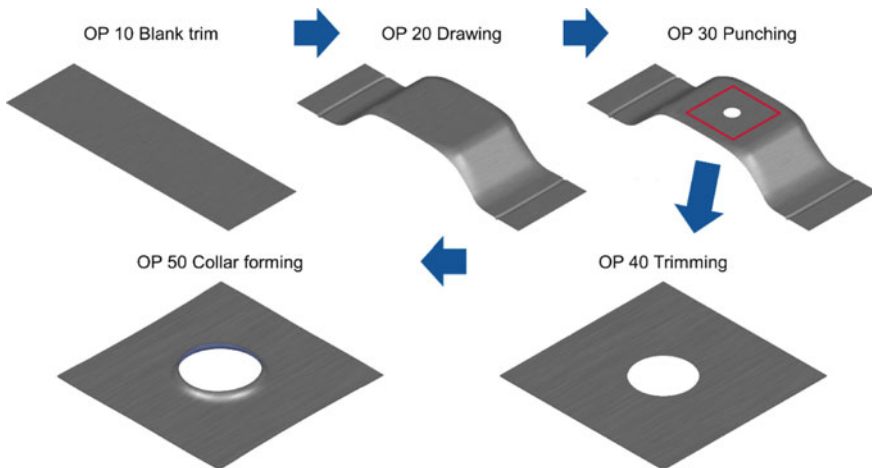


Fig. 8 Sequence of the simulated forming and cutting processes

$\lambda(\beta) = l/l_{FLC}$ according to [8]. Shear cutting operations are identified and the parameters β and λ of all edge elements at the step of the cutting operation are recorded. The pre-strain-dependent *Edge Crack Sensitivity Factor* K_{ec} can be calculated for all elements using the information presented in Fig. 7, whereby the pre-strain state at the step of the cutting operation is decisive for edge elements. If strain ratios exist between the three strain paths defined in chapter “[Characterization of Impurities in Nanomaterials](#)” (uniaxial, plane strain, and biaxial), the *Edge crack Sensitivity Factor* is calculated by linear interpolation between the two adjacent strain paths at the same strain path length ratio λ . The pre-strain-dependent edge crack sensitivity is taken into account in further forming processes of the shear cut edges. For a simple evaluation of manufacturability of the edges, a damage value *EDGEDMG* is implemented in post-processing, whereby the residual forming capacity of the pre-strained material as well as the pre-strain-dependent K_{ec} are included in the calculation. If this value is below 1.0, the component edge can be classified as edge crack-free; if the damage value is above 1.0, local necking and cracking at the edge are to be expected.

The presented evaluation routine is applied to the simulation of the process chain (Fig. 8) for the HCT580X dual-phase steel (initial sheet thickness 1 mm) in combination with the shear cutting parameters shown in Table 1. After pre-straining, homogeneous logarithmic strains of $\varepsilon_1 = 0.035$ and $\varepsilon_2 = -0.006$ are found, whereby the strain state lies between the uniaxial and plane strain paths. The resulting *Edge Crack Sensitivity Factors* K_{ec} at the shear-cut hole are shown in Fig. 9a. These vary

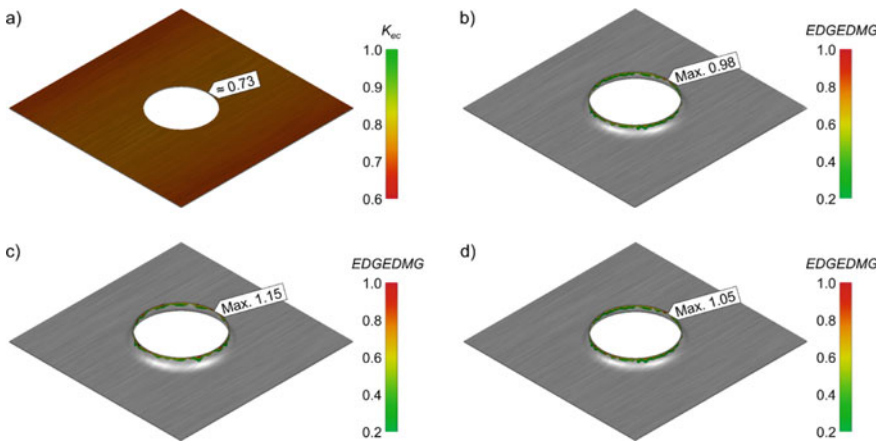


Fig. 9 **a** Pre-strain-dependent *Edge Crack Sensitivity Factor* K_{ec} of the pre-strained and punched specimen; **b** *EDGEDMG* of the specimen after pre-straining, punching, and collar-forming ($\phi_i = 60.0$ mm) with pre-strain-dependent K_{ec} ; **c** *EDGEDMG* of the specimen after pre-straining, punching, and collar-forming ($\phi_i = 62.5$ mm) with pre-strain-dependent K_{ec} ; **d** *EDGEDMG* of the specimen after pre-straining, punching, and collar-forming ($\phi_i = 60.0$ mm) without pre-strain-dependent K_{ec}

only marginally due to the homogeneous pre-strain. With $K_{ec} \approx 0.73$, the edge crack sensitivity is less critical than for the non-pre-strained sheet ($K_{ec} = 0.69$).

Subsequently, the punched hole is expanded into a collar with two different punch diameters ($\varnothing_i = 60.0$ mm; $\varnothing_i = 62.5$ mm) and the *EDGEDMG* damage value is determined at the edge. While the maximum *EDGEDMG* for $\varnothing_i = 60.0$ mm is 0.98 and the collar is thus considered to be manufacturable (Fig. 9b), defects at the collar edge are to be expected for $\varnothing_i = 62.5$ mm with a maximum *EDGEDMG* of 1.15 (Fig. 9c). To illustrate the influence of a non-pre-strain-dependent *Edge Crack Sensitivity Factor* on the manufacturability analysis, Fig. 9d shows the *EDGEDMG* damage value calculated with the initial value of $K_{ec} = 0.69$ for the $\varnothing_i = 60.0$ mm punch. Without the use of a pre-strain-dependent *Edge Crack Sensitivity Factor* K_{ec} , the collar would thus have to be classified as unmanufacturable.

Model Validation Using Collar-Forming Experiments

For a validation of the simulation results from chapter “[Constructing Exact Solutions to Modelling Problems](#)”, a pre-forming condition analogous to the simulation is generated using the forming tool already presented in section “[Experimental Procedure](#)”. Measurements with the GOM Argus optical forming analysis system result in a forming state of $\varepsilon_1 = 0.034$ and $\varepsilon_2 = -0.007$. These agree very well with the pre-strain states from the simulation ($\varepsilon_1 = 0.035$; $\varepsilon_2 = -0.006$). The manufacturing of the 50 mm hole is performed by shear cutting with a high-precision cutting tool, using the cutting parameters listed in Table 1. To realize an open cutting line, a pre-milled hole with a diameter of 42 mm is cut to the final diameter of 50 mm so that a ring with a width of 4 mm is cut out all around. This is intended to generate a stress state in the shear zone during shear cutting analogous to an open cutting line. The correct positioning of the blank in the tool is ensured by positioning pins. The collars are drawn with another tool, using active elements with the punch diameters of $\varnothing_i = 60.0$ mm and $\varnothing_i = 62.5$ mm that have already been simulated (see Fig. 10). Drawing oil is applied to both sides of the sheet to reduce friction. The quality of the specimens is examined visually, whereby collar edges with a crack through the complete sheet thickness are classified as defective. For statistical validation of the results, each collar diameter is repeated five times. The production of one collar diameter is classified as manufacturable if all five specimens show no defects. However, as soon as three defective edges are detected on one collar diameter, further tests are stopped and the diameter is classified as non-manufacturable.

The results of the collar-forming tests with the pre-formed sheet are presented in Fig. 11. Collar-forming with a punch diameter of $\varnothing_i = 60.0$ mm resulted in crack-free edge qualities for all five specimens tested. The larger punch diameter of $\varnothing_i = 62.5$ mm led to edge cracking with all three specimens examined. Thus, these results are consistent with the simulatively predicted results.

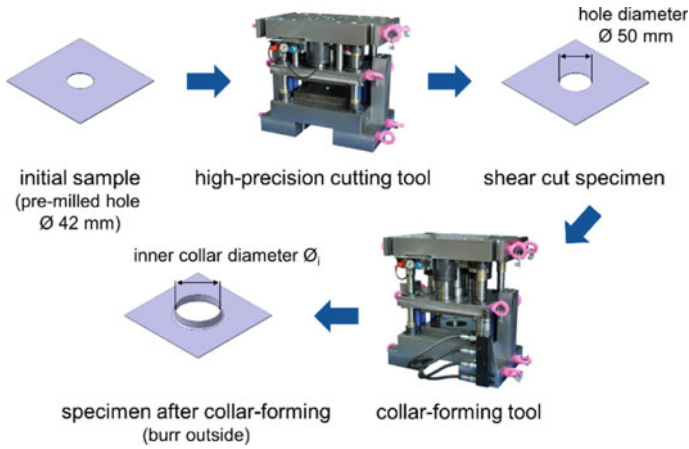


Fig. 10 Procedure of the collar-forming experiments

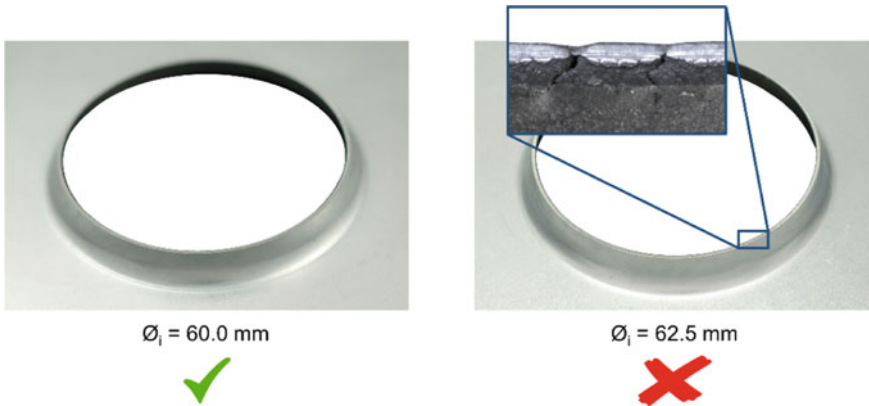


Fig. 11 Comparison of the crack-free collar edge ($\text{Ø}_i = 60.0 \text{ mm}$) and the collar edge with edge cracking ($\text{Ø}_i = 62.5 \text{ mm}$)

Conclusions and Outlook

The investigations have shown that edge crack sensitivity is strongly influenced by previous sheet forming operations. Here, increasing strains from pre-forming resulted in reduced edge crack sensitivities. It is necessary to consider a pre-strain-dependent *Edge Crack Sensitivity Factor* in the FEM simulation in order to use the full forming potential of the component edges. One approach to integrate the pre-strain-dependent edge crack sensitivity into the AutoForm Forming R10 simulation tool has been shown in this work. It should be noted, however, that this approach can so far only be applied to the investigated HCT580X sheet metal material in

combination with the shear cutting parameters defined in Table 1. It is necessary to extend this specific model by means of further experiments with other sheet materials and cutting strategies in order to obtain a generally valid model. In addition, further pre-strain states must be investigated in future works to collect data between the three pre-strain paths investigated in this work. This will contribute to further optimizations of the model.

Acknowledgements The results of this work were performed on the FOSTA P 1445 research project (IGF 21136 N) “Vorhersage des Restumformvermögens an vorverformten schergeschnittenen Bauteilkanten im offenen und geschlossenen Schnitt” [Prediction of the residual formability of pre-formed shear cut component edges using open and closed cutting lines], which is sponsored by the Research Association for Steel Application (FOSTA) and the Federal Ministry for Economic Affairs and Climate Action (BMWK) through the AiF (German Federation of Industrial Research Associations eV) based on a decision taken by the German Bundestag.

Authors’ Contribution Alexander Kindsmueller: Experimental investigations, methodology, programming, simulation, writing—original draft, review and editing, project administration.

Roman Norz: Support and advice for programming and simulation, review, and editing.

Niko Manopulo: Support and advice for programming and simulation.

Wolfram Volk: Supervision, funding administration.

References

1. König W, Klocke F (1995) *Fertigungsverfahren - Blechbearbeitung*. VDI, Düsseldorf
2. Konieczny A, Henderson T (2007) On formability limitations in stamping involving sheared edge stretching. SAE Tech Pap Ser. <https://doi.org/10.4271/2007-01-0340>
3. Iizuka, E, Higai K, Yamasaki Y (2019) Effect of pre-strain on stretch flange deformation limit of steel sheets. In: IDDRG 38th annual conference. <https://doi.org/10.1088/1757-899X/651/1/012017>
4. Feistle M, Kindsmüller A, Pätzold I, Golle R, Volk W (2022) Influence of sheet metal pre-forming on edge crack sensitivity using an AHSS steel grade. *Int J Mater Form*. <https://doi.org/10.1007/s12289-022-01669-5>
5. Weinschenk A, Volk W (2017) FEA-based development of a new tool for systematic experimental validation of nonlinear strain paths and design of test specimens. In: Proceedings of the 20th international ESAFORM conference on material forming. <https://doi.org/10.1063/1.5007966>
6. Feistle M, Krinninger M, Pätzold I, Volk W (2015) Edge-Fracture-tensile-test. In: Tekkaya AE et al (eds) 60 excellent inventions in metal forming. Springer, Berlin, pp 193–198. <https://doi.org/10.1007/978-3-662-46312-3>
7. Volk W, Hora P (2011) New algorithm for a robust user-independent evaluation of beginning instability for the experimental FLC determination. *Int J Mater Form* 4(3):339–346. <https://doi.org/10.1007/s12289-010-1012-9>
8. Volk W, Suh J (2013) Prediction of formability for non-linear deformation history using generalized forming limit concept (GFLC). AIP Conf Proc 1567. <https://doi.org/10.1063/1.4850035>

Prediction of Deformation and Failure Anisotropy for Magnesium Sheets Under Mixed-Mode Loading



Dirk Steglich and Jacques Besson

Abstract Despite the attractive strength-to-weight ratio of magnesium alloys, the application of magnesium sheet structures is restricted. Its anisotropy, the tension–compression asymmetry (the so-called strength differential effect, SD effect) and its poor formability at room temperature challenge engineers. In the current contribution, the deformation and failure behaviour of the innovative magnesium alloy “E-form” AZ31 at room temperature is investigated by means of mechanical tests and respective numerical simulations. Tensile and modified Arcan tests are analysed by digital image correlation (DIC) techniques. Arcan tests impose shear stresses while bending tests are conducted to force simultaneously tensile and compressive stresses in a sample. Irreversible deformation is described by a two-yield surface model, which couples the micromechanical mechanisms of dislocation glide and deformation twinning. Anisotropic failure is modeled using a linear transformation of the strain rate, which allows for a fast and efficient assessment of forming operation.

Keywords Finite elements · Anisotropy · Plasticity · Asymmetry · Strength differential effect · Tensile tests

Introduction

Sheet forming and bending are widely used operations in manufacturing industries. These processes are more frequently applied to magnesium sheets in the last decades, since magnesium alloys bear attractive properties like lightweight, durability, low density attractive in the automotive, rail coach, and aerospace industry. The relative low ductility of the common magnesium alloys, however, demands for reliable prediction tools for the assessment of forming operations.

D. Steglich (✉)

Institute of Material Systems Modeling, Helmholtz-Zentrum Hereon, Max-Planck-Str. 1, 21502 Geesthacht, Germany
e-mail: dirk.steglich@hereon.de

J. Besson

Centre des Matériaux, UMR CNRS 7633, PSL Research University, Mines ParisTech, 91003 Evry Cedex, France

© The Minerals, Metals & Materials Society 2022

K. Inal et al. (eds.), *NUMISHEET 2022*, The Minerals, Metals & Materials Series,
https://doi.org/10.1007/978-3-031-06212-4_55

607

Efforts were made for investigating the dependency of fracture on stress states. The relationship between ductile fracture strain and stress triaxiality is known from the 70 s of the last century [1, 2], for steels, established using notched tensile samples. It is nowadays accepted that ductility is reduced with increasing stress triaxiality. Many ductile fracture models have been developed on this basis and applied in the past: micromechanical-based porous plasticity models [3, 4] as well as phenomenological-based continuum damage models [5, 6]. Despite their respective merits, these approaches are complex because they require finite element analysis, since stress states cannot be directly measured. With the emerging possibilities in digital image correlation techniques, however, strain states can be monitored on the surface, and the use of the strain state for predicting failure appears advantageous.

In this work, the plastic deformation and failure behaviour of a novel magnesium sheet material (AZ31 ‘E-form’) under quasi-static loading conditions at room temperature is studied. This task is pursued using a combined methodology of experimental tests and numerical modelling using finite element simulations. The experimental part includes tensile, compressive, Arcan-like mixed-mode tension tests, and three-point out-of-plane bending tests. Samples were fabricated and tested along the rolling direction (RD), along the transverse direction (TD) and in the case of tensile tests and bending samples additionally 45° to the RD (DD orientation).

The validation is conducted with the use of the finite element (FE) simulation code Zebulon (Z-Set) [7]. A two-yield surface model [8] is adopted to capture anisotropy and asymmetry of the material effectively. The anisotropy parameters are calibrated using mechanical tests. Failure is predicted by a criterion based on linear transforms of the strain caused by dislocation glide.

A magnesium alloy sheet ‘E-form’, Mg–3Al–Zn with an average thickness of 1.17 mm is used here. The main alloying elements are aluminum and zinc with an approximate weight proportion of 3% and 1%, respectively. The material exhibits a weak basal texture [9], which results in a less pronounced anisotropy compared to common magnesium alloys.

Plasticity and Failure Model

A phenomenological two-yield surface (2YS) model is adopted here, which can capture the tension–compression asymmetry and in-plane anisotropy. A symmetric (for glide mechanisms) and an asymmetric yield surface (for twinning mechanisms) are used. The effective stress and strain quantities are defined for each yield surface, namely, $\bar{\sigma}_g$ and $\bar{\varepsilon}_g$ for the glide yield surface, and $\bar{\sigma}_t$ and $\bar{\varepsilon}_t$ for the twinning yield surface. The strain increment is decomposed in an elastic, an inelastic due to glide, and an inelastic contribution due to twinning:

$$d\boldsymbol{\varepsilon} = d\boldsymbol{\varepsilon}^e + d\boldsymbol{\varepsilon}^p = d\boldsymbol{\varepsilon}^e + d\boldsymbol{\varepsilon}_g^p + d\boldsymbol{\varepsilon}_t^p. \quad (1)$$

The inelastic strains are computed from the respective yield surface assuming associated flow. For the description of the glide mechanisms, a Barlat91 [10] formulation is selected:

$$\phi_g = f_g - \tilde{\sigma}_g = \frac{1}{2}(|\beta_2 - \beta_3|^b + |\beta_3 - \beta_1|^b + |\beta_1 - \beta_2|^b)^{\frac{1}{b}} - \tilde{\sigma}_g = 0, \quad (2)$$

where $\tilde{\sigma}_g$ describes the isotropic hardening of the yield surface and b is the yield function exponent. β_1, β_2 , and β_3 are the principal values of a linearly transformed stress tensor β derived from the Cauchy stress B following

$$\beta = L : B, \quad (3)$$

with L including the coefficients of anisotropy.

The inelastic deformation due to twinning is governed by the asymmetric CPB06 [11] criterion:

$$\phi_t = f_t - \tilde{\sigma}_t = (|\delta_1| - k\delta_1)^a + (|\delta_2| - k\delta_2)^a + (|\delta_3| - k\delta_3)^a)^{\frac{1}{a}} - \tilde{\sigma}_t = 0, \quad (4)$$

a being a scalar parameter, δ_1, δ_2 , and δ_3 are the principal values of a linearly transformed stress deviator, δ ,

$$\delta = M : T : \sigma. \quad (5)$$

T is the fourth-order tensor that transforms the stress tensor to its deviator and M is the fourth-order tensor including anisotropy parameters.

The interaction between two deformation mechanisms is achieved through a coupling of the respective hardening laws:

$$\tilde{\sigma}_g(\bar{\varepsilon}_g, \bar{\varepsilon}_t) = R_g + H_g \bar{\varepsilon}_t + Q_{1g}[1 - \exp(-b_{1g} \bar{\varepsilon}_g)] + Q_{2g}[1 - \exp(-b_{2g} \bar{\varepsilon}_g)], \quad (6)$$

$$\tilde{\sigma}_t(\bar{\varepsilon}_t) = R_t + H_t \bar{\varepsilon}_g + Q_{1t}[\exp(b_{1t} \bar{\varepsilon}_t) - 1]. \quad (7)$$

In Eqs. 6 and 7, $R_{g,t}, H_{g,t}, Q_{ig,t}, b_{ig,t}$ are scalar coefficients to be determined from mechanical tests.

In order to predict the onset of cracking in the samples, a strain-based damage criterion is selected using a scalar damage indicator:

$$D^e = \int H(\tilde{\dot{\varepsilon}}_I) \tilde{\dot{\varepsilon}}_I + H(\tilde{\dot{\varepsilon}}_{II}) \tilde{\dot{\varepsilon}}_{II} + H(\tilde{\dot{\varepsilon}}_{III}) \tilde{\dot{\varepsilon}}_{III} dt, \quad (8)$$

where H denotes the Heaviside function. The three principal strain rate components $\tilde{\dot{\epsilon}}_I$, $\tilde{\dot{\epsilon}}_{II}$, and $\tilde{\dot{\epsilon}}_{III}$, are used to define a damage indicator D^ϵ . For the description of the failure anisotropy, the strain rate components need to be transformed by a linear operator [12]. In the present case, the operator does not alter the deviatoric character of the transformed strain rate tensor $\tilde{\dot{\epsilon}}$:

$$\begin{bmatrix} \tilde{\dot{\epsilon}}_{11} \\ \tilde{\dot{\epsilon}}_{22} \\ \tilde{\dot{\epsilon}}_{33} \\ \tilde{\dot{\epsilon}}_{12} \end{bmatrix} = \frac{1}{9} \begin{bmatrix} 4L_1 + L_2 + L_3 & -2L_1 - 2L_2 + L_3 & -2L_1 + L_2 - 2L_3 & 0 \\ -2L_1 - 2L_2 + L_3 & L_1 + 4L_2 + L_3 & L_1 - 2L_2 - 2L_3 & 0 \\ -2L_1 + L_2 - 2L_3 & L_1 - 2L_2 - 2L_3 & L_1 + L_2 + 4L_3 & 0 \\ 0 & 0 & 0 & 9L_4 \end{bmatrix} \begin{bmatrix} \dot{\epsilon}_{11} \\ \dot{\epsilon}_{22} \\ \dot{\epsilon}_{33} \\ \dot{\epsilon}_{12} \end{bmatrix} \quad (9)$$

with four scalar coefficients L_1 , L_2 , L_3 , and L_4 .

Results

Parameter Calibration

The model parameters of the plasticity model are calibrated using an iterative optimisation procedure. Modified Arcan tests in 0° , 15° , 30° , and 45° configuration [9] with sample orientations along the RD and TD are considered for this purpose. Each test is modelled by FE simulations and the global response is compared to the experimentally obtained twin. By this procedure, the parameters listed in Table 1 are identified. The parameters describing shear components along the sheet thickness remain undetermined and hence are set to unity. Figure 1 shows the deformation–force record for the different configurations of the modified Arcan tests and the respective simulation. Table 1 gives the calibrated parameters.

Table 1 Optimised model parameters for the 2YS model and the failure criterion

Elasticity	$E = 43,000 \text{ MPa}$, $\nu = 0.3$
Glide	$b = 5.65$, $l^{LL} = 1$, $l^{TT} = 0.99$, $l^{SS} = 1.09$, $l^{TL} = 1.10$, $R_g = 116.4 \text{ MPa}$, $H_g = 848 \text{ MPa}$; $Q_{1g} = 58.3 \text{ MPa}$, $Q_{2g} = 116.4 \text{ MPa}$, $b_{1g} = 79.0 \text{ MPa}$, $b_{2g} = 13.3$
Twinning	$k = 0.9$, $a = 7.43$, $m^{LL} = 1.0$, $m^{TT} = 1.0$, $m^{SS} = -2.65$, $m^{LT} = 1.0$, $M^{TL} = -1.0$, $M^{TS} = -1.65$, $M^{SL} = -1.87$, $R_t = 45.0 \text{ MPa}$, $Q_{1t} = 54.4 \text{ MPa}$, $b_{1t} = 180$, $H_t = 1852 \text{ MPa}$
Failure	$L_1 = 4.02$, $L_2 = 5.87$, $L_3 = 1.0$, $L_4 = 2.42$

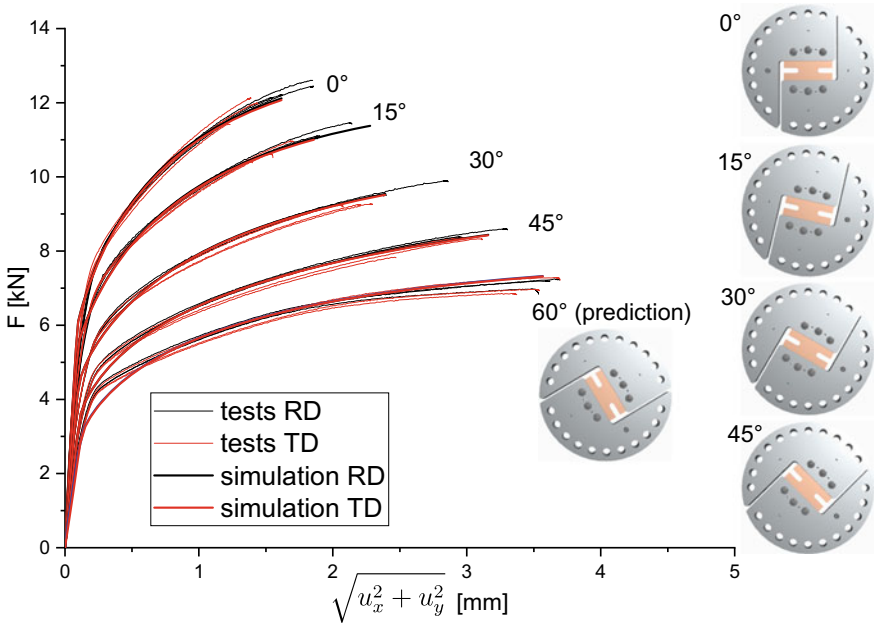


Fig. 1 Force–deformation behaviour of the Arcan samples

Prediction of Three-Point Bending

The model parameters of the 2YS model are validated by three-point bending tests (air bending). A rigid punch of 2 mm radius was symmetrically loading a metal strip of 10 mm width, bending it over cylindrical supports of 5 mm radius. The bending span was 18 mm. In the respective simulations, twofold symmetry was exploited for bending around the RD and TD axes and onefold symmetry for bending around the axis 45° from the RD (DD orientation).

Figure 2 shows the results in terms of global punch force as a function of displacement for the orientations RD, TD, and DD. The fit is excellent over the whole range of deformation and demonstrates the high predictive power of this model. Note that since there is no damage model coupled in the approach, the (early) drop of the load for failed samples is not envisaged to be captured.

Prediction of Crack Initiation

Three features related to failure were apparent during the mechanical tests:

1. Failure is of anisotropic nature, i.e. samples with main loading direction along the TD fail earlier than their counterparts loaded along the RD

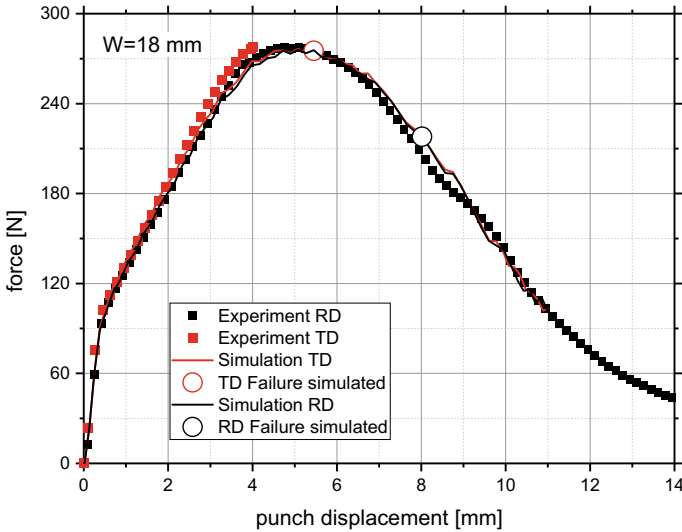


Fig. 2 Results of the three-point bending tests in terms of load vs. deflection; Crack initiation is indicated by symbols

2. With increasing orientation of the Arcan samples, failure is shifted to higher deformation
3. Cracking is initiated at the free surface of the notch; the position of crack initiation varies with the orientation angle.

Since the stress state is uniaxial at the edge of the sample, the selected initiation criterion is not accounting for the stress triaxiality. The parameters introduced in Eqn. [9] were calibrated using the macroscopic failure displacement norm $\sqrt{u_x^2 + u_y^2}$ (see Fig. 1). The results are presented in Fig. 3 together with the standard deviation of the repeated tests for each configuration.

All three features related to crack initiation are met by the simulations: The elevated ductility of samples loaded along the RD, the increase of global deformation with increasing loading angle, and the position of crack initiation of the Arcan samples, see Fig. 4.

It is worth mentioning that the failure criterion is aiming at predicting the onset of failure, i.e. the initiation location and stage of cracking. It is experimentally proven for the modified Arcan tests that crack initiation leads to an unstable crack extension, accompanied by a sudden drop of the external load. Hence, the prediction of the initiation suffices for establishing forming limits. A simulation of crack extension is not required for the assessment of forming operations.

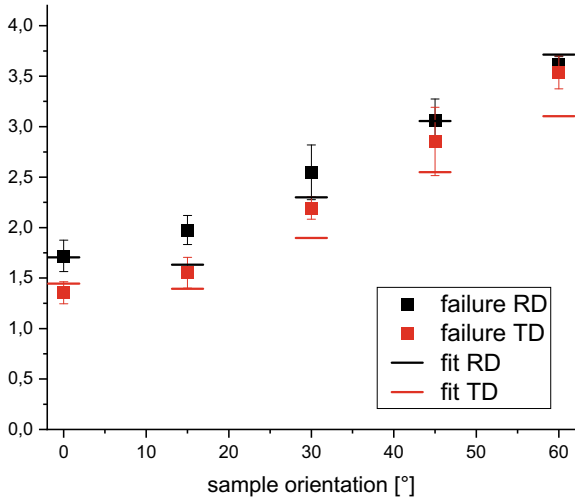


Fig. 3 Performance of the failure calibration in terms of displacement at failure (60° is prediction)

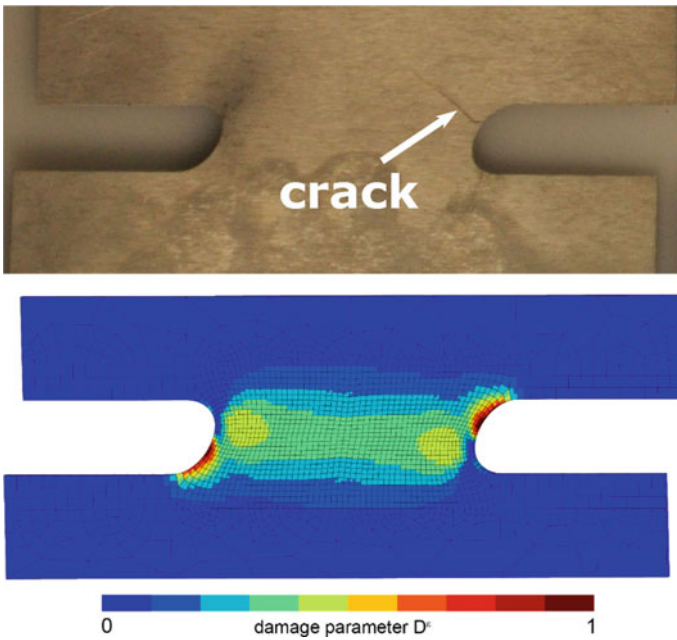


Fig. 4 Location of the crack initiation in case of the 45° TD sample; experiment (top) and damage indicator at the predicted failure load (bottom)

Conclusions and Outlook

The deformation and failure behaviour of a 3rd generation magnesium alloy AZ31 ‘e-form’ is explored by means of mechanical experiments and numerical simulations. In order to carry out a realistic simulation, a comprehensive experiment was established to characterise the material behaviour at room temperature. Using this database, material constitutive equations constituting anisotropy, elastoplastic behaviour with isotropic non-linear hardening was determined. An evolving anisotropy and a tension–compression asymmetry are quantified. While the stress anisotropy is less pronounced compared to other magnesium alloys, the strength differential effect is strong and has to be accounted for in the modelling of inelastic deformation.

A two-yield surface model (2YS) was constituted which allows good prediction of load vs displacement curves obtained from several mechanical tests in tensile and shear modes tests. The predictive power of the two-yield surface model is demonstrated. The model considers both deformation types, dislocation glide and mechanical twinning. This is particularly relevant in bending modes, since twinning is active in the zones undergoing compressive loadings.

A failure model based on the linear transformation of strain rates in the system of orthotropy was applied in order to assess the mechanical tests. It is able to predict the onset of failure, which was experimentally observed to start to form the edge of the Arcan samples. The model’s weakness of underestimating tensile failure along the RD is related to the strain localization in this particular test, see Fig. 5. While in the experiment little diffuse necking is observed (right part of Fig. 5), the simulation predicts localized necking with the maximum intensity of damage in the center of the sample (left part of Fig. 5).

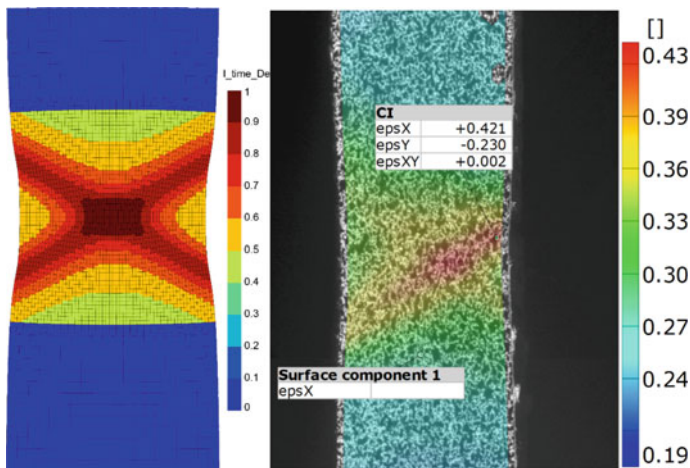


Fig. 5 Damage and strain localisation in a tensile experiment along the RD: damage indicator (left) at the predicted failure point, DIC image with axial logarithmic local strain prior to failure (right)

References

1. Hancock JW, Mackenzie AC (1976) On the mechanisms of ductile failure in high-strength steels subjected to multi-axial stress-states. *J Mech Phys Solids* 24:147–169
2. Mackenzie AC, Hancock JW, Brown DK (1977) On the influence of state of stress on ductile failure initiation in high strength steel. *Eng Fract Mech* 9:167–188
3. Gurson AL (1977) Continuum theory of ductile rupture by void nucleation and growth: part-1 yield criteria and flow rules for porous ductile media. *J Eng Mater Technol* 99:2–15
4. Tvergaard V, Needleman A (1984) Analysis of the cup-cone fracture in round tensile bar. *Acta Metall* 32:157–169
5. Lemaitre J (1985) A continuous damage mechanics model for ductile fracture. *J Eng Mater Technol-Trans Asme* 107:83–89
6. Rousselier G (1987) Ductile fracture models and their potential in local approach of fracture. *Nucl Eng Des* 105:97–111
7. Besson J, Foerch R (1997) Large scale object-oriented finite element code design. *Comput Methods Appl Mech Eng* 142:165–187
8. Steglich D, Tian X, Besson J (2016) Mechanism-based modelling of plastic deformation in magnesium alloys. *Eur J Mech A Solids* 55:289–303
9. Steglich D (2020) Mixed-mode deformation and failure of a magnesium sheet quantified using a modified arcan fixture. *Exp Mech* 60:109–118
10. Barlat F, Lege DJ, Brem JC (1991) A six-component yield function for anisotropic materials. *Int J Plast* 7:693–712
11. Cazacu O, Plunkett B, Barlat F (2006) Orthotropic yield criterion for hexagonal closed packed metals. *Int J Plast* 22:1171–1194
12. Jia Y, Bai Y (2016) Ductile fracture prediction for metal sheets using all-strain-based anisotropic eMMC model. *Int J Mech Sci* 115–116:516–531

Prediction of Necking Initiation in Case of Abrupt Changes in the Loading Direction



R. Norz, N. Manopulo, M. Sigvant, A. R. Chezan, and W. Volk

Abstract FEM simulations are nowadays an integral part of nearly every forming tool development process, especially for the prediction of the overall process feasibility. The traditional forming limit curve (FLC), often fails in delivering a good prediction as many parts fail under non-proportional loading. The Generalized Forming Limit Concept (GLFC) extends the traditional FLC to account for this effect. However, the original GLFC is an isotropic approach and it thus does not account for changes in the loading direction with respect to the rolling direction. In this paper, the functionality of the new 3D-GFLC, which accounts for the mentioned parameter, is demonstrated using a real industrial component. For this purpose, the 3D-GFLC was implemented into the FEM software and validated based on experimental investigations.

Keywords Non-proportional loading · Sheet metal forming · FE-simulation

Introduction

Non-proportional load paths occur in almost every deep-drawn sheet metal part. The prediction of failure after such complex strain paths is not possible in an accurate way when using a linear FLC; therefore, this topic has been the focus of research for many years. Many different approaches have been published. Many approaches are stress-based, e.g. the PEPS-model of Stoughton and Yoon [1], the modified maximum

R. Norz (✉) · W. Volk
Chair of Metal Forming and Casting, Technical University Munich, Walther-Meißner Straße 4,
85748 Garching, Germany
e-mail: roman.norz@utg.de

N. Manopulo
AutoForm Development GmbH, Technoparkstrasse 1, 8005 Zuerich, Suisse

M. Sigvant
Volvo Cars, 81110 Strategy & Concept, 29338 Olofstroem, Sweden

A. R. Chezan
Tata Steel R&D, P.O. Box 10.000, 1970 CA Velsen-Noord, The Netherlands

force criteria of Hora [2], or the method of Yao and Cao using an anisotropic yield function with induced back stress [3]. The reliability and the robustness of these stress-based models strongly depend on the stress–strain relations. Werber et al. [4] have found that the yield locus has an enormous impact on the results and that the Forming Limit Stress Curve (FLSC) is strain path-dependent. The accuracy and the applicability of the FLSC are also dependent on the work-hardening behaviour after pre-forming, due to the fact that the path independence is no longer valid for certain behaviours [5]. To overcome the obstacles of stress-based methods, phenomenological models have been proposed. Using a phenomenological model, Drotleff and Liewald have developed a model based on 36 different tensile tests to calculate FLCs after pre-forming and initial FLCs [6]. Volk et al. [7] also used a phenomenological approach, based on the results of 72 bilinear Nakajima experiments under different pre-forming conditions, the so-called Generalized Forming Limit Concept (GFLC). Those phenomenological models are isotropic approaches. For most sheet metal parts, their accuracy in predicting failure is sufficient. Nevertheless, for strain paths with an abrupt change in loading direction, these models fail to predict failure accurately. Therefore, the GFLC-model has been extended to a 3D-GFLC to cover such very complex strain paths as well [8]. Using a novel experimental setup with a complex strain distribution, the so-called MUC-test by Eder et al. [9], the method was successfully validated. The 3D-GFLC model also requires a database. This database consists of four different pre-forming states with two different pre-forming heights for each investigated rolling direction. The experimental effort for the database is therefore higher than for the GFLC-model. As the database can be scaled within a material class, for example, ferritic steels or dual-phase steels, the experimental effort can be reduced [7].

In this paper, an industrial sheet metal part from Volvo Cars is investigated. The material for this sheet metal part is a ferritic CR4 with high formability. When using FEM tools to predict the producibility of this part, the strains are all below the linear FLC, even when a safety margin (FLC FEM—Input Volvo in Fig. 1) is considered. Therefore, in the simulations, no cracks are predicted in the part. Still, the real part showed cracks after the forming process, see Fig. 1a. The critical strain path is shown in Fig. 1b.

The critical strain path shows an abrupt change in the loading direction after the material has passed the draw bead and the material is pulled into the radius. It seems that only a very reduced formability is left when a change in loading direction of 90° occurs after a plane-strain pre-forming up to $\varepsilon_1 = 0.18$. The initial loading direction is 90° with respect to the initial rolling direction.

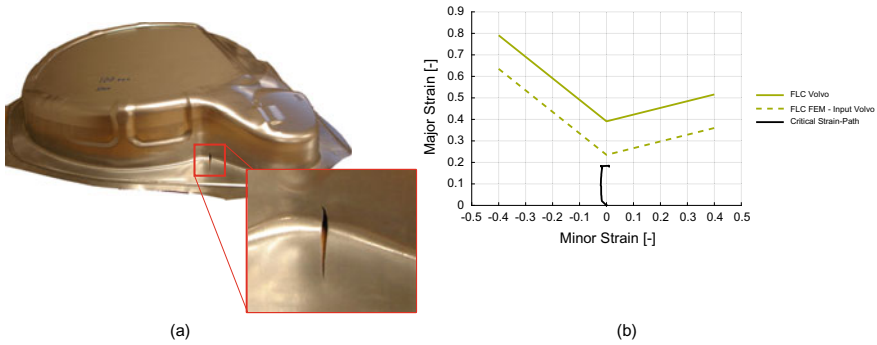


Fig. 1 a Failed part with crack and b the critical strain path in comparison to the linear FLC and the FLC with safety margin

Experimental Setup

In order to recreate the critical strain path in the industrial part, a modified Marciniak tool, developed by Weinschenk and Volk [10] comes into use. This setup has already been successfully used to create the database used in this paper for the 3D-GFLC [8]. To ensure an accurate recreation of the critical strain path, the specimen is numerically optimized. The final geometry as well as the Marciniak tool can be found in Fig. 2. The punch speed was set to a constant value of 15 mm/s. The pre-forming process was done in multiple forming steps, with increasing drawing depth. Before each step, the blank was lubricated with deep drawing oil in order to reduce friction between the blank and the punch. This procedure allows a homogeneously pre-formed area at the center of the specimen. To measure the pre-forming in the critical area, an optical measuring system from GOM is used. From this homogeneously pre-formed area, the Nakajima specimens are cut out, in comparison to the results of the linear FLC, a specimen width of 110 mm is chosen for the plain-strain post-forming step. To show the influence of the change in the loading direction, five specimens with no change

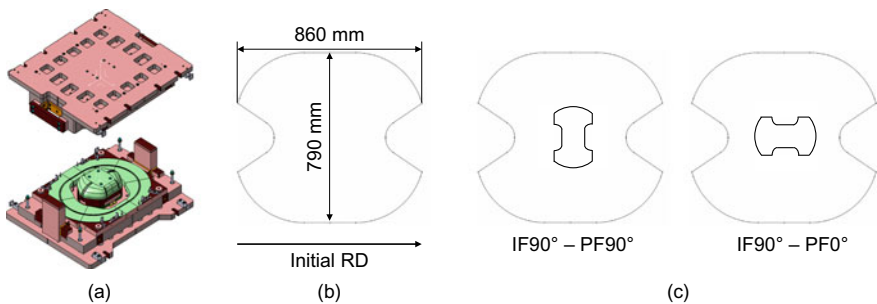


Fig. 2 a Modified Marciniak tool, b specimen for the pre-forming process, c cutting process with for the two investigated load cases

in loading direction, and five specimens with a change in loading direction of 90° are tested. The configuration with the change in loading direction is the same as in the industrial part, recreating the most critical strain path leading to material failure in the real part. The cutting process in order to obtain the pre-formed Nakajima specimens is shown in Fig. 2c.

The Nakajima experiments for the linear FLC as well as the non-proportional Nakajima experiments are conducted on a BUP 1000. The experimental setup is according to ISO12002-2, with a constant punch speed of 1 mm/s. To minimize friction, lubrication in form of a PVC-pad and lubrication paste is adapted. For the strain measurement, an ARAMIS 4 M System with a frame rate of 10 Hz was used. The evaluation of the strains was carried out according to the cross-section method as well as the time-dependent evaluation method (TDEM) according to Volk [11]. In order to enable a statistically valid statement, at least three valid tests per configuration were carried out. Since the GFLC, as well as the 3D-GFLC, require a linear FLC that is well resolved, nine different specimen widths were investigated. In order to determine a possible dependence of the formability on the rolling direction in the initial state, the linear FLC experiments were conducted at 0° and 90° with respect to the initial rolling direction.

Experimental Results

The linear FLC's of the material CR4 show that the rolling direction has almost no influence on the formability of the material. Both orientations show a very high formability, as expected for this material grade. A comparison of the linear FLCs with those of Volvo shows that, despite different evaluation methodologies, the curves are quite similar. The determination of the FLC by Volvo is done by using the method of standard deviations. A more precise description of this method can be found in [12]. The lowest FLC is used by Volvo in their FEM simulations and has a safety margin of $\varepsilon_1 = 0.156$ independent of the minor strain ε_2 . The FLCs assessed by TDEM are above those assessed by the cross-section method, which is expected as the cross-section methods deliver a more conservative result (Fig. 3).

Following the critical strain path of the real part, a plane-strain pre-forming up to $\varepsilon_1 = 0.18$ is required, followed by another plane-strain increment orthogonal to the first increment. To receive valid and reliable results for the post-forming step, a homogeneous pre-forming in the contact area between the Nakajima punch and the blank is required, as well as only a little deviation between the six pre-formed specimens. Figure 4a shows the strain distribution in the critical area. It can be seen, that within the contact area of the punch, marked by a circle with a diameter of 100 mm, the strain is homogeneous. For all six pre-formed specimens, the pre-forming strains are plotted in Fig. 4b. The pre-forming is even below the safety margin FLC of Volvo and shows only a little deviation between the specimens.

The Nakajima experiments with the pre-formed material reveal a strong dependency of the formability on the loading direction. When the loading direction is the

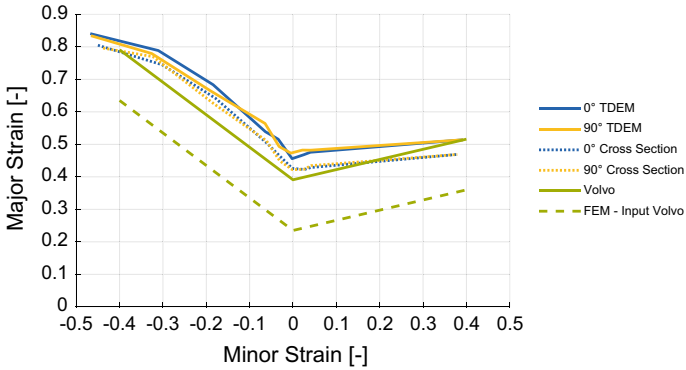


Fig. 3 Linear forming limit curves for CR4 obtained by different evaluation methods

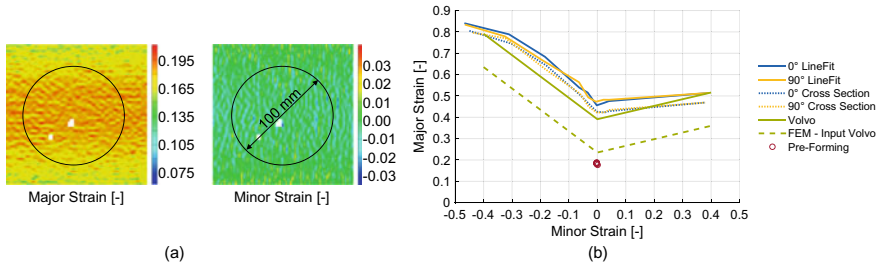


Fig. 4 **a** Major and minor strain distribution in the center of the specimen, **b** pre-forming height in comparison to the linear FLC

same as for the pre-forming (0–0 specimens), the strains are close to those from the initial Nakajima experiments. After a change in loading direction by 90° (0–90 specimens), a significant loss of formability can be observed, see Fig. 5b. This is also visible in the punch travel–force curves, shown in Fig. 5a. Therefore, the results from the industrial part can be recreated with the experimental setup used in this paper.

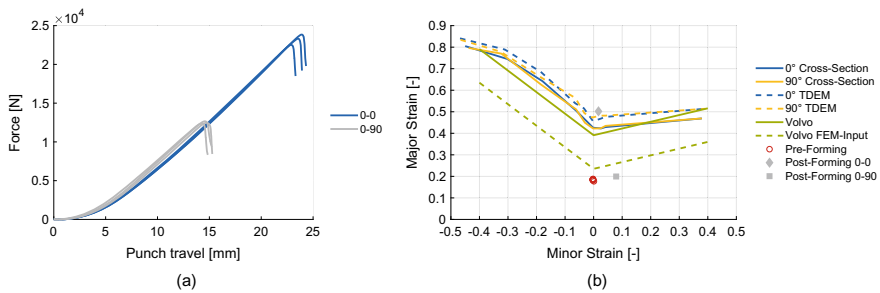


Fig. 5 Punch travel–curves for the 0–0 and 0–90 specimens **(a)** and the failure strains **(b)**

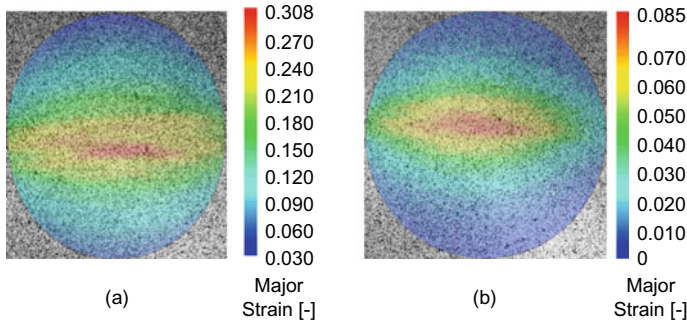


Fig. 6 Major strain distribution at the onset of necking for **a** 0–0 specimens and **b** 0–90 specimens

Also the strains at the onset of necking in Fig. 6 show that, for both specimens, the strain localization has begun. It is also visible that, for the 0–90 specimens, the strains surrounding the necking zone are a lot lower compared to the 0–0 specimens. This indicates that the strain localization starts almost immediately after the beginning of the forming process, leaving most of the specimen almost undeformed. For the 0–0 specimens, the strains are increased over a wider area, leading to a higher punch travel which is possible.

Implementation of the 3D-GFLC into a Commercial FEM-Software

To predict failure after such a complex strain path with an abrupt change in loading direction already during FEM simulations, the 3D-GFLC of Volk et al. [8] is implemented into an FEM software. The AutoForm R10 version allows the implementation of user-defined functionalities via the R&D plug-in. The results of the user-defined functionalities can be plotted in the post-processing and allow continuous monitoring of the results throughout the simulation.

To use this plug-in, the 3D-GFLC is coded in Visual Studio using the programming language C. The code is later compiled into a.dll-file which can be read by AutoForm R10. The user-defined variables can be set as an output parameter in the post-processing menu. Currently, up to 15 user-defined variables can be plotted. The parameters like the material parameters, stresses, and strains are already calculated by AutoForm for each increment and can be used by the user for their user-defined functionalities. It has to be noted that only the current increment can be used for the calculations, therefore, only the values of the variables from the prior time step and the current time step can be used for the calculations. For the 3D-GFLC, the current strain increment, the loading ratio $\beta (\beta = \varepsilon_2/\varepsilon_1)$ as well as the current loading direction angle α of the increment are needed. This angle defines the loading direction between the last and current steps with regard to the initial loading direction.

With this input data, the variable λ , which indicates failure when the value is above 1, can be calculated. The precise description of the calculation can be found in [8]. For this calculation, an experimental database is needed. In this case, the existing database of a ferritic CR300LA-steel is used. The adaption of this database is done by a scaling procedure of the linear FLC of the CR300LA and the CR4. This procedure has already been used by Volk et al. to predict failure for an HC450X based on the experimental results of an HC300X [7]. Nevertheless, this procedure is only valid for materials of the same grade. As in this paper, the steels used for the database, as well as the experiments presented in this paper, are ferritic, this procedure is valid. The experimental database is calculated in a different tool and is manually added to the source code.

During the simulation, the user-defined variables are calculated for each step so that the evolution of the variables can be followed during the whole simulation. In Fig. 7, the failure variable λ from the 3D-GFLC is compared to the failure variables “Linear failure” and “Advanced failure” after the forming process. It can be seen that the currently in AutoForm R10 implemented failure evaluation methods, the linear FLC as well as the GFLC-model, show no risk of failure, even when the FLC with safety margin is used in the FEM simulation. The maximum failure value for the linear FLC is $\lambda = 0.975$ and for the GFLC-model the maximum value is $\lambda = 0.937$. On the other hand, λ shows values above 1 when failure is determined by the 3D-GFLC method and therefore indicates failure in the area where the split occurs in the real part. In the most critical area in the industrial part, a failure value λ of 1.444 is determined.

Nevertheless, it has to be stated that the current implementation shows also false positive areas. This is the cause due to very small strain increments, where the angle

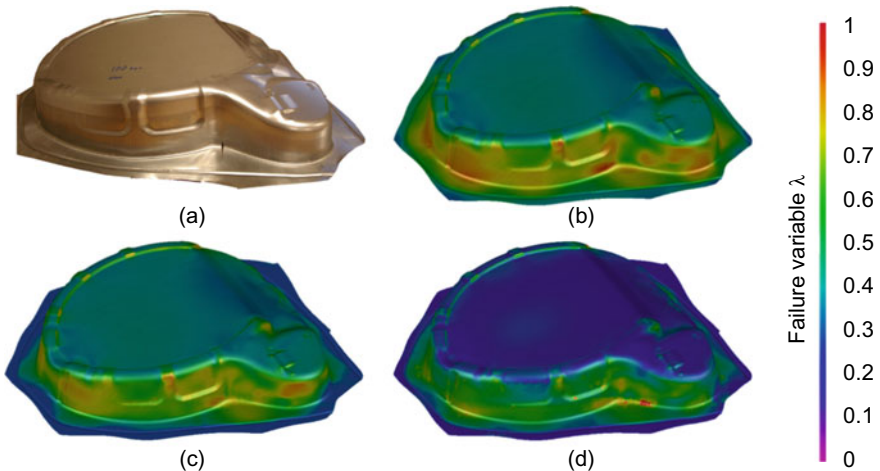


Fig. 7 Failure variable λ for different evaluation methods, **b** linear FLC, **c** GFLC-model, and **d** 3D-GFLC, compared to the real part with crack (**a**)

α is unstable and indicates many changes in the loading direction. An a posteriori valuation of the strain path with the 3D-GFLC is currently not possible. Also, the 3D-GFLC model is only used when the major strain is above 0.1 and a change in loading direction occurs. The investigations used for the database showed that below a certain pre-forming a change in loading direction has a negligible influence on the formability, therefore, the GFLC-model is used for low strains. It is also notable that only angles between 0° and 90° are taken into account. A change in loading direction by for example 135° is handled like a change in loading direction by 45° . Nevertheless, with this example, the functionality of the R&D plug-in is shown as a rather complex model.

Conclusion and Outlook

In this paper, the influence of abrupt changes in the loading direction on the failure behaviour of a mild, ferritic CR4 steel is investigated in an industrial part. The critical strain path in the area where the splits occur in the real part is recreated and is further investigated. It was possible to show the loss of formability after a change in loading direction for the plain-strain pre-formed material. The loss of formability is quite significant even though the pre-forming height is way below the linear FLC.

As such a failure behaviour cannot be predicted by the linear FLC nor the GFLC-model, which are currently implemented in AutoForm R10, the R&D plug-in was used to implement the 3D-GFLC model. By using this method, failure was successfully predicted in the areas where the splits occur in the industrial part. It still has to be noted that there are still some areas which show a false-positive result. The main cause for those areas is the angle α , which indicates a change in loading direction. For small strain increments, this angle is quite unstable and therefore changes quite often. As the remaining formability is very low, already small increases in the strains lead to a significant increase in the failure value. Yet, the functionality of the 3D-GFLC model could be verified for this industrial part.

Acknowledgements The authors would like to thank the German Research Foundation (DFG) for the financial support under grant number 455960756.

References

1. Stoughton TB, Yoon JW (2012) Path independent forming limits in strain and stress spaces. *Int J Solids Struct* 49:3616–3625. <https://doi.org/10.1016/j.ijsolstr.2012.08.004>
2. Hora P, Tong L (2008) Numerical prediction of FLC using the enhanced modified maximum force criterion. In: *Proceedings of the FLC*, pp 31–36
3. Yao H, Cao J (2002) Prediction of forming limit curves using an anisotropic yield function with prestrain induced backstress. *Int J Plast* 18:1013–1038. [https://doi.org/10.1016/S0749-6419\(01\)00022-5](https://doi.org/10.1016/S0749-6419(01)00022-5)

4. Werber A, Liewald M, Nester W, Grünbaum M, Wiegand K, Simon J, Timm J, Hotz W (2013) Assessment of forming limit stress curves as failure criterion for non-proportional forming processes. *Prod Eng Res Devel* 7:213–221. <https://doi.org/10.1007/s11740-013-0446-6>
5. Yoshida K, Suzuki N (2008) Forming limit stresses predicted by phenomenological plasticity theories with anisotropic work-hardening behavior. *Int J Plast* 24:118–139. <https://doi.org/10.1016/j.ijplas.2007.02.008>
6. Drotleff K, Liewald M (2018) Application of an advanced necking criterion for nonlinear strain paths to a complex sheet metal forming component. *IOPConf Ser: Mater Sci Eng* 418:12041. <https://doi.org/10.1088/1757-899X/418/1/012041>
7. Volk W, Hoffmann H, Suh J, Kim J (2012) Failure prediction for nonlinear strain paths in sheet metal forming. *CIRP Ann* 61:259–262. <https://doi.org/10.1016/j.cirp.2012.03.111>
8. Volk W, Gruber M, Norz R (2020) Prediction of limit strains during non-proportional load paths with a change in loading direction. *IOPConf Ser: Mater Sci Eng* 967:12069. <https://doi.org/10.1088/1757-899X/967/1/012069>
9. Eder M, Gruber M, Manopulo N, Volk W (2021) Potentials for material card validation using an innovative tool. *IOPConf Ser: Mater Sci Eng* 1157:12067. <https://doi.org/10.1088/1757-899X/1157/1/012067>
10. Weinschenk A, Volk W (2017) FEA-based development of a new tool for systematic experimental validation of nonlinear strain paths and design of test specimens. *AIP Conference Proceedings* 1896:020009. <https://doi.org/10.1063/1.5007966>
11. Volk W, Hora P (2011) New algorithm for a robust user-independent evaluation of beginning instability for the experimental FLC determination. *Int J Mater Form* 4:339–346. <https://doi.org/10.1007/s12289-010-1012-9>
12. Sigvant M, Mattiasson K, Larsson M (2008) The definition of incipient necking and its impact on experimentally or theoretically determined forming limit curves. In: *Proceedings of the IDDRG*

Strain Rate-Dependent Hardening Behavior of Weld Metal in Laser Welded Blanks with GEN3 AHSS



Minki Kim, Jiahui Gu, and Hyunok Kim

Abstract This paper introduces the effects of the strain rate on the hardening behavior of weld metal in laser welded blank (LWB) with GEN3 AHSS. Mini-tensile specimens were prepared from the LWB to characterize the weld properties. Tensile tests were then performed at strain rates from 0.001 to 0.1/s which are relevant to sheet metal forming. Deformation of the specimen was measured with a digital image correlation (DIC) system to identify strain behavior. Experimental results of the base metal and the weld metal show different hardening behaviors concerning the strain rate. The hardening rate and strain rate sensitivity (SRS) of the base and the weld metals were found to be different from each other. From the calculation of the SRS, changes in the strain rate effect were confirmed. Three different hardening models were used to extrapolate the flow stress of the weld metal for a larger strain.

Keywords Laser welded blank (LWB) · Advanced high-strength steel (AHSS) · Digital image correlation (DIC)

Introduction

The automotive industry has increasingly used laser welded blank (LWB) for the lightweighting of the vehicle body structure. The LWB is fabricated by laser welding of either the same or different sheet metals. The LWB with conventional low-carbon steels is effective for a good quality of products during sheet metal forming processes because the weld and the heat-affected zone (HAZ) are stronger than base metals. However, advanced high-strength steels (AHSS) and generation-three (GEN3) steels show more often fractures on weld or HAZ rather than base metals [1]. Therefore,

M. Kim (✉)

Korea Institute of Industrial Technology (KITECH), Incheon, South Korea

e-mail: mkim@kitech.re.kr

J. Gu · H. Kim

EWI, Columbus, OH 43221, USA

e-mail: hkim@ewi.org

© The Minerals, Metals & Materials Society 2022

K. Inal et al. (eds.), *NUMISHEET 2022*, The Minerals, Metals & Materials Series,

https://doi.org/10.1007/978-3-031-06212-4_57

more research on the material properties of LWB with AHSS and GEN3 steel is needed to find the root cause of this phenomenon.

To characterize the material properties of the LWB, standard tensile tests are normally conducted with dog bone specimens. The difference between tensile tests of the base metal and weld metal is that the dog bone contains the weld zone at the center of the gauge section which is aligned with the transverse direction from the loading direction [2]. The transversely aligned weld of the tensile specimen is proper to obtain the strength of the weld from observation of fracture location. However, a narrow weld seam limits large enough plastic strains to characterize the hardening behavior of the weld metal. To obtain the hardening behavior of the weld metal with a large strain, the tensile test specimen should incorporate the weld line parallel to the axial loading direction. Since the width of the weld line is typically very small for the LWBs, the gauge section of the dog bone includes both the weld and the base [3]. In this case, it is difficult to accurately obtain the stress–strain curve since eccentric load results in non-uniform strain distribution of the weld and tied base metal in the gauge width. Recently, Kim et al. [4] proposed a specimen geometry with the longitudinal weld line at the center of the gauge section to obtain hardening curves with a large strain. The gauge section of the specimen contains the weld metal only. Furthermore, the specimen can be utilized with a conventional universal material testing machine (UTM) rather than a miniature tensile testing machine. Both strain and strain rates of the sheet material vary during sheet metal forming. The limiting-dome-height (LDH) testing is widely used to evaluate the formability and fracture of the LWB in a laboratory environment. When necking starts during the test, the strain rate rapidly increases until a fracture occurs. The hardening curve including the strain-rate effect is expected to improve the accuracy of the finite element method (FEM) simulation to predict necking and failure of the LWB in sheet metal forming. Most studies on tensile properties of AHSS with different strain rates have been conducted with the standard dog bone with a transverse weld line in the gauge section [5, 6].

Based on the literature review, this paper introduces the strain rate-dependent hardening behavior of weld metal for sheet metal forming of LWB. The LWB is the combination of GEN3-980 sheet and DP600 sheet with the same thickness of 1.5 mm. Tensile tests were performed under different strain rate conditions from 0.001 to 0.1/s. The effect of the strain rate on tensile properties is addressed to characterize the weld and the base metals.

Experiments

In this paper, the LWB particularly refers “GEN3-980/DP600” that was laser welded of GEN3-980 and DP600 of the same 1.5 mm thickness. Sub-size dog bone specimens were prepared for the base metals, GEN3-980 and DP600 according to the ASTM-E8. The mini-tensile specimens with the longitudinal weld line were cut using the wire-EDM based on a newly developed specimen design shown in Fig. 1 [4]. A 3D-scan Keyence system was used to measure the dimensions of the machined specimens.

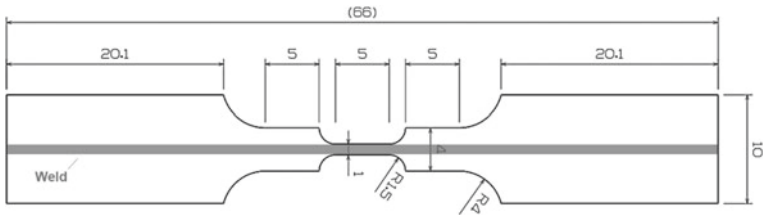


Fig. 1 Mini-tensile specimen for weld metals (unit: mm)

Tensile tests for both base and weld metals were conducted in the Instron 5500 at nominal strain rates of 0.001, 0.01, and 0.1 s⁻¹. Strain data were measured with a 3D digital image correlation (DIC) system, the VIC-3D. Sampling rates of the force and the strain are given in Table 1.

Figure 2 shows the experimental set-up of the mini-weld tensile tests for the weld. All the specimens were spray-painted in the black and white random pattern before testing to measure strain during the test using DIC. The load cell data from the Instron machine and the strain data from DIC were synchronized to establish the hardening curves.

Figure 3 compares stress–strain curves of base metals and weld metal for three different strain rates. Engineering and true stress–strain curves are depicted in

Table 1 Data sampling rates

Strain rate (/s)	Sampling rate (Hz)
0.001	20
0.01	53
0.1	300

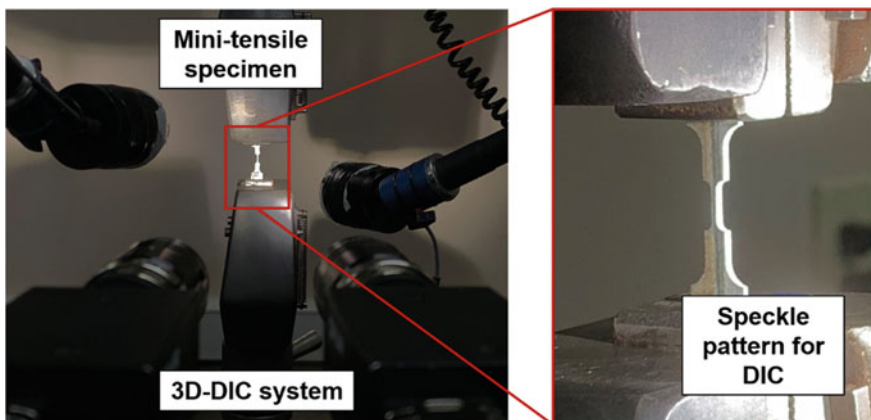


Fig. 2 Experimental set-up for testing of the mini-weld tensile sample

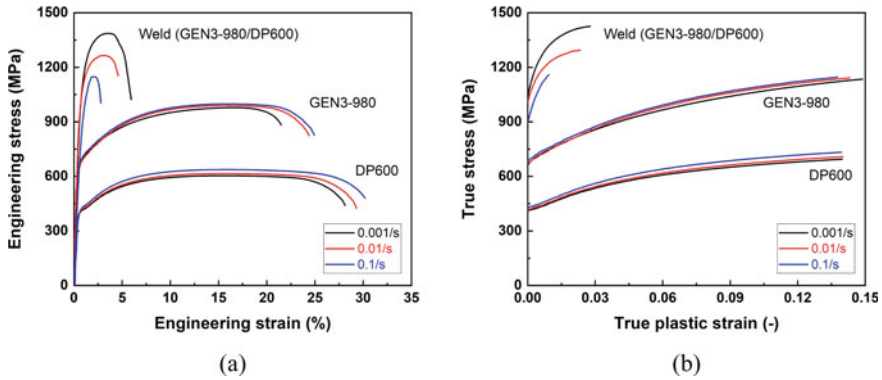


Fig. 3 Uniaxial tensile test results: **a** Engineering stress–strain curves; **b** true stress–strain curves

Figs. 3a, b, respectively. For the engineering stress–strain curves, the base metals show large ductility higher than 20% total elongation (TE) while the weld shows a poor ductility of about 5% TE. In addition, strain hardening of the weld metal is much faster than the one of the base metals. Regarding strain rate sensitivity (SRS) on flow stress, the base metals show a positive SRS that flow stress increases as the strain rate increases. However, the weld metal shows a negative SRS. The true stress–strain curves were obtained from the engineering stress–strain data up to the uniform elongation limit and extrapolating strains larger than the uniform elongation (UE) as shown in Fig. 3b. The UE of the base metals is higher than 12% but the weld metal shows below 3% UE.

Figures 4a, b compare tensile properties of flow stresses and elongations according to the strain rate. The yield stress (YS) is determined by offsetting 0.2% elastic strain and the ultimate tensile strength (UTS) indicates the maximum engineering stress that corresponds to the uniform elongation limit. The YS and UTS of the base metals

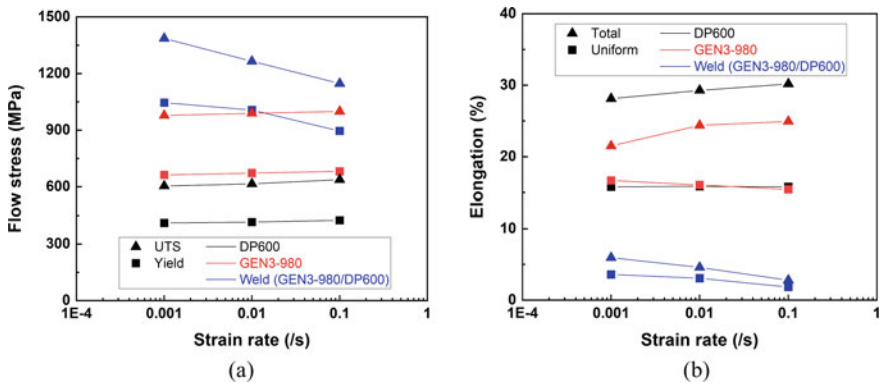


Fig. 4 Tensile properties: **a** Flow stresses; **b** elongations

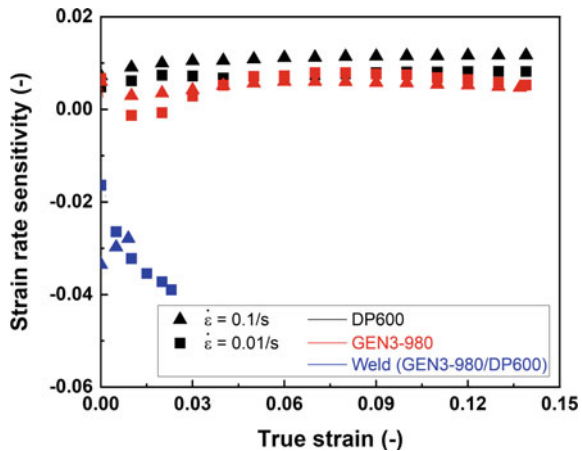
slightly increase as the strain rate increases. However, the flow stress of the weld metal significantly decreases as the strain rate increases. In Fig. 4b, as strain rate increases, both GEN3-980 and DP600 show similarly constant UE, while TE of both base metals slightly increases. However, both the UE and TE of the weld metal are decreased as the strain rate increases.

To observe changes in the SRS regarding the strain, the SRS index (m) is defined by Eq. (1).

$$m = \frac{\log(\sigma/\sigma_0)}{\log(\dot{\epsilon}/\dot{\epsilon}_0)} \Big|_{\epsilon} \tag{1}$$

Figure 5 shows the m-value (SRS) changes for cases of the base and the weld metals. The reference strain rate ($\dot{\epsilon}_0$) was set to 0.001/s. The square and the triangle symbols depict the SRS calculated with the current strain rate ($\dot{\epsilon}$) of 0.01 and 0.1/s, respectively. The SRS of the base metals remains positive regardless of strain rates and shows saturated value as strain increases. However, the SRS of the weld metal remains in negative values and gradually decreases up to the UE. The SRS of the weld metal increases with a 0.1/s strain rate, while it decreases with a 0.01/s strain rate. This means the strain rate hardening behavior of the weld metal is opposite to the one of the base sheet metals and its amounts are depending on the current strain rate and the deformation as well. Therefore, the SRS of the weld metal significantly changes with both strain and strain rate. This weld metal behavior should be considered to improve the material modelling for LWB.

Fig. 5 Strain rate sensitivity of base and weld metals



Evaluation of Hardening Models

To obtain reliable simulation results, it is important to accurately define the material hardening curve with a large strain range. The uniform elongations of the weld metal for 0.001–0.1/s were lower than 5%. This is an insufficient strain range to accurately define the material properties for FE simulations. Therefore, the hardening data were extrapolated using hardening models to obtain the material properties for larger strains over 5%. Three different hardening models were used to define the weld metal hardening behavior. The Swift, Voce, and a modified Hockett–Sherby models are described in Eqs. (2), (3), and (4), respectively.

$$\text{Swift: } \bar{\sigma}(\bar{\epsilon}_p) = C_1(C_2 + \bar{\epsilon}_p)^{C_3} \tag{2}$$

$$\text{Voce: } \bar{\sigma}(\bar{\epsilon}_p) = C_1 + C_2[1 - \exp(-C_3\bar{\epsilon}_p)] \tag{3}$$

$$\text{Modified Hockett – Sherby: } \bar{\sigma}(\bar{\epsilon}_p) = C_1 - C_2 \exp(-C_3\bar{\epsilon}_p^{C_4}) + C_5\bar{\epsilon}_p \tag{4}$$

The hardening models are functions of the equivalent plastic strain ($\bar{\epsilon}_p$). The material coefficients ($C_{1\sim 5}$) are determined by fitting the hardening behavior. Among the various hardening models, these three models are widely used due to their simplicity with a small number of coefficients. The modified Hockett–Sherby contains an additional first-order polynomial term to the Hockett–Sherby model to better describe material behavior for a large strain. Figure 6 shows the fitted results of hardening curves using three selected models and differences between the model and tensile test data for the weld metal. The detailed coefficients of fitted curves are summarized in Table 2. In Fig. 6a, the symbols are the experimental data and the lines are the fitted results. Within the uniform elongation, the three fitted curves are comparable however they were diverged for a large strain range over uniform elongation.

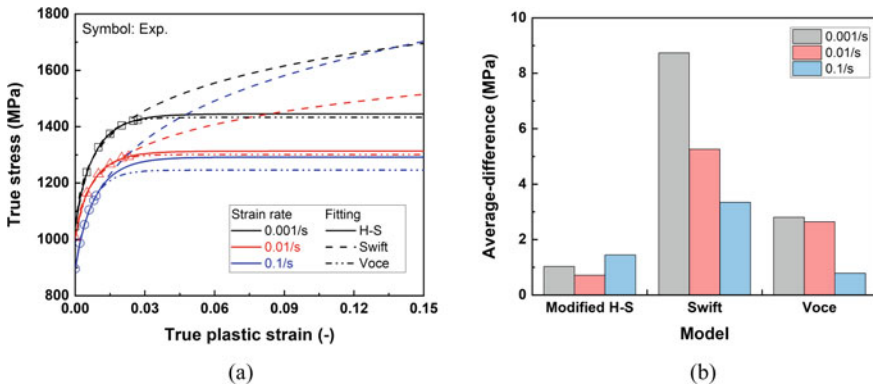


Fig. 6 Model evaluation: **a** Fitting results; **b** model performance

Table 2 Coefficient of fitted curves

	Strain rate (/s)	C_1	C_2	C_3	C_4	C_5
Swift	0.001	2031.9	0.001	0.096	–	–
	0.01	1765.6	0.001	0.081	–	–
	0.1	2249.7	0.002	0.148	–	–
Voce	0.001	1045.3	388.2	130.9	–	–
	0.01	1006.6	294.6	145.2	–	–
	0.1	895.8	350.3	149.1	–	–
Modified Hockett–Sherby	0.001	1445.2	400.0	77.4	0.902	1.0
	0.01	1313.1	306.5	80.5	0.893	1.0
	0.1	1291.9	396.2	84.3	0.928	1.0

Because the Swift model is a power-law type, the amount of hardening is significant as the strain increases. However, the Voce and the modified Hockett–Sherby models show saturated behavior due to their exponential terms in mathematical equations. To evaluate the model performance quantitatively, the average difference ($D_{\dot{\epsilon}}$) in curve fitting of data is defined as Eq. 5.

$$D_{\dot{\epsilon}} = \frac{1}{n} \sum |\bar{\sigma}_{\text{exp}} - \bar{\sigma}_{\text{pred}}| \quad (5)$$

The difference at each strain rate ($D_{\dot{\epsilon}}$) was determined by averaging differences between measured stresses and the model-predicted stresses regarding the number of data (n) for different strain rates. Figure 6b shows differences meaning the fitness for all strain rates of 0.001, 0.01, and 0.1/s. The modified Hockett–Sherby model showed the best match with experimental data for the weld metal at 0.001–0.1/s.

The developed material models for the weld metal should be evaluated in FE simulations of sheet metal forming of the LWB and the correlation with experimental results in the future.

Conclusions

This paper introduces the strain rate-dependent hardening behavior of the LWB of GEN3-980/DP600. The strain rate sensitivity on the stress levels of the weld metal is opposite to the base metals. In addition, the SRS was found to be dependent on strain rate and strain. This implies a need to consider the effects of strain and strain rate in the weld material model. Since the uniform elongation of the weld is relatively small (<5%), the hardening curve can be better described with the modified Hockett–Sherby model. The obtained properties must be validated through comparison of experiment and FE simulation of sheet metal forming tests in a larger strain range.

References

1. Kim H, Gu J, Stubbleski D (2021) Unique formability characteristics of the laser welded blank (LWB) of GEN3 AHSS. In: Great designs in steel (GDIS), Livonia, MI
2. Bandyopadhyay K, Panda SK, Saha, P, Baltazar-Hernandez VH, Zhou YN (2016) Microstructures and failure analyses of DP980 laser welded blanks in formability context. *Mater Sci Eng A* 652:250–263
3. Zhao KM, Chun BK, Lee JK (2001) Finite element analysis of tailor-welded blanks. *Finite Elem Anal Des* 37:117–130
4. Kim M, Gu J, Kim H (2022) A novel tensile testing method to characterize the weld metal properties for laser welded blank (LWB) with AHSS. In: SAE Technical Paper 2022-01-0243. <https://doi.org/10.4271/2022-01-0243>
5. Liu Y, Dong D, Wang L, Chu X, Wang P, Jin M (2015) Strain rate dependent deformation and failure behavior of laser welded DP780 steel joint under dynamic tensile loading. *Mater Sci Eng A* 627:296–305
6. Jia Q, Guo W, Peng P, Li M, Zhu Y, Zou G (2016) Microstructure- and strain rate-dependent tensile behavior of fiber laser-welded DP980 steel join. *J Mater Eng Perform* 25:668–676

The Importance of the Choice of the Yield Criterion in Triaxiality Evaluation for Highly Anisotropic Zirlo Sheets



Felix Rickhey and Seokmoo Hong

Abstract Recent ductile damage models have in common that the fracture strain is a function of stress triaxiality (η), defined as the ratio of mean to equivalent stress. η is usually obtained by tensile testing using different specimen geometries. Since the formulation for the equivalent stress depends on the yield criterion, η values associated with a specimen shape are expected to differ, and deviations to increase with anisotropy. We therefore chose the highly anisotropic zirconium alloy Zirlo for investigating this yield criterion dependence and the evolution of η with strain. Analytical solutions for η are presented for three common yield criteria: von Mises, Hill48, and Barlat89. Using digital image correlation (DIC), we derived local principal strains for three specimen shapes, extracted Lankford coefficients for 0° , 45° , and 90° from uniaxial tensile tests and calculated η . By comparing η -values with analytical solutions for uniaxial tension and showing the yield-criterion dependence for shear and notched specimens, we reveal the significance of, and the problems involved in, the choice of the yield criterion for highly anisotropic sheets.

Keywords Stress triaxiality · Anisotropy · Sheet metal · Digital image correlation · TFD

Introduction

The prediction of failure in sheet metal forming has been a major challenge. However, the variation of necking and fracture strains with stress triaxiality η , along with the Lode parameter, is generally accepted [1]. Under plane-stress conditions, the Lode parameter can be neglected. The stress triaxiality, or just triaxiality, η , is defined as the mean stress normalized by the equivalent stress. It has entered numerous failure criteria, ranging from the traditional McClintock model [2] over the popular Johnson–Cook model [3] to more recent models such as CrachFEM or the generalized incremental stress–strain-dependent damage model (GISSMO) [4]. While the

F. Rickhey · S. Hong (✉)

Department of Automotive and Mechanical Engineering, Kongju National University, Cheonan 31080, Republic of Korea

e-mail: smhong@kongju.ac.kr

© The Minerals, Metals & Materials Society 2022

K. Inal et al. (eds.), *NUMISHEET 2022*, The Minerals, Metals & Materials Series, https://doi.org/10.1007/978-3-031-06212-4_58

635

definition of the mean stress is unambiguous, that of the equivalent stress is not, it varies with the yield criterion. Haufe et al. investigated the influence of the yield criterion, but limited anisotropy to the use of the normal anisotropy and to the Hill48 yield criterion as the only anisotropic yield criterion for analytical solutions [5]. Further investigation is lacking, and the topic has not got the attention it needs. In most cases and for the sake of simplicity, the isotropic von Mises criterion has been applied, and this, however, can lead to inaccuracies of unknown dimension, especially for highly anisotropic material.

In this study, we therefore investigate the influence of the choice of the yield criterion on the resulting triaxiality (η) value. Analytical solutions are derived for three popular yield criteria (von Mises, Hill48, and Barlat89) and compared with experimental results for special cases. As material, the zirconium alloy Zirlo is chosen due to its high degree of anisotropy, which is expected to facilitate highlighting the importance of the choice of the yield criterion. Tensile tests with uniaxial tension (UT), notched (N16), and shear specimens (SH15) are conducted. Strains are obtained on a local level by digital image correlation (DIC). From the principal strains, Lankford values are derived and applied to the yield models. η -values are then calculated for the three yield criteria. Finally, deviations from the analytical solution for UT, for which η is known, and differences between the results for the different yield criteria are discussed.

Theory and Experiment

Yield Model-Dependent Analytical Solutions for Triaxiality η

To find analytical expression for the stress triaxiality η , we first introduce the principal strain ratio β and the principal stress ratio α , which are defined as

$$\beta \equiv \frac{\varepsilon_2}{\varepsilon_1}; \alpha \equiv \frac{\sigma_2}{\sigma_1}, \quad (1)$$

where ε_1 and ε_2 (σ_1 and σ_2) are the major and minor in-plane principal strains (stresses) and η is defined as the ratio of the mean stress σ_m to the equivalent stress $\bar{\sigma}$; assuming plane-stress conditions, we can write

$$\eta = \frac{\sigma_m}{\bar{\sigma}} = \frac{\sigma_1 + \sigma_2}{3\bar{\sigma}}, \quad (2)$$

where σ_1 and σ_2 are the major and minor in-plane principal stresses, respectively. The expression for $\bar{\sigma}$ depends on the chosen yield criterion. Here, we compare three commonly applied yield models: (i) the isotropic von Mises yield criterion; (ii) the anisotropic Hill48 yield criterion; and (iii) the anisotropic Barlat89 yield criterion.

Plane stress conditions, monotonic loading, and associated flow are assumed. For the sake of brevity, details on the derivation are omitted. Also note that for the cases analyzed herein ($\eta \geq 0$), the maximum principal stress is always positive.

Von Mises Yield Criterion

The von Mises yield criterion can be expressed as

$$\bar{\sigma} = |\sigma_1| \sqrt{1 - \alpha + \alpha^2}. \tag{3}$$

Applying the associated flow rule ($d\varepsilon_i/d\lambda = \partial\bar{\sigma}/\partial\sigma_i$), where λ is the plastic multiplier and $i = 1, 2$, we eventually arrive at

$$\eta = \frac{1 + \alpha}{3\sqrt{1 - \alpha + \alpha^2}} \text{sign}(\sigma_1) = \frac{\beta + 1}{\sqrt{3}\sqrt{1 + \beta + \beta^2}} \text{sign}(\sigma_1). \tag{4}$$

Hill48 Yield Criterion

For the Hill48 yield criterion, the equivalent stress becomes

$$\bar{\sigma} = |\sigma_1| \sqrt{1 - \frac{2r_0}{1 + r_0}\alpha + \frac{r_0(1 + r_{90})}{r_{90}(1 + r_0)}\alpha^2} \tag{5}$$

where r_0 and r_{90} are the Lankford coefficients from uniaxial tension tests with sheet specimens, whose axis is parallel and transverse to the rolling direction ($\theta = 0^\circ$ and 90° orientations), respectively.

$$\eta = \frac{1 + \alpha}{3\sqrt{1 - \frac{2r_0}{1+r_0}\alpha + \frac{r_0(1+r_{90})}{r_{90}(1+r_0)}\alpha^2}} \text{sign}(\sigma_1); \quad \alpha = \frac{\beta \frac{1+r_0}{r_0} + 1}{\frac{1+r_{90}}{r_{90}} + \beta}. \tag{6}$$

Barlat89 Yield Criterion

The equivalent stress for the Barlat89 (B89) yield criterion can be expressed as follows:

$$\begin{aligned} \bar{\sigma} &= \frac{1}{2^{1/m}} [a|K_1 + K_2|^m + a|K_1 - K_2|^m + c|K_2|^m]^{1/m} \\ K_1 &= \frac{\sigma_x + h\sigma_y}{2}; \quad K_2 = \sqrt{\left(\frac{\sigma_x - h\sigma_y}{2}\right)^2 + p^2\sigma_{xy}^2} \\ a &= 2 - c = 2 - 2\sqrt{\frac{r_0}{1+r_0} \frac{r_{90}}{1+r_{90}}}; \quad h = \sqrt{\frac{r_0}{1+r_0} \frac{1+r_{90}}{r_{90}}}, \\ m &> 0, \in \mathbb{N}; \quad a, p, h > 0 \text{ (isotr. = 1)}; \quad a < 2 \end{aligned} \tag{7}$$

where K_1 and K_2 denote stress invariants and $a = 2 - c$, h and p are material coefficients. The exponent m depends on the microstructure; we use $m = 8$, although the authors are aware that this may not be the ideal choice for HCP structures. Since shear stresses do not occur in the regions of interest, which could be confirmed by finite element analysis, the term involving p can be neglected. For η , we obtain

$$\eta(\alpha) = \frac{2^{1/m}}{3} \frac{1 + \alpha}{[a + a(h\alpha)^m + (2 - a)|1 - h\alpha|^m]^{1/m}} \text{sign}(\sigma_1)$$

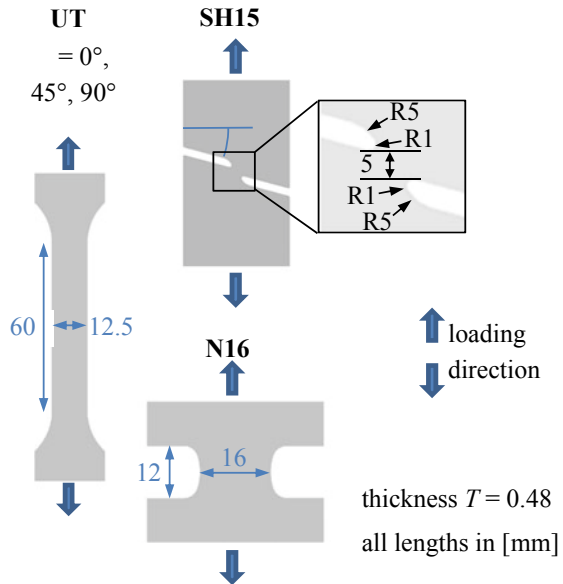
$$\beta(\alpha) = h \frac{(h\alpha)^{m-1} - [\text{sign}(1 - h\alpha)]^m \frac{2-a}{a} \frac{\sigma_1^m}{|\sigma_1|^m} (1 - h\alpha)^{m-1}}{1 + [\text{sign}(1 - h\alpha)]^m \frac{2-a}{a} \frac{\sigma_1^m}{|\sigma_1|^m} (1 - h\alpha)^{m-1}}$$
(8)

Note that for the Barlat89 yield criterion, an implicit method is required to obtain η from β .

Experiment

Tensile testing was conducted to analyze the evolution of η . The specimen shapes shown in Fig. 1 were used to induce different loading conditions in the non-negative η -region. Digital image correlation (DIC) was employed to determine the strains in the specimen centers. To do so, a speckled pattern was sprayed onto the specimen surface; the irregular pattern was then recorded by a high-speed camera with frame

Fig. 1 Specimen geometries



rates of 25 and 100 Hz; and the images were then converted to displacement and strain fields using GOM Aramis Professional 2018 [6]. The test velocity was set to 5 mm/min (UT) and 3 mm/min (others). Each test was performed four times (twice with 25 Hz and twice with 100 Hz).

Results and Discussion

Uniaxial Tension (UT)

From uniaxial tension tests, we first determine the Lankford coefficients (width-to-thickness strain ratio $r_\theta = \varepsilon_W / \varepsilon_T$) for the $\theta = 0^\circ$ and 90° orientations. Local strain values are used for this purpose. Lankford coefficients are assumed to be constant for the region up to maximum load F_{max} , which coincides with necking initiation. We obtain $r_0 = 5.159$ and $r_{90} = 6.776$.

The same strain values are then used to calculate η based on the equations presented in Sect. 2.1. The evolution of η with major strain ε_1 is plotted in Fig. 2. The curves were smoothed by considering the average over ten consecutive values. The vertical line annotated by F_{max} gives the point of incipient necking. The influence of the choice of the yield criterion becomes apparent instantly. Applying the von Mises criterion, we obtain η -values that are far below the theoretical value of $1/3$ (approximately 0.1 for all of the three orientations). Considering anisotropy through the Hill48 or the Barlat89 criteria, experimental values come much closer to $1/3$; the Barlat89 criterion, however, gives the best results for all θ ; η is close to $1/3$, and further remains more or less constant up to fracture (the latter applies also to the von Mises criterion), indicating that $m = 8$ is an appropriate choice.

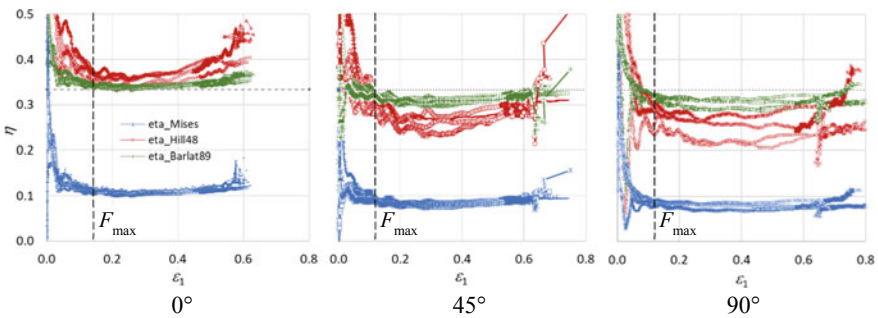


Fig. 2 Evolution of η with ε_1 in uniaxial tension ($\theta = 0, 45^\circ, 90^\circ$)

Notched and Shear Specimens

The same was then performed for the N16 and SH15 specimens. $\eta - \varepsilon_1$ plots are shown in Fig. 3. For the N16 specimens, we find that, as was the case for UT, the curves for the von Mises and Barlat89 yield criteria are nearly horizontal (when neglecting the low-strain region, where fluctuation is inevitable), while the Hill48 curve shows some increase towards fracture. We arrive at approximately $\eta = 0.2$ (von Mises), 0.41 (Barlat89), and 0.65 (Hill48, around necking point). For the SH15 specimen, it is found that high resolution is required for accurate strain evaluation; results for 100 Hz are therefore excluded here. While all curves approach an approximately constant η -value, values vary significantly with the definition of $\bar{\sigma}$ (von Mises, 0.066; Hill48, 0.18; Barlat89, 0.28). It is to note that for near-pure shear conditions ($\beta = -1$), the application of the Barlat89 model can become problematic for high m because of the steep slope $d\eta/d\beta$ in the region around $\beta = -1$; consequently, small changes in β will lead to high changes of η .

Summary and Concluding Remarks

In this study, we investigated how the choice of the yield criterion affects the value of η , which is an important parameter in failure prediction. It was highlighted that η becomes strongly yield criterion dependent for the highly anisotropic sheet metal Zirlo. The η -value associated with a certain specimen shape is thus not universal, and it, as well as the TFD, should be accompanied by the yield criterion. Further, the η -curve should remain on a constant level up to fracture. This criterion was shown to be met by the Barlat89 yield criterion, which further gives the best agreement with the theoretical value for UT. The von Mises criterion clearly underestimates η for UT and the Hill48 criterion tends to rise towards fracture. Of the yield criteria

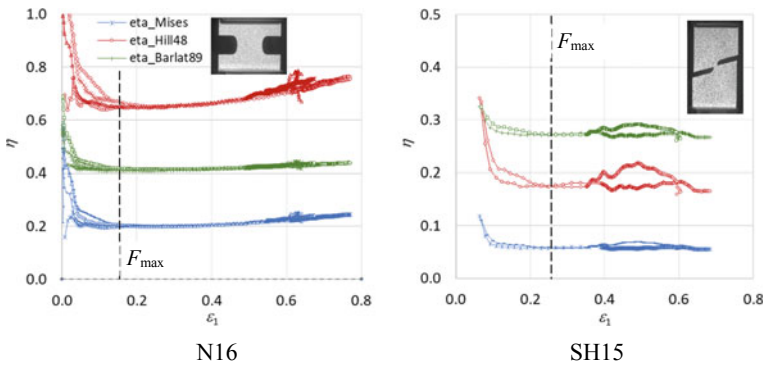


Fig. 3 Evolution of η with ε_1 for N16 and SH15 specimens

investigated here, the Barlat89 model is therefore recommended. With the specimen shapes used in this study, the $\eta = 0$ region associated with the Barlat89 yield criterion, however, could not be covered. Due to the high sensitivity in the $\beta = -1$ region, the analysis of the shear region thus remains a challenge and a specimen geometry that allows extremely accurate strain measurement will be necessary to measure the failure strain in shear.

References

1. Wierzbicki T, Bao Y, Lee YW, Bai Y (2005) Calibration and evaluation of seven fracture models. *Int J Mech Sci* 47:719–743
2. McClintock FA (1968) A criterion for ductile fracture by the growth of holes. *J Appl Mech* 35(2):363–371
3. Johnson GR, Cook WH (1985) Fracture characteristics of three metals subjected to various strains, strain rates, temperatures and pressures. *Eng Fract Mech* 21:31–48
4. Neukamm F, Feucht M, Haufe A (2008) Consistent damage modelling in the process chain of forming to crashworthiness simulations. *LS-DYNA Anwenderforum* 30:11–20
5. Andrade F, Conde S, Feucht M, Helbig M and Haufe A (2019) Estimation of stress triaxiality from optically measured strain fields. In: 12th European LS-DYNA Conference 2019, Koblenz, Germany
6. ARAMIS (2018) Manual aramis professional 2018. GOM-Gesellschaft für Optische Messtechnik mbH, Braunschweig, Germany

Part VIII
Modelling of Friction

A Numerical Study of Local Elastic Tool Deformation in Sheet Metal Forming Simulation



Mats Larsson and Daniel Wiklund

Abstract Dies in sheet metal forming simulation are commonly modeled as rigid, although they are elastic. The influence of elastic response in the dies can be split into two types, global and local deformation. Local deformation occurs where large pressure in the tool prevails typically in the die radii. A numerical study on local elastic tool deformation was performed. Three different blank materials and three tool materials were used. The geometry was from the FTF 2015 conference, triangle die. The blank was modeled with the same material model, and a simple failure criterion as a reference marker was introduced. An important result from the study was: The draw depth difference for the chosen evaluating condition between rigid tools and elastic tools was in the region 5–12.5% deeper using elastic tools.

Keywords Sheet metal forming simulation · Elastic tools · Finite element analysis

Introduction

Sheet metal forming simulation is in many ways a mature tool for developing sheet metal parts to be. Improvements have to be made. The common usage of rigid tool surfaces is of course beneficial from several points of view, easy preprocessing, and low computational time. The increasing use of high-strength materials makes the assumption of rigid tools inadequate. Switching from rigid tools to elastic tool material by the use of solid elements is addressed herein. With this transition, it follows much more complex preprocessing and demands for additional computer resources. The tool deformation is divided into two separate characteristics: (1) global stiffness and (2) local deformation. Tool deformation based on global stiffness is spring behaviour that requires a relatively coarse finite element mesh to correctly capture tool deformation. A typical example are dies for a tailgate to a sedan automobile. The

M. Larsson (✉)

University West, Department of Engineering Science Trollhättan, Trollhättan, Sweden
e-mail: mats.larsson@hv.se

D. Wiklund

RISE Research Institutes of Sweden, Department of Manufacturing Processes, Mölndal, Sweden

V-shape for such panels generates issues on how to design the dies that are designed with a big enough cross section to prohibit the die yawns. Global stiffness type of problems has been addressed successfully in [1–3]. The second characteristic, local deformation, is typically found at die radii, and the higher the interface pressure, the more tool deformation is expected [4]. To study local deformation behaviour using elastic tools versus rigid ones, a slightly extended model was established based on the benchmark example used at the FTF conference in 2015 [5]. The extension made was that two dies were used with two different die radii 3 and 6 mm, respectively. For the computations, the commercial software LS-DYNA was used. Attempts to reduce the number of degrees of freedom as in [6] have not been made. Preprocessing issues on the usage of hexahedrons versus tetrahedrons, mesh densities, and gradients to receive a minimum number of elements in the elastic tools is intentionally left out in this paper, though it is a very important issue for a successful implementation of elastic tools in industry.

The Finite Element Model

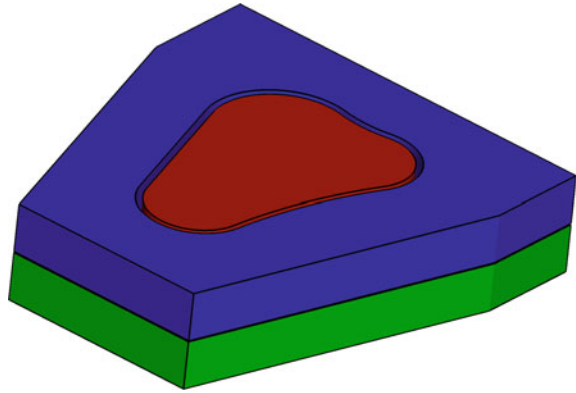
Model Geometry

The blank is modeled with 168349 quadratic fully integrated shell elements, type 16 in LS-DYNA [7] with a typical element length of 0.65 mm. The tools, punch, die, and blankholder are modeled with fully integrated S/R solid elements [8] with a typical element length of 0.75 mm in the interface surfaces between the blank and tool parts, detailed data about the number of elements is given in Table 1. Figure 1 shows the tool finite element model, the height for each individual part is 40 mm. The contact definition used between the blank and the different tool parts is the Mortar contact formulation. Coulumb friction was used and a simple failure criterion based on plastic strain was used. This failure criterion should be interpreted as cut-off criterion, so the different tool geometries and materials for the different blank materials can be

Table 1 Number of solid elements for the tools

	Elastic	Rigid	Total
Punch	779820	21627	801447
Die R3	1057251	42263	1099514
Blankholder R3	988975	39559	1028534
Die R6	1058603	42263	1100866
Blankholder R6	921375	36855	958230
In total: tools R3	2929495		
In total: tools R6	2860543		

Fig. 1 Punch, Blankholder, and Die



compared. The definition of failure herein is the last state without any visible crack in the blank. No mass scaling or adaptivity was used. Figure 2 shows the position in the model where the section cut is made. The finite element mesh of the die in this cut is shown in Fig. 3. The blankholder has exactly the same mesh as the die as it is reflected from the die, only the die radius area is deleted from the blankholder. The distance between the die and blankholder was kept constant.

Fig. 2 Punch, blankholder, and die

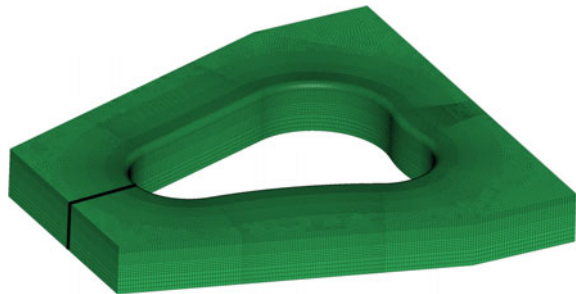
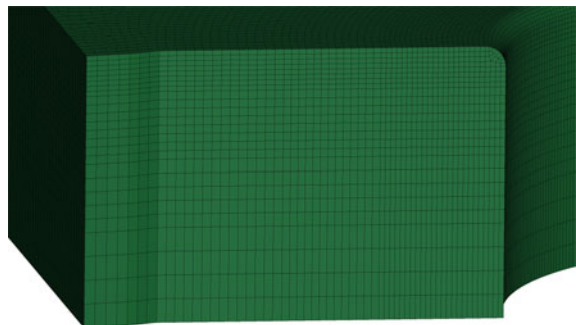


Fig. 3 Snittet



Blank and Tools Materialdata

Three different blank materials are studied a high-strength stainless steel, H800, an isotropic medium-strength steel, HC260, and an aluminium material, AC200V3. The blank materials are modeled with the Barlat2000 material model. The stress–strain curves and the anisotropic coefficients are shown in Fig. 4. The strain-hardening and the yield stresses are very different between the blank materials used, the resulting loading on the tools is therefore expected to be significantly different. Apart from rigid tools, the tool material is either steel or nodular iron. The only difference between the elastic tool materials is the Youngs modulus; $E_{\text{steel}} = 2 \cdot E_{\text{nodular iron}}$. The question is: Which impact has this on the tool deformation?

Results

Draw Depth at Failure

In Table 2 is shown the draw depth for the different blank materials with respect to the die materials and the two different die radii. A significant increase in draw depth is identified when comparing the models with rigid dies to realistic die materials, though there is a larger draw depth difference for the die radius R6 than R3. This is due to different draw-in behaviors and thinning/thickening distributions of the blank material. To be able to draw further conclusions, there is a need to introduce virtual spotting in the model. The results from the table are used to define the evaluation states in the following.

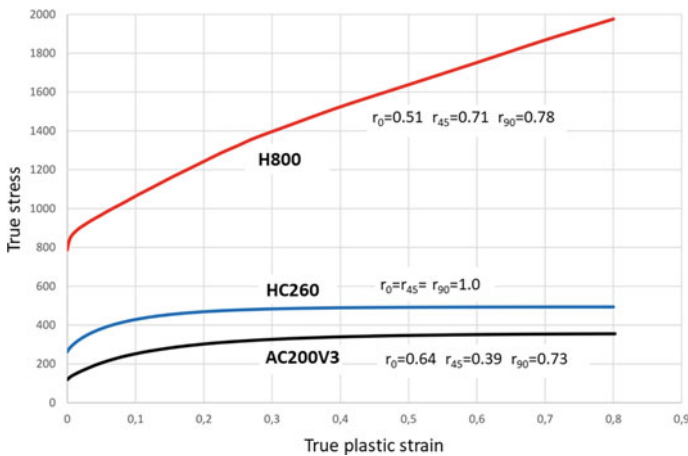


Fig. 4 Stress–strain curves

Table 2 Draw depth at failure (mm)

Die mtrl & Die radius	AC200V3	Blank material HC260	H800
Rigid & R3	31.3	17.0	21.2
Steel & R3	32.8	17.8	23.1
Nodular iron & R3	32.8	19.0	23.1
Rigid & R6	32.3	19.8	27.5
Steel & R6	33.8	21.0	29.5
Nodular iron & R6	34.8	21.9	31.0

Interface Pressure

The pressure distribution for the model with blank material H800 using tool material nodular iron and die radius R3 is shown in Fig. 5. Two states are shown with 11 mm and 22 mm draw depths, respectively. The interface pressure acting on the die radius is established at a high level early on in the process. The legend shows that the pressure is well above 250 MPa in the die radius. Then, the conclusion is drawn that the die deformation is significant throughout the whole stroke. The figure also shows a pressure increase on the flat blank surface due to the local thickening when the draw depth increases, generally because of the specific press process at hand and virtual spotting should be utilized to optimize the process, this will be ad/dressed in a forthcoming paper.

Local Tool Deformation

In Fig. 6, the z-displacement of one die configuration, nodular iron, and die radius R3 are shown together with the blank outline at state 0 and state “failure”, respectively. The blank material was H800. The deformation is significantly more than 0.03 mm

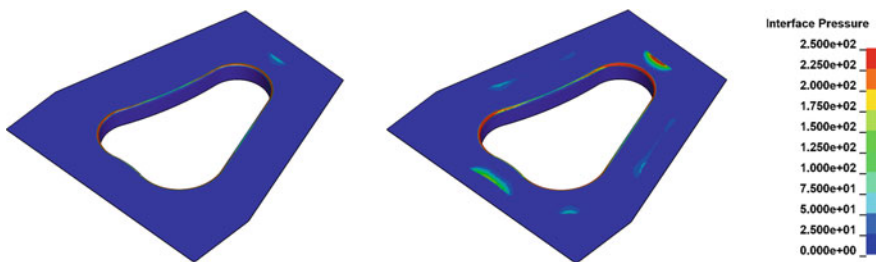
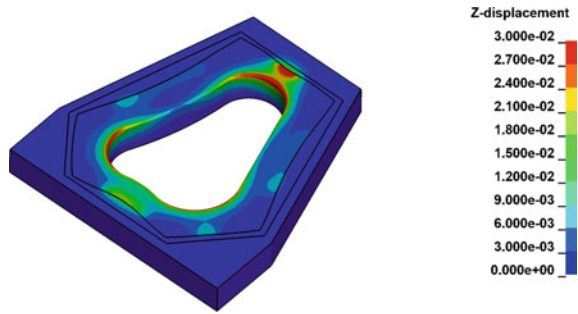


Fig. 5 Pressure distribution cast-iron die

Fig. 6 z-displacement nodular iron die



with a maximum value of 0.039 mm. At the far end of the die, there is a substantial deformation of the tool. This is due to the drawing and local thickening of the blank, this results in a local large interface pressure. Local morphing of the die and blankholder geometries based on the amount of local deformation will eliminate this effect, virtual compensation of thickness increases, similar to common knowledge when compensating for springback.

The local elastic deformation pattern of the die and blankholder depicted in Fig. 7, blank material H800, shows that the local elastic deformation is not only a thin layer phenomenon at the tool surface but it has a significant distribution in depth, z-direction, also. The minimum to maximum values are from 0 to 0.032 mm in steps of 0.002 mm. For the nodular iron tool material, it is concluded that 30 mm of the tool thickness of 40 mm has a significant amount of local elastic deformation. For the steel tool setup, the corresponding distance is 20 mm. The maximum elastic deformation found in die radius is 40% of the maximum increase of the blank thickness for the nodular iron tools and 25% for the steel tools. In Figs. 8 and 9, the minimum to maximum values are from 0 to 0.012 mm in steps of 0.002 mm. The corresponding tool readings for the blank material AC200V3 were 20 mm for nodular iron tools and 10 mm for steel tools and the percentage readings were 17.5% and 8.5%, respectively. Finally, for the blank material HC260, the readings were 30 mm and 20 mm and the percentage figures were 27.5% and 15%, respectively (Table 3).

Table 3 Maximum resultant displacement in section cut (mm)

Die mtrl & Die radius	AC200V3	Blank material HC260	H800
Nodular iron & R6	0.018	0.018	0.057
Nodular iron & R3	0.016	0.015	0.038
Steel & R6	0.009	0.009	0.029
Steel & R3	0.008	0.008	0.021

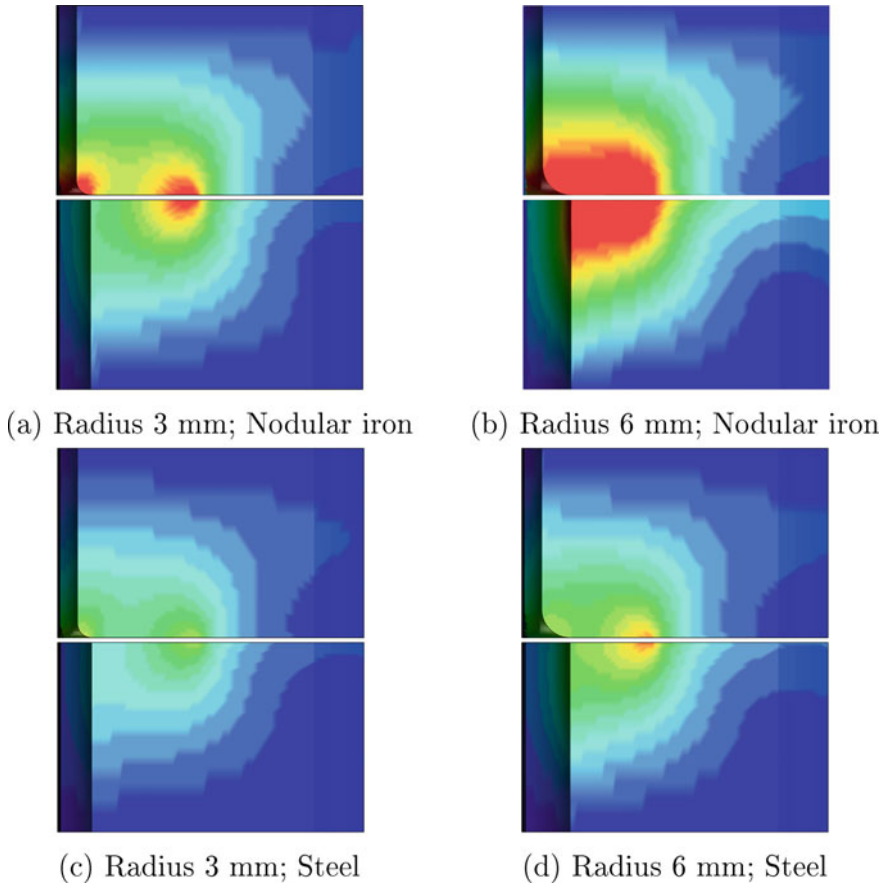


Fig. 7 H800, tool deformation, legend 0–0.032 mm

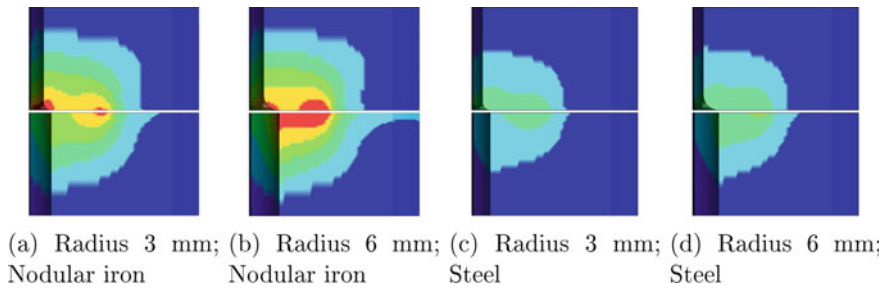
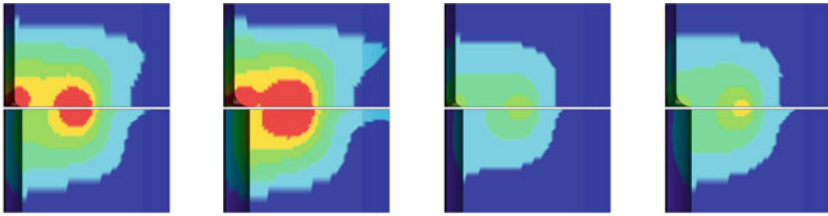


Fig. 8 AC200V3, tool deformation, legend 0–0.012 mm



(a) Radius 3 mm; (b) Radius 6 mm; (c) Radius 3 mm; (d) Radius 6 mm;
Nodular iron Nodular iron Steel Steel

Fig. 9 HC260, tool deformation, legend 0–0.012 mm

These observations indicate a big influence on tool deformation when high-strength materials are to be stamped. But also, much softer blank materials show a significant amount of tool deformation. The results suggest that local tool deformation has potential to improve the precision in sheet metal forming simulation.

Conclusion

It is concluded based on this numerical study that, to include elastic tools in sheet metal forming simulation, one has to create models that account for the two different modes of deformation, thus both the global stiffness and the local deformation behaviour. The draw depth difference for the chosen evaluating condition between rigid tools and elastic tools was in the region 5–12.5% deeper using elastic tools (dependent on die radius and nodular iron or steel in the tools).

Discussion

In order to be able to implement a complete virtual tryout process where elastic tools are used there is a need to account for both global stiffness (deformation) and local deformation of the tools. An initial computer run will show where the blank will increase its thickness locally, a thickness compensation method has to be implemented. Such a procedure is analogous to how springback compensation is performed, preprocessing morphing of the initial die surfaces should be made. As the solid modeling of the tools, there is a need to be able to create such models automatically or at least with a minimum of manual work. A development of preprocessors, so it is possible to generate solid meshes, only hexahedrons or tetrahedrons or a mix of them, so it is possible to define gradients with more degrees of freedom to let the mesh grow in several directions simultaneously so meshes with a minimum number of elements can be created. Here, the section cut was divided into

30 subareas to create the mesh shown. Still, the models will become big therefore demands for computer power will be larger than if rigid tools are used so methods to reduce computer demands are welcomed. To fully utilize the use of elastic tools, it is recommended to explore the possibilities that advanced variable friction models have to offer.

References

1. Pilthammar J, Sigvant M, Kao-Walter S (2018) Introduction of elastic deformation in sheet forming simulations. *Int J Solids Struct* 151:76–90. <https://doi.org/10.1016/j.ijsolstr.2017.05.29>
2. Vrolijk M, Ogawa T, Camanho A, Biasutti M, Lorenz D (2018) A study with ESI PAM-STAMP registered on the influence of tool deformation on final part quality during a forming process. *AIP Conf Proc* 1960:160029. <https://doi.org/10.1063/1.5035055>
3. Penter L, Ihlenfeldt S, Pierschel N (2018) Compensation for tool deformation and expansion in virtual try-outs of hot stamping tools. In: Proceedings of the 37th annual conference international deep drawing research group of IOP conference series: material science and engineering, vol 418, p 012012. <https://doi.org/10.1088/1757-899X/418/1/012012>
4. Chen J, Dongkai X, Xia G, Li X, Chen J, Zhang J, Yan W, Li Y (2013) Geometric compensation for automotive stamping die design integrating structure deflection and blank thinning. *Int J Adv Manuf Technol* 66:1449–1456. <https://doi.org/10.1007/s00170-012-4422-7>
5. Daimler AG (2015) Problem 3: Failure Prediction Benchmark—Triangle Die. Advanced constitutive models in sheet metal forming. In: Hora P (ed) 8th forming technology forum Zurich 2015. Institute of Virtual Manufacturing, ETH Zurich, Switzerland
6. Haufe A, Roll K, Bogon P (2008) Sheet metal forming simulation with elastic tools in LS-Dyna. In: Proceedings of the Numisheet 2008, Interlaken, Switzerland
7. LSTC (2018) LS-DYNA keyword user's manual, vol I, LS-DYNA R11. <http://www.lstc.com>
8. LSTC (2019) LS-DYNA theory manual, LS-DYNA Dev. <http://www.lstc.com>

Analysis and Evaluation of the Clamping Force on the Tool Surface During the Blanking Process



Philipp Schumann , Daniel M. Martin , Christian Kubik ,
Timo Schneider, and Peter Groche 

Abstract Blanking is one of the most important processes for manufacturing sheet metal parts with complex geometry in high precision. Abrasive wear of the cutting edge and adhesive wear of the lateral surface of the punch as a result of the high sliding speed and local pressure have a decisive influence on the tool life. In addition to the forces in the cutting phase, the clamping force by the punched sheet during punch withdraw has a significant influence on the wear on the lateral surface. The FE simulation used in this work enables an estimation of the tribological stress collective in all relevant process phases. The model is validated using experimental investigations on a test tool with different punch wear conditions and cutting parameters. Detailed parameter variations are then carried out to investigate the influences of different process parameters on the load of the tool and the resulting geometry.

Keywords Blanking · Clamping force · Friction · Damage model

Introduction and Motivation

Initial Situation

Blanking is one of the most important industrial processes for separating defined component geometries from sheet metal. The product quality of a component depends mainly on the dimensional accuracy of the cutting line and the quality of the cut surface. On the one hand, material properties such as yield strength and sheet thickness, on the other hand, process parameters such as cutting-edge radius and clearance have a significant influence on the quality of the cut surface. Tool wear changes some of these process parameters [1]. Damage to the punch is caused by high contact normal stresses, relative movement (sliding), and friction between the contacting tool sur-

P. Schumann (✉) · D. M. Martin · C. Kubik · T. Schneider · P. Groche
Technische Universität Darmstadt, Institute for Production Engineering and Forming Machines,
Otto-Berndt-Straße 2, 64287 Darmstadt, Germany
e-mail: philipp.schumann@ptu.tu-darmstadt.de

© The Minerals, Metals & Materials Society 2022
K. Inal et al. (eds.), *NUMISHEET 2022*, The Minerals, Metals & Materials Series,
https://doi.org/10.1007/978-3-031-06212-4_60

faces [2]. The wear is reflected in the component quality by an increase in the cutting burr, which is an important quality feature [2, 3].

FE analysis (FEA) is commonly used to improve the cutting process in terms of product quality and tool life. Most of the simulation models are based on two-dimensional models due to the axial symmetry of the cutting tools [4–6]. Myint et al. implemented an FEA using the Cockroft–Latham and Oyane damage criteria. It can be shown that the product quality depends significantly on the cutting clearance, the cutting edge, and die radius [7, 8]. Dalloz et al. used an anisotropic Gurson–Tvergaard–Needleman (GTN) model to simulate the shear cutting process on a dual-phase steel. This gave them a good prediction of the general level of punch force in the cutting phase [9]. Using a similar approach, Gutknecht et al. were able to accurately predict the punch force. The cutting geometries obtained are in satisfactory agreement with the experimental investigations [10].

A robust and low-wear blanking process is the focus of research to increase the tool life and to make the process more economically efficient [11]. The focus is mainly on the consideration of the cutting phase and changes in the cutting force [12–15]. Nevertheless, combinations of certain process parameters lead to a pronounced withdraw phase [16]. To evaluate the material selection for the punch, Baer et al. investigated the loads in the withdraw phase during fine blanking employing a FEA. For this purpose, the acting clamp force of the sheet metal on the punch is determined numerically and experimentally. The model achieves a satisfactory agreement [17].

Objective

A high withdraw force can be identified as an additional tribological load and indicates high contact normal stresses. To assess the effects that occur, a reliable prediction and analysis of the physical phenomena in all phases of the cutting process is of technological relevance. Quantities that are difficult to quantify by measurements, such as the load of the sheet metal on the surface, can be determined by a numerical simulation.

In order to evaluate the withdraw phase a FEM was set up using a combination of the Cockroft–Latham and Lemaitre damage model. In this work, physical phenomena that occur and their effects on tribology in the withdraw phase are examined. These effects are considered for an accurate prediction of the experimental results in the withdraw of the shear cutting process based on an FE model.

Experimental Setup

In order to validate the simulation in this study, force signals during the blanking process are measured considering varying parameters of tool, process, and semi-finished product.

Table 1 Mechanical properties of the material used in this study

Material	Tensile strength in MPa	Elongation at break in %	Sheet thickness in mm	Carbon in vol. %
1.0347 (DC01)	299.8 ± 2.9	34.7 ± 1.3	2 ± 0.02	0.1

Thereby, all experiments were conducted on a high-speed press from Bruderer AG (BSTA 810). The machine parameters for the experiments were set to a stroke distance of 51 mm and stroke speed of 100–500 strokes per minute (spm). A cylindrical punch with a diameter of 6 mm which immerses 4.4 mm into the die was chosen. The material used for the investigations in this study was a cold-rolled steel (1.0347). As no additional lubrication was used only the lubricant remaining after the manufacturing of the sheet metal strip is available for the blanking operation. According to technical conditions of supply in the automotive industry, an average lubrication quantity of $1 \pm 0.25 \text{ g} \cdot \text{mm}^{-2}$ is assumed. Table 1 summarizes the mechanical properties of the cold-rolled steel.

As shown in Fig. 1a, the force signals are measured with an uniaxial piezoelectrical force washer (Kistler 9054A) integrated to the upper part of the tool. The signal is digitized with an analog acquisition module (National Instruments 9201 ± 10 V) using a sampling frequency of 20 kHz. The measured force curve is characterized by three phases as shown in Fig. 1b. During the punch phase (I), the tool hits the sheet and starts to elastically deform the material. Thereby, the material behavior changes from a linear-elastic phase to a plastic deformation until the stresses in the forming zone exceed the maximum shear strength. At this point, shearing stresses exceed the shear fracture limit and the material begins to break abruptly releasing the stored elastic energy to the system. During the push phase (II), the blanked workpiece is pushed out of the die and the punch passes through the bottom dead center. Finally, in the withdraw phase, the punch is pulled out of the die leading to withdrawal forces which result from a clamping between sheet and punch.

Since the characteristic of the force signal is determined by a variety of parameters this study considers clearance, cutting radii, stroke speed, and sheet thickness as

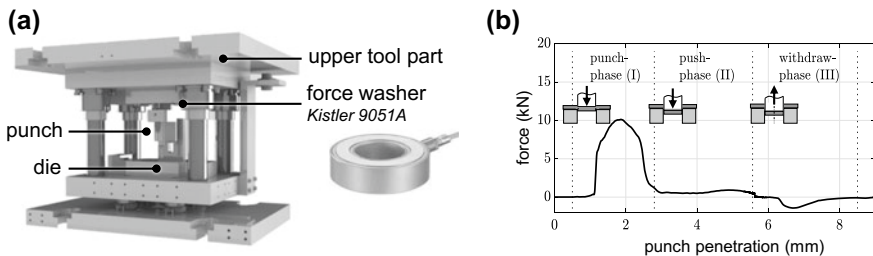


Fig. 1 a Sensorial equipped blanking tool for measuring force signals; b shear cutting phases with corresponding force–displacement curve [16]

Table 2 Parameters of the blanking process varied during the experiments

Parameter	Edge radii in mm	Stroke speed in spm	Sheet thickness in mm	Clearance in μm
Variation	0, 0.1, 0.3, 0.5	100, 300, 500	1.7, 1.8, 1.9, 2.0	75, 150, 300

influencing parameters. These are set by specific adjustments to the tool, the semi-finished products, and the press listed in Table 2. While the tool-sided variations (clearance and cutting-edge radii) are caused by wear [18, 19] material-sided variations (sheet thickness) are related to the manufacturing process of the semi-finished product [20].

FEM Model

For the numerical estimation of the tribological loads on the tool considering varying process parameters, an FEM model is built using Simufact Forming version 16. The FEM model represents the blanking operation from sheet metal strip with a width of 20 mm for the tool shown in Fig. 1a. The model is used to vary the process parameters from Table 2 in order to determine their influences on the process forces and the resulting product geometry. The validation of the FEM model is based on the reference tool configuration described by a clearance of 15 μm , a sharp cutting-edge radii (0.0 mm), a stroke rate of 300 spm, and a sheet thickness of 2 mm. Special attention is paid to the discretization and the choice of the damage model.

Modeling Approaches

The process is divided into the two process phases, punch and withdraw phases, which are calculated in two separate simulations, with the calculated results at the end of the punching phase being used as starting conditions for the simulation of the withdraw phase.

Geometrical Model

The geometry of the model is based on the tool shown in Fig. 1a. The die tool components that come into contact with the workpiece during the punching process (die and punch) are modeled deformable. These are extended via rigid connections to the press (punch link and die base) in order to specify the boundary conditions and to be able to output the punch force. Above the sheet metal there is a stationary

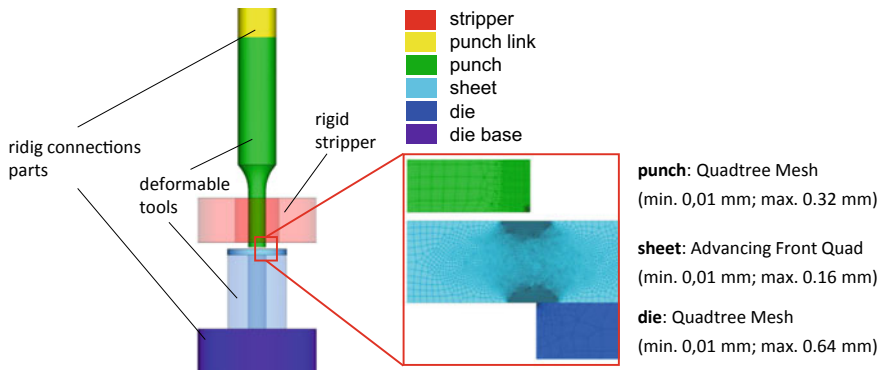


Fig. 2 Setup of the simulation model

stripper, which is modeled rigidly and serves to strip the sheet metal moving upwards with the punch. The simulation is performed in 2D as a comparison with a 3D model in preliminary investigations showed only small deviations. Due to the rotational symmetry of the tool geometry, a 2D approach as used by many other authors [10, 21, 22] is permissible (Fig. 2).

Material Model

To model the plastic and fracture behavior, a material characterization is carried out using tensile tests with flat tensile specimens. Plastic strains up to 0.3 are achieved in the tensile tests. For higher plastic deformation, the flow stress is extrapolated using the Ludwik equation. In the tensile tests carried out, strain rates of only 0.1 1/s can be realized. However, much higher strain rates occur during the stamping process. To take the strain rate-dependent material behavior into account, the flow curves for higher strain rates up to 1000 1/s are therefore extrapolated from the flow curves determined at two different strain rates according to a power function $f(x) = a \cdot x^b$, with $a = 8719.2$ and $b = 0.0254$. The influence of temperature on the plastic behavior of the material is neglected in this work. The yield curves used in the simulation for the material DC01 with a sheet thickness of 2 mm and the used coefficients for the extrapolation are shown in Fig. 3.

The material damage is described using the Lemaitre damage model, with the material parameters required being determined from the tensile test data. To increase the accuracy of the damage prediction, the tensile test is simulated for different material thicknesses using the Lemaitre model in an FEM simulation and the values of damage resistance S are validated according to the time when fracture occurs in the real tests. Since the Lemaitre damage model implemented in the simulation software does not allow element removal, simulations of the shear cutting process with sheet thicknesses of 1.8, 1.9, and 2.0 mm are carried out in preliminary investigations

Fig. 3 Flow curves for DC01 of sheet thickness 2 mm (measured curves displayed with solid lines, dashed lines symbolize extrapolated curves)

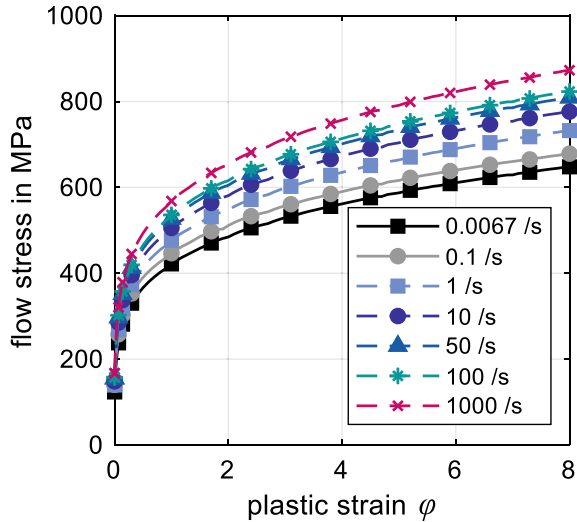


Table 3 Critical damage values for Cockroft–Latham model for DC01 with varying sheet thickness and cutting clearance

Sheet thickness	Clearance		
	75 μm	150 μm	300 μm
1.8 mm	–	1.7	–
1.9 mm	–	1.8	–
2.0 mm	2.2	2.0	1.8

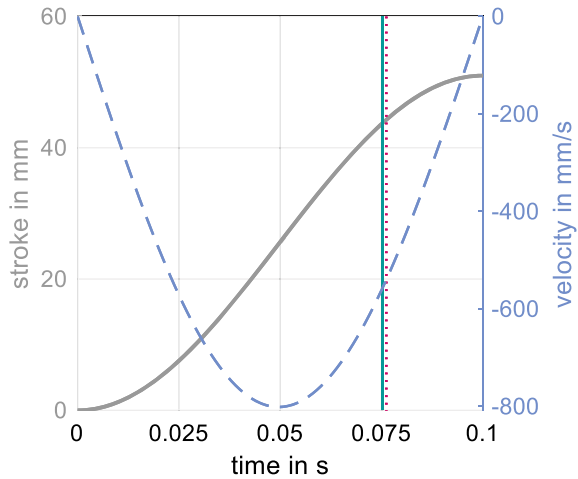
using both the Lemaitre model and the Cockroft–Latham model. By matching the Lemaitre relative damage parameter, the used critical damage parameters d_{crit} of the Cockroft–Latham model are successively adjusted so that the fracture times in each of the two models match. Since the critical damage parameter must be adjusted for each variation of material, thickness, and cutting clearance [7], the values listed in Table 3 are used in the further simulations.

Process Kinematics and Contact Definition

In order to calculate the occurring strain rates correctly, the punch movement near the bottom dead centre is modeled based on the piston formula (Fig. 4). Depending on the simulated case, the punch speed over time given as a boundary condition at the punch link is adapted according to the stroke rate. The punch speed is specified in tabular form.

A node-to-segment contact condition is used for contact formulation, the use of which also allows for element separation between punch and sheet during an

Fig. 4 Stroke path and velocity of the punch (vertical line = start of simulation; dotted line = impingement on sheet surface)



increment. The contact tolerance is set to zero with a bias factor of 0.05 between punch and sheet and 0 between all other bodies.

To take into account the friction between components moving relative to each other, the Coulomb friction model with a constant friction coefficient μ is used. In the model optimized for the stamping process, μ is set to 0.15. The stiffness of the tool is taken into account by Young’s modulus of the tools in the model.

Numerical Discretization

The time discretization is done with an adaptive step size adjustment, which specifies the step size depending on the element distortion to ensure the stability of the simulation. The maximum number of steps is 20.000.

Adaptive remeshing based on element strain is used to adapt the computational grid to the present deformation. When selecting an adequate criterion for the remeshing, the following requirements have to be taken into account, which are partly in conflict with each other: the most accurate representation of the cutting force magnitude, the smallest possible fluctuations in the force curve due to the remeshing, the representation of the fracture time point as well as the minimization of the required calculation time. An element strain of 0.2 is identified as the optimum value for the remeshing criterion.

Quadtree mesh generation is chosen for the spatial discretization of punch and die. Elements with an edge length of 0.64mm are used to mesh the die. When meshing the punch, it must be taken into account that the mesh must be fine enough to predict the clamping forces with sufficient accuracy, but the mesh must not be too fine, otherwise detachment between the sheet and the punch will occur, which is not physically reasonable. A very fine mesh with an edge length similar to that of the

Fig. 5 Results for the maximum punch force with different spatial resolution

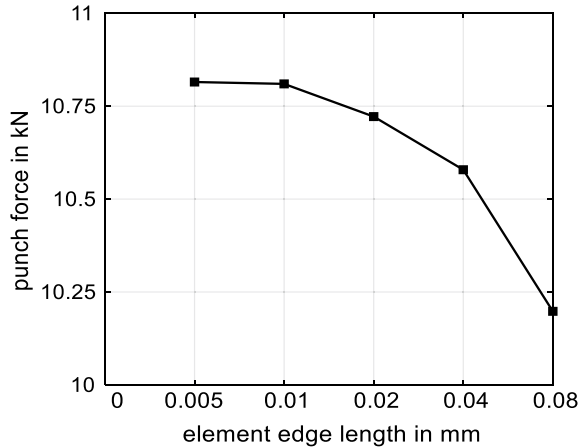


Table 4 Result of the grid convergence study for the maximum punch force using Richardson extrapolation

h_{\min} in mm	0.005	0.01	0.02
ϕ in kN	10.815	10.81	10.722
e_{ext} in %	0.0028	0.0490	0.8627

sheet will result in detachment. This is prevented if the mesh for the punch has at least four times the element edge length of the mesh in the sheet. For this purpose, an element edge length of 0.32 mm is used for the punch in zones far from the critical areas (cutting edge and shell surface).

Advancing front quadrilateral meshing is used for the meshing of the sheet, since it allows changes in element sizes during remeshing, thus ensuring greater stability of the simulation in the presence of large deformations and, in particular, fracture. In areas away from the forming zone, an edge length of 0.16 mm is used for the sheet.

In the area of the cutting edge for both die and punch as well as the forming zone in the sheet, a local mesh refinement with a minimum element edge length of $h_{\min} = 0.01$ mm is applied. This was selected using a grid convergence study. The computational uncertainty due to the spatial discretization was quantified by comparing several simulations of different mesh without varying other settings. Figure 5 shows the results for the maximum punch force during the punching process for different element sizes (plotted against the minimum element edge length in the model). Convergence of the results towards a finite value can be seen. Using Richardson extrapolation following [23], the relative deviation e_{ext} from the extrapolated solution expected on an infinitely fine mesh was calculated from the results of the three finest meshes. These are shown in Table 4. The resulting computational grid is shown in Fig. 2.

Model Validation

The simulation results are compared with experimental data to evaluate the prediction quality and to further optimize the simulation model. The punch force curves during the punch phase and the withdraw phase as well as the geometry of the cutting edge of the punched slugs are used for this purpose.

Figure 6 shows the comparison of the punch forces between simulation and experiment. During the punch phase, both the magnitudes of the maximum force and the qualitative course agree comparatively well. In particular, the time of the fracture, recognizable by the rapid decrease of the force, shows a high agreement. An examination of the force curves in the withdraw phase shows that, with the same settings as during the punch phase ($\mu = 0.15$), there are significant differences in the magnitude of the withdraw force. By reducing the coefficient of friction to $\mu = 0.07$ with otherwise the same settings, significantly better agreement can be achieved. A possible physical explanation for this process-phase-dependent change in the coefficient of friction is discussed in Sect. “Results and Discussion”.

As can be seen in Fig. 7, the contour of the cut edge from the simulations for different edge radii and clearances agrees very well with microscope images of the

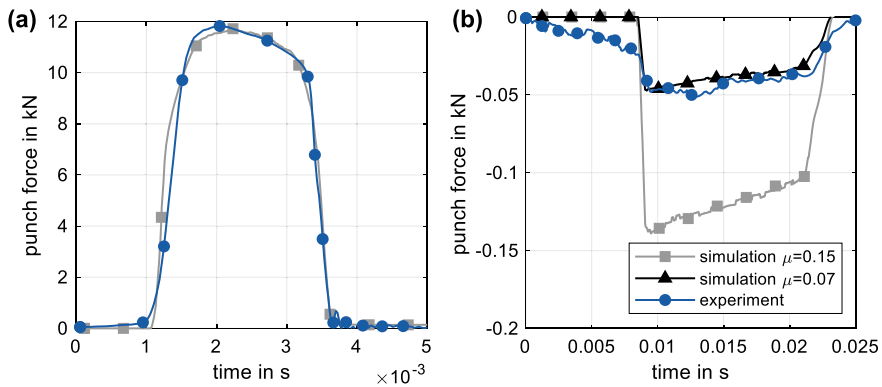


Fig. 6 Comparison of the force curves during punch phase (a) and withdraw phase (b) between simulation and experiment

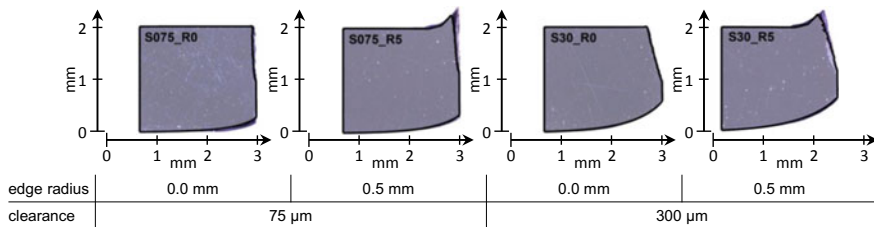


Fig. 7 Comparison of the slug geometries between simulation and experiment

slug cross sections. On closer inspection, it can be observed that the edge indentation shows slight deviations between experiment and simulation for the lower cutting clearance. In cases with a high cutting-edge radius, where there is a lot of burr formation, deviations in the shape of the fracture surface and the burr height can also be seen. These are mainly attributed to the challenging modeling of the part contact between punch and sheet. The shape of the ridge in the simulation model is significantly dependent on the location of crack initiation and thus the location of the locally highest stresses. Therefore, for a precise prediction of the burr formation, an accurate determination of the acting contact normal stresses is important.

Results and Discussion

Punch Force Under Various Conditions

Figure 8 shows the maximum punch forces in the cutting phase for varying process parameters in simulation and experiment. In Fig. 8a, it can be seen that the deviation between the experimental data and the numerical simulation increases with increasing punch edge radius. For a punch with a sharp cutting edge, the deviation for the three investigated clearances averages 0.53 % and is thus very low. For a punch with an edge radius of 0.5 mm, the average deviation for the clearance values shown rises to 5.6%. The largest difference can be found with 6.43% for a clearance of 150 μm and a punch edge radius of 0.5 mm. A distinct influence of the clearance on the maximum punch force could not be observed. A possible explanation for the deviations is inaccuracy in modelling friction at the edge radii in connection with the discretization used. However, overall, the simulation reproduces the experimentally

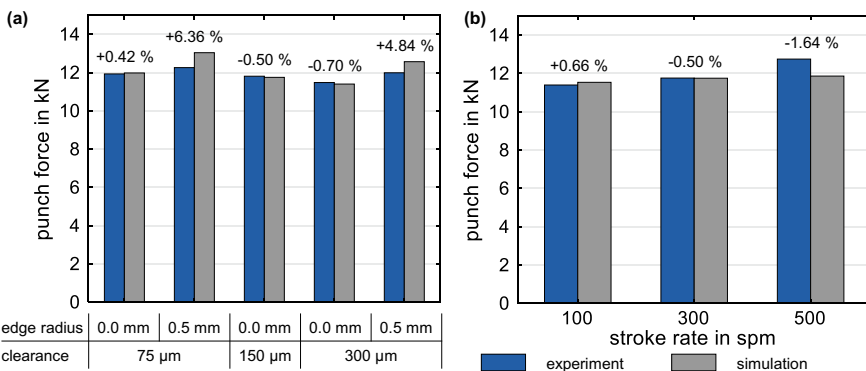


Fig. 8 Comparison of the maximum punch forces of simulation and experiment in the cutting phase for a variation of **a** cutting edge and edge radii and **b** stroke rate

varied process variables appropriately. Both the considered stroke rate, clearance, and edge radii can be mapped with a maximum deviation of 6%.

The results shown in Fig. 8b were produced with a clearance of $150\ \mu\text{m}$, and a punch edge radius of 0 mm under variation of the stroke rate. The maximum deviation of the simulation from the experimentally recorded data is 1.63 % for a stroke rate can be found 500 spm. The assumptions of the simulation are thus in good agreement with the experimental data. The larger deviation at a stroke rate of 500 spm can be explained by the approximation for high strain rates explained in Sect. “Modeling Approaches” and an increasing temperature influence, which is not considered in the model presented in this paper.

Clamping Force

Due to the adjustments described in Sect. “Model Validation”, a high agreement of the simulation with the reference test could be achieved for a clearance of $150\ \mu\text{m}$ and an edge radius of 0 mm. Figure 9 shows the comparison of the maximum force magnitude in the withdraw phase for simulation and experiment of the additionally investigated clearances at a stroke rate of 300 spm. As explained in the model setup, only a small deviation for a cutting gap of $150\ \mu\text{m}$ is achieved by adjusting the friction coefficient in the withdraw phase. For a clearance of $300\ \mu\text{m}$, the deviation increases and the simulation overestimates the experimentally measured force in the withdraw phase. For a punch edge radius of 0 mm, the model deviates by -21.26% , for the punch edge radius of 0.5 mm the deviation further decreases to -77.12% , while the total values for a clearance of $150\ \mu\text{m}$ are relatively low. On the other hand, for the smaller cutting clearance of $75\ \mu\text{m}$, the deviation of the simulation for the punch edge radius of 0 mm is -98.11% and for the punch edge radius of 0.5 mm 78.95% . For small clearances, the maximum withdraw force in the withdraw phase is thus significantly underestimated by the simulation.

Figure 9 has clearly shown the large deviations for a clearance of $75\ \mu\text{m}$. In Fig. 10a, a good fitting of the maxima of simulation and experiment was achieved by an additional increase of the friction coefficient for narrow clearances. However, the plateau after reaching the peak is significantly higher than that observed experimentally. With the lower friction coefficient, on the other hand, a good agreement with the experimental data is achieved for the plateau of the withdraw phase, but it no longer achieves the peak described above as with the significantly higher friction coefficient. In order to be able to reproduce this behavior, a time-dependent friction coefficient was introduced, which decreases after reaching the extremum. As known from literature and shown simulatively in Fig. 7, the smooth cut portion for a narrow clearance is significantly larger in terms of area. The surface topography is the same in both cases, only their proportions differ. According to Archard, this means that the statistical number of micro-contacts in contact with the surface of the punch increases linearly [24]. Accordingly, a larger amount of mechanical work is required to smooth out these roughness peaks. The necessary punch force in the

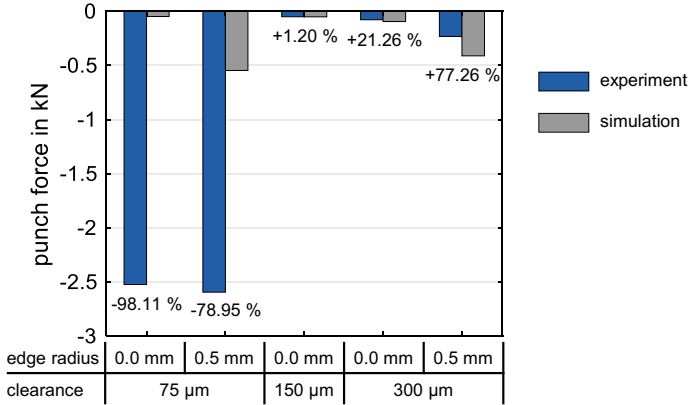


Fig. 9 Comparison of the maximum punch forces of simulation and experiment in the withdraw phase for a variation of cutting edge and edge radii

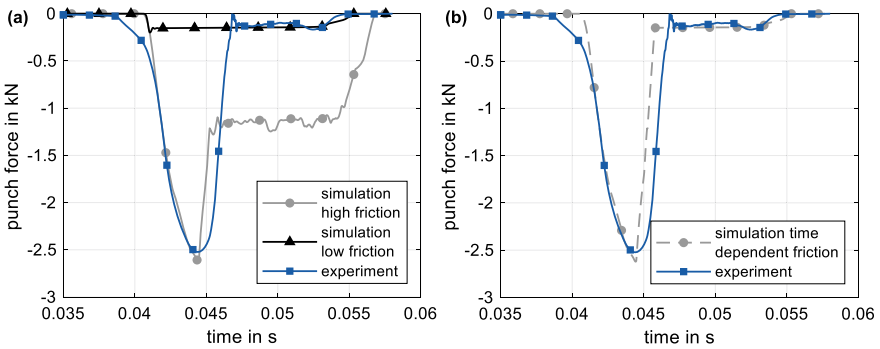


Fig. 10 **a** Influence of various friction coefficients on a small clearance, **b** time-dependent friction coefficient

withdraw phase for narrow clearances is therefore larger. The observed effect and the adjustments made are plausible. The curve obtained in this way is shown in Fig. 10b and is in very good agreement with the experimental data.

Influence of Lubricant

In order to map the behaviour during the withdraw phase adequately in the simulation, significant adjustments in the modeling of the friction behaviour were necessary. Due to the material separation in blanking, dynamically changing conditions occur in all phases of the process. From a tribological point of view, valuable observations for blanking could be made in the present work. These phenomena are discussed below.

It could generally be shown that a high congruence to the experimental data is achieved by reducing the friction coefficient in the simulation model of the withdraw phase, see Fig. 6. The reason for this assumption is a change in the tribological load collective in the withdraw phase, due to a change in the lubrication condition and/or smoothing of the workpiece surface contacting the punch. In order to be able to prove this hypothesis experimentally, the factor of lubrication was also investigated in a further series of tests. For this purpose, a defined length of sheet metal strip was decreased. On the one hand, a complete degreasing as well as degreasing of the upper side of the sheet metal was considered and compared with the conventional lubrication of the delivery condition. The cutting tool was also completely degreased at the beginning of both complete and upper side degreasing test series. A total of 100 strokes were evaluated for each of these three considerations, with approximately a sheet metal strip length corresponding to 50 strokes being degreased. The results of this investigation are shown in Fig. 11, where the maximum of the respective force magnitude in the cutting and withdraw phase is plotted over the examined number of strokes.

Figure 11a clearly shows that the punch force measured in the cutting phase for the fully and partially degreased sheet section is significantly above the reference state. This corresponds to the expectations. For the fully degreased sheet section, it can be seen that after the 50 non-lubricated strokes the punch force decreases. After approximately 75 strokes, the reference state is reached again. The initial stroke is approximately at the same level in the fully and partially degreased state, but the entire force level is below the fully degreased course and then approaches the reference state with a flatter course. This observation shows that adhesion carries lubricant from the underside of the sheet through the punch and thus influences the tribological system under consideration.

Looking at the punch forces in the withdraw phase shown in Fig. 11b, the influence of the lubricant becomes noticeable through a clearly faster response behaviour compared to the cutting phase. In the case of the sheet metal strip degreased on one

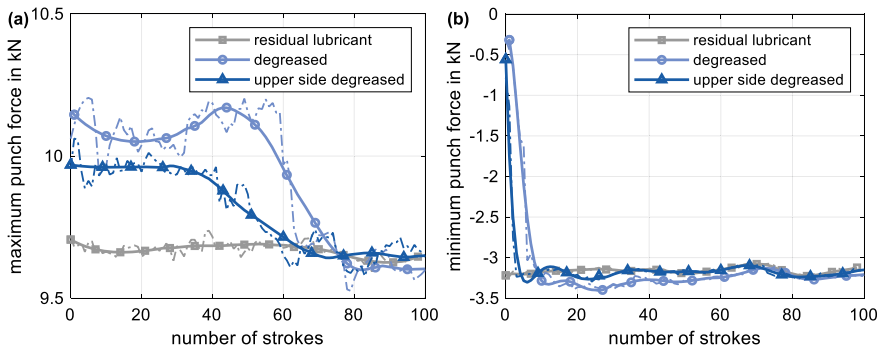


Fig. 11 Maximum punch force per stroke under different lubrication conditions for **a** the cutting phase and **b** the withdraw phase

side, the force curve approaches that of the reference within a few strokes, while the completely degreased sheet metal section only approaches the reference after about 75 strokes. A similar behaviour as could already be observed in the cutting phase. This comparison is an indicator of the considerable more sensitive influence of the lubricant in the withdraw phase. The previously discussed assumptions made in the simulation regarding the reduced friction coefficient can thus be confirmed.

Conclusion and Outlook

A fully coupled elasto-plastic 2D plane strain process that combines the Cockroft–Latham and Lemaitre damage model is applied to blanking. Complementary experiments of the process are conducted to validate the model. The influence of lubrication is taken into account. The findings of this work can be summarized as follows:

- The cutting phase can be modelled by the implemented material and damage model for a wide range of process parameters with a maximum deviation from the experimental data of 6%.
- A reduction of the friction coefficient is necessary for an adequate agreement of the force–time curve in the withdraw phase.
- The increase of the clamping force for narrow clearances in the withdraw phase can only be corrected by further adjustments of the friction coefficient. Phenomenologically, this is attributed to additional frictional contacts due to an increased smooth cut component. The basis is the statistical friction model according to Archard. Experimental studies on this in blanking are necessary.
- A time-dependent behaviour of the roughness coefficient in the withdraw phase could be proven. Explanations are a smoothing of roughness peaks and lubricant influence.
- Experimental studies on lubricant behaviour show a significantly more sensitive influence of the lubricant in the withdraw phase than in the cutting phase.

With the presented work, an important step has been taken towards mapping all phases of the blanking process, but further investigations are required. For a further development of the model, a temperature influence as well as an expansion of the material model for higher strain rates must be considered. In addition, the lubrication condition as well as a possible smoothing behaviour during the withdraw phase due to the sliding of the punch along the cutting edge must be investigated.

Acknowledgements The presented results are part of the research projects “Production-induced properties in the interlocking of stator lamination stacks” (22036 N) and “Tribological optimization of cutting punches through microstructuring by machine hammer peening” (21560 N) of the European Research Association for Sheet Metal Working (EFB) funded by the program for “Industrial Research” (IGF) of the Federal Ministry of Economic Affairs and Climate Action (BMWK) and the German Federation of Industrial Research Associations (AiF) and within the framework of the funding measure “Mittelstand 4.0—Digitale Produktions- und Arbeitsprozesse” provided by the BMWK within the funded project “Mittelstand-Digital Zentrum Darmstadt”. Furthermore, the

authors would like to thank Bruderer AG for providing the high-speed press BSTA 810-145 on which the punching experiments were carried out.

References

1. Altan T, Tekkaya AE (2012) Sheet metal forming: processes and applications. ASM international, Ohio
2. Ersoy-Nürnberg K, Nürnberg G, Golle M, Hoffmann H (2008) Simulation of wear on sheet metal forming tools-an energy approach. *Wear* 265(11–12):1801–1807. <https://doi.org/10.1016/j.wear.2008.04.039>
3. Fang G, Zeng P, Lou L (2002) Finite element simulation of the effect of clearance on the forming quality in the blanking process. *J Mater Process Technol* 112(2–3):249–254. [https://doi.org/10.1016/S0924-0136\(02\)00056-0](https://doi.org/10.1016/S0924-0136(02)00056-0)
4. Myint P, Hagihara S, Tanaka T, Taketomi S, Tadano Y (2001) Finite element model fracture prediction during sheet-metal blanking processes. *Eng Fract Mech* 68(3):365–378. [https://doi.org/10.1016/S0013-7944\(00\)00106-5](https://doi.org/10.1016/S0013-7944(00)00106-5)
5. Ahmed A, Muhamad H (2012) Finite element simulation of blanking process. *IJUM Eng J* 13(2):26. <https://doi.org/10.3390/jmmp2020026>
6. Goijaerts AM, Stegeman YW, Govaert LE, Brokken D, Brekelmans WAM, Baaijens FPT (2000) Can a new experimental and numerical study improve metal blanking? *J Mater Process Technol* 103(1):44–50. [https://doi.org/10.1016/S0924-0136\(00\)00417-9](https://doi.org/10.1016/S0924-0136(00)00417-9)
7. Myint P, Hagihara S, Tanaka T, Taketomi S, Tadano Y (2017) Determination of the values of critical ductile fracture criteria to predict fracture initiation in punching processes. *J Manuf Mater Process* 1(2):12. <https://doi.org/10.3390/jmmp1020012>
8. Myint P, Hagihara S, Tanaka T, Taketomi S, Tadano Y (2018) Application of finite element method to analyze the influences of process parameters on the cut surface in fine blanking processes by using clearance-dependent critical fracture criteria. *J Manuf Mater Process* 2:26. <https://doi.org/10.3390/jmmp2020026>
9. Dalloz A, Besson J, Gourgues-Lorenzon AF, Sturel T, Pineau A (2009) Effect of shear cutting on ductility of a dual phase steel. *Eng Fract Mech* 76(10):1411–1424. <https://doi.org/10.1016/j.engfracmech.2008.10.009>
10. Gutknecht F, Steinbach F, Hammer T, Clausmeyer T, Volk W, Tekkaya AE (2016) Analysis of shear cutting of dual phase steel by application of an advanced damage model. *Procedia Struct Integr* 2:1700–1707. <https://doi.org/10.1016/j.prostr.2016.06.215>
11. Kindsmüller A, Schrepfer A, Stahl J, Pätzold I, Nürnberger A, Golle R, Volk W (2021) Influence of cutting parameters on mechanisms causing slug pulling. *Prod Eng* 15(6):833–842. <https://doi.org/10.1007/s11740-021-01061-3>
12. Wang K, Wierzbicki T (2015) Experimental and numerical study on the plane-strain blanking process on an AHSS sheet. *Int J Fract* 194(1):19–36. <https://doi.org/10.3390/jmmp2020026>
13. Bohdal L, Kukielka L, Chodor J, Kulakowska A, Patyk R, Kaldunski P (2018) 3D finite element modelling of sheet metal blanking process. In: AIP conference proceedings. AIP Publishing LLC, pp 070006. <https://doi.org/10.1063/1.5034902>
14. Zehetner C, Reisinger C, Kunze W, Hammelmüller F, Eder R, Holl H, Irschik H (2021) High-quality sheet metal production using a model-based adaptive approach. In: International conference on industry 4.0 and smart manufacturing. *Procedia computer science*, p 249. <https://doi.org/10.1016/j.procs.2021.01.162>
15. Manopulo N, Tong L, Karadogan C, Hora P (2009) A dual-mesh strategy for the 3d simulation of fineblanking processes. *Int J Mater Form* 2(1):589–592. <https://doi.org/10.1007/s12289-009-0495-8>
16. Hohmann J, Schatz T, Groche P (2017) Intelligent wear identification based on sensory inline information for a stamping process. In: International conference on advanced manufacturing

- engineering and technologies. Springer, Cham, pp 285–295. <https://doi.org/10.1007/978-3-319-56430-2>
17. Baer O, Feuerhack A, Voigts H, Bergs T (2019) Investigation of the mechanical punch loads during fine blanking of high-strength steels with cemented carbide. In: 47th SME North American manufacturing research conference, procedia manufacturing, Pennsylvania, pp 90–100. <https://doi.org/10.1016/j.promfg.2019.06.125>
 18. Kubik C, Hohmann J, Groche P (2021) Exploitation of force displacement curves in blanking-feature engineering beyond defect detection. *Int J Adv Manuf Technol* 113:261–278. <https://doi.org/10.1007/s00170-020-06450-z>
 19. Hernández JJ, Franco P, Estrems M, Faura F (2006) Modelling and experimental analysis of the effects of tool wear on form errors in stainless steel blanking. *J Mater Process Technol* 180(1–3):143–150. <https://doi.org/10.1016/j.jmatprotec.2006.05.015>
 20. German Institute for Standardization: DIN EN 10130:2007-02: Cold rolled low carbon steel flat products for cold forming—Technical delivery conditions; German version EN 10130:2006 (2007). <https://doi.org/10.31030/9758523>
 21. Stanke J, Trauth D, Feuerhack A, Klocke F (2017) Setup of a parameterized FE model for the die roll prediction in fine blanking using artificial neural networks. *J Phys: Conf Ser* 012096:012096. <https://doi.org/10.1088/1742-6596/896/1/012096>
 22. Suzuki Y, Yang M, Murakawa M (2020) Optimum clearance in the microblanking of thin foil of austenitic stainless steel JIS SUS304 studied from shear cut surface and punch load. *Materials* 13(3):678. <https://doi.org/10.3390/ma13030678>
 23. Celik IB, Ghia U, Roache PJ, Freitas CJ, Coleman H, Raad PE (2008) Procedure for estimation and reporting of uncertainty due to discretization in CFD applications. *J Fluids Eng* 130(7):078001-1-4. <https://doi.org/10.1115/1.2960953>
 24. Archard J (1953) Contact and rubbing of flat surfaces. *J Appl Phys* 24(8):981–988. <https://doi.org/10.1063/1.1721448>

Evaluating Lubricants for Warm Forming of Aluminum 6xxx Alloys



Tom Feister, Laura Zoller, Mehdi Shafiei, Paul Bosler, and Hyunok Kim

Abstract The success of the warm forming of aluminum alloys without defects is significantly influenced by a preferred forming temperature range as well as reducing die friction during the forming of the pre-heated aluminum blanks. This paper introduces cup draw testing at different elevated temperatures (200, 240, and 280 °C) with two high-strength 6xxx aluminum alloys and two commercially available lubricants. Finite element simulations were conducted to effectively determine the testing conditions (i.e., temperatures, blank holder force, and the maximum drawing depth), and determine the coefficient of friction inversely by comparing with experiments. One of the tested lubricants showed superior performance regardless of elevated temperatures compared to the other lubricants.

Keywords Warm forming · High-strength aluminum alloys · Cup draw testing · Lubricant · Finite element method · Simulation

Introduction

Lightweighting initiatives are leading to the use of more high-strength aluminum alloys (AA 6xxx–7xxx) in automotive parts. Part complexity often requires warm or hot forming to manufacture parts without defects. Selecting the proper forming temperature and lubricant are key parameters for maximizing formability, decreasing galling, and reducing the overall cost to produce a part.

T. Feister (✉) · L. Zoller · H. Kim
EWI Forming Center, 1250 Arthur E. Adams Drive, Columbus, OH 43221, USA
e-mail: tfeister@ewi.org

M. Shafiei
Novelis, 39550 West 13 Mile Road, Novi, MI 48377, USA

P. Bosler
FUCHS, 17050 Lathrop Avenue, Harvey, IL 60426, USA

Objective

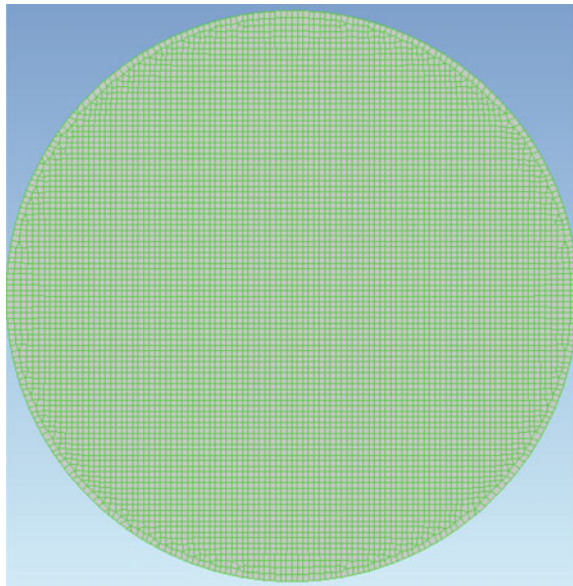
The objective of this study was to evaluate the performance of two lubricants while forming high-strength aluminum alloys at temperatures between 200 and 280 °C. Two lubricants were evaluated to compare the performance as a function of material, temperature, and blank holding force.

Approach

Two aluminum alloys from Novelis were selected for this work. The selected alloys were 2.0-mm-thick Novelis Advanz™ 6HS-s615 and Novelis Advanz™ 6HS-s650. The 6HS-s15 is a more ductile material with a wide variety of part applications, while the 6HS-s650 is a high-strength alloy typically used for structural parts where high crash energy adsorption is required.

PAM-STAMP FEA software was used to predict the forming depth and required blank holding force of the cup drawing process. A shell element mesh with 1-mm uniform element size was used (Fig. 1). Figure 2 shows the tooling setup in PAM-STAMP. Material data for an aluminum alloy with similar chemistry to 6HS-s615 was available from a previous project. The temperature-based hardening curves and forming limits are shown in Fig. 3. Warm material properties for 6HS-s650 were not available. The hardening curves from the 6HS-s615 material were offset upward 41 MPa to account for the increased strength.

Fig. 1 FEA mesh



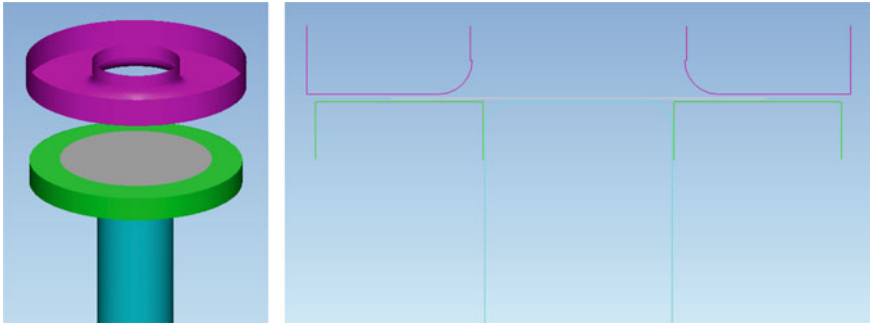


Fig. 2 FEA tooling setup

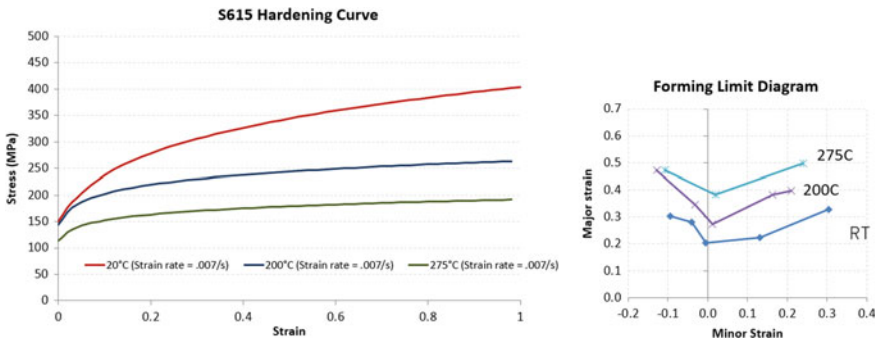


Fig. 3 6HS-s615 material data

Equation 1 was used to determine the minimum blank holding force (BHF) required to prevent wrinkling for both materials at temperatures of 200 and 275 °C. The required force range was determined to be between 3.5 and 5.6 kN. A constant 5-kN BHF was used to determine the maximum forming depth. Simulation predicted that the cups could be fully drawn (~45-mm stroke depth) without necking failure (Fig. 4).

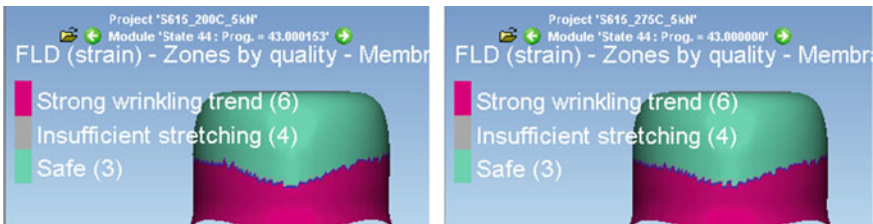


Fig. 4 200 °C forming temperature (left) and 275 °C forming temperature (right) full stroke results at 5-kN BHF

$$p_b = 10^{-3}c \left[(DR - 1)^3 + \frac{0.005d_0}{t_0} \right] S_u \tag{1}$$

where p_b = Blank holder pressure, c = Empirical factor; ranges from 2 to 3, DR = Drawing ratio, d_0/d_p , d_p = Punch diameter, d_0 = Blank diameter, t_0 = Sheet thickness, and S_u = Ultimate tensile strength.

Erichsen Universal Sheet Metal Testing machine was used to trim fifty 100-mm diameter round samples of each material. Two warm forming lubricants were supplied by Fuchs. The lubricants were applied with a sponge according to Table 1. Thermocouple testing was performed to determine the furnace set temperature.

Warm forming testing involves heating the blank holder and die to the target temperature, inserting the blank sample, and then transferring the warm tooling to the Erichsen Universal Sheet Metal Testing machine. Two k-type thermocouple wires were welded to a sample and inserted into the die/blank holder assembly (Fig. 5). A data recorder was used to track the temperature of the sample as the tools were heated from room temperature. Three furnace set temperatures (360, 400, and 410 °C) were used to determine the heating time required to reach the warm forming temperatures and the rate of temperature loss once the heating element is removed and the tools are transferred. Based on this testing, the target furnace set temperature was determined

Table 1 Selected lubricant details

Lubricant name	Forming condition	Description
RENOFORM 1102 ALWF	Warm forming	Water-based dry film lubricant, applied with sponge, ~ 0.5 g/m ²
RENOFORM 2502 ALWF	Warm Forming	Water-based dry film lubricant, applied with sponge, ~ 0.5 g/m ²

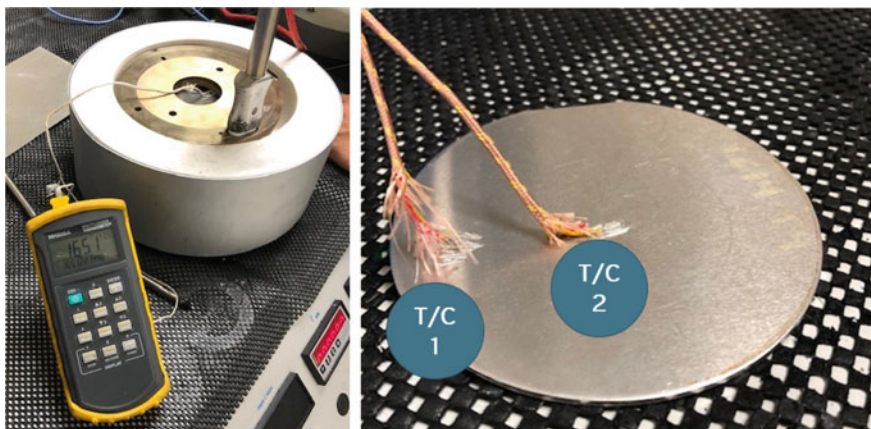


Fig. 5 Erichsen tooling furnace and sample with welded thermocouples

Table 2 Set furnace temperatures for blank temperature (forming temperature)

Furnace temperature (°C)	Blank temperature (°C)
250	200
310	240
350	280

for each forming temperature (Table 2). The temperature loss after removing the heating element was less than 5 °C after 60 s for each of the thermocouple tests. A hand-held thermocouple thermometer was used to measure the tool and sample temperature during testing. The tooling was transferred when the sample reached the target temperature.

Each material was formed at three temperatures (200, 240, and 280 °C) and was tested with multiple blank holding forces and three replicates for each condition. The BHF's for 200 °C forming temperature were determined to be 100 and 200 kN, 240 °C were 50 and 100 kN, and 280 °C were 25 and 50 kN. The forming speed was set at the maximum speed the Erichsen can produce 13.5 mm/s. And the forming depth was set to 30 mm to maintain a flange that could be measured (Fig. 6).

The relative formability and quality of lubrication were determined by measuring the punch force and circumference of the formed samples. Improved lubrication performance was indicated with smaller flange circumferences and lower drawing forces.

Fig. 6 30-mm deep cup



Results

The flange perimeter was measured, averaged, and tabulated in Figs. 7, 8, and 9 for forming temperatures of 200 °C, 240 °C, and 280 °C, respectively. A smaller circumference for a given BHF and forming depth means that the lubrication is more effective, and the material is being stretched less.

The maximum drawing forming force was measured at a stroke of 20 mm as a function of material, blank holding force, and lubrication. Figures 10, 11, and 12 show the maximum drawing force of 200 °C, 240 °C, and 280 °C, respectively. In most cases, the Renoform 2502 ALWF has a lower load than the Renoform 1102 ALWF lubricant.

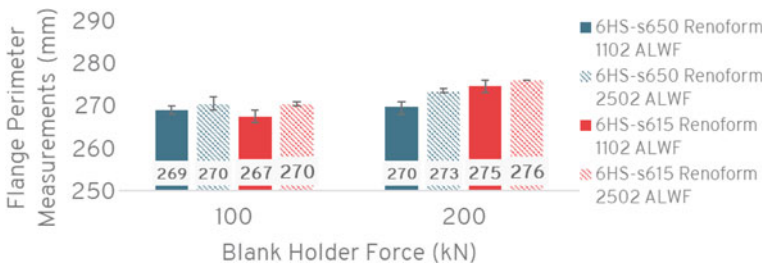


Fig. 7 200 °C flange perimeter results

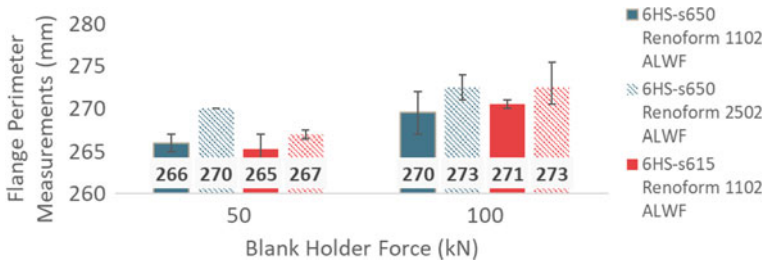


Fig. 8 240 °C flange perimeter results

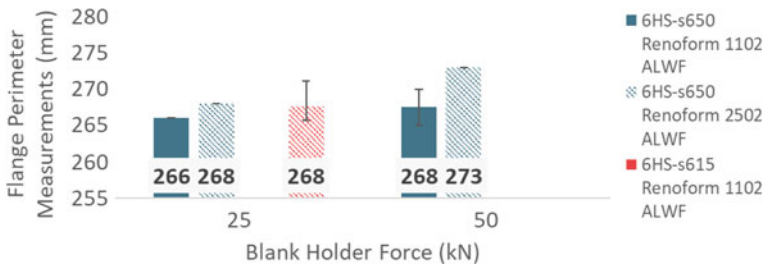


Fig. 9 280 °C flange perimeter results

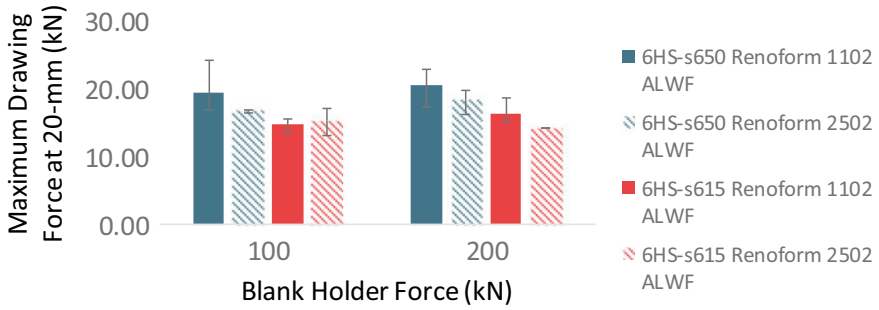


Fig. 10 200 °C drawing force at 20 mm depth results

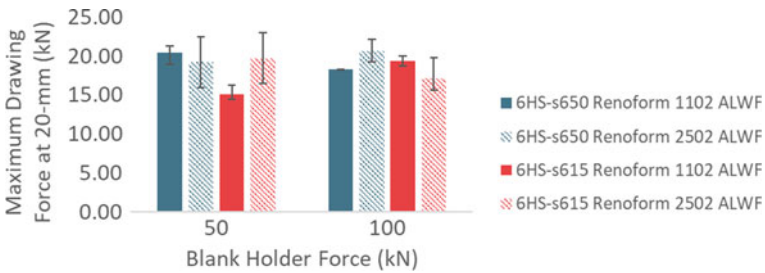


Fig. 11 240 °C drawing force at 20 mm depth results

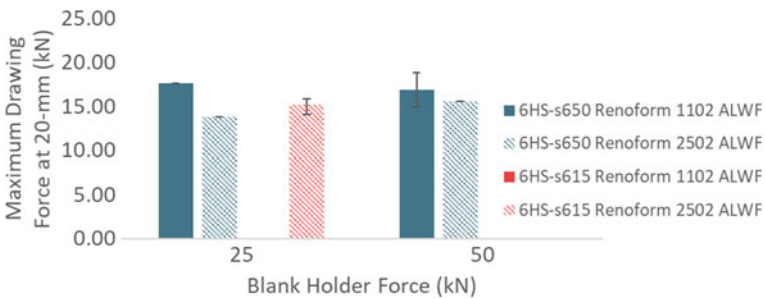


Fig. 12 280 °C drawing force at 20 mm depth results

Conclusions

The measured flange perimeter shows that the Renoform 1102 ALWF lubricant outperforms the Renoform 2502 ALWF for all three temperatures and for each BHF. Renoform 1102 ALWF consistently gave a smaller circumference at a given stroke, temperature, and BHF. This means that the length of line across the cross section is smaller and the material has accumulated less strain.

The maximum forming load measurement should validate the circumference measurement conclusion. The lubricant has the lowest maximum load at a given stroke and BHF gave a better performance. A better-performing lubricant will decrease the friction coefficient, the resistance of sliding motion, and the required punch force. Also, the better lubricant will have less strain hardening which will also show up as a lower load. The maximum forming load results are not as consistent as the circumference measurements. The inconsistency of this method is shown in the 240°C data in Fig. 11. The lubricant with the lowest forming load changes based on material and BHF.

The more consistent output of circumference is believed to be a more accurate factor for determining lubricant performance. The mechanism behind the maximum load inconsistency is not known. It is possible that the small difference in load between the two lubricants (less than 5 kN) is below the resolution that is expected for a load cell that can measure loads up to and above 600 kN.

References

1. Kim H, Hahnen R, Oberhauser P, Austin M, Samant A, Demiralp Y, Tunga V (2018) Design guidelines for warm forming of the high-strength aluminum alloys. In: 37th international deep drawing research group (IDDRG) international conference, Waterloo, Canada, 4–8 June 2018
2. Kim H, Hahnen R, Feister T, Tunga V (2018) Comparison of drawability between warm forming and cold forming of aluminum 6xxx alloys. IOP Conf Ser: Mater Sci Eng 418:012029. In: 37th international deep drawing research group (IDDRG) international conference, Waterloo, Canada, 4–8 June 2018
3. Kim H, Sung J, Sivakumar R, Altan T (2007) Evaluation of stamping lubricants using the deep drawing test. *Int J Mach Tools Manuf* 47(17):2120–2132
4. Bosler P, Kim H (2018) Effects of lubrication on the warm forming of high strength aluminum 7075-T6 alloy. In: 37th international deep drawing research group (IDDRG) international conference, Waterloo, Canada, 4–8 June 2018

Implementation of Real Contact Areas Into Sheet Metal Forming Simulations Using Digital Spotting Images



P. Essig, M. Liewald, C. Bolay, and J. Hol

Abstract Increasing demands on quality of outer car panels and shortened product development processes fundamentally challenge automotive manufacturers. Development times are significantly influenced by the manufacturing process of dies, which are introduced by the time-consuming manual grinding operations carried out during die try-out. Blue color paste is often used to visualize contact areas between die surfaces and blank to provide a spotting image. The spotting image can be used to evaluate and optimize the pressure distribution. A homogeneous pressure distribution positively influences the forming process in terms of flange draw-in and surface quality. This paper presents an approach for implementing real contact areas into forming simulations based on digital spotting images of active surfaces. Spotting images were produced for different drawing depths and subsequently extracted by image processing. The simulation model presented in this study includes different spotting levels in conjunction with the TriboForm friction model to describe tribological conditions during forming more accurately.

Keywords Digitalization · Forming simulation · Spotting image · Data feedback

P. Essig (✉) · C. Bolay
Mercedes-Benz AG, Sindelfingen, Germany
e-mail: peter.e.essig@daimler.com

M. Liewald
Institute for Metal Forming Technology, Stuttgart, Germany

J. Hol
TriboForm Engineering, Hengelosestraat 500, 7521 AN Enschede, The Netherlands

Introduction

Car design departments and part development departments create CAD models for all sheet metal parts. The part geometry is the kick-off for the manufacturing process in an early car development stage. The process plan defines the specifications of the different operations such as forming, cutting, and flanging and is crucial for a robust and feasible final part. Figure 1a depicts the drawing operation of a hood part. The addendum extends the hood by a wall, bearing zone, and draw beads (Fig. 1b).

Corresponding to the complexity of the part, material flow is controlled in the process by means of bearing areas and draw beads in the binder region. An inhomogenous pressure distribution in bearing areas can lead to uneven draw-in of the blank and surface defects due to high pressure areas. It is therefore important to assure a homogeneous pressure distribution in bearing areas to control tribological conditions and material flow during the forming operation.

To improve the pressure distribution in bearing areas the contact areas are manually finished after machining and assembling of the casted tools. The first parts are subsequently pressed on try-out presses similar to the production line. Blue color paste is often applied to both sides of the flat sheet or formed part to evaluate real contact areas between the sheet and the tool. After closing the tool, the color transfers from the sheet to the tool surfaces, which is called a *spotting image*. An ideal spotting image has contact between the upper and lower die at the same time. This method considers the applied forces, the stiffnesses, and the actual surface conditions. Due to straining of the sheet during the forming process, i.e., due to thinning and thickening of the sheet, the initial contact areas can change. Using (ideal) simulation results combined with spotting images help toolmakers to manually improve the contact areas by grinding. Nowadays, the grinded surfaces under applied forces cannot be measured with state-of-the-art systems. However, a novel optical measuring concept is able to capture the real spotting image at a specific drawing state of the forming process [1]. The digital spotting image enables the quantification of the active contact areas which can be used for further optimizing the tools.

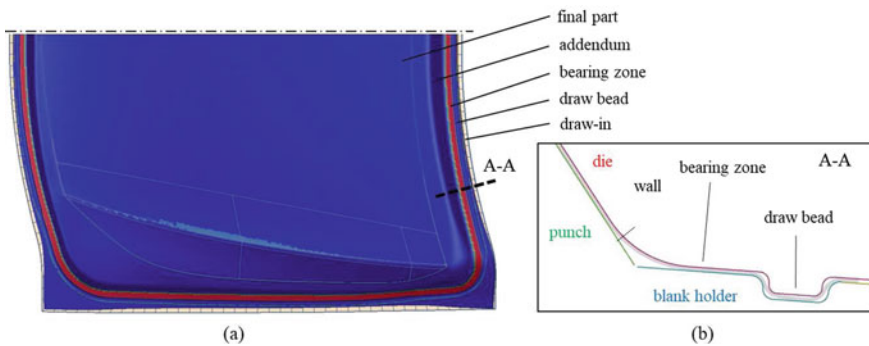


Fig. 1 a Drawing geometry; b cross-section A-A of the addendum

Tribological conditions during forming process determine the material flow and, therefore, the parts dimensional accuracy and surface quality. Tribological conditions depend on pressure distribution, forming velocity, interface temperature, plastic strain, type/amount of lubrication, and the surface topography of both the sheet and the tooling. The improved simulation accuracy by using the TriboForm friction model, accounting for all of these dependencies, has been demonstrated in earlier work of the authors for a body side panel in [2], a door-outer in [3] and a fender in [4]. Combining the TriboForm friction model with an improved description of the pressure distribution in bearing areas will further increase the simulation accuracy, and therefore the prediction capabilities of forming simulations of complex car body parts [5, 6].

Within this paper, a novel method is presented making use of the digital spotting images to accurately describe the bearing areas. This approach closes the process chain with digital feedback from tool try-out to forming simulations to improve forming simulation accuracy. Within the following sections, the part geometry and major objectives are described, followed by the definition of the novel forming simulation approach. The paper concludes with a discussion of the results and outlook for further research.

Validation Rectangle Part

Specifications of the investigated part will be discussed in this section. In addition to the design and material properties of the cup, the digitization process of spotting images in the press is presented as well.

Rectangle Cup

A suitable tool geometry was designed to validate the new simulation approach. Different bead geometries have been defined within this tool geometry, based on the material thickening in corner areas and the tribological change due to variation of the pressure distribution. Figure 2 shows the tool geometry and final part with specific bead geometries. On the long side of the rectangle, a lock bead with a bead radius of 2.5 mm and a height of 5 mm is designed. Compared to the lock bead, the round bead has a bead radius of 6.5 mm and a height of 5 mm. Both bead geometries are specified with the same groove radius on the binder of 8 mm. The active contact surfaces were increased by 0.1 mm, compared to the corner areas, to allow material thickening. Furthermore, clearance behind the bead area of 0.1 mm is defined to prevent tool contact. The lock beads introduce a targeted thinning of the material, which in turn leads to thickening of the sheet in the corner areas. Ensuring the transformability of investigation results, the designed tool geometry reproduces series like die design.

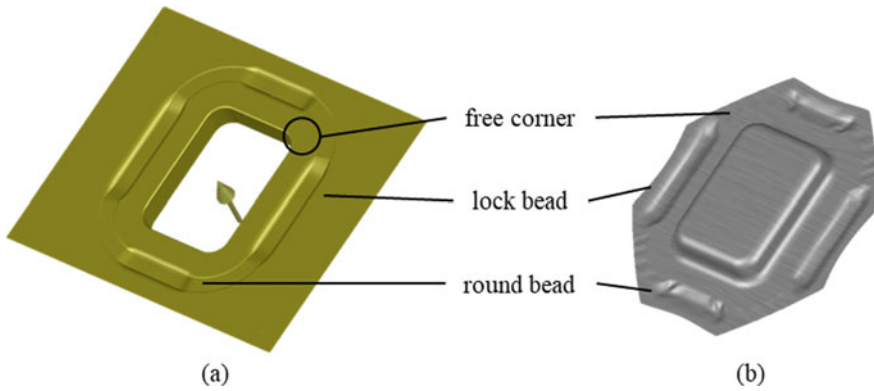


Fig. 2 a Binder geometry with draw beads; b final rectangle cup

Material Properties

Equal to the previous research work by the authors in [1–3], the presented work is focusing on AL6-OUT aluminum blanks [7] with a thickness of one millimeter from the material supplier Constellium.

The binder and the upper die are manufactured from cast iron to represent series tools for outer body parts. The used cast iron material is *EN-JS 2070*. After manufacturing, the tools were manually grinded and finished by the toolmaker equal to the finishing treatment of tools in the try-out process. Due to the grinding process the tools have a specific surface roughnesses. Surface measurements were carried out on the tools and used as input for the TriboForm friction model. Figure 3 shows a top view of the measured surface textures of the blank holder and upper die.

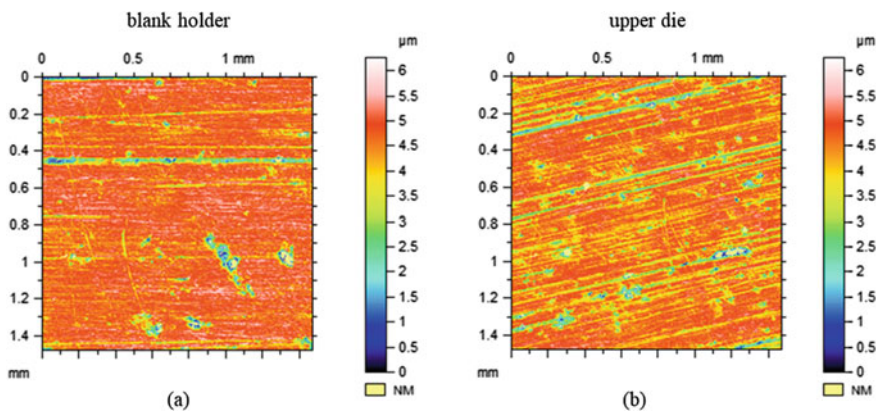


Fig. 3 a Surface properties of the binder with S_a 0.4; b upper die with S_a 0.6

Table 1 Investigated operating conditions with specific forming parameters

Test	Drawing depth (mm)	Binder force (kN)	Lubrication (g/m ²)	Stroke rate (1/min)
RD1	27	90	1.2	7
RD2	23	110	1.2	7
RD3	20	150	1.2	7

Operating Parameters

Three operating conditions were chosen for further investigation based on simulations performed in *AutoForm*. Table 1 shows the investigated operating conditions with characteristic forming parameters. The process window is limited (in terms of binder force and drawing depth) due to the material properties of aluminum and the die design.

The tests were performed on an *AIDA NST-S2-6300* servo press. Core features of the press are as follows:

- Press type: single-action servo-mechanical press with draw cushion
- Nominal force: 6300 kN
- Slide drive: eccentric
- Stroking rate: 1–30 1/min

In order to validate simulation results, the parts were marked with a measurement grid. This grid was applied using electrolytic acid etching. Evaluating the formed parts by using the measurement system *ARGUS* from *GOM GmbH* allows the calculation of major/minor strains and thinning. To ensure the repeatability of the tests at least three parts for each operating condition were prepared with a grid.

Digitalization Setup

The main focus of this investigation is the digitization of the spotting image inside the press and the implementation into forming simulations. The digitization is performed with the *TRITOP* measuring system from *GOM GmbH*. Figure 4 shows the digitization setup.

At first, a reference measurement was generated. This was achieved by placing coded marks, non-coded marks, and scaled objects in the press, see Fig. 4a. The reference images were generated around the measurement object to achieve the smallest possible measurement error. Reproducibility was achieved due to the use of a tripod, shown in Fig. 4b. Images for the spotting image acquisition were reduced to a small number as shown in Fig. 4c.

For the different operating conditions only the relevant spotting images were taken during the tests. Alignment with the reference measurement was established

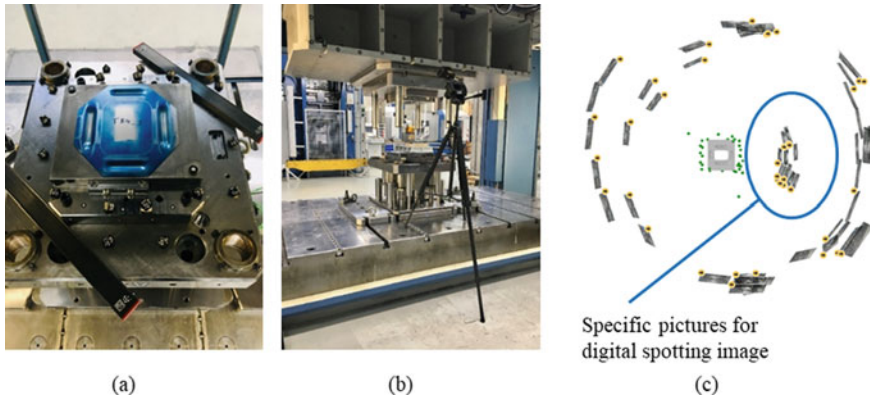


Fig. 4 **a** Different coded measurement elements next to the tool; **b** standardized SLR-camera position with tripod for digital spotting images; **c** digitalization of spotting image with TRITOP

by introducing measurement marks with magnets inside the press. By implementing the reference measurement only once, the process time was significantly reduced. The spotting images were recorded for the binder and the upper die. Additional to the operating conditions from Table 1, different drawing states were investigated. The different drawing states are defined from “0” to “1”. Drawing state “0” is equivalent to binder closure, where only the beads are formed and the active surfaces come into contact. Drawing state “0.5” describes half of the drawing depth for the particular operating point. Finally, drawing state “1” indicates the spotting image of the formed part.

For evaluating the captured spotting images, the color information of each image is mapped onto the 3D CAD surfaces of the binder and the upper die. In this way a colored mesh is generated, which allows a further extraction of the contact surfaces by following the approach described in [8, 9]. In the final step of data processing, boundary curves are generated for the forming simulation. The adaption of the forming simulation by accounting for active contact areas changing over the drawing depth is described in the following section.

Simulation Model Considering Real Contact Areas

In the following section, two simulation models are presented and compared. The first model describes the reference simulation, following the conventional simulation approach of process planning. The second model describes the extended simulation model with real digitized contact areas from the spotting images per operation condition.

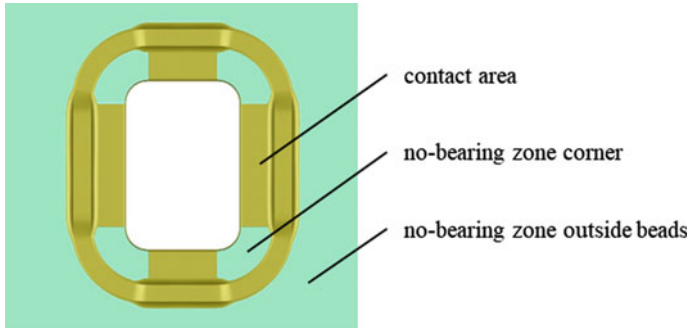


Fig. 5 Specification of active contact areas due to no-bearing zones on the binder geometry

Reference Model

For the reference simulation, AutoForm Forming R8.0 in conjunction with the TriboForm FEM Plug-In for AutoForm was used. To describe the draw beads the 3D bead model was adopted. Bearing zones in the corner areas and behind the bead areas realize the behavior of thickening effects. Due to the no-bearing zones, an applied force results in a homogeneous surface pressure in the retaining contact areas. Figure 5 shows the implemented no-bearing zones. To account for accurate friction conditions, the measured surface roughnesses of the binder and the upper die (see Fig. 3), sheet ($1.1 \mu\text{m}$), and lubrication amount (1 g/m^2) was used as input for the TriboForm friction model.







Spotting Image Simulation Model

As for the reference simulation, the 3D bead model with the TriboForm friction model was used. Active contact areas are extracted from the digitized spotting images from which boundary curves were generated as input for AutoForm. Table 2 shows the contact areas for operation condition RD3 at 150 kN binder force, from which can be observed that the active contact area changes according to the drawing state.

It can be observed that the contact areas are shifting and changing between drawing states 0.5 and 1. Thinning of the blank material in the area of the lock beads reduces the contact area. Contrarily, the sheet metal thickens in the corner areas and additional contact areas are introduced.

Comparing the change in contact areas for the different operation conditions, a conversion to different surface pressures is possible. Figure 6 (left) shows the decrease in surface pressure over the drawing depth. The pressure distribution changes per time step and, therefore, for every drawing depth. Analyzing the contacting surface area for the different spotting images, it becomes clear that the surface pressure decreases due to the increase of surface area. Especially the graph for the binder (Fig. 6 (left)) shows

Table 2 Change of spotting images for binder and upper die, loaded with 150 kN. Linear increase of surface area content for the binder; upper die constant surface area content

Drawing state	0	0.5	1
Binder			
Surface area (mm ²)	5177.2	6545.5	8230.5
Upper die			
Surface area (mm ²)	11560.2	12350.5	11589.9

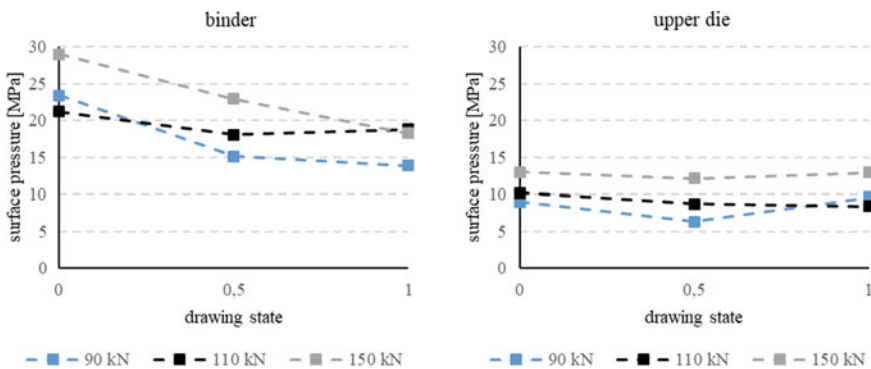


Fig. 6 Line graphs of surface pressure for binder and upper die from zero drawing state 0 to 1 for different binder forces

a linear decrease of the pressure distribution. Compared to the binder, the graph for the upper die shows only a slight change of surface pressure during forming. These average values show the variation of the pressure distribution during the forming process. Therefore, considering the change in contact areas in forming simulations will improve the prediction of the real forming processes. Focussing on the results from the line graphs, only the spotting images from the binder were implemented in the new forming simulation model.

Based on the obtained results, a new simulation model was developed. The new simulation model, including real contact areas, was implemented by generating a simulation model including three drawing operations. For the different operations, the drawing depth was divided into sub-steps as shown in Table 3. In the respective drawing states, boundary curves of the real digitized contact area were imported and defined as bearing zones.

Table 3 Specific drawing states in millimeters for each operating conditions

Drawing state	0	0.5	1
RD1	0–6.75 mm	6.75–20.25 mm	20.25–27 mm
RD2	0–5.75 mm	5.75–17.25 mm	17.25–23 mm
RD3	0–5 mm	5–15 mm	15–20 mm

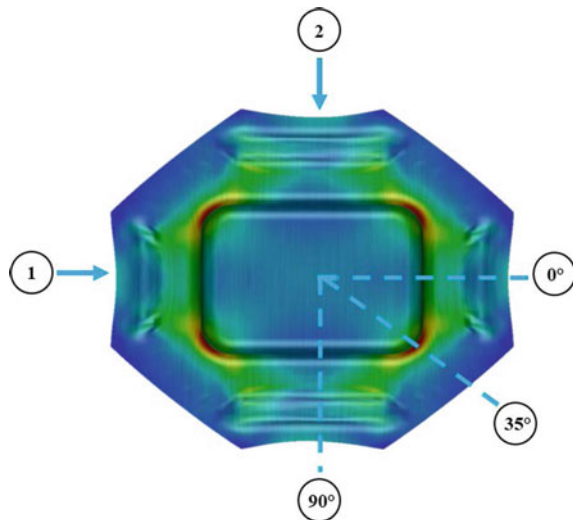
Results

In the following section, the results of the different operation conditions are presented and discussed. Evaluating the obtained results, the draw-in and major strain were chosen as validation measures. Figure 7 shows the measurement locations. Measurement location 1 and 2 describes the location where the draw-in was measured. The major strain is analyzed in three different sections, represented by 90, 35, and 0. In the following figures, the draw-in is shown in the upper left corner and the major strain is plotted in the remaining quadrants. The results are presented from RD1 (lowest binder force) to RD3 (highest binder force).

In Fig. 8, the results corresponding to operation condition RD1 are shown. For RD1 a binder force of 90 kN was used. Analyzing the draw-in data, it becomes clear that the prediction accuracy is increased in the area of the round bead. For the major strain, all three sections give an increased prediction accuracy in the bottom of the part. Towards the round bead, both models give an underprediction compared to the real measured major strains.

For operating point RD2 (see Fig. 9) with a binder force of 110 kN a nearly similar result as RD1 is shown. The major strain in sections 90 and 35 is accurately predicted. The prediction of strains in 0° is limited after the wall area towards the

Fig. 7 Specific part evaluation scheme for main validation parameters draw in and major strain



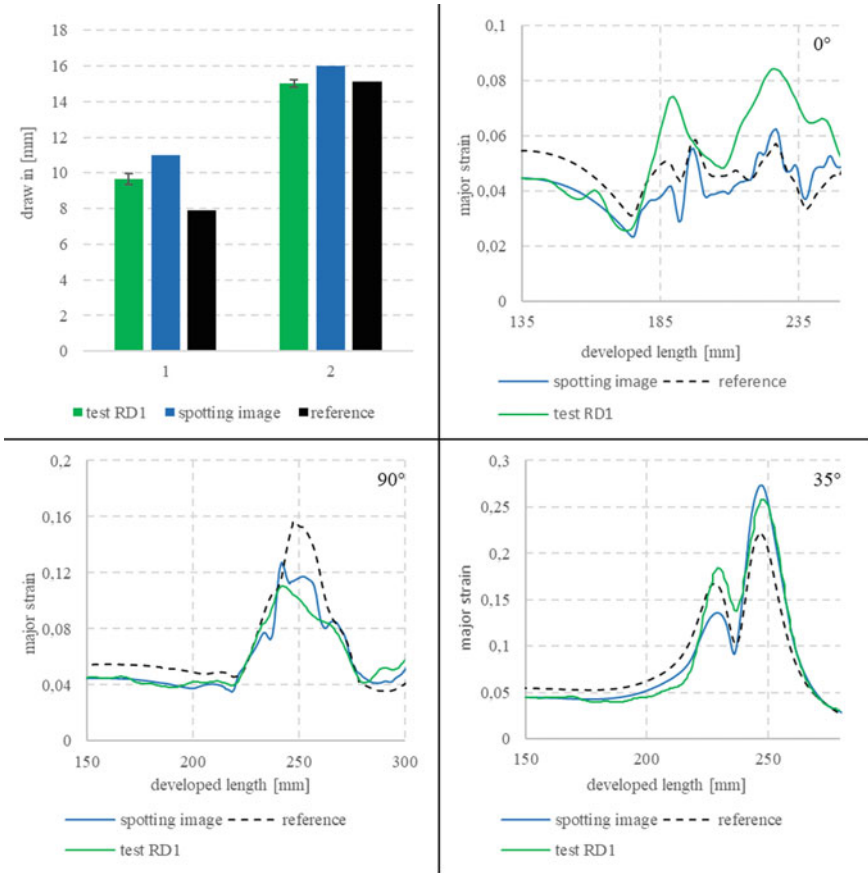


Fig. 8 Result plot for test RD1 with binder force 90 kN and 27 mm drawing depth

bead area. Discrepancies might be introduced by a faulty interpretation of thinning in the spotting image, which might lead to local differences in pressure distribution.

For *RD2*, the major strain is most accurately predicted for the 35° case. This indicates that the shift in contact areas due to thickening is affecting the simulation results.

Results of the last operation condition (*RD3*), with the highest binder force of 150 kN, are shown in Fig. 10. The draw-in for the lock bead (Section “Introduction”) shows a good correspondence. Also the major strain in the lock bead section for the bottom and wall area shows a good correspondence. Due to the smaller drawing depth the major strain in the round bead section is better predicted by the reference model. The ratio of the two parameters binder force and drawing depth influences each other and requires further investigation in series dies to clarify the effect for the round bead section.

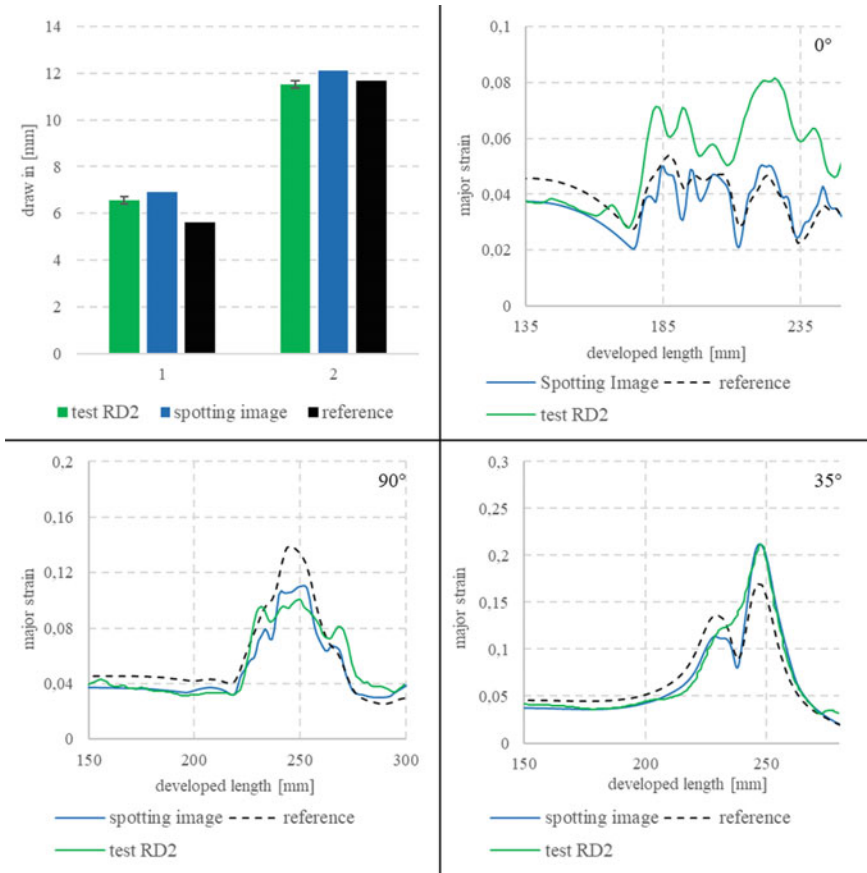


Fig. 9 Result plot for test RD2 with binder force 110 kN and 23 mm drawing depth

Overall, results show that the material flow and the thinning effect can be improved by accounting for active contact areas. This was established by an improved digitalization process to capture more precisely the color of the spotting image. To include spotting images into forming simulations extended effort is required. Therefore the segmentation and image processing was improved with specific python-libraries, enabling an enhanced extraction of real contact areas. In addition, the effort can be reduced significantly by choosing a limited set of spotting images. Transferring the findings of the rectangle cup to series dies/parts prove the benefits of the new simulation approach.

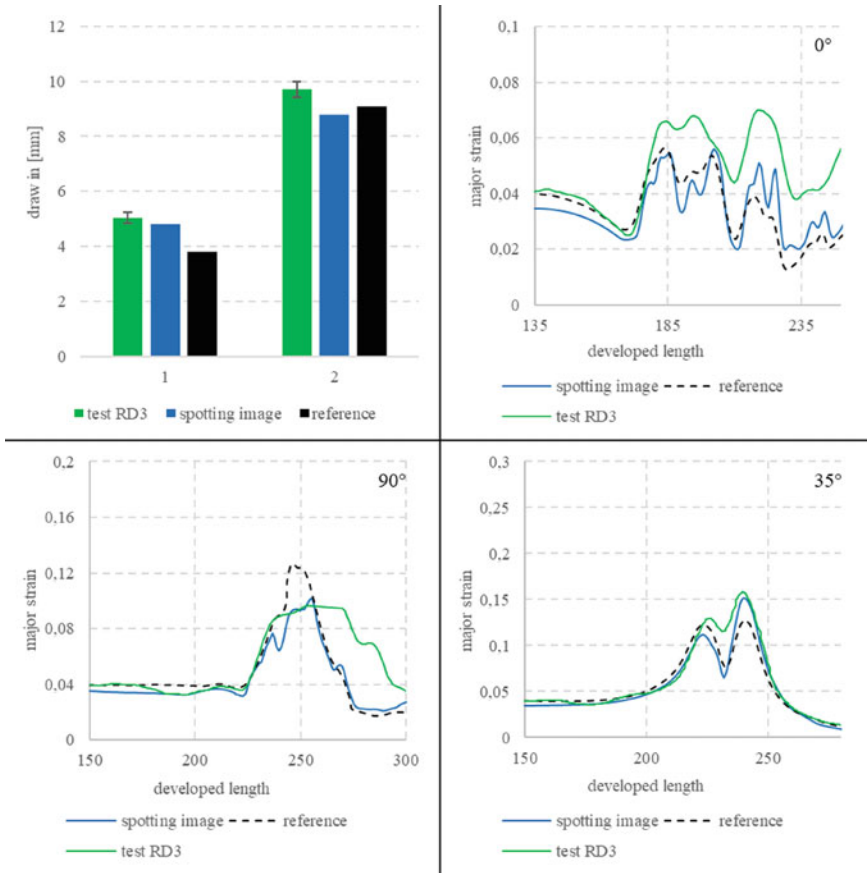


Fig. 10 Result plot for test RD3 with binder force 150 kN and 20 mm drawing depth

Conclusion and Outlook

In this paper it is shown that the spotting image changes over the drawing depth. Thinning/thickening of the sheet during the forming process changes the spotting image and therefore the pressure distribution. The decrease of the pressure distribution due to thickening effects in the corner areas is an important parameter in forming simulations and should be properly accounted for. It is shown in this paper that an increased prediction of the pressure distribution increases the predicting capabilities of the forming simulation. Besides the effect of the material thinning, the spotting image represents press and tool characteristics indirectly. For the die try-out process, this investigation showed that the drawing state to evaluate the die performance best is drawing state 1. This state includes the effect of thinning on pressure distribution during the forming simulation.

Further studies will focus on validating the presented simulation approach on series dies and parts. In addition, other press and tool parameters like cushion pins or tool stiffness will potentially increase the simulation accuracy. Characterizing specific friction conditions for lock beads and round beads can possibly improve the prediction of major strains and draw-in in these areas.

References

1. Essig P, Liewald M, Bolay C, Schubert T (2019) Digital process support in toolmaking by using optical metrology. IOP Conf Ser: Mater Sci Eng 651:012026
2. Bolay C, Wied J, Naegele P, Hol J (2018) Advanced friction modelling in sheet metal forming simulation and their effect on drawbead models. NEBU 2018 – Neuere Entwicklungen in der Blechumformung
3. Hol J, Wiebenga JH, Stock J, Wiegand K, Carleer B (2016) Improving stamping simulation accuracy by accounting for realistic friction and lubrication conditions: application to the door-outer of the Mercedes-Benz C-class Coupé. J Phys Conf Ser 734:032091
4. Hörstge M, Liewald M (2019) Compensation methods to reduce the effects of elastic deformations in the forming process. ESI FORUM Germany
5. Zgoll F, Kuruva S, Götze T, Volk W (2019) Virtual die spotting: compensation of elastic behavior of forming presses. IOP Conf Ser: Mater Sci Eng 651:012021
6. Pilthammar J, Sigvant M, Kao-Walter S (2018) Introduction of elastic die deformations in sheet metal forming simulations. Int J Solids Struct 151:76–90. <https://doi.org/10.1016/j.ijsolstr.2017.05.009>
7. Bolay C, Essig P, Kaminsky C, Hol J, Naegele P, Schmidt R (2019) Friction modelling in sheet metal forming simulations for aluminium body parts at Daimler AG. IOP Conf Ser: Mater Sci Eng 651:012104
8. Liewald M, Essig P, Bolay C (2019) Digitalisierte Tragbilder im Werkzeug-Tryout: Datenrückführung von realen Traganteilen tuschierter Wirkflächen in die Umformsimulation. wt Werkstattstech online 109(10):722–726
9. Liewald M, Essig P, Bolay C (2020) Contact area evaluation of digitalized spotting images as a criterion for die tryout. In: 23rd International conference on material forming (ESAFORM 2020)

Optimization of Slip Conditions in Roll Forming by Numerical Simulation



Marco Becker and Peter Groche

Abstract Energy efficiency is a primary objective in industrial processes nowadays. Roll forming represents a well-established and widespread technology in mass production. In this process, a sheet metal is conveyed by frictional contact with the roll forming tools. The varying roll diameter along the sheet contact line entails different peripheral speeds with decelerating sections leading to undesirable increases of drive torques.

This paper introduces optimizations implemented in a numerical model regarding energy efficient slip conditions between the sheet metal and the forming tools. Different feed settings are investigated locally for each forming step to quantify effects on resulting drive torques. As one measure, changes in gear ratio between top and bottom rolls reduce the difference in upper and lower driving torques in comparison to the initial state and thus lead to an optimized torque balance with significantly lower energy consumption. As a second measure, a systematic decoupling of decelerating roll segments reduces the overall driving torques and results in an energy saving potential of 41.7%. From these results, the preliminary design of industrial roll forming tools can be improved by the use of sliding or rolling bearings in certain roll segments and by provision of an adjustable transmission ratio in the powertrain.

Keywords Roll forming · Energy efficiency · Slip · Torque

Introduction and State of the Art

The industrial sector is annually responsible for more than 50% of the world's energy consumption [1]. Roll forming, as a mass production process for cold rolled products, is an important part of steel processing [2]. According to several studies discussed hereinafter the process offers a high potential for energy saving and can therefore contribute to an improvement of industrial energy efficiency. Due to the fact that

M. Becker (✉) · P. Groche

Institute for Production Engineering and Forming Machines, Technische Universität Darmstadt, Otto-Berndt-Straße 2, 64287 Darmstadt, Germany
e-mail: becker@ptu.tu-darmstadt.de

© The Minerals, Metals & Materials Society 2022

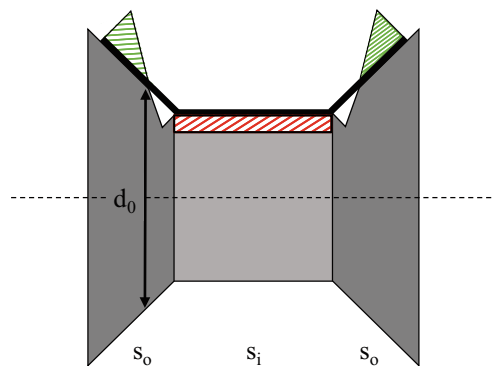
K. Inal et al. (eds.), *NUMISHEET 2022*, The Minerals, Metals & Materials Series,
https://doi.org/10.1007/978-3-031-06212-4_63

693

the forming rolls are responsible for both forming and sheet feeding, the energy demand for each forming step is dependent on the neighboring stages, resulting in complex interactions. Based on the profile geometry and bending angles of each step, the diameter of the rolls varies across the width and thus creates discontinuous slip distributions. According to a theory by Eichler [3], an optimized slip characteristic is achieved with a balanced ratio of accelerating and decelerating areas at each single forming stage, resulting in an overall accelerating torque. The so-called driving shaft diameter d_0 represents the crossover point between positive and negative slip (Fig. 1). However, locating or even specific positioning of the driving diameter is very complex due to the given interactions between the several forming stages. For this reason, torque measuring systems are used in scientific research to understand the powertrain behavior.

Based on the current state of knowledge, there are several influential parameters for increasing energy efficiency in roll forming. Paralikas et al. [4] introduce an energy efficiency indicator by using analytical models. The most influential parameters are found to be the bending angle sequence, the line velocity, and the inter-distance between the forming stands. These findings confirm the impact of the interacting behavior between the neighboring stages. Modifications at individual forming stages were not part of these investigations. Similarly, Shirani Bidabadi et al. [5] achieve positive effects on energy demand by varying the distances between forming stands and changing the bending angle increments for the whole forming line. Their investigations involve a numerical model as well as an experimental setup. Unfortunately, Bidabadi's experiments do not allow a recording of separate torques of each drive shaft, which makes it impossible to locate positive and negative torques for the individual forming stages. In a study by Traub and Groche [6], reaction torques are measured at single-engine units for each top and bottom shaft of a forming stage. These measurement data allow an iterative adjustment of the individual angular velocities of each forming tool in a numerical model to achieve an optimized total torque. For industrial roll forming lines without single-engine units Traub's findings can be used for the design of individual roll diameters depending on the circumferential speed. In this context, it must be noted that enlarged roll diameters lead to

Fig. 1 Accelerating and decelerating parts of a bottom forming roll depending on the driving shaft diameter d_0 according to Eichler's theory [3]



increased mass and therefore to comparatively higher energy demand [4]. In another study Traub et al. [7] investigated the behavior of local torques on separated roll segments of one shaft while changing feed speeds at some of the shafts iteratively. Their results show that through a shift from positive to negative slip on individual roll segments it is possible to achieve an overall balanced driving torque at each forming pass.

Optimization of Slip Conditions in Numerical Simulation

Idea of the Optimization Approach

The idea of this study is to use the knowledge about the interactions between neighboring forming passes and about the effect of varying slip distribution within one stage to investigate suitable measures for increasing the energy efficiency of the whole roll forming line. The aim is an adaption of the forming and sheet feed interactions between the roll segments to obtain feed torques that are better balanced compared to given standard setups. For this purpose, speed variations at individual drive trains are not intended as this is not achievable for most of the industrial roll forming lines that employ one engine for several forming stands. This paper presents the numerical model for two measures, which are technically feasible for systems with group drives: an adaptation of the transmission ratio between top and bottom rolls and a decoupling of individual roll segments for the pre-design of optimized roll forming tools. The numerical setups and findings with combinations of these measures are analyzed by means of the theoretical understanding upon a close examination of the speed characteristics and the related slip behavior.

Description of the Numerical Model

The numerical model needs to describe the contact conditions with great accuracy in order to obtain reasonable torques at the forming tools. Therefore, the sheet metal contains a global mesh as well as a locally more refined area in the forming zone. The model with its basic setup is illustrated in Fig. 2. It has been used and validated in previous investigations by Traub et al. [6, 7]. The sheet metal is driven by friction with the rotating forming rolls. The friction coefficient is set to $\mu = 0.1$ due to findings in strip drawing tests [6]. For the U-channel profile symmetry along the x-z-plane is assumed. Both the top and side rolls are mounted with springs to reproduce the compliance of the forming stands.

In this paper, a numerical pre-design for an optimized gear ratio as well as a separable roll forming tool set is presented. For this purpose, the transmission ratio between top and bottom rolls of the whole forming line is iteratively adapted by

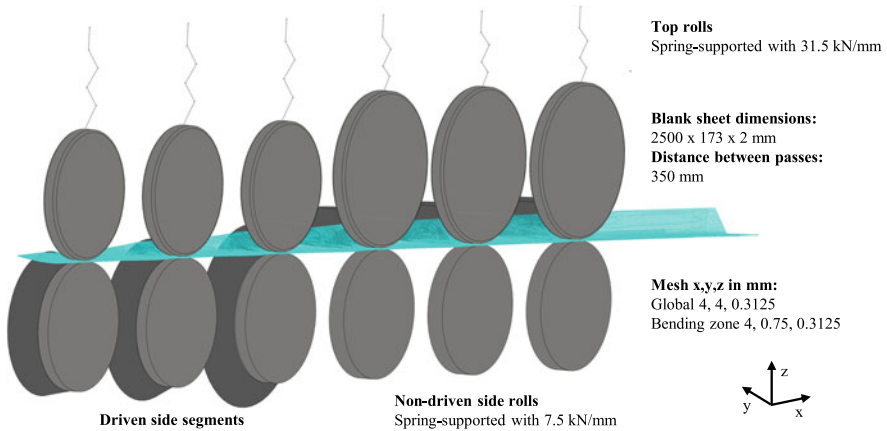


Fig. 2 Numerical model with initial setup

changing the angular speeds of all top rolls. Furthermore, the cylindrical and conical areas of the bottom rolls are separated in order to decouple each section individually from the powertrain.

Theoretical Understanding of Feed Speed and Slip Behavior in Roll Forming

The theoretical understanding of slip behavior in roll forming is illustrated by a six-stage roll forming line with a U-channel profile. Figure 3a shows the differences of the circumferential speeds along the roll lengths. The top rolls only consist of cylindrical center segments to eliminate the decelerating parts in comparison to wider rolls with decreasing diameter from the bending edge to the sheet metal edge. The first three forming stages are fully driven. The bottom rolls consist of increasing diameters towards the edge, resulting in a linear increasing circumferential speed. The last three forming stages are equipped with driving cylindrical center segments at the top and bottom as well as non-driven side rolls. The latter are dragged along by the sheet metal feed speed causing the illustrated circumferential speed profile.

With regard to the theoretical analysis, the bottom rolls 1–3 generate sheet pulling due to the increasing circumferential speed. By contrast, in the transition area to stage 4 the drive speed is reduced abruptly due to the non-driven side rolls—resulting in sheet pushing. Between stages 4 and 6, the decelerating effect of the non-driven side rolls is gradually reduced by their increasing diameters, resulting in a comparatively slight sheet pulling. This observation is confirmed by the required torques in the initial state of the numerical simulation shown in Fig. 3b. The arrows illustrate sheet pulling (solid line), sheet pushing (dotted line) and nearly balanced behavior (dashed line). The cylindrical top rolls with constant circumferential speed in all six stages

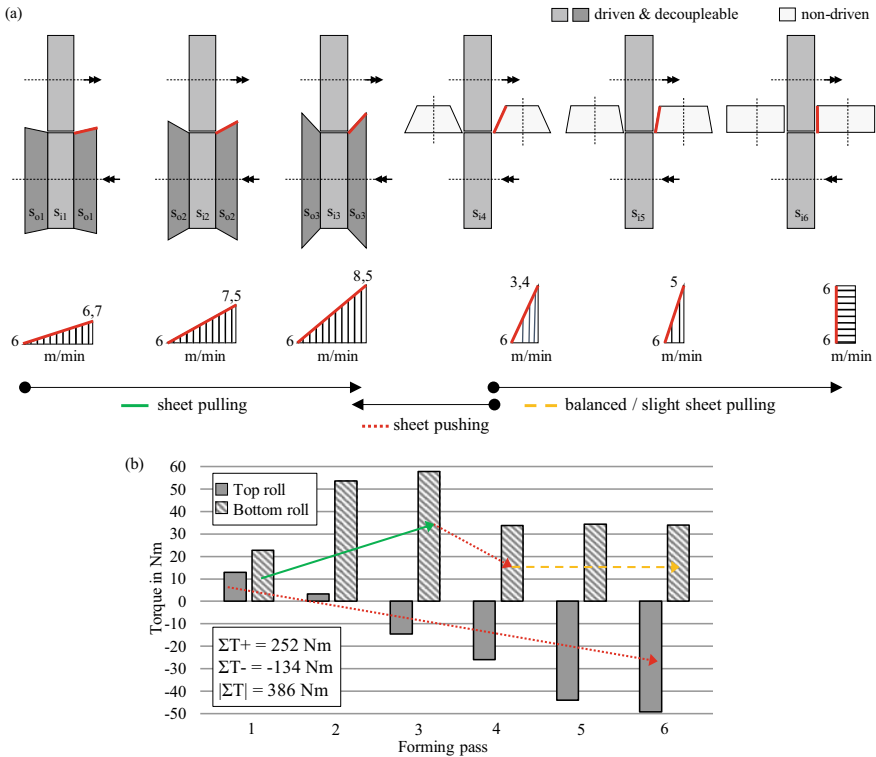


Fig. 3 Circumferential speeds on a six-stage roll forming line (a) and torques on bottom (a) as well as top (b) rolls in the initial state

have decreasing torques from stage 1 to 6 due to the increasing speed of the bottom line. However, the sheet pushing between stages 3 and 4 due to the bottom rolls does not have a noticeable effect on the torques of the top rolls.

Systematic Changes of Transmission Ratio

From the analysis of the torques in the initial state follows that an adjustment of the gear ratio between the overall accelerating bottom rolls and the predominantly decelerating top rolls might lead to an improvement in balance and thus reduce the energy requirement. The effects on torque due to a small adjustment of the transmission ratio by 1.004:1.000 and 1.008:1.000 are shown in Fig. 4a, b. In comparison to the initial state, the torques at the top rolls increase throughout resulting in increased positive torques at the first two passes. Furthermore, a transition from decelerating to accelerating torques at passes 3 and 4 and lower decelerating torques at passes 5 and 6 occur. The sum of the accelerating and decelerating torques as well as the total

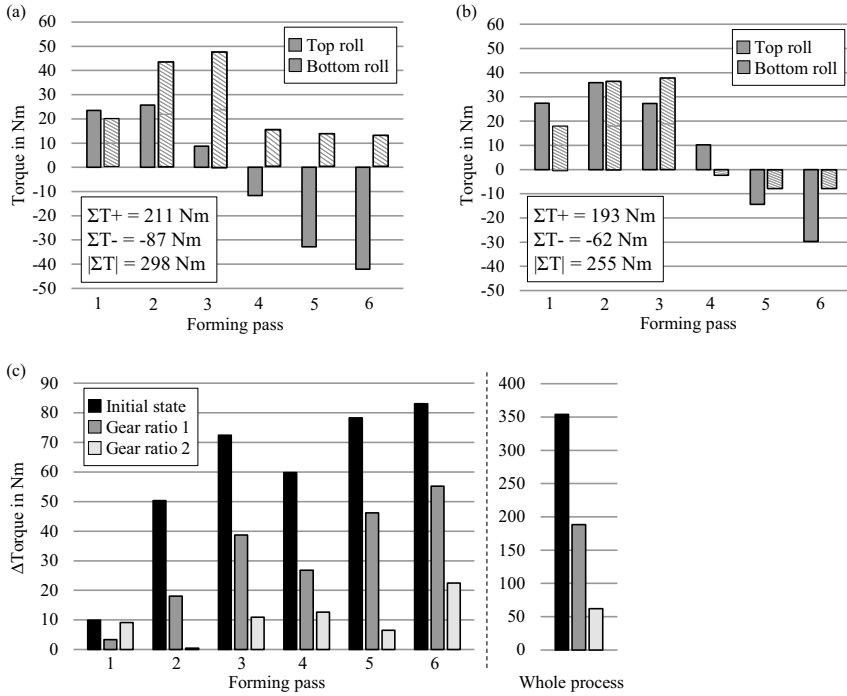


Fig. 4 Torques on top and bottom rolls for gear ratio 1 (a), gear ratio 2 (b), and results for an optimized balance in comparison to the initial state (c)

torque of the forming process is a measure for the energy demand. The energy saving compared to the initial process is therefore 22.8% for gear ratio 1 and 33.9% for gear ratio 2. A comparison of the torque deltas at the bottom and top rolls shows the improvement in balance for each forming step and the overall optimization from the initial state via gear ratio 1 to gear ratio 2 (Fig. 4c). It should be mentioned that in the last two, respectively, three forming steps decelerating torques are applied on both the upper and lower rolls, causing a sheet pulling from stage 4, respectively, stage 3 on with possible disadvantages for the profile geometry. However, the simulation results do not indicate any significant change in the final geometry of the profile.

Decoupling of Tool Segments

By decoupling single roll segments of the roll forming tools, the focus is placed on balanced torque distribution as well as a total reduction of the required driving torques. Since at the upper shafts only cylindrical rolls are installed, the investigation is based on the decoupling of bottom roll segments. There are two different approaches for this:

- The first option is to decouple the slower circumferential moving cylindrical inner segments, which—as can be seen from the theory of Eichler [3] and the results of Traub et al. [7]—can even have decelerating effects. It should be noted that different scenarios are considered because of the setup with three driven side segments and three non-driven side rolls in the initial state of the given roll forming line (compare to Fig. 3). Accordingly, different decoupling combinations are tested in the numerical simulation, whereby the combinations of decoupling the three front inner segments ($s_{i,1-3}$) and all six inner segments ($s_{i,1-6}$) have proven to be most successful.
- The second option is to decouple the first three driven side segments ($s_{o,1-3}$), meaning that all roll forming passes are driven uniformly by their cylindrical tool segments at the same circumferential speed and all side roll segments dragged along without drive.

The torque data of both approaches are illustrated in Fig. 5. The initial state is compared to decoupled outer segments 1–3 $s_{o,1-3}$, decoupled inner segments 1–3 $s_{i,1-3}$, and decoupled inner segments 1–6 $s_{i,1-6}$. The results can be explained by the fact that a decoupling of the outer roll segments $s_{o,1-3}$ leads to reduced torques on these first three bottom rolls and therefore to a better balance due to more similar speed transmission from the cylindrical roll segments (Fig. 5a). The unbalanced behavior in the last three forming stages remains with high accelerating torques at the bottom and decelerating torques at the top rolls. Likewise, a decoupling of the

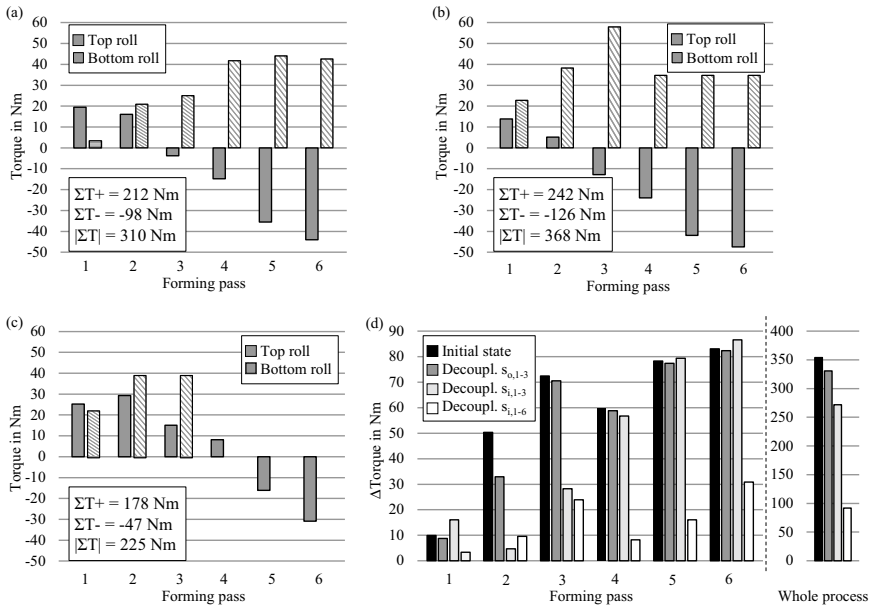


Fig. 5 Torques on top and bottom rolls for $s_{o,1-3}$ (a), $s_{i,1-3}$ (b), $s_{i,1-6}$ (c), and results for an optimized balance in comparison to the initial state (d)

inner roll segments in the first three stages $s_{i,1-3}$ results in a remaining unbalanced torque distribution in the last three stages with even stronger accelerating torques at the bottom and decelerating torques at the top rolls (Fig. 5b). By additionally decoupling the bottom segments at the last three stages to achieve setup $s_{i,1-6}$, the accelerating torques at the bottom are eliminated and the decelerating torques at the top rolls are decreased as well (Fig. 5c). This leads to a comparatively low total torque requirement with an energy saving potential of 41.7%.

Discussion and Conclusion

In this paper, two different measures for changing the slip conditions in a roll forming process have been developed using a numerical model. A better balance of torques between the interacting forming steps as well as a lower energy demand of the whole forming process have been achieved. The measure of decoupling roll segments has a positive effect on the torque distribution, whereas the decoupling of all inner segments $s_{i,1-6}$ obtains the best results. With the improved gear ratio 2 between top and bottom rolls an even better balanced torque distribution is achieved. As illustrated in Fig. 6, this balance distribution is also reflected in the proportion of sheet metal driving energy, which is found to be higher for gear ratio 2 at 85% than for setup $s_{i,1-6}$ at 81%.

However, the calculation of the actual energy savings compared to the initial state shows that setup $s_{i,1-6}$ at 41% has a higher energy saving potential than gear ratio 2 at 32%. This is due to the fact that setup $s_{i,1-6}$ certainly has a slightly worse torque balance, but a significant lower total torque for both accelerating and decelerating torques. It is assumed that a balanced ratio between the top and bottom torques results in a better profile quality with fewer geometrical errors such as vertical bow. Both optimization measures do not show any negative effects on the resulting profile

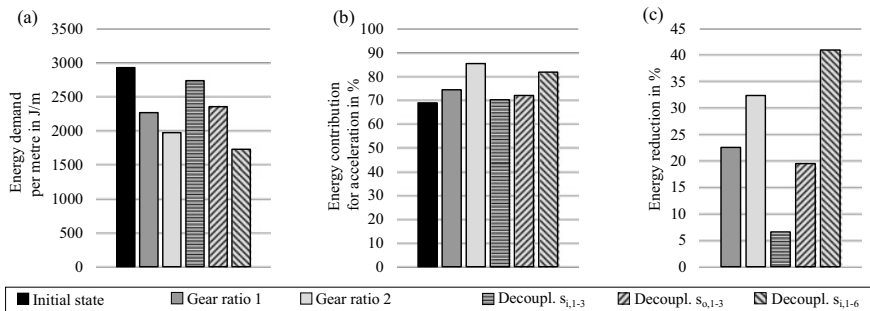


Fig. 6 Results of the investigated measures for energy demand (a), accelerating energy contribution (b), and total energy reduction (c)

quality in the numerical simulations. This is comprehensible as both measures represent an optimization with respect to the initial state. And in the context of these investigations it has been proven experimentally that only a slight vertical bow upwards occurs in the initial state, which is probably caused by strip edge strain and cannot be prevented without adjustment stages. For the two measures developed numerically in this paper, further experimental investigations will verify if changes in profile geometry occur in reality. For this purpose, an industrial roll forming line will be equipped with decoupleable roll segments for a parametric study on the given U-channel profile and other profiles with different slip conditions.

Acknowledgements The investigations presented in this paper were carried out within the AIF ZIM projects ZF4675401PO8 and ZF4016531PO8 supported by: Federal Ministry for Economic Affairs and Energy on the basis of a decision by the German Bundestag. The authors thank the AIF ZIM committee and the project partner DREISTERN GmbH & Co. KG for the cooperation.

References

1. U.S. Energy Information Administration (2019) International Energy Outlook 2019. Report at <https://www.eia.gov/ieo>. Accessed 26 Jan 2020
2. Halmos GT (2006) Roll forming handbook. CRC Press Taylor & Francis Group, Boca Raton
3. Eichler U (1987) Walzprofilieren von Standardquerschnitten auf einer mehrgerüstigen Maschine mit einzeln angetriebenen Werkzeugwellen. Ph.D. thesis, Technische Hochschule Darmstadt, Germany
4. Paralikas J, Salonitis K, Chryssolouris G (2013) Energy efficiency of cold roll forming process. *Int J Adv Manuf Technol* 66:1271–1284. <https://doi.org/10.1007/s00170-012-4405-8>
5. Shirani B, Moslemi H, Azizi R (2017) Experimental and numerical study of required torque in the cold roll forming of symmetrical channel sections. *J Manuf Processes* 27:63–75. <https://doi.org/10.1016/j.jmapro.2017.04.026>
6. Traub T, Groche P (2018) Energy efficient roll forming processes through numerical simulations. *J Phys: Conf Ser* 1063:012182. <https://doi.org/10.1088/1742-6596/1063/1/012182>
7. Traub T, Güngör B, Groche P (2019) Measures towards roll forming at the physical limit of energy consumption. *Int J Adv Manuf Technol*. <https://doi.org/10.1007/s00170-019-03992-9>

Surface Texture Design for Sheet Metal Forming Applications



Meghshyam Shisode, Ton van den Boogaard, and Javad Hazrati

Abstract Sheet metal surfaces are generally textured to improve tribological performance in deep drawing applications. Variations in coefficient of friction in forming processes is one of the major causes of defective products. The major reasons for an unstable friction condition are the tool wear and inhomogeneity in lubricant amount. Textured surfaces can offer enhanced and stable friction condition. However, there is no clear design guidelines available for texturing sheet metal surfaces for a robust friction condition. Various types of texturing methods are available. In this study, the friction sensitivity of surface texture made by laser-texturing method to variations in tool wear and inhomogeneity in lubricant distribution is investigated. The laser-textured surface parameters such as crater diameter and texture density are chosen within the physically attainable range such that a robust friction behavior during forming process is achieved. A multi-scale friction model is used to determine coefficient of friction for textured surfaces in boundary and mixed lubrication conditions. The friction model in combination with surface generating algorithm is used to optimize individual crater geometry and their spacing. The objective is to determine the surface texture which is least sensitive to the potential variations in the tool roughness and lubricant amount in sheet metal forming applications.

Keywords Friction · Sheet metal forming · Texture · Optimization

Introduction

The laser-textured surfaces are gaining increased attention in industry to obtain a stable friction condition and better paint appearance in automotive and packaging applications. Though there are no mass production techniques yet available which can compete with the electro-discharged textured (EDT) sheet metals but the improved performance by the laser-textured surfaces have triggered motivation to develop mass production techniques. The sheet metal components manufactured by deep drawing

M. Shisode · T. van den Boogaard · J. Hazrati (✉)
Faculty of Engineering Technology, Nonlinear Solid Mechanics, University of Twente, Enschede,
The Netherlands
e-mail: j.hazratimarangalou@utwente.nl

© The Minerals, Metals & Materials Society 2022
K. Inal et al. (eds.), *NUMISHEET 2022*, The Minerals, Metals & Materials Series,
https://doi.org/10.1007/978-3-031-06212-4_64

process have number of uncertainties or variations between the product batches or even two consecutive components which may lead to defective products. The major sources of variations are evolving tool topography due to wear, lubricant migration on sheet surface, change in ambient condition, and material properties of the sheet metal. Controlling the tribological system is one of the important factors to improve the productivity. The tribological system is defined by the tool-sheet metal contact condition, their surface topographies and the lubricant. The tool wear is a major reason which results in unstable friction condition at tool-sheet metal leading to product deviations and failures.

Friction between the contacting surfaces is a local phenomenon which depends on the local surface interactions [1, 2] often referred as the real area of contact. The real area of contact depends on the contact loads, materials, and surface topographies of the contacting surfaces [3]. It is very well understood that the surface texture plays a significant role in determining the coefficient of friction. For instance, the surface pockets of the laser-textured surface can act as lubricant reservoir where a hydrodynamic pressure can build up leading to a lower coefficient of friction.

The main goal of this study is to design a laser-textured surface for a robust friction behavior in boundary and mixed lubrication regimes. The robust friction behavior allows the minimum variation in the coefficient of friction for the uncertainties in the tribological system. In this study, surface texture is designed to achieve least variation in friction coefficient due to variations in the tool topography because of wear and uneven lubricant distribution in the blank. For this purpose, laser-textured surfaces are generated for a range of laser texture parameters such as crater depth, diameter, and density. The coefficient of friction is determined using a multi-scale friction model [2, 3] by varying tool topography and lubricant amount within a realistic range as expected in industrial forming tools.

Approach: Robust Friction Behavior

The current study is limited to laser-textured surfaces under boundary and mixed lubrication friction regimes. The tool surface topography and lubricant amount are used as the uncertainty parameters. The tool is assumed to be rigid and the untextured sheet surface used for laser-texturing to be zinc coated steel (GI) sheet with coating thickness of 7 μ m and substrate material of DX54. The material properties of zinc coating and steel substrate are required in the friction model and can be found in [2]. A set of laser-textured surfaces are artificially generated based on the physically attainable range of crater parameters [4]. A validated multi-scale friction model for zinc coated steel sheets is used to determine coefficient of friction at a range of contact loads and different surface topographies of the tool surface [1, 2]. Variation in the coefficient of friction due to change in tool topography is determined for all the surfaces. The optimum surface is selected such that it results in minimum variation in coefficient of friction.

Laser-Textured Surfaces

Figure 1 shows the surface topography of the laser-textured surface manufactured by pico-second pulse laser. The untextured GI sheet manufactured in steel industry has a low surface roughness ($S_q \leq 0.5 \mu\text{m}$ [3]) with a gaussian surface height distribution. However, the surface roughness of the untextured sheet can vary based on the process setting and roughness of the underlying steel substrate. The surface roughness of the untextured sheet can also be changed by further treatment such as sand blasting [3]. The surface is textured with a spherical crater of predefined size and area density.

In this study, the texture pattern is generated on the actual untextured surface of GI sheet obtained right after galvanization process. Figure 2a shows a typical untextured surface with Gaussian height distribution and Fig. 2b shows the textured surface and its resulting height distribution.

Multi-scale Friction Model

A reliable friction model is required to determine the coefficient of friction accounting for different surface textures. Traditionally, a constant Coulomb friction behavior is assumed between the contacting surfaces in the boundary and mixed lubrication regimes. However, the experiments [1, 2, 5] show that the coefficient of friction varies depending on contact pressure, strain, and amount of lubrication in the sheet metal. Local surface texture evolves due to the asperity deformation which consequently changes the local surface interaction between the contacting surfaces. The roughness of the surface decreases due to asperity flattening resulting in a decrease in coefficient of friction.

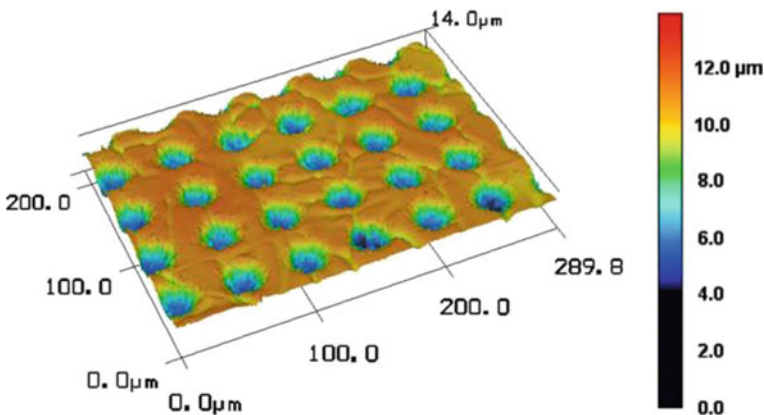


Fig. 1 Laser-textured surface manufactured using pico-second laser [4]

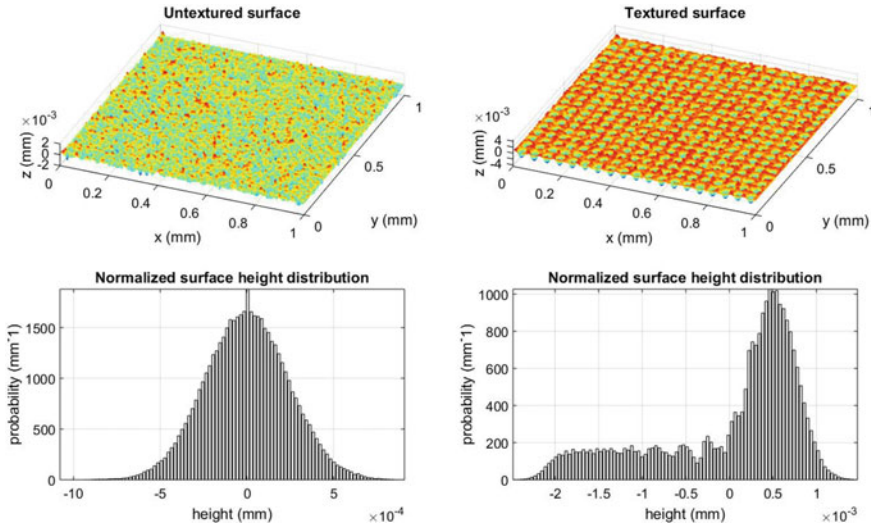
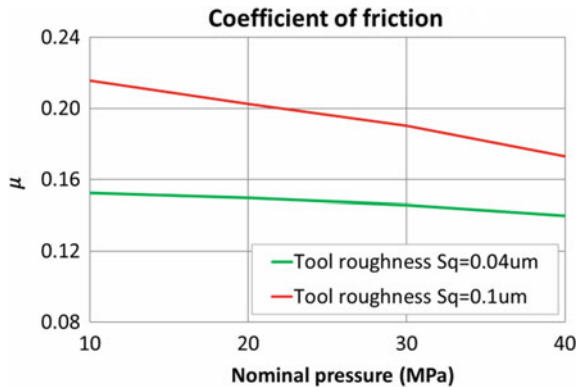


Fig. 2 Left: modeled untextured surface ($Sq_{wp} = 0.3 \mu\text{m}$), and right: textured surface (texture density: 50%, crater diameter: $40 \mu\text{m}$, crater depth: $2.5 \mu\text{m}$)

Recently, Shisode et al. [1] proposed a multi-scale friction model which considers the surface topography of sheet metal and tool, coating effects, contact loads, and hydrodynamic effects of lubricant to determine the coefficient of friction. More details on friction modeling and its implementation in full-scale finite element analyses of deep drawing processes can be found in [1, 2]. The friction model was validated at different scales using different lab-scale experiments. This model is used here to determine the coefficient of friction between different textured surfaces and forming tool at different contact pressures with varying lubricant amount. Figure 3 shows the result of coefficient of friction for a textured surface determined using the boundary friction model at different nominal pressures and tool roughness.

Fig. 3 Model results for textured surface (texture density = 60%, crater diameter = $30 \mu\text{m}$, crater depth = $1.1 \mu\text{m}$ and untextured surface roughness $Sq_{wp} = 0.25 \mu\text{m}$) at different tool roughness



Surface Texture Effects

The design variables for the laser-textured surface are surface roughness of untextured surface (S_{qwp}), crater diameter (DLT), and texture area density (ρ_{LT}). The crater depth (h_{LT}) depends on the crater diameter and setting of the laser beam. Mustafa et al. [4] have performed lab-scale experiments to produce laser-textured surfaces of steel and GI sheets by varying laser energy, pulse time, and number of pulses. Empirical relations are developed to correlate crater diameter and depth. A relation proposed for a pico-second single pulse laser beam for GI sheet is used to determine the crater depth at a given crater diameter. The uncertainty or noise variables in this study are the surface roughness of the tool (S_{qt}) and lubricant amount present in the contact. In a typical deep drawing process, the roughness of the tool is much smaller than the sheet surface. However, it can substantially increase due to tool wear. In this study, a measured tool topography from the die corner region of the Ericson press used in validation of the friction model [1] is considered. The roughness of the tool is scaled appropriately to account for the tool wear. Table 1 shows the design variables and uncertainty parameters used in the current study.

The design variables are assumed to be discrete. The measured roughness of the existing tool is $0.07 \mu\text{m}$. However, a range of tool roughness from 0.04 to $0.1 \mu\text{m}$ is assumed to consider the evolution of tool topography due to wear. The crater area density is defined as the fraction of area covered by the texture. There are in total 54 combinations of the surfaces corresponding to the range and distribution of design variables. The coefficient of friction for each textured surface is determined based on finite element simulation of a strip-draw experiment and varying lubricant amount and tool roughness. For this purpose the friction model is coupled with the finite element simulation. More details on coupling the friction model with the finite element simulations can be found in [1, 2]. Figure 4 shows the schematic of the virtual strip-draw experiment, typical friction curve obtained from FE analysis for different tool roughness and lubricant amounts. Figure 4 right depicts the total contact pressure and lubricant pressure distributions for different lubricant amounts representing boundary and mixed lubrication conditions.

Table 1 Design and uncertainty parameters for optimization

Design variables	
RMS roughness of untextured surface S_{qwp} (μm)	0.3, 0.5
Crater diameter dLT (μm)	30, 45, 60
Crater depth h_{LT} (μm)	1, 3, 5
Crater area density ρ_{LT} (%)	20, 40, 60
Uncertainty parameter	
RMS roughness of the tool S_{qt} (μm)	0.04, 0.07, 0.1
Lubricant amount (g/m^2)	0.2, 2

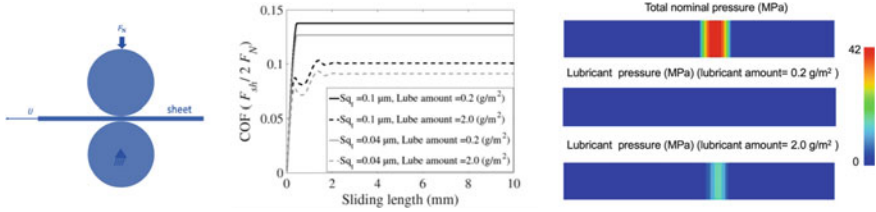


Fig. 4 Schematic of the virtual strip-draw experiment (left), typical coefficient of friction curve result from FE simulation (middle) and total and lubricant contact pressure distributions on the strip (right). The results are shown for the following conditions: $Sq_{\text{wp}} = 0.5 \mu\text{m}$, $\rho_{\text{LT}} = 60\%$, $D_{\text{LT}} = 30 \mu\text{m}$ and $h_{\text{LT}} = 5.0 \mu\text{m}$

Figure 5 shows the coefficient of friction results at different tool roughness values, untextured sheet metal surface roughness of 0.3 and $0.5 \mu\text{m}$ and lubricant amount of 0.2 and 2 g/m^2 where boundary and mixed lubrication regimes are mainly expected, respectively. In the boundary lubrication regime, initial workpiece roughness (untextured) can well affect the coefficient of friction (Fig. 5a–c). For surfaces with crater depth (h_{LT}) of $1 \mu\text{m}$, the lubricant amount of 0.2 g/m^2 is enough to fill surface valleys hence a mixed lubrication condition prevails, therefore coefficient of friction is lower. By increasing the lubricant amount, coefficient of friction in general decreases due to the mixed lubrication regime. The results show that mixed lubrication regime leads to more robust friction behavior and coefficient of friction becomes less sensitive to the workpiece texture parameters. Furthermore, with increase in tool roughness for both 0.2 and 2 g/m^2 lubricant amounts, rise in coefficient of friction can be observed.

Figure 6 shows the maximum deviation in coefficient of friction due to tool roughness variation for each surface texture design with the initial workpiece roughness of $0.5 \mu\text{m}$. It is shown that in the mixed lubrication regime (2 g/m^2), coefficient of friction is less affected with variations in the tool roughness. However, at 60% crater density and larger crater depth, 2 g/m^2 is not sufficient to fill the valleys completely and therefore boundary lubrication will be prevalent. As a general trend, in the boundary lubrication regime (0.2 g/m^2) the sensitivity of workpiece texture to the deviations in tool roughness is reduced by increasing the crater diameter.

Conclusions

In this study, the first steps to determine the surface texture parameters for a robust friction condition in laser-textured GI sheets are taken. The design variables used for the textured surfaces are the crater diameter, crater area density, and surface roughness of initial untextured surface. The uncertainty parameters used in this study are the roughness of tool surface and lubricant amount distribution. The textured surfaces are modeled for the given range of design parameters. A multi-scale friction model is used to determine the coefficient of friction for each surface by varying the tool roughness

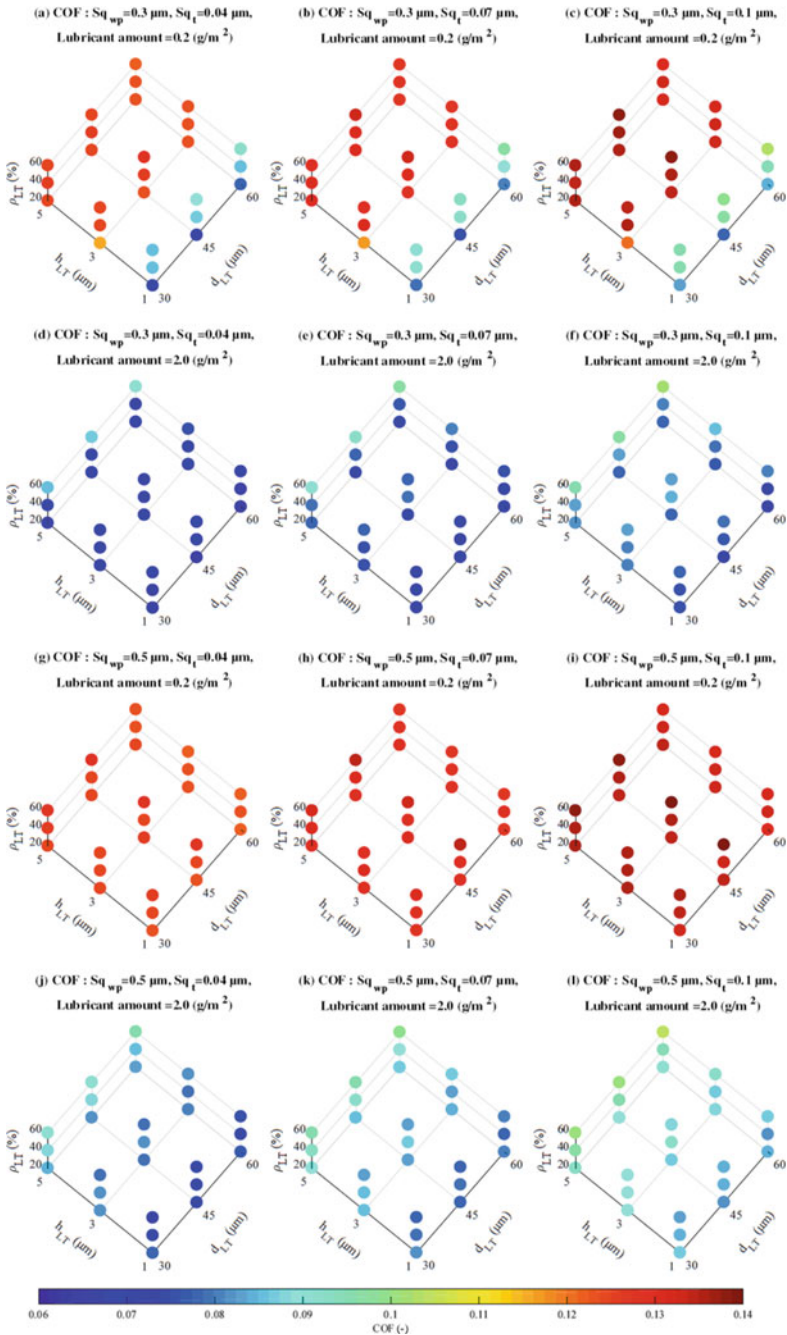


Fig. 5 Coefficient of friction for textured surfaces for the variation in tool roughness and lubricant amount

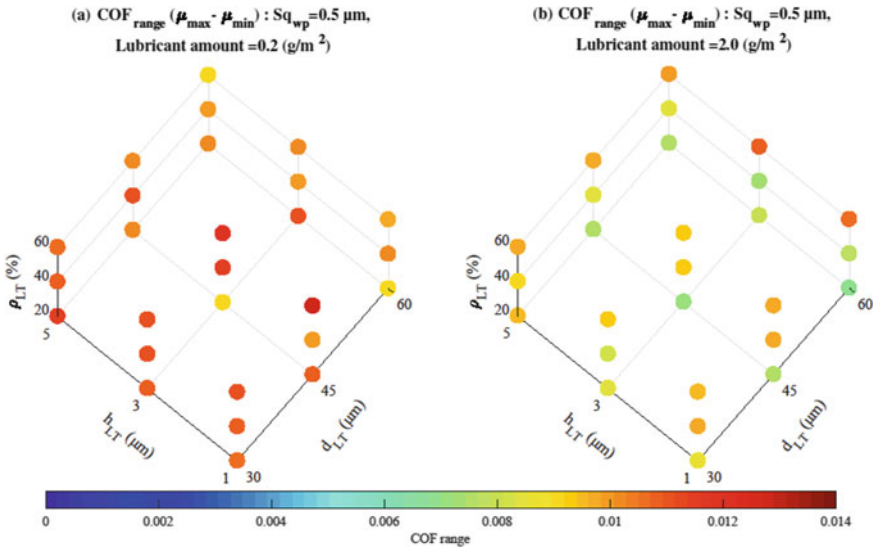


Fig. 6 Range of coefficient of friction with respect to tool roughness at lubricant amounts of (a) 0.2 and (b) 2.0 g/m²

and lubricant amount in boundary and mixed lubrication regimes. The robustness in friction behavior is quantified in terms of variation in friction coefficient for each surface. The variation in coefficient of friction decreases with decrease in roughness of initial untextured surface and increase in crater diameter in boundary lubrication. The results show that mixed lubrication regime is less susceptible to variations in tool roughness.

Acknowledgements This research was carried out under project number S22.1.14520b in the framework of the Partnership Program of the Materials innovation institute M2i (www.m2i.nl) and the Technology Foundation TTW (www.stw.nl), which is part of the Netherlands Organization for Scientific Research (www.nwo.nl).

References

1. Shisode M et al (2021) Modeling boundary friction of coated sheets in sheet metal forming. Tribol Int 153:106554
2. Shisode M et al (2021) Mixed lubrication friction model including surface texture effects for sheet metal forming. J Mater Process Technol 291:117035
3. Shisode M et al (2020) Semi-analytical contact model to determine the flattening behavior of coated sheets under normal load. Tribol Int 146:106182
4. Mustafa H et al (2019) Effect of surface roughness on the ultrashort pulsed laser ablation fluence threshold of zinc and steel. Appl Surf Sci 488:10–21

5. Mustafa H (2019) (Ultra) Short Pulsed Laser Surface Texturing of Zinc. PhD thesis, University of Twente, 2019
6. Westeneng A (2003) Modelling of contact and friction in deep drawing processes. PhD thesis, University of Twente, 2003

Part IX
Challenges and Opportunities in Forming
Aluminum

Effect of Thermal Treatment on Deep Drawability of AA3xxx Alloy



Vivek Srivastava, Sumit Gahlyan, Manali Khandelwal,
and Akshay Deshpande

Abstract Deep drawability of aluminum alloys depends strongly on its microstructure, including metallurgical texture. During production of cold rolled sheet of aluminum, upstream processes like homogenization alter the microchemistry of the alloy and have significant effect on the microstructure of the hot rolled coil. Annealing response post-cold working is found to show strong dependence on heating rate when softening processes interact with microchemistry evolution. Different microstructures and textures were observed in material processed with different homogenization and annealing treatment. VPSC simulations were used to predict deep drawability of these microstructures. Tensile and Erichsen tests were carried out to validate the predictions.

Keywords AA3003 · Homogenization · Annealing · Formability · VPSC

Introduction

AA3xxx alloys are Mn rich alloys used for packaging and architectural applications [1]. These alloys are non-heat treatable and mechanical properties of these alloys are controlled by grain structure. Grain size, preferred crystallographic orientations and their distribution are key factors that determine formability and forming limits of these alloys [2, 3]. Grain size also affects the surface quality of formed components.

Controlled thermo-mechanical processing during hot and cold rolling is, therefore, essential to ensure a microstructure that maximizes the formability and strength [4]. In industrial practice, these alloys are homogenized by soaking at a temperature in the range of 500–600 °C for modification of as-cast constituent particles, removal of micro segregation, precipitation of dispersoids, and controlling the amount of solute present in solid solution. Al_6Mn is the equilibrium phase at high temperatures in these alloys but it is preceded by the formation of BCC $Al_{12}Mn$ (G1) and orthorhombic phases Al_7Mn (G2) at low temperatures [5–7]. G1 and G2 transform

V. Srivastava (✉) · S. Gahlyan · M. Khandelwal · A. Deshpande
Hindalco Innovation Center, Hindalco Industries Limited, MIDC Taloja, Plot No. 2, Raigad, Navi
Mumbai 410 208, India
e-mail: Vivek.s.srivastava@adityabirla.com

into stable orthorhombic Al_6Mn at high temperatures. When Fe and Si are present in the alloy as trace impurities, G1 is the preferred dispersoid phase to be formed. In alloys containing higher levels of Fe and Si, added as alloying elements, the solubility of Mn is greatly decreased and Fe is co-precipitated to form $Al_6(Fe,Mn)$. Si favors precipitation of cubic $Al_{12}Mn_3Si$ or $Al_{12}(Fe,Mn)_3Si$ [8, 9]. For AA3003 alloy, predominantly $Al_{12}(Fe,Mn)_3Si$ dispersoids have been reported previously [10].

Detailed microstructural investigations and conductivity measurements have shown that the number density of these dispersoids is maximum around 400 °C during typical slow heating rates employed during homogenization. At higher temperatures, gradual coarsening occurs as diffusivity increases and Mn can diffuse over longer distances [11]. Number density and size of dispersoids particles have profound effect on recrystallization kinetics, texture, and grain size of the final product and have been the subject of numerous investigations [10, 12–16]. Large constituent particles and dispersoids ($>1 \mu m$) act as sites for Particle Stimulated Nucleation (PSN) as deformation is localized at these particles [17]. Grains nucleated by this mechanism generally lead to randomly oriented grains and reduce anisotropy in the material and lead to improved formability. Fine, closely spaced dispersoids, on the other hand, interact with the grain and sub-grain boundaries and limit their mobility. This phenomenon, called Zener-drag, pins the grain boundaries and significantly retards recrystallization.

During annealing of the cold rolled sheets, further precipitation of elements in solid solution can take place. Depending on the annealing parameters, precipitation can occur during recrystallization, a phenomenon called concurrent precipitation. Concurrent precipitation leads to non-homogenous and coarse grains [17, 18] which are undesirable for the surface finish and sheet metal forming. Similar effect is observed when precipitation occurs prior to recrystallization, but the effect is less pronounced. It is, therefore, desirable to design the annealing treatment such that recrystallization precedes any precipitation during annealing.

Viscoplastic Self Consistent (VPSC) modelling allows correlation of texture and microstructural information to formability [19]. VPSC simulates polycrystalline plasticity considering each grain as an inclusion in a visco-plastic medium. The visco-plastic medium is estimated as an average of the remaining grains as the effective medium. The response of the grain under consideration is coupled to the overall response of the medium and the model has been shown to be capable of accounting for changes in grain structure, like grain shape change, with strain increment. The response of homogenized equivalent medium (HEM) is estimated to account for material flow during each strain increment. Classical Taylor model [20] assumes equal strain across all the grains which leads to rigid interactions. Another approach is to have relaxed constraints (RC) [21] model, but VPSC model following Molinari et.al [22] presents more realistic scenario where grains interact with an anisotropic medium which is the average of the all the surrounding grains.

In this study, two homogenization treatments were given to as-cast rolling ingots to generate markedly distinct dispersoid size distributions and degree of super-saturation prior to hot rolling. Industrially hot and cold rolled samples have been

annealed at different heating rates to study the effect of heating rate on recrystallized microstructure and formability.

Experimental

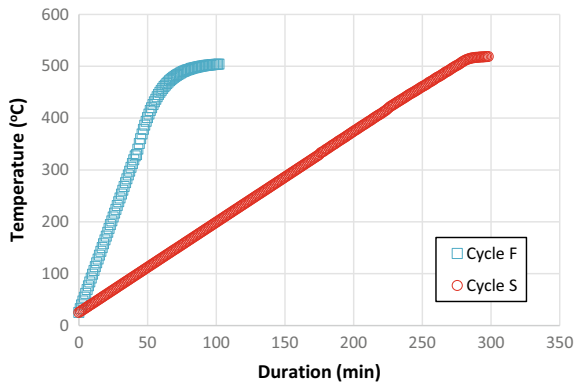
Industrially cast AA3xxx series of alloys was used for this study. Nominal composition of the two alloy ingots is provided in Table 1. Alloy ingot H was homogenized using a two-step treatment. In the first step, the ingot was homogenized at 595°C for a soaking duration of 12 h followed by cooling in the furnace set at 510°C for a duration of 6.5 h. Alloy ingot L, on the other hand, was given a single step homogenization treatment by soaking at 510°C for duration of 6 h. Both the ingots were hot rolled through a two-high reversing mill to hot band gauge of 8.5 and 9.3 mm respectively. The coiling temperature for both the hot bands was in the range of 345 to 360 °C. Hot rolled coils were further cold rolled to 4.0 mm. Samples for cold rolled coils were taken for different annealing treatments and characterization.

Lab annealing was carried out in a Carbolite air circulating oven in the lab. Annealing was carried out by varying the heating rate to the annealing temperature of 500 °C and soaking for a duration of 30 mins. Annealing cycles F and S were employed using a fast and slow heating rate respectively. Figure 1 shows the temperature-time graph from both the cycles. Two specimens from each cold rolled coil were given these annealing treatments and designated as HF, HS, LF, and LS.

Table 1 Nominal composition of the alloy ingots used in this study

	Al	Si	Fe	Mn	Cu	Mg
H	97.57	0.205	0.566	1.124	0.077	0.005
L	97.54	0.300	0.553	1.116	0.066	0.016

Fig. 1 Time temperature plot for annealing cycle F and S



The annealed samples were prepared for metallographic observation after standard metallographic preparation. The grain structure was observed in polarized light through Carl Zeiss (A1M) after electro-etching using Barkers' Reagent in Struers electro-polisher. The samples for EBSD analysis were prepared through standard metallographic procedure to mirror finish and then electro-polishing in 10% perchloric acid in methanol. EBSD analysis was carried out using Hitachi-S3400N SEM with Brukers EBSD system. Post-processing for texture volume fraction, grain boundary characteristics, pole figures, etc. was done using Brukers' Espirit 1.9 and ATEX.

Conductivity measurements were carried out using Fischer SMP10 to estimate the amount of Mn in solid solution at different stages of thermo-mechanical processing. Earing measurements were carried out using a custom built Huxley Bertram device using a cup draw ratio of 1.73. Cupping was carried out using Erichsen cupping machine without lubrication. Tensile tests were carried out to measure the stress-strain curve and anisotropy parameters. The work hardening characteristics were obtained from tensile tests using an in-house code for smoothening and numerical differentiation of the stress-strain curve.

Simulation of r -values was done using VPSC5 code where micro-texture obtained through EBSD was provided as an input for the code. Two procedures, i.e. procedure I and E were followed for the calculation of R values. In procedure I, initial texture obtained from the EBSD data was used after discretizing it into 9000 points. Procedure E employed a virtual tensile test for each of the samples with loading direction being rolling direction. Tensile test resulted in deformed texture owing to grain rotations and hence an evolved microstructure, resultant texture was used an input in this procedure.

Results

Table 2 below shows the conductivity of the cold roll sheet following the homogenization treatments H and L respectively. The conductivity value after homogenization treatment H is lower indicating higher degree of super saturated of Mn in solid solution. For samples HF and HS, a significant rise in conductivity is observed compared to sample H indicating further precipitation of Mn during annealing. For homogenization treatment L, conductivity values post-annealing does not change appreciably indicating no further change in concentration of Mn in solid solution.

Table 2 Conductivity of the samples studied in this work after different thermal treatments

	Ingot H	Ingot L
As-rolled	43.9 ± 0.3	45.7 ± 0.1
Cycle F	44.6 ± 0.3	45.5 ± 0.1
Cycle S	47.2 ± 0.2	45.2 ± 0.1

Figure 2 below shows the micrographs of the dispersoids before and after both F and S annealing cycles. It can be seen that for ingot homogenized using treatment L before annealing has copious precipitation of fine dispersoids. Samples homogenized using treatment H, on the other hand, show presence of coarse dispersoids. Additional precipitation of fine dispersoids is observed in both cases following annealing cycle S, more prominently in case of homogenization treatment H (compare HS with H in Table 3) than in case of homogenization treatment L. Annealing cycle F appears to promote coarsening rather than nucleation of more dispersoids. Image analysis of the dispersoids size and number density confirms the above observations and are plotted in Fig. 3.

It can be seen in Table 3 that the average dispersoids sizes increase significantly for thermo-mechanical treatment HF. In contrast, homogenization treatment L leads to much higher number density and finer dispersoids sizes indicating more nucleation and little opportunity for coarsening of dispersoids due to limited diffusivities at these temperatures.

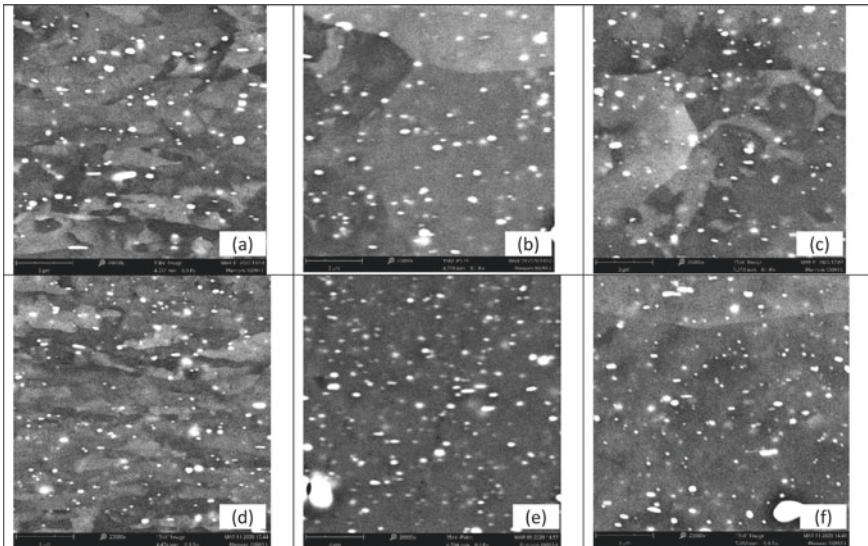
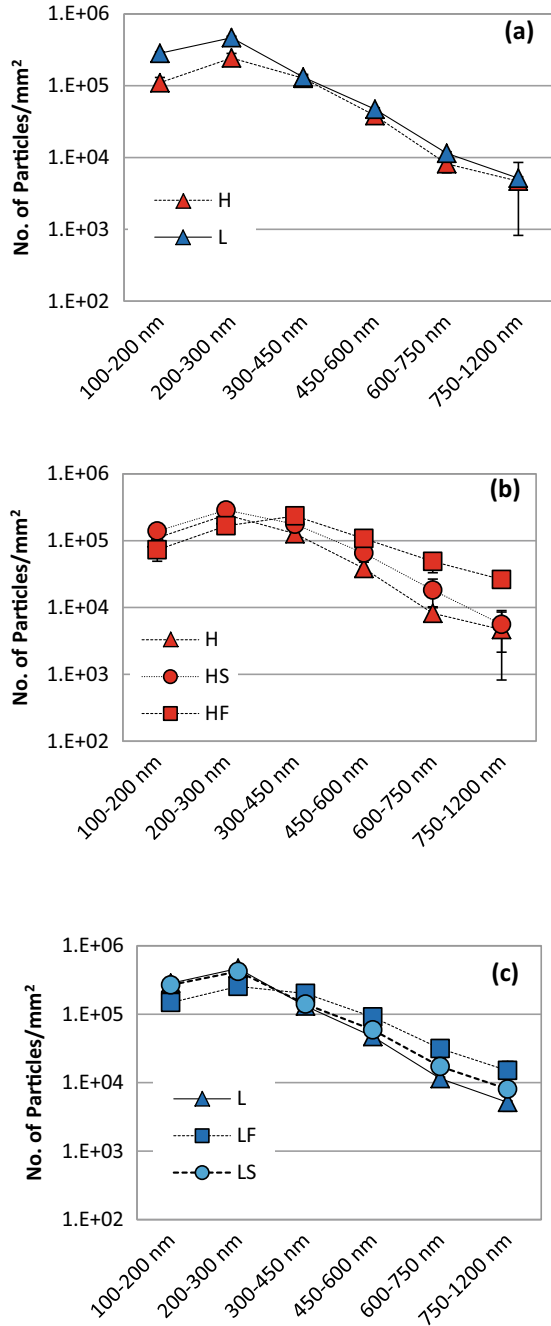


Fig. 2 SEM-BSE micrographs of the cold rolled samples before and after annealing showing dispersoids distribution **a** sample H, **b** sample HF, **c** sample HS, **d** sample L, **e** sample LF, and **f** sample LS

Table 3 Table showing average dispersoids size and number density for all the six samples analyzed in this study

ID	H	HF	HS	L	LF	LS
Avg Size(nm)	291	387	304	260	329	272
Density ($\times 10^6/\text{mm}^2$)	0.53	0.65	0.69	0.94	0.74	0.91

Fig. 3 Histogram showing particle size distribution of the various samples after different thermal treatments



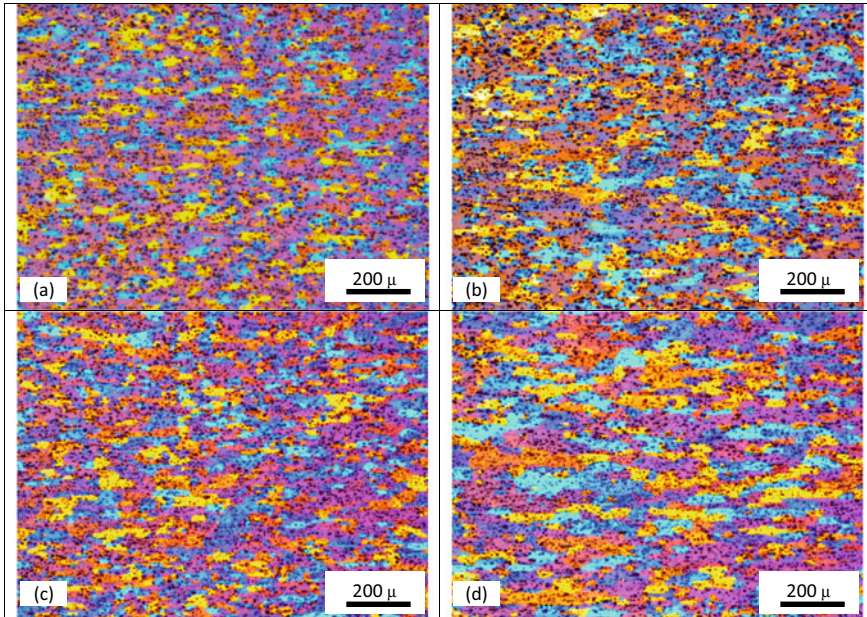


Fig. 4 Transverse grain structure at final gauge after annealing **a** sample HF, **b** sample HS, **c** sample LF, and **d** sample LS

Figure 4 shows the transverse grain structure of final gauge samples after annealing. It can be seen that faster heating rate during annealing promotes nucleation of grains, leading to finer grain sizes. Slow heating leads to recovery prior to recrystallization and has a relatively coarse grain structure. It is also observed that there is a larger gradient in grain size for the samples undergoing homogenization treatment H compared to treatment L. This is believed to be due to higher through thickness temperature gradient for treatment H leading to more non-uniform deformation in the roughing passes during hot rolling.

Figure 5 shows inverse pole figures for all four samples. In all the four cases, moderate rolling texture is observed from the texture components analysis. Intensity of rolling texture is higher for samples homogenized through treatment L. It is observed that annealing cycle F leads to lower texture intensity compared to cycle S. The intensity of cube texture after annealing is fairly low in all cases, indicating particle stimulated nucleation to be the predominant nucleation mechanism leading to random texture in the annealed samples [17]. There is some evidence for higher proportion of formation of cube component for faster annealing following homogenization treatment L.

Figure 6 shows typical tensile curves for two extreme conditions, i.e. HF and LS after annealing. Tensile properties do not show pronounced anisotropy indicating weak texture for all the four cases as seen in Fig. 5. From the elongation data, it can be surmised that sample LS has a higher anisotropy compared to sample HF, as

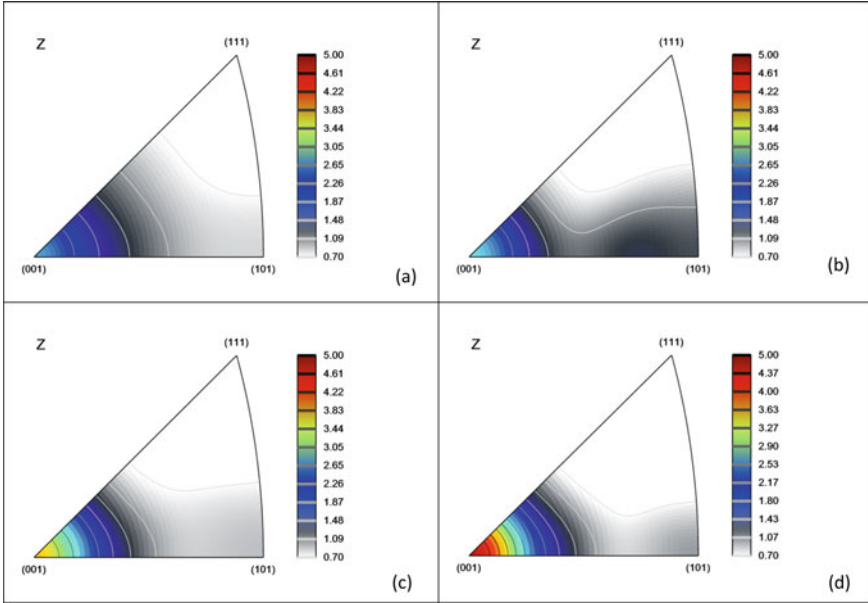


Fig. 5 Inverse pole figures at final gauge after annealing **a** sample LS, **b** sample LF, **c** sample HS, and **d** sample HF

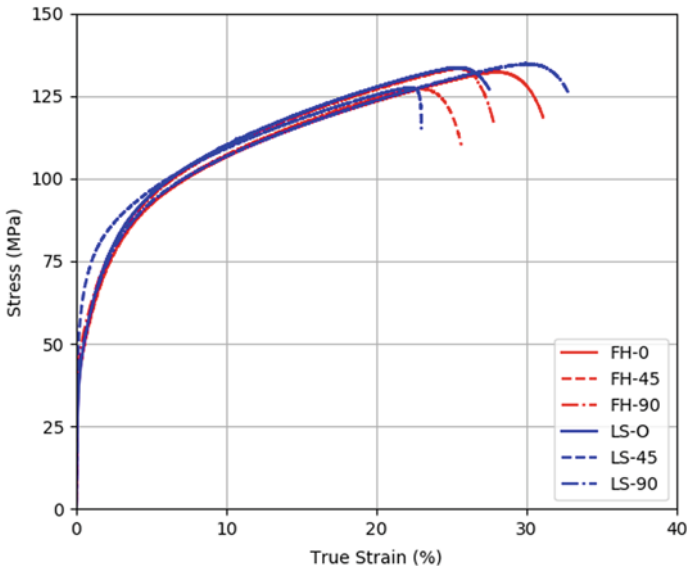


Fig. 6 Typical true stress-strain curve for HF and LS sample post anneal

expected from the texture data. Table 4 lists the strain hardening exponent (n) and Lankford parameter (r) for the four samples. The results indicate homogenization cycle H followed by fast annealing F lead to high n and r-bar. Earing profile for all the four samples is shown in Fig. 7 and mean earing values are reported in Table 4. These results confirm that sample HF leads to lowest earing, more isotropic flow behavior, and enhanced formability. Homogenization cycle L followed by slow anneal S, i.e. sample LS, on the other hand, has the highest mean earing as expected from texture and tensile data.

Table 4 Measured and calculated mechanical properties of the samples studied in this work

Sample	Orientation	N	r	Δ -r	r-bar	Simulated r		Mean Earing (%)
						Procedure I	Procedure E	
HF	0	0.24	0.87	0.01	0.84	0.51	0.58	1.0
	45	0.24	0.84			0.56	0.84	
	90	0.23	0.82			0.66	0.88	
HS	0	0.20	0.76	- 0.21	0.79	0.60	0.62	1.8
	45	0.17	0.90			0.68	0.93	
	90	0.22	0.62			0.66	0.96	
LF	0	0.23	0.56	0.09	0.57	0.36	0.50	1.9
	45	0.23	0.53			0.46	0.79	
	90	0.22	0.67			0.39	0.76	
LS	0	0.24	0.57	- 0.08	0.53	0.43	0.46	2.3
	45	0.17	0.57			0.50	0.72	
	90	0.23	0.42			0.50	0.70	

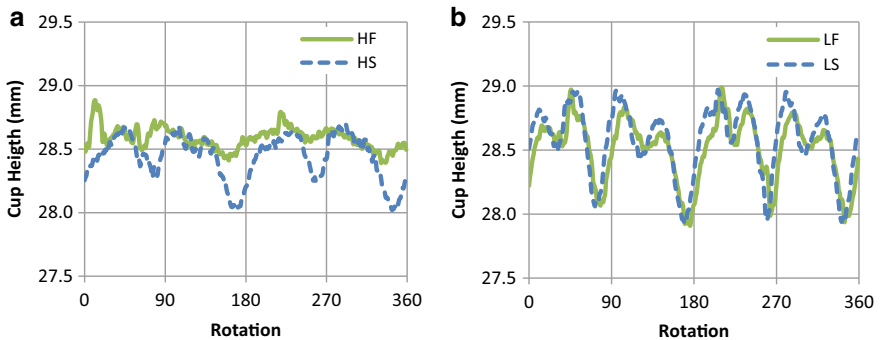


Fig. 7 Trace of earing profile after drawing for samples subjected to different thermal cycles **a** homogenization treatment H and **b** homogenization treatment L

The Lankford parameters in different orientations were calculated based on the texture data using two different procedures as listed in Table 4. Procedure I, based on initial texture data, led to under estimation of the r -values and more specifically for sample HF. Procedure E, using evolved texture, led to overall higher r -values owing to generation of deformed texture in the tensile loading.

Discussion

Precipitation of the dispersoids from the super saturated as-cast microstructure is known to take place during homogenization. This leads to a progressive rise in the conductivity, reaching a maxima at about 480 °C [10]. From the data in Table 2 it can be seen that amount of Mn retained in solid solution is higher for homogenization treatment H compared to treatment L due to higher soaking temperature. A slight drop in Mn in solid solution with increasing soak time during high temperature soaking has been reported by few researchers [10, 18]. This has been explained on the basis of higher Mn content in constituent particles and dispersoids. This phenomenon is also seen in this study as the conductivity of sample HF and HS is observed to be higher than LF and LS.

At high soaking temperatures above 500 °C, re-dissolution of dispersoids takes place due to increased solid solubility of Mn in Al at higher temperatures. The re-dissolution of dispersoids leads to decrease in their number density of fine dispersoids while coarse dispersoids continue to grow [10]. Subsequent cooling from the peak preheating temperature during hot rolling causes renewed precipitation and further growth of coarse dispersoids as observed in Fig. 3a. Fast heating during subsequent annealing has been found to be helpful in further coarsening of the dispersoids.

Mn retained in solid solution is expected to retard recrystallization after hot rolling. Furthermore, fine dispersoids exert a significant retarding force on grain boundaries and inhibit recrystallization. This effect called Zener drag is dependent on the size and volume fraction of the dispersoids present in the alloy [17]. On the other hand, large constituent particles (>1–2 μ m) promote recrystallization by particle stimulated annealing (PSN). This mechanism promotes formation of random grains and leads to more diffused texture. Homogenization treatment H while having higher retained Mn in solid solution leads to coarser dispersoids and constituent particles thus aiding formation of fully recrystallized, randomly oriented grain structure post final annealing. Homogenization cycle L while having low amount of Mn in solid solution, results in precipitation of numerous, fine Mn bearing dispersoids. These dispersoids inhibit formation of equi-axed grains post recrystallization and have slightly elongated grain structure as seen in Fig. 4. At the same time, constituent particles do not have the opportunity to undergo coarsening and are less efficient PSN sites and therefore lead to stronger recrystallization texture and higher earing values. Fast heating rate during annealing provides less time for recovery and promotes formation of multiple nucleation sites for recrystallization [23]. This leads to finer grain sizes as observed in the case of HF and LF compared to HS and LS samples. As

observed from conductivity data, concurrent precipitation is observed in the case of homogenization treatment H during annealing. Interestingly, for annealing cycle F, this leads to more coarsening of dispersoids rather than nucleation of new dispersoids. It therefore does not interfere with recrystallization to the extent expected.

From the above discussion, it is clear that homogenization treatment H combined with fast annealing cycle F leads to the most desirable microstructure from the formability point of view. During deep drawing, planar and normal anisotropy leads to non-uniform strain, plastic instability, and lower formability [2]. It is to be noted that by designing the thermal treatment appropriately, formation of fine, randomly oriented grains can be promoted. This microstructure, in turn, leads to high strain hardening exponent, high r -bar, and low earing in the final sheet.

r value is calculated by conducting a virtual tensile test using texture data as an input. During deformation, grain rotation leads to evolution of texture with strain increment. In calculation procedure I, only the initial texture data is used for calculations while procedure E incorporates the effect of grain rotation and texture evolution. It is observed that procedure E, in general, leads to higher r -values compared to the procedure I. It is due to the generation of higher deformation texture as strain increases, leading to more anisotropy.

Conclusions

From the current study following conclusions are drawn.

- Homogenization treatment H leads to higher degree of super-saturation and coarser dispersoids compared to treatment L.
- Higher heating rate in annealing cycle F results in finer grain sizes and more random texture.
- Thermo-mechanical treatment HF shows enhanced formability, low earing, and better surface finish.

References

1. Joseph R. Davis (1993) ASM specialty handbook: aluminum and aluminum alloys. ASM International
2. Dieter G (1986) Mechanical metallurgy. McGraw-Hill, New York
3. Lumley R (2010) Fundamentals of aluminum metallurgy: production, processing and applications. Woodhead Publishing, Cambridge
4. Robert E (2012) Sanders Jr. Wiley, Aluminum and Aluminum Alloys
5. N.A. Belov, D.G. Eskin (2005) A.A. Askenov, Multi-component phase diagrams: applications for commercial aluminum alloys. Elsevier Ltd, Oxford
6. de Haan PCM, J.v. Rijkom, J.A.H. Sontgerath, (1996) The precipitation behavior of high-purity Al-Mn alloys. Mater Sci Forum 217–222:765–770

7. Goel DB, Roorkee UP, Furrer P, Warlimont H (1974) Precipitation in aluminum manganese (iron, copper) alloys. *Aluminium* 50(1974):511–516
8. Nes E, Naess SE, Hoier R (1972) *Z Metallk* 63:248
9. Lodgaard L, Ryum N (2000) Precipitation of dispersoids containing Mn and/or Cr in Al–Mg–Si alloys. *Mater Sci Eng A* 283:144–152
10. Li YJ, Arnberg L (2003) Quantitative study on the precipitation behavior of dispersoids in DC-cast AA3003 alloy during heating and homogenization. *Acta Mater* 51:3415–3428
11. Gale WF, Totemeier TC (2003) *Smithells metals reference*, Book 8th edn. Butterworth-Heinemann, Oxford
12. Humphreys FJ (1997) Nucleation of recrystallization at 2nd phase particles in deformed aluminum. *Acta Metall* 25:1323–1344
13. Humphreys FJ (1979) Local lattice rotations at 2nd phase particles in deformed metals. *Acta Metall* 27:1801–1814
14. Engler O, Kong XW, Lucke K (2001) Recrystallization textures of particle-containing Al–Cu and Al–Mn single crystals. *Acta Mater* 49:1701–1715
15. Nes E, Embury JD (1975) Influence of a fine particle dispersion on recrystallization behavior of a two phase aluminum-alloy. *Z. Metallkunde* 66:589–593
16. Nes E (1976) Effect of fine particle dispersion on heterogeneous recrystallization. *Acta Metall* 24:391–398
17. Anthony Rollett, F Humphreys, Gregory S., Rohrer M. Hatherly (2004) *Recrystallization and related annealing phenomena*, Elsevier
18. Tangen S, Sjolstad K, Nes E, Furu T, Marthinsen K (2002) The effect of precipitation on the recrystallization behavior of a supersaturated, cold rolled AA3103 aluminum alloy. *Mater Sci Forum* 396–402:469–474
19. Lebensohn RA, Tomé CN (1993) A self-consistent anisotropic approach for the simulation of plastic deformation and texture development of polycrystals: application to zirconium alloy. *Acta Metal. Mater.* 41:2611–2624
20. Taylor GI (1938) Plastic strain in metals. *J. Inst Metals* 62:307–324
21. Van Houtte P (1998) A comprehensive mathematical formulation of an extended Taylor-Bishop-Hill model featuring relaxed constraints, the Renouard-Wintenberger theory and a strain rate sensitivity model. *Textures Microstruct.* 8–9:313–350
22. Molinari A, Canova GR, Ahzi S (1987) A Self consistent approach of the large deformation polycrystal viscoplasticity. *Acta Metal* 35:2983–2994
23. Wang N (2016) KeHuang, YanjunLi, Knut Marthinsen (2016) The influence of processing conditions on microchemistry and the softening behavior of cold rolled al-mn-fe-si alloys. *Metals* 6:61. <https://doi.org/10.3390/met6030061>

Sensitivity Study of Plastic Anisotropy on Failure Prediction in Hole-Expansion



Jinjin Ha and Yannis P. Korkolis

Abstract The influence of yield function parameters on the hole-expansion (HE) predictions is investigated for an AA6022-T4 aluminum sheet. The HE experiment is performed in a fully-instrumented double-action hydraulic press with a flat-headed punch. Full strain fields are measured by a stereo-type digital image correlation (DIC) system. Besides HE, the plastic anisotropy of AA6022-T4 is characterized by uniaxial tension and plane-strain tension experiments. Uniaxial tension is considered as the most important, since it is the stress state along the hoop direction in the hole. The stress state then gradually changes from uniaxial to plane-strain tension to biaxial tension in the radial direction. For the finite element (FE) simulation, Yld2000-2d non-quadratic anisotropic yield function is used with two different parameter sets calibrated by (1) uniaxial tension only (Par 1) and (2) both uniaxial and plane-strain tension (Par 2). Isotropic strain hardening is assumed for both parameter sets. The strain field predictions show a good agreement with the experiments only for Par 2 which takes into account plane-strain as well uniaxial tension. This indicates the importance of biaxial, and in particular the plane-strain mode for the adopted yield function to produce accurate HE simulations.

Keywords Hole expansion · Plastic anisotropy · Aluminum sheet · Digital image correlation

Introduction

Numerical analysis of circular hole-expansion is of high interest in the evaluation of stretch-flangeability of sheet metals. One of the keys is to capture the strain variation around the hole, which can be usually achieved by an appropriate anisotropic yield function for the tested material [1–3]. In the parameter calibration, the anisotropy

J. Ha
University of New Hampshire, Durham, NH, USA

J. Ha · Y. P. Korkolis (✉)
The Ohio State University, Columbus, OH, USA
e-mail: korkolis.1@osu.edu

in uniaxial tension is the main consideration, since this is the stress state around the hole periphery. In contrast, the biaxial stress states, and especially the plane-strain condition, are not necessarily emphasized compared to the uniaxial ones, since they appear at a distance from the critical failure zone, e.g., the hole periphery. In this paper, the influence of plane-strain on the thickness strain variation is investigated through the anisotropic parameter study for Yld2000-2D [4]. Two different parameter sets for AA6022-T4 [5, 6], which give the same prediction for the uniaxial tension but different for plane-strain tension are used, and the predictions are compared with the experiment.

Plasticity Characterization

The material of this study is a AA6022-T4 aluminum alloy of 1 mm thickness. The plastic anisotropy is characterized by uniaxial tension in every 15° from the rolling direction (RD). The experiment is performed using a standard ASTM-E8 specimen and an MTS 250 kN universal testing machine. The stress–strain curves are shown in Fig. 1a: the flow stresses in the RD, 15°, and 30° are slightly higher than the other directions; that in the TD is the lowest. The curve in the RD is used to calibrate a Swift-Voce combined hardening model for the extrapolation (Fig. 1b and Table 1). In addition to the anisotropy in the flow stress, the plastic strain ratio between thickness and width directions, i.e., r-value, is

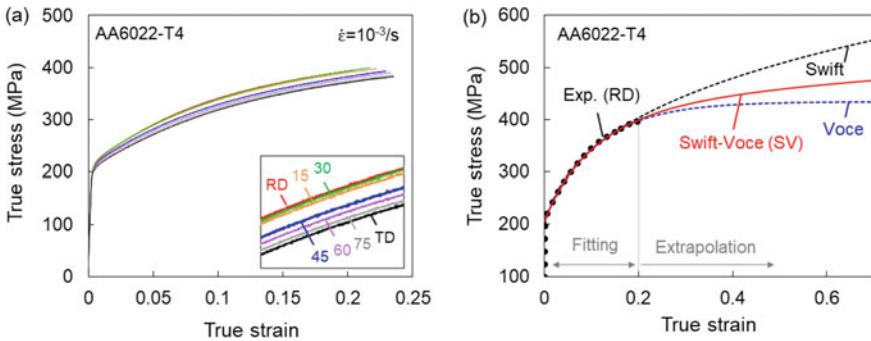


Fig. 1 a Uniaxial stress–strain curves in every 15° from the RD and b the extrapolation of strain hardening using Swift-Voce combined model

Table 1 Parameters for Swift-Voce combined model (Swift-Voce: $\sigma = w_a \cdot \sigma_S + (1 - w_a) \cdot \sigma_V$)

Swift: $\sigma_S = k_0 \cdot (\epsilon_0 + \bar{\epsilon})^n$			Voce: $\sigma_V = k - q \cdot \exp(-\beta \cdot \bar{\epsilon})$			Weight
k_0	ϵ_0	n	k	q	β	w_a
603	0.015	0.262	435	0.519	9.1	0.35

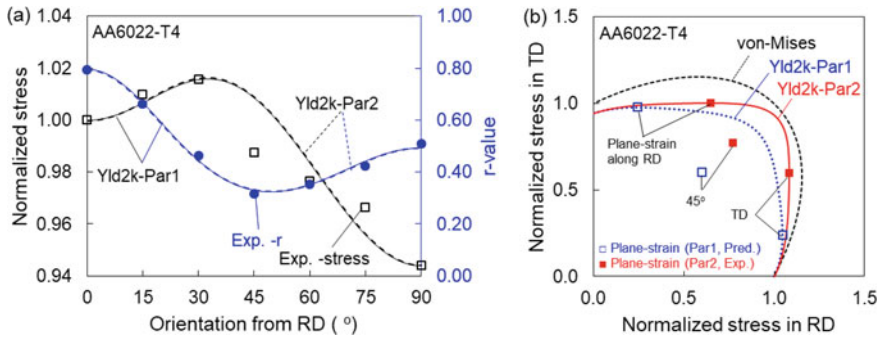


Fig. 2 a Comparison of the experiment and predictions of Yld2k-Par1 and -Par2 for the uniaxial tension and **b** the corresponding yield loci; marked are the plane-strain locations in the RD, 45°, and TD. It should be noticed that the plane-strain conditions for the Yld2k-Par1 are predicted by the given parameter while those for the Yld2k-Par2 are experimentally characterized

Table 2 Yld2000-2D parameters for Yld2k-Par1 and Yld2k-Par2

m=8	α_1	α_2	α_3	α_4	α_5	α_6	α_7	α_8
Yld2k-Par1	0.9702	1.0540	1.2532	1.1281	1.0646	1.2534	0.9400	0.9089
Yld2k-Par2	0.9682	1.0219	1.0673	1.0911	1.0136	0.9771	0.9137	1.0636

identified from the uniaxial tension (Fig. 2a). Compared to the flow stresses, the r-values represent stronger anisotropy as they are far lower than 1 (isotropic value). As the lowest r-value is observed at 45°, it is expected that this direction would have the least resistance to thinning. Beyond uniaxial tension, plane-strain tension in RD, 45°, and TD are conducted using a custom-designed specimen [7–9].

For Yld2000-2D parameter calibration, two anisotropic parameter sets are utilized, based on different sets of experiments: Yld2k-Par1 is calibrated based on the uniaxial tension only while Yld2k-Par2 is done by both uniaxial and plane-strain tensions (Table 2). Since both parameter sets use the uniaxial tension, they give a good agreement with the anisotropy in the uniaxial tension, as seen in Fig. 2a. However, the corresponding yield loci (Fig. 2b) of Yld2k-Par1 and -Par2 show a significant difference regardless of the identical prediction in the uniaxial tension (Fig. 2a).

Hole-Expansion Experiment and FE Simulation

The hole-expansion experiment is performed using a specimen with a circular hole of 35 mm diameter. A flat-headed punch of 100 mm diameter with 12 mm punch radius expands the hole as it travels. Stereo-type digital image correlation (DIC) system is used to measure the surface strain field throughout the process. The thickness strain

evolution is measured at different levels of punch displacement from a hoop with 40 mm initial diameter, i.e. 2.5 mm inland from the hole edge, to avoid the problematic correlation near the hole edge. The same tooling is modeled for the simulation, but only a quarter is used, considering the two symmetry planes. The blank is constructed using 60 shell elements along the quarter hole, which is equivalent to 1.5° per each element.

The experiment and simulation results with two different Yld2000-2D parameters, i.e., Yld2k-Par1 and -Par2, are shown in Fig. 3. In Fig. 3, the thickness strain evolution is described at the different level of punch displacement δ , i.e., $\delta/\delta_{\max} = 0.5, 0.65, 0.8, 0.9, \text{ and } 1$, where δ_{\max} is the punch displacement at the onset of fracture. The experiment shows that the thickness strain variation has the greatest thinning at 45° , intensifying as the punch displacement increases. Indeed, this is the location of the first rupture.

In both parameter sets, the average thickness strain levels are well predicted with the punch displacement, while the thickness strain variation shows a noticeable difference between the two. The prediction for Yld2k-Par2, of which the parameter is calibrated based on both uniaxial and plane-strain tensions, shows a better agreement with the experiment than Yld2k-Par1, calibrated based on uniaxial tension only. This difference seems to be caused by the different plane-strain conditions between Yld2k-Par1 and -Par2 (see Fig. 2b), which means that the plane-strain condition can have a considerable influence on the strain variation in the hole periphery.

Conclusion

The role of plane-strain condition on thickness strain variation in the hole-expansion is investigated through numerical simulation using two different material parameter sets of the anisotropic yield function Yld2000-2D. Both parameter sets can capture the anisotropy of the uniaxial tension, which is the major stress state along the hole edge. However, only Yld2k-Par2, which is calibrated including the plane-strain

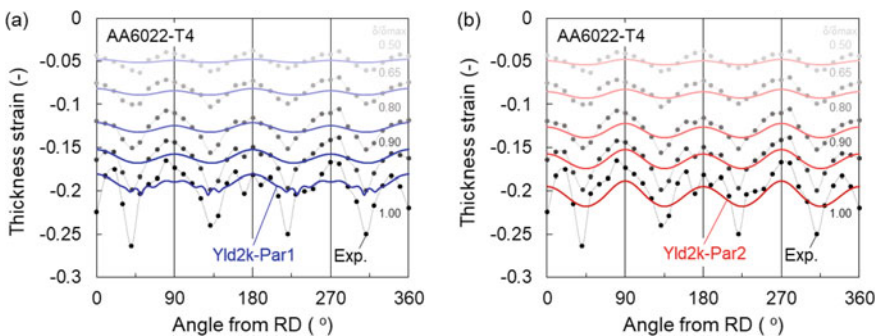


Fig. 3 Thickness strain evolution of **a** Yld2k-Par1 and **b** Yld2k-Par2

condition, shows a good agreement with the experiment. The comparison emphasizes the importance of the plane-strain condition for the accurate prediction of the hole-expansion simulation.

Acknowledgements This work was performed under awards CMMI-1563216 and -1929873 from the U.S. National Science Foundation. The authors specially thank Dr. Edmund Chu, formerly of Alcoa, for providing the sheet material. Fruitful discussions with Ms. Yumi Choi and Prof. Myoung-Gyu Lee of Seoul Nat'l University and Prof. Toshihiko Kuwabara of Tokyo University of Agriculture and Technology are acknowledged with thanks.

References

1. Parmar A, Mellor PB (1978) Plastic expansion of a circular hole in sheet metal subjected to biaxial tensile stress. *Int J Mech Sci* 20(10):707–720
2. Kuwabara T, Hashimoto K, Iizuka E, Yoon JW (2011) Effect of anisotropic yield functions on the accuracy of hole expansion simulations. *J Mat Proc Tech* 211(3):475–481
3. Korkolis YP, Brownell B, Coppieters S, Tian H (2016) Modeling of hole-expansion of AA6022-T4 aluminum sheets with anisotropic non-quadratic yield functions. *J Phys Conference Series NUMISHEET* 734
4. Barlat F, Brem JC, Yoon JW, Chung K, Dick RE, Lege DJ, Pourboghrat F, Choi S-H, Chu E (2003) Plane stress yield function for aluminum alloy sheets-part 1: Theory. *Int J Plast* 19(9):1297–1319
5. Tian H, Brownell B, Baral M, Korkolis YP (2017) Earing in cup-drawing of anisotropic Al-6022-T4 sheets. *Int J Mater Form* 10(3):329–343
6. Ha J, Dirian M, Dunn C, Korkolis YP (2019) Failure of AA6022-T4 sheets in hole-expansion after uniaxial prestrain. *AIP Conf Proc* 2113:180005. <https://doi.org/10.1063/1.5112743>
7. Tardif N, Kyriakides S (2012) Determination of anisotropy and material hardening for aluminum sheet metal. *International Journal of Solids and Structures* 49(25):3496–3506.
8. Ha J, Baral M, Korkolis YP (2018) Plastic anisotropy and ductile fracture of bake-hardened AA6013 aluminum sheet. *Int J Solids Struct*. <https://doi.org/10.1016/J.IJSOLSTR.2018.07.015>
9. M Baral, J Ha, YP Korkolis (2019) Plasticity and ductile fracture modeling of an Al–Si–Mg die-cast alloy. *Int. J. Fract*. <https://doi.org/10.1007/s10704-019-00345-1>
10. J Ha, S Coppieters, YP Korkolis (2020) On the expansion of a circular hole in an orthotropic elastoplastic thin sheet (under review)

Dynamic Deformation Behaviour of Al-Li Alloys Under High Strain Rate Deformation



Ali Abd El-Aty, Yong Xu, Shi-Hong Zhang, Ma Yan, Xunzhong Guo, Jie Tao, Yong Hou, and Myoung-Gyu Lee

Abstract Since high-strength lightweight Al-Li alloys were gained much attention recently, investigating the dynamic behavior of high-strength lightweight AA2060-T8 sheets is crucial because of their outstanding mechanical properties. Thus, uniaxial tensile tests were performed under high strain rate conditions using universal testing machines and split Hopkinson tensile bars. The ductility of AA2060-T8 sheets was improved under HSR deformation because of the adiabatic softening with increasing the strain rate and the inertia effect, which may diffuse necking the necking development and delay the onset of fracture. The present study results can efficiently develop a new manufacturing route based on impact hydroforming technology (IHF) to manufacture sound thin-walled-complex shape components from high-strength lightweight Al-Li alloy sheets at room temperature.

Keywords Al-Li alloys · Dynamic behaviour · High-speed deformation · Impact hydroforming

Introduction

In recent years, Al-Li alloys have acquired much attention for their weight and stiffness-critical structures used in aircraft, military, and aerospace because of their

A. Abd El-Aty (✉) · Y. Hou · M.-G. Lee (✉)

Department of Materials Science and Engineering & RIAM, Seoul National University, Seoul 08826, Republic of Korea
e-mail: aabdlaty@nuaa.edu.cn

M.-G. Lee

e-mail: myounglee@snu.ac.kr

Y. Xu · S.-H. Zhang · M. Yan

Shi-changxu Innovation Center for Advanced Materials, Institute of Metal Research, Chinese Academy of Sciences, Shenyang 110016, P.R. China

X. Guo · J. Tao

College of Material Science and Technology, Nanjing University of Aeronautics and Astronautics, Nanjing 211100, P.R. China

superior outstanding properties, such as a low density and high specific strength, than those of commercial Al alloys. Al-Li alloys' exceptional properties are principally attributed to the added Li, which impacts the elastic modulus, and weight reduction, where 1 wt. % of Li increases the elastic modulus by approximately 6% and reduces the resultant Al alloy's density by approximately 3% [1–3]. Based on the production date, Al-Li alloys are classified into three generations: first-generation Al-Li alloys such as AA1420, AA1421; second-generation Al-Li alloys such as AA8090, AA2090; and third-generation Al-Li alloys such as AA2050, AA2060 [2, 3].

AA2060-T8 is one of the newest candidates in the family of the third-generation Al-Li alloys launched by Alcoa Inc. in 2011 to replace AA2024-T3 and AA7075-T6 for upper and lower wings and fuselage structures [1, 3, 4]. The challenges associated with using AA2060-T8 sheets with conventional forming technologies are (1) poor formability because of the micro-voids and micro-cracks during processing; (2) anisotropic tensile properties, which caused serious issues during press forming; (3) and wrinkling and springback, which is, in turn, adds to the cost of the die and the final products because of the try-out time. The aforementioned issues of AA2060-T8 restrict its board applications [2, 3].

For the reason that AA2060-T8 was launched a few years ago, few studies on understanding the mechanical behavior, deformation mechanism, and anisotropic response of this alloy, notably at elevated temperatures, have been accomplished. For instance, Jin et al. [5] studied mechanical behavior and the texture evolution of AA2060-T8 during the bending process using PRM. Jin et al. [6] learned the dislocation boundary structures of AA2060-T8 during the bending process, and they found that three types of microstructures were formed during bending. Ou et al. [7] revealed the deformation behavior of AA2060-T8 under hot forming conditions. Gao et al. [8] used their outstanding results [7] to investigate the feasibility of manufacturing aircraft components from AA2060-T8 using the HFQ process. Abd El-Aty et al. [4–6] proposed a computational method-based crystal plasticity modelling to link the mechanical response of AA2060-T8 sheets with their microstructural states and predict their deformation behavior at room temperature and different strain rates. Later, Abd El-Aty et al. [3] investigated the mechanical behavior of AA2060-T8 sheets at room temperature and a wide range of strain rates.

From the discussion mentioned above, it is evident that the quasi-static and high-speed deformation behavior of high-strength lightweight AA2060-T8 AL-Li alloy sheets and the constitutive relations which describe the flow behavior of AA2060-T8 sheets under high strain rate conditions are not investigated. Al-Li and Al alloys' flow behavior under high strain rate deformation is complicated because they depend on several factors, such as the deformation mode, strain, and strain rates [9]. These factors control the strain hardening and dynamic softening, which affects the flow behavior and formability of these alloys [10–12]. Thus, characterizing the quasi-static and high-speed deformation behavior of high-strength lightweight AA2060-T8 AL-Li alloy sheets is meaningful to describe their mechanical response at various deformation conditions.

Experimental Procedures

The material used in this study was rolled sheets AA2060-T8 sheet. HSR tensile tests were done using SHTB apparatus at room temperature to investigate the dynamic behavior of AA2060-T8 sheet at RD and strain rates of 1733, 3098, 3651, and 3919 s⁻¹. The sample orientations in HSR tensile tests were not considered since the sample orientations significantly impacted the case of quasi-static strain rates rather than HSR [1, 3]. The experimental setup of the SHTB apparatus and the details of the tensile specimen used in this test are depicted in Fig. 1. The HSR experiment was supposed to be started once the tensile sample was placed between the incident and the transmitter bars. However, the material being studied was rolled sheets with 2 mm thickness. Thus, a novel gripping method (clamp) was designed to integrate it in the SHTB apparatus for providing adequate clamping forces to avoid the tensile specimens from slipping during the experiments and introducing a low mechanical impedance to prevent the distortion of the waves. Once the novel clamp was implemented in the SHTB apparatus, the tensile specimen was placed between the incident and transmitted bars; thereafter, the striker situated on the incident bar impacted the flange, leading to the generation of a tensile wave (incident wave) that propagated along the incident bar, as depicted in Fig. 2. The strain gauge located on the incident bar recorded the incident wave (ϵ_I) once it passed. Once the incident wave (ϵ_I) hits

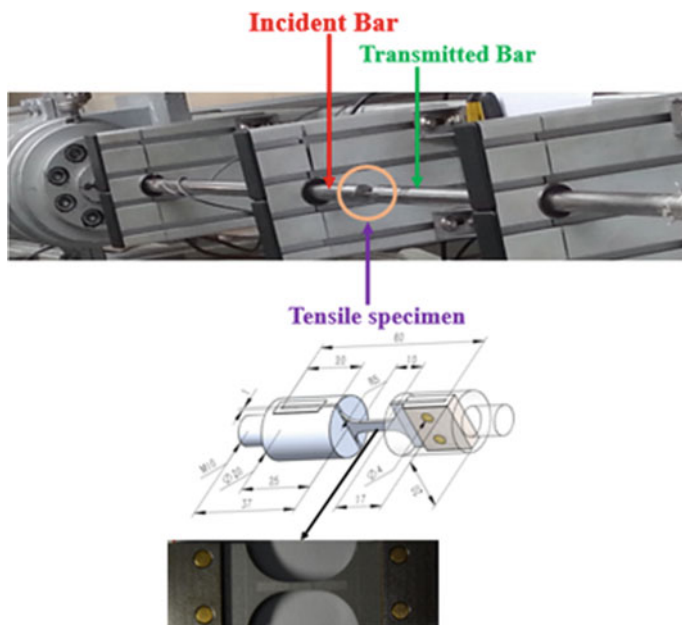


Fig. 1 The actual setup of SHTB apparatus

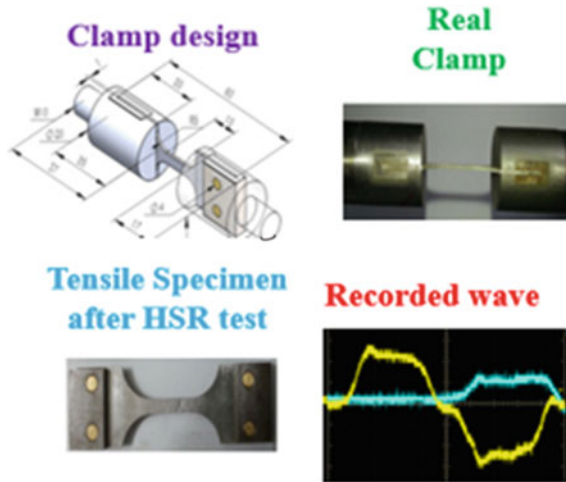


Fig. 2 The final version of the novel clamp used to avert the specimens from slipping during the test

the specimen. It is partly reflected (ϵ_R) through the incident bar and partly transmitted (ϵ_T) through the tensile specimen and the transmitted bar, as shown in Fig. 2. These reflected and transmitted waves were recorded by the strain gauges (using a high-velocity acquisition system, i.e., an oscilloscope) situated on the incident and transmitted bars, respectively. A schematic and a real set of waves detected during the SHTB experiment are depicted in Figs. 3 and 4. The progress of the HSR tensile specimen during HSR tensile testing is illustrated in Fig. 5.

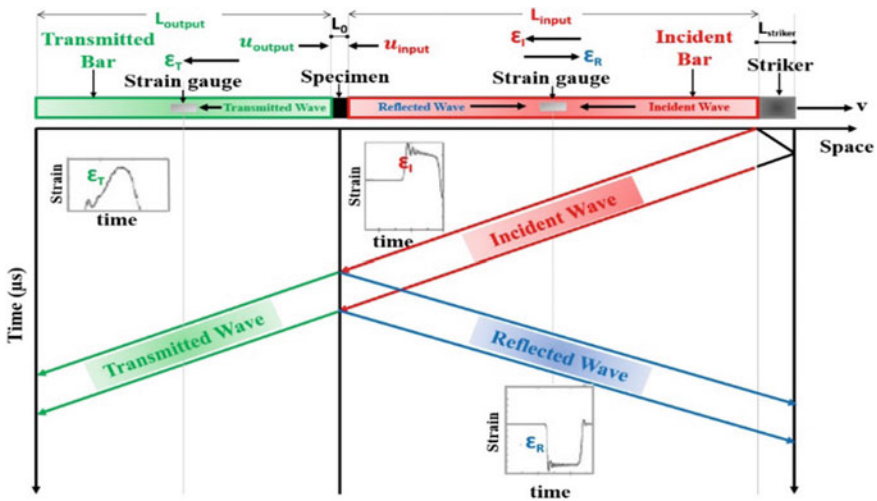


Fig. 3 The schematic representation of stress waves propagation in the bars

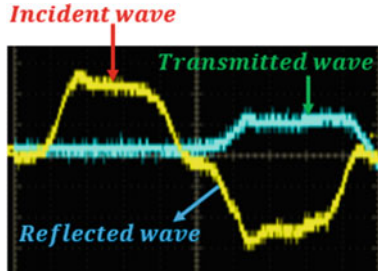


Fig. 4 The waveforms recorded by the oscilloscope during the HSR test

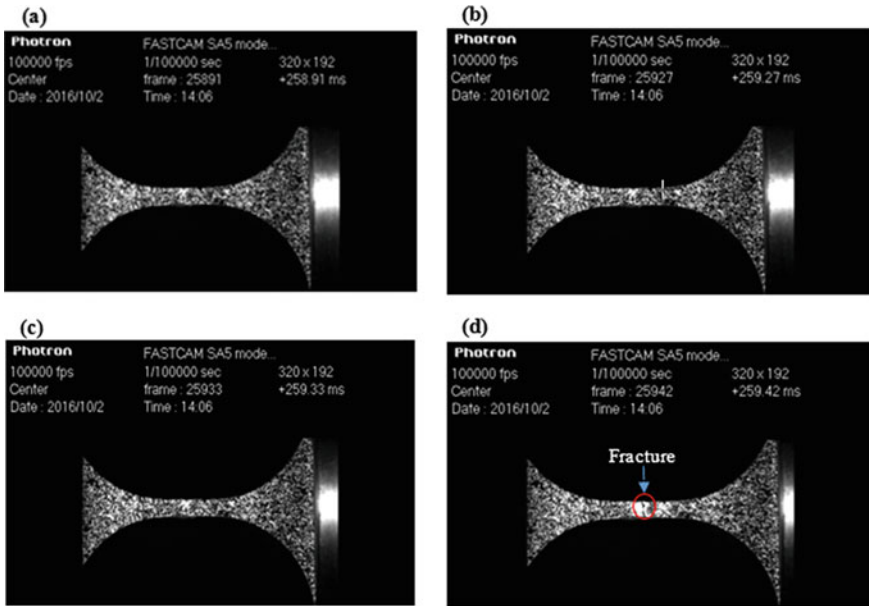


Fig. 5 The HSR tensile specimen **a** at the beginning of HSR tensile testing; **b** after 36 μsec; **c** after 41 μsec, and **d** after 51 μsec from the beginning of HSR testing, in which the tensile specimen was broken

For simplicity, it was assumed that the equilibrium condition was verified during all the tests, thus the mean strain and mean stress are generalized as

$$\epsilon(t) = -\frac{2C}{L_0} \int_0^t \epsilon_R(t) dt \tag{1}$$

$$\sigma(t) = E \frac{A}{A_0} \epsilon_T(t) \tag{2}$$

The promptly axial strain rate ($\dot{\epsilon}$) in the tensile sample was calculated from the first derivative of Eq. 1, so, it can be written as

$$\dot{\epsilon}(t) = \frac{v_{input}(t) - v_{output}(t)}{L_0} = -\frac{2C}{L_0} \epsilon_R(t) \tag{3}$$

From Eq. 3, it could be perceived that with the SHPB equipment, the tests are not performed precisely at a constant strain rate. Only in the ideal case of the perfectly rectangular reflected wave, i.e., an entirely plastic response of the specimen, the strain rate is constant during the whole specimen deformation. In practice, this is almost impossible to observe and, generally, the nominal strain rate (average value of the effective strain rate) which used to indicate the strain rate of tests performed on the Hopkinson Bar apparatus. Thus the HSR experiments were accomplished at strain rates of 1733, 3098, 3651, and 3919 s^{-1} .

Results and Discussion

Stress–Strain Behavior

The (σ_e, e) curves of AA2060-T8 sheets under HSR conditions are shown in Fig. 6. The work hardening behavior observed in HSR testing is more prominent than that detected in QSR and ISR testing [1–3]. Thus, the yield, flow, and ultimate tensile stresses at HSR were higher than their QSR and ISR counterparts, which are generally attributed to the increased strain rates. Notwithstanding, the strain-hardening rate observed in HSR testing was lower than that in QSR and ISR testing. This is attributed to the competition between the strain hardening and thermal softening due to adiabatic

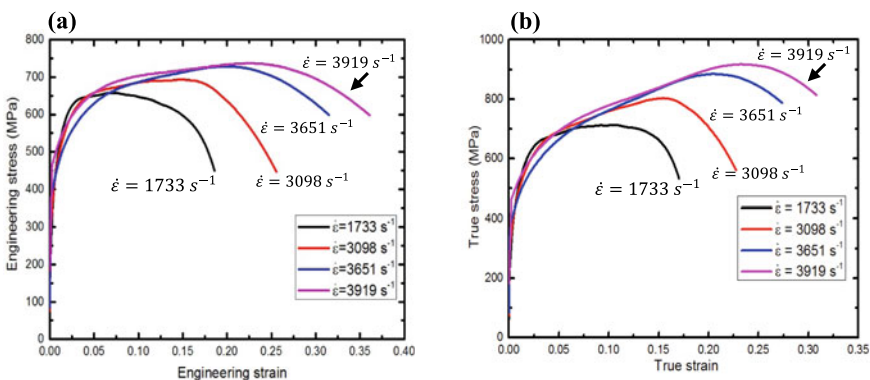


Fig. 6 a Engineering, and b true stress–strain curves of AA2060-T8 sheets at RD and HSR zone (i.e. $\dot{\epsilon} = 1733s^{-1}$, $\dot{\epsilon} = 3098s^{-1}$, $\dot{\epsilon} = 3651s^{-1}$, and $\dot{\epsilon} = 3919s^{-1}$)

temperature rise with increasing the strain rate. Thus, adiabatic softening influence is significant in HSR deformation and leads to abnormal mechanical behavior [34–37]. The strain rate increased to 1733, 3098, 3651, and 3919 s⁻¹ (i.e., strain rate changed from QSR to HSR). The elongation to fracture of AA2060-T8 sheets in the HSR zone was simultaneously improved by increasing the strain rate, which is an appealing feature in HSR deformation. This enhancement is attributed to the adiabatic softening with increasing the strain rate and the inertia effect, which may diffuse necking, slow down the necking development, and delay fracture onset.

Basic Principle of Impact Hydroforming

The basic principle of the impact hydroforming (IHF) is shown in Fig. 7, the high-speed moving impact body impacts the closed liquid chamber to generate high-pressure shock waves and propagates to the material. After the shock wave propagates to the liquid–solid interface, it interacts with the material and drives the sheet to deform. Its load is characterized with instantaneous high pressure, loading time of 100–500 μs, pressure up to 500–1000 MPa.

According to the dynamic yielding of the material and the geometrical characteristics of the part, the pressure requirement for forming can be obtained. According to the impact transfer characteristics, the requirements of the shock wave pressure can be detected. According to the dynamic hardening of the material and the strain requirement of the part, the requirement of forming energy can be proposed, and then the liquid shock wave energy and equipment performance requirements are proposed according to the impact transfer characteristics.

Design and Manufacturing a Novel Machine Based on IHF Technology

Based on the results mentioned above and the results obtained from Ma et al. [13], a new manufacturing route based on HSF was developed and denoted IHF. Based on this new manufacturing route and principle of IHF, an advanced IHF machine was designed and manufactured, depicted as Fig. 8. There are four zones of this machine. Power zone can provide very high acceleration to the projectile, which is as high as 3200 m/s². The acceleration zone supplies the acceleration distance for the projectile and the release rig. The dynamic resistance reduction technology is implemented by controlling the air and adopting a special structure to reach high impact velocity. Forming zone supplies the liquid chamber, binder hydraulic cylinder, and moveable working table. The control zone supplies the control function to all of the hydraulic valves to control the equipment's action. And the machine can run both under manual and automatic mode by inputting the code to the control board. The current research

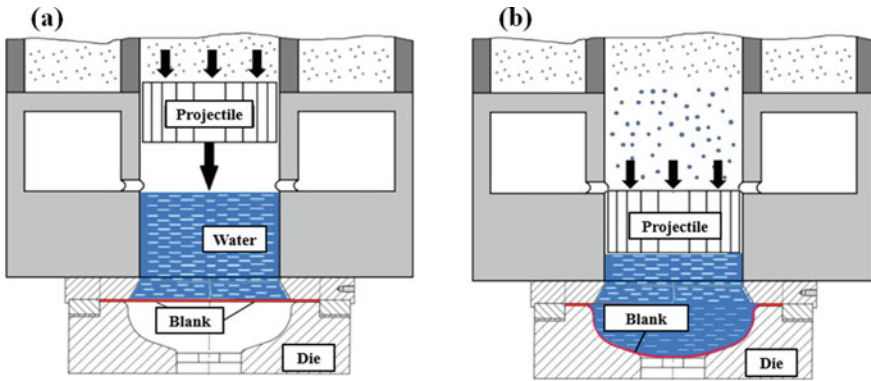


Fig. 7 The schematic of impact hydroforming **a** before forming **b** after forming

equipment’s power source is the hydraulic-driven system, which can provide higher forming energy. For previous works, the power source is a pneumatic or explosive material, and their projectile is a solid cylinder that can freely move in the acceleration tube. The projectile of the current equipment is connected and controlled by a driven rod, capable of realizing more precise control. Furthermore, this equipment is more automatically run, which is suitable for industrial applications. The projectile’s mass and the impact velocity and impact energy of the designed IHF machine are 60 kg (changeable), 10–80 m/s, and 3–200 kJ, respectively. The diameter and the volume of the liquid chamber are 250 mm (changeable) and 3–9 L. The dimensions of the working table are 800 × 800 mm, the max blank holder force is 250 T, and the binder hydraulic cylinder can be opened up to 400 mm.

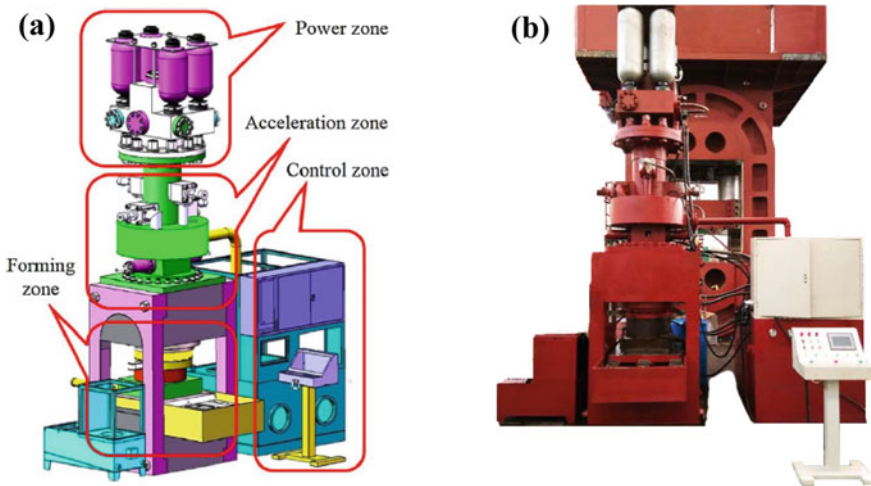


Fig. 8 **a** The schematic description forming, **b** actual setup of IHF machine

Bulging Test

This novel IHF machine was used in this study to conduct a hydro-bulging test to investigate the formability of AA2060-T8 sheets under IHF loads and compare these results obtained from the bulging test under conventional hydroforming (quasi-static loading) loading. The specimens used in the bulging test were machined from AA2060-T8 sheets, and the radius of these samples is 83.6 mm.

Since the IHF machine's impact energy is 3–200 kJ, the impact velocity can be reached up to 80 m/s. As depicted in Fig. 7, the test-specimen placed on the lower die and the upper die was fixed on the master cylinder of the IHF machine by the fixing ring. The locating ring was used to guide the upper die to the right position along the axial direction. After the upper die contacted the test-specimen with suitable clamping pressure, the high-speed hammer accelerated the liquid (Projectile). Thereafter, the test-specimen was formed by the liquid with high energy in the shock wave. The velocity sensor was set in the chamber's lateral wall, whose position was near the liquid's upper surface to detect exactly the final velocity of the accelerated hammer. Each test condition was investigated at least three times to ensure consistency and repeatability.

The bulge height (h_B) of each test-specimen was measured as depicted in Fig. 8 to assess the IHF loading effect on the formability of AA2060-T8 sheets and build up a window to describe the relationship between the impact energy (E_I) and the corresponding bulge height. This window is denoted as bulge height-impact energy ($h_B - E_I$) window, as presented in Fig. 9. The impact energy was used in this study instead of the pressure because the projectile's speed and mass mainly decide the impact energy. Furthermore, it is easy to calculate it compared to the pressure, especially under IHF conditions. As shown in the ($h_B - E_I$) window, under the IHF loading, the bulge heights of the test-specimens were increased by increasing the impact energy up to 16.2 kJ, beyond this value, the test-specimens were ruptured. The max bulge height obtained from IHF loading before rupture was 20.23 mm; however, the max bulge height obtained from conventional hydroforming loading using max pressure

Fig. 9 The measurement tool used to measure the bulge height of each test-specimen



of 28 MPa was 13.3 mm as depicted in ($h_B - E_I$) window. This means and proves that the developed IHF technology can improve the formability of AA2060-T8 sheets at room temperature.

Manufacturing Aircraft Frame Part by IHF Technology

To investigate IHF technology’s feasibility to fabricate thin-walled complex shape components, a complicated aircraft frame part was selected as a case study. The details of the aircraft frame part are depicted in Fig. 13. As shown in Fig. 13a, the aircraft frame part consists of eight convex shapes, outer surfaces, two concaves (concave 1, and concave 2), with drawing ratios (DR) of 3.88 3.52, respectively.

The *DR* in this study was calculated from Eq. 4 as

$$DR = \frac{\text{blank area}}{\text{concave area}} \tag{4}$$

Because of the complexity of the shape of the aircraft frame and high *DR* compared to the common DR limit of steel sheets, 2, many redrawing steps were required to reduce the DR for each step. The convex zones between the two concave zones are relatively easy to crack, as depicted in Fig. 10b since the strain is easy to exceed the forming limits. Furthermore, there are many small fillets (2 mm) at the outer surfaces and the concaves’ bottoms. These small fillets increase the difficulties of forming this component. According to the theories of hydroforming, the smaller the radius, the higher the pressure, since it is challenging to supply the material to the radius

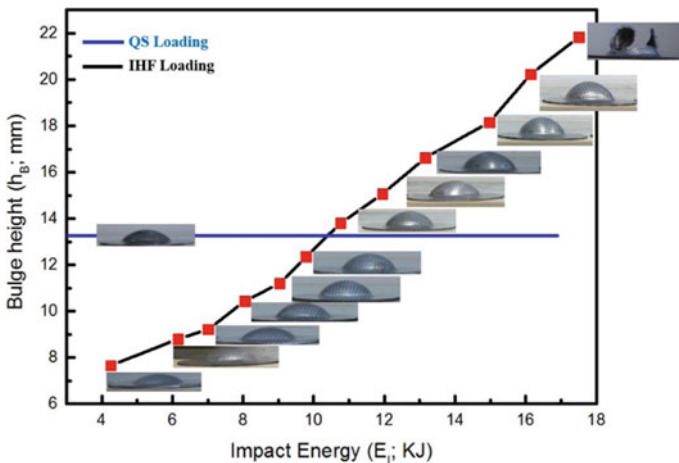


Fig. 10 Bulge height-impact energy ($h_B - E_I$) window describing the relation between the impact energy (k_j) and the corresponding bulge

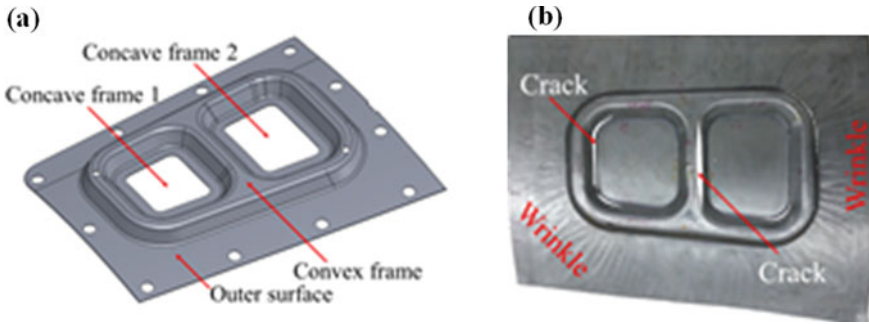


Fig. 11 a The aircraft frame part’s details, b The actual aircraft frame part with wrinkle and crack formed by sheet hydroforming process (SHF)

zone because of the frictions under the high pressure, and form the material which already contacted the surface of the die and supply the material to the radius zone because of the friction under this increased pressure.

In the beginning, actual trials were performed to investigate the feasibility of forming the aircraft frame part using a quasi-static sheet hydroforming process (QS-SHF). As depicted in Fig. 11a, large crack has appeared, and the outer surface of the frame part has a wrinkling tendency. This is because there is not enough material flowing to the fillet area to achieve the feeding effect. The rounded material’s plastic deformation ability cannot meet the forming requirements, thus causing large-area cracking. Therefore, the IHF technology was used to address the issues as mentioned above of QS-SHF. It is observed that the formability of the AA2060-T8 sheets was improved under the HSR condition. Furthermore, the cracking tendency and wrinkling were reduced compared to QS-SHF. However, the final product still has a small crack, as depicted in Fig. 11b. By analysing the results obtained from both one-step QS-SHF and IHF, as shown in Fig. 11, it is challenging to manufacture the frame part by the one-step forming process. This is attributed to the high *DR* of the concave 1 and concave 2. Thus, multi-step forming processes were used to overcome the limitations of the one-step forming process.

Firstly, the pre-forming stage was accomplished using QS-SHF. The pre-forming stage improved and controlled the flow and the distribution of the material during the deformation. After that, to investigate and compare the effect of forming process on the formability and the crack tendency, the second forming stage was performed using either QS-SHF or IHF. Based on the original design of the frame part, the pre-formed parts were proposed as depicted in Fig. 12, since the rounded part of the two cavities’ inner side was increased from 2 to 20 mm. Furthermore, the width of the eight convex shapes is also increased.

After successfully carrying out the pre-forming stage, many trials were performed using both QS-SHF and IHF as a second forming stage. It is observed that the cracks still exist in the frame part produced by QS-SHF. However, no cracks were detected,

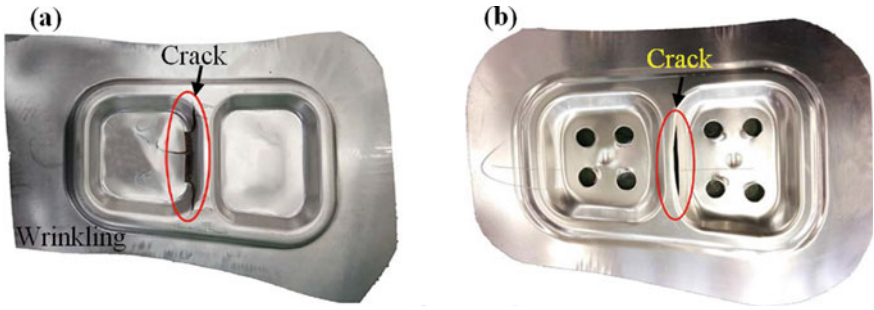


Fig. 12 Actual trials to produce the frame part by one step a QS-SHF, b IHF

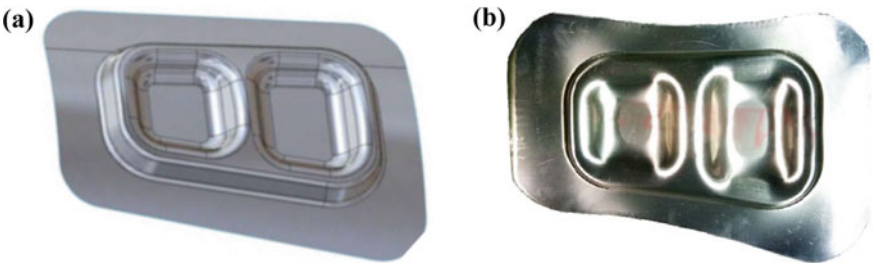


Fig. 13 a The CAD model, and b the actual trial of the pre-formed frame part

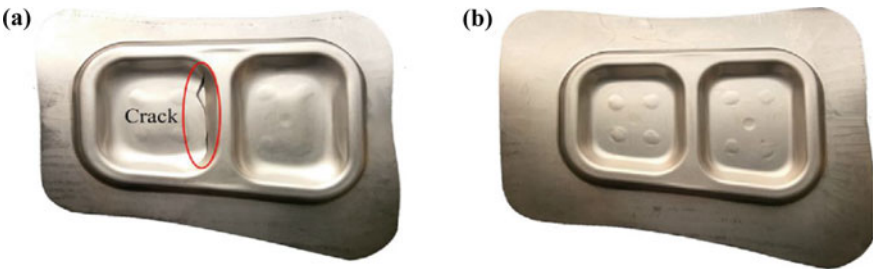


Fig. 14 The frame part was produced by a QS-SHF, b IHF after pre-forming

and the wrinkling was reduced in the frame part produced by IHF, as depicted in Fig. 13.

Conclusions

The main conclusions of this investigation can be deduced based on the achieved results as follows:

1. The work hardening behavior observed in HSR deformation is more prominent than that detected in QSR deformation. Thus, the YS, flow stress, and UTS at HSR were higher than their QSR counterparts. The strain-hardening rate observed in HSR deformation was lower than that in QSR deformation, which was attributed to the competition between the strain hardening and thermal softening due to increasing the adiabatic temperature with increasing the strain rate. The ductility of AA2060-T8 sheets was improved under HSR deformation because of the adiabatic softening with increasing the strain rate and the inertia effect, which may diffuse necking the necking development and delay the onset of fracture.
2. These results obtained from this study were efficiently used to develop a new manufacturing route called impact hydroforming technology (IHF). IHF technology can improve the formability of lightweight metals and manufacture thin-walled complex shaped components from Al-Li and Al alloys.

Acknowledgments The authors greatly acknowledge the financial support by Brain Pool program funded by the Ministry of Science and ICT through the National Research Foundation of Korea (grant number: NRF-2021H1D3A2A01100036), National Natural Science Foundation of China - International (Regional) Cooperation and Exchange Program (No. 5201101342), and Jiangsu Province Science and Technology Project (No. BK20200453), and the National Natural Science Foundation of China (Grant No. 51875548). Finally, MG Lee appreciates a partial support from the KEIT (No. 20010717).

References

1. Abd El-Aty A, Xu Y, Guo X, Zhang S, Ma Y, Chen D (2018) Strengthening mechanisms, deformation behavior, and anisotropic mechanical properties of Al-Li alloys: A review. *J Adv Res* 10:49–67
2. Rioja R, Liu J (2012) The Evolution of Al-Li Base Products for Aerospace and Space Applications. *Metall Mater Trans A* 43A:3325–3337
3. Abd El-Aty A, Xu Y, Zhang S, Ma Y, Chen D (2017) Experimental investigation of tensile properties and anisotropy of 1420, 8090 and 2060 Al-Li alloys sheet undergoing different strain rates and fibre orientation: A comparative study. *Procedia Eng* 207:13–18
4. Abd El-Aty A, Xu Y, Ha S, Zhang S (2018) Computational homogenization of tensile deformation behaviors of a third generation Al-Li alloy 2060–T8 using crystal plasticity finite element method. *Mater Sci Eng A* 731:583–594
5. Abd El-Aty A, Ha S, Zhang S, Xu Y (2018) Prediction of tensile deformation behavior of Al-Li alloy 2060–T8 by computational homogenization-based crystal plasticity finite element method. *J Phys Conf Ser* 1063:12058
6. Abd El-Aty A, Zhang S, Xu Y, Ha S. Deformation behavior and anisotropic response of 2060 Al-Cu-Li alloy: Experimental investigation and computational homogenization-based crystal plasticity modelling. *J Mater Res Technol*. Accepted.
7. Ou L, Zheng Z, Nie Y, Jian H (2015) Hot deformation behavior of 2060 alloy. *J Alloys Compd* 648:681–689

Research on Electric Current-Assisted Draw Bending of AA7075-T6 Sheet



Hongrui Dong, Xiaoqiang Li, Dongsheng Li, Luyi Dou, Haibo Wang, Yanfeng Yang, and Xuebin Zheng

Abstract Electrically-assisted forming is a promising technology to realize the precise forming of materials with poor formability. For stamping process, the typical deformation process of sheet metal is that the sheet metal experiences bending and reverse bending when it passes through the corner of die, and the draw-bending test can well characterize this typical deformation process. Therefore, this paper studies the influence of normalized back force (0.1, 0.25), temperature (25 °C, 65 °C, and 150 °C), current (0A, 830A, 1300A, and 1700A) on the springback of AA7075-T6. The results show that the springback can be reduced by loading current during draw-bending test. Moreover, the larger the normalized back force is, the larger the reduction of springback angle is, which shows that the electroplasticity becomes more obvious with the increase of normalized back force. At the same temperature, with the increase of current, the springback angle decreases. Moreover, the higher the temperature is, the larger the reduction of springback angle is, which shows that pure electroplasticity becomes more obvious with the increase of temperature.

Keywords Aluminum · Draw bending · Electroplasticity · Pure electroplasticity · Springback

H. Dong · X. Li (✉) · D. Li · L. Dou · X. Zheng
School of Mechanical Engineering & Automation, Beihang University, Beijing 100191, China
e-mail: lixiaoqiang@buaa.edu.cn

H. Wang
School of Mechanical and Materials Engineering, North China University of Technology, Beijing 100144, China

Y. Yang
Université de Lorraine, Arts et Métiers ParisTech, 57000 Metz, France

X. Zheng
Shougang Group Co., Ltd. Research Institute of Technology, Beijing 100043, China

Introduction

Lightweight is becoming more and more important in the transportation industry due to the requirement for fuel economy and environmental protection. In the field of sheet metal forming, the use of precipitation-hardening 7XXX series aluminum alloy with high specific strength and specific stiffness can significantly reduce the weight, and its density is only one-third of that of steel. Therefore, the application of aluminum alloy in automobile has become more and more popular.

However, the poor formability of AA7075-T6 at room temperature severely limits its application in automobile. Nikolay Sotirov et al. [1] put forward warm forming, which requires a forming temperature of 200 °C–30 °C. However, high forming temperature will lead to the decrease of part strength and the change of microstructure after forming. Therefore, new forming methods are needed to solve above-mentioned problems.

It is found that the formability of sheet metal will change significantly when the current is applied during forming, such as the increase of plasticity and the decrease of deformation resistance. This phenomenon is called electroplastic effect. It has been found that on the one hand, electric current can increase the temperature of the material through Joule thermal effect, which makes the material soften (thermoplasticity / thermal effect). On the other hand, electric current can directly reduce the flow stress of material (pure electroplasticity / non-thermal effect). Based on existing research, pure electroplastic-assisted warm forming (PEPAWF) process is proposed, which can reduce the forming temperature by using pure electroplastic/non-thermal effect to compensate plasticity loss caused by the decrease of forming temperature. It is expected to greatly improve the forming limit and the forming quality of sheet metal.

Current research is mainly about the influence mechanism of current on the flow behavior of sheet metal by conducting uniaxial tensile test and microscopic test. For stamping process, the typical deformation process of sheet metal is that the sheet metal experiences bending and reverse bending when it passes through the corner of die, and the draw-bending test can well characterize this typical deformation process. Therefore, this paper studies the influence of normalized back force (0.1, 0.25), temperature (25 °C, 65 °C, and 150 °C), current (0A, 830A, 1300A, and 1700A) on the springback of AA7075-T6.

Material and Experiment

Material and Specimen

The material used in the test is AA7075 with T6 temper, whose chemical composition is shown in Table 1. The size of specimen used in electrically-assisted draw-bending test is shown in Fig. 1 and the lugs on the left and right of specimen are used to load current.

Table 1 Chemical composition of AA7075T6 (wt.%)

Zn	Mg	Cu	Si	Fe	Mn	Ti	Cr	others	Al
05.1 ~ 6.1	2.1 ~ 2.9	1.2 ~ 2	≤ 0.4	≤ 0.5	≤ 0.3	≤ 0.2	0.18 ~ 0.28	0.05 ~ 0.15	balance

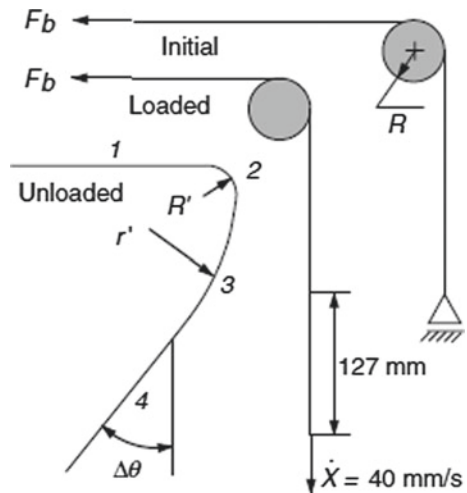


Fig. 1 The size of specimen for electrically-assisted draw-bending test (unit: mm)

Experiment Principle and Procedure

The experiment principle of draw-bending test is shown in Fig. 2 and concrete introduction is referred to reference [2]. Typical unloaded specimen is depicted in Fig. 2, and there are four deformation regions delineated. Regions 1 and 4 remain straight throughout the test. Region 2 is in contact with die just before unloading, whose radius is marked as R' . Region 3 experiences bending and reverse bending during test, whose radius is marked as r' . The total springback angle is marked as $\Delta\theta$. In addition, the back force F_b is characterized by normalized back force (\bar{F}_b) during test, which is expressed as the back force divided by the yielding force of the specimen in uniaxial tension (Eq. 1).

Fig. 2 Schematic of three stages of the draw-bend test and unloaded specimen geometry



$$\bar{F}_b = \frac{F_b}{\sigma_b \cdot b \cdot t} \tag{1}$$

where σ_b is yield strength, b is the width of specimen and t is the thickness of specimen.

Electrically-Assisted Draw-Bending Test Procedure

The experimental procedure for electrically-assisted draw-bending test is as follows:

1. The tension cylinder, which provides back force, is positioned at 30 mm of displacement sensor to ensure the consistency of initial state of draw-bending test and to prevent the contact between tension cylinder and specimen;
2. Grip the left end of specimen with tension cylinder, and then bend the specimen to conform to the die, with 90° of contact. Then grip the right end of specimen with drawing cylinder, as shown in Fig. 3a.
3. Connect the copper wire with the lugs of specimen with bolts, as shown in Fig. 3b. Then turn on the thermal imager to record the temperature change

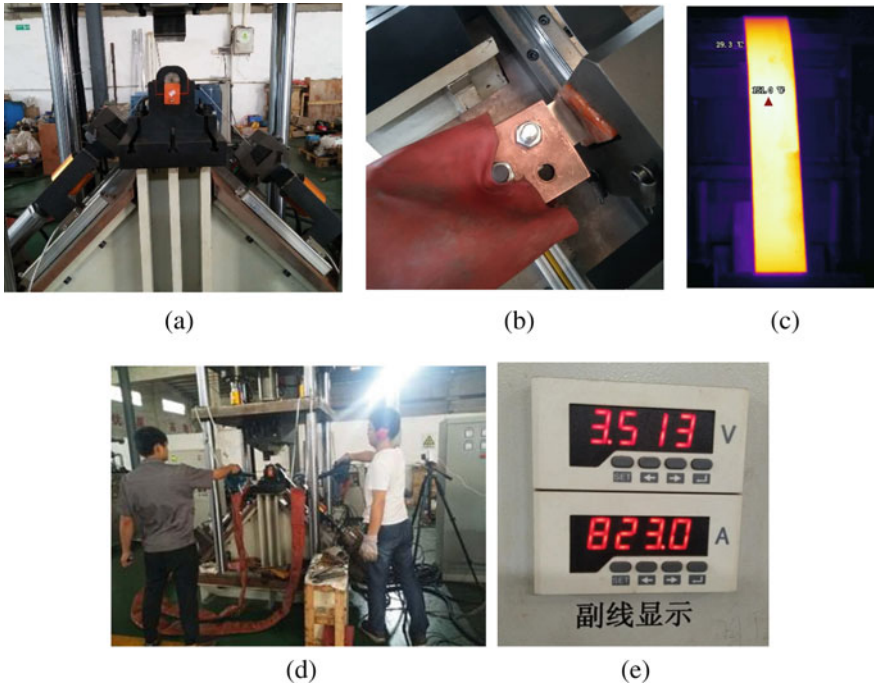


Fig. 3 Schematic diagram of draw-bending test

of the specimen (Fig. 3c), and turn on the blower to control the temperature (Fig. 3d).

4. Turn on the power switch and set the corresponding current parameter (Fig. 3e). When the temperature on specimen reaches the corresponding temperature, set the relevant parameters in the software to carry out the draw-bending test.

Experiment Matrix and Result

In order to study the effect of electroplasticity on the springback of draw bending, designed experiment matrix and corresponding results are shown in Table 2.

In order to study the effect of pure electroplasticity on the springback of draw bending, designed experiment matrix and corresponding results are shown in Table 3.

Table 2 Experiment matrix for the effect of electroplasticity on the springback of draw bending

NO	\bar{F}_b	Current/A	$\Delta\theta/^\circ$	R'	r'
1	0.1	0	47.066	46.5087	93.9589
2		830	47.106	38.7700	97.7425
3		1300	46.9	35.5290	104.1500
4		1700	45.904	31.7973	111.5627
5	0.25	0	42.305	40.8120	117.8091
6		830	41.758	37.3793	117.0187
7		1300	39.147	33.1436	132.2325
8		1700	35.94	31.7268	147.7016

Table 3 Experiment matrix for the effect of pure electroplasticity on the springback of draw bending

NO	Current/A	Temperature/ $^\circ\text{C}$	\bar{F}_b	$\Delta\theta/^\circ$	R'/mm	r'/mm
1	830	65	0.25	41.758	37.3793	117.0187
2	1300	65	0.25	41.409	35.9833	111.6453
3	1700	65	0.25	40.644	38.3860	108.9173
4	1300	150	0.25	39.147	33.1436	132.2325
5	1700	150	0.25	35.74	34.2222	134.3026

Discussion

The Effect of Electroplasticity on the Springback of Draw Bending

In order to observe the effect of electroplasticity on the springback of draw-bending intuitively, the corresponding experimental results in Table 2 are plotted in the Fig. 4. When the current increases from 0 to 1700A, the corresponding springback angle decreases from 47.066° to 45.904° under the condition of $\bar{F}_b = 0.1$. When the current increases from 0 to 1700A, the corresponding springback angle decreases from 42.305° to 35.94° under the condition of $\bar{F}_b=0.25$, which is mainly due to the Joule thermal effect. It can be concluded that springback can be decreased by loading current during draw-bending test. Moreover, the larger the normalized back force is, the larger the reduction of springback angle is, which shows that the electroplasticity becomes more obvious with the increase of normalized back force. Deeply, the springback angle is caused by radii at Region 2 and Region 3. As shown in Fig. 4, r' increases with the increase of current. This is because that the temperature of specimen increases due to Joule thermal effect, which decreases the flow stress of AA7075-T6 and the stress difference between inner and outer sides of specimen. R' decreases with the increase of current. This is because that the high temperature softening effect improves the plasticity of AA7075-T6, which decreases the springback at Region 2 and results in the change law of R' . As introduced in reference [2], the increase of r' makes $\Delta\theta$ decrease and the decrease of R' makes $\Delta\theta$ increase. However, the effect of variation of r' is larger than that of variation of R' , which makes the springback angle decrease with the increase of current.

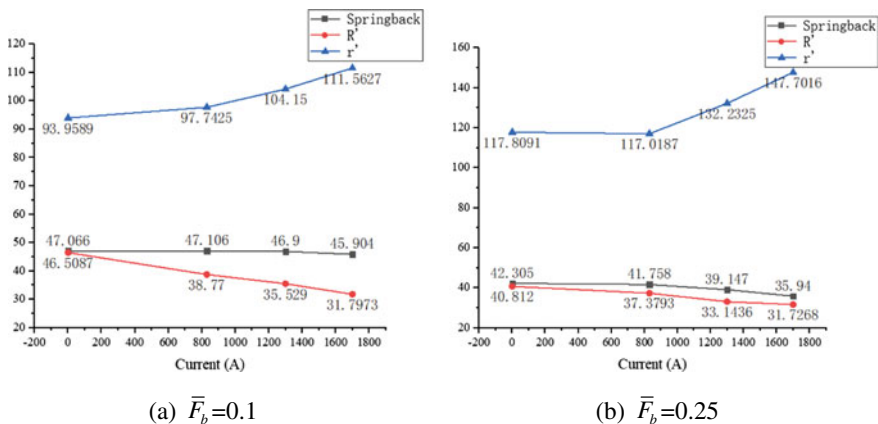


Fig. 4 The effect of current on springback of draw bending under different normalized back force **a** $\bar{F}_b = 0.1$ **b** $\bar{F}_b = 0.25$

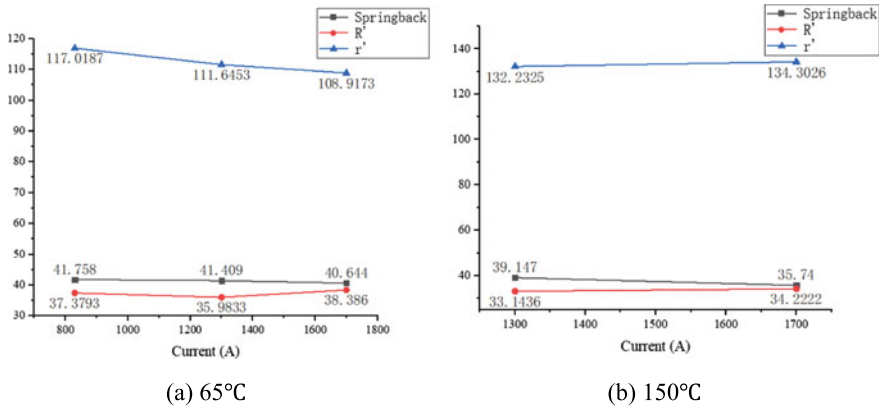


Fig. 5 The effect of pure electroplasticity on springback of draw bending under different temperature **a** 65 °C **b** 150 °C

The Effect of Pure Electroplasticity on the Springback of Draw Bending

In order to observe the effect of pure electroplasticity on the springback of draw bending intuitively, the corresponding experimental results in Table 3 are plotted in the Fig. 5. It is found that the springback angle decreases with the increase of current under the same temperature. Moreover, the higher the temperature is, the larger the reduction of springback angle is. When the temperature is 65 °C and the current increases from 830 to 1700A, the corresponding springback angle decreases from 41.758° to 40.644°. When the temperature is 150 °C and the current increases from 1300 to 1700A, the corresponding springback angle decreases from 39.147° to 35.74°. It can be concluded that the effect of pure electroplasticity becomes more significant with the increase of temperature. When the temperature is 65 °C, r' decreases and R' increases with the increase of current. When the temperature is 150 °C, r' and R' increase with the increase of current. According to reference [2], the larger the values of r' and R' , the smaller the springback angle is. Therefore, the reduction of springback angle at 150 °C with different current is larger than that at 65 °C with different current. Meanwhile, the influence of pure electroplasticity on springback needs further study.

Conclusion

1. The springback can be reduced by loading current during draw-bending test. Moreover, the larger the normalized back force is, the larger the reduction of springback angle is.

2. At the same temperature, with the increase of current, the springback angle decreases. Moreover, the higher the temperature is, the larger the reduction of springback angle is, which shows that pure electroplasticity becomes more significant with the increase of temperature.

Acknowledgements The authors are thankful for the support from the Fundamental Research Funds for the Central Universities (YWF-19-BJ-J-163). Also, the authors are thankful for the suggestions of editors and reviewers.

References

1. Nikolay S, Peter S, Thomas W, et al. (2010) Towards High Strength 7xxx Aluminium Sheet Components Through Warm Forming. Paper presented at the 12th International Conference on Aluminium Alloys. Yokohama, Japan, 5–9 September 2010.
2. Wang JF, Wagoner RH, Matlock DK et al (2005) Anticlastic curvature in draw-bend spring-back[J]. *Int J Solids Struct* 42(5–6):1287–1307

Part X
Other Topics

Numerical Modeling for Progressive Crushing of Composite and Hybrid Metal—Composite Structures



Saarvesh Jayakumar, Lorenz Stolz, Sharath Anand, Amir Hajdarevic, and Xiangfan Fang

Abstract In this present study, the numerical behaviors for progressive crushing of composite materials and hybrid metal composite materials are investigated. State of the art shows the importance of progressive crushing in composites as they lead to superior energy absorption characteristics. Since composite and hybrid materials serve a lightweight potential in structural applications, especially in automotive structures. The usage of these materials in energy absorption applications in automotive structures creates the need for their predictability in numerical simulations. Therefore, a methodology using finite element methods has been proposed to predict the numerical behaviors of composite and hybrid materials under crushing loads. A progressive failure material model is used to simulate the crushing response of a GMT structure. The cohesive zone modeling approach is used to predict the adhesive behaviors between metal and composite structures in numerical simulations. Finally, the cohesive modeling approach is combined with a progressive failure material model to predict the crushing behaviors of Hybrid Metal—Composite Structures.

Keywords Progressive crushing · Cohesive zone modeling · Interlaminar failure modeling

Introduction

Fiber-reinforced thermoplastics (FRP) have demonstrated their ability and are predominantly being used for lightweight design in many load-bearing applications, especially in the automotive sector [1–3]. FRP integration with metallic structures provides additional advantages such as cost savings and exceptional structural stability, justifying their use in automotive applications [4, 5]. Hybrid metal-FRP components, like FRP materials, are becoming more popular due to their combination of beneficial ductile failure behavior of metals with high specific stiffness and localized strength of the FRP material. To use these materials in automotive

S. Jayakumar (✉) · L. Stolz · S. Anand · A. Hajdarevic · X. Fang
Institute of Automotive Lightweight Design, University of Siegen, Siegen, Germany
e-mail: saarvesh.jayakumar@uni-siegen.de

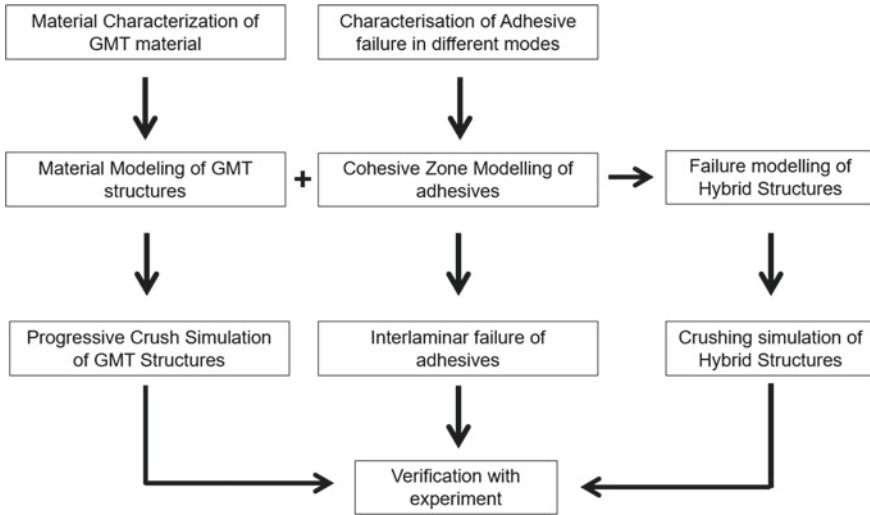


Fig. 1 Process cycle for numerical modeling of GMT and hybrid structures

applications, crashworthiness requirements must be met. To meet the crashworthiness requirements, correct crash simulation results are required during the product development process. Hence a numerical methodology to reproduce the crushing behavior of FRP and Hybrid structures is developed.

Figure 1 describes the methodology for numerical modeling of glass mat thermoplastic material (GMT) and hybrid metal-GMT structures under crushing loads. Since GMT components exhibit anisotropic behavior and more sophisticated energy dissipation mechanisms, material modeling of these materials requires a thorough understanding of their properties [4]. And therefore, the first step in material modeling of GMT materials involves the material characterization of GMT materials for the development of the material card. After the progressive crushing simulation is done and verified with the experimental behavior, the next step is to model the interlaminar behavior of adhesives. The adhesives between the metal and composite materials are characterized under different loadings such as cross tension and lap shear tests. These characteristic data serve as a base for the cohesive modeling of adhesives. After modeling the adhesives, the interlaminar behavior is validated for two extreme loading conditions where a minimum and maximum separation of adhesives are involved. Finally, the progressive failure model of GMT material and interlaminar failure behavior of adhesives through cohesive zone modeling are combined with aluminum material to predict the crushing behavior of hybrid metal-composite structures. Failure modeling of adhesives (interlaminar failure) is crucial because the Metal-FRP material combination leads to complex mutual interactions of aluminum and GMT during axial crushing. Hence, the purpose of this paper is to investigate the material behavior of GMT and adhesive, as well as to create a methodology

for time-efficient numerical modelling of GMT and hybrid structures using finite element methods.

Material Characterization

Material Characterization of GMT Materials

The fiber-reinforced thermoplastic investigated in this study corresponds to a glass mat thermoplastic material (GMT) comprising 40% vol of glass fibers. GMT extrudate material has a complex architecture comprising of both continuous fibers (glass mat layers including two layers of stacked plain weaved woven fabric reinforcement) and discontinuous fibers (long glass fibers) combined with Polypropylene matrix.

Diagrammatic representations of specimen location from the extrudate and pressed components are shown in Fig. 2a, b. It was not possible to use the ISO 527 Norm specimen from the pressed component because the Norm specimens were longer in size in comparison to the component length. Therefore, a smaller specimen size of 110 mm in length, 10 mm in width and 4 mm thickness was used in both extrudate (delivered material) and pressed GMT material to characterize the tensile behavior.

After these specimens were cut in the extrudate, the tensile and compression specimens were cut directly from the U profile, which was formed by compression molding using two plies of GMT material as illustrated in Fig. 2b. To determine the quasi-static mechanical properties of these glass mat thermoplastic materials a tensile test machine of type Zwick Z100 was used, and the tests were carried out at a speed of 2 mm/min. The compression test is performed with a combined loading compression

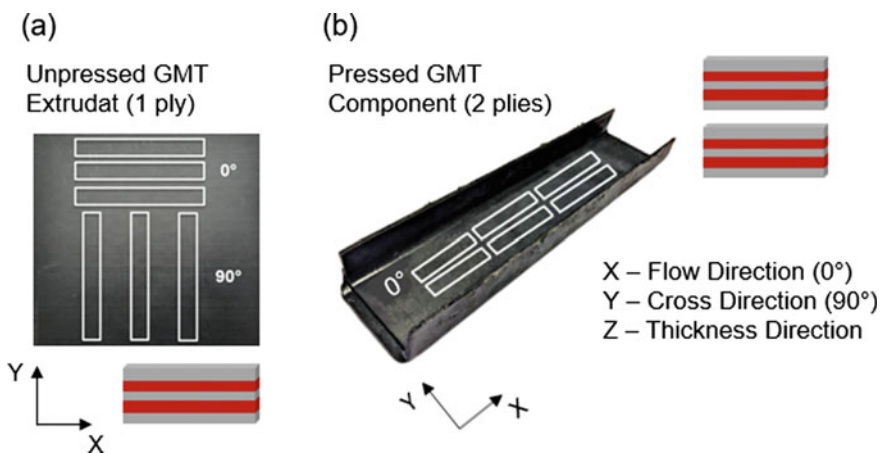


Fig. 2 Specimen location from extrudate (a) and pressed component (b)

(CLC) fixture. Compression tests were carried out on samples according to ASTM D6641 standards. The corresponding deformation strain is measured with the DIC technique (ARAMIS system and 5 M cameras). The characterized specimens from the pressed U profile components provided superior mechanical properties with an 18% increase in tensile strength and a 58% increase in compressive strength in the fiber direction compared to the results characterized from extrudate material. In the pressed GMT, using two plies with two woven layers each increases the number of woven layers to four. Thus, the mechanical properties are expected to be improved in the pressed GMT. The increase in mechanical properties especially compressive strength plays a vital role as it supports a stable crushing mode and prevents the structure to fail catastrophically which is discussed in later sections below.

Aluminum Characterization

The stress–strain behaviors of the base aluminum material 5182 used for the hybrid forming were characterized. For quasi-static tests with lower strain rates, the Zwick Z100 was used, and for high strain rates (from 10 1/s up to 1000 1/s) a high-speed testing machine HTM 5020 was used [6]. The determined strain rate dependency from tensile testing was used for the strain rate-dependent material modeling of the aluminum 5182 in FE Simulations.

Material Characterization of Adhesives

To investigate the interlaminar behavior between Aluminum and GMT in Mode 1 and Mode 2, lap shear and cross tension tests were carried out in the Ibertest Testcom-50 machine. The specimen geometry was based on the DIN EN 1465 standards. The yield stresses 6 MPa and 3.2 MPa were obtained from lap shear and cross tension tests and were further employed to model the interlaminar behavior between hybrid metallic and GMT materials. Figure 3a, b shows the force–displacement behavior of lap shear and cross tension tests respectively.

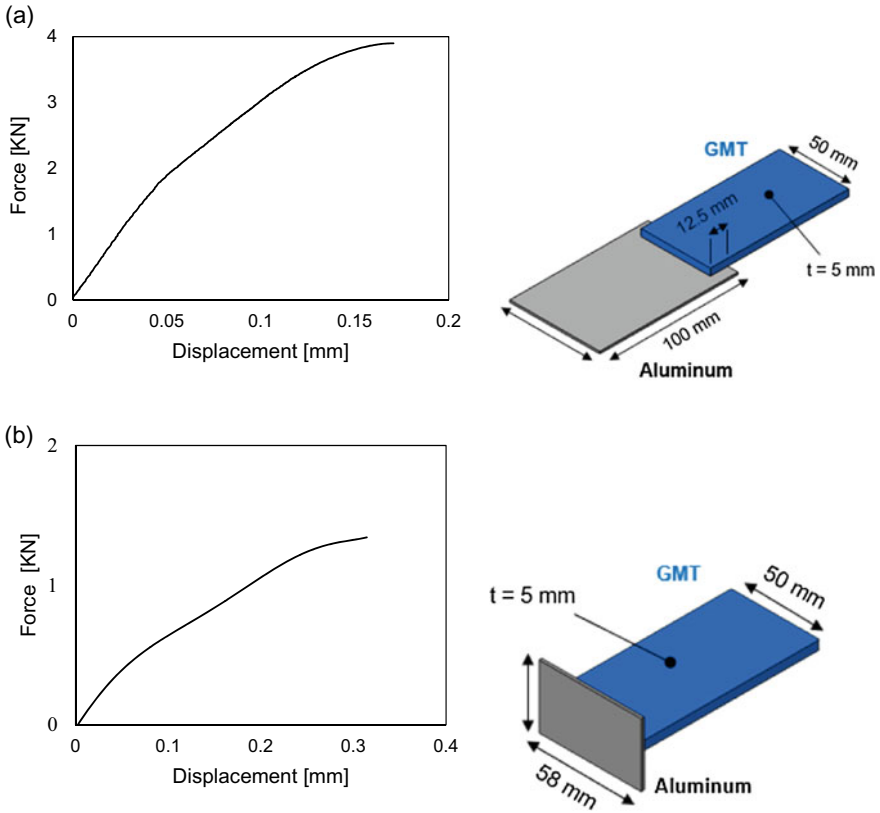


Fig. 3 Force displacement behavior of lap shear test (a) and cross tension test (b)

Material Modeling

Failure Mechanisms and Modeling of FRP Structures

Figure 4 shows the two types of failure mechanisms occurring commonly in composite materials. After the peak load, the material begins to fail under global buckling, fracture, or progressive crushing. The catastrophic failure occurring due to global buckling leads to the sudden growth of fractures in FRP structures. As a result, poor post-peak behavior is seen in the force deformation curve of the FRP structure under catastrophic failure.

Whereas contrary to the catastrophic failure of structures, when the structure undergoes a stable crushing mode called the progressive failure mechanism the post-peak behavior provides a superior force deformation curve. And since the post-peak behavior is superior it provides a better crushing load efficiency and energy absorption characteristics.

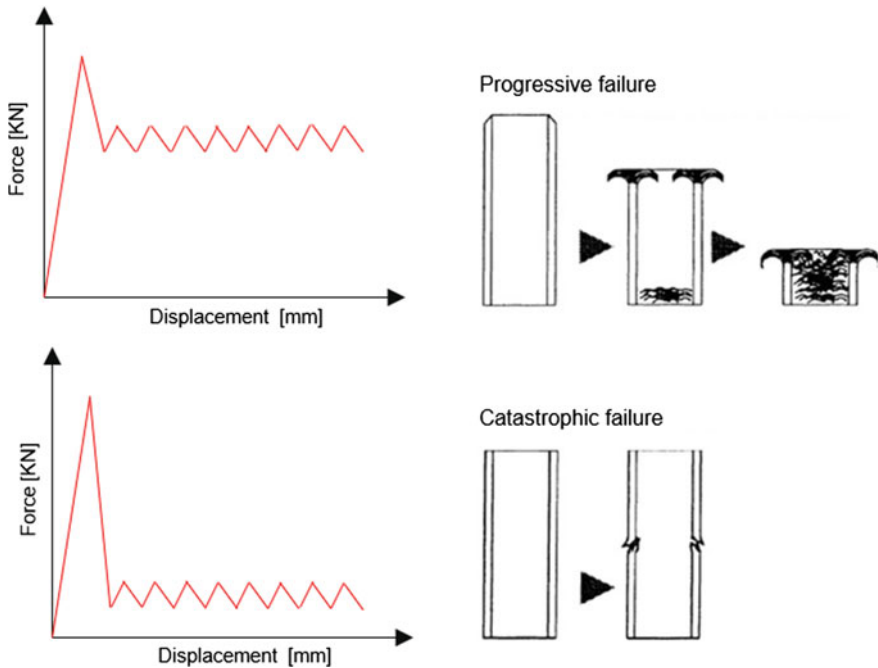


Fig. 4 Characteristic failure mechanisms of FRP structures [7]

The behavior of composite materials under crash conditions presents numerical challenges because it requires material modeling beyond the elastic region and into failure initiation and propagation. Crushing is caused by a combination of failure mechanisms such as matrix cracking and splitting, delamination, fiber tensile fracture, compressive kinking, frond formation and bending, and friction [8]. However, the computational power is insufficient to model all these failure mechanisms in a single numerical analysis, where the lamina-level failure criteria in progressive failure models serve as a great alternative for its pragmatic approach to predicting the onset of damage within laminate codes [9]. After the initiation of failure, the propagation of failure can be carried out using several degradation schemes [10].

Depending upon the specific degradation law used, the constitutive models in LS-Dyna can be categorized into progressive failure models (PFM – MAT54) and continuum damage mechanics models [8, 11].

In PFM, failure criteria for laminated composites are typically strength-based, and material properties are degraded using a ply discount method. The values of the appropriate elastic properties of the ply in the material direction are degraded at the failure surface from the undamaged state of 1 to the fully damaged state of typically 0. Progressive failure is achieved by a ply-by-ply failure within the laminate, with the element being deleted once all plies have failed. The properties are immediately dropped to zero once the ply's strength given in the material model is exceeded [8].

The progressive failure models are increasingly used for modeling composite materials due to their pragmatic approach and for their ease of design optimizations.

For modeling the GMT materials an orthotropic material model Mat_Enhanced_Composite_Damage MAT 54 was chosen with an enhanced Chang- Chang failure criterion.

The damage behavior with different failure modes in tensile and compression are shown below [12, 13].

for the tensile fiber mode,

$$\begin{aligned} \sigma_{11} \geq 0 \rightarrow e_{ft}^2 &= \left(\frac{\sigma_{11}}{X_t} \right)^2 + \beta \left(\frac{\sigma_{12}}{S_c} \right)^2 - 1, \quad e_{ft}^2 \geq 0 \rightarrow \text{failed} \\ E_1 = E_2 = G_{12} = \nu_{21} = \nu_{12} &= 0 \quad e_{ft}^2 < 0 \rightarrow \text{elastic} \end{aligned} \quad (1)$$

for the compressive fiber mode,

$$\begin{aligned} \sigma_{11} < 0 \rightarrow e_{fc}^2 &= \left(\frac{\sigma_{11}}{X_c} \right)^2 - 1 \quad e_{fc}^2 \geq 0 \rightarrow \text{failed} \\ E_1 = \nu_{21} = \nu_{12} &= 0 \quad e_{fc}^2 < 0 \rightarrow \text{elastic} \end{aligned} \quad (2)$$

for the tensile matrix mode,

$$\begin{aligned} \sigma_{22} \geq 0 \rightarrow e_{mt}^2 &= \left(\frac{\sigma_{11}}{X_c} \right)^2 - 1 \quad e_{mt}^2 \geq 0 \rightarrow \text{failed} \\ E_2 = \nu_{21} = 0 \rightarrow G_{12} &= 0 \quad e_{mt}^2 < 0 \rightarrow \text{elastic} \end{aligned} \quad (3)$$

and for the compressive matrix mode,

$$\begin{aligned} \sigma_{22} < 0 \rightarrow e_{mc}^2 &= \left(\frac{\sigma_{22}}{2S_c} \right)^2 + \left[\left(\frac{\sigma_{22}}{2S_c} \right)^2 - 1 \right] \left(\frac{\sigma_{12}}{S_c} \right)^2 - 1 \quad e_{mc}^2 \geq 0 \rightarrow \text{failed} \\ E_2 = \nu_{21} = \nu_{12} &= 0 \rightarrow G_{12} = 0 \quad e_{mc}^2 < 0 \rightarrow \text{elastic} \end{aligned} \quad (4)$$

In the above equations (Eq. 1 – Eq. 4): e_{ft} , e_{fc} , e_{mt} , e_{mc} is called the history variables and e_{ft} , etc. represent the tension and compression for longitudinal direction 1 and e_{mt} , e_{mc} transverse direction 2 respectively. The necessary material parameters X_c , X_t , Y_t , Y_c , E_1 , E_2 , and further for modeling the GMT materials were obtained from the material characterization of GMT materials.

Cohesive Zone Modeling of Adhesives

The Cohesive Zone Model (CZM) describes the failure behavior of very thin layers, such as delaminating of composite structures or adhesive bonding between two different materials. Due to the presence of complex dynamic interactions between the structures, the CZM can be used instead of a more complicated continuum mechanics fracture model in crash simulations of adhesively bonded vehicle structures which is computationally intensive and challenging.

Instead of using classical constitutive equations, the CZM considers the adhesive layer’s continuum mechanical fracture behavior and describes its failure using a simple traction–separation law (Fig. 5) [14–16].

The interlaminar failure between aluminum and GMT material was modeled using *Mat-Cohesive-Mixed-Mode-Elastoplastic-Rate (MAT 240) cohesive material model. The damage initiation and interaction among different delamination modes are described below [14].

The separations Δ_n in normal (peel) and Δ_t in tangential (shear) direction are calculated from the element separations in integration points,

$$\Delta_n = \langle u_n \rangle \text{ and } \Delta_t = \sqrt{u_{t1}^2 + u_{t2}^2}, \langle x \rangle = \begin{cases} x, & \text{if } x > 0 \\ 0, & \text{else} \end{cases} \quad (5)$$

u_n , u_{t1} and u_{t2} are the separations in normal and in both tangential directions of the element coordinate system. The total mixed mode separation Δ_m is determined by

$$\Delta_m = \sqrt{\Delta_n^2 + \Delta_t^2} \quad (6)$$

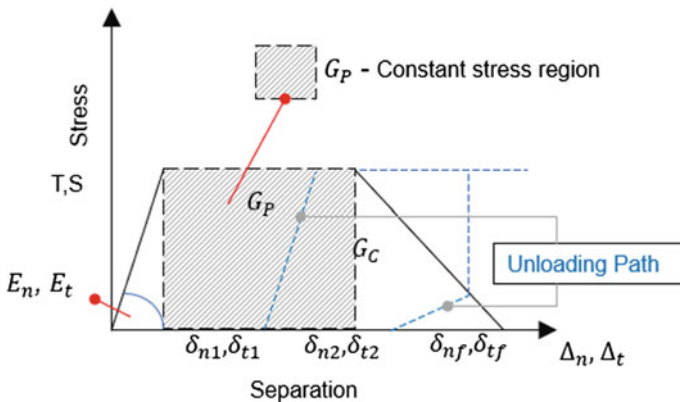


Fig. 5 Trilinear traction separation law used in MAT240 material model [14]

The initial stiffness E_n and E_t in both modes are calculated from the elastic young’s modulus E and the shear modulus G , $E_n = \frac{E}{t_{elem}}$ and $E_t = \frac{G}{t_{elem}}$, where t_{elem} , the element thickness, is an user defined value, which can be obtained from the distance between the initial positions of the corner nodes of the element. The young’s modulus and the shear modulus of the adhesive are obtained from the Lap shear and Cross tension tests and used as input parameters for the cohesive modeling of adhesives.

When the total energy under the traction separation law is given by G_C , one further parameter is needed to describe the exact shape of the traction separation material model. If the energy under the constant stress (plateau) region is denoted G_P (Fig. 5), a parameter f_{Gi} ($i = 1,2$) defines the shape of the traction–separation law.

$$0 \leq f_{G1} = \frac{G_{IP}}{G_{IC}} < 1 - \frac{T^2}{2G_{IC}E_n} < 1 \tag{7}$$

$$0 \leq f_{G2} = \frac{G_{IIP}}{G_{IIC}} < 1 - \frac{S^2}{2G_{IIC}E_t} < 1 \tag{8}$$

where the T and S are the critical stresses for Mode I and Mode II/III, respectively [11, 12]. These yield stresses were obtained from the Lap Shear and Cross Tension tests: $T = 6$ MPa and $S = 3.2$ MPa. Energy release rate G_{IC} in mode I and G_{IIC} in mode II was calibrated to two extreme situations in three-point bending load cases which are presented in Fig. 9. The energy release rate G_{IC} and G_{IIC} obtained from calibrations are 0.8 N/mm. Although the material model MAT 240 posses the ability to model the rate dependency of adhesives. In this study at the first step the strain rate dependent adhesive behavior is not investigated, due to the complex material modelling and the necessity of an extensive experimental investigation for Mode I and Mode II separations respectively.

Finite Element Modeling

Figure 6a shows the finite element model of hat profiles of pure GMT material for axial crush load case. Both the aluminum and GMT in the hybrid hat profile structures were modeled using LS-Dyna as layers using thin shell elements. Thin shells were stacked together and connected by cohesive elements which are shown in Fig. 6b. Thin shell elements used for modeling aluminum and GMT are of Type 16 fully integrated shell elements. 8 noded cohesive element of thickness 0.1 mm with four integration points was centered between two layers of shells (Aluminum and GMT) on the lower and upper surfaces to predict the interlaminar behavior. Figure 6b shows the hybrid aluminum GMT finite element model of both quasi-static three-point bending and dynamic axial crush load cases. Impactor and supports in both three-point bending, and axial crush load cases were modeled as rigid bodies.

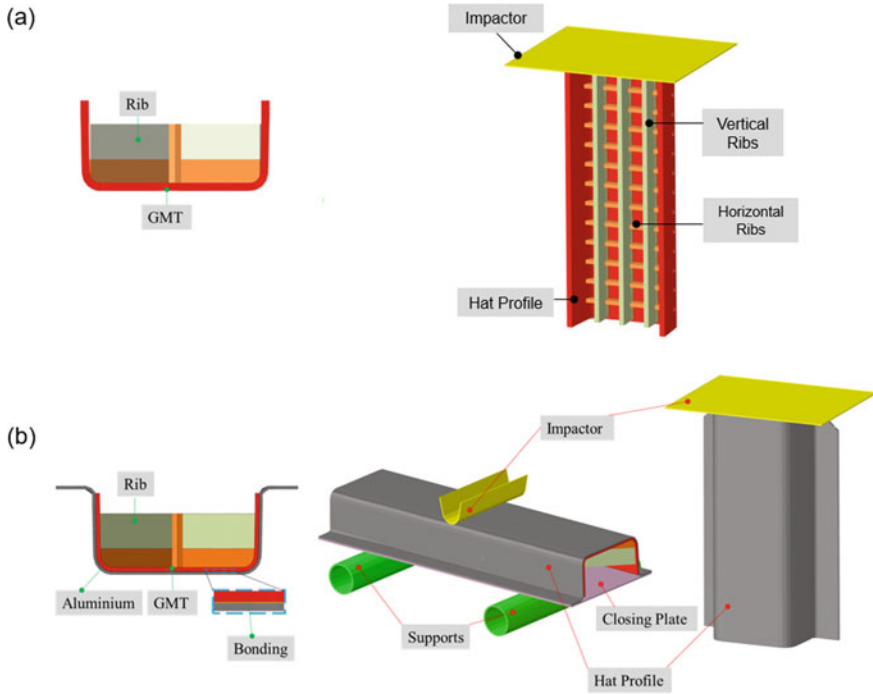


Fig. 6 a GMT Finite element model b Hybrid Aluminum—GMT Finite element model (3 PB and axial crush)

Orthotropy in the GMT layer was specified in MAT 54 material model using AOPT Eq. 3.0 (Material axes option) and with aid of their corresponding component vectors V1, V2, V3 and providing the material axes and element axes respectively. The contact algorithm Contact Automatic Single Surface was used for modeling the contact between impactor, rigid supports, and hybrid hat structures. Further Contact Automatic Surface to Surface was employed to model the contact between aluminum and GMT layers with a friction coefficient of 0.35 for both three-point bending and axial crush load cases. Both to the GMT axial crush model and the Al-GMT axial crush model an additional self-contact was provided in to prevent collision of elements.

Results and Analysis

Crushing Behaviors of GMT Structures

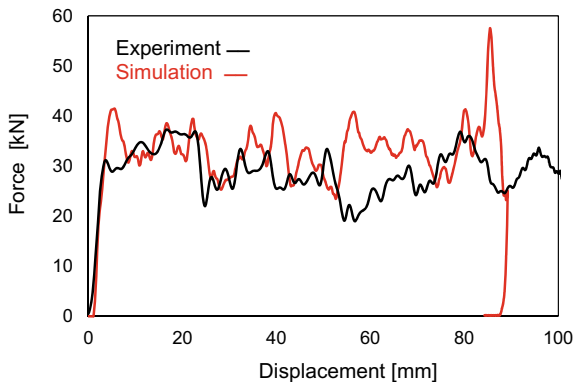
Dynamic axial crushing simulations of GMT structures were carried out with a testing velocity of 5.4 m/s with a falling mass of 200 kg and a kinetic energy of 3 kJ. The bottom portion of the axial crash box is fixed and constrained in all directions upto 50 mm.

Drop tower tests were conducted with above mentioned parameters and finally compared with the numerical simulations. Force–displacement curve in Fig. 7 shows that the crushed sample after the peak load produces a superior energy absorption characteristic. This superior mean force level is caused due to the progressive crushing of the GMT structures. Further the progressive crushing failures is a combination of various failure modes such as delamination, Interlaminar shear, Intralaminar shear, Fiber–Matrix separation and elastic bend formation. The stacking of double plies during the manufacturing of the GMT components played a vital role to produce stable crushing behavior due to their enhanced mechanical properties when compared to the single plies (extrudate).

As mentioned before in the state of the art although the MAT54 material model cannot individually model each failure modes which is computationally intensive and challenging. The simulation model with the Chang–Chang failure criteria could produce a progressive crushing behavior which shows good agreement with the experimental results. The systematic crushing of GMT axial crash box is further illustrated in Fig. 8.

With the verification of axial crushing with experimental results these material model serves as a foundation for further design optimization of crash structures with FRP materials. And these progressive failure models can also be combined with other material models to predict multi material structures.

Fig. 7 Correlation of force-intrusion curves in experiment and simulation of GMT crush profile



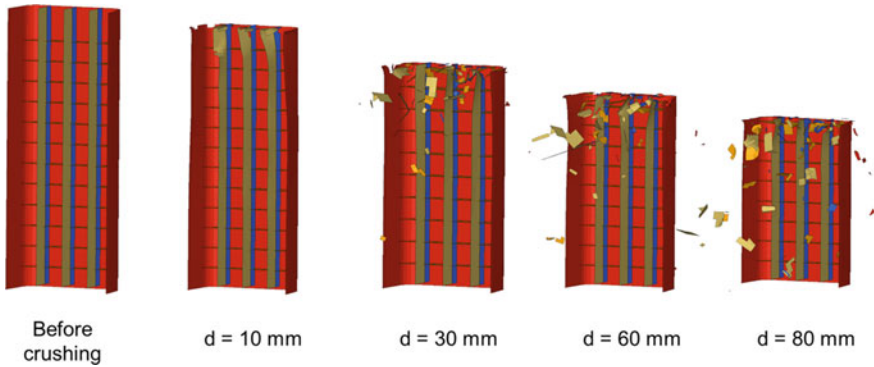


Fig. 8 Systematic crushing of GMT structures in numerical simulations

Numerical Behaviors of Hybrid Metal—Composite Structures

Quasi-Static Bending

In this analysis, quasi-static three-point bending load cases on the hybrid aluminum – GMT hat profiles were modeled. To validate the simulative behavior of the adhesives two three-point-bending tests were compared with experimental investigations under quasi-static loading with and without a closing plate that can be seen in Fig. 9.

Hat profile with a closing plate shows small bending deflection as the closing plate prevent the opening of the profile and the adhesives are only debonded in the middle section of the hat profile where the impactor is in contact as shown in Fig. 9 (left). However, when the profile without closing plate was bent, large bending deflection takes place which causes a strong debonding of the aluminum and GMT, as can be seen in Fig. 9 (right). Thus the simulation and test results are comparable and could qualitatively be validated for both loading conditions.

Crushing Behaviors of Hybrid Aluminum—GMT Structures

Dynamic axial crushing simulations of Hybrid Aluminum-GMT structures were carried out with a testing velocity of 6.2 m/s with a falling mass of 375 kg and a kinetic energy of 7 kJ. The bottom portion of the axial crash box is fixed and constrained in all directions upto 50 mm. Drop tower tests were conducted with above mentioned parameters and finally compared with the numerical simulations. The comparison of experimental and simulation results obtained from dynamic crushing of hybrid profiles is shown in Fig. 10. From the Fig. 10, it can be concluded that the force intrusion behavior of the simulation slightly over-predicts the experimental results till the crushing displacement of 60 mm.

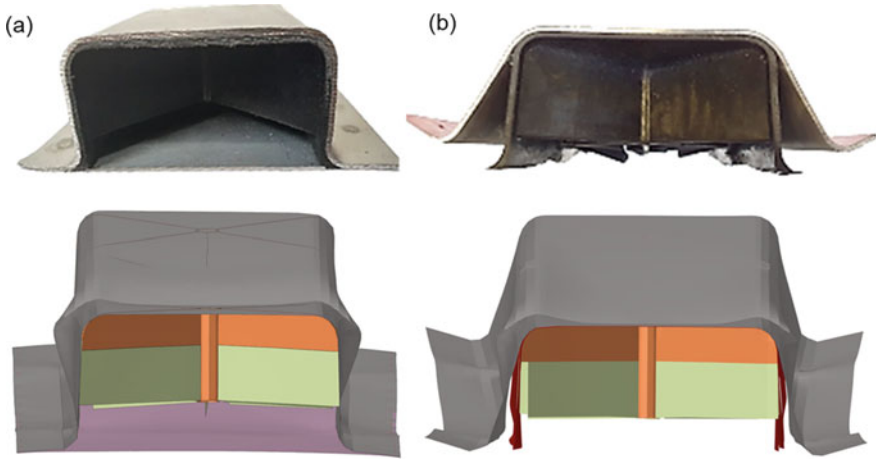


Fig. 9 Validation of adhesive materials under two extreme boundary conditions

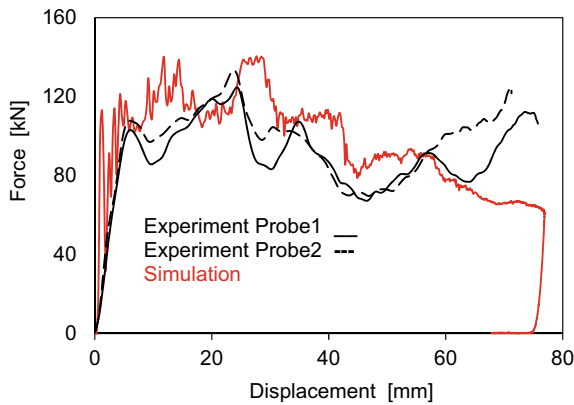


Fig. 10 Correlation of force-intrusion curves in experiment and simulation of hybrid crush profiles with (a) and without trigger (b)

On further comparing the mean force level to the experimental behavior it can be evidenced that the second peak is delayed in the finite element simulations. From Fig. 11 the systematic crushing of the hybrid crush box at different displacement ranges 20 mm, 40 mm, and 60 mm can be seen. The minimal failure of the adhesives in the cut section view at crushing displacement 20 mm was observed. As the crushing proceeds to 60 mm, a predominant failure of adhesives can be depicted from Fig. 11.

The predominant failure of adhesives after crushing displacement 60 mm causes mutual interaction between aluminum folding and GMT crushing (delamination), leading to an unstable complex failure mechanism. This unstable behavior at the end of the crushing process after 60 mm displacement causes substandard repeatability

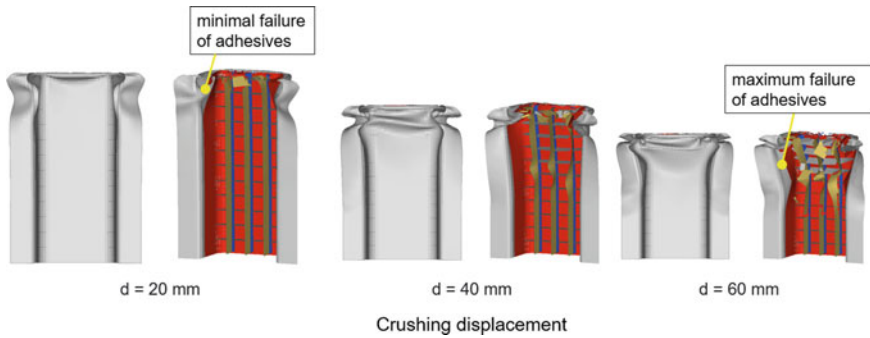


Fig. 11 Crushing behavior of hybrid axial crash box at different displacements

and a higher discrepancy between the simulation and experiments (Fig. 11). The presence of adhesive in the crash box and the corresponding connection strength contributed to a more stable and progressive crushing of the hybrid crash box till the crushing displacement of 60 mm. The folds of the aluminum, crushing of GMT and the separation of aluminum and GMT could be modeled successfully which predict both the crushing characteristics and the crushing parameters such as intrusions and peak force reasonably well.

Summary and Conclusions

In the present work, a methodology for the numerical simulation of GMT and Hybrid GMT structures was developed. Developed FE methodology with MAT54 material model could predict the GMT material behavior and provide good agreement with experiments. First approaches for modeling GMT progressive failure and adhesives interlaminar failure are presented. The cohesive zone material model may reproduce the bonding behavior between Aluminum and GMT materials in three-point bending load cases qualitatively. Due to their simplicity compared to the continuum mechanics fracture models these models can be applied for component development and structures involving the debonding of two materials. The developed material model consisting of the interlaminar failure of the adhesives and intralaminar failure of GMT material could reasonably predict the experimental crushing behavior of the hybrid crash box till the crushing displacement of 60 mm. After crushing displacement 60 mm higher disparity between simulations and experiments was observed due to the predominant failure of adhesives. Since the simulations of axial crushing of FRP and hybrid structures are challenging due to their complexity. And as the FE simulation is a critical step in the dimensioning and design of structures, the methodology developed here can serve as a base for the further improvement and to conduct design and optimization of lightweight structures.

Acknowledgements The authors acknowledge the European regional development funds (EFRE-0801129) for their financial support of the research project “AKTIV”.

References

1. Fang XF, Kloska T (2019) Hybrid forming of sheet metals with long Fiber thermoplastics by a combined deep drawing and compression molding process. *Int. J. of Material Forming*. 13:561–575
2. Ahmad B, Fang XF (2020) Modeling Shear Behavior of Woven Fabric Thermoplastic Composites for Crash Simulations. *Appl Compos Mater* 27:739–765
3. Striewe J, Reuter C (2018) Manufacturing, and crashworthiness of fabric-reinforced thermoplastic composites. *Thin-Walled Structures*. 123:501–508
4. Bambach MR (2010) Axial capacity and crushing of thin-walled metal, fiber-epoxy, and composite metal-fiber tubes. *Thin-Walled Structures*. 48:440–452
5. Reuter C, Tröster T (2017) Crashworthiness and numerical simulation of hybrid aluminum-CFRP tubes under axial impact. *Thin-Walled Structures*. 117:1–9
6. Fang XF (2021) A one-dimensional stress wave model for analytical design and optimization of oscillation-free force measurement in high-speed tensile test specimens. 149:103770
7. Saijod Lau TW, Said MR, Yaakob MY (2012) On the effect of geometrical designs and failure modes in composite axial crushing: A literature review. *Compos Struct* 94:803–812
8. Feraboli P, Wade B (2011) LS-Dyna Mat 54 modeling of the axial crushing of a composite tape sinusoidal specimen. *Composites: Part A*. 42:1809–1825.
9. Hinton MJ, Kaddour AS, Soden PD (2002) A comparison of the predictive capabilities of current failure theories for composite laminates, judged against experimental evidence. *Compos Sci Technol* 62(12–13):1725–1797
10. Xiao X (2009) Modeling energy absorption with a damage mechanics-based composite material model. *J Compos Mater* 43(5):427–444
11. Boria S, Scattina A (2015) Axial energy absorption of CFRP truncated cones. *Compos Struct* 130:18–28
12. Chang F, Chang K (1987) Post-failure analysis of bolted composite joints in tension or shear-out mode failure. *J Compos Mater* 25:809–833
13. Chang F, Chang K (1987) Progressive damage model for laminated composites containing stress concentrations. *J Compos Mater* 22:834–855
14. Marzi S, Hesebeck O, Brede M, Klein F (2009) A rate-dependent, elasto-plastic cohesive zone mixed-mode model for crash analysis of adhesively bonded joints, 7th European LS Dyna Conference, Salzburg, Austria
15. Zhou G, Sun Q (2020) Crushing Behaviors of Unidirectional Carbon Fiber Reinforced Plastic Composites under Dynamic Bending and Axial Crushing Loading. *Int J Impact Eng* 140:103539
16. Zhou G, Sun Q (2019) Experiment and simulation study on unidirectional carbon fiber composite component under dynamic three-point bending loading. *Int J Mater Manufact* 11:499–504

A New Sample for Oscillation-Free Force Measurement at High Strain Rates and Its Physical Principles



Xiangfan Fang

Abstract During high-speed tests using a hydraulic tensile machine, the force measurements are destroyed by the system ringing effect. In this work, the ringing of the test system was analyzed using FEM, which resulted in the development of a new type of test sample. Depending on the material's elastic properties and plastic work hardening rate, the new specimen has a specially designed minor plastic deformation area in addition to the usual plastic deformation zone. A ringing-free sample area can be created so that the test force can be measured there using strain gauge sensors. The plastic deformation and damage behavior can be determined for a wide range of strain rate, from 0.0001 to 5000/s. Based on the equations for one-dimensional stress waves and the stress wave attenuation due to dislocation motion, a simplified model with analytical formulation could be established and programmed in MATLAB. Verifications show a good prediction of the sample's geometry using this simplified model.

Keywords High speed test · Stress wave transmission/reflection · Sample geometry

Introduction

For crash simulations during the development phase of a passenger car, different mechanical material data, such as yield point, fracture strain, stress–strain curves, and instability/failure limit–stress triaxiality curves at different strain rates ranging from 10^{-4} to 1000 1/s, are needed [1–3]. For quasi-static tensile tests, DIN EN ISO 6892–1 [4] conventional tensile test samples with a gauge length of usually 80 mm are used. For higher speeds which correspond to strain rates of more than 10 1/s up to 1000 1/s, tensile tests according to ISO 26203/SEP 1230 [5, 6] are the choice. Its geometry is different from that of DIN EN ISO 6892–1 [4]. In particular, its gauge length is only 20 mm, which increases the eigenfrequency of the sample and thus

X. F. Fang (✉)

Institute of Automotive Lightweight Design, University of Siegen, Breite Straße 11, 57076 Siegen, Germany

e-mail: xiangfan.fang@uni-siegen.de

© The Minerals, Metals & Materials Society 2022

K. Inal et al. (eds.), *NUMISHEET 2022*, The Minerals, Metals & Materials Series, https://doi.org/10.1007/978-3-031-06212-4_70

773

reduces the force oscillation. In all of these tests, the forces are measured directly on the load cell of the tensile test machine. The force oscillation by load cell force measurement is very strong due to the system ringing at high strain rates of more than 50–100 1/s. An exact determination of the stress–strain curves is thus impossible.

Several proposals for the reduction of system ringing have been put forward [7–10], for example, the use of a filtering technique [7, 10] or longer load rising time [9]. The first proposal, which is commonly being used in the industry and by some research institutes, has the disadvantage of manipulating the measurement data without any knowledge of the material’s real behavior. The second method, lengthening the load rising time, usually cannot fulfill the targeted strain rate and thus cannot meet the requirements of high-speed tests. In addition to these proposals, Boehme [8] determined that the forces may be measured in the lower sample clamping area of a SEP/ISO sample [5, 6] with reduced force oscillations by using strain gauge sensors in comparison to the force measurement in the load cell of the test machine (see Fig. 1a). Using this method, the stress–strain curves of steels can be determined with little oscillation up to 200 1/s. Above this strain rate, the force oscillation becomes very large.

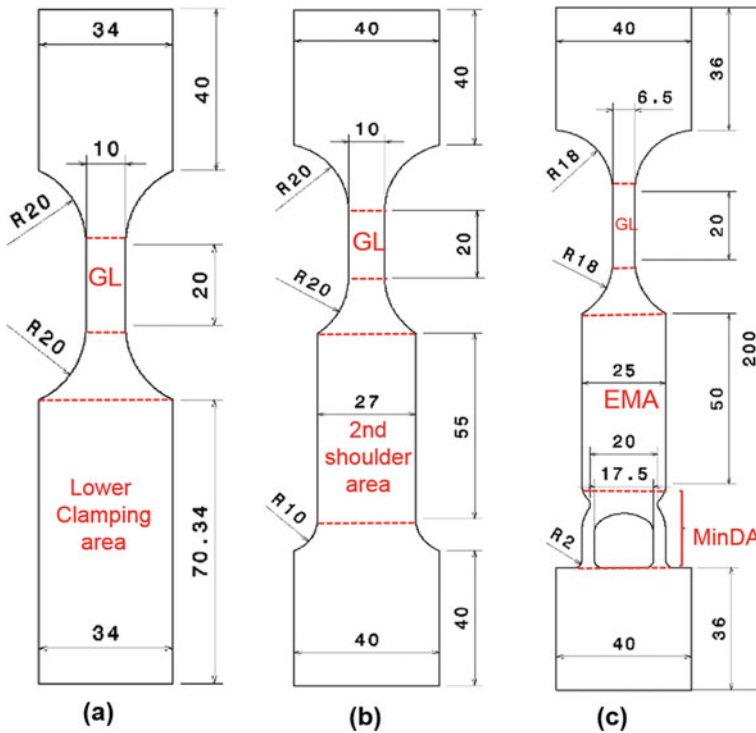


Fig. 1 Geometry of tensile test samples **a** according to SEP 1230/ISO 26203–2, **b** its modification as generation I (Gen. I) sample, and **c** further modification as generation III (Gen. III) sample. EMA: elastic measurement area for strain gauge to measure the force; MinDA: minor deformation area; GL: gauge length of plastic deformation

Based on the idea of [8], the SEP/ISO sample has been further developed [11]; the sample shoulder was enlarged and divided into two parts, as shown in Fig. 1b. This modification of the sample shows a further reduction of the force oscillation when forces were measured in the so-called second shoulder by strain gauges, as in [8]. The modified sample is named the generation I (Gen. I) sample.

In this work, the Gen.I sample is further improved by using FEM which results in the creation of Gen. III sample shown in Fig. 1c. A simplified one-dimensional stress wave model was proposed to explain the physical principle of the Gen. III sample.

Analysis of the System Ringing in a Hydraulic Tensile Test System

For the hydraulic tensile test machine HTM 2050 (ZwickRoell) used in this work, the CAD data of the entire test system were provided by the company so that a FE-Modell could be for the first time built for the whole system, including the test sample and machine. This is the base for the entire development.

The FEM model was built as follows: (a) the CAD data were meshed using solid elements with the following element sizes: hydraulic jack, sliding bar and lower plate = 5 mm and accelerated grip, specimens including EMA, screws and upper plate = 1 mm. Appropriate element orientations were selected to avoid non-physical reflections; (b) both element formulations of LS-DYNA, either constant stress (ELFORM = 1) or fully integrated (ELFORM = 2) could be used; (c) numerical penetrations between colliding parts, such as the sliding bar and acceleration grip, were minimized by using a node-to-node connection. Otherwise, the solver would try to overcorrect the numerical penetrations, thus causing non-physical oscillations. Instead of a single definition of global contact for all components in the model using the LS-DYNA algorithm "CONTACT_AUTOMATIC_SINGLE_SURFACE," local contacts between each colliding pair were defined as "CONTACT_AUTOMATIC_SURFACE_TO_SURFACE" algorithm; (d) the material properties of the sample are given by their quasi-static stress-strain curves and Young's module only. For the plastic deformation, the tabulated material law *MAT_024 (*MAT_PIECEWISE_LINEAR_PLASTICITY) was used, and the failure strain was set at 1.3, which was larger than the actual value, to obtain a few more oscillation periods and to better determine the frequencies; (e) all the machine components were considered rigid. Additionally, components that were fixed together, such as the sample and fixture, were connected by shared nodes in the FEM model; (f) the time step during the simulation was reduced from 3.41E-05 ms to 3.37E-05 ms because of the changes in the smallest element size during the simulation; and (g) to determine the force signal in every part, force sections were used (Fig. 2).

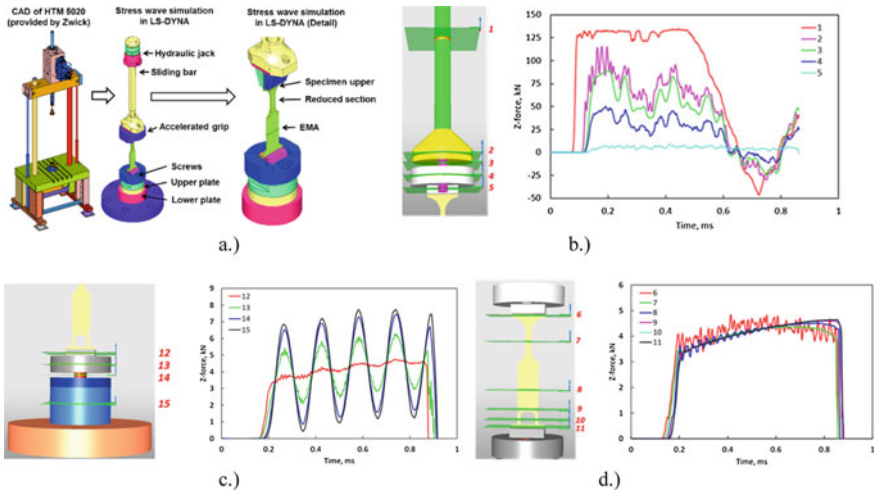


Fig. 2 a FE model of the Zwick HTM5020 hydraulic tensile machine, b section forces in the upper part of the system, c section forces in the lower part of the system, and d section forces in the Gen. III sample. Sample material: austenitic steel FSS 439

Based on this model and the extended SEP/ISO and Gen. I samples, further FE calculations and sample optimizations were performed. Figure 2 shows the results of the developments on a new sample geometry called the generation III (Gen. III) sample [12, 13].

The most important finding in Fig. 2 is that the force oscillation in the area of the hydraulic jack and sliding bar for the sample loading is very large (Fig. 2b), in the area of the load cell in the lower part of the test system, it is large (Fig. 2c) and in the area of the plastic deformation (gauge length area of the sample = section 7) (Fig. 2d) it is nearly zero. Because of this effect, the SEP/ISO sample and its modification, the Gen. I sample (Fig. 1a, b), were further developed. The target was to further reduce the force oscillations in the area of the second shoulder of the Gen. I specimen by changing the detailed geometry of the sample. This process ended with the discovery of the generation III (Gen. III) sample whose geometry is shown in Fig. 1c. In the Gen. III sample, a cut-off in the second shoulder area of the Gen. I sample was added. It should work as a geometric filter to prevent the stress waves being reflected back to the elastic measurement area (EMA) when the downward stress waves, which come from the top of the sample, pass the second shoulder area and are reflected at the lower end of the sample.

With a decrease in the cross section in the weakening area in the second shoulder, a decreasing system ringing could be observed in the EMA. The best results were obtained when a slight plastic deformation occurs in the weakening area in the second shoulder, which is named a minor deformation area (MinDA) in Fig. 1c. Using the sample geometry in Fig. 1c, the section force 8 in Fig. 2d, which is the force in the EMA area (the example here is ferritic stainless steel FSS 439), is almost free of

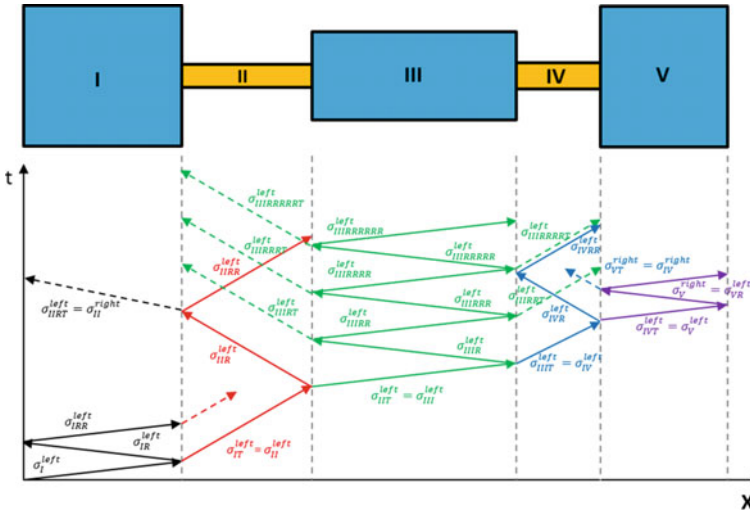


Fig. 3 A simplified one-dimensional beam model of the Gen. III sample, and the transition and reflection of the stress waves on the section boundary

oscillation at 1000 1/s strain rate (20 m/s machine speed). The effect of this slight plastic deformation is much larger than the pure geometric changes, i.e., the cross section reduction. The experimental results of [12, 13] show that a dual-phase steel DP 600 and an European mild steel DC04 at different strain rates up to 1000 1/s are all free of oscillations. These good results for Gen. III are also confirmed on a dual-phase steel DP 600 by real tests, as shown later (Fig. 3) (see Fig. 4).

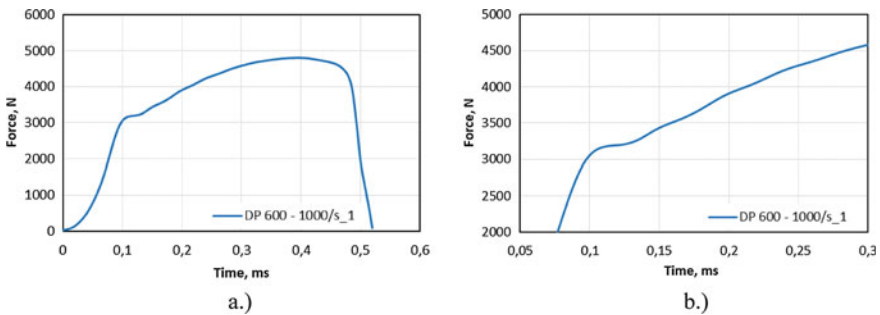


Fig. 4 **a**) A complete force–time curve of DP 600 steel at 1000 1/s, **b**) zoomed force–time curves

Physical Interpretation of the Gen. III Sample

It is well known in physics that stress waves occur if a material is loaded by a sudden impact [14, 15]. The stress waves of a one-dimensional stress wave can be described by a second-order differential equation and the wave propagates with a speed C :

$$C = \sqrt{\frac{1}{\rho_0} \cdot \frac{d\sigma}{d\varepsilon}},$$

With ρ_0 is the initial material density and $\frac{d\sigma}{d\varepsilon}$ is its hardening rate. For elastic deformation, the hardening rate is equal to Young's modulus E . For plastic deformation, it is the slope of the stress-strain curve (strain or work hardening rate), which usually changes during the deformation.

The intensity or amplitude of the stress wave generated by an impact with velocity v is determined by Eq. 1:

$$\sigma = \rho_0 \cdot C_0 \cdot v, \quad (1)$$

where $\rho_0 \cdot C_0$ is the impedance of the material. In an elastic case, it can be written as $\sqrt{E \cdot \rho_0}$. This means that the stress wave amplitude is only determined by the material's elastic properties; the impact mass has no influence. For materials in plastic deformation mode, the impedance is $\sqrt{d\sigma/d\varepsilon \cdot \rho_0}$.

If the stress wave propagates in a bar consisting of different section sizes and materials, wave reflections, and transmissions occur. Depending on the change of geometric section size and materials' impedance, the stress amplitude of the reflected wave may be calculated by Eq. 2:

$$\sigma_R = F \cdot \sigma_I \quad (2)$$

and for transmission by Eq. 3:

$$\sigma_T = T \cdot \sigma_I \cdot \frac{A_1}{A_2} \quad (3)$$

n , F , and T are defined by Eq. 4:

$$n = \frac{(\rho_0 C_0 A)_1}{(\rho_0 C_0 A)_2} = \frac{\left(\sqrt{\frac{d\sigma}{d\varepsilon} \cdot \rho \cdot A}\right)_1}{\left(\sqrt{\frac{d\sigma}{d\varepsilon} \cdot \rho \cdot A}\right)_2} = \frac{A_1}{A_2} \cdot \alpha \quad (4)$$

$$F = \frac{1 - n}{1 + n} \quad (5)$$

$$T = \frac{2}{1 + n}. \quad (6)$$

where α is the ratio between Young’s modulus and the plastic modulus (work hardening rate) according to Eq. 7 if the waves are transmitting from a material section in an elastic state to a material section in a plastic deformation state. If both sections are in an elastic state, $\alpha = 1$.

$$\alpha = \frac{(\rho C)_{el}}{(\rho C)_{pl}}. \tag{7}$$

Another important fact is that the elastic stress waves’ amplitude may be reduced strongly by plastic deformations. This effect can be seen in the forces in sections 7 and 9 of Fig. 2d. In these two areas, the material sustains a plastic deformation. The force vibration is nearly zero, whereas in the neighboring areas, large force vibrations are visible. Maurel et al. [16, 17] suggested that dislocations in materials interact with elastic stress waves through dislocation movement and that these interactions may attenuate the elastic stress waves.

Based on this fact and the work of Wang [14], a one-dimensional stress wave model has been proposed in this work to explain the phenomenon of the Gen. III sample.

At first, the sample geometry in Fig. 1c is simplified as a beam model illustrated in Fig. 3. Beams I and V correspond to the sample clamping area. Beam II is the main plastic deformation area (gauge length area), beam III the EMA, and beam IV the MinDA areas. The beams have different cross sections $A_I - A_V$ and may have different elastic or elastic–plastic properties. Beams I, III, and V should always be in an elastic state, while beams II and IV are initially in an elastic state and change to an elastic–plastic state when the specimen is loaded. The impulse load comes from the left side (beam I), and, on the right side, beam V is fixed on the load cell.

As the lower part of Fig. 3 shows, the incident stress wave σ_I^{left} passes through beam I and is transmitted into beam section II at the boundary between the two beams. This $\sigma_{IT}^{left} = \sigma_{II}^{left}$ can be easily determined using Eqs. 3 and 5. Parallel to the wave transmission, σ_I^{left} is also reflected on the same boundary as σ_{IR}^{left} , which can be calculated by Eqs. 2 and 5.

The same transmission and reflection happen on the boundary between beams II and III as $\sigma_{IIT}^{left} = \sigma_{III}^{left}$ and σ_{IIR}^{left} , between beams III and IV as $\sigma_{IIIT}^{left} = \sigma_{IV}^{left}$ and σ_{IIIR}^{left} , and between IV and V as $\sigma_{IVT}^{left} = \sigma_V^{left}$ and σ_{IVR}^{left} .

There are also many second- to N- order reflections, such as σ_{IIR}^{left} reflected on boundary II to I as σ_{IIRR}^{left} and σ_{IIIR}^{left} , reflected on boundary III to II as σ_{IIIRR}^{left} . The same thing happens in beam IV. When considering beam III, N = 6 times reflections are drawn, with the last one as $\sigma_{IIIRRRRR}^{left}$.

To complete the model, the following assumptions must be made:

- The reflection and transmission of the infinitesimal short waves are considered only in one direction: from left to right or from right to left (indicated as left-side or right-side wave, σ_i^{left} or σ_i^{right} in Fig. 3).
- Since the stress waves are absorbed in the plastic deformation zones GL and MinDA (Fig. 1c), which correspond to beam II and IV in the model in Fig. 3,

the second-order reflected waves such as σ_{IRR}^{left} in beam I and the σ_{IIRR}^{left} in beam II are not followed. This means that after σ_1^{left} is transmitted into beam III, they will be captured inside beam III and be reflected back and forth in beam III after the plastic deformations take place in beam II and IV. The $\sigma_{III...R}^{left}$ are captured in beam III.

- Only the amplitude of the stress waves is considered and not their phase angle. The superposition of several waves is a simple addition of their stress amplitude.
- The beam sections I, III, and V of the Gen. III sample are always in an elastic state, and sections II and IV are always in a plastic deformation state. The transition of the deformation mode from elastic to plastic in sections II and IV is neglected, so that only one impedance for each section would be used.
- In the plastic deformation areas II and IV, the strain hardening rate is constant, which means a linear plastic work hardening.
- Young's modulus is strain rate independent which is commonly accepted.

In order to obtain a fast stress wave attenuation in the sample, the following two conditions must be met:

- (a) The stress amplitude of all transmitted waves must be smaller in comparison to the incident wave ($T < 1$). Therefore, the wave transmission will always reduce the stress wave amplitude.
- (b) The stress amplitude of all reflected waves must be smaller than the incident. This is always true because the n -value in Eq. 4 is always positive, and F is thus always smaller than 1 ($-1 < F < 1$) according to Eq. 5.

Based on the model in Fig. 3 and the abovementioned simplifications, as well as condition a), a total of nine condition equations can be mathematically formulated using Eqs. 2–7 [18].

For the geometry of the Gen. III sample, it can be proved that the sample's geometric dimensions meet the nine conditions. With section sizes of $A_I = A_V = 50 \text{ mm}^2$, $A_{II} = 6.5 \text{ mm}^2$, $A_{III} = 25 \text{ mm}^2$, and $A_{IV} \approx 7.5 \text{ mm}^2$ for the Gen. III sample, the incident stress waves created by the sliding bar of the machine (Fig. 2) need 7 reflections ($N = 7$) in beam III (Fig. 3) of the model to be reduced to less than 1% of their initial amplitude. For the length of beam III (58 mm), this means an attenuation time of 0.06 ms. In this calculation, a α -value of 25 is assumed, which is the beginning of the plastic deformation of steels according to the work hardening rate measured in [13].

In comparison to the results in [13], where no ringing of forces and stresses were observed, the current model predicts that a fast reducing force oscillation (seven reflections) must exist at the beginning of the plastic deformation, as calculated above. Careful inspection of the measured force–time curves (zooming of the curve in Fig. 4a) in fact shows a small but fast reducing force oscillation at the beginning of the deformation, as can be seen in Fig. 4b. The small oscillation after the begin of plastic deformation disappears after approx. 0.1 ms time, which is close to the above forecast of 0.06 ms. The one-dimensional stress wave model can thus not only

describe the physical background of the Gen. III sample, but is also able to predict a phenomenon which has been overlooked until now.

Material Sensitivity of the Sample’s Geometry

Because of the simplicity of the one-dimensional model, its equations can be easily coupled with mathematical optimizations that enable the analysis of the sensitivity of the material properties on geometric section sizes. In this work, the sequential quadratic programming [19] technique, which is already implemented in MATLAB, has been used.

The α -value (Eq. 7) is the only material property in the model. It is obviously a function of strain, since the work hardening $d\sigma/d\varepsilon$ usually decreases with the increasing strain. Using the MATLAB software, the influence of the α -value on both the optimized section sizes A_{III} and A_{IV} , as well as the reflection numbers N, can be determined (see Fig. 5). For this calculation, the section sizes $A_I = A_V = 50 \text{ mm}^2$ and $A_{II} = 6.5 \text{ mm}^2$ were set. The incident stress amplitude should attenuate to $< 1\%$ after the N-reflections. A maximum N-value of almost 350 could be found at $\alpha = 340$, which is very high. For lower or very large α -values, lower N-values can be obtained (Fig. 5a). The value of optimized section sizes for beams III and IV, A_{III} and A_{IV} , are non-steady. There is one jump for A_{IV} and two for A_{III} . A_{IV} may take a value of 20 mm^2 if the α -value > 80 . This is only possible in the real world if the material in beam IV has an elastic modulus which is $1/80$ of Young’s modulus. In the Gen. III sample, the materials in beam IV must deform plastically. The section size of A_{IV} may thus not be much larger than A_{II} . The large value of A_{IV} is non-physical and must thus be ignored.

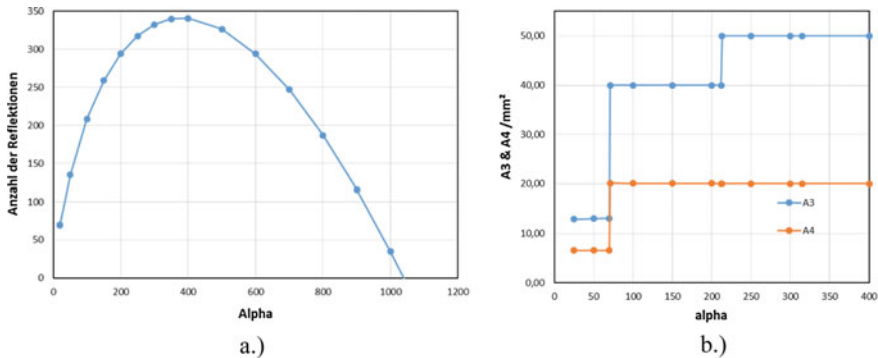


Fig. 5 **a** Influence of the α -value on reflection number N, **b** influence of the α -value on the section sizes of A_{III} and A_{IV} for minimizing the N-value

If A_{IV} may change, as in Fig. 5b, the value of A_{III} may change from 13 mm² to 40 mm² and finally to 50 mm² for minimizing the reflection number (N-value), when the α -value increases.

In a real-world test sample, the value of A_{III} is not only determined by the number of reflections in beam section III, but also by the stress homogeneity condition in beam III. The shape of the transition from beam III to IV plays an important role. From this transition edge, a multi-axial stress state occurs, which results in inhomogeneous stress and strain. The section width and length of beam III must be large enough so that an area of homogeneous strain may be built in its middle for force measurement via strain gauge sensor, as can be seen in Fig. 1c. Hence, the section size of beam III is a compromise between the minimum N-value and strain homogeneity.

Using the MATLAB optimization software, for $\alpha = 25$, if the range of the beam sections of I and V is set from 20 mm² to 500 mm², which is very large for a tensile specimen, an optimum of A_{II} and A_{IV} can be found with $A_{II} = 6, 5$ mm², $A_{IV} = 8, 3$ mm² at $A_{III} = 51$ mm² and $N = 1$. If the α -value changes, the sample sizes change as well.

Conclusions

Starting with the FE modeling of the entire servo-hydraulic test system and based on the former proposal of force measurement directly on the sample shoulder, a novel specimen geometry (Gen. III sample) for oscillation-free force measurement at a nominal strain rate of 1000 1/s was developed in this work. The physical principle of the sample can be explained by a one-dimensional stress wave model. This model is also able to predict phenomenon which has been overseen. It can be used to guide the sample geometry design for materials with different work hardening properties.

Acknowledgements This work was supported by the German Research Foundation (Deutsche Forschungsgemeinschaft, grant No.: FA 1024/5-1), to which I am indebted. The author also thanks Mr. Jens Olschewski for his MATLAB programming and Mr. Chongyang Zeng for his technical support.

References

1. Haufe A (2010) Recent developments in damage and failure modeling with LS-DYNA, Nordic LS-DYNA Users Forum, Nordic LS-DYNA Users Forum-2010
2. Gese H, Dell H, Reisner M, Brenner F (2014) Improved prediction of material fracture with CrachFEM. Paper presented at the 3rd MATFEM Conference, Hohenkammer
3. Klitschke S, Böhme W (2014) Crashverhalten von Stählen im Automobilbau bei unterschiedlichen mehrachsigen Belastungen. Paper presented at Werkstoffprüfung, Halle 2014:213–218
4. DIN EN ISO 6892–1, Metallic materials - Tensile testing - Part 1: Method of test at room temperature (ISO 6892–1:2016), 2016

5. Metallic materials - Tensile testing at high strain rates - Part 2: Servo-hydraulic and other test systems (ISO 26203–2)
6. Ermittlung mechanischer Eigenschaften an Blechwerkstoffen bei hohen Dehraten im Hochgeschwindigkeitszugversuch (SEP 1230)
7. Yan B, Kuriyama Y, Uenishi A, Cornette D, Borsutzki M, Wong C (2006) Recommended practice for dynamic testing for sheet steels - development and round robin tests. SAE Trans 155:147–157
8. Böhme B (2008) FAT-Richtlinie Dynamische Werkstoffkennwerte für die Crashesimulation. Material Test 50:199–205
9. Xiao X (2008) Dynamic tensile testing of plastic materials. Polym Test 27:164–178. <https://doi.org/10.1016/j.polymertesting.2007.09.010>
10. Zhu D, Rajan S, Mobasher B, Peled A, Mignolet A (2011) Modal analysis of a servo-hydraulic high speed machine and its application to dynamic tensile testing at an intermediate strain rate. Exp Mech 51:1347–1363
11. Li J, Fang XF (2014) Stress wave analysis and optical force measurement of servo-hydraulic machine for high strain rate testing. Exp Mech 54:1497–1501. <https://doi.org/10.1007/s11340-014-9929-4>
12. Fang XF, Grams R (2017) Neue Entwicklungen in der Materialprüfung bei sehr hohen Dehnraten. Paper presented at Werkstoffprüfung 2017 - Fortschritt in Werkstoffprüfung in Forschung und Praxis, Berlin, Nov. 2017
13. Fang XF, Grams R (2018) A novel oscillation-free force measurement for the determination of material properties during high-speed tests. ASTM Journal of Testing and Evaluation. <https://doi.org/10.1520/JTE20180887>
14. Wang LL (2007) Foundations of stress waves. Elsevier
15. Achenbach JD (1999) Wave propagation in elastic solids. Elsevier
16. Maurel A, Mercier J-F, Lund F (2004) Elastic wave propagation through a random array of dislocations. Phys Rev B 70:024303. <https://doi.org/10.1103/PhysRevB.70.024303>
17. Maurel A, Pagneux V, Barra F, Lund F (2005) Wave propagation through a random array of pinned dislocations: Velocity change and attenuation in a generalized Granato and Lücke theory. Phys Rev B 72:174111. <https://doi.org/10.1103/PhysRevB.72.174111>
18. Fang X.F. to be published
19. Boggs PT, Tolle JT (1995) Sequential quadratic programming. Acta Numer 4:1–51

A Novel Benchmark Test for Validating the Modelling and Simulation Methodology of Modern Gas-Based Hot Sheet Metal Forming Processes



Naveen Krishna Baru, Tobias Teeuwen, David Bailly, and Gerhard Hirt

Abstract New rapid gas-based hot sheet metal forming processes are being invented to manufacture geometrically complex automotive components from lightweight high-strength aluminum alloys. The complexity of the forming processes necessitates a computationally economic yet sufficiently accurate modelling and simulation methodology to ensure a successful simulation-aided process planning for manufacturing complex components. This includes accurate modelling of process characteristics such as large deformations, complex geometrical features, thermo-mechanical and tribological interactions. The current work aims to establish a finite element method (FEM) based simulation methodology for modern gas-based hot sheet metal forming processes. For this purpose, the conventional cross-die geometry is modified with features of some typical automotive components to establish a complex benchmark geometry that covers a broader spectrum of strain states and strain paths. Moreover, a laboratory-scale hot forming test setup for forming the complex benchmark specimen is realized and the preliminary experiments are conducted. The corresponding FE simulation models are developed and experimentally validated. The applicability of the developed benchmark for establishing and validating the models for complex gas-based hot forming processes is demonstrated.

Keywords Aluminum hot forming · Gas-based forming · Benchmark test · Finite element method · Simulation

N. K. Baru (✉) · T. Teeuwen · D. Bailly · G. Hirt
Institute of Metal Forming (IBF), RWTH Aachen University, Intzestraße 10, 52072 Aachen, Germany
e-mail: naveen.baru@ibf.rwth-aachen.de

T. Teeuwen
e-mail: tobias.teeuwen@ibf.rwth-aachen.de

D. Bailly
e-mail: david.bailly@ibf.rwth-aachen.de

G. Hirt
e-mail: gerhard.hirt@ibf.rwth-aachen.de

Introduction

Nowadays, automotive lightweight design is being done to overcome emission-related environmental pollution and fuel shortage. The potential of lightweight design is being fully exploited through invention of new materials and manufacturing processes. For automotive structural components, one proven approach is to replace steel with lightweight and high-strength aluminum alloys of 6xxx and 7xxx series. The formability of these alloys in terms of ductility and forming limits is significantly higher at elevated temperatures [1]. Even at elevated temperatures, the conventional punch-based deep-drawing processes are limited in terms of achievable part complexity. Therefore, similar to superplastic forming, gaseous medium is being used instead of a mechanical punch and new forming technologies are being developed. Some instances of modern gas-based forming are hot metal gas forming, hot die forming, etc. whereas hybrid processes such as high-speed blow forming involve a combination of deep-drawing and gas-based forming [2]. In these processes, higher part complexity can be achieved due to uniform load exerted by the active medium on the sheet in contrast to the punch in deep drawing [3]. Unlike low strain-rate superplastic forming processes that consume days to weeks, the modern gas-based forming processes are rapid with duration of seconds, which makes them attractive for mass production of automotive components.

Numerical simulations assist in investigating the process and understanding the influence of process parameters on component properties. In recent times, FEM can highly assist an industrial process design and optimization, provided that all the process aspects are thoroughly modelled. Even though sheet metal forming processes are often simulated isothermally, modern warm and hot forming processes involve transient thermal conditions and complex thermo-mechanical interactions, necessitating a coupled thermo-mechanical solver [4]. Another aspect that differentiates the gas-based forming processes from conventional processes is the large local deformation due to extreme stretching of the sheet as shown by Luo et al. [5]. In addition, the material behavior during hot forming is also quite complex since the lightweight aluminum alloys exhibit strain softening and strain-rate hardening at elevated temperature as shown in [6]. Due to these process complexities, selection of accurate, reliable, and robust FE modelling and simulation methods is a cumbersome process considering that the modern FE software packages offer numerous options for modelling each and every process aspect [7]. With help of a suitable benchmark test that generally represents the important process aspects, modelling, and simulation methods can be systematically developed and experimentally validated at laboratory scale before proceeding with the simulation of a complex industrial process [8]. The aim of the current study is to realize a benchmark test suitable for gas-based hot sheet metal forming processes, which assists in establishing and validating the modelling and simulation methods.

State of the Art

A typical sequence of simulation-aided process development starts with the material characterization followed by formability investigation, determination of friction and thermal coefficients under process conditions and finally their implementation into the forming process model, which is then simulated. Generally, the functional part to be formed is directly modelled and simulated and the models are further developed and calibrated via experiments. However, the suitability of the chosen modelling and simulation approach can be sometimes limited, as shown in terms of element types by [9]. The limitations can only be identified during the later experimentation stage. Sometimes, the uncertainty is ambiguous; e.g., incapability of the element type, insufficient representation of the boundary conditions, or material model [10]. Depending on the complexity of the process due to geometrical features or manufacturing route, identification and rectification of the limitation can be quite burdensome.

Benchmark Tests in Sheet Metal Forming

A benchmark test usually encompasses the features of the process and components intended to be manufactured via these processes. For instance, a cylindrical cup is used for studying cold and warm deep-drawing processes as it covers large deformations and exhibits signs of anisotropy in form of earing [11]. On the other hand, open forms such as hat-profile [12] and V-profile [13] are standard tests for predicting springback in stamping processes. The cross-die test covers wide spectrum of strain states and serves multiple purposes. This is used by Kumar et al. to determine the limiting drawing depth during warm forming of AW-7921 [14] and by D'Amours et al. to validate the material modeling method for hot stamping of AA7075 [15]. On the other hand, Venema et al. used a cross-die test for validation of friction model for hot stamping process [16]. For investigation of hot stamping processes, the B-Pillar demonstrator is often used. Even though an automotive B-Pillar is typically not made of aluminum alloys, it is widely used for formability investigations of different materials, for instance, 6xxx and 7xxx alloys in case of Liu et al. [17].

Gas-Based Hot Forming Processes

During gas-based hot forming of complex components, large deformation occurs at the sharp edges and small radii of the components due to sheet stretching. As confirmed by Luckey Jr. et al., element size plays a major role in predicting the sheet thickness at radii [18]. At sharp corners and small radii, sufficient element size must be ensured with help of techniques such as adaptive remeshing [19]. An important aspect is to accurately model the softening behavior of aluminum at hot

forming process temperatures as shown by Hong et al. with help of a miniature automobile component formed via hybrid gas-based forming [20]. Another aspect is the evolving strain dependent friction coefficient during aluminum gas-based superplastic forming as shown by Sorgente et al. [21]. This poses difficulties in calibration of the friction model when a complex component is directly dealt with. Apart from final components, some hybrid gas-based forming studies investigated demonstrator components, e.g. V-trough with wavy bottom [22]. Cheng et al. investigated gas-based hot forming of a tubular component covering complex geometrical scenarios [23]. Such a benchmark study is not yet performed for gas-based sheet metal forming.

Summary and Problem Statement

To summarize, benchmark tests serve as an effective and economic tool for development of modelling and simulation methods for complex processes. For modern non-conventional processes like gas-based forming, the fundamental studies generally used axisymmetric components and there is no well-known benchmark till date. Other investigations directly dealt with modelling and validation of the real component. However, having a fundamentally validated modelling and simulation methodology that represents the process characteristics sufficiently accurately is beneficial. The current study aims at development of a suitable benchmark test representing the features of gas-based forming processes.

Material Characterization

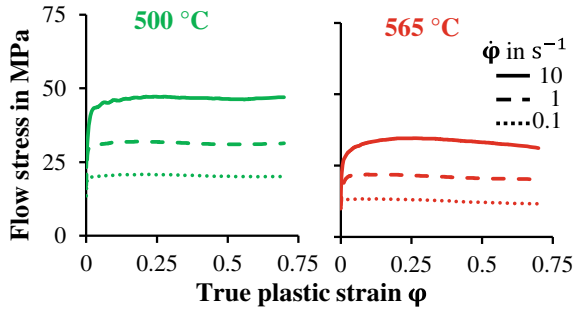
A heat treatable, precipitation hardening Al–Si–Mg aluminum alloy EN AW-6010, which can be used for automotive lightweight applications is investigated. Table 1 shows the chemical composition and the thermal properties of the alloy. The material is first solution heat-treated for 20 min at 565 °C and directly subjected to the forming process at the same temperature. The material characterization is also performed according to this process route followed by initial solution heat treatment for 20 min.

The flow curves of the alloy are determined via hot stacked layer compression tests. A complete lubrication at the specimen-tool interface is not favored due to the risk of specimen shearing, which means slight frictional influence is present on the

Table 1 Investigated alloy, its composition and properties [24]

Alloy	Major alloying elements					Processing temperature in °C		
	Si	Mg	Mn	Cu	Zn	Solution	Solidus	Liquidus
EN AW-6010	0.8–1.2	0.6–1.0	0.2–0.8	≤0.5	≤0.25	565	585	649

Fig. 1 Temperature and strain-rate dependent flow curves of solution heat-treated EN AW-6010 alloy



determined flow curves. However, an appropriate height to diameter ratio (1.5) is chosen for the specimen in order to keep the frictional influence to the minimum [25].

Even though the current hot forming process starts at the solution heat treatment temperature, the sheet might slightly cool down during the gas-based forming. Therefore, the characterization field is extended to temperatures below the solution heat treatment temperature. The flow curves of these alloys at different strain rates and temperatures after temperature compensation are shown in Fig. 1.

From Fig. 1, the flow curves show a noticeable temperature and strain-rate dependence. The material initially exhibits strain hardening and the flow stress remains almost constant as in ideal plastic behavior. At 565 °C, the material exhibits strain hardening followed by slight softening, especially at lower strain rates. A separate analysis of a 6xxx alloy via hot isothermal tensile tests revealed that the material exhibited negligible anisotropy after solution heat treatment. Therefore, anisotropy is neglected for time being.

Forming Process and Tool Setup

General Process Description

The sequence of the current gas-based hot forming process is schematically illustrated in the following Fig. 2. At the beginning of the process, the sheet metal blank is placed in between the die and blank holder. It is then heated-up via conduction until it reaches the process temperature and solutionized for a specific duration depending on the alloy composition. After that, the pressurized gas enters the forming chamber, deforms the blank, and simultaneously draws it into the die cavity as shown in the second step of Fig. 2. The drawing process nearly ends once the sheet touches the bottom of the die and the form-filling begins where the free zone of the sheet material locally stretches under the increasing gas-pressure and fills the die cavity completely. This phase can be termed as calibration. Finally, the fully formed component is

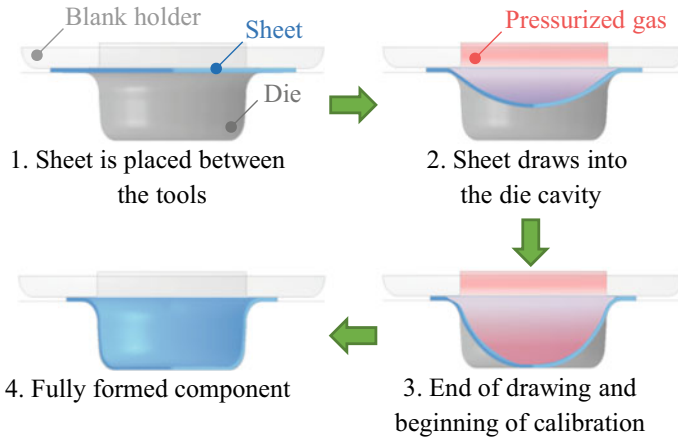


Fig. 2 Schematic illustration of gas-based hot forming of an axisymmetric component

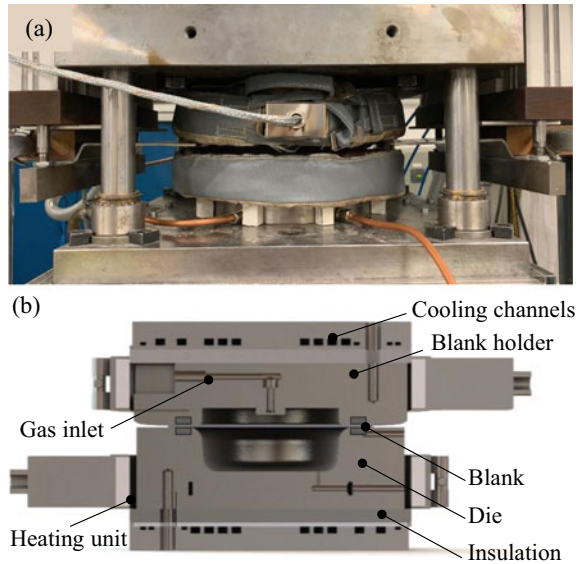
ejected and further heat treatment is performed according to the requirements. During the experiments, a suitable combination of blank holder force and gas-pressure profile is necessary to obtain components with good properties without failure.

Experimental Test Setup

The forming process is realized on a servohydraulic press that can incorporate two tool units, a force or displacement controlled translatable lower tool (die) and a fixed upper tool (blank holder) as shown in Fig. 3a. Moreover, the pressurized gaseous forming medium enters the forming chamber via an inlet provided through the blank holder. Within this study, to maintain nearly constant temperature of the sheet material during the forming process for enhanced formability, the tools are heated up to the process temperature. For this, the tools are equipped with circumferential heating collars, insulation plates, and cooling channels. The temperature of the tools is continuously measured by the embedded thermocouples and the heat supply is regulated using a PID temperature controller to maintain the system at required temperature.

The upper and lower tool units can be geometrically adapted for manufacturing various components. For instance, the tool setup for manufacturing an axisymmetric cup is depicted in Fig. 3b. This setup is used in the author's previous study [9] to investigate the suitability of different finite element discretization methods for modelling the gas-based hot sheet metal forming processes. Within the current study, different upper and lower tools are manufactured for forming a conventional cross-die specimen and a complex benchmark specimen.

Fig. 3 **a** Assembled tool setup and **b** cross-sectional view of setup for manufacturing an axisymmetric cup



Investigation With a Conventional Cross-Die Test

The goal of this preliminary investigation is to establish a FE model of the current gas-based hot forming processes with help of a well-known benchmark test and validate it. Therefore, the investigation started with a conventional cross-die, a typical benchmark test used for sheet metal drawing processes.

Cross-Die Test Conception, Specimen Design, and Experimentation

As a first step, a closed bottom cross-die specimen is designed based on the design of an existing miniature cross-die specimen that is used for studying the deep-drawing processes at the IBF. The depth is chosen to be similar to the length of the arm, i.e., 30 mm. Other dimensions of the cross-die are depicted in the following Fig. 4a, b. In order to facilitate the material draw-in, a suitable blank size and shape are necessary. Therefore, the size and shape of the blank is adjusted according to the geometry of the cross-die specimen. Initially an octagonal blank of suitable size is designed, and it is further slenderized and its corners are filleted until the blank in Fig. 4c is obtained so that it draws in uniformly from the flange region.

The experiments were performed on the cross-die test setup shown in Fig. 5a with the sheet metal blanks manufactured from 2 mm thick EN AW-6010 alloy via laser cutting. The blank and the tool surfaces are uniformly sprayed with Boron Nitride

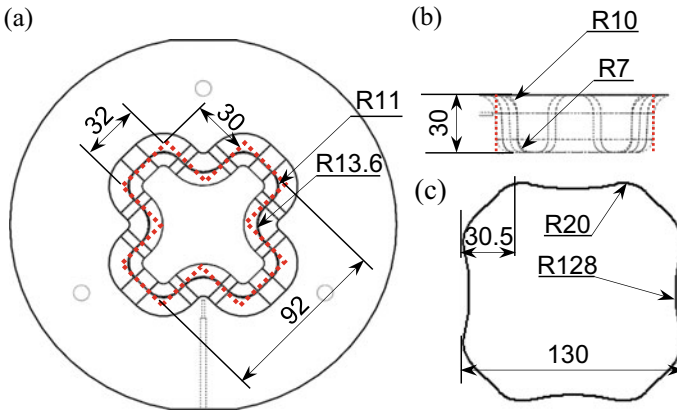


Fig. 4 a, b Dimensions of the cross-die and c blank geometry

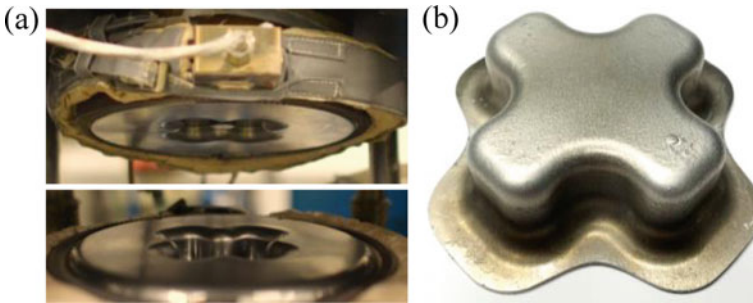


Fig. 5 a Experimental setup and b successfully formed cross-die specimen

lubricant. During the experiments, the gas-pressure is set to increase linearly at the rate of 5 MPa/s. The blank holder force is a critical parameter that influences the amount of material draw-in and the resulting component thinning. Based on previous experience from [9, 26], the blank holder force is set to be linearly varying during the gas-forming process. With help of trials with few failed components showing cracks or insufficient form-filling, the blank holder force varying from 10 to 70 kN resulted in components without failure. A cross-die specimen resulting from the experiments is shown in Fig. 5b.

FE Modelling of Cross-Die Test and Convergence Analysis

As shown in Fig. 6a, the model is setup in LS-PrePost-4.3 analog to the test setup with three parts: die, blank holder, and sheet metal blank. The tools are modelled as rigid bodies and the blank is modelled as an elastoplastic body. As

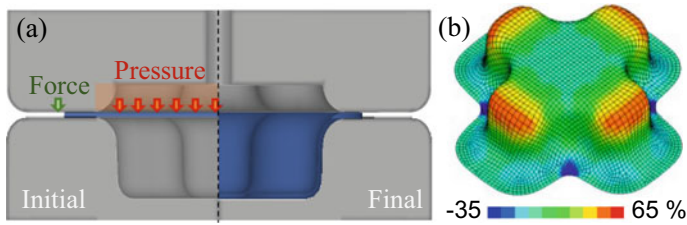


Fig. 6 a Model setup and b simulated cross-die showing the thinning distribution

discussed in the previous study [9] fully integrated shell elements of Type-16 with thick thermal shell formulation are suitable for modelling 2 mm thick sheets, and are eventually chosen for discretizing the blank. The blank holder force and gas-pressure are applied according to the experiments using the `Load_Rigid_Body` and `Load_Mask` on the blank holder and blank surface, respectively. The contact and interactions between the tools and the blank are modelled according to Coulomb friction model through `Contact_Forming_Surface_to_Surface`. The flow curves of blank material shown in Fig. 1 are modelled via 3D-Table option in the material card `Mat_Thermo_Elasto_Viscoplastic_Creep` considering only viscoplasticity and ignoring the creep effects. Moreover, the sheet cools down via forced convection due to gas flow, and this phenomenon is modelled using `Boundary_Convection_Set` option with a convection coefficient of $300 \text{ W/m}^2\text{K}$. The simulations are performed with a coupled thermo-mechanical explicit solver of LS-Dyna R12.0.0 with an automatic time-step increment.

Convergence and Friction Sensitivity Analysis

The convergence analysis showed that an element size of 2 mm with 9 thickness integration points for discretization of the blank gave converged results with a reasonable computational time. According to the datasheet given by the supplier, the friction coefficient of Boron Nitride is 0.17. Since this number is not experimentally confirmed yet, a simulative sensitivity analysis is performed by varying it within the range relevant for Boron Nitride application in hot forming processes, i.e., from 0.1 to 0.3. Results showed that with increasing friction, the draw-in decreased and the maximum sheet thinning increased. When the friction coefficient is varied from 0.17 within the mentioned range, the draw-in and thinning deviate by a maximum of 12% and 7% respectively. Therefore, for time being, the interactions are modelled with the friction coefficient of 0.17 as suggested by the material datasheet. A result of the simulation is shown in Fig. 6b.

Analysis and Validation of the Results

First of all, complete form-filling is ensured by analyzing the geometries of experimental components with help of 3D surface measurement device and comparison with target geometry. In this case, the pressure required for complete form-filling obtained from the simulations is around 9.5 MPa. The corresponding pressure during the experiments cannot be determined because the gas keeps on storming into the forming chamber according to the pre-set profile even after form-filling is complete. The sheet cools down by approximately 20 °C during the simulation. This still needs to be experimentally validated. For time being, the properties of the final component are used for validation of modelling simulation methods.

The resulting thinning distributions along the three characteristic symmetry lines of the cross-die specimen are extracted and comparatively shown in Fig. 7. In this, the dots represent the average thinning values measured from three experimental components with help of a screw-gauge whereas the line represents the simulated thinning. It can be seen that the results correspond to each other with an absolute deviation of less than 5%. The experimental draw-in values along lines 1 and 3 are 6 mm and 11.5 mm, respectively, which are slightly lower than the corresponding simulated draw-in of 6.2 and 13.7 mm. This is mainly due to the compressive deformation of the sheet in flange region and outward material flow from sheet thickness in the experiments, which cannot be modelled through Type-16 shell elements used in this study. The slight deviations in thinning distribution can be due to the unmeasured parameters such as friction coefficient or thermo-mechanical boundary conditions. In the future, the models can be further improved by determination and implementation of the unknown thermos-mechanical parameters as well as testing the other discretization options.

Development of a Complex Benchmark Test

After the initial investigation with cross-die, a more representative benchmark test applicable to gas-based hot forming processes is to be developed, which is also the main objective of this paper. For instance, the automobile body component produced

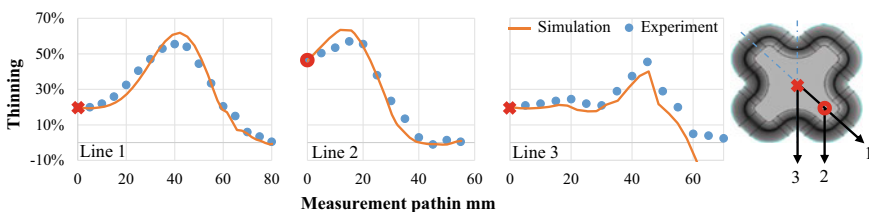


Fig. 7 Comparison of thinning from experiments and simulations along the symmetry lines

via high-speed blow forming [2] or the shock absorber housing produced by hybrid forming [20] show sharp edges and corners, stepped features, and local protrusions in the components which are not covered by the conventional cross-die. The idea behind the new benchmark is to come closer to components produced by modern hot forming processes in terms of their geometrical complexity, which also increases the deformation degree the material undergoes during forming. Another goal is to obtain a higher number of validation parameters for a robust validation of the modelling and simulation methods.

Conception of Benchmark Geometry and Experimentation

The new benchmark is conceived with four geometrically different arms, in contrast to the identical arms in the conventional cross-die. As shown in Fig. 8a, each of these arms has a geometrically different feature, Arm-1 similar to that of the cross-die but with a smaller corner radius, a ramp in Arm-2 down to the bottom of the die, an inbuilt step within Arm-3, and finally a protruded rib in Arm-4. The overall contour indicated by red dotted line in Fig. 8a and the general dimensions such as the arm length, width, and die depth are retained as in the cross-die. The major dimensions of the characteristic features of the four arms are shown in Fig. 8b.

The new benchmark die is manufactured and the tool setup is updated with it as shown in Fig. 9a. For better comparative analysis, same blank geometry as in previous case is used. The experiments are performed on the benchmark test setup under similar experimental conditions as in the previous case. The experimental boundary conditions are retained as in the cross-die test except for higher calibration pressure in the final forming stage to achieve complete form-filling. The formed cross-die specimen is shown in Fig. 9b.

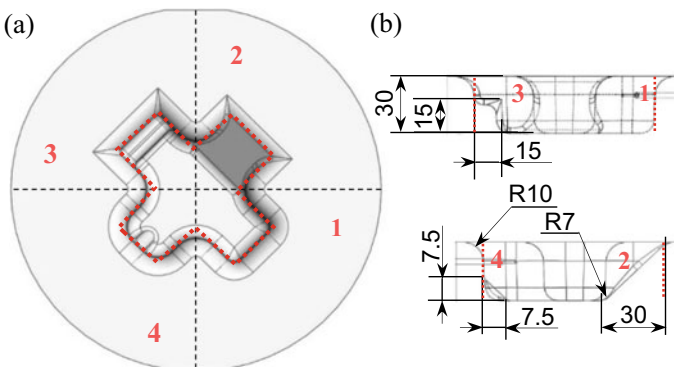


Fig. 8 a Concept and b dimensions of the new benchmark die

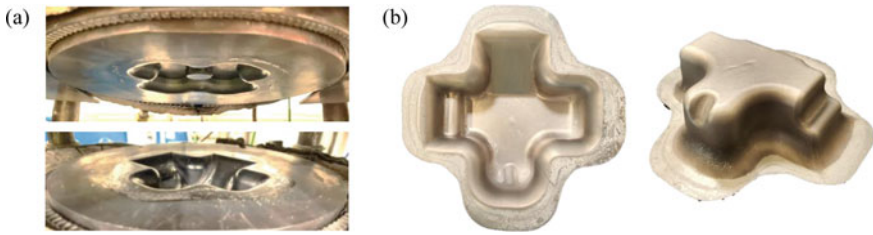


Fig. 9 a Experimental setup and b formed benchmark specimen

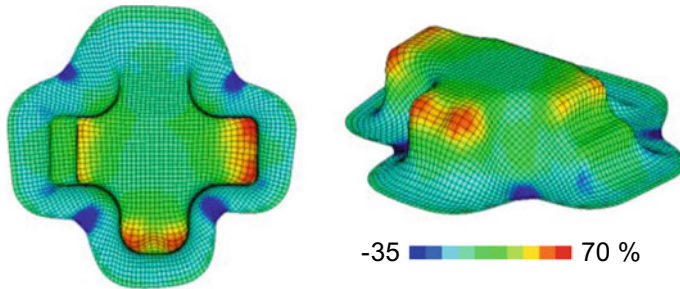


Fig. 10 Simulated benchmark showing the sheet thinning distribution

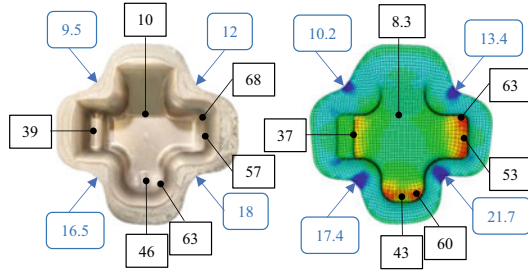
FE Modelling of Benchmark Test

The die in the cross-die model is replaced with the benchmark die. The blank holder force and gas-pressure are applied according to the experiment. All the other aspects such as the material models, thermal, and contact boundary conditions are retained as in the previous cross-die test. The discretization of the blank is optimized, where the mesh orientation is adjusted so that a better form-filling for complex geometrical features in the Arm-3 and Arm-4 is obtained. Moreover, the previous element size of 2 mm is not sufficient and hence 1.5 mm is chosen for meshing the blank to obtain a converged and reliable result within reasonable simulation time. The simulation result is shown in Fig. 10.

Analysis of the Results

Upon analyzing the resulting components from the experiments, it is observed that the components exhibited complete form-filling. From the simulations, the pressure required for complete form-filling is above 15 MPa, which is significantly higher than that of conventional cross-die specimen. Since the current geometry has several characteristic features, for time being, the thinning at characteristic regions of each

Fig. 11 The resulting thinning in % (indicated by black dots) and draw-in in mm (indicated by blue arrows) at some characteristic points of the benchmark



arm are measured and plotted in Fig. 11. The sheet draw-in is also measured and shown with help of arrows in Fig. 11.

A comparison of the results shows that the local thinning and draw-in at each arm are quite different. The maximum thinning occurs in Arm-1, the one similar to that of the conventional cross-die, but with a smaller corner radius. Also, in this case, the results show slight deviations between simulations and experiments. This can be due to the unmeasured parameters such as friction coefficient, which can be more complex due to higher geometrical complexity and surface enlargement. Other than that, the accuracy of modelling the thermal boundary conditions can be an influencing factor. The draw-in values show a similar trend as in the previous case, due to the compressive stresses and outward material flow in experiments. Apart from implementation of unknown thermo-mechanical parameters, adaptive remeshing options can be explored to further improve the models of the benchmark test.

Comparative Analysis of Cross-Die and Benchmark Tests

In order to understand the advantages of the new benchmark test, a comparative analysis is performed with the same blank shape, similar boundary conditions, and process parameters. The foremost aspect is the high degree of deformation of the sheet. The maximum sheet thinning in the cross-die specimen is about 63% whereas in benchmark specimen, it is 67%. This shows that the deformation degree in benchmark specimen is slightly higher than that of the cross-die specimen. Following this, the major and minor strains are extracted from the simulations and the results are plotted in Fig. 12.

Upon comparing the simulated strain states followed by the cross-die specimen with those of the benchmark specimen, it is clear that the new benchmark geometry exhibited wider spectrum of strain states compared to the conventional cross-die specimen. Within the benchmark specimen, due to high local strains under biaxial stretching, the surface enlargement is also higher, which can be seen in terms of increased size on the right-side of the strain-state diagram. This might offer higher potential for calibrating and validating the evolving strain dependent friction models

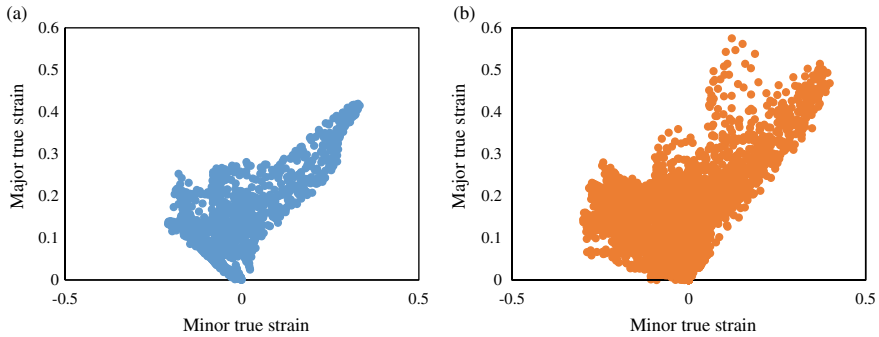


Fig. 12 Strain states of **a** cross-die and **b** benchmark specimen under current boundary conditions

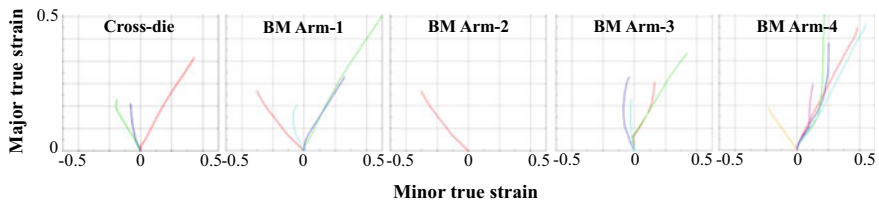


Fig. 13 Strain paths covered by the cross-die and each arm of the benchmark specimen under present conditions

for the aluminum hot forming processes. In the future, these simulated major and minor strains can be validated by experimental strain measurements with help of an optical measurement system.

As a next step, the strain paths of some elements showing the highest strains (the extremities in Fig. 12) are extracted and plotted in Fig. 13. The cross-die specimen shows simple and slightly non-linear strain paths covering most of the diagram. The benchmark specimen, especially Arm-3 and Arm-4, exhibits non-linear strain paths with complex transitions from biaxial to plane-strain, which can potentially influence the local formability and forming limits of the material. Therefore, the benchmark can be used for validation of complex strain paths and strain path transitions, and non-linear forming limits of the material.

Apart from the above analysis, parameter studies and further experiments (out of the scope of this paper) revealed that the new benchmark geometry is more sensitive to the loads and boundary conditions compared to the cross-die specimen. The process parameter window of a successfully formed benchmark specimen without failure is quite small. Moreover, it offers a higher validation potential with several thinning and draw-in zones. Similar to the punch force curve in deep-drawing processes, the forming load, i.e., the gas-pressure curve can be used as a validation parameter by analyzing the form-filling. In cross-die the corner radius is 7 mm in all arms whereas

the radii within the benchmark vary from 3 mm to 7 mm, which help in validating the material flow stress.

Conclusion and Outlook

In this study, laboratory-scale cross-die and benchmark tests are realized for establishing and validating the modelling and simulation methods of gas-based hot sheet metal forming processes. Based on these two components, the FE modelling methodology is established and comparatively evaluated for EN AW-6010 aluminum alloy. The following conclusions can be drawn:

- The benchmark test represents the complex geometrical scenarios as in gas-based hot forming processes and offers more validation parameters.
- The benchmark test shows higher deformation degree and covers a broader spectrum of strain states and complex strain path transitions compared to the cross-die specimen. This helps in robust validation of the forming limits compared to the cross-die specimen.
- The benchmark geometry also offers higher potential for validation of the process aspects such as evolving surface enlargement dependent friction under gas-based hot forming process conditions.

The proposed cross-die and benchmark tests can be used for selection of the process-modelling methodology for gas-based warm and hot forming processes. In the future, these tests will be used for validating the material models, forming limits as well as robust investigation of modelling and simulation methods for 6xxx and 7xxx alloys.

Acknowledgements The authors would like to thank Speira Research & Development, Bonn (previously Hydro Aluminium Rolled Products) for providing the aluminum sheets.

Conflict of Interest The authors declare that there is no conflict of interest.

References

1. Neugebauer R, Altan T, Geiger M et al (2006) Sheet metal forming at elevated temperatures. *CIRP Ann* 55(2):793–816. <https://doi.org/10.1016/j.cirp.2006.10.008>
2. Majidi O, Jahazi M, Bombardier N (2018) Finite element simulation of high-speed blow forming of an automotive component. *Metals* 8(11):901. <https://doi.org/10.3390/met8110901>
3. Bell C, Corney J, Zuelli N et al (2020) A state of the art review of hydroforming technology. *Int J Mater Form* 13:789–828. <https://doi.org/10.1007/s12289-019-01507-1>
4. Bach M, Degenkolb L, Reuther F et al (2020) Conductive heating during press hardening by hot metal gas forming for curved complex part geometries. *Metals* 10(8):1104. <https://doi.org/10.3390/met10081104>

5. Luo Y, Luckey SG, Friedman PA, Peng Y (2008) Development of an advanced superplastic forming process utilizing a mechanical pre-forming operation. *Int J Machine Tools Manuf* 48(12–13):1509–1518. <https://doi.org/10.1016/j.ijmachtools.2007.12.010>
6. Bobbili R, Madhu V, Gogia AK (2016) Tensile behaviour of aluminium 7017 alloy at various temperatures and strain rates. *J Mater Res Technol* 5(2):190–197. <https://doi.org/10.1016/j.jmrt.2015.12.002>
7. Pimentel AMF, de Carvalho Martins Alves JL, de Seabra Merendeiro NM et al (2018) Comprehensive benchmark study of commercial sheet metal forming simulation softwares used in the automotive industry. *Int J Mater Form* 11:879–899. <https://doi.org/10.1007/s12289-018-1397-4>
8. Santos AD, Reis A, Duarte JF et al (2004) A benchmark for validation of numerical results in sheet metal forming. *J Mater Process Technol* 155–156:1980–1985. <https://doi.org/10.1016/j.jmatprotec.2004.04.290>
9. Baru NK, Teeuwen T, Teller M et al (2021) On appropriate finite element discretization in simulation of gas-based hot sheet metal forming processes. *IOP Conf Ser Mater Sci Eng* 1157:012027. <https://doi.org/10.1088/1757-899X/1157/1/012027>
10. Lafon P, Adragna PA, Nguyen VD (2016) Multi-objective optimization under uncertainty for sheet metal forming. *MATEC Web Conf* 80:10004. <https://doi.org/10.1051/mateconf/20168010004>
11. Noder J, Abedini A, Rahmaan T et al (2018) An experimental and numerical investigation of non-isothermal cup drawing of a 7XXX-T76 aluminum alloy sheet. *IOP Conf Ser Mater Sci Eng* 418:012019. <https://doi.org/10.1088/1757-899X/418/1/012019>
12. Maeno T, Mori K, Yachi R (2017) Hot stamping of high-strength aluminium alloy aircraft parts using quick heating. *CIRP Ann* 66(1):269–272. <https://doi.org/10.1016/j.cirp.2017.04.117>
13. Zhou J, Yang X, Wang B et al (2022) Springback prediction of 7075 aluminum alloy V-shaped parts in cold and hot stamping. *Int J Adv Manuf Technol* 119:203–216. <https://doi.org/10.1007/s00170-021-08204-x>
14. Kumar M, Ross NG (2016) Influence of temper on the performance of a high-strength Al–Zn–Mg alloy sheet in the warm forming processing chain. *J Mater Process Technol* 231:189–198. <https://doi.org/10.1016/j.jmatprotec.2015.12.026>
15. D'Amours G, Ilinich A (2018) Development of a material model for AA7075 aluminium hot stamping. *J Phys Conf Ser* 1063. <https://doi.org/10.1088/1742-6596/1063/1/012033>
16. Venema J, Atzema E, Hazrati J et al (2020) Modelling of friction in hot stamping. *Procedia Manuf* 47:596–601. <https://doi.org/10.1016/j.promfg.2020.04.184>
17. Liu Y, Zhu Z, Wang Z et al (2017) Formability and lubrication of a B-pillar in hot stamping with 6061 and 7075 aluminum alloy sheets. *Procedia Eng* 207:723–728. <https://doi.org/10.1016/j.proeng.2017.10.819>
18. Luckey SG, Friedman PA, Weinmann KJ (2007) Correlation of finite element analysis to superplastic forming experiments. *J Mater Process Technol* 194(1–3):30–37. <https://doi.org/10.1016/j.jmatprotec.2007.03.122>
19. Gedikli H, Cora ÖN, Koç M (2011) Comparative investigations on numerical modeling for warm hydroforming of AA5754-O aluminum sheet alloy. *Mater Des* 32(5):2650–2662
20. Hong JH, Kim H, Kim W et al (2021) Failure with strain localization of aluminum alloy 7075 sheets at elevated temperature and its application to two-step hybrid forming. *Metals Mater Int* 28:871–886. <https://doi.org/10.1007/s12540-020-00949-6>
21. Sorgente D, Lombardi A, Coviello D et al (2022) A strain-dependent model for the coefficient of friction in the tool-blank interaction in superplastic forming. *J Manuf Process* 73:791–798. <https://doi.org/10.1016/j.jmapro.2021.11.050>
22. Lee S, Tang JS, Chu CL (2016) Prior sheet buckling leading to wrinkling formation in a gas forming a V-trough with wavy bottom. *J Manuf Process* 21:101–106. <https://doi.org/10.1016/j.jmapro.2015.12.001>
23. Cheng P, Ge Y, Xia Y, Zhou Q (2018) Numerical and experimental investigation on tube hot gas forming process for UHSS. *J Phys Conf Ser* 1063:01217. <https://doi.org/10.1088/1742-6596/1063/1/012172>

24. Boyer HE, Gall TL (1985) Metals handbook. American Society for Metals, Materials Park, OH
25. Bernrath G, Volles R, Kopp R (2006) Multi-layer compression tests under hot forming conditions. *Steel Res Int* 77(4):265–270. <https://doi.org/10.1002/srin.200606384>
26. Teeuwen T, Baru NK, Tilly KJ et al (2022) Development of a high-temperature double-layer bulge test for failure prediction in gas-based hot forming of a high-strength aluminium alloy. Paper presented at the 41st IDDRG Conference, Lorient, France, 06–10 June 2022

Analysis on Deformation Behavior of High-Strength Steel Using the Finite Element Method in Conjunction with Constitutive Model Considering the Elongation at Yield Point



S. C. Yoon, K. J. Kim, G. H. Yim, J. S. Hyun, and Y. D. Chung

Abstract Tensile tests are widely used for estimating mechanical properties of materials including flow curves as well as Young's modulus, yield strength, tensile strength, and yield point elongation. This paper aims at analyzing the plastic flow behavior of high-strength steels for automotive bodies using the finite element method in conjunction with the viscoplastic model considering the yield point elongation phenomenon. The plastic flow behavior of the high-strength steel was successfully predicted, by considering an operating deformation mechanism, in terms of normalized dislocation density, strain hardening, and accumulative damage of high-strength steel using the modified constitutive model. In addition, the finite element method is employed to track the properties of the high-strength steel pertaining to the deformation histories in a skin pass mill process.

Keywords High strength steel · Mechanical properties · Yield point elongation · Constitutive model · Finite element method

Introduction

Recently, the issues regarding the future environment are becoming a global interest, and many studies are being conducted to cope with these future environmental chal-

S. C. Yoon (✉) · K. J. Kim · G. H. Yim · J. S. Hyun · Y. D. Chung
Hyundai Steel Company, Dangjin-Si, Korea
e-mail: scyoon@hyundai-steel.com

K. J. Kim
e-mail: kijungkim@hyundai-steel.com

G. H. Yim
e-mail: gyim88@hyundai-steel.com

J. S. Hyun
e-mail: hjs401@hyundai-steel.com

Y. D. Chung
e-mail: ydchung@hyundai-steel.com

lenges. In the automotive industry, the substitution of high-strength lightweight materials from existing materials is increasing for the main automotive parts to improve fuel efficiency and reduce carbon dioxide emissions. In order to maximize the vehicle weight reduction, many research teams are examining the technical issues regarding Advanced High-Strength Steel (AHSS) [1–6]. In the case of high-strength steel for lightweighting, the material's performance is highly dependent on the strain path because of the large difference in effective stress generated according to the degree of work hardening. In the case of a metal material, in general, the increase and decrease of dislocation propagation is determined according to the average glide distance, and as a result, microscopic structure and grains appearing inside the material may vary. These small differences can provide inaccurate information about the physical behavior of high-strength steel materials, which can make it difficult to accurately predict the enhancement of material performance and satisfaction of safety regulation under different strain path conditions. As such, prior studies must be carried out to accurately predict them simultaneously [7–14].

Since the physical property and behavior of steel materials are highly dependent on the strain path change of the material, many research groups have recently proposed constitutive models for implementing the material's microstructure regarding the strain path change [15–20]. Although progress is being made, effective solutions for preventing yield point elongation in steel are still unclear, hindering accurate prediction. Thus, research attempts for more accurate prediction are still ongoing [19–28]. The purpose of this study is to investigate the plastic deformation characteristics based on the constitutive model considering the yield point elongation, deformation characteristics, and the effect of strain path change for high-strength steel.

Constitutive Model and Finite Element Analysis

In this study, viscoplastic model was used to implement the deformation behavior of steel according to the grain size and microstructure. Additionally, the proposed model can evaluate plastic deformation in consideration of the effect of the microstructural factors such as solute atom effect, grain size, and alloying. Since the classical plasticity theory is independent of strain rate, the time-dependent deformation is introduced through the classical creep model, but in the classical theory, plasticity and creep are mutually independent [15–18]. Therefore, the viscoplastic model was used in this study in an attempt to eliminate this distinction between plasticity and creep, and this integrated theory allows rather convenient analysis because elastic and inelastic deformation exists at all loading stages.

In this study, the total strain rate was separated into elastic and inelastic components in order to describe the overall mechanical behavior. Hook's law was used to describe the elastic components as time derivatives, and Prandtl–Reuss flow rule was used to describe the inelastic components. In addition, the yield point elongation section was inserted for these components to implement the yield point elongation. Above all, yield point elongation is observed generally when immobile dislocations are generated by the diffusion of carbon or nitrogen atoms towards the surplus sur-

face of the edge dislocation with lowest energy. The dislocation line energy can be represented as shown in Eq. (1).

$$\sigma_{yp} = \frac{4Ga^3\varepsilon}{br_c^2} \tag{1}$$

where a is the Shear modulus, b is the Burgers vector, and $r_c \approx 2 \times 10^{-10}$ m is the distance from the center of the potential dislocation to the solidification atomic line. The lattice deformation around the point defect shows an approximate spherical shape and its radius is marked a . In addition, the elongation of yield points and stress generated was faster as strain rate increased. In this study, limited values based on the experiment were used for yield point elongation, and the effect of grain size on the yield point elongation will be implemented as a function in the future work. Also, the stress generated at deformation was correlated with the work hardening of the material through normalization of the dislocation density, allowing the combination of escape energy of dislocation with the initial stress of the integrated viscoplastic model. Based on this model, it was possible to determine the stress of the materials by using the initial stress as a material variable.

For monotonic uniaxial loading, it suffices to use the simplest version of the unified theory. The total strain rate is assumed to be separable into plastic and inelastic (plastic) components. The elastic component is given by the times derivative of Hooke’s law while the Prandtl–Reuss flow law is applied to the inelastic strain components (see below). In the unified constitutive model with one internal variable, the equivalent (von Mises) plastic strain rate associated with the unified constitutive model of a crystallite $\dot{\varepsilon}^*$ is related to the equivalent stress, σ_0 through a power-law [15–18].

$$\dot{\varepsilon}^p = \dot{\varepsilon}_* (\sigma/\sigma_0)^m Z^{-m/2} \tag{2}$$

Here Z is the dislocation density normalized by its initial value. The quantity σ_0 is related to the initial dislocation density. The parameter $\dot{\varepsilon}^*$ is a constant normalization factor with units of strain rate. The evolution of the dislocation density with the equivalent (von Mises) plastic strain ε^p is described by

$$\frac{dZ}{d\varepsilon^p} = C + C_1\sqrt{Z} - C_2Z \tag{3}$$

where

$$C_2 = C_{20} \left(\frac{\dot{\varepsilon}^p}{\dot{\varepsilon}_0} \right)^{-1/n} \tag{4}$$

Equations (1)±(4) provide a complete constitutive description for the strain hardening of the crystallite. For steel metals at low temperatures (below half of the melting temperature, say), the parameters $C_1, C_{20}, \sigma_0, \dot{\varepsilon}_*, \varepsilon_0, m, n$ can all be considered constant. The exponent’s m and n are inversely proportional to the absolute temperature T and can be considered constant for a given temperature. It should be noted that the first two terms in the parentheses are strain hardening terms and C_2Z is a recovery term, as suggested by its negative sign. In the present context, it is interesting to

note that the term C is inversely proportional to the grain size (Eq. 4) [15–18]. The viscoplastic model defined in this way implies that the crystallites are plastically isotropic. The C_1 , C_{20} , σ_0 , ε_* , ε_0 , m , and n can be obtained from deformation data for bulk reference material by means of the evolution strategy-based parameter evaluation technique. Here m and n can be regarded as functions of absolute temperature T but it was constant at room temperature. More specifically C was taken to be inversely proportional to the grain size, implying that the dislocation mean free path is determined by the grain size [15–18].

$$C = M \frac{b}{d} \left(\frac{M \alpha G}{\sigma_0} \right)^2 \quad (5)$$

Here b is the magnitude of the dislocation Burgers vector, G is the Shear modulus, M is the Taylor factor, d is dislocation mean free path, and α is a numerical constant. Based on the abode constitutive model, there were separated the three type models for most optimization. (Model 1 on removing the yield point elongation section, model 2 on involving the yield point elongation section, model 3 for modified component model considering the yield point elongation interval.)

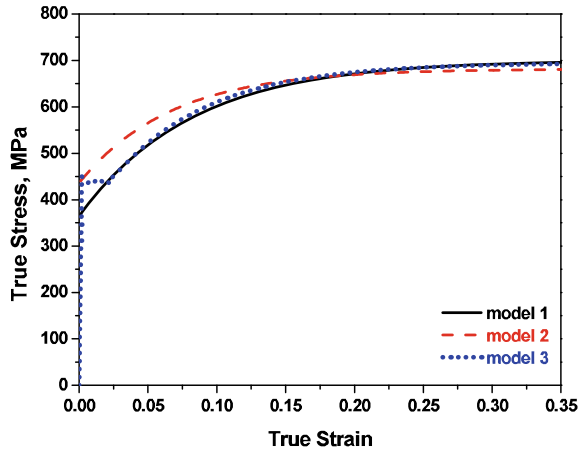
On the other hand, strain behavior was implemented using user subroutine for model 3 with modified configuration model considering yield point elongation interval for the finite element method. At first, the finite element analysis of the tensile test was performed to predict the validity of model 3 at strainrate $1 \times 10^{-3} \text{ s}^{-1}$ and applied 3,000 elements. To save time for the finite element analysis, a computed deformation area was established considering symmetry, and for the initial potential dislocation density, it was required to be randomly distributed to elements within a minimum range of deviations based on the initial values, in order to it does not affect overall deformation. Also, to remove elongation sections of yield points from steel, an approximate 2% Skin Pass Mill (SPM) process is added to minimize surface defects. For the implementation and interpretation of this additional skin pass rolled process, the deformation behavior pass is considered using a finite element analysis in conjunction with the model 3 constitutive model. In this study, the purpose of this research was to be implemented using 590 MPa grade steel (precipitation hardening type), which is applied to automotive steel sheet.

Results and Conclusion

Evaluation of Deformation Behavior Through Numerical Analysis

Figure 1 shows the uniaxial tensile behavior for each of the models 1, 2, and 3 described above. Each model shows a similar behavior to the automotive steel sheet 590 MPa grade material. Based on this model variable relationship, Fig. 1 shows all the stress curves generated by all models. Here, it can be seen that model 1 and model

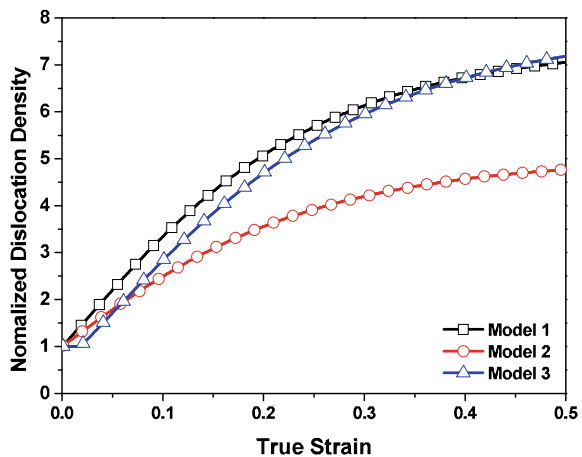
Fig. 1 Comparison of each model through the theoretical strain–stress curves



3 have similar work hardening rates, and model 2 and model 3 have similar initial stress values. When the steel material with yield point elongation undergoes a large deformation process, there was no significant difference from the actual behavior when model 1 was used, but the initial micro-deformation was different. On the contrary, model 2 showed no significant difference in terms of micro-deformation, but the deformation behavior differs as the effective deformation increases.

Therefore, it is evident that the model 3, presented in this study, is effective in explaining the actual material deformation of steel with yield point elongation. Figure 2 shows the normalized dislocation densities obtained from the material variables used in this study and it can be observed that the dislocation density increase ratio is different for each model. As mentioned above, in the case of model 3, the stress of the material at the yield point elongation section does not reach the initial

Fig. 2 Normalization dislocation density curves as a function true strain through the theoretical each model



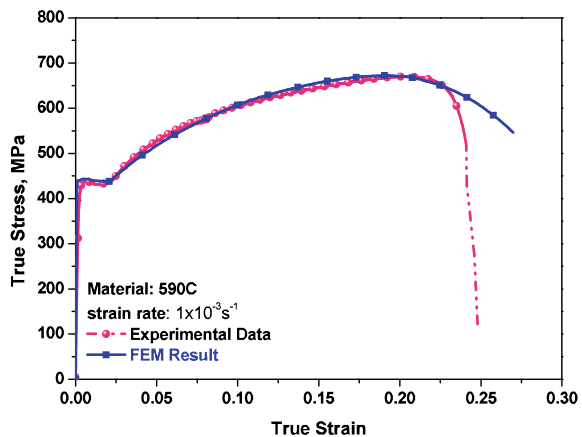
stress that considers material's dislocation escape and the set value for the yield point elongation section, thereby delaying dislocation interaction. It can be concluded that dislocation density increase ratio that influences microstructure and the grain size of the material has a strong impact on the material properties [13, 14, 28].

Evaluation of Deformation Behavior by Using Finite Element Analysis

Based on the numerical analysis mentioned above, model 3, which is similar to the actual deformation behavior, was implemented through using DEFORM, a commercial finite element code. The stress–strain curves from finite element analysis and actual test are shown in Fig. 3. As shown in Fig. 3, the results from model 3, which was obtained through finite element analysis, show that the deformation behavior is almost identical to the 590 MPa grade steel sheet. Figure 4 shows the results of the effective strain distribution for the tensile deformation through finite element analysis, showing the nominal stress–strain curve and the strain distribution during the entire tensile test.

In the case of high-strength steel, since the resistance to external deformation is relatively large, it can be seen that the increase in the effective strain in the uniform deformation region is small. Where (1) is the initial state, (2) the yield point elongation section, (3) the yield point elongation end point, (4) uniform elongation section, (5) maximum stress point, (6) local elongation section, and finally (7) is the final fracture section (the point at which the necking cross section corresponds to about 40 % of the initial cross-sectional area). The macroscopic phenomenon is similar to that of other materials. Effective strain rate distribution at the yield point elongation section of the 590 MPa grade material was divided into (8) ~ (14).

Fig. 3 Experiment and FEM data regarding the strain–stress curves by the model 3



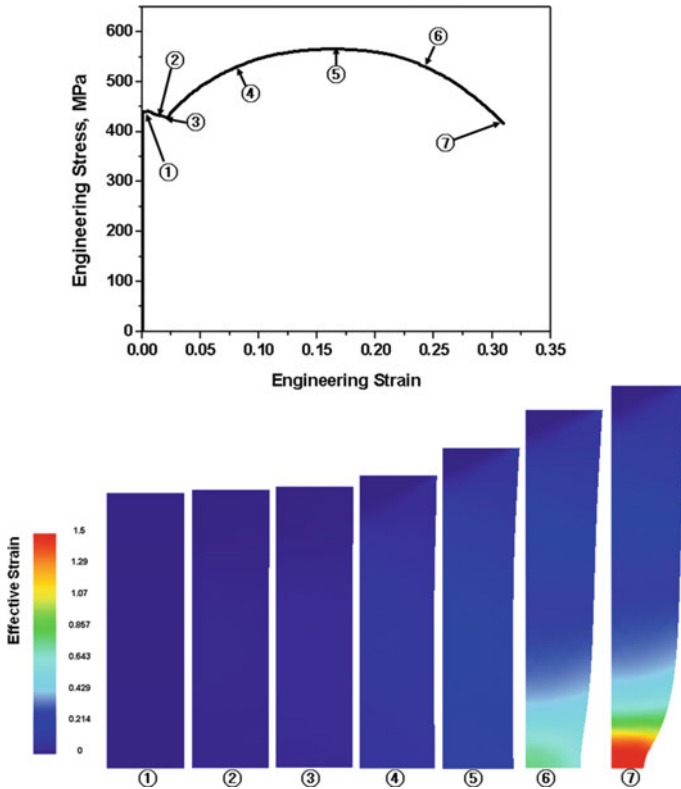


Fig. 4 Effective strain distribution during tensile test using the finite element method at each step with engineering stress–strain curve of 590 MPa

In Fig. 5, it can be seen that the effective strain rate occurs between the grip and the center of the specimen at the effective strain yield point elongation section and spreads to the center of the specimen. The deformation behavior of the yield point elongation section is observed to be very similar to that of stretcher strain. Meanwhile, skin pass mill, a process for preventing surface defects that may occur during sheet forming, is used to eliminate the stretcher strain generated in high-strength steel. As seen in Fig. 6, skin pass mill process was carried out by using the proposed model 3 in this study. A reduction ratio of about 2% was applied and the rolling was performed at a constant speed. The friction coefficient used was about 0.3, and the finite element method was performed only for the upper skin pass mill section, which is the 1/2 symmetric model for the whole process. The effective strain distribution range after temper rolling process was about 0.03 ~ 0.06 for 590 MPa grade material. In addition, in order to confirm the effect of the skin pass mill process, Fig. 7 shows the physical properties of the 590 MPa material in the 0° direction before and after skin pass mill process.

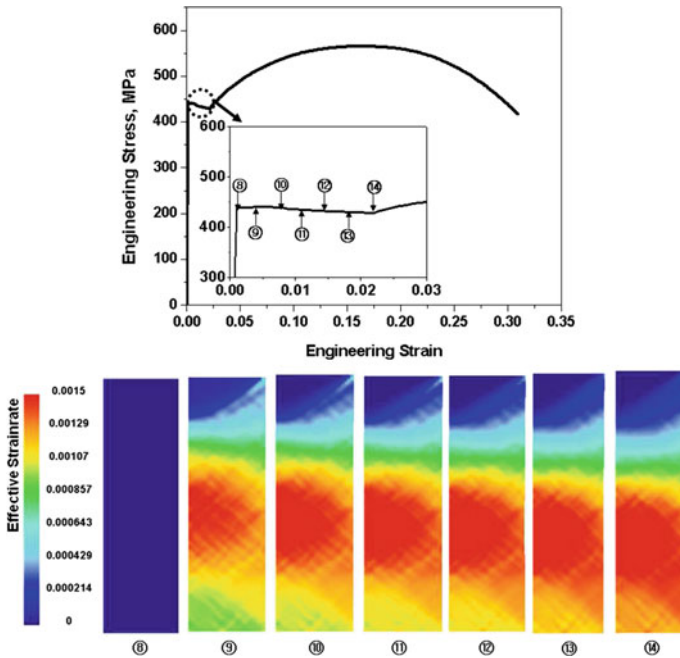
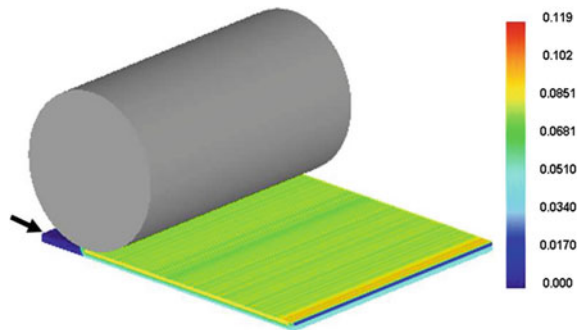


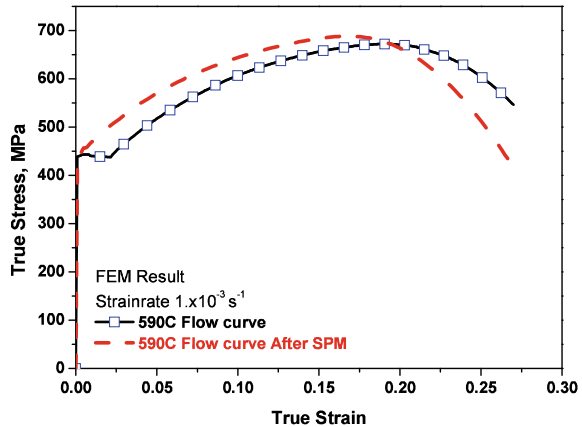
Fig. 5 Effective strain rate distribution during tensile test by the finite element method at yield point elongation range

Fig. 6 Effective strain distribution during skin pass mill process by the finite element method



It can be seen that the yield point elongation section disappears by skin pass mill process done for the removal of the stretcher strain. Therefore, it is possible to conclude that the simulation proposed model can not only derive accurate simulation results for the tensile behavior of high-strength steel, but also reasonable prediction about material deformation and performance after skin pass mill.

Fig. 7 The flow curves of finite element method result by the skin pass mill process for removing the yield point elongation



Conclusion

In this study, finite element analysis for the deformation behavior and skin pass mill of high-strength steel was carried out through the modified constitutive model considering yield point elongation in steel materials.

- (1) It is evident that the deformation behavior of high-strength steel can be more accurately predicted through the constitutive model considering the yield point elongation. Through each model, significant difference was confirmed for whether the yield point elongation was considered or not for the stress and normalized dislocation density. In addition, the finite element analysis was able to evaluate the geometrical characteristics for the deformation behavior of steel materials by using the different material value obtained from each model.
- (2) The finite element analysis was done through model 3, which considers the yield point elongation, to simulate skin pass mill that is used to eliminate the stretcher strain formed by the deformation behavior of 590 MPa grade material. The elimination of the yield point elongation section in the high-strength steel after the process by using model 3 was confirmed. It can be concluded that the model 3, presented in this study, is more effective in predicting the actual material deformation behavior of high-strength steel than the existing constitutive models.

References

1. Khalid FA (2002) Mater Sci Eng A 325:281
2. Bayraktar E, Isac N, Arnold G (2005) J Mater Pro Tech 162–163:471
3. Bouaziz O, Guelton N (2001) Mater Sci Eng A 391:246
4. Vercammen S, Blanpain B, De Cooman BC, Wollants P (2004) Acta Mater 52:2005
5. Yoo JD, Hwang SW, Park KT (2009) Mater Sci Eng A 508:234

6. Hamada AS, Karjalainen LP, Somani MC (2007) *Mater Sci Eng A* 467:114
7. Miller WS, Zhuang L, Bottema J, Wittebrood AJ, De Smet P, Haszler A, Vieregge A (2000) *Mater Sci Eng A* 280:37
8. Stearns J, Srivatsan TS, Prakash A, Lam PC (2004) *Mater Sci Eng A* 366:262
9. Mendoza R, Alanis M, Alvarez-Fregoso O, Juarez-Islas JA (2000) *Scr Mater* 43:771
10. Choi ID, Kim DM, Bruce DM, Matlock DK, Speer JG, Park SH (2005) *J Kor Inst Met Mater* 43:263
11. Berbenni S, Favier V, Lemoine X, Berveiller M (2004) *Scr Mater* 51:303
12. De AK, Vandeputte S, De Cooman BC (1999) *Scr Mater* 41:831
13. Yoon SC, Seo MH, Kim HS (2006) *Scr Mater* 55:159
14. Baik SC, Estrin Y, Kim HS, Hellmig RJ (2003) *Mater Sci Eng A* 351:86
15. Estrin Y, Mecking H (1984) *Acta Metall* 32:57
16. Follansbee PS, Kock UF (1988) *Acta Metall* 36:81
17. Baik SC, Estrin Y, Kim HS, Hellmig R, Jeong H-T (2002) *Mater Sci Forum* 408–412:697
18. Baik SC, Estrin Y, Hellmig RJ, Jeong HT, Brokmeier H-G, Kim HS (2003) *Zeit Metallkd* 94:1189
19. Usnishi A, Teodosiu C (2004) *Int J Plast* 20:915
20. Kim HS, Suryanarayana C, Kim S-J, Chun BS (1998) *Powder Metall* 41:217
21. Kim YM, Kim SK, Kim YJ, Kim NJ (2002) *ISIJ Int* 42:1571
22. Kato B (1990) *ISIJ Int* 30:1003
23. Kim YM, Kim SK, Kim NJ (2005) *Mater Sci Forum* 475–479:289
24. Kim NJ, Thomas G (1985) *Mater Sci Tech* 1:32
25. Umemoto M, Liu ZG, Sugimoto S, Tsuchiya K (2000) *Metall Trans A* 31:1785
26. Kim SK, Kim YM, Lim YJ, Kim NJ (2006) *Metal Mater Int* 12:131
27. Goel NC, Chakravarty JP, Tangri K (1987) *Metall Trans A* 18A:5
28. Kim HS, Kim SH, Ryu WS (2005) *Mater Trans* 46:2159

Automatic Extraction and Conversion of the Bending Line from Parametric and Discrete Data for the Free-Form Bending Process



Lorenzo Scandola , Daniel Maier, Matthias Konrad Werner, Christoph Hartmann, and Wolfram Volk

Abstract The free-form bending process is particularly suited for small-batch components of arbitrary three-dimensional shape. Nevertheless, the target geometry is usually input as a discrete set of bending instructions. The derivation of every bending operation from the CAD file is a complex task and can result in a cumbersome decomposition process. On the other hand, a list of sequential bending operations only contains information for each individual bent. In this contribution, an automated tool for turning parametric CAD data into bending instructions and vice versa is proposed. Regardless of the input type, the target bending line is computed as a NURBS curve, which can in turn be exported as a CAD file or bending table. The tool is validated by two case studies processing respectively a discrete and parametric bending line description. Finally, the outcome of the presented strategy is demonstrated by performing a surface-to-surface comparison between the target CAD component and the obtained bent part.

Keywords Free-form bending · NURBS reconstruction · Metal forming · Dimensional accuracy

Introduction

Free-form bending allows to perform multiple bending operations on a single component. With the use of a single tool, different bending radii and bending angles can be realised on distinct planes [1]. This widens significantly the typical design freedom for bent components with respect to other common bending processes, such as rotary draw bending or three-roll bending [2]. In addition, different kinematic profiles can result in the same geometry but different mechanical properties and residual stresses [3]. Such an increased flexibility translates into a higher complexity in the design phase of free-form bent parts and requires new tools for the engineering of the pro-

L. Scandola (✉) · D. Maier · M. K. Werner · C. Hartmann · W. Volk
Technical University of Munich, Chair of Metal Forming and Casting, Walther-Meißner-Straße 4,
85748 Garching b. München, Germany
e-mail: lorenzo.scandola@utg.de

cess [4]. In this context, a higher level CAD/CAM integration is required to optimise the process [5], which should first of all identify the bending features [6]. The crucial object describing the target geometry can be identified as the bending line, namely the line connecting the cross sections' gravity centres of the part [7]. This is typically conveyed as parametric data, i.e. a CAD drawing, from the design point of view, while it is expressed in form of discrete data, namely as a set of bending instructions, in the production line, Fig. 1. While the process of transition from the parametric to the discrete description can be trivial and fast for bending lines conceived for traditional bending processes, it can result in a cumbersome and complex task for free-form bent curves in the three-dimensional space. In this paper, an automated tool for the extraction of the bending instructions from parametric to discrete data and vice versa is presented. The translation of the CAD part into bending instructions is introduced first, followed by the derivation of the bending table from the CAD file, by means of two case studies. Finally, the part described as a bending table is manufactured and measured, and the surface-to-surface comparison is carried out with the aid of the tool. The developed strategy ensures a robust data exchange and allows for a more integrated process line, where the bent product can be solely described by its bending line in the design step, as well as in the production phase and along the quality control route. The developed tool enhances the robustness of free-form bending and contributes to the wide spreading of the process in the future.

Extraction of the Bending Line to NURBS

In order to efficiently switch from parametric CAD data to a discrete set of bending instructions and vice versa, an additional super-ordinate description is proposed exploiting Non-Uniform Rational B-Spline (NURBS) curves. Independently of the original description of the bending line, the translation into NURBS allows to dispose of a fundamental mathematical object, which guarantees a unique representation of the curve. In this way, the comparison of different bending lines is made easier and the export to CAD data or bending table is immediate. NURBS curves are defined as follows [8]:

$$\mathbf{C}(u) = \frac{\sum_{i=0}^n N_{i,p}(u)w_i \mathbf{P}_i}{\sum_{i=0}^n N_{i,p}(u)w_i} = \sum_{i=0}^n R_{i,p}(u) \mathbf{P}_i, \quad 0 = a \leq u \leq b = 1 \quad (1)$$

where p is the degree of the curve, \mathbf{P}_i are the $n + 1$ control points which generate the control polygon, $N_{i,p}$ are the basis functions, and $U = \{a, \dots, a, u_{p+1}, \dots, u_{m-p-1}, b, \dots, b\}$ is the knot vector consisting of $m + 1$ knots. The fundamental relation $m = n + p + 1$ allows to retrieve the number of required knots, given the number of control points and degree. The choice of NURBS curves over the simpler Bézier curves or B-splines is justified by the capability of the former of representing rational curves. This is ensured by the proper adaption of the

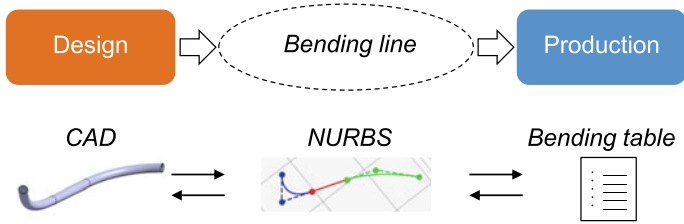


Fig. 1 Data flow in the process chain from the design up to the production step

$m + 1$ weights w_i , which enable the representation of conic sections, such as hyperbola, parabola, ellipse, and circle [9]. This is particularly important, as it allows to describe all possible bending line features occurring in free-form bending, namely lines, arcs, and splines, with the same mathematical object only adjusting its parameters. This property is the core of the extraction tool, which is thoroughly described in the following.

NURBS Reconstruction from CAD Data

The translation of the CAD data into NURBS requires as input a *.stp file. This allows the tool to be CAD software-independent and to work with a normed file type, specified in [10]. The choice of the *.stp over the *.iges format derives from the greater diffusion of the former in the context of 3D design and construction. In addition, the *.stp standard is more easily human-readable and more recent, so that it is set as the format of choice also with respect to future applications. Nevertheless an integration of the tool for handling the *.iges format as well is feasible. The first step for translating the bending line to NURBS is to parse the *.stp file with respect to its keywords [11]. In order to do so, the only requirement is to dispose of the bending line as a single merged curve, which can be easily achieved in any CAD software. The proposed custom parser searches for the global bending line entity, ('COMPOSITE_CURVE'), and retrieves the multiple segments in which it is divided ('COMPOSITE_CURVE_SEGMENT'). Each segment is furthermore described as a curve bounded between its starting and ending point, ('TRIMMED_CURVE'), and represented by its feature, namely a line, a circle, a B-spline, or a NURBS ('LINE', 'CIRCLE', 'B_SPLINE_CURVE_WITH_KNOTS', or 'RATIONAL_B_SPLINE_CURVE'). The hierarchy and decomposition of the bending line is summarised in Fig. 2. At this point, the necessary attributes for obtaining a NURBS are parsed depending on the type of segment feature. This includes the degree of the curve, its control points, the knots, and the weights. For a line, the parsing of the *.stp file allows to retrieve the starting and ending points ('CARTESIAN_POINT'). These are set as the NURBS control points, the degree is set to 1 and the 4 required knots are taken as shown

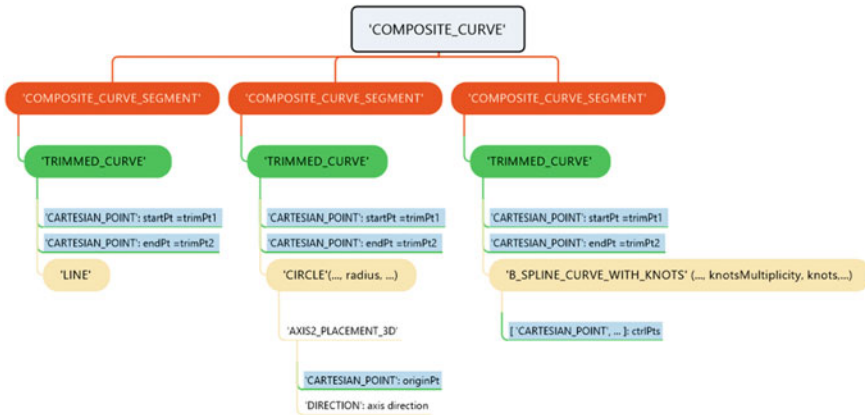


Fig. 2 Hierarchy of bending line in .stp files

in Fig. 7a, b. In the case of an arc, the information available from the CAD are the extremes, the radius (from the entity 'CIRCLE'), the direction and origin of the axis (AXIS2_PLACEMENT_3D), and the ascribed angle, which can be derived as follows (Fig. 7c):

$$\begin{cases} \alpha = \arccos\left(\frac{P_1O \cdot P_0O}{|P_1|P_0|}\right), & \text{if } n \cdot (P_0O \times P_1O) \geq 0 \\ \alpha = 2\pi - \arccos\left(\frac{P_1O \cdot P_0O}{|P_1|P_0|}\right), & \text{if } n \cdot (P_0O \times P_1O) < 0 \end{cases} \quad (2)$$

The translation to NURBS is performed setting the degree to 2 and distinguishing four cases for the derivation of control points, knots, and weights, depending on the ascribed angle (≤ 90 , ≤ 180 , ≤ 270 , and ≤ 360) as described in Fig. 7c, d, e, f, g, h, i, and j. For B-splines and NURBS, the respective parameters are directly parsed. With this procedure, the bending line is extracted from the original CAD geometry and turned to a sequence of NURBS segments, which independently of their original feature can be universally described and compared by their degree, control points, knots and weights.

NURBS Reconstruction from Bending Instructions

When expressed in form of a set of bending line instructions, or a bending table, the bending line can only be constituted by line and arc segments. While lines are just described by their length, arcs are identified by a bending radius, a bending angle, and an additional angle indicating the position of the bending plane. Since this description is purely discrete, the additional information of the normal plane

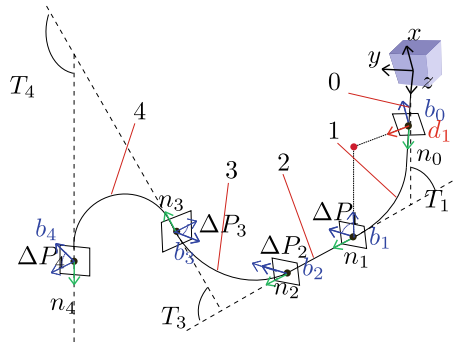


Fig. 3 Extraction of NURBS from bending table description

and of the bending plane unit vectors must be retrieved for each segment in order to generate a NURBS in the Cartesian space. The algorithm works sequentially and requires for every segment the actual point and the normal and bending plane unit vectors, respectively n_i and b_i in Fig. 3. At the beginning the origin is set as the point $O = (0, 0, 0)$, while the initial bending plane and normal plane are respectively the x - and the z -axis unit vectors. In this way, the z -axis points towards the evolving bending, namely in the opposite direction of the feed. These inputs are user-defined, and depending on their choice the same curve can be described in different spatial configurations, which is helpful to evaluate the feasibility of a bent in the process. In addition, it should be pointed out that the normal and bending planes are always referred to the end of the bent segment, and that while the T angle is already a relative angle on the bending plane between the normals at the beginning and end of the bent, the P angle between the bending planes is always absolute, so that ΔP must be considered, i.e. the difference between the next bending plane angle and the previous. In the case of a line, the current normal and bending planes are maintained, and the ending extreme is retrieved at a distance equal to the parsed length L along the normal axis. In addition, the difference in bending plane angle, ΔP , is set to zero. For an arc, the parsing of the bending table delivers the bending angle T , radius R , and plane P , and in order to find the ending extreme of the arc, the origin and the axis have to be calculated. First, the actual bending plane is rotated along the actual normal plane by the relative angle ΔP . Then, the actual normal plane is rotated along the new bending plane by the absolute angle T , namely the angle of the bend. Successively, the origin point of the arc is found at a distance equal to R from the starting point, along the origin axis direction calculated as the cross product between the new bending plane and the previous normal plane unit vectors:

$$d_i = b_i \times n_{i-1} \quad (3)$$

Finally, the ending point of the arc is calculated by rotating the starting point along the bending plane axis displaced in the origin of the arc. All rotations are realised

with a versatile rotation function, allowing to rotate an object along and axis with a given origin:

$$R = T^{-1}T_{xz}^{-1}T_z^{-1}R_z(\theta)T_zT_{xz}T \tag{4}$$

In this way, also a bending line described with a bending table can be translated into a sequence of NURBS.

NURBS Properties

The NURBS description of the bending line allows the computation of two different reference frames, describing in turn the intrinsic geometry of the curve at every point and its position with respect to the machine during the process.

First of all, the Frenet Frame [12] of every segment is calculated. The motivation behind the choice of this frame is that it is an invariant property of the curve. It describes uniquely its intrinsic geometry with the tangent T , normal N , and binormal B vector, which can be calculated for every point from its spatial derivatives, x' , x'' as:

$$T = \frac{x'}{|x'|}, \quad B = \frac{x' \times x''}{|x' \cdot x''|}, \quad N = B \times T \tag{5}$$

While for lines the only non-zero vector is the tangent, for arcs and splines all vectors are different from zero. The normal vector points always towards the origin of the osculating circle [13], and the binormal defines the plane on which the curve lies. This allows to recognise the original feature of the curve in the NURBS representation. In addition, the Frenet Frame satisfies the following differential equations:

$$\begin{bmatrix} T' \\ N' \\ B' \end{bmatrix} = \begin{bmatrix} 0 & k & 0 \\ -k & 0 & \tau \\ 0 & -\tau & 0 \end{bmatrix} \begin{bmatrix} T \\ N \\ B \end{bmatrix} \tag{6}$$

where k and τ are, respectively, the curvature and the torsion of the curve, which can be calculated as:

$$k = \frac{|x' \times x''|}{|x'|^3}, \quad \tau = \frac{x''' \cdot (x' \times x'')}{|x' \times x''|^2} \tag{7}$$

In this way, the curvature and hence radius can be easily computed at any point of the curve.

On the other hand, the Parallel Transport frame is computed to represent the position of the machine on the curve during the evolving bent. This is obtained by setting an initial frame representing the machine position. The tangent vector T is chosen as the opposite of the feed direction, the first normal vector N_1 points in the direction leading to a bent in the vertical direction ($P = 90^\circ$), and the second normal vector N_2 is the cross product of the two. At every point, the first normal is rotated along the second normal by the angle between the two tangents, and so the

frame is rigidly moved along the curve [14]. The Parallel Transport frame satisfies the following equations:

$$\begin{bmatrix} T' \\ N'_1 \\ N'_2 \end{bmatrix} = \begin{bmatrix} 0 & k_1 & k_2 \\ -k_1 & 0 & 0 \\ -k_2 & 0 & 0 \end{bmatrix} \begin{bmatrix} T \\ N_1 \\ N_2 \end{bmatrix} \quad (8)$$

and allows to retrieve at every point on the curve the position of the machine. This is specifically represented by the P angle which can be computed as the angle between the first normal N_1 of the Parallel Transport frame and the binormal B vector of the Frenet frame:

$$P_i = \arccos(N_1^{PT} \cdot B_i^{FF}) \quad (9)$$

It is important to notice that independently of its curvature profile every segment possesses a non-vanishing Parallel Transport frame at any point, in contrast to the Frenet frame.

Conversion of NURBS to Bending Line

Once the bending line is available in a NURBS description, the tool can easily perform the opposite operation of parsing and export it to an *.stp file as well as to a bending table.

NURBS Conversion to Bending Table

The translation of a NURBS bending line deriving from the CAD to a bending table is straightforward. Every segment composing the bending line is parsed, and a bending instruction is generated depending on its feature. For lines, just the length L is extracted. For the case of arcs, the value of the bending radius is calculated as the reciprocal of the curvature $R = 1/k$, the bending angle T is retrieved as the ending angle of the arc, and the P angle is calculated by comparing the Frenet and Parallel Transport frames as shown above. As a validation example, the part shown in Fig. 4a is considered. It represents the half frame of a rocking chair and consists of 13 segments, Fig. 4b, distributed on several bending planes, Fig. 4d, and resulting in different bending radii and angles Fig. 4c. The corresponding extracted bending table is summarised in Table 1. It is important to notice that retrieving the set of every single operation from the CAD would result in a lengthy and imprecise operation, while thanks to the tool the bending table is returned automatically.

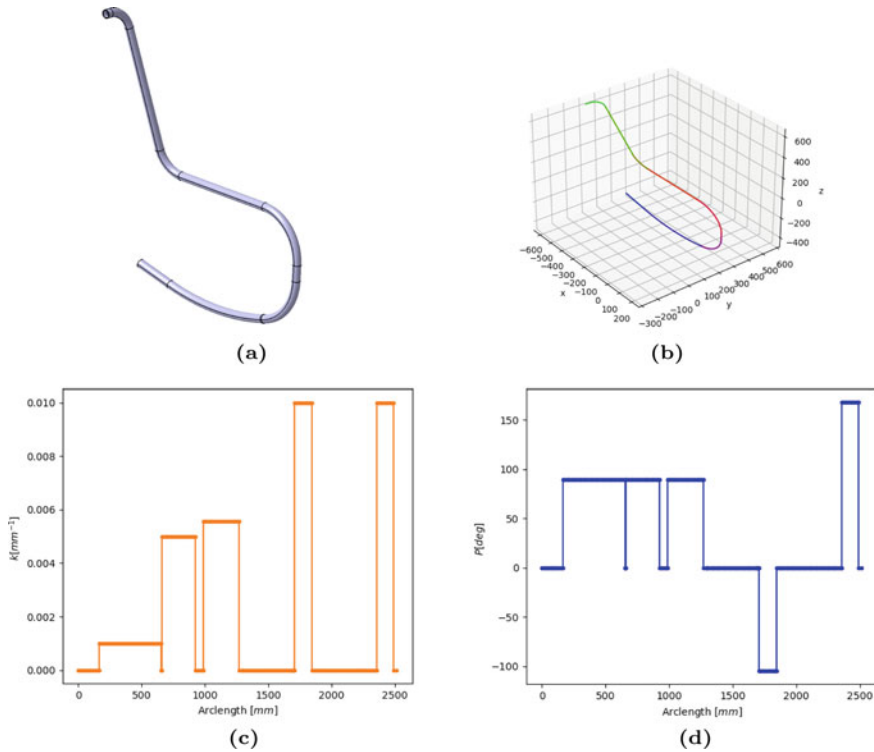


Fig. 4 Validation case study for the transition of CAD data to bending table: **a** input *.stp data; **b** corresponding bending line; **c** curvature profile k ; **d** bending plane profile P

Table 1 Bending table corresponding to CAD case study

Segment	1	2	3	4	5	6	7	8	9	10	11	12	13
L (mm)	162.3		6.2		63.8		20.0	400.0	13.8		512.1		21.4
R (mm)		1000.0		200.0		180.0				100.0		100.0	
T (deg)		28.1		76.0		90.0				81.5		76.3	
P (deg)		89.5		89.5		89.5				-104.4		167.7	

NURBS Conversion to CAD Data

In order to export a NURBS bending line from a bending table to a CAD file in *.stp format, the tool extracts the first control point of the bending line and its first normal vector N_1 . These are set as the starting origin and the unit vector of the first bending plane. Successively, every NURBS curve composing the bending line is represented as a complex entity in the *.stp file ('RATIONAL_B_SPLINE_CURVE'), its starting and ending point are introduced ('TRIMMED_CURVE'), and it is stored

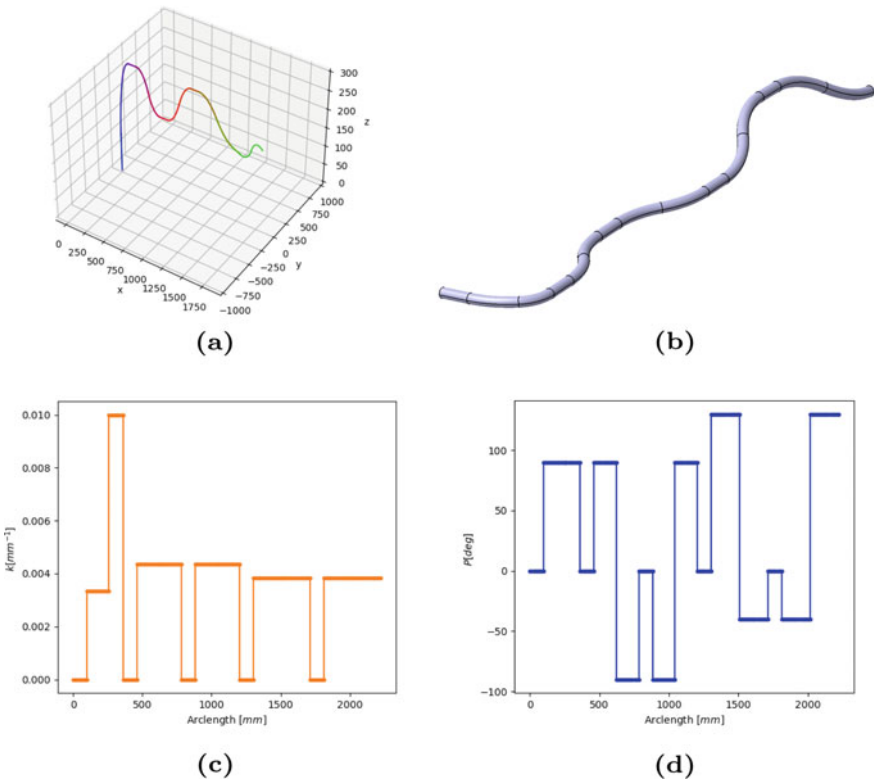


Fig. 5 Validation case-study for the transition of bending table to CAD data: **a** corresponding bending line; **b** output *.stp data; **c** curvature profile k ; **d** bending plane profile P

Table 2 Validation case study for the transition of bending table to CAD data

Segment	1	2	3	4	5	6	7	8	9	10	11	12	13	14	15
L [mm]	100.0			100.0			100.0			100.0			100.0		
R [mm]		300.0	100.0		230.0	230.0		230.0	230.0		260.0	260.0		260.0	260.0
T [deg]		30.0	60.0		40.0	40.0		40.0	40.0		45.0	45.0		45.0	45.0
P [deg]		90.0	90.0		90.0	-90.0		-90.0	90.0		130.0	-40.0		-40.0	135.0

as a single segment ('COMPOSITE_CURVE_SEGMENT'). Finally, all segments are grouped in a single bending line object ('COMPOSITE_CURVE').

The process is validated through the case study described in the bending table in Table 2, which is a prototypical example resembling the geometry of a side frame part of a truck. The corresponding bending line is shown in Fig. 5a, including its curvature Fig. 5c and bending plane profiles Fig. 5d, while the resulting CAD file is shown in Fig. 5b. The tool enables a fast reconstruction of the bent part in the CAD environment and allows for a direct quality assessment, which is discussed in the next section.

Validation Through Target-Obtained Part Comparison

In order to demonstrate the advantages of the developed tool, the case study involving a bending table description is taken into account. The assessment of the quality of a bent part is typically evaluated in the production route by comparing the bending radii and angles of the obtained and the target part. While this can suffice for simple bent geometries consisting of constant radii and in-plane bents, such as those obtained by rotary draw bending, this is not suitable for free-form bent geometries evolving over different planes. In this context, the tool allows to dispose of the target CAD geometry also for bending lines defined by bending tables, and so the quality assessment can be done through a surface-to-surface comparison. The results are the deviations of the tube at any location, and in addition it is possible to define if the obtained part respects some other geometrical requirement, such as the distance between its extremes or the location of particular points involving soldering or screw connections. The bent raw material consists of a hollow tube of diameter 33.7 mm and thickness 2 mm of steel *P235TR1*. The machine is calibrated with respect to the given batch using 13 calibration points, described in Table 3. The calibration curves for the deflection and rotation of the bending head are obtained by piecewise cubic spline interpolation (PCHIP), as described in [15]. The typical evaluation methodology consists in comparing the target and obtained bending radius and angle for every bending operation. The target and measured values are shown in Table 4. It can be seen that the radii are generally met in a very precise way, with a maximum deviation in the bending 14 of $\Delta R_{max}^{(14)} = 8.3 \text{ mm}$. This corresponds to $\Delta R_{max\%} = 3.2\%$ of the target value, while the mean percentage error through all the bendings is $\Delta R_{avg\%} = 0.06\%$. On the other side, the bending angles show more prominent deviations, up to a maximum of $\Delta T_{max}^{(2)} = 5.6^\circ$ in the bending 2. The maximum percentage deviation is found at the bending 5, $\Delta T_{max\%}^{(5)} = 11.6\%$, while the average percentage error is $T_{avg\%} = 6.72\%$. Although the obtained component is completely characterised by means of this information, it is difficult to evaluate its quality and accuracy regarding

Table 3 Calibration tests

	1	2	3	4	5	6	7	8	9	10	11	12	13
R_0 [mm]	101.1	134.8	168.5	212.3	235.9	337	539.2	674.0	842.5	1348.0	2123.1	2696.0	3370.0
R [mm]	80.0	100.9	126.7	159.2	180.5	251.0	392.1	499.6	643.6	1192.6	2124.6	2913.1	3055.8
T_0 [deg]	110.0	90.0	70	55	50.0	70.0	45	35.0	30	25.0	15.0	10.0	10.0
T [deg]	95.1	89.2	74.0	61.8	57.3	90.6	60.8	47.4	39.5	29.0	12.2	5.5	4.2
u [mm]	24.2	18.5	15.4	12.9	11.9	9.2	6.6	5.7	4.9	3.6	2.7	2.3	2.0
a [deg]	36.4	31.1	27.4	24.0	22.5	18.2	13.6	11.9	10.3	7.7	5.9	5.1	4.5

Table 4 Target-obtained value comparison for the single bents

	2	3	5	6	8	9	11	12	14	15
R_{tgt} [mm]	300.0	100.0	230.0	230.0	230.0	230.0	260.0	260.0	260.0	260.0
R_{obt} [mm]	299.8	99.9	234.5	230.6	227.5	228.5	267.4	257.6	251.7	264.2
T_{tgt} [deg]	30.0	60.0	40.0	40.0	40.0	40.0	45.0	45.0	45.0	45.0
T_{obt} [deg]	26.8	65.6	35.8	37.2	35.4	35.4	39.9	43.4	43.6	41.8

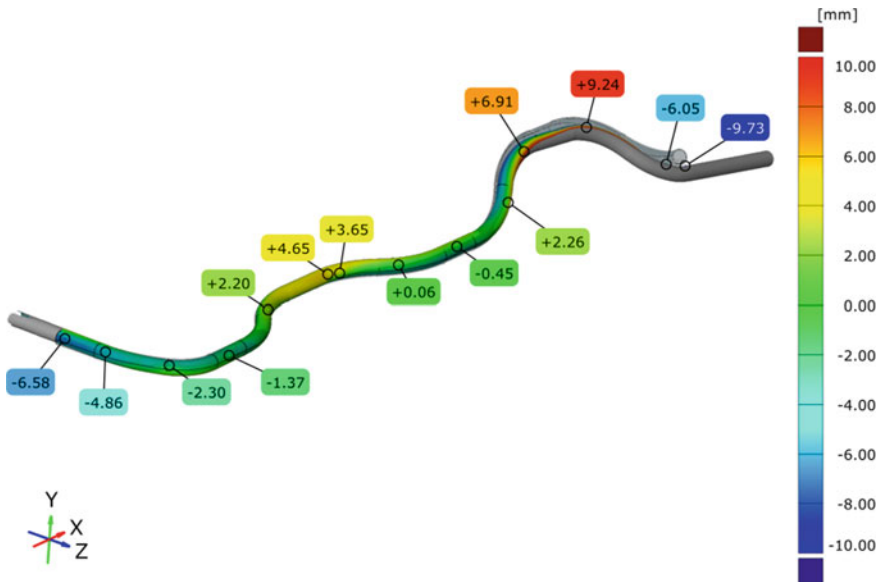


Fig. 6 Surface-to-surface comparison and deviation analysis

the fulfilment of geometrical requirements at reference positions. Local geometrical features such as the distance between the starting and ending point of the component or the location of connecting elements cannot be evaluated efficiently through the analysis of the obtained bending radii and angles. To investigate this further, the surface-to-surface comparison is carried out with the software GOM-Inspect and shown in Fig. 6. The obtained part is scanned with a Zeiss T-Scan device, and the resulting data is oriented to the target part with a best-fit approach. This can be done thanks to the automatic extraction tool, which makes the CAD target geometry of the component available by feeding the target bending table. The impact of the calculated deviations in Table 4 is not uniform along the part. The mean deviation along the whole part is $u_{mean} = 0.19$ mm, with a standard deviation of $\delta u = 3.65$ mm. It can be seen that the regions exhibiting the higher deviations are those related to the bent numbers 15, 14, 2, and 8. Although the deviation calculation is affected by the orientation of the part, these bendings are not identified as the most critical according to Table 4, but are in turn those which should be optimised first in a compensation step. In this framework, the surface-to-surface comparison allows to evaluate a free-form bent component in a more detailed and complex way with respect to the discrete comparison of bending radii and angles. The dimensional accuracy of the part can be hence assessed by investigating local geometrical features related to the component function, such as point-to-point distances or the locations of weld as well bolt connections. This is achieved by switching from parametric indicators, such as bending radii and angles values, to Cartesian indicators, namely deviations

values. This is in turn made possible by the developed tool, which automatically gives the CAD geometry to compare with for any user-defined bending table.

Conclusions and Outlook

The implemented strategy represents a powerful tool for the optimisation of the free-form bending process. Through the automatic extraction of the bending line from CAD data as well as from bending tables, the data exchange process between the design phase and the production is made faster, more rigorous, and less error prone. In addition, the user-dependency in the evaluation and definition of the corresponding bending line is reduced. The tool allows a bidirectional information flow, from CAD to bending instructions and vice versa, taking as reference description solely NURBS curves. This in turn allows to completely characterise every bending line in terms of its intrinsic geometry as well as with respect to the position of the semi-finished part in the machine during the process. This data is achieved thanks to the definition of two distinct reference frames, the Frenet frame as well as the Parallel Transport frame, and the differential properties of the NURBS, such as the curvature, the torsion, and the bending plane angle. Finally, the tool allows to accomplish a dual purpose, namely to directly retrieve the bending instructions from a CAD component as well as to turn a bending table into a CAD part. This is particularly useful in the framework of deviation assessment, as it widens the process beyond the comparison of the bending radii and angles. The presented work represents the first part of a wider automatic assistance system tool for free-form bending. Future investigations include the derivation of the kinematics of the bending head directly from the bending line, an automated strategy for the compensation of deviations at relevant locations and the derivation of the bending line from simulated as well as measured parts. A paradigm change can be obtained with the presented tool if also splines freely designed in the 3D space can be directly bent without intermediate steps.

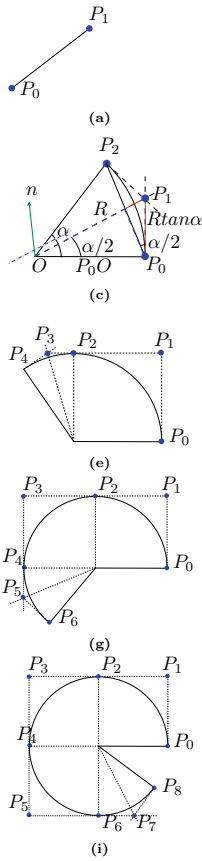
Acknowledgements The authors would like to thank Hörmann Automotive GmbH for the financial support and J. Neu GmbH for providing the machine.

Conflict of Interest The authors declare that they have no conflict of interest.

Appendix

Translation of Line and Arcs to NURBS

See Fig. 7.



NURBS parameter	values
Control Points	P_0, P_1
Knot vector	$[0, 0, 1, 1]$
Weights	$[1, 1]$
(b)	
NURBS parameter	values
Control Points	P_0, P_1, P_2
Knot vector	$[0, 0, 0, 1, 1, 1]$
Weights	$[1, \cos(\frac{\alpha}{2}), 1]$
(d)	
NURBS parameter	values
Control Points	P_0, P_1, P_2, P_3, P_4
Knot vector	$[0, 0, 0, 1/2, 1/2, 1, 1, 1]$
Weights	$[1, \cos(\frac{\pi}{4}), 1, \cos(\frac{\pi}{2}), 1]$
(f)	
NURBS parameter	values
Control Points	$P_0, P_1, P_2, P_3, P_4, P_5, P_6$
Knot vector	$[0, 0, 0, 1/3, 1/3, 2/3, 2/3, 1, 1, 1]$
Weights	$[1, \cos(\frac{\pi}{4}), 1, \cos(\frac{\pi}{4}), 1, \cos(\frac{\alpha}{2}), 1]$
(h)	
NURBS parameter	values
Control Points	$P_0, P_1, P_2, P_3, P_4, P_5, P_6, P_7, P_8$
Knot vector	$[0, 0, 0, 1/4, 1/4, 2/4, 2/4, 3/4, 3/4, 1, 1, 1]$
Weights	$[1, \cos(\frac{\pi}{4}), 1, \cos(\frac{\pi}{4}), 1, \cos(\frac{\pi}{4}), 1, \cos(\frac{\pi}{4}), 1, \cos(\frac{\alpha}{2}), 1]$
(j)	

Fig. 7 Data for representing lines and arcs as NURBS: **a** Line; **b** NURBS data; **c** Arc ≤ 90 ; **d** Arc ≤ 90 NURBS data; **e** Arc ≤ 180 ; **f** Arc ≤ 180 NURBS data; **g** Arc ≤ 270 ; **h** Arc ≤ 270 NURBS data; **i** Arc ≤ 360 ; **j** Arc ≤ 360 NURBS data

References

1. Murata M (2011) Tube bending of new generation by mos bending machine. In: TU Dortmund (ed) 1st International tube and profile bending conference, Institut für Umformtechnik und Leichtbau, pp 9–18
2. VDI-Gesellschaft Produktion und Logistik (2014) Vdi 3430: Rotationszugbiegen von profilen
3. Maier D, Stebner S, Ismail A, Dölz M, Lohmann B, Münstermann S, Volk W (2021) The influence of freeform bending process parameters on residual stresses for steel tubes. *Adv Ind Manuf Eng* 2:100047. <https://doi.org/10.1016/j.aime.2021.100047>
4. Gantner P (2008) The characterisation of the free-bending technique. Thesis (Ph.d.), Glasgow Caledonian University
5. Nasr EA, Kamrani AK (2007) Computer-based design and manufacturing: an information-based approach, manufacturing systems engineering, vol 7. Springer Science+Business Media LLC, Boston
6. Subrahmanyam S, Wozny M (1995) An overview of automatic feature recognition techniques for computer-aided process planning. *Comput Ind* 26(1):1–21. [https://doi.org/10.1016/0166-3615\(95\)80003-4](https://doi.org/10.1016/0166-3615(95)80003-4)
7. VDI-Gesellschaft Produktion und Logistik (2016) Vdi 3431: Biegen von profilen - prüfhinweise für profilbiegebauteile
8. Piegl L, Tiller W (1997) The NURBS book, 2nd edn. Monographs in visual communication. Springer, Berlin. <https://doi.org/10.1007/978-3-642-59223-2>
9. Hughes T, Cottrell JA, Bazilevs Y (2005) Isogeometric analysis: Cad, finite elements, nurbs, exact geometry and mesh refinement. *Comput Methods Appl Mech Eng* 194(39–41):4135–4195. <https://doi.org/10.1016/j.cma.2004.10.008>
10. International Organization for Standardization, Geneva, Switzerland (2004–11) ISO 10303-11:2004: Industrial automation systems and integration - product data representation and exchange: part 11: description methods: the express language reference manual
11. Step Tools I (2022) Step tools: express documentation. https://www.steptools.com/stds/stp_aim/html/
12. Eisenhart LPA (1960) Treatise on the differential geometry of curves and surfaces. Dover, New York
13. Struik DJ (1961) Lectures on classical differential geometry. Addison-Wesley Pub. Co, Reading
14. Bishop R (1975) There is more than one way to frame a curve. *The American mathematical monthly*, vol 82. Mathematical association of America. <https://doi.org/10.2307/2319846>
15. Werner MK, Maier D, Scandola L, Volk W (2021) Motion profile calculation for freeform bending with moveable die based on tool parameters. In: ULiège Library (ed) Proceedings of the 24th international conference on material forming. <https://doi.org/10.25518/esaform21.1879>

Characterization of Cohesive Zone Model Properties of Laminated Metal Sheet with a Thin Adhesive Layer



Hyeonil Park, Se-Jong Kim, Jinwoo Lee, and Daeyong Kim

Abstract Double cantilever beam (DCB) test associated with the measurement of crack tip opening displacement (CTOD) is a practical method to experimentally evaluate cohesive zone model (CZM) properties in mode I. However, it has an obvious limitation that does not allow the plastic deformation of adherends during the test, making it difficult to evaluate the polymer layer inserted in the laminated metal sheet comprising thin metal sheets which are vulnerable to the plastic deformation. This paper provides an experimental technique for evaluating the mode I CZM properties of ductile adhesive layers inserted in the laminated metal sheet, while suppressing the plastic deformation of the thin metal adherends. To suppress the plastic deformation of the thin adherends during the DCB test, the supporting tools were designed and bonded to the both outer surfaces of the laminated metal sheet. Until delamination occurred, the evolution of fracture toughness (G) was evaluated, and the CTOD was measured in the stereo image using a digital image correlation system. Then, a traction (T)–separation (δ) law in mode I was established based on the differentiation of the relation between the evolution of G and CTOD. Finally, the mode I CZM properties were successfully obtained from the bilinear-fitted T – δ law.

Keywords Double cantilever beam test · Laminated metal sheet · Cohesive zone model · Ductile adhesive layer

Introduction

Various techniques for analyzing adhesive layers have been developed and improved over the last decade, and a cohesive zone model (CZM) is increasingly used to describe the mechanical behavior of ductile adhesive layers [1, 2]. The CZM is defined by a traction–separation law, which represents the constitutive behavior of interfacial bonding traction (T) as function of the separation (δ) between two bonded points, and the under area of the curve represents the critical fracture toughness

H. Park · S.-J. Kim · J. Lee · D. Kim (✉)

Materials Deformation Department, Korea Institute of Materials Science, 797 Changwondaero, Changwon, Gyeongnam 515508, Republic of Korea
e-mail: daeyong@kims.re.kr

© The Minerals, Metals & Materials Society 2022

K. Inal et al. (eds.), *NUMISHEET 2022*, The Minerals, Metals & Materials Series,
https://doi.org/10.1007/978-3-031-06212-4_74

(G^c). The elastic energy-based calculation during beam bending tests is the well-known method to characterize G^c , and a differentiation concept between the evolution of fracture toughness (G) and the crack tip opening displacement (CTOD) has been developed to experimentally establish T - δ law [3–5]. However, the calculation method based on the elastic deformation of adherends was originally designed to target composite adherends, which allows only elastic deformation; therefore, they are not suitable for the evaluation of the ductile adhesive layer inserted in the laminated metal sheets comprising thin metal sheets that are vulnerable to plastic deformation [6, 7].

This paper provides a practical experimental technique for evaluating the mode I CZM properties of the ductile adhesive layer inserted in the laminated metal sheet, while suppressing plastic deformation of the thin metal adherends. To evaluate the mode I CZM properties of the ductile adhesive layer, the mode I beam bending test, namely, double cantilever beam (DCB) test standardized by ASTM [8], was performed. The supporting tools for suppressing the plastic deformation of the thin metal adherends were designed and bonded to the both outer surfaces of the laminated metal sheet. Until delamination occurred, the evolution of G was evaluated, and the CTOD was measured in the stereo image using a digital image correlation (DIC) system. Then, the T - δ law was established based on the differentiation of the relation between the evolution of fracture toughness and CTOD. Finally, the mode I CZM properties were obtained from the bilinear-fitted T - δ law.

Experimental Procedure

Adherend Material

The adherend material is dual phase (DP) 590 MPa grade high strength steel sheets with 0.7 mm thickness. In order to investigate the mechanical properties of the steel sheets, a uniaxial tensile test along the rolling direction was carried out on ASTM-E8 standard specimens with a universal testing machine (UTM) using the quasi-static rate of 0.001/s [9]. The laminated metal sheet was fabricated by passing through roller after inserting acrylic-based adhesive layer between two steel sheets having size of 300 mm \times 300 mm (Table 1).

Table 1 Characteristics of the base steel sheet

Elastic modulus (GPa)	Yield stress (MPa)	Ultimate tensile stress (MPa)	Uniform elongation (%)	Total elongation (%)	Lankford value
210.3	347.6	635.9	18.5	27.0	0.84

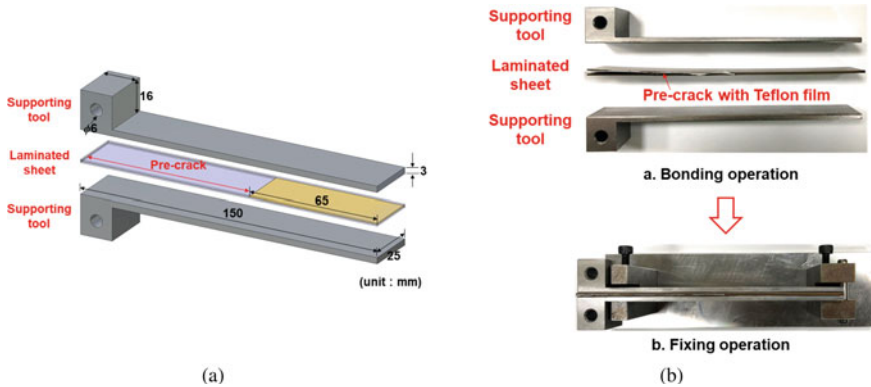


Fig. 1 Apparatus of supporting tools: **a** detailed dimension, and **b** bonding procedure

Design of Supporting Tool

To suppress the plastic deformation of the thin adherends during the DCB test, the supporting tools were designed and made of the ion-nitrided SM45C structural carbon steel. They were bonded to the both outer surfaces of the laminated metal sheet using the epoxy-based strong adhesive (S/N: 3 M 460NS). Detailed dimension of supporting tools and their bonding procedure is shown in Fig. 1 a, b, respectively.

Double Cantilever Beam Test

DCB test was performed using UTM to experimentally evaluate cohesive zone model (CZM) properties in mode I. On the specimen prior to tests, a stochastic pattern was applied to the surface of side wall using white and black spray. Until delamination occurred, the applied load (P) and loading point displacement (U) were measured from the UTM, and synchronized with CTOD measured in the stereo image using the DIC system. The apparatus of DCB test specimen and the measurement procedure of CTOD are shown in Fig. 2a, b, respectively.

Adhesive Characterization

During the DCB test, the evolution of fracture toughness (G) can be evaluated by the Irwin-Kies equation as follows [10]:

$$G = \frac{P^2}{2B} \frac{dC}{da} \tag{1}$$

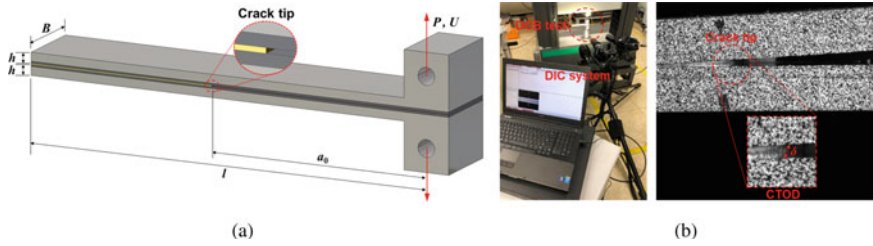


Fig. 2 Apparatus of DCB test: **a** test specimen, and **b** measurement of CTOD

where P , B , and a are the applied load, specimen width, and crack propagation length, respectively. C is the compliance, and defined by

$$C = \frac{U}{P} \tag{2}$$

where U is the loading point displacement, and P is the applied load. C is also calculated by the Timoshenko beam theory based on the equivalent crack (a_{eq}) concept as follows:

$$C = \frac{8a_{eq}^3}{E_{eq} B h^3} + \frac{24(1 + \nu)a_{eq}}{5E_{eq} B h} \tag{3}$$

where ν , B and h are the Poisson’s ratio, width, and thickness of the adherend, respectively. E_{eq} is the equivalent elastic modulus, and given by

$$E_{eq} = \frac{8a_0}{C_0 B h} \left(\frac{a_0^2}{h^2} + \frac{3(1 + \nu)}{5} \right) \tag{4}$$

where a_0 and C_0 are the pre-crack length and initial compliance obtained from the early linear part in Eq. (2). By introducing Eq. (3) into Eq. (1), G can be derived as follows:

$$G = \frac{6P^2}{E_{eq} B^2 h} \left(\frac{2a_{eq}^2}{h^2} + \frac{2(1 + \nu)}{5} \right) \tag{5}$$

Because G is determined as a function of P , the δ - P curve measured during the DCB test can be converted to the G - δ curve, then the T - δ law can be established by differentiating the G - δ curve against δ as follows:

$$T(\delta) = \frac{dG}{d\delta} \tag{6}$$

Results and Discussion

Figure 3 shows the established $T-\delta$ law of ductile adhesive inserted in the laminated metal sheet during the DCB test. The $G-\delta$ curve and its derivative, $T-\delta$ law, are shown in Fig. 3a, b, respectively. The mode I CZM properties were extracted from the bilinear-fitted $T-\delta$ law (see the red line in Fig. 3b), as listed in Table 2. In addition, to verify the established $T-\delta$ law, the numerical simulation of the DCB test was performed by inputting the obtained mode I CZM properties, and its result was compared with the experimental one as shown in Fig. 3c. Resultantly, although there was some error due to the simple shape of the bilinear model, the overall tendency was predicted well.

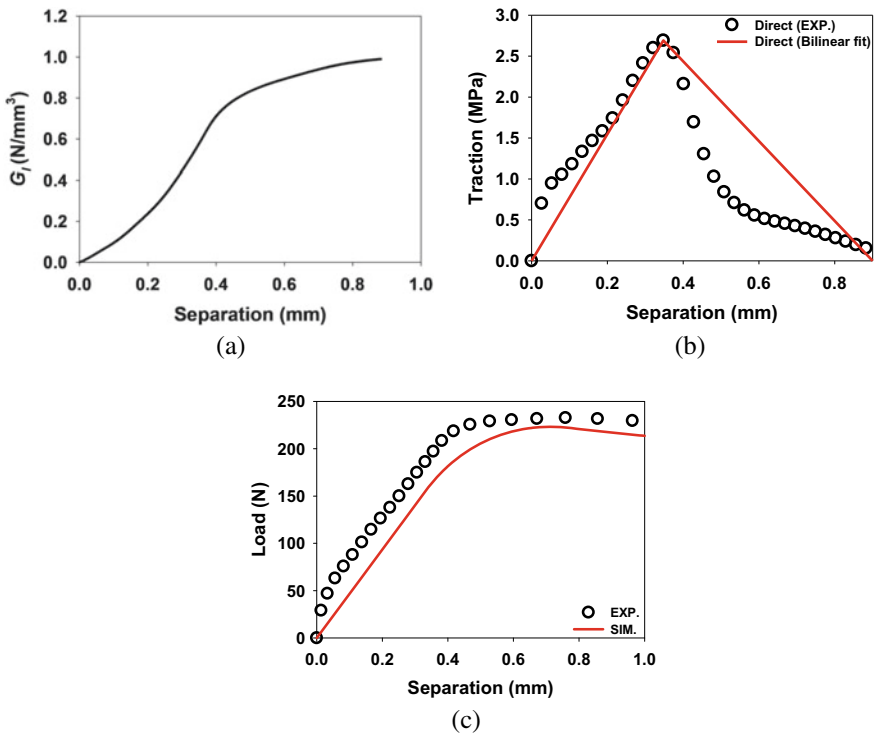


Fig. 3 Established $T-\delta$ law of ductile adhesive inserted in laminated metal sheet: **a** $G-\delta$ curve, **b** $T-\delta$ law, and **c** $P-\delta$ curve

Table 2 Mode I CZM properties of ductile adhesive inserted in laminated metal sheet

K (N/mm ³)	T^{\max} (MPa)	G^c (N/mm)
7.74	2.69	1.21

Summary

This study provided practical experimental technique to evaluate mode I CZM properties of ductile adhesive layer inserted in the laminated metal sheet. To suppress the plastic deformation of the thin metal adherends during the DCB test, the supporting tools were designed and bonded to the both outer surfaces of the laminated sheet. As a results, the T - δ curve was successfully established based on the differentiation of the relation between the evolution of fracture toughness and CTOD. Finally, the mode I CZM properties were extracted from the bilinear-fitted T - δ law. In addition, to verify the established T - δ law of the ductile adhesive, the numerical simulation of the DCB test was performed by inputting the mode I CZM properties, and its result was not significantly different from the experimental one.

Acknowledgements This study was financially supported by the Fundamental Research Program (PNK6000) of the Korea Institute of Materials Science funded by the Ministry of Science and ICT and the Industrial Technology Innovation program (10063579) funded by the Ministry of Trade, Industry and Energy, Republic of Korea.

References

1. Camanho PP, Davila CG, De Moura MF (2003) Numerical simulation of mixed-mode progressive delamination in composite materials. *J Compos Mater* 37:1415–1438
2. De Moura MF, Gonçalves JPM, Chousal JAG, Campilho RDSG (2008) Cohesive and continuum mixed-mode damage models applied to the simulation of the mechanical behaviour of bonded joints. *Int J Adhes Adhes* 28:419–426
3. De Moura MF, Gonçalves JPM, Magalhães AG (2012) A straightforward method to obtain the cohesive laws of bonded joints under mode I loading. *Int J Adhes Adhes* 39:54–59
4. Fernandes RMRP, Chousal JAG, De Moura MF, Xavier J (2013) Determination of cohesive laws of composite bonded joints under mode II loading. *Compos Part B* 52:269–274
5. Khoramishad H, Hamzenejad M, Ashofteh RS (2016) Characterizing cohesive zone model using a mixed-mode direct method. *Eng Fract Mech* 153:175–189
6. Park H (2019) Mechanical behavior of high strength laminated steel sheets with thin adhesive interlayers (Doctoral dissertation). Pusan National University, Republic of Korea
7. Park H, Kim S-J, Lee J, Kim JH, Kim D (2020) Delamination behavior analysis of steel/polymer/steel high-strength laminated sheets in a V-die bending test. *Int J Mech Sci* 2020:105430
8. ASTM Standard D5528–13 (2013) Standard test method for mode I interlaminar fracture toughness of unidirectional fiber-reinforced polymer matrix composites. ASTM International
9. Park H, Kim S-J, Lee J, Kim JH, Kim D (2019) Characterization of the mechanical properties of a high-Strength laminated vibration damping steel sheet and their application to formability prediction. *Metals Mater Int* 25:1326–1340
10. Kanninen MF, Popelar CH (1985) *Advanced fracture mechanics*. University Press, Oxford

Clinching in In Situ CT—A Novel Validation Method for Mechanical Joining Processes



Daniel Köhler, Robert Kupfer, Juliane Troschitz, and Maik Gude

Abstract Force–displacement measurements and micrograph analyses are commonly used methods to validate numerical models of clinching processes. However, these methods often lead to resetting of elastic deformations and crack-closing after unloading. In contrast, the in situ computed tomography (CT) can provide three-dimensional images of the clinch point under loading conditions. In this paper, the potential of the in situ investigation of a clinching process as validation method is analyzed. For the in situ testing, a tailored test set-up featuring a beryllium cylinder for load-bearing and clinching tools made from ultra-high-strength titanium and Si₃N₄ are used. In the experiments, the clinching of two aluminum sheets is interrupted at specific process steps in order to perform the CT scans. It is shown that in situ CT visualizes the inner geometry of the joint at high precision and that this method is suitable to validate numerical models.

Keywords Clinching · Non-destructive testing · Computed tomography · In situ CT

Introduction

The increased interest in lightweight components in the automotive industry requires joining methods, which are able to join versatile materials. Furthermore, the ever-increasing legal requirements on material recycling [1] demand a separation of multi-material systems into their components with low contamination [2]. Clinching is a mechanical joining method applicable to various materials, as it creates a joint by locally deforming two join partners creating a form lock. There is no particular surface preparation and, usually, no heat input is required. Thus, this is a versatile and cost-efficient [3] joining method which also facilitates material separation during recycling [4]. However, versatility regarding material, geometry, and field of application can only be achieved when the manufacturing of a clinch point can be reliably simulated.

D. Köhler (✉) · R. Kupfer · J. Troschitz · M. Gude
Institute of Lightweight Engineering and Polymer Technology, Technische Universität Dresden,
Dresden, Germany
e-mail: daniel.koehler3@tu-dresden.de

The validation of numerical models of a clinching process is usually done using the force–displacement measurement during manufacturing and destructive methods such as microsectioning [5]. Non-destructive validation methods such as computed tomography (CT) can improve the validation. However, these *ex situ* methods cannot consider elastic effects and closing cracks, which occur after unloading. Thus, the deformation and damage chronology is not consistently given. Consequently, possible deviations between a numerical model and the respective experiment cannot be fully understood. Therefore, methods describing the clinching process *in situ* can improve the validation process of numerical models.

The CT testing method uses several scans of an object from different angles allowing reconstruction of a three-dimensional image of the object [6]. Thus, in contrast to microsectioning, the complete three-dimensional inner geometry of the object is known for reducing the number of necessary samples. Therefore, it has become an established method for geometry and structural analyses. It is used to investigate the microstructure of both homogeneous (e.g. aluminium alloy [7]) and heterogeneous material systems, such as concrete [8] or composites [9]. The testing method was already used for damage analysis, e.g. for semi-tubular self-piercing riveting of fibre-reinforced plastics (FRP) and aluminium (Al) [10]. Recently, it also has been applied to support numerical modelling or for validation. For example, Mckinley et al. used synchrotron-based micro-CT to assist the modelling of adhesive bonds in wood [11]. The validation method is further improved by conducting the CT in *in situ* measurements. Huang et al. and Qsymah validated numerical models of concrete using *in situ* CT [12, 13]. Füßel et al. investigated *in situ* the damage in joints using a single overlapping adhesively bonded riveted lap joint of FRP and Al [14]. Furthermore, Pottmeyer et al. applied *in situ* CT to analyze the deformation and damage of metal inserts in FRP [15].

While there are numerous references about applying *in situ* CT for testing processes, there are only a few cases where manufacturing processes were investigated. Kratz et al. used *in situ* CT in order to observe gaps in prepreg laminates during consolidation and curing [16]. However, to the author's knowledge, there are no reports about an *in situ* investigation of the manufacturing process of mechanical joints. In this paper, a test set-up for investigating the accurate deformation chronology during the clinching process in *in situ* CT is described (cf. Fig. 1). Furthermore, the potential of this method for the validation of numerical models is demonstrated in a first proof-of-concept.

Materials and Methods

In Situ CT-Clinching Setup

The CT-system VITOMEIX L450 from GE Sensing & Inspection Technologies GmbH (300 kV microfocus X-ray tube with flat detector) is used. The test set-up

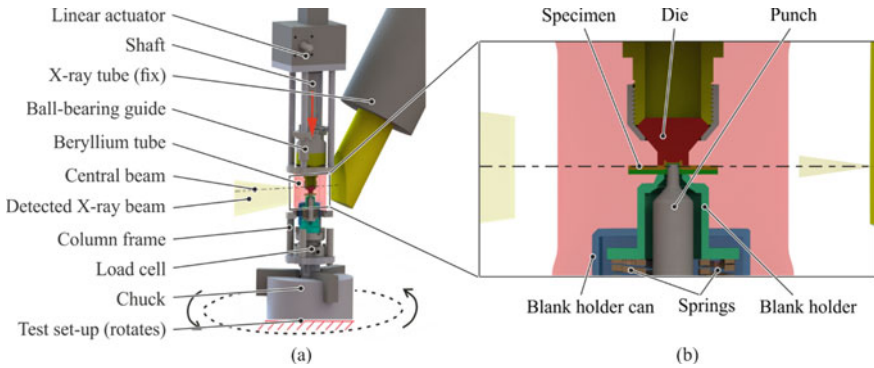


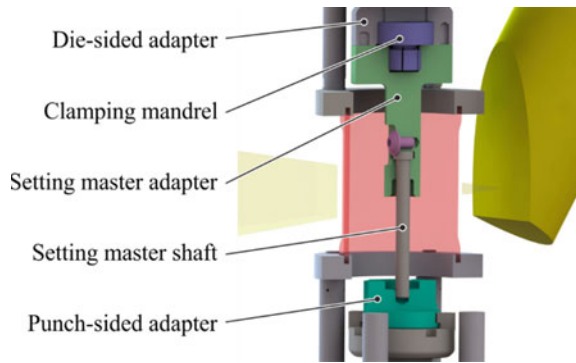
Fig. 1 In situ test set-up in the CT system (detector not displayed) (a) and close-up view (b) with the test specimens

consists of a linear actuator and a column frame (cf. Fig. 1). The force is transmitted via a shaft on the die, while ball-bearing guides prevent lateral shifting of the shaft. A beryllium tube is used allowing a constant and low X-ray absorption by the frame. The set-up is clamped in a chuck which rotates in order to adjust the scanning angles during CT. The linear actuator is the screw jack system HSG-4-SVA-300-L-GG-AB-KGS32×5 with ball screw, worm gear, and a transmission ratio of 28:1. A handwheel for manual operation is mounted on the worm gear in order to apply small movements to the shaft. To measure the clinching force, there is a load cell series K (nominal force 50 kN, nominal value 2 mV/V) from GTM Testing and Metrology GmbH underneath the adapters of the punch. The force signal is amplified using the amplifier 9243 from burster präzisionsmesstechnik GmbH & co kg. The signal is recorded using a measuring card (frequency 50 Hz). Consequently, with this set-up, the clinching process can be conducted path- and force-controlled.

In Situ CT Tools and Specimen

The clinching tools consist of the die, the punch, and the blank holder. The die and the blank holder are made of the high-strength titanium alloy Ti-355 from AMT Advanced Materials Technology GmbH. The tools are hardened to exhibit a Yield strength of 1.420 MPa. The punch is made of silicon nitride (Si3N4) from FCT Ingenieurkeramik GmbH. Previous investigations identified these materials as suitable tool materials for in situ CT-Clinching [17, 18]. Especially high-strength titanium alloy exhibits a sufficiently high toughness while leading to a low X-ray absorption. It could be shown that a die made of Si3N4 breaks during clinching [19]. A buckling of the sheets is avoided by the blank holder. The punch movement is coupled with the blank holder via four springs, which have a total stiffness of 465 N/mm and a preload force of 785 N.

Fig. 2 Aligning the die- and the punch-sided adapters to each other using the setting master



Two aluminum sheets made of Al EN AW 6014, a common material in automotive industry [20], are clinched in T4 state (thickness: 2 mm diameter: 40 mm). Since CT is based on X-ray attenuation caused by the object's material, the interface between the aluminum sheets is only visible when there is a small gap or interface layer between the surfaces. However, in the clinch point, the sheets are pressed so tightly that the sheet interface is hardly visible in CT scans [18]. In order to enhance the visibility of the interface, the application of a 10 μm thick tin foil (diameter 12 mm) between the aluminum sheets proved to be suitable [18]. To facilitate the removal of the specimen from the die, grease is applied to the respective surfaces on the die and the sheet.

Because of the complex buildup of the in situ testing set-up and the resulting addition of tolerances, an axial alignment of punch and die within the set-up is necessary. For this purpose, a separate setting master is used. On the upper side of the die, the setting master is mounted to a clamping mandrel (cf. Fig. 2). By moving the setting master shaft into a hole in the punch-sided adapter, the die- and the punch-sided adapters are aligned to each other (cf. Fig. 2). Then, the adapters are fixed, the setting master is removed, and die and punch are mounted to the adapters.

CT Measurement and Image Analysis

The specimen is X-ray scanned at five measuring points (MP) which are set manually by the handwheel:

- MP1—The punch is at the neutral position,
- MP2—The sheets are pushed into the cavity of the die but have not touched the anvil,
- MP3—The sheet material is drawn radially along the anvil,
- MP4—The sheet material fills the radial groove,
- MP5—The targeted bottom thickness is reached.

Table 1 Applied parameters for the CT measurement and image analysis

	Parameter	Unit	Value
CT measurement	Acceleration voltage	[kV]	250
	Tube current	[μ A]	150
	X-ray projections		1440 (4 per 1°)
	Exposure time	[ms]	1000
	Voxel size	[μ m]	12
	Magnification		16.5
Image analysis	Canny—threshold		0.19
	Canny—standard deviation of the filter		2

After the CT scan is conducted, the three-dimensional volumes are reconstructed. Then, the CT volume of each MP is investigated in cross-sectional images using a MATLAB script (R2019a) with the edge detection function “Canny”. The CT and image analysis parameters are shown in Table 1.

Results

In the CT scans, generally, good image quality is achieved (cf. Fig. 3a–e) and the interface is well visible over the clinch point. The clinching process and the material deformation can be clearly identified. However, the die’s front face and the tin foil cause moderate streak artefacts in the sheet material (cf. Fig. 3d). Furthermore, the tin foil exhibits a small fracture at the feed of the clinch point (cf. Fig. 3c). The punch movement and the axial forces at the respective MP are displayed in Fig. 3f.

The edge detection algorithm identified the sheet edges and the edges of the tin sheet properly in most cases (cf. Fig. 4). Additionally, the tool edges are detected. Gaps can be found primarily at the punch-sided sheet at MP1 (cf. Fig. 4a) and between the sheets’ outer contour and the tool edges. Furthermore, the streak artefacts are misinterpreted as edges. Although they can be removed manually, gaps residue in the punch-related edge (cf. Fig. 4b).

Summary, Discussion, and Conclusions

In order to achieve a broad application of the clinching technology, reliable simulations of the manufacturing process are necessary. Likewise, there is an increase in using in situ CT-measurements for validating numerical models. When validating numerical models of a clinching process, this approach can be advantageous as elastic

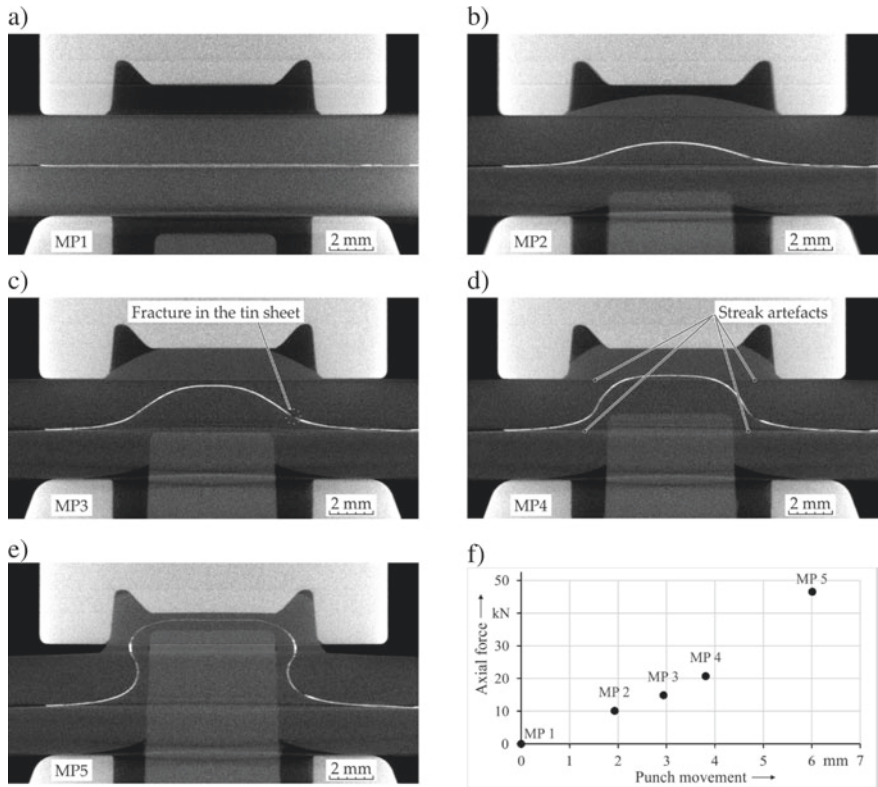


Fig. 3 CT images of the in situ clinching process (a–e) and process force and punch movement during the clinching process (f). The streak artefacts and the fracture in the tin foil are exemplarily highlighted

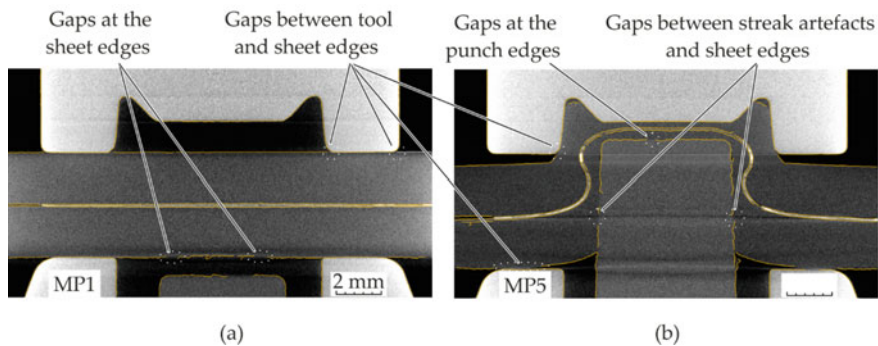


Fig. 4 CT images at MP1 and MP5 overlaid with the detected edges (yellow) using the Canny algorithm. Gaps in the detected edges are highlighted and streak artefacts which are wrongly detected as edges are removed in (b)

deformations and cracks that would close after unloading can be observed. Furthermore, the nearly complete deformation chronology can be given for an individual specimen. Therefore, in this paper, a method for in situ CT testing of a clinching process is described and the potential for validating numerical models is shown. Two aluminium sheets are clinched using a die and a blank holder made of high-strength titanium alloy and a punch made of Si₃N₄. Additionally, a tin foil is placed between the sheets in order to visualize the sheet interface at the clinch point. The clinching process is interrupted for CT scans at five stages. The results show an overall good CT image quality with few streak artefacts. To the author's knowledge, this is the first report of such an in situ method for the clinching process.

Since classic tool materials like steel are difficult to penetrate by X-rays, they are replaced by tools made of Si₃N₄ and high-strength titanium alloy. Even though a good image quality can be achieved, streak artefacts reduce the value of the CT scans as they are wrongly detected as edges. In experiments with single clinch points, these streak artefacts could be reduced by tilting the clinch point. Consequently, tilting the in situ clinching set-up is subject to further research. Additionally, there are gaps in the lower edge of the punch-sided sheet at MP1. They can be explained by the blurry edge in the CT image, which can be improved by tiling the in situ set-up as well. Nevertheless, the experiment and the image analysis prove the potential of in situ CT of clinching processes to validate numerical models. In the next step, the influence of the tin foil will be investigated and the identified sheet and tool edges will be used for validation studies with a respective numerical model.

References

1. European Commission (2018) A European Strategy for Plastics in a Circular Economy: Communication from the Commission to the European Parliament, the Council, the European Economic and Social Committee and the Committee of the Regions. Brussels
2. Ragaert K, Delva L, van Geem K (2017) Mechanical and chemical recycling of solid plastic waste. *Waste Manag* 69:24–58. <https://doi.org/10.1016/j.wasman.2017.07.044>
3. Varis J (2006) Economics of clinched joint compared to riveted joint and example of applying calculations to a volume product. *J Mater Process Technol* 172:130–138
4. Heibeck M, Rudolph M, Modler N, Reuter M, Filippatos A (2021) Characterizing material liberation of multi-material lightweight structures from shredding experiments and finite element simulations. *Miner Eng* 172:107142. <https://doi.org/10.1016/j.mineng.2021.107142>
5. Bielak C, Böhnke M, Beck R, Bobbert M, Meschut G (2021) Numerical analysis of the robustness of clinching process considering the pre-forming of the parts. *J Adv Join Proces* 3:100038. <https://doi.org/10.1016/j.jajp.2020.100038>
6. Carmignato S, Dewulf W, Leach R (2018) *Industrial x-ray computed tomography*. Springer, Cham
7. Nicoletto G, Anzelotti G, Konečná R. (2010) X-ray computed tomography vs. metallography for pore sizing and fatigue of cast Al-alloys. *Procedia Eng* 2(1):547–54. <https://doi.org/10.1016/j.proeng.2010.03.059>
8. Du Plessis A, Boshoff WP (2019) A review of X-ray computed tomography of concrete and asphalt construction materials. *Constr Build Mater* 199:637–651. <https://doi.org/10.1016/j.conbuildmat.2018.12.049>

9. Gröger B, Köhler D, Vorderbrüggen J, Troschitz J, Kupfer R, Meschut G et al (2021) Computed tomography investigation of the material structure in clinch joints in aluminium fibre-reinforced thermoplastic sheets. *Prod Eng Res Dev* 16(2–3):203–212. <https://doi.org/10.1007/s11740-021-01091-x>.
10. Drossel WG, Mauermann R, Grütznert R, Mattheß D (2013) Numerical and experimental analysis of self piercing riveting process with carbon fiber-reinforced plastic and aluminium sheets. *KEM* 554–557:1045–1054
11. Mckinley P, Kamke F, Ching D, Zauner M, Xiao X (2016) Micro X-ray computed tomography of adhesive bonds in wood. *Wood Fiber Sci: J Soc Wood Sci Technol* 48:2–16
12. Huang Y, Yang Z, Ren W, Liu G, Zhang C (2015) 3D meso-scale fracture modelling and validation of concrete based on in-situ X-ray computed tomography images using damage plasticity model. *Int J Solids Struct* 67–68:340–352. <https://doi.org/10.1016/j.ijsolstr.2015.05.002>
13. Qsymah A (2016) In-situ X-ray computed tomography tests and numerical modelling of ultra high performance fibre reinforced concrete [PhD]. The University of Manchester, Manchester
14. Füßel R, Gude M, Mertel A (2016) In-situ X-ray computed tomography analysis of adhesively bonded riveted lap joints. In: 17th european conference on composite materials. Munich
15. Pottmeyer F, Bittner J, Pinter P, Weidenmann KA (2017) In-Situ CT damage analysis of metal inserts embedded in carbon fiber-reinforced plastics. *Exp Mech* 57(9):1411–1422
16. Kratz J, Galvez-Hernandez P, Pickard LR, Belnoue J, Potter K (2021) Lab-based in-situ micro-CT observation of gaps in prepreg laminates during consolidation and cure. *Compos A Appl Sci Manuf* 140:106180. <https://doi.org/10.1016/j.compositesa.2020.106180>
17. Köhler D, Kupfer R, Gude M (2020) Clinching in in-situ CT—A numerical study on suitable tool materials. *J Adv Join Process* 2:100034. <https://doi.org/10.1016/j.jajp.2020.100034>
18. Köhler D, Kupfer R, Troschitz J, Gude M (2021) Clinching in In-situ CT—Experimental study on suitable tool materials. *ESAFORM* 2021. <https://doi.org/10.25518/esaform21.2781>
19. Köhler D, Stephan R, Kupfer R, Troschitz J, Brosius A, Gude M (2022) Investigations on combined In-situ CT and acoustic analysis during clinching. *ESAFORM 2022* (accepted)
20. Bhattacharya R, Stanton M, Dargue I, Williams G, Aylmore R (2010) Forming limit studies on different thickness aluminium 6xxx series alloys used in automotive applications. *Int J Mater Form* 3(S1):267–270. <https://doi.org/10.1007/s12289-010-0758-4>

Design Guideline of the Bolt Hole Based on the Parametric Formability Analysis



Inje Jang, Gihyun Bae, Junghan Song, Namsu Park, Jongsup Lee, Sehwan Jeong, and Heejong Lee

Abstract This paper deals with the formability analysis of the bolt hole. Mechanical properties were evaluated by the tensile test and Nakajima test in order to construct a material model for the sheet metal forming simulation. A quantitative formability evaluation method was proposed based on the simulation result, such as the strain distribution and the thinning. By using the proposed evaluation method, the parametric study was performed to investigate the effect of design parameters in the bolt hole shape. Finally, a design methodology was suggested to improve the formability of the bolt hole by controlling the main design parameters.

Keywords Bolt hole · Design guideline · Stamping · Formability analysis

Introduction

Fastening of mechanical structures is an important research field in the structural design of home appliances in order to obtain good performance without undesired vibration and noise. General methods for connecting structures are welding, bolting, and riveting, etc. Among these methods, bolting is the most traditional and essential method. The bolted joint has significant effects on the structural behavior. Therefore, the proper design is necessary because it has a great influence on the reduction of performance and durability due to stress concentration or fatigue failure [1–4]. In recent years, it is difficult to achieve fine appearance and high stiffness of a bolt hole because the structure has severe geometrical constraints and requires a strong fastening force. However, the design method of the bolt hole shape still depends on the engineer's experience and know-how in spite of the enormous failure cost. Therefore,

I. Jang · G. Bae (✉) · J. Song · N. Park · J. Lee
Metal Forming R&D Group, Korea Institute of Industrial Technology, 156, Gaetbeol-ro
(Songdo-dong), Yeonsu-gu, Incheon 21999, Republic of Korea
e-mail: baegh@kitech.re.kr

S. Jeong · H. Lee
Core Technology Team, Production Engineering Research Institute, 222, LG-ro, Jinwi-myeon,
Pyeongtaek-si, Gyeonggi-do, Republic of Korea

it is necessary to establish an efficient design guideline based on the quantitative formability evaluation of the bolt hole with respect to the design parameter.

In this study, formability analysis of the bolt hole was performed by the parametric study in order to identify the effectiveness of the design parameters of the bolt hole. Sheet metal forming simulation was conducted for bolt hole formability analysis. The mechanical properties of the forming simulation were evaluated by the tensile test and Nakajima test. The simulation results were analyzed to quantify the formability variation based on the major/minor strain distribution and the local thinning. The parametric study was performed with respect to the geometrical parameters of the bolt hole in order to suggest the main factors in formability of the bolt hole. Finally, the parametric study result can be utilized to construct a design guideline to improve the formability of bolt holes for various home appliances.

Material Characterization

Tensile Test

HXKE4K 0.42t mild steel sheet used for general home appliances was selected as the target material for the formability analysis of the bolt hole. A tensile test was carried out by using MTS 810 universal tester with a capacity of 10 tons. ARAMIS DIC system was used to measure the strain distribution on the specimen surface during the tensile test. The specimen was prepared by referring to ASTM E8M standard specimen specifications. The strain rate was 0.001/s for the quasi-static loading condition. The gauge length for the strain measurement was 25 mm at the specimen center. In order to evaluate the anisotropy characteristics, specimens were prepared along the loading direction of 0° (Rolling Direction, RD), 45° (Diagonal Direction, DD), and 90° (Transverse Direction, TD). Figure 1a shows the flow stress curves according to the loading angle from the rolling direction. The mechanical properties are presented in Table 1. Hill's 48 yield function expressed by Eq. (1) was used in order to consider the anisotropic behavior of the sheet material. Hill's 48 yield locus as shown in Fig. 1b was constructed by using the r -value and the yield stress.

The linear combination of Swift $K(\varepsilon + \varepsilon_0)^n$ and Hockett–Sherby $(\sigma_{sat} - (\sigma_{sat} - \sigma_i)e^{-c\varepsilon^p})$ hardening law with weighting value α was used to describe the isotropic expansion behavior of the yield surface. The calibrated coefficients of the Swift/Hockett–Sherby model are shown in Table 2.

$$\bar{\sigma} = \sqrt{(G + H)\sigma_{xx}^2 - 2H\sigma_{xx}\sigma_{yy} + (H + F)\sigma_{yy}^2 + 2N\sigma_{xy}^2} \quad (1)$$

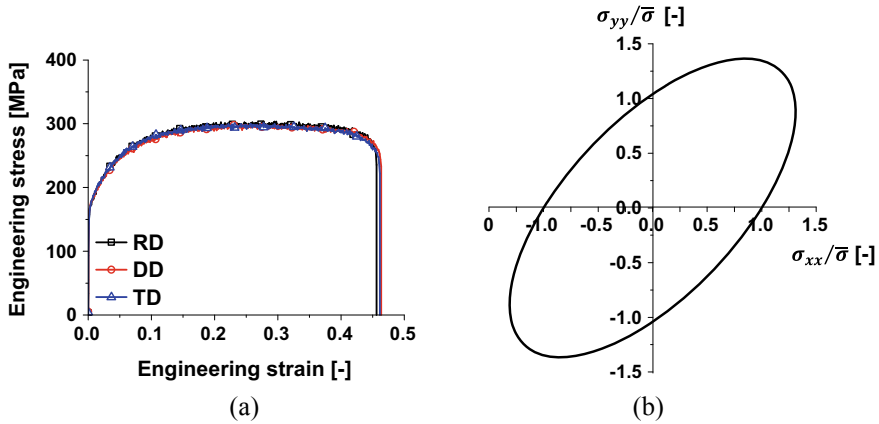


Fig. 1 Tensile test results: **a** Eng. stress–Eng. strain curve; **b** Hill's 48 yield locus

Table 1 Mechanical properties according to the loading angle from the rolling direction

Loading direction [°]	ϵ_u [-]	ϵ_f [-]	YS [MPa]	UTS [MPa]	r -value [-]	\bar{r} [-]	Δr [-]
0 (RD)	0.26	0.46	169.26	303.48	1.64	1.84	0.02
45 (DD)	0.27	0.46	168.31	299.40	1.82		
90 (TD)	0.21	0.46	169.18	299.79	2.06		

Table 2 Parameters of Swift/Hockett–Sherby hardening law

K [MPa]	ϵ_0 [-]	n [-]	σ_i [MPa]	σ_{sat} [MPa]	c [-]	P [-]	α [-]
540.71	0.0076	0.25	157.61	489.90	2.89	0.66	0.25

Nakajima Test

The Nakajima test was performed for evaluating the forming limit of the test material. The specimen shape follows ISO 12004 standard. Specimens with various widths were prepared to induce a wide range of linear loading paths. This test was performed with a universal formability test machine with a capacity of 200 tons. The blank holding force was 20 tons for preventing the material draw-in at the flange. The punch speed was 1 mm/s and the test was performed after applying grease to the blank and punch for lubrication. Finally, the forming limit curve was obtained as shown in Fig. 2b based on the forming limits in various loading paths.

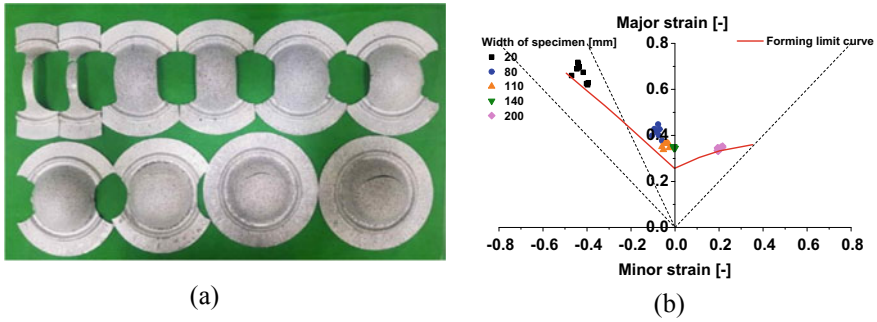


Fig. 2 Nakajima test result: **a** Specimen after Nakajima test; **b** Forming limit diagram

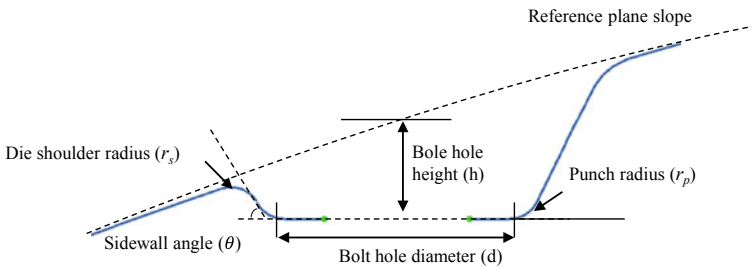


Fig. 3 Schematic diagram of the bolt hole shape and main geometrical parameters

Bolt Hole Formability Analysis

Shape Analysis of Bolt Hole

The bolt hole shape was investigated from home appliances to evaluate the influence on the formability during the sheet metal forming process. Recently, the bolt hole of general home appliances is formed on the smooth curved surface. Figure 3 shows the schematic shape of the bolt hole and its parameters in general home appliances. Table 3 shows the range of design parameters which are selected by referring to the shape of general home appliances.

Quantitative Evaluation of the Bolt Hole Formability

The bolt hole formability was quantified by FE analysis using Autoform R8. Figure 4a shows the FE modeling for the sheet metal forming simulation. Strain distribution on forming limit diagram (FLD) and thinning was selected to quantify the formability.

Table 3 Shape design parameters for bolt hole formability analysis

Design parameter	Reference value	Design range
Thickness [mm]	0.5	0.4–0.6
Sidewall angle [deg.]	25	15–35
Bolt hole height [mm]	3	2–4
Die shoulder radius [mm]	15	1–2
Bolt hole diameter [mm]	8	6–10
Punch radius [mm]	1.5	1–2

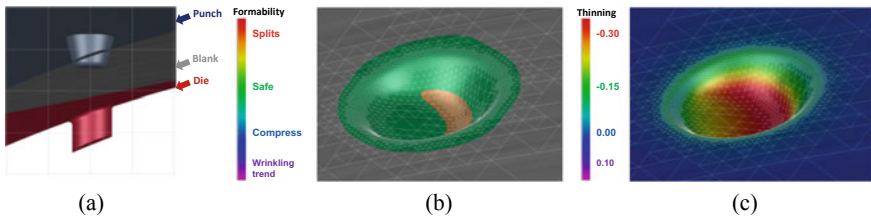


Fig. 4 FE model and simulation result of the bolt hole forming process: **a** FE model; **b** Formability; **c** Thinning

The simulation result as described in Fig. 4b, c shows that severe formability occurs at the punch corner.

The maximum amount of thinning can be directly used for quantitative evaluation of the formability. On the other hand, a proper method is required to quantify the major and minor strain distribution on FLD. The strain path at the punch corner, where maximum deformation occurs, is under the biaxial loading as shown in Fig. 5. Based on this information, FLD ratio, which is the ratio between FLD_{Ref} and FLD_{mar} , was proposed as a new parameter for the quantitative evaluation of the strain distribution. Here, FLD_{Ref} and FLD_{mar} are the distance of the origin point and the nearest point on FLD from FLC under the biaxial loading condition, respectively.

Parametric Study

A parameter study was conducted to investigate the effect on the formability of shape parameters in the design range. The results of the quantitative evaluation of formability according to the shape design parameters are summarized in Table 4 and Fig. 6. The bolt hole height was evaluated as the most influential parameter, and the sheet thickness and the die shoulder radius were evaluated as insignificant parameters. The results also show that design parameters related to the punch corner shape, which are the bolt hole height and the punch radius, have large effectiveness on

Fig. 5 Quantification of formability based on FLD

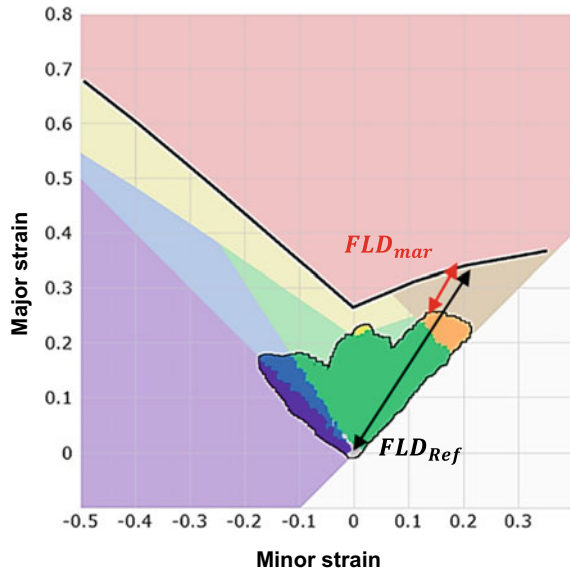
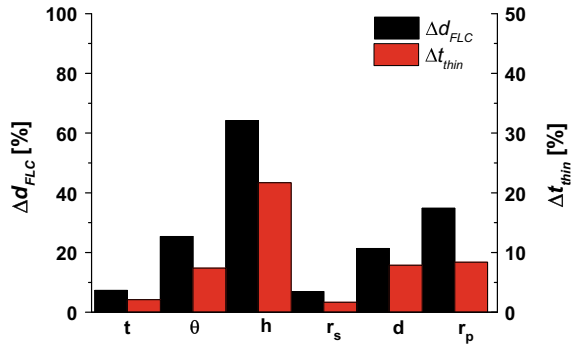


Table 4 Parametric study results of the bolt hole formability

Design parameter	Case	$d_{FLCratio}$ (%)	$\Delta d_{FLCratio}$ (%)	t_{thin} (%)	Δt_{thin} (%)
Thickness (t)	t_{lower} : 0.4 mm	33.1	7.3	29.5	2.1
	t_{upper} : 0.6 mm	25.8		31.6	
Sidewall angle (θ_w)	$\theta_{w,lower}$: 15 deg.	17.5	25.4	33.9	7.4
	$\theta_{w,upper}$: 35 deg.	42.9		26.5	
Bolt hole height (h)	h_{lower} : 2 mm	58.3	64.1	19.9	21.7
	h_{upper} : 4 mm	-5.8		41.6	
Die shoulder radius (r_s)	$r_{s,lower}$: 1 mm	27.1	7.0	31.7	1.7
	$r_{s,upper}$: 2 mm	34.1		30.0	
Bolt hole diameter (d)	d_{lower} : 6 mm	16.1	21.3	35.5	7.9
	d_{upper} : 10 mm	37.4		27.6	
Punch radius (r_p)	$r_{p,lower}$: 1 mm	3.9	34.8	36.4	8.4
	$r_{p,upper}$: 2 mm	38.7		28.0	

the formability due to the deformation concentration. This information can be utilized as a design guideline for improving the formability when a local crack occurs at the bolt hole during the forming process.

Fig. 6 Sensitivity analysis of the bolt hole formability according to shape design parameters



Conclusion

In this study, the parametric study was performed based on the quantitative formability evaluation in order to establish the bolt hole design guideline. Bolt hole forming simulation was carried out to evaluate the formability and the mechanical properties required for the simulation were obtained through the tensile test and Nakajima test. Simulation results show that the deformation is concentrated at the punch corners. It means that the formability can be quantified by using the strain distribution in this area. From the parameter study, it was confirmed that the parameters related to the punch corner shape where the deformation is concentrated had a great influence on the formability. It would be effective to design or improve the bolt hole forming process by controlling the main parameters. This design scheme will be useful for enhancing forming process design efficiency and reducing the manufacturing failure cost.

References

1. Cho JH, Kang OS, Kim DS (2005) Structural analysis of clearance effects on system with bolted joint. Proc KSAE Fall Conf 2:1485–1490
2. Yoon JC, Kang BS, Kim J (2003) A study on finite element modeling of the structure with bolted joints. J Korean Soc Precis Eng 20(8):205–212
3. Chang H, Cho SS, Lee KW (2006) Procedure development for determination of optimal preload for engine connecting-rod bolts using CAE (Computer-Aided Engineering). Proc KSAE Spring Conf 2:1248–1255
4. Kwon YD, Goo NS, Cho MH (2002) Finite element modeling for static and dynamic analysis of structures with bolted joints. Trans Korean Soc Mech Eng A 26(4):667–676

Experimental and Numerical Evaluation of DP600 Fracture Limits



Yang Song, Iman Sari Sarraf, and Daniel E. Green

Abstract The main objective of this research is to evaluate the performance of the digital image correlation (DIC) method and the numerical models used to determine and predict the fracture strains of DP600 steel sheets subjected to various strain paths. Accordingly, Nakazima [1] tests along with 3D-DIC strain measurements were conducted to evaluate necking and fracture strains. Fracture strains were experimentally determined assuming plane-strain deformation after the onset of necking, using DIC surface strain and in situ thickness measurement at the fracture site. In addition, quasi-static and dynamic uniaxial tension tests and hydraulic bulge tests were carried out to calibrate a modified Johnson–Cook (mJC) hardening function, and two versions of the JC damage models. It was shown that the fracture strains predicted by the numerical simulations are in good agreement with the experimental DIC data. Therefore, the proposed DIC method can be effectively used to estimate the necking and fracture limit diagrams of sheet metals.

Introduction

There is an increasing demand in the automotive industry to reduce both vehicle weight and gas emissions [2]. Finite element (FE) simulation is widely used to predict the forming behaviour of higher strength lower formability materials such as advanced high strength steels (AHSS), in order to produce strong lightweight automotive components. Nakazima tests are frequently used along with DIC to quantify the forming limit of sheet materials, due to its simplicity in the experimental setup, and also its capability of reaching a wide range of strain states [3] which produces

Y. Song (✉) · I. S. Sarraf · D. E. Green
University of Windsor, 401 Sunset Ave., Windsor, ON N9B 3P4, Canada
e-mail: songw@uwindsor.ca

I. S. Sarraf
e-mail: sarisa@uwindsor.ca

D. E. Green
e-mail: dgreen@uwindsor.ca

a more complete forming limit diagram (FLD). The process-dependent effects in necking limit determined by Nakazima tests can be compensated using a process proposed by Min et al. [3]. The DIC method is a non-contact method for tracking surface deformation history that has gained popularity in the past few decades; it has many advantages [4] over the previous standardized method that uses a grid measurement system [5]. The hydraulic bulge test is a near biaxial stretching test in which a fluid is pressurized in a chamber sealed by the sheet specimen. The bulge test data produces flow curves up to a higher strain level than uniaxial tensile tests, which is inherently due to stretching in a near biaxial stress condition. This is advantageous for implementation in numerical models to predict material behaviour at higher strain levels.

This manuscript investigates the effectiveness of fracture strain estimation of DP600 steel sheets using DIC strain data, which is validated against FE simulations using calibrated JC constitutive and damage models.

DP600 Sheet Material

A galvanized DP600 sheet steel with a 1.5-mm nominal thickness was used in this research. It has a volume fraction of 4.7%, 3.3%, and 92.0% for martensite, bainite, and ferrite, respectively [6]. The material exhibits relatively low anisotropy [7, 8] and low strain rate dependency [8, 9].

Constitutive Models and Finite Element Simulations

One of the essential steps in modelling the mechanical behaviour of engineering materials is to utilize accurately determined hardening functions and damage criteria. In order to define the hardening behaviour of DP600 sheet specimens, two hardening functions were chosen: (a) a modified version of the Johnson–Cook (mJC) hardening function as an unbounded hardening model (Eq. 1a) and (b) a multiplicative combination of the Voce equation and modified Johnson–Cook function (VmJC) as a saturated model (Eq. 1b). A combination of the non-linear regression and Markov Chain Monte Carlo (NLR+MCMC) method was used to find the best parameters that fit the experimental data points obtained through uniaxial tension and hydraulic bulge tests [2, 10, 11].

The JC damage criterion [12] was chosen to predict the ductile fracture in the simulation of the Nakazima tests. Unlike micro-mechanical damage models where the accumulation of damage is defined by nucleation growth and coalescence of voids, damage accumulation in JC damage criterion is separated from the constitutive model and damage parameters are determined based on the fracture behaviour of the material under various strain paths and stress states [13]. It predicts the critical fracture strain as a function of equivalent plastic strain (ϵ_p), strain rate ($\dot{\epsilon}_p$), temperature (T), and

stress triaxiality (η) as shown in Eq. 1c. $C_{1...5}$ in Eq. 1a and Eq. 1b are hardening function constants, which are determined by an appropriate fitting procedure, and $D_{1...5}$ in Eq. 1c are material dependent constants which are determined based on the quasi-static and dynamic behaviour of the material. It is worth noting that the damage parameters were determined based on the uniaxial tension tests, hydraulic bulge test, and a multi-stage rolling process [14–16].

$$\sigma(\varepsilon_p, \dot{\varepsilon}_p) = (C_1 + C_2\varepsilon_p^{C_3}) \left[1 + C_4 \left(\ln \frac{\dot{\varepsilon}_p}{\dot{\varepsilon}_0} \right)^{C_5} \right] \tag{1a}$$

$$\sigma(\varepsilon_p, \dot{\varepsilon}_p) = C_1 - (C_1 - C_2)(1 - \exp(-C_3\varepsilon_p)) \left[1 + C_4 \left(\ln \frac{\dot{\varepsilon}_p}{\dot{\varepsilon}_0} \right)^{C_5} \right] \tag{1b}$$

$$\varepsilon_f = [D_1 + D_2 \exp(D_3\eta)] \left[1 + D_4 \ln \left(\frac{\dot{\varepsilon}_p}{\dot{\varepsilon}_0} \right) \right] [1 + D_5 T^*] \tag{1c}$$

Table 1 shows the hardening function constants and JC damage parameters that were calibrated to the experiments.

To simulate the Nakazima tests, the punch, blank holder, and the upper die as shown in Fig. 1, were considered rigid bodies, while the test specimen was modelled as a deformable part. Since the DP600 sheet that was used in this research did not show any significant anisotropy, only one quarter of the sheet specimens were modelled and meshed using 8-node reduced integration-brick elements (C3D8R) in order to reduce the computational cost. Mesh sensitivity studies were carried out using element sizes ranging from 1 mm to 0.1 mm in the centre of the specimen where the damage is more likely to occur. Consequently, an element size of 0.3 mm with five elements through the thickness demonstrated the best results. Symmetric boundary conditions were applied. The hardening functions were implemented in a VUHARD subroutine code, and a dynamic explicit approach was employed to simulate the Nakazima tests. General contact with a coefficient of friction of 0.5 was used for all surfaces in contact except the contact between the punch and the bottom surface of the sheet specimens where that coefficient of friction was considered as

Table 1 Calibrated hardening coefficients and damage function parameters obtained for DP600

	C_1	C_2	C_3	C_4	C_5
mJC (1a)	225.35	850.10	0.3194	0.0037	1.5715
VmJC (1b)	400.21	795.19	9.0236	0.0015	1.9430
	D_1	D_2	D_3	D_4	D_5
JC (damage, 1c)	0.56	0.47	4.5	-0.006	0

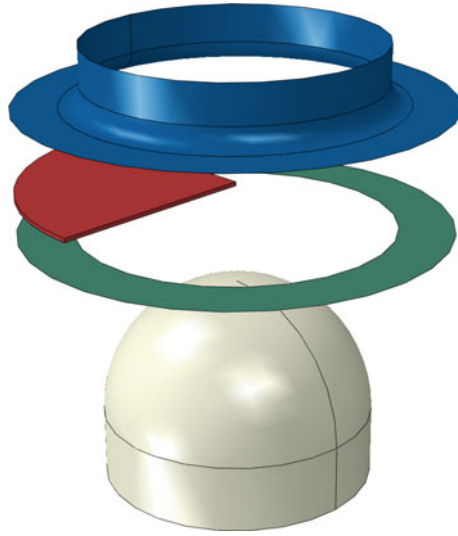


Fig. 1 Finite element model of the Nakazima test (BT). From top to bottom: upper die, test piece, blank holder, hemispherical punch

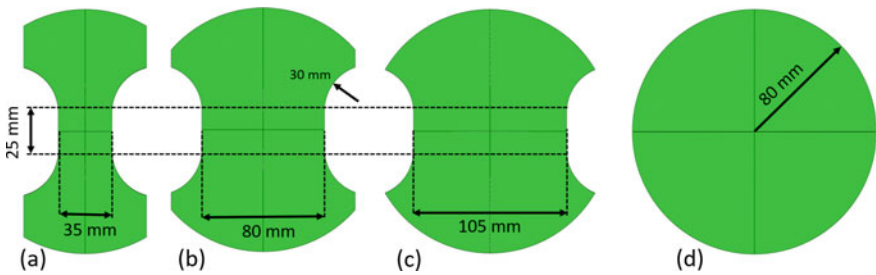


Fig. 2 Specimen geometry for Nakazima tests: **a** uniaxial tension (UT), **b** plane strain 1 (PS1), **c** plane strain 2 (PS2), and **d** biaxial tension (BT)

0.02 due to the lubrication that was used to minimize friction. The finite element model used to simulate the Nakazima tests as well as the geometry of the specimens used to generate different strain paths are shown in Figs. 1 and 2, respectively.

Calibration Tests

The large deformation work hardening behaviour of DP600 sheets was determined using a combination of tensile tests and hydraulic bulge tests, as described by Sari Sarraf et al. [11].

Tensile Tests

Uniaxial tension tests were used to characterize the DP600 sheet in terms of work hardening and damage behaviour. Tests were conducted at strain rates ranging from quasi-static (0.001, 0.1, and 1 s^{-1}) to elevated strain rates (10 and 100 s^{-1}), with DIC strain measurements. The testing apparatus, setup, specimen geometries, and detailed experimental procedures are provided by Rahmaan et al. [8].

Hydraulic Bulge Tests

Bulge tests were carried out according to ISO-16808:2014 standard [17] using a custom set of tools in a double-action hydraulic press, which controls the pressure of the fluid to form the specimen. The specialized tools feature a 135-mm-diameter cavity, an 8.5-mm fillet at clamp ring contact, and are equipped with an in cavity pressure transducer to track the fluid pressure history. Details of the test equipment are provided by Vasilescu [18]. Two cameras, equipped with 35-mm lenses, mounted at 30°C from each other were used to access the top surface of the test specimen for DIC strain measurement. The camera frame rate was set 10Hz. An improved method to estimate the instantaneous sheet thickness at the pole [19] was adopted to increase the accuracy of strain measurements. Bulge test data were used to extend the flow curve acquired from uniaxial tensile tests.

Nakazima Tests

Nakazima tests were performed in the same double-action hydraulic press, using a set of specialized tools with dimensions conforming to ISO 12004-2:2008 standard [20]. The detailed apparatus and experimental setup can be found in previous work by Song et al. [4]. The setup of the DIC camera system and the parameters used in DIC post-processing were very similar to those of the bulge test. Specimen geometries of different widths were designed to generate five various strain paths. All geometries except the full blank for biaxial tension condition (geometry #5), have a gauge length of 25 mm and a transitional radius of 30 mm. Geometries #1, 2, 3, and 4 have gauge widths of 35 mm, 80 mm, 105 mm, and 160 mm, respectively. This minimum specimen width is the dominant parameter for controlling the strain path during forming. Figure 3 shows the strain paths achieved in the Nakazima tests and the corresponding specimen geometries. A tribo-system composed of double-layer PTFE films and petroleum jelly was placed between the punch and the specimen to minimize friction.

The necking limits for the tested Nakazima specimens were analyzed using commercial DIC software Vic-3D and a custom MATLAB code. The surface slope

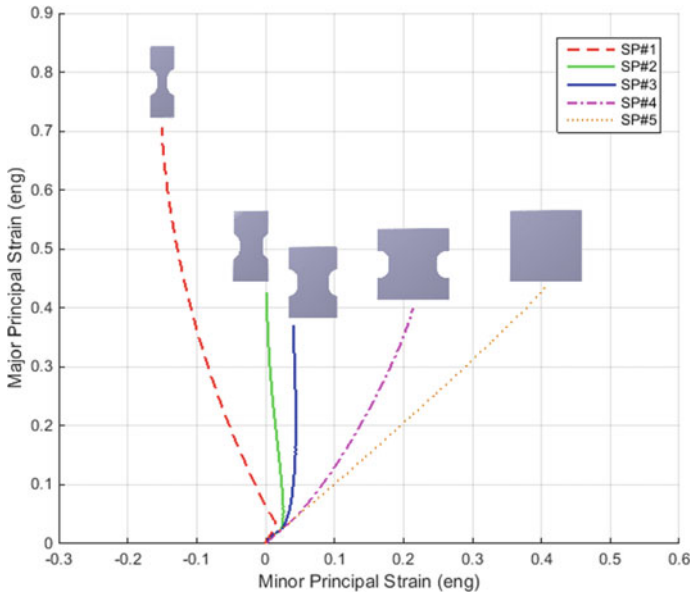


Fig. 3 Nakazima test strain paths and the corresponding geometries: #1 uniaxial tension (UT), #2 plane strain 1 (PS1), #3 plane strain 2 (PS2), #4 intermediate stretch (IS), and #5 biaxial tension (BT)

necking criterion, a time- and geometry-dependent necking criterion adopted from Martínez-Donaire et al. [21] with minimal modification [4], was used to identify the onset of necking. The determined necking limit strains were then corrected for process-dependent effects with the method proposed by Min et al. [3].

Fracture strains were measured assuming plane-strain deformation after the onset of necking [22]. The minor strain was measured using DIC in close vicinity to the location of the onset of fracture, at the last frame before fracture. The thickness strain was physically measured post-forming using a calibrated ultrasonic probe directly at the fracture site. The major strain was then calculated assuming volume constancy.

Results and Discussion

The necking and fracture limits determined using Nakazima tests are shown in Fig. 4. Linear and quadratic functions representing the Necking and Fracture FLCs (NFLCs and FFLCs) are also shown in Fig. 4. It is observed that the lowest point of the necking limit curve (NFLC) is shifted to about 4.3% minor strain. This is typical of Nakazima test data and is effectively corrected back to plane-strain (minor strain equal to zero) using the compensation method [3], as shown in Fig. 5.

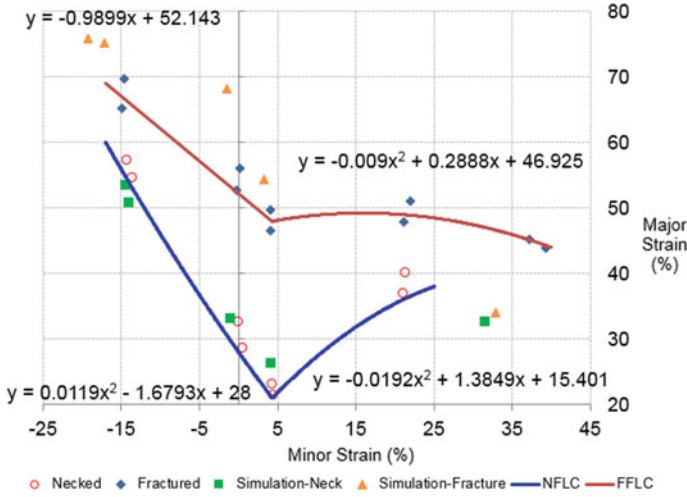


Fig. 4 NFLC and FFLC of 1.5mm DP600 obtained from Nakazima tests and simulation

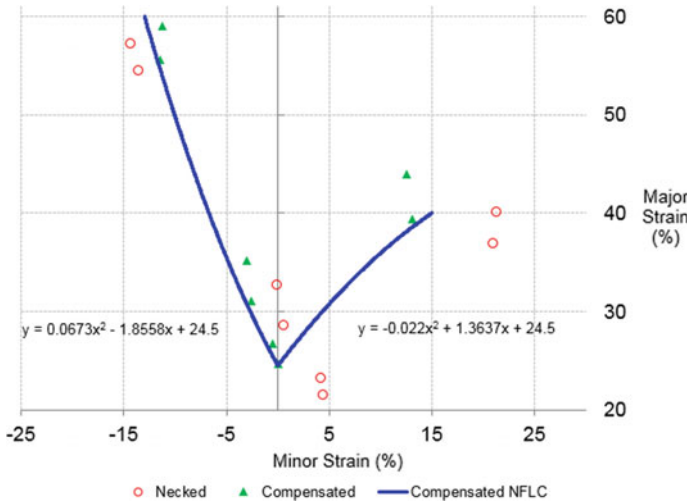


Fig. 5 Compensated Necking FLD—Nakazima—DP600

It is also observed that the FFLC follows a trend that is similar to that of the NFLC, where the lowest major strain limit occurs at geometry #3 (PS2). This same trend is observed in other studies [23, 24]. The difference between NFLC and FFLC decreases toward positive minor strains, which is justified by the fact that DP600 sheet material does not show localized necking under biaxial tension.

Since the NFLC from FE simulation is constructed based on the onset of necking, it is necessary to utilize a precise approach to extract the limiting strains throughout the simulation of Nakazima tests that can efficiently be applied for various strain paths.

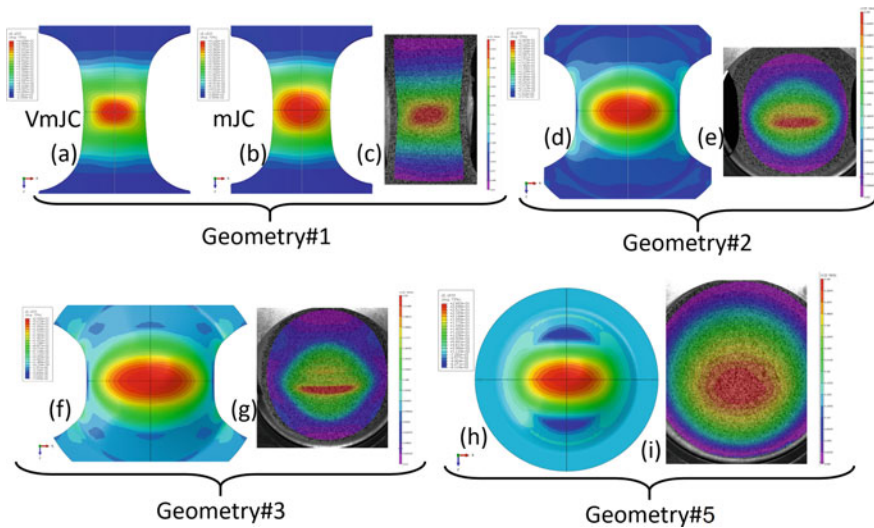


Fig. 6 Distribution of the major strain on Nakazima specimens, **a, b, d, f, h** numerical models and **c, e, g, i** DIC results

Therefore, a criterion was determined based on the first derivative of the thickness strain, where a sudden change in the rate of deformation occurs at the onset of plastic instability. As described by Sarraf et al. [2], the thickness strain and its first derivative were obtained from the numerical results. Two polynomial functions were then fitted to the two branches of the $\epsilon \dot{\epsilon}_t$, and the intersection point of two bifurcation branches was considered as the onset of the necking [2, 25] and the time associated with this point was determined as the critical necking time. Consequently, the major and minor strains corresponding with the critical time were considered the limiting strains on the FLD. Figure 6 shows the distribution of the major strain on the Nakazima test specimens obtained using numerical simulations and through DIC method from experiments in different strain paths. It can be seen that both the location of strain localization and the strain distribution around the neck were predicted successfully using the combination of VmJC or mJC as the hardening function and JC as the ductile damage model. However, the diffuse neck in the middle of the gauge area in geometry #1 (UT) is more evident when using VmJC compared to mJC because the VmJC reaches a plateau (zero strain-hardening) at high strains, while mJC shows approximately constant positive strain hardening.

The geometry of the fracture and the distribution of the equivalent plastic strain on the Nakazima test specimens predicted by the simulations are presented in Fig. 7. As the experimental test showed, the fracture starts from the middle of the specimens for various strain paths and propagates towards the edge of the gauge area. As mentioned previously, the distribution of the strain around the damaged area in Geometry #1 is more localized when using the VmJC compared to the mJC hardening models due to their saturated and unbounded behaviours at high strain levels.

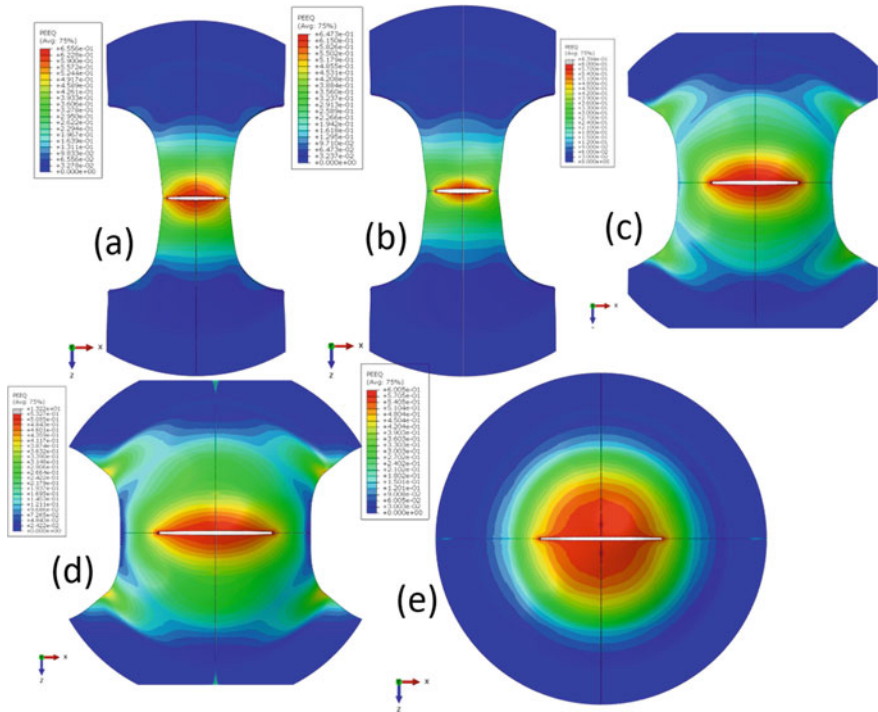


Fig. 7 Geometry of the fracture and distribution of the equivalent plastic strain on the FE models, **a** Geometry #1 (mJC), **b** Geometry #1 (VmJC), **c** Geometry #2, **d** Geometry #3, and **e** Geometry #5

The critical points in terms of the necking and fracture strains obtained through numerical simulations for various strain paths are presented in Fig. 4. It can be seen that there is a good agreement between the numerically predicted and experimentally obtained necking and fracture strains for geometries #1 and 2. The model slightly overestimates the necking strains for geometry #3 and significantly underestimates the limiting strains in geometry #5. Further investigations on the evolution of damage in biaxial stretching conditions will be carried out. It is noteworthy that the effect of the hardening function on the prediction of the critical strains was found to be negligible. The overprediction of the fracture strain for geometries #1, 2, and 3 can be attributed to the fact that the critical strain at the onset of fracture can be accurately determined based on a damaged element that is located exactly in the middle of the fractured area while the experimental procedure relies on the last frame of the DIC strain measurement in the vicinity of the crack initiation. Moreover, it is shown that the post uniform deformation and fracture are microstructure- and inhomogeneity-dependent, and incorporating these non-uniformities in a numerical model would increase the accuracy of the simulations [26].

Conclusions

The following conclusions can be made from the results of current research:

- the DIC method is reliable in estimating the necking and fracture limits for Nakazima formability tests,
- the combination of mJC or VmJC hardening functions with the JC damage model successfully predicted the limiting and fracture strains in uniaxial tension and plane-strain testing conditions.

References

1. Nakazima K, Kikuma T, Hasuka K (1968) Study on the formability of steel sheets. Yawata Tech Rep 264:8517–8530
2. Sari Sarraf I (2017) Meso-scale modelling of deformation, damage and failure in dual phase steels. PhD thesis, University of Windsor
3. Min J, Stoughton TB, Carsley JE, Lin J (2016) Compensation for process-dependent effects in the determination of localized necking limits. *Int J Mech Sci* 117:115–134
4. Song Y, Green DE, Rose A (2019) Investigation of various necking criteria for sheet metal formability analysis using digital image strain data. *Int J Mater Form* 1–10
5. ASTM International (2015) Standard test method for determining forming limit curves
6. Samei J, Green DE, Cheng J, de Carvalho Lima MS (2016) Influence of strain path on nucleation and growth of voids in dual phase steel sheets. *Mater Des* 92:1028–1037
7. Hassannejadasl A, Rahmaan T, Green DE, Golovashchenko SF, Worswick MJ (2014) Prediction of DP600 flow surfaces at various strain-rates using yld2004-18p yield function. *Procedia Eng* 81:1378–1383
8. Rahmaan T, Bardelcik A, Imbert J, Butcher C, Worswick M (2016) Effect of strain rate on flow stress and anisotropy of DP600, TRIP780, and AA5182-O sheet metal alloys. *Int J Impact Eng* 88:72–90
9. Maris C, Hassannejadasl A, Green DE, Cheng J, Golovashchenko SF, Gillard AJ, Liang Y (2016) Comparison of quasi-static and electrohydraulic free forming limits for DP600 and AA5182 sheets. *J Mater Process Technol* 235:206–219
10. Sarraf IS, Jenab A, Boyle KP, Green DE (2017) Effect of rate-dependent constitutive equations on the tensile flow behaviour of DP600 using Rousselier damage model. *Mater Des* 117:267–279
11. Sarraf IS, Green DE (2018) A numerical method to predict the rate-sensitive hardening behaviour of sheet materials using uniaxial and biaxial flow curves. In: *IOP conference series: materials science and engineering*, vol 418, p 012087
12. Johnson GR, Cook WH (1985) Fracture characteristics of three metals subjected to various strains, strain rates, temperatures and pressures. *Eng Fract Mech* 21(1):31–48
13. Hassannejadasl A, Green DE, Altenhof WJ, Maris C, Mason M (2013) Numerical modeling of multi-stage tube hydropiercing. *Materials & Design* 46:235–246
14. Hassannejadasl A, Green DE, Golovashchenko SF, Samei J, Maris C (2014) Numerical modelling of electrohydraulic free-forming and die-forming of DP590 steel. *J Manuf Process* 16(3):391–404
15. Sarraf IS, Green DE, Jenab A (2018) Damage evolution and void coalescence in finite-element modelling of DP600 using a modified Rousselier model. *Eng Fract Mech* 196:168–190

16. Sarraf IS, Green DE (2019) Prediction of damage accumulation in the multi-stage rolling of DP600 steel sheets. In: NUMIFORM 2019: The 13th international conference on numerical methods in industrial forming processes
17. ISO (2014) Metallic materials - sheet and strip - determination of biaxial stress-strain curve by means of bulge test with optical measuring systems. In: ISO16808
18. Vasilescu M (2016) Development of a hydraulic bulge test to determine the work hardening behaviour of sheet materials. Master's thesis, University of Windsor
19. Min J, Stoughton TB, Carsley JE, Carlson BE, Lin J, Gao X (2017) Accurate characterization of biaxial stress-strain response of sheet metal from bulge testing. *Int J Plast* 94:192–213
20. International Organization for Standardization (2008) Metallic materials - sheet and strip - determination of forming-limit curves - part 2: determination of forming-limit curves in the laboratory
21. Martínez-Donaire A, García-Lomas F, Vallellano C (2014) New approaches to detect the onset of localised necking in sheets under through-thickness strain gradients. *Mater Des* 57:135–145
22. Borrego M, Morales-Palma D, Martínez-Donaire A, Centeno G, Vallellano C (2019) Analysis of formability in conventional hole flanging of AA7075-O sheets: punch edge radius effect and limitations of the FLC. *Int J Mater Forming* 1–14
23. Cardoso M, Moreira L (2015) Forming limit analysis of DP600-800 steels. *Int J Mater Metall Eng* 9(9):1123–1130
24. Lian JH, Liu PF, Münstermann S (2013) Modeling of damage and failure of dual phase steel in nakajima test. *Key Eng Mater* 525:69–72; *Trans Tech Publ*
25. Zhang C, Leotoing L, Guines D, Ragneau E (2009) Theoretical and numerical study of strain rate influence on AA5083 formability. *J Mater Process Technol* 209:3849–3858
26. Gorji MB, Manopulo N, Hora P, Barlat F (2016) Numerical investigation of the post-necking behavior of aluminum sheets in the presence of geometrical and material inhomogeneities. *Int J Solids Struct* 102–103:56–65

FE Simulations About the Influence of Work Hardening Derived from Embossing Process on Hole-Expansion of Duplex Embossed Sheet



You Yu, Wuyang Liu, and Takashi Iizuka

Abstract Embossing process is a prevalent method of enhancing the flexural rigidity of sheet metal. Also, it could realize multifunctions due to its good performances in heat radiation, energy absorption, sound insulation, etc. It is well known that its mechanical properties depend on the crystal texture generated by the rolling process and subsequent heat treatment. Theoretically, formability has a good correlation to mechanical properties. As for the apparent mechanical properties of embossed sheets, there were many investigations conducted. However, as for embossed sheets, the investigation of formability has not been conducted so much, yet. In order to investigate the stretch flange deformation of duplex embossed sheet, in this study, the FE simulations of hole-expansion for embossed sheets were conducted. Stretch flange deformation behavior of embossed sheets with and without work hardening was compared. Finally, the effects of preliminary work hardening and embossing direction on hole-expansion were also discussed.

Introduction

In recent decades, in order to protect the environment, lightweight was more and more demanded. As for lightweight, the use of sheet metal with thinner thickness could reduce the weight to some extent. However, the flexure rigidity and formability of thinner sheet metal are usually weaker than that of the thicker or heavier sheet metal. In order to overcome these problems, although many strategies were proposed [1, 2], the usage of embossed sheets can be thought of as one of the most effective methods to realize lightweight together with high rigidity and high formability.

Embossing process, which can be alternatively named the dimple process, could be conducted using roll forming or stamping process. When a plain sheet metal is subjected to embossing process, a periodic convex–concave structure would be formed. In other words, cross section of the sheet becomes wavy, so the flexural rigidity would be enhanced due to the increase of the sectional secondary moment.

Y. Yu (✉) · W. Liu · T. Iizuka

Kyoto Institute of Technology, Matsugasaki Goshokaido-cho, Sakyo-ku, Kyoto 606-8585, Japan
e-mail: m9623105@edu.kit.ac.jp

© The Minerals, Metals & Materials Society 2022

K. Inal et al. (eds.), *NUMISHEET 2022*, The Minerals, Metals & Materials Series,
https://doi.org/10.1007/978-3-031-06212-4_78

In addition, it has been reported that by giving appropriate embossing patterns, resistance to deep drawing in the flange area decreased and the strength at the punch shoulder increased [3]. Also, there are many functional merits derived from embossing structures, such as heat radiation-ability, heat diffusivity, sound insulation, friction reduction, etc. Thanks to these merits, embossed sheets are getting more and more widely applied as architecture material, automotive component, and so on. On the other hand, understanding of mechanics and formability of embossed sheet is insufficient, and forming of embossed sheet has still been conducted mainly on the basis of empirical ways at practical press shops. When an embossed sheet is regarded as a kind of tailored or designed material, it would be a good attempt to confirm whether formability of such a sheet could be discussed in the theoretical framework for plain sheet metals or not.

As for plain sheet metals, it is well known that the mechanical properties depend on crystal texture derived from rolling process and subsequent heat treatment. And theoretically, formability like deep-drawability, stretchability, and hole-extensibility has good correlations to Lankford value, work hardening exponent, and local elongation, respectively. When a plain sheet metal is embossed, 'apparent' mechanical properties of the sheet would be changed from those for plain sheet to new ones depending on the quasi-uniform embossing structure. Through previous reports, it was verified that the periodical embossing structure provided new apparent mechanical properties and their new anisotropy to the sheet [4] and that the apparent plastic anisotropy of embossed sheets emerges as a superposition of both anisotropies for crystal texture and embossing structure [5]. It was also reported that these apparent mechanical properties of embossed sheet changed by annealing process because the process could almost remove the effects of work hardening experienced during embossing [6]. Kim et al. reported that apparent yield locus of an embossed sheet was different from those for the original plain sheet close to Tresca's criterion and had more round corner around equi-biaxial tension state [7]. Apparent elastic properties of embossed sheets have also been investigated and the difference in springback amount of embossed sheets from that of the original plain sheet was examined [8, 9]. Moreover, improvement of energy absorption by the usage of embossed sheets has also been attempted until now [10].

On the other hand, formability of embossed sheets has still not been studied so much, yet. In the previous studies, deep drawing test and Erichsen test using duplex embossed sheet metal were only attempted and the Limiting Drawing Ratio (LDR) and Erichsen value were compared to those for original plain sheets [11, 12]. Here, hole-expansion test of embossed sheets has still not been conducted yet and there is no information on stretch flange formability of embossed sheets. Therefore, in this study, FE (Finite Element) simulations of the hole-expansion test of embossed sheets were conducted in order to obtain elementary information on stretch flange formability of an embossed sheet. Stretch flange deformation behavior was compared between embossed sheets with and without work hardening derived from embossing process. Finally, differences in the way of hole-expansion were also discussed in terms of the existence of preliminary work hardening and of embossing direction.

FE Simulation Method

Duplex Embossing Process

As shown in Fig. 1, multi-punch stretching was adopted as a duplex embossing process referring to previous studies [11, 12]. In this embossing process, many hemispherical punches were arranged with a lattice pattern on both upper die and lower die. The center of punches on one die was set to locate in the center of lattice made by punches on the other die. The lower die was immovable, and a plane sheet was initially put on this die. Then, the upper die, which was movable, traveled towards the lower die, and embossing was done. The traveling stroke of the upper die was set to be $2h$, in which h is called embossing height here and represents a degree of the embossing.

Duplex embossing pattern formed on the sheet plane is shown in Fig. 2. All punches used for embossing had a diameter of 2.0 mm. This pattern was a periodic convex-concave pattern and the distance from a concavity to the nearest convexities was 3.0 mm. An embossing-based direction (E.D.), which was used for referring to the direction relating to embossing pattern, was defined as the direction that the nearest convexities or the nearest concavities lined up.

Fig. 1 Duplex embossing apparatus and embossing process

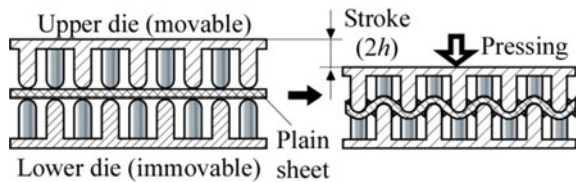


Fig. 2 Arrangement of multi-punches (embossing pattern) and embossing based direction

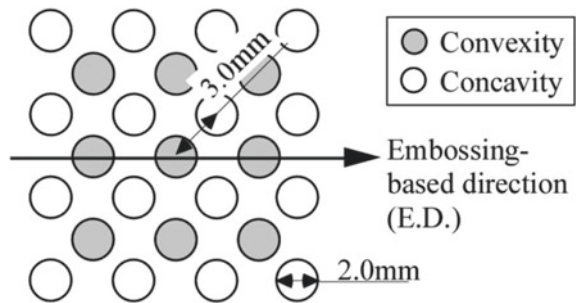
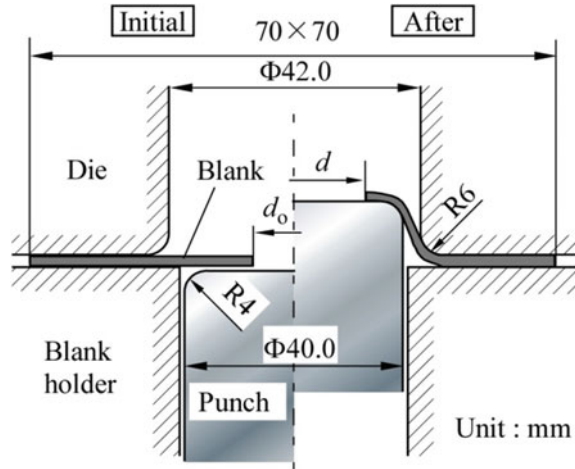


Fig. 3 Schematic diagram of hole-expansion test



Hole-Expansion Test

Hole-expansion test was simulated assuming the system shown in Fig. 3. In this system, diameter and shoulder radius of the punch were set to be 40.0 mm and 4 mm, respectively. Die had an inner diameter of 42.0 mm and a shoulder radius of 6 mm, so the clearance on one side was 1.0 mm. Blank, which was an embossed sheet in this study, was square with one side length of 70 mm. In the center of the blank, a circle hole with an initial diameter d_o existed. The blank was held between the die and a blank holder by the force of 25kN during a test. Then, when the punch was progressed toward the die hole, the blank was stretched and the hole would be expanded to a diameter d .

Finite Element Modeling

In this simulation, an isotropic material model, which obeys the von Mises yield criterion, was used in order to consider only the influence of periodic embossing structure and to ignore metallurgical anisotropy. As the target material, soft aluminum was supposed and Young's modulus E of 69 GPa and Poisson's ratio ν of 0.30 was assigned. As the flow curve, a working hardening rule of Hollomon power law, $\sigma_{eq} = F\varepsilon_{eq}^n$, was adopted. Here, σ_{eq} and ε_{eq} denote equivalent stress and equivalent strain, respectively. F is a strength coefficient and was set to be 147 MPa. Work hardening exponent n of 0.27 was also adopted in this study. These material parameters are summarized in Table 1.

Table 1 Material parameters, embossing condition, and test condition

Young's modulus E/GPa	69
Poisson ratio ν	0.30
Work hardening exponent n	0.27
Strength coefficient F/MPa	147
Initial thickness t_0/mm	0.80
Embossing height h/mm	0 (plain), 0.5, 1.0
Initial diameter of hole d_0/mm	10.0
Friction coefficient μ	0

SIMUACT13.0 was used for FE analysis of this study. Initial thickness of the plain sheet was 0.80 mm, and in the actual simulation, a system of 1/4 size was used in consideration of the orthogonal symmetry in the sheet plane. A solid element was adopted and the size was set to be almost 0.20 mm. The initial number of layers in the thickness direction was six and remeshing was conducted reflecting the equivalent strain during simulation.

Flow of the simulation is shown in Fig. 4. The whole simulation was mainly divided into three steps. In the first step, embossing process of a plain sheet was conducted to obtain an embossed sheet with realistic thickness distribution and local work hardening. Three types of embossed sheet with different embossing heights were prepared at this step. The embossing heights h were 0 (i.e. a plain sheet), 0.5 mm, and 1.0 mm, respectively. After that, in the second step, virtual annealing, which means the removal of strain history from all elements, was performed in the case of annealed model. As for the ordinal embossed sheet with local work hardening,

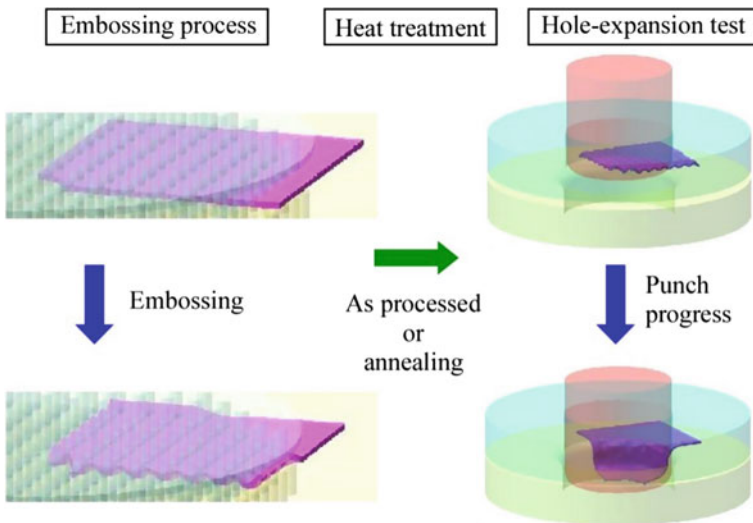


Fig. 4 Flow of the simulation

no treatment was done at this step. And at the final step, hole-expansion test of emboss sheets with the shape formed by the first step was carried out until punch stroke of eight millimeters. Friction coefficient between tool and sheet was set to 0 in the whole simulation supposing to an ideal state.

Simulation Result

Punch Load–Stroke Curves

Punch load–stroke curves obtained from FE simulations are compared between as-processed condition and annealed condition in Fig. 5. In this figure, the curve for plain sheet is also presented as a reference. In the case of $h = 0.5$ mm, which is shown in Fig. 5a, an obvious difference was seen between those two conditions. Punch load for as-processed condition was higher in the whole stroke. Because the curve for annealed condition showed almost the same variation as that for the original plain sheet, it is thought that the difference seen here was derived from work hardening that occurred during the embossing process. On the other hand, embossing structure, of which embossing height was relatively low, looks less influential on punch load.

As for the case where embossing height was large, simulation results for $h = 1.0$ mm are shown in Fig. 5b. In this case, both curves for as-processed condition and annealed condition showed similar variation. The punch load for embossed sheets was higher than that for the original plane sheet in the small stroke region, but they became almost the same level in the large stroke region. In addition, the punch load for embossed sheets with high embossing height looked lower than that for as-processed embossed sheet with $h = 0.5$ mm. These results would mean that amount of work hardening derived from embossing process was no longer a definitive factor, and that embossing structure became more dominant for hole-expansion load. The

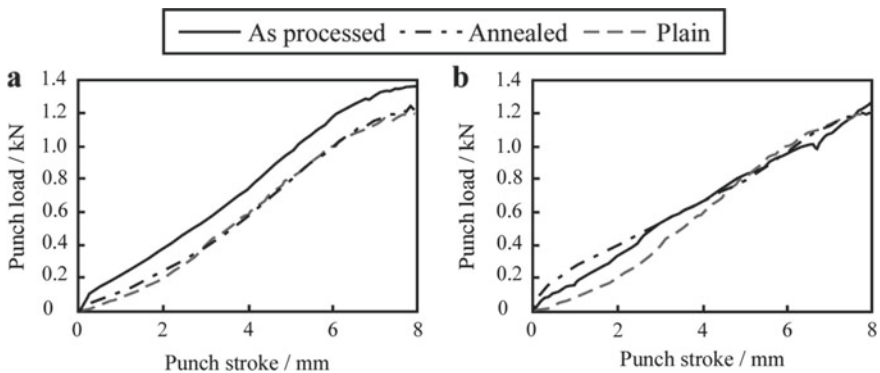


Fig. 5 Punch load–stroke curves of specimens during hole-expansion; **a** $h = 0.5$ mm, **b** $h = 1.0$ mm

rise in punch load for embossed sheet compared to plain sheet would result from an increase in the bending rigidity. Because this hole-expansion test was the type of punch stretching, it could be thought that, in the region of large stroke, the effect of bending would become smaller and that deformation would occur mainly on the punch head. Therefore, the effect of embossing structure would probably have been smaller in this region.

Deformation Behavior

In Figs. 6 and 7, variations in the distribution of equivalent strain increment are compared between as-processed condition and annealed condition. For each embossed sheet, distributions of equivalent strain increment with three punch strokes, which were 0 mm, 4 mm, and 8 mm, are shown. At first, in Fig. 6, numerical results for embossed sheets with $h = 0.5$ mm are compared. In this figure, embossed sheets are looked down from above die hole. A quarter-circle denoted by the broken line indicates the inside region of the die hole and embossing directions of all sheets are parallel to both the horizontal direction and the vertical direction.

From the initial state, in which punch stroke was 0, it can be confirmed that the bottom of concavities existed near the hole-edge at the positions of 0° , 45° , and 90° from the horizontal direction. When the punch stroke reached 4 mm, embossed sheets were deformed uniformly to some extent on the punch head, but four lines with locally high equivalent strain increment emerged. This means that deformation had occurred mainly on these lines. Especially it is found that the largest deformation regions appeared in vertical and horizontal directions from the bottom point of concavity at the hole-edge in a 45° direction. Although, in this stroke, no clear difference was

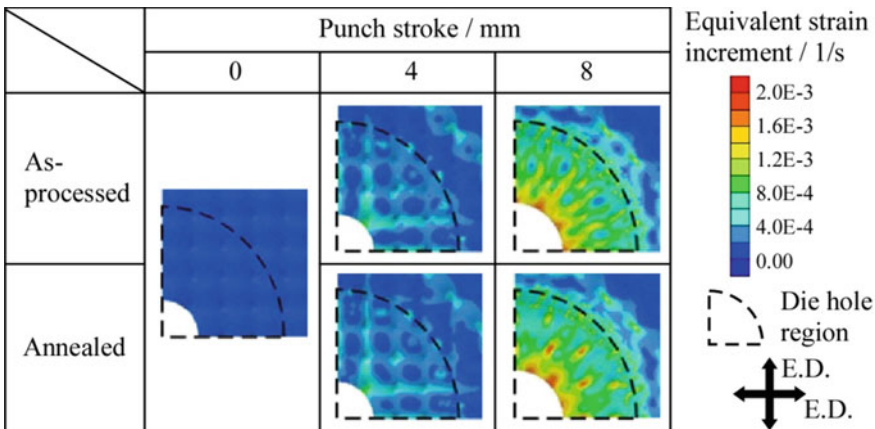


Fig. 6 Variations in the distribution of equivalent strain increment of embossed sheets with $h = 0.5$ mm

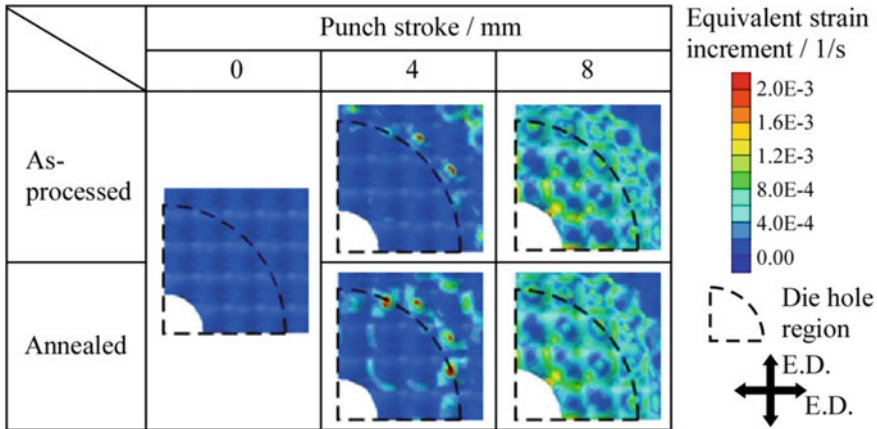


Fig. 7 Variations in the distribution of equivalent strain increment of embossed sheets with $h = 1$ mm

seen between as-processed condition and annealed condition, when the punch stroke comes to 8 mm, some differences were seen between these two conditions.

In the case of as-processed condition, local concentration of equivalent strain increment had taken place at four points on the hole-edge. It is thought that these points almost corresponded to the region between a concavity and a convexity near hole-edge and that large deformation lines appeared avoiding bottoms of concavity and tops of convexity from these points. On the other hand, in the case of annealed condition, local concentration of equivalent strain increment had taken place at three points on the hole-edge. It is thought that these points correspond to the vicinity of bottom of concavity or top of convexity. And, some local concentrations of deformation were seen in the direction connecting concavities to convexities. In embossing process of punch stretching type, the region near the top of semi-spherical punch would be deformed the most largely. Therefore, this region would also bring about the largest work hardening but become the thinnest. So, it is thought that, in as-processed sheet, the concentration of deformation occurred in the line connecting regions where work hardening was the least, and that, in annealed sheet, it occurred in the region around which the thickness was the least.

Next, in Fig. 7, numerical results for embossed sheets with $h = 1$ mm are compared to Fig. 6. Different from the case of $h = 0.5$ mm, large deformation could not be seen on the punch head in this case. Instead, local concentrations of deformation were seen at top of convexities around die shoulder. These tendencies were not changed so much between as-processed condition and annealed condition. This would mean that bending or compression of bosses at die shoulder was the main deformation in this stroke. When punch stroke comes to 8 mm, embossed sheets became to be deformed quasi-uniformly on the punch head. At the position of 45° direction on the hole-edge, the strongest local concentration of deformation was seen, but a net-like deformation region appeared avoiding bottoms of concavity and tops of convexity.

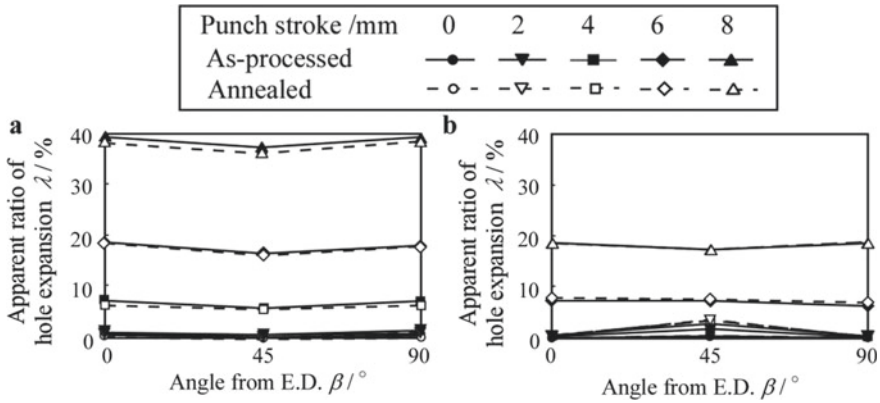


Fig. 8 Variations in anisotropy of local apparent ratio of hole-expansion; **a** $h = 0.5$ mm, **b** $h = 1.0$ mm

Even in this stage, there would not be clear differences between the two conditions, and it seems that this is reflected in less difference in punch load–stroke relations. And, this net-like deformation would result from structural dependence.

Anisotropy in Apparent Ratio of Hole-Expansion

In Fig. 8, variations in anisotropy of local apparent ratio of hole-expansion are compared between as-processed condition and annealed condition. Figures 8a and 8b are the results for $h = 0.5$ mm and $h = 1.0$ mm, respectively. Local apparent ratio of hole-expansion was calculated using the distance from hole-center to hole-edge obtained after a test in each direction. It is seen from Fig. 8a that there was only a little difference between two conditions. From the results for large punch strokes, the apparent hole-expansion ratio seems to be a little smaller for annealed embossed sheet. As for anisotropy, local apparent hole-expansion ratio was smaller in the 45° direction from E.D than that in the 0° direction. However, the anisotropy was not so large.

As for $h = 1.0$ mm, hole-expansions were smaller than that for $h = 0.5$ mm. As seen in Figs. 6 and 7, in the case of $h = 1.0$ mm, embossed sheet on the punch head was hardly deformed, so the small ratio of hole-expansion would be obtained. And differing from the case of $h = 0.5$ mm, the apparent ratio of hole-expansion was a little larger for annealed embossed sheet. The difference seemed to become smaller in the progress of punch stroke, and at punch stroke of 8 mm, hole-expansion became almost the same between two conditions. As for anisotropy, a reversal phenomenon was seen. In the small stroke stages, contrary to the case of $h = 0.5$ mm, local apparent hole-expansion ratio was larger in the 45° direction from E.D than that in the 0° direction. The difference between 0° direction and 45° direction was getting

smaller as punch stroke progressed, and, finally, local apparent hole-expansion ratio in the 0° direction became larger like the case of $h = 0.5$ mm. Invariance of hole diameter in small punch stroke stage would mean that some material flew in the die-hole from flange or die shoulder portion. It is thought that some compression of bosses at die shoulder took place and material flew in die hole less at 45° direction in an early stage. When materials on the punch head become to be deformed in large punch stroke stage, deformation behavior changed to that of the case of $h = 0.5$ mm, so such a reversal phenomenon of anisotropy would be occurred.

Conclusions

In this paper, FE simulations of hole-expansion test of embossed sheets were conducted, and elementary information on stretch flange formability of an embossed sheet was investigated. Stretch flange deformation behavior was compared between embossed sheets with and without work hardening derived from embossing process.

From the results, it was found that punch load–stroke curve was changed by the influence of work hardening derived from embossing process. However, such an influence of work hardening became smaller when embossing height was larger, and, finally, embossing structure becomes the more dominant factor. Deformation behavior was also different between as-processed embossed sheet and annealed embossed sheet. Like results seen in punch load–stroke curve, this difference becomes smaller for embossed sheets with larger embossing height. It was also found that apparent ratio of hole-expansion had anisotropy depending on embossing structure. Although this anisotropy was not so large, a reversal phenomenon of anisotropy was seen in the case of large embossing height.

Acknowledgements This study was conducted as a part of the study of the Light Metal Educational Foundation, Inc. We show big gratitude to all the support.

References

1. Kleiner M, Geiger M, Klaus A (2003) Manufacturing of lightweight components by metal forming. *CIRP Ann* 52(2):521–542
2. Kleiner M, Chatti S, Kalus A (2006) Metal forming techniques for lightweight construction. *J Mater Process Technol* 177(1–3):2–7
3. NaIlloco CS Jr, Iizuka T, Narita K, Takakura N, Yamaguchi K (2007) Effects of embossing and restoration process on the deep drawability of aluminum alloy sheets. *J Mater Process Technol* 187–188:202–206
4. Iizuka T, Yamagata S, Hatanaka N, Takakura N (2008) Fundamental study on deformation and In-plane anisotropy of stainless steel sheet subjected to embossing on both sides. *Steel Res Int* 79(2):669–676
5. Liu WY, Iizuka T (2019) Fundamental apparent plastic anisotropy of duplex embossed aluminum sheet. *Int J Mech Sci* 163:105125

6. Liu WY, Iizuka T (2016) Variation of apparent mechanical anisotropy of cold-formed embossed sheet by annealing. AIP Conf Proc 1769:200003
7. Kim Y, Oh S, Do V, Lee B (2006) Evaluation of the plastic yield locus for embossed sheet using biaxial tensile tests. Metals Mater Int 22(6):974–981
8. Liu WY, Suzuki Y, Iizuka T, Shiratori T, Komatsu T (2018) Variation of tensile and bending rigidities of a duplex embossed steel sheet by small uniaxial tensile deformation. J Mater Process Technol 261:123–139
9. Oh S, Ahn D, Kim Y (2016) A study on the mechanical properties and springback of 3D aluminum sheets. Int J Precis Eng Manuf 17(5):671–677
10. Liang CS, Wang CJ, Nguyen VB, English M, Mynors D (2017) Experimental and Numerical study on crashworthiness of cold-formed dimpled steel columns. Thin-Walled Struct 112:83–91
11. Liu WY, Iizuka T (2017) Investigation on flange deformation behavior of duplex embossed sheet metal subjected to deep drawing. AIP Conf Proc 1896:020011
12. Liu WY, Iizuka T (2019) Trials to evaluate bulging formability of duplex embossed A1050-O sheet using Erichsen test. AIP Conf Proc 2113:160014

Identification and Validation of Brass Material Parameters Using Single Point Incremental Forming



Ehssen Betaieb, Laurent Duchêne, and Anne Marie Habraken

Abstract The identification of material parameters of a brass alloy using single point incremental forming (SPIF) is presented. The determination of accurate law parameters for metal sheets in the whole range of their plastic deformation field is a challenge in order to reach efficient forming simulations of manufacturing processes. The identification is performed using a homemade optimization code based on Levenberg–Marquardt algorithm. To validate the previously identified material data, an identifiability method is developed. This method consists in measuring the influence of a material parameter on the SPIF test by analyzing the sensitivity matrix. Such information permits to assess the capacity of a SPIF test to be used to identify the material parameters. A consisting scalar (the identifiability index), concluded from the highest and the lowest eigenvalues of the Fisher’s matrix, gives an indication about the most appropriate SPIF tests to identify the material data.

Keywords Brass · SPIF · FE simulations · Identifiability

Introduction

Due to its high malleability and excellent corrosion resistance [1], brass became very useful in plumbing applications, water components, and standard fittings (tubes, drains, pipes...). The brass grade CuZn37 or also called yellow brass is known for its formability (excellent capacity for cold working), its conductivity, and especially its low price [2].

As stated by [3], CuZn37 is composed, according to EN 12,163:2011, of 62%–64% of copper, 0.1% (max) of lead, 0.1% (max) of iron, 0.3% (max) of nickel, and the rest is zinc ($\approx 37\%$).

Incremental sheet forming (ISF) is a type of forming process where the final piece is formed by a series of small successive deformations. The deformation is due to localization of repeated contact between a tool and the sheet metal. The ISF is a

E. Betaieb (✉) · L. Duchêne · A. Marie Habraken
University of Liège, ArGenCo dpt, MSM team, 9 allée de la Découverte, 4000 Liège, Belgium
e-mail: ehssen.betaieb@uliege.be

flexible process, which can be performed with high precision using a CNC machine. Hence, ISF stands as a remarkably slow option to classical forming processes, being particularly suitable to form complex parts in small batch productions.

In [4], the basic elements of incremental sheet metal forming and its different categories (forming method, formed sheet, forming path and tool path strategy, forming tool, forming limits) are discussed. One of them is the SPIF, which is the main focus of this paper as it is the simplest version of ISF.

The identification of accurate law parameters for metal sheets in the whole range of their elastic and plastic deformation field by just one or two tests would be an interesting progress for the efficiency of forming simulations and manufacturing processes. The final aim of this study is to replace a large set of classical experimental homogeneous tests with a few tests performed by SPIF process able to reach very large plastic strains.

An identifiability technique is proposed by Brun et al. [5] which is applied in the environmental sciences models. The same technique is adapted here to the mechanical modelling as already proposed by Richard et al. [6].

The current work establishes such a methodology which consists in measuring the capacity of a SPIF test to be used for the identification of a material parameter by analyzing the sensitivity matrix of different geometries.

Parameter Identification

A CuZn37 brass sheet of 1.0 mm in thickness has been selected. A hypothesis of isotropy in the three directions of the sheet is currently assumed. LAGAMINE finite element code possesses a large library of laws and elements. Its capacity to model SPIF has been checked in previous studies [7] An elasto-plastic constitutive law is used in this paper. The elasticity is described by the linear Hooke's law. The isotropic hardening is depicted by the Hollomon's law:

$$\sigma = C \varepsilon^n \quad (1)$$

where σ and ε are the equivalent stress and equivalent strain, respectively. C and n are the hardening parameters.

A tensile test, as specified in NBN EN ISO 6892–1, was performed on the material in order to identify the isotropic hardening (Fig. 1). The test was repeated four times to ensure reproducibility. ZWICK ROELL uniaxial machine (Fig. 2a) with a capacity of 100 kN was used to carry out this test. Figure 2b shows the geometry of the sample.

Young's modulus is obtained from the tensile test ($E = 105$ Gpa). Hollomon's parameters are provided in Table 1.

The identified set of parameters in Table 1 is used to create a SPIF virtual experimental campaign which allows identifying the material data through a SPIF test.

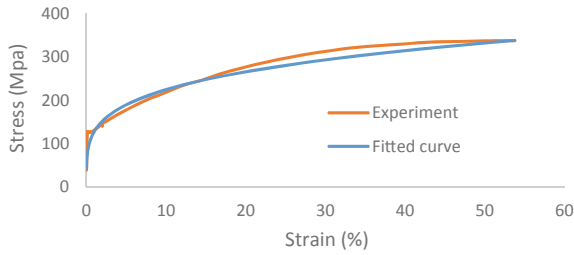
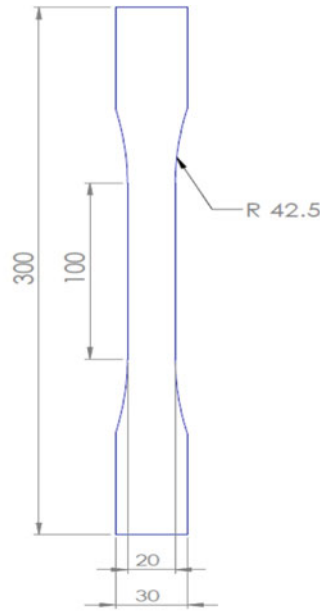


Fig. 1 Stress–strain curve for CuZn37 brass



(a)



(b)

Fig. 2 **a** ZWICK ROELL Z100KN uniaxial machine (University of Liege); **b** Geometry of the tensile test specimen (mm)

Table 1 Material data

C (Mpa)	n
128.21	0.2428

The Identifiability Method

An identifiability method has been developed in order to evaluate the capacity of a characterization test (in general) or an SPIF test (in our case) to identify the material set of parameters. This study is based on analyzing the eigenvalues of Fisher’s matrix.

A Python script was developed to calculate the sensitivity matrix to the elasto-plastic law used. The identifiability (conditioning) technique proposed by [5] is based on sensitivity functions. This technique quantifies the dependence of the solution of a numerical problem on the input of this problem. The components of the sensitivity function at time t_i are defined by the following relation:

$$\mathbf{S}_{ij} = \frac{\partial R(\theta_j, t_i)}{\partial \theta_j} \frac{\Delta \theta_j}{SC_i} \quad (2)$$

where R is the numerical value of a target result (the vertical component of the tool force F_z in this case), θ_j is the parameter to perturb, and $\Delta \theta_j$ is the uncertainty range of the parameter θ_j . According to [8], if there is no information about $\Delta \theta_j$, the value of the parameter itself can be used. SC_i represents typical magnitudes of the numerical response R . In this paper, based on [9], the maximum value of the force F_z is used for this parameter.

The Jacobian $\frac{\partial R(\theta_j, t_i)}{\partial \theta_j}$ is numerically approximated using forward differences (1st order accuracy):

$$\frac{\partial R(\theta_j, t_i)}{\partial \theta_j} = \frac{R(\theta_j + \delta \theta_j, t_i) - R(\theta_j, t_i)}{\delta \theta_j} \quad (3)$$

Also, it can be calculated using central differences (second-order accuracy):

$$\frac{\partial R(\theta_j, t_i)}{\partial \theta_j} = \frac{R(\theta_j + \delta \theta_j, t_i) - R(\theta_j - \delta \theta_j, t_i)}{2\delta \theta_j} \quad (4)$$

In this work, in order to minimize the number of numerical simulations, the forward difference formula is chosen. The influence of θ_j on the numerical result R is quantified by the level of the index value δ (sensitivity ranking) computed by the following equation:

$$\delta_j = \frac{1}{N} \sum_{i=1}^N |S_{ij}| \quad (5)$$

where N is the number of measurement points or the number of time steps. δ_j gives an indication about the influence of the parameter θ_j on the numerical result R . A high value of δ_j means that the parameter θ_j has an important influence on the numerical result, while a value of zero indicates that the latter is independent of this parameter. To measure the multicollinearity, the identifiability index (collinearity index) is given as follows:

$$I = \log_{10} \left(\frac{\lambda_{\max}}{\lambda_{\min}} \right) \quad (6)$$

where λ_{\max} and λ_{\min} are, respectively, the biggest and the smallest eigenvalues of Fisher’s matrix H defined by

$$H = S^T S \tag{7}$$

According to Gujarati [10], a low value of I (<2) implies a low collinearity (good identifiability), if I is between 2 and 3, there is moderate to strong collinearity (moderate identifiability), and if I exceeds 3, there is severe or high collinearity (low identifiability).

Numerical Modelling

Three SPIF tests were simulated using the FE code LAGAMINE. The chosen material is a brass ZnCu37 described in Sect. 2. The same tool was used in all the simulations, it is a spherical tool, fixed against rotation, with a diameter of 10 mm.

A cone test with a wall angle of 55° was modelled (Fig. 3). The sheet was clamped along the outer circumferential part. Z-constant strategy was used with a step down of 0.5 mm between two successive contours. Therefore, 60 contours were performed during this simulation to reach 30 mm of depth.

A one-slope pyramid was also simulated as illustrated in Fig. 4. For the boundary conditions, the squared sheet was clamped along its edges. Z-constant strategy with a step down of 1 mm was used to carry out the 30 contours of the simulation and reach 30 mm of depth.

A line test tries to represent a simple test of SPIF. A squared metallic sheet is clamped along its edges and deformed plastically. Figure 5 describes the movement of the tool during the simulation. The tool plunges into the material twice; 3 mm at each vertical indent is chosen.

The FE meshes for the three SPIF processes are presented in Fig. 6. Table 2 summarizes the information about these three simulations. Note that RESS element

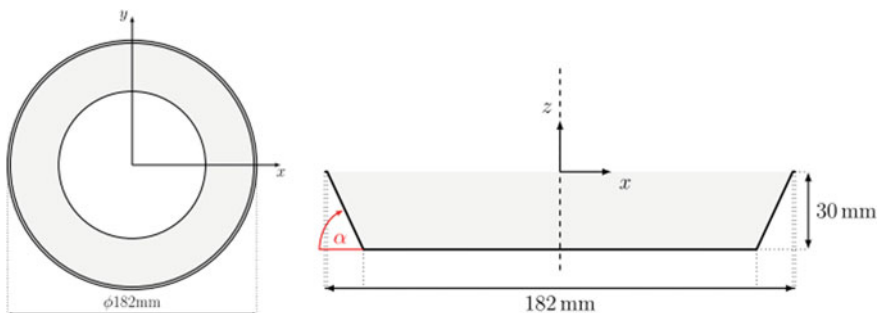


Fig. 3 Cone geometry (Guzman et al. [11])

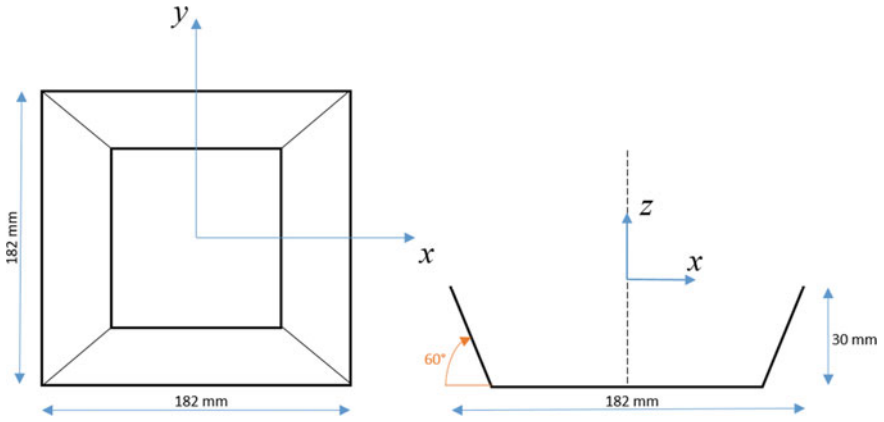


Fig. 4 One-slope pyramid geometry

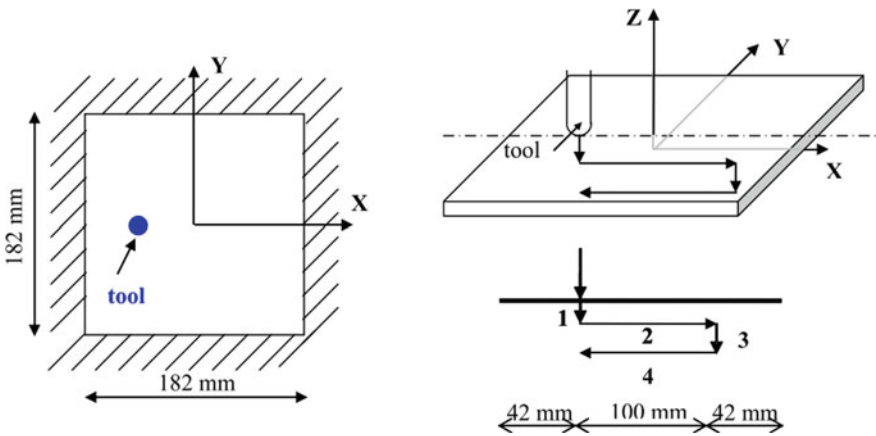


Fig. 5 Description of the line test (Bouffioux et al. [12])

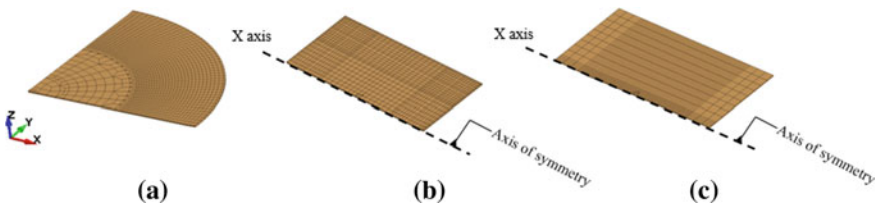


Fig. 6 Finite element meshes exploiting symmetries for the three geometries: **a** Cone test; **b** Pyramid test; **c** Line test

Table 2 Information about the simulations

	Elements	Contact elements	Simulated part	Boundary conditions	CPU time
Cone test	1492 RESS (solid-shell elements)	1344 CFI3D	90° angle pie	Rotational BC*	5 h. 27 m. 48 s
Pyramid test	1058 RESS (solid-shell elements)	1058 CFI3D	Half of the sheet	Rotational BC*	2 h. 3 m. 7 s
Line test	806 RESS (solid-shell elements)	806 CFI3D	Half of the sheet	Symmetry BC X-axis (Y = 0)	0 h. 5 m. 13 s

*Rotational boundary conditions are discussed in more detail in [7]

is a solid shell element [13], while CFI3D is a contact interface element used with a penalty Coulomb model here (3D extension of the general 2D element presented in [14]). No friction is applied between the tool and the sheet.

Results

Inverse modelling coupled with LAGAMINE software allows us to identify the material data (Hollomon’s parameters) referencing the virtual experimental campaign mentioned in the previous section. The Levenberg–Marquardt algorithm is used to iteratively adjust the set of parameters in order to minimize the objective function X:

$$X(\theta) = \sum_{i=1}^n [R_{ref_i} - R_{num_i}(t_i, \theta)]^2 \tag{8}$$

With n is the number of the measuring points, R_{ref} is the reference curve, and R_{num} is the numerical result based on θ represents the set of parameters to optimize.

The selected SPIF test to identify the material data is the cone with a 55° for the wall angle α (see Fig. 3). In order to minimize the cost of this operation in terms of CPU time, the optimization in the first step was performed only on the first half of the simulation (until 300 s). Starting with a set of parameters far from those of the virtual experimental tests, after nine iterations of Levenberg–Marquardt (step 1) we reached roughly the wanted experimental curve (Fig. 7a). Zooming the first part (until 100 s) and taking into consideration the scale of the force values, we assumed that extra Levenberg–Marquardt iterations are still required to enhance the identification.

More iterations are performed on the first four contours of the cone (step 2) in order to achieve the virtual experimental curve (Fig. 7b). Starting with the parameters

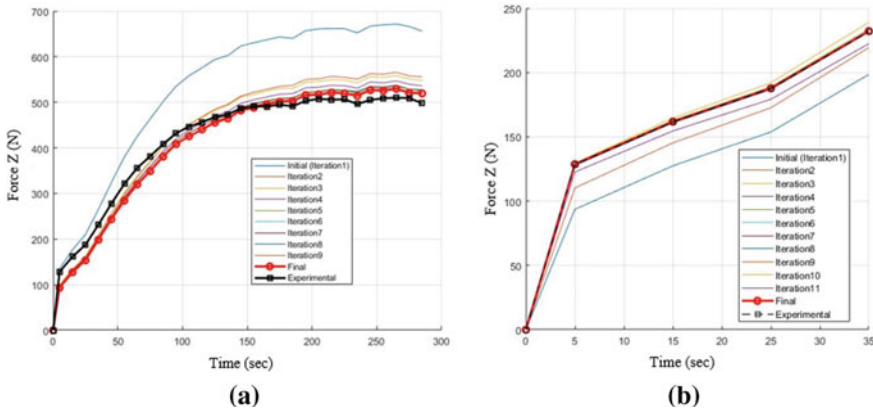


Fig. 7 Iterations of Levenberg–Marquardt Algorithm: **a** step 1; **b** step 2

($C = 145.99$; $n = 0.3327$) identified in the first step of the fitting procedure and after 11 iterations on the first 4 contours, we reached the virtual experimental results with values of C and n ($C = 128.69$; $n = 0.2434$) approximately the same as the values presented in Table 1.

The cumulative error of the force prediction using the parameters identified in the last iteration of step 1, and the last iteration of step 2 is presented in Fig. 8.

The Pyramid and the Line tests were then used to validate the identified parameters. Figure 9 shows the comparison between the numerical and experimental results (F_z) for the three geometries.

From the simplest test of the SPIF (line test), to more complicated cases (cone and pyramid tests) of this process, we analyzed the sensitivity of the vertical component of the forming force (F_z) to the identified set of parameters. The identifiability method of the Sect. 3 was applied to the three studied geometries in order to confirm the capacity of SPIF tests in terms of mechanical parameter identification. A first study consisted in measuring the effect of Hollomon’s parameters (C and n) on the numerical result

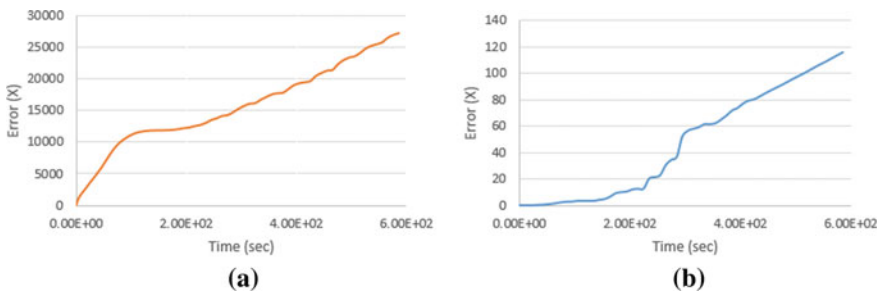


Fig. 8 Cumulative error for the last iteration of: **a** step 1; **b** step 2

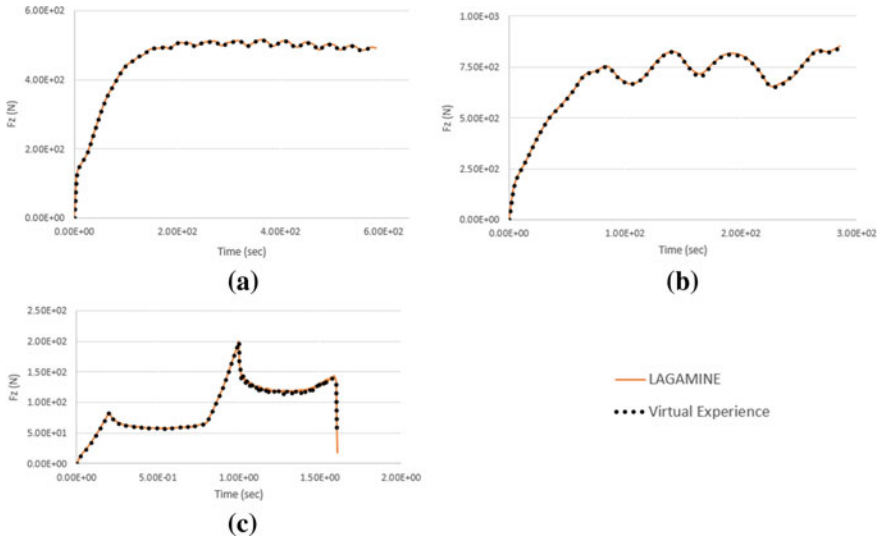


Fig. 9 Comparison between numerical and experimental results: **a** Cone test (identification process) and validation of the identified data set by: **b** Pyramid test; **c** Line test

(Fig. 10a). A second study allowed us to ensure the ability of these tests to identify the material data based on the analysis of Fisher’s matrix and its eigenvalues (Fig. 10b).

The high sensitivity of C parameter in the pyramid test, according to our tests, strongly depends on the mesh refinement.

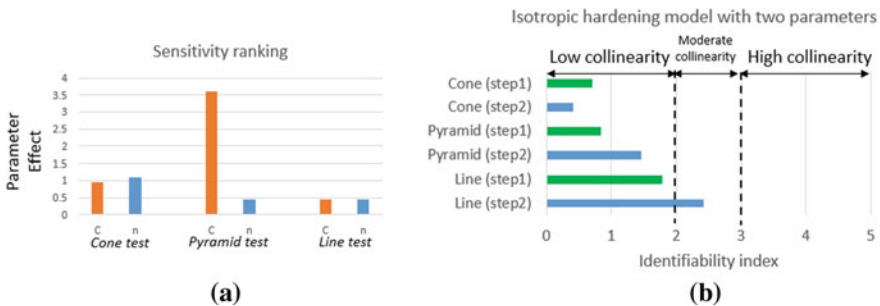


Fig. 10 Sensitivity analysis results: **a** Sensitivity ranking (Eq. 5); **b** Identifiability index (Eq. 6)

Conclusions

Numerical results show the capacity of the Levenberg–Marquardt algorithm to identify the material parameter of a sheet through an SPIF cone experiment (virtual here). Note that the initial set of parameters was relatively far from the optimal solution. The robustness of this algorithm is proved in this paper.

SPIF simulations of three different shapes were performed in this work. The simulations present sensitivity enough to identify the material data as confirmed by the sensitivity analysis. Results show the superiority of the cone and pyramid tests and especially the cone test which has been already demonstrated in [9]. Note that this ranking of the three tests is kept at the end of each step. The richness of the SPIF platform by including other geometries and applying the helical strategy can expand the current procedure.

The research perspectives concern more complicated constitutive laws taking into account the kinematic hardening and the anisotropy. Such analyses could modify the SPIF tests ranking. The ongoing real experimental campaign demonstrated also that force prediction by such a simple model is not possible. Both anisotropy and kinematic hardening play a role.

Additionally, performing the SPIF tests on just one material is not enough to validate and confirm a method. The use of another material will extend and validate the identifiability method.

Acknowledgements FNRS Research Director A.M. Habraken acknowledges the support from Belgian Fund for Scientific Research (FRS-FNRS). This SPIF research is funded by the PDR MatSPIF-ID FRS-FNRS.

References

1. La Fontaine A, Keast VJ (2006) Compositional distributions in classical and lead-free brasses. *Mater Charact* 57:424–429
2. Alaboodi AS, Al-Mufadi F, Modeling BP (2018) Cold deformation of dezincification resistant yellow brass for plumbing Cold deformation of dezincification resistant yellow brass for plumbing applications. *Mater Manuf Process* 33(15):1693–1700
3. Skibicki D, Pejkowski Ł (2017) Low-cycle multiaxial fatigue behaviour and fatigue life prediction for CuZn37 brass using the stress-strain models. *Int J Fatigue* 102:18–36
4. Echraf SBM, Hrairi M (2011) Research and progress in incremental sheet forming processes. *Mater Manuf Process* 26(11):1404–1414
5. Brun R, Reichert P, Künsch HR (2001) Practical identifiability analysis of large environmental simulation models. *Water Resour Res* 37(4):1015–1030
6. Richard F, Villars M, Thibaud S (2013) Viscoelastic modeling and quantitative experimental characterization of normal and osteoarthritic human articular cartilage using indentation. *J Mech Behav Biomed Mater* 24:41–52
7. Henrard C, Bouffieux C, Eyckens P, Sol H, Dufloy JR, Van Houtte P, Van Bael A, Duchêne L, Habraken AM (2011) Forming forces in single point incremental forming: prediction by finite element simulations, validation and sensitivity. *Comput Mech* 47:573–590

8. Reichert P, Vanrolleghem P (2001) Identifiability and uncertainty analysis of the river water quality model no. 1 (RWQM1). *Water Sci Technol* 43(7):329–338
9. Ben Hmida R (2014) Identification de lois de comportement de tôles en faibles épaisseurs par développement et utilisation du procédé de microformage incremental. PhD Thesis, Supervisor: S.Thibaud, University of Franche-Comté
10. Gujarati D (2004) *Basic econometrics*
11. Guzmán CF, Yuan S, Duchêne L, Saavedra Flores EI, Habraken AM (2018) Damage prediction in single point incremental forming using an extended Gurson model. *Int J Solids Struct* 151:45–56
12. Bouffioux C, Henrard C, Eyckens P, Aerens R, Van Bael A, Sol H, Duflou JR, Habraken AM (2008) Comparison of the tests chosen for material parameter identification to predict single point incremental forming forces. In: *Proceedings IDDRG 2008 International conference*, Olofström, Sweden, pp 133–144
13. Ben Bettaieb A, Velosa de Sena JI, Alves de Sousa R, Valente R, Habraken AM, Duchêne L (2015) On the comparison of two solid-shell formulations based on in-plane reduced and full integration schemes in linear and non-linear applications. *Finite Elem Anal Des* 107:44–59
14. Habraken AM, Cescotto S, Banning Q (1998) Contact between deformable solids: the fully coupled approach. *Math Comput Model* 28(4):153–169

Improvement of the Strength of an Aluminum Liner by Beading Under Consideration of Internal Pressure and Low Temperatures



A. Reimer, C. Hartmann, R. Norz, P. Sturm, and W. Volk

Abstract Increasing public interest in decarbonization and regulatory requirements to reduce emissions have led to a steady progress of hydrogen power technology in the commercial vehicle sector in recent years. In addition to important aspects of safety in the handling of pressurized gas liners, the driving performance or range as well as the consideration of the lightweight construction idea are key criteria from an economic and technical point of view. Therefore, a design of the aluminum liner that meets the requirements is essential as an important component in the system of hydrogen power technology. In the evaluation of different liner geometries, the achieved stiffness and the point of occurring plastification play a decisive role. In this paper, the influence of geometric beads on the stiffness of an aluminum liner under internal pressure loading and cryogenic temperature conditions is investigated by means of an FE simulation.

Keywords Hydrogen power technology · Aluminum liner · Hydroforming · FE-simulation

Introduction

From a European and global perspective, the transport sector is characterized by a significant increase in energy consumption. Not only is there a dependence on increasingly limited fossil resources but also the sector contributes to the greenhouse effect as a contributor. In Germany, approximately 20% of greenhouse gas emissions could be attributed to transport in 2020 [1].

According to the VDI publication [2], around 200,000 zero-emission vehicles will have to be deployed in Europe by 2030 in order to meet the CO₂ targets for heavy trucks. Accordingly, the shares of fuel cell and battery-electric powertrains for freight transport should reach 75% and 24%, respectively. Therefore, great efforts have been

A. Reimer (✉) · C. Hartmann · R. Norz · P. Sturm · W. Volk
Chair of Metal Forming and Casting, Technical University Munich, Walther-Meißner Strasse 4,
85748 Garching, Germany
e-mail: alina.reimer@utg.de

made in recent years to advance the development of alternative drive technologies and fuels.

In the field of electrically powered vehicles, it is apparent that the limited range, in particular, is a challenge for the application in heavy long-distance trucks. These include the required battery weight, which leads to a reduction in payload, and the time-intensive and low-power charging [2]. The weaknesses identified would be solved by using hydrogen in fuel cell-powered commercial vehicles, as demonstrated by trucks from Hyundai already in trial operation [3, 4].

State of the Art

The implementation of zero-emission fuel cell drive technology in the commercial vehicle sector necessitates fulfillment of the requirements resulting from its usage. For a long-distance truck, the requirements therefore result in high storage capacities of around 70–80 kg of hydrogen in order to achieve ranges of approx. 800–1000 km with one tank filling. On the other hand, there are restrictions in terms of installation space and permissible weight, which influence both the design of the hydrogen storage unit to be integrated and the storage technology. In addition, fast and easy refueling is required [5].

On-Board Hydrogen Storage Technologies

In principle, a distinction can be made between three technological approaches for mobile hydrogen storage in vehicles. One option is material-based storage of hydrogen on the surface of solids by adsorption or in solids by absorption (metal hydrides). Other options include physically based gaseous storage at ambient temperatures and pressures up to 700 bar (CGH₂: Compressed Gaseous Hydrogen) and the use of liquid hydrogen (LH₂: Liquid hydrogen), which is stored at cryogenic temperatures close to the boiling point [6].

However, in view of the above-mentioned requirements of the commercial vehicle sector, the stated storage methods are reaching their technical limits and feasibility. In particular, the 35 MPa and 70 MPa compressed gas storage technology (CGH₂ 35/70 MPa), which has already been tested in the passenger car sector, has not yet been able to establish itself for long-distance applications. The fuel cell trucks with 35 MPa CGH₂ storage technology used by Hyundai in Switzerland have a range of 400–450 km, which is too limited for use in long-distance trucks [7]. Although liquid gas storage technology (LH₂) achieves the highest gravimetric and volumetric storage densities, the high evaporation losses that occur during the parking time, the losses during refueling, and the low-pressure supply capability are disadvantages [7, 8].

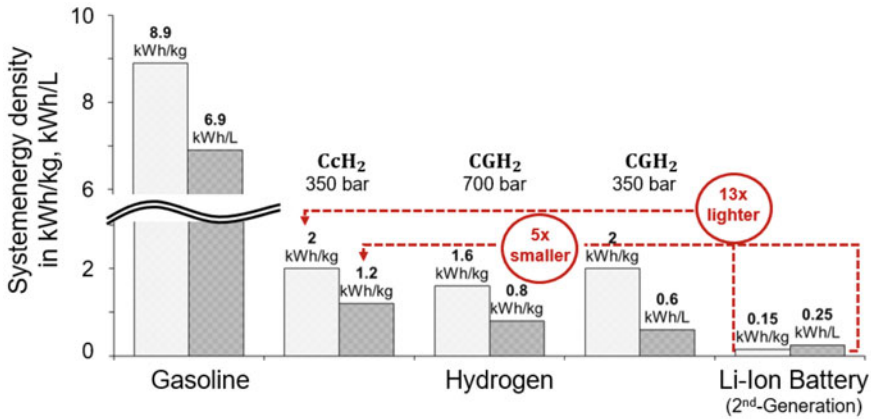


Fig. 1 Comparison of the energy densities of different vehicle storage technologies [9]

Therefore, the sLH₂ technology approach (subcolled LH₂) by Daimler and Linde on the one hand, and the cryogenic compressed gas storage technology (CcH₂ = Cryo-compressed Hydrogen) by BMW on the other hand were developed as successors for the LH₂ storage and refueling technology [9].

This paper focuses on BMW’s cryogenic compressed gas storage. The hydrogen is stored at operating pressures of 350 bar and temperatures between 30 and 360 K. In this case, the gaseous hydrogen is in a so-called supercritical state so that it is no longer possible to distinguish between the liquid and gas phases on the basis of the distance between the molecules. Figure 1 shows that this storage technology can achieve superior volumetric and gravimetric storage densities compared with the 35 MPa/70 MPa compressed gas storage and lithium-ion batteries used [7, 10].

Types of Pressure Vessels and Their Manufacture

For the storage of hydrogen, the pressure vessels can be of four different types as shown in Fig. 2.

In general, the vessels have a cylindrical shape in order to achieve the most uniform pressure distribution possible. Metallic pressure vessels belong to type I. Type II vessels are wrapped with a fiber–resin composite in the cylindrical area. Type III and Type IV, on the other hand, are fully wrapped with carbon fibers embedded in a polymer matrix. If the internal liner contributes to the mechanical strength of the pressure vessel, it is a Type III (usually metallic liner); if it does not, it is a Type IV tank. A Type IV design is characterized by a polymer liner, in a few cases, an extremely thin metallic liner is also possible [6]. Although the use of carbon fiber-reinforced plastic (CFRP) proves to be particularly advantageous in terms of mechanical properties and weight, it also represents the most cost-intensive size of

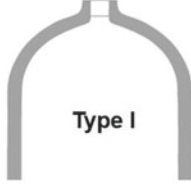
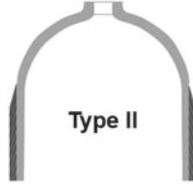
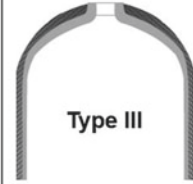
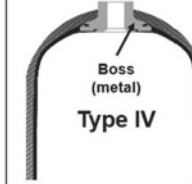
			
Metallic pressure vessel	Metallic pressure vessel wrapped on the cylindrical part with composite (fiber and resin)	Metallic liner fully wrapped with composite (fiber and resin)	Polymer liner fully wrapped with composite (fiber and resin)

Fig. 2 Different types of pressure vessels [6]

the storage system. Therefore, when selecting the pressure vessel design, cost should be considered in addition to the intended application and technical performance. For the mobile hydrogen storage systems of fuel cell-powered commercial vehicles, Type III and Type IV can be selected [11].

The polymer liners of Type IV pressure vessels can be made by rotational molding, blow molding, or welding injection-molded domes to an extruded polymer tube. Metal parts, such as the boss, can be inserted into the domes during the molding process or bonded to the liner in a second step [12].

The pressure vessel of Type I and the liners of Type II, as well as Type III, can be manufactured from three different semi-finished products [12] as shown in Fig. 3.

Different process routes are possible for the production of liners from sheet metal. In most cases, the initial production of a hollow body is carried out by (multi-stage) deep drawing or draw-gliding [13]. The hollow bodies are subsequently closed by

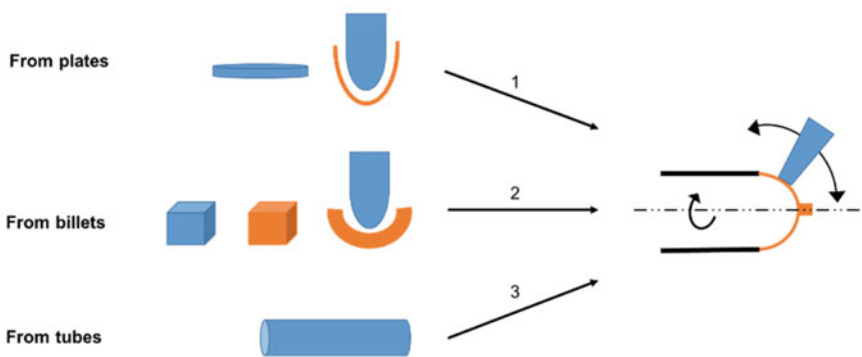


Fig. 3 Possible production routes of pressure vessels starting from three different semi-finished products [12]

incremental processes, such as (hot-) spinning or draw-forming [14, 15]. A final heat treatment enables the adjustment of the desired mechanical properties [16].

If instead a solid billet is used as a semi-finished product, a (hot-) cup reverse extrusion can be used to form the hollow body [13, 17]. In an additional subsequent incremental forming process, the hollow bodies can be expanded to achieve the targeted dimensions. Closure and final modification of the mechanical properties are carried out in the same way as for the production of sheet metals [16].

In the production of liners from seamless tubes, only the domes are formed by (hot-) spinning or stretch-gliding [13, 18]. Here, the initial tube diameter defines the final diameter of the liner.

Combinations of the given process routes are also implemented, for example, to achieve certain geometric characteristics (dimension, wall thickness distribution, etc.) [19].

For pressure vessels that are only exposed to low pressures, thermal processes are also used in which a tube is welded with two caps. This results in two or three weld seams, which are potential sources of defects in the component.

Selection of Materials

When selecting suitable materials and structures for liner production, in addition to the static and dynamic loads resulting from the operating conditions, the compatibility of the gas with the materials must also be taken into account. The aim must be to prevent the risk of failure of the pressure vessel due to bursting or leakage during operation and to ensure the technical performance of the system.

The most commonly used materials for the metallic liner are 6061 or 7060 aluminum alloys or chrome-molybdenum or INOX steels [12].

In general, metallic materials, especially steel, tend to hydrogen embrittlement, which leads to the degradation of mechanical properties and premature cracking. The mechanism of hydrogen embrittlement is still a subject of research in industry and academia in terms of improved alloy production, component composition selection, and mechanical testing [20, 21].

Usually, the effect of hydrogen embrittlement is observed at ambient temperatures and is negligible at elevated temperatures ($>100\text{ }^{\circ}\text{C}$). In the case of austenitic stainless steels used for cryogenic applications, an increased manifestation of the effect is observed at $-100\text{ }^{\circ}\text{C}$, which turns negligible at temperatures lower than $-150\text{ }^{\circ}\text{C}$ [12].

In view of the cryogenic temperatures, changes in mechanical properties, temperature-induced expansion and contraction processes and embrittlement play an important role. Especially for liners of type III, which have a carbon fiber-reinforced plastic wrap, expansion and contraction processes have a great influence on the pressure vessel system.

Approach

This paper addresses the production of large-volume aluminum liners with a volume of around 600 L for the commercial vehicle sector. In addition, various liner geometries are investigated by means of Finite Element (FE) simulations with regard to their achieved stiffness and their point of plastification under internal pressure and cryogenic temperature conditions. Figure 4 shows the general underlying procedure of the paper.

In view of the liner dimensions, the forming manufacturing processes presented in the prior state of the art reach their limits in terms of series-production capability and robustness.

For example, the ejection of the component from the die at the end of the cup reverse extrusion process requires a large working range for the aimed dimensions, which severely limits the selection of suitable presses [22]. In addition, when seamless tubes are used as semi-finished products, the diameter is limited by the initial diameter.

Therefore, the hydroforming process is considered a promising process for the production of large-volume liners.

Selected Liner Geometries

A comparative study of the manufacturability and load resistance of three different liner geometries is carried out. The classic cylindrical liner geometry is used as a reference and compared with liners that have geometric stiffening beads in the

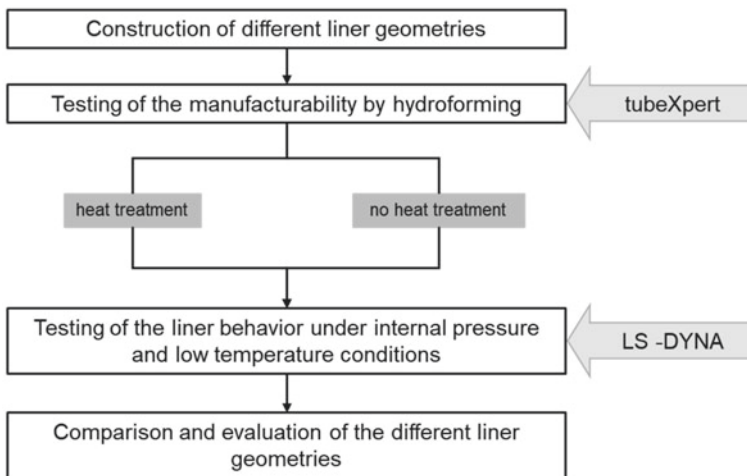


Fig. 4 General approach of the investigations in this paper

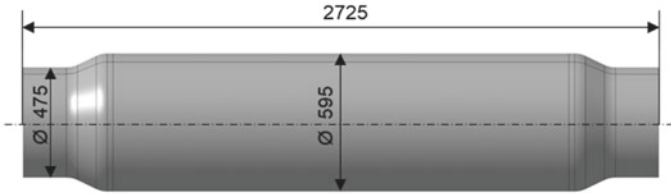


Fig. 5 Geometry of the reference liner

longitudinal direction on the one hand and in the circumferential direction on the other. The basic geometry diameter of the reference geometry according to Fig. 5 of 595 mm is retained for all designs.

The circumferential beads are intended to contribute to the increasing resistance to compressive loads in a similar way to reinforcing rings or bands wrapped around the shell surface. Based on the idea, that subdividing the longitudinal direction of the cylinder into smaller segments with ends stiffened by beads, leads to a reduction in the lever arm for the applied surface load, when internal pressure is applied. Figure 6 shows the liner geometry considered here with four circumferential internal beads, which have a bead diameter of 490 mm.

In the case of longitudinal bead geometry, on the other hand, the principle of action of the beads increases the second moment of inertia, which means that the deflection can be reduced. At the same time, this means that a greater bending moment in the direction of the longitudinal axis caused by internal pressure can be tolerated. The four longitudinal beads of this geometry have an outer diameter of 610 mm (see Fig. 7).

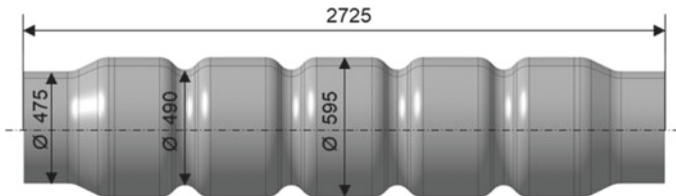


Fig. 6 Geometry of the liner with internal circumferential beads

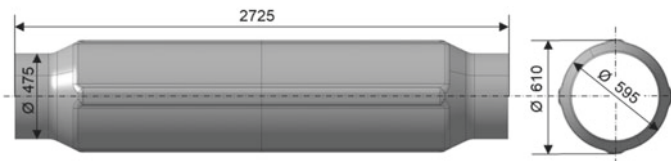


Fig. 7 Geometry of the liner with external beads in longitudinal direction

Manufacturability by Hydroforming

In the first step, the manufacturability of the different liner geometries in the hydroforming process is examined using Autoform's FEM software tubeXpert.

The total thickness and the forming limit diagram (FLD) are used as evaluation parameters. For the wall thickness distribution, this means that the thickness must not fall below 9 mm.

The material investigated in this paper is aluminum alloy 6061 in the T4 condition. Furthermore, the influence of a heat treatment carried out after the hydroforming process on the later resistance to internal pressure loading is analyzed. The heat treatment is performed at temperatures above the recrystallization temperature and therefore leads to an elimination of work hardening.

Numerical Load Test

The liner geometries generated in tubeXpert using hydroforming are imported into the FE software LS-DYNA together with their stress and strain tensors and their wall thickness distribution. In the FE model, the various liners are analyzed with regard to the thermomechanical loads occurring later during usage. For this purpose, on the one hand, an internal pressure according to Fig. 8a is built up over the simulation time and, on the other hand, the influence of extremely low temperature (approx. $-196\text{ }^{\circ}\text{C}$) on the material behavior is taken into account by using an appropriate flow curve for the 6061-T4 aluminum alloy (see Fig. 8b) [23]. The yield curve was approximated using a Swift/Hockett–Sherby approach and extrapolated beyond the range of uniform strain. The fitting was done according to the least squares method.

The analysis of the resistance of the different liner geometries against the internal pressure is carried out on the basis of the strains reached during the loading. For this purpose, elements are selected in LS-DYNA that are located in the middle area of the

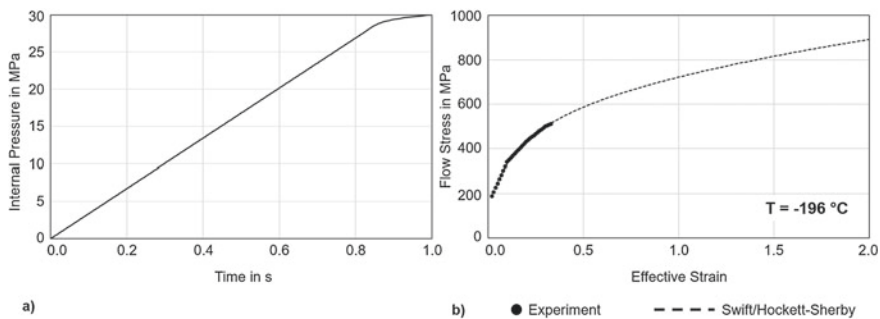


Fig. 8 **a** Internal pressure versus the simulated time; **b** Used flow curve of aluminum alloy 6061 T4 at a low temperature of $-196\text{ }^{\circ}\text{C}$ in LS-DYNA [23]

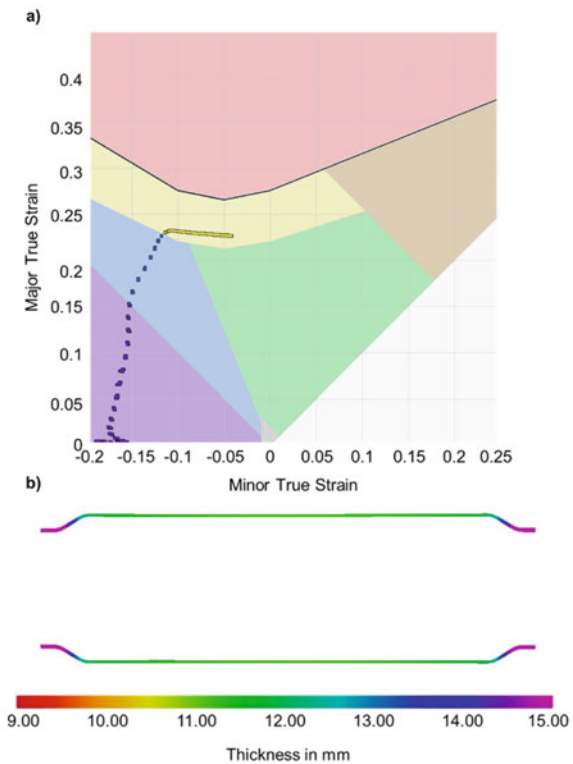
liner, since this is where the largest stresses and strains result from the pressure during the simulation. A jump of the strain values by two-thousandth marks the transition from the elastic to the plastic range (yield strength $R_{p0.2}$) and is used as a failure criterion of the liner since plastic deformation during loading must be excluded. The pressure endured up to this point can be used as a measure of the liner's stiffness.

Results and Discussion

The results of the process simulation using tubeXpert show that the hydroforming process is basically suitable for producing the required large-volume aluminum liners. Figure 9 shows an example of the FLD (a) of the reference tank geometry and the wall thickness distribution (b). The required press force is around 7000 t and can be applied with presses available in the industry. The requirement for a wall thickness greater than 9 mm is clearly met over the entire cross section of the liner.

The aim of introducing beads is to increase stiffness in order to be able to withstand higher loads. In addition to the realization of the lightweight design idea through beading, the manufacturing costs, which as already mentioned in the state of the art

Fig. 9 a The Forming Limit Diagram and b The wall thickness distribution of the reference geometries after hydroforming by using tubeXpert



correlate primarily with the CFRP used, can also be reduced through lower material needs. The results of the load simulation with LS-DYNA are shown below in Figs. 10 and 11. The results without heat treatment are shown on the right and those with heat treatment on the left. As already mentioned, the heat treatment eliminates the work hardening previously introduced by the hydroforming process.

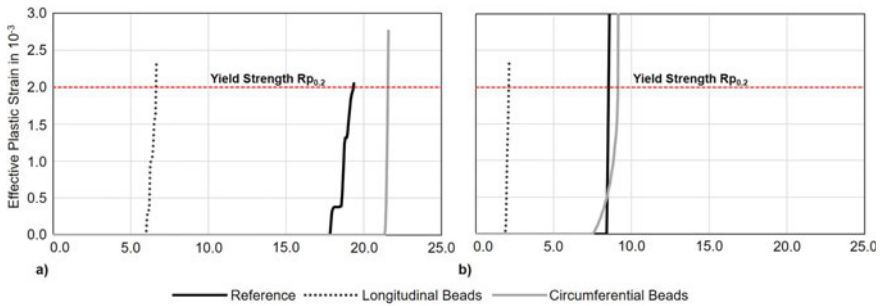


Fig. 10 Effective plastic strain during pressure loading for the different liner geometries (a) without and (b) with subsequent heat treatment after hydroforming. The red dotted line represents the change from elastic to elastic–plastic forming behavior

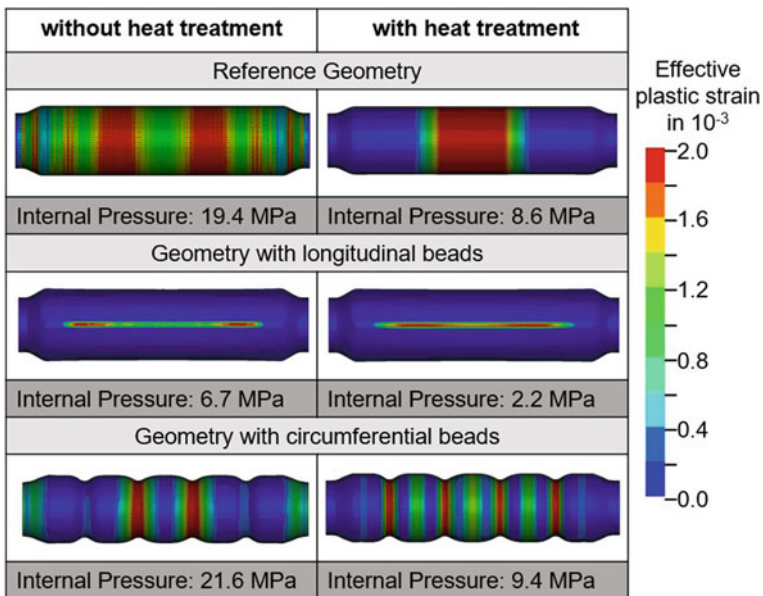


Fig. 11 Overview of simulated liner geometries in LS-DYNA under internal pressure. Shows the effective plastic strain distribution of the liner at the time when the yield strength $Rp_{0.2}$ is reached. In addition, the corresponding internal pressure loads are indicated

An analysis of the occurring strains and the determination of the plasticizing pressure is carried out in areas where failure would be expected in the further course and therefore concentrates on the middle area of the liner.

A comparison of the two diagrams in Fig. 10 shows that a subsequent heat treatment of the liner and an associated reduction in strain hardening generally leads to an earlier failure, i.e. a transition from purely elastic to elastic–plastic behavior, at lower pressures.

In the case of a heat treatment carried out following the hydroforming process, the geometry with introduced longitudinal beads exhibits the lowest resistance and thus also stiffness to the acting internal pressure.

The yield strength $R_{p0.2}$ is already reached a pressure of 2.2 MPa. In contrast, failure of the reference or circumferential bead geometry occurs at a pressure four times higher.

A similar picture in the sequence of the liner geometries with respect to the plastification and thus failure pressures also appears in the right-hand diagram of Fig. 10, where no subsequent heat treatment takes place. In general, consideration of the introduced strain hardening in the load simulation leads to a later onset of flow at higher stresses so that the critical transition from elastic to plastic behavior occurs at higher internal pressures. The first liner to fail is the one with longitudinal beads. This is followed by the reference geometry before the liner with circumferential beads fails at a pressure of 21.6 MPa. However, it is noticeable here that the difference between reference and circumferential bead geometry is more pronounced than is the case with subsequent heat treatment. This can be attributed to the higher strain hardening generated during the hydroforming process.

An examination of the strain distribution in Fig. 11 illustrates very well the effect of the bead geometries introduced compared to the reference liner. The longitudinal beads show that they cannot contribute to an increase in stiffness and thus to an improvement in resistance to internal pressure loading. The critical strains leading to the fulfillment of the failure criterion occur first at the top flange of the inserted beads. This can be explained by the smaller wall thicknesses present in these areas after the hydroforming process. When the liner is subjected to internal pressure, the shell surface in particular is loaded along the longitudinal axis so that it is precisely the longitudinal beads with their lower wall thickness that represent the weak points.

In contrast, the inner circumferential beads with their effect contribute to an increase in stiffness. Figure 11 shows the clear segmentation of the liner with the stiffened bead ends. These lead to a reduction in the lever arm for the applied surface load and contribute to higher compression resistance.

Conclusion and Outlook

The application of CcH2 technology for mobile hydrogen storage in the commercial vehicle sector poses new challenges for the production and design of pressurized gas vessels. In addition to the selection of a suitable process route for the production

of large-volume aluminum liners for the Type III container, the thermomechanical loads and their effects on the material behavior in particular have been insufficiently investigated the present extent. This paper, with its simplified simulation models, was intended to provide an initial discussion of the manufacturability of the required liner dimensions in the hydroforming process and to illustrate the potential of introduced geometric stiffening beads on the resistance of the liner to internal pressure loads. This is also with regard to the possibility of reducing the CFRP material consumption in order to achieve further economical as well as ecological advantages in the field of climate-friendly commercial vehicles.

The investigation into manufacturability was generally able to show that it is possible to produce the required liner dimensions by hydroforming. The presses available in the industry are also capable of applying the required forces, which means that robust series production is possible. The consideration that the introduction of geometric beads leads to an increase in liner stiffness and thus an improvement in resistance to compressive loads could be confirmed for the circumferential internal beads. In the case of the longitudinal beads, however, the greater wall thickness thinning in the area of the top flange results in weak points in the pressurized shell surface so that failure occurs at low pressures.

If a heat treatment follows the hydroforming process, which eliminates the strain hardening, then the tolerable pressures for all three liner geometries are significantly lower than in the case without heat treatment. In general, the introduced strain hardening contributes to an increase in the yield point, which has a positive effect on the failure criterion defined here (transition from elastic to elastic–plastic material behavior).

Further investigations are planned with regard to other materials (e.g. stainless steel) and bead geometries. In addition, the construction of a more complex material model that takes into account the interaction of liner material and CFRP wrapping for the Type III pressure vessel under different loading conditions would be interesting. Moreover, new questions arise regarding the wrapping strategy when the liner has geometric beads.

References

1. Umweltbundesamt. Dokumentation der Abschlusskonferenz zur Klimawirkungs- und Risikoanalyse 2021 für Deutschland. <https://www.umweltbundesamt.de/service/termine/klimawirkungs-risikoanalyse-2021-des-bundes>
2. VDI Verein Deutscher Ingenieure e.V., Klimafreundliche Nutzfahrzeuge. Vergleich unterschiedlicher Technologiepfade für CO₂-neutrale und -freie Antriebe. www.vdi.de
3. Hong BK, Kim SH (2018) (Invited) recent advances in fuel cell electric vehicle technologies of hyundai. ECS Trans 86(13):3–11. <https://doi.org/10.1149/08613.0003ecst>
4. Mark Freymueller. Vorstellung Hyundai Hydrogen Mobility. KNI Workshop. https://www.kn-i.de/fileadmin/user_upload/20210707_HyundaiHydrogenMobilty_Wasserstoff.pdf.
5. U.S. DOE. Hydrogen storage. <https://www.energy.gov/eere/fuelcells/hydrogen-storage>. Accessed 26 March 2022

6. Rosen PA (2018) Beitrag zur Optimierung von Wasserstoffdruckbehältern Wiesbaden: Springer Fachmedien Wiesbaden
7. Kircher O, Greim G, Burtscher J, Brunner T (2011) Validation of cryo-compressed hydrogen storage (CCH₂)—a probabilistic approach. In: 4th ISFEH Conference. <https://h2tools.org/bibliography/validation-cryo-compressed-hydrogen-storage-cch2-probabilistic-approach>. Accessed 23 May 2022
8. Brunner T, Kircher O, Lutz J (2006) On the way to a new generation of production passenger car-integrated liquid hydrogen storage systems. In: WHEC 16, 13–16 June 2006, Lyon (France). <https://www.cder.dz/A2H2/Medias/Download/Proc%20PDF/PARALLEL%20SESSIONS/%5BS13%5D%20Storage%20-%20Liquid%20Hydrogen/14-06-06/196.pdf>. Accessed 23 May 2022
9. H2 MOBILITY Deutschland GmbH & Co. KG. Overview hydrogen refuelling for heavy duty vehicles. https://h2-mobility.de/wp-content/uploads/sites/2/2021/08/H2-MOBILITY_Overview-Hydrogen-Refuelling-For-Heavy-Duty-Vehicles_2021-08-10.pdf. Accessed 27 March 2022
10. Ahluwalia RK, Hua TQ, Peng J-K, Lasher S, McKenney K, Sinha J, Gardiner M (2010) Technical assessment of cryo-compressed hydrogen storage tank systems for automotive applications. *Int J Hydrogen Energy* 35(9):4171–4184. <https://doi.org/10.1016/j.ijhydene.2010.02.074>
11. Gangloff JJ, Ordaz G, Adams J, Stetson N (2016) Technical challenges and R&D needs for compressed hydrogen storage on-board fuel cell electric vehicles. In: 31st annual technical conference at Williamsburg, Virginia (USA)
12. Barthelemy H, Weber M, Barbier F (2017) Hydrogen storage: recent improvements and industrial perspectives. *Int J Hydrogen Energy* 42(11):7254–7262. <https://doi.org/10.1016/j.ijhydene.2016.03.178>
13. Hoffmann H, Neugebauer R, Spur G (eds) (2012) Handbuch Umformen, 2, vollständig neu, bearbeitete. Hanser, München
14. Crawshaw FD (2018) Metall spinning mechanics handbooks classic reprint. Forgotten Books, London
15. Kalaycıoğlu B, Dirikolu MH (2010) Investigation of the design of a metal-lined fully wrapped composite vessel under high internal pressure. *High Pressure Res* 30(3):428–437. <https://doi.org/10.1080/08957959.2010.504420>
16. Kohtz D (1994) Wärmebehandlung metallischer Werkstoffe Berlin. Springer, Berlin Heidelberg
17. Luxfer Gas Cylinders Ltd. <https://www.luxfercylinders.com/>
18. Samtech Co. Ltd. <http://www.samtech.co.jp/english/index.html>
19. Chalandon B, Daval R, Hepples W. Method of manufacturing pressure vessel liners, US 9.433.995 B2 (14. März)
20. Hydrogen embrittlement-related issues and needs in the hydrogen value chain. In: Somerday BP, Sofronis P (eds) (2014) International Hydrogen Conference (IHC 2012). ASME Press, pp 1–24
21. Colom S, Weber M, Barbier F (2008) Storhy: A european development of composite vessels for 70MPa hydrogen storage. In: 17th world hydrogen energy conference 2008 (WHEC (2008) Brisbane], Queensland, Australia, 15–19 June 2008: Red Hook, NY, p 2009
22. Reichel M (2017) Fertigungstechnik – Umformen. Springer Fachmedien Wiesbaden, Wiesbaden
23. Schneider R, Heine B, Grant RJ, Zouaoui Z (2015) Aluminium sheet metal forming at low temperatures. *IOP Conf Series: Materi Sci Eng* 74:12014. <https://doi.org/10.1088/1757-899X/74/1/012014>

Influence of Loading Direction on the Mechanical Parameters of Pre-formed Materials in Tensile Test



R. Norz and W. Volk

Abstract In the recent years, the determination of non-proportional loading paths has been the focus of many publications. Different models for the prediction of necking after non-proportional loading paths have been published and validated. Lately, also a change in loading direction has been investigated. It was found out that next to the deformation history, a change in loading direction leads to different Forming Limit Curves (FLC). The aim of this paper is the characterization of the influence on the mechanical parameters in tensile test. Pre-formed tensile tests with and without a change in loading direction under different strain rates and temperatures are investigated in order to determine the influences on a micro-alloyed steel and an aluminium alloy. Next to those parameters, the fracture surfaces are studied to assess the different fracture modes. These results contribute to a better understanding of the anisotropic hardening effects and the different fracture modes.

Keywords Pre-formed tensile tests · Non-proportional loading · Temperature

Introduction

To optimize forming processes, Finite Element Analyses (FEA) are widely used. To provide accurate results, a precise knowledge of the material behaviour is essential [1]. As complex forming processes undergo non-proportional loading paths, it is necessary to determine the material behaviour after pre-forming [2]. Barlat et al. [3] have shown that pre-forming, as well as a change in loading direction and load case, have a significant influence on the stress–strain curve. The dislocation structure plays a major role after non-proportional loading for AA1050-O material. They characterized this anisotropic behaviour in three stages. At the beginning of the experiment up to 2% strain, the Bauschinger effect is dominant, at higher strains, the reorganization of dislocations, and at large strains, the texture evolution is in control. The effect of pre-forming on the yield point and yield locus for AA6111 alloy was

R. Norz (✉) · W. Volk
Chair of Metal Forming and Casting, Technical University Munich, Walther-Meißner Strasse 4,
85748 Garching, Germany
e-mail: roman.norz@utg.de

investigated by Wu et al. [4]. A change in loading direction under uniaxial tension leads to a different shape of the yield locus. For their simulations, they modelled the transition effect by residual stresses generated during the pre-forming. Zandrahimi et al. [5] have shown that next to the yield point and yield locus, the uniform elongation is influenced by pre-forming. The higher the pre-forming strain and the change in loading direction, the earlier diffuse necking begins. This effect was also observed for a DP800 by Tarigopula et al. [6, 7]. The larger the change in loading direction, the bigger the transient behaviour of the pre-formed material in tensile-, shear-, and plane strain experiments is. To describe this plastic hardening behaviour after non-proportional loading paths, purely isotropic or kinematic hardening is not sufficient. A mixed isotropic and kinematic hardening model was used by Larsson et al. [8] to successfully model this behaviour in FEA.

In this paper, the effect of pre-forming and a change in loading direction on a micro-alloyed steel HC340LA as well as an aluminium alloy AA6082 are investigated. Tensile tests with pre-formed specimens under different strain rates and temperatures were conducted in order to quantify the influence of pre-forming, the change in loading direction, the strain rate and temperature on the mechanical parameters. To explain the results, the microstructure and the fracture surfaces are studied.

Experimental Setup

The pre-forming of the specimen was done by an oversized Marciniak tool [9] on a hydraulic Dieffenbacher press, see Fig. 1. This tool allows different pre-forming states by varying the specimen geometry. A flat, homogeneously pre-formed area allows the extraction of different pre-formed specimen geometries. The drawing depth of the punch is varied to achieve a stated pre-forming strain. The specimens were pre-formed under 0° to the rolling direction (IF0°). For the strain measurement after pre-forming, a GOM Argus System was used. Therefore, a grid was applied

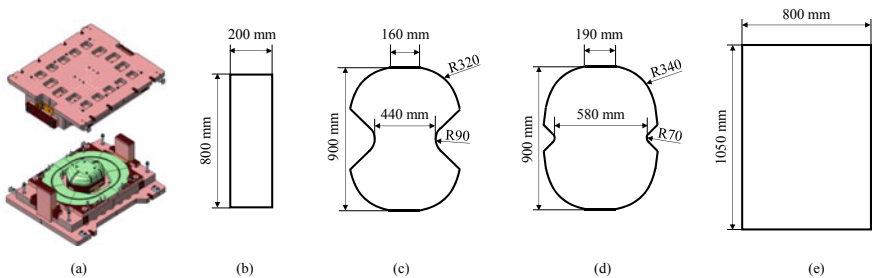


Fig. 1 a Marciniak tool used for pre-forming and the used specimen geometries for the b uniaxial, c plane strain, d $\varphi_1/\varphi_2 = 0.5$, and biaxial e strain state

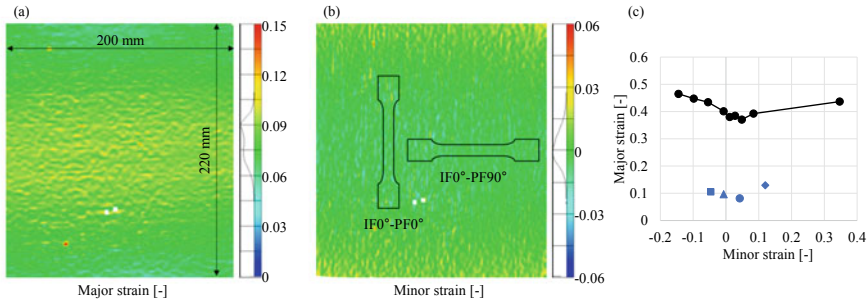


Fig. 2 a Major and b minor strain distribution of a plane strain pre-forming and the different pre-forming states in comparison to the linear FLC in rolling direction (c)

by electrochemical etching on all specimens. The tensile tests at elevated temperatures, 150 °C for the aluminium AA6082 and 300 °C for the steel HC340LA, were conducted on a Zwick DUPS 1484 with a maximum force of 200 kN, while the tensile tests at room temperature were conducted on a Zwick Z150. The strain rates were set to a constant value of 0.001 1/s, 0.01 1/s and 0.1 1/s.

The tensile test specimens were extracted under two different directions with respect to the initial rolling direction. Specimens without a change in loading direction are denoted as IF0°-PF0°, while specimens with a change in loading direction of 45° or 90° are denoted as IF0°-PF45° and IF0°-PF90°, respectively, see Fig. 2b. The tensile test specimen geometry is according to DIN EN ISO 50125, with a length of 165 mm and a width of 12.5 mm.

Results

Pre-Forming

Several specimens are pre-formed in order to extract tensile test specimens. To ensure a homogeneously pre-formed area, deep drawing oil as lubrication is used. The specimens are formed in a single forming operation with a constant punch speed of 15 mm/s. It can be seen that the deviation of the strains in the pre-formed specimen is negligible for the extraction area of the specimen. The height of the pre-forming strains is approximately 25% of the linear Forming Limit Curve (FLC). Per pre-formed specimen four tensile test specimens are extracted.

In the uniaxial pre-forming state, 25% of the linear FLC are approximately 50% of the uniform elongation. Therefore, sufficient remaining formability for the HC340LA and the AA6082 is ensured.

Tensile Test

To investigate the influence of pre-forming on the material, tensile tests with the initial material are conducted. For the HC340LA at room temperature (20 °C), a pronounced yield strength was found, independent of the loading direction. For the pre-formed specimens, no pronounced yield strength is detectable. For the uniaxial pre-formed specimen IF0°-PF0°, the flow curve is almost congruent with the reference flow curve under 0° as it is expected. At room temperature, a significant influence of the pre-forming state and a change in loading direction is detectable. An increase in yield strength and a distinct reduction in total elongation can be determined for uniaxial, the plane strain, and the $\beta = 0.5$ pre-forming with a change in loading direction. All IF0°-PF45° and IF0°-PF90° specimens show an instant strain localization, regardless of the pre-forming state, while for the IF0°-PF0° only, the $\beta = 0.5$ and the biaxial pre-forming show this behaviour. It is also visible that a bigger change in loading direction leads to a smaller total elongation (Fig. 3).

It can be clearly seen that the smaller the strain ratio β , the bigger the influence of a change in loading direction is. For the biaxial pre-formed specimens, the change in loading direction does not affect the flow curve, as the pre-forming is isotropic. The immediate localization for the $\beta = 0.5$ and the biaxial pre-formed specimens can be explained by the fact that a pre-forming of 25% of the linear FLC leads to an equivalent strain which is beyond the uniform elongation of the material.

For further investigations, the combination with the most significant influence is chosen. Therefore, the uniaxial pre-forming with a change in loading direction by 90° is further investigated. The formability of the material is not affected by the strain rate. A slight reduction can be observed for the initial material. For the uniaxial pre-formed material, the total elongation for the IF0°-PF90° material is detectable and an increased strength is found for the pre-formed material (Fig. 4).

The stress-overshoot for the IF0°-PF90° leads to a rotation of the stress state from uniaxial to the plane strain state and therefore early failure [10]. An influence of the loading direction can also be observed for a uniaxial pre-formed aluminium alloy

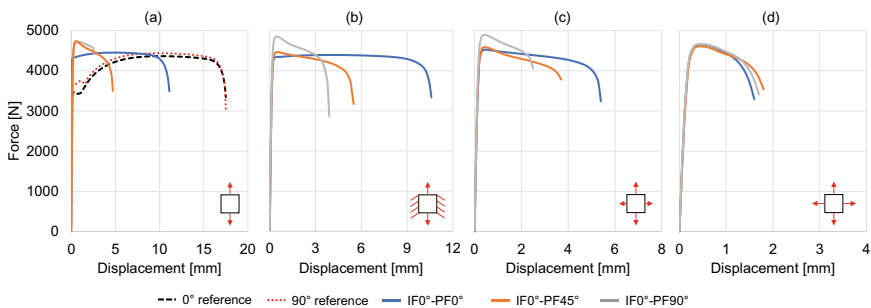


Fig. 3 Flow curve of the uniaxial (a), plane strain (b), $\beta = 0.5$ (c), and biaxial (d) pre-formed specimens for the HC340LA at a strain rate of 0.001 1/s

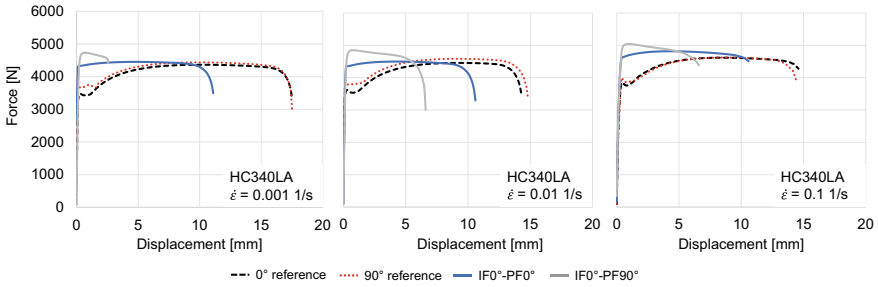


Fig. 4 Influence of the strain rate on the pre-formed HC340LA at room temperature

AA6082. The aluminium alloy is pre-formed up to 50% of the uniform elongation. A change in loading direction leads to a decrease in formability, regardless of the applied strain rate. Nevertheless, the influence of a change in loading direction is significantly smaller than for the micro-alloyed HC340LA steel. A stress overshoot can be observed for the IF0°-PF0° specimens, caused by latent hardening, while a cross-loading contraction effect is visible for the IF0°-PF90° specimens. These results are in good agreement with those from Manopulo et al. [10]. The material is not strain rate-sensitive, as expected for an AA6082 alloy (Fig. 5).

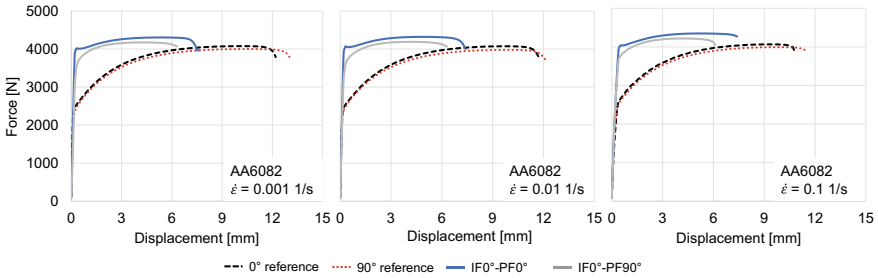


Fig. 5 Influence of the strain rate on the pre-formed AA6082 at room temperature

Tensile Tests at Elevated Temperatures

One explanation for this behaviour is the increase in dislocation density and the orientation of those dislocations [11, 12]. At elevated temperatures, the annihilation of those dislocations is increased for aluminium alloys as well as iron. At temperatures of $T/T_m > 0.15$, the dislocation annihilation is increased [13, 14]. Those elevated temperatures support the overcome of obstacles and therefore the dislocations can move more easily.

The strength for the HC340LA is not affected by the increased temperature while the formability of the initial material is increased. The pronounced yield strength has vanished and a PLC—effect occurs at low strains. At this temperature, an increased annihilation rate is observed by Malguyin [14] for BCC-materials. This is due to increased diffusion of the interstitial atoms [15]. Nevertheless, the pre-formed specimen does not show an increased formability. For the aluminium AA6082, a significantly lower strength and a significantly increased formability can be observed for the initial material. The pre-formed specimen shows a decrease in strength but no increase in formability. Both materials show a decreasing Young’s modulus (Fig. 6).

The fact that the formability of the pre-formed material is not increased at elevated temperatures leads to the conclusion, that the dislocations play a role for the initial material but have only little to no effect on the pre-formed material. Hence, the microstructure and the fracture surfaces of the two materials are investigated.

Microstructure Analysis

The microstructure of the micro-alloyed steel HC340LA shows a ferritic matrix with small amounts of coagulated carbides. For the specimens with no change in loading direction, the grains are elongated in loading direction, see Fig. 7. The IF0°-PF90° specimens show biaxial formed grains. This effect is more pronounced for the HC340LA in comparison to the aluminium alloy AA6082. The silver and black

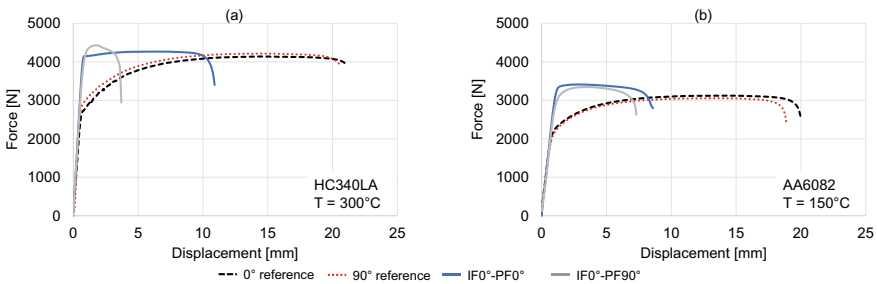


Fig. 6 Tensile tests at elevated temperatures for the HC340LA and the AA6082 at a strain rate of 0.001 1/s

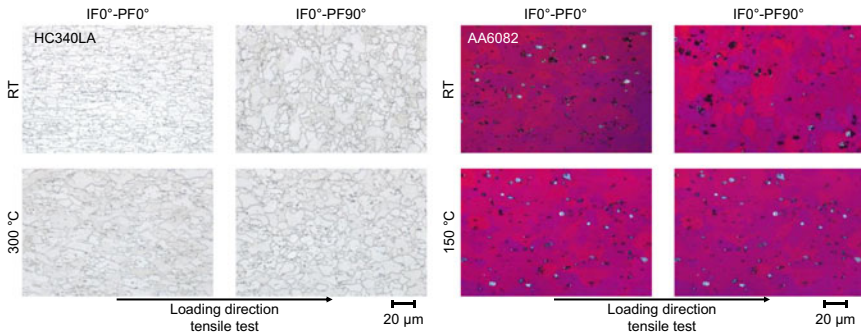


Fig. 7 Microstructure of the tensile test specimen at different temperatures after fracture

areas in the microstructure of the AA6082 are non-metallic inclusions, which are removed by the etching process. The investigated area is approximately 5 mm away from the fracture zone because in the fracture zone, all grains are elongated in the tensile test loading direction and no differences are detectable.

The fracture surfaces for the uniaxial pre-formed specimens are shown in Fig. 8. A significant increase in voids is detectable for the surfaces of the HC340LA specimens with a change in loading direction. The increased number of voids leads to an early failure of the specimens as the cross section of the tensile test specimen is reduced and therefore a local increase in stress occurs. For the AA6082, the fracture is initiated by cracks inside the hard and brittle inclusions, see Fig. 9. Therefore, only small voids occur before fracture.

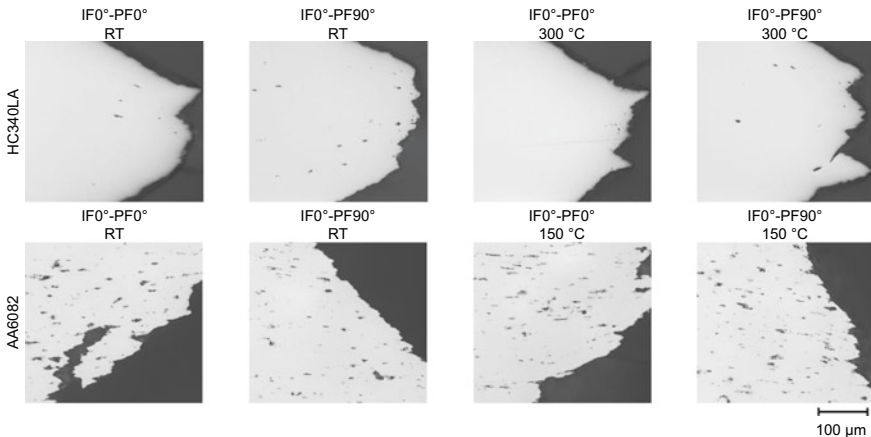


Fig. 8 Microvoids at the fracture surface for the HC340LA and the AA6082 at different temperatures

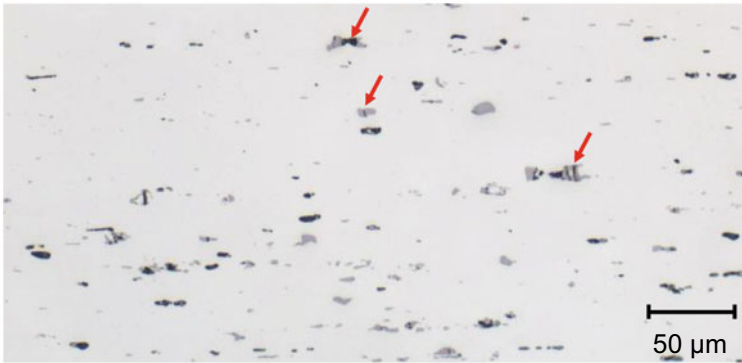


Fig. 9 Brittle fracture inside the inclusions before crack initiation

The significant amount of voids at the fracture surface for the IF0°-PF90° HC340LA specimens indicates that damage plays an important role after a change in loading direction. For the aluminium alloy AA6082, only small differences between the IF0°-PF0° and the IF0°-PF90° specimens are visible.

Conclusion and Outlook

In this paper, the influence of different pre-forming states and a change in loading direction on the flow curve are investigated. A micro-alloyed steel HC340LA and an aluminium alloy AA6082 are therefore tested. It is found that a change in loading direction has an influence on the total elongation of the material. This effect is occurring especially when a uniaxial or a plane strain pre-forming state is present. The formability can be enhanced when higher strain rates are applied for the HC340LA material, where the strain rate has almost no influence on the formability of pre-formed AA6082 specimens. Tensile tests at elevated temperatures show that the formability of the initial material is increased. The pre-formed specimens and the influence of a change in loading direction are not affected by an increased temperature. The reason for the observed material behaviour is found in the microstructure of the material. During pre-forming, the microstructure of the material is affected and the grains are elongated in loading direction. If a change in loading direction in the following tensile test takes place, the grains are stretched perpendicular to the initial forming direction. The fracture surfaces show that a change in loading direction leads to an increase in void size and number for the HC340LA steel. The fracture surfaces of the aluminium alloy AA6082 show only a small increase in void number. This observation is in good agreement with the results from tensile test, where the HC340LA, with its very pure microstructure, is more sensitive to a change in loading direction than the aluminium with its hard and brittle inclusions. Nevertheless, further

investigations are necessary to gain a deeper understanding of the different mechanisms in the pre-formed micro-alloyed steel and the aluminium alloy, which lead to the different material behaviours in tensile test. In addition, more materials have to be investigated to determine the dependency of the mechanical parameters on the loading direction. Especially steels with hard and brittle inclusions like dual-phase steels have to be investigated.

Acknowledgements The authors would like to thank the German Research Foundation (DFG) for the financial support under grant number 455960756.

References

1. Bruschi S, Altan T, Banabic D, Bariani PF, Brosius A, Cao J, Ghiotti A, Khraisheh M, Merklein M, Tekkaya AE (2014) Testing and modelling of material behaviour and formability in sheet metal forming. *CIRP Ann* 63:727–749. <https://doi.org/10.1016/j.cirp.2014.05.005>
2. Merklein M, Suttner S, Brosius A (2014) Characterisation of kinematic hardening and yield surface evolution from uniaxial to biaxial tension with continuous strain path change. *CIRP Ann* 63:297–300. <https://doi.org/10.1016/j.cirp.2014.03.039>
3. Barlat F, Ferreira Duarte JM, Gracio JJ, Lopes AB, Rauch EF (2003) Plastic flow for non-monotonic loading conditions of an aluminum alloy sheet sample. *Int J Plast* 19:1215–1244. [https://doi.org/10.1016/S0749-6419\(02\)00020-7](https://doi.org/10.1016/S0749-6419(02)00020-7)
4. Wu PD, MacEwen SR, Lloyd DJ, Jain M, Tugcu P, Neale KW (2005) On pre-straining and the evolution of material anisotropy in sheet metals. *Int J Plast* 21:723–739. <https://doi.org/10.1016/j.ijplas.2004.05.007>
5. Zandrahimi M, Platias S, Frice D, Barrett D, Bate PS, Roberts WT (1989) Effects of changes in strain path on work hardening in cubic metals. *Metall Trans A* 20:2471–2482. <https://doi.org/10.1007/BF02666682>
6. Tarigopula V, Hopperstad OS, Langseth M, Clausen AH (2008) Elastic-plastic behaviour of dual-phase, high-strength steel under strain-path changes. *Eur J Mech A Solids* 27:764–782. <https://doi.org/10.1016/j.euromechsol.2008.01.002>
7. Tarigopula V, Hopperstad OS, Langseth M, Clausen AH (2009) An evaluation of a combined isotropic-kinematic hardening model for representation of complex strain-path changes in dual-phase steel. *Eur J Mech A Solids* 28:792–805. <https://doi.org/10.1016/j.euromechsol.2008.12.004>
8. Larsson R, Björklund O, Nilsson L, Simonsson K (2011) A study of high strength steels undergoing non-linear strain paths—Experiments and modelling. *J Mater Process Technol* 211:122–132. <https://doi.org/10.1016/j.jmatprotec.2010.09.004>
9. Weinschenk A, Volk W (2017) FEA-based development of a new tool for systematic experimental validation of nonlinear strain paths and design of test specimens. *AIP Conference Proceedings* 1896. <https://doi.org/10.1063/1.5007966>
10. Manopulo N, Hora P, Peters P, Gorji M, Barlat F (2015) An extended modified maximum force criterion for the prediction of localized necking under non-proportional loading. *Int J Plast* 75:189–203. <https://doi.org/10.1016/j.ijplas.2015.02.003>
11. Peeters B, Kalidindi SR, Teodosiu C, van Houtte P, Aernoudt E (2002) A theoretical investigation of the influence of dislocation sheets on evolution of yield surfaces in single-phase B.C.C. polycrystals. *J Mech Phys Solids* 50:783–807. [https://doi.org/10.1016/S0022-5096\(01\)00094-1](https://doi.org/10.1016/S0022-5096(01)00094-1)
12. Rauch EF, Thuillier S (1993) Rheological behaviour of mild steel under monotonic loading conditions and cross-loading. *Mater Sci Eng, A* 164:255–259. [https://doi.org/10.1016/0921-5093\(93\)90673-3](https://doi.org/10.1016/0921-5093(93)90673-3)

13. Malygin GA (1999) Dislocation self-organization processes and crystal plasticity. *Phys-Usp* 42:887–916. <https://doi.org/10.1070/PU1999v042n09ABEH000563>
14. Malygin GA (2005) Structure factors that influence the stability of plastic strain of BCC metals under tensile load. *Phys Solid State* 47:896. <https://doi.org/10.1134/1.1924852>
15. Ananthakrishna G (2007) Current theoretical approaches to collective behavior of dislocations. *Phys Rep* 440:113–259. <https://doi.org/10.1016/j.physrep.2006.10.003>

Microstructure Modelling of the HEC Behaviour of a Novel Vanadium DP980 Cold Rolled Alloy



Bruce Williams, Khaled Abu-Samk, Jia Xue, Babak Shalchi Amirkhiz, and Colin Scott

Abstract Cold rolled high-strength dual-phase (DP) ferrite/martensite steels are the most commonly used advanced high-strength steels (AHSS) in automotive body in white applications, particularly for components where good formability is required. However, these alloys have limitations for parts where high stretch flange formability is required. The latter is usually characterised by the hole expansion coefficient (HEC). We have recently developed a vanadium microalloyed DP980 steel with tensile properties that are stable over a wide range of intercritical annealing (IA) temperatures. Interestingly, the HEC behaviour shows a strong IA dependence. We propose that this is related to a complex combination of microstructural parameters including ferrite grain size, martensite fraction, vanadium precipitate distribution, and, in this particular case, to the fraction of epitaxial ferrite formed during fast cooling. For as-quenched DP steels, it is well established that fracture initiates by void nucleation at the ferrite/martensite interface due to strain incompatibilities. The microstructural parameters can be optimised to reduce the local triaxiality at these interphase boundaries and hence reduce the void nucleation and growth rate during straining. For an improved understanding of this effect, finite element (FE) simulations at both the continuum and local scale were carried out. Continuum FE simulations of the HEC test were performed to capture the global state of stress and strain at fracture. A model was used in which the effective strain at fracture was dependent on stress triaxiality and Lode angle. The stress and strain state predicted at failure in the continuum model was then used as the boundary condition for local FE models of two different DP microstructures. The results of the local FE models are linked to the measured HEC response.

Keywords Hole expansion coefficient · Dual-phase steel · Microstructure · Finite element analysis

B. Williams (✉) · J. Xue · B. Shalchi Amirkhiz · C. Scott
CanmetMATERIALS, Natural Resources Canada, 183 Longwood Road South, Hamilton, Canada
e-mail: bruce.williams@nrcan-rncan.gc.ca

K. Abu-Samk
Department of Materials Science and Engineering, McMaster University, 1280 Main St. W,
Hamilton, Canada

© Her Majesty the Queen in Right of Canada, as represented by the Minister of Natural Resources 2022

K. Inal et al. (eds.), *NUMISHEET 2022*, The Minerals, Metals & Materials Series,
https://doi.org/10.1007/978-3-031-06212-4_82

Introduction

Dual-Phase (DP) steels with good strength and tensile elongation have been utilised for lightweighting in-vehicle body-in-white (BIW) components for more than 30 years. However, there is still a need to improve the fracture response of these alloys under a variety of loading conditions, particularly those encountered in parts that require good stretch flange formability. This requires an improved understanding of the interaction between the ferrite and martensite structure and damage mechanisms. In untempered DP steels, microvoids first nucleate at ferrite–martensite interfaces, primarily related to strain incompatibilities caused by the large difference in strength between the two phases. This difference between the soft ferrite and hard martensite strengths can be quantified by the Phase Strength Ratio (PSR) and it can be shown that there is a benefit in reducing this ratio.

Recently Scott et al. [1, 2] and Pushkareva et al. [3] described a vanadium microalloyed (DP-V) steel that was shown to have improved ductility without a loss of strength compared to a reference DP steel with no V additions. Approximately 0.16 wt.% V was added to a reference DP composition, resulting in significant refinement of both the ferrite and martensite grain sizes. After cold rolling and continuous annealing V(C,N), precipitates in ferrite grains were smaller and much more numerous than those observed in the martensite phase. This led to selective precipitation strengthening of the ferrite phase (hence to a lower PSR ratio) and improved ductility, without loss of strength. It was shown in [1, 3] that reducing the PSR by tempering the martensite phase is much more efficient than selectively strengthening the ferrite for improved failure performance. In other words, reducing the mean PSR by strengthening ferrite does not greatly improve fracture resistance. It is noted that PSR is far from being the only microstructure parameter controlling DP damage response and is possibly not even the most important. For example, the martensite fraction and distribution seem to have a larger impact on failure. In the nano-indentation studies, it was shown that neighbouring martensite islands in as-quenched DP can take an extremely wide range of hardness values (3–10 GPa). This range is much bigger than could be achieved by any realistic ferrite strengthening mechanism (~1 GPa). Consequently, in the as-quenched condition, there are always going to be critical local configurations for damage initiation around the hardest martensite islands. Now, temper softening kinetics are known to be the fastest for very hard (high carbon) martensite. This means that tempering is a much more efficient way to preferentially eliminate the most critical local configurations where damage is initiated.

It is known that the fracture response of ductile metals is dependent upon stress triaxiality and Lode angle. The damage and fracture response of DP980 has recently been studied by Park et al. [4] using an anisotropic fracture model, Wang et al. [5] with the Oyane fracture model, Pack et al. [6] using a modified Hosford–Coulomb model, and Darabi et al. [7] using the Modified Mohr–Coulomb (MMC) fracture model. In these studies, a number of mechanical tests were performed using tensile, shear, notched, and biaxial test geometries to produce a range of loading conditions. The

experimental results were used in combination with FE simulation and optimization methods to determine fracture model coefficients for DP980. One commonality between the fracture models was that they were all dependent on stress triaxiality but considered only the global and not the local response.

To gain a better understanding of the influence of the microstructure on the stress triaxiality of dual-phase steels, local modelling was carried out in the current work. A recently published structure-properties model for DP steel was used to obtain the local stress versus strain response of the ferrite and martensite phases. The stress and strain states applied in the local model were determined by first performing global finite element simulations of the Hole Expansion (HE) test.

Dual-Phase Vanadium Alloyed Steel

Material, Processing, Annealing, and Tempering

Several DP-V ingots were produced at CanmetMATERIALS (CMAT) using a vacuum induction furnace. The chemical composition was Fe with (0.14–0.18) C, (1.7–1.9) Mn, 0.2 Si, (0.03–0.7) Cr, (0–0.14) Mo, 0.15 V, and (0.06–0.08) N. The ingots were then processed to 1 mm strips on the CMAT hot and cold pilot rolling mill. Hot and cold rolling parameters can be found in [1, 2]. Following cold rolling, a continuous annealing simulator (CASIM) was used to simulate processing on both continuous annealing (CAL) and galvanising (GI) lines. From each annealed blank (200 mm × 100 mm), either two (100 mm × 100 mm) HE coupons or four 12.5 mm × 50 mm tensile specimens were cut for testing. Physical GI annealing simulations were carried out using an infrared furnace. Strips were intercritically annealed at either 750, 800, or 810 °C for 100 s followed by fast gas cooling at approximately 30 °C/s to 460 °C. After holding for 200 s, the strips were gas quenched to room temperature at an initial rate of about 20 °C/s. Additional CAL simulations were made on strips which were water quenched after holding 100 s at 750 and 800 °C. In all cases, the heating rate was 4 °C/s.

Tensile and Hole Expansion Tests

HE tests were performed using the standard test procedure outlined in ISO16630 [8]. Prior to performing the HE tests, a 10 mm diameter hole was punched in the 1 mm thick sheet (using a 10.3 mm diameter die). A four-post punch fixture with linear bearings ensured strict alignment of the punch and die system when punching the holes. The HE test was carried out at a punch displacement rate of 0.1 mm/s with a camera frame rate of 10 Hz. After testing, the images were examined and the Hole Expansion Coefficient (HEC) was calculated based on the first through-thickness

crack wider than about 0.1 mm. The images at which the HEC was calculated for the 750 and 810 °C GI samples are shown in Fig. 1.

The engineering stress versus strain response of tensile specimens is shown in Fig. 2a. The corresponding HEC versus intercritical annealing (IA) temperature results are shown in Fig. 2b with four–five repeats shown per condition. The tensile responses for the 800 and 810 °C GI conditions are very similar with only a small decrease in elongation of about 2% at 810 °C. However, there was a significant improvement in HEC from an average of 17%, 27%, and 37% between 750, 800, and 810 °C, respectively. As expected, quenching increased the tensile strength and decreased the uniform elongation. However, there was only a small decrease in HEC for the 750 and 800 °C quenched samples (16% and 24%, respectively) compared to samples that were not quenched. These results confirm that there is no correlation between elongation in a tensile test and HEC. Consequently, it is important to capture the stress and strain state from HE testing in modelling efforts.

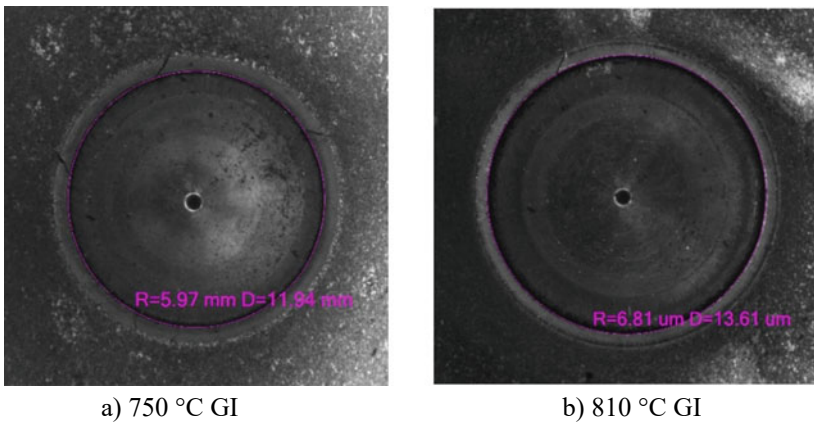


Fig. 1 Images showing crack formation of 1 mm through the thickness of DP-V sheet

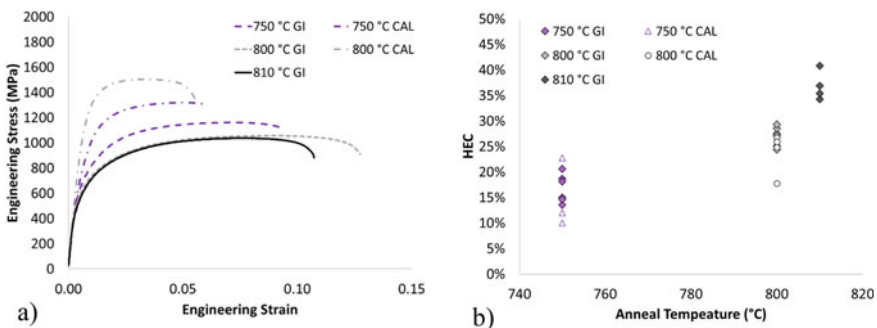


Fig. 2 a Engineering stress versus strain and b Hole Expansion Coefficient (HEC) versus IA anneal temperature response of DP-V

Microstructure

An FEI Osiris FEG-S/TEM equipped with a Super-X EDS detector system was used to analyse the microstructure of the DP-V steel. Figure 3a shows a STEM bright-field micrograph of a DP-V sample after GI annealing at 800 °C. Ferrite grains appear light and martensite grains appear dark. The image is superimposed with V and Mn EDX maps. The red dots indicate fine V(C,N) precipitates mainly within the ferrite grains with fewer, coarser particles in the martensite grains. These features are detailed further in [1–3].

An interesting result is observed in the EDS map of Mn in Fig. 3b. The Mn-rich martensite grains can be readily distinguished. However, two distinct types of ferrite are now noticeable. The original intercritical ferrite, F_I , grains, and then new epitaxial ferrite, F_E , which has grown outwards from F_I into the surrounding austenite during the first seconds of the fast gas cooling step. The epitaxial ferrite can grow very quickly as there is no nucleation barrier to overcome. Only carbon has time to partition so the F_E regions are clearly revealed by Mn enrichment within ferrite in the vicinity of the martensite islands. Figure 2a showed there was a decrease of tensile strength of about 83 MPa between 750 and 810 °C GI cycles. This seemed counter-intuitive as the martensite fraction should be higher at the higher IA temperature. However, a significantly larger amount of epitaxial ferrite formed during gas cooling from 810 °C leading to an overall lower strength.

The primary damage mechanism in DP steel is void nucleation, growth, and coalescence at ferrite/martensite boundaries due to strain incompatibilities. It is suggested that the combination of F_I , F_E , and M phases leads to an improved distribution of stress and strain leading to an improved fracture response. This will be

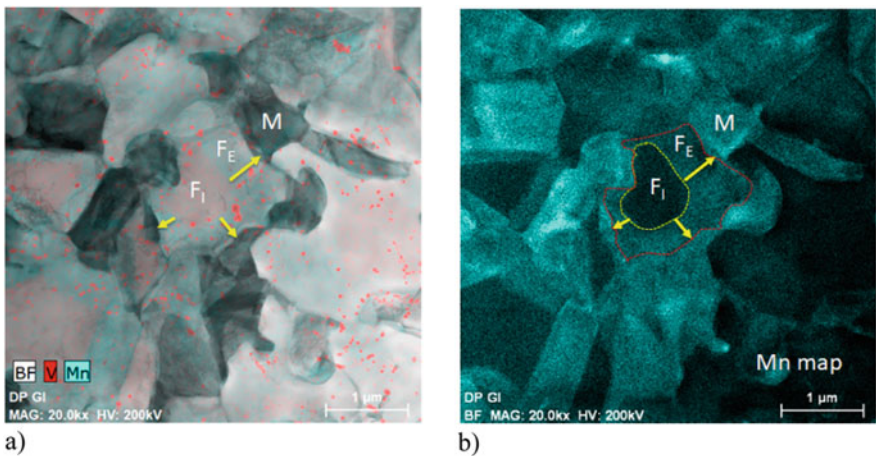


Fig. 3 a) STEM bright-field micrograph and b) EDS map of Mn for DP-V microstructure

explored below using local micromechanical modelling based on an accurate state of stress and strain obtained from global FE modelling of the HE test.

Global and Local Finite Element Simulations of DP-V Steel

FE Model of Hole Expansion Tests

The HE test was modelled in Abaqus using approximately 1,000 axisymmetric elements with an element size near the location of failure of 0.14 mm. The flow stress of the material was described by $\tilde{\sigma} = 542(1 + 446.2\bar{\epsilon}^p)^{0.216}$ which was based on the 810 °C anneal sample shown in Fig. 2a and extrapolated to a higher effective plastic strain, $\bar{\epsilon}^p$. Neither anisotropic deformation nor anisotropic fracture as discussed by Darabi et al. [7] was considered.

The MMC model used in the current work is given by [7, 9]

$$\epsilon_f = \left\{ \frac{A}{C_2} \left[C_3 + \frac{\sqrt{3}}{2 - \sqrt{3}}(1 - C_3) \left(\sec\left(\frac{\theta_L \pi}{6}\right) - 1 \right) \right] \left[\sqrt{\frac{1 + C_1^2}{3}} \cos\left(\frac{\theta_L \pi}{6}\right) + C_1 \left(\eta + \frac{1}{3} \sin\left(\frac{\theta_L \pi}{6}\right) \right) \right] \right\}^{-1/n} \quad (1)$$

where C_1, C_2, C_3, A , and n are material constants. The strain to initiate fracture, ϵ_f , depends on stress triaxiality, η , and Lode angle, θ_L . The stress triaxiality is given by the mean stress divided by the effective stress ($\eta = \sigma_m/\tilde{\sigma}$). In the models of Pack et al. [6] and Darabi et al., [7] elements are deleted when the damage equals unity and the material softens from the onset of plastic strain with the damage rate increasing near failure. The slightly alternative approach detailed by Paredes et al. [9] was used in the current work. In this model, damage accumulates from the onset of plastic strain but the element is not softened until an initial damage, D_0 , is reached. Then, the strength of the element is weakened according to $\varpi = [(D_c - D)/(D_c - D_0)]^m$ until a critical damage level, D_c , is achieved when the element is deleted from the model. The model coefficients used for DP980 are given in Table 1 and the D_0 and

Table 1 MMC fracture model coefficients for DP980

Model	A	n	C1	C2	C3	D0	Dc	m
MMC (Darabi et al. [7])	1695.12	0.153	0.15	900	0.925	0	1	–
MMC-current	446.2	0.216	0.23	205	0.925	1	1.8	0.1

D_c curves for a normalized Lode angle of unity are shown in Fig. 6. The model was implemented as a user-defined subroutine in Abaqus according to Simha and Williams [10].

A contour plot of stress triaxiality predicted just before the first element deletion is shown in Fig. 4. The predicted force versus punch displacement profile is compared to corresponding experimental data in Fig. 5 showing reasonable agreement with the 810 °C annealed tests. The effective strain versus stress triaxiality profile taken from an element near the location of failure is shown in Fig. 6 and compared against the fracture envelope of DP980 for a normalized Lode angle of unity. The stress ratio during loading at an element on the hole edge was about $\hat{\sigma}_{xx} : \hat{\sigma}_{yy} : \hat{\sigma}_{zz} = 1.0:0.0:0.0$ with a stress triaxiality of 0.33. The strain ratio was about $\hat{\epsilon}_{xx} : \hat{\epsilon}_{yy} : \hat{\epsilon}_{zz} = 1.0:-0.43:-0.57$ with an effective strain of 0.33 at first element deletion. These conditions are close to uniaxial tension (with the major load in the circumferential direction). These stress and strain conditions were applied in the local models. Away from the edge, the stress and strain state approaches equi-biaxial tension with a triaxiality of about 0.66. The x, y, and z directions correspond to the circumferential, radial, and thickness directions, respectively.

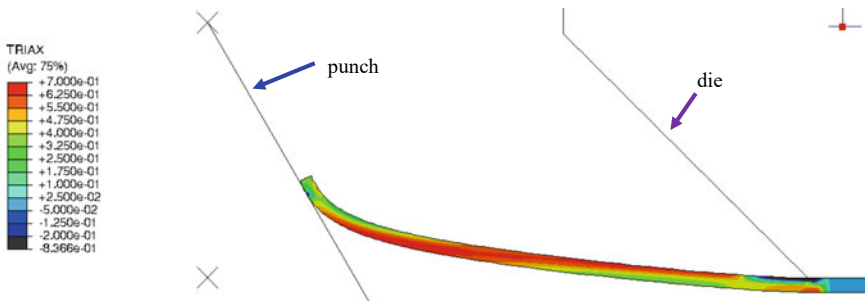


Fig. 4 Contour plot of stress triaxiality predicted in HE test

Fig. 5 Predicted versus measured load profile from HE test

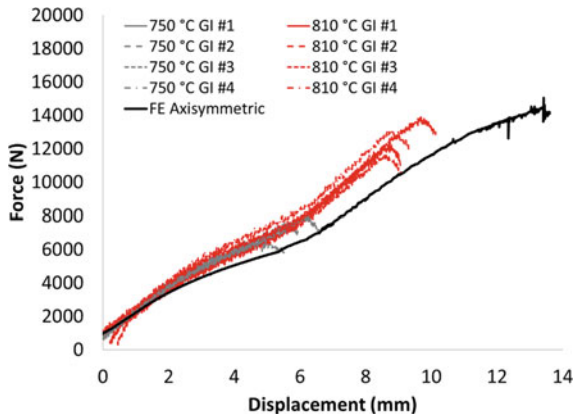
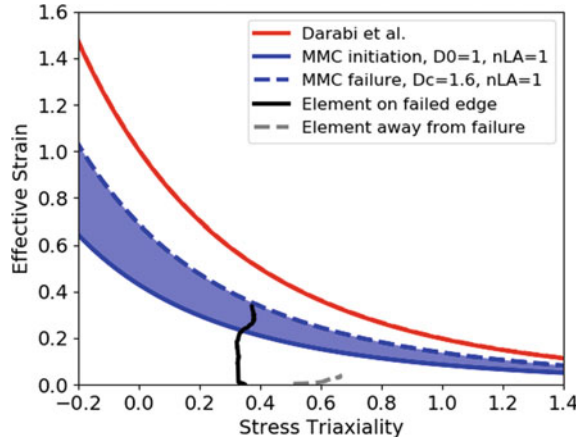


Fig. 6 Fracture envelope for DP980

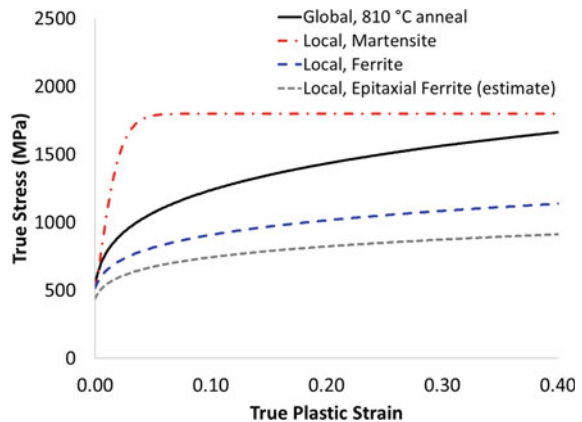


Microstructure Modeling of DP980

FE was used to assess how the stress distribution is influenced by the ferrite and martensite phases. Although F_E grains cannot be classified as a new phase, distinct mechanical properties of F_I and F_E phases were specified in the models such that a three-phase material was essentially modelled. Duchaussoy et al. [11] detail a method, referred to as ASTAR, of using crystal orientation mapping to obtain grain structures from TEM images. This method was not available in the current work so a representative microstructure based on Fig. 3 was modelled. SEM-EBSD images of the grain structure should also be considered for FE modelling.

Allain et al. [12] detail a structure-properties model that characterizes the stress versus strain response of ferrite and martensite in DP steel. The true stress versus strain responses shown in Fig. 7 used for the ferrite (F_I) and martensite (M) phases in

Fig. 7 Stress versus strain response of F_I , F_E , and M phases compared to the bulk behaviour



the local FE model were based on the local responses predicted from the structures–properties model for a DP-V steel in [1]. Also shown is the global response for the 810 °C GI material. The epitaxial ferrite (F_E) was taken to be slightly softer than intercritical ferrite (F_I) due to lower precipitation strengthening. An estimated stress–strain response of the F_E phase is seen in the figure, which was based on the ferrite stress–strain response in a DP steel with no V additions as presented in [1].

Two-phase and three-phase microstructures were modelled based on the microstructural images shown in Fig. 8. OOF2 [13] was used to generate an FE mesh from the images. The meshes comprised about 15,000 solid elements with one element through the thickness (in the z-direction). Simulations were performed using the explicit solver in Abaqus. Displacements were applied to the surface edges to produce a strain ratio of about $\hat{\epsilon}_{xx} : \hat{\epsilon}_{yy} : \hat{\epsilon}_{zz} = 1.0 : -0.43 : -0.57$ with a stress ratio of $\hat{\sigma}_{xx} : \hat{\sigma}_{yy} : \hat{\sigma}_{zz} = 1.0 : 0.0 : 0.0$. In some simulations, it was necessary to enforce the z-strain to prevent premature localization to achieve a large effective strain of 0.33.

Predicted contour plots of stress triaxiality (TRIAx) for the two- and three-phase simulations are shown in Figs. 9 and 10 for an effective strain of 0.02 and 0.06, respectively. The figures indicate a large variation in stress triaxiality from less than -0.02 to some local regions with a value greater than 1.4. Localization occurred early in simulations with no z-constraint (z-free) as highlighted in Fig. 10. The strain levels at which localization occurred were well below the predicted effective strain at failure in the HE tests of about 0.33. To produce this level of effective strain without localization, a small constraint was necessary in the z-direction (thickness).

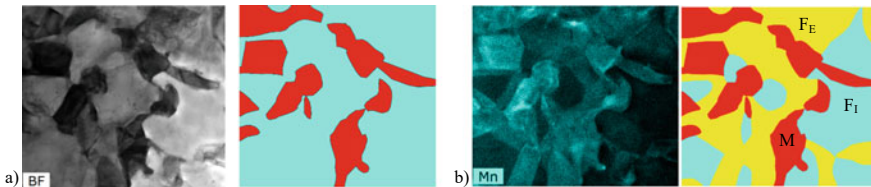


Fig. 8 Representative of a 2-phase (F_I and M) and b 3-phase (F_I , F_E , and M) microstructure

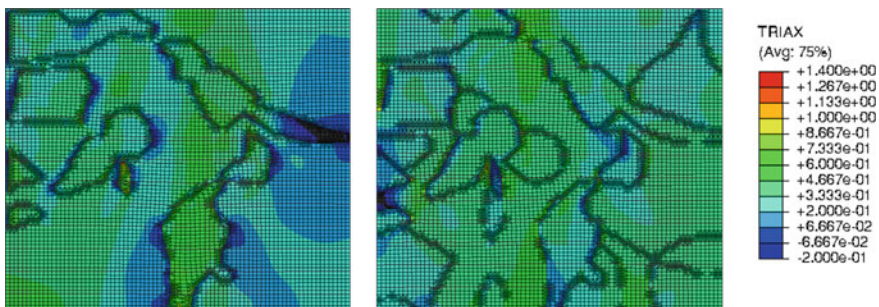


Fig. 9 Contour plot of triaxiality at an effective strain of 0.02 (z-free): Left 2-phase, Right 3-Phase

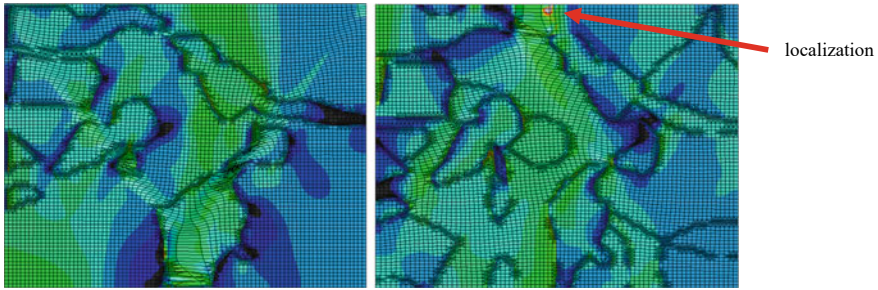


Fig. 10 Plot of triaxiality at an effective strain of 0.06 (z-free): Left 2-phase, Right 3-Phase

The predicted triaxiality at an effective strain of 0.33 is compared between the two- and three-phase microstructure in Fig. 11. The microstructures are elongated in the x -direction but compressed in y - and z -directions. Triaxiality is predicted to be higher in the ferrite phase. For the three-phase microstructure, the triaxiality between the martensite and ferrite (F_I and F_E) phases is slightly greater than for F_I alone and the local regions of high triaxiality are more apparent. The triaxiality averaged over the microstructure increased slightly to 0.49 for the three-phase simulation compared to 0.44 for the two-phase simulation. This trend is unexpected and may be attributed to using a lower strength F_E phase. Further work is required to understand the strength of F_E and correlate the shift of triaxiality to the fracture response of the material.

Conclusions

Previously, it was shown that V precipitates in Dual-Phase steels (DP-V) produce a more efficient phase strength ratio by selectively increasing the ferrite strength leading to improved fracture resistance. In the current work, the role of intercritical annealing was further examined for DP-V steel. It was found that the Hole Expansion Coefficient (HEC) increased from an average of 17–37% when performing a GI annealing sequence at either 750 °C or 810 °C, respectively. This large increase in HEC was accompanied by only a slight decrease in tensile strength of 83 MPa, from

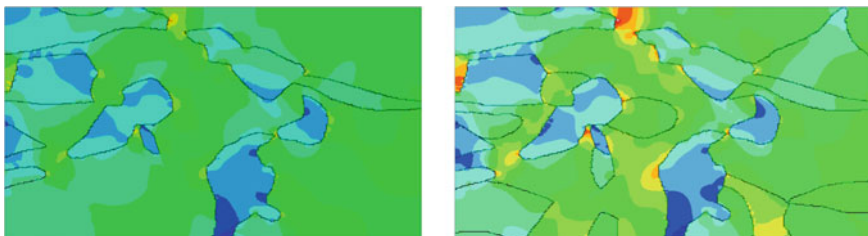


Fig. 11 Plot of triaxiality at an effective strain of 0.33 (z-constrained): Left 2-phase, Right 3-Phase

1161 to 1078 MPa. TEM investigations revealed an Mn-rich epitaxial ferrite (F_E) zone formed between the M and intercritical ferrite (F_I) phases. Local FEA analysis of the microstructure was performed to study the stress triaxiality during deformation. Global FEA of the HE test was first performed to obtain the stress and strain state near the location of failure and was then applied in the microstructural FEA model. Though F_E was not a distinct phase, it was treated as such in the local FEA model and was prescribed a lower strength than the F_I zone due to lower precipitation hardening. A slight shift in stress triaxiality was predicted between the two-phase (M and F_I) and three-phase (M, F_I , and F_E) microstructures. Further FEA analysis is required to correlate local triaxiality to fracture.

Acknowledgements The authors would like to acknowledge the casting and rolling groups at CanmetMATERIALS as well as Lucian Blaga and Jie Liang for performing the annealing and mechanical testing. Ongoing support and discussion with Vanitec, Stelco, and Arcelor Mittal-Dofasco is well appreciated. Funding for this project was provided by Natural Resources Canada.

References

1. Scott CP, Shalchi-Amirkhiz B, Pushkareva I, Fazeli F, Allain SYP, Azizi H (2018) New insights into martensite strength and the damage behaviour of dual phase steel. *Acta Mater* 159:112–122
2. Scott CP, Fazeli F, Shalchi-Amirkhiz B, Pushkareva I, Allain SYP (2017) Structure-properties relationship of ultra-fine grained V-microalloyed dual phase steels. *Mater Sci Eng A* 703:293–303
3. Pushkareva I, Scott CP, Goune M, Valle N, Redjaimia A, Moulin A (2013) Distribution of carbon in martensite during quenching and tempering of dual phase steels and consequences for damage properties. *ISIJ Int* 53:1215–1223
4. Park N, Huh NJB, Jung CG (2015) Anisotropy effect on the fracture model of DP980 sheets considering the loading path. *Int J Automot Technol* 16:73–81
5. Wang H, Yan Y, Jia F, Han F (2016) Investigations of fracture on DD980 steel sheet in roll forming process. *J Manuf Process* 22:177–184
6. Pack K, Tancogne-Dejean T, Gorgi MB, Mohr D (2018) Hosford–Coulomb ductile fracture model for shell elements: experimental identification and validation for DP980 steel and aluminum 6016–T4. *Int J Solids Structures* 151:214–232
7. Darabi AC, Guski V, Butz A, Kadkhodapour J (2020) A comparative study on mechanical behavior and damage scenario of DP600 and DD980 steels. *Mech Mater* 143:1–13
8. ISO 16630:2017 Metallic materials—sheet and strip—hole expanding test, International Organization for Standardization
9. Paredes M, Sarzosa DFB, Savioli R, Wierzbicki T, Jeong DY, Tyrell DC (2018) Ductile tearing analysis of TC128 tank car steel under mode I loading condition. *Theor Appl Fract Mech* 96:658–675
10. Simha CHM, Williams BW (2016) Modeling failure of Ti-6Al-4V using damage mechanics incorporating anisotropy, rate and temperature on strength. *Int J Fracture* 198:101–115
11. Duchaussoy A, Sauvage X, Edalati K, Horita Z, Renou G, Deschamps A, De Geuser F (2019) Structure and mechanical behavior of ultrafine-grained aluminum-iron alloy stabilized by nanoscaled intermetallic particles. *Acta Mater* 167:89–102

12. Allain SYP, Bouaziz O, Pushkareva I, Scott CP (2015) Towards the microstructure design of DP steels: a generic size-sensitive mean-field mechanical model. *Mater Sci Eng A* 637:222–234
13. Langer SA, Reid ACE, Coffman VR, Doğan G, Haan S-III, García RE, Lua RC (2019) OOF: finite element analysis of microstructures THE OOF2 Manual: revision 4.0.0 for OOF2 Version 2.1.1. National Institute of Standards and Technology

Numerical Description of the Physical Properties of Stretch Web Connectors in Progressive Die Stamping



Florian Steinlehner, Annika Weinschenk, Sven Kolb, Stefan Laumann,
and Wolfram Volk

Abstract The design of the strip layout and in particular, the geometry of the stretch web connector in progressive die stamping has so far been predominantly experience-based aiming for material utilization and cost optimization. Disruptive vibrations of the highly dynamic transportation of the strip can lead to reduced part quality and at worst, to a component collision and a damaging of the tooling. Therefore, the stroke rate and the production rate often need to be reduced. A physical model is developed, which describes the mechanical properties of the stretch web, taking the requirements of the progressive die stamping process into account. These properties are material- and geometry-dependent and are determined by a finite element model, which is validated by experimental tensile and impact modal testing. Based on the most common stretch web shapes found in industrial applications, a study of the influence of the stretch web geometry on its physical properties for the use of progressive die stamping is conducted to.

Keywords Progressive die stamping · Stretch web connector · Sheet metal forming · Strip-layout design

F. Steinlehner (✉) · S. Kolb · W. Volk

Chair of Metal Forming and Casting, Technical University of Munich, Walther-Meissner-Strasse 4, 85748 Garching, Germany
e-mail: Florian.Steinlehner@utg.de

S. Kolb

e-mail: Sven.Kolb@tum.de

W. Volk

e-mail: Wolfram.Volk@utg.de

A. Weinschenk

Hexagon Canada, 555 Michigan Drive, Oakville, ON, Canada

e-mail: Annika.Weinschenk@hexagon.com

S. Laumann

Men at Work GmbH, Hertzstrasse 1, 76467 Bietigheim, Germany

e-mail: Stefan.Laumann@maw-cax.de

Introduction

The aim of this work is to optimize the geometrical design of stretch web connectors used in progressive die stamping tools regarding their specific application and the requirements of the produced product. Therefore, the requirements of stretch web connectors which are derived from the progressive die stamping process itself and the produced part are described by a physical model. The physical characteristics of the stretch web connectors are experimentally and numerically determined using a tensile and an impact modal test. The obtained properties of different stretch web designs can afterwards be used to choose a suitable connector for a given product.

Progressive Die Stamping

Progressive die stamping is mainly used for high-volume production and is therefore designed to operate at a high speed rate. Due to the high acquisition costs of a progressive die, the design of the tooling and of the strip layout is often made in an early stage and often can not be changed while in operation. A tooling for progressive die stamping consists of several single stages through which a coiled strip material runs progressively while the part is produced. Each of the tooling stages performs one or multiple operations on the part and has different requirements. Operations performed to produce the product are, for example, deep drawing, piercing, coining, and cutting. The produced part usually remains connected to one or more carrier strips via stretch web connectors throughout the forming process. Pilot holes are often used to position the strip via pilot punches in their exact position on the single stages and are usually integrated into the carrier strip or the stretch web connector. Feeding machines are used to move the strip through the tooling. This feeding requires a lifting of the whole strip if the strip has areas with any three-dimensional structures, e.g. deep-drawn cups on it. The components of a progressive die strip are shown in Fig. 1 [1–4].

Requirements of Stretch Web Connectors

The design and development of progressive dies and the used geometry of the stretch web connector still lie largely in the hands of artisans and craftsmen. Nowadays, the design focuses to a high degree on **material utilization** and does often not take process-specific requirements into account. There are various requirements on the stretch web connector due to the specific processes. For accuracy and feeding aspects, a high **stiffness** in the connection between the carrier and the part is desired to suppress vibrations and inertial effects while transporting the strip through the tooling. Nevertheless, vibrations and disturbances can still occur randomly or due

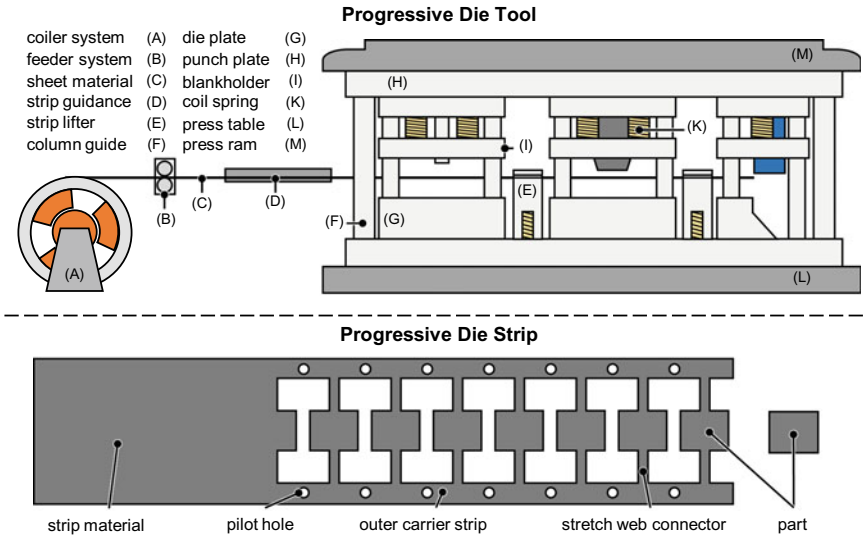


Fig. 1 Components of a progressive die tooling and a progressive die strip

to the process. A high overall **damping** on the strip is desired to help regulate the vibrations and to stabilize the feeding process. Forming operations often have their own specific requirements, such as the **retention** capability, which is strongly dependent on the actual process. For deep drawing operations, material flow of the surrounding material and a high **deformation capability** is preferred, whereas a strong restraining force is favoured for a stretch forming process. Due to safety reasons, a high overall **strength** of the stretch web is desired to keep the strip in its exact position and to avoid collisions with the surrounding tooling components. With an asymmetrically placed stretch web connector, which is often used due to spatial constraints and the utilization of material, **cross forces** can occur. Such forces will tend to weaken the stretch web in terms of its stiffness and damping behavior. Besides, they can lead to a disruptive motion and reduced part-accuracy. Cross forces are defined here as any force that is not parallel to the loading force. The following charts in Fig. 2 show some of the specific requirements for exemplary applications with normalized attributes on each of its axes [2]. With the help of a physical description, a finite element analysis (FEA) model is used to generate a property chart for different stretch web geometries to find a suitable design for a given use case, taking all physical requirements into account.

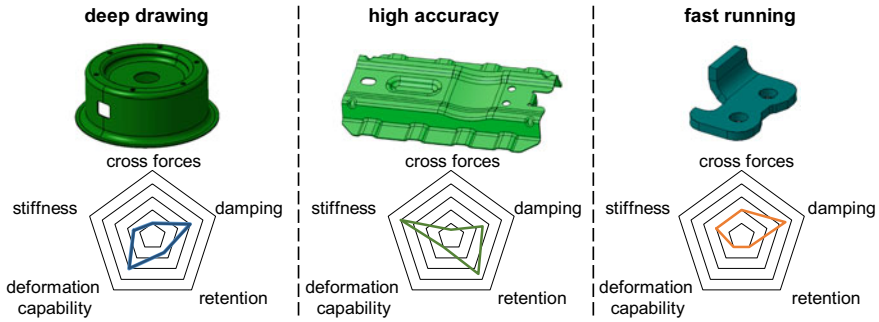


Fig. 2 Spider charts showing the required properties for exemplary applications in progressive die stamping

Physical Model Properties of the Stretch Web Connector

Next to the material’s characteristics, the behavior of a stretch web connector is mainly determined by its geometry. To specify a suitable stretch web design with an approach focused on the requirements of the part, the description of the physical model must be geometrically independent and generally valid. In this work, a spring–damping system with a single degree of freedom is used to describe the connector properties in all three dimensions in space. Thereby, the part can move in every direction on the strip within adjustable ranges. The physical model for a strip with two outer carriers is shown in Fig. 3.

The substantial requirements of stretch web connectors make it necessary to describe the strength, stiffness, cross forces, retention, deformation capability, and damping properties of the spring and the damper system:

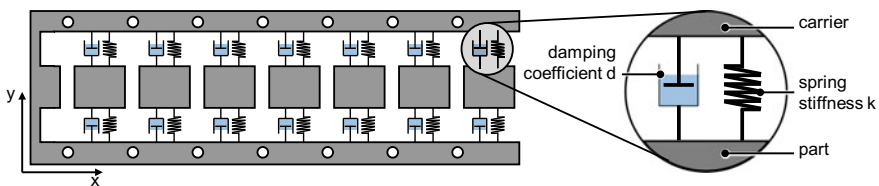


Fig. 3 Visualization of the physical model used to describe the geometrically independent stretch web connector with the help of a spring–damper system with a single degree of freedom

Physical Properties of Stretch Web Connector Derived from Part Requirements

In general, the **stiffness** of a structure is specified as the force needed for deformation along a certain axis. It can be obtained by the derivation of the force–displacement curve as $\frac{dF}{dx}$. For small deformations where no plasticity occurs, the stiffness of an ideal material can be modelled via Hooke’s law, as seen in Eq. (1).

$$\sigma(x) = E\varepsilon(x) \tag{1}$$

For larger deformations, however, as plasticity begins to develop, this relationship becomes non-linear and difficult to express in a mathematical model [5]. Additionally, geometric structures often result in non-linear stress–strain relationships, as deformations become increasingly complex.

The **retention** force is physically very similar to the stiffness, although its value is dependent on the current forming process and the actual force from the stretch web that is restricting the material from flowing into the die. The retention is specified as the force in the opposite direction of the material flow $F_{Retention}$. The strength of a material describes the maximum stress it can withstand before material failure occurs at $x_{failure}$. It is usually evaluated experimentally using standardized tests, although more complex geometric structures can influence the ultimate strength of a structure, necessitating further tests with specific geometries.

The **deformation capability** of a structure can be defined as total elongation until failure $\Delta x_{deformation}$. This parameter mainly depends on the total amount of material used in the structure and is thus highly geometry-specific.

Cross forces can also be obtained via the force–displacement curve and are measured as their maximum value at the occurring axis $F_{CF,i}$. For a generic mass oscillator with one degree of freedom, the basic equation of motion can be written as shown in Eq. (2) [6].

$$m\ddot{x} + d\dot{x} + kx = 0 \tag{2}$$

where m = mass, d = dampingcoefficient, k = stiffness

This equation can be rearranged to Eq. (3).

$$\ddot{x} + 2D\omega_0\dot{x} + \omega_0^2x = 0 \tag{3}$$

using $\omega_0 = \sqrt{\frac{k}{m}}$ and $D = \frac{d}{2\sqrt{km}}$ [6].

D is called **damping ratio**, and it can be used to characterize the global damping properties of a system as follows:

$D = 0$	$0 < D < 1$	$D = 1$	$D > 1$
Undamped system	Underdamped system	Critically damped system	Overdamped system

A solution of the differential Eq. (4) is given by [6]

$$x(t) = e^{-D\omega_0 t} \left[x_0 \cos \omega t + \frac{v_0 + D\omega_0 x_0}{\omega} \sin \omega t \right] \tag{4}$$

where $\omega = \omega_0 \sqrt{1 - D^2}$.

This equation can be interpreted as a periodic oscillation multiplied with an exponentially decaying term governed by D , describing the damped oscillation of a system at one frequency [6].

For more complex systems, however, modelling via a damped oscillator with singular mass and one degree of freedom is often not sufficient to represent the physical behavior of the system due to nonlinearities. This yields the necessity for more sophisticated damping models.

A model widely used in FEA is called Rayleigh damping. This model relies on two coefficients, α and β , which describe mass- and stiffness-proportionate damping, respectively. The relationship between the damping ratio and Rayleigh damping coefficients is given by Eq. (5).

$$D = \frac{\alpha}{2\omega} + \frac{\beta\omega}{2} \tag{5}$$

The Rayleigh coefficients α and β can be adjusted to match experimentally evaluated damping behavior at one or two natural frequencies using $\omega_i = 2\pi \cdot f_i$. The geometries discussed in this paper mostly show one dominant natural frequency and a few much weaker frequencies, which makes the Rayleigh damping model a suitable choice in this context [7].

Specimen Geometry and Approach

There are five general basic types of stretch web geometries, used for industrial applications. Those stretch web geometries are following referred to as *I-type A*, *O-type A*, *S-type A*, *U-type A*, and *L-type A* due to their geometrical resemblance to alphabetic letters. The idealized geometries are shown in Fig. 4.

The test specimens for this work are the basic types shown above and some variants of the *I-type* and the *O-type*. With the help of the validated finite element model, the investigation of unknown geometries is possible. Each of the stretch web geometries has advantages and disadvantages, which make them suited for different use cases. The most common stretch web geometry is the *I-type*, because of its simplicity and its

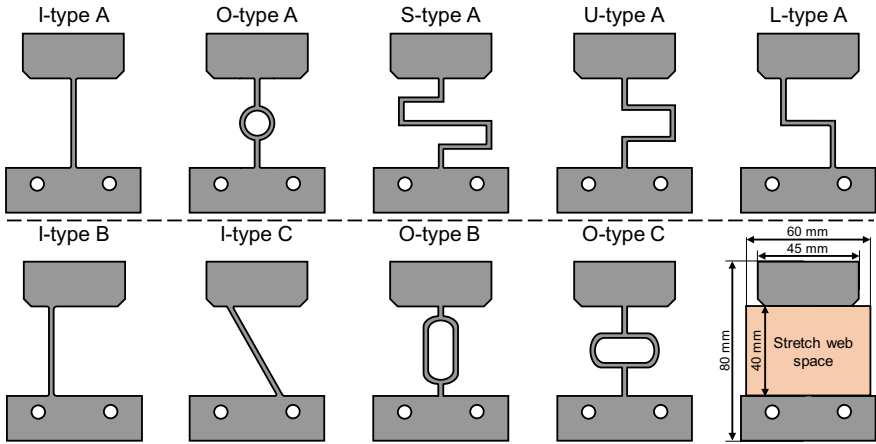


Fig. 4 Industrially used basic types (*I*, *O*, *S*, *U*, and *L*) for stretch web geometries and their variants

high space and material utilization. The *O-type* is used in many different variations to achieve higher retention and stiffness. In contrast, the *S-type*, the *U-type*, and the *L-type* behave very similarly and allow the structure to behave more elastically and give more flexibility to the process.

Experimental and Numerical Test Setup

The test specimens were experimentally and numerically investigated using tensile test and impact modal test. For the experimental tensile test, a universal testing machine Z150 TL, Zwick GmbH & Co. KG, Ulm, Germany, was used. The numerical tensile testing was implemented using the FEA software Abaqus FEA, Dassault Systèmes, Vélizy-Villacoublay, France. The setup of the experimental and numerical tensile test is shown in Fig. 5.

The test specimens are clamped on both ends, allowing deformation of the stretch web connector. For the experimental testing, mechanical clamping jaws are used to fix and move the clamped parts, whereas boundary conditions on the nodes are used for the FEA testing. The experimental testing in Y-direction is used to validate the finite element model. This model is used to investigate the stretch web’s behavior in X-, Y- and Z-directions.

The experimental impact modal testing is done using a vice to clamp the section of the carrier and a small hammer to provide an impulse into the area of the test specimen representing the part. The impulse is in Y-direction and the system’s vibration response is measured in the same direction with a laser vibrometer Polytec CLV-2534, Polytec GmbH, Waldbronn, Germany. Boundary conditions on the nodes are used to fix the carrier and to induce the impulse on the part side of the specimen

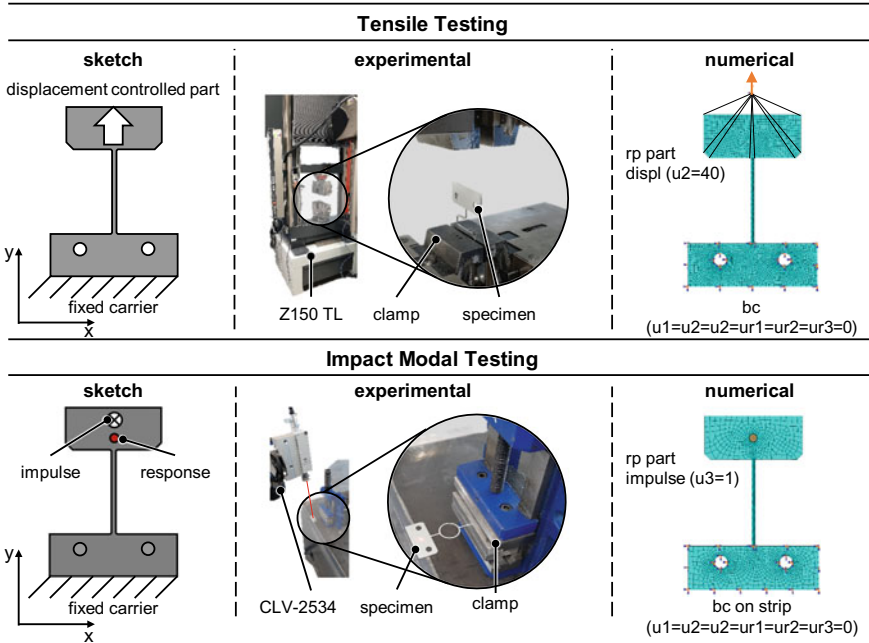


Fig. 5 Test setup for the experimental and numerical tensile testing and impact modal testing

in the Z-direction. The system’s response to the impulse can be measured in X-, Y-, and Z-directions with FEA. The damping is modelled using Rayleigh damping parameters calculated via the approach in Chap. 2, with $f_1 = 1.0$ Hz and f_2 being the experimentally obtained dominant natural frequency of each structure. The testing parameters for the experimental and numerical tensile and impact modal test are shown in following Table 1.

Table 1 Testing parameters for experimental and numerical tensile test and impact modal test

Tensile testing		Impact modal testing	
Experimental testing			
Load case	Y	Load case	Z
Output	Y	Output	Z
Drawing velocity	0.1 mm/s	Sampling frequency	38,400 Hz
Numerical testing			
Solver	Abaqus/Standard	Solver	Lanczos
Element type	C3D8R, C3D6	Element type	C3D8R, C3D6
Load case	X, Y, Z	Load case	X, Y, Z
Output	X, Y, Z	Output	X, Y, Z
Drawing velocity	40 mm/s	Sampling frequency	38,400 Hz

Table 2 Mechanical and chemical properties of the testing material AA5182

Mechanical Properties	$R_{p0.2}$ (MPa)		R_m (MPa)	A_{eq} (%)		A_{80} (%)	n_5 (-)	r_{10} (-)	
	135		280	22		25	0.3	0.63	
Chemical Properties	Si	Fe	Cu	Mn	Mg	Cr	Zn	Ti	other
	0.2	0.35	0.15	0.2–0.5	4.0–5.0	0.1	0.25	0.1	0.05

AA5182 with a sheet thickness of 1.5 mm was used for the experimental and numerical testing of the stretch web connectors. The material was characterized by a tensile test [8] and a Nakajima test [9]. The mechanical properties and the chemical composition of the material are shown in Table 2.

Validation of Numerical Model with Experimental Data

To validate the numerical model, the basic type stretch web connectors (*I*-, *O*-, *S*-, *L*-, and *U*-type *A*) are compared with the experimental results of the tensile and the impact modal testing in following Fig. 6. The force–displacement curve from the tensile testing gives information about the strength, the retention, the elasticity, and from the curves’ derivative, the stiffness. The global dampening parameter of the stretch web connector can be calculated from the decay curve produced by the impact modal testing.

The force–displacement curves of the numerical model are a good representation of the experimental data. The first 60% of the displacement are particularly well fitted and are the most relevant area of operation of stretch web connectors, as a certain safety factor must be considered while designing the stretch web geometry, to ensure a maximum displacement less than $x_{failure}$. One anomaly occurs for the *O*-type specimen. Here, the material failure in the experimental test takes place in one of the two strands of the oval-shaped area, whereas the failure in the numerical test occurs in the single-stranded part of the stretch web just before the carrier strip, outside the oval-shaped area. This behavior has to be taken into account when recommending and choosing an *O*-type stretch web connector for a given product.

Results of the Physical Properties of the Stretch Web Specimen

The physical properties of the test specimens as described in Chap. 2 are evaluated with the validated numerical model and visualized in the spider charts in Figs. 7, 8 and 9 for each test specimen. In general, a point further outside the center of the diagram indicates a higher value for each property, with the exception of cross forces. As these are generally undesired, a point further outside indicates lower cross forces.

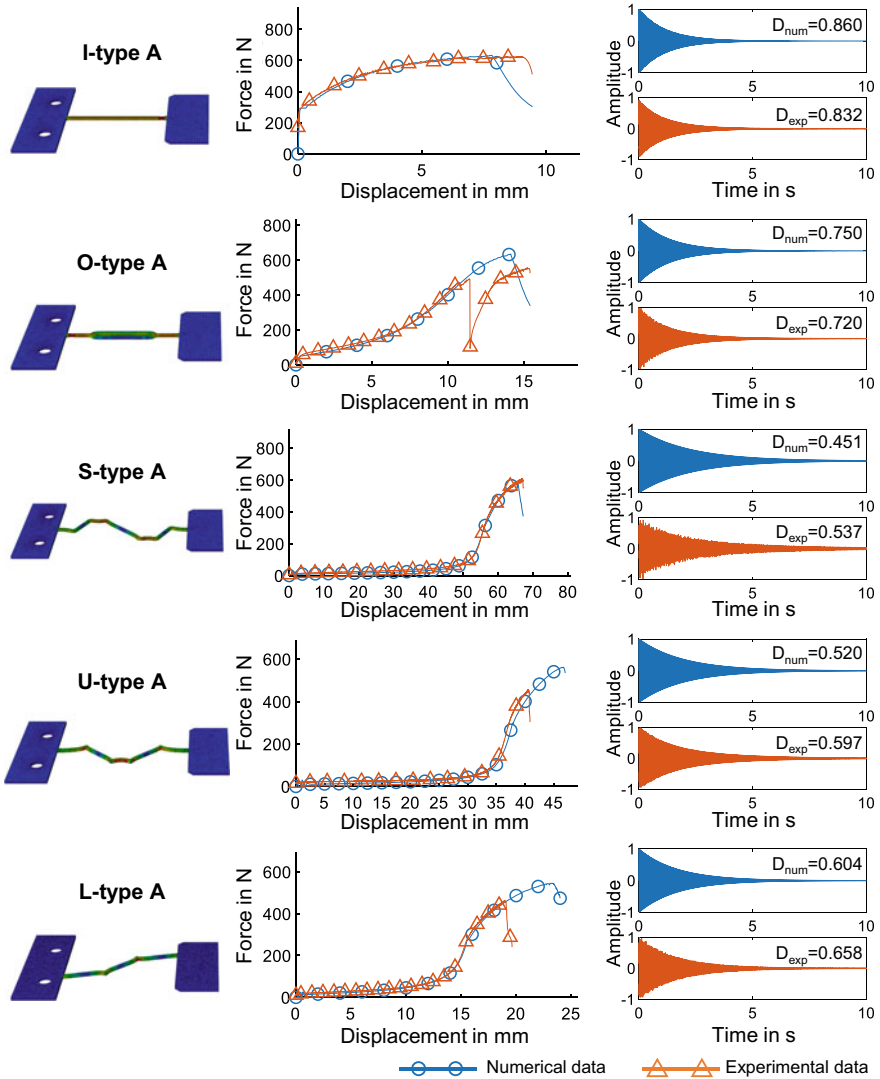


Fig. 6 Comparison of the experimental and numerical results of the tensile test and the impact modal test

To determine the physical properties the results of the tensile test are shown as force–displacement curves with the pulling force acting in X-, Y-, and Z-directions, and the resulting reference forces are measured in X-, Y-, and Z-directions, respectively. The damping factors are obtained by measuring the systems’ response in X-, Y-, and Z-directions to an applied single force impact on one side of the stretch web connector in Z-direction. All magnitudes obtained from the tensile and impact modal testing

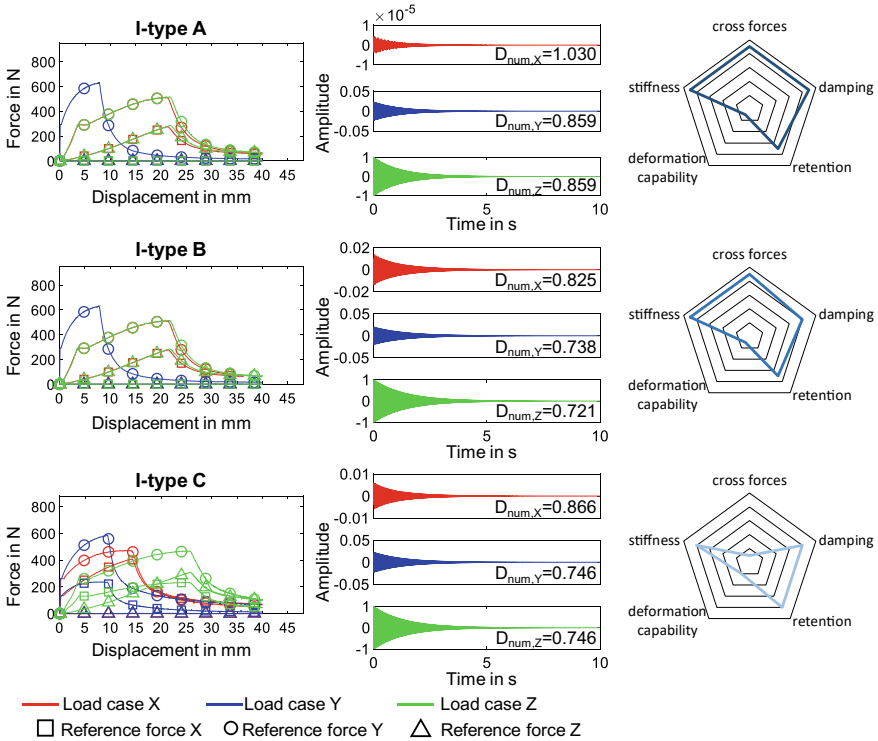


Fig. 7 Numerical results of the tensile and impact modal test for test specimens *I-type A*, *I-type B*, and *I-type C* for three load cases in X-, Y-, and Z-directions and derived properties shown in a spider chart

to describe the physical properties shown in the spider charts are normalized, to the maximum occurring value of each property.

I-Type

The *I-type* stretch web geometry is characterized by its immediate reaction to an applied force. Therefore, the retention of the structure is high for small displacements. The specimen also shows a high overall stiffness but has little deformation capability. The results of the numerical tensile and impact modal testing for the three *I-type* specimens are shown in following Fig. 7.

All *I-type* geometries have relatively large damping coefficients, and due to symmetry, *I-type A* shows almost no reaction in X-direction upon impact compared to the other two variants. Due to the immediate reaction, the capability to modify the force–displacement curves by altering the geometry is limited. A huge advantage of

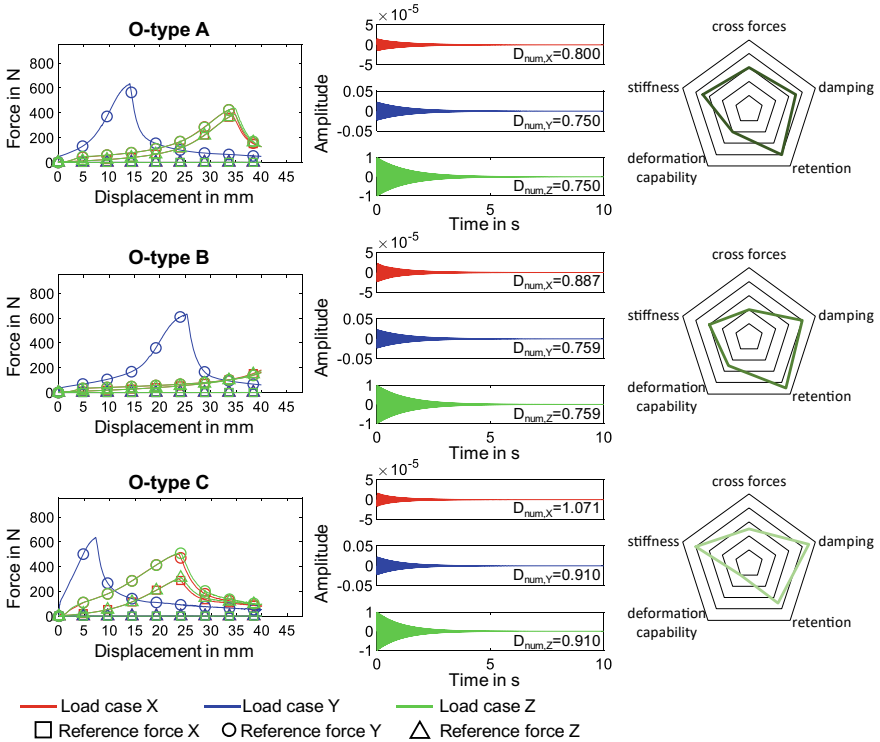


Fig. 8 Numerical results of the tensile and impact modal test for test specimens *O-type A*, *O-type B*, and *O-type C* for three load cases in X-, Y-, and Z-directions and derived properties shown in a spider chart

this stretch web geometry is the fact that it is easy to implement and can be designed with a high degree of material utilization. However, as specimen *I-type C* shows, the cross forces become very high when an offset angle is used, which makes it useable on only a small range of variants.

O-Type

One disadvantage of the *O-type* specimen is the need of another punch for cutting the hole in the stretch web geometry when realizing this stretch web in the tooling. However, the drawback of this additional operation is compensated by increased flexibility in the behavior of the connector. By changing the geometrical parameters of the oval-shaped hole, one can shift the location of maximum stiffness, maximum retention, and damping to a displacement level, where those properties are desired. *O-type B* shows the stiffest behavior at a displacement of 25 mm, whereas the *O-type*

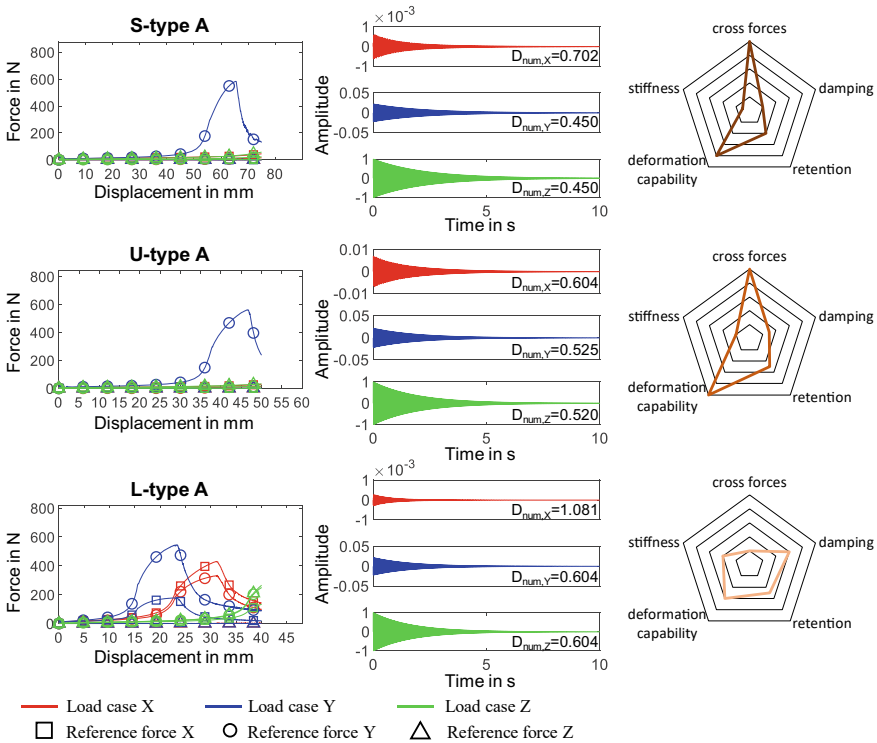


Fig. 9 Numerical results of the tensile and impact modal test for test specimens *S-type A*, *U-type A*, and *L-type A* for three load cases in X-, Y-, and Z-directions and derived properties shown in a spider chart

C specimen has the same amount of stiffness already at a displacement of 5 mm. Medium retention forces are present from the beginning of the load. Furthermore, the cross forces and the multi-axial stability can be influenced, by changing the shape of the connector. The *O-type* damping coefficients are in a similar range as the *I-type* geometries, which are relatively high. Due to their symmetric properties, all *O-type* variants show hardly any reaction in the X-direction upon impulse excitation. The results of the numerical tensile and impact modal testing for the three *O-type* specimens are shown below in Fig. 8.

S-, U-, and L-Type

The characteristics of the *S-, U-, and L-type* stretch web connectors are very similar, as all possess a very high deformation capability. In contrast to the *I-type* (< 5 mm) and the *O-type* (<10 mm) the *S-, U-, and L-type* geometries can undergo a very

large deformation with little retention before the stiffness increases. These high deformations are rarely reached during operation. The *S-type* geometry has a narrow range of displacement where the stiffness is higher at around 30 mm, whereas the *L-type* specimen becomes stiffer at 15 mm and still retains some deformation capability. The *S-* and *U-type* stretch web connectors show no cross forces for any load case but have negligible stiffness and retention behavior in X- or Z-direction. In contrast, the *L-type* connector causes higher cross forces due to the moment resulting from the lever arm of the applied forces. This can be used in cases where multi-axial behavior in X-, Y-, and Z-directions is more important. The *S-*, *L-*, and *U-type* geometries all display much weaker damping compared to the *I-* and *O-types*. This can be attributed to the increasing length of the structures through which vibrations propagate. The results of the numerical tensile and impact modal testing for the *S-*, *U-*, and *L-type* specimens are shown in following Fig. 9.

Conclusion

The results show that it is possible to fully describe the stretch web connector's behavior with its physical properties using a validated finite element model. The physical properties stiffness, retention, damping, elasticity, and cross forces can be used to estimate the usability of stretch web connectors for typical products for deep drawing, high accuracy, or fast running progressive die stamping applications.

In general, the *O-type* geometry shows the best flexibility, when an adaption of the requirements is considered. Nearly all physical properties can be influenced by the design of the oval-shaped hole. For operations where the material is subjected to large deformations, a *U-type* geometry offers a good amount of flexibility and has lower cross forces compared to the *L-type* specimen. The *S-type* shows very similar behavior compared to the *U-type* but lacks stiffness in cases where little deformation occurs on the stretch web. Due to its simplicity, the *I-type* is a good all-around choice and has advantages in punch design and material utilization. All variants of the *I-* and *O-type* geometries display relatively strong damping behavior compared to the other types, making them more suitable for preventing the propagation of harmful vibrations into the carrier strip, whereby the symmetrical variants are especially well suited due to their minimal X-directional response to Z-directional impulses.

The developed model and description of the physical stretch web properties can be used to test unknown geometries and to estimate the feasibility of certain designs and their suitability for specific products. A database with the most important physical properties can be created to choose a suitable stretch web geometry in the designing phase of a progressive die tooling.

Acknowledgements The authors thank Prof. Mike Worswick and Dylan Budnick (University of Waterloo). The authors acknowledge the financial support of the German Aerospace Center (DLR), the German Federal Ministry of Education and Research (BMBF), and the National Research Council Canada (NRC).

References

1. Duffey MR, Sun Q (1991) Knowledge-based design of progressive stamping dies. *J Mater Process Technol* 28(1–2):221–227. [https://doi.org/10.1016/0924-0136\(91\)90221-Y](https://doi.org/10.1016/0924-0136(91)90221-Y)
2. Naranje V, Shailendra K (2010) AI applications to metal stamping die design—a review. *World Acad Sci Eng Technol* 44:1526–1532
3. Kumar S, Singh R (2008) Automation of strip-layout design for sheet metal work on progressive die. *J Mater Process Technol* 195(1–3):94–100. <https://doi.org/10.1016/j.jmatprotec.2007.04.11>
4. Ngoi B, Kai CC (1994) A knowledge-based system for strip layout design. *COMPUT IND* 25(1):31–44. [https://doi.org/10.1016/0166-3615\(94\)90030-2](https://doi.org/10.1016/0166-3615(94)90030-2)
5. Gould PL, Feng Y (2018) *Introduction to linear elasticity*. Springer, Cham
6. Shabana AA (2019) *Theory of vibration*. Springer, Cham
7. Spears RE, Jensen SR (2012) Approach for selection of Rayleigh damping parameters used for time history analysis. *J Press Vessel Technol* 134(6):061801 (7 pages)
8. DIN 50125 (2016). <https://doi.org/10.31030/2577390>
9. DIN EN ISO 12004-2 (2009). <https://doi.org/10.31030/1443061>

Numerically Coupled Tools for Double-Sided Incremental Sheet Forming



Vincent Raymond and Jean Savoie

Abstract Research on incremental sheet forming started decades ago but has not yet found its momentum. To become a mainstream technology, two key enablers are required: geometrical accuracy and usability. The added formability and accuracy provided by double-sided incremental forming (DSIF) is a promising improvement but comes with additional challenges, such as toolpath definition. This paper is presenting a novel strategy to determine tool positioning without using a squeezing factor, sine law, or other conventional techniques. First, the master toolpath is calculated with CAM software. Then, a coupling between the master and the slave is numerically imposed to precisely simulate their positions while ensuring continuous contact and a variable support force. Upstream deformations are thus minimized throughout the complete forming of the part. This strategy was applied to a step cone geometry, and the numerical results show only slight deviations from computer-aided design (CAD).

Keywords Sheet metal · Dieless · Incremental · Double-sided · Robotic · Toolpath

Introduction

The idea of forming sheet metal without die emerged more than 50 years ago [1] and, since then, generated more than 100 patents worldwide, but there is still no mature enough technology for straightforward industrialization. Former variants, such as single-point incremental sheet forming (SPIF) and two-point incremental forming (TPIF) do not offer the accuracy or the flexibility required by most applications. Many different strategies, such as numerical compensation [2] and warm forming [3], can be used to improve geometrical accuracy but the strain distribution is not perfectly controlled, especially for complex geometries with small radii. In order to improve formability and accuracy, Meier et al. [4] and Maidagan et al. [5] tested in 2007 the double-sided incremental forming (DSIF) variant where two tools are used

V. Raymond (✉) · J. Savoie
National Research Council Canada, Boucherville, Québec, Canada
e-mail: vincent.raymond@nrc-cnrc.gc.ca

to create localized deformations. DSIF is now an active field of research and multiple groups have published promising results (see Ref. [6] for an exhaustive review). This variant is more complex since a second synchronous tool path is required to form the part. Any loss of contact critically reduces formability and accuracy since induced deformations are no longer localized. Defining toolpaths that preserve a continuous contact between the blank and the tools is a major challenge since the blank thickness evolves throughout the process. To predict the thickness, the sine law is known to be inaccurate, even with a squeezing factor [7]. A modified sine law model with additional parameters was proposed and successfully tested on a single geometry by Moser et al. [8]. However, the model requires iterative fitting specific to the material, tools, geometry, etc., which is a drawback for prototyping. A different solution is to add actuation to the forming tools to compensate for the thickness variations [9]. This additional degree of freedom needs to be closely controlled and may lead to an imprecise coupling due to tool compliance and/or dynamic effects. To avoid the thickness prediction requirement, a new innovative variant called ADSIF was introduced by Kiriden et al. [10]. The principle is to first form inside features and progress toward the external periphery of the part in order to only form a new material with the original blank thickness. The downside is that it requires smaller toolpath increments and the accuracy for steep walls is still being investigated [11]. Thus, a gap remains for toolpath generation and sheet thickness prediction in DSIF.

This paper will present a new DSIF strategy to numerically impose the coupling and avoid loss of contact using a preprocessing step based on FEA. First, the basics of the coupling model are explained in [Tool Coupling](#) section, then the implementation methodology, including material characterisation, is detailed in [Methodology](#) section. Finally, simulation results are presented in [Results](#) section.

Tool Coupling

In the proposed methodology, the relative orientation between the master and the slave is ensured by modeling numerically the coupling of the tools with a translational joint. The master tool position and orientation as a function of time are prescribed. Master rotation will force the slave to maintain a specific orientation with respect to the master for each forming increment. A force $F \rightarrow$ is then applied along the joint to ensure contact between the two tools and the blank (the slave is free to move along the joint). In this first proposed method, the direction of the force is coincident with the vector between tool centers and translational joint (see Fig. 1). The orientation of the translational joint has to be set and doesn't have to be necessarily aligned along with the contact normal $n \rightarrow$. Results from a previous work by Meier et al. [12] showed that a positive offset θ_1 relative to the normal of the nominal geometry is beneficial for both formability and conformation with the CAD.

In the second method, the configuration decouples the force directions by adding a second master (see Fig. 2). The translational joint in this case is between Master 2 and the slave, along which the force is applied. The slave position is now controlled

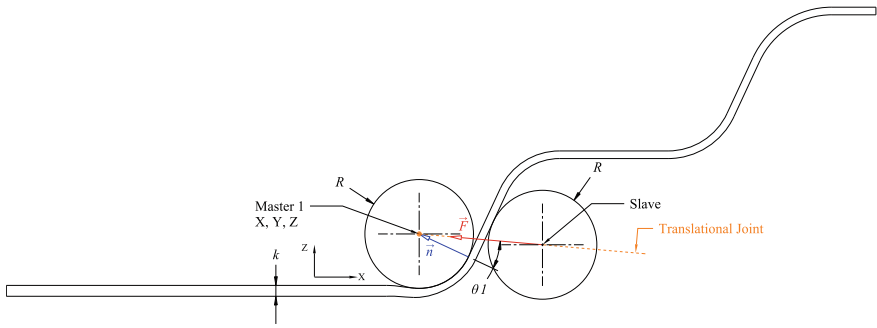


Fig. 1 Schematic definition method 1: force along with tool centers

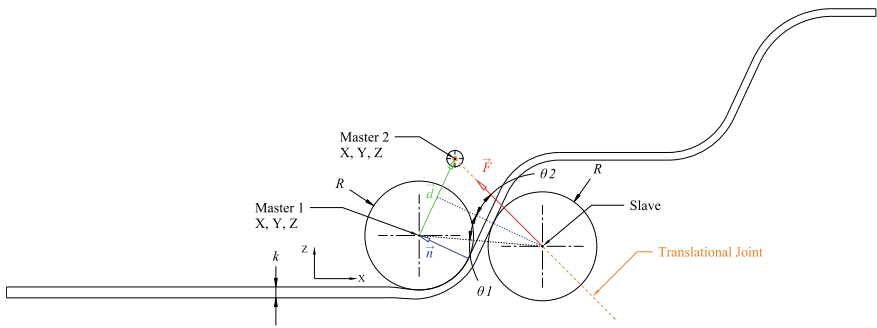


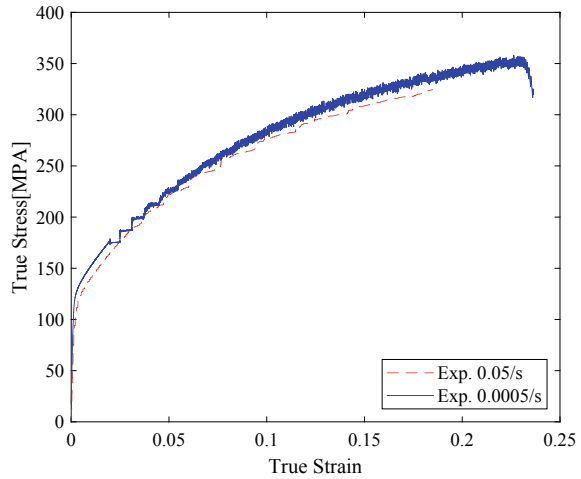
Fig. 2 Schematic definition method 2: independent force orientation

by the translational joint and master 2, positioned at a specific distance from Master 1 defined by the following relation:

$$\|\vec{d}\| = (2 \cdot R + k)(\sin(\theta 1) + \sin(\theta 2)) \tag{1}$$

where R is the tool radius and k the initial sheet thickness. The vector \vec{d} is perpendicular to the geometrical normal $n \rightarrow$ at the location of master 1. For simplification, its magnitude (Eq. (1)) is approximated by considering the triangle, formed by $\theta 1$ and $\theta 2$, isosceles, and neglecting the sheet thickness variation as well as the angle through the thickness. Master 2 is rotated by $\theta 2$ around an axis originating at its center, perpendicular to the plane defined by vectors $n \rightarrow$ and $F \rightarrow$. The larger the magnitude of \vec{d} and \vec{F} , the more bending will be imposed on the work piece during forming. The purpose of this bending is to improve formability and reduce springback [9].

Fig. 3 AA5182-O strain rate sensitivity



Methodology

Material Characterization

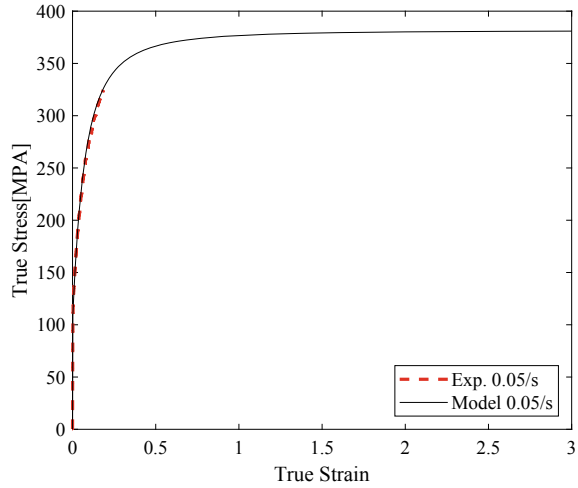
The selected material was AA5182-O. Material properties were measured at room temperature on an MTS Alliance RT100 with TestSuite software at two different strain rates: a slow standard rate of 0.0005/s and a faster rate of 0.05/s since materials with high Mg content, such as 5182, display negative strain rate sensitivity at room temperature (see Fig. 3). Strain rates for the incremental sheet forming process were estimated to 1/s, however, the properties at such high rates were not yet measured. For this study, the difference was considered negligible. As the maximum strain during forming exceeds the experimental range, the experimental curves at 0.05/s were extrapolated up to a true strain of 3 using a strain rate sensitive rigid-plastic crystal plasticity code [13]. Anand hardening law [14] implemented at the slip system level was used (see Fig. 4).

Friction coefficients between the aluminium workpiece and the steel tool were measured using a CETR ball-on-disk apparatus with CETR Data viewer software. Several petroleum-based and water-based lubricants were tested. The measured friction coefficients ranged between 0.09 and 0.11. A value of 0.10 was used in finite element models.

Master Toolpath Definition

To test the coupling strategy, a step cone geometry was first used. It was created with relatively steep walls, small radii, and flat sections to help quickly assess the

Fig. 4 Modeling AA5182-O, with high strain extrapolation



efficiency of the coupling law: final perpendicularity is linked to the quality of the support throughout the forming. The dimensions are given in Fig. 5.

The next step was creation of Master 1 toolpath with a commercial CAM software. Figure 6 shows a section view of the path followed by Master 1 tool center point (blue) inside the step cone geometry (shaded grey). The diameter of the forming tool was 10 mm, using Z-level contours with straight transitions, 0.15 mm axial step for walls, and 0.1 mm radial step for flat sections. No toolpath was generated for the bottom flat surface (\varnothing 24 mm surface). The output was a generic NC-code file.

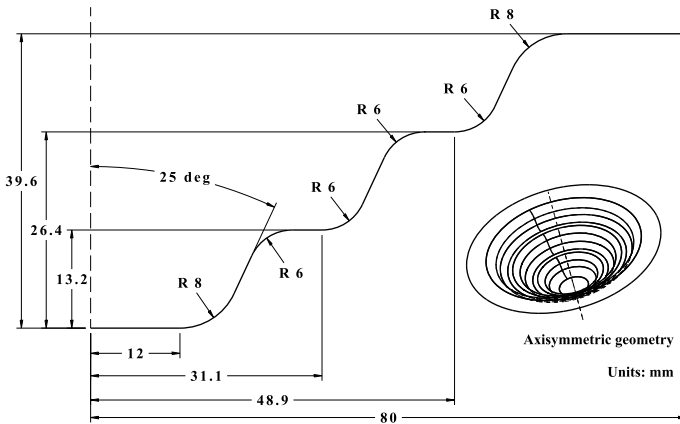


Fig. 5 Step cone geometry dimensions



Fig. 6 Section view, master 1 toolpath (thin lines)

Preprocessing

To impose the tool coupling, Master 1 toolpath needs to be discretized in points. This discretization is required to control the forming tool in the simulation and then, in the robotic controllers. A custom NC-code interpreter function was developed for that purpose. The code reads sequentially the NC commands and subdivides each movement using a specific increment, for this particular case: 0.5 mm. For simplification, a constant non-dimensional velocity between points was used. Once completed, the list of point coordinates as a function of time (t) is passed to a custom parallel point-to-CAD function. Based on Open CASCADE, this second function takes each point individually and finds the minimum distance from the final geometry to create normal vectors. To avoid dynamic effects or erratic movements, orientation gradients must be minimized by selecting an appropriate discretization increment and using a rich representation of the geometry (untessellated). Finally, a third function creates all the positioning and orientation of the two master tools in multiple tables using a specific LS-DYNA card named “*DEFINE_CURVE”. This last function has several options to control the coupling of the tool by specifying the following relations: $\theta_1(t)$, $\theta_2(t)$, and $\|\vec{F}\|(t)$. Those relations were parametrized to create additional support through position and orientation variation of Master 2 entity, creating more bending when forming the walls and maintaining flatness in the plateaus. The slave trajectory is thus numerically coupled with the master to ensure continuous contact and a variable support force while minimizing upstream deflections during forming.

Simulation

The proposed coupling strategy implies a mandatory simulation step. The position and orientation of master tools 1 & 2, calculated in [Preprocessing](#) step, are used as inputs for the simulation in order to predict the slave position with respect to the imposed constraints and local sheet thickness. The first master tool and the slave form the blank, while master 2 is only an entity required to create a joint to respect the pre-defined force orientation. In subsequent steps not presented in this paper, master 1 and slave tool positions and forces are exported and post-treated to control the actual robotic forming of the part.

For the simulation, LS-DYNA version R11.0.0, double-precision, MPP, explicit solver was run with 19 cores on a desktop computer. The blank was meshed with 30,375 deformable fully integrated solid elements (1.25 mm elements, two elements through the thickness). Material behaviour was modeled with MAT24 (piecewise linear plasticity). The 10 mm master and slave tools are modelled with rigid shell elements (about 1.25 mm) with a dynamic and static friction coefficient of 0.1. The joint between master and slave is set with the card `**CONSTRAINED_JOINT_TRANSLATIONAL`. All translational and rotational degrees of freedom are defined by `**BOUNDARY_PRESCRIBED_MOTION_RIGID` and `**BOUNDARY_PRESCRIBED_ORIENTATION`, respectively. The slave forces were imposed along the joint with `**LOAD_RIGID_BODY`. For the contact, several options are available. However, none is really optimized for increment sheet forming for which the elements in contact continuously change (most options are designed for conventional stamping simulations). The option `**CONTACT_FORMING_ONE_WAY` is more adapted for such contacts but can be noisier. After multiple trials, `**CONTACT_AUTOMATIC_SURFACE_TO_SURFACE` was chosen because of its numerical stability while fulfilling DSIF requirements. For the boundary condition of the blank, all the nodes within the clamping region are fixed (all DOF). The total computational time, using a speed scaling factor of $\sim 1,000$, was 65.5 h on a workstation with 2 Intel Xeon CPU E5-2660 v3 2.60 GHz and 64 Go RAM. An example of the model is depicted in Fig. 7, where the mesh size, the contact, and tool coupling behaviour can be observed.

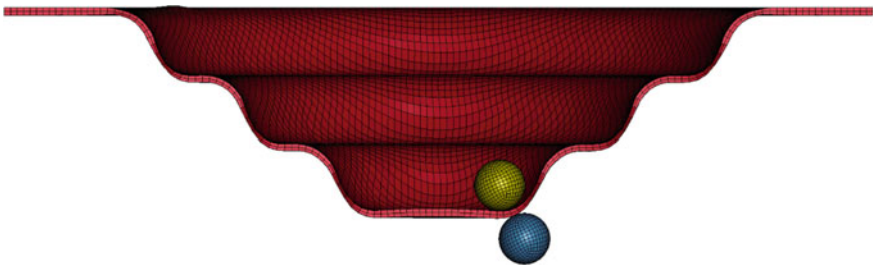


Fig. 7 Simulation model near completion, with coupled master (inside) and slave (outside)

Results

To validate the geometrical accuracy, nodal positions from the final simulated state were compared to the CAD. Note that only the upper nodes (towards master toolpath) from the solid elements are presented. Additionally, since the part is axisymmetric, nodal coordinates were converted to a polar coordinate system for 2D section plotting. The final geometrical accuracy for section views normal to X and Y axes are shown in Figs. 8 and 9, respectively. The simulation produces very accurate results, and

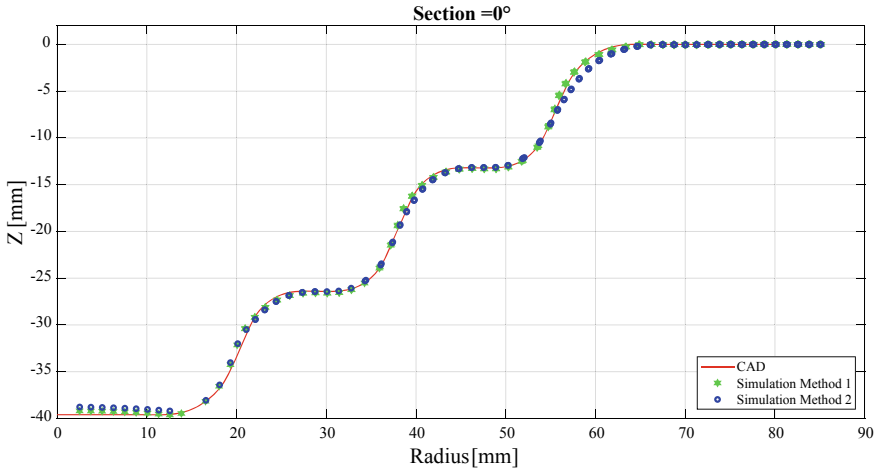


Fig. 8 Final state, nodal positions, section normal to X

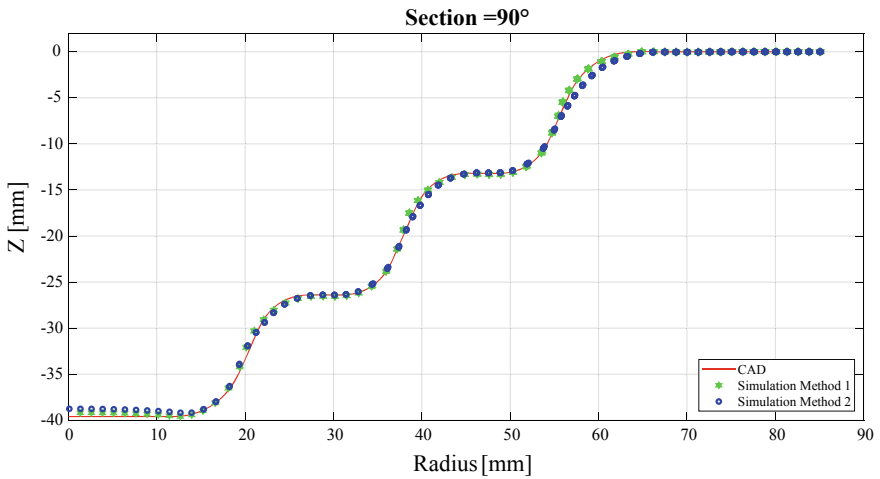


Fig. 9 Final state, nodal positions, section normal to Y

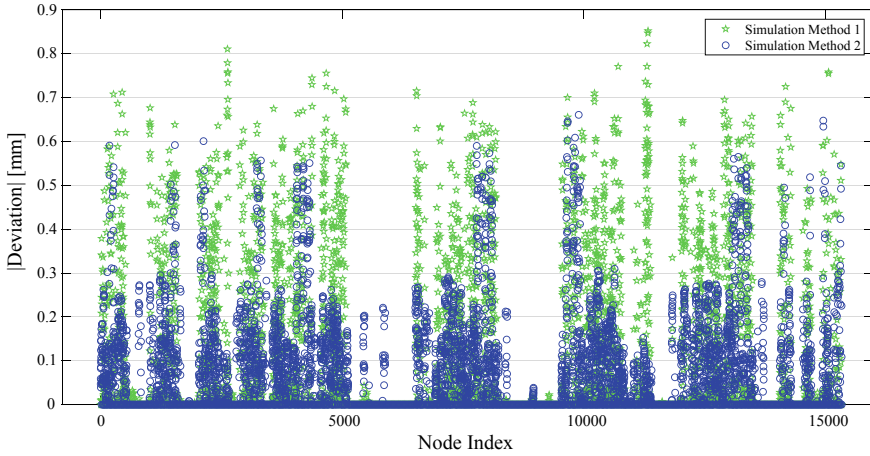


Fig. 10 Error distribution, 11 mm < polar coordinate R < 79 mm

only minor deviations can be observed for both methods. The plateaus are straight and the wall angles are nearly perfect. Method 1 consistently produces steeper walls for all steps, while Method 2 produces slightly different wall angles. This is directly linked to the level of support throughout the forming: finding the right support force evolution $\|\vec{F}\|(t)$ is critical, especially for Method 2. All sections studied showed similar results.

To better quantify the deviations from CAD, the minimum distance between the ideal surface and all upper nodes (within the forming range) was evaluated. As shown in Fig. 10, the numerical deviations are small. The simulated accuracy is smaller than ± 0.9 mm with Method 1 and smaller than ± 0.7 mm with Method 2. This is with a single pass, without iterative experimental correction loops. Experimental trials will determine the final achievable accuracy.

Another way to visualize the coupling efficiency is to look at the plastic strains (see Fig. 11). Larger deformations are, as anticipated, localized in steep wall regions. The maximum strain for Method 1 is 1.57 and 1.70 for Method 2, both located in the deepest wall. In the first wall, less deformation is observed in Method 2 since the predicted angle is shallower than the theoretical one (CAD), clearly observable in the section plots.

As seen in Fig. 7, significant thinning is observed. A multi-step forming methodology could help reduce thickness variation by distributing more uniformly the deformation.

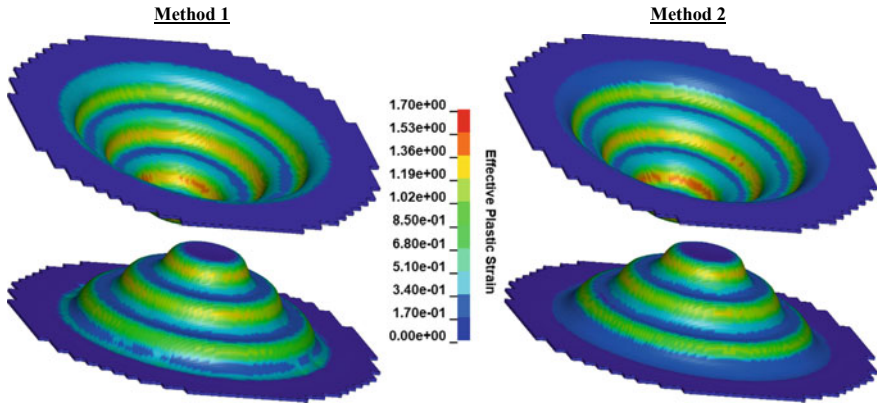


Fig. 11 Plastic strain results, methods 1 and 2 comparison

Conclusion

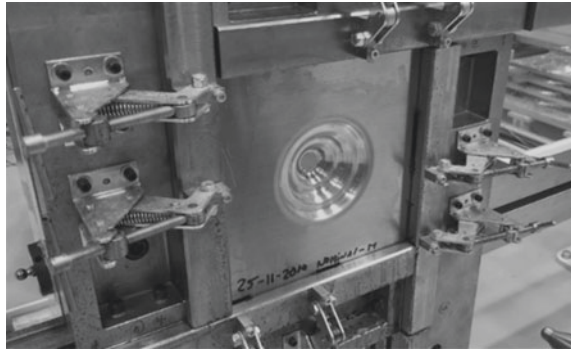
The aim of this modeling effort was to find a methodology suitable for DISF that would not rely on numerous experimental trials, and ultimately reduce the lead time to form and test new prototypes. This was accomplished by using a numerical model that couples the forming tools within FEA. The proposed methods reproduce the CAD shape of the step cone with good precision. The maximum predicted geometrical errors with Method 2 is better than ± 0.7 mm, which is relatively small and could be further improved by optimizing the force profile. Such results give confidence that experimental implementation of the simulated toolpath will yield parts with acceptable geometrical tolerances, even after taking into account robotic errors.

Ongoing and Future Work

The new methods will be extensively tested by varying the force amplitude and its direction to better understand how much and where bending is beneficial. A mesh size sensitivity analysis is also currently being performed to assess its effect on geometry, forming forces, and strains. To validate model assumptions, SPIF experiments on a CNC will be carried out for forces, strains (digital image correlation), and springback comparison.

In parallel, experimental implementation of the calculated toolpath will be completed on NRC robotic DISF workbench (see Fig. 12). Development of robotic calibration, compensation, and synchronisation is still being investigated to eliminate compliance effects and minimize toolpath deviations. If experiments are successful, the proposed methods will be applied to more complex industrial shapes for robustness assessment.

Fig. 12 NRC ongoing DSIF experimental tests, step cone geometry



Acknowledgements This strategy was developed by the National Research Council Canada (NRC) in support of the robotic incremental sheet forming project within ALTec industrial research and development group [15].

References

1. Leszak E Apparatus and process for incremental dieless forming. US3342051A
2. Ren H, Xie J, Liao S, Leem D, Ehmann K, Cao J (2019) In-situ springback compensation in incremental sheet forming. *CIRP Ann* 68(1):317–320. <https://doi.org/10.1016/j.cirp.2019.04.042>
3. Mohammadi A, Qin L, Vanhove H, Seefeldt M, Van Bael A, Dufloy JR (Jun. 2016) Single point incremental forming of an aged AL–Cu–Mg alloy: influence of pre-heat treatment and warm forming. *J Mater Eng Perform* 25(6):2478–2488. <https://doi.org/10.1007/s11665-016-2055-y>
4. Meier H, Smukala V, Dewald O, Zhang J (2007) Two point incremental forming with two moving forming tools. *Key Eng Mater* 344:599–605. <https://doi.org/10.4028/www.scientific.net/KEM.344.599>
5. Maidagan E, Zettler J, Bambach M, Rodríguez PP, Hirt G (2007) A new incremental sheet forming process based on a flexible supporting die system. *Key Eng Mater* 344:607–614. <https://doi.org/10.4028/www.scientific.net/KEM.344.607>
6. Peng W, Ou H, Becker A (2019) Double-sided Incremental Forming: a Review. *J Manuf Sci Eng* 141(5):050802. <https://doi.org/10.1115/1.4043173>
7. Malhotra R, Cao J, Ren F, Kiridena V, Cedric Xia Z, Reddy NV (2011) Improvement of geometric accuracy in incremental forming by using a squeezing toolpath strategy with two forming tools. *J Manuf Sci Eng* 133(6):061019. <https://doi.org/10.1115/1.4005179>
8. Moser N et al (2016) Effective forming strategy for double-sided incremental forming considering in-plane curvature and tool direction. *CIRP Ann* 65(1):265–268. <https://doi.org/10.1016/j.cirp.2016.04.131>
9. Wang H, Zhang R, Zhang H, Hu Q, Chen J (2018) Novel strategies to reduce the springback for double-sided incremental forming. *Int J Adv Manuf Technol* 96(1–4):973–979. <https://doi.org/10.1007/s00170-018-1659-9>
10. Kiridena VS, Arbor A, Xia ZC Method of incrementally forming a workpiece. US8302442B2
11. Ndiip-Agbor E et al (2016) Optimization of relative tool position in accumulative double sided incremental forming using finite element analysis and model bias correction. *Int J Mater Form* 9(3):371–382. <https://doi.org/10.1007/s12289-014-1209-4>

12. Meier H, Magnus C, Smukala V (2011) Impact of superimposed pressure on dieless incremental sheet metal forming with two moving tools. *CIRP Ann* 60(1):327–330. <https://doi.org/10.1016/j.cirp.2011.03.134>
13. Tóth LS, Neale KW, Jonas JJ (1989) Stress response and persistence characteristics of the ideal orientations of shear textures. *Acta Metall* 37(8):2197–2210. [https://doi.org/10.1016/0001-6160\(89\)90145-4](https://doi.org/10.1016/0001-6160(89)90145-4)
14. Kalidinix SR, Bronkhorst CA, Anand L (1992) Crystallographic texture evolution in bulk deformation processing of FCC metals. *J Mech Phys Solids* 40(3):537–569. [https://doi.org/10.1016/0022-5096\(92\)80003-9](https://doi.org/10.1016/0022-5096(92)80003-9)
15. NRC Canada (2015) ALTec industrial R&D group. 08 May 2015. Accessed 05 Jan 2020. <https://nrc.canada.ca/en/research-development/research-collaboration/industrial-rd-groups/altec-industrial-rd-group>

Overcoming Major Obstacles of Springback Compensation by Nonlinear Optimization



Luca Hornung, Sebastian Denz, and Vojtech Cvrcek

Abstract The compensation of die surfaces to obtain parts that are dimensionally accurate after springback involves numerous serious challenges. In this article, we introduce a nonlinear optimization technique on mesh level that extrapolates a vector field defined in certain nodes to the whole mesh respecting defined constraints. This method is especially defined to preserve arc lengths as good as possible within the extension procedure. We apply this technique to all steps required in a compensation, the compensation of the blank against a target surface, the smooth modification of the tool surfaces, the treatment of undercut, and the application of fixing and symmetry constraints. Finally, we prove the flexibility of our vector field extension with an application to the offset problem of low-quality meshes. Last but not least, we discuss practical examples simulated in the commercial code Stampack Xpress.

Introduction and State of the Art in Springback Compensation

Springback occurs when the press opens and the elastic energy is released. This deformation results in deviations to the formed parts, that are often out of the allowed dimensional tolerance range. Usually, this is measured by comparing the final part after springback with the desired nominal part. Although there are many ways to reduce the springback effect like increasing blank holder forces, drawbead restraining forces, or introducing further plasticity in the part by reinforcement beads, springback cannot be fully eliminated. Thus, a common approach to get parts in dimensional tolerance is to modify the die surfaces by the amount of springback in opposite direction to the springback. The assumption of this approach is that the springback remains the same within this small modification and thus, the part is in tolerance.

L. Hornung (✉)
Stampack GmbH, Bietigheim, Germany
e-mail: luca.hornung@stampack.com

S. Denz · V. Cvrcek
Men at Work GmbH, Bietigheim, Germany

In a ground-breaking work, Gan and Wagoner [2] introduced the so-called Displacement–Adjustment (DA) method that iterates several comparisons between target geometry and springback geometry in combination with the corresponding adjustments in the sheet and in the tool geometry. Several improvements to this method have been developed. Amongst others, we mention the smooth displacement adjustment method (SDA) by Petzoldt et al. [4]. This method improves the (DA) with an approximation method that provides continuous compensation displacement fields and a smooth extension from the blank area to the tool area. These two properties of the method are essential for a good compensation and will also play a huge role in our approach.

All these approaches are based on the following simple iterative idea that is visualized in Fig. 1. Imagine we have the springback geometry S_j after the j -th iteration, we measure the j -th displacement field D_j from target geometry to springback geometry. Then, we adjust the geometry C_j before springback by the vector field $-D_j$ to get the compensated geometry C_{j+1} of the next, the $(j + 1)$ -th, iteration.

A more recent and remarking approach for springback compensation is the physical displacement adjustment method by [1]. Their method is not based on modifying the blank node by node, but they deform the blank with forces normal to the blank in an additional elastic finite element simulation until they reach their desired compensated shape. The major advantage of this approach is that it preserves arc lengths and surface areas within the compensation process. They show that this enhanced method results in an improved compensation convergence compared to the existing commercial codes.

Major Challenges in Springback Compensation

Before we show the details of our approach, we first repeat the major challenges of springback compensation.

- (1) Have a robust sheet metal forming process.
- (2) Have an excellent springback prediction result.

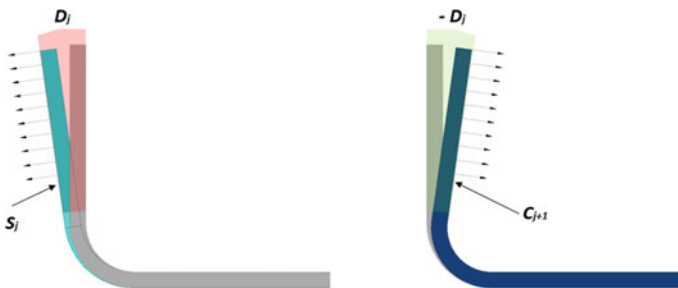


Fig. 1 Left distance to target after springback S_j . Right compensated geometry C_{j+1}

- (3) Compensate the blank against a given target preserving arc lengths.
- (4) Mapping the compensation from the blank to the tool surfaces.
- (5) Applying constraints, for example, in the blank holder area.
- (6) Remove undercut in compensated sidewalls.

Obviously having a solution for the challenges (1) and (2) is critical before coming to compensation. However, in this article, we focus on a new approach to solve challenges (3)–(6) with a vector field extension method based on a nonlinear optimization method that is described in the next section. Later on, we apply this quite general method step by step to overcome challenges (3)–(6).

Smooth Vector Field Extension by Nonlinear Optimization

We start with a triangular surface mesh S and a vector field V given in a subset of all nodes in the mesh. We assume that the magnitude of V is small compared to the size of the triangulated surface. Our method extends this vector field to a smooth vector field V^* defined on the whole surface S (Fig. 2).

The first step is to formulate the minimal conditions we have on our extension field V^* .

- (1) $V = V^*$ on the set of nodes where V is defined.
- (2) The extended vector field V^* should be defined in a way that the surface with node coordinates $S + V^*$ should be as close as possible to the surface with node coordinates S , i.e., the difference of mesh triangle sizes l and internal mesh triangle angles α between S and $S + V^*$ should be as small as possible.
- (3) Additional linear equality constraints of the form $AV^* = B$ or linear inequality constraints of the form $AV^* \leq B$ for all choices of V^* , where A is a $k \times n$ matrix and B is a k -dimensional vector. Here, n is the number of nodes in S and k is the number of constraint nodes (Fig. 3).

Condition (1) describes the need to extend the vector field from a predefined base. Condition (2) leads to a nonlinear minimization problem. We use it to define a nonlinear functional ϑ of the form

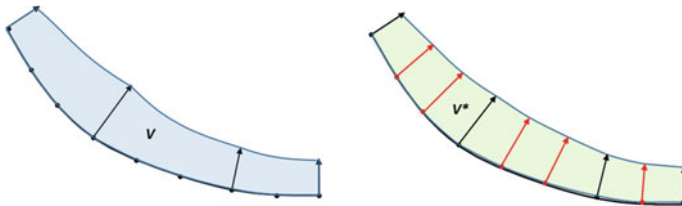
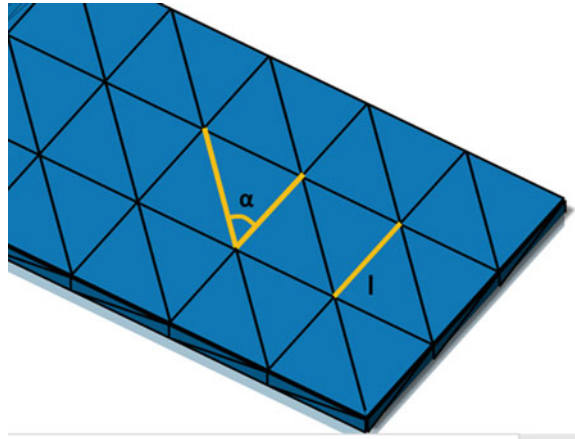


Fig. 2 Left vector field V in few nodes (black). Right extended vector field V^* (red)

Fig. 3 Angles and lengths, to be changed as little as possible



$$\vartheta(V^*) = \sum_T \sum_{i=1}^3 \vartheta_{1,T}(|\alpha_i(S) - \alpha_i(S + V^*)|) + \vartheta_{2,T}(|l_i(S) - l_i(S + V^*)|)$$

with a given error function $\vartheta_{1,T}$ and $\vartheta_{2,T}$ on each triangle T in S . These error functions depend on the displacement field V^* or more precisely on the triangle size changes and triangle angle changes in each triangle of the surface when we compare the surfaces with node coordinates S with the surface with node coordinates $S + V^*$. Condition (3) is not physically motivated. It is chosen as the maximum a state-of-the-art optimization solver allows. We will use this flexibility in our application to solve real-world problems. We solve this optimization problem with a constrained trust region solver with an initial guess given by a smoothed version of $V^* = V$, where V is defined and $V^* = 0$ in the other nodes.

The upside of this procedure is that due to Condition (2) it provides by construction a result displacement field V^* that provides a result surface $S + V^*$ that is smooth from triangle to triangle. Moreover, Condition (2) allows just minimal arc length deviations, a fact we need in our application to come closer to the great benefit of the physical compensation method, the length-of-line preservation, by Birkert et al. [1] than the traditional methods.

The application shows that our method is also stable in case of non-smooth input meshes S . However, due to convergence issues, this method is not applicable when the basic vector field V deforms the initial surface mesh too much. Hence, this approach is not applicable to general mesh morphing. Nevertheless, it turns out that it is sufficient for the springback compensation challenges and for offsetting die surface meshes by a sheet thickness. Before we show how to apply our extension method, we show an example where the arc length preservation is well illustrated.

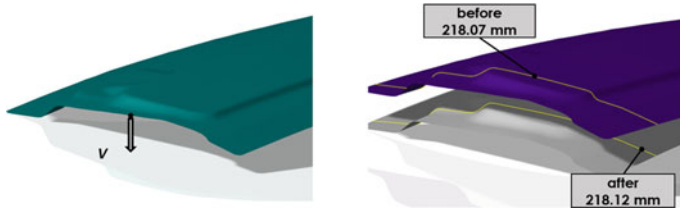


Fig. 4 Left vector field V on the surface S . Right comparison of the arc lengths between S and $S + V^*$.

Example: Windshield Cover

We take a 1 m large sheet metal part; a windshield cover; as surface S and we choose V in a simple way. V is defined in two nodes, one in the centre of the part and one in the centre of the arc highlighted in Fig. 4. We set $V = 0$ in the centre of the part and V is a deformation in $-z$ direction by length 20 mm in the centre of the arc. Our extension procedure yields a deformation vector field V^* defined on the whole surface and we compare the arc lengths of the surface S and the surface $S + V^*$. The arc length changes in this deformation process from 218.07 mm on the initial surface to 218.12 mm on the result surface.

Application of Vector Field Extension to Springback Compensation

No matter how difficult springback is in practical applications, its magnitude is always small compared to the part size and the springback deformation is always smooth. Thus, it turns out that even for huge springback magnitudes occurring, for example, in large automotive parts, the method provides excellent results. The key is to define the constraints in an appropriate way depending on what we want to achieve. Hence, we treat challenges (3)–(6) one by one with a different choice of the predefined vector field V , the area where V is defined and the constraints we impose.

Compensate the Blank Against a Target

It is well known [3] that springback can be compensated very well when the springback direction is normal to sheet, whereas it has limitations when the springback direction is more tangential to the sheet. Our approach is to choose V in the area where the springback is perpendicular to the sheet up to a tolerance (Area A). In this area, we set V as the inverted distance vector field from blank to target. The rest of the nodes are unconstrained (Area B). Our optimization scheme yields an extended

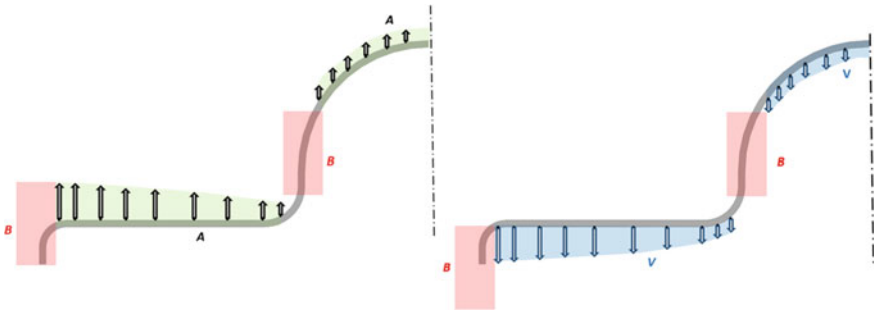


Fig. 5 **Left** springback perpendicular to blank in area A. **Right** compensation field V in area A

vector field V^* and we take $S + V^*$ as the compensated blank surface. In simple terms, we use the conventional displacement–adjustment method described in Fig. 1 in the areas where springback is almost perpendicular to the blank and treat the other areas with the optimization scheme (Fig. 5).

Extend the Compensation from the Blank to the Die Surfaces

In this step, the challenge is that typically the die surfaces are larger than the blank. Once we know how to compensate the blank, we map the compensation field from the blank to the area on the die that is in contact with the blank. Afterwards, we call our optimization algorithm with given displacement V in the area close to the blank and without constraint in the rest of the die. As a result, we get a smooth extension V^* of the compensation field to the whole die surface (Fig. 6).

Application of Constraints

Fixed areas, in real-world cases typically the blank holder area, can be obtained by defining $V = 0$ on the area to be fixed and to set an unconstrained smoothing zone around the fixed area as in Fig. 7. Outside the fixed area and the smoothing zone, V is defined as in Sect. “Compensate the Blank Against a Target”. The optimization scheme then lets the fixed area fixed and provides a smooth extension to the rest of the part.

More sophisticated constraints, like a symmetry constraint in a certain area, can be achieved by using Condition (3) of our optimization scheme. Here, we enforce a symmetry in a predefined area and leave an unconstrained smoothing zone around the area with a symmetry condition.

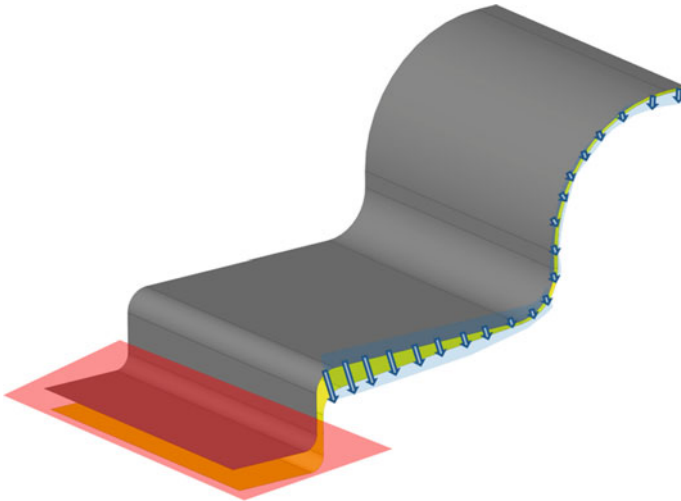


Fig. 6 Grey die before compensation, V is given by blue vector field, red zone is where V is not defined. **Yellow** die after compensation

Remove Undercut in Sidewalls

The linear inequality constraints are applied to remove the undercut, which is a constraint in our optimization scheme especially designed for sidewall areas. With this approach, we can treat areas that do not have undercut before the compensation

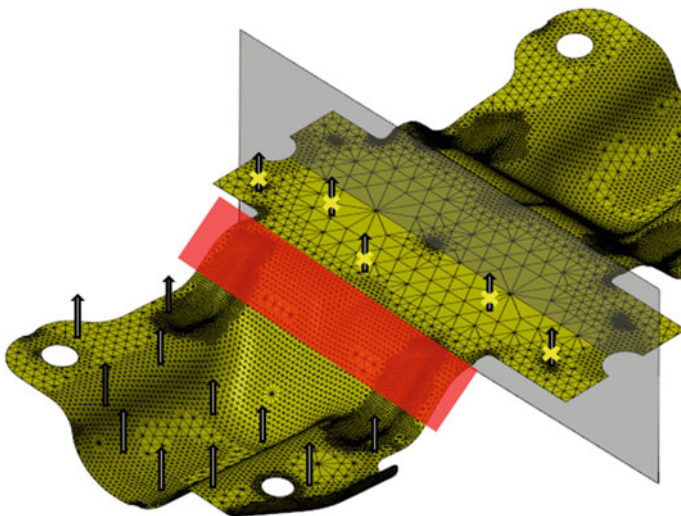


Fig. 7 Symmetric part fixed in the middle. Red zone is where V is not defined

and fall into undercut during the compensation procedure. To detect areas that fall into undercut, we take the following simple but useful criterion. We check in each node the normal vector n at node, and we say that a node has undercut if and only if the condition $n_z > 0$ before compensation and $n_z < 0$ after compensation holds true. This description can be used to define a constraint as in condition (3) together with an unconstraint smoothing area around the undercut zone. The optimization scheme forbids vector fields V^* leading to a surface $S + V^*$ with undercut. To get a smooth result, it is necessary to give an unconstraint smoothing area around the undercut area (Fig. 8).

Example: Springback Compensation of B-Pillar

We apply our method to compensate the springback of a B-Pillar. In this part, two iteration loops are sufficient to match the given tolerance $\pm 0.7mm$. We see that the distance to the target is not monotonously decreasing, but that the part that is initially above the target is then below. However, the absolute distance values are decreasing in a satisfactory way (Fig. 9).

Example: Flatness Tolerance in a Rear Wall Panel

The following example is a joint work with **Pengfei GmbH Deutschland**, a subsidiary of China-based **Pengfei Group** (www.pengfei-mold.com) with more than 2300 employees producing about 1000 tools per year for a worldwide customer base.

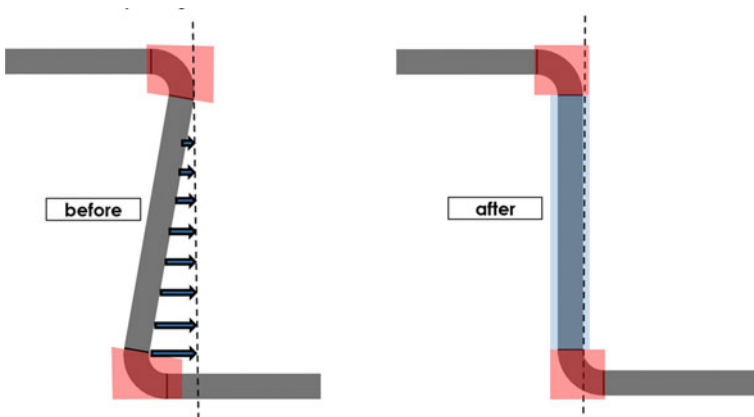


Fig. 8 **Left** vector field that avoids $n_z < 0$, Red zone is unrestricted smoothing zone. **Right** Result after undercut removal

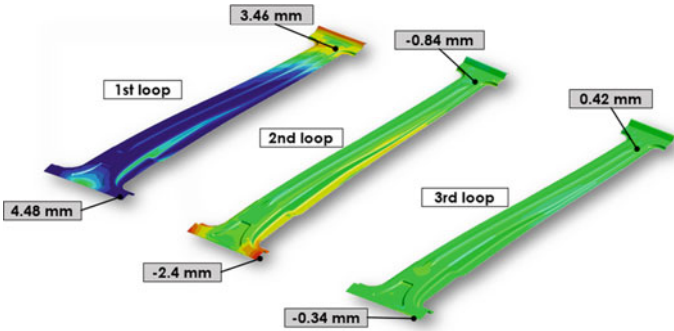


Fig. 9 Displayed is the distance to the target in each iteration loop

It is 345 mm large and 1.2 mm rear wall panel made of HX420LA. The challenge in this part is a flatness tolerance ± 0.25 mm in the outer area, which is more than ten times smaller than the amount of springback. To compensate this springback from a simulation point of view demands a high accuracy of the forming simulation, an extremely precise prediction of springback and a good compensation algorithm. We choose Stampack's solid element technology with three elements across the thickness. The iterative application of our compensation algorithm converges in a base simulation and three correction loops to the desired accuracy (Fig. 10).

Example: Remove Undercut

The following example is an application of the undercut removal introduced in Chapter 3.4. It is a bracket made of the AHSS high-strength steel CP1400 with springback of 2.51 mm in the base simulation. The main difficulty is the vertical wall, that would fall into undercut in a naive compensation (Figs. 11 and 12). However, for production, it is mandatory to have tools without undercut and we have to apply our undercut removal. The convergence is again not monotone, the first correction is an overcompensation where just the absolute values are reduced. After the second correction loop, the part is in the required tolerance of ± 0.5 mm and, after another loop, we end up with a part that is after springback just 0.18 mm away from the target.

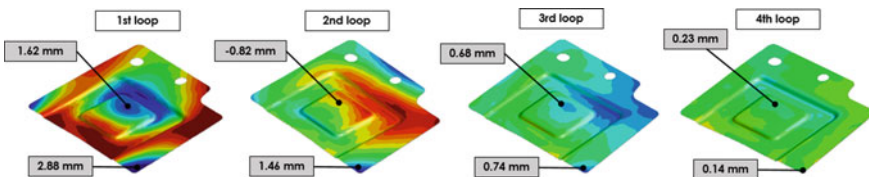


Fig. 10 Displayed is the distance to target each compensation loop

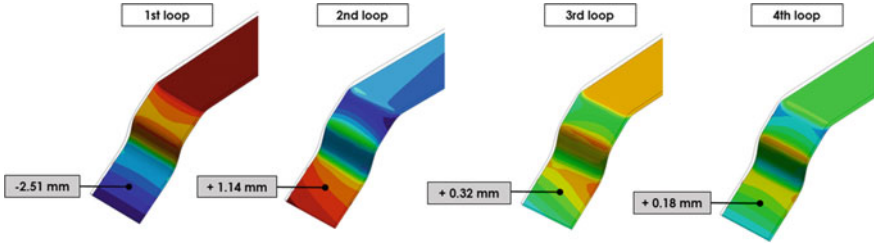
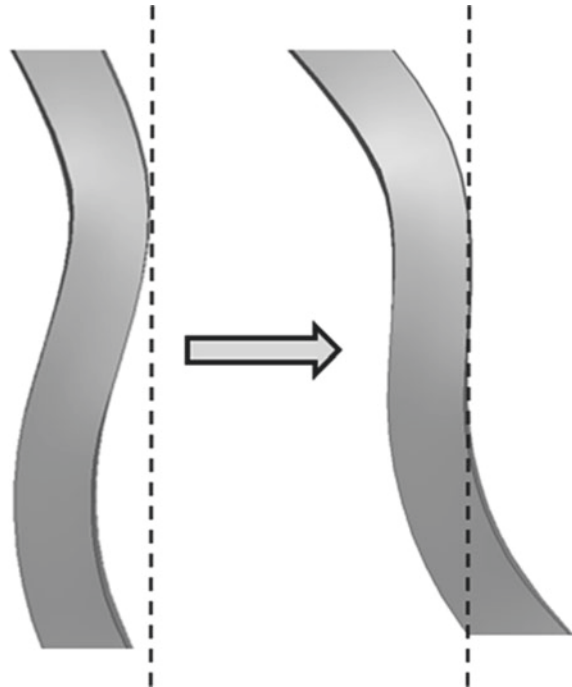


Fig. 11 Displayed is the distance to target each compensation loop

Fig. 12 Left: blank without undercut removal. Right: blank with undercut removal



Application of Vector Field Extension to Offsetting to Low-Quality Meshes

Another application of our extrapolation technique is the offset of low-quality triangular surface meshes by a small length. In applications, the offset length is typically the thickness of the sheet. Basically, offsetting a surface means to move each node in normal direction by the offset length L . Especially, when working with non-smooth tessellations, we face a huge problem. These meshes contain triangles with side lengths less than 0.002 mm, whereas we need an offset of 1–2 mm. A simple

offset in normal direction would result in huge element distortions in these triangles (Figs. 13 and 14).

We approach this difficulty by covering the whole surface with patches. In each patch, we choose one node with a well-defined normal. Next, we set $V = normal * L$ in these nodes. Then, we extend V to a smooth vector field V^* in the whole surface and obtain the offset surface $S + V^*$.

It turns out that the limitation of our approach is the offset of sharp edges and more severely, the offset of a radius R by $L > R$ in contractive direction. In these cases,

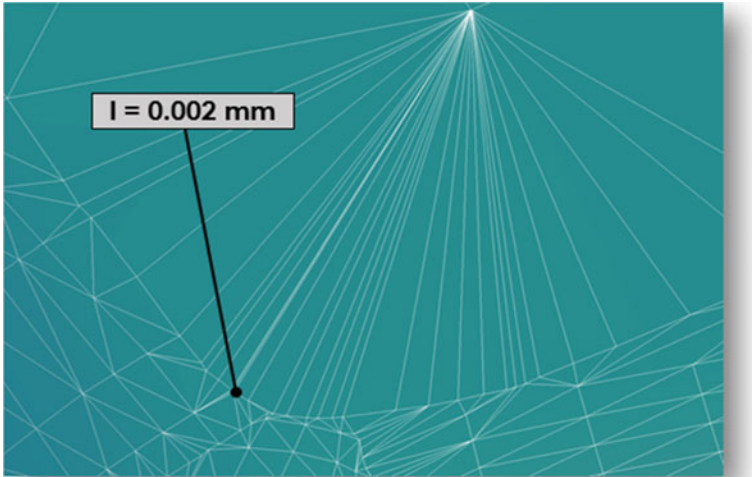
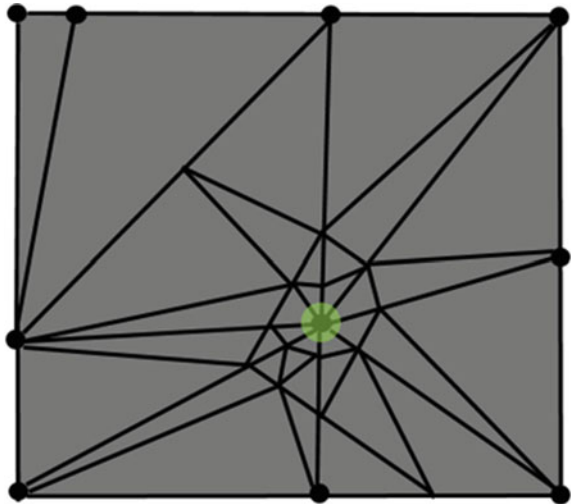


Fig. 13 Low-quality mesh

Fig. 14 V Defined in one node per patch



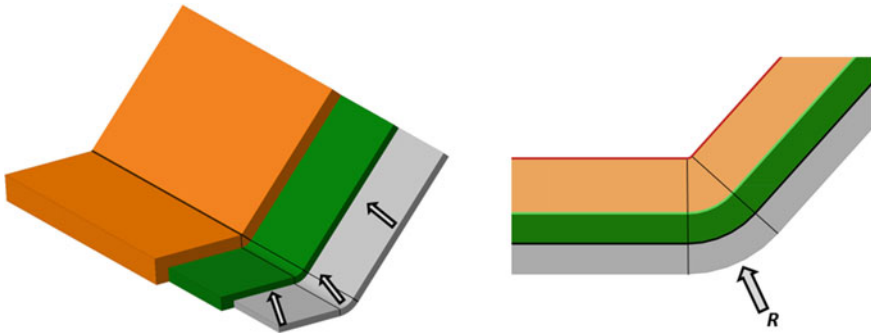


Fig. 15 Green: Offset by offset-length $R/2$. Orange: Offset by offset-length R with sharp edge

our approach fails due to triangle distortions in the offset surface. The borderline case $L = R$ gives in theory a sharp edge (see Fig. 15). In practical examples, we see that our approach is only stable when we have $L < 0.9 * R$. However, in typical sheet metal applications of automotive panels, this limitation is not that severe, since in these parts, we typically have radii much larger than the sheet thickness.

Conclusion and Future Work

We introduced a new approach to springback compensation. In the classical methods like the displacement–adjustment method, it was necessary to define for every node the appropriate compensation vector. In contrast, our method defines the compensation vectors just in those areas where springback is normal to the sheet and lets the optimization scheme finalize the job. We highlighted that this optimization method has the flexibility to extend the compensation from the blank to the larger die, to constrain defined areas and to remove undercuts in vertical walls. Finally, we apply the optimization scheme to the offset problem of non-smooth meshes. The limitation of our method is that a surface mesh cannot be deformed too much compared to the topology of the initial mesh. However, both springback compensation and offset of about 1–2 mm in automotive sheet metal parts do not require a general mesh morphing.

The method we propose is implemented in the commercial code Stampack Xpress. Still open is a detailed comparison between our approach and the other commercial and non-commercial methods to distinguish the strength and weaknesses of each method. However, we are confident that our springback compensation by nonlinear optimization opens a new way of thinking about springback compensation.

References

1. Birkert A, Hartmann B, Straub M (2017) New method for springback compensation for the stamping of sheet metal components. IOP Conf Ser J Phys Conf Ser 896
2. Gan W, Wagoner R (2004) Die design method for sheet springback. *Int J Mech Sci* 46(7):1097–1113
3. Lingbeek R, Meinders T, Ohnimus S, Petzoldt M (2006) Springback compensation fundamental topics and practical application. Proceedings of the 9th ESAFORM Conference, pp 403–406
4. Petzoldt M, Weiher J, Rietman B, Kose K, Ohminus S, Weiher J (2004) Controlling springback with compensation strategies. NUMIFORM Ohio State University, pp 1011–1015

Sheet Metal Forming Simulation System Strongly Coupled with Die Tool Deformation



Masahi Arai and Naoki Ichijo

Abstract Deformation of die tools caused by high pressing force has been concerned in a practical sheet metal forming process. The deformations introduce changes in the contact condition between the die faces and the work-piece, affecting product quality such as formability, springback, and surface deflection. To research these issues, we have developed a system that performs stamping simulation considering the tool deformation. Whereas increases in time for modeling and calculation are typical problems with computing structural behavior of the tools, both can be drastically reduced in this system by a model reduction technique, in which fine die face mesh is coupled to coarse solid mesh. Additionally, this system provides a feature to create simple structure shapes, then simulations can be performed without practical complex shapes. We present some examples of applying this system to automotive parts. The results demonstrate that the consideration of the tool deformation affects the draw-in of work-piece and improves springback prediction, and the developed system can suppress the increase in lead time of the simulation.

Keywords Sheet metal forming · Tool deformation · Elastic die · Springback · High tensile strength steel

Introduction

Deformation of die tools caused by high pressing force has been concerned in a practical sheet metal forming process. The deformations introduce changes in the contact condition between the die faces and the work-piece, affecting product quality such as formability, springback, and surface deflection. Moreover, the use of high

M. Arai (✉)

Research and Development Department, Engineering Technology Division, JSOL Corporation, 1-8-12 Harumi, Chuo-ku, Tokyo 104-6205, Japan
e-mail: arai.masahi@jsol.co.jp

N. Ichijo

Productization Production Engineering Division, Mid-Size Vehicle Company, Toyota Motor Corporation, 1 Motomachi Aichi Prefecture, Toyota City 471-8573, Japan
e-mail: naoki_ichijo@mail.toyota.co.jp

© The Minerals, Metals & Materials Society 2022

K. Inal et al. (eds.), *NUMISHEET 2022*, The Minerals, Metals & Materials Series,
https://doi.org/10.1007/978-3-031-06212-4_86

963

tensile strength steel has been increasing in recent years. This means that forming condition has become more severe and the tool deformation is of even greater concern.

To address such a concern, restraining the deformation by rigidifying the tools would be ideal, but difficult to achieve. This is because practical die manufacturing involves various requirements such as manufacturing cost, energy-saving, and facility restrictions. Therefore, weight and stiffness of the tools are limited and the die design requires to handle the tool deformation.

FE simulation could be effective to study this issue. Sheet metal forming simulation has been already widely used in the die design process. However, the tools are generally assumed to be rigid in the simulation. Thus, simulation methods considering the tool deformation have been desired to be established.

Conventional Methods to Consider Tool Deformation

Several numerical methods have been proposed to consider the elastic behavior of die tools.

The most typical method is to model the tool structure with elastic solid elements and calculate deformations of work-piece and tools simultaneously [1–6]. In this method, the structure models can capture realistic behavior because the shape of the tools sequentially updating. This leads to higher prediction capability. However, a fine solid mesh is required to achieve faithful geometry of the die face, and meshing of the structure models requires advanced skill and large operation time. Furthermore, an increase in the number of solid elements results in a significantly large computational time.

A method that considers the tool deformation only at a specific moment is also widely used [7]. It can be called the weak coupling method. This method consists of three steps. First, a normal forming simulation is performed with rigid tools. Second, obtained contact force distribution of the die faces at a specific moment is mapped to solid structure models. Then a static simulation is performed to calculate the deformation of the structures. Third, the shapes of the rigid die faces are updated with the displacement of the static structural simulation, and the forming simulation is performed again. In this method, the accuracy is improved efficiently by limiting the deformation state to a moment when the contact force increases, such as at the bottom dead center. If a mapping system is used, there is no need to match the mesh patterns between the die face and the structure. This reduces the difficulty of solid meshing. However, the calculation time contains still an issue because the forming simulation must run twice.

As an advanced version of the weak coupling method, Vrolijk et al. proposed a method in which the forming simulation and the structural analysis are performed in parallel [8]. In this method, the contact force distribution calculated in forming analysis using the dynamic explicit scheme is mapped to the structural analysis model every few cycles. The tool deformation is calculated in implicit solver, and the die face shape is updated according to the displacement of structural analysis.

This method can capture the tool behavior more accurately than the offline weak coupling above, updating the die face shape multiple times. However, if the update cycle is shortened, an increase in time for the coupling processing is concerned, because the coupling is achieved through the mapping. Additionally, some care must be taken for the boundary conditions in the implicit analysis.

Haufe et al. proposed a method using modal analysis and static condensation [9]. In this method, behavior of the tool structure is represented by the superposition of linear modes, and the degree of freedom inside the structure is reduced by static condensation to save computational time. However, this method involves some issues in practical use: Eigenmode analyses of the structure models must be conducted in advance. The behavior of tool structure depends on the number of modes to be considered. The calculation time increases when the number of the modes increases.

Issues in Die Design and Manufacturing Process

Shifting the focus from the numerical methods to a die design process exposes other big issues in considering the tool deformation. The design validation by stamping simulation is usually conducted in parallel with the die face design. However, the structural design of the die tools is usually started after the die face design has been almost completed. That is, during the phase in which the simulations run frequently, the tool deformation cannot be considered because the structural data is not available. Moreover, at the time the data is available, the design study is coming to an end, and the simulation must be performed in a very short time. To overcome these issues in the design process, several improvements are required: faster calculation time, a way to assemble the tool structure models quickly, and a way to prepare structure models even in the early stages of the die design.

As described above, there still remain some challenges in conducting the stamping simulation considering the tool deformation. This study aims to solve these challenges. In this paper, we propose a method to consider the tool deformation while saving time and try to put that method to practical use. Additionally, we have developed a system that can assemble die structure models in stamping analysis quickly and create simple structure shapes based on the die faces. This system has been implemented in JSTAMP, an integrated forming simulation system, and applied to automotive parts to verify the benefits.

Model Reduction Technique by Coupling Coarse Solid and Fine Shell

Here, we propose a numerical method to consider tool deformation while saving time. In our method, the deformations of work-piece and tools are calculated simultaneously, as in the conventional typical method. Although the conventional method is extremely time-consuming, a model reduction technique can solve this issue. Figure 1 shows the schematic view of this technique. In this technique, the FE mesh of the structure used for calculating its deformation is modeled with elastic solid elements, and the FE mesh of the die face used for calculating the contact with the work-piece is modeled with shell elements having no rigidity. Both are coupled so that the deformation of the die face follows the deformation of the structure model. Specifically, the relative coordinates of the nodes on shell elements are constrained to the corresponding solid element surface using a kind of contact condition. Although the concept of this technique was introduced by Haufe et al., it is mentioned that “great care” must be taken in the setting of contact conditions to combine different meshes as intended [9], and applying this technique to practical models has been difficult. Thus, we have developed a system that can apply this technique robustly and succeeded in putting it to practical use.

The greatest advantage of this method is that different mesh patterns can be applied to the die face and the structure. It is easy to assume that the model resolution required for structural analysis of tools is different from that for the contact calculation with work-piece. In the structural analysis, it is expected to capture the global deformation of the tools. Fine meshes are thus unnecessary, and the solid element size can be increased accordingly. This can remarkably reduce the number of solid elements and the difficulty of meshing. In contrast, the die faces with fine shell elements ensure the accuracy of the contact calculation with the work-piece. Additionally, the setup is quite simple because there is no need to process mapping, which is used in the weak coupling, and the entire model is calculated using the dynamic explicit scheme.

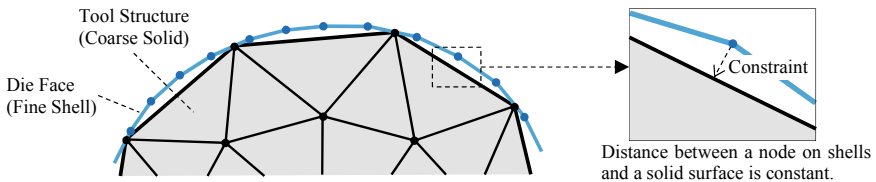


Fig. 1 Schematic view of the model reduction technique

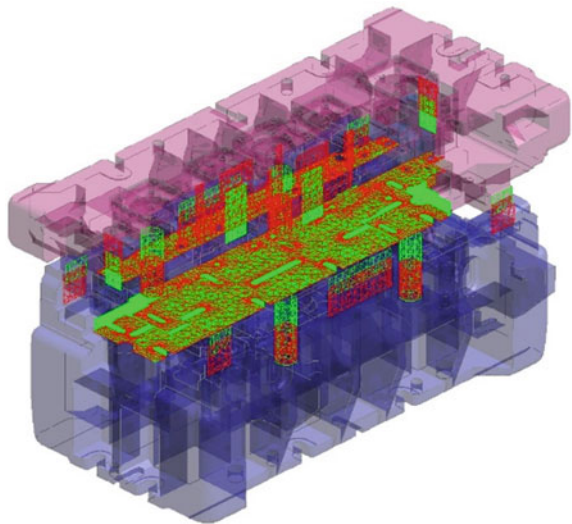
Feature for Assembling Structure Models

To conduct a simulation considering tool deformation in a short time, the structure models must be assembled quickly in addition to reducing the calculation time. The developed system thus provides a feature to assemble the structures based on a rigid tool model. Usually, the setup of the contact surfaces between the die tools is the most time-consuming in assembling the structures. Specifying the contact areas of the structures is effective to stabilize and speed up the contact calculation, but it takes a lot of time to extract the contact surfaces from the FE meshes. Additionally, converting boundary conditions such as load and constraint from rigid tool model to deformable tool model is cumbersome and mistakable. The system provides commands to perform these tasks easily and reliably. Figure 2 shows an example of contact surfaces of the structures extracted using this system. These commands can reduce the time for pre-processing markedly.

Feature for Generating Simplified Shape of the Tool Structure

Next, we introduce a feature to create a simplified shape of the tool structure. With this feature, a volume can be created by simple geometric processing such as extrusion based on the die face. Figure 3b shows an example of the simplified shape created. Although creating details such as cast hole and ribs is unsupported currently, the system provides commands to create a volume after changing the outer shape of the

Fig. 2 Contact surfaces between die tools



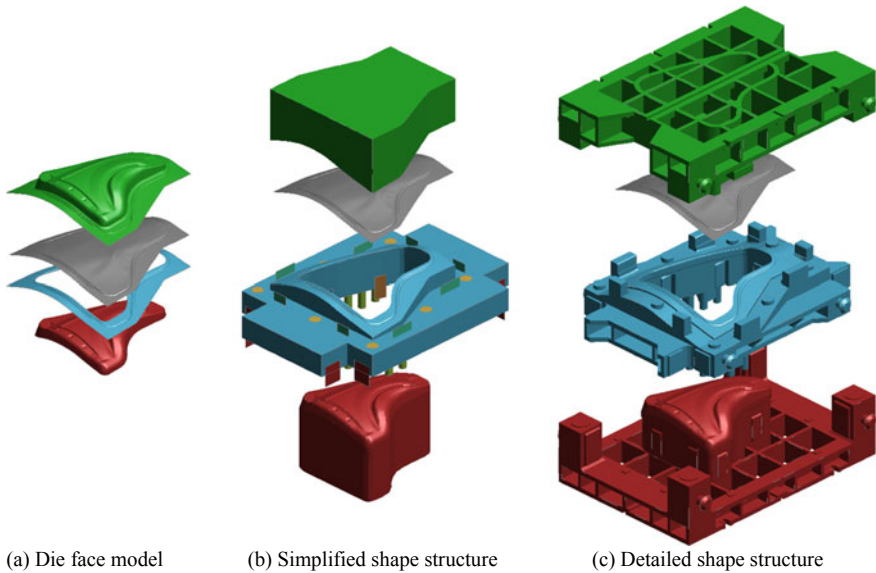


Fig. 3 Example of die tool structure model

die face and to specify the positions of the cushion pins, the guide slides, and the distance blocks. This allows the boundary conditions to be set according to the actual conditions. We think that even such a model can sufficiently capture the tendency of the overall behavior of the structure despite a rough approach. This system thus enables simulation considering the tool deformation even before designing the die structure.

Feasibility Study of the Proposed Method

Now, we report the feasibility of the proposed method with a drawing process of a fender panel shown in Fig. 3. Several simulations are performed and compared here. Table 1 shows the test cases. Case 0 is a standard rigid tool model, Case

Table 1 Test cases of feasibility study

ID	Tool Modeling		
	Meshing	Shape	Remarks
Case 0	–	–	Rigid tool
Case 1	Fine mesh	Detailed shape	Conventional typical method
Case 2	Coarse mesh	Detailed shape	Proposed method
Case 3	Coarse mesh	Simplified shape	Proposed method

1 is a deformable tool model using the conventional typical method, Case 2 is a deformable tool model using the proposed method with the detailed shape, and Case 3 is a deformable tool model using the proposed method with the simplified shape. Figure 4 shows the mesh pattern of Case 3 as a sample of the coupling technique.

First, some information related to the solid models and the pre-process is shown.

Figure 5a shows the operation time for the solid meshing. The meshes were generated in the following procedures using a general-purpose mesh generator: the surface mesh of the structure was first generated, and then tetra elements were generated inside. The fine mesh—detailed shape model used in Case 1 took 5.3 h for the meshing. The coarse mesh—detailed shape model used in Case 2 took only 0.5 h, which was about 1/10 of Case 1. Case 3 is excluded because the mesh generation is included in the pre-process.

Figure 5b shows the number of solid elements. Case 2 and Case 3, in which Coarse meshes are used, have only 1/13 and 1/16 as much elements as Case 1, indicating a drastic decrease in solid processing.

Figure 6 shows the operation time for assembling the deformable tool models based on the rigid tool model (Case 0). In Case 1, a general-purpose pre-processor was

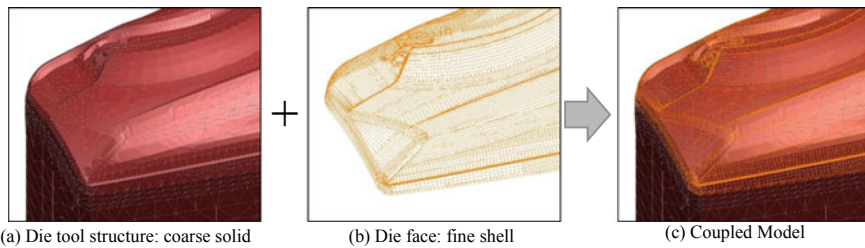


Fig. 4 Coupling of coarse solid and fine shell

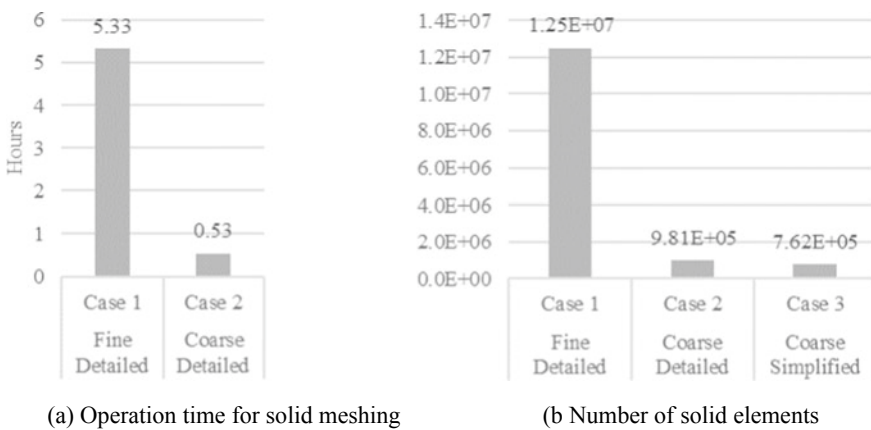


Fig. 5 Property of solid structure model

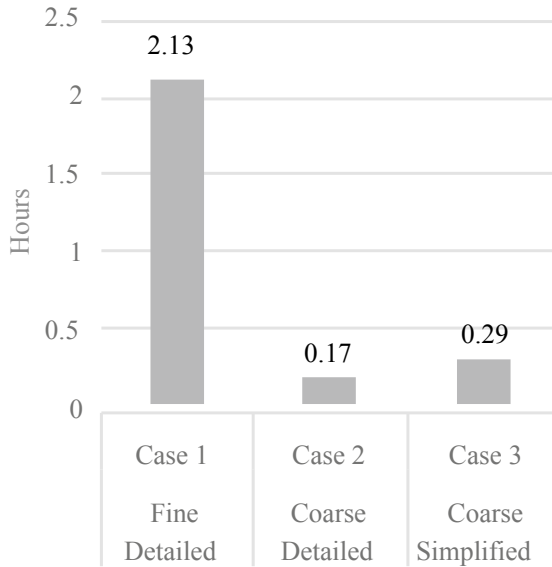


Fig. 6 Operation time for assembling tool models

used, and operations such as extracting contact surfaces between tools and converting boundary conditions are included. This represents the standard way to assemble a conventional typical model. Case 2 took much less time than Case 1, because the most of operations were automated by using the developed system. The system was also applied to Case 3. Although the operation to create the simplified shapes is included, the time is greatly saved.

Subsequently, simulation results are introduced.

Figure 7 shows the calculation time of each case. Case 1 took 6.8 times longer than Case 0, exhibiting it was very time-consuming. Case 2 took 1.6 times longer and Case 3 took 1.4 times longer than case 0, indicating its time efficiency.

Figure 8 shows the draw-in at the edges of work-piece. Maximum difference of about 10 mm is observed between the cases in which the deformation is considered and the case in which the deformation is not considered. Moreover, the lines of Cases 1, 2, and 3, in which the deformation is considered, are almost overlapped, indicating that the results are almost the same.

In summary, this investigation demonstrates the following: The proposed coupling technique can be applied to the practical model and calculated in a reasonable time. The developed system allows quick setup of the deformable tool model. Consideration of the tool deformation affects the draw-in of the work-piece. The mesh resolution and the shape roughness of the structure have little effect on the draw-in.

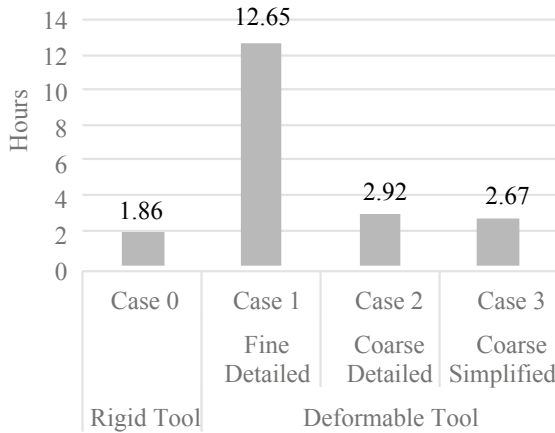


Fig. 7 Calculation time (MPP 32 cores)

Application to an Actual Automotive Part

Next, an example of applying this system to an actual automotive part is shown. Here, the effects of tool deformation and shape roughness on springback predictions have been investigated by comparing simulation results with a tryout result. A bending process of the front floor center panel shown in Fig. 9 was employed. The material of work-piece is 590 MPa high-tensile strength steel with 1.1 mm thickness. Figure 10 shows the configuration of the die tools. The upper tools are composed of a pad, a bending die, and a die holder. The lower tools are composed of a punch and a punch holder.

Table 2 shows test cases. Case 0 is a rigid tool model. Case 1 is a deformable tool model with coarse mesh and detailed shape. Case 2 is a deformable tool model with coarse mesh and simplified shape.

Figure 11 shows the springback evaluation of the simulation results. Shape deviation between the tryout panel and the simulation results after springback was

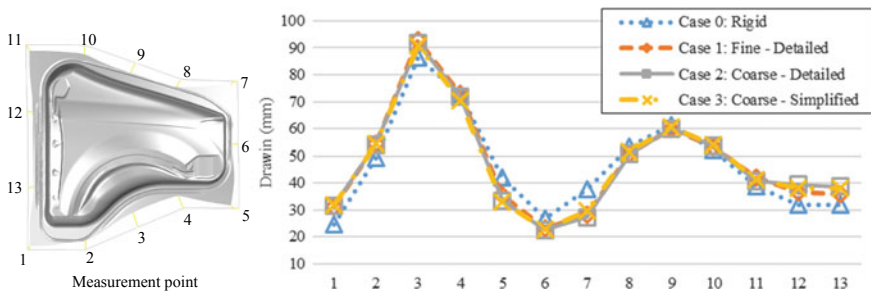


Fig. 8 Draw-in at the edges of work-piece



Fig. 9 Front floor center panel

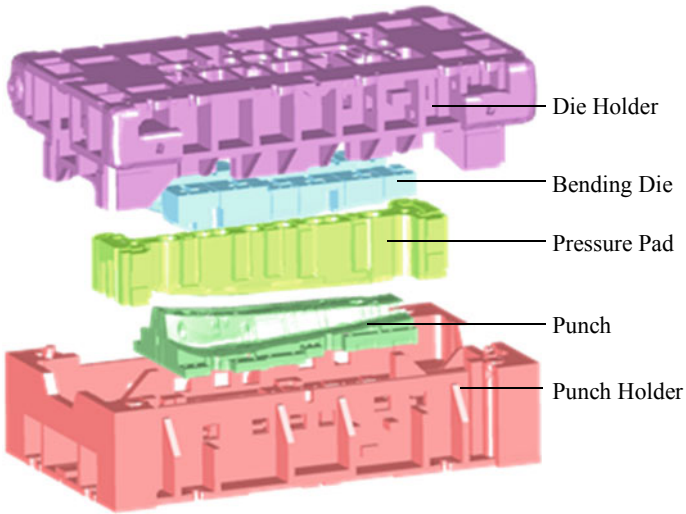


Fig. 10 Die tool configuration

Table 2 Test cases of springback evaluation

ID	Tool modeling		
	Meshing	Shape	Remarks
Case 0	–	–	Rigid tool
Case 1	Coarse mesh	Detailed shape	Proposed method
Case 2	Coarse mesh	Simplified shape	Proposed method

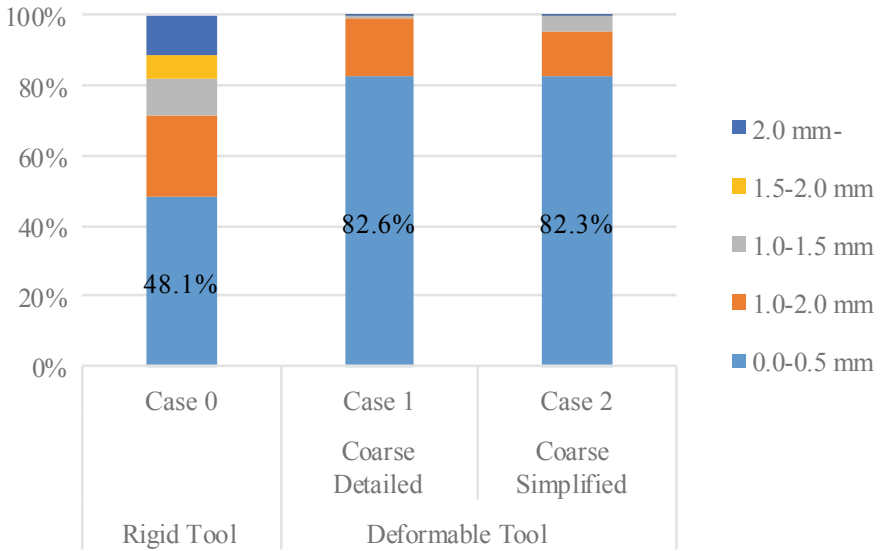


Fig. 11 Shape deviation between the tryout panel and the simulation results after springback

measured and classified into several ranges. The percentage of the area occupied by each range is illustrated. It can be seen that the accuracy of springback prediction is largely improved by considering the tool deformation, and the simplified shape model has almost the same accuracy as the detailed shape model.

Conclusion

In this study, we have proposed the method to perform stamping simulations in consideration of the tool deformation while suppressing the increase of the lead time and have succeeded in practical use. Moreover, we have developed the system for assembling the structure models quickly and for generating simplified structure shapes. This system has been implemented in JSTAMP and applied to automotive parts to verify the proposed method. Our results show the following: The proposed method can be applied to the practical model and calculated in a reasonable time. The developed system allows quick setup of the deformable tool model. The consideration of the tool deformation affects the draw-in of the work-piece and improves the springback prediction although the mesh resolution and the shape roughness of the structure have little effect.

Notably, the deformation behavior of the actual die tools during stamping has not been sufficiently analyzed yet because of the difficulty of measurement. That is why the simulation can contribute a lot to examining the tool behavior, and we believe that the developed system can help it. We will keep making efforts to clarify the mechanism by which the deformation of the tool affects the panel quality and to realize rational structure design.

References

1. Tsutamori H, Iwata N, Suzuki N (2003) Prediction of the geometrical defects of sheet metal in 3 dimensional shape: numerical prediction of springback behavior of a stamped metal sheet III. *J Jap Soc Technol Plast* 44(513):1024–1028
2. Takamura M, Ohura K, Sunaga H, Kuwabara T, Makinouchi A, Teodosiu C (2006) Sheet forming simulation using static explicit FEM program coupled with elastic deformation of tools. *J Jap Soc Technol Plast* 47(540):64–68
3. Großmann K, Wiemer H, Hardtmann A, Penter L (2007) Faster to sound parts by advanced forming process simulation—advanced forming process model including the elastic effects of the forming press and tool. *Steel Res Int* 78(10–11):825–830
4. Clarke M, He J (2008) Sheet metal forming simulation and real world tooling. Proceedings of the 10th International LS-DYNA conference, pp 2–27—2–34
5. Ishiwatari A, Hiramoto J, Urabe T, Kuwabara T (2015) Influence of elastically modeled parts of press machine on Torsion prediction —improvement of CAE springback prediction by considering elastic deformation of tools I. *J Jap Soc Technol Plast* 56(651):311–316
6. Tsutsumi M, Ikeda T, Koike K (2017) Die deflection analysis—evaluation of dies and processes by sheet metal forming simulation. *J Jap Soc Technol Plast* 58(681):908–912
7. Pilthammar J, Sigvant M, Kao-Walter S (2016) Including die and press deformations in sheet metal forming simulations. *Proc Numisheet* 2016:032036
8. Vrolijk M, Ogawa T, Camanho A, Biasutti M, Lorenz D (2018) A study with ESI PAM-STAMP® on the influence of tool deformation on final part quality during a forming process. *Proc ESAFORM* 2018:160029
9. Haufe A, Roll K, Bogon P (2008) Sheet metal forming simulation with elastic tools in LS-DYNA. *Proc Numisheet* 2008:743–748

Author Index

A

Abd El-Aty, Ali, 733
Abeyrathna, Buddhika, 61
Abu-Samk, Khaled, 909
Adewale, Kemi Y., 25
Ahmad, Shahin, 173
Aibinu, Mathew O., 25, 39
Alankar, Alankar, 173
Alharbi, Mohammed, 365
Amirthalingam, Murugaiyan, 105
Anand, Sharath, 757
Arai, Masahi, 963
Ayoub, Georges, 15

B

Bae, Gihyun, 355, 841
Bailly, David, 785
Balan, Tudor, 241
Bansal, Ankush, 141
Banu, Mihaela, 141
Bardelcik, A., 499
Barth, K., 275
Baru, Naveen Krishna, 785
Bashford-Rogers, Thomas, 411
Baudouin, Cyrille, 241
Baumgartner, Iris, 539
Becker, Marco, 693
Bekele, Tsegaye, 197, 219
Beri, Habtamu, 197, 219
Berisha, B., 275
Besson, Jacques, 607
Betaieb, Ehssen, 873
Bielak, Ch.R., 165, 575
Birkert, Arndt, 401

Bobbert, M., 165, 575
Böhnke, M., 165, 575
Bolay, C., 679
Bortucen, S., 301
Boskovic, Vladimir, 539
Bosler, Paul, 671
Brünig, Michael, 423

C

Cao, Jian, 141, 345
Chalal, Hocine, 241
Chen, Da-Yong, 483
Cheng, Randy, 141
Chezan, A. R., 617
Chung, Y. D., 803
Connolly, Daniel S., 523
Cui, Zhenshan, 155, 471
Cvrcek, Vojtech, 949

D

Dasu, Raj, 309
Date, Prashant, 185
Dayong, L. I., 81
Debattista, Kurt, 411
den Boogaard van, Ton, 703
Deng, Zhi, 309
Denz, Sebastian, 949
Deshpande, Akshay, 715
Dhara, Sisir, 287
Domitner, Josef, 539
Dong, Hongrui, 747
Dou, Luyi, 747
Duchêne, Laurent, 873

E

Ehmann, Kornel, 141
 Engel, Bernd, 125
 Essig, P., 679
 E. Wilkosz, Daniel, 61

F

Fang, Xiangfan, 445, 757, 773
 Feister, Tom, 671
 Figiel, Łukasz, 287
 Friedlein, Johannes, 329
 Frohn-Sörensen, Peter, 125

G

Gahlyan, Sumit, 715
 Gerke, Steffen, 423
 Green, Daniel E., 433, 849
 Groche, Peter, 655, 693
 Grünbart, Florian, 539
 Gude, Maik, 833
 Gu, Jiahui, 627
 Guo, Xunzhong, 733

H

Hajdarevic, Amir, 757
 Ha, Jinjin, 389, 727
 Hartmann, Benjamin, 401
 Hartmann, Christoph, 263, 813, 885
 Hazra, Sumit, 287, 411
 Hazrati, Javad, 703
 Hirt, Gerhard, 785
 Hodgson, Peter, 61
 Hol, J., 679
 Hong, Seokmoo, 635
 Hora, P., 275
 Hornung, Luca, 949
 Hou, Yong, 733
 Huang, Lu, 345
 Hughes, Darren, 287
 Hyun, J. S., 803

I

Ichijo, Naoki, 963
 Iizuka, Takashi, 861
 Ilinich, Andrey, 15
 Inal, Kaan, 49, 523

J

Jäger, A., 511
 Janaki Ramulu, Perumalla, 197, 219
 Jang, Inje, 841
 Jayakumar, Saarvesh, 757
 Jeong, Sehwan, 841
 Joshi, Yogendra, 557
 Jun, S. H., 457

K

Khandelwal, Manali, 715
 Khazaie, Pedram, 71
 Kičin, Mustafa, 539
 Kim, Daeyong, 827
 Kim, H. S., 457
 Kim, Hyunok, 627, 671
 Kim, J. J., 115
 Kim, J. S., 457
 Kim, K. J., 803
 Kim, Minki, 389, 627
 Kim, Se-Jong, 827
 Kim, Y. S., 115
 Kindsmueller, Alexander, 595
 Kohar, Christopher P., 49, 523
 Köhler, Daniel, 833
 Kolb, Sven, 921
 Konrad Werner, Matthias, 813
 Korkolis, Yannis P., 389, 727
 Kotkunde, Nitin, 251, 549
 Kridli, Ghassan, 15
 Krishnamraju, M., 321
 Krishnaswamy, Hariharan, 105
 Kubik, Christian, 655
 Kumar Gupta, Amit, 549
 Kumar Singh, Swadesh, 251, 549
 Kupfer, Robert, 833

L

Larsson, Mats, 645
 Laumann, Stefan, 921
 Lee, Heejong, 841
 Lee, Jinwoo, 827
 Lee, Jongsup, 355, 841
 Leem, Dohyun, 141, 345
 Lee, Myoung-Gyu, 733
 Lian, Junhe, 375
 Li, Dayong, 491
 Li, Dongsheng, 747
 Liewald, M., 679
 Lihui, Lang, 209

Li, Qian, 155
 Liu, Jiaru, 471
 Liu, Wuyang, 861
 Li, Xiaoqiang, 747
 Li, Y. Larry, 49
 Lloyd, D. J., 585
 Löbbe, C., 511
 Luo, Shuai, 471

M

Mahalle, Gauri, 549
 Maier, Daniel, 813
 Maier, L., 263
 Makki, Mustapha, 15
 Manopulo, Niko, 595, 617
 Marie Habraken, Anne, 873
 Martin, Daniel M., 655
 Martschin, J., 511
 Meng, Qingdang, 91
 Mergheim, Julia, 329
 Meschut, G., 165, 575
 Mishra, Raja K., 49, 523
 Moein, Sajjad, 71
 Mohamed, Mohamed, 557
 Moon, M. S., 457
 Morchhale, Ayush, 251
 Moser, Newell, 141
 Moyo, Sibusiso, 39
 Münstermann, Sebastian, 375
 Mu, Zhenkai, 91

N

Narasimhan, K., 173, 321
 Nayak, Kanhu, 185
 Norz, Roman, 595, 617, 885, 899
 Nowack, Moritz, 401

P

Pandre, Sandeep, 251
 Park, Hyeonil, 827
 Park, Namsu, 355, 841
 Peng, Yinghong, 491
 Pereira, Michael P., 61
 Praveen Kumar Reddy, P., 197
 Putschkat, D., 511

Q

Quach, H., 115

R

Raymond, Vincent, 937
 Reimer, A., 885
 Rickhey, Felix, 635
 Rolfe, Bernard F., 61
 Rongfeng, L. I. U., 81

S

Sachdev, Anil K., 309
 Sahinoglu, U., 301
 Sahu, Sandeep, 321
 Samei, Javad, 433
 Sardar, Arshdeepsingh, 499
 Sarraf, Iman Sari, 433, 849
 Savoie, Jean, 937
 Scandola, Lorenzo, 813
 Schiller, Michael, 125
 Schneider, Timo, 655
 Schumann, Philipp, 655
 Schwarz, Christian, 401
 Scott, Colin, 909
 Shafiei, Mehdi, 671
 Shahzamanian, M. M., 585
 Shalchi Amirkhiz, Babak, 909
 Shen, Fuhui, 375
 Sheng, Jie, 231, 365
 Shin, Jaekwang, 141
 Shisode, Meghshyam, 703
 Shollock, Barbara, 287
 Sigvant, M., 617
 Sijja, Sheng, 209
 Simha, C. H. M., 499
 Singh, Amarjeet Kumar, 321
 Singh, Aru Ranjan, 411
 Siraji, Amirela, 197, 219
 Solomon, Joshua, 345
 Sommitsch, Christof, 539
 Song, Junghan, 355, 841
 Song, Yang, 433, 849
 Srivastava, Vivek, 715
 Steglich, Dirk, 607
 Steinlehner, Florian, 921
 Steinmann, Paul, 329
 Stolz, Lorenz, 757
 Stoughton, Thomas B., 355
 Sturm, P., 885
 Sulaiman, H., 511
 Suresh, Kurra, 251
 Szegda, Damian, 557

T

Takalkar, Prathamesh, [549](#)
Tamer, M. E., [301](#)
Tao, Jie, [733](#)
Tathavadkar, Vilas, [173](#)
Taub, Alan, [141](#)
Taylor, Scott, [287](#)
Teeuwen, Tobias, [785](#)
Tekkaya, A. E., [511](#)
Thakur, Surendra C., [39](#)
Tiwari, Jai, [105](#)
Tong, Wei, [3](#), [231](#), [365](#)
Troschitz, Juliane, [833](#)

U

Ünver, B., [263](#)

V

Vanjani, Amin L., [499](#)
Venkateswar Reddy, P., [219](#)
Vincze, Gabriela, [241](#)
Volk, Wolfram, [263](#), [595](#), [617](#), [813](#), [885](#),
[899](#), [921](#)

W

Wang, Haibo, [747](#)
Wang, Haoran, [91](#)
Wang, Huamiao, [491](#)
Wang, Hui-ping, [345](#)
Weber, Johannes, [401](#)
Weinschenk, Annika, [921](#)
Weiss, Matthias, [61](#)
Wiklund, Daniel, [645](#)

Williams, Bruce, [909](#)
Wu, P. D., [585](#)
Wu, Peidong, [491](#)

X

Xiao, X., [115](#)
Xu, Dongkai, [155](#)
Xue, Jia, [909](#)
Xu, Yong, [733](#)

Y

Yadav, Vipin, [185](#)
Yang, Hao, [491](#)
Yang, Seung-Yong, [3](#), [231](#), [365](#)
Yang, Yanfeng, [241](#), [747](#)
Yan, Ma, [733](#)
Yim, G. H., [803](#)
Yoon, Jeong Whan, [355](#)
Yoon, S. C., [803](#)
Yun, K. H., [457](#)
Yu, You, [861](#)

Z

Zeng, Chongyang, [445](#)
Zhang, Haiming, [155](#), [471](#)
Zhang, Peng, [61](#)
Zhang, Shi-Hong, [483](#), [733](#)
Zhao, Jun, [91](#)
Zheng, Xuebin, [747](#)
Ziane, Mustapha, [557](#)
Zimmermann, Philipp, [401](#)
Zistl, Moritz, [423](#)
Zoller, Laura, [671](#)

Subject Index

A

AA3003, 716
AA5052, 173–182
AA5083, 173–182
Adhesion, 197
Advanced high strength steels (AHSSs),
471, 472, 477, 480, 539, 540, 547,
627, 628
AISI 304, 321
Al-Cu-Mg alloy, 484
Al-Li Alloys, 733, 734
Al-Mg alloys, 173, 174, 182
Aluminium alloy, 557, 558, 562
Aluminum, 748
Aluminum alloy, 275, 276, 280
Aluminum hot forming, 798
Aluminum liner, 885, 890, 893, 896
Aluminum sheet, 727
Angle bracket, 345–348, 352
Anisotropic plasticity, 231, 232, 366, 367
Anisotropic damage, 16, 21
Anisotropic hardening, 355, 357
Anisotropic plasticity, 16
Anisotropy, 155–157, 160–163, 375–377,
379, 381, 383–385, 607–610, 614,
635, 636, 639
Annealing, 715–719, 721–725
Assembly simulation, 402, 404
Asymmetry, 607, 608, 614
AutoForm, 457–460, 469

B

Barlat'89 yield criteria, 549
Bauschinger effect, 329, 330, 333, 337, 343
Benchmark test, 786–788, 791, 794–797,
799

Bendability, 585, 586, 589, 590
Biaxial experiments, 423, 424, 427
Bipolar plate, 61, 62
Blank holding force, 219, 221, 223–228
Blanking, 655–658, 666, 668
Body manufacturing process, 402
Body shop, 401
Bolt Hole, 841, 842, 844–847
Boundary condition, 209, 214
Brass, 873, 874, 875, 877
Brittle damage, 437

C

Cellular automata, 433–435, 442
Clamping Force, 655, 661, 665, 668
Clinching, 329, 330, 335, 337, 338, 343,
833–835, 837–839
Cohesive element, 209, 212, 213, 216
Cohesive zone model, 827, 829
Cohesive zone modeling, 757, 758, 764
Collar-Forming, 595, 596, 603–605
Combined tension-shear, 389–391, 393,
396
Computed Tomography (CT), 834
Constitutive model, 105–107, 111, 113,
803–806, 811
Continuum Damage Mechanics, 16
Coupled analysis, 457, 458
Coupled Process Analysis (CPA), 402, 403,
405–409
Cross section adapted, 129
Cruciform specimen, 389, 390
Crystal plasticity, 155–159, 161–163, 471,
472, 475–477, 479, 480, 491, 493,
497
Cup draw testing, 671

D

Damage, 375–380, 382–385, 423–425, 427, 430, 575–578, 581, 583
 Damage model, 656, 658, 659, 668
 Data reduction, 264, 272
 Deep learning, 411–413, 418
 Deep drawing, 219–222, 224, 226, 228, 263, 264, 268, 539–541, 545, 547
 Design Guideline, 842, 846, 847
 Die compensation, 458, 465, 467, 468
 Die deformation, 457, 459, 468, 469
 Die design, 74
 Dieless, 937
 Differential strain hardening, 365, 370, 371, 373
 Digital Image Correlation (DIC), 276–278, 627, 629, 635, 636, 638, 727, 729
 Digitalization, 683, 684, 689
 Dimensional accuracy, 823
 Dislocation density, 105–108, 111–113
 Dome height, 197, 202, 205, 207, 208
 Double cantilever beam test, 829
 Double-Sided, 937
 Draw bending, 751–753
 Dual-Phase (DP) steel, 251–253, 260, 433–435, 439, 911, 918
 Ductile damage, 435, 439
 Ductile metals, 424
 Ductile adhesive layer, 827, 828, 832
 Ductile fracture, 61, 321, 325, 326
 Dynamic behaviour, 733, 735

E

Edge Crack, 595–599, 601–605
 Elastic tools, 645, 646, 648, 652, 653
 Elastic die, 964
 Electric-assisted forming, 105, 106
 Electroplasticity, 747, 751, 752
 Energy efficiency, 693–695
 Exact solutions, 40–44, 46, 47

F

Ferrite, 25, 26
 FE simulation, 185
 FE simulations, 877
 Fiber metal laminates, 209, 210, 213–216
 Finite element, 433, 434, 437, 442
 Finite Element Analysis (FEA), 62, 64, 67–69, 919
 Finite Element (FE)-simulation, 885, 890

Finite Element Method (FEM), 71–75, 585, 588, 595, 596, 602, 605, 785, 803, 806, 809–811
 Finite Element Method (FEM) simulation, 401–403
 Finite Element Modelling, 289
 Finite Elements, 608
 Finite element simulation, 345, 346
 Flashless forging, 71–77
 Flexibility, 125, 127, 128, 131, 137, 138
 Flow rule, 376, 378, 379, 382
 Fluid structure interaction, 483, 484
 Formability, 49, 50, 54, 55, 57, 58, 173, 174, 177, 181, 182, 197–199, 204–206, 208, 321, 322, 715–717, 723, 725
 Formability Analysis, 841, 842, 844, 845
 Forming, 125–127, 129–131, 135, 137, 138, 301–303, 305, 306, 308
 Forming Limit Curve (FLC), 173, 175, 177, 178, 182
 Forming Limit Diagram (FLD), 549–551, 553–555
 Forming simulation, 679, 681, 683, 684, 686, 689, 690
 Fracture, 375–378, 380, 382, 383, 385, 423–425, 427, 429, 430, 585, 586, 588–590, 592, 593
 Free-form bending, 813–815, 824
 Friction, 557, 558, 560–564, 569–572, 655, 661, 663–668, 703–710

G

Gas-based forming, 786, 788, 789
 Generalized traveling-wave, 41–44, 46
 Geometrical accuracy, 251, 253
 GISSMO, 512, 513, 519, 520
 Grain size, 321, 322, 325, 327, 328

H

Heat and wave equations, 45, 46
 Heat treatment/quenching, 557, 558
 Hierarchy modeling approach, 471, 472, 476, 480
 High-strength steel, 803, 804, 808–811
 High-speed deformation, 734
 High-speed tensile test, 446
 High strain rate formability, 483
 High strength aluminum alloys, 671, 672
 High tensile strength steel, 964
 Hole expansion, 471, 472, 474–480, 727

Hole expansion coefficient, 909, 911, 912, 918
 Homogenization, 49, 50, 52, 715–719, 721, 723–725
 Hot deep drawing, 185
 Hot stamping, 511, 513
 Hybrid forming-heating process, 539, 540, 542, 547, 548
 Hydroforming, 890, 892–896
 Hydrogen power technology, 885

I

Identifiability, 873–877, 880–882
 Image classification, 417
 Impact hydroforming, 483–490
 IN718 alloy, 550, 551, 553, 554
 Incremental, 937, 940
 Incremental forming, 251, 253
 In-situ Computed Tomography (CT), 833–835, 837, 839
 In-situ SEM and EBSD, 287
 Inverse fitting, 276
 Isotropic strain hardening, 365, 373

J

Joule's heating, 105–107, 110, 111, 113

K

Kinematic hardening, 329–333, 335–339, 341–343

L

Laminated metal sheet, 827–829, 831, 832
 Laser Welded Blank (LWB), 627, 628, 631, 633
 Limit dome height, 197, 199–206, 208
 Load adapted, 125, 127, 129, 130, 138
 Local heat treatment, 539, 540, 547
 Lubricant, 671, 672, 674, 676–678

M

Machine learning, 402, 403
 Magnetic, 25–27, 31–33, 35
 Material modelling, 329–331
 Mechanical properties, 803
 Mechanical characterization, 301–303, 308
 Mechanical joining, 165, 575, 577
 Metal forming, 813
 Micro-stamping, 61, 62, 64, 65, 67–69

Microstructure, 909–911, 913, 916–919
 Midas MeshFree, 457–460, 464
 Modified Johnson—Cook model, 483
 MPM Sandwich, 198–200

N

Nakajima, 173–177, 179–182
 Nakazima experiments, 275–278, 280, 284
 Nakazima test, 549, 550
 Nanomaterials, 25
 Nanoparticles, 25–27, 29, 32
 Neutron diffraction, 491–493, 497, 498
 Newton iteration, 4, 9
 Non-proportional loading, 423, 424, 426, 428–430
 Non-associated flow rule, 355
 Non-destructive testing, 834
 Non-proportional loading, 617, 899, 900
 Numerical simulation, 166, 167, 575, 576, 581, 582
 NURBS reconstruction, 815, 816

O

Optimization, 707
 Oscillation-free force measurement, 445, 446, 448

P

PAM-STAMP™, 174, 179, 180, 182, 221, 228
 Parameter identification, 333, 335
 Plane stress, 232–234
 Plane Strain, 275–282, 284
 Plane-strain tension, 231, 233–236, 238
 Plastic anisotropy, 727, 728
 Plasticity, 608, 610
 Plasticity potentials, 12
 Plastic strain ratio, 185, 187
 Precipitation hardening, 51, 58
 Pre-formed tensile tests, 899
 Pre-Forming, 595–602, 604, 605
 Press brake, 345–349, 353
 Progressive crushing, 757, 758, 761, 767, 770
 Progressive die stamping, 921, 922, 924, 934
 Proportional loading, 15, 16, 22, 23
 Punch test, 575, 577–581
 Pure electroplasticity, 747, 748, 751, 753

Q

Q&P Steel, 491

R

Reaction-diffusion, 40, 41, 47
 Reverse engineering, 263, 264
 Reverse fitting, 91, 92, 98, 101, 102
 Rigidity evaluation, 346, 351, 352, 354
 Robotic, 942, 943, 946
 Roll forming, 693–701
 Rousselier model, 433–435, 438
 R-value, 91, 92, 94–102, 160

S

Scalability, 125, 137
 Shape optimization, 390, 391, 393, 396
 Shear cutting, 512–514, 518, 595, 596, 598, 600, 601, 603, 604, 606
 Sheet metal, 91, 92, 101, 102, 301–303, 308, 635, 640, 937
 Sheet metal forming, 355, 356, 363, 367, 703, 963, 964
 Sheet metal forming simulation, 645, 652
 Sheet metal stamping, 411–413, 418
 Simulation, 671, 673, 785–788, 793–797, 799
 Simulation/modelling, 557, 558, 563, 564, 566, 568–571
 Single Point Incremental Forming (SPIF), 873–875, 877, 879, 880, 882
 Slip, 693–696, 700, 701
 Smart data, 401
 Specimen design, 389, 390, 393
 Specimen geometry, 445–447
 Spotting image, 679–681, 683–686, 688–690
 Springback, 539–541, 547, 548, 747–749, 751–754, 963, 971, 973
 Springback compensation, 263, 264, 267
 Stiffening dart, 345–349, 351–353
 Strain distribution, 275–281, 283
 Strain Non-uniformity Index (SNI), 185, 193, 194
 Strain path, 251, 256, 257
 Strain path change, 287–294, 299, 300
 Strain rate, 165, 167–171, 445–449, 452–454
 Strength differential effect, 607, 614

Stress state, 375–379, 382–385, 389, 390, 445–447, 453, 454
 Stress triaxiality, 635, 636
 Stretch-flanging, 251–255
 Stretch web connector, 921–925, 927, 929, 930, 933, 934
 Subroutines, 209, 211, 212, 216
 Surface roughness, 251, 253, 259
 Swift power hardening law, 549

T

Temperature, 165–171, 899–906
 Tensile test, 92, 93, 95, 100
 Tensile tests, 608
 Texture, 703–708
 TFD, 640
 Thermomechanical modelling, 535
 Thin flash, 71–74, 77
 3D-swivel-bending, 125, 127–138
 Time dependent, 275, 277, 278, 284
 Tool deformation, 963–968, 970, 971, 973
 Toolpath, 937, 938, 940–942, 944, 946
 Torque, 693–700
 Trial stress, 3–6, 8–12
 Trimming, 511, 512, 518
 TRIP steel, 524, 535
 Tube hydroforming, 321, 322
 Tungsten Inert Gas (TIG) welding, 321, 322, 325, 326

U

Ultra-thin sheet, 61

V

Vegter yield locus, 275–278, 280, 284
 Viscoplastic Self Consistent (VPSC), 715, 716

W

Warm forming, 671, 674
 Width to thickness ratio, 585

Y

Yield point elongation, 803–811
 Yield locus, 275–281, 284
 Yield surface evolution, 356, 357, 359